

**OPEN ACCESS**

## Volume IV. The DUNE far detector single-phase technology

To cite this article: B. Abi *et al* 2020 *JINST* **15** T08010

View the [article online](#) for updates and enhancements.



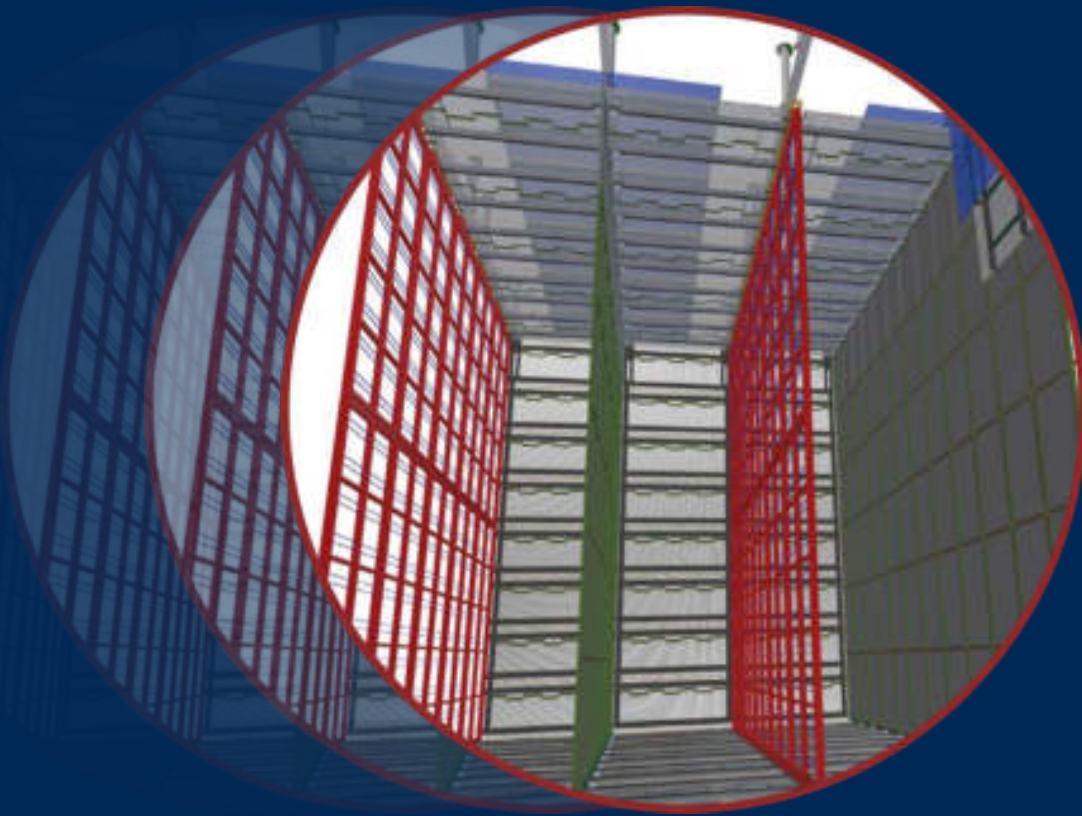
**IOP ebooks™**

Bringing together innovative digital publishing with leading authors from the global scientific community.

Start exploring the collection—download the first chapter of every title for free.

# Deep Underground Neutrino Experiment (DUNE) Far detector technical design report

## Volume IV The DUNE far detector single-phase technology



The DUNE collaboration

**DUNE**  
DEEP UNDERGROUND  
NEUTRINO EXPERIMENT

# Contents

|   |             |
|---|-------------|
| <b>Contents</b>   | <b>i</b>    |
| <b>List of Figures</b>                                    | <b>ix</b>   |
| <b>List of Tables</b>                                     | <b>xvii</b> |
| <b>A roadmap of the DUNE technical design report</b>      | <b>1</b>    |
| <b>1 Executive summary</b>                                | <b>2</b>    |
| 1.1 Introduction  | 2           |
| 1.2 The single-phase liquid argon time-projection chamber | 3           |
| 1.3 The DUNE single-phase far detector module             | 4           |
| 1.4 The liquid argon                                      | 7           |
| 1.5 Photon detection system                               | 8           |
| 1.6 High voltage, cathode planes and field cage           | 9           |
| 1.7 Anode planes  | 11          |
| 1.8 Electronics   | 12          |
| 1.9 Data acquisition                                      | 13          |
| 1.10 Calibration  | 15          |
| 1.11 Installation   | 16          |
| 1.12 Schedule and milestones                              | 17          |
| 1.13 Conclusion   | 18          |
| <b>2 Anode plane assemblies</b>                           | <b>19</b>   |
| 2.1 Anode plane assembly (APA) overview                   | 19          |
| 2.2 Design  | 22          |
| 2.2.1 APA design parameters                               | 23          |
| 2.2.2 Support frames                                      | 28          |
| 2.2.3 Grounding mesh                                      | 29          |
| 2.2.4 Wires   | 31          |
| 2.2.5 Wire boards and anchoring elements                  | 33          |
| 2.2.6 The APA pair  | 37          |
| 2.2.7 APA structural analysis                             | 39          |
| 2.3 Quality assurance                                     | 41          |

2020 JINST 15 T08010

|          |   |           |
|----------|---|-----------|
| 2.3.1    | Results from ProtoDUNE-SP construction                  | 41        |
| 2.3.2    | Results from ProtoDUNE-SP operation                     | 45        |
| 2.3.3    | Final design prototyping and test assemblages           | 50        |
| 2.4      | Interfaces  | 51        |
| 2.4.1    | TPC cold electronics                                    | 52        |
| 2.4.2    | Photon detection system                                 | 53        |
| 2.4.3    | Cable routing   | 53        |
| 2.5      | Production plan   | 53        |
| 2.5.1    | Assembly procedures and tooling                         | 57        |
| 2.5.2    | APA production sites                                    | 59        |
| 2.5.3    | Material supply   | 61        |
| 2.5.4    | Quality control in APA production                       | 62        |
| 2.6      | Handling and transport to SURF                          | 66        |
| 2.6.1    | APA handling  | 66        |
| 2.6.2    | APA transport frame and shipping strategy               | 67        |
| 2.6.3    | APA quality control during integration and installation | 70        |
| 2.7      | Safety considerations                                   | 70        |
| 2.8      | Organization and management                             | 71        |
| 2.9      | Schedule and risks                                      | 74        |
| 2.9.1    | Schedule  | 74        |
| 2.9.2    | Risks   | 75        |
| <b>3</b> | <b>High voltage</b>                                     | <b>81</b> |
| 3.1      | High voltage system overview                            | 81        |
| 3.1.1    | Introduction and scope                                  | 81        |
| 3.1.2    | Design specifications                                   | 82        |
| 3.1.3    | Design overview   | 86        |
| 3.1.4    | HV system safety  | 89        |
| 3.2      | HV Power Supply and Feedthrough                         | 91        |
| 3.3      | CPA arrays  | 93        |
| 3.4      | Field cage  | 95        |
| 3.4.1    | Field cage profiles                                     | 96        |
| 3.4.2    | Ground planes   | 97        |
| 3.4.3    | Maximum field distortions                               | 99        |
| 3.4.4    | Top and bottom field cage modules                       | 99        |
| 3.4.5    | Endwall field cages (EWFC)                              | 100       |
| 3.4.6    | Voltage divider boards                                  | 102       |
| 3.5      | Electrical interconnections                             | 103       |
| 3.6      | ProtoDUNE-SP high voltage experience                    | 105       |
| 3.6.1    | Summary of HV construction                              | 105       |
| 3.6.2    | HV commissioning and beam time operation                | 107       |
| 3.6.3    | Post-beam stability runs with cosmic rays               | 108       |
| 3.6.4    | Lessons from ProtoDUNE                                  | 110       |

|          |   |            |
|----------|---|------------|
| 3.6.5    | Future R&D                                    | 112        |
| 3.7      | Interfaces                                    | 113        |
| 3.8      | Production and assembly                       | 114        |
| 3.8.1    | Power supplies and feedthrough                | 114        |
| 3.8.2    | Cathode plane assembly                        | 115        |
| 3.8.3    | Field cages                                   | 116        |
| 3.8.4    | Electrical interconnections                   | 118        |
| 3.8.5    | Production safety                             | 119        |
| 3.9      | Quality control, transport, and installation  | 120        |
| 3.9.1    | Quality control                               | 120        |
| 3.9.2    | Transport and handling                        | 121        |
| 3.9.3    | Safety during handling                        | 122        |
| 3.10     | Organization and management                   | 122        |
| 3.10.1   | Institutional responsibilities                | 122        |
| 3.10.2   | Risks   | 124        |
| 3.10.3   | High-level schedule                           | 126        |
| 3.11     | Appendix: alternatives                        | 129        |
| 3.11.1   | Optical reflectors on CPA                     | 129        |
| 3.11.2   | Calibration laser penetrations                | 130        |
| <b>4</b> | <b>TPC electronics</b>                        | <b>131</b> |
| 4.1      | System overview                               | 131        |
| 4.1.1    | Introduction                                  | 132        |
| 4.1.2    | Requirements and specification                | 134        |
| 4.1.3    | Design  | 137        |
| 4.2      | System design                                 | 140        |
| 4.2.1    | Grounding and shielding                       | 140        |
| 4.2.2    | Distribution of bias voltages                 | 142        |
| 4.2.3    | Front-end motherboard                         | 142        |
| 4.2.4    | Infrastructure inside the cryostat            | 164        |
| 4.2.5    | Cold cables and cold electronics feedthroughs | 165        |
| 4.2.6    | Warm interface electronics                    | 169        |
| 4.2.7    | Timing distribution and synchronization       | 172        |
| 4.2.8    | Services on top of the cryostat               | 174        |
| 4.2.9    | ProtoDUNE-SP results                          | 175        |
| 4.2.10   | ProtoDUNE-SP lessons learned                  | 179        |
| 4.2.11   | Remaining design and prototyping tasks        | 184        |
| 4.3      | Quality assurance                             | 186        |
| 4.3.1    | Initial design validation                     | 187        |
| 4.3.2    | Integrated test facilities                    | 188        |
| 4.3.3    | Reliability studies                           | 193        |
| 4.4      | Production and assembly                       | 195        |
| 4.4.1    | Spares plan                                   | 195        |

|          |  |            |
|----------|--|------------|
| 4.4.2    | Procurement of parts                           | 196        |
| 4.4.3    | Assembly                                       | 196        |
| 4.4.4    | Quality control                                | 198        |
| 4.4.5    | Test facilities                                | 202        |
| 4.5      | Integration, installation, and commissioning   | 202        |
| 4.5.1    | Timeline and resources                         | 202        |
| 4.5.2    | Internal calibration and initial commissioning | 204        |
| 4.6      | Interfaces                                     | 204        |
| 4.6.1    | APA  | 205        |
| 4.6.2    | DAQ  | 206        |
| 4.6.3    | HV   | 206        |
| 4.6.4    | Technical coordination                         | 206        |
| 4.6.5    | Other interfaces                               | 207        |
| 4.7      | Safety   | 208        |
| 4.7.1    | Personnel safety during construction           | 208        |
| 4.7.2    | Detector safety during construction            | 209        |
| 4.7.3    | Detector safety during operation               | 210        |
| 4.8      | Risks  | 211        |
| 4.8.1    | Design and construction risks                  | 212        |
| 4.8.2    | Risks during commissioning                     | 214        |
| 4.8.3    | Risks during operation                         | 215        |
| 4.9      | Organization and management                    | 216        |
| 4.9.1    | Consortium organization                        | 217        |
| 4.9.2    | Planning assumptions                           | 218        |
| 4.9.3    | Institutional responsibilities                 | 220        |
| 4.9.4    | High-level cost and schedule                   | 221        |
| <b>5</b> | <b>Photon detection system</b>                 | <b>225</b> |
| 5.1      | Introduction                                   | 225        |
| 5.2      | Design specifications and scope                | 226        |
| 5.2.1    | Specifications                                 | 226        |
| 5.2.2    | Scope  | 228        |
| 5.3      | Photon detector system overview                | 229        |
| 5.3.1    | Principle of operation                         | 229        |
| 5.3.2    | Design considerations                          | 229        |
| 5.3.3    | Design overview                                | 232        |
| 5.3.4    | Options to improve uniformity of response      | 236        |
| 5.3.5    | Overview summary                               | 236        |
| 5.4      | Light collectors                               | 237        |
| 5.5      | Silicon photosensors                           | 242        |
| 5.6      | Electronics                                    | 243        |
| 5.6.1    | SiPM signal ganging                            | 244        |
| 5.6.2    | Front-end electronics baseline design          | 245        |

|        |  |     |
|--------|--|-----|
| 5.6.3  | Electronics next steps                             | 247 |
| 5.7    | Calibration and monitoring                         | 249 |
| 5.8    | Design validation                                  | 251 |
| 5.8.1  | Photosensors and active ganging                    | 251 |
| 5.8.2  | Standard ARAPUCA (S-ARAPUCA)                       | 254 |
| 5.8.3  | Extended ARAPUCA (X-ARAPUCA)                       | 259 |
| 5.8.4  | Materials selection, testing and validation        | 268 |
| 5.8.5  | Calibration and monitoring                         | 270 |
| 5.9    | Production and assembly                            | 273 |
| 5.9.1  | Light collector module component fabrication       | 273 |
| 5.9.2  | Photon detector module assembly                    | 274 |
| 5.9.3  | APA frame mounting structure and module securing   | 276 |
| 5.9.4  | Photosensors and photosensor modules               | 280 |
| 5.9.5  | Electronics  | 281 |
| 5.9.6  | Calibration and monitoring                         | 283 |
| 5.9.7  | Outline of PD system assembly plan                 | 283 |
| 5.10   | System interfaces                                  | 285 |
| 5.10.1 | Overview   | 285 |
| 5.10.2 | Anode plane assembly                               | 285 |
| 5.10.3 | TPC cold electronics                               | 287 |
| 5.10.4 | Cathode plane assembly and high voltage system     | 287 |
| 5.10.5 | Data acquisition                                   | 288 |
| 5.10.6 | Cryogenics instrumentation and slow control        | 289 |
| 5.10.7 | Facility, integration and installation interfaces  | 290 |
| 5.10.8 | Calibration and monitoring                         | 290 |
| 5.10.9 | Physics, software and computing                    | 291 |
| 5.11   | Risks  | 292 |
| 5.11.1 | Physics performance specification risks            | 293 |
| 5.11.2 | Design risks                                       | 294 |
| 5.11.3 | Risks during integration                           | 295 |
| 5.11.4 | Risks during installation/commissioning/operations | 295 |
| 5.12   | Transport and handling                             | 296 |
| 5.13   | Quality assurance and quality control              | 296 |
| 5.13.1 | Design quality assurance                           | 297 |
| 5.13.2 | Production and assembly quality assurance          | 297 |
| 5.13.3 | Production and assembly quality control            | 298 |
| 5.13.4 | Installation quality control                       | 299 |
| 5.14   | Safety   | 299 |
| 5.15   | Organization and management                        | 300 |
| 5.15.1 | High-level schedule                                | 301 |
| 5.15.2 | High-level cost narrative                          | 304 |
| 5.16   | Appendix   | 304 |
| 5.16.1 | Simulation   | 304 |

|          |  |            |
|----------|--|------------|
| 5.16.2   | Options to enhance light yield uniformity      | 310        |
| <b>6</b> | <b>Calibration hardware for single-phase</b>   | <b>314</b> |
| 6.1      | Introduction                                   | 314        |
| 6.2      | Calibration overview                           | 315        |
| 6.2.1    | Scope  | 316        |
| 6.2.2    | Design considerations and requirements         | 317        |
| 6.2.3    | Strategy                                       | 319        |
| 6.3      | Calibration systems                            | 321        |
| 6.3.1    | Cryostat configuration for calibration systems | 321        |
| 6.3.2    | Laser calibration: ionization system           | 322        |
| 6.3.3    | Laser calibration: beam location system        | 333        |
| 6.3.4    | Laser calibration: photoelectron system        | 336        |
| 6.3.5    | Pulsed neutron source system                   | 340        |
| 6.3.6    | Validation of calibration systems              | 347        |
| 6.4      | Interfaces with other consortia                | 349        |
| 6.4.1    | Calibration data volume estimates              | 349        |
| 6.5      | Construction and installation                  | 353        |
| 6.5.1    | Quality control                                | 353        |
| 6.5.2    | Installation, integration and commissioning    | 353        |
| 6.5.3    | Safety   | 355        |
| 6.6      | Organization and management                    | 356        |
| 6.6.1    | Consortium organization                        | 356        |
| 6.6.2    | Institutional responsibilities                 | 358        |
| 6.6.3    | Risks  | 358        |
| 6.6.4    | Schedule and milestones                        | 361        |
| 6.7      | Appendix                                       | 363        |
| 6.7.1    | Laser system alternative designs               | 363        |
| 6.7.2    | PNS system alternative designs                 | 363        |
| 6.7.3    | Proposed radioactive source calibration system | 365        |
| <b>7</b> | <b>Data acquisition</b>                        | <b>375</b> |
| 7.1      | Introduction                                   | 375        |
| 7.2      | Design overview                                | 376        |
| 7.2.1    | Requirements and specifications                | 376        |
| 7.2.2    | Interfaces                                     | 385        |
| 7.3      | Data acquisition system design                 | 388        |
| 7.3.1    | Overview                                       | 388        |
| 7.3.2    | Upstream DAQ                                   | 389        |
| 7.3.3    | Data selection                                 | 392        |
| 7.3.4    | Back-end DAQ                                   | 398        |
| 7.3.5    | Control, configuration, and monitoring         | 400        |
| 7.3.6    | Data quality monitoring                        | 406        |



|          |   |            |
|----------|---|------------|
| 7.3.7    | Timing and synchronization                          | 406        |
| 7.4      | Design validation and development plans             | 407        |
| 7.4.1    | ProtoDUNE test beam                                 | 408        |
| 7.4.2    | Ongoing development                                 | 410        |
| 7.4.3    | Plan for future development                         | 417        |
| 7.5      | Production, assembly, installation and integration  | 417        |
| 7.5.1    | Production and assembly                             | 417        |
| 7.5.2    | Installation and integration                        | 418        |
| 7.6      | Organization and project management                 | 420        |
| 7.6.1    | Consortium organization                             | 420        |
| 7.6.2    | Schedule and milestones                             | 421        |
| 7.6.3    | Safety and risks                                    | 421        |
| <b>8</b> | <b>Cryogenics instrumentation and slow controls</b> | <b>428</b> |
| 8.1      | Introduction  | 428        |
| 8.1.1    | Scope   | 430        |
| 8.1.2    | Design considerations                               | 432        |
| 8.1.3    | Fluid dynamics simulation                           | 434        |
| 8.2      | Cryogenics instrumentation                          | 440        |
| 8.2.1    | Thermometers  | 440        |
| 8.2.2    | Purity monitors                                     | 451        |
| 8.2.3    | Liquid level meters                                 | 456        |
| 8.2.4    | Pressure meters                                     | 457        |
| 8.2.5    | Gas analyzers                                       | 458        |
| 8.2.6    | Cameras   | 461        |
| 8.2.7    | Cryogenics instrumentation test facility            | 465        |
| 8.2.8    | Validation in ProtoDUNE                             | 465        |
| 8.3      | Slow controls                                       | 466        |
| 8.3.1    | Slow controls hardware                              | 466        |
| 8.3.2    | Slow controls infrastructure                        | 468        |
| 8.3.3    | Slow controls software                              | 468        |
| 8.3.4    | Slow controls quantities                            | 469        |
| 8.3.5    | Local integration                                   | 469        |
| 8.3.6    | Validation in ProtoDUNE                             | 471        |
| 8.4      | Organization and management                         | 471        |
| 8.4.1    | Institutional responsibilities                      | 473        |
| 8.4.2    | Schedule  | 474        |
| 8.4.3    | Risks   | 475        |
| 8.4.4    | Interfaces  | 479        |
| 8.4.5    | Installation, integration, and commissioning        | 479        |
| 8.4.6    | Quality control                                     | 484        |
| 8.4.7    | Safety  | 488        |

|          |  |            |
|----------|--|------------|
| <b>9</b> | <b>Detector installation</b>                 | <b>489</b> |
| 9.1      | Introduction                                 | 489        |
| 9.2      | Logistics                                    | 493        |
| 9.2.1    | Logistics planning                           | 494        |
| 9.2.2    | Logistics quality control                    | 497        |
| 9.2.3    | Logistics safety                             | 498        |
| 9.3      | Detector infrastructure                      | 499        |
| 9.3.1    | Detector support system                      | 499        |
| 9.3.2    | Cryostat roof infrastructure                 | 506        |
| 9.3.3    | Cryostat internal infrastructure             | 509        |
| 9.3.4    | Cleanroom and cleanroom infrastructure       | 511        |
| 9.3.5    | Cryogenics and Cold boxes                    | 516        |
| 9.3.6    | Prototyping and testing (QA/QC)              | 520        |
| 9.4      | Detector installation                        | 521        |
| 9.4.1    | Installation process description             | 521        |
| 9.4.2    | Installation prototyping and testing (QA/QC) | 542        |
| 9.5      | Detector commissioning                       | 554        |
| 9.6      | Schedule                                     | 556        |
| 9.7      | Environmental, safety, and health (ES&H)     | 560        |
| 9.7.1    | Documentation approval process               | 560        |
| 9.7.2    | Support and responsibilities                 | 560        |
| 9.7.3    | Safety program                               | 560        |
|          | <b>Acknowledgments</b>                       | <b>563</b> |
|          | <b>Glossary</b>                              | <b>564</b> |
|          | <b>Bibliography</b>                          | <b>582</b> |
|          | <b>The DUNE collaboration</b>                | <b>593</b> |

# List of Figures

|      |   |    |
|------|---|----|
| 1.1  | The single-phase (SP) LArTPC operating principle                  | 3  |
| 1.2  | A 10 kt DUNE far detector SP module                               | 4  |
| 1.3  | A far detector (FD) cryostat                                      | 5  |
| 1.4  | The underground layout of the SURF laboratory                     | 6  |
| 1.5  | A stack of two anode plane assemblies (APAs)                      | 7  |
| 1.6  | Photon detector (PD) modules, mounted in an APA                   | 9  |
| 1.7  | An X-ARAPUCA PD cell  | 9  |
| 1.8  | A ProtoDUNE-SP cathode plane assembly (CPA)                       | 10 |
| 1.9  | A section of the field cage (FC)                                  | 11 |
| 1.10 | Schematic and photo of an APA                                     | 11 |
| 1.11 | Geometry boards and wire-support combs on an APA                  | 13 |
| 1.12 | A block diagram of the APA readout electronics                    | 14 |
| 2.1  | A 10 kt DUNE far detector SP module                               | 20 |
| 2.2  | Illustration of the APA wire layout                               | 21 |
| 2.3  | Cross section view of the head end and wire layers of an APA      | 22 |
| 2.4  | A completed APA for ProtoDUNE-SP                                  | 23 |
| 2.5  | Electron-photon separation dependence on wire pitch and angle     | 26 |
| 2.6  | Field line simulation around wire planes                          | 27 |
| 2.7  | Bare APA frame drawing  | 29 |
| 2.8  | APA frame construction details                                    | 30 |
| 2.9  | Photos of APA grounding mesh                                      | 32 |
| 2.10 | Wire carrier board layout on the APA frames                       | 33 |
| 2.11 | Wire board stack at the head end of an APA                        | 34 |
| 2.12 | APA side boards showing traces that connect wires around openings | 35 |
| 2.13 | APA side boards on the frame                                      | 36 |
| 2.14 | APA pair diagram with dimensions                                  | 37 |
| 2.15 | APA-to-APA connections  | 38 |
| 2.16 | Yoke that connects an APA pair to the DSS                         | 38 |
| 2.17 | APA-to-APA gaps   | 39 |
| 2.18 | A drift region in ProtoDUNE-SP with installed APAs                | 41 |
| 2.19 | ProtoDUNE-SP wire tensions as measured during production          | 43 |
| 2.20 | ProtoDUNE-SP wire tension measurement plots                       | 44 |

|      |   |     |
|------|---|-----|
| 2.21 | ProtoDUNE-SP wire tension before and after cold tests                     | 44  |
| 2.22 | ProtoDUNE-SP event display; impact of a grounded electron diverter        | 46  |
| 2.23 | ProtoDUNE-SP event display; track crossing gap without electron diverter  | 47  |
| 2.24 | $dQ/dx$ distributions for ProtoDUNE-SP with different diverter conditions | 47  |
| 2.25 | Average charge deposition on tracks vs. height                            | 48  |
| 2.26 | ProtoDUNE bias voltage scan data  | 50  |
| 2.27 | Ash River APA pair integration tests                                      | 51  |
| 2.28 | APA interface with TPC electronics  | 52  |
| 2.29 | APA interface with PDs in ProtoDUNE-SP                                    | 54  |
| 2.30 | TPC electronics cable routing in the APAs                                 | 55  |
| 2.31 | APA-to-APA connection and cable routing                                   | 56  |
| 2.32 | Winding machine schematic showing ongoing development                     | 57  |
| 2.33 | APA wire winding machine  | 58  |
| 2.34 | The upgraded APA wire winding machine                                     | 58  |
| 2.35 | APA on a process cart during construction                                 | 59  |
| 2.36 | Layouts of APA production sites   | 60  |
| 2.37 | Observed resonant frequency in electrical wire tension method             | 65  |
| 2.38 | APA edge lifting fixture  | 67  |
| 2.39 | APA transport frame   | 68  |
| 2.40 | APA loading into the mine shaft   | 69  |
| 2.41 | APA consortium organizational chart                                       | 71  |
| 2.42 | APA construction organizational chart                                     | 72  |
|      |   |     |
| 3.1  | SP module schematic with one unit of top and bottom FC modules            | 82  |
| 3.2  | Electric field distribution in the TPC                                    | 88  |
| 3.3  | Simulated CPA discharge event   | 90  |
| 3.4  | Power supply photos and schematic of HV delivery system to the cryostat   | 92  |
| 3.5  | Photo and drawing of a HV feedthrough                                     | 92  |
| 3.6  | HV input connection to CPA array  | 94  |
| 3.7  | Completed ProtoDUNE-SP CPA panel on production table                      | 95  |
| 3.8  | Benefit of field-shaping strip concept                                    | 96  |
| 3.9  | E field map and equipotential contours of profiles at $-180$ kV           | 97  |
| 3.10 | Current baseline FC+GP module design; changes relative to ProtoDUNE-SP    | 98  |
| 3.11 | Coupling between FC and GP  | 98  |
| 3.12 | E field at edge of field cage   | 99  |
| 3.13 | Fully assembled top FC module with GP                                     | 100 |
| 3.14 | Endwall FC panels   | 101 |
| 3.15 | ProtoDUNE-SP HV resistor divider board                                    | 102 |
| 3.16 | E field distortion from broken voltage divider path                       | 103 |
| 3.17 | HV interconnection topology   | 104 |
| 3.18 | Photo of ProtoDUNE-SP drift volume with HV components                     | 106 |
| 3.19 | ProtoDUNE-SP HV performance during the test beam run                      | 108 |
| 3.20 | ProtoDUNE-SP HV autorecovery procedure                                    | 109 |

|      |   |     |
|------|---|-----|
| 3.21 | Photon detector activity on streamers   | 110 |
| 3.22 | CPA mockup panels at Ash River  | 116 |
| 3.23 | Top and bottom FC module frame assembly procedure                               | 117 |
| 3.24 | Endwall FC assembly table   | 118 |
| 3.25 | Hanging endwall FC frames   | 119 |
| 3.26 | HVS production and installation schedule for first SP detector module           | 128 |
| 3.27 | Concept to attach reflector to a CPA panel                                      | 130 |
| 3.28 | SBND laser arrangement  | 130 |
|      |   |     |
| 4.1  | The reference architecture for the TPC electronics                              | 133 |
| 4.2  | Connections between the signal flanges and APA                                  | 138 |
| 4.3  | APA wire bias schematic diagram, including the CR board                         | 143 |
| 4.4  | The complete FEMB assembly as used in ProtoDUNE-SP                              | 144 |
| 4.5  | Modified design of the cold data cable and of the FEMB PCB                      | 144 |
| 4.6  | FE ASIC channel schematic   | 146 |
| 4.7  | FE ASIC response and layout   | 147 |
| 4.8  | ColdADC block diagram   | 148 |
| 4.9  | Circuit blocks in each ADC pipeline stage                                       | 149 |
| 4.10 | ADC stage transfer function   | 150 |
| 4.11 | Static linearity of ColdADC   | 152 |
| 4.12 | Dynamic Linearity   | 153 |
| 4.13 | ColdDATA block diagram  | 154 |
| 4.14 | ColdDATA fast command timing  | 155 |
| 4.15 | ColdDATA output eye diagram   | 156 |
| 4.16 | Lifetime projection of the COTS ADC   | 158 |
| 4.17 | Noise measurement of FEMBs with COTS ADC  | 158 |
| 4.18 | Overall architecture of the CRYO ASIC   | 159 |
| 4.19 | CRYO FE section architecture and typical front-end response                     | 160 |
| 4.20 | CRYO ADC architecture   | 160 |
| 4.21 | Photos of CRYO ASIC prototype   | 161 |
| 4.22 | CRYO ASIC FE response at liquid nitrogen temperature                            | 162 |
| 4.23 | Example of a pulse injected in a CRYO ASIC channel                              | 162 |
| 4.24 | Differential and integral non-linearities for the CRYO ADC                      | 163 |
| 4.25 | Prototype CE box used in ProtoDUNE-SP   | 165 |
| 4.26 | Views of various cable and CE cold boxes supports                               | 166 |
| 4.27 | TPC cold electronics feedthrough  | 167 |
| 4.28 | Exploded view of the cold electronics signal flange for ProtoDUNE-SP            | 170 |
| 4.29 | PTC and timing distribution to the WIB and FEMBs                                | 171 |
| 4.30 | Low voltage power distribution to the WIB and FEMBs                             | 171 |
| 4.31 | Warm interface board  | 172 |
| 4.32 | Services on top of the cryostat   | 176 |
| 4.33 | ProtoDUNE-SP APA #2 ENC levels measured in GN <sub>2</sub> in the CERN cold box | 176 |
| 4.34 | TPC ENC levels measured at ProtoDUNE-SP after LAr fill                          | 178 |

|      |   |     |
|------|---|-----|
| 4.35 | TPC ENC levels for all channels of the ProtoDUNE-SP detector                    | 178 |
| 4.36 | Raw data from a ProtoDUNE-SP event  | 179 |
| 4.37 | Raw data from a MicroBooNE event  | 180 |
| 4.38 | Signal over noise for cosmic muon tracks reconstructed in ProtoDUNE-SP          | 181 |
| 4.39 | Pulse shape on a ProtoDUNE-SP wire showing the ledge effect                     | 182 |
| 4.40 | Image of a connector for the cold cables lifted from the FEMB                   | 183 |
| 4.41 | Spectrum of the noise on the ProtoDUNE-SP APA wires                             | 183 |
| 4.42 | The Cryogenic Test System   | 188 |
| 4.43 | ICEBERG cryostat and top plate spool piece                                      | 190 |
| 4.44 | ICEBERG TPC and DAQ rack  | 191 |
| 4.45 | ENC levels for all channels of the ICEBERG TPC                                  | 192 |
| 4.46 | One side of the 40 % APA with four FEMBs and the CE flange                      | 193 |
| 4.47 | Parts flow for the detector components inside the cryostat                      | 197 |
| 4.48 | Parts flow for the detector components on top of the cryostat                   | 197 |
| 4.49 | Organization chart of the TPC electronics consortium                            | 218 |
| 4.50 | Construction responsibilities for the TPC electronics consortium                | 222 |
| 4.51 | Schedule for the construction of the TPC electronics detector components        | 224 |
| 5.1  | Schematic of scintillation light production in argon                            | 230 |
| 5.2  | Arrangement of APAs in a SP module and position of PD modules in APA frame      | 231 |
| 5.3  | Schematic representation of the X-ARAPUCA operating principle                   | 233 |
| 5.4  | 3D model of PDs in the APA  | 234 |
| 5.5  | PD Module being inserted into an APA frame                                      | 234 |
| 5.6  | X-ARAPUCA conceptual model  | 238 |
| 5.7  | X-ARAPUCA module indicating four supercells                                     | 239 |
| 5.8  | Exploded X-ARAPUCA supercell  | 239 |
| 5.9  | X-ARAPUCA SiPM mounting and signal routing boards                               | 241 |
| 5.10 | Overview of the PD system signal path   | 244 |
| 5.11 | SiPM signal summing board circuit   | 245 |
| 5.12 | PD system 64-channel front-end board  | 248 |
| 5.13 | PD system front-end electronics controller module                               | 248 |
| 5.14 | PD system front-end electronics grounding scheme                                | 248 |
| 5.15 | Calibration system diffuser locations on the SP CPA                             | 250 |
| 5.16 | Photosensors signal ganging scheme  | 251 |
| 5.17 | Photosensors signal ganging with 48 SiPMs                                       | 252 |
| 5.18 | Time walk from 48 ganged MPPCs  | 253 |
| 5.19 | Performance of candidate FBK SiPMs  | 253 |
| 5.20 | Readout of 72-MPPC active ganging array with the Mu2e electronics readout board | 254 |
| 5.21 | Event display from ProtoDUNE-SP showing the location of the PD modules          | 256 |
| 5.22 | Full-scale S-ARAPUCA array installed in ProtoDUNE-SP APA 3                      | 256 |
| 5.23 | S-ARAPUCA module prototype assembly   | 257 |
| 5.24 | PD system response to 7 GeV/c momentum electrons and muons in ProtoDUNE-SP      | 259 |
| 5.25 | PD system timing measurements with ProtoDUNE-SP                                 | 259 |

|      |   |     |
|------|---|-----|
| 5.26 | PD system energy response to ProtoDUNE-SP electron beam                         | 260 |
| 5.27 | Stability of the PD system during ProtoDUNE-SP running                          | 260 |
| 5.28 | X-ARAPUCA test cell   | 261 |
| 5.29 | Coated dichroic filters and vacuum coating system                               | 262 |
| 5.30 | X-ARAPUCA test stand  | 262 |
| 5.31 | Alpha particle energy spectrum in an X-ARAPUCA test cell                        | 263 |
| 5.32 | ICEBERG TPC model and assembled APA   | 264 |
| 5.33 | Single supercell ICEBERG PD module  | 265 |
| 5.34 | SBND X-ARAPUCA modules  | 266 |
| 5.35 | PD system coating test stand  | 269 |
| 5.36 | ProtoDUNE-SP UV calibration and monitoring system                               | 271 |
| 5.37 | ProtoDUNE-SP S-ARAPUCA response to UV calibration and monitoring system         | 271 |
| 5.38 | ProtoDUNE-SP gain monitoring with UV calibration and monitoring system          | 272 |
| 5.39 | ProtoDUNE-SP UV calibration and monitoring system stability                     | 272 |
| 5.40 | PD module scanner   | 276 |
| 5.41 | PD mounting rails in APA frame  | 277 |
| 5.42 | PD cable routing in APA frames  | 278 |
| 5.43 | PD cable connectors   | 278 |
| 5.44 | PD mechanical support analysis  | 280 |
| 5.45 | Supernova neutrino energy resolution from the TPC                               | 308 |
| 5.46 | SNB neutrino energy resolution from the PD system                               | 309 |
| 5.47 | Predicted light yield with WLS-coated reflector foils on the CPA                | 312 |
| 5.48 | Simulation of LAr scintillation light with and without Xe doping in a SP module | 312 |
| 6.1  | Calibration consortium subsystem chart  | 316 |
| 6.2  | Cryostat penetration map with calibration ports                                 | 322 |
| 6.3  | Impact on E field of CPA position distortions                                   | 323 |
| 6.4  | Impact on E field of FC resistor failures                                       | 324 |
| 6.5  | MicroBooNE laser calibration system schematics                                  | 328 |
| 6.6  | MicroBooNE laser calibration system drawings                                    | 329 |
| 6.7  | View of top field cage and laser coverage estimation                            | 330 |
| 6.8  | Laser periscope penetrating the field cage                                      | 331 |
| 6.9  | Simulation of impact on E field of FC penetration                               | 331 |
| 6.10 | Cluster assembly of the miniCAPTAIN LBLs  | 334 |
| 6.11 | Mirror-based laser beam location system   | 335 |
| 6.12 | Placement of phototargets on the cathode plane assembly                         | 337 |
| 6.13 | Anticipated positions and number of phototargets on the cathode plane assembly  | 338 |
| 6.14 | View of the CPA illumination with fibers on the APA                             | 338 |
| 6.15 | Cross sections enabling the PNS concept   | 341 |
| 6.16 | Neutron capture gamma spectrum measured by ACED                                 | 342 |
| 6.17 | Conceptual design of the PNS  | 343 |
| 6.18 | Energy of moderated neutrons produced by the PNS                                | 343 |
| 6.19 | PNS baseline design   | 345 |

|      |   |     |
|------|---|-----|
| 6.20 | Pulsed neutron system neutron capture positions inside a DUNE-sized TPC             | 346 |
| 6.21 | Top view of the ProtoDUNE-SP cryostat showing various penetrations                  | 348 |
| 6.22 | Organizational chart for the calibration consortium                                 | 357 |
| 6.23 | CAD drawing of the double rotary flange for the end-wall laser calibration ports    | 364 |
| 6.24 | PNS two designs   | 364 |
| 6.25 | Pulsed neutron system neutron capture positions inside a DUNE-sized TPC             | 365 |
| 6.26 | Fish-line deployment scheme in DUNE for an encapsulated radioactive source          | 367 |
| 6.27 | Detected charge from 9 MeV gamma-ray source with radiological backgrounds           | 371 |
| 6.28 | Measured E field and $e^-$ lifetime from 9 MeV gamma; with radiological backgrounds | 372 |
| 7.1  | DAQ conceptual design overview for one module                                       | 377 |
| 7.2  | Expected physics-related activity rates in one FD module                            | 379 |
| 7.3  | DAQ system overview   | 389 |
| 7.4  | DUNE upstream DAQ subsystem and connections   | 390 |
| 7.5  | Flow diagram of the DUNE upstream DAQ subsystem.                                    | 390 |
| 7.6  | Data selection strategy and hierarchy   | 393 |
| 7.7  | DUNE DAQ data selection subsystem   | 394 |
| 7.8  | DUNE DAQ back-end operation   | 398 |
| 7.9  | DAQ CCM subsystem interaction   | 401 |
| 7.10 | DAQ control subsystem roles and services  | 402 |
| 7.11 | DAQ CCM subsystem interaction   | 403 |
| 7.12 | DAQ monitoring subsystem roles and services   | 404 |
| 7.13 | ProtoDUNE DAQ system  | 409 |
| 7.14 | Topology of the FELIX-based upstream DAQ of ProtoDUNE                               | 411 |
| 7.15 | CPU core-time for primitives and CPU utilization in live data                       | 412 |
| 7.16 | Trigger primitives in ProtoDUNE-SP data   | 413 |
| 7.17 | Trigger primitive rates in ProtoDUNE-SP, four categories                            | 414 |
| 7.18 | Efficiency for forming trigger candidates as input trigger primitives               | 414 |
| 7.19 | Efficiency for forming trigger candidates from ionization activity                  | 415 |
| 7.20 | Supernova burst trigger efficiency  | 416 |
| 7.21 | Layout of the DUNE underground areas  | 418 |
| 7.22 | Layout of the DUNE data room and work area in CUC                                   | 419 |
| 7.23 | DAQ counting room in the CUC  | 420 |
| 7.24 | DAQ consortium org chart  | 421 |
| 7.25 | DAQ schedule for first 10 kt module   | 424 |
| 8.1  | CISC subsystem chart  | 429 |
| 8.2  | CFD example   | 437 |
| 8.3  | SP CISC geometry layout   | 438 |
| 8.4  | Streamlines for LAr flow inside ProtoDUNE-SP  | 439 |
| 8.5  | Distribution of temperature sensors inside the cryostat                             | 441 |
| 8.6  | Principle of cross-calibration with dynamic T-gradient monitor                      | 442 |
| 8.7  | Temperature profile for dynamic T-gradient with pumps-off                           | 443 |



|      |  |     |
|------|--|-----|
| 8.8  | Dynamic T-gradient monitor overview                                      | 444 |
| 8.9  | Sensor-cable assembly for dynamic T-gradient monitor                     | 444 |
| 8.10 | ProtoDUNE-SP static T-gradient results                                   | 445 |
| 8.11 | Temperature sensor resolution and reproducibility                        | 445 |
| 8.12 | Conceptual design of the static T-gradient monitor                       | 446 |
| 8.13 | Cryostat bolts and temperature sensor support                            | 447 |
| 8.14 | ProtoDUNE-SP instrumentation map   | 448 |
| 8.15 | ProtoDUNE-SP T-gradient results  | 448 |
| 8.16 | ProtoDUNE-SP bottom sensor results                                       | 449 |
| 8.17 | The ProtoDUNE-SP purity monitoring system                                | 452 |
| 8.18 | Measured electron lifetimes in the three purity monitors at ProtoDUNE-SP | 452 |
| 8.19 | Schematic diagram of the baseline purity monitor design                  | 454 |
| 8.20 | Block diagram of the purity monitor system                               | 455 |
| 8.21 | LAr level measurements   | 457 |
| 8.22 | Pressure sensors installed on a flange in ProtoDUNE-SP                   | 458 |
| 8.23 | A gas analyzer switchyard valve assembly                                 | 459 |
| 8.24 | Impurity levels during the pre-fill stages for 35 ton prototype phase 1  | 460 |
| 8.25 | O <sub>2</sub> just after the 35 ton prototype was filled with LAr       | 460 |
| 8.26 | Camera locations in ProtoDUNE-SP   | 461 |
| 8.27 | A camera enclosure   | 462 |
| 8.28 | Inspection camera design   | 464 |
| 8.29 | Example schematic for LED chain  | 465 |
| 8.30 | Slow controls connections and data                                       | 466 |
| 8.31 | Rack monitoring box prototype for the SBND; based on MicroBooNE design   | 467 |
| 8.32 | Diagram of the ProtoDUNE-SP control system topology                      | 472 |
| 8.33 | CISC consortium organization   | 473 |
| 9.1  | Material flow diagram for LBNF and DUNE                                  | 494 |
| 9.2  | Simplified model of the Ross Cage  | 495 |
| 9.3  | Planned usage of underground space during installation setup             | 496 |
| 9.4  | QC and shipping data flow diagram for logistics                          | 498 |
| 9.5  | 3D model of the DSS  | 500 |
| 9.6  | DSS vertical support feedthrough   | 503 |
| 9.7  | DSS support for lateral loads  | 504 |
| 9.8  | 3D models of the shuttle beam end of the DSS                             | 504 |
| 9.9  | Prototype of the motorized DSS trolley                                   | 505 |
| 9.10 | Mezzanine and electronics racks  | 505 |
| 9.11 | Electronics rack contents  | 506 |
| 9.12 | Cryostat crossing tube design  | 508 |
| 9.13 | Layout of the internal cryogenics piping                                 | 510 |
| 9.14 | Installation Cleanroom layout  | 511 |
| 9.15 | Installation Integration Lower Rail System                               | 514 |
| 9.16 | APA cabling tower  | 515 |

## List of Figures

---

|      |  |     |
|------|--|-----|
| 9.17 | Cleanroom platforms and material transport system                    | 516 |
| 9.18 | Installation cold box  | 517 |
| 9.19 | Cold box cryogenics support system based on mechanical refrigeration | 519 |
| 9.20 | Cold box cryogenics support system based on LN2                      | 520 |
| 9.21 | High level installation schedule                                     | 522 |
| 9.22 | Layout of the DUNE underground areas                                 | 523 |
| 9.23 | Layout of the DUNE data room and work area in CUC                    | 524 |
| 9.24 | Top view of the installation area highlighting the infrastructure    | 525 |
| 9.25 | Installation of electronics crosses                                  | 526 |
| 9.26 | DSS feedthrough installation   | 527 |
| 9.27 | DSS I-Beam lifting setup   | 527 |
| 9.28 | Design of the instrumentation feedthroughs                           | 529 |
| 9.29 | Distribution of various CISC devices inside the cryostat.            | 530 |
| 9.30 | Endwall hoisting infrastructure                                      | 531 |
| 9.31 | Installation of the first endwall                                    | 531 |
| 9.32 | Single row of APA and CPA  | 532 |
| 9.33 | Typical APA installation schedule                                    | 532 |
| 9.34 | Photon detector and APA integration                                  | 533 |
| 9.35 | Initial APA testing and pair assembly                                | 534 |
| 9.36 | APA cabling and cold test  | 535 |
| 9.37 | CPA assembly steps   | 536 |
| 9.38 | Cold Electronics cabling inside the cryostat                         | 538 |
| 9.39 | Model of the electronics and photon detector cabling                 | 539 |
| 9.40 | CPA installation   | 540 |
| 9.41 | Installation of final row of detector components                     | 541 |
| 9.42 | Second endwall FC installation                                       | 541 |
| 9.43 | NOvA Assembly Area at Ash River                                      | 544 |
| 9.44 | Photon detector scanner used for ProtoDUNE-SP                        | 553 |
| 9.45 | Overview of the single-phase schedule                                | 558 |

# List of Tables

|      |  |     |
|------|--|-----|
| 1.1  | Key parameters for a 10 kt FD SP module  | 5   |
| 1.2  | Key milestones and dates   | 17  |
| 2.1  | APA specifications.  | 24  |
| 2.2  | APA wire plane nominal bias voltages   | 27  |
| 2.3  | APA design parameters  | 28  |
| 2.4  | Beryllium copper (CuBe) wire properties  | 32  |
| 2.5  | Disconnected channel counts in ProtoDUNE-SP                                      | 45  |
| 2.6  | Dead channel counts in ProtoDUNE-SP  | 45  |
| 2.7  | APA interfaces   | 52  |
| 2.8  | APA consortium institutions  | 72  |
| 2.9  | APA production institutional responsibilities                                    | 73  |
| 2.10 | APA consortium review schedule   | 74  |
| 2.11 | APA consortium schedule  | 75  |
| 2.12 | APA risks  | 76  |
| 3.1  | HV specifications.   | 84  |
| 3.2  | HV cathode components  | 86  |
| 3.3  | HV field cage components   | 87  |
| 3.4  | HV system interconnections   | 105 |
| 3.5  | HV system interfaces   | 114 |
| 3.6  | HVS consortium institutions  | 123 |
| 3.7  | HV risks   | 124 |
| 3.8  | HVS consortium schedule  | 127 |
| 4.1  | TPC electronics specifications.  | 134 |
| 4.2  | TPC electronics components and quantities for a single APA                       | 139 |
| 4.3  | Voltage drop and power dissipation in the FEMBs power cables inside the cryostat | 168 |
| 4.4  | Power requirements of FEMBs, WIBs, and WIECs                                     | 174 |
| 4.5  | Status of the design of the different CE detector components                     | 185 |
| 4.6  | TPC electronics system interfaces  | 205 |
| 4.7  | TPC electronics risks  | 211 |
| 4.8  | TPC electronics consortium institutions  | 216 |
| 4.9  | Leadership positions in the TPC electronics consortium                           | 217 |

## List of Tables

---

|      |   |     |
|------|---|-----|
| 4.10 | Number of TPC electronics components for one detector module                    | 219 |
| 4.11 | TPC electronics consortium schedule   | 223 |
| 5.1  | PDS specifications.   | 226 |
| 5.2  | PDS baseline configuration  | 229 |
| 5.3  | Candidate photosensors characteristics  | 243 |
| 5.4  | Shrinkage of PD materials   | 279 |
| 5.5  | Relative shrinkage of PD components and APA frame                               | 280 |
| 5.6  | PDS interfaces  | 286 |
| 5.7  | PD system risks   | 292 |
| 5.8  | PDS consortium institutions.  | 300 |
| 5.9  | PD working groups   | 302 |
| 5.10 | PDS consortium schedule.  | 302 |
| 5.11 | PD system efficiency for nucleon decay events                                   | 306 |
| 5.12 | Fraction of beam events with channels that saturate                             | 310 |
| 6.1  | Calibration specifications.   | 318 |
| 6.2  | Full specifications for calibration subsystems                                  | 320 |
| 6.3  | Work function and other features of candidate metal targets for laser PE system | 337 |
| 6.4  | Calibration system interfaces   | 350 |
| 6.5  | Calibration DAQ summary   | 351 |
| 6.6  | Calibration consortium institutions   | 357 |
| 6.7  | Institutional responsibility for calibrations                                   | 358 |
| 6.8  | Calibration risks   | 360 |
| 6.9  | Calibration consortium schedule   | 362 |
| 6.10 | Full specifications for the radioactive source deployment system                | 367 |
| 6.11 | Key milestones for commissioning RSDS in ProtoDUNE-2                            | 369 |
| 6.12 | Calibration DAQ summary for RSDS  | 372 |
| 6.13 | Radioactive source calibration system risks                                     | 373 |
| 7.1  | Expected DAQ yearly produced TPC data volumes                                   | 380 |
| 7.2  | DAQ specifications.   | 381 |
| 7.3  | Key DAQ parameters  | 385 |
| 7.4  | DAQ system interfaces   | 386 |
| 7.5  | DAQ consortium institutions   | 422 |
| 7.6  | DAQ consortium schedule   | 423 |
| 7.7  | DAQ risks   | 424 |
| 8.1  | CISC specifications.  | 433 |
| 8.2  | Specifications for CISC subsystems (1)  | 435 |
| 8.3  | Specifications for CISC subsystems (2)  | 436 |
| 8.4  | CFD parameters for ProtoDUNE  | 439 |
| 8.5  | Slow controls quantities  | 470 |
| 8.6  | CISC consortium institutions  | 474 |

## List of Tables

---

|      |  |     |
|------|--|-----|
| 8.7  | Institutional responsibilities in the CISC consortium      | 475 |
| 8.8  | SP CISC schedule and milestones                            | 476 |
| 8.9  | CISC risks   | 478 |
| 8.10 | CISC system interfaces                                     | 480 |
| 9.1  | Installation specifications.                               | 490 |
| 9.2  | SP module installation risks                               | 491 |
| 9.3  | DSS Loads  | 500 |
| 9.4  | Cold box cryogenics system parameters                      | 518 |
| 9.5  | Summary of the tests at Ash River                          | 547 |
| 9.6  | SP installation, integration, and commissioning milestones | 557 |

2020 JINST 15 T08010

# A roadmap of the DUNE technical design report

The Deep Underground Neutrino Experiment (DUNE) far detector (FD) technical design report (TDR) describes the proposed physics program, detector designs, and management structures and procedures at the technical design stage.

The TDR is composed of five volumes, as follows:

- Volume I (Introduction to DUNE) provides an overview of all of DUNE for science policy professionals.
- Volume II (DUNE physics) describes the DUNE physics program.
- Volume III (DUNE far detector technical coordination) outlines DUNE management structures, methodologies, procedures, requirements, and risks.
- Volume IV (The DUNE far detector single-phase technology) and Volume V (The DUNE Far Detector Dual-Phase Technology) describe the two FD liquid argon time-projection chamber (LArTPC) technologies.

The text includes terms that hyperlink to definitions in a volume-specific glossary. These terms appear underlined in some online browsers, if enabled in the browser's settings.

# Chapter 1

## Executive summary

### 1.1 Introduction

The overriding physics goals of the DUNE are the search for leptonic charge parity (CP) violation, the search for nucleon decay as a signature of a Grand Unified Theory underlying the Standard Model, and the observation of supernova neutrino bursts (SNBs) from supernovae. Central to achieving this physics program is the construction of a detector that combines the many-kiloton fiducial mass necessary for rare event searches with sub-centimeter spatial resolution in its ability to image those events, allowing us to identify the signatures of the physics processes we seek among the numerous backgrounds. The single-phase (SP) LArTPC [1] allows us to achieve these dual goals, providing a way to read out with sub-centimeter granularity the patterns of ionization in 10 kt volumes of liquid argon (LAr) resulting from the MeV-scale interactions of solar and SNB neutrinos up to the GeV-scale interactions of neutrinos from the Long-Baseline Neutrino Facility (LBNF) beam.

To search for leptonic CP violation, we must study  $\nu_e$  appearance in the LBNF  $\nu_\mu$  beam. This requires the ability to separate electromagnetic activity induced by charged current (CC)  $\nu_e$  interactions from similar activity arising from photons, such as photons from  $\pi^0$  decay. Two signatures allow this: photon showers are typically preceded by a gap prior to conversion, characterized by the 18 cm conversion length in LAr; and the initial part of a photon shower, where an electron-positron pair is produced, has twice the  $dE/dx$  of the initial part of an electron-induced shower. To search for nucleon decay, where the primary channel of interest is  $p \rightarrow K^+\bar{\nu}$ , we must identify kaon tracks as short as a few centimeters. It is also vital to accurately fiducialize these nucleon-decay events to suppress cosmic-muon-induced backgrounds, and here the detection of argon-scintillation photons is important for determining the time of the event. Detecting a SNB poses different challenges: those of dealing with a high data-rate and maintaining the high detector up-time required to ensure we do not miss one of these rare events. The signature of a SNB is a collection of MeV-energy electron tracks a few centimeters in length from CC  $\nu_e$  interactions, spread over the entire detector volume. To fully reconstruct a SNB, the entire detector must be read out, a data-rate of up to 2 TB/s, for 30 s to 100 s, including a  $\sim 4$  s pre-trigger window.

In this Executive Summary, we give an overview of the basic operating principles of a SP LArTPC, followed by a description of the DUNE implementation. We then discuss each of the

subsystems separately, connecting the high-level design requirements and decisions to the overriding physics goals of DUNE.

## 1.2 The single-phase liquid argon time-projection chamber

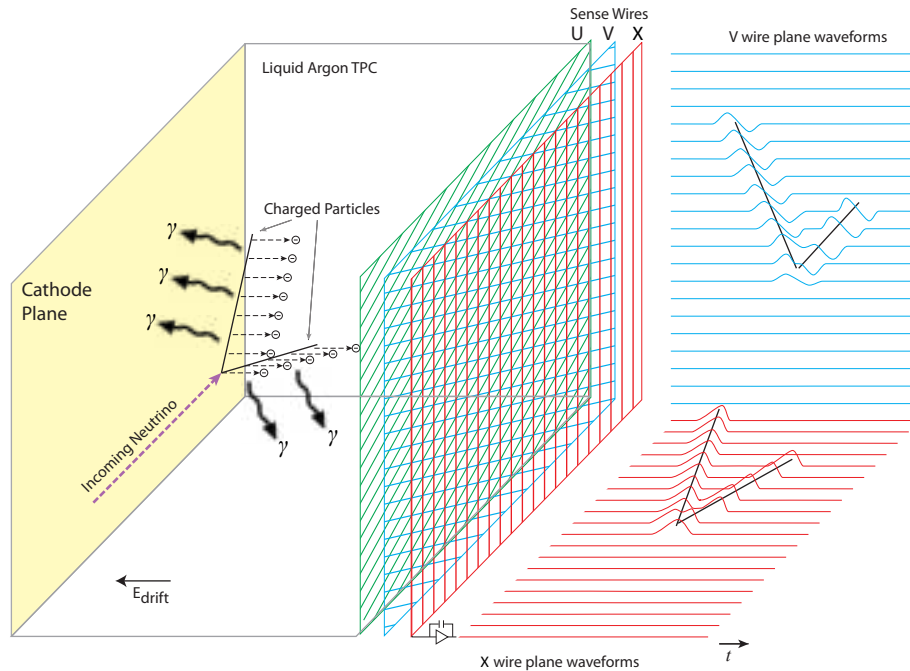


**Figure 1.1.** The general operating principle of the single-phase liquid argon time-projection chamber.

Figure 1.1 shows a schematic of the general operating principle of a SP LArTPC, as has been previously demonstrated by ICARUS [2], ArgoNeuT [3], MicroBooNE [4], LArIAT [5], and ProtoDUNE [6]. A large volume of LAr is subjected to a strong electric field of a few hundred volts per centimeter. Charged particles passing through the detector ionize the argon atoms, and the ionization electrons drift in the E field to the anode wall on a timescale of milliseconds. This anode consists of layers of active wires forming a grid. The relative voltage between the layers is chosen to ensure all but the final layer are transparent to the drifting electrons, and these first layers produce bipolar induction signals as the electrons pass through them. The final layer collects the drifting electrons, resulting in a monopolar signal.

LAr is also an excellent scintillator, emitting VUV light at a wavelength of 127 nm. This prompt scintillation light, which crosses the detector on a timescale of nanoseconds, is shifted into the visible and collected by photon detector (PD) devices. The PDs can provide a  $t_0$  determination for events, telling us when the ionization electrons begin to drift. Relative to this  $t_0$ , the time at which the ionization electrons reach the anode allows reconstruction of the event topology along the drift direction, which is crucial to fiducialize nucleon-decay events and to apply drift corrections to the ionization charge.

The pattern of current observed on the grid of anode wires provides the information for reconstruction in the two coordinates perpendicular to the drift direction. A closer spacing of the



wires, therefore, results in better spatial resolution, but, in addition to increasing the cost of the readout electronics due to the additional wire channels, a closer spacing worsens the signal-to-noise (S/N) of the ionization measurement because the same amount of ionization charge is now divided over more channels. S/N is an important consideration because the measurement of the ionization collected is a direct measurement of the  $dE/dx$  of the charged particles, which is what allows us to perform both calorimetry and particle identification.

### 1.3 The DUNE single-phase far detector module

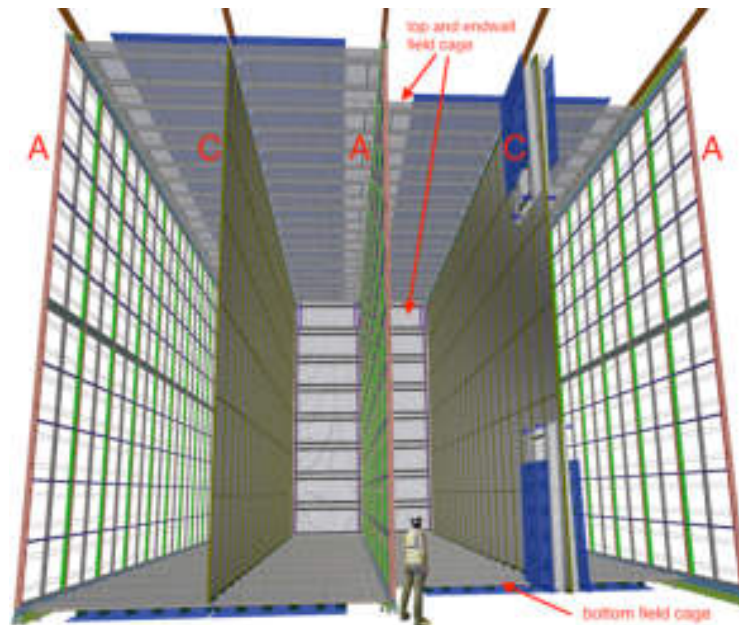


**Figure 1.2.** A 10 kt DUNE FD SP module, showing the alternating 58.2 m long (into the page), 12.0 m high anode (A) and cathode (C) planes, as well as the FC that surrounds the drift regions between the anode and cathode planes. On the right-hand cathode plane, the foremost portion of the FC is shown in its undeployed (folded) state.

The DUNE SP LArTPC consists of four modules of 10 kt fiducial mass (17.5 kt total mass), contributing to the full 40 kt FD fiducial mass. Figure 1.2 shows a 10 kt module, and the key parameters of a SP module are listed in table 1.1. Inside a cryostat of outer dimensions  $65.8 \text{ m} \times 17.8 \text{ m} \times 18.9 \text{ m}$  (shown in figure 1.3), four 3.5 m drift volumes are created between five alternating anode and cathode walls, each wall having dimensions of  $58 \text{ m} \times 12 \text{ m}$ .

The FD is located underground, at the 4850 ft level of the Sanford Underground Research Facility (SURF) in South Dakota. The detector is 1300 km from the source of the LBNF neutrino beam at Fermi National Accelerator Laboratory (Fermilab); this baseline provides the matter effects necessary for DUNE to determine the neutrino mass hierarchy. The SURF underground campus is shown in figure 1.4. The four 10 kt FD modules will be located in the two main caverns, which are each 144.5 m long, 19.8 m wide and 28.0 m high. Each cavern houses two 10 kt modules, one either side of the central access drift. Between the two caverns is the central utility cavern (CUC),

**Table 1.1.** Key parameters for a 10 kt FD SP module.

| Item                        | Quantity                 |
|-----------------------------|--------------------------|
| TPC size                    | 12.0 m × 14.0 m × 58.2 m |
| Nominal fiducial mass       | 10 kt                    |
| APA size                    | 6 m × 2.3 m              |
| CPA size                    | 1.2 m × 4 m              |
| Number of APAs              | 150                      |
| Number of CPAs              | 300                      |
| Number of X-ARAPUCA PD bars | 1500                     |
| X-ARAPUCA PD bar size       | 209 cm × 12 cm × 2 cm    |
| Design voltage              | −180 kV                  |
| Design drift field          | 500 V/cm                 |
| Drift length                | 3.5 m                    |
| Drift speed                 | 1.6 mm/μs                |

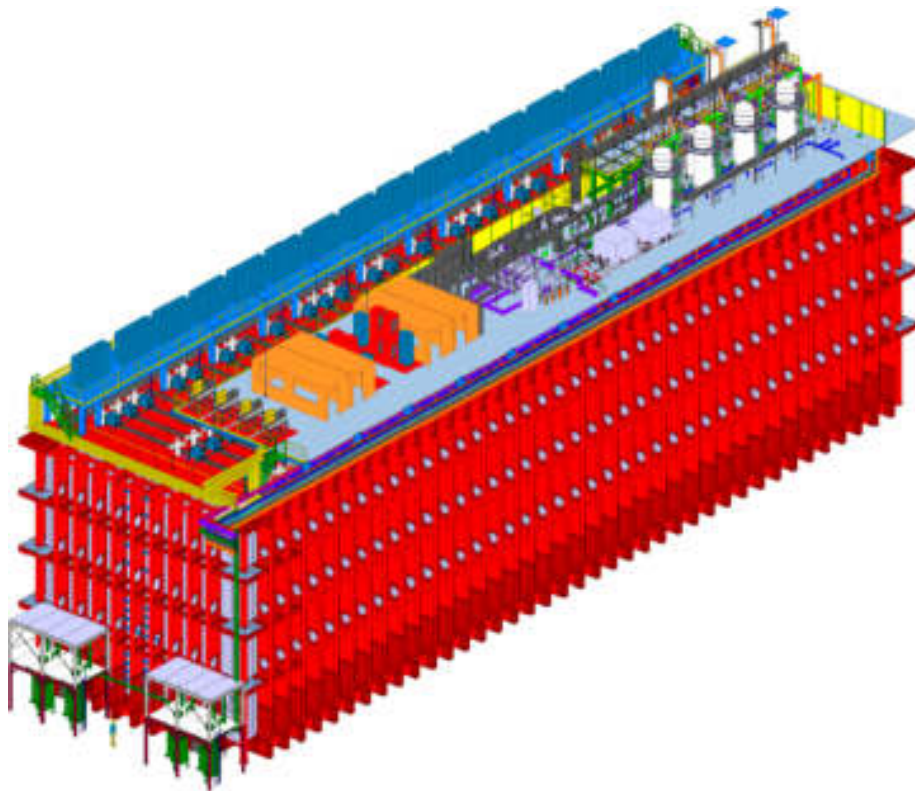


**Figure 1.3.** A 65.8 m (L) by 18.9 m (W) by 17.8 m (H) outer-dimension cryostat that houses a 10 kt FD module. A mezzanine (light blue) installed 2.3 m above the cryostat supports both detector and cryogenics instrumentation. At lower left, between the LAr recirculation pumps (green) installed on the cavern floor, the figure of a person indicates the scale.

a 190 m long, 19.3 m wide, 11.0 m high cavern in which many of the utilities and the upstream data acquisition (DAQ) reside.

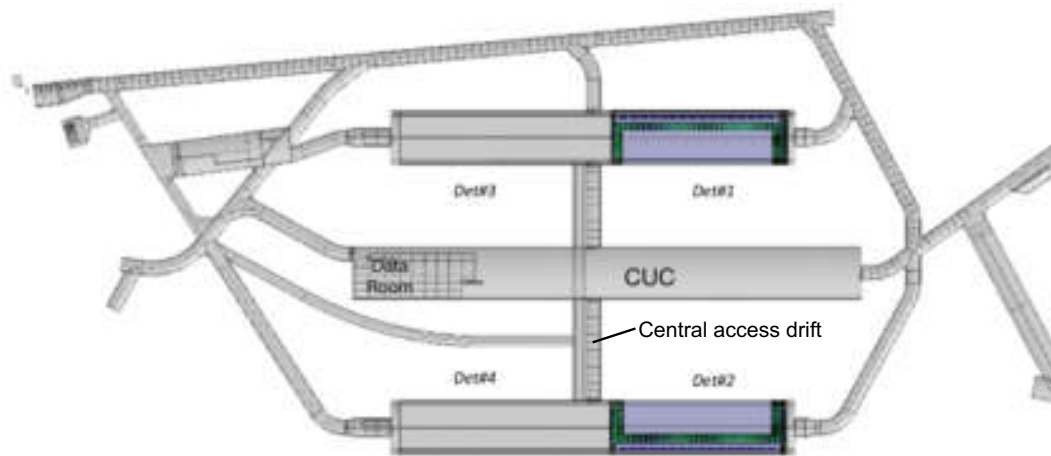


**Figure 1.4.** The underground layout of the SURF laboratory. The two main caverns each hold two 10 kt modules, one either side of the central access drift. The CUC houses utilities and the upstream DAQ.

Each cathode wall in a module is called a cathode plane assembly (CPA) array. The CPA is the  $1.2\text{ m} \times 4\text{ m}$  panel from which the CPA arrays are formed; each CPA array contains 150 CPAs. The CPA arrays are held at  $-180\text{ kV}$ . With the anode walls held close to ground, this results in a uniform  $500\text{ V/cm}$  E field across the drift volume. A FC surrounds the remaining open sides of the time projection chamber (TPC), ensuring the field is uniform to better than 1% throughout the active volume. A typical minimum ionizing particle passing through the argon produces around  $60k$  ionization electrons per centimeter, which drift towards the anodes at around  $1.6\text{ mm}/\mu\text{s}$ ; the time taken to drift the full distance from cathode to anode would therefore be around  $2.2\text{ ms}$ .

The anode walls are each made up of 50 anode plane assembly (APA) units that are  $6\text{ m} \times 2.3\text{ m}$  in dimension. As shown in figure 1.5, the APAs hang vertically; each anode wall is two APAs high and 25 APAs wide. The APAs are two-sided, with three active wire layers and an additional shielding layer, also called a grid layer, wrapped around them. The wire spacing on the layers is  $\sim 5\text{ mm}$ . The collection layer is called the X-layer; the induction layer immediately next to that is called the V-layer; the next induction layer is the U-layer; and the shielding layer is the G-layer. X-layer and G-layer wires are vertical; the U- and V-layer wires are at  $\pm 35.7^\circ$  to the vertical.

Readout electronics, called cold electronics (CE), are attached to the top end of the top APA and the bottom end of the bottom APA. These front-end (FE) electronics benefit from the low LAr temperature through the reduction of thermal noise. The front-end electronics shape, amplify, and digitize the signals from the induction and collection wires thanks to a series of three different types of ASIC through which all signals pass. Cables from the CE pass through feedthroughs on the roof of the cryostat; cables from the motherboards on the bottom APA pass through the inside of the hollow APA frames up to the top.

Once signals from APAs leave the cryostat through feedthroughs, they are passed to warm interface boards that put the signals onto 10 Gbps optical fibers, ten fibers per APA, which carry the signals to the upstream DAQ system located in the CUC. Each 10 kt module has its own, independent

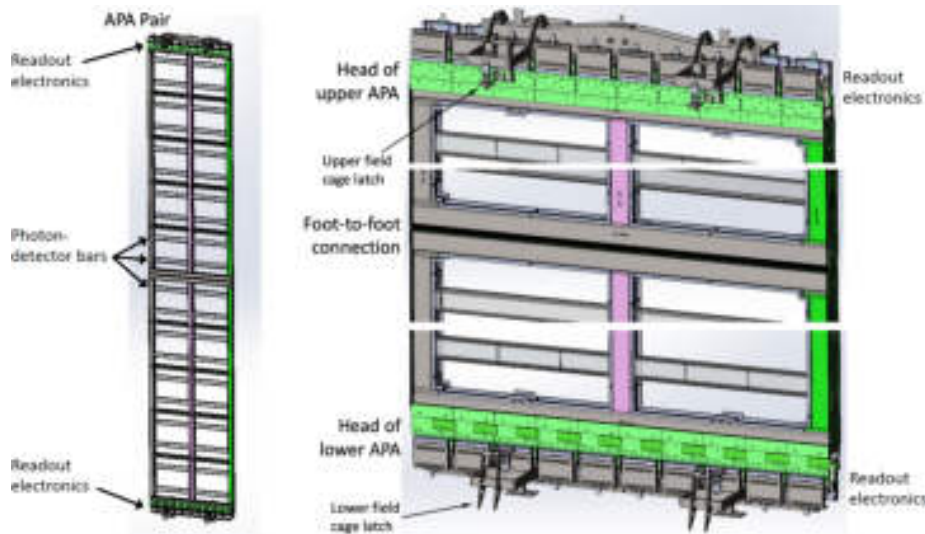


**Figure 1.5.** Left: two APAs linked together to form one unit of an APA wall. PD bars can be seen installed across the width of the APAs. Right: a zoom into the top and bottom ends of the APA stack showing the readout electronics, and the center of the stack where the APAs are connected together.

DAQ system, built around the Front-End Link eXchange (FELIX) system, developed by European Organization for Nuclear Research (CERN), which is responsible for triggering, buffering, and shipping data out to permanent storage above ground; when triggered, each 10 kt module will provide data at a rate of up to 2 TB/s. This separation of DAQ systems allows each module to run as an independent detector to minimize any chance of a complete FD outage. Modules can, however, provide the others with a supernova trigger signal. The DAQ system also provides the detector clock. A Global Positioning System (GPS) one-pulse-per-second signal (1PPS signal) is used to time-stamp events, both to allow matching to the beam window and to allow time-stamping of supernova triggers. Within a 10 kt module a 62.5 MHz master clock keeps all detector components synchronized to within 1 ns.

In addition to the ionization, charged particles passing through the argon produce approximately 24,000 scintillation photons per MeV. These photons are collected by devices called X-Arapucas, which are mounted in the APAs, in between the two sets of wire layers, as shown in figure 1.5. There are ten X-Arapucas on each APA, which are bars running the full 2.3 m width of the APA. The X-Arapuca bars consist of layers of dichroic filter and wavelength-shifter that shift the VUV scintillation light into the visible and trap these visible photons, transporting them to silicon photomultiplier (SiPM) devices. The signals from these SiPMs are sent along cables that pass through the hollow APA frames, up to feedthroughs in the cryostat roof. The signals are then sent along 10 Gbps optical fibers, one fiber per APA (ten X-Arapuca bars), to the DAQ system where the PD and APA-wire data-streams are merged.

#### 1.4 The liquid argon

The primary requirement of the LAr is its purity. Electronegative contaminants such as oxygen or water absorb ionization electrons as they drift. Nitrogen contaminants quench scintillation photons.

The target purity from electronegative contaminants in the argon is  $<100$  ppt (parts per trillion)  $\text{O}_2$  equivalent, which is enough to ensure a  $>3$  ms ionization-electron lifetime at the nominal 500 V/cm drift voltage. This target electron lifetime means that, for a charged particle traveling near a CPA array, there is 48% attenuation of the ionization by the time it reaches the anode, which ensures that we achieve S/N ratios of  $S/N > 5$  for the induction planes and  $S/N > 10$  for the collection planes, which are necessary to perform pattern recognition and two-track separation. We have an additional requirement for electronegative impurities released into the argon by detector components of  $<30$  ppt, to ensure such sources of contamination are negligible compared to the contamination inherent in the argon. Data from ProtoDUNE has shown that we can exceed our target argon purity, with electron lifetimes in excess of 6 ms achieved.

Nitrogen contamination must be  $<25$  ppm (parts per million). This is necessary to ensure we achieve our requirement of at least 0.5 photoelectrons per MeV detected for events in all parts of the detector, which in turn ensures, through the timing requirements discussed in section 1.5, that we can fiducialize nucleon decay events throughout the detector.

Fundamental to maintaining argon purity is the constant flow of argon through the purification system. It is, therefore, important to understand the fluid dynamics of the argon flow within the detector to ensure there are no dead regions where argon can become trapped. This fluid dynamics also informs the placement of purity, temperature, and level monitors.

### 1.5 Photon detection system

Compared to the ionization electrons, which can take milliseconds to drift across the drift volume, the scintillation photons are fast, arriving at the PDs nanoseconds after production. This scintillation light provides a  $t_0$  for each event. By comparing the arrival time of ionization at the anode with this  $t_0$ , reconstruction in the drift direction becomes possible. A  $1\ \mu\text{s}$  requirement on the timing resolution of the PD system enables  $\sim 1$  mm position resolution for 10 MeV SNB events. The PD  $t_0$  is also vital in fiducializing nucleon-decay events, which allows us to reject cosmic-muon-induced background events that will occur near the edges of the detector modules. We must be able to do this throughout the entire active volume with  $>99\%$  efficiency, leading to a requirement of at least 0.5 photoelectrons per MeV detected for events in all parts of the detector. These requirements are discussed later in chapter 5.

PD modules, shown in figure 1.6, are  $209\ \text{cm} \times 12\ \text{cm} \times 2\ \text{cm}$  bars, ten of which are mounted in each APA between the wire layers. Each bar contains 24 X-Arapuca<sup>1</sup> cells, grouped into four supercells. An X-Arapuca cell is shown in figure 1.7. The outer layers are dichroic filters transparent to the 127 nm scintillation light. Between these filters is a wavelength-shifting (WLS) plate, which converts the UV photons into the visible spectrum (430 nm); one WLS plate runs the full length of each supercell. Visible photons emitted inside the WLS plate at an angle to the surface greater than the critical angle reach SiPMs at the edges of the plates. Visible photons that escape the WLS plates are reflected off the dichroic filters, which have an optical cutoff, reflecting photons with wavelengths more than 400 nm back into the WLS plates.

---

<sup>1</sup>An arapuca is a South American bird trap, the name used here in analogy to the way the X-Arapuca devices trap photons.

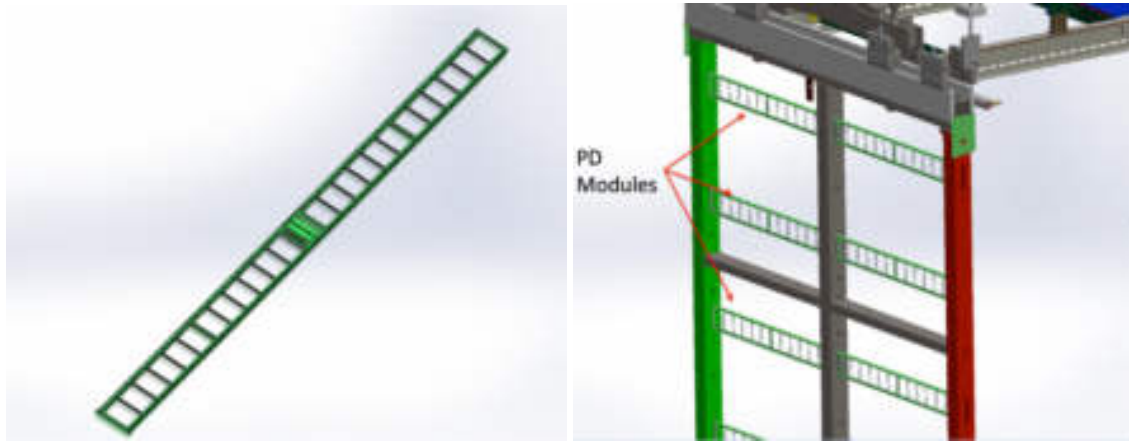


**Figure 1.6.** Left: an X-ARAPUCA PD module. The 48 SiPMs that detect the light from the 24 cells are along the long edges of the module. Right: X-ARAPUCA PD modules mounted inside an APA.

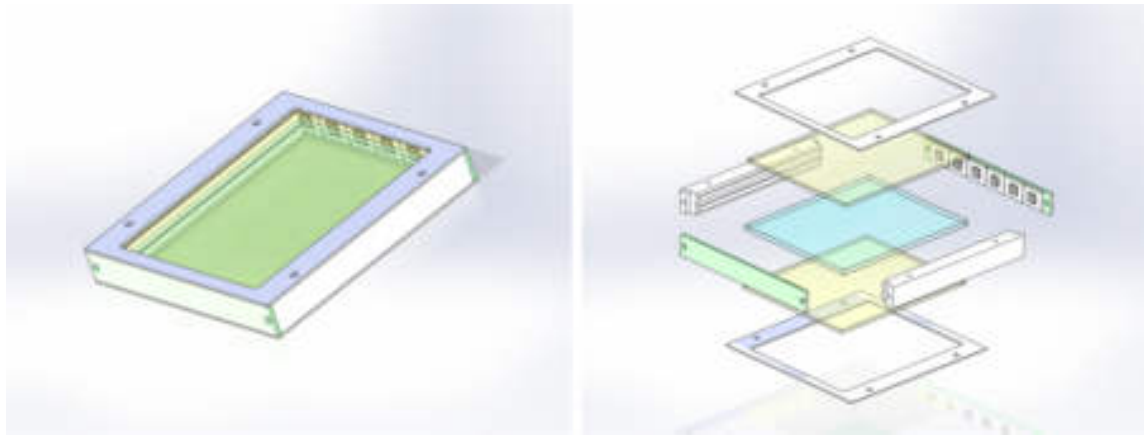


**Figure 1.7.** Left: an X-Arapuca cell. Right: an exploded view of the X-Arapuca cell, where the blue sheet is the wavelength-shifting plate and the yellow sheets the dichroic filters.

The 48 SiPMs on each X-Arapuca supercell are ganged together and the signals are collected by front-end electronics, mounted on the supercell. The design of the front-end electronics is inspired by the system used for the Mu2e cosmic-ray tagger [7], which uses commercial ultrasound ASICs. The front-end electronics define the  $1 \mu\text{s}$  timing resolution of the PD system.

## 1.6 High voltage, cathode planes and field cage

The design voltage at which the DUNE TPC will operate is  $-180 \text{ kV}$ , corresponding to  $500 \text{ V/cm}$  across each drift volume. This voltage is a trade off. A higher voltage results in more charge collected, and hence better S/N ratio, better calorimetry, and lower detection thresholds, as well as less saturation of free charge at the point of ionization. A higher voltage, however, also reduces the amount of scintillation light produced and requires more space between the CPAs and the cryostat walls to prevent discharges, reducing the fiducial volume. The ProtoDUNE experience shows that

we can achieve this design voltage; nevertheless, from MicroBooNE, we also know that a drift voltage of 250 V/cm achieves an adequate S/N ratio.

The high voltage (HV) is supplied to the CPA arrays. Each CPA array (two per 10 kt module) has its own independent high voltage supply. These commercial high voltage devices will supply a current of 0.16 mA at  $-180$  kV. The voltage is delivered, via  $\sim 30$  m length commercial cables, through a series of few-M $\Omega$  filtering resistors that act as low-pass filters to reduce noise and thereby satisfy the ripple-voltage requirement of  $< 0.9$  mV on the CPA array, which corresponds to a requirement of  $< 100 e^-$  of noise injected into the TPC by the high-voltage system. The supply unit monitors the voltage and current every 300 ms; toroids mounted on the cables are sensitive to much faster changes in current and enable responses to current changes on a timescale of 0.1  $\mu$ s to 10  $\mu$ s.

The high voltage passes into the cryostat through a feedthrough based on the ICARUS design [2], the stainless steel conductor of which mates with the CPA array via a spring-loaded feedthrough. When at  $-180$  kV, each CPA array stores 400 J of energy, so the CPAs must have at least 1 M $\Omega$ /cm<sup>2</sup> resistance to prevent damage if the field is quenched. The CPA, an example of which from ProtoDUNE is shown in figure 1.8, is a 1.2 m  $\times$  4 m planar unit, each side of which is a 3 mm thick FR-4 sheet, onto which is laminated a thin layer of carbon-impregnated Kapton that forms the resistive cathode plane.



**Figure 1.8.** A ProtoDUNE-SP cathode plane assembly. The black surface is the carbon-impregnated Kapton resistive cathode plane.

The field must be uniform throughout the active TPC volume to within 1%, and this is achieved by a FC that surrounds the drift volumes. The FC is built from field-shaping aluminum profiles, terminated with 6 mm thick ultra-high molecular-weight polyethylene caps (see figure 1.9). All surfaces on these profiles must be smooth to keep local fields below 30 kV/cm, a requirement that reduces the possibility of voltage breakdowns in the argon; the shape of the profiles leads to a maximum local field near the surface of the FC of  $\sim 12$  kV/cm. The aluminum profiles are connected together via a resistive divider chain; between each profile, two 5 G $\Omega$  resistors, arranged in parallel, provide a 2.5 G $\Omega$  resistance to create a nominal 3 kV drop.



**Figure 1.9.** A section of the field cage, showing the extruded aluminum field-shaping profiles, with white polyethylene caps on the ends to prevent discharges.

### 1.7 Anode planes

The APAs are  $6\text{ m} \times 2.3\text{ m}$  planes that form the three anode walls of the TPC. An APA is shown in figure 1.10. In the FD, the APAs are mounted in pairs, in portrait orientation, one above another, with the head end of the top APA at the top of the detector and the head end of the bottom APA at the bottom of the detector.

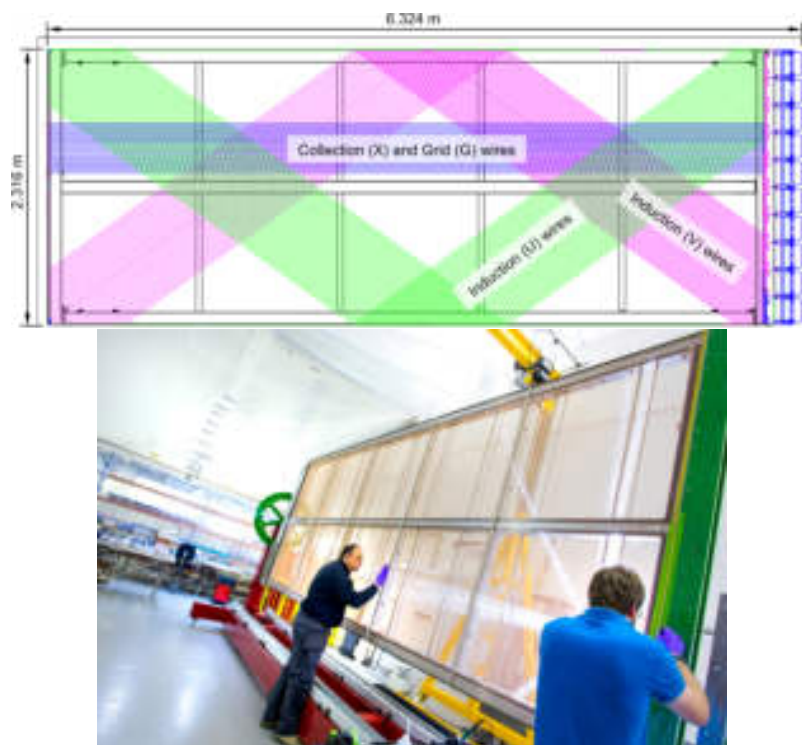


**Figure 1.10.** Top: a schematic of an anode plane assembly. In black is the steel APA frame. The green and pink areas indicate the directions of the induction wire layers. The blue area indicates the directions of the induction and shielding (grid) wire layers. The blue boxes at the right-hand end are the CE. Bottom: a ProtoDUNE APA in a wire-winding machine. The right-hand end of the APA as shown in this picture is the head end, onto which the CE are mounted.



The basic building block of the APA is the steel frame that can be seen outlined in figure 1.10, consisting of three long steel bars, a head shaft onto which the CE are mounted, a foot shaft, and four thinner cross-braces. The two outer long sections are 4 inch  $\times$  4 inch square-profile steel tubes through which run the PD cables and the CE cables from the bottom APA of a pair. The PDs are mounted into the APAs, after production, through slots in these long sections.

Mounted directly onto both sides of the APA frame is a grounding mesh, which ensures any ionization produced inside the APA cannot cause signals on the active wire layers. The four wire layers, consisting of 152  $\mu\text{m}$  diameter copper-beryllium wire, are wound around the grounding mesh. The inside layer is the collection layer, called the  $X$ -layer, the 960 wires of which run parallel to the long axis of the APA. Next are the two induction layers, the  $U$ - and  $V$ -layers, each with 800 wires at  $\pm 35.7^\circ$  to the long axis. Finally, the uninstrumented shielding layer, the  $G$ -layer, has 960 wires running parallel to the  $X$ -layer wires; this layer shields the three active layers from long-range induction effects. The wire spacing on each layer is 4.79 mm for the  $X$  and  $G$  layers and 4.67 mm for the  $U$  and  $V$  layers; the inter-plane spacing is 4.75 mm. The wire spacing on each plane defines the spatial resolution of the APA; it is wide enough to keep readout costs low and S/N high, but small enough to enable reconstruction of short tracks such as few-cm kaon tracks from proton-decay events. The tolerance both on the wire spacing in the plane and on the plane-to-plane spacing is 0.5 mm; this is most important in the plane-to-plane direction where the spacing ensures that the induction planes remain transparent to the drifting charge.

The wires are soldered to printed circuit boards located around the four sides of the APA. These boards, shown in figure 1.11, are called geometry boards since they define the wire spacing in all dimensions; they consist only of pads and traces: no active components. At the head end, these boards lie flat in the plane of the APA, and the wires are terminated onto these boards for readout. On the remaining three sides, the boards sit on the sides of the APA, perpendicular to the wire planes, and control the wrapping of the wires around the APA. These wrap boards have insulating pins on their edges, around which the wires are wrapped, to set the wire spacing. At the head end, additional active boards are installed after all wires are wound:  $G$ -bias boards provide the necessary capacitance to the  $G$ -layer and a resistor to provide the bias voltage;  $CR$ -boards provide the interface between the  $X$  and  $U$  layers and the CE, resistors providing the bias voltages and capacitors providing DC blocking. Relative to the ground, the four wire layers are biased to 820 V ( $X$ -layer), 0 V ( $V$ -layer),  $-370$  V ( $U$ -layer), and  $-665$  V ( $G$ -layer). To maintain the wire spacing across the APA, wire-support combs, also shown in figure 1.11, run along the four cross-braces across the short dimension of the APA.

### 1.8 Electronics

The job of the readout electronics is to send out of the cryostat digitized waveforms from the APA wires. To enable us to look at low-energy particles, we aim to keep noise to below  $1000 e^-$  per channel, which should be compared to the  $20k$ – $30k e^-$  per channel collected from a minimum-ionizing particle traveling parallel to the wire plane and perpendicular to the wire orientation. For large signals, we require a linear response up to  $500k e^-$ , which ensures that fewer than 10% of beam events experience saturation. This can be achieved using 12 analog-to-digital converter (ADC) bits. In addition, the electronics are designed with a front-end peaking time of 1  $\mu\text{s}$ , which matches the

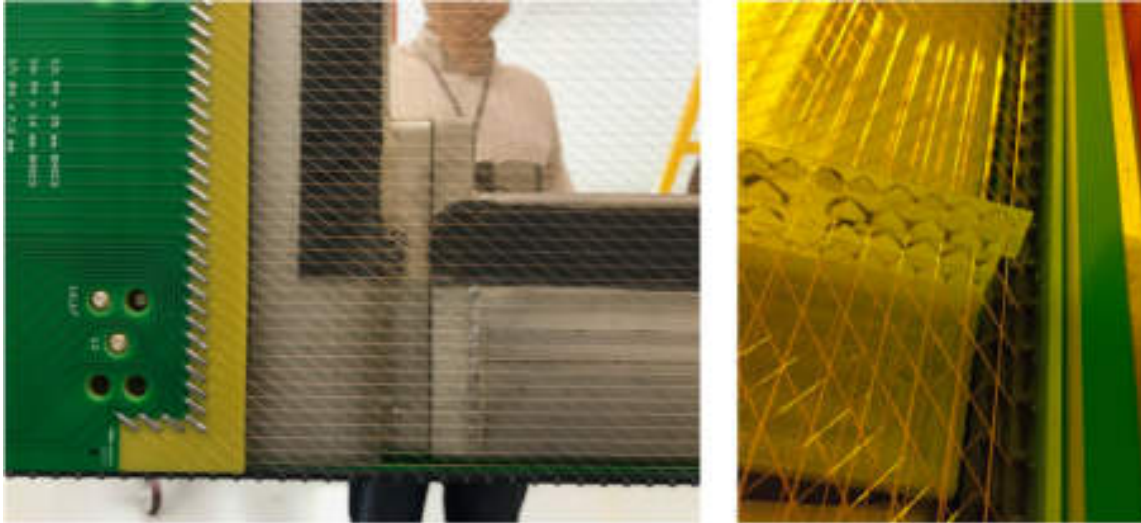


**Figure 1.11.** Left: V-layer geometry boards, showing the head-end boards face-on and the wrap boards along the bottom. Back plastic insulating pins are visible on the edges of the wrap boards. The V-layer wires can be seen running diagonally, and the X-layer wires, horizontal in this picture, are visible behind those. Right: wire-support combs, showing all four layers of wires.

time for the electrons to drift between wires planes on the APA; this then leads to a design sampling frequency of 2 MHz to satisfy the Nyquist criterion.

The digitization electronics are mounted on the head ends of the APAs in the LAr and are therefore referred to as CE. The low, 87 K temperatures reduce thermal noise. Figure 1.12 shows a block diagram of the front-end mother board (FEMB)s mounted on the APAs. Each APA is instrumented with 20 FEMBs, each of which takes the signals from 40 U-layer wires, 40 V-layer wires, and 48 X-layer wires. The signals pass through a series of three ASICs. The first ASIC, the front-end ASIC, shapes and amplifies the signals. The next ASIC, the ADC ASIC, performs the analogue-to-digital conversion. Finally, a COLDATA ASIC merges the data streams from the preceding ASICs for transmission to the outside world; this COLDATA ASIC also controls the front-end motherboard and facilitates communications between the motherboard and the outside world.

The data passes out of the cryostat through feedthroughs in the roof. Mounted directly to each feedthrough is a warm interface electronics crate (WIEC). Each WIEC contains five warm interface board (WIB)s, each of which processes the signals from five FEMBs. A WIEC also contains a power and timing card (PTC) that provides the fiber interface to the timing system, fanning out timing and control systems, as well as the low-voltage power, to the WIBs via a power and timing backplane (PTB).

## 1.9 Data acquisition

The DAQ is divided between an upstream section, located underground in the CUC, and a downstream DAQ back-end subsystem (DAQ BE) above ground at SURF. All trigger decisions are made underground, and the data buffered underground until the DAQ BE indicates it is ready to receive

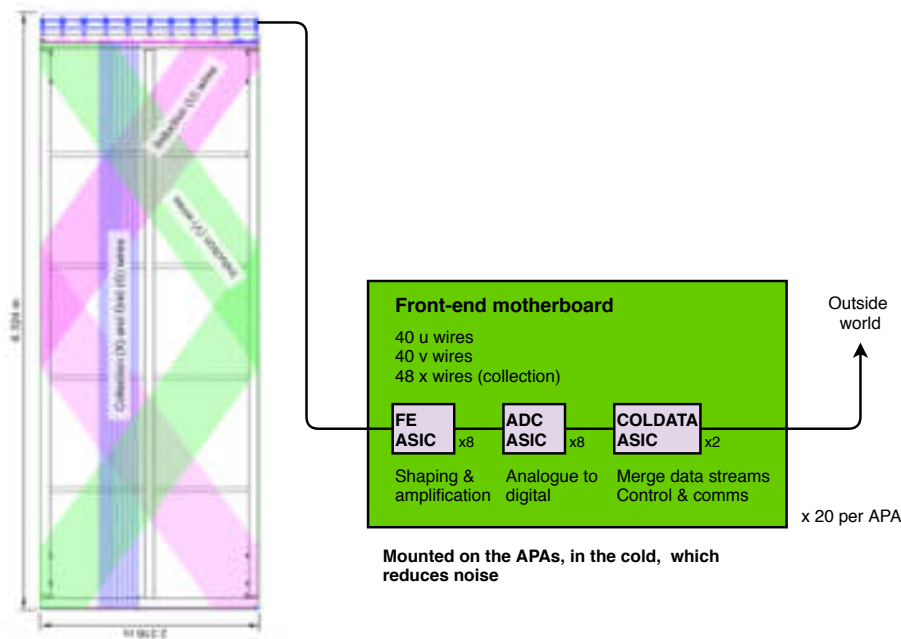


**Figure 1.12.** Left: an APA with 20 FEMBs installed on the head end. Right: a block diagram of the readout electronics mounted on the APAs.

data, in order to minimize the rate of data flowing to the surface. An end-goal of the DAQ is to achieve a data-rate to tape of no more than 30 PB/year.

The DAQ architecture is based on the FELIX system designed at CERN and used for the LHC experiments. The 150 APAs from each 10 kt module are processed by 75 DAQ readout unit (DAQ RU); each DAQ RU contains one FELIX board. The PDs from the module will have a lower data-rate since the PD electronics, unlike that of the TPC, perform zero-suppression; therefore the PDs of a module will be processed by six to eight additional DAQ RUs. The DAQ will be partitionable: it will be possible to run multiple instances of the DAQ simultaneously so that the majority of the detector can be taking physics data whilst other DAQ instances are running test runs for development or special runs such as calibration runs. A key philosophy is that all the primary DUNE physics goals can be achieved using only the TPC as the trigger; information from the PDs can then further enhance the trigger.

There will be two basic triggers operating. Beam, cosmic and nucleon decay events will be triggered using the localized high-energy trigger. This will trigger on localized regions of visible activity, for example in a single APA, with a  $> 99\%$  trigger efficiency at 100 MeV and a trigger threshold as low as 10 MeV. A localized high-energy trigger will open a readout window of 5.4 ms, enough to read out the full TPC drift around an event. For SNBs, we will use an extended low-energy trigger. This will look for coincident regions of low-energy deposits, below 10 MeV, across an entire module and in a 10 s period. An extended high-energy trigger will open a readout window of 100 s to capture a full SNB. The upstream DAQ identifies per-channel regions of interest and forms them into trigger primitives. These are then formed into trigger candidates that contain information from an entire module; on these trigger candidates, trigger decisions are made. Once

a trigger decision has been made, this will be communicated to the surface, and the data buffered underground until the DAQ BE indicates it is ready to receive data.

The DAQ must also provide the system clock that keeps the detector components synchronized and provides the timestamp for all data. The timestamp derives from a GPS 1PPS signal that is fed into the DAQ with 1  $\mu$ s precision, adequate to timestamp beam and supernova events. To provide the finer synchronization between detector components, a 10 MHz reference clock drives the module's 62.5 MHz master clock, which is fanned out to all detector components, providing an overall synchronization to a precision of 1 ns.

## 1.10 Calibration

The challenge of calibrating the DUNE FD is to control the response of a huge cryogenic detector over a period of decades, a challenge amplified by the detector's location deep underground and therefore shielded from the cosmic muons that were typically used as standard candles by previous LArTPCs.

To achieve our  $O(\text{GeV})$  oscillation and nucleon decay physics goals, we must know our fiducial volume to 1–2% and have a similar understanding of the vertex position resolution; understand the  $\nu_e$  event rate to 2%; and control our lepton and hadron energy scales to 1% and 3%, respectively. At the  $O(\text{MeV})$  scale our physics requirements are driven by our goal of identifying, and measuring the spectral structure of, a SNB; here, we must achieve a 20–30% energy resolution, understand our event timing to the 1  $\mu$ s level, and measure our trigger efficiency and levels of radiological background. These are all high-level calibration requirements, but the underlying detector parameters that we are characterizing are parameters such as the energy deposited per unit length ( $dE/dx$ ), ionization electron drift-lifetimes, scintillation light yield and detection efficiency, E field maps, timing precision, TPC alignment, and the behavior (noise, gain, cross-talk, linearity, etc.) of electronics channels.

The tools available to us for calibration include the LBNF beam, atmospheric neutrinos, atmospheric muons, radiological backgrounds, and dedicated calibration devices that will be installed in the detector. At the lowest energies, we have deployable neutron sources and intrinsic radioactive sources; in particular the natural  $^{39}\text{Ar}$  component of the LAr with its 565 keV end-point can, given its pervasive nature across the detector, be used to measure the spatial and temporal variations in electron lifetime. The possibility of deploying radioactive sources is also being explored. In the 10 MeV to 100 MeV energy range we will use Michel electrons, photons from  $\pi^0$  decay, stopping protons and both stopping and through-going muons. We will also have built-in lasers, purity monitors and thermometers, and the ability to inject charge into the readout electronics. Finally, data from the ProtoDUNE detectors will be invaluable in understanding the response and particle-identification capabilities of the FD.

Once the first 10 kt module is switched on, there will be a period of years before LBNF beam sources are available for calibration — and even then the statistics will be limited. In this time, cosmic muons will be available, but the low rate of these means that it will take months to years to build up the necessary statistics for calibration. The inclusive cosmic muon rate for each 10 kt module is  $1.3 \times 10^6$  per year. However, for calibrations such as APA alignment, the typical rate of useful muons is 3000–4000 per APA per year. For energy-scale calibrations, stopping cosmic

muons are the most relevant and here the rate is 11000 per 10 kt module per year. Therefore the earliest calibrations will come from dedicated calibration hardware systems and intrinsic radiological sources.

A 266 nm laser will be used to ionize the argon, and this can be used to map the E field and to make early measurements of APA alignment. The laser system will be used throughout the lifetime of the detector to measure the gradual changes in the E field map as positive ions accumulate and flow around the detector. An externally deployed pulsed neutron source provides a triggered, well defined energy deposition from neutron capture in argon which is an important component of signal processes for SNB and long-baseline (LBL) physics. A radioactive source deployment system, which is complementary to the pulsed neutron system, can provide at known locations inside the detector a source of gamma rays in the same energy range as SNB and solar neutrino physics

Over time, the FD calibration program will evolve as statistics from the cosmic rays and the LBNF beam amass and add to the information gained from the calibration hardware systems. These numerous calibration tools will work alongside the detector monitoring system, the computational fluid dynamics models of the argon flow, and ProtoDUNE data to give us a detailed understanding of the FD response across the DUNE physics program.

### 1.11 Installation

A major challenge in building the DUNE SP modules is transporting all the detector and infrastructure components down the 1500 m Ross shaft, to the detector caverns. To aid the planning of the installation phase, installation tests will be performed at the NOvA FD site in Ash River, Minnesota, USA. These tests will allow us to develop our procedures, train the installation workers, and develop our labor planning through time and motion studies.

Once the module's cryostat has been installed, a temporary construction opening (TCO) is left open at one end through which the detector components are installed. A cleanroom is built around the TCO to prevent any contamination entering the cryostat during installation. The detector support system (DSS) is then installed into the cryostat, ready to receive the TPC components.

Inside the cryostat, the various monitor devices (temperature, purity, argon level) are installed at the end furthest from the TCO. The far end of the FC is then installed. Rows of APAs and CPAs, along with the top and bottom FC sections, are then installed and cabled, working from the far end of the detector towards the TCO. The integration of the PDs and CE with the APA happens in the cleanroom immediately outside the TCO. Finally, the second FC end-wall is installed across the TCO, along with the monitoring devices at the TCO end. The TCO can then be closed up and the cryostat is ready to purge and fill with LAr. The warm electronics and DAQ are installed in parallel with the TPC installation.

Throughout the installation process, safety is the paramount consideration: safety both of personnel and of the detector components. Once the detectors are taking data, safety is still the priority with the DUNE detector safety system (DDSS) monitoring for argon level drops, water leaks and smoke. A detailed detector and cavern grounding scheme has been developed that not only guards against ground loops, but also ensures that any power faults are safely shunted to the facility ground.

Throughout the project, quality assurance (QA) and quality control (QC) are written into all processes. Most detector components are constructed off-site at collaborating institutions; strict QC procedures will be followed at all production sites to ensure that components are working within specifications before delivery to SURF. Underground at SURF integrated detector components are tested in the cleanroom to ensure functionality, before passing them through the TCO for installation. Finally, QC is performed on all integrated components inside the cryostat, in particular to ensure that all connections have been made through to the CUC.

## 1.12 Schedule and milestones

A set of key milestones and dates have been defined for planning purposes in the development of the TDR. The dates will be finalized once the international project baseline has been defined. Table 1.2 shows the key dates and milestones (colored rows) and indicates the way that detector consortia will add subsystem-specific milestones based on these dates (no background color). A more detailed schedule for the detector installation is discussed in chapter 9.

**Table 1.2.** (Sample subsystem) construction schedule milestones leading to commissioning of the first two FD modules. Key DUNE dates and milestones, defined for planning purposes in this TDR, are shown in orange. Dates will be finalized following establishment of the international project baseline.

| Milestone   | Date (Month YYYY) |
|---|-------------------|
| Technology Decision Dates   | April 2020        |
| Final Design Review Dates   | June 2020         |
| Start of module 0 component production for ProtoDUNE-2              | August 2020       |
| End of module 0 component production for ProtoDUNE-2                | January 2021      |
| Start of ProtoDUNE-SP-II installation                               | March 2021        |
| Start of ProtoDUNE-DP-II installation                               | March 2022        |
| South Dakota Logistics Warehouse available                          | April 2022        |
| production readiness review dates                                   | September 2022    |
| Beneficial occupancy of cavern 1 and CUC                            | October 2022      |
| Start procurement of (subsystem) hardware                           | December 2022     |
| CUC counting room accessible  | April 2023        |
| Top of detector module #1 cryostat accessible                       | January 2024      |
| Start of detector module #1 TPC installation                        | August 2024       |
| Top of detector module #2 cryostat accessible                       | January 2025      |
| End of detector module #1 TPC installation                          | May 2025          |
| Start of detector module #2 TPC installation                        | August 2025       |
| End of detector module #2 TPC installation                          | May 2026          |
| Full (subsystem) commissioned and integrated into remote operations | July 2026         |

### 1.13 Conclusion

This executive summary has provided an overview of the design of the 10 kt SP LArTPC modules of the DUNE FD, explaining how key design choices have been made to ensure we can achieve our primary physics goals of searching for leptonic  $CP$  violation, nucleon decay and neutrinos from supernova bursts. The chapters that follow go into significantly more detail about the design of the SP FD modules. In addition to describing the design and requirements, these chapters include details on the construction, integration and installation procedures, the QA and QC processes that have been developed to ensure that the detector will function for a period of decades, and the overall project management structure. The chapters also describe how the design has been validated and informed by ProtoDUNE.

2020 JINST 15 T08010

## Chapter 2

# Anode plane assemblies

### 2.1 Anode plane assembly (APA) overview

The anode plane assemblies, or wire planes, are the DUNE SP module elements used to sense, through both signal induction and direct collection, the ionization electrons created when charged particles traverse the LAr volume inside the SP module. All elements of the DUNE physics program depend on a high performing system of APAs and their associated readout CE.

Volume II of this TDR, DUNE physics, describes the simulations that rigorously establish the requirements for achieving the needed performance. Here we summarize some of the APA capabilities required for the key elements of neutrino charge-parity symmetry violation (CPV) and associated long-baseline oscillation physics, nucleon decay (NDK), and intra-galactic SNB searches. As a multipurpose detector accessing physics from MeV to multi-GeV scales, the DUNE LArTPC cannot be optimized for a narrow range of interaction signatures in the manner of noble liquid TPCs dedicated to direct dark matter (DM) or neutrino-less double beta decay searches. The APAs must collect ionization charge in a way that preserves the spatial and energy profiles of ionization events that range from few hundred keV point-like depositions (from low energy electrons and neutrons created in SNB neutrino interactions) to the double-kinked  $K \rightarrow \mu \rightarrow e$  decay chain with its combination of highly- and minimum-ionizing particles (HIPs and MIPs) that is a key signature in proton decay searches. The APAs must record enough hits on tracks within a few cm of a neutrino interaction vertex to differentiate the 1 minimum ionizing particle (MIP)  $dE/dx$  signature of a  $\nu_e$ -induced electron from the 2 MIP signature of a  $\nu$  neutral current photon conversion to enable the  $\nu_\mu - \nu_e$  separation demanded for CPV physics; and they must provide the pattern recognition and calorimetry for multi-GeV neutrino interaction products spread over cubic meters of the detector needed for the precision neutrino energy estimates that allow separation of CPV effects from those related to matter effects.

Anode planes in the APA must be well-shielded from possible high voltage breakdown events in the detector module. The APA wire spacing and orientations must maximize pattern recognition capabilities and S/N in a cost-effective manner. The APA wires must maintain their positions to a level that is small compared to the wire spacing so that energy estimators based on range and multiple Coulomb scattering remain reliable over two decades of operation. The wires must hold their tension, lest microphonic oscillations develop that degrade S/N or anode plane field distortions



arise that inhibit the transmission of drifting electrons through the induction planes to the collection plane. Any wire break would destroy fiducial volumes (FVs), so the APA design must both minimize the possibility of this occurrence and contain the extent of any damage that would ensue should it happen. An APA implementation that meets all these goals follows in the remainder of this chapter, along with a summary of significant validations achieved through dedicated simulations and ProtoDUNE-SP construction and operations.

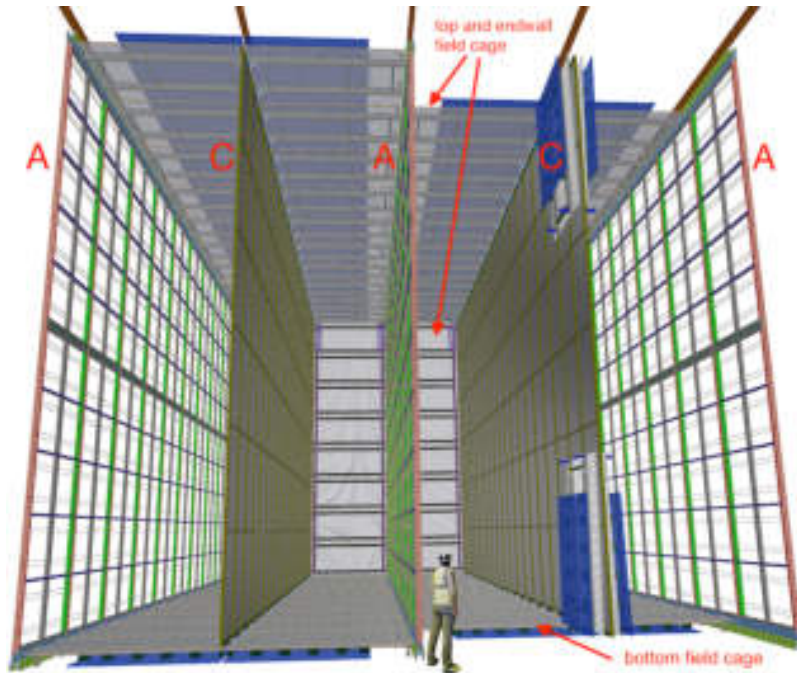


**Figure 2.1.** A 10 kt DUNE FD SP module, showing the alternating 58.2 m long (into the page), 12.0 m high anode (A) and cathode (C) planes, as well as the field cage (FC) that surrounds the drift regions between the anode and cathode planes. On the right-hand cathode plane, the foremost portion of the FC is shown in its undeployed (folded) state.

To facilitate fabrication and installation underground, the anode design is modular, with APAs tiled together to form the readout system for a 10 kt detector module. A single APA is 6 m high by 2.3 m wide, but two of them are connected vertically, and twenty-five of these vertical stacks are linked together to define a 12.0 m tall by 58.2 m long mostly-active readout plane. As described below, the planes are active on both sides, so three such wire readout arrays (each one 12.0 m  $\times$  58.2 m) are interleaved with two HV surfaces to define four 3.5 m wide drift regions inside each SP module, as figure 2.1 shows in the detector schematic views. Each SP 10 kt module, therefore, will contain 150 APAs.

Each APA frame is covered by more than 2500 sense wires laid in three planes oriented at angles to each other: a vertical collection plane,  $X$ , and two induction planes at  $\pm 35.7^\circ$  to the vertical,  $U$  and  $V$ . Having three planes allows multi-dimensional reconstruction of particle tracks even when the particle propagates parallel to one of the wire plane directions. An additional 960 wires that are not read out make up an outer shielding plane,  $G$ , to improve signal shapes on the  $U$  induction channels. The angled wires are wrapped around the frame from one side to the other,

allowing all channels to be read out from one end of the APA only (the top or bottom), thereby minimizing the dead regions between neighboring APAs. Signals induced or collected on the wires are transferred through soldered connections to wire termination boards mounted at the end of the APA frame that in turn connect to FE readout CE sitting in the LAr. Figures 2.2 and 2.3 illustrate the layout of the wires on an APA, showing how they wrap around the frame and terminate on wire boards at the head end where readout CE are mounted.

The APAs are a critical interface point between the various detector subsystems within the SP module. As already mentioned, the TPC readout CE mount directly to the APA frames. The PDs for detecting scintillation light produced in the LAr are also housed inside the frames, sandwiched between the wires on the two sides, requiring careful coordination in frame design as well as requiring transparency for the APA structures. In addition, the electric field cage (FC) panels connect directly to the edges of the APA frames. Finally, the APAs must support routing cables for both the TPC electronics and the PD systems. All these considerations are important to the design, fabrication, and installation planning of the APAs.

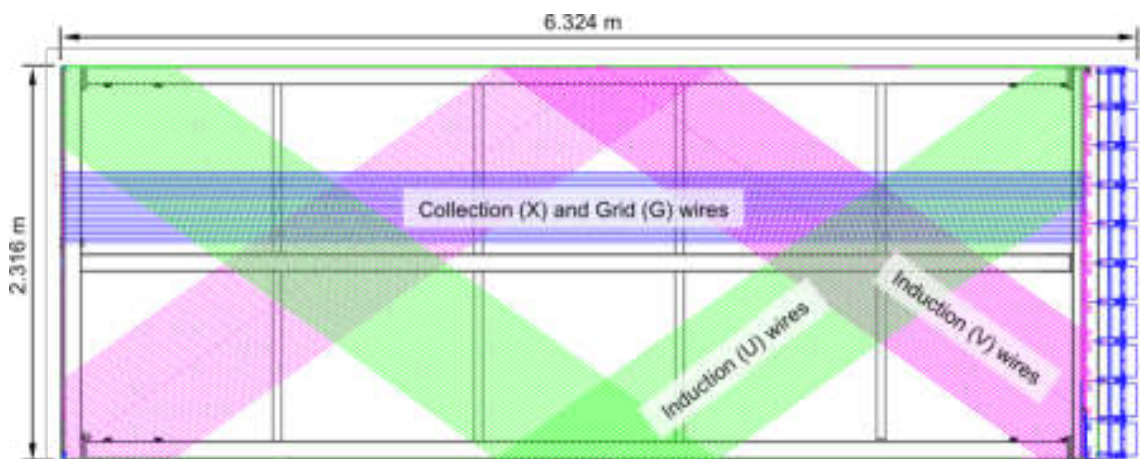


**Figure 2.2.** Illustration of the DUNE APA wire wrapping scheme showing small portions of the wires from the three signal planes ( $U$ ,  $V$ ,  $X$ ). The fourth wire plane ( $G$ ) above these three, and parallel to  $X$ , is present to improve the pulse shape on the  $U$  plane signals. The TPC electronics boxes, shown in blue on the right, mount directly to the frame and process signals from both the collection and induction channels. The APA is shown turned on its side in a horizontal orientation.

The APA consortium oversees the design, construction, testing, and installation of the APAs. Several APA production sites will be set up in both the US and the UK with each nation producing half of the APAs needed for the SP modules. Production site setup is anticipated to begin in 2020, with APA fabrication for the first 10 kt SP module running from 2021–2023.

The Physical Sciences Laboratory (PSL) at the University of Wisconsin and the Daresbury Laboratory in the UK have recently produced full-scale APAs for the ProtoDUNE-SP project at CERN. Figure 2.4 shows a completed APA produced at PSL just before shipment to CERN. This effort has greatly informed the design and production planning for the DUNE detector modules, and ProtoDUNE-SP running has provided valuable validation for many fundamental aspects of the APA design.

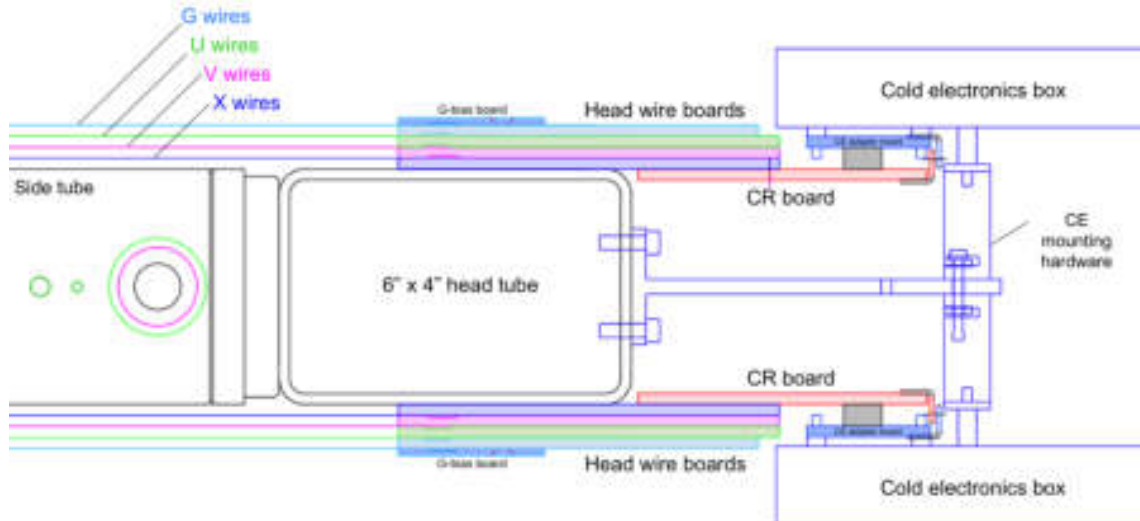


**Figure 2.3.** Cross section view of an APA frame near the head end showing the layers of wires ( $G, U, V, X$ ) on both sides of the frame that terminate on wire boards, which connect to TPC readout CE through a capacitor-resistor chain on the CR boards and a connector adapter board.

The remainder of this chapter is laid out as follows. In section 2.2, we present an overview of the design of the APAs, focusing on the key design parameters and their connection to the physics requirements of DUNE. In section 2.3, we discuss quality assurance for the design with an emphasis on lessons learned from ProtoDUNE-SP construction and operations and a summary of remaining prototyping efforts being planned before the start of production next year. Section 2.4 summarizes three important interfaces to the APAs: TPC cold electronics (CE), photon detectors (PD), and the cable routing for both systems. In section 2.5, we detail the production plan for fabricating the large number of APAs needed for the experiment including a description of the main construction sites being developed in the US and UK by the APA consortium. Section 2.6 describes some requirements for handling the large and delicate APAs throughout construction and presents the design for a custom transport system for delivery to the far detector site for installation. Section 2.7 reviews the safety considerations for APA construction and handling. Finally, section 2.8 summarizes the organization of the APA consortium that is responsible for building the APAs and provides the high-level cost, schedule, and risk summary tables for the project.

## 2.2 Design

The physics performance of the SP module is a function of many intertwined detector parameters including argon purity, drift distance, E field, wire pitch, wire length, and noise levels in the readout CE. Energy deposits from MIPs originating anywhere inside the active volume of the detector should be identifiable with near 100% efficiency. This requirement constrains aspects of the APA design, specifically, the limits on wire pitch, wire length, and choice of wire material. This section details the design of an individual APA. We begin with an overview of the key fundamental parameters of the APAs and their connection to the physics requirements of the DUNE experiment.

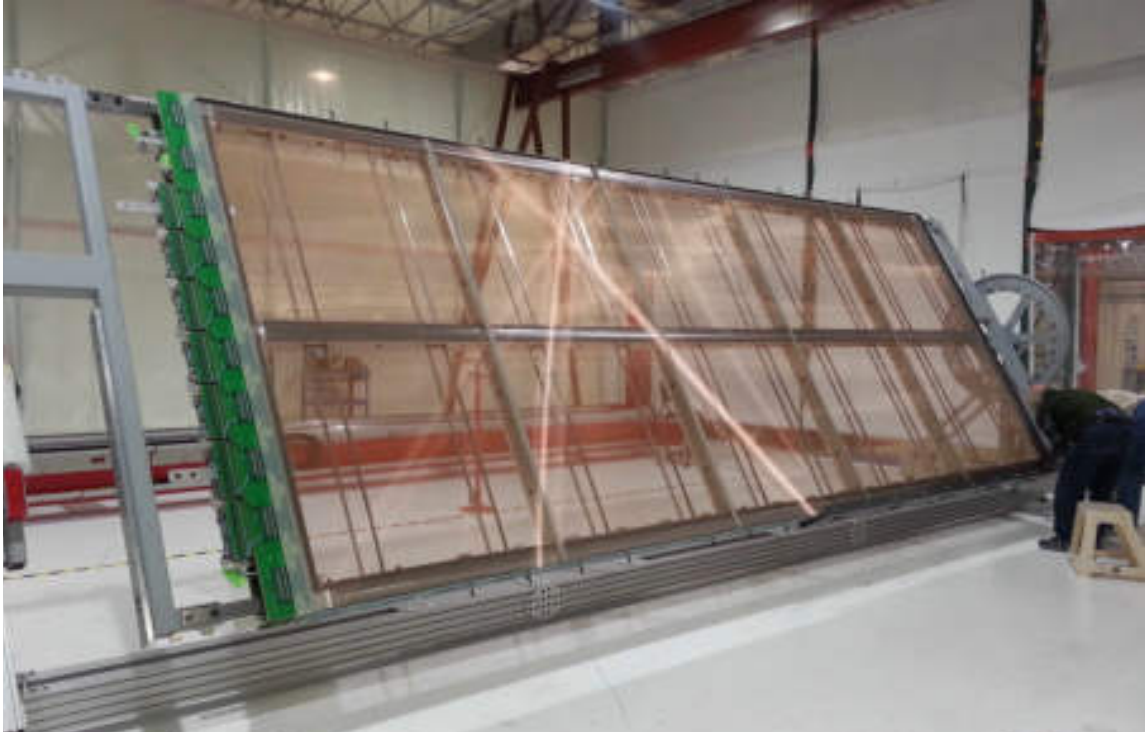


**Figure 2.4.** Completed ProtoDUNE-SP APA ready for shipment to CERN.

### 2.2.1 APA design parameters

Each APA is 6 m high, 2.3 m wide, and 15 cm thick. The underlying support frame is made from stainless steel hollow tube sections that are precisely machined and bolted together. A fine, conducting mesh covers the rectangular openings in the frame on both sides to define a uniform electrical ground plane (GP) behind the wires. The four layers of sense and shielding wires at varying angles relative to each other completely cover the frame. The wires terminate on boards that anchor them as well as provide the electrical connection to the TPC readout CE. Starting from the outermost wire layer, there is first an uninstrumented shielding (grid) plane (strung vertically,  $G$ ), followed by two induction planes (strung at  $\pm 35.7^\circ$  to the vertical,  $U, V$ ), and finally the collection plane (vertical,  $X$ ). All wire layers span the full height of the APA frame. The two planes of induction wires wrap in a helical fashion around the long edges and over both sides of the APA. Figures 2.2 and 2.3 illustrate the layout of the wire layers. Below, we summarize the key design parameters and the considerations driving the main design choices for the APAs. A tabulated summary of APA specific requirements is also provided in table 2.1.

**Table 2.1:** APA specifications.

| Label    | Description                                       | Specification (Goal)  | Rationale   | Validation   |
|----------|---|---|---|--|
| SP-FD-6  | Gaps between APAs                                 | < 15 mm between APAs on same support beam;<br>< 30 mm between APAs on different support beams | Maintains fiducial volume. Simplified construction.                     | ProtoDUNE  |
| SP-FD-7  | Drift field uniformity due to component alignment | < 1 % throughout volume   | Maintains APA, CPA, FC orientation and shape.                           | ProtoDUNE  |
| SP-FD-8  | APA wire angles                                   | 0° for collection wires, $\pm 35.7^\circ$ for induction wires                                 | Minimize inter-APA dead space.  | Engineering calculation  |
| SP-FD-9  | APA wire spacing                                  | 4.669 mm for U,V;<br>4.790 mm for X,G   | Enables 100% efficient MIP detection, 1.5 cm $yz$ vertex resolution.    | Simulation   |
| SP-FD-10 | APA wire position tolerance                       | $\pm 0.5$ mm  | Interplane electron transparency; $dE/dx$ , range, and MCS calibration. | ProtoDUNE and simulation   |
| SP-APA-1 | APA unit size                                     | 6.0 m tall $\times$ 2.3 m wide  | Maximum size allowed for fabrication, transportation, and installation. | ProtoDUNE-SP   |
| SP-APA-2 | Active area                                       | Maximize total active area.   | Maximize area for data collection                                       | ProtoDUNE-SP   |
| SP-APA-3 | Wire tension                                      | 6 N $\pm$ 1 N   | Prevent contact between wires and minimize break risk                   | ProtoDUNE-SP   |
| SP-APA-4 | Wire plane bias voltages                          | The setup, including boards, must hold 150% of max operating voltage.                         | Headroom in case adjustments needed                                     | E-field simulation sets wire bias voltages. ProtoDUNE-SP confirms performance. |
| SP-APA-5 | Frame planarity (twist limit)                     | <5 mm   | APA transparency. Ensures wire plane spacing change of <0.5 mm.         | ProtoDUNE-SP   |
| SP-APA-6 | Missing/unreadable channels                       | <1%, with a goal of <0.5%   | Reconstruction efficiency   | ProtoDUNE-SP   |

- **APA size:** the size of the APAs is chosen for fabrication purposes, compatibility with over-the-road shipping, and for eventual transport to the 4,850L at SURF and installation into a cryostat. The dimensions are also chosen so that an integral number of electronic readout channels and boards instrument the full area of the APA.
- **Detector active area:** APAs should be sensitive over most of the full area of an APA frame, with any dead regions between APAs due to frame elements, wire boards, electronics, or cabling kept to a minimum. The wrapped style shown in figure 2.2 allows all channels to be read out at the top of the APA, eliminating the dead space between APAs that would otherwise

be created by electronics and associated cabling. In addition, in the design of the SP module, a central row of APAs is flanked by drift-field regions on either side (figure 2.1), and the wrapped design allows the induction plane wires to sense drifted ionization that originates from either side of the APA. This double-sided feature is also effective for the APAs located against the cryostat walls where the drift field is on only one side; the grid layer facing the wall effectively blocks any ionization generated outside the TPC from drifting in to the wires on that side of the APA.

- **Wire angles:** the  $X$  wires run vertically to provide optimal reconstruction of beam-induced particle tracks, which are predominantly forward (in the beam direction). The angle of the induction planes on the APA,  $\pm 35.7^\circ$ , was chosen to ensure that each induction wire only crosses a given collection wire once, reducing the ambiguities that the reconstruction must address. Simulation studies (see next item) show that this configuration performs similarly to an optimal  $45^\circ$  wire angle for the primary DUNE physics channels. The design angle of the induction wires, coupled with their pitch, also satisfies the requirement of using an integer multiple of electronics boards to read out one APA.
- **Wire pitch:** the wire spacing, 4.8 mm for  $(X, G)$  and 4.7 mm for  $(U, V)$ , combined with key parameters for other TPC systems can achieve the required performance for energy deposits by MIPs while providing good tracking resolution and good granularity for particle identification. The SP requirement that it be possible to determine the fiducial volume to 1% implies a vertex resolution of 1.5 cm along each coordinate direction. The  $\sim 4.7$  mm wire pitch achieves this for the  $y$  and  $z$  coordinates. The resolution on  $x$ , the drift coordinate, will be better than in the  $y$ - $z$  plane because of the combination of drift velocity and electronics sampling rate. Finally, as already mentioned, the total number of wires on an APA will match the granularity of the electronics boards (each FEMB can read out 128 wires, mixed between the  $U, V, X$  planes). This determines the exact wire spacings of 4.8 mm on the collection plane and 4.7 mm on the induction planes. To achieve the reconstruction precision required (e.g., for  $dE/dx$  reconstruction accuracy and multiple Coulomb scattering determination), the tolerance on the wire pitch is  $\pm 0.5$  mm.

In 2017, the DUNE FD task force, using a full FD simulation and reconstruction chain, performed detector optimization studies to quantify the impact of design choices, including wire pitch and wire angle, on DUNE physics performance. The results indicated that reducing wire spacing (to 3 mm) or changing wire angle (to  $45^\circ$ ) would not significantly affect the performance for the main physics goals of DUNE, including  $\nu_\mu$  to  $\nu_e$  oscillations and CPV sensitivity. A key low-level metric for oscillation physics is the ability to distinguish electrons versus photons in the detector because photon induced showers can fake electron showers and create neutral current (NC) generated backgrounds in the  $\nu_e$  CC event sample. Two important handles for reducing this contamination are (1) the visible gap between the vertex of the neutrino interaction and the start of a photon shower, and (2) the accordance of the energy density at the start of the shower with one MIP instead of two.

A detector spatial resolution much smaller than the radiation length for photons (0.47 cm vs. 14 cm) allows the gap between the neutrino interaction vertex and a photon conversion point

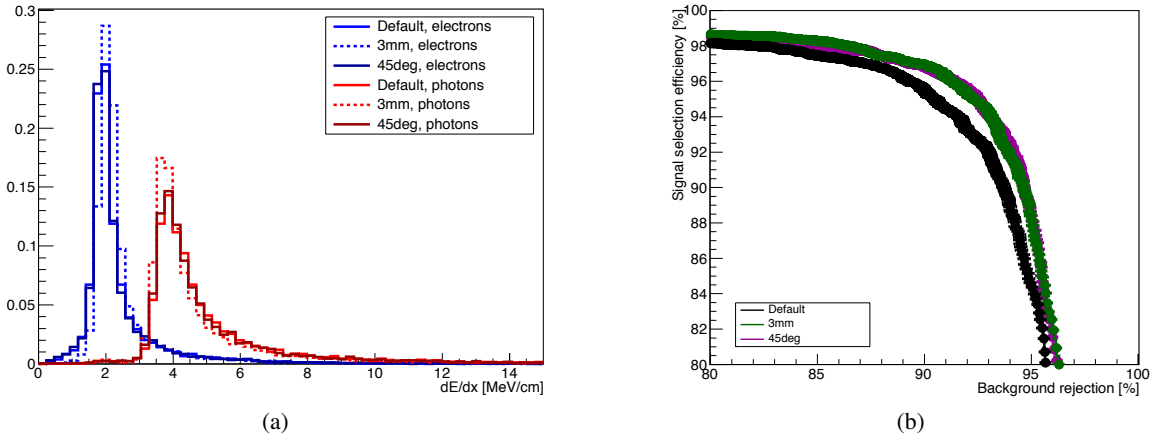


**Figure 2.5.** Summary of electron-photon separation performance studies from the DUNE FD task force. (a)  $e-\gamma$  separation by  $dE/dx$  for the nominal wire spacing and angle (4.7 mm/37.5°) compared to 3 mm spacing or 45° induction wire angles. (b) Electron signal selection efficiency versus photon (background) rejection for the different detector configurations. The 3 mm wire pitch and 45° wire angle have similar effects, so the 45° curve is partly obscured by the 3 mm curve.

to be easily visible, and figure 2.5(a) shows the reconstructed ionization energy loss density ( $dE/dx$ ) in the first centimeters of electron and photon showers, illustrating the separation between the single MIP signal from electrons and the double MIP signal when photons pair-produce an  $e^+e^-$ . In the figure, the ( $dE/dx$ ) separation for electrons and photons is compared for finer wire pitch (3 mm) and optimal wire angle (45°). The final electron signal selection efficiency is also shown as a function of the background rejection rate for different wire configurations in figure 2.5(b). At a signal efficiency of 90 %, for example, the background rejection can be improved by about 1 % using either 3 mm spacing or 45° wire angles for the induction planes. This slight improvement in background rejection with more dense hit information or more optimal wire angles is not surprising, but the effect on high-level physics sensitivities from these changes is very small. The conclusions of the FD task force, therefore, were that the introduction of ambiguities into the reconstruction by increasing the wire angles is not a good trade off, and the increase in cost incurred by decreasing the wire pitch (and, therefore, increasing the number of readout channels) is not justified.

- **Wire plane transparency and signal shapes:** the ordering of the layers, starting from the active detector region, is  $G-U-V-X$ , followed by the grounding mesh. The operating voltages of the APA layers are listed in table 2.2. These were calculated by COMSOL software in order to maintain a 100% ionization electron transparency as they travel through the grid and induction wire planes. Figure 2.6 shows the field simulation and expected signal shapes for the bias voltages listed in the table. When operated at these voltages, the drifting ionization follows trajectories around the grid and induction wires, terminating on a collection plane wire. The grid and induction layers are completely transparent to drifting ionization, and the collection plane is completely opaque. The grid layer is present for pulse-shaping and not connected to the electronics readout; it effectively shields the first induction plane from

the drifting charge and removes a long leading edge from the signals on that layer. These operating conditions were confirmed by a set of dedicated runs in ProtoDUNE-SP taken with various bias voltage settings during spring 2019 (see section 2.3.2 for a detailed discussion).

**Table 2.2.** Baseline bias voltages for APA wire layers for a 100% ionization electron transparency as they travel through the grid and induction wire planes. These values were calculated by COMSOL software and confirmed by analytical calculations based on the conformal representation theory as well as dedicated data from ProtoDUNE-SP.

| Anode Plane           | Bias Voltage |
|-----------------------|--------------|
| <i>G</i> - Grid       | -665 V       |
| <i>U</i> - Induction  | -370 V       |
| <i>V</i> - Induction  | 0 V          |
| <i>X</i> - Collection | 820 V        |
| Grounding Mesh        | 0 V          |

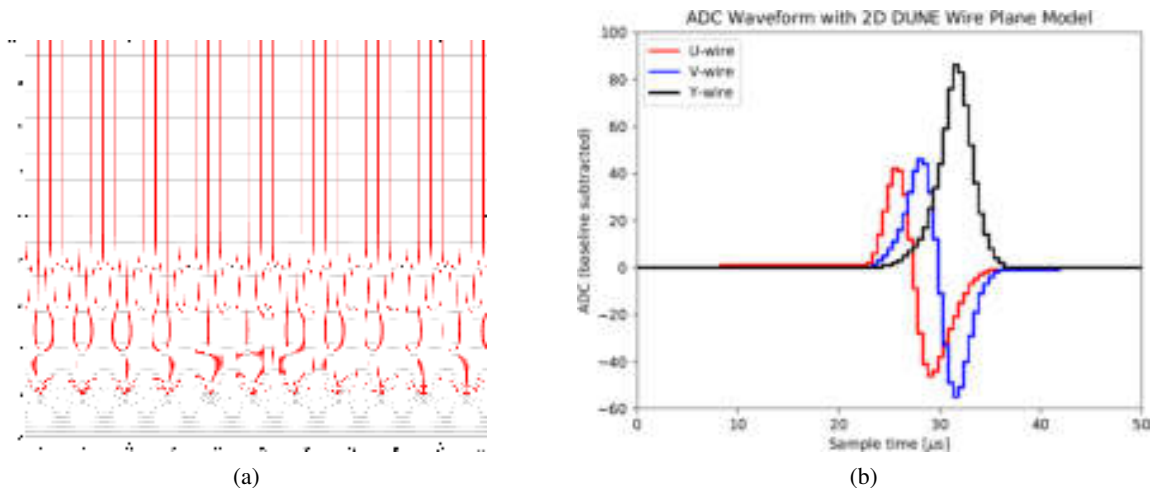


**Figure 2.6.** Field lines (a) and resulting signal shapes on the APA induction and collection wires (b) according to a 2D electric field simulation. The bi-polar nature of the induced signals on the *U* and *V* wires together with the uni-polar collection signals on *Y* are clearly illustrated.

- **Wire type and tension:** the wire selected for the APAs is 152  $\mu\text{m}$  beryllium (1.9%) copper wire, chosen for its mechanical and electrical properties, ease of soldering, and cost. The tension on the wires, combined with intermediate support combs on the APA frame cross beams (described in section 2.2.5.4), ensure that the wires are held taut in place with minimal sag. Wire sag can affect the precision of reconstruction, as well as the transparency of the TPC wire planes. The tension must be low enough that when the wires are cooled, which increases their tension due to thermal contraction, they stay safely below the break load of the beryllium copper wire. A tension of  $6 \pm 1$  N is the baseline for DUNE, to be confirmed after ProtoDUNE-SP analysis is completed. See section 2.2.4 for more details about the APA wires.



Table 2.3 summarizes some of the principal design parameters for the SP module anode plane assemblies.

**Table 2.3.** APA design parameters.

| Parameter                               | Value  |
|---|--|
| Active height                           | 5.984 m  |
| Active width                            | 2.300 m  |
| Wire pitch ( $U, V$ )                   | 4.7 mm   |
| Wire pitch ( $X, G$ )                   | 4.8 mm   |
| Wire pitch tolerance                    | $\pm 0.5$ mm                                       |
| Wire plane spacing                      | 4.8 mm   |
| Wire plane spacing tolerance            | $\pm 0.5$ mm                                       |
| Wire Angle (w.r.t. vertical) ( $U, V$ ) | $\pm 35.7^\circ$                                   |
| Wire Angle (w.r.t. vertical) ( $X, G$ ) | $0^\circ$  |
| Number of wires / APA                   | 960 ( $X$ ), 960 ( $G$ ), 800 ( $U$ ), 800 ( $V$ ) |
| Number of electronic channels / APA     | 2560   |
| Wire material                           | beryllium copper                                   |
| Wire diameter                           | 152 $\mu\text{m}$                                  |

### 2.2.2 Support frames

The APA frames are built of rectangular hollow section (RHS) stainless steel tubes. Figure 2.7 shows three long tubes, a foot tube, a head tube, and eight cross-piece ribs that bolt together to create the 6.0 m tall by 2.3 m wide frame. All hollow sections are 10.2 cm (4 in) deep with varying widths depending on their role.

The head and foot tubes are bolted to the side and center pieces via abutment flanges welded to the tubes. In production, the pieces can be individually machined to help achieve the flatness and shape tolerances. During final assembly, shims are used to create a flat, rectangular frame of the specified dimensions. The central cross pieces are similarly attached to the side pieces. Figure 2.8 shows models of the different joints.

The APA frames also house the photon detection system (PD system) (chapter 5). Rectangular slots are machined in the outer frame tubes and guide rails are used to slide in PD elements from the edges. (See section 2.4 for more details on interfacing with the PD system.)

In a FD SP module, pairs of APA frames will be mechanically connected to form a 12.0 m tall structure with electronics for TPC readout at both the top and bottom of this two-frame assembly and PDs installed throughout. The APA frame design, therefore, must support cable routing to the top of the detector from both the bottom APA readout electronics and the PDs mounted throughout both APAs. Section 2.4 discusses the interfaces.

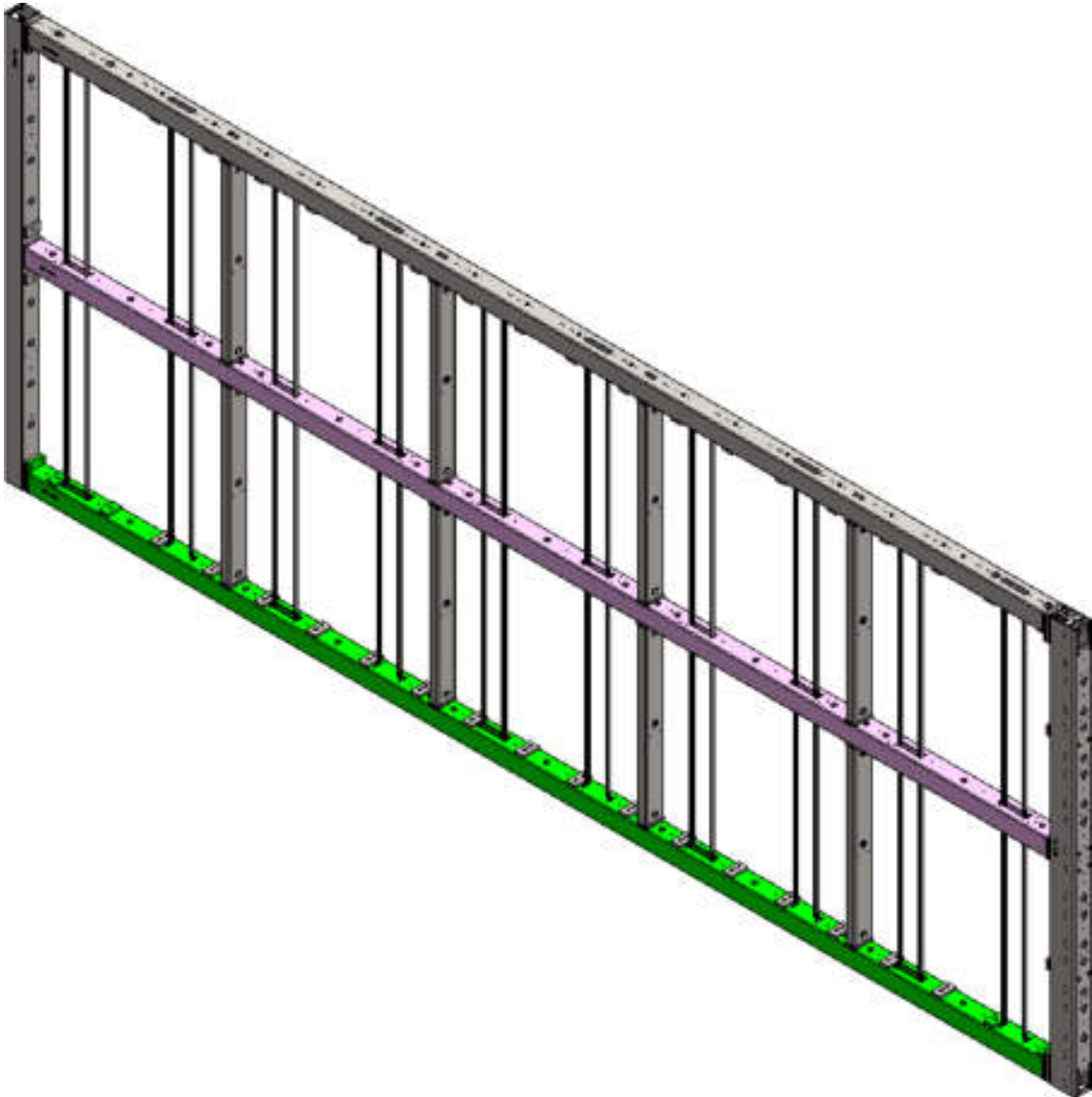


**Figure 2.7.** A DUNE APA frame showing the 13 separate stainless steel tube sections that bolt together to form a complete frame. The long tubes and foot tube are a  $10.2 \times 10.2$  cm ( $4 \times 4$  inch) cross section, the head tube is  $10.2 \times 15.2$  cm ( $4 \times 6$  inch), and the ribs are  $10.2 \times 5.1$  cm ( $4 \times 2$  inch).

### 2.2.3 Grounding mesh

Beneath the layers of sense wires, the conducting surface should be uniform to evenly terminate the E field and improve the uniformity of field lines around the wire planes. A fine woven mesh that is 85% optically transparent is used to allow scintillation photons to pass through to the PDs mounted inside the frame. The mesh also shields the APA wires from spurious electrical signals from other parts of the APA or the PD system.

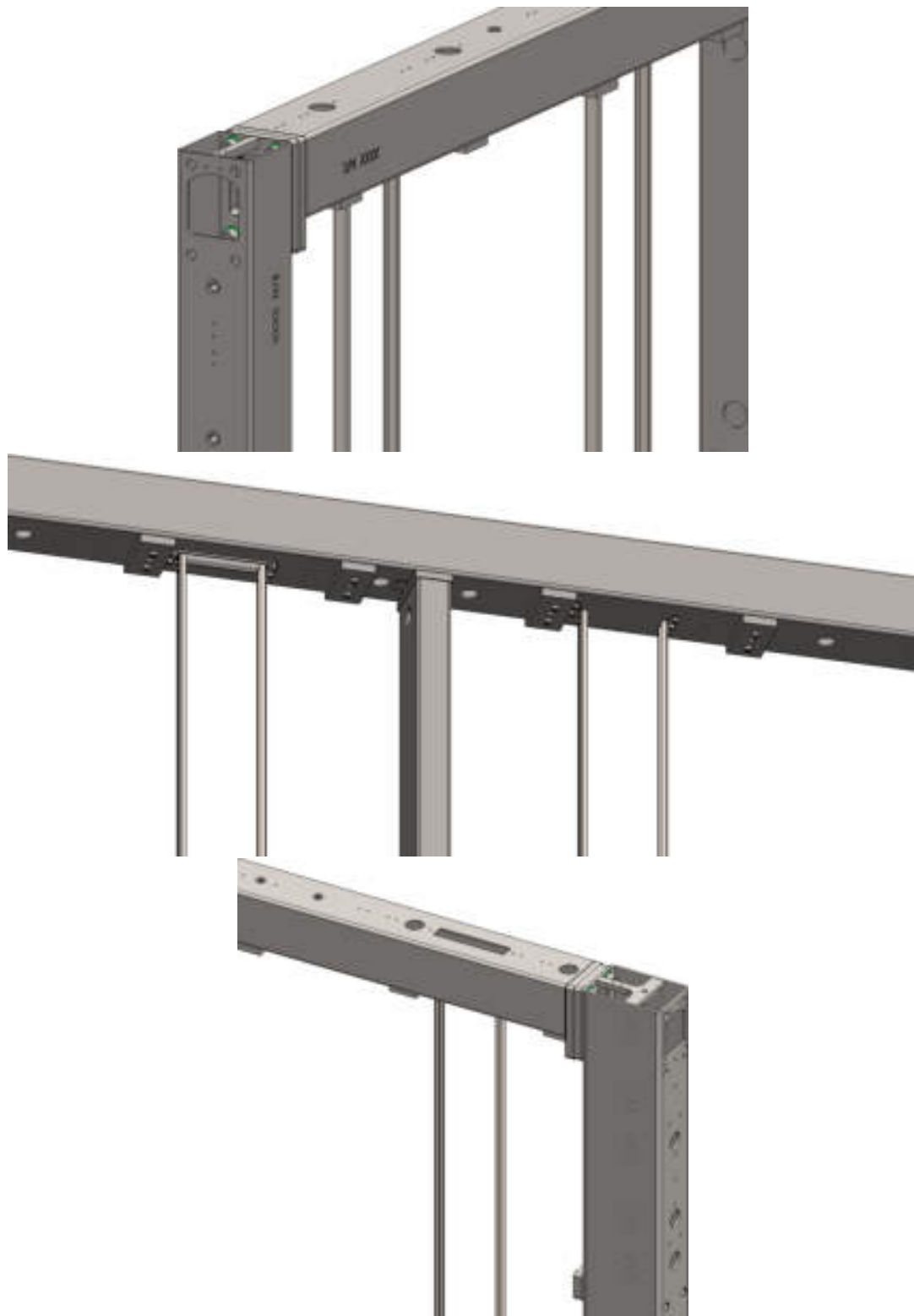


**Figure 2.8.** APA frame construction details. Top: the corner joint between the foot tube and the side tube. Middle: the joint between the side tube and a rib. Bottom: the joint between the head tube and the side tube.

2020 JINST 15 T08010

In the ProtoDUNE-SP APAs, the mesh was installed in four long sheets, along the length of the left- and right-hand halves of each side of the APA and epoxied directly to the frame. This approach to mesh installation was found to be slow and cumbersome. For the DUNE mass production, a modular window-frame design is being developed, where mesh is pre-stretched over smaller sub-frames that can be clipped into each gap between cross beams in the full APA frame. This improves the reliability of the installed mesh (more uniform tension across the mesh) and allows much easier installation on the APA frame. The mesh will be woven of conducting 304 stainless steel 89  $\mu\text{m}$  wire. It will be mounted on 304 stainless steel 20 mm  $\times$  10 mm box section frames, stretched over the frame with jigs and pneumatic actuators built for the purpose, and TIG welded around the top surface and again around the side surfaces. Five different panel designs are needed to match the openings in the APA frames: two for the foot end, two for the head end, and one for the central panels that are all the same. There are 20 panels per APA. Stainless steel brackets will be fixed to the inner window sections of the APA frame and the panels will be secured into position using steel fasteners. The design ensures good electrical contact between the mesh and the frame. A full-scale APA (APA-07) has been built at Daresbury Lab for CE testing at CERN using the mesh panel design. Figure 2.9 shows images of the mesh design and the prototypes built for APA 7.

### 2.2.4 Wires

The 152  $\mu\text{m}$  (0.006 in) diameter beryllium copper (CuBe) wire chosen for use in the APAs is known for its high durability and yield strength. It is composed of 98 % copper, 1.9 % beryllium, and a negligible amount of other elements. Each APA contains a total of 23.4 km of wire.

The key properties for its use in the APAs are low resistivity, high tensile or yield strength, and a coefficient of thermal expansion suitable for use with the APA's stainless steel frame (see table 2.4 for a summary of properties). Tensile strength of the wire describes the wire-breaking stress. The yield strength is the stress at which the wire starts to take a permanent (inelastic) deformation and is the important limit for this case. The wire spools purchased from Little Falls Alloys<sup>1</sup> for use on ProtoDUNE-SP were measured to have tensile strength higher than 1380 MPa and yield strength more than 1100 MPa (19.4 N for 152  $\mu\text{m}$  diameter wire). The stress while in use is approximately 336 MPa (6 N), leaving a comfortable margin.

The CTE describes how a material expands or contracts with changes in temperature. The CTEs of CuBe alloy and 304 stainless steel are very similar. Integrated down to 87 K, they are 2.7 mm/m for stainless steel and 2.9 mm/m for CuBe. The wire contracts slightly more than the frame, so for a wire starting at 6 N at room temperature the tension increases to around 6.5 N when everything reaches LAr temperature.

The rate of change in wire tension during cool-down is also important. In the worst case, the wire cools quickly to 87 K before any significant cooling of the much larger frame. In the limiting case with complete contraction of the wire and none in the frame, the tension would peak around 11.7 N, which is still well under the 19 N yield tension. In practice, however, the cooling will be done gradually to avoid this tension spike as well as other thermal shocks to the detectors.

---

<sup>1</sup>Little Falls Alloys<sup>TM</sup>, <http://www.lfa-wire.com/>.

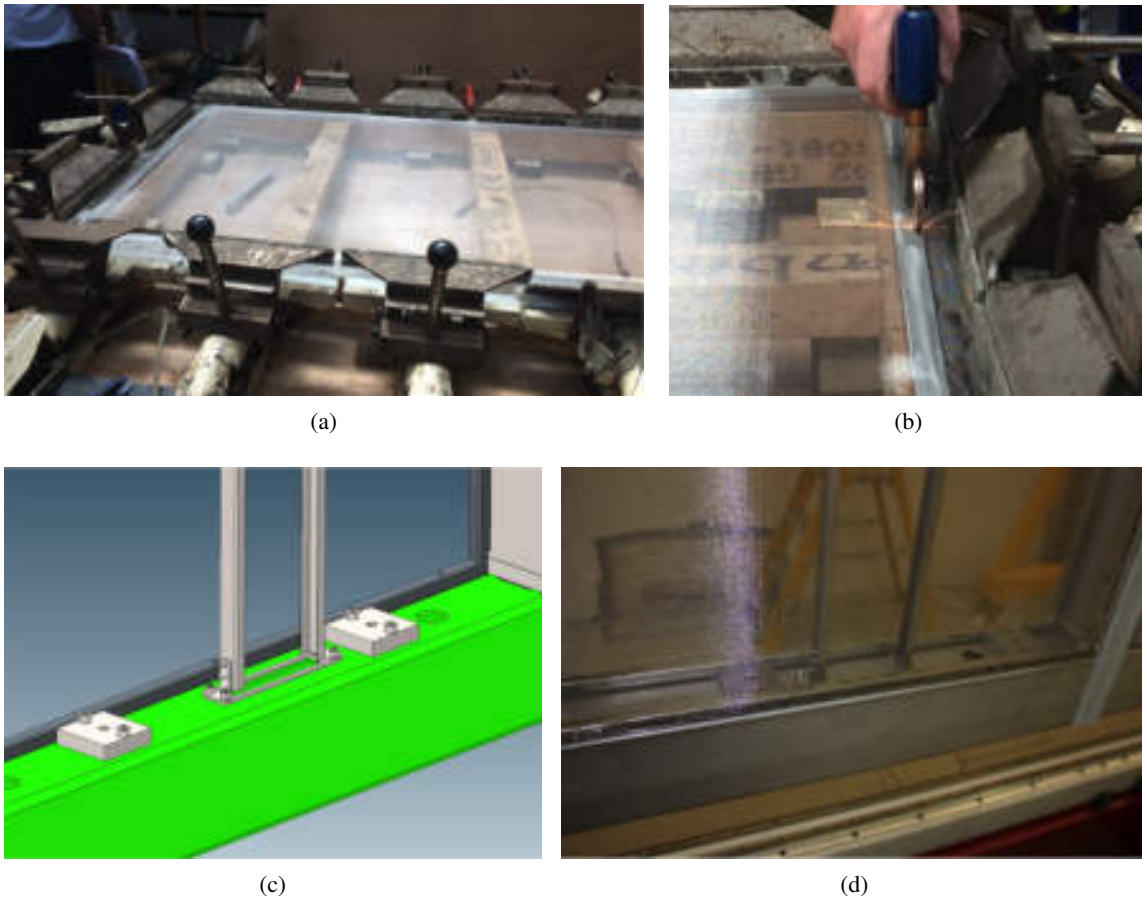


**Figure 2.9.** APA grounding mesh construction and installation. a) The mesh panel stretching jig, b) mesh being welded to the support frame, c) model showing the mesh sub-frame (in dark gray) fitting into the APA frame (in green), and d) photo of an installed mesh panel in APA 7.

**Table 2.4.** Summary of properties of the beryllium copper wire used on the APAs.

| Parameter                                  | Value                                  |
|--|--|
| Resistivity                                | 7.68 $\mu\Omega$ -cm @ 20° C           |
| Resistance                                 | 4.4 $\Omega$ /m @ 20° C                |
| Tensile strength (from property sheets)    | 1436 MPa / 25.8 N for 152 $\mu$ m wire |
| CTE of beryllium copper integrated to 87 K | $2.9 \times 10^{-3}$ m/m               |
| CTE of stainless steel integrated to 87 K  | $2.7 \times 10^{-3}$ m/m               |

### 2.2.5 Wire boards and anchoring elements

To guide and secure the 3520 wires on an APA, stacks of custom FR-4 circuit boards attach all along the outside edges of the frame, as shown in the engineering drawings in figure 2.10. There are 337 total circuit boards on each APA (50,550 in an SP module with 150 APAs), where this number includes 204 wire boards ( $X/V/U/G = 30/72/72/30$ ), 72 cover boards to protect the wire solder pads and traces on the top layer of wire boards, 20 capacitive-resistance (CR) boards, 20 adapter boards to connect the CRs to the CE, 20  $G$ -layer bias boards, and one safe high voltage (SHV) board to distribute bias voltages to the planes. Figure 2.3 shows the positions of the boards at the head of the APA and the path connecting TPC wires to the CE.

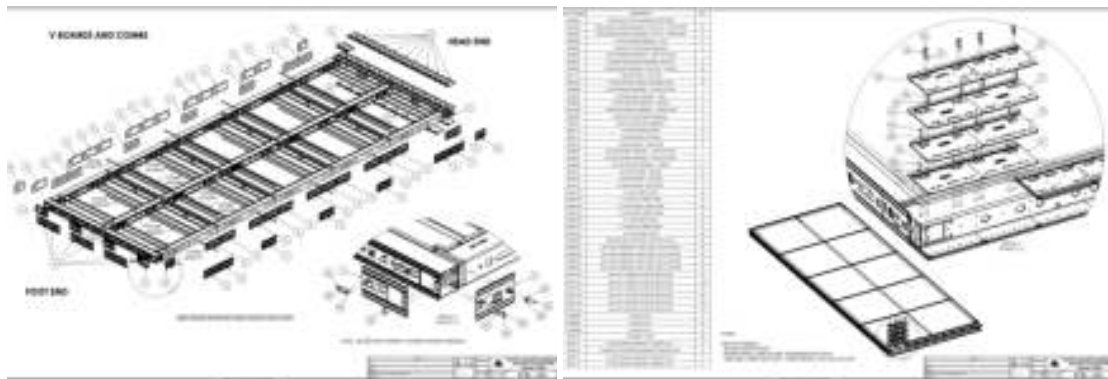


**Figure 2.10.** Engineering drawings that illustrate the layering of the wire carrier boards that are secured along the perimeter of the APA steel frames. Left: the full set of  $V$ -layer boards. Right: detail showing the stack of four boards at the head end of the APA (bottom to top:  $X, V, U, G$ ).

#### 2.2.5.1 Head wire boards

All APA wires terminate on wire boards stacked along the electronics end of the APA frame. The board stack at the head end is shown in an engineering drawing in the right panel of figure 2.10. A photograph showing the head boards and  $G$ -bias boards on one of the completed ProtoDUNE-SP APAs is shown in figure 2.11. Attaching the wire boards begins with the  $X$ -plane (innermost). Once the  $X$ -plane wires are strung on both sides of the APA frame, they are soldered and epoxied to their wire boards and trimmed. Next, the  $V$ -plane boards are epoxied in place and the  $V$  wires installed, followed by the  $U$ -plane boards and wires, and finally the  $G$ -plane boards and wires. The wire plane spacing of 4.8 mm is set by the thickness of these wire boards.

Mill-Max<sup>2</sup> pins and sockets provide electrical connections between circuit boards within a stack. They are pressed into the circuit boards and are not repairable if damaged. To minimize the possibility of damaged pins, the boards are designed so that the first wire board attached to the frame has only sockets. All boards attached subsequently contain pins that plug into previously mounted boards. This process eliminates exposure of any pins to possible damage during winding, soldering, or trimming.

The  $X$ ,  $U$  and  $V$  layers of wires are connected to the CE (housed in boxes mounted on the APA) either directly ( $V$ ) or through DC-blocking capacitors ( $U, X$ ). Ten stacks of wire boards are

<sup>2</sup>Mill-Max™, <https://www.mill-max.com/>.

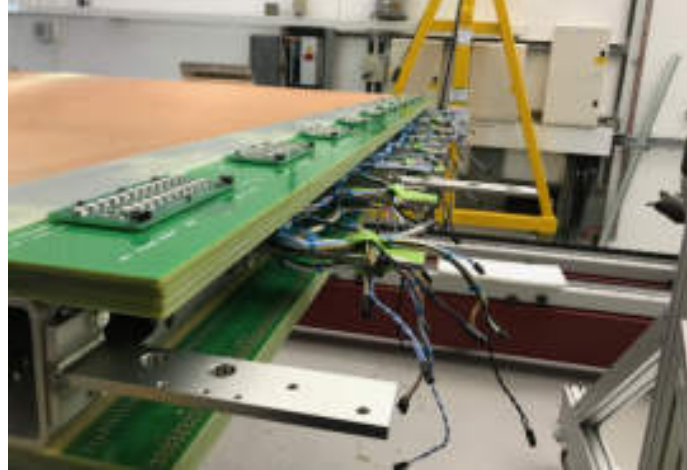


**Figure 2.11.** The wire board stack at the head end of an APA. The four wire boards within a stack can be seen on both the top and bottom sides of the APA. Also visible are the T-shaped brackets that will hold the CE boxes when electronics are installed.

installed across the width of each side along the head of the APA. The *X*-layer board in each stack has room for 48 wires, the *V*-layer has 40 wires, the *U*-layer 40 wires, and the *G*-layer 48 wires. Each board stack, therefore, has 176 wires but only 128 signal channels since the *G* wires are not read out. With a total of 20 stacks per APA, this results in 2560 signal channels per APA and a total of 3520 wires starting at the top of the APA and ending at the bottom. Many of the capacitors and resistors that in principle could be on these wire boards are instead placed on the attached CR (capacitive-resistance) boards (section 2.2.5.3) to improve their accessibility in case of component failure.

### 2.2.5.2 Side and foot wire boards

The boards along the sides and foot of the APA have notches, pins, and other location features to hold wires in the correct position as they wrap around the edge from one side of the APA to the other.

The edge boards need a number of hole or slot features to provide access to the underlying frame (see figure 2.12 for examples). In order that these openings not be covered by wires, the sections of wire that would go over the openings are replaced by traces on the boards. After the wires are wrapped, the wires over the opening are soldered to pads at the ends of the traces, and the section of wire between the pads is snipped out. These traces can be easily and economically added to the boards by the many commercial fabricators who make circuit boards.

The placement of the angled wires are fixed by teeth that are part of an injected molded strip glued to the edge of the FR-4 boards. The polymer used for the strips is Vectra e130i (a trade name for 30% glass filled liquid crystal polymer, or LCP). It retains its strength at cryogenic temperature and has a CTE similar enough to FR-4 that differential contraction is not a problem. The wires make a partial wrap around the pin as they change direction from the face of the APA to the edge.

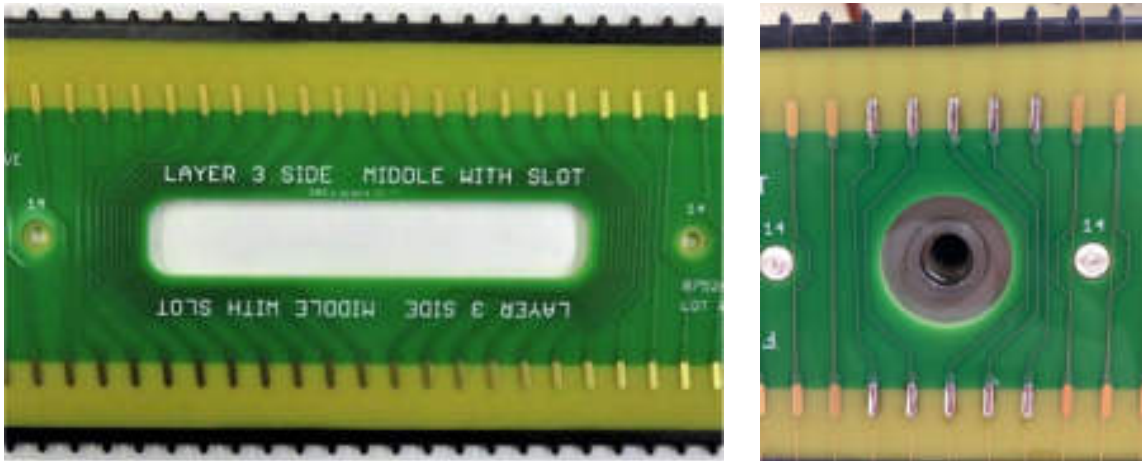


**Figure 2.12.** Side boards with traces that connect wires around openings. The wires are wound straight over the openings, then soldered to pads at the ends of the traces. The wire sections between the pads are then trimmed away.

### 2.2.5.3 Capacitive-resistive (CR) boards

The CR boards carry a bias resistor and a DC-blocking capacitor for each wire in the  $X$  and  $U$ -planes. These boards are attached to the board stacks after fabrication of all wire planes. Electrical connections to the board stack are made through Mill-Max pins that plug into the wire boards. Connections from the CR boards to the CE are made through a pair of 96-pin Samtec<sup>3</sup> connectors.

Surface-mount bias resistors on the CR boards have resistance of 50 M $\Omega$  and are constructed with a thick film on a ceramic substrate. Rated for 2.0 kV operation, the resistors measure 3.0 mm  $\times$  6.1 mm (0.12 in  $\times$  0.24 in). The selected DC-blocking capacitors have capacitance of 3.9 nF and are rated for 2.0 kV operation. Measuring 5.6 mm  $\times$  6.4 mm (0.22 in  $\times$  0.25 in) across and 2.5 mm (0.10 in) high, the capacitors feature flexible terminals to comply with PCB expansion and contraction. They are designed to withstand 1000 thermal cycles between the extremes of the operating temperature range. Tolerance is also 5%.

In addition to the bias and DC-blocking capacitors for all  $X$  and  $U$ -plane wires, the CR boards include two R-C filters for the bias voltages.<sup>4</sup> The resistors are of the same type used for wire biasing except with a resistance of 5 M $\Omega$ , consisting of two 10 M $\Omega$  resistors connected in parallel. Wire plane bias filter capacitors are 39 nF, consisting of ten 3.9 nF surface-mount capacitors connected in parallel. They are the same capacitors as those used for DC blocking.

The selected capacitors were designed by the manufacturer to withstand repeated temperature excursions over a wide range. Their mechanically compliant terminal structure accommodates CTE mismatches. The resistors use a thick-film technology that is also tolerant of wide temperature excursions. Capacitors and resistors were qualified for ProtoDUNE-SP by testing samples repeatedly at room temperature and at  $-190$  °C. Performance criteria were measured across five thermal cycles, and no measurable changes were observed. During the production of 140 CR boards, more than

<sup>3</sup>Samtec™ <https://www.samtec.com/>.

<sup>4</sup>The  $V$ -plane does not carry a bias voltage, so does not require these components.



10,000 units of each component were tested at room temperature, at LAr temperature, and again at room temperature. No failures or measurable changes in performance were observed.

### 2.2.5.4 Support combs

Support combs are glued at four points along each side of the APA, along the four cross beams. These combs maintain the wire and plane spacing along the length of the APA. A dedicated jig is used to install the combs and also provides the alignment and pressure as the glue dries. The glue used is the Gray epoxy 2216 described below. Before the jig can be removed and production can continue, an eight-hour cure time is required after comb installation on each side of the APA. Figure 2.13 shows a detail of the wire support combs on a ProtoDUNE-SP APA.



**Figure 2.13.** Left: APA corner where end boards meet side boards. The injection molded teeth that guide the  $U$  and  $V$  wires around the edge are visible at the bottom. Right: the wire support combs.

### 2.2.5.5 Solder and epoxy

The ends of the wires are soldered to pads on the edges of the wire boards. Solder provides both an electrical connection and a physical anchor to the wire pads. A 62% tin, 36% lead, and 2% silver solder was chosen. A eutectic mix (63/37) is the best of the straight tin-lead solders, but the 2% added silver gives better creep resistance. The solder contains a no-clean flux and does not need to be removed after soldering. Most of it is encapsulated when subsequent boards are epoxied in place. At room temperatures and below, the flux is not conductive or corrosive.

Once a wire layer is complete, the next layer of boards is glued on; this glue provides an additional physical anchor. Gray epoxy 2216 by 3M<sup>5</sup> is used for the glue. It is strong and widely used (therefore much data is available), and it retains good properties at cryogenic temperatures.

<sup>5</sup>3M™ <https://www.3m.com/>.

### 2.2.6 The APA pair

In an SP module, pairs of 6 m tall APA frames are mechanically connected at their ends to form a 12 m tall readout surface. Figure 2.14 shows a connected pair (turned on its side) with dimensions. The TPC readout electronics require that the individual APA frames be electrically isolated. The left panel of figure 2.15 shows the design for mechanically connecting APAs while maintaining electrical isolation. The two APAs are connected through a stainless steel link that is attached to both frames with a special shoulder screw. The steel part of the link is electrically insulated from the frames using a G10 panel. The links connect to the side tubes with a special shoulder screw that screws into plates welded to the frame.



**Figure 2.14.** Diagram of an APA pair, with connected bottom and top APA. The dimensions of the APA pair, including the accompanying cold electronics and mechanical supports (the yoke), are indicated.

The APA yoke, shown in figure 2.16, is a bolted stainless steel structural assembly with a central support point and a pair of pins to connect to the load. Two T-shaped brackets, referred to as the structural tees, mount to the head tube of the top APA and provide the mating pin holes to connect the yoke to the APA. The center support point consists of a M20 stainless steel bolt, oversize washers, and a PEEK washer for electrical isolation. The yoke is mounted to the top APA before an APA pair is assembled. To move into the cryostat, the pair is hung from two trolleys that connect to the structural tees. Once in final position, the load of the APA pair can be transferred from the trolleys to the DSS in the cryostat through the center support point of the yoke. To accomplish this, the M20 bolt and washer assembly is inserted from the bottom of the yoke and the threaded end of the bolt connects to the DSS.

Adjacent APA pairs are kept in plane with each other by simple insertion pins at the top and bottom of the side tubes. The pins are made up of a screw and an insulating sleeve to ensure electrical isolation, and each pin engages a slot in the adjacent APA pair side tubes. The right panel of figure 2.15 shows a schematic of the side pin connectors before and after insertion.

Once installed in the detector, a physical gap of 12 mm exists along this vertical connection between all adjacent APAs at room temperature. Since the APAs are suspended under the stainless steel DSS beams, which contract similarly to that of the APA frames, the gaps between most adjacent

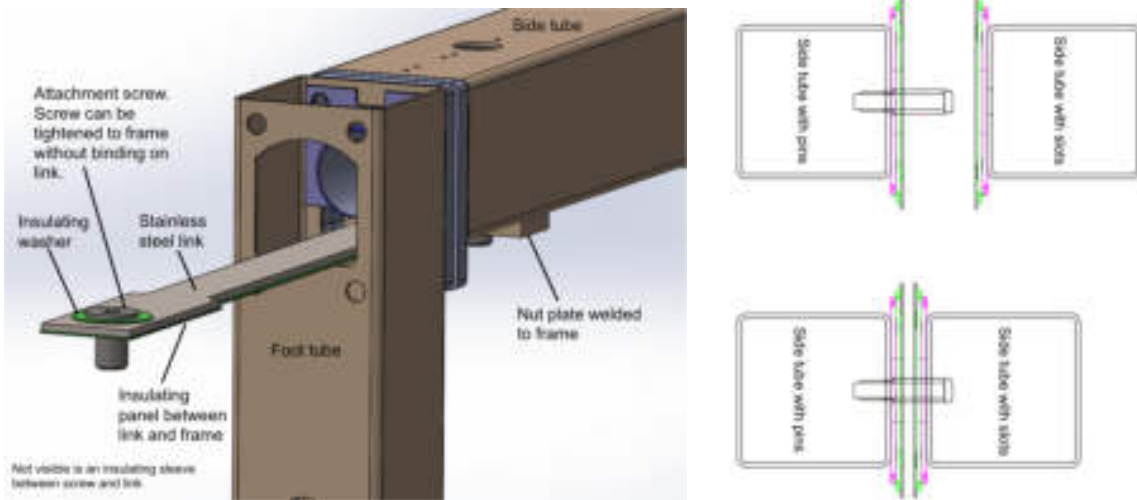


**Figure 2.15.** Design for the APA-to-APA connections. Left: for the vertical connection there are two steel links joining the upper APA to the lower APA; one link connected to one APA is shown here. The steel part of the link is electrically insulated from the frames. Right: along adjoining vertical edges, two pins keep neighboring APAs in plane. Two side tubes before engagement with the screw and insulating sleeve installed are shown at the top, and the engaged side tubes are shown below.

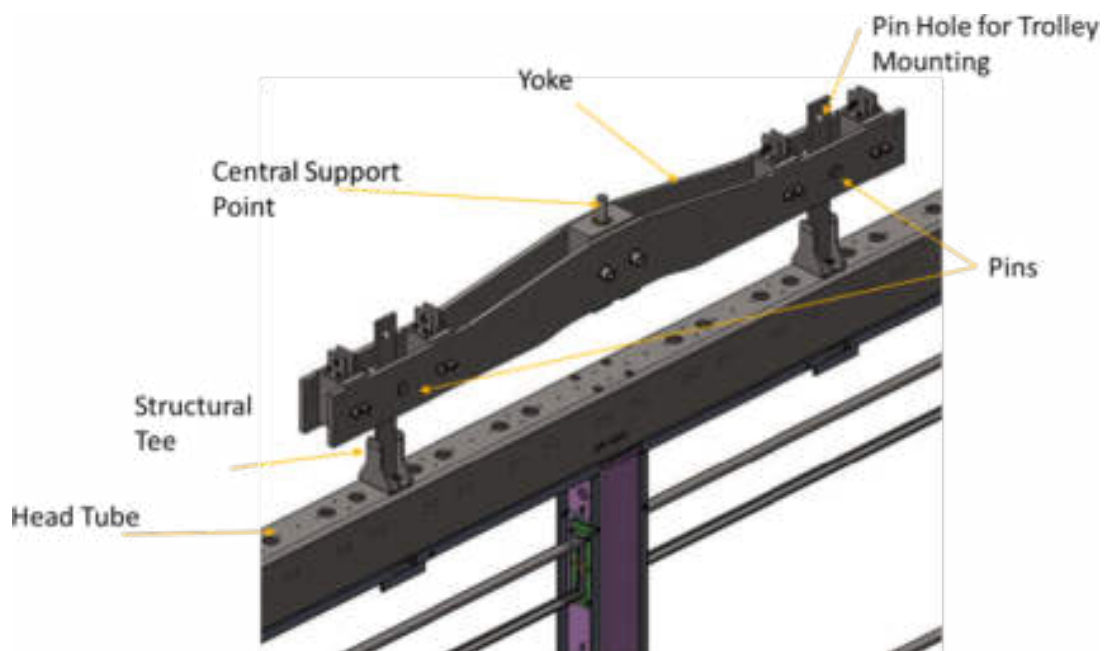


**Figure 2.16.** The yoke at the top of an APA pair that provides connection to the DSS.

APAs stay about the same (12 mm) in the cold. The DSS beams, however, are segmented at 6.4 m length, and each beam segment is independently supported by two DSS feedthroughs, one of which does not allow lateral movement. As a result, the gaps between DSS beams open up in the cold by another 17 mm, making the physical gaps 29 mm as shown in figure 2.17. The actual gap between the APAs active width 28 mm is approximately 16 mm wider than the physical gap (45 mm) in the two scenarios described above.

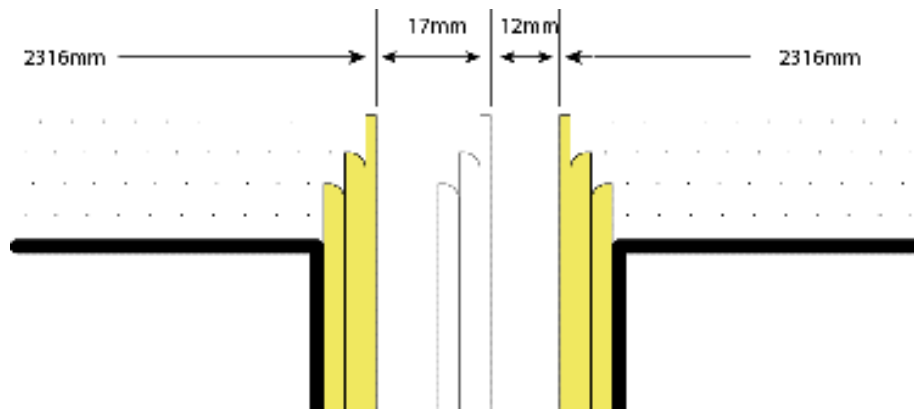


**Figure 2.17.** Illustration of the gap width between APAs.

To minimize the loss of signal charge over the gaps between APAs in ProtoDUNE-SP, special electrodes (electron diverters) were installed along the vertical gaps to nudge the incoming electrons into the active regions of the APAs. The data from ProtoDUNE-SP are being used to study the impact of using electron diverters and determine the need for them in DUNE. See section 2.3 for a discussion of the ProtoDUNE-SP data analysis (ProtoDUNE-SP had some gaps with electron diverters installed and some without, enabling comparisons of the tracking and calorimetry performance in the two cases).

### 2.2.7 APA structural analysis

The APAs will be subjected to a variety of load conditions throughout construction, installation, and operation of the experiment, so it is important to analyze carefully and confirm the design of the mechanical components. A structural and safety analysis was performed to confirm the strength of the APA frame, the APA yoke, and the APA-to-APA link. The full report can be found at [8]. As noted, the way the APA frame is supported and loaded changes during the construction and transport of the APA. Twenty different load cases were checked. These load cases cover the handling of the bare frame, the APA during wiring, the fully integrated APA, and the APA pair. The analysis covered the loaded APA pair in the installed warm and dry state as well as spatial and transient thermal gradients that might be encountered during cool down.

The masses of components mounted on the frame were determined from the material densities and the geometry defined in the 3D models. Loads from the supported masses and the APA wire load were applied to the frame in the analysis to replicate the way loads are applied to the actual frame. The analysis was performed in accordance with the standard building code for large steel structures, the ASICs Specification for Structural Steel Buildings (AISC document 360-10). For

stainless steel structures, the ASIC publication Design Guide 27: Structural Stainless Steel was also applied. The analysis was performed using the Load and Resistance Factor Design method (LRFD).

Per LRFD, a load factor of 1.4 was applied to all loads and to the self-weight of the APA frame. The factored loads were used to calculate the required strength or stress. Strength reduction factors were assigned to the strength or stress rating of the component or material. The strength reduction factors determined the allowable strengths and the design was considered to meet code as long as the allowable strength of the material or component is greater than the required strength as determined by the factored loading.

In order to evaluate the structure, a finite element analysis (FEA) model of the APA frame was built in SolidWorks Simulation.<sup>6</sup> For each load case, proper constraints were defined and factored loads were applied. The stress in the frame members were directly extracted from the model. Also extracted from the model were the forces and moments acting on the welded and bolted joints. These forces and moments and methods from code were used to determine the required strength. The allowable strength was also determined using methods from the code. For transportation cases, the analysis was used to determine that the maximum shock or g-load the APA frame can tolerate is 4g (39.2 m/s<sup>2</sup>). This value has been incorporated into the requirements for the design of the transport frame.

Two thermal cases were run. In one case, a steady state thermal gradient of 17 K/m was applied to the frame in addition to the installed state loading. The second thermal case was a transient case. In this case, the fastest cool down rate the APA frame can tolerate without over stressing the wires and wire solder/epoxy joints was estimated. The wire cools faster than the frame and the cool-down rate is limited by a 75°C allowable differential temperature between the frame and the wire. The estimation of the differential was done using a conservative method that is described in the section that presents the results for case 20 in the APA analysis document. The allowable cool down rate of the ambient environment is 70°C/hr.

In addition to the frame, the yoke was also analyzed for strength. These components are not subjected to multiple load states and see their maximum loads when in the installed state. The yoke was analyzed using FEA to check stress and buckling of the side plates. The APA -to-APA link was checked using methods for pinned connections defined in code.

Results for the frame analysis show the frame members are most heavily stressed in the transportation cases. This is expected because the g-load was increased until strength limits were reached. Here the ratio of allowable to required strength is 1.1 for both the beam structural members and for the welds and 1.5 for the bolts. The results for the yoke analysis show that the allowable stress over the required strength for the yoke plates is 2.2. The ratio of the load that will cause buckling to the applied load is 33.

The structural analysis clearly shows the APA frame members, welds, and bolts are strong enough to carry the loads.

---

<sup>6</sup><https://www.solidworks.com/>.

### 2.3 Quality assurance

The most important and complete information for assuring the quality of the APA design, components, materials, and construction methods comes from the construction and operation of ProtoDUNE-SP. We have learned much about the design and fabrication procedures that has informed the detailed design and plans for the DUNE APA construction project. ProtoDUNE-SP included six full-scale DUNE APAs instrumenting two drift regions around a central cathode. Four of the ProtoDUNE-SP APAs were constructed in the USA at the University of Wisconsin-PSL, and two were made at Daresbury Laboratory in the UK. All were shipped to CERN, integrated with PDs and CE, and tested in a cold box prior to installation into the ProtoDUNE-SP cryostat. Figure 2.18 shows one of the drift regions in the fully constructed ProtoDUNE-SP detector.

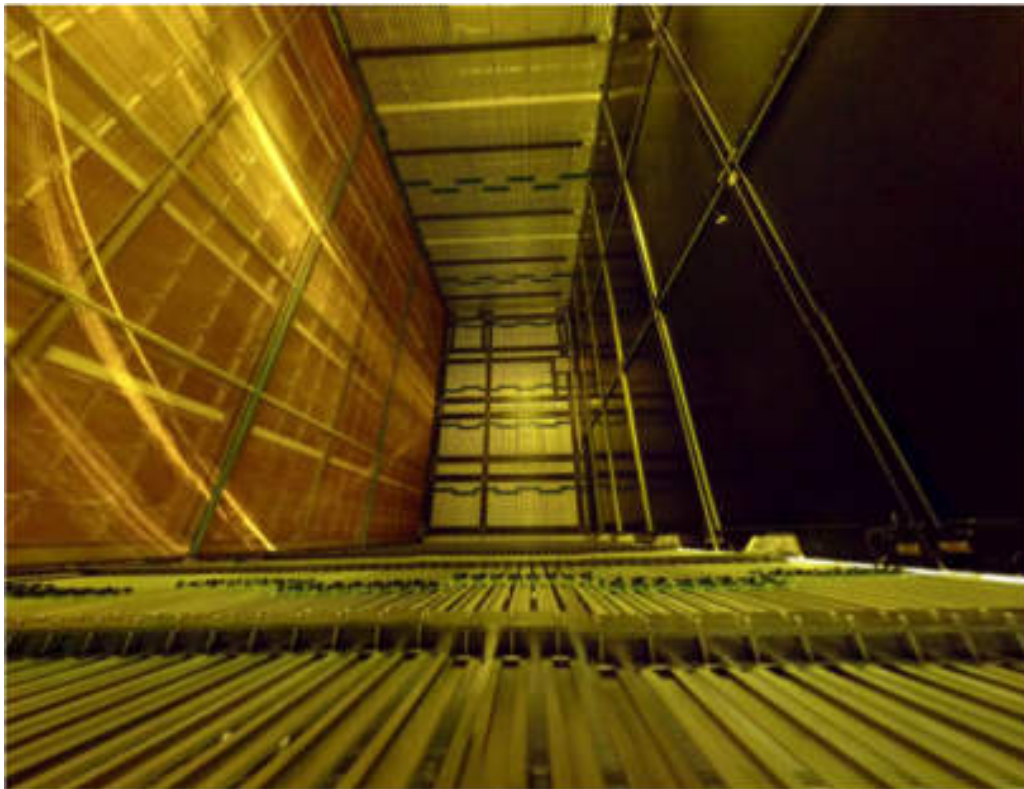


**Figure 2.18.** One of the two drift regions in the ProtoDUNE-SP detector at CERN showing the three installed APAs on the left.

#### 2.3.1 Results from ProtoDUNE-SP construction

A thorough set of QC tests were performed and documented throughout the fabrication of the ProtoDUNE-SP APAs. The positive outcomes give great confidence in the quality of the overall APA design and construction techniques. Here we summarize some of the testing that was done for ProtoDUNE-SP and the results.

After each wire layer was applied to an APA, electrical continuity between the head and foot boards was checked for each wire. This test is most useful for the  $U$  and  $V$  layers, where metal

traces on the side boards can be damaged during construction. All boards were visually inspected as construction proceeded.

Channels were checked for isolation. In the beginning, wire-to-wire isolation was measured over a long period of time, and no problems arose. In the end, each wire was individually hipot tested (a dielectric withstand test) at 1 kV. No failures were ever seen. However, leakage currents were seen to be highly dependent on relative humidity. The surface of the epoxy has some affinity for moisture in the air and provides a measurable leakage path when relative humidity exceeds about 60 %. Tests have confirmed that in a dry environment, such as the LAr cryostat, these leakage currents disappear.

Wire tension was measured for all wires at production. Figure 2.19 displays the measured tensions for wires on the instrumented wire planes ( $X, U, V$ ) for the six ProtoDUNE-SP APAs, four constructed at PSL in the US and two at Daresbury Laboratory in the UK. In total, 4.4 % of the 14,972 wires considered for this analysis had a tension below 4 N, and 22.5 % were above 6 N. A wire which has a tension higher than specification should not impact the physics in any meaningful way. Wires with tension lower than specification could move slightly out of position and impact detector function primarily through modifying the local E field. E field modification can lead to the number of ionization electrons being incorrectly reconstructed in the deconvolution process or alter the transparency so that less than 100 % of the ionization electrons reach the collection plane. Because these processes change the amount of reconstructed charge, they would alter the reconstruction of the energy deposited by charged particles near these wires. A further complication from very low-tension wires might be an increase in noise level, introduced by wire vibrations, which can lead to vortex shedding. Each of these impacts is expected to be quite small, but to confirm, cosmic muon tracks in ProtoDUNE-SP data are now being used to test if differences in response can be seen on wires with particularly low tension. The target tension for DUNE APAs has already been increased to 6 N, and these ProtoDUNE-SP studies will quantitatively inform a minimum tension requirement, but no challenges in meeting specifications are foreseen based on current knowledge from ProtoDUNE-SP construction.

Wire tension measurements were also performed for a subset of wires on each APA after arriving at CERN. Figure 2.20 shows the comparison of tension values measured at CERN versus at the production site for the selected subset of wires from each wire plane. Based on the traveler documents provided by the production sites, wires having outlier tension values were selected from each APA for re-measurement at CERN. In addition, a set of randomly selected wires from each plane was measured. In total, for six APAs, ~1500 wires had their tension re-measured at CERN. Measurements took place in the clean room with APAs hanging vertically, the first time the tensions were sampled in this orientation. Tension measurements were performed by using the laser-photodiode based method, the same as at the production sites.

Finally, to test if a cold cycle had any effect on the wire tension, samples of wires were measured again after the cold box tests at CERN. This is the only tension data we have after a cold-cycle for ProtoDUNE-SP APAs. Figure 2.21 presents the results, showing no significant change in the resonant frequency of the wires, indicating cold cycle does not have a significant effect on wire tension.

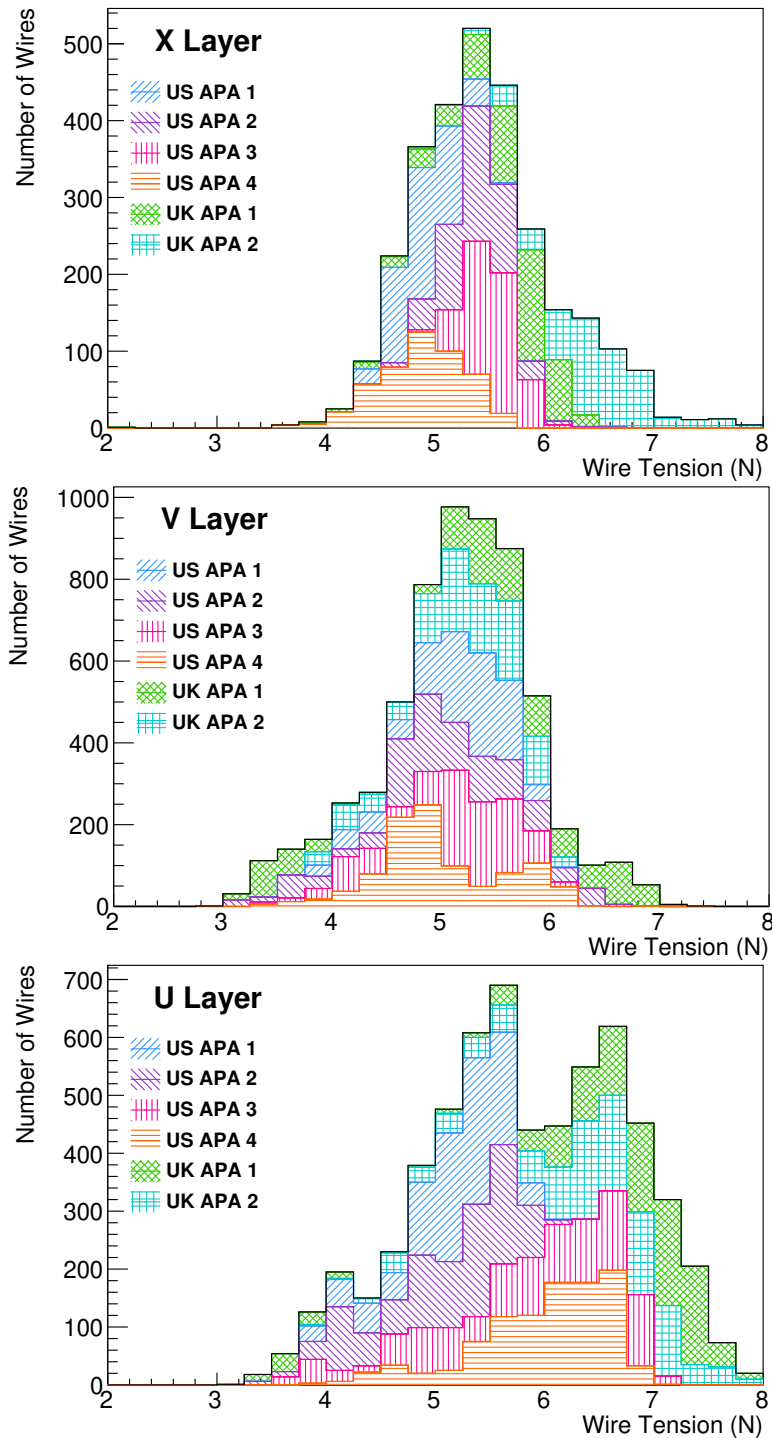


**Figure 2.19.** Distributions of wire tensions in the ProtoDUNE-SP APAs for wires longer than 70 cm, as measured during production at PSL and Daresbury. For the X-plane, every wire has the same length (598.39 cm), and so every wire is included. The histograms for the six APAs are stacked.

2020 JINST 15 T08010



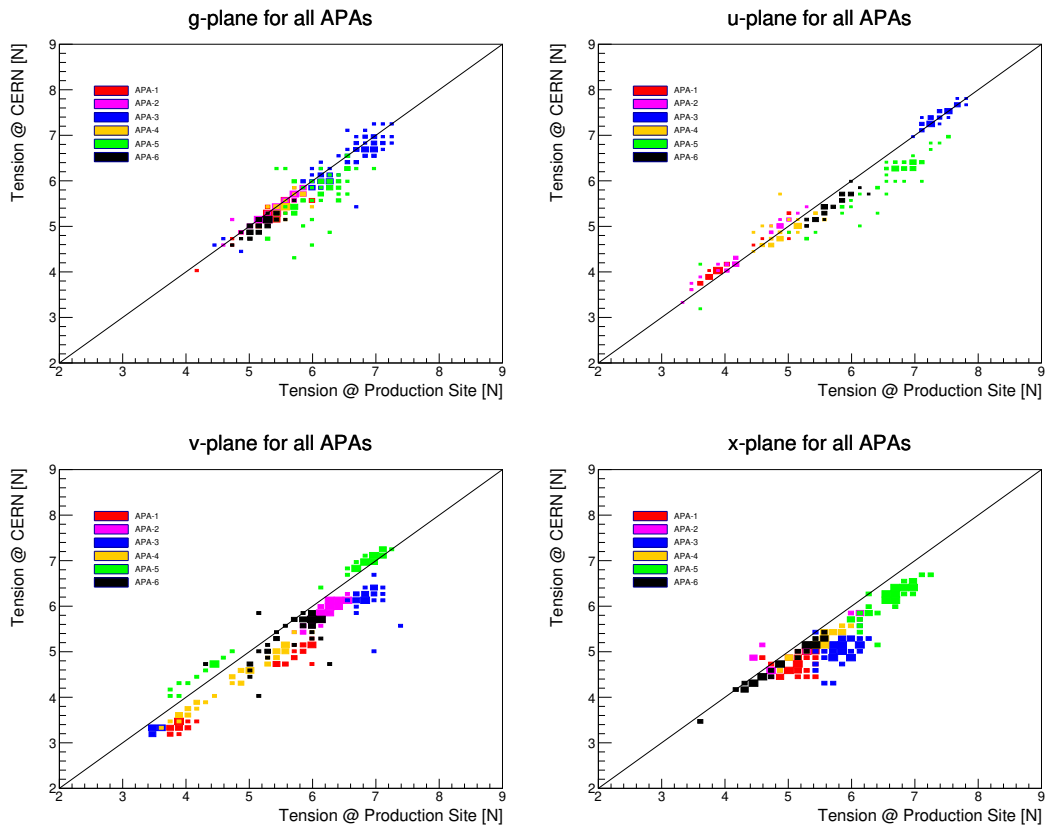


**Figure 2.20.** Comparison of wire tensions upon arrival at CERN versus at the production sites for a sample of wires on each of the ProtoDUNE-SP APAs.

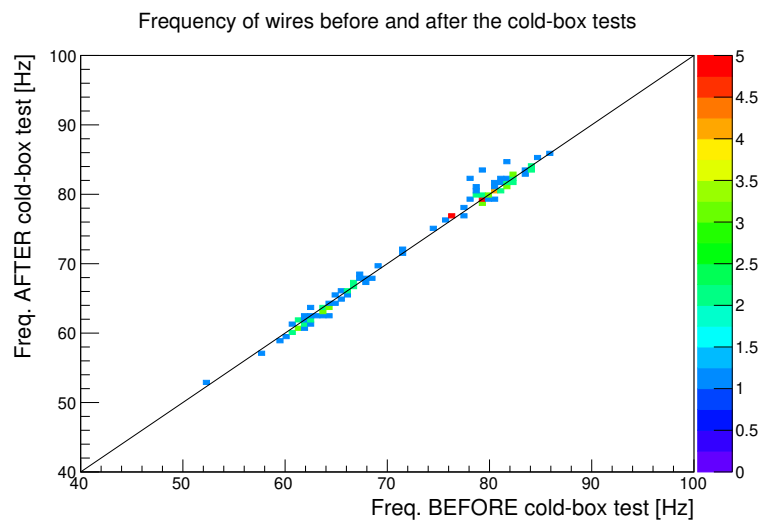


**Figure 2.21.** Comparison of wire tensions after the cold box test versus before at CERN for a sample of wires on each of the ProtoDUNE-SP APAs.

2020 JINST 15 T08010

### 2.3.2 Results from ProtoDUNE-SP operation

Several useful analyses for evaluating the APA design have been carried out including monitoring the number of non-responsive or disconnected channels in the detector, studying the impact of the electron diverters on reconstruction and calorimetry, and measuring the change in electron transparency with wire bias voltage. The status of these studies is presented below.

#### 2.3.2.1 Disconnected channels

APA channels with a “broken connection” can be identified in ProtoDUNE-SP data by comparing channels that do not record hits during detector runs against channels that do respond to the internal calibration pulser system on the FEMBs. If pulser signals are seen on a channel with no hits, this most likely points to a mechanical failure in the wire path to the electronics. The failure could be, for example, at a bad solder connection, a damaged trace on a wire board, or a faulty connection between a wire, CR, and CE adapter boards. Studies have been done using data throughout the ProtoDUNE-SP run, looking for channels non-responsive to ionization. Note that this analysis is insensitive to the  $X$ -plane wires that face the cryostat walls since no ionization arrives at those wires.

The results show a very low count of permanently disconnected channels in the ProtoDUNE-SP APAs (28 channels out of 12,480 channels facing the drift volume). In addition, we identified 21 channels that are intermittently not responsive, most probably due to APA problems. This is summarized in tables 2.5 and 2.6. The fractions of disconnected and intermittent channels are low, 0.22% and 0.17%, respectively.

**Table 2.5.** Summary of disconnected channels per plane in ProtoDUNE-SP due to mechanical failures in the APAs.

|              | $U$ -plane | $V$ -plane | $X$ -plane | Total Channels | Rate  | Total |
|--------------|------------|------------|------------|----------------|-------|-------|
| Disconnected | 16         | 8          | 4          | 12,480         | 0.22% | 0.39% |
| Intermittent | 7          | 7          | 7          |                | 0.17% |       |

**Table 2.6.** Summary of disconnected channels per APA in ProtoDUNE-SP due to mechanical failures in the APAs.

|              | APA 1 | APA 2 | APA 3 | APA 4 | APA 5 | APA 6 |
|--------------|-------|-------|-------|-------|-------|-------|
| Disconnected | 4     | 5     | 8     | 3     | 1     | 7     |
| Intermittent | 10    | 0     | 1     | 4     | 3     | 3     |

So far, analysis of data throughout the ProtoDUNE-SP run shows no evidence of increasing numbers of disconnected or intermittent channels.

#### 2.3.2.2 Effect of electron diverters on charge collection

Active strip-electrode electron diverters were installed in ProtoDUNE-SP between APAs 1 and 2 (ED12) and between APAs 2 and 3 (ED23), which are both on the beam-right side of ProtoDUNE-

SP for the 2018–2019 run. The two inter-APA gaps on the beam-left side did not have electron diverters in them. ED12 developed an electrical short early in the run, and as a consequence, both ED12 and ED23 were left unpowered for the beam run and all but a small number of test runs after the beam run. A voltage divider on the electron diverter HV distribution board provided a path to ground, and so the electron diverter strips were effectively grounded. Since they protrude into the drift volume in front of the APAs, the grounded diverters collect nearby drifting charge instead of diverting it towards the active apertures of the APAs, leading to broken tracks with charge loss in the gaps. When powered properly, charge is primarily displaced away from the gap, and tracks that are more isochronous provide good measurements of the charge arrival time delays due to the longer drift paths of diverted charge. Figure 2.22 shows the collection-plane view of the readout of APAs 3 and 2 for a test run in which ED23 was powered at its nominal voltage. Figure 2.23 shows the collection-plane view of a track crossing the drift volumes read out by APAs 6 and 5, which do not have an electron diverter installed between them. Timing and spatial distortions in the absence of diverters appear minimal.

The impact of charge distortions can be seen in figure 2.24, which shows the average  $dQ/dx$  distributions for ProtoDUNE-SP run 5924, which has ED12 at ground voltage, ED23 at nominal voltage, and no diverters on the beam-left side of the detector between APAs 4, 5, and 6. Pronounced drops in the charge collected near ED12 (grounded diverter) are seen, while much smaller distortions are seen elsewhere. Run 5924 was taken while the grid plane in APA 3 was charging up, resulting in artifacts in the  $dQ/dx$  measurements with a period of three wires. APA 2 has an artifact from an ASIC with a slightly different gain reading out channels near the boundary with APA 1, causing even and odd channels to be offset.

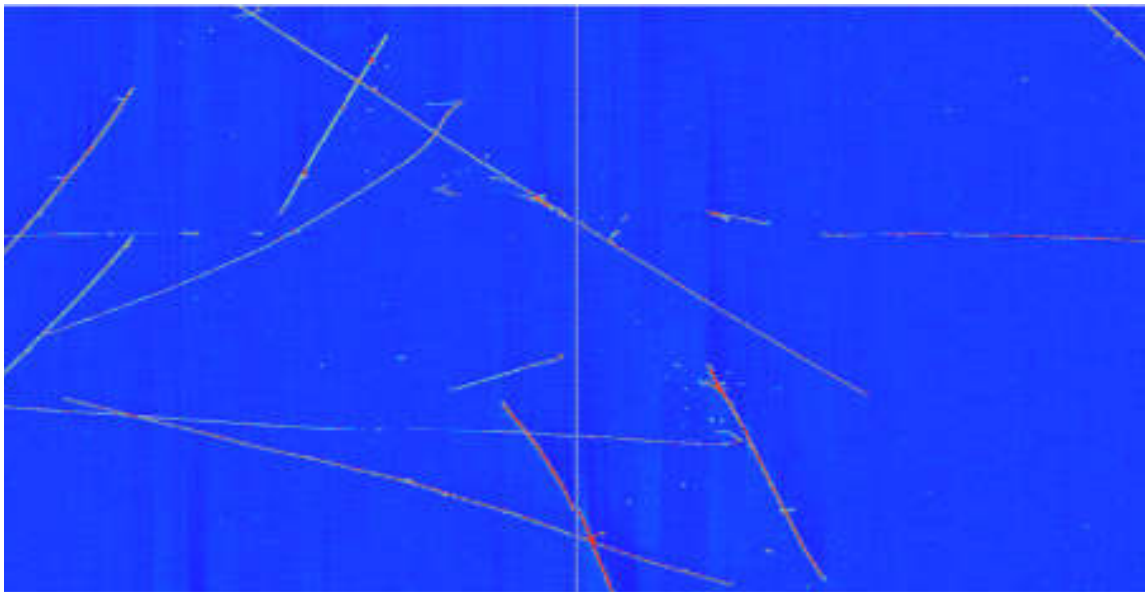


**Figure 2.22.** Collection-plane charge signals in ProtoDUNE-SP for a single readout window in APAs 3 (left) and 2 (right) for a test run in which ED23 was powered at its nominal voltage. The horizontal axis is wire number, arranged spatially along the beam direction, and the vertical axis is readout time. The event is run 5924, event 275.

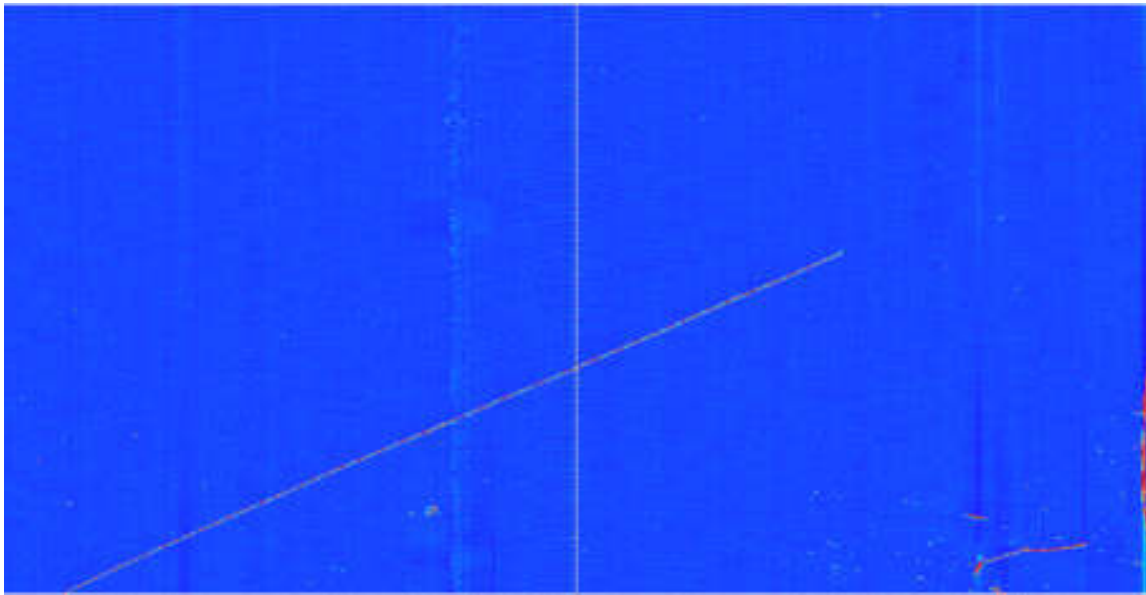


**Figure 2.23.** Collection-plane event display for APAs 6 (left) and 4 (right). No electron diverter was installed between these two APAs. The event is run 5439, event 13.

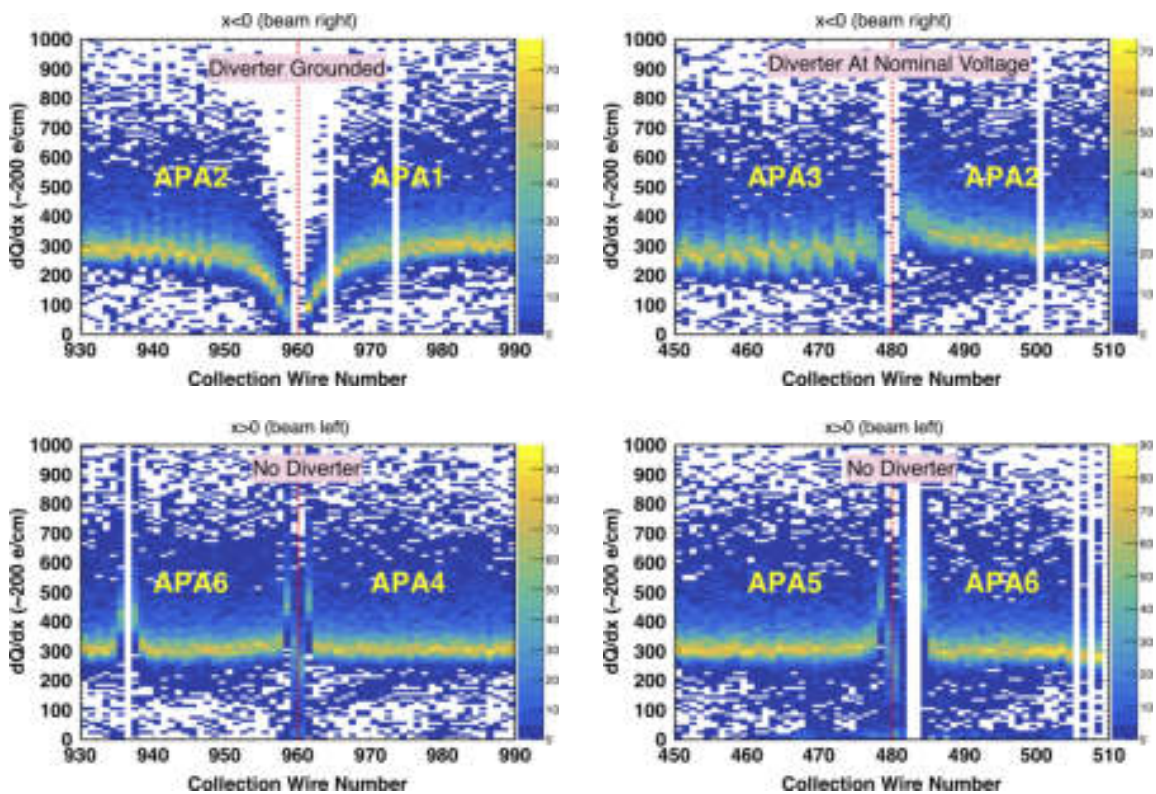


**Figure 2.24.** The  $dQ/dx$  distributions as a function of the collection wire number zoomed in near the gaps, using cosmic ray muons in ProtoDUNE-SP run 5924. The electron diverters are only instrumented for the gaps at the beam right side ( $x < 0$ ). The electron diverter between APA 2 and APA 3 was running at the nominal voltage while the electron diverter between APA1 and APA 2 was turned off.

2020 JINST 15 T08010

### 2.3.2.3 Effect of wire support combs on charge collection

Inclusive distributions of charge deposition on each channel can be made with ProtoDUNE-SP data using the cosmic-ray tracks. Tracks that cross from the cathode to the anode have unambiguous times even without association with PDs, and thus distance-dependent corrections to the lifetime can be made. The reconstruction of tracks in three dimensions makes use of the charge deposited in each of the three wire planes. Maps of the median  $dQ/dx$  response have been made for each plane in each APA in the  $(y, z)$  plane, the plane in which the APA resides. The granularity of these maps is the wire spacing, in both dimensions, and so the charge response of small segments of wires is measured. These maps are projected onto the  $U$ ,  $V$ ,  $y$ , and  $z$  coordinate axes in order to visualize more easily the impacts of localized detector inhomogeneities.

The wire-support combs are approximately evenly spaced in the  $y$  coordinate. In order to investigate the impact of the wire combs on charge collection and induction signals, the average of the median binned  $dQ/dx$  values as a function of  $y$  is shown for  $U$ ,  $V$ , and collection-plane ( $Z$ ) wires in figure 2.25. APA 6, which is in the middle of the detector and thus is minimally affected by features on the neighboring field cages, is chosen so the effects of the combs are most visible, though similar effects are seen in all six APAs in ProtoDUNE-SP. Localized dips of the order of 2% in the average signals can be seen at the locations of the combs in the  $U$  and  $V$  views, while the collection-plane channels show smaller dips and other features. Charge is expected to divert around the dielectric combs after they charge up, and if the diversion is purely in the vertical direction, then the impact on the collection-plane response is expected to be suppressed. The induction-plane response may be understood as the result of the dielectric comb locally polarizing in the field of the drifting charge, thus modifying the  $E$  field at the wires. This analysis well exhibits the uniformity of the response of the ProtoDUNE-SP APAs as well as the level of detail that can be extracted from TPC data for the precise calibration of the SP modules.

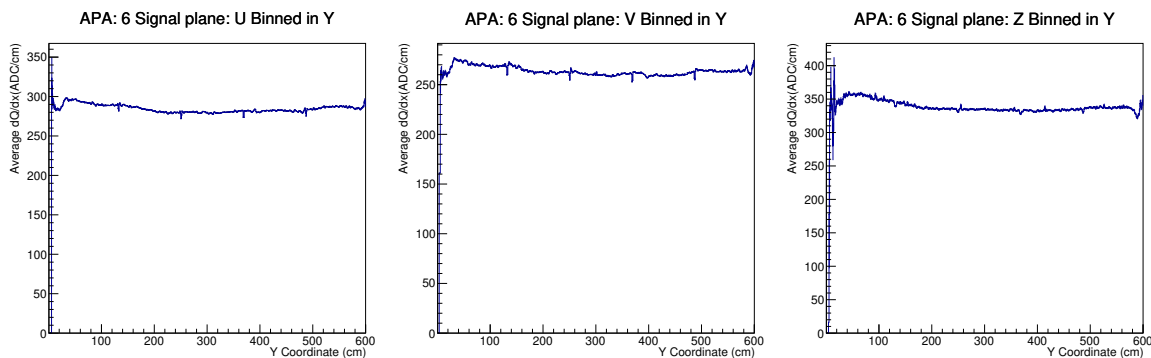


**Figure 2.25.** Average  $dQ/dx$  on the  $U$ ,  $V$ , and collection-plane ( $Z$ ) wires in APA 6 as a function of the height  $y$  from the bottom of the ProtoDUNE-SP detector.

### 2.3.2.4 Wire bias voltage scans and electron transparency

A set of dedicated runs were taken at ProtoDUNE-SP in order to confirm the bias voltage settings calculated by the COMSOL software and presented in section 2.2.1. In particular, the bias voltages in the  $G$  (grid), (induction)  $U$ , and (collection)  $X$  wire plane were uniformly reduced from 5% to

30% relative to the nominal settings. For each wire plane, the transparency condition depends on the ratio of the E field before and after the wire plane. Therefore, in the situation of uniform reduction of the bias voltages, some ionization electrons are expected to be collected by the grid plane, leading to a loss of ionization electrons collected by the X wires. Figure 2.26 shows the results from each of six APAs in ProtoDUNE-SP. The ratio “R”, ranging from 0.7 (30% reduction) to 0.95 (5% reduction), represents the different bias voltage settings used in these runs. “T” represents the transparency of the ionization electrons, which is proportional to the number of ionization electrons collected by the X wire plane. As a result of the significant space charge effect in ProtoDUNE-SP, the sources of ionization electrons (presumably dominated by cosmic muons) are different for different APAs. To facilitate the comparison among different APAs, the transparency at each bias voltage setting is normalized by the transparency at the highest bias voltage setting (R=0.95). Except for APA 3, all APAs show a similar trend in the change of transparency. The spread represents the uncertainty in calculating the transparency. The grid plane of APA 3 was found to be disconnected since December 2018, which led to incorrect bias voltage settings in these runs. This explained the abnormal behavior in its transparency data. Two sets of predictions (COMSOL vs. Garfield) are compared with the ProtoDUNE-SP data. The ranges of R in these predictions are different from that of the ProtoDUNE-SP data, since these two predictions were obtained prior to the ProtoDUNE-SP data taking. The COMSOL prediction is clearly confirmed by the ProtoDUNE-SP data, which also validates the nominal bias voltage settings listed in section 2.2.1. The incorrect prediction from the Garfield simulation is attributed to inaccurate E field calculations near the boundary of the wires (152  $\mu\text{m}$  diameter), which is much smaller than the wire pitch ( $\sim 4.79$  mm).

### 2.3.2.5 Abnormal behavior of G-plane on APA 3

Dedicated studies of  $dQ/dx$ , the recorded ionization charge per unit path length from cosmic muon tracks, have been performed for each APA. For runs immediately after periods when the cathode HV was off for an extended length of time, of the order of a few days, the average of the  $dQ/dx$  distribution on APA 3 collection and induction planes was found to be systematically lower than for the other APAs. The  $dQ/dx$  would then slowly increase with time. Detailed investigations showed that this behavior is explained by the assumption that the G-plane on APA 3 is not connected to a proper reference voltage. When the cathode HV is turned on after a long off period, the G-plane, initially at a floating potential close to ground, slowly charges up towards a negative HV, re-establishing transparency for the ionization electrons towards the signal planes. It takes about 100 hours for the G-plane to reach a negative potential close to the nominal value that allows full transparency.

We are presently evaluating more accessible locations for the connection of the bias HV cables from the cryostat feedthroughs to the APAs, to minimize connection problems with the SHV connectors. In addition, during installation, we will include as part of the standard checkout procedure either a direct confirmation of the bias connection between a wire plane and its bias input on the feedthrough flange, or an indirect measurement of the connection by recording the charging current in the bias line when increasing the bias voltage to its nominal value. The construction and integration tests with a pre-production APA, described below in section 2.3.3, will fully test any changes to the SHV system.

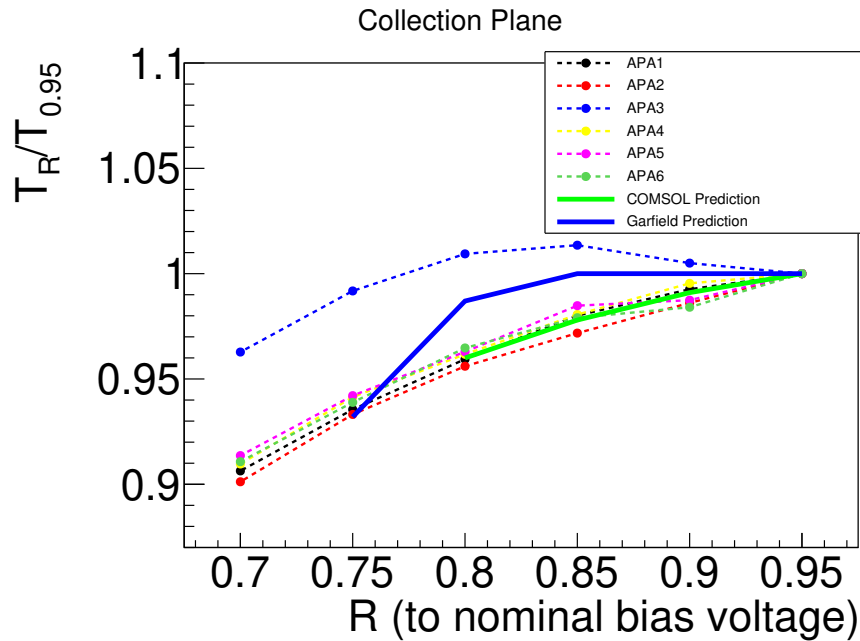


**Figure 2.26.** The transparency results from the bias voltage scan in ProtoDUNE-SP. “R”, the ratio to the nominal bias voltages, represents different bias voltage settings. “T” represents the transparency of the ionization electrons, which is proportional to the number of ionization electrons collected by the X wire plane. The prediction of COMSOL (Garfield) is confirmed (refuted) by the ProtoDUNE-SP data. The abnormal behavior of APA 3 is a result of incorrect bias voltage settings. See section 2.3.2.5 for more discussion.

### 2.3.3 Final design prototyping and test assemblages

To confirm modifications made to the APA design and production process since ProtoDUNE-SP and to work through the multi-APA assembly procedures, several prototypes are planned for 2020.

A seventh ProtoDUNE-SP-like APA was completed at Daresbury Laboratory by utilizing an upgraded winding machine with the new interface arm design (see section 2.5.1). This APA was shipped to CERN in March 2019 for a test of the CE in the cold box, expected to be performed in 2020. In addition, work is in progress to implement a new winding head on the APA winding machines, with automatic tension feedback and control on the wires. These same upgrades will be implemented on the winding machine at PSL in 2020.

A top and bottom version of the new supporting APA frame design were built in spring 2019 at PSL and shipped to Ash River. A full test of the APA pair assembly procedure was successfully completed in early October 2019 (see figure 2.27). The procedure of routing the CE cables along the side tubes of the APA pair was also successfully tested. In addition, a preliminary test of the installation of PD system prototype cables inside the APA frames and the mating of cable connections between the lower and upper APA was performed. See section 2.4.3 for more information on cable routing in the APA frames.

Also planned is the construction of a pre-production APA for an integration test with the CE and PD system systems at CERN, which will fully test all interface aspects. This test will inform the final design review of the APA system in May 2020.

In addition, three fully wound APAs with pre-installed PD system cables, will be built by the end of 2020 for deployment in ProtoDUNE-SP-II, replacing the detectors of one of the drift volumes. This will allow a test of all APA components, including the larger size frames and geometry boards and a final tuning of the winding machines. The three APAs will be shipped to CERN, integrated with CE boxes and PD system detectors, and tested in the cold box before installation in ProtoDUNE-SP. The pre-production APA mentioned above could serve as one of the three if no design modifications are required. These final prototyping activities will serve to test all critical aspects of the APA design before starting DUNE APA production in 2020.



**Figure 2.27.** APA pair assembly and integration tests at Ash River.

### 2.4 Interfaces

The interfaces between the APA consortium and other detector consortia, facilities, and working groups covers a wide range of activities. Table 2.7 lists the interface control documents under development. In the following sections, we elaborate slightly on the interfaces with the TPC readout electronics and the PD system, as well as the cable routing plan for both systems. Other important interfaces are to the TPC HV system (the FC) and the DSS inside the DUNE cryostats.



**Table 2.7.** APA Interface Links.

| Interfacing System           | Linked Reference |
|------------------------------|------------------|
| TPC electronics              | DocDB 6670 [9]   |
| Photon detector system       | DocDB 6667 [10]  |
| Drift high voltage system    | DocDB 6673 [11]  |
| DAQ                          | DocDB 6676 [12]  |
| Slow controls and cryogenics | DocDB 6679 [13]  |
| Integration facility         | DocDB 7021 [14]  |
| Facility interfaces          | DocDB 6967 [15]  |
| Installation                 | DocDB 6994 [16]  |
| Calibration                  | DocDB 7048 [17]  |
| Software computing           | DocDB 7102 [18]  |
| Physics                      | DocDB 7075 [19]  |

#### 2.4.1 TPC cold electronics

The TPC readout electronics (CE) are directly mounted to the APA and thus immersed in LAr to reduce the input capacitance and inherent electronic noise. With the wire-wrapped design, all 2560 wires to be read out (recall 960 are *G*-plane wires used for charge shielding only and are not read out) terminate on wire boards that stack along one end (the head) of the APA frame. The 2560 channels are read out by 20 FE motherboards (128 channels per board), each of which includes eight 16-channel FE ASICs, eight 16-channel ADC ASICs, LV regulators, and input signal protection circuits. Figure 2.28 shows a ProtoDUNE-SP APA during integration at CERN with the TPC electronics partially installed and a cable tray mounted above.

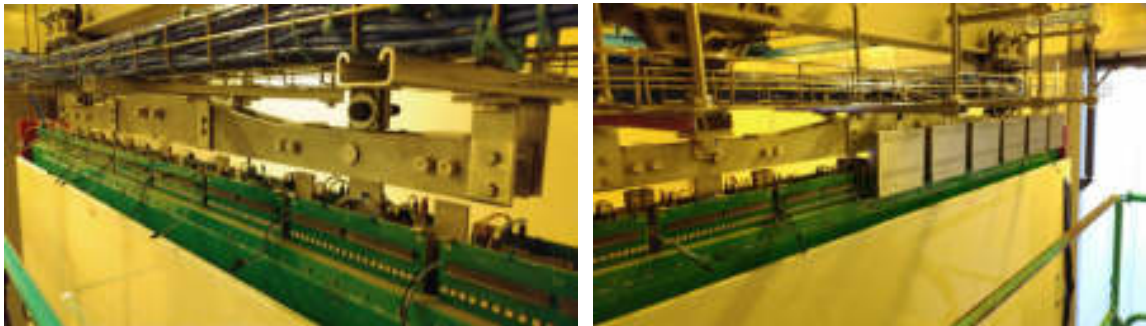


**Figure 2.28.** The head region of an APA frame during installation at ProtoDUNE-SP. On the left the head wire boards, CR boards, and yoke are clearly visible. On the right, five of the 20 CE boxes have been installed.

The mechanical interface includes the support of the 20 CE boxes, each housing a 128 channel FEMB. They are the gray vertically oriented boxes on the right in figure 2.28.

The electrical interface covers the choice of wire-bias voltages to the four wire planes so that 100% transparency can be achieved for drifting ionization electrons, cable connection for the

wire bias voltages from the cryostat feedthroughs to the CR boards, interface boards connecting CR boards and CE boxes, filtering of wire-bias voltages through CR boards to suppress potential electronic noise, and an overall grounding scheme and electrical isolation scheme for each APA. The last item is particularly important to achieve the required low electronic noise levels. See section 4.2 for information on all parts of the CE system.

### 2.4.2 Photon detection system

The PD system is integrated into the APA frame to form a single unit for detecting both ionization charge and scintillation light. The APA frame design must also accommodate cables for the PDs. Individual PD units are inserted through 10 slots machined in the side steel tubes of the frame and supported by rails mounted in the APA. Figures 2.7 and 2.8 show examples of these features in the frame. Figure 2.29 shows a PD module being inserted into a slot in the frame and mating with an electrical connector mounted along the center tube in the APA.

The interface between the PD system and APAs involves the mechanical hardware design and production, cable routing, and integration, installation, and testing procedures. The electrical interface includes a grounding scheme and electrical insulation. The strict requirements on noise from the CE means the electrical interface must be defined together with the SP TPC electronics consortium.

For more information on the PD system, see chapter 5.

### 2.4.3 Cable routing

Cable routing schemes for both the TPC electronics and PD system must be integrated into the design of the APAs. The CE signal and power cables must be routed so that the head end of the lower APA in the two-APA assembly can be reached. CE cables, therefore, will be routed inside the two side beams of the APA frames. Figure 2.30 depicts such a cable routing scheme. The CE cables at the lower end of the lower APA are formed into two bundles, each about 50 mm in diameter. Installation of the cables through the side tubes of the two stacked APAs is done by pulling them through a large, smooth conduit placed inside each of the side tubes. To fully accommodate the cables, the APA frame hollow tube sections were enlarged relative to the PD design from 7.6 cm to 10.2 cm (3 in to 4 in) deep. Prototyping of this solution was carried out at PSL during summer 2018, as shown in the right photograph in figure 2.30.

The concept being developed for the cables of the PDs is depicted in figure 2.31. The cables run along the outside of the central tube in the APA frame, joining together into a bundle of five cables by the time they reach the top of the frame. Cables from the bottom APA in a stack are fed through the foot tubes to the upper APA and ran along the outside tubes on either side. In this way, all PD cables make it to the head of the upper APA.

## 2.5 Production plan

The APA consortium oversees the design, construction, and testing of the DUNE SP module APAs. Production sites are being planned in the USA and UK. This approach allows the consortium to produce APAs at the rate required to meet overall construction milestones and, at the same time, reduce risk to the project if any location has problems that slow the production pace.

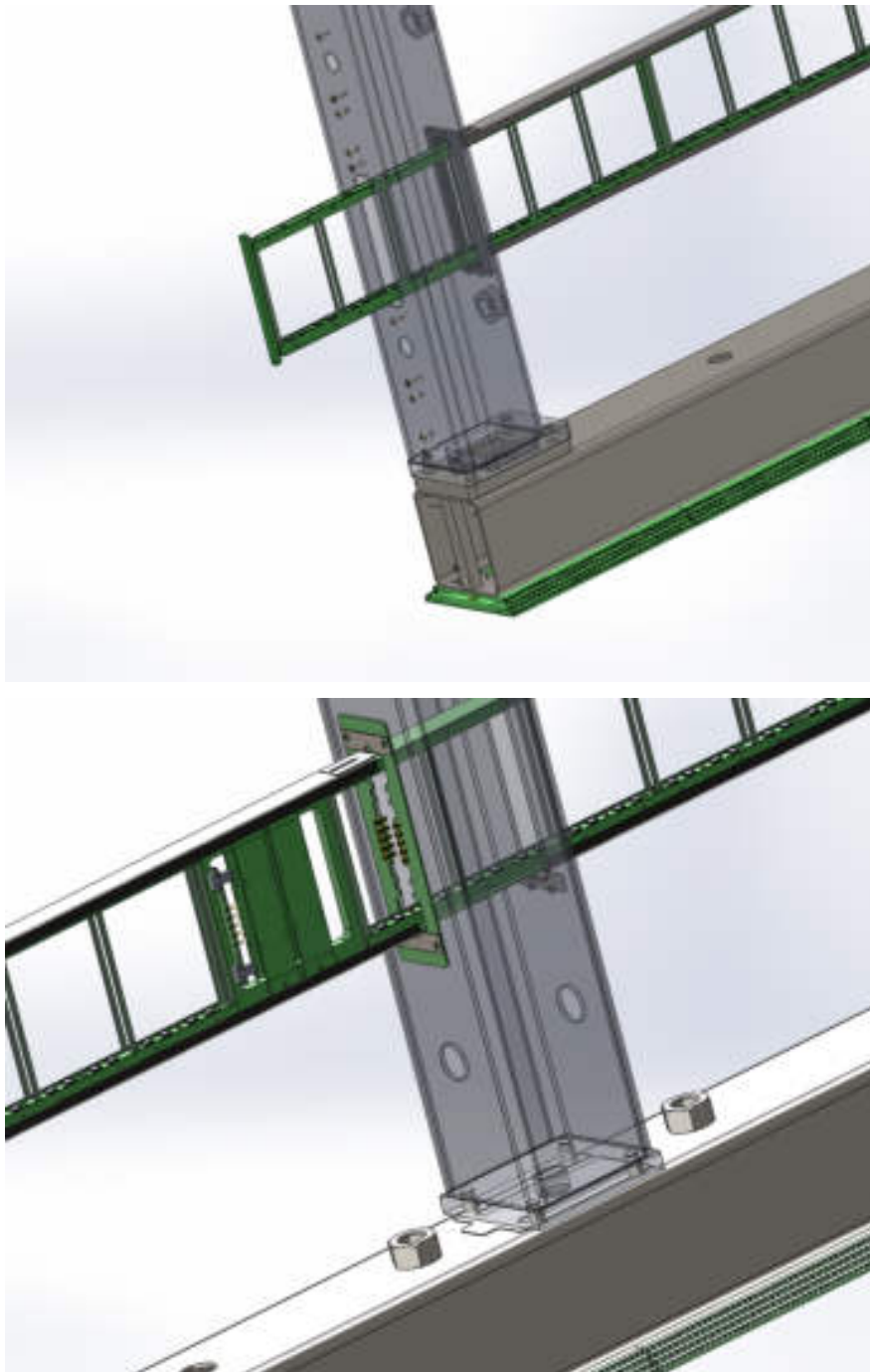


**Figure 2.29.** Top: a PD module in ProtoDUNE-SP being inserted into a slot in the frame. Bottom: the PD unit mating with an electrical connector mounted along the center tube in the APA.

2020 JINST 15 T08010

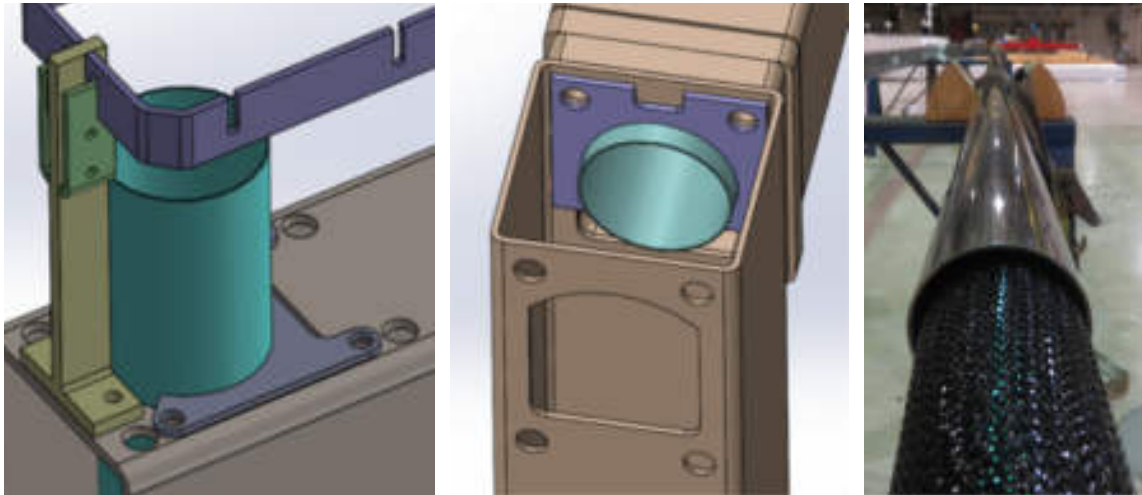


**Figure 2.30.** Cable routing scheme. Left: conduit for the CE cables protruding from the end of the long side tubes of the APA frame. Right: one of the CE cable bundles being pulled through conduit of equal length to the two stacked APAs. The cable bundle is wrapped with a protective cover of braided PET plastic.

The starting point for the APA production plan for DUNE SP modules is the experience and lessons learned from ProtoDUNE-SP construction. For ProtoDUNE-SP, the APAs have been constructed on single production lines set up at PSL in the USA and at Daresbury Laboratory in the UK. The plan now is to construct APAs for DUNE at US and UK collaborating institutions with ten total production lines, four in the UK and six in the US.

A production line is centered around a wire winding robot, or winder, that enables continuous wrapping of wire on a 6 m long frame (see figures 2.32 and 2.33). Two process carts are needed to support the APA during board epoxy installation and QC checks, among other construction processes. A means of lifting the APA in and out of the winder is also required. A gantry-style crane was used for ProtoDUNE-SP construction.

The fabrication of an APA is a three-stage process requiring about 50 eight-hour shifts to complete, with a mix of engineering, technical, and scientific personnel. The first stage, estimated at about four shifts, is a preparation stage in which PD system cables and rails, wire mesh panels, comb bases,  $X$ -plane wire boards, and tension test boards are installed on the bare APA frame. In the second and longest stage, lasting 38–40 shifts, the APA occupies a winding machine. All the wires are strung and attached in this stage, and tension and electrical tests of each channel are performed. The third and final stage, requiring an estimated 8 shifts, is completed in a process cart and involves the installation of wire harnesses, G-bias boards, and cover boards. Protection panels are then installed over the wire planes and the completed APA is transferred to a transport frame (see section 2.6). During ProtoDUNE-SP construction, we were able to complete an APA in 64 shifts, on average. Several improvements to the process and tooling have been developed since then to reduce this to the maximum allowed 50 shifts.

The approximately 40 shifts that an APA spends in the winding machine combined with the total number of winders determines the overall pace of production since the pre- and post-winding stages can be done in parallel with winding. The overall production model assumes that the APA

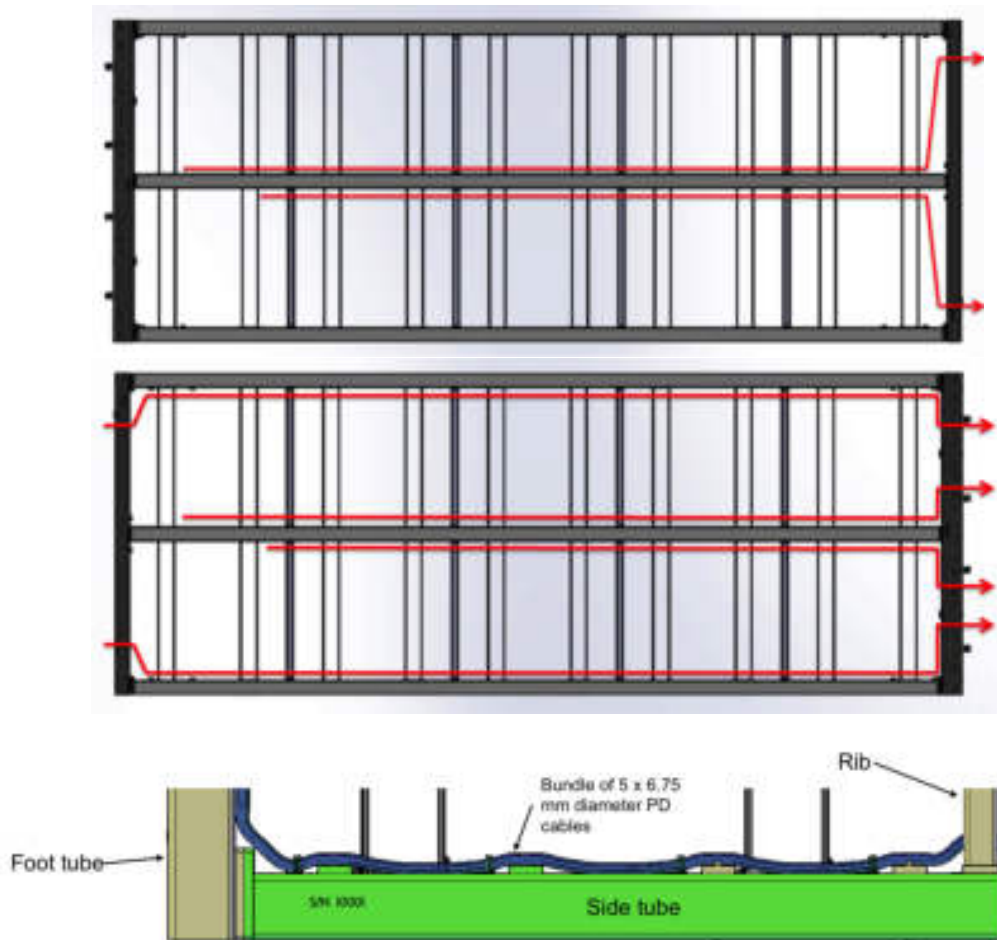


**Figure 2.31.** A concept for PD system cable routing (shown horizontal). Top: the bottom APA. The PDs are the ten transparent pieces spanning the frame — two between each set of ribs. They connect to their cables at the center tube. The cables run up either side of the center tube (outside the tube) joining with others and forming two bundles of five cables by the time they reach the foot tube at the right end of this image. Middle: the top APA. The two five-cable bundles from the lower APA continue to the head tube of the upper APA (at the right in this image) where they go through the head tube. The cables from the PDs in the upper APA run up the outside of the center tube and form bundles which also go through the head tube. Bottom: detail showing the five PD system cables gathered together at the foot tube (the top) of the bottom APA.

production sites run one shift per day, that all winding machines are operated in parallel, and that two weeks per year are devoted to maintaining equipment. The work plan at production sites further assumes a steady supply of the necessary hardware for APA wiring, such as completed frames, grounding mesh panels, and wire boards. Detailed planning is underway within the APA consortium for collaborating institutions to help source and test components and ensure their on-time delivery to production sites.

Having several APA production sites in two different countries presents quality assurance and quality control (QA/QC) challenges. A key requirement is that every APA be the same, regardless of where it was constructed. To achieve this goal, we are building on ProtoDUNE-SP experience

where six identical APAs were built, four in the US and two in the UK. The same tooling, fabrication drawings, assembly, and test procedures were used at each location, and identical acceptance criteria were established at both sites. This uniform approach to construction is necessary, and the APA consortium is developing the necessary management structure to ensure that each production line follows the agreed-upon approach to achieve APA performance requirements.

### 2.5.1 Assembly procedures and tooling

The central piece of equipment used in APA production is the custom-designed wire winder machine, shown schematically in figure 2.32 and in use in figure 2.33. An important centerpiece of the winder machine is the wiring head. The head releases wire as motors move it up and down and across the frame, controlling the tension in the wire as it is laid. The head then positions the wire at solder connection points for soldering by hand. The fully automated motion of the winder head is controlled by software, which is written in the widely used numerical control G programming language. The winder also includes a built-in vision system to assist operators during winding, which is currently used at winding start-up to find a locator pin on the wire boards.

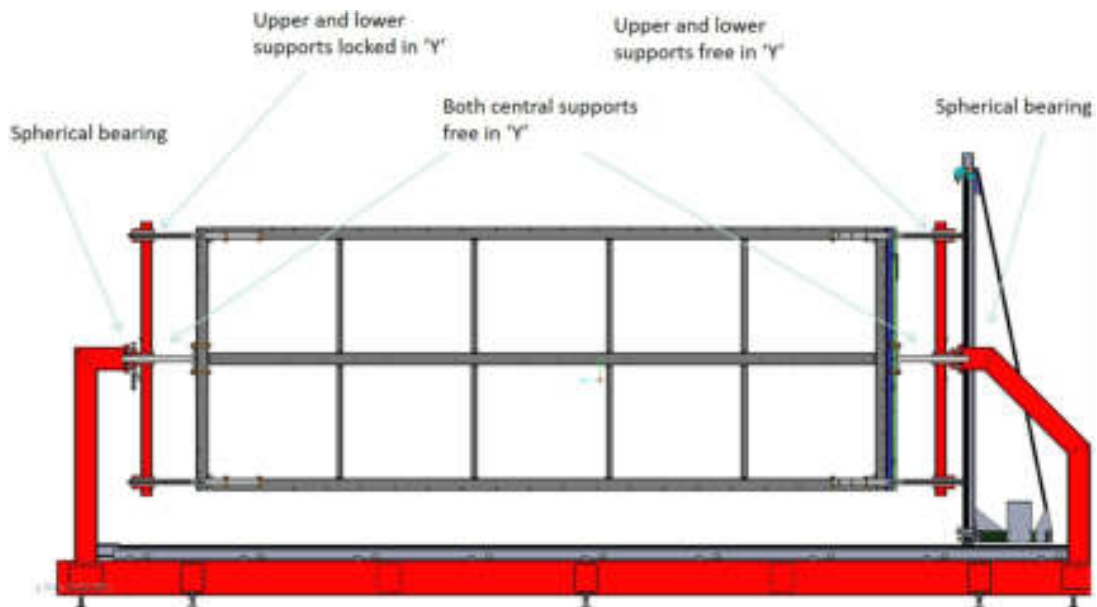


**Figure 2.32.** Schematic of the custom-designed APA wiring machine. This shows the updated version with upper and lower supports and the spherical bearings for rotating the APA on the winder.

In the scheme used for wiring the ProtoDUNE-SP APAs, an APA moved on and off the winder machine several times for wiring, soldering, and testing. Several design changes were developed in 2018–2019 to enable the APA to remain on the winding machine throughout the wiring process. The design concept allows the winder head to pass from one side to the other nearly continuously. The interface frames at either end have been replaced by retractable linear guided shafts. These can be withdrawn to allow the winding head to pass around the frame over the full height of the frame. These shafts have conical ends and are in shafts fixed to the internal frame tube to provide guides to location. This design change does not alter the design of the frame itself, but it does



**Figure 2.33.** Left: partly wired ProtoDUNE-SP APA on the winding machine at Daresbury Lab, UK. Right: partly wired ProtoDUNE-SP APA on the winding machine during wire tension measurements at PSL.

allow for rotation in the winding machine. It is now possible to carry out board installation, gluing, and soldering all while on the winding machine. This eliminates any transfer of the APA to the process cart for the entire production operation, making it an inherently safer and faster production method. The upgraded design has been implemented on the winding machine at Daresbury, which has been used to build a new prototype, APA 7 (figure 2.34). All winding, board installation, gluing, soldering and testing operations are being carried out in the winding machine. APA 7 also incorporates the pre-built grounding mesh sub-frames, another new feature that saves significant time in production.



**Figure 2.34.** Left: upgraded winding machine with new interface arm design being used to wire APA-07. Fitted mesh panels are also shown installed. Right: the V-layer soldering process at the head end of APA-07. Soldering can now be done with the APA in the winding machine.

The wiring head has also been updated. The upgraded design offers real-time tension feedback and control, which will save time in wiring and produce better tension uniformity across wires. A prototype of the new head has been constructed and is undergoing extensive commissioning and qualification.

An important element in the long-term use of the winders will be maintenance. During ProtoDUNE-SP construction winding machine problems traceable to a lack of routine maintenance occurred from time to time, shutting the production line down until repair or maintenance was performed. We will formulate a routine and preventive maintenance plan that minimizes winder downtime during APA production for the SP module.

The large process carts are important to the flow of activities during production (figure 2.35). The process carts are used to hold APAs during wiring preparations, for QC checks after wiring, and to safely move APAs around within the assembly facility. Process carts are fitted with specialized 360° rotating casters that allow the cart, loaded with a fully assembled APA, to maneuver corners while moving the large frames between preparation, assembly, and packing/shipping areas.



**Figure 2.35.** A ProtoDUNE-SP APA being moved around the PSL production facility on a process cart.

### 2.5.2 APA production sites

Multiple APA production lines spread over several sites in the USA and the UK will provide some margin on the production schedule and provide backup in the event that technical problems occur at any particular site.

The space requirements for each production line are driven by the size of the APA frames and the winding robot used to build them. The approximate dimensions of a class 100,000 clean space needed to house winder operations and associated tooling is 175 m<sup>2</sup>. The estimated requirement for inventory, work in progress, and completed APAs is about 600 m<sup>2</sup>. Each facility also needs temporary access to shipping and crating space of about 200 m<sup>2</sup>. Floor layouts at each institution are being developed, with current layouts shown in figure 2.36. Adequate space is available at each site, and the institutions have offered commitments for space for this purpose.

At Daresbury Laboratory in the UK, the existing single production line used for ProtoDUNE-SP construction will be expanded to four. The Inner Hall on the Daresbury site has been identified



as an area that is large enough to be used for DUNE APA construction. It has good access and crane coverage throughout. Daresbury Laboratory management has agreed that the area is available, and a working environment that meets DUNE's safety standards is now being prepared, starting with clearing the current area of existing facilities, obsolete cranes, and ancillary equipment. The renovation of a plant room is also in progress, so that it can be used for storage and as a shipping area. The production area is designed to hold four winding machines and associated process equipment and tooling. A production site design review of the Daresbury facility is planned for January 2020, and a production site readiness review is anticipated for June 2020, followed by the start of APA production for DUNE detector module #1 in August 2020.

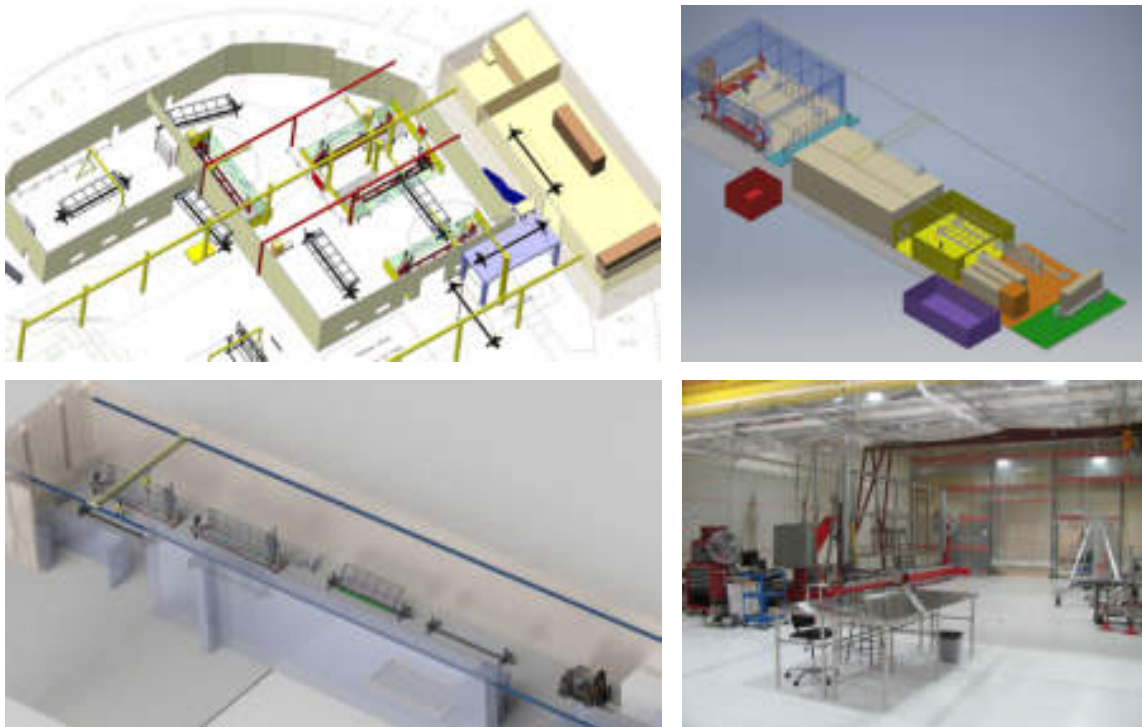


**Figure 2.36.** Developing concepts for production site layouts at Daresbury Lab (top left), University of Chicago (top right), and Yale University (bottom left), and the existing APA production area at PSL (bottom right).

In the USA, there will be six total production lines at three sites: two at the University of Chicago, two at Yale University, and two at the University of Wisconsin's PSL, including the existing winder where the construction for ProtoDUNE-SP was carried out.

The APA production site at the University of Chicago will be housed in the Accelerator Building on the campus in Hyde Park. The building has hosted the assembly of large apparatuses for numerous experiments over the course of its history and features an extensive high bay with an overhead crane, an indoor truck bay, clean laboratory spaces, a professional machine shop, and proximity to faculty and staff offices. Winding will be done inside a clean room installed on the first floor-level mezzanine, where there is 234 m<sup>2</sup> of floor space above the machine shop. A 2 ton capacity bridge crane will be installed inside this clean room to move APAs between the two winders

and the process carts that will be located here. APAs will enter and exit the mezzanine by way of a loading deck external to the cleanroom. Preparation of APA frames, including mesh installation, will be done inside a second clean room on the basement level floor of the high bay. Ample space, roughly 170 m<sup>2</sup>, between this clean room and the truck bay allows for simultaneous receiving of bare frames or other larger items, hoisting of APAs to and from the mezzanine, and packaging of completed APAs for outbound shipment. When needed, additional off-site storage will be available for holding excess inventory and completed APAs before they are transported to South Dakota.

Yale's Wright Laboratory will host another of the USA-based APA production sites in a recently renewed area named "The Vault" where the nuclear accelerator operated previously. The Vault is approximately 720 m<sup>2</sup> of total floor space and it satisfies all the safety and space requirements for an APA production site. Indeed, the area, which is planned to be completely transformed into a cleanroom, can easily host two winders and four processing carts and has sufficient space for crating the APAs for shipment and receiving and stocking all the material, e.g., bare frames, electronics boards, and mesh panels. A large high bay door at one end offers direct road access, allowing trucks to back inside the room where a 10 ton crane operates all along the length. Moreover, Wright laboratory has good support infrastructure, including cleanrooms and modern mechanical and prototyping workshops that are directly connected to the Vault. Faculty, researchers and postdoc offices are located upstairs in the same building.

The Physical Sciences Laboratory (PSL) Rowe Technology Center has up to 1850 m<sup>2</sup> (20,000 ft<sup>2</sup>) total space available for continued DUNE activities. A clean work area that houses the existing winding machine used for ProtoDUNE-SP is already in place and will be used for DUNE APA construction. A second APA production line using the updated winder design will be assembled in 2020, and the existing winder will be upgraded. PSL will host other major activities as well, including the assembly of bare APA frames for wiring in the USA, production of CR boards, and fabrication of APA pair linkage and installation hardware.

Development work relevant for local planning at each site is rapidly advancing. Figure 2.36 shows current conceptual layouts for the future production setups at Daresbury, Chicago, and Yale and a photograph of the existing APA production facility at PSL-Wisconsin. Production Site Design Reviews of the Chicago and Yale facilities are planned for early in 2020.

### 2.5.3 Material supply

Ensuring the reliable supply of raw materials and parts to each APA production site is critical to keeping APA production on schedule through the years of construction. Here the consortium institutions are pivotal in taking responsibility for delivery of APA sub-elements. Supplier institutions will be responsible for sourcing, inspecting, cleaning, testing, QA, and delivery of hardware to each production site. In particular, the critical activities to supply production sites with the minimum needed APA components for assembly include:

- **Frame construction:** there will be separate sources of frames in the USA and the UK. The institutions responsible will rely on many lessons learned from ProtoDUNE-SP. The effort requires specialized resources and skills, including a large assembly area, certified welding capability, large-scale metrology tools and experience, and large-scale tooling and crane support. We are considering two approaches for sourcing: one is to outsource to an industrial

supplier; the other is to procure all the major machined and welded components and then assemble and survey in-house. Material suppliers have been identified and used with good results on ProtoDUNE-SP.

- **Grounding mesh supply:** the modular grounding mesh frame design allows the mesh screens to be produced outside of the APA production sites and supplied for APA construction. Suitable vendors to supply the needed units (20 mesh frames per APA) will be identified in both the USA and UK.
- **Wire wrapping board assembly:** multiple consortium institutions will take on the responsibility of supplying the tens of thousands of wire-wrapping boards required for each SP detector module. The side and foot boards with electrical traces are procured from suppliers and a separately bonded tooth strip is installed to provide wire placement support. The institutions responsible for boards will work with several vendors to reduce risk and ensure quality.
- **Wire procurement:** Approximately 24 km of wire is required for each unit. During ProtoDUNE-SP construction, an excellent supplier worked with us to provide high-quality wire wound onto spools that we provide. These spools are then used directly on the winder head with no additional handling or re-spooling required. Wire samples from each spool are strength-tested before use.
- **Comb procurement:** each institution will either work with our existing comb supplier or find other suppliers who can meet our requirements. The ProtoDUNE-SP supplier has been very reliable.

### 2.5.4 Quality control in APA production

QC testing is a critical element of APA production. All QC procedures are being developed by the consortium and will be implemented identically at all production sites in order to ensure a uniform quality product as well as uniform available data from all locations. Important QC checks are performed both at the level of components, before they can be used on an APA, as well as on the completed APAs, to ensure quality of the final product before leaving the production sites. In addition, a 10% sample of the completed APAs produced at each of the production sites each year will be cold cycled in a cryogenic test facility available at PSL.

#### 2.5.4.1 APA frame acceptance tests

Each APA support frame must meet geometrical tolerances in order to produce a final APA that meets requirements for physics. In particular, the wire plane-to-plane spacing must be within the specified tolerance of  $\pm 0.5$  mm (see section 2.2.1). Flatness of the support frame, therefore, is a key feature and is defined as the minimum distance between two parallel planes that contain all the points on the surface of the APA. Although the frame could be distorted out of plane in several ways, the most likely causes are: (1) a curve in the long side tubes causing the frame to bow out of plane, (2) a twist in the frame from one end to the other, or (3) a fold down the center-line (if the ends of the ribs are not adequately square).

As detailed in section 2.2.2, APA frames are constructed of 13 separate rectangular hollow steel sections. Before machining, a selection procedure is followed to choose the sections of the steel most suited to achieving the geometrical tolerances. After assembly, a laser survey is performed on the bare frames before they can be delivered to an APA production site. Three sets of data are compiled into a map that shows the amount of bow, twist, and fold in the frame. A visual file is also created for each APA from measured data.

A study was performed to determine the tolerances on the three distortions characterized above and is documented in [20]. It was determined that a 0.5 mm change in the final wire plane spacing could result from:

1. An 11 mm out-of-flatness caused by curved long side tubes.
2. A 6 mm out-of-flatness due to a twist in the frame. This is assumed to be evenly distributed between each of the 5 cells of the APA with ~1.2 mm out-of-flatness per cell.
3. A 1.2 mm out-of-flatness due to a fold down the middle of the APA.

The bow, twist, and fold extracted from the survey data will be compared against these allowable amounts before the support frame is used to build an APA. Later, during APA wiring at the production sites, a final frame survey will be completed after all electrical components have been installed, and the as-built plane-to-plane separations will be measured to verify that the distance between adjacent wire planes meets the tolerances.

Another check performed at the APA production site before the frame is transferred to a winder will confirm sufficient electrical contact between the mesh sub-panels and the APA support frame. A resistance measurement is taken immediately after mesh panel installation for all 20 panels before wiring begins.

### **2.5.4.2 Material supply inspections**

All components require inspection and QC checks before use on an APA. Most of these tests will be performed at locations other than the APA production sites by institutions within the consortium before the hardware is shipped for use in APA construction. This distributed model for component production and QC is key to enabling the efficient assembly of APAs at the production sites. The critical path components are the support frames (one per APA), grounding mesh panels (20 per APA), and wire carrier boards (204 per APA). Section 2.8 provides details about which consortium institutions in the US and UK will be responsible for each of these work packages.

### **2.5.4.3 Wire tension measurements and channel continuity and isolation checks**

The tension of every wire will be measured during production to ensure wires have a low probability of breaking or moving excessively in the detector. Every channel on the completed APAs will also be tested for continuity across the APA and isolation from other channels. The plan is to perform all tests at once, using the methods described in this section. As will be described in section 2.5.4.4, it is also planned that 10% of the APAs will be shipped to PSL for a cold test, where the full APA will be brought to LN<sub>2</sub> temperature. Following the cold test, the wire tensions and continuity will be remeasured. Finally, for this 10% sample of APAs, a measurement of the wire plane spacing will

be performed using a Faro arm that can precisely record the position of each wire plane in space. This checks that the QC on the flatness of the support frames remains sufficient.

Wire tensions will be measured after each new plane of wires is installed on an APA. The optimal target tension has been set at 6 N based on ProtoDUNE-SP experience. ProtoDUNE-SP data, where the tensions did have substantial variation, is also being used to study the effects of varying tensions and finalize the allowed range of values.

The technique used to measure tensions for the APAs of ProtoDUNE-SP was based on a laser and a photodiode system [21]. In this method, the laser shines on an individual wire and its reflection is captured by the photodiode. An oscillation is produced in the measured voltage when a vibration is induced on the wire, such as by manually plucking it. This oscillation is dominated by the fundamental mode of the wire, which is set by the wire's tension. Since the length and density of the wire are known, the measured fundamental frequency can be converted into a tension value. The method works very well, but due to the necessity of aligning the laser and exciting and measuring wires individually, this technique can take tens of seconds per wire. Given the large number of wires per detector module, development of a faster technique represents a major opportunity for the full DUNE construction.

A technique that can reduce the overall time required to measure the tension of every wire is currently being developed [22]. In this method, DC and AC voltages are applied on the neighboring wires of a wire under test. A sine wave of the same frequency as that of the applied AC voltage is measured from the tested wire, since it is capacitively coupled to its neighbors. The amplitude of the sine wave exhibits a resonant behavior when the frequency of the AC voltage corresponds to the fundamental frequency of the wire. Thus, a frequency sweep of the AC voltage can be performed to determine at which frequency there is a resonance, from which the wire tension can be obtained. As electrical signals can be injected and measured in several wires simultaneously, this technique has the potential of measuring the tension of many wires at once.

A wire tension measurement device based on the electrical method is being developed within the context of the DUNE APAs. While the underlying principle of the electrical method has been demonstrated, its technical implementation requires consideration. The wire pitch of the APAs requires summed input voltages on the order of 500 V to reasonably discern resonances against noise. The head boards, cf. section 2.2.5.1, have been designed to withstand temporarily such large differential voltages across neighboring channels. Additionally, the components of the CR boards or of the CE would interfere with the method and need to be absent.

The exact specifications of the measurement system are being finalized. It is planned to connect to one of the twenty head board stacks at a time. Within a given stack, the device is projected to inject and read out signals by groups of sixteen wires simultaneously. The device could be used to measure the tension of any wire layer at any stage of the production process, in particular after the winding of a wire layer or after all the wires are wound. The designs of the winder machine and of the APA protection panels have clearance provisions for the usage of such a measurement device.

The measurement system design is a combination of a commercial field programmable gate array (FPGA) board and a custom printed circuit board for analog signal processing. An FPGA board is used as it can produce a square wave at any frequency that is expected to be encountered while measuring a wire's fundamental frequency, i.e., below 5 kHz. In addition, the FPGA board can be used for digital signal processing of the readout signal. The analog circuitry would act as a

bridge between the FPGA and the APA wires. It is needed to filter the square wave into a sine wave, to amplify that sine wave before sending it to the wires and to digitize the readout signal before sending it to the FPGA. The analog board is also needed to provide electrical connections to the head boards. With such a design, it is expected that the concurrent tension measurement of eight wires would take on the order of ten seconds.

A prototype of the measurement device has been built. The main difference between the prototype and the planned design is that the former is restricted to three wires instead of sixteen: a single readout wire and two stimulus wires. The prototype has been employed on a test bench in which wires with the same physical properties as those that will be used in the APAs have been wound. The wires were wound according to these wire parameters, which are similar to those of the APAs: 6 N tension, 6 m length, 4.7 mm pitch. The applied voltages were 400 V DC and 26 V for the AC peak amplitude. The results obtained are shown in figure 2.37. The expected resonant frequency is 16.1 Hz. The observed resonant frequency is obtained from the raw data by offline data analysis using numerical algorithms that can be implemented directly in the FPGA. The value obtained is 16.0 Hz, corresponding to a tension value of 5.9 N, which is within a few percent of the physical value.

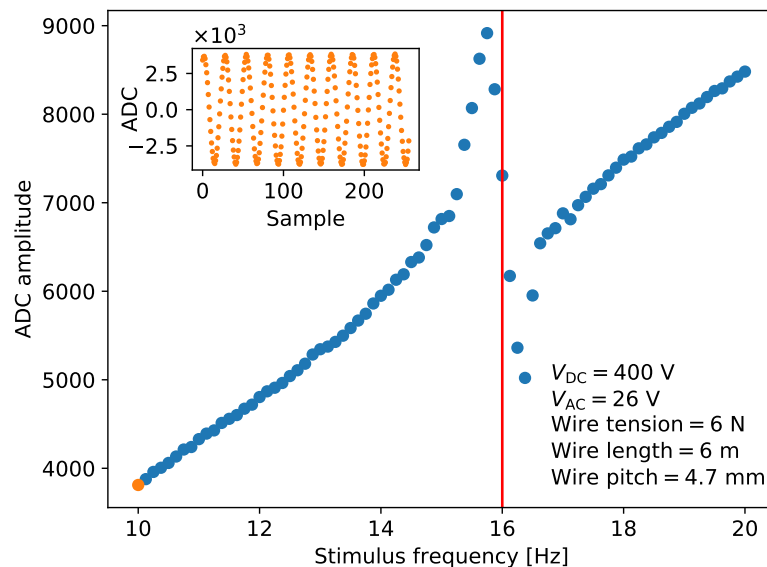


**Figure 2.37.** Amplitude of the readout signal as a function of the stimulus frequency, as used in the electrical wire-tension method. The vertical line is located at the observed resonant frequency. The raw digitized signal values corresponding to the first data point of the main plot are shown in the inset plot.

In this test bench setup, no wire support combs, cf. section 2.2.5.4, are present. Their presence shortens the wire length that needs to be considered in this method, resulting in several higher resonant frequencies per wire. A similar effect happens for the wire channels that wrap around the APA frame. Although they are a succession of wire segments electrically connected, the segments are mechanically independent and can have different tension values. Several resonant frequencies can be present per readout channel, possibly corresponding to different tension values.

In addition to measuring tension values, the measurement device is envisioned to be able to test wires for electrical isolation and electrical continuity, given the flexibility of the FPGA

and provisions put in place in the design of the analog circuitry. Injecting a signal in a readout channel and detecting it in a different channel would indicate that these channels are not electrically isolated, for example, due to a solder bridge. The electrical continuity could be tested by sending a pulse down a channel and measuring the time it takes to travel through the wire and back to the measurement device. If the measured time is shorter than expected, this could indicate cold solder joints, for example.

A final review of the electrical tension measuring system design will take place in spring 2020. Once completed, mobile APA test stands will be built for each of the APA production sites, the South Dakota Warehouse Facility (SDWF), and SURF. The introduction of the electrical testing methods for APAs presents a fantastic opportunity for more efficient APA fabrication and more flexible testing during the integration and installation phases.

### 2.5.4.4 Cold testing of APAs

The six APAs produced for ProtoDUNE-SP have demonstrated clearly that the APA design, materials, and fabrication methods are sufficiently robust to operate at LAr temperature. No damage or change in performance due to cold have been identified during ProtoDUNE-SP running. Nevertheless, over a five year construction effort, it is prudent to cold cycle a sample of the APAs produced to ensure steady fabrication quality. A cold testing facility sized for DUNE APAs exists at PSL and can be used for such tests. Throughout the construction project, it is anticipated that 10% of the produced APAs will be shipped to PSL for cold cycling. This amounts to about 1 APA per year per production site during the project. It is planned that all APAs will still be cold tested during integration at SURF and before installation in the DUNE cryostats.

### 2.5.4.5 Documentation

Each APA is delivered with a traveler document in which specific assembly information is gathered, initially by hand on a paper copy, then entered into an electronic version for longer term storage. The traveler database contains a detailed log of the production of each APA, including where and when the APA was built and the origin of all parts used in its construction.

Assembly issues that arise during the construction of an APA are gathered in an issue log for each APA, and separate short reports provide details of what caused the occurrence, how the issue was immediately resolved, and what measures should be taken in the future to ensure the specific issue has a reduced risk of occurring.

## 2.6 Handling and transport to SURF

Completed APAs are shipped from the APA production sites to the SDWF in South Dakota. As they are transported to the 4850L, they are integrated with the TPC FE electronics and PDs followed by installation in the cryostat. Extensive QC testing will be performed before installation to ensure the fully integrated APAs function properly. Installation activities at SURF are described in chapter 9.

### 2.6.1 APA handling

The handling of the APAs must ensure their safety. Several lifting and handling fixtures will be employed for transferring and manipulating the APAs during fabrication, integration, and installa-

tion. At the production sites a fixture called the edge lift kit will be used to transfer the APA to and from the process cart and the winder, as well as to the transport containers. The lift kit is shown schematically in figure 2.38. It is essential that the fixture connect to the APA along an outer edge because after wires are attached to the support frame, it can no longer be grabbed anywhere on the front or back face of the frame.

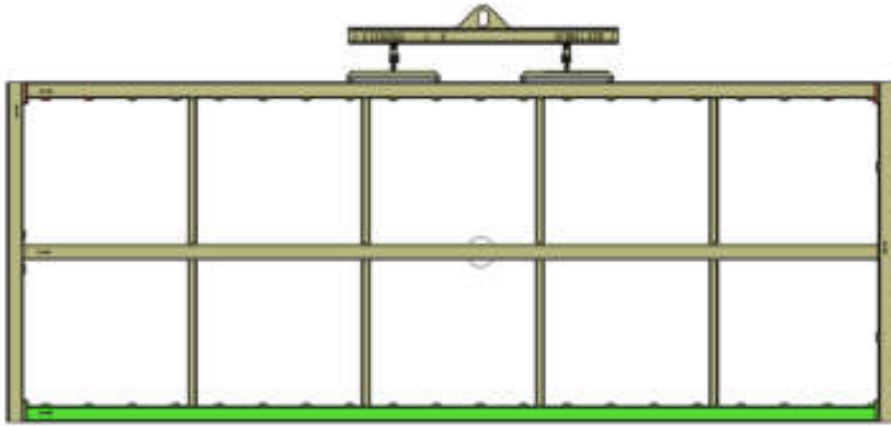


**Figure 2.38.** A custom lifting fixture is used to pick up an APA from the long edge and safely handle it during the various construction steps at the production sites.

### 2.6.2 APA transport frame and shipping strategy

The transport packaging for the APAs is designed to safely transport them from the production sites to the SDWF. The design of the packaging is shown in figure 2.39. Light rigid metalized foam protective panels are attached via clamps affixed to the APA frames and provide the primary protection for the wire planes. Pairs of APAs (one upper and one lower in an APA pair) are loaded onto welded structural steel transport frames at the factory. The APA frames are bolted to mounts on the transport frames that incorporate shock-attenuating coil springs designed to reduce possible accelerations on the APA frames to less than 4g. The APAs and transport frames will be instrumented with accelerometers to find out if the APAs were subject to shocks above their specifications. Removable side frames, made from aluminum, are then bolted to the transport frames providing a structure around the APAs, and this whole structure is then sealed in plastic sheeting.

The packaged transport frames from the US sites will be covered in wooden panels, loaded on custom pallets, and shipped via truck from the APA factories to the SDWF. The packaged transport frames from the UK will be packed, in pairs, inside wooden crates for shipping. They then will be trucked to the nearby port in Liverpool, transported by ship to the port of Baltimore, and then shipped by truck to the SDWF. APAs may be stored for three years or longer at the SDWF — an APA crate cannot arrive at SURF until it is required underground.

The size of the packaging and rigging hardware is constrained by the Ross headframe dimensions and over-the-road shipping requirements in the US. The design of the protective panels and the side frames allow for temporarily removing a portion of the shipping packaging and protective panels to access the APA head boards for wire tension, isolation, and continuity tests after shipment and after transport underground.



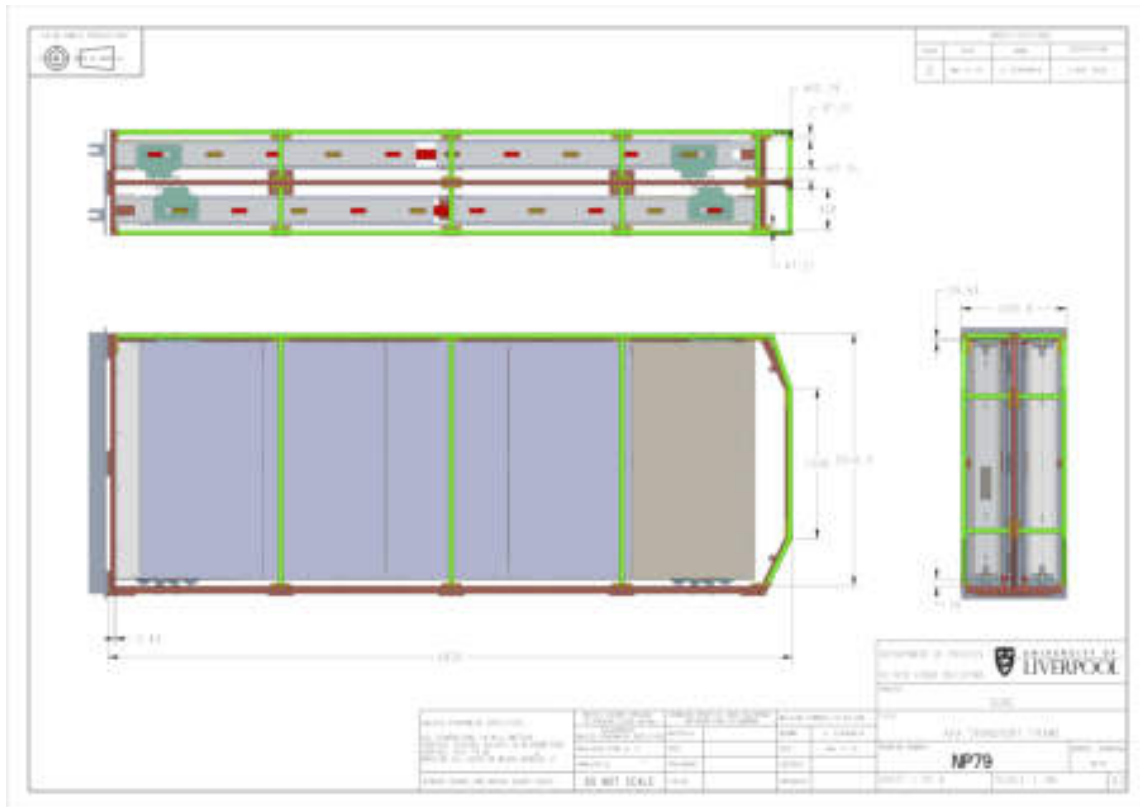


**Figure 2.39.** The current design of the APA shipping frame (maroon) and removable side frames (green) with two APAs covered with protective panels (shown in grey and tan). The external wooden packaging is not shown in this view.

When a crate is required underground, it will be stripped of its wooden crating and transported via Conestoga-type trailer to the headframe area. Near the headframe, the crates will be moved by forklift onto a cart on a rail system and rolled into the headframe. The inside portion of the headframe will have rigging gear attached to hard points on both short ends of the crate. The crate's upper end will be attached to the hoist below the cage and will be used to lift the crate from horizontal to vertical and pull it into the shaft. The shipping frame is designed to clear the headframe during this operation. The other end (lower) will be used to attach a horizontal tigger that will control the crate as it is pulled into the shaft station (figure 2.40). When in the shaft, fixtures on the sides of the crate will engage wooden guides in the shaft to keep the crate from swinging or rotating while being lowered down the shaft. This operation is consistent with standard slung-load transport procedures at SURF. When the crate arrives underground, it will be pulled out of the shaft by reversing the shaft rigging operation; it will land on the opposite long edge of the crate that was used on the surface. The crate is placed on a transport cart and pulled down the drift to the cavern. When in the cavern, the APAs will be uncrated, rotated to vertical by the cavern crane, mounted on a vertically oriented cart, tested, and stored temporarily (a few weeks) in the cavern adjacent to the clean room prior to final integration and installation. The transport frames and carts have been designed to be stable in each of these configurations.

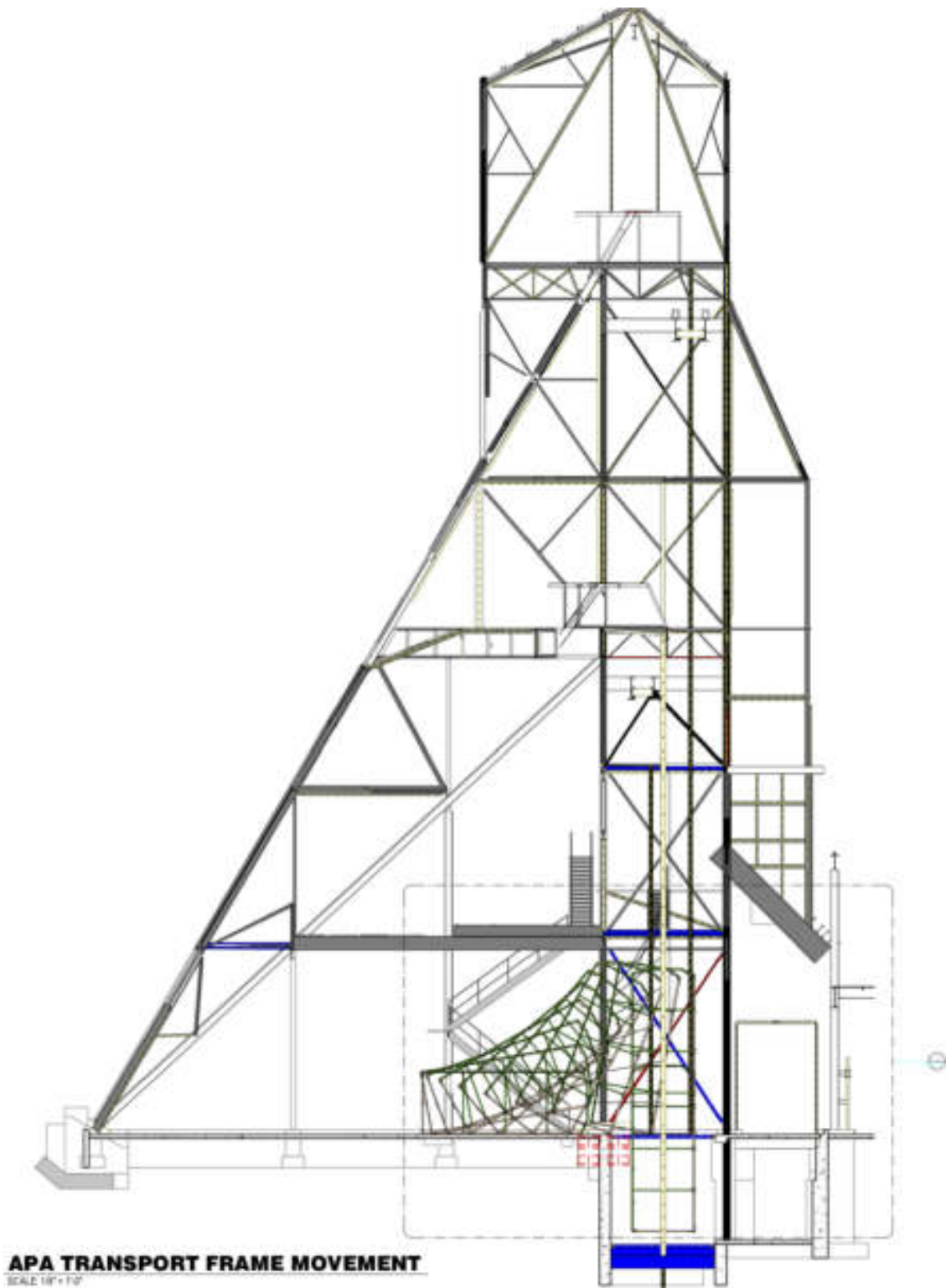


Figure 2.40. Motion study of loading an APA frame into the shaft.

2020 JINST 15 T08010

### 2.6.3 APA quality control during integration and installation

All active detector components are shipped to the SDWF before final transport to SURF. After unpacking an APA (underground at SURF), a visual inspection will be performed and wire continuity and tension measurements will be made. Tension values will be recorded in the database and compared with the original tension measurements performed at the production sites, as was done for ProtoDUNE-SP and shown in figure 2.20. Definite guidance for the acceptable tension values will be available to inform decisions on the quality of the APA. Clear pass/fail criteria will be provided as well as clear procedures to deal with individual wires lying outside the acceptable values. This guidance will be informed also by the ProtoDUNE-SP experience. In addition, a continuity test and a leakage current test is performed on all channels and the data recorded in the database.

When all tests are successful, the APA can be prepared for integration with the other components. This step is critical for ensuring high performance of the integrated APAs. The procedures for APA transport to the 4850L at SURF, integration with the PD system and CE, and the schedule for testing the integrated APA are addressed in chapter 9. APA consortium personnel will play direct and key roles throughout the integration and installation activities.

## 2.7 Safety considerations

The LBNF and DUNE project (LBNF/DUNE) is committed to ensuring a safe work environment for workers at all institutions and facilities, from APA fabrication to installation. The project utilizes the concept of an Integrated Safety Management System (ISMS) as an organized process whereby work is planned, performed, assessed, and systematically improved to promote the safe conduct of work. The LBNF/DUNE Integrated Environment, Safety and Health Management Plan [23] contains details on LBNF/DUNE integrated safety management systems. This work planning and hazard analysis (HA) program utilizes detailed work plan documents, hazard analysis reports, equipment documentation, safety data sheets, personnel protective equipment (PPE), and job task training to minimize work place hazards.

Prior to APA production, applying the experience of ProtoDUNE-SP, the project will coordinate with fabrication partner facilities to develop work planning documents, and equipment documentation, such as the Interlock Safety System for APA winding machines to implement an automated protection against personnel touching the winding arm while the system is in operation. Additionally, the project will work with the local institutions' environment, safety and health (ES&H) coordinators to ensure that ES&H requirements within the home institution's ES&H Manual address the hazards of the work activities occurring at the facility. Common job hazard analyses may be shared across multiple fabrication facilities.

Handling of the large but delicate frames is a challenge. Procedures committed to the safety of personnel and equipment will be developed for all phases of construction, including frame assembly, wiring, transport, and integration, and installation in the cryostat. This documentation will continue to be developed through the Ash River trial assembly process, which maps out the step-by-step procedures and brings together the documentation needed for approving the work plan to be applied at the far site.

As is Fermilab's practice, all personnel have the right to stop work for any safety issues.

## 2.8 Organization and management

Coordination of the groups participating in the DUNE APA consortium is critical to successfully executing the large-scale multi-year construction project that is needed to produce high-quality APAs for the DUNE SP modules. The APA consortium comprises 21 institutions, of which 14 are in the USA and 7 in the UK (see table 2.8). The consortium is organized along the main deliverables, which are the final design of the APA and the APA production and installation procedures (see figure 2.41). The two main centers of APA construction are in the USA and the UK, so usually the leaders of a working group are chosen to represent the main stakeholders to ensure that common procedures and tooling are developed. We plan to produce half of the DUNE APAs in the USA and half in the UK.

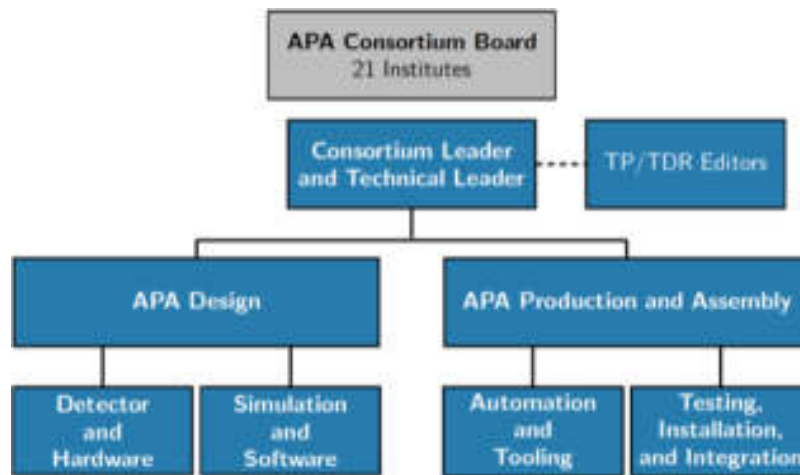


**Figure 2.41.** APA consortium organizational chart.

The university groups and Brookhaven National Laboratory (BNL) are responsible for validating the design, while engineering and the production set up is being developed at PSL (USA) and Daresbury Laboratory (UK), where the APAs for ProtoDUNE-SP have been built. In addition to PSL and Daresbury Laboratory, the University of Chicago and Yale University are developing detailed plans for the layouts, activities, and schedule at each site.

In addition to the APA production sites, a successful production effort will require significant and sustained contributions from university groups throughout the production process. Table 2.9 and figure 2.42 list the main work packages that are part of the overall APA construction process and the institutions in the USA and UK who are taking the leading roles in each effort. The tasks range from the production of bare support frames, to the assembly and testing of many thousands of wire boards, to the procurement of the custom transport crates for shipping the completed APAs. The on-time supply of materials to each of the APA production sites will be imperative to maintaining the production schedule, and detailed plans are being developed for the execution of the project in both countries.

Table 2.8. Current APA consortium institutions and countries.

| Institution  | Country |
|--|---------|
| University of Cambridge  | UK      |
| Daresbury Laboratory — Science and Technology Facilities Council | UK      |
| Lancaster University   | UK      |
| University of Liverpool  | UK      |
| University of Manchester   | UK      |
| University of Sheffield  | UK      |
| University of Sussex   | UK      |
| Brookhaven National Laboratory                                   | USA     |
| University of Chicago  | USA     |
| Colorado State University  | USA     |
| Harvard University   | USA     |
| University of Houston  | USA     |
| University of Iowa   | USA     |
| University of Mississippi  | USA     |
| Northern Illinois University                                     | USA     |
| Syracuse University  | USA     |
| University of Texas at Arlington                                 | USA     |
| Tufts University   | USA     |
| College of William & Mary  | USA     |
| University of Wisconsin-Madison, Physical Sciences Laboratory    | USA     |
| Yale University  | USA     |

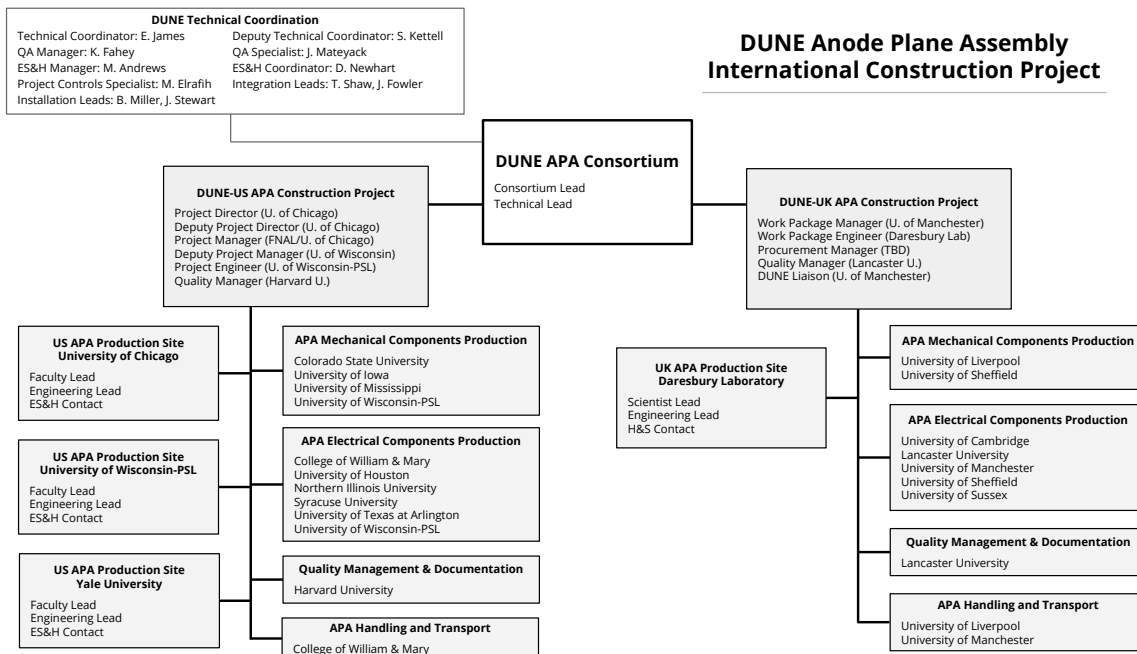


Figure 2.42. APA construction project organizational chart.

2020 JINST 15 T08010

**Table 2.9.** Institutional responsibilities for APA production in the UK and USA.

| APA Construction Work Packages  | Institutions   |
|---------------------------------|--|
| <b>Production in the UK</b>     |  |
| APA production site             | Daresbury Laboratory                                   |
| U/V-plane wire boards           | University of Cambridge, University of Sussex          |
| X/G-plane wire boards           | Lancaster University, University of Sheffield          |
| G-bias boards                   | University of Manchester                               |
| CR boards                       | University of Manchester                               |
| Cold electronics adapter boards | University of Sheffield                                |
| Grounding mesh frames           | University of Sheffield                                |
| APA frames                      | University of Liverpool                                |
| APA transport crates            | University of Liverpool, University of Manchester      |
| Yokes and structural tees       | University of Liverpool                                |
| QA/QC management                | Lancaster University                                   |
| <b>Production in the US</b>     |  |
| APA production site             | University of Wisconsin-PSL                            |
| APA production site             | University of Chicago                                  |
| APA production site             | Yale University  |
| U/V-plane wire boards           | College of William & Mary                              |
| X-plane wire boards             | University of Texas at Arlington                       |
| G-plane wire boards             | University of Houston                                  |
| G-bias boards                   | Syracuse University                                    |
| CR boards                       | University of Wisconsin-PSL                            |
| Cold electronics adapter boards | Northern Illinois University                           |
| Grounding mesh frames           | University of Chicago                                  |
| APA frames                      | University of Iowa, University of Wisconsin-PSL        |
| APA transport crates            | College of William & Mary                              |
| Yokes and structural tees       | University of Wisconsin-PSL                            |
| CE interface hardware           | Colorado State University, University of Wisconsin-PSL |
| QA/QC management, wire tension  | Harvard University                                     |

## 2.9 Schedule and risks

### 2.9.1 Schedule

A schedule for key design and production readiness reviews leading up to the start of APA production is provided in table 2.10. The high-level milestones for the final design and construction of the DUNE APAs between 2019 and 2026 are given in table 2.11.

**Table 2.10.** Planned review schedule for the APA design and production preparations.

| Review  | Date          |
|---|---------------|
| APA Electrical Preliminary Design Review                    | November 2019 |
| APA Production Site Design Internal Review — UK             | January 2020  |
| APA Transport Frame Preliminary Design Review               | April 2020    |
| Wire Tension Measurement Internal Review                    | March 2020    |
| APA Production Site Design Internal Review — USA            | April 2020    |
| APA Final Design Review                                     | May 2020      |
| Production Site Readiness Review — UK                       | June 2020     |
| Production Sites Readiness Review — U. of Wisconsin-PSL     | November 2020 |
| Production Sites Readiness Review — U. of Chicago & Yale U. | April 2021    |

Analysis of the ProtoDUNE-SP data will inform the decision on the electron diverters. Additional design considerations that cannot be directly tested through ProtoDUNE-SP, like the APA pair assembly and related cabling issues require the full test with cabling of an APA pair frame assembly, planned to be performed at Ash River. Also planned is the construction of a pre-production APA for an integration test with CE and PD systems at CERN in spring 2020, which will fully test all interface aspects. This test will inform the final design review of the APA system in May 2020.

Design reviews of APA production sites in the UK and USA, to validate the layout of the production lines, are planned for early 2020, together with the finalization of the winding machine modifications. Production site readiness reviews are planned in June 2020 in the UK and in December 2020 in the USA.

Production of three APAs for a final test in ProtoDUNE-SP-2 is foreseen in the second half of 2020. The pre-production APA used for the integration test at CERN in spring 2020 could be used for installation in ProtoDUNE-SP-2, if no additional modifications are required.

Dates are also provided in table 2.11 for the start and end of APA production for detector modules #1 and #2. Steady-state production rates are 24 APAs/year at Daresbury Laboratory with four production lines, 12 APAs/year both at Yale and Chicago, each with two production lines, and six APAs/year at PSL, with one production line. The production time for detector module #1 takes into account a gradual start-up of the production lines, and the different start dates and number of production lines in the UK and USA. The end of APA production for detector module #1 happens comfortably ten months before the start of installation. In the UK, with four assembly lines, in order to meet the installation date for detector module #2 the APA production time would need to be reduced by about seven months. This could be achieved by a reduction of the APA assembly time,

**Table 2.11.** Schedule milestones for the production and installation of anode plane assemblies for two SP DUNE far detector modules.

| Milestone  | Date           |
|--|----------------|
| Final report on the necessity and design of electron diverters | August 2019    |
| Completion of APA pair frame assembly & cabling at Ash River   | October 2019   |
| Decision on the wire tension measurement method                | April 2020     |
| Completion of winding machine modifications and commissioning  | April 2020     |
| Start of APA Components Production — UK                        | June 2020      |
| Start of APA production for ProtoDUNE-SP-II                    | July 2020      |
| Start of APA Production for DUNE — UK                          | August 2020    |
| Completion of APA integration test with CE and PDS at CERN     | September 2020 |
| Start of APA Components Production — USA                       | November 2020  |
| End of APA production for ProtoDUNE-SP-II                      | December 2020  |
| Start of APA Production for DUNE — U. of Wisconsin-PSL         | January 2021   |
| Start of ProtoDUNE-SP-II installation                          | March 2021     |
| Start of APA Production for DUNE — U. of Chicago & Yale U.     | June 2021      |
| South Dakota Logistics Warehouse available                     | April 2022     |
| Beneficial occupancy of cavern 1 and CUC                       | October 2022   |
| CUC counting room accessible                                   | April 2023     |
| End of APA Production — detector module #1                     | September 2023 |
| Start of APA Production — detector module #2                   | October 2023   |
| Top of detector module #1 cryostat accessible                  | January 2024   |
| Start of detector module #1 TPC installation                   | August 2024    |
| Top of detector module #2 accessible                           | January 2025   |
| End of detector module #1 TPC installation                     | May 2025       |
| Start of detector module #2 TPC installation                   | August 2025    |
| End of APA Production — detector module #2                     | April 2026     |
| End of detector module #2 TPC installation                     | May 2026       |

an opportunity mentioned in section 2.9.2, and, if necessary, by increasing the number of working shifts per week.

### 2.9.2 Risks

Risks have been identified for the finalization of the APA design and the prototyping phase, for the setup of the production sites, for the production of APAs, and for installation at SURF. Risks are summarized in table 2.12. For each risk source, we describe a brief mitigation strategy as well as an estimation of the probability of occurring (P) and the impact that risk would have on costs (C) and on schedule (S). These are each indicated as Low (L), Medium (M), or High (H) probability of impact. One opportunity is also listed and uses the same probability and impact indicators.



**Table 2.12:** APA risks (P=probability, C=cost, S=schedule) The risk probability, after taking into account the planned mitigation activities, is ranked as L (low < 10 %), M (medium 10 % to 25 %), or H (high > 25 %). The cost and schedule impacts are ranked as L (cost increase < 5 %, schedule delay < 2 months), M (5 % to 25 % and 2–6 months, respectively) and H (> 20 % and > 2 months, respectively).

| ID           | Risk   | Mitigation   | P | C | S |
|--------------|--|--|---|---|---|
| RT-SP-APA-01 | Loss of key personnel  | Implement succession planning and formal project documentation                           | L | L | M |
| RT-SP-APA-02 | Delay in finalisation of APA frame design  | Close oversight on prototypes and interface issues                                       | L | L | M |
| RT-SP-APA-03 | One additional pre-production APA may be necessary                               | Close oversight on approval of designs, commissioning of tooling and assembly procedures | L | L | L |
| RT-SP-APA-04 | APA winder construction takes longer than planned                                | Detailed plan to stand up new winding machines at each facility                          | M | L | M |
| RT-SP-APA-05 | Poor quality of APA frames and/or inaccuracy in the machining of holes and slots | Clearly specified requirements and seek out backup vendors                               | L | L | M |
| RT-SP-APA-06 | Insufficient scientific manpower at APA assembly factories                       | Get institutional commitments for requests of necessary personnel in research grants     | M | M | L |
| RT-SP-APA-07 | APA production quality does not meet requirements                                | Close oversight on assembly procedures   | L | M | M |
| RT-SP-APA-08 | Materials shortage at factory  | Develop and execute a supply chain management plan                                       | M | L | L |
| RT-SP-APA-09 | Failure of a winding machine - Drive chain parts failure                         | Regular maintenance and availability of spare parts                                      | L | L | L |
| RT-SP-APA-10 | APA assembly takes longer time than planned                                      | Estimates based on protoDUNE. Formal training of every tech/operator                     | L | M | M |
| RT-SP-APA-11 | Loss of one APA due to an accident   | Define handling procedures supported by engineering notes                                | M | L | L |
| RT-SP-APA-12 | APA transport box inadequate   | Construction and test of prototype transport boxes                                       | L | L | M |
| RO-SP-APA-01 | Reduction of the APA assembly time   | Improvements in the winding head and wire tension measurements                           | M | M | M |

Risks with medium or greater probability and/or medium or greater impact are discussed in more detail below:

- RT-SP-APA-01, Loss of key personnel:
  - *Description:* if loss of key personnel happens, it will cause delays as knowledge is lost and new team members will need to come up to speed.
  - *Mitigation:* implement succession planning and formal project documentation at all stages. All key tasks to be shared between multiple people, including production site management.

- *Probability and impact*: while the post-mitigation probability is low, below 10%, if the risk is realized, the impact on the schedule could range from a couple of months to a half-year.
- RT-SP-APA-02, Delay in finalization of APA frame design:
  - *Description*: if problems are encountered with the APA pair frame assembly and cabling tests at Ash River, or with the integration test of the pre-production APA at CERN, this will delay the finalization of the APA frame design.
  - *Mitigation*: oversight of the APA Consortium on the schedule of components procurement for the Ash River tests and close coordination with the Ash River team. Close coordination with CE and PD systems consortia on all interface issues, to be formalized in the interface documents.
  - *Probability and impact*: on the basis of the work done up to now we believe that the probability of this risk is low. However, if materialized, it would imply a delay in the start of APA production from a couple of months to a half-year.
- RT-SP-APA-04, APA winders construction takes longer than planned:
  - *Description*: if the construction of the winding machines takes longer than planned, the schedule for APA production will be delayed, and additional labor for winders production will be needed. We plan the construction of four additional winders in the USA and the modification of winder, presently at PSL, as well as the construction of three additional winders in the UK, in addition to the modification and relocation of the winder at Daresbury Lab. The estimated time for the production of the additional winders is approximately one year, both in the UK and the USA.
  - *Mitigation*: get commitments from the relevant institutions for the necessary resources for winder production, both for space and skilled manpower availability. Develop and execute a detailed plan to set up new winding machines at each production site. This plan will include contingencies in the event that technical problems cause schedule delays.
  - *Probability and impact*: winders are complex machines, and we estimate a medium probability for this risk, of less than 25%. The impact on the schedule is also medium, with possible delays up to a half-year.
- RT-SP-APA-05, Poor quality of APA frames and/or inaccuracy in the machining of holes and slots:
  - *Description*: APA frames are constructed from structural stainless steel tubing. The quality of the material provided by the vendor may change with time and be outside the required tolerances. Problems with QA during machining of holes and slots may result in unusable products. If this happens, it may delay the supply of frames of sufficient quality, which would delay the APA construction schedule.

- *Mitigation*: all requirements must be clearly specified in the purchase contracts. We will establish a well managed relationship with a vendor to provide the stainless steel tubing and the machining for the components of an APA frame. In addition, through our prototyping efforts, we will seek out at least one solid backup vendor for material supply and machining in both the USA and UK.
- *Probability and impact*: while the post-mitigation probability is low, below 10%, if the risk is realized, the impact on the schedule is medium, since finding a new vendor may take up to a half-year.
- RT-SP-APA-06, Insufficient scientific manpower at APA assembly factories:
  - *Description*: for US production, if it is not possible to recruit scientific resources, costed professional manpower is needed and costs will increase. This risk does not apply to the UK production since the required scientific staff is costed and awarded on project.
  - *Mitigation*: proactively contact institutions and get their commitments for inclusion of the necessary personnel in their research grants.
  - *Probability and impact*: this is a medium probability risk; we estimate a 50% probability that 50% of the US scientific resources may be missing. The cost impact is also medium, up to 20%.
- RT-SP-APA-07, APA production quality does not meet requirements:
  - *Description*: if wire planes are outside the required tolerances, they will need to be reworked, and the APA production schedule will be affected. A point of concern is to stay within limits for the tension of the wires.
  - *Mitigation*: the overall quality of each constructed APA will be ensured by following detailed procedures for every step of the assembly process (e.g., mesh installation, board placement and gluing, soldering, wire winding, etc.). These procedures already exist from our ProtoDUNE-SP work and are in the process of being modified to the final design of the DUNE FD APAs. For critical steps, an operator and quality control representative will record information in travelers for each APA.
  - *Probability and impact*: given the ProtoDUNE-SP experience and the steps outlined in the mitigation strategy, we can keep this risk probability low, below 10%. If realized, we assume a maximum impact on cost and schedule of 20%, corresponding to a medium impact.
- RT-SP-APA-08, Materials shortage at an APA production site:
  - *Description*: a material shortage at an APA production site would delay production.
  - *Mitigation*: as part of our comprehensive production strategy, we are in the process of developing and executing a supply chain management plan. This plan will include the details of material source, delivery logistics, critical milestones, and personnel resources required to meet APA production site needs for efficient APA production. All suppliers (vendors, laboratories, academic institutions) will be included in the implementation

of the supply chain plan. A key part of this plan will be the establishment of supplier metrics that will be gathered and reported to DUNE management by the APA production manager. These metrics will serve as an early warning of potential problems and trigger mitigation efforts early in the cycle.

- *Probability and impact*: even with mitigation, this is a realistic risk with an estimated probability of up to 25%. Delays on the schedule would probably not exceed a couple of months, making the impact low.
- RT-SP-APA-10, APA assembly takes longer than planned:
  - *Description*: if the labor for APA assembly is underestimated, it will correspondingly lengthen the time to produce APAs. We estimate an upper limit on the additional required labor of 10%.
  - *Mitigation*: APA assembly time estimates have been based on ProtoDUNE-SP experience and improvements to the winding machine. Formal training of every technician/operator of the winding machine should maintain a high production efficiency.
  - *Probability and impact*: we believe that this risk probability is low, below 10%, but even a 10% increase in the required labor would have a medium impact on both cost and schedule.
- RT-SP-APA-11, Loss of an APA due to an accident:
  - *Description*: if during APA assembly or integration/installation an accident happens, this may cause the destruction of an APA. We already plan to build two spare APAs for each detector module. In addition, we assume a probability of up to 10% to lose an additional APA during assembly or integration/installation.
  - *Mitigation*: we define procedures to handle APAs at all stage of fabrication, integration/installation, together with associated engineering notes for all modes of handling. Wire planes are delicate, and once damaged they would not be repairable.
  - *Probability and impact*: this is a marginally medium risk, with low impact both on cost and schedule.
- RT-SP-APA-12, APA transport box inadequate:
  - *Description*: if the transport box will not provide enough mechanical protection for the safe transportation of the APAs or if the size of the box is inadequate for transfer to the underground location, it will impact the schedule.
  - *Mitigation*: construct and test prototype transport boxes. Test all handling steps at Ash River and SURF. Coordinate closely with the team at SURF and APA Consortium oversight of transport boxes.
  - *Probability and impact*: given the mitigation steps, we estimate a probability for this risk of less than 10%. In case of redesign, it may have a medium impact on the schedule.

- RO-SP-APA-01, Reduction of the APA assembly time:
  - *Description*: if the new winding head will provides better uniformity in wire tension, it will reduce the time necessary for re-tensioning of the wires. If the new electrical method for wire tension measurements work as planned, it will reduce substantially the time required for wire tension measurements. A saving of up to 10% in APA assembly time will be possible with these improvements.
  - *Opportunity*: this is an opportunity that the APA Consortium is actively pursuing with ongoing testing of a new winding head design and development of the electronic tension measurement method. The APA boards have been already redesigned to allow for electronic tension measurements.
  - *Probability and impact*: given the preliminary results obtained up to now, we estimate a medium probability for this opportunity. A saving of 10% in the APA assembly time could be realized, corresponding to a medium impact for both cost and schedule.

## Chapter 3

# High voltage

### 3.1 High voltage system overview

#### 3.1.1 Introduction and scope

A LArTPC requires an equipotential cathode plane at HV and a precisely regulated interior electric field (E field) to drive electrons from particle interactions to sensor planes. To achieve this, the DUNE SP TPC consists of

- vertical cathode planes, called CPA arrays, held at HV;
- vertical anode planes, called APA arrays, described in chapter 2; and
- formed sets of conductors at graded voltages surrounding the drift volumes to ensure uniformity of the E field; the conductors are collectively called the FC.

The SP TPC configuration is shown in figure 3.1. The drift fields transport the ionization electrons towards the APAs at the sides and center.

The scope of the SP HV system, provided by the DUNE high voltage system (HVS) consortium, includes the selection and procurement of materials for, and the fabrication, testing, delivery, and installation of systems to generate, distribute, and regulate the voltages that create a stable and precise E field within a SP module.

The HV system consists of components both exterior and interior to the cryostat. The voltage generated at the HV power supplies passes through the cables, filters, and the HV feedthrough into the cryostat. From the point of delivery into the cryostat, components that form part of the TPC structure further distribute the voltage. The internal HV components in fact form a large fraction of the total internal structures of the TPC itself, and effectively bound the fiducial volume of the detector module.

The SP HV system consists of

- HV power supplies, cables, filters, and feedthrough;
- CPA array;
- top field cage (top FC), bottom field cage (bottom FC), and GPs; and
- endwall field cage (endwall FC).

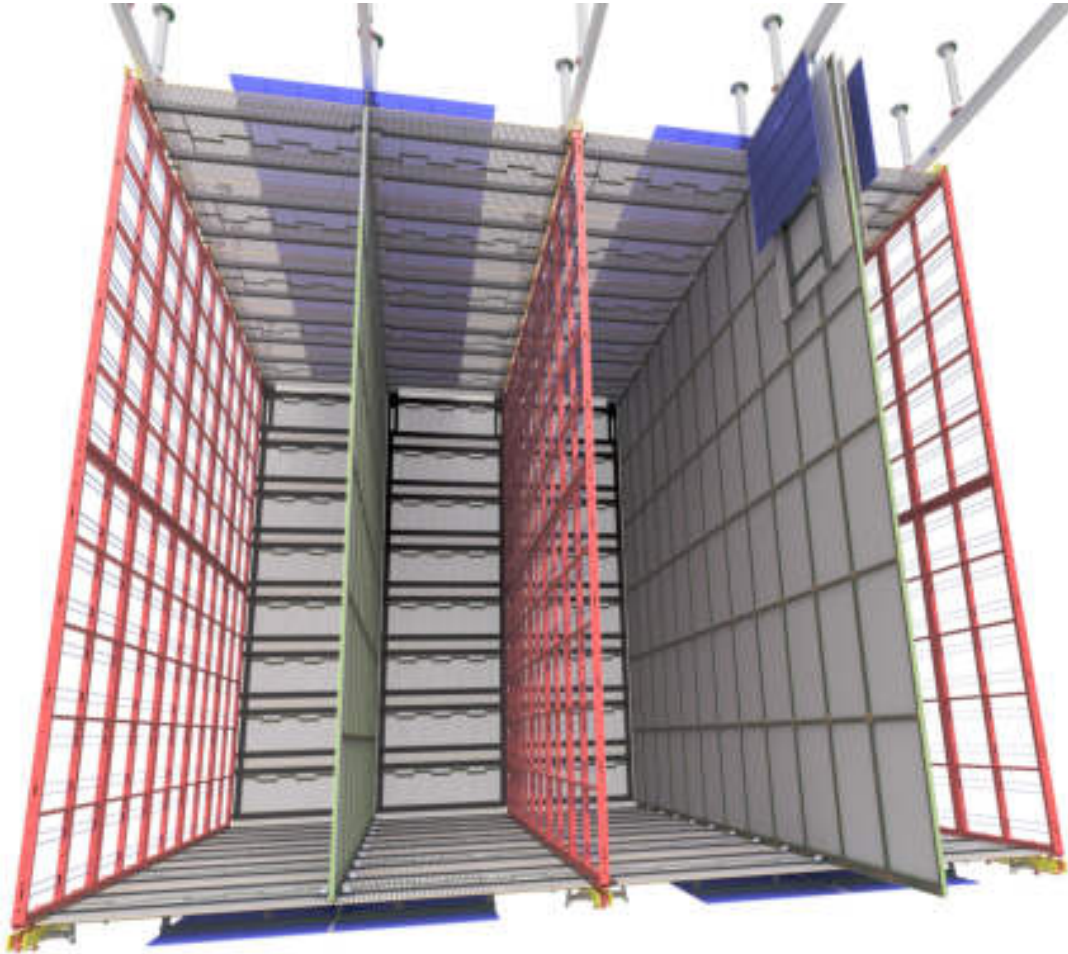


**Figure 3.1.** A schematic of a SP module showing the three APA arrays (at the far left and right and in the center, all of which span the entire 58.2 m detector module length) and the two CPA arrays, occupying the intermediate second and fourth positions. The top and bottom FC modules are shown with GPs in blue. On the right, the front top and bottom FC modules are shown folded up against the CPA panels to which they connect, as they are positioned for shipping and insertion into the cryostat. The CPAs, APAs, and FC together define the four drift volumes of the SP module. The sizes and quantities of the FC and CPA-array components are listed in tables 3.2 and 3.3 and represented in this image.

The system operates at the full range of voltages,  $-180$  kV to ground, inside the TPC volume.

The SP and dual-phase (DP) modules will implement similar designs for some of the HV system components, in particular, aspects of the FC and its supporting beams. This chapter describes the SP versions.

### 3.1.2 Design specifications

The working principle of the LArTPC relies on the application of a very uniform strong E field in ultra-pure LAr. A number of detector performance parameters benefit from such an E field in ways that directly support the core components of the DUNE physics program. Some of these are

examined in detail in Volume II, DUNE physics. Here we present a qualitative description of E field impacts on physics to set context.

Since free electron drift velocity in LAr is a function of E field, a uniform E field leads to a simple time versus position mapping along the drift direction, enabling precise and efficient 3D reconstruction. This allows, for example, the establishment of a well defined fiducial volume for beam neutrino events reconstructed in the FD. Since a neutrino CPV measurement or neutrino mass hierarchy (MH) test at root consists of the comparison of normalized spectra for electron and muon neutrino and antineutrinos interactions in the fiducial volume of the FD as projected from the near detector (ND), fiducial volume characterization is critical.

The optimal E field range at which to operate the LArTPC is a trade-off of detector performances that improve with increasing field against others that degrade. For instance, spectral information is necessary to separate CP and MH effects, necessitating efficient tracking and shower reconstruction and good energy resolution. To accomplish this, higher E field strength is generally better; more free charge is created at the ionization points, as electron-ion recombination decreases at higher fields, improving S/N and calorimetry.

Drift times are reduced, resulting in less free electron capture from residual electronegative impurities, and hence better S/N, even under less than optimal purity conditions. Spatial resolution improves, as free electron diffusion (proportional to the square root of the drift time) lessens.

Higher free charge production and lower electron capture allows for lower detection thresholds for components of electromagnetic showers, improving shower energy reconstruction. Lower detection thresholds also lead to higher detection efficiency for MeV-scale electron, photon, and neutron signatures of low-energy  $\nu_e$  interactions from SNB events.

The electron-ion recombination more strongly affects highly ionizing particles, usually protons. With decreased recombination, less saturation of free charge production occurs, leading to better particle identification and more precise energy measurements. Lower recombination particularly aids in proton-kaon separation by  $dE/dx$ , a key component of a search for  $p \rightarrow K^+ \nu$  baryon decay events.

However, the E field should not be raised beyond certain limits. For example, while free charge production increases with E field, scintillation photon production decreases, resulting in fewer photons available for triggering and determination of  $t_0$ . Two-track separation can degrade if the drift velocity is increased while keeping the anode wire separation and electronic wave form sampling frequency fixed. The distance between the TPC boundaries and the cryostat walls might need to be increased for very high E fields to prevent electrostatic discharge. This would in turn reduce the fraction of LAr in the FV. The impacts of the first two effects are modest, and all effects are subsidiary to technical challenges in the delivery of high voltage to the cryostat and the maintenance of highly stable HV surfaces for multiple decades of operation. These challenges require development of non-commercial cryogenic HV feedthroughs, HV ripple-repression through custom HV RC circuits, careful construction and deployment of HV cables, redundant HV connections, high-precision monitoring, and best practices at all stages of design, installation, and operation.

To the best of present common knowledge, the response and stability of a LArTPC to HV is strongly dependent on many boundary conditions that are not fully related to the HV design. There are for instance hints and tests that suggest that gas bubble formation as well as residual dust circulating in the LAr are primary sources of HV instability. Insulator charging up can also



affect HV performance in the long term. Finally, because we found no information on applying  $-180$  kV in an LAr detector, our approach to designing the HV system relied heavily on past experience, applying in addition sufficient safety margins from previous designs. ProtoDUNE-SP has provided experience and understanding of HV behavior, giving us confidence that the upgraded design documented in this TDR is appropriate for underground long-term operation.

Two decades of design and operational experience that began with ICARUS have established that a  $500$  V/cm field is an appropriate trade-off value that can be realistically achieved through utilization of cost-effective design and construction methods. In practice, achieving this design goal has been challenging as the drift distance has been progressively increased to the  $3.5$  m foreseen for the SP module, and overall detector optimization has proved to be important. For example, MicroBooNE operates at  $273$  V/cm (lower than its nominal value of  $500$  V/cm) and is able to operate well by exploiting its very high argon purity, (characterized by an electron lifetime in excess of  $15$  ms), as well as an excellent S/N ratio from the FE CE. MicroBooNE (and a number of other noble liquid TPCs) compensated for electrostatic instability problems by achieving higher purity, and DUNE might well operate in this mode during its run.

In DUNE, the minimum requirement of the drift E field has been set to  $250$  V/cm, with a goal of  $500$  V/cm for long-term stable operation. With good free electron lifetime ( $>10$  ms), and the electronics S/N demonstrated in ProtoDUNE-SP, experience shows that DUNE will be able to operate above  $250$  V/cm. The advantage of running at higher E field is that the lower electron-ion recombination rate and the higher electron drift velocity can compensate for any lower purity conditions that could arise during the planned operation period.

Running ProtoDUNE-SP at a higher HV value (as allowed by HV cables and filtering systems) is under consideration to gain better understanding of the HV stability issues.

Positive ProtoDUNE experience (see section 3.6.4) indicates that the  $500$  V/cm E field goal is within reach. This goal, combined with high LAr purity and a large S/N ratio, will allow a wide range of possible operating points to optimize detector performance for maximum physics potential over decades of stable conditions and very high live-time. The specification minimum of  $250$  V/cm will provide adequate detector performance, assuming achievable purity and electronics parameters.

The HV system is designed to meet the physics requirements of the DUNE experiment, both physical (e.g., E fields that allow robust event reconstruction) and operational (e.g., avoiding over-complication that could affect the time available for collecting neutrino events). The important requirements and specifications for the HV system are given in table 3.1.

**Table 3.1:** HV specifications.

| Label    | Description                       | Specification (Goal)            | Rationale   | Validation               |
|----------|-----------------------------------|---------------------------------|---|--------------------------|
| SP-FD-1  | Minimum drift field               | $> 250$ V/cm<br>( $> 500$ V/cm) | Lessens impacts of $e^-$ -Ar recombination, $e^-$ lifetime, $e^-$ diffusion and space charge. | ProtoDUNE                |
| SP-FD-11 | Drift field uniformity due to HVS | $< 1\%$ throughout volume       | High reconstruction efficiency.   | ProtoDUNE and simulation |

|          |   |  |   |   |
|----------|---|--|---|---|
| SP-FD-12 | Cathode HV power supply ripple contribution to system noise | $< 100 e^-$  | Maximize live time; maintain high S/N.  | Engineering calculation, in situ measurement, ProtoDUNE |
| SP-FD-17 | Cathode resistivity   | $> 1 M\Omega/\text{square}$<br>( $> 1 G\Omega/\text{square}$ ) | Detector damage prevention.   | ProtoDUNE   |
| SP-FD-24 | Local electric fields                                       | $< 30 \text{ kV/cm}$   | Maximize live time; maintain high S/N.  | ProtoDUNE   |
| SP-FD-29 | Detector uptime   | $> 98\%$<br>( $> 99\%$ )                                       | Meet physics goals in timely fashion.   | ProtoDUNE   |
| SP-FD-30 | Individual detector module uptime                           | $> 90\%$<br>( $> 95\%$ )                                       | Meet physics goals in timely fashion.   | ProtoDUNE   |
| SP-HV-1  | Maximize power supply stability                             | $> 95\%$ uptime  | Collect data over long period with high uptime.   | ProtoDUNE   |
| SP-HV-2  | Provide redundancy in all HV connections.                   | Two-fold<br>(Four-fold)  | Avoid interrupting data collection or causing accesses to the interior of the detector. | Assembly QC   |

We note that specification SP-FD-1 is discussed in the text above table 3.1. SP-FD-2 is met in case of stable HV operation (lessons from ProtoDUNE-SP). The noise contribution from HV instabilities is unclear and under investigation with ProtoDUNE-SP. The remaining requirements specific to the HV system, summarized here, are all addressed and referred to in the remainder of this chapter.

- SP-FD-11: non-uniformity could be due to defects in resistor chains; muon and laser calibrations will mitigate this effect. [section 3.4]
- SP-FD-12: lessons learned from ProtoDUNE-SP demonstrate that the present filtering scheme is adequate. [3.2, 3.4.1]
- SP-FD-17: the CPA design is based on few  $M\Omega/\text{square}$  resistivity surfaces. Such surfaces have been demonstrated in ProtoDUNE-SP to be adequate to prevent fast discharges that could potentially damage CE and the cryostat (no event was ever recorded). Underground operation will allow higher resistivity, thus further slowing down the potential release of stored energy. [3.3, 3.4.1]
- SP-FD-24 is met by calculation in ProtoDUNE-SP. In the present design, the E field in the critical region between FC and GP is further reduced. [3.4.1, 3.5]
- SP-FD-29, 30: these uptime requirements are already met in ProtoDUNE-SP; the much lower ionization density in underground operation and optimization in the design (FC to GP distance) will ensure meeting the requirement even in the case of the much wider detector surface.
- SP-HV-1: the HV distribution and filtering has been tested in ProtoDUNE-SP; the design of these items will be revised to minimize long-term degradation and maintenance requirements. [3.4.1]

- SP-HV-2: two-fold redundant connections to the CPA are foreseen. The HV feedthrough and its connection to the CPA is designed in such a way that it could be extracted and replaced even with the detector filled with LAr (based on ICARUS experience). [3.3, 3.5]

### 3.1.3 Design overview

#### 3.1.3.1 Cathode plane assembly (CPA) arrays

CPA arrays are made up of adjacent resistive cathode panels, secured in frames and connected by an HV bus. HV cups are mounted at both ends to receive input from the power supply.

Two CPA arrays span the length and height of the SP module, as shown in figure 3.1. Each array is assembled from a set of 25 adjacent full-height CPA planes, each of which consists of two adjacent full-height panels. Each panel consists of three stacked units, approximately 4 m in  $y$  (height) by 1.2 m in the  $z$ -coordinate (parallel to beam). A unit consists of two vertically stacked resistive panels (RPs) framed by FR-4<sup>1</sup> members. The HV cathode components are listed in table 3.2 and will hereafter be referred to by their names as defined in this table.

**Table 3.2.** HV cathode components.

| Component and Quantity       | Length (z) | Height (y) | Per SP module |
|------------------------------|------------|------------|---------------|
| CPA array (2 per SP module)  | 58 m       | 12 m       | 2             |
| CPA plane (25 per CPA array) | 2.3 m      | 12 m       | 50            |
| CPA panel (2 per CPA plane)  | 1.2 m      | 12 m       | 100           |
| CPA unit (3 per CPA panel)   | 1.2 m      | 4 m        | 300           |
| RP (2 per CPA unit)          | 1.2 m      | 2 m        | 600           |

The RPs are made of a highly resistive material. An installation rail supports the CPA panels from above through a single mechanical link.

The cathode bias is provided by an external HV power supply through an HV feedthrough connecting to the CPA array inside the cryostat.

#### 3.1.3.2 Field cage

In the SP module, an FC covers the top, bottom, and endwalls of all the drift volumes, thus providing the necessary boundary conditions to ensure a uniform E field, unaffected by the presence of the cryostat walls. The FC is made of adjacent extruded aluminum open profiles (electrodes) running perpendicular to the drift field and set at increasing potentials along the 3.5 m drift distance from the CPA HV (−180 kV) to ground potential at the APA sensor arrays.

The FC modules come in two distinct types: the identical top and bottom modules, which are assembled to run the full length of the detector module, and the endwall FC modules, which are assembled to complete the detector at either end. The profiles in both types of modules are supported by FRP<sup>2</sup> (fiber-reinforced plastic) structural beams.

<sup>1</sup>NEMA grade designation for flame-retardant glass-reinforced epoxy laminate material, multiple vendors, National Electrical Manufacturers Association™, <https://www.nema.org/pages/default.aspx>.

<sup>2</sup>Fiber-reinforced plastic, a composite material made of a polymer matrix reinforced with fibers, many vendors.

The top FC and bottom FC modules extend nominally 2.3 m in  $z$  and 3.5 m in  $x$ ; the top and bottom of the SP module each requires 25 modules lengthwise in  $z$  and four across in  $x$ . The endwall FC modules are 3.5 m wide by 1.5 m in high; each endwall requires four adjacent stacks, eight units high. A GP consisting of modular perforated stainless steel sheets runs along the outside surface of each of the top FC and bottom FC, with a 30 cm clearance. The endwall FC modules do not require a GP because the distance to the cryostat wall is sufficient, approximately 2 m.

To provide a linear voltage gradient within each drift volume, a chain of resistive divider boards connects the adjacent pairs of aluminum profiles along each FC module.

Table 3.3 lists the FC components.

**Table 3.3.** HV field cage components.

| Component   | Count                 | Length<br>(z) | Width<br>(x) | Height<br>(y) | Submodules | Grand<br>Total |
|---|-----------------------|---------------|--------------|---------------|------------|----------------|
| Top FC modules  | 100 ( $4 \times 25$ ) | 2.3 m         | 3.5 m        | -             | -          | 100            |
| Bottom FC modules                                     | 100 ( $4 \times 25$ ) | 2.3 m         | 3.5 m        | -             | -          | 100            |
| Profiles per module (all top and bottom module types) | 57                    | 2.3 m         | -            | -             | -          | 11400          |
| GP modules per top or bottom FC module                | 5                     | 2.3 m         | 0.7 m        | -             | -          | 1000           |
| Endwall FC plane                                      | 2                     | -             | 14.4 m       | 12 m          | 4          | 2              |
| Endwall FC modules per endwall FC                     | 32                    | -             | 3.5 m        | 1.5 m         | -          | 64             |
| Profiles per endwall FC module                        | 57                    | -             | -            | 1.5 m         | -          | 3648           |

### 3.1.3.3 Electrical considerations

As shown in figure 3.1, the outer APA arrays face the cryostat walls, and the CPA arrays are installed between the APA arrays in two of the three interior positions (A-C-A-C-A). In this configuration, as opposed to C-A-C-A-C, most of the cathode plane surfaces are far away from the grounded cryostat walls, reducing electrostatic breakdown risks and decreasing the total energy stored in the E field to 800 J.

Figure 3.2 maps out the E field strength over a cross section of a drift volume. The energy is stored mostly in the high E field region between the FC and the facing GPs. In the case of an unexpected HV breakdown, the entire 400 J associated with one CPA array could be discharged to ground, potentially causing physical damage. Given the difficulty of predicting the distribution of energy along a discharge path, we treat the possibility of discharged energy, conservatively, as a risk to the TPC components and the cryostat membrane.

Previous large LArTPCs (e.g., ICARUS and MicroBooNE) have used continuous stainless steel tubes as their FC electrodes; however, a continuous electrode in a DUNE detector module would need to be at least 140 m long. This would increase the stored energy in each electrode and, in turn, increase the risk of damage in the case of a discharge.

Subdividing the FC into electrically isolated modules limits the stored energy in each FC module, thereby minimizing the risk of damage. Each FC module must have its own voltage divider

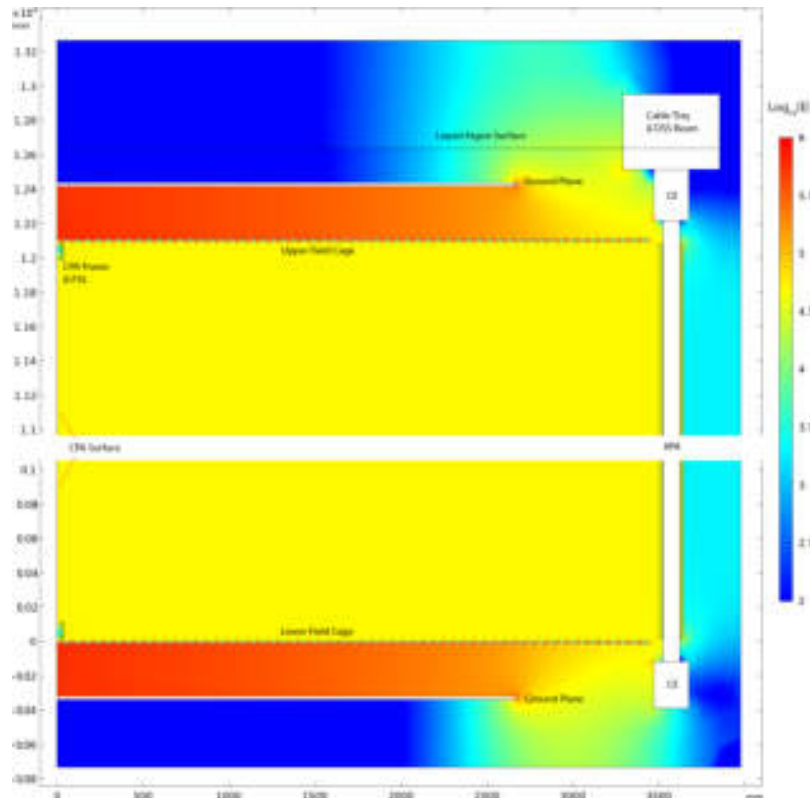


**Figure 3.2.** A simplified cross sectional view of an outer drift volume of the TPC showing the distribution of the static E field (in V/m). Since the electrostatic potential energy is proportional to  $E^2$ , most of the energy is stored between the FC modules and their facing GPs.

network to create a linear voltage gradient. Dividing the FC into mechanically and electrically independent modules also eases the construction and assembly of the FC and greatly restricts the extent of drift field distortion caused by a resistor failure on the divider chain of a FC module.

An HV discharge onto a metallic cathode could cause the electrical potential of the entire cathode surface to swing from its nominal bias (e.g.,  $-180\text{ kV}$ ) to  $0\text{ V}$  in a few nanoseconds, inducing a large current into the analog FE amplifiers connected to the sensing wires on the APAs (mostly to the first induction wire plane channels). An internal study [24] has shown that with a metallic cathode structure, an HV discharge could swing the outer wire plane by nearly  $100\text{ V}$  and inject  $0.9\text{ A}$  current into the input of the FE amplifiers connected to the first induction plane, possibly overwhelming the internal electrostatic discharge (ESD) protection in the FE ASICs.

On the other hand, a highly resistive cathode structure can significantly delay the change in its potential distribution in a discharge event due to its large distributed RC time constant. Such a delay reduces both the current flowing through the discharge path and the current induced on the anode readout amplifiers. The upper limit in the cathode surface resistivity is determined by the voltage drop between the center and the edges of the cathode array driven by the ionization current flowing to the cathode. For example, a surface resistivity of  $1\text{ G}\Omega/\text{square}$  will have a voltage drop less than  $1\text{ V}$  from the  $^{39}\text{Ar}$  ionization flux at the underground site. Figure 3.3 illustrates the two main benefits in such a design in an event of HV discharge at the edge of the cathode: (1) reducing

the rate of transfer of the stored energy in the cathode plane to reduce the risk of damage to the HVS and cryostat membrane; and (2) slowing down the change in cathode voltage distribution that capacitively injects charge into the readout electronics. With a surface resistivity of  $1 \text{ G}\Omega/\text{square}$  on the entire cathode, the time constant of a discharge is on the order of a few seconds. An HV discharge on the edge of the cathode would inject a maximum current of only about  $50 \mu\text{A}$  into the FE ASICs, avoiding damage.

### 3.1.3.4 Structural considerations

The frames around the CPA panels and the frames supporting the FC aluminum profiles are made from materials with similar thermal expansion coefficients, minimizing issues of differential thermal expansion. The FC frames are restrained at only one location. The CPAs and APAs support the top FC and bottom FC modules, whereas installation rails above the CPAs and APAs support the endwall FC modules.

All structural members of the CPAs and FCs are made of either FR-4 or FRP with very similar coefficients of thermal expansion (CTE). However, the structures supporting the CPAs and FCs are made of stainless steel, with a CTE about 50% greater. To accommodate the mismatch in the CTEs, small expansion gaps are added between CPAs at installation time. These gaps are set during installation between CPA panels by adjusting the distance between the CPA hanger bars and between CPA planes at the top of the TPC on the CPA beam; these 3 mm gaps, 49 of them in total, will disappear once the TPC is submerged in LAr.

### 3.1.3.5 Design validation

Successful ProtoDUNE running and extensive testing has validated the mechanical and electrical properties of materials selected for the HV system. These are fully documented in references [25–27]. More details follow in section 3.6.

Issues identified in earlier testing form the basis of an ongoing R&D program.

Operations experience from ProtoDUNE-SP is summarized in section 3.6. It revealed some instabilities in the HVS operations. Design changes (see section 3.4.2) have been introduced to the top and bottom FC assemblies to further decrease the overall E field between the profiles and the GPs.

## 3.1.4 HV system safety

Safety is central to the design of the HV system and is the highest priority concern in all phases: fabrication, installation, and operations. Documentation of assembly, testing, transport, and installation procedures is in progress and systematically catalogued. Particular attention was paid to these procedures in the design and construction of ProtoDUNE-SP, with the explicit understanding that they be applicable to the SP module. The most critical procedures are also noted in the current HV risk assessment.

The structural and electrical designs for the SP module HV are closely modeled on designs that were vetted and validated in the ProtoDUNE-SP construction. Prior to ProtoDUNE-SP, a full-voltage and full-scale HV feedthrough, power supply, filtering, and monitoring system were tested at Fermilab, along with the HV connection cup and arm, after completing full safety reviews.

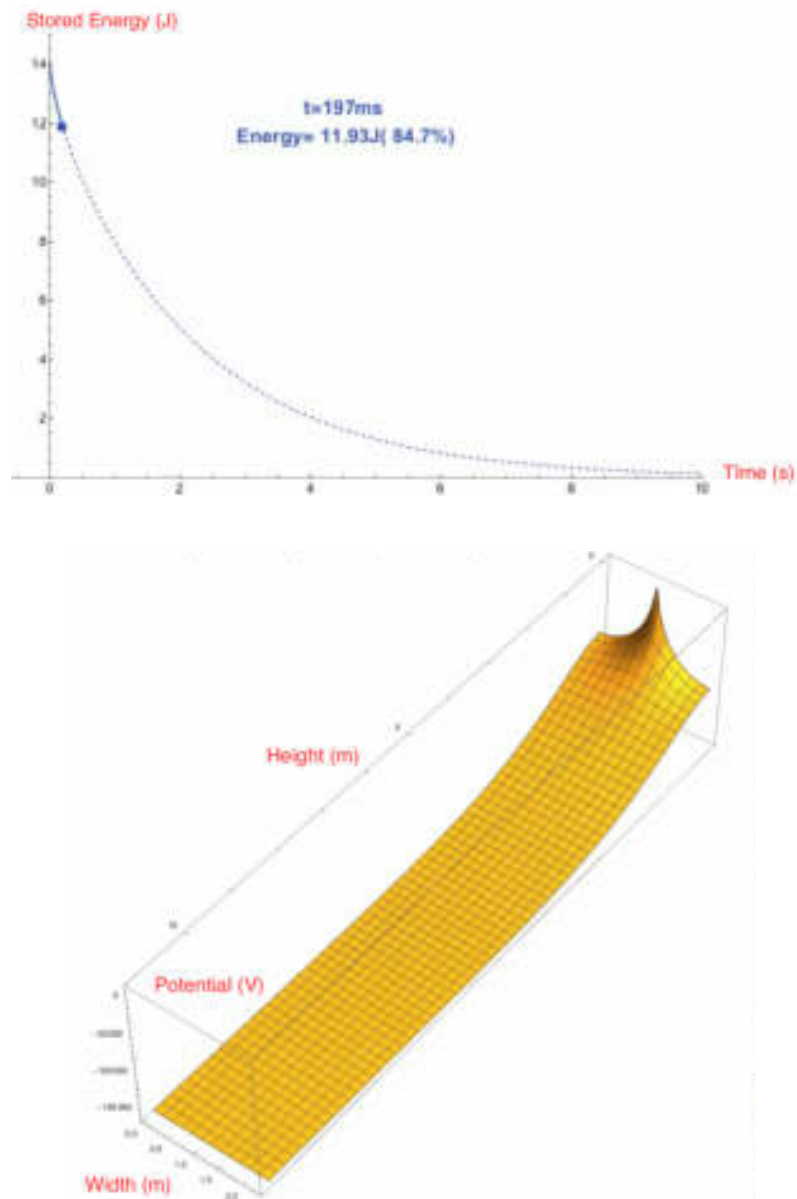


**Figure 3.3.** Simulated discharge event on a highly resistive cathode surface with a surface resistivity of  $1 \text{ G}\Omega/\text{square}$ . Top: stored energy on the cathode as a function of elapsed time from an HV discharge. 0.2 second after the discharge, only about 15% of the stored energy contributes to the discharge. Bottom: voltage distribution on a section of the cathode ( $2.3 \text{ m} \times 12 \text{ m}$ ) 0.2 s after the discharge at the upper right edge. Due to the long time constant of the cathode, most of the surface area remains at the  $-180 \text{ kV}$  operating potential. Only the region close to the discharge site shifts positively toward  $0 \text{ V}$ . Charge injection to the wire readout electronics, proportional to  $dV/dt$  averaged over the cathode area facing an APA, is therefore greatly suppressed.

These devices worked as designed and were used in ProtoDUNE-SP. They will be reproduced for the SP module, except for specific optimizations described in this chapter.

At full operating voltage, the FC stores a substantial amount of energy. As discussed in section 3.1.3.3, the CPA is designed to limit the power dissipated during a power supply trip or other failure that unexpectedly drops the HV. Its design has succeeded in tests at full voltage over 2 m<sup>2</sup> surfaces and at larger scale in ProtoDUNE-SP.

Integral to the ProtoDUNE-SP and SP module design is the concept of pre-assembled modular panels of field-shaping conductors with individual voltage divider boards. The structural design and installation procedures used in ProtoDUNE-SP were selected to be compatible with use at the FD site and were vetted by project engineers, engineering design review teams, and safety engineers at the CERN. Any revisions to these designs based on lessons learned in ProtoDUNE-SP installation and operations will be reviewed both within the project and by Fermilab ES&H personnel. The safety features of the overall design are on solid footing.

### 3.2 HV Power Supply and Feedthrough

The HV delivery system consists of

- two power supplies,
- HV cables,
- filter resistors, and
- HV feedthrough into the cryostat.

For HV delivery, two power supplies generate the voltage, one for each CPA array. This separated setup accommodates any necessary different running voltages between the two CPA arrays. The cryostat design has two feedthrough ports for each CPA array, one at each end of the cryostat. Correspondingly, two HV receiving cups are mounted on the CPA array frame. The spare downstream port provides redundancy against any failure of the primary HV delivery system. In addition, the HV feedthrough is designed to be extracted and replaced in case of misbehavior.

Each CPA array separates and services two adjacent drift volumes, presenting a net resistance of 1.14 G $\Omega$  to each power supply. At the nominal 180 kV cathode voltage, each power supply must provide 0.16 mA. The power supply model planned for the SP module is similar to that used on ProtoDUNE-SP.<sup>3</sup> The HV cables are commercially available models compatible with the selected power supplies.

Filter resistors are placed between the power supply and the feedthrough. Along with the cables, these resistors reduce the discharge impact by partitioning the stored energy in the system. The resistors and cables together also serve as a low-pass filter reducing the 30 kHz voltage ripple on the output of the power supply. With filtering, such supplies have been used successfully in other LArTPC experiments, such as MicroBooNE and ICARUS. Figure 3.4 shows the HV supply circuit.

The requirement on low electronics noise sets the upper limit of residual voltage ripple on the cathode to be 0.9 mV.

---

<sup>3</sup>Heinzinger, PNC HP300000 HV power supply, Heinzinger™ Power Supplies, <http://www.heinzinger.com/>.



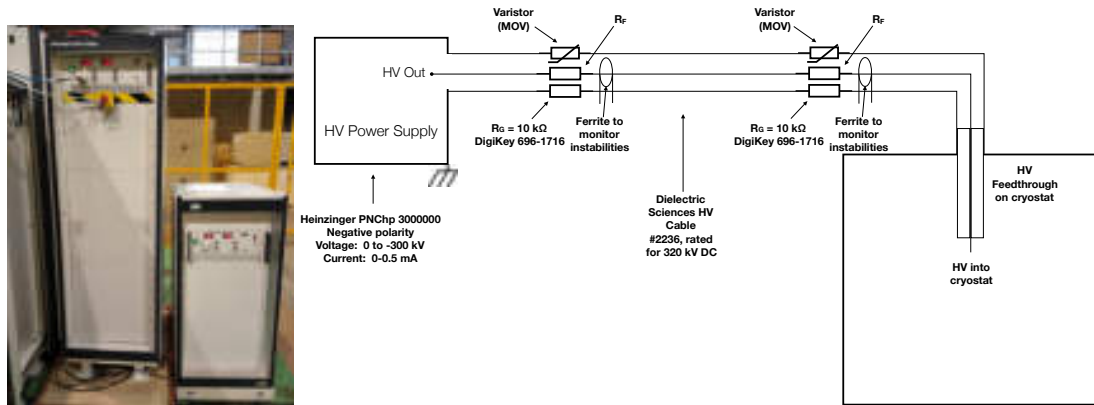


**Figure 3.4.** Left: photo of 300 kV and 200 kV power supplies. Right: a schematic showing the HV delivery system to the cryostat. One of the two filter resistors sits near the power supply; the other sits near the feedthrough.

Typically, commercial supplies specify a ripple variation limit of 0.001 % around an absolute precision in nominal voltage of  $\pm 50$  mV. Assuming cable lengths of 30 m and 3 m between the filters themselves and between the filter and feedthrough, respectively, calculations and experience confirm that resistances as low as a few  $M\Omega$  yield the required noise reduction.

The filter resistors are of a cylindrical design. Each end of a HV resistor is electrically connected to a cable receptacle. The resistor must withstand a large over-power condition. A cylindrical insulator is placed around the resistor.

The HV feedthrough is based on the successful ICARUS design [2], which was adapted for ProtoDUNE-SP. The voltage is transmitted by a stainless steel center conductor. On the warm side of the cryostat, this conductor mates with a cable end. Inside the cryostat, the end of the center conductor has a spring-loaded tip that contacts a receptacle cup mounted on the cathode, delivering HV to the FC. The center conductor of the feedthrough is surrounded by ultra-high molecular weight polyethylene (UHMWPE), an insulator. This is illustrated in figure 3.5.

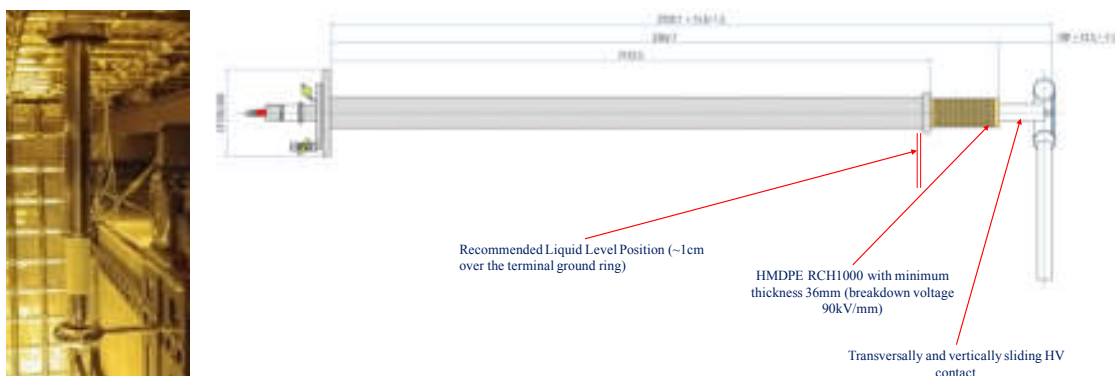


**Figure 3.5.** Photograph and drawing of a HV feedthrough. Photograph shows ProtoDUNE-SP installation. The distance from the cup to the top surface is approximately 1.3 m.

On a feedthrough, to a first approximation, the operating voltage upper bound is set by the maximum E field. This E field can be reduced by increasing the insulator radius. For the target voltage, the feedthrough uses a UHMWPE cylinder of approximately 15 cm diameter. In the gas space and into at least 15 cm of the liquid, the insulator is surrounded by a tight-fitting stainless steel ground tube. A Conflat industry-standard flange is welded onto the ground tube for attachment to the cryostat.

Outside the cryostat, the HV power supply and cable-mounted toroids monitor the HV. The power supplies have capabilities down to tens of nA in current read-back and are able to sample the current and voltage every 300 ms. The cable-mounted toroids are sensitive to fast changes in current; the polarity of a toroid's signal indicates the location of the current-drawing feature as either upstream or downstream of it. Experience from the DUNE 35 ton prototype installation suggests that sensitivities to changing currents are on a timescale between 0.1  $\mu$ s to 10  $\mu$ s.

Inside the cryostat, pick-off points near the anode monitor the current in each resistor chain. Additionally, the voltage of the GPs above and below each drift region can diagnose problems via a high-value resistor connecting the GP to the cryostat. In the DUNE 35 ton prototype, such instrumentation provided useful information on HV stability and locations of any stray charge flows.

Both commercial and custom HV components must be rated for sufficient voltage and must satisfy tests to meet the specifications summarized in section 3.1.2. Section 3.9.1 provides further details on these tests.

The resistances in the filters, in combination with the capacitances between the HV system and the cathode, determine the attenuation of the tens-of-kHz ripple from the power supply. The filters are designed such that the ripple is reduced to an acceptable level when installed in the complete system, thus satisfying specification SP-FD-12 that the power supply ripple be negligible.

### 3.3 CPA arrays

Two vertical, planar CPA arrays held at HV each provide constant-potential surfaces at  $-180$  kV. Each CPA array also distributes HV to the first profile on the top and bottom FC and to the endwall FCs. The configuration of the CPA arrays is described in section 3.1.3.1.

RPs form the constant-potential surfaces of each CPA unit. The RPs are composed of a thin layer of carbon-impregnated Kapton<sup>4</sup> laminated to both sides of a 3 mm thick FR-4 sheet of 1.2 m  $\times$  2 m size.

A CPA array receives its HV via the feedthrough that makes contact with the HV bus mounted on the CPA frame through a cup assembly attached to the frame, as shown in figure 3.6. One cup assembly attaches to each end of the two CPA arrays, for a total of four. Details on the electrical connections are in section 3.5.

In accordance with specification SP-FD-17, the surface resistivity of the RPs is required to be greater than 1 M $\Omega$ /square to provide for slow reduction of accumulated charge in the event of a discharge. Given the anticipated higher stored energy at the FD relative to the prototypes, we set a goal of 1 G $\Omega$ /square to further protect against potential discharges.

To maintain the position and flatness of the cathode, 6 cm thick FR-4 frames are placed at 1.2 m intervals between the CPA panels. This design ensures the cathode distortion caused by a small

---

<sup>4</sup>DuPont™, Kapton® polyimide film, E. I. du Pont de Nemours and Company, <http://www.dupont.com/>.

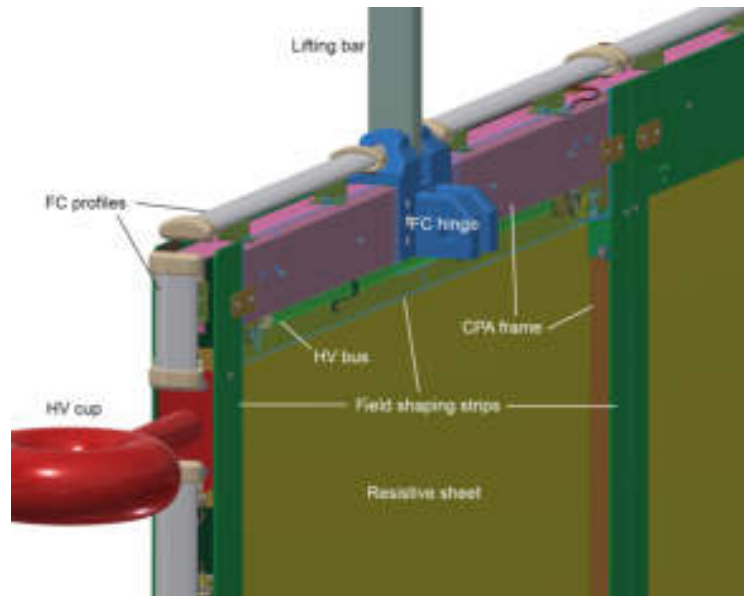


**Figure 3.6.** HV input cup connection to CPA array.

pressure differential (up to 1 Pa) across the cathode surface from the convective flow of the LAr is less than 1 cm, meeting the specification of less than 3 cm, which causes a field uncertainty of 1%.

The CPA frames are required to support, in addition to the HV components, the top FC and bottom FC units attached to both sides of the CPA plane. The arrangement and deployment of these components is identical to that in ProtoDUNE-SP. Figure 3.7 shows a completed ProtoDUNE-SP CPA panel on the production table ready for lifting into vertical position.

Since FR-4 is a good insulator at cryogenic temperatures with a dielectric constant different from that of LAr, the presence of the CPA panel frames causes a local E field distortion that can become pronounced if the frame surface becomes charged from ionization in the TPC. To minimize this distortion, resistive field-shaping strips (FSS) are placed on the frame and biased at a different potential. Figure 3.8 illustrates the drift field uniformity improvement with these strips.

Other HV components of the CPA arrays include edge aluminum profiles (to act as the first elements of the FC) and cable segments forming the HV bus.

There are at least two instances of electrical connections on the CPA array and between the CPA array and other HV system components (top, bottom, and endwall FCs), and four connections between RPs in a CPA unit. Each of the different types of electrical connections on the CPA were tested in a LN<sub>2</sub> tank at BNL [25] and in ProtoDUNE-SP. No failures occurred at either BNL or ProtoDUNE-SP. The HV connection from the HV power supply is a closed loop around the CPA that can sustain at least one broken connection without loss of the cathode HV. This ensures compliance with requirement 3.1.

Visual inspection of these items during the assembly process is done to ensure that no accidental sharp points or edges have been introduced. The surface resistivity of the CPA RPs and the FSS are checked multiple times during assembly, first when the resistive panels and strips are received and after assembly into CPA units on the table. Coated parts that do not meet the minimum surface

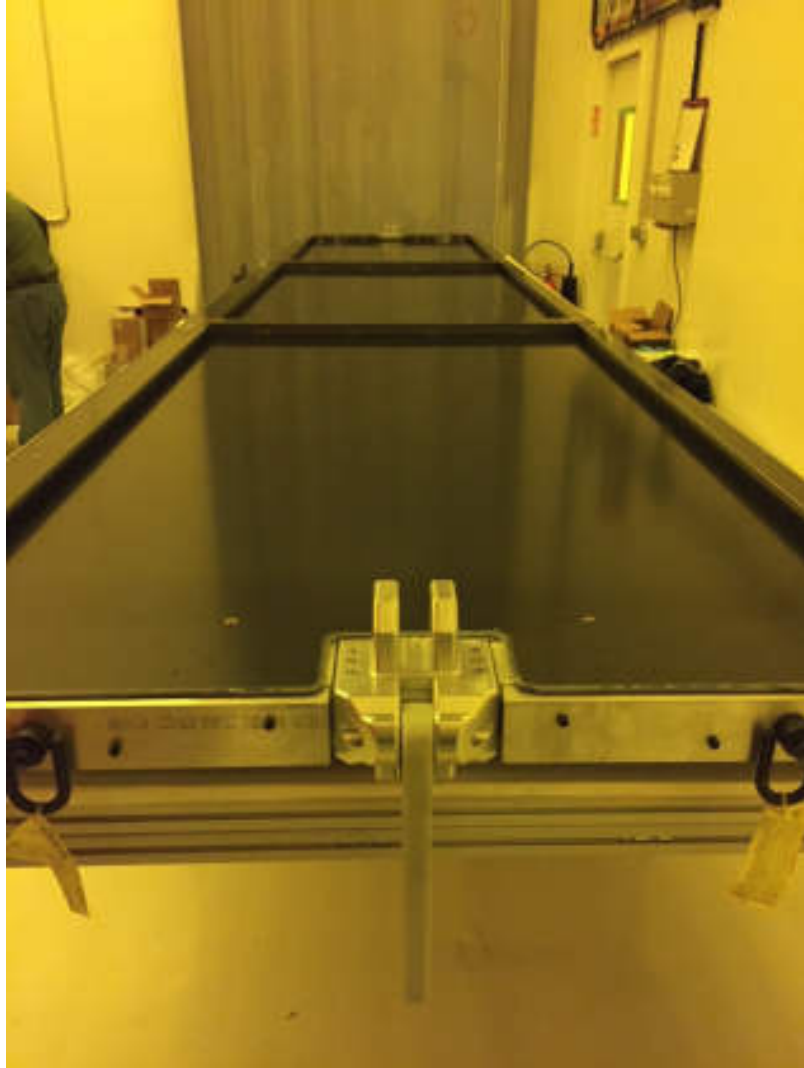


**Figure 3.7.** Completed 6 m long ProtoDUNE-SP CPA panel on production table. A CPA plane is made up of two panels side-by-side.

resistivity requirement are replaced. This ensures that requirement SP-FD-17 is satisfied. No discharges were observed in ProtoDUNE, so no additional cryogenic tests are planned for the CPAs for DUNE.

### 3.4 Field cage

The FC is introduced in section 3.1.3.2. Its function, basic characteristics, and components are described there. The FC is designed to meet the system specifications listed in section 3.1.2. To allow the system to reach the design E field uniformity (specification SP-FD-11), all components other than the aluminum profiles, GPs, and electronic divider boards are made of insulating FRP and FR-4 materials, and the end of each profile is covered with a UHMWPE end cap.

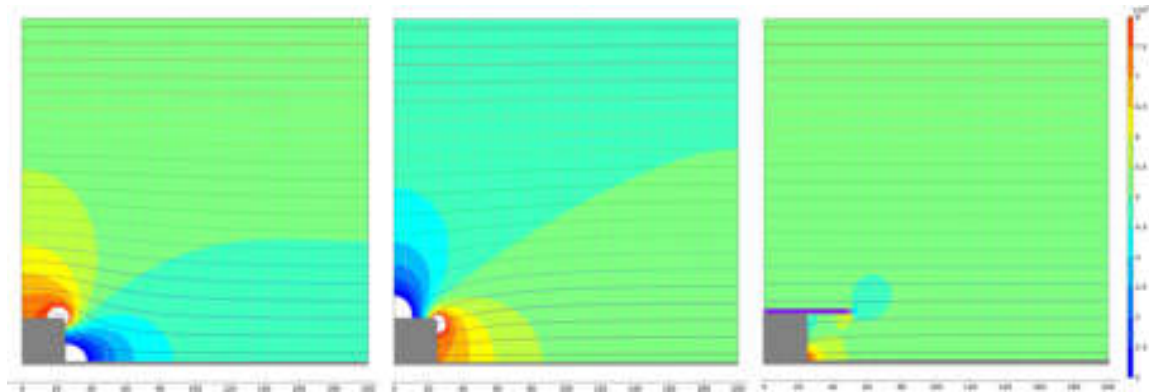


**Figure 3.8.** A comparison of three cathode cross sections to illustrate the benefit of the FSS. Both equipotential lines (horizontal) and E field lines (vertical) are shown. The amplitude of the E field is shown as color contours. Each color contour is a 10% step of the nominal drift field. The gray rectangles represent the frame and the resistive sheet in each case. Left: a conductive/resistive frame similar to that of ICARUS or SBND; middle: an insulating frame with the insulating surfaces charged to an equilibrium state; right: an insulating frame covered with FSS (purple) and biased at the optimum potential.

All voltage divider boards provide redundancy for establishing the profile-to-profile potential differences with only minor distortions to the E field in case of failure of any individual part, and two redundant boards provide the connection from the FCs modules to the CPA (specification 3.1). The aluminum profiles are attached to FRP pultruded structural elements, including I-beams and box beams. Pultruded FRP material is non-conductive and strong enough to withstand the FC loads in the temperature range of  $-150\text{ C}$  and  $23\text{ C}$ , as certified by vendors. Testing of the FRP joints were conducted at  $\text{LN}_2$  temperatures [26]. The material was stronger at these temperatures than at room temperature, providing confidence in the material behavior at LAr temperature. The FRP material meets class A standards for fire and smoke development established by the International Building Code characterized by ASTM E84.<sup>5</sup>

The top and bottom FCs are supported by the CPA and APA arrays. The endwall FC modules, 1.5 m tall by 3.5 m long, are stacked eight units high (12 m) and are supported by the installation rails above the CPA and APA arrays.

### 3.4.1 Field cage profiles

The FC consists of modules of extruded aluminum field-shaping profiles, as listed in table 3.3. The shape of these profiles is chosen to minimize the strength of the E field between a given profile and its neighbors and between a profile and other surrounding parts, including the GP. For example, with a 30 cm separation between the FC and the GP, the maximum E field on the profiles surface is under  $10\text{ kV} \cdot \text{cm}^{-1}$  over the straight sections of the profiles at  $-180\text{ kV}$  bias (figure 3.9).

The profile ends have higher surface E field, especially those at the corners of the FC. To prevent high voltage breakdown in the LAr, the ends of the profiles are encapsulated by custom

<sup>5</sup>ASTM E84-20, Standard Test Method for Surface Burning Characteristics of Building Materials, ASTM International, West Conshohocken, PA, 2020, <https://www.astm.org>.

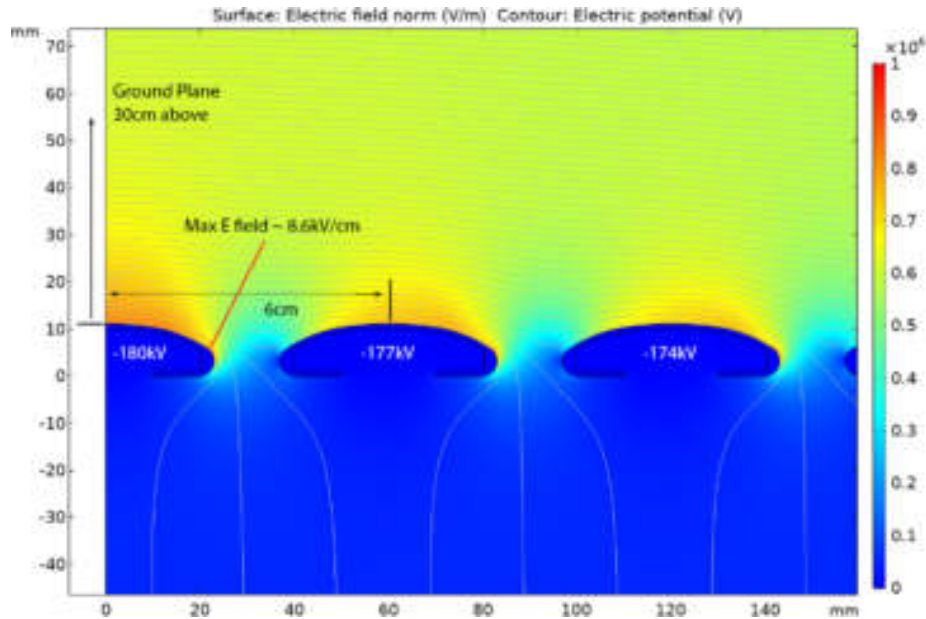


**Figure 3.9.** E field map (color) and equipotential contours of an array of the FC profiles biased up to  $-180$  kV and a ground clearance of 30 cm.

UHMWPE caps. These caps are designed and experimentally verified to withstand the full voltage across their 6 mm thickness.

The profiles and their end caps have been carefully modeled to ensure the resulting E field does not approach 30 kV/cm [28] (specification SP-FD-24). This design concept was validated in a small-scale test setup at CERN before it was adapted for the SP module. These features are designed to avoid sparking and thus to draw very small stable currents, which should produce a consistent load on the power supply (specifications 3.1, 3.1, and 3.1).

### 3.4.2 Ground planes

For safe and stable operation of the LAr cryogenics system, the cryostat requires a small fraction of its volume to be filled with gaseous argon. This small volume is commonly referred to as the ullage. To optimize use of the LAr in the cryostat, we will place the upper FC, which forms the top boundary of the TPC, just below the liquid surface.

The ullage contains many grounded conducting components with sharp features, near which the E field could easily exceed the breakdown strength of gaseous argon if directly exposed to the upper FC. To shield the high E field from entering the gas ullage and thereby prevent such breakdowns, ground planes (GPs), in the form of tiled, perforated stainless steel sheet panels, are mounted on the outside surface of the top FC module with a 30 cm clearance. While critical over the region near the cathode, the need for such shielding diminishes toward the APA end of the FC due to the lower voltages on the FC profiles in that region. The 30 cm FC-GP distance represents a 50% increase over the value used in ProtoDUNE-SP, to further reduce the maximum E field in the TPC and thus the possibility of discharges. The 20 cm distance in ProtoDUNE-SP was due to an early DUNE design, where 20 cm was the maximum possible distance that could maintain the GP

below the liquid level. With the current cryostat and SP module design, more space is available, allowing an increase in the FC-to-GP distance.

In addition to the increase in FC to GP clearance, we are also eliminating most of the insulating standoffs used in ProtoDUNE-SP that support GP tiles from the FC I-beams, in particular, those near the CPA end of the FC. These standoffs are deemed at risk of aiding discharges by providing a short path from FC to GP along corresponding straight edges. Figure 3.10 illustrates the new configuration. Figure 3.11 shows a test stand built to demonstrate the coupling between FC and GP, with the standoffs near the cathode end removed. Tests in Ash River are confirming that no changes in the assembly or deploying procedures are needed and that the mechanical stability of the full system is unaffected. An upcoming review will examine the design changes and related tests and calculations. Final validation of the complete HV design for the SP module will be performed in future ProtoDUNE running.

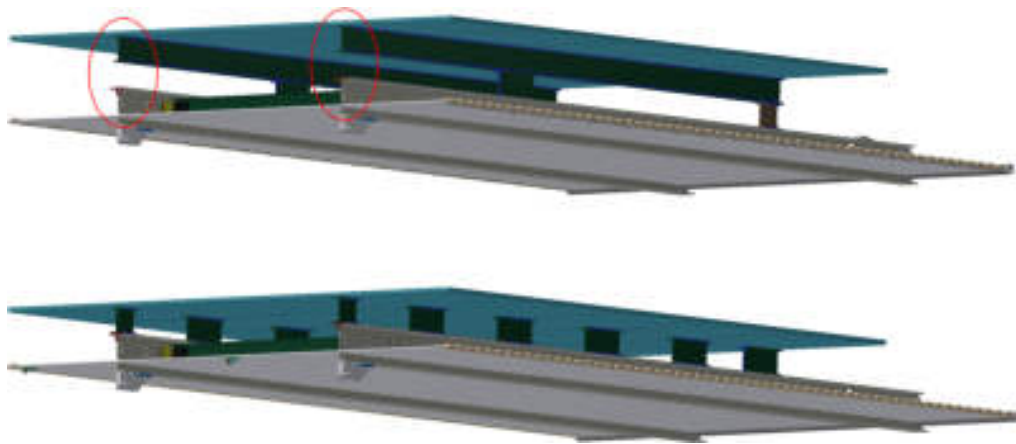


**Figure 3.10.** Comparison between the FD top FC module (top) and the ProtoDUNE-SP counterpart (bottom). The changes to the CPA side standoffs in the FD version are highlighted in red circles. The increase in the FC to GP separation is also shown here.

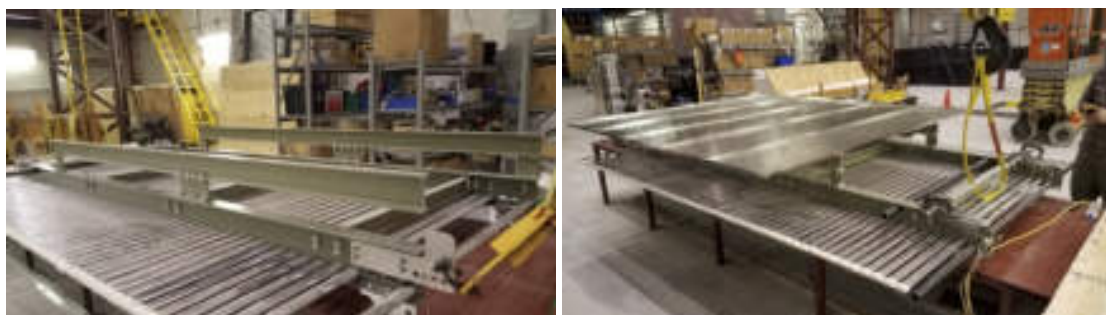


**Figure 3.11.** Photos of a test module demonstrating the coupling between the FC and GP, with the standoffs near the cathode end (towards the right) removed.

On the bottom of the cryostat a similar set of GPs will protect against breakdown in the liquid near cryogenic pipings and other sensors with sharp features. The same clearance will be used. No GPs are planned beyond the two endwall FCs since there is sufficient clearance in those regions.

### 3.4.3 Maximum field distortions

The FCs are designed to produce a uniform E field with understood characteristics. The largest known E field distortion in the TPC occurs around a large gap in the FC between the endwall module and its neighboring top and bottom modules. This gap is necessary to allow the top and bottom modules to rotate past the endwall FC during deployment. Figure 3.12 illustrates the extent of the distortion in this limiting scenario. In the SP module, a total LAr mass of 160 kg along these four edges of the TPC suffers > 5% E field distortions. If the non-uniformity is not accounted for in reconstruction, this will result in uncertainties in  $dE/dx$  in these regions exceeding 1%.

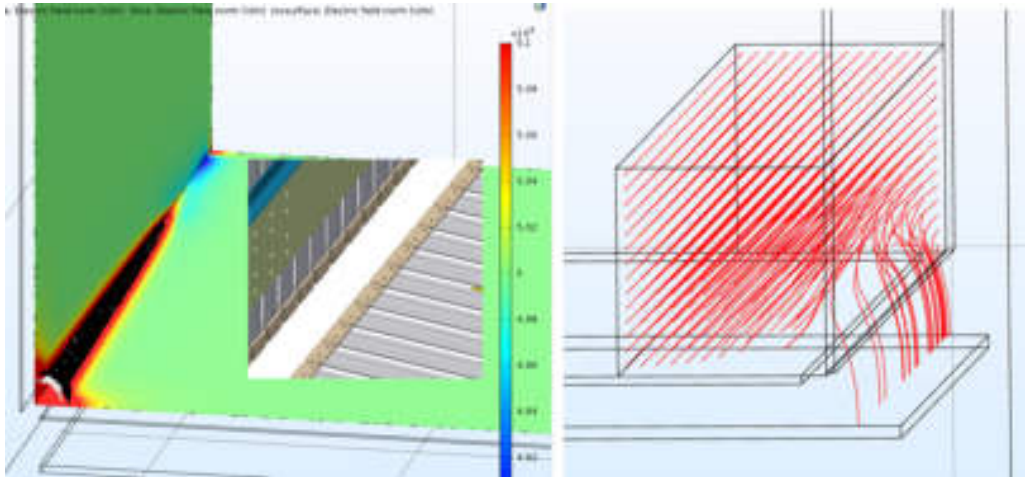


**Figure 3.12.** E field at a corner between the bottom and endwall FC modules, showing effects of a 7 cm gap. Left: the extent of 5% E field non-uniformity boundary (black surface, contains less than 10 kg of LAr) and 10% non-uniformity boundary (white surface, contains ~6 kg of LAr) inside the TPC's active volume. The inset is a view from the CAD model. Right: electron drift lines originating from the cathode surface.

### 3.4.4 Top and bottom field cage modules

The top FC and bottom FC module dimensions are listed in table 3.3. The length, 3.5 m, is set by the length of the two 15.2 cm (6 in) FRP I-beams that form the primary support structure of the modules. The I-beams are connected to each other by three 7.6 cm (3 in) FRP cross beams. The connections between the longitudinal and cross I-beams are made with L-shaped FRP braces that are attached to the I-beams with FRP spacer tubes, and secured with FRP threaded rods, FRP hex-head nuts, and custom-machined FR-4 washer plates.

The 2.3 m module width corresponds to the length of the aluminum profiles, including the UHMW polyethylene end caps. Profiles are secured to the FRP frame using custom-machined double-holed stainless steel slip nuts that are slid into and electrically in direct contact with the aluminum profiles such that they straddle the webbing of the 15 cm I-beams, and are held in place with screws that penetrate the I-beam flanges. The profile offset with respect to the FRP frame is different for modules closest to the endwall FCs, and modules in the center of the active volume.

Five GPs are connected to the outside (i.e., the non-drift side) of each top FC and bottom FC module. The GPs are positioned ~30 cm away from the profiles, and begin at the CPA end of the



module, leaving the last 14 profiles (88 cm) on the APA end of the module exposed. Between the GPs and the 15 cm I-beams standoffs made of short sections of 10.2 cm (4 in) FRP I-beams are connected with FRP threaded rods and slip nuts. The electrical connection between the GPs is made with copper strips.

The connections between the top and bottom modules and the CPAs are made with aluminum hinges, 2.54 cm (1 in) in thickness, that allow the modules to be folded in on the CPA during installation. The hinges are electrically connected to the second profile from the CPA. The connections to the APAs are made with stainless steel latches that are engaged once the top and bottom FC modules are unfolded and fully extended toward the APA.

The voltage drop between adjacent profiles is established by voltage divider boards screwed into the drift-volume side of the profiles. A custom-machined nut plate is inserted into the open slot of each profile and twisted 90° to lock into position. Two additional boards to connect the modules to the CPAs screw into the last profile on the CPA end of the module. This system is more fully described in section 3.5. A fully assembled module is pictured in figure 3.13.



**Figure 3.13.** A fully assembled top field cage (top FC) module with ground plane (GP) is shown.

### 3.4.5 Endwall field cages (EWFC)

Each of the four drift volumes has two endwall FCs, one on each end. Each endwall FC is in turn composed of eight endwall FC modules. The two endwalls are identical in construction, and are installed with an 180° rotation front to back. Figure 3.14 illustrates the layout for the topmost and the other panels, respectively.

Each endwall FC module is constructed of two FRP box beams, each 3.5 m long, as shown in 3.14. The box beam design also incorporates cutouts on the outside face to minimize charge build

up. Box beams are connected using 1.27 cm (0.5 in) thick FRP plates. The plates are connected to the box beams using a shear pin and bolt arrangement. The inside plates facing the active volume are connected using special stainless steel slip nuts and stainless steel bolts. The field-shaping profiles are connected to the top box beam using stainless steel slip nuts, an FRP angle, and two screws each that pass through matching holes in the wings of the aluminum profiles. At the bottom box beam, the profiles are pulled against another FRP angle with a single screw and a slip nut that is held in place by friction.

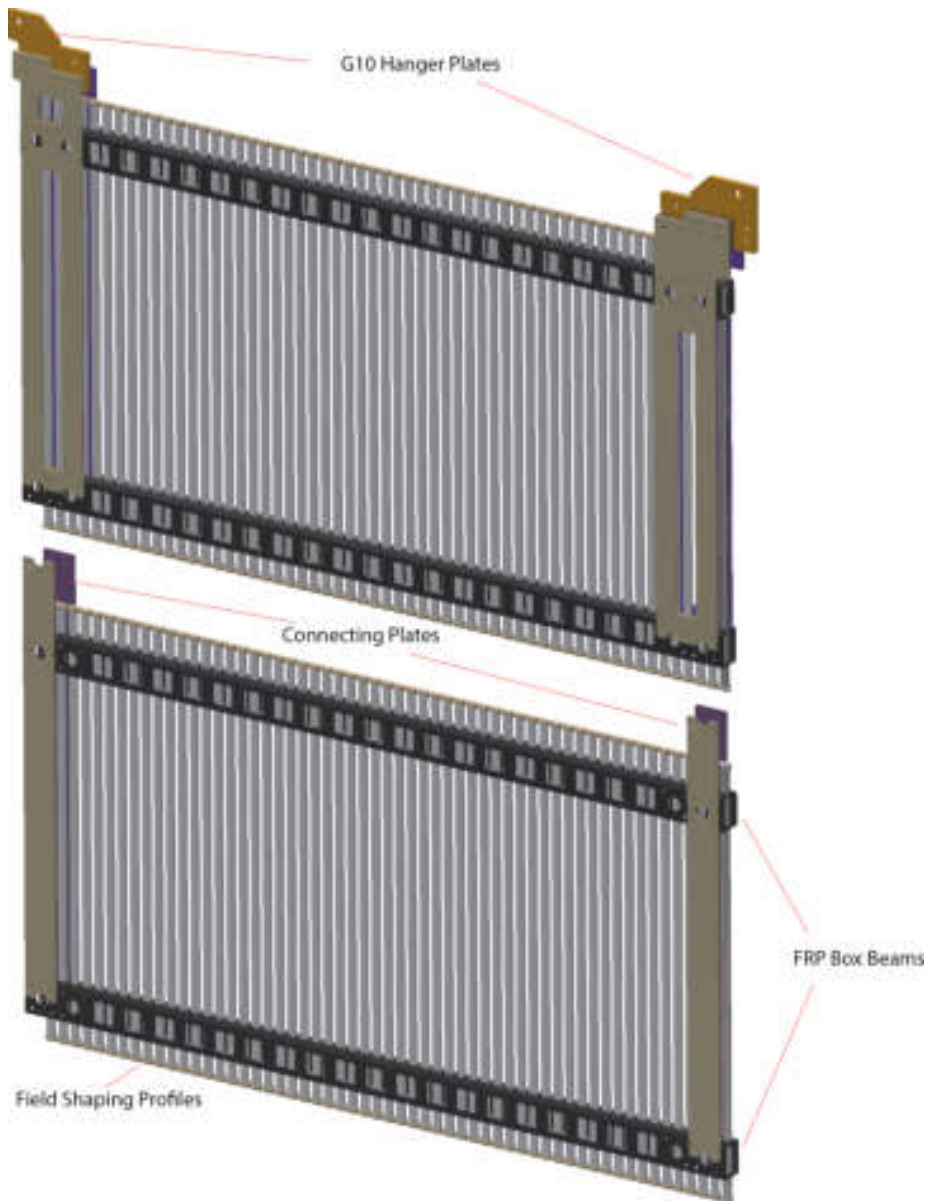


**Figure 3.14.** Top: uppermost module of the endwall FC. The two G10 hanger plates connect the endwall FC to the DSS beams above the APAs and CPAs. Bottom: regular endwall FC module. Seven such modules stack vertically with the top module to form the 12 m total height.

### 3.4.6 Voltage divider boards

A resistive divider chain interconnects all the metal profiles of each FC module to provide a linear voltage gradient between the cathode and anode planes.

The resistive divider chain is a chain of resistor divider boards each with eight resistive stages in series. Each stage (corresponding to 6 cm gap between FC profiles) consists of two  $5\text{ G}\Omega$  resistors in parallel yielding a parallel resistance of  $2.5\text{ G}\Omega$  per stage to hold a nominal voltage difference of 3 kV. Each stage is protected against high voltage discharge transients by transient/surge absorbers (varistors). To achieve the desired clamping voltage, three varistors (with 1.8 kV clamping voltage) are wired in series and placed in parallel with the associated resistors. A schematic of the resistor divider board is shown in figure 3.15; an illustration of the resistor divider board used in ProtoDUNE-SP is shown as well. These boards will be identical to the ones successfully mounted in the ProtoDUNE-SP FC.

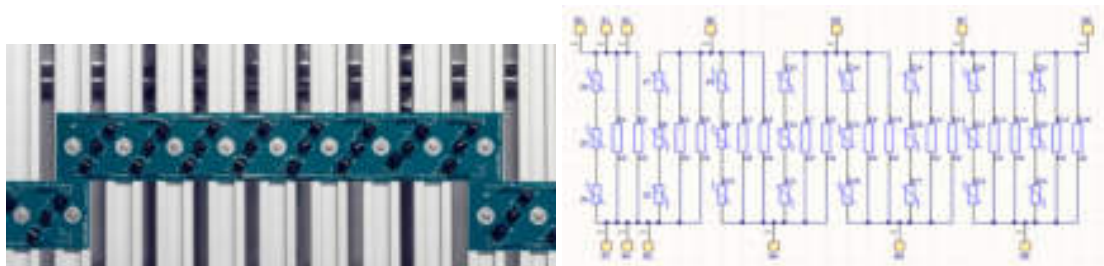


**Figure 3.15.** Left: a ProtoDUNE-SP resistor divider board. Right: schematic diagram of resistor divider board.

The current drawn by each divider chain is about  $1.2\ \mu\text{A}$  at the nominal E field of 500 V/cm. A total of 132 resistive divider boards are connected in parallel to each CPA array for a total of about  $158\ \mu\text{A}$ , well within the capability of the selected HV power supply.

There are about 30,000 resistors used on the FCs in an SP module. A resistor failure is a possible risk to the TPC. An open resistor on the divider chain, the most common failure mode, would approximately double the voltage across the remaining resistor to 6 kV. This larger voltage would force the three varistors in parallel to that resistor into conduction mode, resulting in a voltage drop of roughly 5 kV ( $1.7\text{ kV} \times 3$ ), while the rest of the divider chain remains linear, with a slightly lower voltage gradient. Because the damage to the divider would be local to one module, its impact to the TPC drift field is limited to region near this module, a benefit of the modular FC design. An example of a simulated E field distortion that would be caused by a failed resistor is shown in figure 3.16.

The effect of the non-uniformity in resistor values can also be scaled from this study. A 2% change in a resistor value (1% change from the  $2R$  in parallel) would give about 1.5% of the distortion from a broken resistor, i.e. less than 1 mm of transverse distortion in track position, with no noticeable drift field amplitude change inside the active volume.

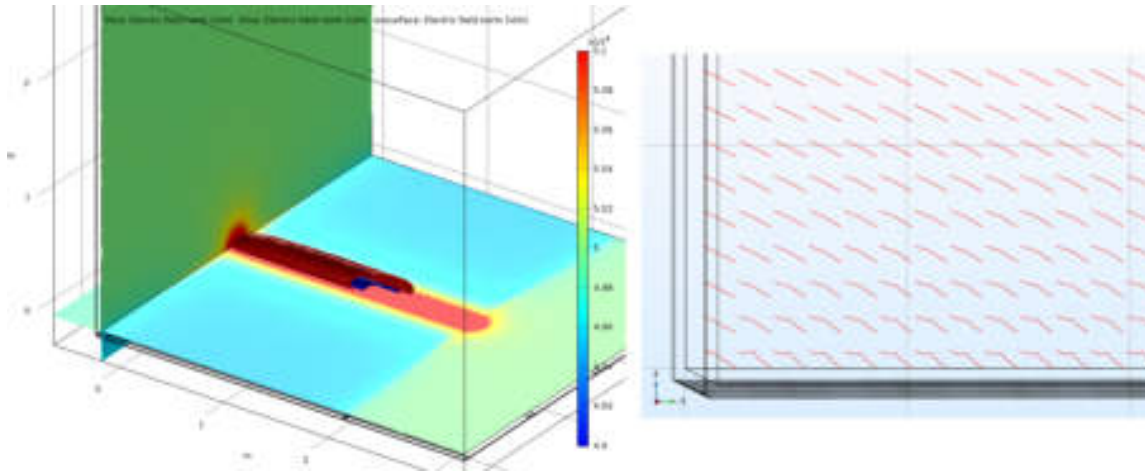


**Figure 3.16.** Simulated E field distortion from one broken resistor in the middle of the voltage divider chain on one bottom FC module. The benefit of the redundancy scheme is emphasized by the limited extent of the E field distortions. Left: extent of E field non-uniformity in the active volume of the TPC. The green planes mark the boundaries of the active volume inside the FC. The partial contour surfaces represent the volume boundaries where E field exceeds 5% (dark red, contains less than 100 kg of LAr) and 10% (dark blue, contains less than 20 kg of LAr) of the nominal drift field. The units are  $\text{V} \cdot \text{m}^{-1}$  in the legend. Right: electron drift lines connecting the CPA to APA in a bottom FC corner. The maximum distortion to the field line is about 5 cm for electrons starting at mid-drift at the bottom edge of the active volume.

### 3.5 Electrical interconnections

Electrical interconnections are needed among the HV delivery system, CPA panels, FC modules, and termination boards on the APA modules, as well as between resistive dividers and the field-forming elements on the CPAs and FCs. Redundancy is needed to avoid single points of failure. Some connections must be insulated in order to avoid creating a discharge path that might circumvent the discharge mitigation provided by the resistive CPA surface and FC partitioning. Certain connections must be flexible in order to allow for FC deployment, thermal contraction, and motion between separately supported CPAs components. Figure 3.17 shows a high-level overview of the interconnections between the HV, CPA, and FC modules.

High voltage feedthroughs connect to cups mounted on the CPA frame that attach to an HV bus running through the CPAs. HV bus connections between CPA panels are made by flexible wires through holes in the CPA frame. The HV bus is a loop that mitigates any risk of a single failure point; the feedthrough at each end of each CPA panel mitigate risk of a double-break failure. Voltage dividers on each CPA panel bias the FSS and the resistive dividers on the top and bottom FCs. The CPA-to-FC connections are made using flexible wire to accommodate FC deployment. To further increase redundancy, two CPA panels connect to each top or bottom field cage, and two connections are also made to each endwall FC. Resistor divider boards attach directly to the interior side of the FC profiles with screws. A redundant pair of flexible wires connects a circuit board on the last profile of each FC to a bias-and-monitoring board mounted on the corresponding APA.

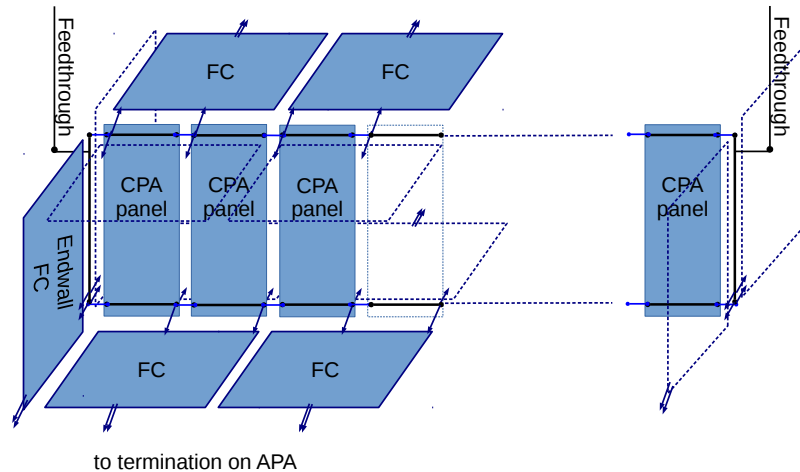


**Figure 3.17.** High-level topology of the HV interconnections for one CPA array and adjacent field cages. Each pair of adjacent CPA panels is connected to two top field cage modules and two bottom field cage modules. A high voltage bus supplies the CPA panels at the top and bottom, and also supplies the endwall field cage modules. All field cages are terminated at the APAs (not shown).

Short sections of flexible wire at the ends of each HV bus segment attach to screws in brass tabs on the CPA resistive panels (CPA RPs). Vertical HV bus segments on the outer ends of each CPA plane connect the top and bottom HV buses to complete the loop. Solid wire is used to connect resistive panels within a CPA panel.

Each FC module is as electrically independent as possible in order to mitigate discharge. However, only the bottom module of each endwall can make connections to the HV bus and APA, so each endwall module is connected to its upper neighbor at its first and last profile using metal strips.

Each FC divider chain connects to an FC termination board in parallel to a grounded fail-safe circuit at the APA end. The FC termination boards are mounted on the top of the upper APAs and bottom of lower APAs. Each board provides a default termination resistance, and an SHV cable connection to the outside of the cryostat, via the CE signal feedthrough flange, through which we can either supply a different termination voltage to the FC or monitor the current flowing through the divider chain.

All flexible wires have ring or spade terminals and are secured by screws in brass tabs. Spring washers are used with every electrical screw connection in order to maintain good electrical contact with motion and changes of temperature.

Table 3.4 summarizes the interconnections required for the HV system.

The redundancy in electrical connections described above meets requirement 3.1. The HV bus and interconnections are all made in low field regions in order to meet requirement 6.1. The HV bus cable is rated at the full cathode HV such that even in case of a rapid discharge of the HV system no current can flow to the cathode or FC except at the intended contact points, preserving the ability of the resistive cathode and FCs to meet requirement 3.1.

**Table 3.4.** HV system interconnections.

| Connection                            | Method   |
|---------------------------------------|--|
| HV cup to HV bus                      | wire to screw in HV cup mount on CPA frame                         |
| HV bus between CPA panels             | wire between screws in brass tabs                                  |
| HV bus to FSS                         | wire to circuit board mounted on FSS                               |
| FSS to top FC and bottom FC           | wire to circuit board on first FC profile, two per FC module       |
| HV bus to endwall FC                  | wire to circuit board mounted on first FC profile, two per endwall |
| FC divider circuit boards             | directly attached to profiles using screws and SS slip nuts        |
| FC to bias and monitoring termination | redundant wires from board mounted on last FC profile              |
| HV bus to CPA panels                  | brass tab on CPA resistive panel                                   |
| CPA RP interconnections               | solid wire between screws in brass tabs                            |
| Endwall FC module interconnections    | metal strips, first and last profiles only                         |

### 3.6 ProtoDUNE-SP high voltage experience

ProtoDUNE-SP [6] is a prototype for an SP module. Approximately one twentieth the size of a SP module, this detector implements an A-C-A configuration with one CPA array that bisects the TPC and two APA arrays, one along each side. The CPA array consists of six CPA panels, each 1.2 m wide by 6.0 m high (half-height relative to an SP module), and is positioned 359 cm away from each APA array, matching the maximum drift distance of an SP module.

Six top and six bottom FC modules connect the horizontal edges of the CPA and APA arrays, and four endwall FCs connect the vertical edges (two per drift volume). One of the drift volumes is pictured in figure 3.18. Each endwall FC comprises four endwall modules (half-height relative to a SP module). A Heinzinger  $-300$  kV 0.5 mA HV power supply delivers voltage to the cathode. Two HV filters in series between the power supply and HV feedthrough filter out high-frequency fluctuations upstream of the cathode.

#### 3.6.1 Summary of HV construction

The ProtoDUNE-SP HV components underwent various levels of pre-assembly offsite prior to transport and final assembly in the ProtoDUNE-SP cleanroom adjacent to the cryostat.

Parts for the top and bottom FC frames were procured and test fit at Stony Brook University before being shipped to CERN for module assembly in a cleanroom about 5 km away from the detector hall. Fully assembled modules were transported individually to the detector hall for storage until installation. CERN provided the GPs for the top and bottom FCs as well as the field shaping profiles for all FCs.

Louisiana State University (LSU) provided all the voltage divider boards, then procured and test fit the endwall FC frame parts before shipping them fully assembled to CERN. These profiles and the voltage divider boards were installed in the same CERN cleanroom facility as the other FC components.

Argonne National Laboratory shipped the CPA material to the detector hall as single pre-assembled resistive panels held in a FR-4 frame; i.e., as CPA units (table 3.2). In the cleanroom



**Figure 3.18.** One of the two drift volumes of ProtoDUNE-SP. The FC modules shown enclose the drift volume between the CPA array (at the center of the image) and the APA array (upper right). The endwall FCs are oriented vertically; the top and bottom units are horizontal. The staggered printed circuit boards connecting the endwall FC profiles are the voltage divider boards.

adjacent to the ProtoDUNE-SP cryostat, three CPA units were mechanically and electrically connected to produce a CPA panel. The CPA panels (one of which is pictured in figure 3.7) were first assembled horizontally and then lifted and rotated to a vertical orientation where they were paired to make a  $6.0\text{ m} \times 2.3\text{ m}$  CPA plane.

At this point, two top and two bottom FC modules were brought to the cleanroom to be lifted, rotated to vertical, and attached to the CPA plane. To fit through the TCO, the top FCs were suspended from their support at the top of the CPA plane to hang vertically, and the bottom FCs were folded up and temporarily attached to their top FC counterparts. The resulting CPA-FC assemblies were rolled onto the central bridge beam inside the cryostat and deployed.

Also in the ProtoDUNE-SP cleanroom, sets of four pre-assembled endwall FCs were each assembled into one endwall FC plane. Although not a component of the SP module design, the beam plug was installed onto its corresponding module before the beam-right, upstream endwall FC was built. An electric hoist lifted the top module to a height at which the next module could be wheeled underneath and connected via FRP plates. The hoist then raised the pair, and the procedure would continue in this way until the endwall FC was four modules tall. The load of the assembled endwall was then transferred to a trolley on a transport beam, which allowed it to be pushed into the cryostat onto the appropriate bridge beam.

The TPC components of ProtoDUNE-SP were installed first for the drift space to the right of the delivered beam (beam-right), and then for the beam-left drift space. The APAs and the CPA array were locked into position along their respective bridge beams, and then the bridge beams were locked into their positions along the drift direction. Next, the two endwall FCs were moved and

rotated into their upstream and downstream positions to bridge the gap between the vertical edges of the corresponding APA and CPA. The endwall FCs loads were transferred onto the APA and CPA bridge beams, which freed the intermediate bridge beam for top and bottom FC deployment. Two mechanical hoists were used to lower (raise) the bottom (top) FC to bridge the gap between the horizontal edges of the APAs and CPAs. Finally, the HV cup was connected on the downstream CPA, and the HV feedthrough was lowered through the cryostat penetration to make contact with the cup.

### 3.6.2 HV commissioning and beam time operation

During cool-down and LAr filling, a power supply was used to supply  $-1$  kV to the cathode and monitor the current draw of the system. As the system cooled from room temperature to LAr temperature, the resistance increased by  $\sim 10\%$ , consistent with expectations. Once the LAr level had exceeded the height of the top GPs, the voltage was ramped up to the nominal voltage.

The initial week of HV operations showed no signs of any anomalous instabilities. Over the following weeks, the HV power supply showed signs of instabilities that affected the quality of the HV provided to the cathode plane. Replacement of the power supply midway through the run resulted in higher stability of the warm side of the HV system. The original power supply was sent to Heinzinger for inspection. The malfunctioning was confirmed to be due to unexpected excessive moisture that had accumulated in the HV cable socket.

In addition, two types of instabilities emerged in the cold side of the HV system. The first type was the so-called current blips, during which the system draws a small excessive current that persists for no more than a few seconds. The magnitude of the excess current during such events increased over the subsequent three weeks from  $1\%$  to  $20\%$ . The second type of instability, labeled “current streamers,” exhibited persistent excessive current draw from the HV power supply with accompanying excessive current detected on a GP and on the beam plug. These two types of instabilities were experienced periodically throughout the duration of the ProtoDUNE-SP beam run. The frequency of both types increased over time after the system was powered on, until a steady state of about ten current blips/day and one current streamer every four hours was reached. These effects are consistent with a slow charging-up process of the insulating components of the FCs supports, which then experience partial discharges that are recorded as HV instabilities. This process appears to restart after every long HV-off period.

In addition, these processes seem to be enhanced by the LAr bulk high purity, which allows the electric current to develop. At low purity electronegative impurities act as quenchers, blocking the development of the leakage current. Despite the presence of two types of instabilities, the HV system was able to consistently achieve  $>95\%$  uptime during the beam runs. The downtime was the result of short manual interventions to quench a current streamer (figure 3.19).

In some cases, mostly outside of the beam run period, we turned off the HV system momentarily to allow the HV system components to discharge. This is reflected as larger dips in the uptime plot. During moments when the rest of the subsystems (including the beam) were stable, the moving 12-hour HV uptime fluctuated between  $96\%$  and  $98\%$ .

The up-time during the week starting October 11th (Oct 11 in figure 3.19) is lower than the subsequent three beam-on weeks because the current streamers were addressed differently in these two periods. In the beginning, they were left to develop until they quenched themselves or until the



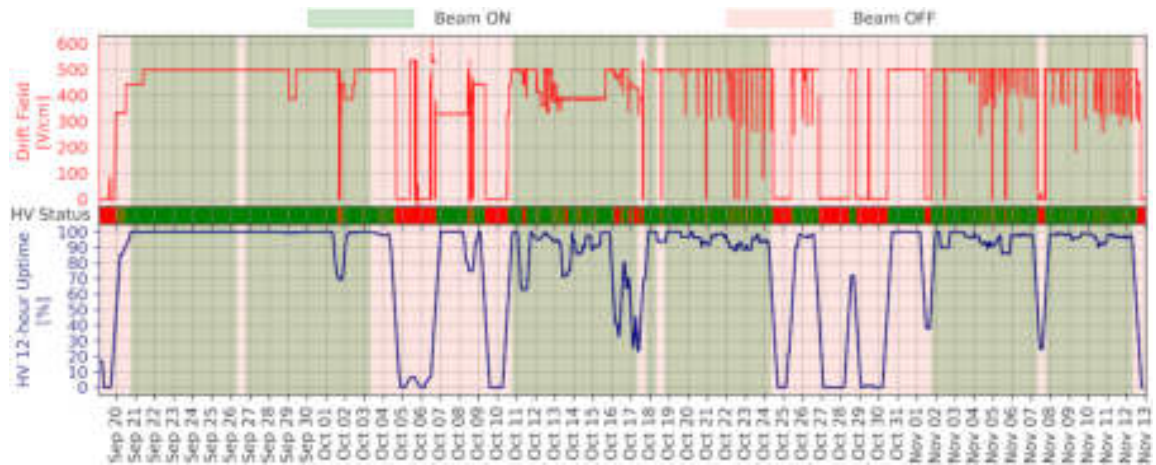


**Figure 3.19.** The performance of the HV system across the test beam period, September-November 2018. The top panel shows the drift field delivered to the TPC, the middle panel indicates HV cuts during periods when the system is not nominal (some periods not visible due to their short timescale), and the bottom panel shows the moving 12-hour uptime of the HV system based on these HV cuts.

HV was manually ramped down. The HV was brought back up when the current draw returned to nominal, according to the FC resistance value. Automated controls to quench the current streamers were then successfully implemented in an auto-recovery mode. These helped significantly to increase the up-time, by optimizing the ramping down and up of the HV power supply voltage, which was performed in less than four minutes (figure 3.20).

### 3.6.3 Post-beam stability runs with cosmic rays

During the 2018 beam run periods, priority was given to operating the ProtoDUNE-SP detector with maximal up-time in order to collect as much beam data as possible at the nominal HV conditions. Therefore, investigating the long-term behavior of the HV instabilities and understanding their origin became goals of the long-term operation of ProtoDUNE-SP in 2019.

As mentioned above, it appears that the current streamer effect is a charging-up process with its frequency increasing with time after a long HV-off period. This behavior has been repeatedly observed and confirmed in 2019. The current streamer rate stabilized at 4–6 per day, and the location was essentially always on the same single Ground Plane (GP#6) out of the 12 monitored GPs. Their rate and location were approximately independent of the HV applied on the CPA in the 90 kV to 180 kV range.

More recently, after a change of the LAr re-circulation pump (April 2019), the detector was operated for several months in very stable cryogenic conditions and with very high and stable LAr purity (as measured by purity monitors and cosmic rays). During this period, the HV system was set and operated at the nominal value of 180 kV at the CPA for several weeks without interruption. A significant evolution in the behavior of the HV system was observed.

To better understand the current streamers phenomenon, the HV system was operated for about fifty days without the auto-recovery script, and the current streamers were left to evolve naturally. They typically lasted 6 to 12 hours, exhibiting steady current and voltage drawn from the HV power

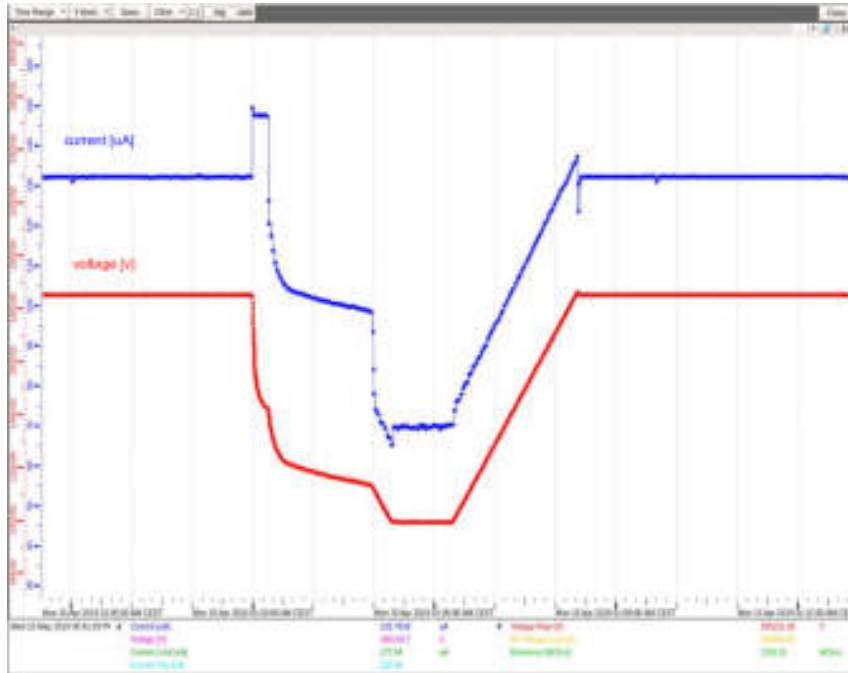


**Figure 3.20.** Example of the HV automatic recovery procedure developed to detect and quench the current streamers: whenever an excess sustained current from the HV PS is detected (obtained by continuously monitoring the total detector resistance experienced by the PS), the HV delivered by the PS is lowered in discrete steps. At each step the total resistance is checked again, and if it agrees with the nominal detector resistance the HV is ramped up again to its nominal value; otherwise the HV is lowered to the next step.

supply and they eventually self-quenched without any intervention. The repetition rate was highly reduced to about one current streamer every 10–14 days; this rate can be compared to the 4–6 per day in the previous periods with auto-recovery on.

The auto-recovery script was then re-enabled and the current streamer rate stabilized at about one in every 20 hours; in addition, the intensity of the current streamer on the GP was reduced with respect to the previous periods. As in the previous runs, the current streamers occurred always on the same GP (GP#6) with a small leakage current on the beam plug hose, which is close to GP#6.

This behavior is a further indication that the current streamers are in fact a slow discharge process of charged-up insulating materials present in the high-field region outside of the FC. The auto-recovery mode does not allow a full discharge, so the charging up is faster, and the streamer repetition rate is shorter.

The LAr purity loss experienced at the end of July, 2019, was accompanied by the complete disappearance of any HV instabilities. They gradually reappeared when the electron lifetime again exceeded 200 microseconds, and their intensity constantly increased as purity improved. This behavior replicated that observed after the initial filling, and supports the hypothesis that the HV instabilities are enhanced by the absence of electronegative impurities in high-purity LAr.

The effects of the current streamers on the FE electronic noise and the PD background rate have been investigated. We have not observed any effect of the current streamers on the FE electronics. On the other hand, recent analysis of the data collected by the PD system during active current

streamers has indicated a high single photon rate on the upper upstream part of the TPC. This is consistent with the activities recorded on GP#6, which is located exactly at this upper upstream area. The analysis of the photon detection data is in progress with the main goal of narrowing down the position of current streamers and the localization of it, if possible (figure 3.21) Visual inspection of this location when the detector is emptied will be required to further understand the HV instability issues.

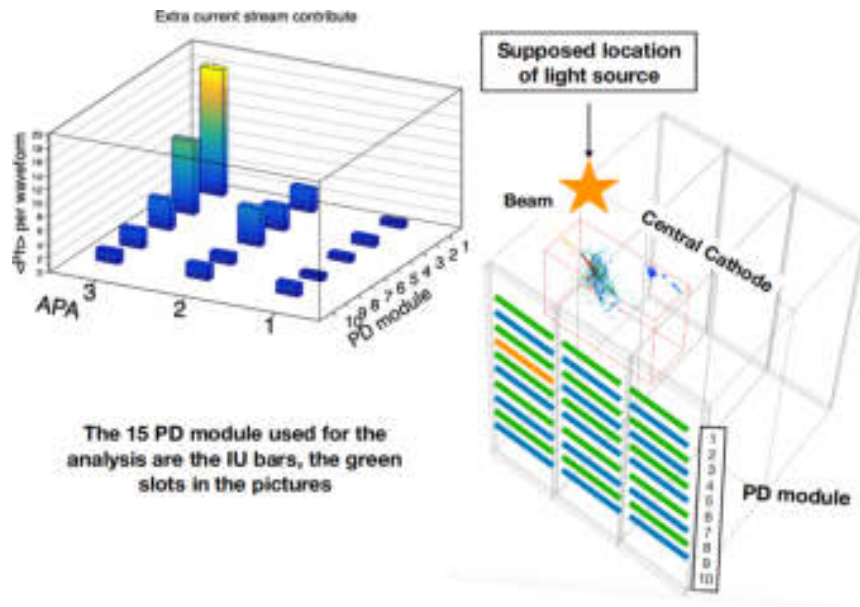


**Figure 3.21.** Preliminary analysis of the single photon activity rate in coincidence with a current streamer as a function of the position of the PDs in the APAs (beam right site). The rate clearly decreases proportionally to the distance of the PD from the supposed location of the current streamer. More refined analysis is ongoing (including the beam left PDs) to better locate the light source.

It is planned to continue monitoring the HV behavior, and in particular, before the end of the run, we plan to increase the HV above the nominal value to possibly enhance anomalous effects in the HV chain. Furthermore, the possible role of macroscopic impurities (metallic or insulating dust) circulation within the LAr is still to be understood, and specific running conditions will be implemented in ProtoDUNE-SP to better investigate this issue as well.

Although we do not yet have precise knowledge of the origin of the current streamers, it is certainly safe to state that, in a time scale of nearly one year, we did not observe any degradation of the HV system performance. On the contrary, the up-time has constantly improved (now it is above 99%), and the instability rate and intensity have decreased.

### 3.6.4 Lessons from ProtoDUNE

The ProtoDUNE-SP HV experience was, in general, very encouraging, having demonstrated an ability to operate the TPC with a drift field of 500 V/cm. However, throughout the run, the system experienced various instabilities, discussed above. Systematic study of these instabilities continues.

### 3.6.4.1 Design

The success of ProtoDUNE-SP validated the general design of the DUNE HV system, but various opportunities for improvement during its construction and operation appeared. In particular, we chose the following:

- adopt a “pot-style” filter resistor design (with input and output cables on the same end) to prevent leaks from causing interventions for refilling;
- raise the HV feedthrough cable insert to be above the cold insulation space, if space allows (to allow removing the cable while preventing moisture from entering and freezing on the walls, which could affect electrical contact);
- add toroid signals to the feedthrough; and
- improve stability by increasing the distance between the GPs and field-shaping profiles and eliminating direct paths for potential surface currents.

The instrumented GPs on the top and bottom FCs proved invaluable for collecting information during moments of instability. A dedicated DAQ read out the signals from the GP monitoring system, the beam plug current monitor, and the power supply at a rate of 20 kHz on a trigger provided useful information for diagnosing the HV behavior inside the TPC. This system was not operated continuously due to correspondingly large data disk storage requirements. Toroid signals from the HV filters were also helpful in localizing sources of instability, specifically for distinguishing issues on the warm side from issues inside the TPC.

### 3.6.4.2 Production, handling and quality control

The production and handling of HV components must be approached with great care to avoid scratching and potentially compromising the electrical components. Part production should be carried out to avoid introducing sharp edges wherever possible. The corners of the GP panels had to be smoothed after some buckling was introduced during the pressing process, and a number of support hinges and clevises had sharp features removed by polishing. The aluminum field-shaping profiles are particularly prone to scratches and must be packaged and handled so as to avoid direct contact with other profiles and materials. Kapton strips were used to separate the profiles from the FRP of the FC frames as they were being inserted to protect against scratching or removal of the profile coating. Any scratches found in the FRP beams were covered with epoxy to prevent fibers from escaping into the LAr.

QC tests were conducted on HV modules and individual components at every step: part procurement, production, integration, and installation. For example, checklist forms were completed for component parts of detector modules as production proceeded. Also, during the production process, documented procedures included QC steps with checklist forms. Printed copies of the checklists completed in the procurement and production stages were included as travelers in shipping crates. To ensure that nothing was compromised during transport, QC tests were repeated on individual components and assembled pieces after shipping. Resistance between steps on the voltage divider boards was measured and verified to be within specification both after their production at

LSU and after they were shipped to CERN. Once the voltage divider boards were mounted onto an assembled FC module, the resistance between adjacent profiles was measured to verify sound electrical connection. In a similar way, QC checks of connections between CPA modules and between CPA and FC modules were performed after installation.

QC tests on the HV components of ProtoDUNE-SP required many measurements to be made with several different test devices. Extrapolating these measurements to the scale of DUNE will require development of dedicated tools so that the QC process can be made more efficient and optimal at each step. For example, devices to measure the resistivity of CPA coated resistive panels and field shaping strips will be provided to each of the designated production factories. Also, designing a rig that can latch onto the FC modules in such a way to make contact with all electrodes and control their voltages independently would allow for an automated loop across all steps. Such dedicated equipment and automated procedures will be required en route to a full SP module.

### 3.6.4.3 Assembly and installation

The ProtoDUNE-SP experience allowed for a realistic estimation of the time involved to produce various HV components for an SP module. The time involved for ProtoDUNE-SP was approximately as follows:

- FC module assembly: 1.5 days/module with 2 workers,
- endwall FC module assembly: 1.5 days/module with 2 workers,
- CPA (2-panel) plane: 2 days/plane with 4 workers,
- CPA plane + FC integration: 1 day/assembly with 4 workers,
- endwall FC frame assembly: 7 days/module with 2 workers,
- endwall FC final assembly: 4 hours/wall with 4–6 workers.

These estimates include time needed to perform the required QC tests at each stage of the assembly and installation.

The ProtoDUNE-SP installation sequence had the beam-right drift volume deployed before the beam-left. As anticipated from calculation and testing, asymmetries in the weight distribution before the beam-left drift was deployed produced temporary misalignments that propagated throughout the entire detector until the final left drift deployment, which corrected them. The process of connecting individual endwall modules to build an endwall exposed another alignment issue. The first endwall was significantly bowed initially. A tool was built to adjust the angle between adjacent modules, which straightened out the wall. The tool was also used while connecting modules for the remaining three endwalls, and no significant bowing was observed.

### 3.6.5 Future R&D

The present HV system design derives closely from the one in operation in ProtoDUNE-SP. Operation of this detector in 2019 has allowed us to gain further confidence in depth concerning the long term stability and reliability of the HV system under nominal conditions. The present R&D program, which will not extend beyond early 2020, has the goal to further improve, if required, the reliability of the system. In the R&D program we plan to

- evaluate the charge and discharge behavior of the UHMWPE caps on the end of the profiles compared to metallic capped profiles. The goal is to check if the end caps contribute to HV instability.
- compare the high voltage stability of a new version of end wall profiles to the ProtoDUNE version. The new version bends the top and bottom of the end wall profiles 90 degrees towards the ends of the top or bottom profiles, reducing the gap between field cage components at the two detector module ends and lowering the E fields on the surfaces of the UHMWPE caps and profiles near the profile ends.
- evaluate resistive versus metallic caps. If the UHMWPE caps are problematic, find an alternative solution to maintain separated FC modules.
- study the surface-charging behavior of the FC insulation structures. Evaluation of general insulator performance for LArTPCs, including charge-up effects and geometry, remains an outstanding task. In this test, the goal is to find out if any geometrical feature or surface treatment can reduce HV instability.
- evaluate higher-resistivity Kapton films. The goal is to check the feasibility of increasing the surface resistivity of the cathode plane up to 1 G $\Omega$ /square. The task includes verifying the lamination quality on FR-4 sheet and production availability.
- perform further simulation of HVS discharge behavior. Although modeling other FC designs and DUNE itself will take considerable effort, understanding the source of instabilities or exposing any design weaknesses would be worthwhile.

### 3.7 Interfaces

The HVS has the largest surface area on the TPC and interfaces with many other systems. Table 3.5 summarizes the interfaces with other consortia, highlights the key elements, and provides the links to the existing interface documents.

The two most important mechanical interfaces are with the DSS and the APA. The entire weight of the CPAs, endwall FC and half the weight of the top and bottom FC are supported by rails provided by the DSS. The other half of the top and bottom FC weight is transferred to the APAs through latches mounted on the APAs. All CPAs and most of the FC modules are also transported along the DSS rails to their final positions. The DSS rails ultimately determine the final locations of the CPAs and FCs on the TPC.

Electrically, since the APAs are at the detector ground, all HVS field cage termination and fail-safe circuits are connected to the APAs. All cables used for the FC termination pass through the APA frame, to connect to the SHV cables provided by the CE through the CE signal flanges. The TPC electronics consortium also provides HVS the FC termination power supplies.

**Table 3.5.** HV system interface links.

| Interfacing System                                 | Description   | Linked Reference |
|--|---|------------------|
| DSS  | Support, positioning, and alignment of all CPA, FC modules inside the cryostat both warm and cold                             | DocDB 16766 [29] |
| APA  | FC support (top, bottom, and end wall) on APA frames; mounting of FC termination filter boards and FC fail-safe terminations; | DocDB 6673 [11]  |
| CE   | FC termination wire connectors on CE feedthrough flange, FC termination wires routed with CE cables                           | DocDB 6739 [30]  |
| PD system  | Mounting of PD calibration flash diffusers and routing of their fibers to CPAs; possible TPC coated reflector foil on CPAs.   | DocDB 6721 [31]  |
| facility   | Locations and specifications of the HV feedthrough ports; gas and LAr flow velocities and patterns.                           | DocDB 6985 [32]  |
| calibration  | FC openings for the calibration laser heads   | DocDB 7066 [33]  |
| cryogenic instrumentation and slow controls (CISC) | HV vs. LAr level interlock, sensor locations in high field regions, cold/warm camera coverage, HV signal monitoring, etc.     | DocDB 6787 [34]  |
| SDWF   | Storage buffer, inspections/tests, repackage for underground delivery   | DocDB 7039 [35]  |
| physics  | Requirements: range of operating drift field, uniformity of the drift field; supply detector geometry and E field map.        | DocDB 7093 [36]  |

### 3.8 Production and assembly

#### 3.8.1 Power supplies and feedthrough

We plan to buy commercial power supplies through, among other vendors, Heinzinger. The HV cable is commercially available.

The power supply is tested extensively along with the controls and monitoring software. Features to be included in the software are

- the ability to ramp, or change, the voltage, set the ramp rate, and pause the ramp. In previous installations, the ramp rate was typically between 60 V/s to 120 V/s.
- an input for a user-defined current limit. This parameter is the electric current (I) value at which the supply reduces the voltage output to stay below the current limit. The current-limiting is done in hardware.

- an input for a trip threshold. At this current reading, the program would reduce the voltage output through software. In previous experiments, the trip function in software would set the output to 0 kV.

Additionally, the software must record the current and voltage read-back values with a user-defined frequency, as well as any irregular current or voltage events.

The HV feedthrough and filters are custom devices. As for ProtoDUNE-SP, the feedthrough designs are made by collaborators and fabricated by an external company or major laboratory. Raw materials such as stainless steel, UHMWPE rods, and flanges are readily available and are machined to make a feedthrough. Similarly, the resistors, steel or aluminum, and insulator material for the filters are readily available. The feedthrough and filters require testing before being delivered to the SDWF.

### 3.8.2 Cathode plane assembly

The component parts of the CPA array will be mainly produced by commercial companies except for specific items that are more efficiently produced by university collaborators. Parts will be packaged into kits, each to contain the parts for a single CPA panel (three CPA units). The parts in each kit are

- manufactured FR-4 RP frames,
- carbon-impregnated Kapton-coated RPs and FSS,
- HV cable segments and wire jumpers making up the CPA HV bus and RP interconnects,
- resistor boards connecting the RPs to FSS (for raising the RP HV by 1.5 kV),
- machined brass tabs for connecting RPs, HV bus, and FSS, and
- top, bottom, and exterior edge profiles and associated connection hardware.

The kits are sent to the production factories, the locations of which will be determined later. The CPA construction unit for installation into the SP module at the SURF is a pair of CPA panels called a CPA plane. The production factories thus ship partially-assembled CPA panels to SURF where panel assembly is completed and two panels are paired in the underground cleanroom to form a CPA plane. During production, some storage (up to one month's installation rate) of CPA shipping crates can occur at the SDWF while waiting for movement into the SURF cleanroom. No unpacking of crates is needed at the SDWF; only visual inspection will be done to determine if any damage occurred during shipping.

The most basic element of the CPA is an RP mounted in a machined slot in the top, bottom and sides of FR-4 frames. There are three different RP types: an upper, which has as its top frame the CPA mounting bracket and top FC hinge, a middle, and a lower, which has as its bottom frame a bottom FC hinge. Pairs of RPs are bolted together and pinned to form CPA units of size 1.2 m × 4 m for shipment. Three types of pairings are constructed to make a full six-RP, 12 m tall CPA panel: (1) an upper and a middle, (2) two middle, and (3) a middle and a lower.

The order in the shipping crate from top to bottom is: middle-and-lower, middle-and-middle, and upper-and-middle. Two CPA panels are shipped together in one crate; they are paired at SURF



to form one CPA plane. The SP module requires 100 upper, 100 lower, and 400 middle RPs to make up the 100 CPA panels (50 CPA planes) of the TPC.

In addition to the frames and RPs, FSS are mounted on the exposed sides of the FR-4 frames, aluminum profiles are attached to the exterior edges of the upper and lower RPs, and cables are attached to the RPs to form segments of the HV bus.

The CPA units are assembled horizontally on a smooth, flat, highly stable table to ensure flatness and straightness of the entire panel before units are pinned together. There is one table per factory with up to three factories making CPAs.

Figure 3.22 shows a 6 m ProtoDUNE-SP CPA panel (rear) and a 12 m ProtoDUNE-SP CPA panel (foreground) at Ash River Laboratory in Minnesota, USA.



**Figure 3.22.** A 12 m DUNE-SP CPA mock-up panel (foreground) and a half-height 6 m ProtoDUNE-SP panel mock-up (rear) at Ash River, Minnesota.

### 3.8.3 Field cages

#### 3.8.3.1 Top and bottom field cages

Firms that specialize in the machining of fiberglass components for electrical applications will produce the FRP and FR-4 components of the top and bottom FCs, as was successfully done for ProtoDUNE-SP. All the machined edges except the small circular holes are to be coated with translucent epoxy. The stainless steel and aluminum components will be produced in university and commercial machine shops. University groups will likely fabricate the voltage divider boards and FC and CPA connection boards.

The FRP frame assembly process consists primarily of fastening together FRP I-beams with FRP threaded rods and hex nuts, and securing them with a limited and specified torque to avoid damage to the threads. Detailed views of this procedure are shown in figure 3.23.

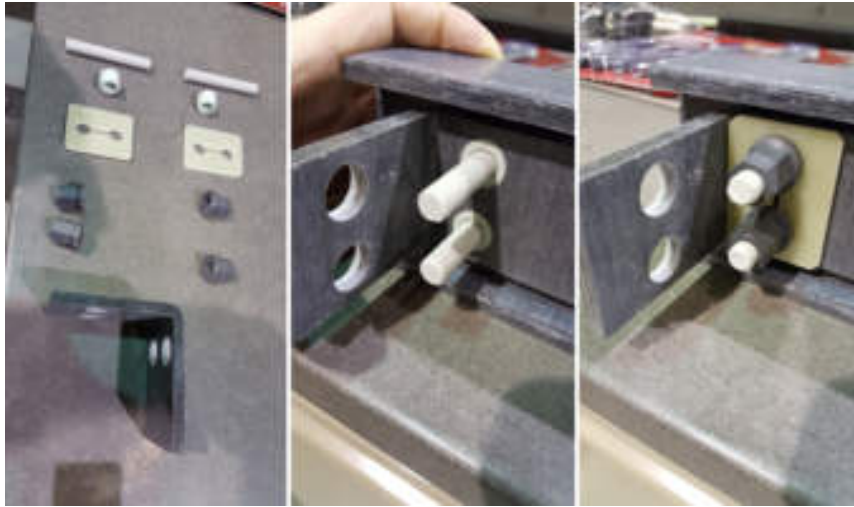


**Figure 3.23.** The figure shows the procedure for connecting the cross beams to the main I-beams for the top FC. Left: a display of the components of each connection, which (from top to bottom) are the threaded rods, the spacer tubes, washer plates, the hexagonal nuts, and an L-shaped FRP brace. An intermediate stage (middle) and final stage (right) of the assembly are also shown.

Prior to sliding each profile into the FRP frame, the holes are covered with Kapton tape to avoid damage to the profile coating. An end cap is attached to each profile using plastic rivets, and then the profiles are aligned against an alignment fixture running the length of the FC. After securing each profile to the frame, the tension in the mounting screws is adjusted to remove any angular deflection in the extended portion of the profile.

The GPs are attached to the 10 cm stand-off I-beam sections with threaded rods and a machined plate. The copper strips are connected to adjacent modules at the same locations. Care must be taken to avoid bending the corners of the GPs toward the profiles, particularly on the CPA side of the module.

### 3.8.3.2 Endwall field cages

For the endwall FCs, all FRP plates are commercially cut to shape by water jet, as are the cutouts in the FRP box beams. Holes that accommodate G10 bushings are reamed in a machine shop. FRP frames are pre-assembled to ensure proper alignment of all FRP parts and holes (the profiles are not inserted at this stage). The FRP modules are hung off of each other by means of interconnecting FRP plates to ensure accurate alignment.

Next, parts are labeled, and the frames are taken apart. All components are cleaned by pressure washing or ultrasonic bath. All cut FRP surfaces are then coated with polyurethane, which contains the same main ingredient as the FRP resin, allowing it to bond well to the FRP fibers. Final panels are constructed from cleaned and inspected parts. Since assembly requires access to both sides of a module, a dedicated assembly table has been manufactured that allows convenient module rotation.

Figure 3.24 shows a partially assembled endwall FC FRP frame on the assembly table. The FRP box beams are sandwiched between 1.27 cm (0.5 in) thick FRP panels that are held on one side by means of G10 bushings and rods with square nuts. On the other side M10 stainless steel bolts, which are clearly visible in figure 3.25, engage with large slip nuts that are inserted into the aluminum profiles. The profiles are pulled towards a 2.5 cm thick FRP plate located on the inside of the box beam.



**Figure 3.24.** Assembly table with partially assembled endwall FC module. Box beams, cross beams, and slots for mounting of aluminum profiles are visible.

Aluminum profiles are inserted into the cutouts of the box beams and attached with screws and stainless steel slip nuts to L-shaped FRP brackets that are mounted on the FRP box beams. Small changes in part sizes will help to simplify the assembly procedure with respect to the one used for ProtoDUNE-SP. Currently, we expect that pre-assembly of the FC endwall frames will no longer be required. The full modules will be assembled at the factory (LSU), and then complete endwall FC panels will be shipped to the SDWF.

### 3.8.4 Electrical interconnections

All electrical fasteners and wires used on the CPA arrays and FC are produced to specification by commercial vendors and packaged with the CPA or FC modules. As discussed in sections 3.8.2 and 3.8.3), this includes. e.g., the HV cable segments, wire jumpers, and machined brass tabs.

University shops will produce and test circuit boards for HV interconnections according to the same design used for ProtoDUNE-SP. The FC voltage dividers were produced for ProtoDUNE-SP at LSU, and the boards for CPA frame bias and CPA-FC connections were produced at Kansas State University (KSU). Both institutions have created custom test apparatuses for verifying proper



**Figure 3.25.** Top and center endwall FC module frames hanging.

operation of the boards at full voltage and over-voltage conditions, keeping the boards free of solder flux and flux-remover. These institutions may scale up production and testing by the required order of magnitude for the SP module or share this work with other institutions, whichever best meets the needs of the project.

### **3.8.5 Production safety**

Production of the FC panels and resistor-divider boards will involve collaboration technical, scientific, and student labor and does not present unusual industrial hazards. The HVS consortium will work closely with each production site to ensure that procedures meet both Fermilab and institutional requirements for safe procedures, PPE, environmental protection, trained materials handling, and training. The vast majority of production part fabrication will be carried out commercially and shipping will be contracted through approved commercial shipping companies. Prior to approving

a site as a production venue, it will be visited and reviewed by an external safety panel to ensure best practices are in place and maintained.

Testing of the HV feedthrough will be done in a closed cryostat to avoid exposure to high voltage and to assure the nominal voltage is functional. The power supply is grounded to the cryostat as a further safety measure. Tests for the ProtoDUNE-SP HV feedthrough were done at CERN after a safety electrical and cryogenic review mainly focusing on the grounding of the whole test stand (power supply, cable, and cryostat where the feedthrough was tested) as well as interlocks. A safety document (PPSPS) was created, reviewed, and approved for this test. Similar testing and documentation will be done for the SP module.

### 3.9 Quality control, transport, and installation

The HVS consortium has developed a comprehensive quality control (QC) plan for the production, shipping, and installation of the SP module HV components. It is based partly on QC procedures developed and implemented on ProtoDUNE-SP and on the NOvA experiment's successful use of barcode tagging for identifying and tracking detector components. Inventory tagging and tracking each component is crucial. Documentation in the form of printed checklists is maintained [37].

Travelers have been replaced by a system of tags with bar codes attached to the units, which key to electronic QC data. The tags will be large and brightly colored enough to be seen from both ends of the cryostat. A particularly suitable choice is to use bright yellow cattle tags, plastic tags of about 10–12 square inches ( $\sim 70 \text{ cm}^2$ ) on which a unique QR<sup>6</sup> or bar code can be printed; they can be purchased very inexpensively in quantities of hundreds or thousands.

Scanned tags are removed after completion of electronic checklist forms linked to the tag's bar code. At the end of TPC installation, all QC data for components at a particular location in the detector are stored electronically and linked to that location.

#### 3.9.1 Quality control

Power supply devices used in an SP module will be tested before installation. Output voltages and currents will be checked on a known load.

The feedthrough and filters will be tested at the same time, with the selected power supply. The feedthrough must be verified to hold the required voltage in TPC-quality LAr ( $\tau \geq 1.6 \text{ ms}$ ) for several days. The ground tube submersion and E field environment of the test setup will be comparable to the real FC setup or more challenging (e.g., the test liquid level can be lower than that in the SP module but not higher). Additionally, the feedthrough must be leak-tight to satisfy cryogenics requirements.

The QC tests concerning the voltage divider boards are as follows: all individual resistors and varistors are submitted to a warm and cold (87 K) current-voltage measurement. This forms the basis for selecting components that meet specifications: all electrical components must pass visual inspection for mechanical damage; all measurement values (resistance, clamping voltage) must be within  $2\sigma$  of the mean for entire sample both in warm and cold tests.

---

<sup>6</sup>Quick Response Code, The QR<sup>TM</sup> code system was invented in 1994 by the Japanese company Denso Wave. <https://www.qrcode.com/en/index.html>.

The QC process for mechanical components starts at the production factories by attaching a cattle tag with a unique code to each production element. A file linked to each code contains the individual measurements and properties contained in the QC checklists for that element. The following is an example of how this system will be implemented for the CPA components:

1. During assembly, QC checklists are filled out electronically using a smart phone or tablet. Once a CPA unit is completely assembled and all checklists are complete, a coded temporary cattle tag is attached and scanned, linking the checklist information to the code on the tag. (The CPA unit's individual parts are not tagged separately.)
2. A shipping crate will contain six CPA units, each with its removable coded tag, plus any included hardware packages, each with a coded sticker.
3. A coded label on the shipping crate (paper sticker) will identify the contents of the crate (six codes + codes of hardware packages). The code on the label is used only for shipping purposes and for inventory purposes.
4. In the SURF cleanroom, the first CPA panel is assembled. A coded tag is attached to the CPA panel and scanned. Then the three individual CPA unit tags are scanned and removed, linking them to the CPA panel code.
5. The same procedure is followed for the second CPA panel from the crate. Each CPA panel now has a single tag attached to it.
6. The CPA panels are then combined into a CPA plane, and a single coded tag is attached to the CPA plane and scanned. The two individual CPA panel tags are then scanned, linking their codes to the that of the CPA plane.
7. Top and bottom FC modules are attached to both sides of the CPA plane, and a single coded tag is placed on this CPA/FC assembly identifying the codes of each of the four FC modules and the code of the CPA planes; these five tags are removed after scanning.
8. When moving the panel into the cryostat the code of the position tag on the DSS is scanned as well as the tag on the CPA/FC assembly, and then both tags are removed.

At this point, a sequence of linked codes associated with QC checklists identify which CPA and FC modules are mounted in which DSS positions, and no tagging material remains in the cryostat. A similar sequence is anticipated for the production of the top and bottom FC units up to step 6; the endwalls are done separately but similarly. At the completion of installation in the cryostat and before top and bottom FC deployment, visual inspection will confirm the absence of any tags.

### **3.9.2 Transport and handling**

The HVS consortium has studied options for transportation from HVS production sites to the SDWF and packaging of the shipped elements. We found that using reusable underground crates and returning them to the factories when empty is less expensive than using inexpensive, disposable crates for shipment from the factories to the SDWF, even with the extra shipment costs.

We have identified a vendor that produces honeycombed PVC sheets of varying thicknesses that can be formed into crates. These can be loaded at the production sites, shipped to the SDWF, and sent underground at SURF. We will require 50 shipments of crates containing two CPA panels each to complete the SP module. The reusable underground crate scheme requires only 20 crates to make the 50 shipments. Similar reductions are obtained for the top and bottom FC modules.

Crates would be available at each factory at the start of production. As production proceeds, individual assembly units are bagged and sealed inside them. When a full shipment of crates is ready at a factory, crates are sent by flatbed truck from the factory to the SDWF. The full crates are stored at the SDWF until they can be received at SURF. Some components may require QC and/or minor assembly procedures to be done at the SDWF before shipping to SURF.

At SURF, the crates are lowered into the staging area outside the cleanroom where they are unpacked. The assembly units are removed from their bags and taken into the cleanroom for installation. Only cleaned assembly units are allowed into the cleanroom; the crate is restricted to the staging area only. The empty crate is returned to the SDWF and then sent back to a production factory for reloading.

### 3.9.3 Safety during handling

In the current installation scenario, no assembly activities are foreseen at the SDWF site for any components of the HV system. Only visual inspection of the HVS modules crate condition will be performed to verify the integrity after shipping. No disruption in installation should occur in the event of shipping damage since there is a one-month storage period at the SDWF and two week's installation storage underground at SURF. The HVS consortium will coordinate procedures for underground handling with technical coordination.

A detailed Gantt chart on the production and installation schedule for the HVS of the first SP module is shown in figure 3.26.

The installation activities are described in chapter 9.

## 3.10 Organization and management

### 3.10.1 Institutional responsibilities

The HVS consortium includes all the institutions that have participated in the design, construction, and assembly of the HV systems for both ProtoDUNE-SP and ProtoDUNE-DP. They are listed in table 3.6. The consortium currently comprises several USA institutions and CERN, the only non-USA participant.

As it has been for ProtoDUNE, CERN is heavily committed to a significant role in the FD in terms of funding, personnel, and the provision of infrastructure for R&D and detector optimization. Moreover, CERN will be responsible for a significant fraction of subsystem deliverables; as such CERN is actively in search of additional European institutions to attract into the consortium.

At present, in the HV current consortium organization, each institution is naturally assuming the same responsibilities that it assumed for ProtoDUNE-SP and ProtoDUNE-DP. The consortium organizational structure includes a scientific lead (from CERN), a technical lead (from BNL), and an HVS design and integration lead (from Argonne National Laboratory (ANL)).

The successful experience gained with the ProtoDUNE-SP detector has demonstrated that the present HVS consortium organization and the number of institutions are appropriate for the construction of the HV system of the SP module. Funding and the predominant participation of USA institutions are presently open issues that would benefit from more international participation.

The consortium is organized into working groups (“WG” below) addressing the design and R&D phases of development, and the hardware production and installation.

- WG1: design optimization for SP module and DP module; assembly, system integration, detector simulation, physics requirements for monitoring and calibrations;
- WG2: r&D activities, R&D facilities;
- WG3: SP-CPA: procurement of resistive panels, frame strips, electrical connections of planes; assembly, QC at all stages, and shipment of these parts;
- WG4: DP cathode and GP: material procurement; construction, assembly, shipment to SDWF QA, QC;
- WG5: modules: SP-top/bottom-FC module, SP-endwall modules, DP-FC modules: procurement of mechanical and electrical components, assembly and shipping to SDWF; and
- WG6: HV supply and filtering, HV power supply and cable procurement, R&D tests, filtering and receptacle design and tests.

Taking advantage of identified synergies, some activities of the SP and DP working groups are merged: HV feedthrough, voltage dividers, aluminum profiles, FRP beams, and assembly infrastructure.

**Table 3.6.** Institutions participating in the HVS consortium.

| Institution                              | Country     |
|--|-------------|
| CERN                                     | Switzerland |
| Argonne National Lab                     | USA         |
| Brookhaven National Lab                  | USA         |
| University of California Berkeley / LBNL | USA         |
| University of California Davis           | USA         |
| Fermilab                                 | USA         |
| University of Houston                    | USA         |
| Kansas State University                  | USA         |
| Louisiana State University               | USA         |
| SUNY Stony Brook                         | USA         |
| University of Texas Arlington            | USA         |
| Virginia Tech                            | USA         |
| College of William and Mary              | USA         |



3.10.2 Risks

Table 3.7 presents a summary of the risk items identified for the HV system of the FD SP module.

**Table 3.7:** HV risks (P=probability, C=cost, S=schedule) The risk probability, after taking into account the planned mitigation activities, is ranked as L (low < 10 %), M (medium 10 % to 25 %), or H (high > 25 %). The cost and schedule impacts are ranked as L (cost increase < 5 %, schedule delay < 2 months), M (5 % to 25 % and 2–6 months, respectively) and H (> 20 % and > 2 months, respectively).

| ID          | Risk   | Mitigation   | P | C | S |
|-------------|--|--|---|---|---|
| RT-SP-HV-01 | Open circuit on the field cage divider chain                               | Component selection and cold tests. Varistor protection.   | L | L | L |
| RT-SP-HV-02 | Damage to the resistive Kapton film on CPA                                 | Careful visual inspection of panel surfaces. Replace panel if scratches are deep and long          | L | L | L |
| RT-SP-HV-03 | Sole source for Kapton resistive surface; and may go out of production     | Another potential source of resistive Kapton identified. Possible early purchase if single source. | M | L | L |
| RT-SP-HV-04 | Detector components are damaged during shipment to the far site            | Spare parts at LW. FC/CPA modules can be swapped and replaced from factories in a few days.        | L | L | L |
| RT-SP-HV-05 | Damages (scratches, bending) to aluminum profiles of Field Cage modules    | Require sufficient spare profiles for substitution. Alternate: local coating with epoxy resin.     | L | L | L |
| RT-SP-HV-06 | Electric field uniformity is not adequate for muon momentum reconstruction | Redundant components; rigorous screening. Structure based on CFD. Calibration can map E-field.     | L | L | L |
| RT-SP-HV-07 | Electric field is below goal during stable operations                      | Improve the protoDUNE SP HVS design to reduce surface E-field and eliminate exterior insulators.   | M | L | L |
| RT-SP-HV-08 | Damage to CE in event of discharge   | HVS was designed to reduce discharge to a safe level. Higher resistivity cathode could optimize.   | L | L | L |
| RT-SP-HV-09 | Free hanging frames can swing in the fluid flow                            | Designed for flow using fluid model; Deformation can be calibrated by lasers or cosmic rays.       | L | L | L |
| RT-SP-HV-10 | FRP/ Polyethene/ laminated Kapton component lifetime is less than expected | Positive experience in other detectors. Gain experience with LAr TPC's; exchangeable feedthrough.  | L | L | L |
| RT-SP-HV-11 | International funding level for SP HVS too low                             | Cost reduction through design optimization. Effort to increase international collaboration.        | M | M | M |
| RT-SP-HV-12 | Underground installation is more labor intensive or slower than expected   | SWF contingency, full-scale trial before installation. Estimates based on ProtoDUNE experience.    | L | L | L |

The first five risks refer to the construction and operation phases; risks 6 through 12 apply to the installation and/or detector operation phase.

2020 JINST 15 T08010

Most of the cited risks have already been addressed during the construction, commissioning, and operation of ProtoDUNE-SP. None have caused significant problems, with the partial exception of risk 9. Risk 9 requires an accurate analysis of collected muon data (this activity is in progress), and the disentangling of space charge effects.

Given the much larger detector scale and the more complex underground installation environment, the listed risks still apply to the detector modules. However, the positive experience gained with ProtoDUNE justifies the low risk probabilities assigned to most of the items. To better justify these statements, brief explanations are given below, together with the identified mitigation actions.

Risk 1: an open circuit on the FC could occur if a resistor in the conventional voltage dividers were to fail in the open condition, which could result in HV discharges across the open circuit gap. Mitigation: perform stringent component selection and cryogenic testing. Use parallel resistor chains to provide redundancy. Varistors, capable of withstanding several thousand amperes of current impulses, have been added in parallel with the resistor chains to protect them from large current surges. Check resistances several times during FC fabrication and assembly phases, including once after the FC deployment.

Risk 2: limited, local scratches could occur from accidental contacts during module assembly or installation. No mitigation is required if a scratch is limited in size. For larger scratches that can induce delamination, the mitigation is to replace the panel with a spare.

Risk 3: about 12 rolls of resistive Kapton are needed (4 ft wide, 300 m per roll) for the CPA panels of one SP module. The cost is 20k\$ per roll from the only vendor available up to now. Mitigation: recently another source of resistive Kapton has become available and is being investigated. An early purchase is also under consideration in case of a single source condition.

Risk 4: poor shipping techniques could cause damage to delicate components (e.g., broken CPA panels, bent or heavily scratched aluminum profiles) that would cause the modules to fail QC tests. If significant repairs to detector components are needed, they may require replacements. Mitigation: plan for an adequate number of spare elements and implement a documented QA program for shipment packing with detailed review of shipping procedures, shipping containers, and testing in crates after arrival.

Risk 5: the surface of the aluminum profiles is very delicate and deep scratches could locally increase the E field to close to the critical field of 30 kV/cm. The surface can be damaged during transport or manipulation in the assembly area. In case of significant damage, it cannot be repaired due to its conductive coating. For mitigation, ensure the availability of sufficient spare profiles on-site to allow last-minute substitutions. Alternatively, use a local coating with epoxy resin.

Risk 6: unexpected changes in FC resistor values, cathode/FC non-planarity or movement, and surface or space charge buildup can distort the E field. As a consequence, the momentum of non-contained muons, measured by estimating the multiple scattering rate for the observed track segments, could be incorrectly estimated, thereby degrading the momentum resolution for non-contained muons.  $\nu_\mu$  disappearance analyses and three-flavor fits could be affected leading to feed-down of high-energy neutrino backgrounds to low-energy reconstructed categories. Mitigation: consider addition of a laser calibration if calibration with cosmic crossing muons is not sufficient.

Risk 7: in ProtoDUNE, HV instabilities appeared as current streams occurring at intervals of several hours and localized on a specific FC module. These required a several-minute ramp-down of the HV from the nominal  $-180$  kV to a lower value, typically  $-140$  kV; see section 3.6.

Investigations are underway to characterize and mitigate this risk. Recently, understanding of this risk has significantly progressed thanks to the long-term operation of ProtoDUNE-SP in 2019 while exposed only to cosmic rays. There are strong hints that the instabilities are due to charging-up processes on insulators. In addition, the current streamers are confirmed to have been localized mainly on one GP (of 12). No degradation of the detector performance due to HV instabilities has been observed. Moreover, these instabilities appear to decrease gradually in rate and intensity. At present, the detector down-time due to these instabilities is less than 1%.

ProtoDUNE long-term operation is also indicating that LAr purity does not play a significant role in the onset of the HV instability (for free electron lifetime above  $\sim 1$  ms). The impact of the HV instabilities on APA/CE and PDs is also under investigation and at the moment appears to be negligible.

The mitigation for risk 7 involves improvement at the design level to increase as much as possible the distance between the FC and GPs and to avoid high-field regions by smoothing all electrodes exposed to HV. ProtoDUNE-DP, with a comparable design, will help determine the validity of these improvements.

Risk 8: a sudden discharge on the HV system would inject charge to the FE ASICs, overwhelming the protection circuits and causing permanent damage. Mitigation: key aspects of the HVS design were aimed at reducing the charge injection to a safe level for the CE, such as segmenting the FC and making the cathode planes resistive. We are still searching for higher-resistivity material on the cathode to increase the safety factor.

Risk 9: each cathode is made of lightweight, non-porous material with an area of  $58\text{ m} \times 12\text{ m}$  that could move under the convective flow of the LAr. Mitigation: the CPA structure is designed to withstand pressure from LAr flow based on fluid model predictions. Static deformation can be calibrated by lasers or cosmic rays.

Risk 10: aging of insulator components in LAr could pose a problem, but experience in ATLAS (Kapton & PCB, 20+ years), ICARUS (G10, feedthrough 4+ years; feedthrough exchangeable) is trending favorably. Mitigation: Continue to gain experience with LArTPCs. Make feedthrough exchangeable.

Risk 11: current costing suggests that international funding could be insufficient. Mitigation: implement cost reduction through design optimization and scaling. Make efforts to include more international institutions.

Risk 12: underground installation is more labor-intensive or slower than expected. Mitigation: add labor contingency. Carry out full-scale installation trials at the Ash River site prior to installation. The estimates are based on ProtoDUNE experience. With the present knowledge, the HV system is not on the critical path for installation.

### 3.10.3 High-level schedule

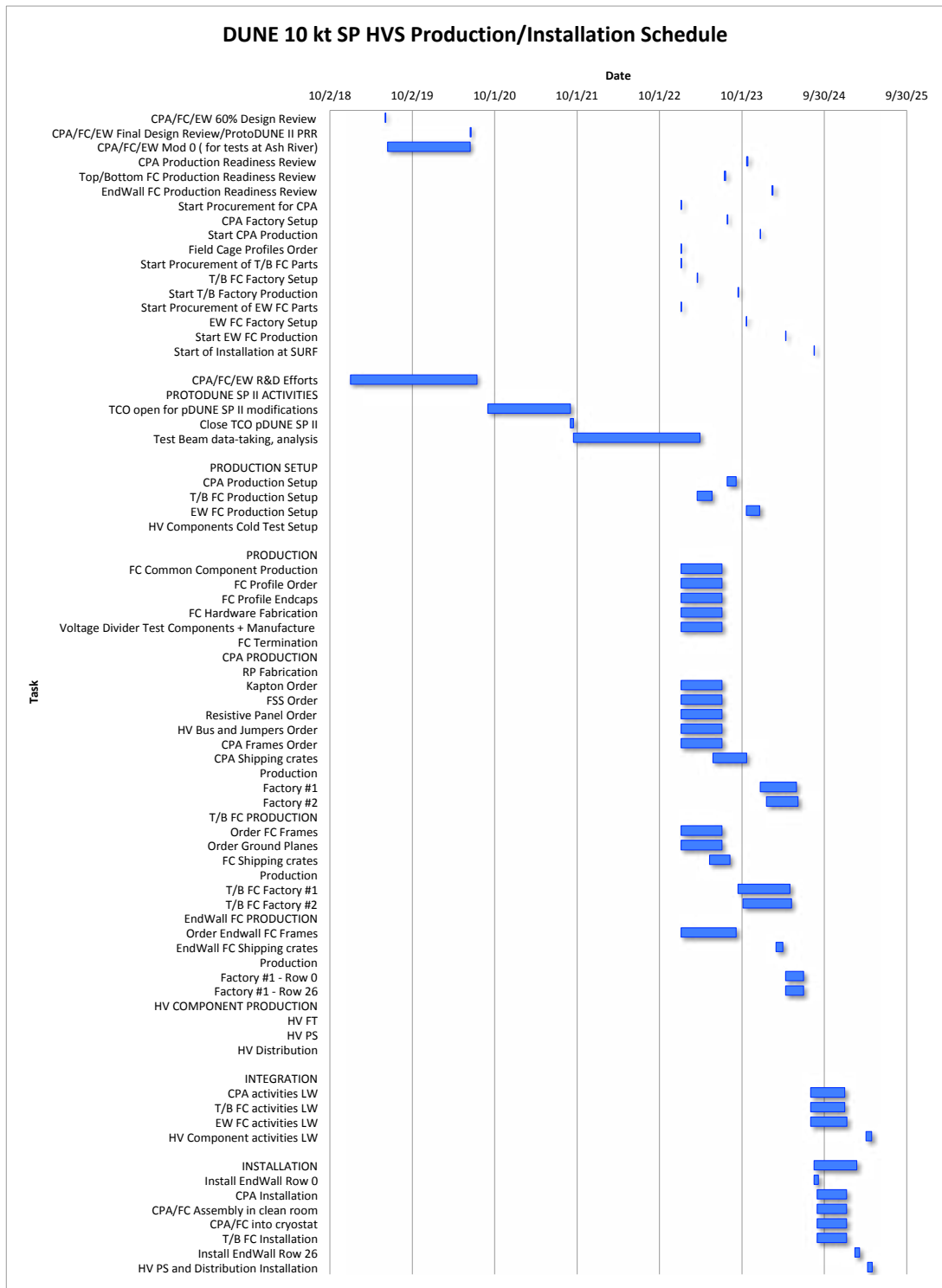
Table 3.8 lists the most high-level milestones for the design, testing, production, and installation of the SP module HVS. Dates in this tentative schedule are based on the assumed start of installation of the first SP module at SURF. The dates for the HVS production of a second SP module are included as a reference.

The production scenario for the schedule presented in table 3.8 assumes two factory sites for the CPA construction, two for the top/bottom FC modules and one for endwall FC modules. Given

the present starting date for the first SP module installation, this assumption is fully compatible with the time available after the operation of the ProtoDUNE-2 prototype. A more detailed schedule for production and installation of the first SP module is found in figure 3.26.

**Table 3.8.** High level Milestones and Schedule for the production of the HVS of the SP module.

| Milestone  | Date (Month YYYY)     |
|--|-----------------------|
| Technology Decision                                    |                       |
| CPA/FC/Endwall 60% Design Review                       | June 2019             |
| CPA/FC/Endwall Mod 0 (for tests at Ash River)          | June 2019 – June 2020 |
| Final Design Review                                    | June 2020             |
| Start of module 0 component production for ProtoDUNE-2 | June 2020             |
| End of module 0 component production for ProtoDUNE-2   | March 2021            |
| Start of ProtoDUNE-2 installation                      | March 2021            |
| Start of ProtoDUNE-2 installation                      | March 2022            |
| South Dakota Logistics Warehouse available             | April 2022            |
| Beneficial occupancy of cavern 1 and CUC               | October 2022          |
| CUC counting room accessible                           | April 2023            |
| Top/Bottom FC production readiness review              | July 2023             |
| Start of Top/Bottom FC production                      | September 2023        |
| CPA production readiness review                        | October 2023          |
| Start of CPA production                                | December 2023         |
| Top of detector module #1 cryostat accessible          | January 2024          |
| Endwall FC production readiness review                 | February 2024         |
| Start of Endwall FC production                         | April 2024            |
| End of CPA production Detector #1                      | August 2024           |
| End of Top/Bottom FC production Detector #1            | August 2024           |
| End of Endwall FC production Detector #1               | August 2024           |
| Start of detector module #1 TPC installation           | August 2024           |
| Start of detector module #1 TPC installation           | August 2024           |
| Top of detector module #2 accessible                   | January 2025          |
| End of detector module #1 TPC installation             | May 2025              |
| Start of detector module #2 TPC installation           | August 2025           |
| End of CPA production Detector #2                      | September 2025        |
| End of Top/Bottom FC production Detector #2            | October 2025          |
| End of Endwall FC production Detector #2               | January 2026          |
| End of detector module #2 TPC installation             | May 2026              |



2020 JINST 15 T08010

**Figure 3.26.** Gantt chart providing a detailed view of the production and installation schedule for the HVS for the first SP module.

### 3.11 Appendix: alternatives

#### 3.11.1 Optical reflectors on CPA

Since the PDs in the current TPC design are installed only on the APA side of the drift volume and have low coverage, their responses to ionization inside the TPC are highly dependent on drift distance and severely biased toward the APA. In order to improve the uniformity of response along the drift direction, the PD consortium has proposed adding reflector foils coated with WLS to convert the UV photons arriving at the cathode into visible photons and bounce them back to the PDs inside the APAs. Simulations have shown that addition of the reflectors significantly improves the uniformity of response.

Implementing this concept, however, could dramatically alter the current CPA characteristics and design. The HVS consortium has developed several concepts to accommodate the reflectors with minimal change to the CPA design. The main issue is the conductivity of the reflector foil versus the highly resistive nature of the CPA. To improve the light output, it would be best to cover as much of the cathode surfaces as possible, but large area coverage with conductive, (e.g., aluminum-coated) reflectors could short-circuit the resistive cathode and render it ineffective in slowing down the energy transfer during a potential HV breakdown. On the other hand, reflector foils made of insulating material would intercept the ionization charges drifting toward the cathode and become charged. This would alter the drift field uniformity and, worst yet, could result in random breakdown through the foil.

A design concept that is fairly simple to implement is depicted in figure 3.27. A 3M Vikuiti<sup>7</sup> reflector foil or equivalent is laminated onto a thin FR-4 backing sheet to maintain thermal expansion compatibility with the resistive CPA panel, which also has an FR-4 core. The reflector foil assembly is perforated at regular intervals to allow collection of electrons through the holes to the RP surface, minimizing the voltage build-up from charging of the non-perforated surfaces. Several such foil assemblies are then tiled onto the existing RPs with screws.

In order to advance the CPA design while providing the option of adding the reflector foils at a later time, the HVS consortium will design a hole pattern on the RPs that could be used for mounting of reflector foils or panels, or left unused without negative consequences. In the meantime, HVS and PD consortia are conducting joint R&D to evaluate a few design concepts and material choices.

---

<sup>7</sup>Vikuiti™ is a light enhancement film produced by the 3M Company, <http://multimedia.3m.com/mws/media/419882O/vikuititm-rear-projection-displays-brochure>.

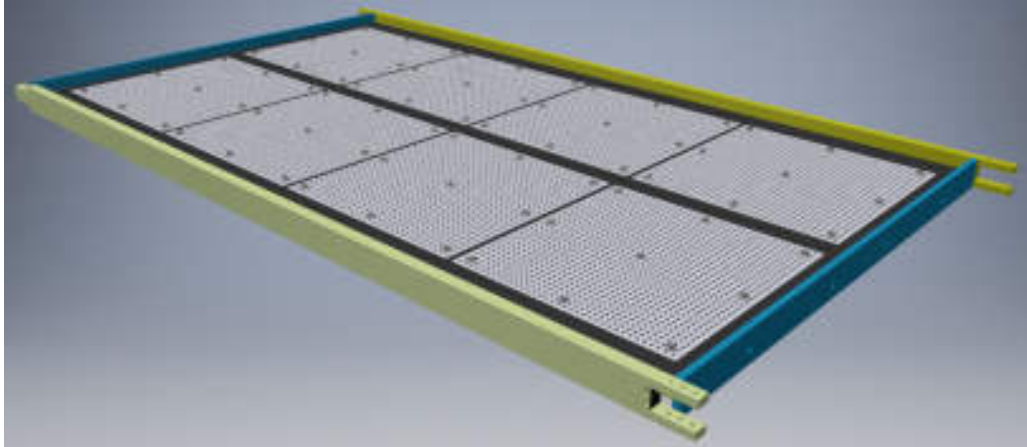


**Figure 3.27.** A concept to attach reflector foils to a CPA panel. (Credit: BNL)

### 3.11.2 Calibration laser penetrations

The calibration consortium is developing requirements for calibrating the E field. One existing technique is to use UV laser beams to ionize the LAr and generate straight tracks along known trajectories. Because the FC surrounds the TPC active volume, we can either shoot through the gaps between the FC profiles (as in MicroBooNE) or make openings in the FC for the laser heads to pass through (as in SBND). Figure 3.28 shows the design of a corner of the SBND TPC with a FC opening and a calibration laser head through the opening. Implementing such openings is straightforward if the openings are at the FC module boundaries. Doing so through the interior surface of a FC panel is more complicated but still simpler than the beam plug we designed for ProtoDUNE-SP. There will be some minor drift field distortion around the openings. Preliminary FEA studies have shown the field distortion to be negligible.

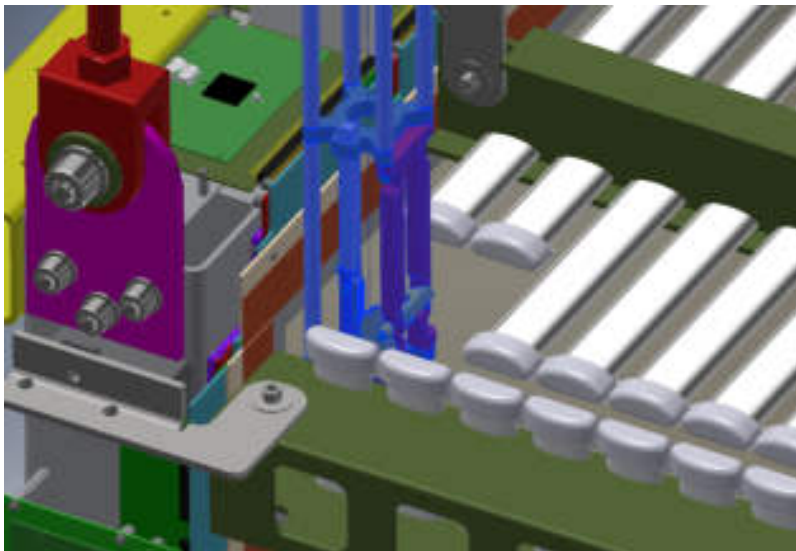


**Figure 3.28.** SBND field cage opening to allow a calibration laser head to pass through. (Credit: BNL)

## Chapter 4

# TPC electronics

### 4.1 System overview

The TPC electronics encompass the hardware systems necessary to amplify, digitize, and transmit the TPC ionization charge signals out of a DUNE SP LArTPC. This includes the cryogenic FE electronics (amplifiers, digitizers, digital controllers), power and data cabling and their cryostat feedthroughs, external (non-cryogenic) digital control electronics and power supplies, in addition to the system providing the bias voltage to the anode plane assemblies. The TPC electronics as presented here does not include the electronics associated with the detection and recording of LAr scintillation photons, nor the DAQ computing systems needed to capture and record these data.

The main difference between the DUNE SP detector module and previous experiments or prototypes using LAr technology is that for the first time all the signal processing for the readout of the wires of the APAs takes place inside the LAr, in boards that are directly mounted on the APA. This approach to the TPC readout was tested for the first time in the DUNE 35 ton prototype, and extensively tested in the ProtoDUNE-SP prototype. It has also been adopted by the SBND experiment. The TPC FE readout components immersed in the LAr are also referred to as the CE.

The FE electronics are mounted inside the LAr to exploit the fact that charge carrier mobility in silicon is higher, and thermal fluctuations are lower, at LAr temperature than at room temperature. For CMOS electronics, this results in substantially higher gain and lower noise at LAr temperature than at room temperature [38]. Mounting the FE electronics on the APA frames also minimizes the input capacitance, which further contributes to the noise reduction. Furthermore, placing the digitizing and multiplexing electronics inside the cryostat reduces the total number of penetrations into the cryostat and minimizes the number of cables coming out of it.

As the full TPC electronics chain for the SP module includes many components on the warm side of the cryostat as well, the DUNE consortium designated to develop this system is formally called the DUNE SP TPC electronics consortium.

This overview section starts with a review of the considerations that have led to the proposed design for the DUNE SP detector, then discusses how the detector requirements follow from the physics goals of the experiment. The reader will find a detailed description of all the TPC electronics detector components in section 4.2, including a discussion of how the lessons learned from the construction, integration, installation and commissioning of ProtoDUNE-SP have informed the



design of the DUNE SP module and how the early data from ProtoDUNE-SP validate this design. The description of the detector design is then followed by discussions of the QA program and the plans for production and assembly, and for integration, installation and commissioning, in sections 4.3–4.5. Section 4.6 discusses the interfaces with detector components provided by other consortia, with technical coordination, and with the physics group. Sections 4.7–4.9 conclude the chapter with plans for addressing safety issues and risks during the construction, installation, and operation of the detector, and an outline of the organization of the TPC electronics consortium, with a timeline for the detector module construction and an estimate of the resources required.

### 4.1.1 Introduction

In the DUNE SP module a MIP deposits on average between  $20\text{ ke}^-$  and  $30\text{ ke}^-$  on each collection wire, assuming a drift E field of  $500\text{ V/cm}$  and an electron lifetime of  $6\text{ ms}$ , as discussed in chapter 1, and assuming full transparency during the electron transport through the grid plane of the APA and its two planes of induction wires, as discussed in chapter 2. The larger of the two numbers is for MIPs close to the anode plane, and the smaller takes into account the electron capture by electronegative impurities during the electron drift for tracks close to the cathode plane.

The DUNE SP TPC is a unit-gain device where the electrical signal is produced by the drift of the charges near the wires, in contrast to signal production in gaseous wire chambers, where the E field is strong enough to provide additional ionization and signal multiplication. The signal induced in the DUNE SP module wires is bipolar on the induction wires, negative when the electrons drift toward the wires, and positive when they drift away from the wires. On the collection wires signals are unipolar (negative). The signal duration is of the order of microseconds, and tends to be narrower for the collection plane due to the enhancement of the weighting field for the collection wires. Due to the lack of amplification of electrons inside LAr, low noise is essential for the CE to reliably extract the ionization electron signal from both the collection and induction wire planes.

The reduction in noise level obtained with the CE greatly extends the reach of the DUNE physics program. It allows measurement of smaller charge deposits, which mitigates the risks of inability to reach the desired drift field or a lower electron lifetime than desired due to electronegative impurities. For example, given an electron lifetime of  $3\text{ ms}$  and a drift E field of  $0.25\text{ kV/cm}$ , the charge deposited in the collection wires from a MIP close to the cathode plane is reduced to  $10\text{ ke}^-$ . The exact minimal S/N required for pattern recognition depends on the tracking algorithms and the offline signal processing. We use the minimal requirement of a total equivalent noise charge (ENC) less than  $1000\text{ e}^-$ , consistent with a S/N of at least 10 on the collection wires, even in the pessimistic case where the electron lifetime and the E field just meet the required design values discussed in chapter 3. Considering the difference in signal amplitudes between collection and induction wires and the bipolar shape of the signal on the latter, this requirement corresponds to a S/N of at least 5 on the induction wires. This asymmetric requirement for the minimal S/N on the collection and induction wires was first adopted by the SBND experiment [39].

The goal is to keep the total noise level as low as possible. For example, an increase in the S/N above 15 allows the observation of MeV-scale photons, as recently demonstrated by ArgoNeuT [40]. This enables reconstruction of both photons released during de-excitation of the nucleus and part of the energy transferred to final-state neutrons. Low noise is also crucial for the baseline oscillation analysis described in Volume II, DUNE physics, chapter 5. The event classification is based on a

convolutional visual network (CVN) that uses as inputs three images of the neutrino interactions, one for each of the three readout views, using the reconstructed hits on the individual wire planes. This approach relies on low noise levels. Decreasing the noise level also increases the reach of low-energy physics measurements like those associated with stellar core-collapse SNB. Finally, a low noise level opens up the possibility of using  $^{39}\text{Ar}$  beta decays to calibrate the DUNE SP module [41]. Instead of zero suppression, the DUNE DAQ system uses lossless data compression, as discussed in section 7.2.1, that becomes more efficient as the noise level is reduced. Therefore, the noise level also affects the bandwidth requirements for the DAQ system, discussed in chapter 7; these bandwidth requirements can be a limiting factor for low-energy physics signals, particularly those of astrophysical origin.

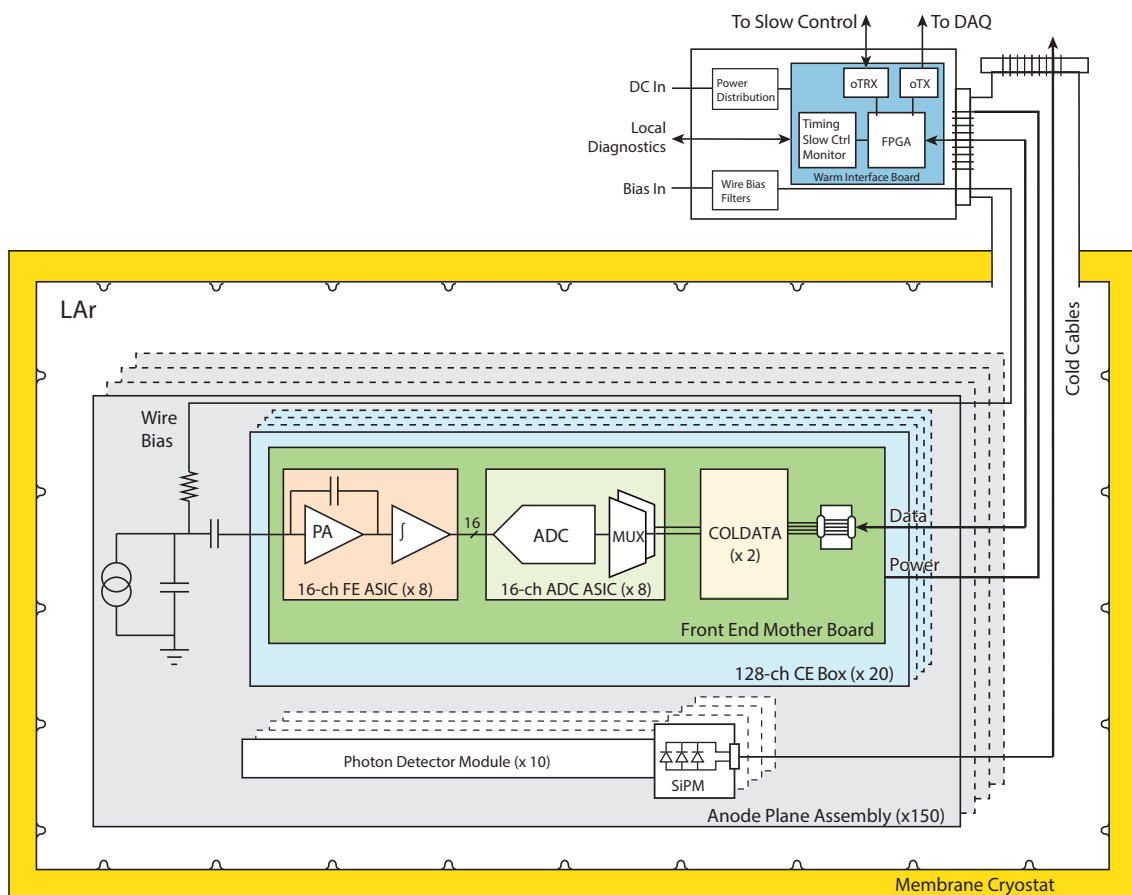


**Figure 4.1.** The reference architecture for the TPC electronics. The basic unit is the 128-channel FEMB. The scheme includes also the SiPMs used for the readout of the PDs, as discussed in chapter 5.

To retain maximum flexibility in optimizing reconstruction algorithms after the DUNE data is collected, the TPC electronics are designed to produce a digital record representing the waveform of the current produced by charge collection and induction on the anode wires. Each anode wire signal is input to a charge-sensitive amplifier, followed by a pulse-shaping circuit and an ADC. To minimize the number of cables and cryostat penetrations, the ADCs as well as the amplifier/shapers are located in the LAr, and digitized data from many wires merge onto a much smaller set of high-

speed serial links. The TPC signal processing is implemented in ASICs using CMOS technology. The TPC is continuously read out, resulting in a digitized ADC sample from each APA channel (wire). The ASICs used for the readout of the 2560 wires of each APA are mounted on front-end mother boards (FEMBs), as shown in figure 4.1. These are connected to WIBs located outside of the cryostat via the CE signal cable flange located at the CE feedthrough at the top of the cryostat. The WIBs are installed, together with power and timing cards (PTCs) that distribute the power and the clock and control signals, in a WIEC that is mounted on the signal flange. From the WIBs the data is sent to the DAQ back-end on an optical fiber network, as discussed in chapter 7.

#### 4.1.2 Requirements and specification

A number of specifications are imposed on the TPC electronics in addition to the noise requirement ( $ENC < 1000 e^-$ ). Some of them, labeled as SP-FD in table 4.1, are derived from DUNE's overall physics goals. The rest, labeled as SP-ELEC, are engineering specifications derived from the design choices for the CE.

**Table 4.1:** TPC electronics specifications.

| Label     | Description                                    | Specification (Goal)  | Rationale  | Validation                                |
|-----------|--|---|--|---|
| SP-FD-2   | System noise                                   | $< 1000 e^-$  | Provides $>5:1$ S/N on induction planes for pattern recognition and two-track separation.      | ProtoDUNE and simulation                  |
| SP-FD-13  | Front-end peaking time                         | $1 \mu\text{s}$   | Vertex resolution; optimized for 5 mm wire spacing.  | ProtoDUNE and simulation                  |
| SP-FD-14  | Signal saturation level                        | $500,000 e^-$<br>(Adjustable so as to see saturation in less than 10 % of beam-produced events) | Maintain calorimetric performance for multi-proton final state.                                | Simulation                                |
| SP-FD-19  | ADC sampling frequency                         | $\sim 2 \text{ MHz}$  | Match $1 \mu\text{s}$ shaping time.  | Nyquist requirement and design choice     |
| SP-FD-20  | Number of ADC bits                             | 12 bits   | ADC noise contribution negligible (low end); match signal saturation specification (high end). | Engineering calculation and design choice |
| SP-FD-21  | Cold electronics power consumption             | $< 50 \text{ mW/channel}$   | No bubbles in LAr to reduce HV discharge risk.   | Bench test                                |
| SP-FD-25  | Non-FE noise contributions                     | $\ll 1000 e^-$  | High S/N for high reconstruction efficiency.   | Engineering calculation and ProtoDUNE     |
| SP-FD-28  | Dead channels                                  | $< 1 \%$  | Minimize the degradation in physics performance over the $> 20$ -year detector operation.      | ProtoDUNE and bench tests                 |
| SP-ELEC-1 | Number of baselines in the front-end amplifier | 2   | Use a single type of amplifier for both induction and collection wires                         | ProtoDUNE                                 |

|           |   |  |  |   |
|-----------|---|--|--|---|
| SP-ELEC-2 | Gain of the front-end amplifier   | $\sim 20$ mV/fC<br>(Adjustable in the range 5 mV/fC to 25 mV/fC) | The gain of the FE amplifier is obtained from the maximum charge to be observed without saturation and from the operating voltage of the amplifier, that depends on the technology choice. |   |
| SP-ELEC-3 | System synchronization  | 50 ns<br>(10 ns)   | The dispersion of the sampling times on different wires of the APA should be much smaller than the sampling time (500 ns) and give a negligible contribution to the hit resolution.        |   |
| SP-ELEC-4 | Number of channels per front-end motherboard  | 128  | The total number of wires on one side of an APA, 1,280, must be an integer multiple of the number of channels on the FEMBs.  | Design  |
| SP-ELEC-5 | Number of links between the FEMB and the WIB  | 4 at 1.28 Gbps<br>(2 at 2.56 Gbps)                               | Balance between reducing the number of links and reliability and power issues when increasing the data transmission speed.   | ProtoDUNE, Laboratory measurements on bit error rates |
| SP-ELEC-6 | Number of FEMBs per WIB   | 4  | The total number of FEMB per WIB is a balance between the complexity of the boards, the mechanics inside the WIEC, and the required processing power of the FPGA on the WIB.               | ProtoDUNE, Design                                     |
| SP-ELEC-7 | Data transmission speed between the WIB and the DAQ backend                                       | 10 Gbps  | Balance between cost and reduction of the number of optical fiber links for each WIB.  | ProtoDUNE, Laboratory measurements on bit error rates |
| SP-ELEC-8 | Maximum diameter of conduit enclosing the cold cables while they are routed through the APA frame | 6.35 cm (2.5")   | Avoid the need for further changes to the APA frame and for routing the cables along the cryostat walls  | Tests on APA frame prototypes                         |

- SP-FD-13: the FE peaking time must be in the range 1 to 3  $\mu$ s to match the time required for the drifting charges to travel from one plane of anode wires to the next, which corresponds to the typical duration of the signal observed on the wires. The planes of anode wires are separated by 4.75 mm (see chapter 2), and the drift velocity for the E fields considered for DUNE is in the range 1.2 mm/ $\mu$ s to 1.6 mm/ $\mu$ s (1.4 mm/ $\mu$ s to 2.1 mm/ $\mu$ s for the gaps between the APA wire planes). A FE peaking time similar to the typical signal duration improves the detector's two-track resolution.

- SP-FD-14: the system must have a linear response up to an impulse input of at least  $500,000 e^-$ . This corresponds roughly to the largest ionization signals expected. These occur in events where multiple protons are produced in the primary event vertex, in particular, when the trajectories of one or more of the protons are parallel to the wire, leading to collection of charge over a long path length within a short time.
- SP-FD-19: the ADC sampling frequency must be  $\sim 2$  MHz, This value is chosen to match a FE shaping time of  $1 \mu\text{s}$  (approximate Nyquist condition) while minimizing the data rate.
- SP-FD-20: the ADC must digitize the charge deposited on the wires with 12 bits of precision. The lower end of the ADC dynamic range is driven by the requirement that the digitization not contribute to the total electronics noise, as defined by requirement SP-FD-25. The upper end is defined by SP-FD-14. Combining this with SP-FD-02 on the total electronics noise results in the need for 12 bits digitization.
- SP-FD-21: preliminary studies indicate that the power dissipated by the electronics located in the LAr should be less than  $50 \text{ mW/channel}$ . Lower power dissipation is desirable because the mass of the power cables scales with power. Ongoing studies focus on whether the amount of power dissipated by the electronics should be minimized further because of potential complications from argon boiling.
- SP-FD-25: the components of the readout chain, including the ADC and the bias voltage supplies, together must not contribute significantly to the overall noise. The ADC specifications for non-linearity and noise will depend on the gain of the FE. Like in the case of the requirement on the noise caused by voltage ripples on the cathode (SP-FD-12) discussed in section 3.1.2 we are aiming to keep all sources of noise other than the FE amplifier below  $100 e^-$ .
- SP-FD-28: the fraction of non-functioning channels over DUNE's nominal 20 years lifetime must not exceed 1%. Ongoing studies will quantify the effect of failures in the TPC and electronics, including single wire failures, and failures of groups of 16, 64, or 128 channels.
- SP-ELEC-1: the FE must have an adjustable baseline such that a single amplifier can process both the bipolar signal from the induction wires and the mostly unipolar signal from the collection wires.
- SP-ELEC-2: the FE must have a gain that allows using the entire voltage range provided by the chosen chip fabrication technology and operating voltage without saturation for physics signals up to those specified in SP-FD-14. Multiple gain settings could be made available to allow for optimization of the detector performance.
- SP-ELEC-3: the dispersion of the sampling times on the different wires of all the APAs in one DUNE SP detector module should be less than  $50 \text{ ns}$ . This value is much smaller than the time difference between two subsequent samples on the same wire as defined by the sampling frequency (SP-FD-19) such that it gives a negligible contribution to the single hit resolution (assuming a drift velocity of  $1.6 \text{ mm}/\mu\text{s}$ , the requirement of  $50 \text{ ns}$  corresponds to a contribution to the single hit resolution of  $80 \mu\text{m}$ ).

- SP-ELEC-4: the readout electronics for the APA wires must be organized into FEMBs containing 128 channels. This number is a sub-multiple of the number of wires on an APA and is determined by geometrical considerations, e.g., the number, size, and form factor of the CR boards introduced in section 4.2.2.
- SP-ELEC-5: the data from the FEMBs must be transmitted to the WIBs on a maximum of four links per board, each with a maximum speed of 1.28 Gbps, to minimize the number of connections on the cryostat penetrations. This requires data transmission at high speeds, which increases the power consumption inside the LAr. A reduction in the number of links per FEMB to two (with a link speed of 2.56 Gbps) will be investigated.
- SP-ELEC-6: each WIB must read out four FEMBs. This number is chosen to balance the complexity of the boards, the mechanics of the WIEC that houses the WIBs, and the required processing power in the FPGA inside the WIB.
- SP-ELEC-7: each WIB must transmit data to the DAQ back end on optical links at a speed of  $\sim 10$  Gbps. This speed is a compromise between the cost of optical transmitters and receivers and the complexity of the readout fiber plant.
- SP-ELEC-8: all the cables required to provide the low-voltage power and the control and readout for the FEMBs mounted on the bottom APA, plus the bias voltage cables for the same APA, must fit inside two conduits with a diameter of 6.35 cm (2.5 inch) that are inserted in the frame of the APA, as discussed in section 4.6.1.

### 4.1.3 Design

The reference design of the TPC electronics detector components is based on the specifications presented in section 4.1.2. Each individual APA has 2560 channels read out by 20 front-end mother boards (FEMBs), with each FEMB enabling digitized wire readout from 128 channels. One cable bundle connects each FEMB to the outside of the cryostat via a CE signal cable flange located at the CE feedthrough at the top of the cryostat, where a single flange services each APA, as shown in figure 4.2. Two CE signal flanges are on each feedthrough and together account for all electronics channels associated with a pair of APAs (upper and lower, vertically arranged). Each cable bundle contains wires for low-voltage (LV) power, high-speed data readout, and clock or digital-control signal distribution. Eight separate cables carry the TPC wire bias voltages from the signal flange to the APA wire bias boards, in addition to the bias voltages for the field cage termination electrodes and for the electron diverters. An additional flange on the top of each feedthrough services the PD system cables associated with the APA pair. Low-voltage power supplies and bias-voltage power supplies are located on the top of the cryostat.

The reference design for the CE calls for three types of custom ASICs inside the LAr:

- a 16-channel FE ASIC for amplification and pulse shaping (referred to as LArASIC);
- a 16-channel 12-bit ADC ASIC operating at  $\sim 2$  MHz (referred to as ColdADC); and
- a 64-channel control and communications ASIC (referred to as COLDATA).

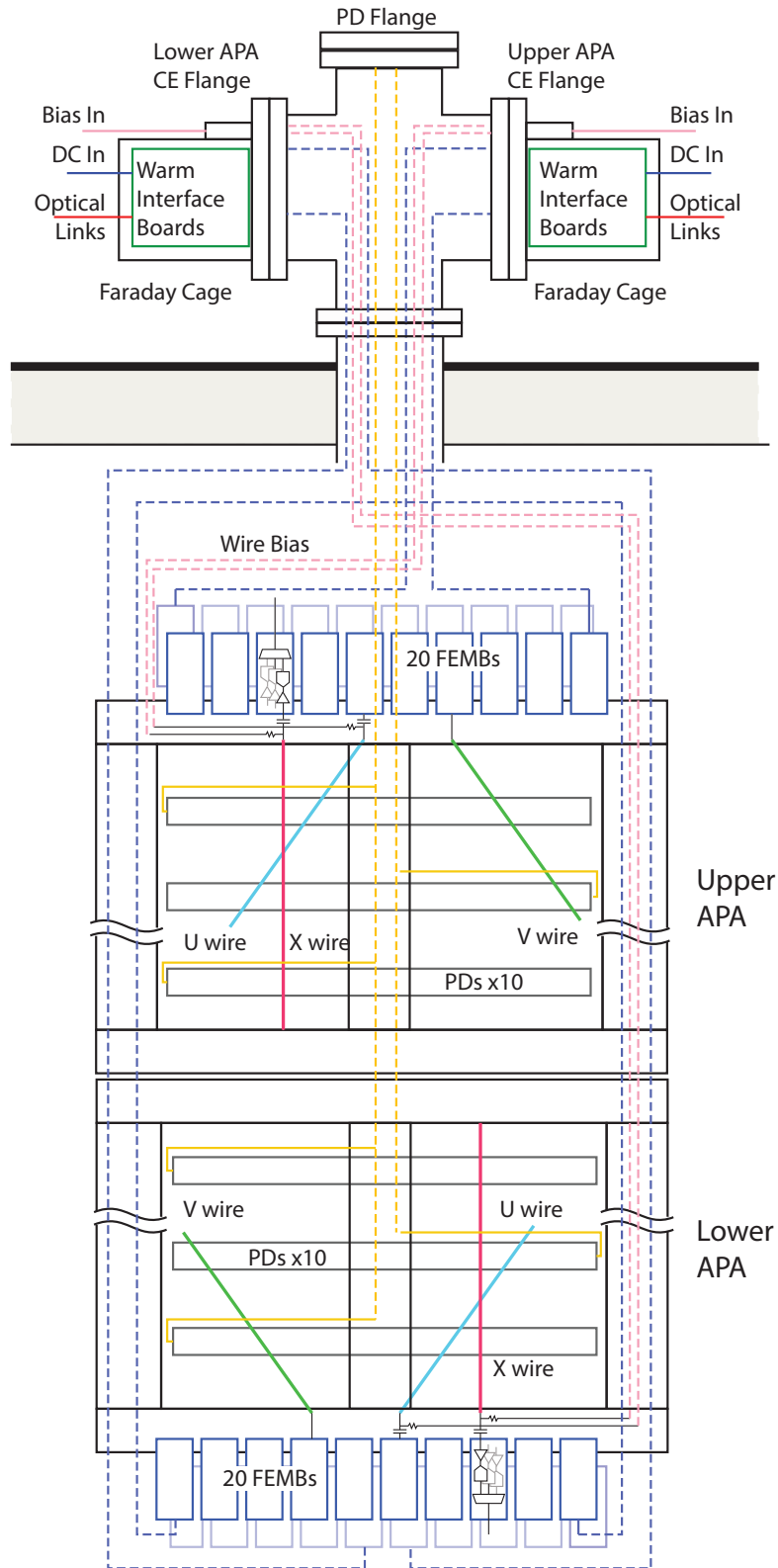


**Figure 4.2.** Connections between the signal flanges and APA. The lower APA shares the PD flange with the upper APA but has a separate TPC readout flange.

The TPC electronics detector components required for one APA are:

- FEMBs, on which the ASICs are mounted, and which are installed on the APAs;
- cables for the data, clock, and control signals; LV power; and wire bias voltages between the APA and the signal flanges (cold cables);
- signal flanges with a CE feedthrough to pass the data, clock, and control signals; LV power; and APA wire bias voltages between the inside and outside of the cryostat; and the corresponding cryostat penetrations and spool pieces;
- WIECs mounted on the signal flanges containing the WIBs and a PTC for further processing and distribution of the signals entering and exiting the cryostat; low voltage power and clock and control signals are transmitted from the PTCs to the WIBs on the PTB.
- cables for LV power and wire bias voltages between the signal flange and external power supplies (warm cables); and
- LV power supplies for the CE and bias-voltage power supplies for the APAs.

The number of channels (wires) connected to each of these components is given in table 4.2.

**Table 4.2.** TPC electronics components and quantities for a single APA of the DUNE SP module.

| Element                                 | Quantity       | Channels per element |
|---|----------------|----------------------|
| Front-end mother board (FEMB)           | 20 per APA     | 128                  |
| FE ASIC chip                            | 8 per FEMB     | 16                   |
| ADC ASIC chip                           | 8 per FEMB     | 16                   |
| COLDATA ASIC chip                       | 2 per FEMB     | 64                   |
| Cold cable bundle                       | 1 per FEMB     | 128                  |
| Signal flange                           | 1 per APA      | 2560                 |
| CE feedthrough                          | 1 per APA pair | 5120                 |
| Warm interface board (WIB)              | 5 per APA      | 512                  |
| Warm interface electronics crate (WIEC) | 1 per APA      | 2560                 |
| Power and timing card (PTC)             | 1 per APA      | 2560                 |
| Power and timing backplane (PTB)        | 1 per APA      | 2560                 |

The electronics located inside the cryostat cannot be replaced or repaired after the cryostat has been filled with LAr. Successful operation of the readout electronics in LAr for the 20 years of DUNE operation imposes technological choices for the SP module ASICs, and specific constraints on commercial components that are installed inside the LAr. While the higher charge carrier mobility [42] at LAr temperature than at room temperature is central to improving the performance of the CE, it also leads to the hot-carrier effect [43], which limits the lifetime of ASICs. In n-type CMOS transistors, the carriers (electrons) can acquire enough kinetic energy to ionize silicon in the active channel. This charge can become trapped and lead to effects (including threshold shifts)



similar to those caused by radiation damage, which can cause CMOS circuits to age much more quickly at LAr temperature, reducing performance and potentially causing failure. To mitigate the hot carrier effect, the maximum E field in transistor channels must be lower than that which could be used reliably at room temperature. The reduction of the maximum E field is achieved by operating the ASICs at a reduced bias voltage and by increasing by  $\sim 50\%$  the length of the transistors' channels. Another drawback of integrated circuits operated at LAr temperature is that the spread of the transistor properties becomes larger, making it more difficult to rely on transistor matching for circuit design. We must carefully test any commercial circuits used in the LAr to ensure they will perform well for the expected experiment lifetime. Reliability studies for TPC electronics designs under consideration are discussed in section 4.3.3.

## 4.2 System design

In order to achieve the lowest possible overall noise in the readout of the APA wire planes, all possible sources of noise need to be kept to a minimum. This requires minimizing the noise sources in each of the components of the readout chain of the APA wires, such as the FE amplifier noise. It also requires that all system aspects are taken into account, including avoiding channeling noise inside the cryostat through ground connections and through the readout chain of other detector components, like the PD system, the HVS, or the cryogenic instrumentation.

In this section we describe the overall system design of the TPC electronics, starting in section 4.2.1 with a description of the grounding and shielding scheme adopted in the DUNE SP module to minimize the overall noise in the detector, followed in section 4.2.2 by a discussion of the bias voltage distribution system. Later, we describe in section 4.2.3 the FEMBs, including the design of the ASICs that are being considered for use in DUNE. In section 4.2.4 we discuss the infrastructure for the CE inside the cryostat, which includes the cold boxes that shield the FEMBs, the cold cables, and the cable trays. Then in sections 4.2.5–4.2.8 we discuss the infrastructure on the top of the cryostat, including the feedthroughs, the WIECs, the timing distribution and synchronization system, and the services that provide the low voltage power and the bias voltage to the TPC electronics. The design presented here is very similar to the one used for ProtoDUNE-SP. The results obtained with this detector are discussed in section 4.2.9. Then in section 4.2.10 we discuss how the lessons learned from the construction, installation, commissioning, and operation are informing the final design of the DUNE SP detector module. Later in section 4.2.11 we conclude with a discussion of the design maturity and of the remaining prototype activities that are required prior to the beginning of the detector construction. Other aspects of system design pertaining to the interfaces with other detector components, including their grounding, are discussed in section 4.6.

### 4.2.1 Grounding and shielding

The overall approach to minimizing the system noise in the SP module relies on enclosing the sensitive wire planes in a nearly hermetic Faraday cage, and then carefully controlling currents flowing into or out of that protected volume through the unavoidable penetrations needed to build a working detector. Done carefully, this can result in avoiding all unwanted disturbances that result in detector noise. Such disturbances could either be induced on the signal wires by changing currents flowing inside the cryostat or even on the cryostat walls as, for instance, a temperature sensing

circuit that acts as a receiving antenna on the outside of the cryostat and a transmitting antenna on the interior of the cryostat. In addition, unwanted signals might be injected into the electronics either in the cold or just outside the cryostat by direct conduction along unavoidable power or signal connections to other devices. This approach to minimizing the detector noise by using appropriate grounding and shielding procedures is discussed in detail in [44]. It results in the following set of requirements that need to be respected during the design and the construction of the SP module:

- The APA frame shall be connected to the common of all the FE ASICs;
- All electrical connections (low voltage power, bias voltage, clock, control, and data readout) from one APA shall lead to a single signal feedthrough (SFT);
- All APAs shall be insulated from each other;
- The common of the FE ASIC and the rest of the TPC readout electronics shall be connected to the common plane of the FEMB;
- The return leads of the APA power line and any shield for the clock, control, and data readout shall be connected to the common plane of the FEMB at one end and to the flange of the SFT at the other end; this shall be the only connection of the APA frame to the cryostat;
- The mechanical suspension from the frame of the APA to the cryostat shall be insulated;
- The last stage of the sense wire and grid bias filters shall be connected to the common of all the FE ASICs and therefore to the APA frame.
- Similarly the last element of the FC divider chain shall be connected with an appropriate termination to the APA frame, as discussed in section 3.5.

These requirements have been followed already for the construction of the ProtoDUNE-SP prototype. As discussed in section 4.2.9, the initial results from the online monitoring and the analysis of ProtoDUNE-SP indicate that the system noise requirements for the DUNE SP module can be met.

To minimize system noise, the TPC electronics cables for each APA enter the cryostat through a single CE flange, as shown in figure 4.2. This creates, for grounding purposes, an integrated unit consisting of an APA frame, FEMB ground for all 20 CE modules, a TPC flange, and warm interface electronics. The input amplifiers on the FE ASICs have their ground terminals connected to the APA frame. All power-return leads and cable shields are connected to both the ground plane of the FEMB and to the TPC signal flange.

The only location where this integrated unit makes electrical contact with the cryostat, which defines the detector ground and acts as a Faraday cage, is at a single point on the CE feedthrough board in the TPC signal flange where the cables exit the cryostat. Mechanical suspension of the APAs is accomplished using insulated supports. To avoid structural ground loops, the APA frames described in chapter 2 are insulated from each other.

Filtering circuits for the APA wire-bias voltages are locally referenced to the ground plane of the FEMBs through low-impedance electrical connections. This approach ensures a ground-return

path in close proximity to the bias-voltage and signal paths. The close proximity of the current paths minimizes the size of potential loops to further suppress noise pickup.

Signals associated with the PD system, described in chapter 5, are carried directly on shielded, twisted-pair cables to the signal feedthrough. The cable shields are connected to the cryostat at the PD flange shown in figure 4.2, and to the PCB shield layer on the PDs. The cable shields have no electrical connection to the APA frame or the TPC electronics.

Further aspects of the DUNE grounding scheme are discussed in Volume III, DUNE far detector technical coordination, chapter 5 and in [45].

#### 4.2.2 Distribution of bias voltages

Each side of an APA includes four wire layers, as described in section 2.2. Electrons passing through the wire grid must drift unimpeded until they reach the  $X$ -plane collection layer. The nominal bias voltages, chosen to result in this electrically transparent configuration, are given in section 2.2.

The filtering of wire bias voltages and the AC coupling of wire signals passing onto the charge amplifier circuits is done on CR boards that plug in between the APA wire-board stacks and FEMBs. The CR boards have already been described in section 2.2.5.3; here we focus on the rationale for the choice of the resistance and capacitor values and their impact on the wire signals. Each CR board includes single RC filters for the  $X$ - and  $U$ -plane wire bias voltages, while the  $V$ -plane wires have a floating voltage. In addition, each board has 48 pairs of bias resistors and AC coupling capacitors for  $X$ -plane wires, and 40 pairs for the  $U$ -plane wires. The coupling capacitors block DC levels while passing AC signals to the FEMBs. On the FEMBs, clamping diodes limit the input voltage received at the amplifier circuits to between  $1.8\text{ V} + U_D$  and  $0\text{ V} - U_D$ , where  $U_D$  is the threshold voltage of the diode, approximately 0.7 V at LAr temperature. The amplifier circuit has a 22 nF coupling capacitor at the input to avoid leakage current from the protection clamping diodes. Tests of the protection mechanism have been performed by discharging 4.7 nF capacitors holding a voltage of 1 kV (2.35 mJ of stored energy). The diodes survived more than 250 discharges at LN<sub>2</sub> temperature. A schematic diagram of the APA wire bias subsystem, identical to the one used in ProtoDUNE-SP, appears in figure 4.3.

Bias resistance values should be at least 20 M $\Omega$  to maintain negligible noise contributions. The higher value helps achieve a longer time constant for the high-pass coupling networks. Time constants should be at least 25 times the electron drift time so that the undershoot in the digitized waveform is small and easily correctable. As discussed in section 2.2.5.3, the bias resistance value is 51 M $\Omega$ , while the DC-blocking capacitors on each wire have a value of 3.9 nF. This gives a time constant of 0.2 s that is much larger than the drift time for electrons from tracks passing near the cathode ( $\sim 2.3$  ms).

The bias-voltage filters are RC low-pass networks. Resistance values should be much smaller than the bias resistances to control cross-talk between wires and limit the voltage drop if any of the wires becomes shorted to the APA frame. As discussed in section 2.2.5.3, these resistors have a resistance of 5 M $\Omega$ , while the bias filter capacitors have a capacitance of 39 nF.

#### 4.2.3 Front-end motherboard

Each APA is instrumented with 20 FEMBs. The FEMBs plug into the APA CR boards, making the connections from the wires to the charge amplifier circuits as short as possible. Each FEMB

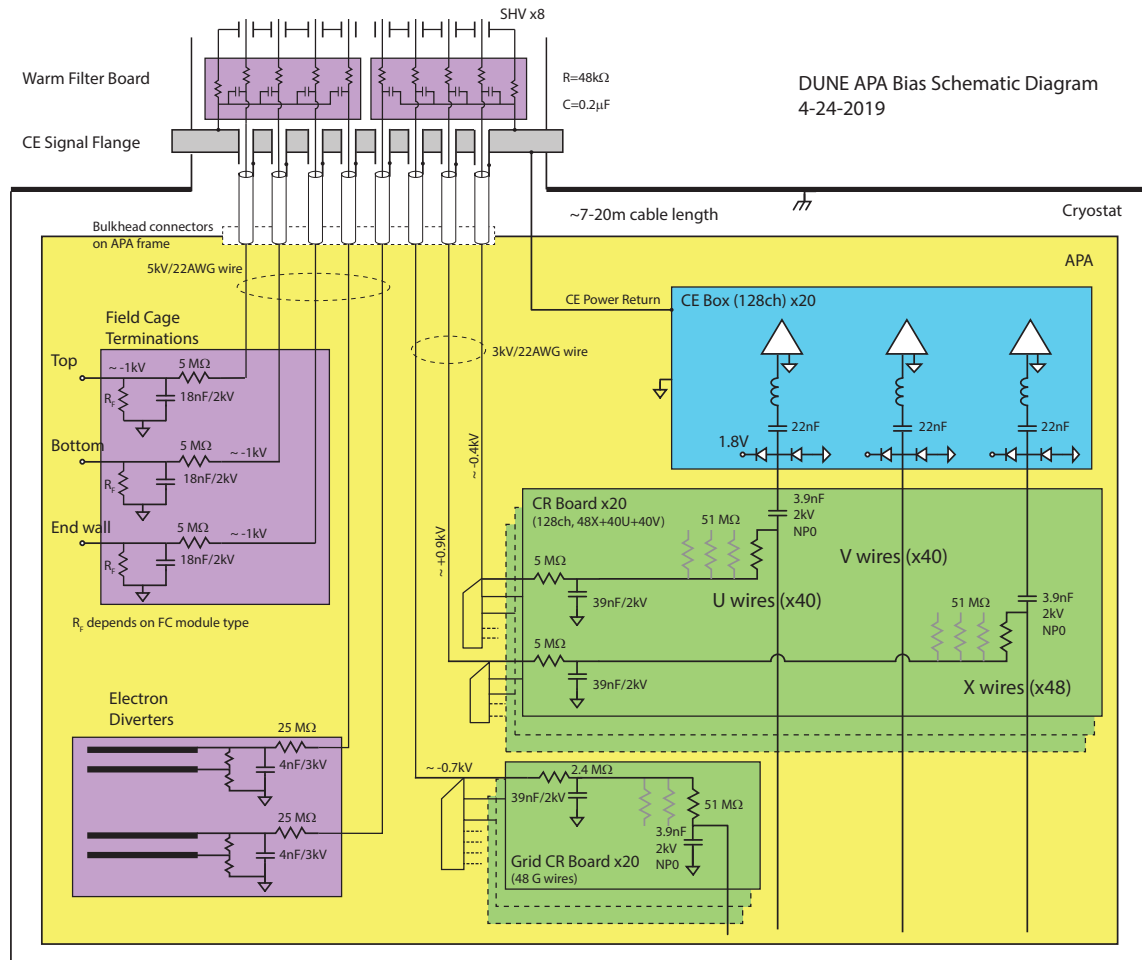
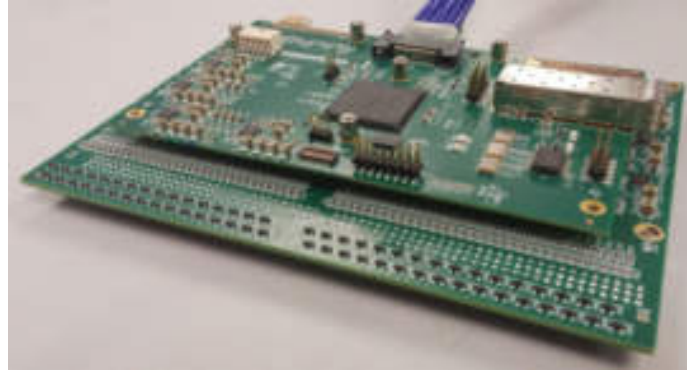


Figure 4.3. DUNE APA wire bias schematic diagram including the CR board.

receives signals from 40  $U$  wires, 40  $V$  wires, and 48  $X$  wires. The reference FEMB design contains eight 16-channel LArASIC chips, eight 16-channel ColdADC ASICs, and two COLDATA control and communication ASICs (see figure 4.1). The FEMB also contains regulators that produce the voltages required by the ASICs and filter those voltages, and a micro-electromechanical system oscillator that provides a 40 MHz reference to the COLDATA Phase-Locked Loop (PLL). The LArASIC inputs are protected by an external series inductor and two diodes as well as the internal diode protection in the chip.

The ProtoDUNE-SP version of the FEMB (which uses a single FPGA on a mezzanine card instead of two COLDATA ASICs) is shown in figure 4.4. In the rest of this section we describe the ASICs that will be installed on the FEMBs and discuss the procedure that will be followed to choose the ASIC design to implement in the SP module. In addition to describing LArASIC, ColdADC, and COLDATA, we also discuss two alternative solutions, one based on a commercial off-the-shelf (COTS) ADC, and one where the functionality of the three-ASIC is implemented in a single chip, CRYO.



**Figure 4.4.** The complete FEMB assembly as used in the ProtoDUNE-SP detector. The cable shown is the high-speed data, clock, and control cable.

The functionality of the FEMB for DUNE will be almost identical to that of the FEMB used in ProtoDUNE-SP. The design will change slightly to accommodate the new ASICs, which will also entail changing the connections to the WIB, and changing the number of voltage regulators. In addition, the connector for the control and data cold cables will be replaced to address an issue observed in ProtoDUNE-SP that will be discussed in section 4.2.10. The new design, shown in figure 4.5, adds wings to the PCB soldered to the cold cable, with standoffs to ensure the planarity of the connector to the FEMB, and a cutout in the PCB to preclude any stresses introduced by height variations.

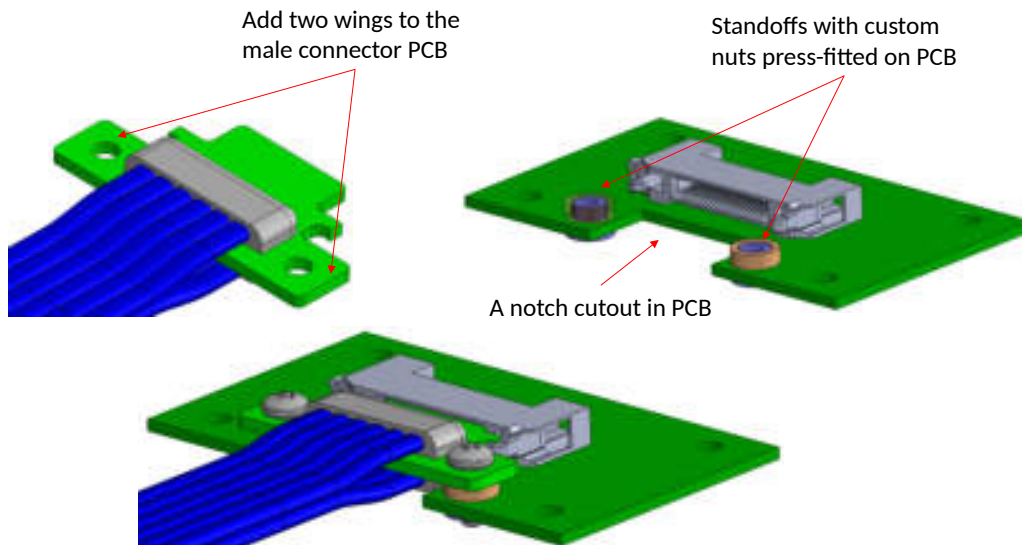


**Figure 4.5.** Modified design of the cold data cable and of the FEMB PCB.

All the discrete components mounted on the FEMB have been characterized for operation in LAr. In some cases (resistors, capacitors, diodes) the components used on the ProtoDUNE-SP FEMB belong to the same family of components already used for other boards operating in cryogenic environment, namely the boards used for the ATLAS accordion LAr calorimeter, providing relevant information on the lifetime of these components, which is discussed later in section 4.3.3. There

we also discuss procedures for the measurement of the lifetime of discrete components that have been adopted in recent years to demonstrate that the TPC electronics can survive in LAr. These types of measurements have been performed already for other neutrino experiments using the LAr TPC technology, while for the micro-mechanical oscillator we rely on characterizations performed by NASA [46].

In the case of custom ASICs, appropriate steps must be taken prior to starting the layout of the chips. Both COLDATA and ColdADC are implemented in the TSMC 65 nm CMOS process [47]. The designs were done using cold transistor models produced by Logix Consulting.<sup>1</sup> Logix made measurements of TSMC 65 nm transistors (supplied by Fermilab) at LN<sub>2</sub> temperature and extracted and provided to the design teams SPICE [48] models valid at LN<sub>2</sub> temperature. These models were used in analog simulations of COLDATA and ColdADC subcircuits. In order to eliminate the risk of accelerated aging due to the hot-carrier effect [43], no transistor with a channel length less than 90 nm was used in either ASIC design. A special library of standard cells using 90 nm channel-length transistors was developed by members of the University of Pennsylvania and Fermilab groups. Timing parameters were developed for this standard cell library using the Cadence Liberate tool<sup>2</sup> and the Logix SPICE models. Most of the digital logic used in ColdADC and COLDATA was synthesized from Verilog code using this standard cell library and the Cadence Innovus tool.<sup>3</sup> Innovus was also used for the layout of the synthesized logic. The design of the CRYO ASIC and of LArASIC are implemented in the TSMC 130 nm and 180 nm CMOS process [49, 50], respectively. In the case of LArASIC, the design uses models that were obtained by extrapolating the parameters of the models provided by TSMC, which are generally valid in the 230 K to 400 K. In the case of the CRYO ASIC, cold transistor models were based on data taken at SLAC National Accelerator Laboratory (SLAC) with TSMC-produced 130 nm transistors.

#### 4.2.3.1 Front-end ASIC

LArASIC [38] receives current signals from the TPC sense wires and provides a way to amplify and shape the signals for downstream signal digitization. LArASIC has 16 channels and is implemented using the TSMC 180 nm CMOS process [50]. It integrates a band-gap reference to generate all the internal bias voltages and currents. This guarantees high stability of the operating point over a wide range of temperatures, including cryogenic temperatures. The channel schematic of LArASIC is shown in figure 4.6.

Each LArASIC channel has a dual-stage charge amplifier and a 5<sup>th</sup> order semi-Gaussian shaper as an anti-aliasing filter for the TPC signals. It has programmable gain selectable from one of 4.7, 7.8, 14, and 25 mV/fC (corresponding to full-scale charge of  $1.9 \times 10^6$ ,  $1.1 \times 10^6$ ,  $625 \times 10^3$ , and  $350 \times 10^3 e^-$ ), programmable peaking time selectable from one of 0.5, 1, 2, and 3  $\mu$ s, and programmable baseline for operation with either the collection ( $\sim 200$  mV) or the induction ( $\sim 900$  mV) wires. All these parameters can be set only at the ASIC level, i.e., they affect the behavior of 16 readout channels. The design of LArASIC has been optimized for the capacitive loads expected in the case of the DUNE detector (i.e., in the range 170 pF to 210 pF). Each channel has an option

<sup>1</sup>Logix<sup>TM</sup> Consulting, <http://www.lgx.com/>.

<sup>2</sup>Cadence Liberate<sup>TM</sup>.

<sup>3</sup>Cadence Innovus<sup>TM</sup>.

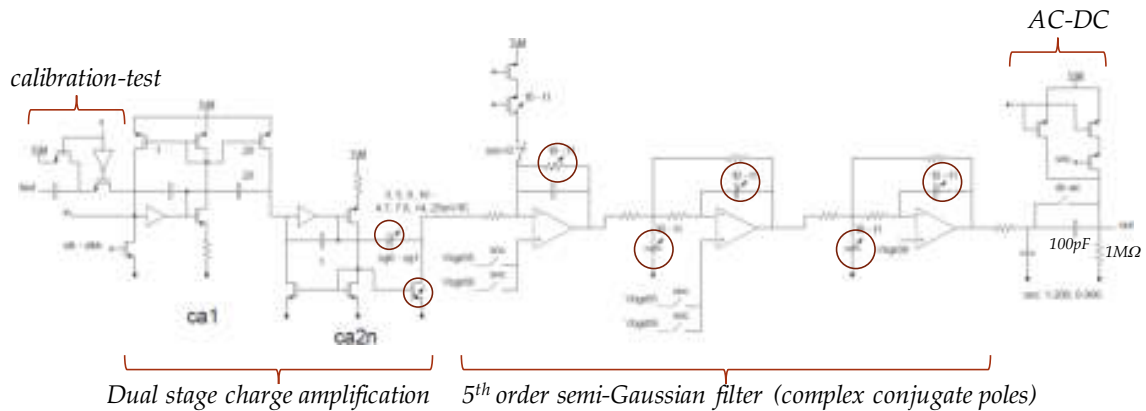


**Figure 4.6.** Channel schematic of LArASIC, which includes a dual-stage charge amplifier and a 5<sup>th</sup> order semi-Gaussian shaper with complex conjugate poles. Circuits in red circles are programmable to allow different gain and peaking time settings.

to enable the output monitor to probe the analog signal, and an option to enable a high-performance output driver that can be used to drive a long cable.

Each LArASIC channel has a built-in charge calibration capacitor that can be enabled or disabled through a dedicated register. Measurements of the injection capacitance have been performed using an external precisely calibrated capacitor. These measurements show that the calibration capacitance is extremely stable against temperature variations, changing from 184 fF at room temperature to 183 fF at 77 K. This result and the measured stability of the peaking time demonstrate the high stability of the passive components as a function of temperature. Channel-to-channel and chip-to-chip variation in the calibration capacitor are typically less than 1%. The variations of the calibration capacitors could be characterized prior to the beginning of DUNE data taking, using the QC process, discussed in section 4.4.4.

Shared among the 16 channels in LArASIC are the digital interface, programming registers, a temperature monitor, and a band-gap reference monitor. It is also possible to enable AC coupling as mitigation of baseline variations induced by vibrations of the APA wire, a programmable input bias current selectable from one of 0.1, 0.5, 1, or 5 nA, as well as a programmable pulse generator with a 6-bit DAC for calibration. The possibility of configuring various parameters controlling the FE amplifier (gain, peaking time, baseline) has allowed ProtoDUNE-SP to reduce the impact of the saturation effect discussed in section 4.2.10, at the cost of a reduction in dynamic range for the collection wires.

The power dissipation of LArASIC is about 5.5 mW per channel at 1.8 V supply voltage when the output buffer is disabled (the output buffer is required only for transmitting analog signals over long distances; it is not needed when LArASIC is mounted close to the ADC on the FEMB). The ASIC is packaged in a commercial, fully encapsulated plastic 80 pin QFP. Figure 4.7 shows the response of LArASIC for all gains and peaking times and both baselines. Note that the gain is independent of the peaking time; the same amount of charge, in the impulse approximation, produces the same peak voltage signal regardless of the peaking time.

Prototype version P2 LArASIC chips have been evaluated and characterized at room temperature and LN<sub>2</sub> temperature (77 K). 960 P2 chips, totaling 15.360 channels, have been used to

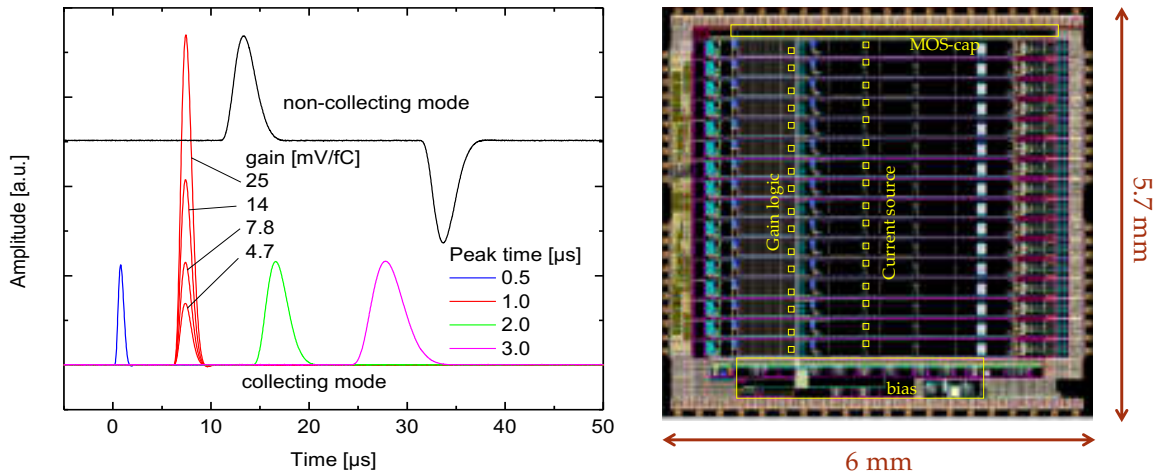


**Figure 4.7.** Response of LArASIC for four gains, four peaking times, and both baseline values (left; the time distance between the positive and negative pulse for the induction wires has been exaggerated for clarity reasons); layout of 16-channel LArASIC version P3, where revisions with reference to version P2 are highlighted in yellow boxes (right).

instrument six ProtoDUNE-SP APAs successfully. Excessive stress in the package of LArASIC at cryogenic temperature causes FE channels to have a non-uniform baseline in collection mode, while the baseline DC voltage in induction mode is uniform. A new prototype, version P3, was fabricated in March 2018 to address this issue by making DC circuits for the collection mode similar to the induction mode. At the same time, the default gain setting was changed to 14 mV/fC. The layout of P3 LArASIC is also shown in figure 4.7, with modifications highlighted in yellow boxes. The P3 LArASIC chips were received and evaluated in September 2018. We have verified that with the new design the FE channels have a uniform baseline when operated in the collection mode, and that 14 mV/fC is the new default gain setting.

P3 LArASIC will be further evaluated on FEMBs in various integration test stands for performance studies, including the 40% APA at BNL, the ICEBERG R&D cryostat and electronics (ICEBERG) TPC at Fermilab and the seventh ProtoDUNE APA in the cold box at CERN. Analysis of the ProtoDUNE-SP data has highlighted a saturation problem in the design of the P2 LArASIC that we have observed also in bench tests of the P3 version. This problem, discussed in detail in section 4.2.10, will be addressed in the design of the next version of LArASIC, P4, for which we are also planning to implement a single-ended-to-differential converter as an interface to the recently developed ColdADC. The plan for solving the saturation problem in LArASIC is discussed in section 4.2.11.

#### 4.2.3.2 ColdADC ASIC

ColdADC is a low-noise ADC ASIC designed to digitize 16 input channels at a rate of  $\sim 2$  MHz, as required for the DUNE SP module. ColdADC was designed to operate with an external 64 MHz clock and an external 2 MHz digitization clock. The 2 MHz clock is aligned on the rising edge of one of the 64 MHz transitions, as discussed in section 4.2.3.3. For the remainder of this section we assume that the main clock is operating at 64 MHz, but in the DUNE SP module this external



clock will operate at 62.5 MHz as discussed in section 7.3.7, and the waveforms from the APAs will be digitized every 512 ns. ColdADC is implemented in the TSMC 65 nm CMOS technology and has been designed by a team of engineers from Lawrence Berkeley National Laboratory (LBNL), BNL, and Fermilab. The ASIC uses a conservative, industry-standard design including digital calibration. Each ColdADC receives 16 voltage outputs from a single LArASIC chip. The voltages are buffered, multiplexed by 8, and input to two 15-stage pipelined ADCs operating at 16 MHz. The 16 MHz clock is generated internally in ColdADC and shares its rising edge with the 2 MHz clock. The ADC uses the well known pipelined architecture with redundancy [51]. Digital logic is used to correct non-linearity introduced by non-ideal amplifier gain and offsets in each pipeline stage [52], and an automatic calibration procedure is implemented to determine the constants used in this logic. The ADC produces 16-bit output which is expected to be truncated to 12 bits.

The ADC is highly programmable to optimize performance at different temperatures. Many circuit blocks can be bypassed, allowing the performance of the core digitization engine to be evaluated separately from the ancillary circuits. A block diagram of the chip is shown in figure 4.8. Each of the major blocks is described below.

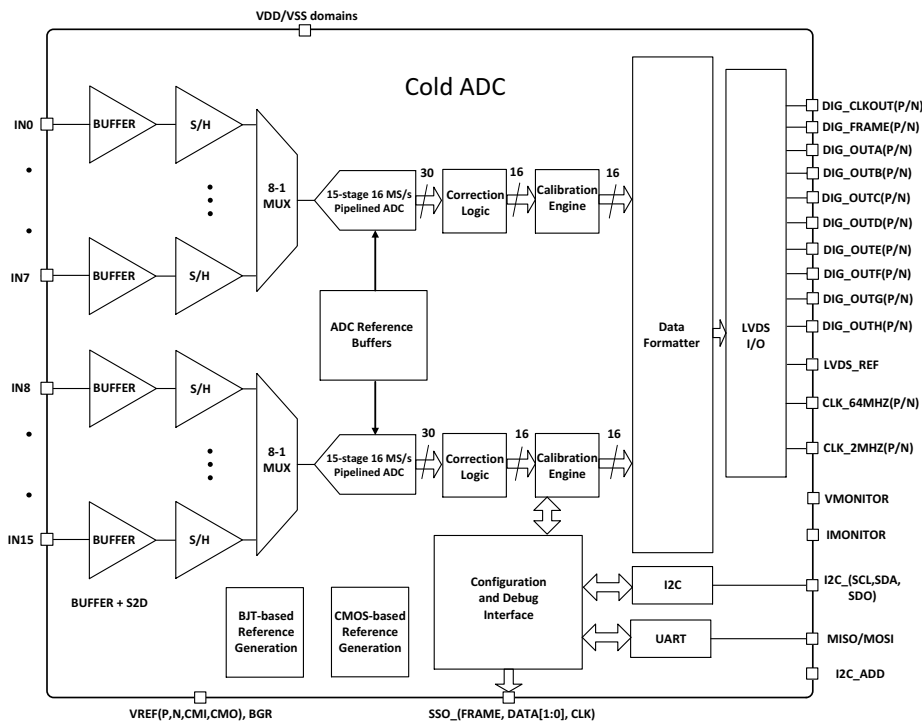
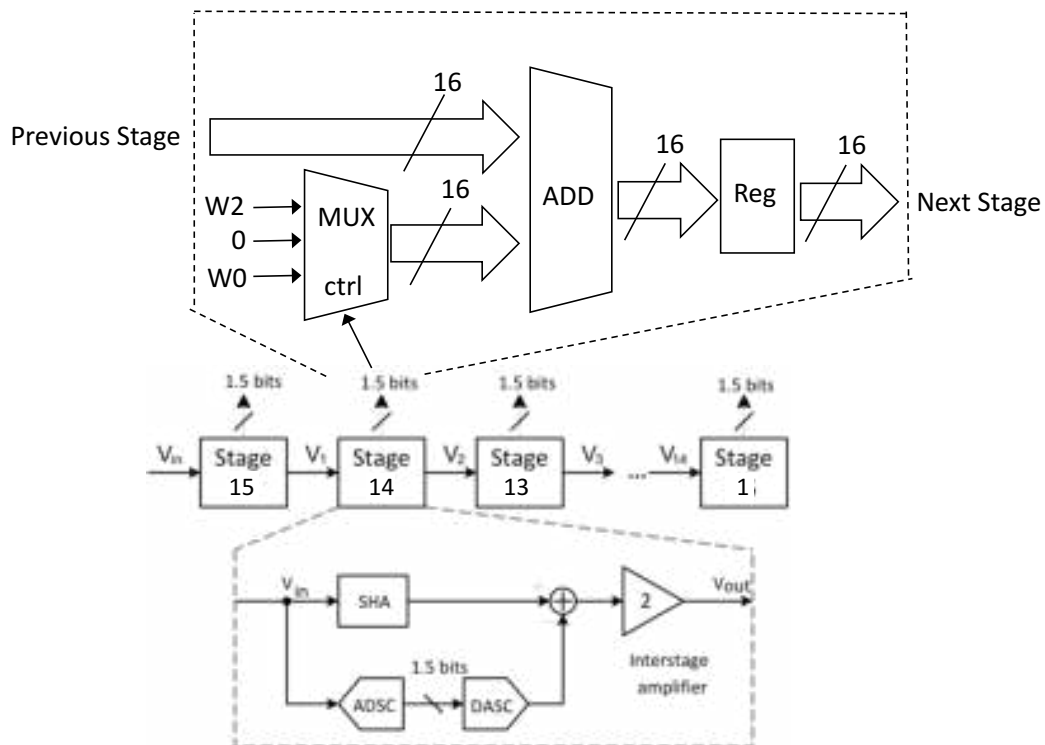


Figure 4.8. ColdADC block diagram.

All required reference voltages and currents are generated on-chip by programmable circuit blocks. Independently adjustable bias voltage levels and currents are provided for the input buffers, sample-and-hold amplifiers, ADCs, and ADC reference buffers. The most accurate reference voltage circuit is a band-gap reference based on a PNP transistor. However, measurements made at BNL and LBNL of a large PNP transistor indicate that the foundry-provided SPICE model does not adequately describe the device operation at LAr temperature. Thus, a CMOS-based voltage

reference has also been included in ColdADC. As discussed below, bench tests of ColdADC prototypes show that both reference blocks perform well and meet requirements.

ColdADC has four possible ways to interface with LArASIC. It can accept either single-ended inputs (provided by existing LArASIC chips) or differential inputs (foreseen for the future LArASIC P4 upgrade). In either case, it is also possible to bypass the input buffers and apply the inputs directly to the sample-and-hold amplifiers. The role of the input buffers is to present a well defined and easy-to-drive load to LArASIC. The sample-and-hold amplifiers are separated into two groups of eight. They sample the waveform at the rising edge of the (2 MHz) sampling clock. The 16 MHz clock is then used to clock an 8-to-1 multiplexer that presents eight samples in turn to one of the two ADC pipelines.



**Figure 4.9.** Circuit blocks in each ADC pipeline stage. MUX selects one of three values as the digitized output of the current stage and presents it to the ADD circuit, which adds it to the result calculated by previous pipeline stages. SHA is a sample-and-hold amplifier, and ADSC and DASC are low resolution 1.5 bit analog-to-digital and digital-to-analog subconverters, respectively.

A block diagram of an ADC pipeline is shown in figure 4.9. Each of the 15 stages contains a low-resolution 1.5-bit analog-to-digital subconverter containing two comparators, a 1.5-bit digital-to-analog subconverter that produces a voltage based on the two comparator outputs, an analog subtractor, a sample-and-hold amplifier, and a gain stage (with a nominal gain of two). The transfer function of each stage is identical and is shown in figure 4.10 along with the nominal “weights” ( $W_0$  and  $W_2$ ) that are added to form the output of the pipeline. Each pipeline stage makes a three-level coarse decision based on the analog input voltage, selects one of three digital weights to be added to the results of previous stages, and passes a voltage to the next stage that is proportional to the

difference between the input voltage and the voltage corresponding to the digital output of the stage. Because the stages are weighted by a factor of two, but have three possible digital results, there is redundancy between stages that makes the final result independent of errors in the comparator thresholds (up to  $\pm V_r/4$  where the stage range is  $[-V_r, V_r]$ ). An “error” in the output of one stage is corrected in subsequent stages (usually the next stage). In order to take advantage of this redundancy provided by the pipelined architecture it is necessary to include at least one “extra” stage in the pipeline.

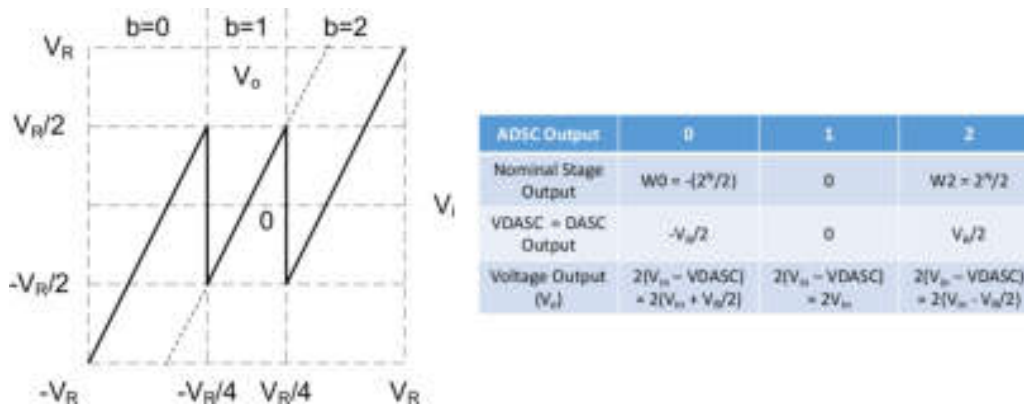


**Figure 4.10.** 1.5-bit stage transfer function and digital output. The voltage range of the ADC as a whole, and of each individual stage is  $[-V_r, V_r]$ . Note that the voltage passed to the subsequent stage will not exceed the stage range even if a comparator threshold is wrong by up to  $V_r/4$ .

The calibration logic allows the correction of errors caused by imperfections in the voltage that are passed from one stage to the next. These imperfections arise from errors in each stage corresponding to  $\pm V_r/2$  from the resistive dividers and non-ideal effects in the gain and offset of the interstage amplifiers. The calibration procedure relies on the fact that the required precision is easily satisfied by the last stages of the pipeline. The number of stages to be calibrated (maximum seven) is set by a programmable register. An iterative calibration procedure is used. Starting with the least significant stage to be calibrated, the input to the stage is set to the threshold levels of  $\pm V_r/4$  and the normal comparator outputs are overridden and forced first to 1 and then to 0. The lower stages of the ADC digitize the analog value output from the stage being calibrated and the difference between the ADC output when the comparator is forced to 1 and the ADC output when the comparator is forced to 0 is calculated. These two differences ( $W_0$  expressed as a negative number and  $W_2$  expressed as a positive number) are stored and used as two of the three possible digital outputs of the stage being calibrated (the third possible output being 0). This procedure is then repeated for the next most significant pipeline stage until stage 15 has been calibrated.

The number of ADC bits that are useful depends on the effective noise of the various subcircuits of the ADC. The noise of the first few pipeline stages (associated with the most significant bits) contributes more heavily than subsequent stages. For this reason, the first stages are designed to be larger, lower noise, and to require more power than later stages. The capacitance is reduced by a factor of two, relative to that of the sample-and-hold amplifier, for each of the first three stages, and then kept constant. The total effective noise expected is  $\sim 130 \mu\text{V}$  root mean square (RMS). This is similar to the quantization error of an ideal 12-bit ADC with a voltage range of 1.5 V (slightly

larger than the output range of LArASIC, 0.2 V to 1.6 V) for which the bin width is  $\sim 366 \mu\text{V}$  and the quantization error is  $\sim 106 \mu\text{V}$ .

In normal operation, each pipelined ADC passes a 16-bit result to the data formatter on the rising edge of the 16 MHz clock. The data formatter separates the two 16-bit words into eight 4-bit nibbles and serializes the nibbles for output (most significant bit first) at 64 MHz. An output clock and a frame marker are also generated. The frame marker indicates the most significant bit in each nibble of the first of eight channels digitized by one of the ADC pipelines in each 2 MHz sample period. The output data is generated on the falling edge of the output clock and is latched by the COLDATA ASIC using the rising edge of the same clock.

A second mode of operation is included for debugging purposes. In this mode, 2-bit raw stage results from each of the 15 stages of one of the two pipelines are formatted into the most significant 15 bits of two 16-bit words, broken into nibbles, and output in the same manner as normal data.

Ten differential output drivers are used for the 64 MHz output clock, frame marker, and ADC data. The output drivers source and sink a current whose value can be digitally controlled. The minimum current is  $165 \mu\text{A}$ , which corresponds to approximately 3 mV peak-to-peak with  $100 \Omega$  termination. Seven additional levels spaced by  $275 \mu\text{A}$  can be selected. The maximum current is 2.07 mA, about  $2/3$  of the LVDS standard of 3.5 mA.

The operation of ColdADC is controlled by a number of 8-bit registers. These registers can be written to and read back using either an Inter-Integrated Circuit (I2C) interface [53] or a Universal Asynchronous Receiver/Transmitter (UART). COLDATA will use the I2C interface. The UART is included in the first ColdADC prototype to facilitate chip testing and for risk mitigation.

ColdADC was received at the end of January 2019. Bench tests were performed at BNL, Fermilab, and LBNL. These tests used ADC chips mounted directly on printed circuit boards, and were done at both room temperature and cryogenic temperature. The tests concentrated first on functionality and later on performance. A small number of problems were found during bench testing and will be described below. These problems will not prevent system tests from being done with prototype ColdADC chips.

Both control interfaces (I2C and UART) operate as designed. All of the digital control bits can be written and read. The LVDS I/O operates as designed and the drive current of the LVDS can be selected as designed. The ADC pipeline functions as designed, as does the data formatter. The automatic calibration logic does not work, but the pipelines can be calibrated off-chip using register-controlled debugging modes to force all of the steps of the calibration procedure. The sample-and-hold amplifiers and the multiplexer that connects the sample-and-hold outputs to the ADC pipelines operate correctly. Both the CMOS reference generation block and the band-gap reference block operate as designed, although a minor error in a digital-to-analog converter in the band-gap reference block means that it must operate with the (nominally 2.3 V) analog voltage set to 2.7 V. Another error was discovered in the input buffer block. Level shifters intended to translate control bits in the 1.2 V domain to the 2.5 V domain were omitted. As a result, the 1.2 V digital supply must be set to 2.1 V. All of these design errors (including the auto-calibration failure) have been understood and are easily corrected. Bench tests have proven that the ColdADC prototypes can be run at the required elevated voltage settings for many days without damage to the chips.

Performance measurements of ColdADC have also been done. The performance of many of the sub-circuits have been measured separately as well as the performance of the entire ADC. Here we present two measurements made at LN<sub>2</sub> temperature.

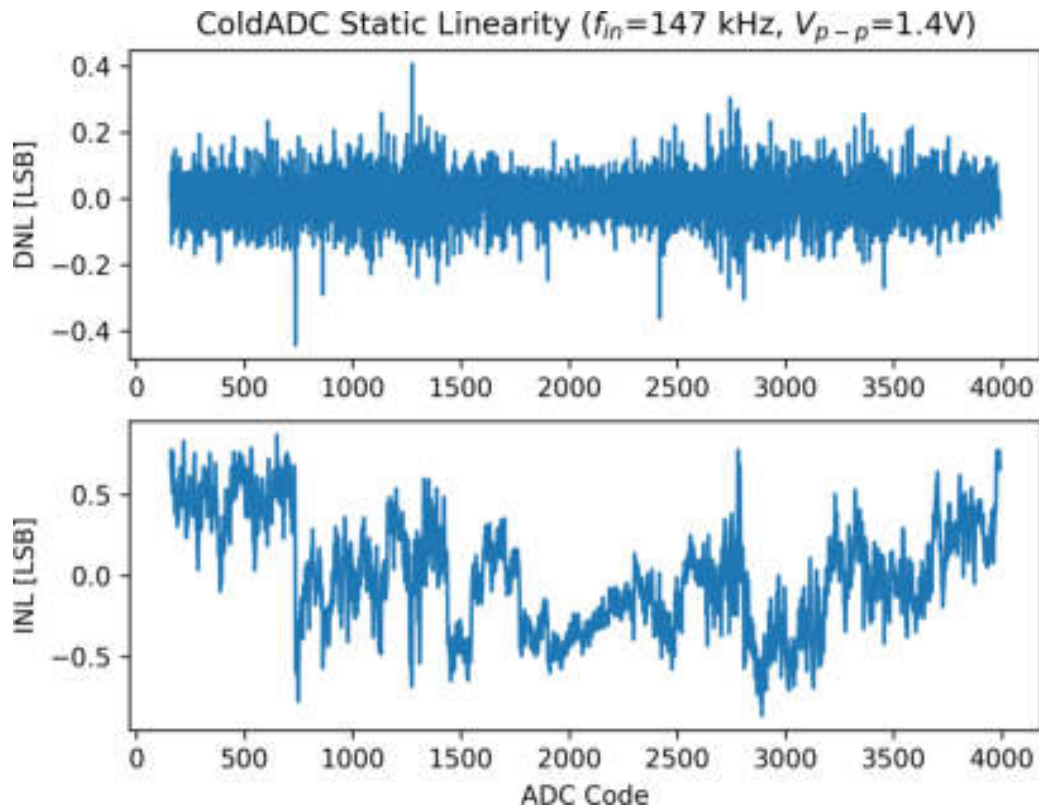


**Figure 4.11.** DNL (top) and INL distributions as a function of ADC code for ColdADC.

The static linearity of the pipeline ADC was measured using a filtered sine wave connected to the test inputs of ColdADC. The measured histogram of ADC codes was fitted to the probability density function for a sine wave. The calculation of the residuals to the fit yields the differential non-linearity (DNL) as a function of ADC code; the integral of DNL is the integral non-linearity (INL). These two distributions are shown in figure 4.11, which was obtained using a sine wave of amplitude of 1.4 V peak-to-peak (matching the LArASIC dynamic range) and the nominal reference voltage settings (corresponding to a 1.5 V dynamic range).

Dynamic linearity was also measured using a filtered sine wave. In this case, ADC codes were collected for an integer number of sine wave cycles and a FFT was performed on the data. The signal to noise and distortion ratio (SNDR), effective number of bits (ENOB), spurious free dynamic range (SFDR), and the total harmonic distortion (THD) were extracted from the FFT. An example of the FFT is shown in figure 4.12, which was obtained using a sine wave of amplitude 1.5 V (matching the full range of the ADC). The extracted ENOB is over 11, despite the non-linearity evident in figure 4.11, because the ADC noise is very low. The dominant source of non-linearity has been demonstrated to be insufficient open-loop gain of the operational amplifier used in each pipeline stage. The design has already been modified to address this deficiency.

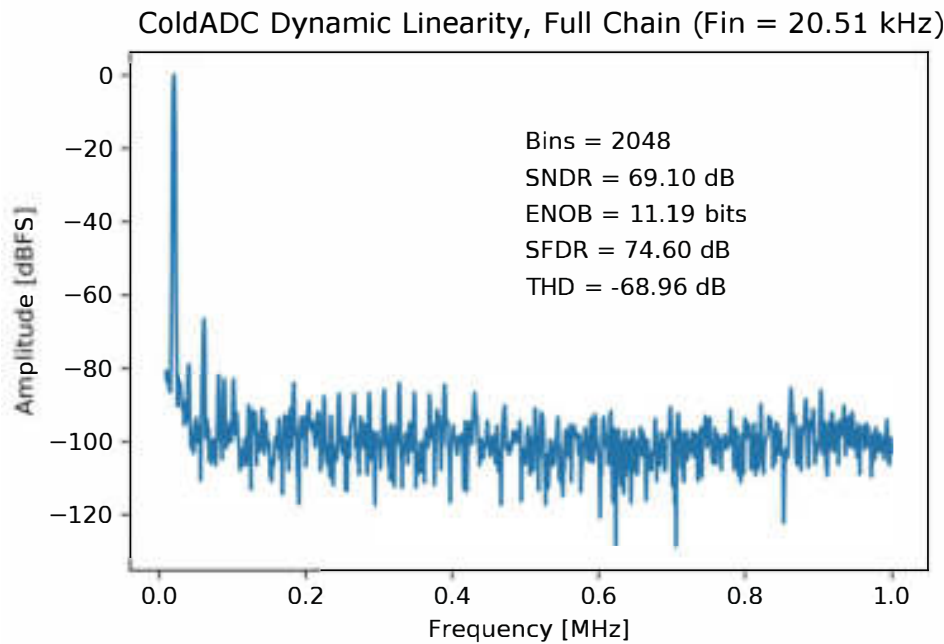


**Figure 4.12.** Fourier transform of ADC codes collected with a coherently sampled sine wave input to a single-ended input buffer.

#### 4.2.3.3 COLDATA ASIC

The COLDATA ASIC was designed by engineers from Fermilab and Southern Methodist University. It is responsible for all communications between the FEMBs and the electronics located outside the cryostat. Each FEMB contains two COLDATA chips. COLDATA receives command-and-control information from a WIB. Each COLDATA provides clocks to four ColdADCs and relays commands to four LArASICs and four ColdADCs to set operating modes and initiate calibration procedures. Each COLDATA receives data from four ColdADCs, merges the data streams, provides 8b/10b encoding, serializes the data, and transmits the data to the warm electronics over two 1.28 Gbps links. These links are driven by line drivers with programmable pre-emphasis. Figure 4.13 is a block diagram of COLDATA.

The commands for the control of all the ASICs on a FEMB are sent from a WIB using an I2C-like protocol [53]. The protocol used in COLDATA differs from the standard I2C one. Because of the long cables required between the WIEC and the FEMBs, COLDATA uses LV differential pairs for both the I2C clock and data. Separate point-to-point links are used for data sent from warm-to-cold and for data sent from cold-to-warm. In order to reduce the number of cables required, only one of the two COLDATA chips on an FEMB has its main I2C interface directly connected to a WIB. That COLDATA chip relays I2C commands and data to the secondary COLDATA chip and relays I2C responses from the secondary COLDATA to the WIB. Each COLDATA also relays I2C commands and data sent from the WIB to one of the four ColdADC chips, and it relays data back to the WIB from one of the four ColdADC chips. The links on the FEMB between COLDATA chips and ColdADC chips use single-ended (2.25 V) CMOS signals.

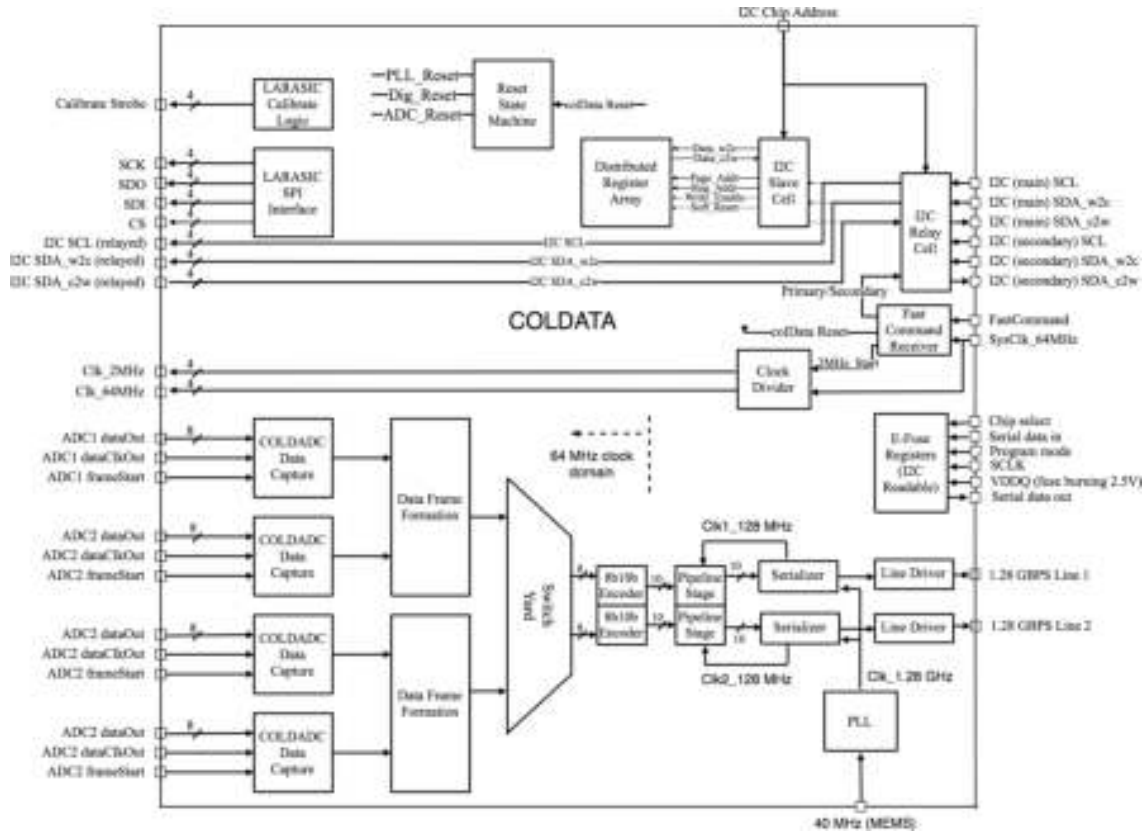
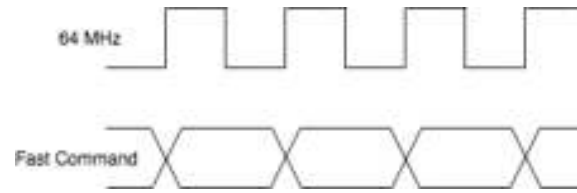


Figure 4.13. COLDATA block diagram.

The controls intended for the LArASIC chips are interpreted inside COLDATA and transmitted to the appropriate ASIC using a Serial Peripheral Interface (SPI)-like interface that uses single-ended (1.8 V) CMOS signals. The configuration registers in LArASIC are configured to be loaded as a single-shift register. As data is shifted into LArASIC on the master out slave in (MOSI) line, bits from the other end of the shift register are shifted out on the master in slave out (MISO) line. It is thus only possible to read LArASIC configuration registers while writing new configuration data.

In addition to the configuration commands, COLDATA receives a master clock and a fast command signal on a LV differential pair from the WIB. Currently the master clock is 64 MHz, but it will be changed to 62.5 MHz to simplify the overall DUNE SP module synchronization, as already discussed in the case of ColdADC. The clock used for sampling the ADC is created inside COLDATA by dividing the master clock by 32. The relative phase of the 2 and the 64 MHz clocks is set by an appropriate fast command sent from the WIB. Both the master clock and the ADC sampling clocks are passed from COLDATA to the four ColdADC chips that it controls. Depending on the master clock frequency the ADC will convert input data every 500 or 512 ns, corresponding to a frequency of 2 or 1.95 MHz. Signals that must be executed at a known time use the fast command line. COLDATA uses the falling edge of the master clock to sample fast command bits as shown in figure 4.14. All legal fast commands are DC balanced. An “alert” pattern is used to establish the 8-bit fast-command word boundary. An “idle” pattern is used when no command is being sent. Four commands are defined: “Edge,” which moves the rising edge of the ADC

sampling clock to coincide with the next rising edge of the master MHz clock; “Sync,” which zeros the 8-bit timestamp that is incremented on the rising edge of each ADC sampling clock; “Reset,” which resets COLDATA; and “Act,” the function of which is determined by an 8-bit register that is programmed using the I2C interface.



**Figure 4.14.** Fast command timing: the leading edges of the fast command and of the master clock are equal time when produced on the WIB. The fast-command bits are captured by COLDATA on the falling edge of the master clock and shifted into a register on the next positive edge.

COLDATA receives digitized waveform data from four ColdADC ASICs. Each ADC presents its data on eight serial streams operating in parallel. Data from the ADCs is captured using the ADC “dataClkOut” signal (one per ADC) and the start of a sample period is indicated by the “frameStart signal” (one per ADC). Each ADC digitizes 16 channels of information and puts out 16 bits of data per channel. Information from two ADCs are merged by a Data Frame Formation block. The Data Frame Formation circuitry converts the two groups of sixteen 16-bit words into one of three types of data frame. For normal data taking, either a 12-bit format or a 14-bit ADC format can be selected, discarding either the four or two lowest order bits. When the 12-bit format is selected, a data frame consists of an 8b/10b command character (K28.2) and an 8-bit time stamp, followed by 48 bytes of ADC data and two bytes of parity information. When the 14-bit format is selected, a data frame consists of an 8b/10b command character (K28.3) and an 8-bit time stamp, followed by 56 bytes of ADC data and two bytes of parity information. Two debugging frame formats are also defined. When the “Frame-12 Test” format is selected, a data frame consists of an 8b/10b command character (K28.0) and an 8-bit time stamp, followed by 48 bytes of predefined data and two bytes of parity information. The final format is used when the ColdADCs are read out in debug mode. In this case, 30 bits of raw pipeline stage data are read out from one of the two pipelined ADCs in each ColdADC ASIC and passed from ColdADC to COLDATA using two 16-bit frames. When the “Frame-15” format is selected, a COLDATA output data frame consists of an 8b/10b command character (K28.6) and an 8-bit time stamp, followed by 60 bytes of ADC data (30 bytes from each ColdADC). No parity information is generated when this format is selected. This is to ensure that at least one idle character (K28.1) will be sent between each “Frame-15.” A series of 8b/10b command characters (K28.5) is sent at the end of each frame of 12-bit or 14-bit data to ensure synchronization of the high-speed links.

The serializers and output drivers operate asynchronously in a separate clock domain that is not related to the master clock signal received from the WIB. Instead they use clocks derived from a 40 MHz micro-electromechanical system oscillator on the FEMB. A single PLL generates a 1.28 GHz clock for both serializers and output drivers. The 10-bit serializers are implemented using two 5:1 multiplexers (clocked at 128 MHz) followed by a single 2:1 multiplexer (clocked at 640 MHz). Each serializer derives the 640 MHz and 128 MHz clock from the 1.28 GHz clock



provided by the PLL and provides its 128 MHz clock to the Data Frame Formation block, which uses it at the output stage of a clock-domain-crossing FIFO. A link synchronization sequence of 8b/10b command characters (K28.5) is used when the link is reset to establish the boundary between 10-bit “words.” Idle characters (K28.1) are inserted by the Data Frame Formation block when no data is ready for serialization (between data frames). The 1.28 Gbps output drivers include programmable pre-emphasis. The pre-emphasis is achieved using a combination of a voltage mode circuit at the input to the current mode driver and current mode pre-emphasis integrated into the driver circuit. Measurements were made of the insertion loss (“S parameters”) as a function of frequency using 25 m and 35 m lengths of the twinax cable identical to the cable used in ProtoDUNE-SP, and the output driver circuit including pre-emphasis was simulated using a SPICE model based on these measurements. The PLL and serializer circuits used in COLDATA were included in the first partial prototype (CDP1) test chip that was produced in fall 2017 and shown to work as designed. The measured eye diagram after 25 m of twinax cable immersed in LAr using a commercial equalizer on the receiving end is shown in figure 4.15. The pre-emphasis circuit has been added to the current mode driver, which was verified in CDP1 and can be disabled if desired.

A conservative estimation of the power consumption of COLDATA, that is dominated by the power required for the LVDS transmitters and receivers, amounts to 195 mW for each 64-channel ASIC.

Prototype COLDATA chips were received in July 2019 and the first round of room and LN<sub>2</sub> temperature bench tests has been completed. All of the I2C control paths have been verified. COLDATA registers can be written and read using either the LVDS interface or the CMOS interface. ColdADC registers can be written and read using the I2C relay. Fast commands are interpreted as designed; the 2 MHz clock phase can be controlled, and the various “Act” commands are executed as intended. The PLL locks and the link speed is correct. Bench tests of COLDATA were completed in December 2019. Data integrity was verified more completely using test equipment capable of checking for link errors in test periods of days. The LArASIC control path will also be more completely verified and later system tests with packaged ASICs will be performed.

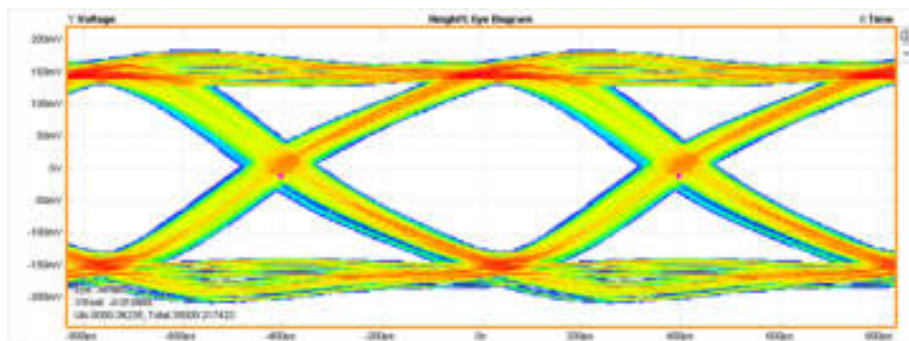


**Figure 4.15.** Eye diagram after 25 m of ProtoDUNE-SP twinax at LN<sub>2</sub> temperature for the COLDATA 1.28 Gbps output link.

#### 4.2.3.4 Alternative ASIC solutions

##### 4.2.3.4.1 Commercial off-the-shelf ADC option

The SBND collaboration has been exploring the COTS ADC option for the TPC readout electronics development since spring 2017 [54]. After a market survey, a few candidate ADCs using the SAR architecture were identified that would continue to operate correctly when immersed in LN<sub>2</sub>. Starting in July 2017, a lifetime study plan was developed to evaluate a COTS ADC option in two different phases: exploratory and validation. The lifetime study focused on the Analog Devices AD7274,<sup>4</sup> implemented in TSMC 350 nm CMOS technology, and has demonstrated better performance in cryogenic operation compared to other candidates.

During the exploratory phase, fresh samples of the COTS ADC AD7274 were stressed with higher than nominal operation voltage, e.g. 5 V, while power consumption (drawn current) was monitored continuously. Periodically, the sample would be operated at nominal voltage (setting the power supply input,  $V_{DD}$ , at 2.5 V, and the voltage reference input,  $V_{REF}$ , at 1.8 V) for a performance characterization test, where both the DNL and INL were monitored and analyzed in addition to the current. Stress test results were used to extrapolate the lifetime of the COTS ADC. The relation between the CMOS transistor lifetime  $\tau$  and the drain-source voltage  $V_{ds}$ ,  $\log \tau \propto 1/V_{ds}$ , is based on the creation of interface states by hot electrons and has been studied in the past extensively [55]. The linear extrapolation of  $\log \tau \propto 1/V_{ds}$  is also used in industry (e.g. IBM) for accelerated stress testing. It was determined that a current drop of 1% on  $V_{DD}$  would be used as the degradation criterion for the lifetime study. Following the development of this criterion, more devices were tested later to validate what was learned in the exploratory phase.

The lifetime projection of the AD7274 ADC from the stress test with  $V_{DD} > 5$  V is shown in figure 4.16. With the AD7274 operating at 2.5 V, which is lower than the nominal 3.6 V for the 350 nm CMOS technology, the projected lifetime is more than  $1 \times 10^6$  years.

Based on the lifetime study of AD7274, a FEMB with the COTS ADC was developed and characterized for the SBND experiment. The integration test was carried out with 40% APA at BNL and showed satisfactory noise performance as seen in figure 4.17. The noise measurements obtained with the 40% APA at BNL indicate that the AD7274 gives a negligible contribution to the overall system noise, as expected given that the ADC has an ENOB of 11.4. The COTS ADC AD7274 serves as a backup solution for the SP module TPC readout electronics system. The current plan is to evaluate this ADC in the small TPC installed in ICEBERG at Fermilab. Ten FEMBs with the COTS ADC have been fabricated and will be used to instrument the ICEBERG TPC for system integration tests in spring 2020. The main drawback of the AD7274 ADC is that it is a single-channel chip, complicating the assembly of the FEMBs.

##### 4.2.3.4.2 CRYO option

The SLAC CRYO ASIC differs from the reference three-chip design by combining the functions of an analog pre-amplifier, ADC, and data serialization along with transmission for 64 wire channels into a single chip. It is based on a design developed for the Enriched Xenon Observatory (nEXO) experiment [56] and differs from it only in the design of the pre-amplifier, which is modified for

<sup>4</sup>AnalogDevices, AD7274™, <https://www.analog.com/en/products/ad7274.html>.

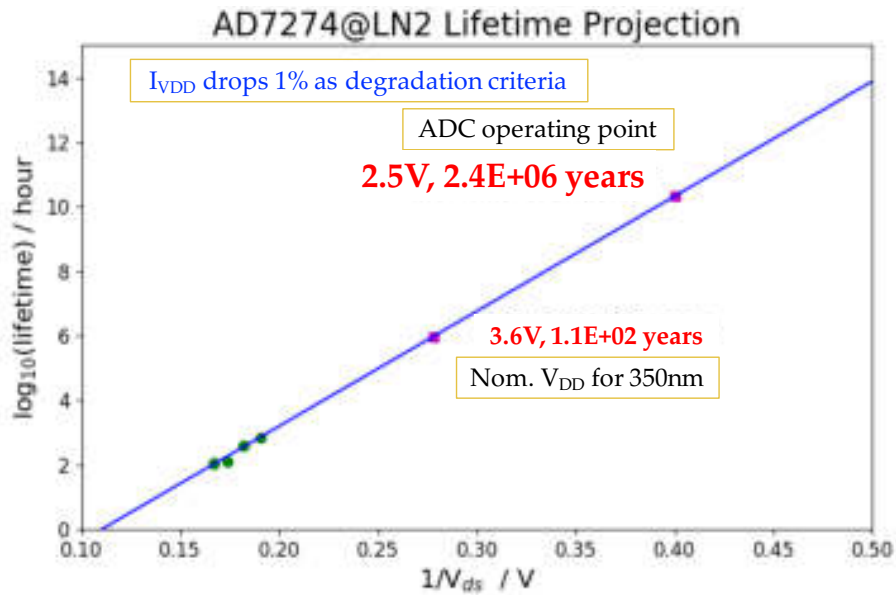


**Figure 4.16.** Lifetime projection of the COTS ADC AD7274 from the stress test with  $V_{DD} > 5\text{ V}$ . The current drop of 1% on  $V_{DD}$  is used as the degradation criterion. With nominal operation voltage of 3.6 V for the 350 nm CMOS technology, the lifetime is projected to be more than 100 years. For SBND and the DUNE FD, the AD7274 will be operated at 2.5 V to add an additional margin; the expected lifetime is more than  $1 \times 10^6$  years.

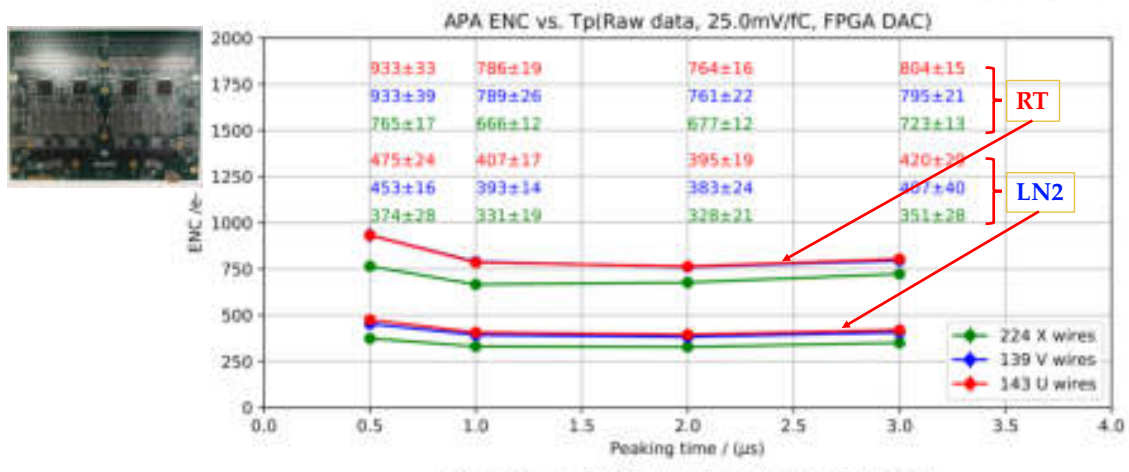


**Figure 4.17.** The noise measurement of FEMBs with COTS ADCs mounted on the 40% APA at BNL. A picture of the FEMB is shown in the top left corner. The induction plane (4 m wire length) has an ENC level of  $\sim 400\text{ e}^-$  with  $1\ \mu\text{s}$  peaking time, while the collection plane (2.8 m wire length) has a noise level of  $\sim 330\text{ e}^-$  with  $1\ \mu\text{s}$  peaking time.

2020 JINST 15 T08010

the higher capacitance of the DUNE SP module wires compared to the short strips of nEXO. The FEMBs constructed using this chip would use only two ASICs, compared to the 18 (eight LArASICs, eight ColdADCs, and two COLDATAs) needed in the reference design. This drastic reduction in part count may significantly improve FEMB reliability, reduce power (40 mW per channel), and reduce costs related to production and testing.

Figure 4.18 shows the overall architecture of the CRYO ASIC, which is implemented in 130 nm CMOS. It comprises two identical 32-channel blocks (banks) and a common section providing biasing voltages and currents, as well as the controls signals, the clocks generation, and the configuration of the registers.

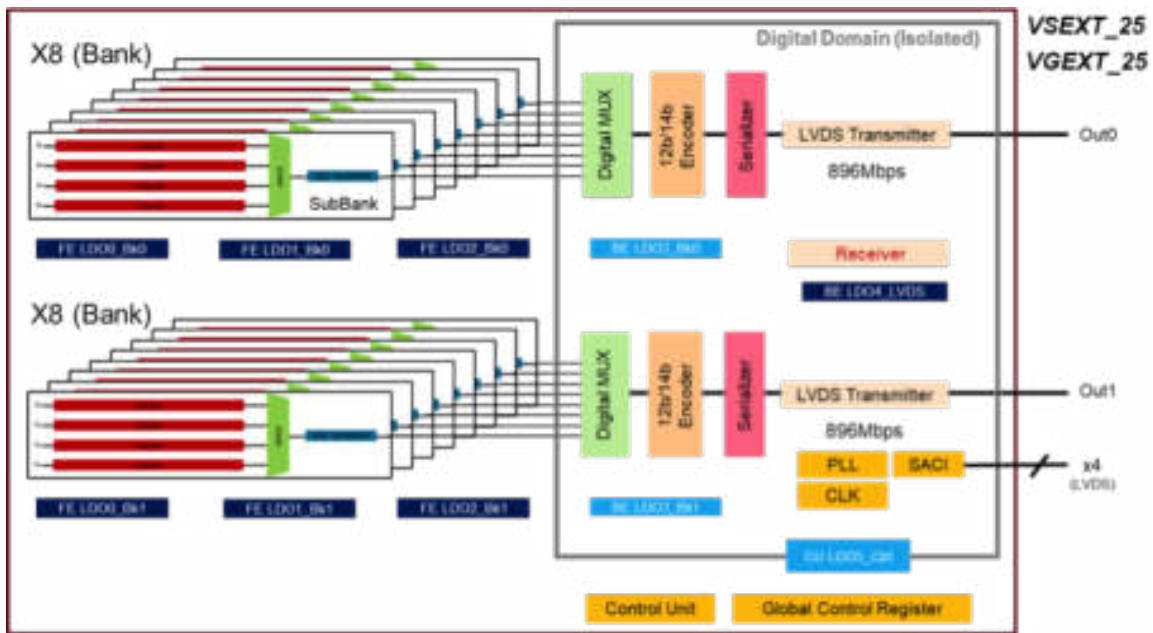


**Figure 4.18.** Overall architecture of the CRYO ASIC.

The current signal from each wire is amplified using a pre-amplifier with pole-zero cancellation [38] and an anti-alias fifth-order Bessel filter (figure 4.19). Provisions are also made for injection of test pulses. Gain and peaking time are adjustable to values similar to those of the reference design. The four programmable gain settings of 6X, 3X, 1.5X, and 1X correspond to full-scale signals of  $3.2 \times 10^5 e^-$ ,  $6.4 \times 10^5 e^-$ ,  $1.28 \times 10^6 e^-$ , and  $1.92 \times 10^6 e^-$ . A filter with a Bessel shape has been chosen because of its flat group delay characteristic that minimizes waveform distortion as well as provides noise shaping performance similar to more classic semi-Gaussian shaper implementations. The four programmable peaking times of the filter are  $0.6 \mu s$ ,  $1.2 \mu s$ ,  $2.4 \mu s$ , and  $3.6 \mu s$ , corresponding to filter bandwidths equivalent to the ones used in the reference solution. Similarly to the reference design with three ASICs, each channel can be configured, independently from the other channels, to have a baseline for operation consistent with either the collection or the induction wires. The outputs of the FE amplifiers can be connected, one-at-a-time, to an analog monitor to probe the analog signal.

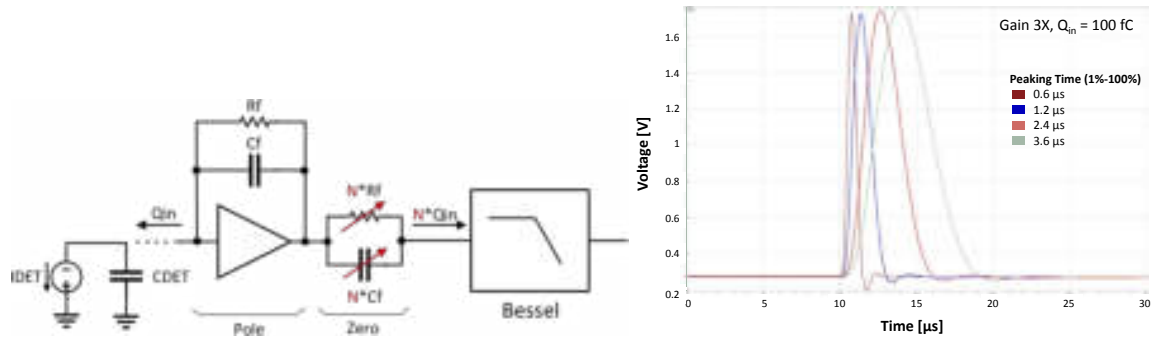


Figure 4.19. CRYO front-end section architecture (left); typical response of the CRYO front-end (right).

Four input channels are multiplexed onto a single fully differential 12-bit 8 MSPS ADC. Signals from the four channels are concurrently sampled onto a sample-and-hold stage. An ADC driver after the multiplexer performs the single-ended to differential conversion. The ADC has a pure SAR architecture (figure 4.20) with a split-cap DAC based on  $V_{cm}$  switching [57], and has the option to be calibrated for offset compensation. External signals can be routed to the input of each single ADC allowing standalone characterization.

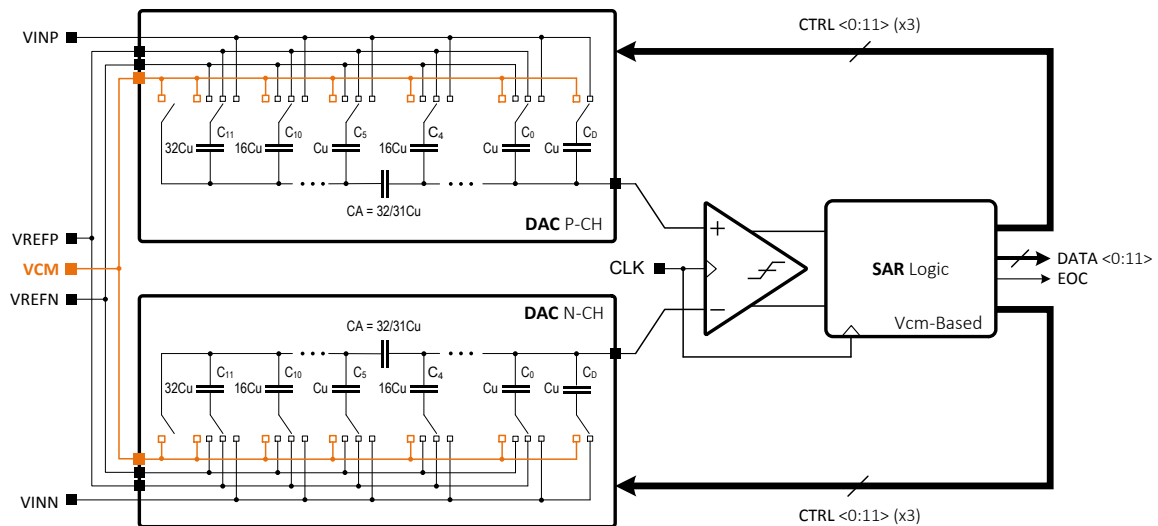


Figure 4.20. CRYO ADC architecture.

The data serialization and transmission block uses a custom 12b/14b encoder, so 32 channels of 12-bit 2 MSPS data can be transmitted with a digital bandwidth of only 896 Mbps, which is significantly lower than the required bandwidth of the reference design (1.28 Gbps).

One key concern with mixed-signal ASICs is the possibility of interference from the digital side causing noise on the very sensitive pre-amplifier. To avoid this interference, the CRYO design uses well established techniques for isolating the substrate; these are described in the literature [58] and have been successfully used in previous ASICs. Furthermore, power domains of the various sections of the ASICs are isolated using multiple internal low-dropout regulators (LDOs).

For reliability purposes the analog section of the ASIC using thick oxide devices is biased at 2 V (20% less than nominal voltage) and does not use minimum length devices. The digital section

of the ASIC uses core devices biased at 1 V (again 20% less than nominal voltage).

The infrastructure requirements for a CRYO ASIC-based system are similar to those of the reference option. However, in most cases, somewhat fewer resources are needed; for instance:

- A single voltage is needed for the power supply. This is used to generate the two supply voltages using internal voltage regulators.
- The warm interface is different. CRYO operates synchronously with a 56 MHz clock, does not require a fast command, and uses the SACI protocol [59] for configuration rather than I2C.

Simulation-based studies have been performed: using the  $1.2 \mu\text{s}$  peaking time and an input capacitance of 220 pF (close to that expected in the SP module), the noise level is approximately  $500 e^-$ , similar to that expected with the reference LArASIC design in LAr with the same input capacitance.

The first iteration of the CRYO ASIC design (see figure 4.21) was submitted to MOSIS for fabrication in November 2018. The first prototypes were delivered at the end of January 2019.

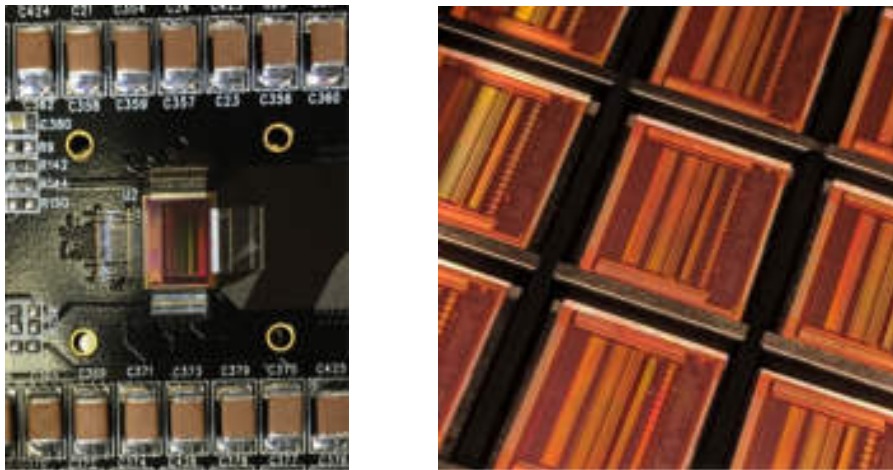


**Figure 4.21.** Photo of the prototype CRYO cold board (left); zoomed-in photo of CRYO ASICs (right).

The prototypes are under test in an existing test stand at SLAC using the CTS described in section 4.3.1. Subsequent system tests are planned using the facilities described in section 4.3.2.

The first prototype of the ASIC is functional at both room temperature and  $\text{LN}_2$  temperature. In particular, all the key blocks have been verified. Configuration of all the 64 channel registers (13 bits each) and the 17 (16-bit) global registers has been verified. Optimization of the register values is ongoing at both room and cold temperature. Initialization procedures for the ASIC power-up have been established. Operation of the on-chip LDOs has been verified and expected supply levels are stable against changes in temperature. The analog monitor can be used to spy on the output of the amplifier for injected pulses on the FE channels, prior to the digitization of these signals by the internal ADCs, as shown in figure 4.22.

Encoded data are transmitted and correctly decoded in the external FPGA. Figure 4.23 shows an example of a pulse injected in a channel visible on both the analog monitor as well as in the data acquired by the ASIC. Data are acquired at  $\text{LN}_2$  temperature at the nominal  $\sim 2 \text{ MSPS}$  rate.

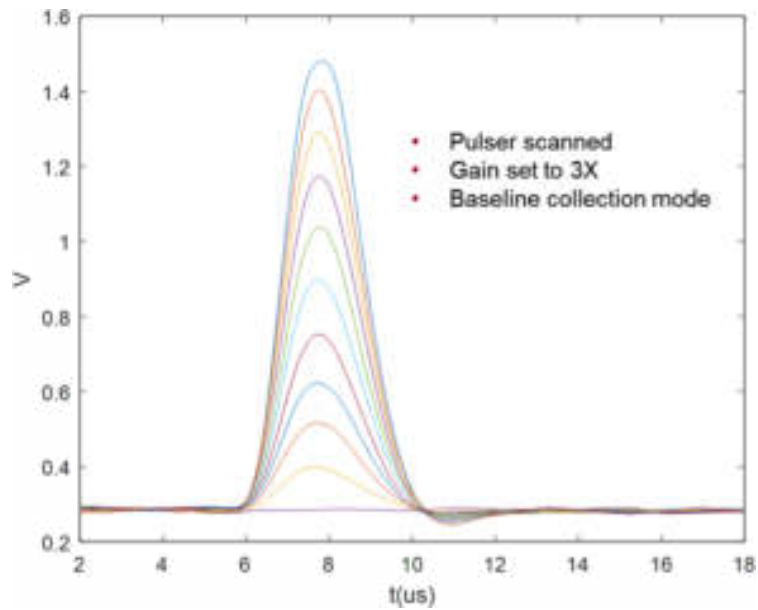


**Figure 4.22.** CRYO ASIC front-end response at liquid nitrogen temperature, presented at the analog monitor and acquired with an external 50 MSPS ADC.

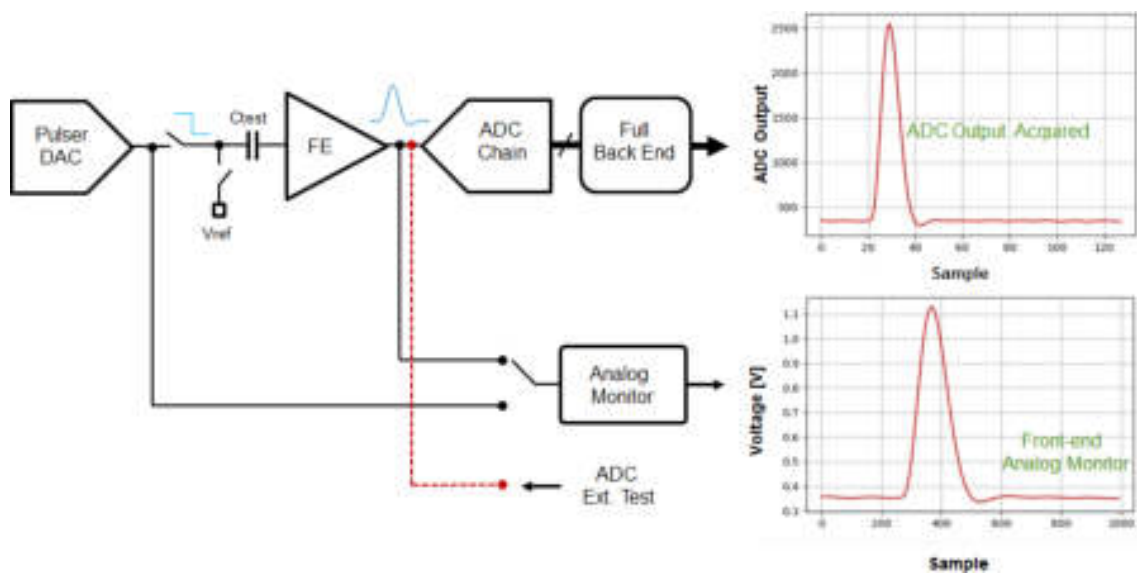


**Figure 4.23.** Example of a pulse injected in a CRYO ASIC channel, visible on both the analog monitor and in the output data.

From the functional point of view, a single unexpected behavior has been identified in the digital multiplexer that is used at the input of the encoders. The latches at the input of the multiplexer show poor driving capability, resulting in the presence of a ghost from a previously multiplexed channel. The effect is not present on the first 12 channels of each block which show expected behavior. The effect has been replicated in simulation and a trivial fix has been implemented for the next version of the ASIC.

Initial results on the performance of the ADC block of CRYO have been obtained by directly injecting a linear voltage ramp (generated by an external 20-bit DAC) into the ADC. The distributions of the DNL and INL obtained from these measurements are shown in figure 4.24. The maximum deviations of the DNL and INL from the reference signal are 0.74 and 1.27 ADC counts, respectively, within a usable dynamic range of  $\sim 3000$  ADC counts. From these distributions, the values of 65.75 dB and of 10.63 are estimated for the SNDR and ENOB, respectively. These results indicate that, from a static point of view, the ADC block of CRYO meets the required performance for the DUNE TPC readout. Further work is ongoing to characterize the dynamic response of the ADC and to determine the overall linearity and noise performance of the entire readout chain including the FE amplifier.

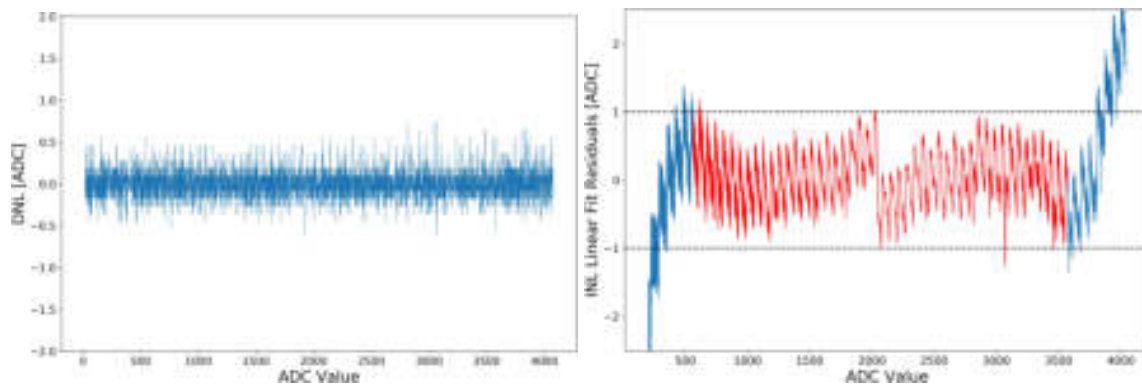


**Figure 4.24.** Distribution of the DNL (left) and INL (right) for the ADC block of CRYO.

#### 4.2.3.5 Procedure and timeline for ASIC selection

We are currently pursuing two different ASIC designs and planning on qualifying the COTS ADC solution that will be used for the SBND experiment. We plan to continue developing both the three-ASIC solution and the CRYO ASIC for at least a second iteration before deciding which ASIC solution to implement in the DUNE SP module. This plan requires that multiple versions of the FEMB are also designed and tested. The FEMBs populated with the first set of prototypes of the two kinds of ASICs will be available in spring 2020 and are expected to perform similarly to the boards used for ProtoDUNE-SP. We plan to review the results of the system tests and of the component lifetimes discussed in section 4.3 in early 2020. In that review, we will also decide whether to change anything on the list of specifications for the ASICs and to further develop the two custom ASIC solutions, including fixing any issues found during the tests of the first version of the ASICs. We expect that the subsequent iteration of the design, fabrication, and testing of the ASICs and FEMBs will take an additional twelve months. At the end of this process, when results



from standalone tests of the ASICs and system tests of the FEMBs are available, we will have all the information required to select the ASIC solution to be used in DUNE. We are assuming that the second design iteration of the ASICs design will meet all the DUNE requirements. The schedule for the construction of the DUNE SP module currently has between eight and fourteen months of float for the ASICs and FEMBs, which would allow for a third design iteration, if needed, as discussed in section 4.9.2. This does not apply for the second run of ProtoDUNE-SP (discussed later in section 4.3.2.1). Ideally, the ASICs from the engineering run would be used for the second run of ProtoDUNE-SP, but this is not compatible with the currently planned date for the installation of the FEMBs on the APAs. In order to meet the current goal for the starting date of the second run of ProtoDUNE-SP, ASICs from the second round of prototyping would have to be used. In case a third round of prototypes is necessary, the second run of ProtoDUNE-SP would have to be delayed by one year.

The selection of the ASIC(s) to be used for the construction of the SP detector module will be based on performance, reliability, power density criteria, as well as consideration of the costs and resources required during the construction and testing of the FEMBs. We have not yet decided the weights to assign to these criteria. Reliability would in principle favor the single-ASIC solution that requires FEMBs with fewer connections, while power density considerations could be less favorable to CRYO option. We plan to charge a committee to draft a series of recommendations on the ASIC selection in spring 2020, at least one year ahead of the expected decision date. These recommendations could also inform the second cycle of design for ASICs and FEMBs. Once the second cycle of design and testing is complete, these recommendations will be used by the committee charged with the final design review to suggest a preferred option for the ASIC solution. The committee's recommendation will then be passed to the DUNE executive board (EB), which is tasked with the final ASIC decision.

#### 4.2.4 Infrastructure inside the cryostat

Each FEMB is enclosed in a mechanical CE box to provide support, cable strain relief, and control of bubbles of gaseous argon generated by heat from an FEMB attached to the lower APA, which could, in principle, lead to discharge of the HV system. The CE box, illustrated in figure 4.25, is designed to make the electrical connection between the FEMB and the APA frame, as discussed in section 4.2.1. Mounting hardware inside the CE box connects the ground plane of the FEMB to the box casing. If argon bubbles form inside the CE box, they must get channeled through the two side tubes of the APA's frame, from where they would reach the top of the cryostat. As already discussed in section 4.1.2, a test setup has been prepared at BNL to measure the maximum power that can be dissipated in LAr at a depth equivalent to that of the FEMBs installed on the bottom APA. Initial measurements indicate that the ASICs mounted on the FEMBs are not going to cause boiling of the LAr inside the CE boxes. We have measured the power required to cause boiling at a pressure equivalent to that of 12 m of LAr. We have also observed that with the current ASIC designs and power dissipation we have a safety factor of 20 in terms of total power and of at least two in terms of power density. These measurements will be repeated once prototype FEMBs with the three-ASIC and CRYO solutions become available.

The CE box casing is electrically connected to the APA frame via the metal mounting hardware called the "Omega bracket" (not shown in figure 4.25). The input amplifier circuits are connected



**Figure 4.25.** Prototype CE box used in ProtoDUNE-SP.

to the CR board and terminate to ground at the APA frame, as shown in figure 4.3. As a backup solution, the casing is also connected to the APA frame via a wire.

In addition to the CE box and mounting hardware, cable trays for support and routing the cold cables will be installed in the cryostat. One set of cable trays, shown in figure 4.26 (left column), will be attached to the upper APAs to hold the CE and PD cables. A different cable tray design, also shown in figure 4.26 (right column), will support the CE cables underneath the lower hanging APAs. A final set of cable trays will be installed inside the cryostat after the APAs are fixed in their final location to support the cables as they are routed to the CE and PD feedthroughs.

#### 4.2.5 Cold cables and cold electronics feedthroughs

All cold cables originating inside the cryostat connect to the outside warm electronics through PCB feedthroughs installed in the signal flanges that are located on the cryostat roof. The data rate from each FEMB with four cables is sufficiently low ( $\sim 1$  Gbps) that LVDS signals can easily be driven over more than 22 m of twin-axial transmission line. Additional transmission lines are available to distribute LVDS clock and control signals, which are transmitted at a lower bit rate. The connections between the WIBs on the signal flanges and the DAQ (see chapter 7) and slow control systems (see chapter 8) are made using optical fibers.

The design of the signal flange includes a four-way cross spool piece, separate PCB feedthroughs for the CE and PD system cables, and an attached crate for the TPC warm electronics, as shown in figure 4.27. The wire bias voltage cables connect to standard SHV connectors machined directly into the CE feedthrough, ensuring no electrical connection between the wire bias voltages and other signals passing through the signal flange. Each CE feedthrough serves the bias voltage, power, and digital I/O needs of one APA.

Data and control cable bundles send system clock and control signals from the signal flange to the FEMB and stream the  $\sim 1$  Gbps high-speed data from the FEMB to the signal flange. Each FEMB connects to a signal flange via one data cable bundle, leading to 20 bundles between one APA and one flange. For the reference ASICs configuration, ten low-skew shielded twin-axial cables are required to transmit the following differential signals between the WIB and the FEMB:

- four 1.28 Gbps data lines (two from each COLDATA);
- two 64 MHz clock signals (one input to each COLDATA);

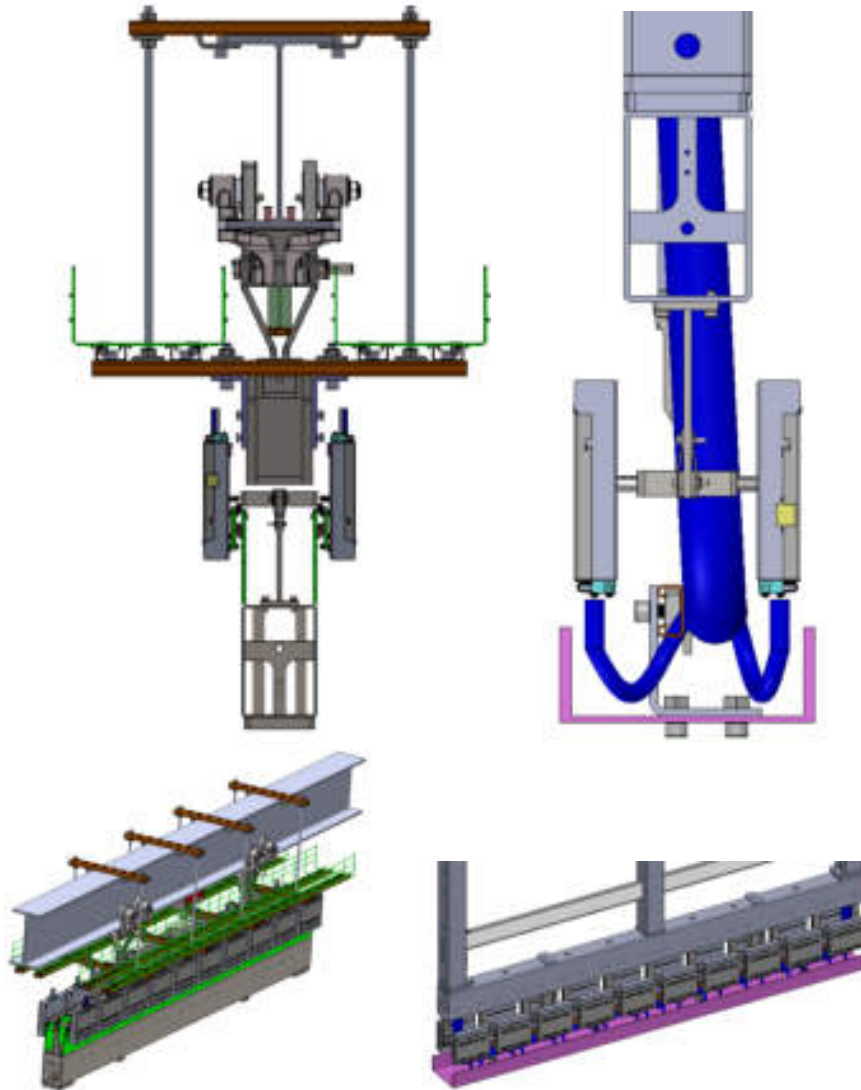


**Figure 4.26.** Side and end views of mechanical supports for the CE boxes on the upper (left column) and lower (right column) APAs. Shown are the APA cable trays in green and pink, the CE boxes in dark gray, and the Omega brackets and mounting hardware between the CE boxes and APA frame in light gray. The CE cables are shown in blue; the PD cables are not shown.

- one fast command line (shared between the two COLDATA ASICs); and
- three I2C-like control lines (clock, data-in, and data-out, also shared between the two COLDATA ASICs).

As discussed later, this number of connections is compatible with routing the cables that bring the power and transmit the data and controls for the lower APA through the APA frames. We are making the assumption that the fast command line can be shared between the two COLDATA ASICs, but will also consider other possibilities, like sharing the 64 MHz clock between the two ASICs or increasing the data transmission speed to 2.56 Gbps, thereby reducing the number of

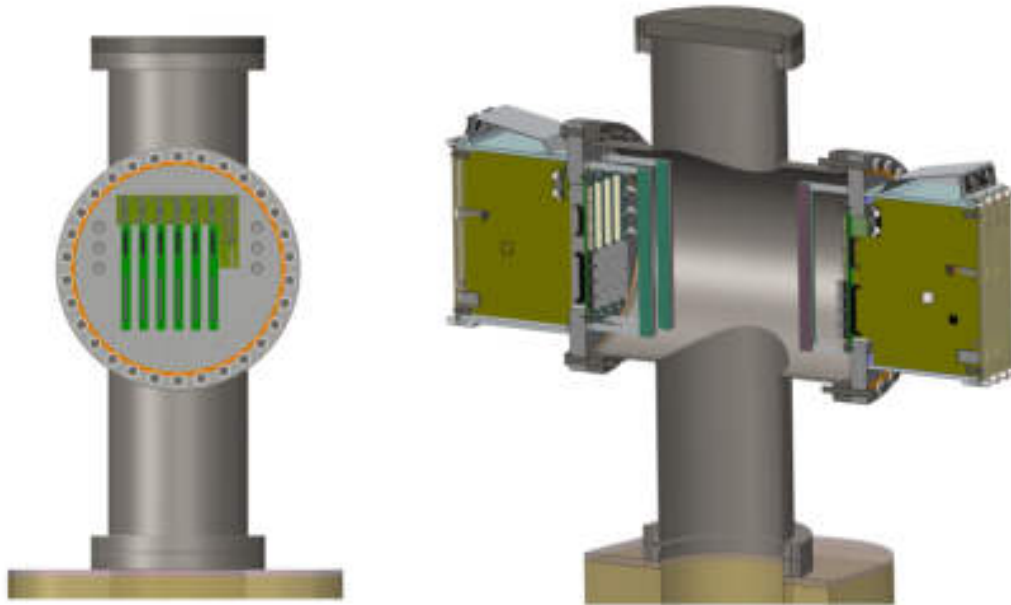


**Figure 4.27.** TPC CE feedthrough. The WIBs are seen edge-on in the left panel and in an oblique side-view in the right panel, which also shows the warm crate for an SP module in a cutaway view.

data transmission lines to two for each FEMB. This assumption will be tested as soon as the first prototypes of COLDATA become available.

The LV power is passed from the signal flange to the FEMB by bundles of 20 AWG twisted-pair wires, with half of the wires serving as power feeds and the other half as returns. Using the measured power consumption for LArASIC and ColdADC and the estimates for COLDATA, the total power required to operate each FEMB is estimated as 6 W (2.4 A at 2.5 V), including the power dissipated in the linear voltage regulators. This assumes that linear voltage regulators are used on the FEMB to reduce the 2.5 V provided by the WIB down to the various voltages required by the three ASICs:

- 1.8 V for LArASIC, and
- 2.25 V and 1.1 V for ColdADC and COLDATA.

We currently assume that only 2.5 V will be provided by the WIB, since the largest fraction of the power required by the FEMB is at 2.25 V. We are currently planning on using a total of eight 20 AWG twisted-pair wires, seven of which will be used for bringing the 2.25 V to the FEMB, with the eighth one reserved for the 5 V bias for the linear voltage regulators (this connection carries a very low current). With this cable plant, the resistance of the cable bundle is 41 m $\Omega$  for the upper APAs (9 m cable length) and 101 m $\Omega$  for the lower APAs (22 m cable length). To account for the voltage drop along the wires and the returns in the case of operation at room temperature, prior to filling the cryostat, the WIB needs to provide 2.7 V and 3.0 V for the upper and lower APAs, respectively. For one FEMB, the power dissipated in the cables is 0.5 W and 1.2 W for the upper and lower APAs, respectively. The values for the power dissipated in the cables are reduced by a factor of three for operation in LAr, which allows for a reduction of the voltage provided by the WIB. The voltage drop and power dissipation values are summarized in table 4.3. We will

also consider the possibility of using one pair of wires to deliver a separate voltage to LArASIC (2.0 V that will be reduced to the required 1.8 V on the FEMB). This solution may provide a better overall noise performance for the readout electronics, but will have a slightly larger voltage drop on the cold cables. The size of the cable bundles planned for DUNE represents a small reduction compared to that used for ProtoDUNE-SP, where bundles of nine 20 AWG twisted-pair wires were used. Overall, the total resistance of the power return wires are 2 m $\Omega$  and 5 m $\Omega$  for the upper and lower APAs, respectively, numbers that are reduced by a factor of three for operation in LAr. For each APA pair, the total power dissipated inside the power cables ( $\sim 11$  W at LAr temperature) is small compared to the total power dissipated in the FEMBs, 240 W.

**Table 4.3.** Voltage drop and power dissipation in the cables bringing power to the FEMBs at room and at LAr temperature for the cable lengths corresponding to the upper (9 m) and the lower (22 m) APAs. The FEMBs require 2.4 A at 2.5 V to operate. At room temperature, the resistances of the seven 20 AWG twisted-pair wires are 41 m $\Omega$  and 101 m $\Omega$  for the upper and the lower APAs, respectively. These resistances are reduced to 14 m $\Omega$  and 34 m $\Omega$  inside the LAr.

|                               | Voltage       | Voltage drop  | Power dissipation |
|-------------------------------|---------------|---------------|-------------------|
| WIB output (room temperature) | 2.7 V / 3.0 V | 0.2 V / 0.5 V | 0.5 W / 1.2 W     |
| WIB output (LAr temperature)  | 2.6 V / 2.7 V | 0.1 V / 0.2 V | 0.25 W / 0.5 W    |

The cable plant for one APA in the LAr also includes the cables that provide the bias voltages applied to the  $X$ -,  $U$ -, and  $G$ -plane wire layers, three FC terminations, and an electron diverter, as shown in figure 4.3. The voltages are supplied through eight SHV connectors mounted on the signal flange. RG-316 coaxial cables carry the voltages from the signal flange to a patch panel PCB mounted on the top of the APA that includes noise filtering. From there, wire bias voltages are carried by single wires to various points on the APA frame, including the CR boards, a small PCB mounted on or near the patch panel that houses a noise filter and termination circuits for the FC voltages, and a small board mounted near the electron diverter that also houses the wire bias voltage filter described in section 4.2.2.

In sections 2.4.3 and 4.6.1 we discuss the problem of routing the cold cables (data, control, power, and bias voltages) for the bottom APAs through the frames of both the top and bottom APAs. Routing tests were initially performed with the ProtoDUNE-SP cable bundles, and even after increasing the cross section of the side tubes from  $7.62 \times 7.62$  cm<sup>2</sup> (3"  $\times$  3") to  $10.16 \times 10.16$  cm<sup>2</sup> (4"  $\times$  4"), routing was difficult. After understanding that we could reduce the number of cables, we ran a second set of tests with fewer sets of cables (nine rather than ten sets of 12 data and control cables, nine rather than ten sets of nine twisted-pair wires for power, and eight bias voltage cables as before). This insertion test was successful once a 6.35 cm (2.5") diameter conduit was inserted inside the APA frame to present a uniform cross section to the cables and the cables were restrained with a mesh. These tests have been successfully repeated in October 2019 at Ash River using the setup with two stacked APA frames, described in section 2.3.3.

The cable plant discussed above for the reference design with the three ASICs can be used also for FEMBs populated with the CRYO ASIC. In that case, the power requirements are reduced (5 W at 2.5 V), and the internal LDOs do not require an external bias line. Six of the eight 20 AWG

twisted-pair wires could be used to bring the low-voltage power to the FEMB, while the remaining two could be used to sense the voltage on the FEMB. This configuration would entail a small increase ( $\sim 14\%$ ) of the total resistance seen on the return wires. The same number of low-skew shielded twin-axial cables are required to transmit the following differential signals between the WIB and the FEMB:

- four 896 Mbps data lines (two from each CRYO ASIC);
- two 56 MHz clock signals (one for each CRYO ASIC); and
- four shared SACI signals.

In the current design of CRYO ASIC a total of five SACI signals are required: three of them are shared between the two ASICs on the FEMB, and two separate ones are required to send commands to the two CRYO ASICs. We are planning to implement internal addresses in a future version of CRYO, such that the two ASICs can share the command line.

The proposed cable plant is also compatible with the use of the COTS ADC. The current design of the SBND FEMB uses 12 low-skew shielded twin-axial cables, instead of ten, but some of the signals are not used. The low-voltage power is transmitted with a bundle of nine 20 AWG twisted-pair wires, but two of them are used for the bias of the linear voltage regulators, which require very little current.

In all possible configurations of the FEMB, it is very likely that the cable plant required to bring the low-voltage power and controls to the FEMBs and to read out the data from the FEMBs is compatible with the option of routing the cables through the APA frames. This, however, does not leave much room for building redundancy in the system. The cable connections need to be extremely reliable because the loss of one connection could result in an entire FEMB becoming unresponsive.

### 4.2.6 Warm interface electronics

The warm interface electronics provide an interface between the CE, DAQ, timing, and slow control systems, including local power control at the flange and a real-time diagnostic readout. They are housed in the WIECs attached directly to the CE flange. A WIEC, shown in figure 4.28, contains one PTC, five WIBs and a passive PTB that fans out clock signals and LV power from the PTC to the WIBs. The WIEC must provide Faraday-shielded housing and robust ground connections from the WIBs to the detector ground (section 4.2.1). Only optical connections are used for the communication to the DAQ and the slow controls, to avoid introducing noise in the CE feedthrough.

The WIB receives the system clock and control signals from the timing system and provides processing and further distribution of those signals to four FEMBs. It also receives high-speed data signals from the same four FEMBs and transmits them to the DAQ system over optical fibers. The data signals from the FEMBs are recovered on the WIB with commercial equalizers. The WIBs are attached directly to the TPC CE feedthrough on the signal flange. The feedthrough board is a PCB with connectors to the cold signal and LV power cables fitted between the compression plate on the cold side and sockets for the WIB on the warm side. Cable strain relief for the cold cables is provided from the back end of the feedthrough.

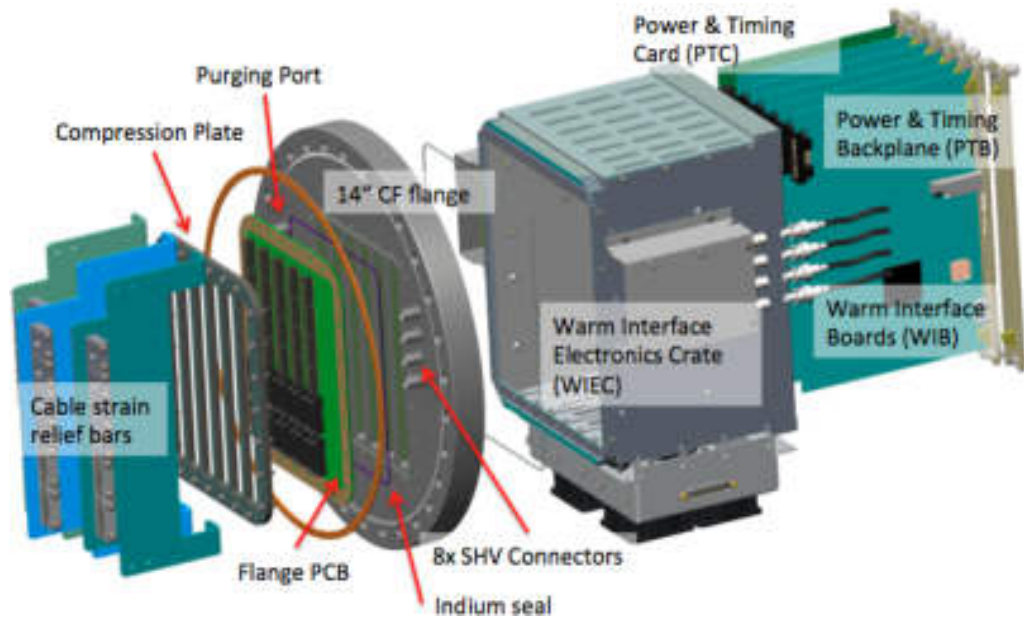


**Figure 4.28.** Exploded view of the CE signal flange for ProtoDUNE-SP. The design for the DUNE SP module CE signal flange will be very similar (with two CE signal flanges per feedthrough).

The PTC provides a bidirectional fiber interface to the timing system. The clock and data streams are separately fanned out to the five WIBs as shown in figure 4.29. A clock-data separator on the WIB separates the signal received from the timing system into clock and data signals. Timing endpoint firmware for receiving and transmitting the clock is integrated into the WIB FPGA. The SP module timing system, described in section 7.3.7, is a further development of the ProtoDUNE-SP system and is expected to have nearly identical functionality at the WIB endpoint.

The PTC receives 48 V LV power for all TPC electronics connected through the TPC signal flange: one PTC, five WIBs, and 20 FEMBs. The LV power is then stepped down to 12 V via a DC-DC converter on the PTC. The output of the PTC converters is filtered with a common-mode choke and fanned out on the PTB to each WIB, which provides the necessary 12 V DC-DC conversions and fans the LV power out to each of the FEMBs supplied by that WIB, as shown in figure 4.30. The output of the WIB converters is also filtered by a common-mode choke, and each voltage line provided to the FEMBs is individually controlled, regulated, and monitored.

Because the WIBs can provide local power to the FEMB and real-time diagnostic readout of all channels, each TPC electronics system for each APA is a complete, stand-alone readout unit. The FEMBs and cold cables are shielded inside the cryostat, and the WIBs and PTC are shielded inside the Faraday cage of the WIEC, with only shielded power cables and optical fibers connecting to external systems.

As shown in figure 4.31, the WIB can receive the encoded timing signal over bidirectional optical fibers on the front panel; it can then process them using either the on-board FPGA or clock synthesizer chip to provide the clock required by the TPC electronics. The reference ASIC design currently uses 8b/10b encoding; if the SLAC CRYO ASIC is selected for the DUNE SP module, 12b/14b encoding will be used instead of 8b/10b.

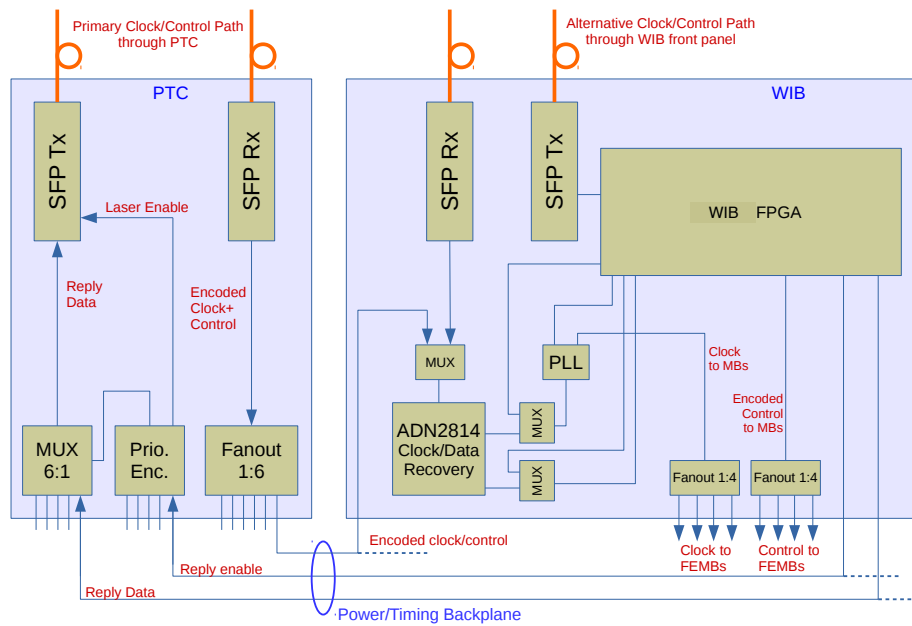


**Figure 4.29.** PTC and timing distribution to the WIB and FEMBs used in ProtoDUNE-SP. A similar design will be adopted for the DUNE SP module.

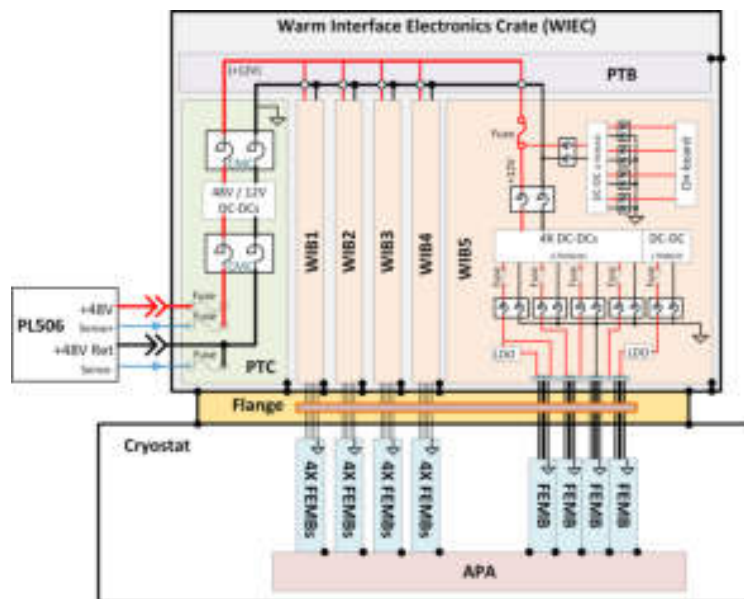


**Figure 4.30.** LV power distribution to the WIB and FEMBs for DUNE. In the current design, up to four separate voltages can be provided from the WIB to each FEMB. Measurements with prototype FEMBs will inform the final design of the power distribution, and the number of different voltages sent to the WIB will be chosen to reduce the voltage drops along the cold cables and to minimize the readout noise.

2020 JINST 15 T08010



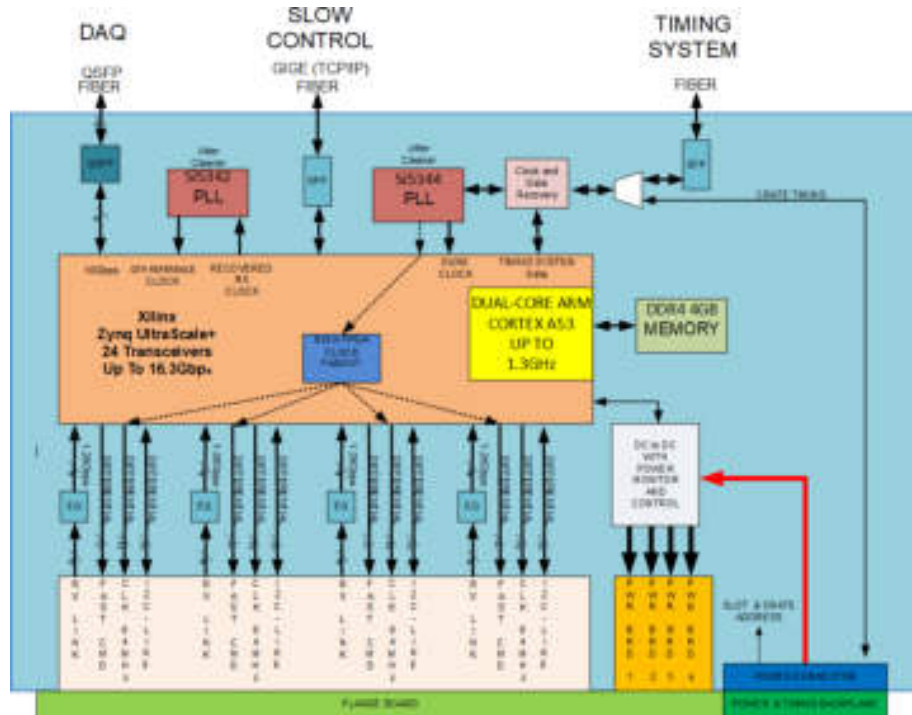


**Figure 4.31.** WIB block diagram including the fiber optic connections to the DAQ backend, slow controls, and the timing system, as well as the data readout, clock, and control signals to the FEMBs.

The FPGA on the WIB will have transceivers that can drive the high-speed data to the DAQ system up to 10 Gbps per link, meaning that all data from two FEMBs ( $2 \times 5$  Gbps) could be transmitted on a single link. The FPGA will have an additional transceiver I/O for an optical 1 Gbps Ethernet connection, which provides real-time monitoring of the WIB status to the slow control system.

For system tests, discussed later in section 4.3.2, the WIEC, WIB, and PTC developed for ProtoDUNE-SP are being used. A special version of the WIB has been developed for use with FEMBs equipped with the CRYO ASIC, which require a different power and clock distribution scheme. Plans are being put in place to redesign the WIB, and eventually make minor changes also to the PTC and the WIEC, to use less expensive FPGAs and to be able to program independently the voltage rails used to provide power to the FEMBs. While in the current WIB it is possible to monitor and turn on and off these voltage rails independently, the redesign will include the capability of setting independent voltage and current limits on each one of them. In addition, it is planned to add the possibility of measuring the delay of the propagation of the clock signals between the WIB and the FEMBs. With this feature, it will be possible to align the sampling time of different FEMBs to a precision of a few ns in situ without relying on the measurement of the cable lengths, which was necessary in ProtoDUNE-SP.

#### 4.2.7 Timing distribution and synchronization

The charge deposited on each wire of the APAs installed in the DUNE SP module is digitized at a frequency of 2 MHz, as discussed in section 4.1.2. This requires that the TPC electronics

be synchronized to a level of the order of 10 ns, which is much smaller than the time difference between two charge samples. This level of error in the synchronization between the sampling time of different FEMBs contributes negligibly to the expected resolution of the reconstructed space points measurement, both in the APA plane and along the drift distance. The timing distribution and synchronization system for the SP module is described in section 7.3.7. Each WIEC has a bidirectional optical connection with the timing system in the PTC. Inside the PTC the optical signal from the timing system is converted, as discussed in the previous section, to an electrical signal and distributed via the backplane to the WIBs that constitute an endpoint for the timing distribution system. Each WIB contains a standalone jitter-reducing PLL that forwards the clock to all the FEMBs. The FPGA contained inside the WIB implements the protocol [60, 61] for aligning the phase of the clock at the endpoint of the distribution tree.

The timing distribution and synchronization system ensures that all the WIBs are synchronized to within 3 ns. One possible way of synchronizing the FEMBs is the one that was used in ProtoDUNE-SP, which relies on the fact that all the cables connecting the WIBs to the FEMBs have approximately the same length (a length difference of 0.5 m corresponds to a difference in the sampling time of 2.5 ns). The same approach could be used for the DUNE SP module, correcting for the top-bottom APA cable length difference (corresponding to  $\sim 65$  ns) inside the FPGA of the WIB. The exact correction factor could be obtained by measuring the time propagation difference for a sample of short and long cables prior to the installation of the FEMBs on the APAs. Synchronizing the CE with the PD system requires one additional time constants that correspond to the transit time of the fast command sent from the WIB to COLDATA and from there to the ColdADC, which includes the propagation time along the cables (45 ns for the 9 m long cables to the top APAs and 110 ns for the 22 m long cables to the bottom APAs) plus the propagation time inside the ASICs. This overall time constant can be obtained offline from the data, but it represents at most a correction of  $O(150 \mu\text{m})$  on the position of a track along the drift distance. Instead of relying on cable measurements, we are also considering the addition of a timer inside the WIB's FPGA to measure the transit time of a command sent to the FEMB and its corresponding return message. This study will help us understand whether the relative phases of the FEMB and the WIB can be aligned more precisely.

The communication between the WIB and the DAQ backend is asynchronous and the 64-bit time-stamp, which is used to indicate the time at which the signal waveform was sampled 7.3.7, is inserted in the data frame in the WIB's FPGA. For the three-ASIC solution, the communication from the FEMB to the WIB is also asynchronous and a 8-bit time stamp is sent to count the number of ADC samples (triggered by the FEMB with a fast command) from the last "Sync" signal, as discussed in section 4.2.3.3. This 8-bit time stamp is used only to ensure that the FEMB and the WIB are still synchronized.

In contrast to the three-ASIC solution, in the CRYO solution the communication between the FEMB and WIB is entirely synchronous, and instead uses a 56 MHz clock. In order to properly align the phase of the ADC sampling for the top and bottom APAs, appropriate delays must be added to the sampling command in the WIB's FPGA. The requirements listed above for synchronizing the CE relative to the PD system remain valid for this case.

#### 4.2.8 Services on top of the cryostat

Table 4.4 summarizes the power requirements of the FEMBs, WIBs, and WIECs, which were discussed in sections 4.2.5 and 4.2.6. As shown in figure 4.30, each PTC receives 48 V from a power supply installed on the top of the cryostat; this voltage is stepped down via voltage regulators to 12 V, which is distributed to each WIB. Inside each WIB the 12 V is further reduced to the 2.7 or 3.0 V that is used to power the FEMBs, as discussed in section 4.2.5. For these estimates, an efficiency of 80% is assumed for each voltage regulation step, while the power requirements for the FPGA and the optical components on the WIBs are based on the measurements from ProtoDUNE-SP.

The overall power required for each WIEC is in the range 335 W to 360 W, corresponding to the range 7 A to 7.5 A at 48 V. The LV power is delivered to the PTC using a power mainframe that can operate in the 30 V to 60 V range, providing a maximum of 13.5 A and 650 W to each APA. Using a 10 AWG cable, and assuming a distance of 20 m between a LV power supply on the detector mezzanine and the most distant cryostat penetration for a row of APAs, no voltage drop over 1 V should occur along the cable. At most  $\sim 150$  W is dissipated inside the cryostat, and another  $\sim 200$  W is dissipated inside the (air-cooled) WIEC; only a few watts are dissipated in the warm cables located below the false flooring on top of the cryostat. Multiplying by the total number of WIECs, less than 1 kW of power is dissipated in the cabling system over the entire surface of the cryostat.

**Table 4.4.** Power requirements for the FEMBs, WIBs, and PTCs.

| Component  | Current        |                | Power |
|--|----------------|----------------|-------|
| FEMB (assume 80% efficiency in the 12 V $\rightarrow$ 2.7/3.0 V conversion)          |                |                |       |
| Lower APA  | 2.4 A at 2.7 V | 0.68 A at 12 V |       |
| Upper APA  | 2.4 A at 3.0 V | 0.75 A at 12 V |       |
| WIB (4 FEMB + FPGA, assume 80% efficiency in the 48 V $\rightarrow$ 12 V conversion) |                |                |       |
| 4 FEMBs lower APA  | 2.7 A at 12 V  |                |       |
| 4 FEMBs upper APA  | 3.0 A at 12 V  |                |       |
| FPGA and optical components  | 1.7 A at 12 V  |                |       |
| Total lower APA  | 4.4 A at 12 V  | 1.4 A at 48 V  | 67 W  |
| Total upper APA  | 4.7 A at 12 V  | 1.5 A at 48 V  | 72 W  |
| WIEC (5 WIBs + PTC)  |                |                |       |
| Total lower APA  | 7 A at 48 V    |                | 335 W |
| Total upper APA  | 7.5 A at 48 V  |                | 360 W |

Four wires are used for each PTC module; two 10 AWG, shielded, twisted-pair cables for the power and return; and two 20 AWG, shielded, twisted-pair cables for the sense. The primary protection is the over-current protection circuit in the LV supply modules, which is set higher than the  $\sim 8$  A current draw of the WIEC. Secondary sense line fusing is provided on the PTC. Tests are being performed in ProtoDUNE-SP to check which is the best scheme for connecting the shields of

the power cables. In ProtoDUNE-SP the shield of the warm power cables is connected to ground on both the power supply side and on the CE flange. Other shield connection schemes are being investigated in ProtoDUNE-SP and the connection scheme yielding the lowest readout noise will be used for DUNE.

Switching power supplies controlled by the slow controls system provide power to the heaters (12 V) and the fans (24 V) that are installed on the CE flanges. Temperature sensors mounted on the flanges, and power consumption and speed controls from the fans are connected to the interlock system that is part of the DDSS, in addition to being monitored by the slow controls system.

Bias voltages for the APA wire planes, the electron diverters, discussed in section 2.2.6, and the last FC electrodes are generated by supplies that are the responsibility of the TPC electronics consortium. The current from each of these supplies should be very close to zero in normal operation. However, the ripple voltage must be carefully controlled to avoid injecting noise into the FE electronics. RG-58 coaxial cables connect the wire bias voltages from the bias voltage supply to the standard SHV connectors that are machined directly into the CE feedthrough and insulated from the low voltage and data connectors.

Optical fibers are used for all connections between the WIECs and the DAQ and slow control systems. The WIB reports its temperature and the current draw from each FEMB to the slow control system, while the current draw for each APA is monitored at the mainframe itself.

To support the electronics, fan, and heater power cables, as well as optical fibers on top of the cryostat, cable trays are installed below the false flooring on top of the cryostat. These cable trays run perpendicular to the main axis of the cryostat and connect the three cryostat penetrations for one row of APAs to the detector mezzanine near the cryostat roof, as shown in figure 4.32. All the necessary LV supplies and the bias voltage supplies are installed in these racks. Patch panels for the optical fiber plant used for the control and readout of the detector are also installed on the detector mezzanine.

#### 4.2.9 ProtoDUNE-SP results

The ProtoDUNE-SP detector features a LArTPC with 15,360 sense wires with a fiducial mass of roughly 700 tons of LAr. The system was deployed in a hadrons and electrons beamline at the CERN Neutrino Platform in 2018 and continues to take cosmic event data. The goal of the ProtoDUNE-SP TPC readout was to validate the concept and the design of the integrated APA+CE readout and measure the performance of the TPC electronics system with components as close as possible in design to those in the final DUNE TPC readout. In the case of the TPC electronics, most of the detector components used in ProtoDUNE-SP are prototypes of the DUNE FD ones discussed in the previous sections. The major difference is the FEMB (and associated ASICs), where an early version of LArASIC (P2) is used for the FE ASIC, followed by the first prototype (P1) of a different ADC, using the “domino” architecture and implemented in the 180 nm technology, and finally by an FPGA that provided the data serialization functionality.

Each of the six ProtoDUNE-SP APA+CE readout units consists of 2,560 sense wires, of which 960 are 6 m long collection wires and 1,600 are 7.4 m long induction wires. Five of the six APAs were tested in a full-scale cold box in cold gaseous nitrogen ( $\text{GN}_2$ ) with a complete TPC electronics readout system, identical to the one deployed in ProtoDUNE-SP, before installation in the cryostat; the sixth was installed without first going through the cold box testing. Figure 4.33 shows the measured noise level, represented by the ENC in units of electrons, for the collection ( $X$ ) plane and

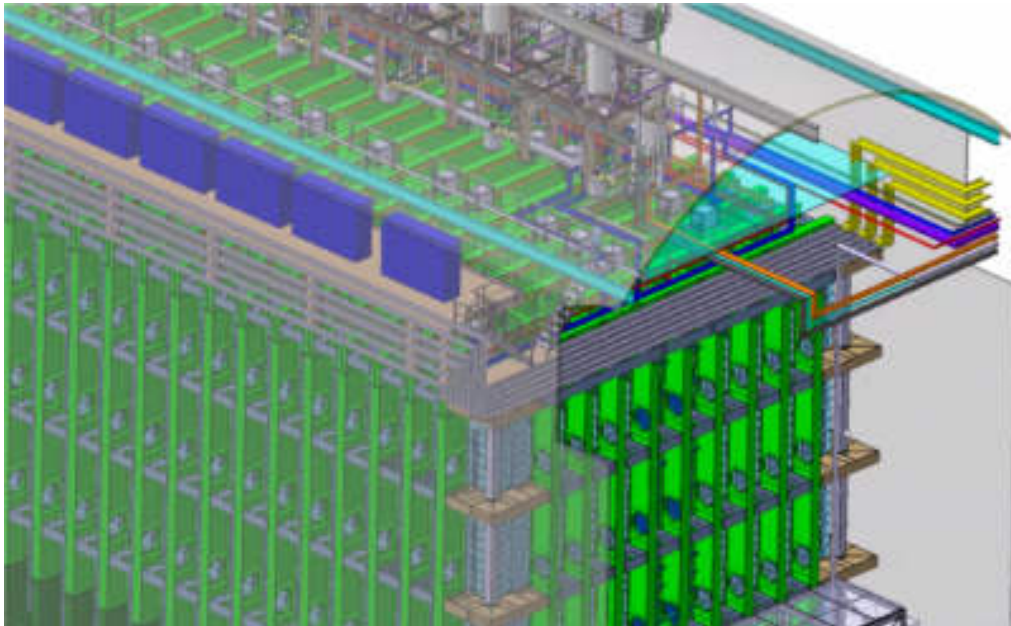


**Figure 4.32.** Services on top of the cryostat. The racks for the LV power supplies are shown in blue.

the two induction ( $V$ ,  $U$ ) planes as well as the FEMB temperature in the cold box as a function of the cold cycle time. At a stable temperature of 160 K, the ENC for all three wire planes is less than  $500 e^-$ .

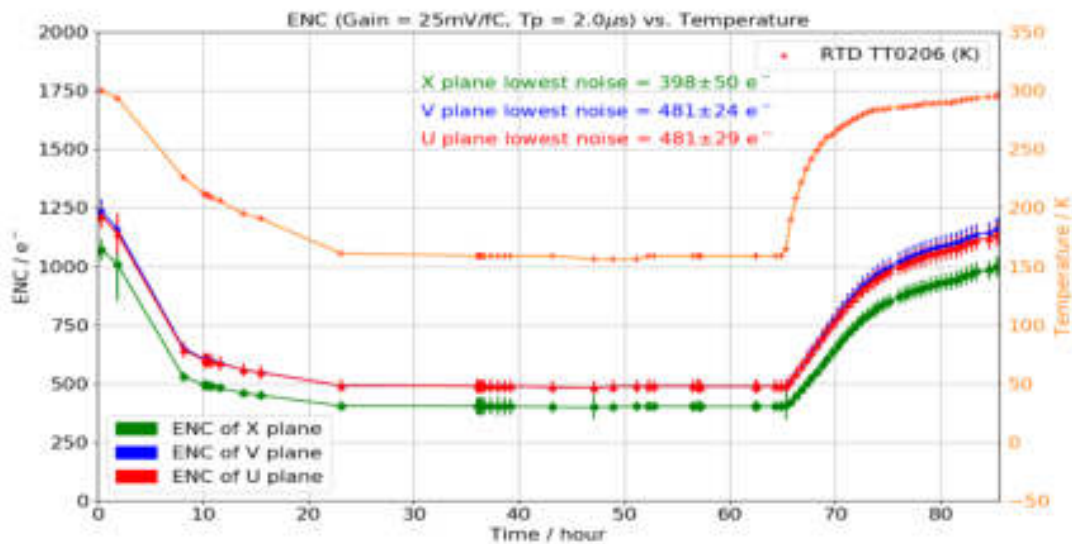


**Figure 4.33.** Left y axis: ENC (in electrons) for  $U$ ,  $V$ , and  $X$  (red, blue, and green curves) sense wire planes as a function of time (hours) for the APA 2 cold cycle in  $GN_2$  in the CERN cold box; right y axis: temperature (orange curve) measured at the level of the FE electronics.

After the cryostat was filled with LAr and the drift and wire bias voltages were set to their nominal values, 99.7% of the TPC readout channels were found to be functioning properly. A total of 42 channels were found to be unresponsive. Of these:

- 14 channels were identified based on tests performed prior to the insertion of the APA into the cryostat as having no capacitive load on the FE electronics, suggesting an open connection somewhere upstream of the CE system;
- 24 additional channels showed the same problem after the cryostat was filled with LAr (three of these, all on the first APA, were already observed during testing in the cold box); and
- four channels were associated with the FE electronics not functioning properly: two of these channels appeared in tests performed after the cathode high voltage was raised to 120 kV, and two more appeared when the high voltage reached 160 kV.

As discussed in section 2.3.2.1, the number of disconnected channels due to mechanical failures in the connection between the APA wire and the FE electronics has changed with time, with some channels becoming again active, and others becoming inactive. Only one additional dead channel is caused by a permanent failure of the FE electronics. If these numbers are indicative of the normal rate of channel loss, it would imply that over the 20 years of DUNE operations at most 0.5% of the readout channels would fail. A similar upper limit can be obtained from the operational experience of MicroBooNE, considering also an additional scale factor for the additional ASICs immersed in LAr (in MicroBooNE only the FE amplifier is in the liquid). Further operation of ProtoDUNE-SP, as well as operation of SBND in the coming years, will provide additional information on the long term stability of the active electronics components immersed in LAr.

With the detector operating under nominal conditions, the measured ENC by the online monitoring program was approximately  $550 e^-$  on the collection wires and approximately  $650 e^-$  on the induction wires, averaged over all operational channels. The noise increased relative to the tests performed inside the cold box due to the larger dielectric constant of LAr relative to  $GN_2$ . These noise measurements are consistent with the ratio of the corresponding capacitances of the APA wires. Figure 4.34 shows the ENC (in electrons) for all channels of one APA+CE readout unit. The collection channels with ENC larger than  $1500 e^-$  had a problem in the P1-ADC ASIC; this problem had already been identified prior to their installation on the FEMBs. The channels on all three planes with ENC smaller than  $300 e^-$  have an open connection somewhere in front of the CE system. Figure 4.35 summarizes ENC levels in the entire ProtoDUNE-SP detector both before and after the application of a simple offline common-mode noise filter similar to the one used in MicroBooNE [62]; an improvement of roughly  $100 e^-$  is seen on all planes.

The overall performance of the CE system in ProtoDUNE-SP satisfies the CE noise specification for the SP module listed in section 4.1.2. A comparison of the raw data from a ProtoDUNE-SP event (figure 4.36) to that from a MicroBooNE event (figure 4.37 [62]) demonstrates the improvements achieved in LArTPC performance. The ProtoDUNE-SP event was collected very early in the data taking period when the charge collection efficiency was still limited by the amount of impurities in the LAr; it shows very little noise and appears to be of the same quality as the MicroBooNE event display after offline noise removal.

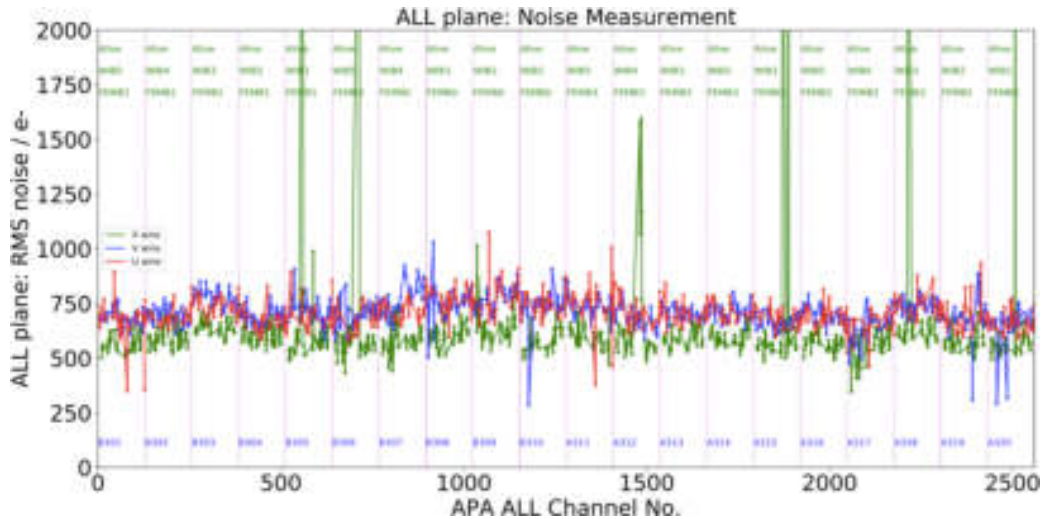


**Figure 4.34.** ENC (in electrons) for all  $U$ ,  $V$ , and  $X$  (red, blue, and green curves) sense wire planes for one ProtoDUNE-SP APA under nominal operating conditions.

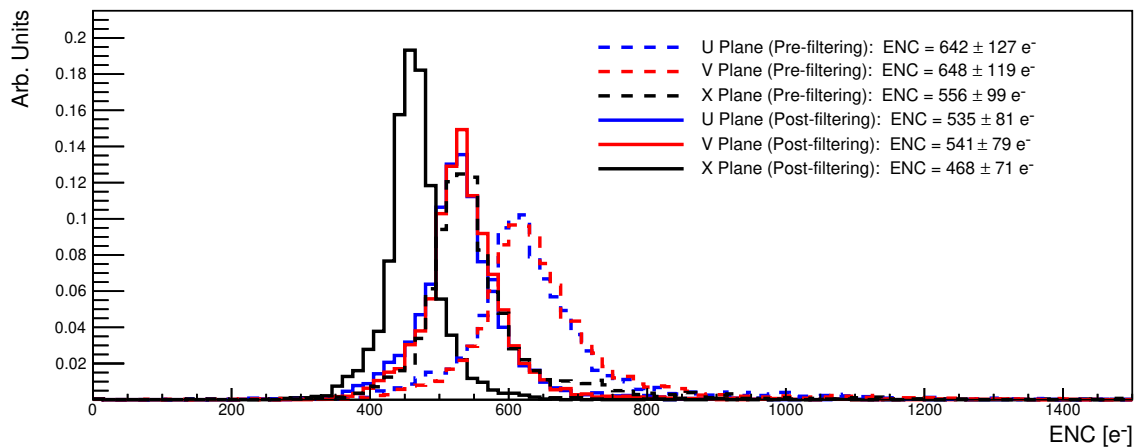


**Figure 4.35.** ENC levels (in electrons) for all channels of the ProtoDUNE-SP detector, both before and after the application of a simple offline common-mode filter.

The  $S/N$  has been evaluated using a selected cosmic muon sample, with tracks crossing the LAr volume at shallow angle with respect to the anode plane and large angle with respect to the direction of the wires in each plane considered for  $S/N$  characterization. The charge deposited on each wire in a given plane is evaluated using the pulse height (peak) of the hit found in the raw waveform. A correction taking into account different relative angle between track and wire direction has been applied to normalize the hit response. The noise value is extracted from the width of the Gaussian fitted on the pedestal distribution of the waveform baseline. The electric field in the TPC volume was at the nominal level of 500 V/cm, and the LAr purity for the runs considered in this analysis was about 5.5 ms as measured by the purity monitors, corresponding to  $\sim 35\%$  charge loss due to attachment for tracks close to the cathode. This measurement ignores the effect of the space charge, which introduces distortions of the electric field in the TPC volume that may locally change the

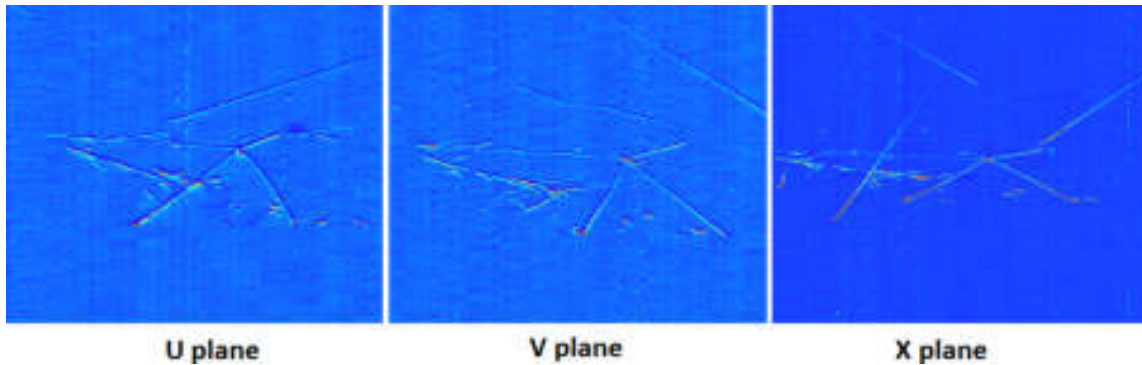


**Figure 4.36.** Display of the charge deposited on the collection wires (wire number on the  $x$ -axis) as a function of the drift time (on the  $y$ -axis) for a ProtoDUNE-SP event that includes two electromagnetic showers and a four tracks in the final state of the interaction. The color associated with each time sample on the APA wires gives a measurement of the charge measured by the CE readout, with blue representing the smallest charge values and red representing the largest charge values.

recombination factor and therefore affect the S/N value. Finally, the measurement is made both before and after the application of a simple offline common-mode noise filter. The distribution of the S/N for all the wires in the sample of muon tracks considered is shown in figure 4.38 [63]. Looking before (after) the application of the common-mode noise filter, for the collection plane the mean value of the S/N distribution is 38 (49), for the first induction plane it is 16 (18), and for the second induction plane it is 19 (21).

#### 4.2.10 ProtoDUNE-SP lessons learned

As discussed in section 4.2.9, the initial data from ProtoDUNE-SP show that the SP module can meet the noise specification. The experience with the TPC electronics in ProtoDUNE-SP nonetheless motivates several improvements to the TPC electronics system design, some of which have already been implemented and discussed in the previous sections. A complete list of the lessons learned from the construction, testing, integration, installation, commissioning of the TPC electronics detector components is available [64]. This reference also discusses the plans and timeline for addressing the issues observed in ProtoDUNE-SP. This TDR section and the following cover only the main issues and the plans for their resolution and implementation in the SP module.

During the commissioning of ProtoDUNE-SP, violations of the grounding rules described in section 4.2.1 have been observed with one of the readout boards for the PD system and with the cameras immersed inside the LAr. The power supply used to provide the HV to the cathode plane has also been observed to cause noise inside the detector and has been replaced. The overall success of ProtoDUNE-SP owes much to the fact that the grounding rules were properly implemented and that any violation was discovered and addressed during the detector commissioning.

The main problem with the ProtoDUNE-SP TPC electronics readout is the poor performance of the P1-ADC ASICs. This problem was observed as early as 2017 while these ASICs were being tested prior to their installation on the FEMBs. The “domino” architecture [65] used in this design relies on excellent transistor matching, which unfortunately is worse at LAr temperature. In ProtoDUNE-SP, this problem results in a fraction (about 3.2%) of the readout channels having



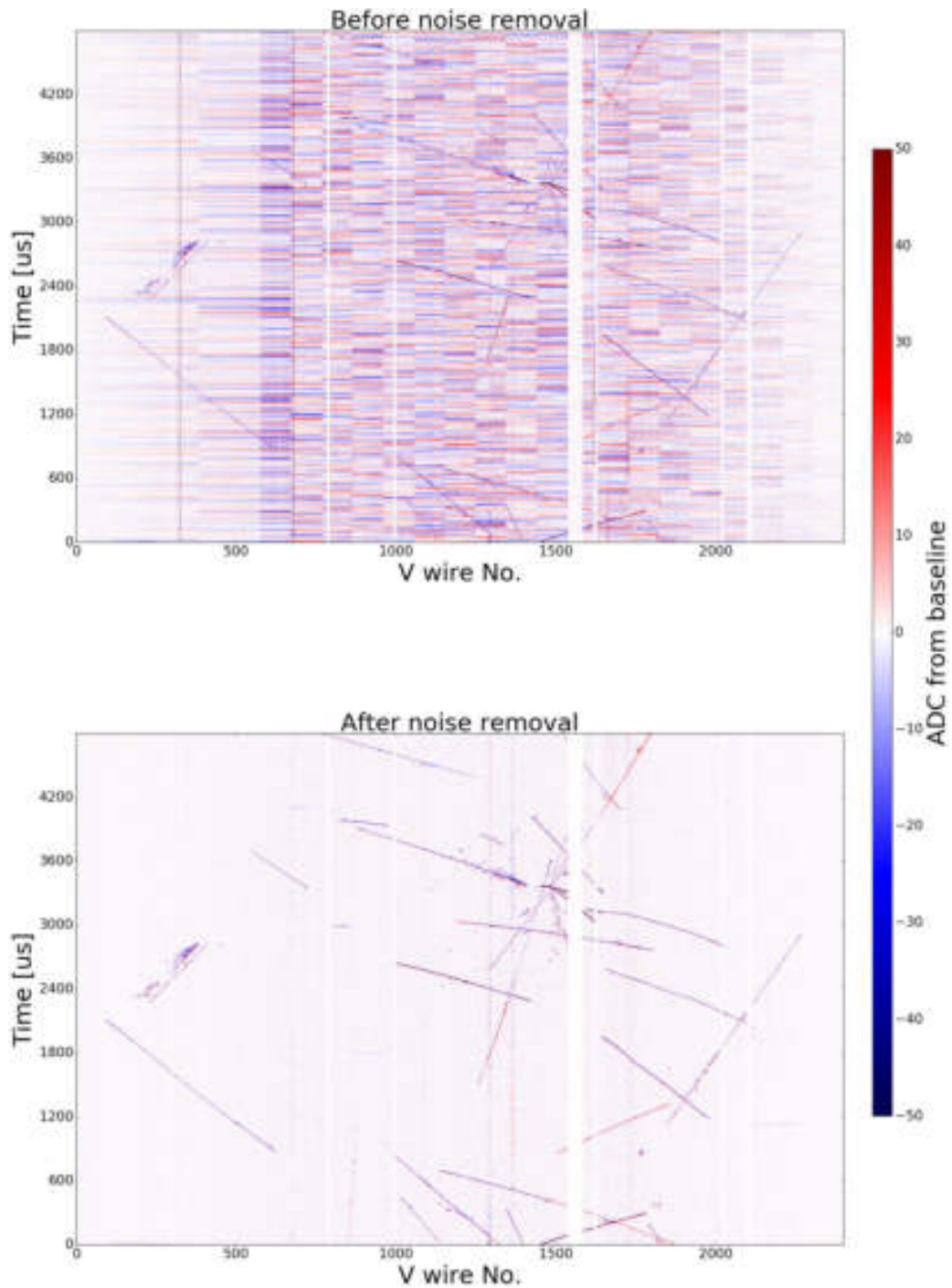


**Figure 4.37.** MicroBooNE 2D event display of the V plane from run 3493 event 41075 showing the raw signal (a) before and (b) after offline noise filtering. A clean event signature is recovered once all of the identified noise sources are subtracted [62].

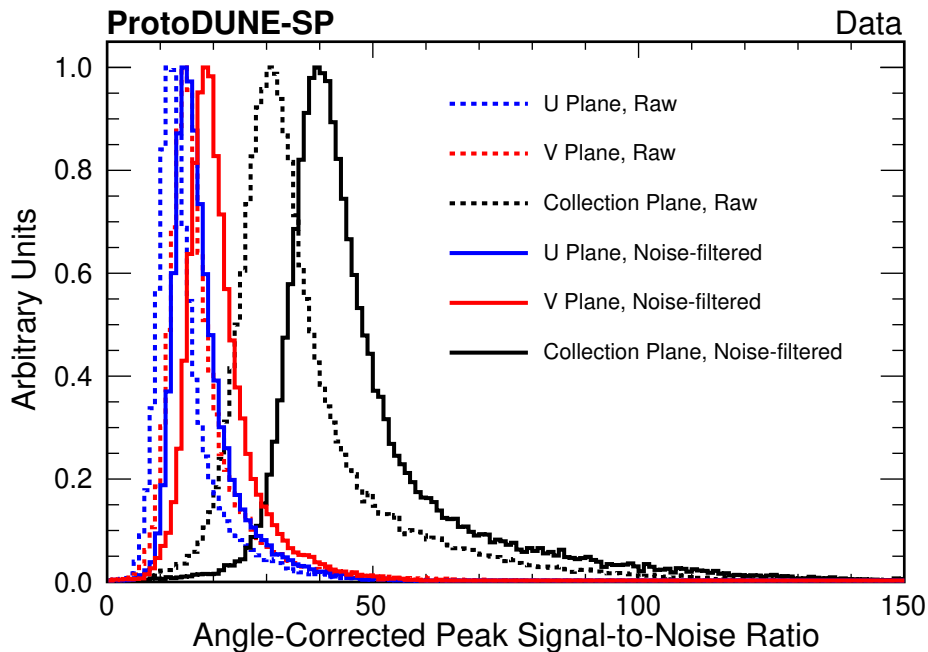


**Figure 4.38.** Angle-corrected peak signal-to-noise ratio for reconstructed cosmic muon tracks in ProtoDUNE-SP, both before and after noise filtering is applied [63].

a fixed value for some of the ADC bits, independent of the input voltage. In a majority of the cases an approximate value for the charge can be obtained via interpolation. For about 0.9% of the channels, the problem is so severe that the only solution is to remove the channels from the analysis, resulting in a loss of efficiency. This problem prompted us to abandon this design and to develop the completely new ColdADC, to adapt the CRYO ASIC for use in DUNE, and to follow the approach of the SBND collaboration and consider the COTS ADC option as well.

Initial analysis of the ProtoDUNE-SP data has uncovered a new problem with LArASIC that occurs when more than  $50\text{ fC}$  is collected over a period of  $10\text{ }\mu\text{s}$  to  $50\text{ }\mu\text{s}$  and the baseline configuration of the amplifier for the collection wires is used. The feedback mechanism of the FE amplifier stops working for several hundred  $\mu\text{s}$ . During this period, the readout does not function and signals following the large charge deposited can be completely lost. A ledge is observed in the output of the FE amplifier, followed by a slow decay and a sudden turn-on of the amplifier. Figure 4.39 shows an example of this behavior.

This problem has been reproduced in the laboratory and is being actively studied. It affects all versions of LArASIC fabricated after the one used for the MicroBooNE experiment. The problem occurs when the threshold on the injected charge is small and therefore affects with larger probability the collection wires, where the  $200\text{ mV}$  baseline is used, compared to the induction wires, which have a  $900\text{ mV}$  baseline. After the problem and this difference between the two baselines were observed, the decision was taken to operate the CE in ProtoDUNE-SP using the  $900\text{ mV}$  baseline for the collection wires as well, sacrificing the dynamic range. Data from the wires where the problem occurs can be masked in analysis, resulting in a loss of efficiency. This problem affected a very small fraction of the events: with the  $200\text{ mV}$  baseline about  $0.1\%$  of the waveforms were

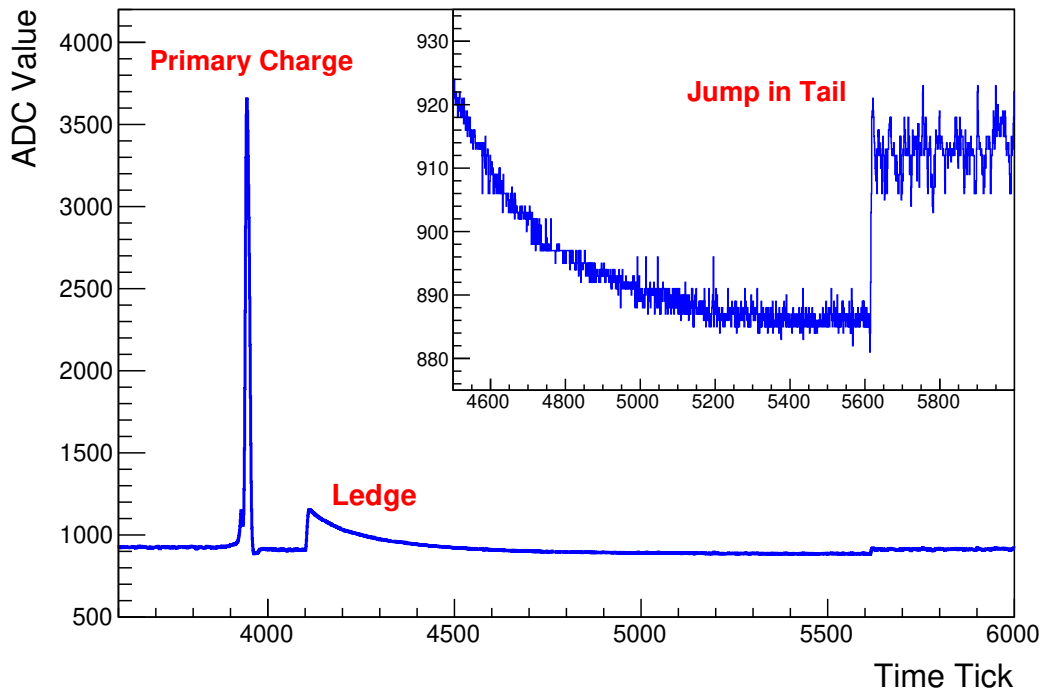


**Figure 4.39.** Waveform of a channel showing a ledge following significant charge deposition on the wire, followed by a discharge and a subsequent jump to the normal baseline ADC value.

affected, and this number became almost completely negligible after switching to the 900 mV baseline. It should be noted that the problem occurs more often in ProtoDUNE-SP than is expected in the DUNE SP module due to the presence of cosmic rays traveling parallel to the APA wires. The problem could, however, affect the SP module’s ability to detect electromagnetic showers — one of the main physics signals. Section 4.2.11 discusses the plans and timeline for addressing this issue in a new LArASIC prototype.

During the integration of the FEMBs onto the APAs and the cold tests that preceded the APA installation inside the ProtoDUNE-SP cryostat, multiple connectors detached from the FEMBs, causing a loss of communication. We replaced the FEMBs on all of the APAs that had been tested in the cold box. One additional FEMB was replaced on the APA that had been installed without undergoing the test in the cold box. This detachment may also be the cause of the loss of the external clock signal on one of the FEMBs that was observed after cool-down. The problem with the connector has been traced to a mechanical interference between the PCB of the FEMB and the epoxy deposited as a protective measure on the small printed circuit board to which the cold cables are soldered and which forms the male part of the connector. The height of the epoxy can cause the female part of the connector to lift from the PCB, as shown in figure 4.40. Section 4.2.3 discusses the redesign of the connection to address this problem.

Analysis of the ProtoDUNE-SP data has made significant progress throughout 2019, leading to many insights on the detector behavior and on the interactions between its different components. The level of noise mentioned in section 4.2.9 (approximately  $550 e^-$  on the collection wires, and approximately  $650 e^-$  on the induction wires) was measured with raw data, without any filtering



**Figure 4.40.** Image of a connector for the cold readout and signal cables, which has been lifted from the FEMB due to the presence of excess epoxy on the connection between the cold cables and the printed circuit board that acts as the “male” part of the connector.

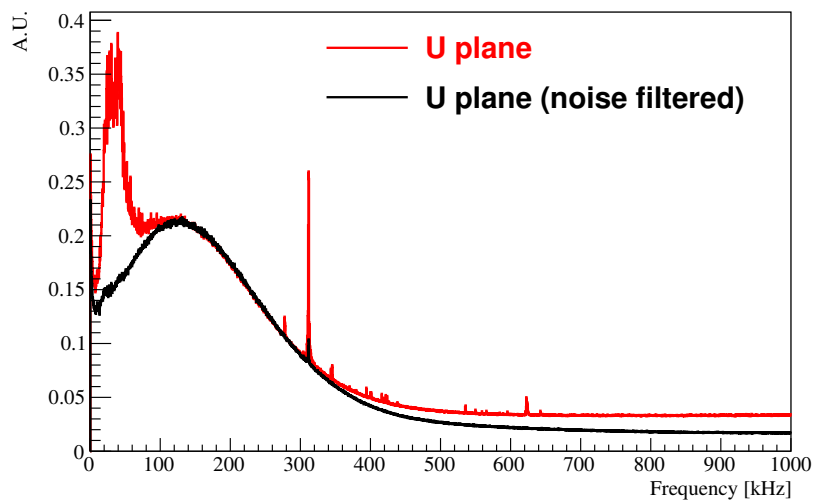


**Figure 4.41.** Spectrum of the noise on the first induction plane of the ProtoDUNE-SP APAs before and after applying a simple offline common-mode filter and partially mitigating ADC issues in software [63].

or selection applied to the pulses on the APA wires. A simple offline common-mode filter can significantly reduce the noise, particularly at low frequencies, as shown in figure 4.41, which compares the noise spectrum of the first induction plane of the APA before and after the filtering [63]. The spectrum prior to the filtering shows a significant increase at frequencies smaller than 60 kHz that in MicroBooNE had been associated with the low-voltage regulators that are installed on the FEMBs [62]. This contribution to the noise has been significantly reduced compared to initial observations at MicroBooNE by means of RC filters that have been added on the ProtoDUNE-SP FEMBs. Further work is required to understand why these RC filters do not completely suppress this specific noise source, as indicated by tests performed in other setups. The noise spectrum prior to the filtering also shows spikes at multiple discrete frequencies, and in some cases the associated noise

sources have been identified: for example, the operation of cameras inside the cryostat contributes to the peaks at 310 kHz and 630 kHz; malfunctioning bias voltage supplies also contribute to the noise. Finally, the reduced level of white noise in the spectrum at higher frequencies is due to the application of an algorithm to partially recover from the ADC problems described above [63]. We expect that further data analysis and tests with ProtoDUNE-SP will result in improvements to the TPC electronics design that already demonstrates excellent performance.

#### 4.2.11 Remaining design and prototyping tasks

ProtoDUNE-SP was built with multiple goals, one of which was to demonstrate that the specifications for DUNE could be met with a design that would only require a simple scale up of the detector size. The data collected with ProtoDUNE-SP in fall 2018 has demonstrated that noise levels well below the target of  $1000 e^-$  can be achieved in LAr, validating the detector system design approach planned for the DUNE SP module.

Still, additional design and prototyping work is required in several areas before the start of SP module construction, with differing levels of risk and engineering work, as estimated in table 4.5.

For example, changing the number and arrangement of cryostat penetrations to accommodate two CE flanges in addition to the PD system flange can be considered a relatively minimal modification. It may require some structural reinforcement and additional FEA simulations to estimate the proper flow of argon in order to avoid any back-diffusion of oxygen into the cryostat (in case of leaks on the flanges), as well as to ensure an acceptable temperature gradient in the LAr.

On the other hand, changes in the design of the ASICs, with the development of ColdADC and COLDATA, are more involved.

The area that requires most work is that of the ASICs that are mounted on the FEMBs. LArASIC has already gone through eight design iterations, the last three directly targeted for DUNE, and has already been used (in two of its earlier versions) for MicroBooNE and for ProtoDUNE-SP, where it has reached the noise levels specified for the DUNE SP module. At least one additional design iteration is required to address the issues observed during ProtoDUNE-SP operations and to implement a single-ended to differential converter to improve the interface with the newly developed ColdADC. To ensure the success of the next design iteration, we are investing in the development of appropriate transistor models for the 180 nm CMOS technology for operation in LAr, such that the saturation effect observed in ProtoDUNE-SP can be properly addressed first in simulation and then with improvements in design. It should be noted that, so far, approximate models that were originally developed for the same 180 nm technology (but with different design rules) have been used for the LArASIC development, and therefore it should not be a surprise that LArASIC may have limitations in certain cases. The circuitry for the single-ended to differential converter has already been developed in the 65 nm technology and needs to be ported to the 180 nm technology used for LArASIC. Various measures have been put in place to minimize the risk associated with the need of a further prototyping iteration; nevertheless, in section 4.8.1 we consider a generic risk for a delay in the availability of ASICs and argue that this delay would not have an impact on the beginning of DUNE FD operations.

It should be noted that even if the reference design for the SP module makes use of custom ASICs for the ADC and the data serialization functionality, a solution based on commercial components is available and has been demonstrated to work by the SBND collaboration. This solution is based on

**Table 4.5.** Status of the design of the different CE detector components as well as the expected amount of engineering and prototyping required prior to construction.

| Component                       | Status               | Expected work   |
|---------------------------------|----------------------|---|
| LArASIC                         | Advanced             | Fix issues observed in ProtoDUNE-SP, port differential output from ColdADC design |
| COTS ADC                        | Complete             | None  |
| ColdADC                         | See text for details |   |
| COLDATA                         | See text for details |   |
| CRYO                            | See text for details |   |
| FEMB                            | Advanced             | Experience with multiple prototypes, final design will follow the ASIC selection  |
| Cold cables                     | Very advanced        | Minor modifications, additional vendor qualification                              |
| Cryostat penetrations           | Advanced             | Add CE flange for bottom APA  |
| WIEC                            | Very advanced        | Add air filters and hardware interlock system                                     |
| WIB                             | Advanced             | Update design to use cheaper FPGA, modify FEMB power, new firmware                |
| PTC                             | Very advanced        | Add interface to interlock system   |
| Power supplies                  | Very advanced        | Investigate possible additional vendors, rack arrangement                         |
| Warm cables                     | Very advanced        | Finalize cable layout, identify vendors   |
| Readout and control fiber plant | Very advanced        | Finalize plant layout   |

the use of a COTS ADC and an FPGA for the data serialization, and further validation is planned for spring 2020. We consider this solution as a fall-back solution for DUNE. Custom solutions for the ASICs are being developed to simplify the FEMB assembly and reduce the power dissipated by the electronics in the LAr.

The reference solution for the ADC and the data serialization is based on two new ASICs, ColdADC and COLDATA. The first iteration of the ColdADC was submitted for fabrication at the end of October 2018, and the chips were delivered in January 2019. Initial results from the tests of the ColdADC prototypes have been discussed in section 4.2.3.2. The results obtained so far are encouraging, despite the fact that some flaws have been identified in the design. Even if one additional design iteration is required, we think that the status of ColdADC can be characterized as having reached the “Advanced” status.

We are also considering an alternative solution for the readout, where the three ASICs are replaced with a single one, the CRYO chip that has a development timeline similar to that of ColdADC. Also in this case the chips from the first submission have been delivered in January 2019; initial results from the tests of the CRYO prototypes have been discussed in section 4.2.3.4.2. As in the case of ColdADC, the results obtained so far are encouraging. As soon as the noise issue observed in the first prototype is understood, CRYO should also be characterized as having reached the “Advanced” status.

The first complete prototype of COLDATA was submitted in April 2019 and the chips have been delivered in July. As discussed in section 4.2.3.3, all test results for COLDATA have been positive, and so in this case it can also be claimed that the design of the ASIC has reached the “Advanced” design status.

There have already been multiple iterations of FEMBs that have been fabricated and tested and used for data taking in MicroBooNE and in ProtoDUNE-SP. The SBND collaboration is starting the production of FEMBs based on the COTS ADC and FPGA solution. The design of the FEMB needs to be adapted for the different ASIC solutions that are being considered for DUNE. This development is already ongoing, as system tests where the FEMBs are connected to an APA are part of the qualification tests. The design status for the FEMB is already at the “Advanced” level, and it will reach the “Very advanced” level at the time of the ASIC selection. At that point, only minor modifications may be required.

The only other TPC electronics detector components that do not yet reach the “Very advanced” level are the cryostat penetrations, as discussed above, and the WIB, where small design changes will be done prior to production in order to use a more modern and cheaper FPGA. Additional changes to the power distribution scheme will be required as the number of power lines (and the corresponding voltages) will be reduced compared to ProtoDUNE-SP. The transition to a more modern FPGA will allow more extensive data monitoring inside the WIB, but may also require developing new software and porting the firmware from one family of FPGAs to another.

For all other detector components, the estimate of the design maturity is considered “Very advanced” based on the experience gained with commissioning and operation of ProtoDUNE-SP. The cold signal cables will be modified to reduce the number of connections and to address the issues observed with the connector on the FEMB. The design of the WIEC needs to be modified to include air filters to minimize the possible damage from dust and/or chemical residues from explosives during the lifetime of the experiment at SURF. The PTC is going to be modified to add an interface to the hardware interlocks of the detector safety system. For cables and fibers on the top of the cryostat, the only work that remains to be done is the design of the actual cable plant, which will then determine the length of the cables. The arrangement of power supplies in the racks on top of the cryostat is the only other remaining design task. For many components, the qualification of additional vendors could also be considered as part of value engineering; this will reduce the risk of vendor lock-in and help minimize costs.

### 4.3 Quality assurance

The TPC electronics consortium is developing a QA plan consistent with the principles discussed in Volume III, DUNE far detector technical coordination, chapter 9. The goal of the QA plan is to maximize the number of functioning readout channels in the detector that achieve the performance specifications for the detector discussed in section 4.1.3, particularly on noise. Minimizing the noise levels in the detector requires that all system aspects are considered starting from the design phase, and in this respect, the experience gained with the ProtoDUNE-SP prototype is extremely valuable as it informs necessary design changes in the detector components. The lessons learned during the construction of ProtoDUNE-SP, the commissioning of the detector, and the initial data taking period have already been discussed in section 4.2. Further operation of ProtoDUNE-SP in 2019 has provided information on the long term stability of the detector components.

Apart from the number of channels, the most important difference between ProtoDUNE-SP and DUNE is the projected lifetime of the detector. This is relevant because a significant fraction of the detector components provided by the TPC electronics consortium are installed inside the

cryostat and cannot be accessed or repaired during the operational lifetime of the detector. The graded approach to QA indicates that particular care must be used for the CE components that will be installed inside the cryostat.

A complete QA plan starts with ensuring that the designs of all detector components fulfill the specification criteria, considering also system aspects, i.e. how the various detector components interact among themselves and with the detector components provided by other consortia. We discuss validating the design in section 4.3.1 and the facilities that we use to investigate the interactions among different detector components in section 4.3.2.

The other aspects of the QA plan involve documenting the assembly and testing processes, storing and analyzing the information collected during the QC process, training and qualifying personnel from the consortium, monitoring procurement of components from external vendors, and assessing whether the QC procedures are applied uniformly across the various sites involved in detector construction, integration, and installation. The TPC electronics consortium plan involves having multiple sites using the same QC procedures, many of which will be developed as part of system design tests during the QA phase, with the possibility of a significant turnover in the personnel performing these tasks. To avoid problems during most of the production phase, we plan to emphasize training as well as documentation of the QA plan. Reference parts will be tested at several sites to ensure consistent results. At a single site, some parts will be tested repeatedly to ensure that the response of the apparatus does not change and that new personnel involved in testing detector components are as proficient as more experienced personnel.

All data from the QC process will be stored in a common database, and the yields of the production will be centrally monitored and compared among different sites. The procedures adopted for detector construction will evolve from the experience gained with ProtoDUNE-SP. A first version of the testing procedures will be put in place in 2020, while the final designs of the detector components are completed and new prototypes are tested. The QC procedures will then be reviewed during the engineering design review that precedes pre-production. Lessons learned during pre-production will be analyzed, and a final and improved QC process will be developed before the production readiness review that triggers the beginning of production. During production, the results of the QC process will be reviewed at regular intervals in production progress reviews. In case of problems, production will be stopped and the problematic issues assessed, followed by changes in the procedures if necessary.

### 4.3.1 Initial design validation

As described in section 4.2, four ASIC designs are being developed for the DUNE FD single-phase TPC readout (LArASIC, ColdADC, COLDATA, and CRYO). When a new prototype ASIC is produced, the groups responsible for the ASIC design will perform the first tests of ASIC functionality and performance. These tests may use either packaged parts or dice mounted directly on a printed circuit board and wire bonded to the board. The goal of these tests is to determine the extent to which the ASIC functions as intended, both at room temperature and at LN<sub>2</sub> temperature. For all chips, these tests include exercising digital control logic and all modes of operation. Tests of FE ASICs include measurements of noise levels as a function of input capacitance, baseline recovery from large pulses, cross-talk, linearity, and dynamic range. Tests of ADCs include measurements of the effective noise levels and of differential as well as integral non-linearity. Tests of the COLDATA



and CRYO ASICs include verification of both the control and high-speed data output links using cables with lengths of 9 m and 22 m as required for the DUNE FD. After the initial functionality tests by the groups that designed the ASICs, further tests will be performed by other independent groups; then the ASICs will be mounted on FEMBs so noise measurements can be repeated with real APAs attached to the readout chain.

Tests of ASICs and FEMBs in a cryogenic environment are performed in LN<sub>2</sub> instead of LAr for cost reasons, ignoring the small temperature difference. These tests can be performed immersing the detector components in a dewar containing LN<sub>2</sub> for the duration of the tests. Condensation of water from air can interfere with the tests or damage the detector components or the test equipment, particularly during their extraction from the LN<sub>2</sub>. A test dewar design developed by Michigan State University, referred to as the CTS, has been developed to avoid this problem and to automate the immersion and the retrieval of the components being tested. Several CTS units were deployed at BNL during the ProtoDUNE-SP construction and used for the QC on the ASICs and FEMBs for ProtoDUNE-SP. Later they were also used to perform similar tasks during the construction of the electronics for SBND. Several other CTS units have been deployed to institutions involved in developing ASICs to test the first prototypes of ASICs and FEMBs for the DUNE FD. Two CTS units in operation at BNL are shown in figure 4.42.



**Figure 4.42.** Cryogenic Test System (CTS): an insulated box is mounted on top of a commercial LN<sub>2</sub> dewar. Simple controls allow the box to be purged with nitrogen gas and LN<sub>2</sub> to be moved from the dewar to the box and back to the dewar.

### 4.3.2 Integrated test facilities

The investigation of the system issues that can arise from the interaction of different detector components requires that a full system test of a slice of the entire detector is performed. These tests are performed with FEMBs attached to APAs enclosed in a structure that provides the same grounding environment planned for the final DUNE FD. Power, control, and signal readout connections will be provided using cryostat penetrations similar to those planned for use in the DUNE FD. Prototypes of the final DUNE FD DAQ will be used for readout and control of the detector, and if possible the PD system will also be included. We have identified three such system test stands that we can use for system tests: the ProtoDUNE-SP facility at dwordcern, the ICEBERG facility at Fermilab, and the 40% APA at BNL. We discuss these three setups in this section.

#### 4.3.2.1 ProtoDUNE-SP and cold box at CERN

ProtoDUNE-SP is designed as a full slice of the DUNE SP module using components with a design as close as possible to the one that will be used in production. It contains six full-size DUNE APAs instrumented with 20 FEMBs each for a total readout channel count of 15,360 digitized sense wires. Critically, the wires on each APA are read out via a full TPC electronics readout system, including a CE flange and WIEC with five WIBs and one PTC. Each combined APA and CE readout unit follows the grounding guidelines described in section 4.2.1 to operate in a fully-isolated way with respect to the rest of the detector.

ProtoDUNE-SP took beam data in the CERN Neutrino Platform in 2018 and will continue to take cosmic data throughout spring 2020. As described in section 4.2.9, the live channel count (99.7%) and average noise levels on the collection and induction wires (ENC  $\sim 550 e^-$  and  $\sim 650 e^-$ , respectively) satisfy the DUNE-SP requirements described in section 4.1.2. Several lessons learned from the production and testing of the TPC electronics and the ProtoDUNE-SP beam data run will be incorporated into the next iteration of the system design for the DUNE SP module, as discussed in section 4.2.10.

Five of the six APAs were tested in the ProtoDUNE-SP cold box before they were installed in the cryostat. These tests were critical in identifying issues with CE components after installation on the APA. Therefore, a very similar set of cold box tests are planned at SURF with the fully-instrumented DUNE APAs. A seventh APA was delivered to CERN in March 2019 and will be first equipped with ProtoDUNE-SP FEMBs. This APA was characterized in October 2019 in the cold box like the APAs installed in ProtoDUNE-SP, establishing a reference point for further tests that will be performed after replacing half of the FEMBs with new prototypes FEMBs (equipped with prototypes of the new ASIC designs). Tests will be performed in early 2020 using FEMBs equipped with the COTS ADC, FEMBs with the CRYO ASIC, and FEMBs with the new ColdADC and COLDATA ASICs. The cold box will also be used to study the effect of low temperature on the low-voltage power and bias-voltage power cables as they are routed through the APA frame.

The DUNE APAs and the readout electronics will differ from the ones used in ProtoDUNE-SP. For this reason, we are planning to re-open the ProtoDUNE-SP cryostat and replace three of the six APAs with final DUNE FD prototypes that also include the most recent prototypes of the FEMBs built using the chosen ASIC solution. If possible, ASICs from the engineering run will be used to populate the FEMBs instead of using prototypes from a multi-purpose wafer fabrication run. A total of 60 FEMBs are required to populate the three final DUNE APA prototypes to be installed in ProtoDUNE-SP. A second period of data taking with this new configuration of ProtoDUNE-SP is planned for 2021–2022. This will also allow another opportunity to check for interference between the readout of the APA wires and the PD system or other cryogenic instrumentation.

#### 4.3.2.2 Small test TPC (ICEBERG)

While the cold box test at CERN and ProtoDUNE-SP operations provide important validation of the TPC electronics for DUNE, a new cryostat (ICEBERG) has been built to test multiple CE prototypes in a LArTPC environment. ICEBERG will be used for LAr detector R&D and for system tests of the CE prototypes. The ICEBERG cryostat allows for rapid turn-around in testing new configurations of the CE. One cycle, including installing new FEMBs, filling the cryostat, performing measurements,

and finally emptying the cryostat, can be completed in less than one month. While this is slower than the turn-around that can be achieved with the cold box at CERN, the advantage of ICEBERG is that it houses a small TPC which allows measurements with ionization tracks, which is not possible when performing tests in the cold box. In addition, ICEBERG enables system-wide studies with new prototypes of the PD system because the scaled-down APA is mechanically compatible with the new design of the PD system, which is not the case for the seventh ProtoDUNE-SP APA.

The ICEBERG cryostat, shown in figure 4.43, is installed at the Proton Assembly Building at Fermilab. It has an inner diameter of 152 cm and can hold about 35,000 liters of LAr, sufficient to house a TPC with dimensions 115 cm × 100 cm × 60 cm. For DUNE purposes, this cryostat will house a 1,280-channel TPC, shown in figure 4.44, with an APA and two FCs that together enclose two sensitive ionization drift volumes. Each drift volume has a maximum drift distance of 30 cm. The APA has been built using wire boards and anchoring elements identical to those of ProtoDUNE-SP, as described in section 2.2.5. It has dimensions of 1/10<sup>th</sup> of a DUNE APA. The APA mechanics are designed to accommodate two half-length ProtoDUNE-SP PDs with dimensions and connectors that already include the design modifications planned for the DUNE FD.

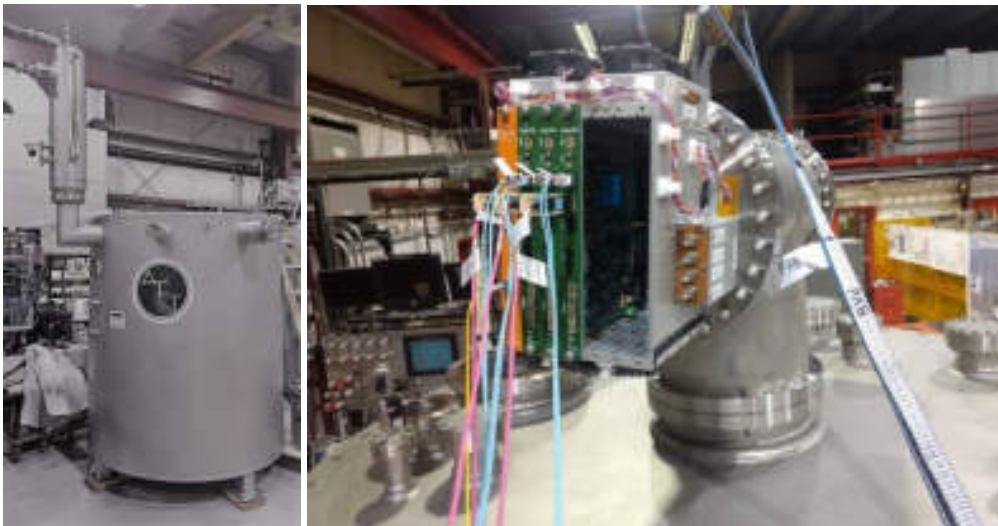


**Figure 4.43.** ICEBERG cryostat (left) and top plate spool piece (right).

Power, readout, and controls use equipment identical to those used for ProtoDUNE-SP. The interface between the FEMBs and the APA wires uses the same CR boards used for ProtoDUNE-SP and described in section 2.2.5. The TPC is read out via a DAQ system (also shown in figure 4.44) identical to that of ProtoDUNE-SP. The power and signal cables for the detector are routed through a spool piece installed on the center port of a movable flange on the top of the cryostat, which is also used to support the TPC. The movable flange contains fourteen additional ports that are available for different utilities, including HV, purity monitoring, cryogenic controls, and visual inspection. A condenser as well as LAr fill and vacuum ports are on the side of the cryostat, providing easy access to the detector.

The FC for the TPC is constructed using printed circuit boards and designed to provide up to 30 cm of drift length on both sides of the APA. The cathode plane is made of a printed circuit board

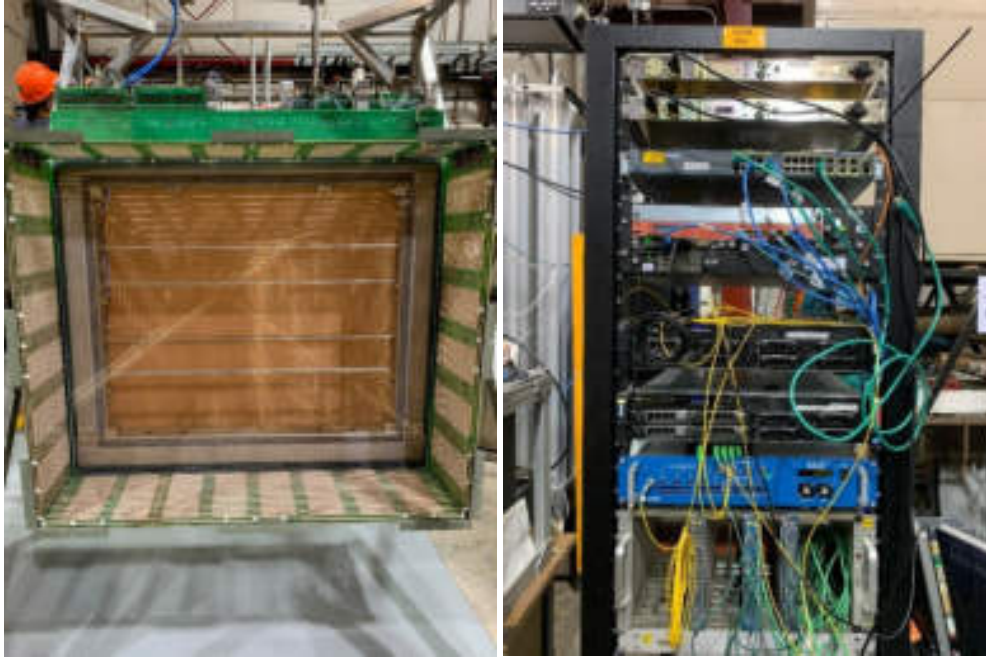


**Figure 4.44.** ICEBERG TPC (left) and DAQ system (right).

coated with copper and is powered with  $-15$  kV DC power. A  $1$  G $\Omega$  resistance between the strips of the FC creates a gradient field changing from  $-15$  kV at the cathode to  $-1$  kV near the APA. In the initial configuration, the sides of the FCs are terminated on the APA ground with  $156$  M $\Omega$  resistors, which is different from that which has been planned for the DUNE FD, where the last electrode of the FCs is also connected to a separate bias voltage supply.

The ICEBERG power system that provides power to the detector, electronics, DAQ, and cryogenics controls was designed with extreme care to isolate the detector and building grounds, following the same principles adopted for ProtoDUNE-SP and including a new  $480$  V transformer. The impedance between the detector and building grounds is continuously monitored. The distribution panel, which is at detector ground, provides both  $208$  V and  $120$  V lines for the TPC electronics rack, providing both the low-voltage power to the TPC electronics components and the bias voltage to the APA wire planes through the WIEC and SHV connectors located on the cryostat penetration. A single WIENER MPOD provides  $-665$  V,  $-370$  V,  $0$  V, and  $820$  V to the  $G$ ,  $U$ ,  $V$ , and  $X$  planes of the APA, respectively. It is also used to provide the  $-15$  kV to the cathode plane. A WIENER PL506 provides the low-voltage power to the PTC, to the fans, and to the heaters located on the flange that is mounted on the spool piece at the top of the cryostat.

The DAQ for ICEBERG is a copy of the system used for the readout of five of the ProtoDUNE-SP APAs at CERN. The core of the DAQ system consists of two Linux PCs that communicate over  $10$  Gbps optical fibers with processing units called reconfigurable computing elements (RCEs), which are FPGAs that are housed on industry-standard Advanced Telecommunications Computing Architecture (ATCA) shelves on cluster on board (COB) motherboards. The RCEs can perform data compression and zero suppression. They also buffer the data while waiting for a trigger and then send it to the Linux PCs where the data can be analyzed using the artdaq framework. A pair

of scintillators at the top and bottom of the cryostat generates a cosmic trigger for the DAQ. The system is modular and could be upgraded to follow the overall DUNE FD DAQ development.

The ICEBERG cryostat was filled for the first time with LAr in March 2018, with ProtoDUNE-SP FEMBs installed on the TPC. The initial data taking run uncovered some issues with the pressure regulation system of the cryostat and with the field cage. Once these problems were addressed, a second data taking period started in June 2019, demonstrating stable operations of the cryostat and TPC. The baseline performance of the ICEBERG TPC has been established using ProtoDUNE-SP FEMBs. As shown in figure 4.45, noise levels of  $\sim 300 e^-$  have been measured on the collection and induction wires, which are of similar length, in line with expectations given the input capacitance to the FE electronics. A small number of channels have larger noise levels as a result of the underperforming ADC electronics, as in the case of ProtoDUNE-SP. TPC noise levels remained constant while the PD system was being operated, demonstrating that there is no interference between that system and the TPC electronics. Moving forward, ICEBERG will be used to test new FEMB prototypes, equipped with the new ASICs under development.

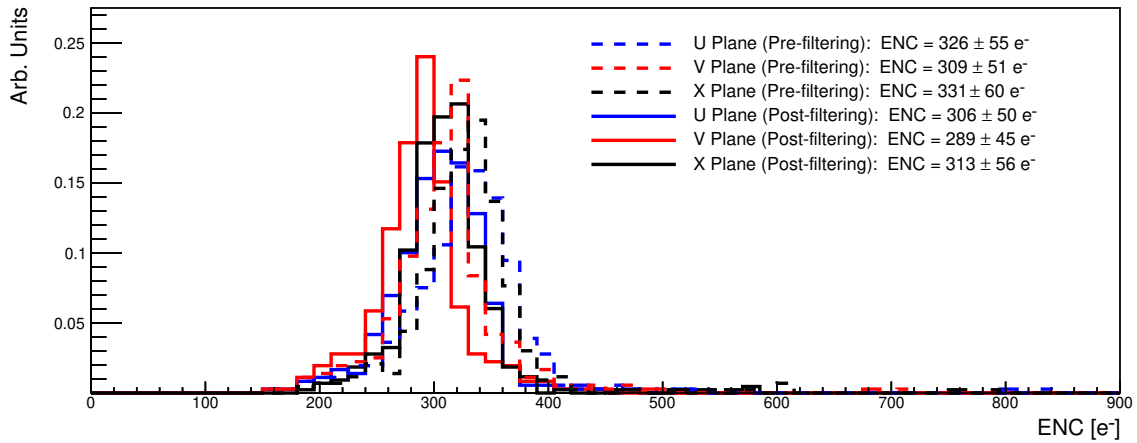


**Figure 4.45.** ENC levels (in electrons) for all channels of the ICEBERG TPC, both before and after the application of a simple offline common-mode noise filter.

#### 4.3.2.3 40% APA at BNL

One additional facility where the FEMB prototypes can be connected to an APA inside a shielded environment is the 40 % APA test stand at BNL. The 40 % APA at BNL is a 2.8 m × 1.0 m three-plane APA with two layers of 576 wrapped (*U* and *V*) wires and one layer of 448 straight (*X*) wires. It is read out by up to eight FEMBs with the full length (7 m) ProtoDUNE-SP data and LV power cables. The readout uses the full TPC electronics system, including the CE flange and WIEC, as shown in figure 4.46. Detailed integration tests of the ProtoDUNE-SP CE readout performance were done at the 40 % APA. During these tests the DUNE grounding and shielding guidelines were strictly followed. This system was also used for initial studies of the COTS ADC option that is described in section 4.2.3.4.1 and will be used again for new FEMB prototypes.

Each of the three setups (APA in the cold box at CERN, ICEBERG TPC at Fermilab, and 40 % APA test stand at BNL) that can be used for system tests has advantages and disadvantages. Only the ICEBERG TPC can be used to perform measurements with tracks, but the APA is much smaller



**Figure 4.46.** Left: one side of the 40 % APA with four FEMBs. Right: the full CE feedthrough and flange.

than the DUNE FD APA (which is also an advantage because it allows us to determine the ultimate performance of the electronics because the detector capacitance is reduced). The ICEBERG TPC is for the moment the only setup compatible with the new PD system design. Tests performed in the cold box at CERN and with the 40 % APA at BNL are limited to noise measurements. These tests are not performed at LAr temperature in the CERN setup. The advantage of the cold box at CERN and of tests performed in ProtoDUNE-SP is that the APA size is the one used in the DUNE FD, while the ICEBERG detector is much smaller. We plan to continue using all these setups for testing during the development of new ASICs and FEMBs designs.

### 4.3.3 Reliability studies

The TPC CE system of the DUNE SP FD must meet stringent requirements, including a very small number of failures ( $< 1\%$  of the total number of channels) for components installed on the detector inside the cryostat during the 20 years of detector operation. Initial studies of the impact of dead channels indicate that there is minimal impact on physics measurements even for a large ( $\sim 5\%$ ) number of channel failures randomly distributed in the detector, given the very high granularity of the TPC. Further studies are ongoing to understand the impact of failures affecting groups of neighboring channels, which could arise from the failure of ASICs (16–64 channels) or FEMBs (128 channels). Reliability must be incorporated in the design of all components, and a dedicated analysis of the physics impact of all possible failure modes, including a consideration of the number of readout channels affected, is required before finalizing the design of all ASICs, printed circuit boards, cables, connectors, and their supports, all of which are housed inside the DUNE FD cryostat.

A few HEP detectors have operated without intervention for a prolonged period, with few readout channel losses, in extreme conditions that are similar to those in the DUNE FD cryostats:

- The NA48/NA62 liquid krypton (LKr) calorimeter has 13,212 channels of JFET pre-amplifiers installed on the detector. It has been kept at LKr temperature since 1998. The total fraction of failed channels is  $< 0.2\%$  in more than 20 years of operation.
- The ATLAS LAr accordion electromagnetic barrel calorimeter has approximately 110,000 readout signal channels, with up to seven connections and different circuit boards populated with resistors and diodes inside the cryostat. This calorimeter has been cold since 2004, for a total of 15 years of operation. So far, the number of readout channels that have failed is approximately  $0.02\%$  of the total channel count.

- The ATLAS LAr hadronic endcap calorimeter has approximately 35,000 GaAs pre-amplifiers summed into 5,600 readout channels that are mounted on cold pre-amplifier and summing boards. The ATLAS LAr hadronic endcap calorimeter CE have been in cold since 2004, with 0.37% of the channels failing during 15 years of operation.

Since neither NA48/NA62 nor the ATLAS LAr hadronic endcap calorimeter use CMOS electronics, the procedures used in the construction and QC of PCBs and for the selection and QC of connectors and discrete components mounted on the PCBs represent the most relevant aspect for the DUNE FD.

In addition, FERMI/GLAST is an example of a joint project between NASA and HEP groups with a minimum mission requirement of five years, and is on its way to achieving a stretch goal of ten years of operations in space. Although the requirements are somewhat different, examining and understanding the various strategies for a space flight project can inform the DUNE project.

A preliminary list of reliability topics to be studied for the TPC electronics operated in LAr environment are:

- The custom ASICs proposed for use in DUNE (LArASIC, ColdADC, COLDATA, and CRYO) incorporate design rules intended to minimize the hot-carrier effect [55, 66], which is recognized as the main failure mechanism for integrated circuits operating at LAr temperature.
- For COTS components, accelerated lifetime testing, a methodology developed by NASA [67] will be used to verify the expected lifetime of operation at cryogenic temperatures. A COTS ADC has undergone this procedure and has been qualified as a solution for the SBND experiment [54].
- Printed circuit board assemblies are designed and fabricated to survive repeated immersions in LN<sub>2</sub>.
- A study will be undertaken to give guidance on how much components (capacitors, resistors, etc.) should be de-rated for power dissipation, operating voltage, etc. in order to achieve the desired reliability.
- Similarly, connectors and cables, usually major sources of detector channel failures, will require a separate study to identify optimal choices.
- In addition to the QA studies noted above, a very detailed and formal set of QC checks of the production pieces will be required in order to ensure a reliable detector. The QC plans for the TPC electronics detector components are discussed in section 4.4.4.

The TPC electronics consortium has formed a working group tasked with studying the reliability of these components, which is preparing recommendations for the choice of ASICs, the design of printed circuit boards, and testing procedures. This working group will review the segmentation of the CE to understand which failures will most affect data taking, revisit recommendations for the ASIC design, beyond those aimed at minimizing the hot-carrier effect, revisit the industry and NASA standards for the design and fabrication of printed circuit boards, connectors, and cables, and recommend QC procedures to be adopted during fabrication of the CE components. The working

group will also review system aspects, to understand where it is desirable, necessary, and feasible to implement redundancy in the system in order to minimize data losses due to single component failures.

#### 4.4 Production and assembly

In this section, we discuss the production and assembly plans, including the plans for the spares required during the detector construction and for operations, for procurement, assembly, and quality control.

##### 4.4.1 Spares plan

The APA consortium plans on building 152 APAs for the first SP detector. This means that at least 3,040 FEMBs with the corresponding bundles of cold cables will be required for the integration (3,040 power cables, 3,040 data cables, and 1,216 bias voltage cables; half the cables will be long enough for integration on the top APAs, while the other half will be compatible with the bottom APAs). To have spare FEMBs, the TPC electronics consortium plans to build at least 3,200 FEMBs, 5% more than necessary. If more spares are needed during the QC process or during integration, additional FEMBs can be produced quickly as long as any components that have long lead times are on hand. For these components, we plan to keep on hand a larger number of spares. The ASICs require a long lead time; a plan for those spares is discussed below. For other discrete components (capacitors, resistors, connectors, voltage regulators, oscillators), plans will be put in place once the final design of the FEMB is available and vendors contacted.

For the ASICs, the number of spare chips is driven by the fact that fabrication requires batches of 25 wafers at a time. Given the dimensions of the current prototype ASICs, the expected number of chips per wafer is about 700 for LArASIC, 930 for ColdADC, 230 for COLDATA, and 220 for CRYO. These numbers are based on the assumption that ColdADC and COLDATA are fabricated on the same wafer. To estimate the number of usable chips for installation on the FEMBs, we assume that 10% of the chips will fail during the QC process described later in this section, and an additional 5% of the chips will fail during dicing and packaging. With these assumptions, one would need at least 43 LArASIC wafers, 33 ColdADC and COLDATA wafers, and 35 CRYO wafers for one SP FD module. Wafers must be ordered in batches of 25 which implies that we will have a significant number of spares, meaning that additional batches of wafers would be needed only if the overall yield of LArASIC falls below 75% or if the overall yield of the other ASICs falls below 60%. The number of spare chips available can be reduced if wafers are purchased for two SP detectors at a time; however, the wafers are relatively inexpensive and the chosen processes may not be available after a few years so generous spares of these custom devices are likely advisable.

In general, for other components, we plan to procure between 5 and 10% additional components for spares for the construction of the first SP FD module. We will need more spares for components that have a larger risk of damage during integration and installation. For example, for cold cables, we plan for 10% additional spare cables for the bottom APA because they must be routed through the APA frames, but for the top APA, we foresee needing only 5% additional spare cables. Assuming we will have unused spares from the first detector, we will reduce the number of spares for the second SP FD module.



The components on top of the cryostat (power supplies, bias voltage supplies, cables, WIECs with their WIB and PTC boards) can be replaced while the detector is in operation. For these components, additional spares may be required during the 20 years operation period of the DUNE FD. The initial plan is to purchase 10% additional components for spares for the first SP FD module and use them for the second SP FD as well (i.e. effectively having 5% additional components for spares). Once the design of the WIBs is finalized, we will decide if extra spares should be purchased for FPGAs and optical transmitters and receivers. These are commercial components that may no longer be available after a certain number of years of operation, which could prevent the TPC electronics consortium from fabricating additional spare WIBs if required. This risk is discussed in section 4.8.3, one that could be alleviated by placing commercial components on mezzanine cards to minimize any necessary redesign of boards if these components are no longer available. We can also stock additional components if market trends show that the components will become harder or impossible to find in the future.

### 4.4.2 Procurement of parts

The construction of the detector components for DUNE requires many large procurements that must be carefully planned to avoid delays. For the ASICs, the choice of vendor(s) is made at the time the technology used in designing the chips is chosen. For almost all other components, several vendors will bid on the same package. Depending on the requirements of the funding agency and of the responsible institution, this may require a lengthy selection process. The cold cables used to transmit data from the FEMBs to the WIBs represent a critical case. In this case a technical qualification, including tests of the entire cold chain (from the FEMB to the receiver on the WIB) is required. Another problem is the large numbers of components required. In some cases, the number of components of a given type (resistors, capacitors) may far exceed the number of components that the usual resellers keep in stock. This will require careful planning to avoid stopping the assembly chain for the FEMBs, for example, because one kind of component runs short. Figures 4.47 and 4.48 show the flow of the TPC electronics detector components through procurement, assembly, QC testing, and finally integration and installation at SURF using a color code to indicate the activities that are performed by external vendors, those that take place at one of the consortium institutions, and those that take place at SURF.

### 4.4.3 Assembly

The TPC electronics consortium plans to minimize the amount of assembly work at any one of the participating institutions. When assembly work is required, it will be performed by external companies; examples are the installation of surface mount components, ASICs, FPGAs on the printed circuit boards for the FEMBs and the WIBs, and the assembly of the crossing tube cable supports. One of the few exceptions is the assembly of the WIECs that involves mechanical and electrical connections at the backplane and crate supports. Other activities that require work performed at one of the consortium institutions are the assembly of the plugs attached to the cold cables, which are used to protect the FEMBs from ESD damage, and the preparation of the bundles of low-voltage power, clock signal, trigger, data readout, and bias voltage cables. During the engineering phase and for components fabricated in small quantities, like boards used for testing other components, the plan is to have one of the consortium's institutions assemble the components.

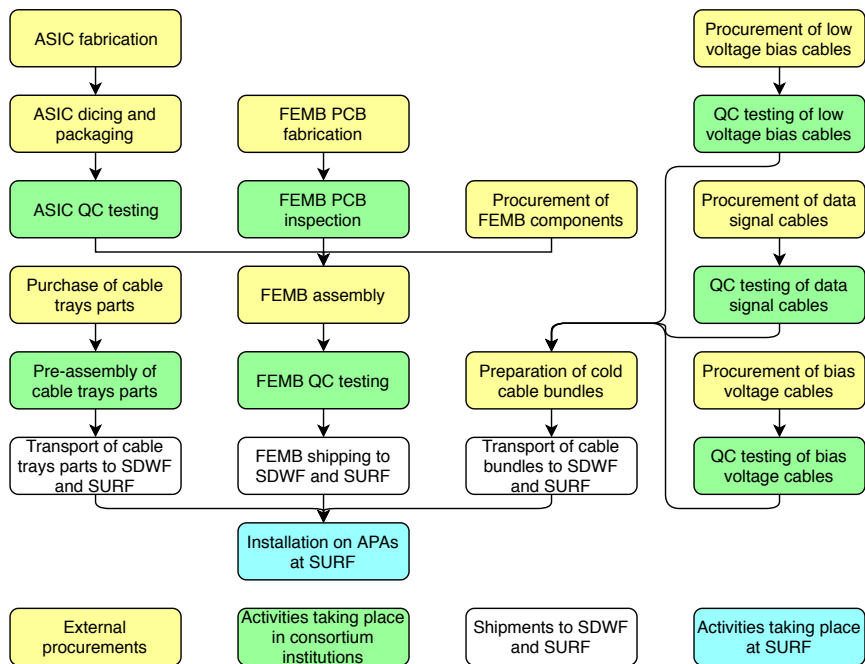


Figure 4.47. Parts flow for the TPC electronics detector components installed inside the cryostat.

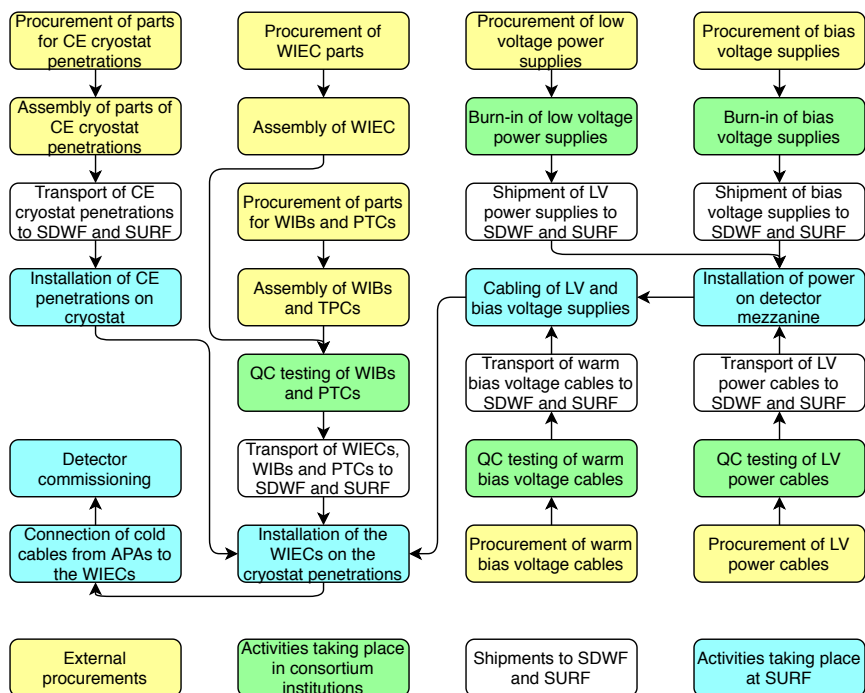


Figure 4.48. Parts flow for the TPC electronics detector components installed on top of the cryostat.

After assembly and testing, discussed below in section 4.4.4, all detector components are shipped to the SDWF and later to SURF, where the final detector assembly takes place as discussed in chapter 9.

### 4.4.4 Quality control

Once the APAs are installed inside the cryostat, only limited access to the detector components will be available to the TPC electronics consortium. After the TCO is closed, no access to detector components will be available; therefore, they should be constructed to last the entire lifetime of the experiment (20 years). This puts very stringent requirements on the reliability of these components, which has been already addressed in part through the QA program discussed in section 4.3. The next step is to carefully apply stringent QC procedures for detector parts to be installed in the detector. All detector components installed inside the cryostat will be tested and sorted before they are prepared for integration with other detector components prior to installation. The full details of the QC plan have not been put in place yet, and the specific selection criteria for the components will be defined only after the current design and prototyping phase is completed. For each detector component, a preliminary version of the QC program will be developed before the corresponding engineering design review. The program will then be used for qualification of components fabricated during pre-production. It will be modified as needed before the production readiness review that triggers the start of production of detector components used for assembling the detector. In most cases the QC program will be informed by the experience gained with the tests of the corresponding parts fabricated for ProtoDUNE-SP. Yields from the testing of LArASIC and of other discrete components mounted on the FEMBs are discussed below.

Some of the requirements for the QC plans can be laid out now based on the lessons learned from constructing and commissioning the ProtoDUNE-SP detector. Experience with ProtoDUNE-SP shows that a small fraction (roughly 4%) of the LArASIC chips that pass the qualification criteria at room temperature fail the tests when immersed in LN<sub>2</sub>. Therefore, we plan to test all ASICs in LN<sub>2</sub> before they are mounted on the FEMBs; cryogenic testing of the FEMBs is also planned. The goal of testing the ASICs in LN<sub>2</sub> is to minimize the need to rework the FEMBs. This is more important if the three ASICs solution is chosen for the FEMB. Since in this case there are 18 ASICs on the FEMB, an upper limit of 2% on the fraction of FEMBs that require reworking translates into a requirement of less than 0.1% of the ASICs failing during immersion in LN<sub>2</sub>. If the CRYO solution is chosen for the ASICs to be used on the FEMBs, the 2% requirement for the number of FEMBs to be reworked changes to a maximum failure rate of 1%, given that there are only two ASICs on the FEMBs. Based on experiences at ProtoDUNE-SPs, discrete components like resistors and capacitors need not undergo cryogenic testing before they are installed on the FEMBs. Capacitors and resistors are commonly sold in reels of a few thousand components, which should be typically sufficient for the fabrication of ten FEMBs. For these components, we are planning to perform cryogenic tests on samples of a few components from each reel prior to using the reel in the assembly of FEMBs. Some other components installed on the FEMBs, like voltage regulators and crystal oscillators, will have to be qualified like the ASICs in LN<sub>2</sub> before being mounted on the FEMBs. In the case of the voltage regulators, it was found that the number of failures were negligible and that cryogenic testing was not necessary. One component used for ProtoDUNE-SP

that we are not planning to use for the DUNE FD FEMBs, the memory card used to store the FPGA programming, had instead a very high failure rate ( $> 50\%$ ).

ASIC testing is performed with dedicated test boards that allow tests of the functionality of the chips and are also used to determine the initial calibration constants that are stored in a database for later use. The dedicated test boards reproduce the entire readout chain where the input to the FE amplifier or to the ADC is replaced by an appropriate signal generator, and some parts of the backend may be replaced by a simple FPGA that is directly connected to a computer. Tests of the FEMBs can be performed by connecting them directly to a standalone WIB, as discussed in section 4.2.6. Given the large number of ASICs and FEMBs required for one DUNE FD SP detector, we plan to distribute the corresponding QC activities among multiple institutions belonging to the TPC electronics consortium. Up to six test sites are needed for the ASICs plus an additional five sites for the FEMBs, with each test equipped with a cryogenic system such as the CTS. All tests will be performed following a common set of instructions.

The choice of distributing the testing activities among multiple institutions has been made based in part on the experience gained with ProtoDUNE-SP, where all associated testing activities were concentrated at BNL. While this approach had some advantages, like the direct availability of the engineers that had designed the components, a strict conformance to the testing rules, and a fast turn-around time for repairs, it also required a very large commitment of personnel from a single institution. Personnel from other institutions interested in the TPC electronics participated in the test activities but could not commit for long periods of time. For this reason, we are planning to distribute the QC testing activities for ASICs and FEMBs among multiple institutions belonging to the TPC electronics consortium. It should be noted that this approach is used in the LHC experiments for detector components like the silicon tracker modules where both the assembly and QC activities take place in parallel at multiple (of the order of ten) institutions. To ensure that all sites produce similar results, we will emphasize training experienced personnel that will overview the testing activities at each site, and we will have a reference set of ASICs and FEMBs that will be initially used to cross-calibrate the test procedures among sites and then to check the stability of the test equipment at each site. All testing activities for ASICs and FEMBs will be monitored by a member of the management of the TPC electronics consortium who will also have the responsibility of training the personnel at all sites and conducting site inspections to ensure that all safety and testing rules and procedures are applied uniformly. Test results will be stored in a database, and criteria will be developed for the acceptance of ASICs and FEMBs. The acceptance rate will be monitored, and in case of problems, the failures will be analyzed and root cause analyses will be performed. If necessary, the test program will be stopped at all sites while issues are being investigated. In the case of CRYO, since each FEMB will only have two chips, it may be possible to bypass chip-level testing altogether. If the chip-level failure rate is low enough, it may be sufficient to simply test assembled FEMBs and reject or rework those that fail the tests.

For the large numbers of ASICs required for one DUNE FD SP detector (6,000 or 54,000 chips depending on the ASIC solution chosen), manual testing of the chips requires excessive amounts of resources and, based on the lessons learned from constructing ProtoDUNE-SP, would lead to unacceptable rejection factors. Ideally, the entire testing process would be performed using a robotic system, where a robotic arm picks up the ASIC from a tray, places it on a test board, and holds it in place while the test is performed, followed by sorting it into a second tray based upon the test

result. The requirement that the test be performed in LN<sub>2</sub> prevents us from using this scheme. Two of the biggest problems observed during the construction of ProtoDUNE-SP were related to the QC of ASICs in LN<sub>2</sub>. The first one, related to condensation on the test boards, has been addressed with the development of the CTS, discussed in section 4.3.1. The second one is related to placement of the chips into the sockets on the test boards, and leads to test failures and in some cases damage to the chips and/or the sockets. To overcome problems with the manual placement of the chips into the sockets, we plan to develop a robotic system to perform this operation. Once the ASICs are placed on test boards, they will be moved manually into upgraded versions of the current CTS that can house multiple test boards. At the end of the testing procedure, the robotic system will then remove the chips from the test boards and sort them according to the test results. Based on the experience with the tests of the ProtoDUNE-SP ASICs, as well as from other experiments, we plan to have the sockets on the test boards cleaned on a regular basis and then replaced after a certain number of testing cycles.

Before assembly, the printed circuit boards for the FEMBs will be tested by the production vendor for electrical continuity and shorts. The usual approach for particle physics experiments is to perform a visual inspection of the boards before installing the discrete components and the ASICs. This inspection will be repeated after installation and before the functionality test, which for DUNE will be performed in LN<sub>2</sub>. The specifications on vias and pads for the printed circuit boards for the FEMBs are not outside the industrial vendors' capabilities, and therefore we do not expect these inspections to be absolutely necessary. We will perform visual inspections on a sample of production units, with a higher rate of sampling at the beginning of the production. We will also investigate the possibility of using other, possibly automatic, inspection methods for the bulk of the production. After assembly, each FEMB will be tested in LN<sub>2</sub> using the current CTS design. Nine CTSs have already been fabricated and are being distributed among the institutions in the consortium.

The test procedures are likely to be very similar to the ones adopted for ProtoDUNE-SP, with the main difference that the tests will not be performed with the final cables to be used in the experiment but with a set of temporary cables. The final cables will be tested separately as described below. The tests of the FEMBs are performed using the CTS, which allows a turnaround time of about one hour per FEMB. In the test, the FEMB is connected to a capacitive load that simulates the presence of APA wires. This allows connectivity checks for each channel as well as measurements of the waveform baseline and of the channel noise level. Calibration pulses will be injected in the front-end amplifier, digitized, and read out. These injected pulses will also be used to determine the calibration constants of the ADC. The test setup requires one WIB and a printed-circuit board similar to those used on the cryostat penetration, allowing simultaneous testing of four FEMBs. A standalone 12 V power supply is required, and the readout of the WIB uses a direct Gb Ethernet connection to a PC. The setup used for ASIC testing is similar. In both cases, the data can be processed locally on the PC, and the results from the tests and calibrations are then stored in a database. The plan is to have the capability to retrieve these test and calibration results throughout the entire life of the experiment. As in the case of ASIC testing, we will monitor the test results to ensure that all sites have similar test capabilities and yields and to identify possible problems during production. Further tests will be performed on the FEMBs before and after their installation on the APAs, as discussed in section 9.4.

The final component provided by the TPC electronics consortium and installed inside the cryostat is the ensemble of cold cables: the cables carrying the bias voltage for the APA wires and the field cage termination electrodes; the cables carrying the low-voltage power to the FEMBs; and the data cables that carry the clock and control signals to the FEMBs that are also used for signal readout. It is neither feasible nor necessary to test these cables in LN<sub>2</sub> because they will usually perform better at cold temperatures than room temperature. We will perform checks on all cables during production at room temperature before they are installed and connected to the FEMBs. These tests will involve continuity checks and resistance measurements on the low-voltage power and the bias voltage cables, and also bit-error rate measurements on the clock/control and data readout cables. Connectors will be visually inspected to ensure that they show no sign of damage. Further tests will take place when the APAs are tested in the cold boxes at SURF prior to installation inside the cryostat.

Stringent requirements must be applied to the cryostat penetrations in order to avoid argon leaks. The cryostat penetrations have two parts: the first is the crossing tube with its spool pieces, and the second one is the three flanges used for connecting the power, control, and readout electronics with the CE and PD system components inside the cryostat. On each cryostat penetration there are two flanges for the CE and one for the PD system. The crossing tubes with their spool pieces are fabricated by industrial vendors and pressure-tested and tested for leaks by other vendors. The flanges are assembled by institution that are members of the TPC electronics and PD system consortia; the flanges must undergo both electrical and mechanical tests to ensure their functionality. Electrical tests comprise checking all of the signals and voltages to ensure they are passed properly between the two sides of the flange and that there are no shorts. Mechanical tests involve pressure-testing the flange itself, including checking for leaks. Further leak tests are performed after the cryostat penetrations are installed on the cryostat and later after the TPC electronics and PD system cables are attached to the flanges. These leak tests are performed by releasing helium gas in the cryostat penetration and checking for the presence of helium on top of the cryostat. Similar tests were performed during the ProtoDUNE-SP installation.

All other detector components that are a responsibility of the TPC electronics consortium can be replaced, if necessary, even while the detector is in operation. Regardless, every component will be tested before it is installed in SURF to ensure smooth commissioning of the detector. The WIECs will be assembled and tested with all of the WIBs and PTC installed. Testing requires a slice of the DAQ back-end, power supplies, and at least one FEMB to check all connections. All cables between the bias voltage supplies and the end flange, as well as all of the cables between the low-voltage power supplies and the PTCs will be tested for electrical continuity and for shorts. All power supplies will undergo a period of burn-in with appropriate loads before being installed in the cavern. Optical fibers will be tested by measuring the eye diagram for data transmission at the required speed. All test equipment used for qualifying the components to be installed in the detector will be either transported to SURF or duplicated at SURF in order to be used as diagnostic tools during operations.

After the completion of the initial QC testing, all detector parts are transported first to the SDWF and later to SURF, where all the integration activities will take place as discussed in section 4.5 and in chapter 9.

#### 4.4.5 Test facilities

The QC plan described in the previous section requires multiple test stands that must be put in place and used before the beginning of production. For the testing of ASICs, a setup similar to the CTS (see section 4.3.1) will be used. In this setup, several test boards housing up to 24 chips will be immersed in LN<sub>2</sub> before running the electronics tests; the test boards will later be warmed to room temperature in a nitrogen atmosphere to avoid condensation on the chips and boards. As mentioned previously, placing the chips on the test boards will be performed using a robotic system. The test setups, one for each kind of ASIC, will be an evolution of those used initially for characterizing the ASIC and similar to the setups used for qualifying the chips used in the ProtoDUNE-SP construction. The tests of the FEMBs will be performed with setups that include using CTSs units for the cryogenic part but are otherwise simple modifications (with newer WIBs) of the setups used to characterize the FEMBs for ProtoDUNE-SP. Cold and warm power and bias voltage cables will be characterized with test stations using appropriate power supplies and some cable testing equipment; these cables will most likely be COTS components. For the test of the data cables, we will probably rely on a setup using waveform generators and a high end oscilloscope that can handle 2.56 Gbps signals and measure eye diagrams. Burn-in stations, with custom-designed loads, may be required for the commercial low-voltage power and bias voltage supplies. A test setup to check WIECs with their WIBs and PTCs installed will require a minimal DAQ back-end that the DAQ consortium should provide.

Given the delay between the beginning of the DUNE FD APAs production and the production of the TPC electronics components, it is desirable to integrate the FEMBs on some of the APAs and perform tests in cold boxes. For APAs fabricated in the UK, these tests will be performed at CERN using the ProtoDUNE-SP cold box. A similar setup needs to be put in place in the US (most probably at the University of Wisconsin) to perform these tests ahead of the shipment of the APAs to SDWF and SURF. Both the setup at CERN and the one in the US will require a full power, control, and readout system, similar to the one described in section 9.4.2.

#### 4.5 Integration, installation, and commissioning

Chapter 9 provides a complete discussion of the plans for integrating, installing, and commissioning the detector. Here, we briefly discuss the responsibilities of the TPC electronics consortium for the activities taking place at SURF, with the exception of the QC process that is discussed in detail in section 9.4.2. We also discuss the timeline and the resources for the integration and installation activities. Finally, we conclude with a discussion of the commissioning of the TPC electronics detector components that take place while the cryostat is being filled and immediately after the fill is completed.

##### 4.5.1 Timeline and resources

The current TPC electronics consortium plan is to receive all detector components at the SDWF, where they are stored temporarily prior to being transported to SURF for integration and installation. Only the FEMBs will undergo a reception test, either in a laboratory on the surface at SURF or in a nearby institution, prior to integration with the other DUNE SP detector components. All other

integration takes place at SURF in the clean room in front of the detector cryostat. After a pair of APAs are connected and moved inside the clean room, the CE cables for the bottom APA are routed through the APA frames. The cables are then connected to the FEMBs, and the bundles of cables are placed in the trays at the top of the APA pair. At this point, the pair of APAs is moved into one of the cold boxes, and the cables are connected to a patch panel inside the cold box to save the time that would be required for routing the cables through the cryostat penetration of the cold box and connecting them to the end flange. The CE is then tested at both room temperature and at a temperature close to that of LN<sub>2</sub>, much like what was done for the APAs installed in the ProtoDUNE-SP detector.

Later, the pair of APAs is moved to its final position inside the cryostat. The CE and PD system cables are routed through the cryostat penetration and connected to the corresponding warm flanges, and final leak tests are performed on the cryostat penetration. At this point, the WIEC is attached to the warm flange and all of the cables and fibers required to provide power and control signals to the TPC electronics and for data readout are connected. This permits additional testing with the full DAQ readout chain and the final power and controls signals distribution system. Once initial tests are completed successfully, more APAs can be installed, and the APAs and their FEMBs can remain accessible until the FC are deployed.

This installation sequence assumes that all the TPC electronics detector components required for readout of a pair of APAs on top of the cryostat are installed before APAs are inserted into the cryostat. This includes the WIECs with their boards, the power supplies in the racks, and all cables and fibers required to distribute power and control signals as well as for detector readout. Installation should occur at least two weeks before the APAs are inserted into the cryostat to allow time for final checks.

One exception is installing the cryostat penetrations with the warm flanges for both the CE and the PD system. The cryostat penetrations should be installed, at the latest, at the same time the detector support structure is installed inside the cryostat. This ensures the cryostat is almost completely sealed to minimize the amount of dust entering the cryostat. During the routing of the CE and PD system cables through the cryostat penetrations, dust entering the cryostat will be minimized by having a small over-pressure inside the cryostat and by isolating each penetration from the cavern using a tent mounted over the work area.

The schedule of activities at SURF is designed so all APAs can be installed in the cryostat on a timescale of eight months, proceeding at a rate of one row of six APAs per week and allowing for a ramp-up period at the beginning of the process. This requires that personnel from the TPC electronics consortium be available for two 10-hours shifts per day at SURF at all times, including weekends. A total of 30 FTEs/week will be needed to install and test the APAs, under the assumption that there will be a maximum of four shifts per person per week.

The installation of all other TPC electronics detector components takes place on the top of the cryostat. The cryostat penetrations are installed ahead of the installation of the APAs inside the cryostat, ideally as soon as the welding of the cold membrane is completed in part of the cryostat. This activity requires a team of eight FTEs, split over two shifts per day, for a period of one month. A similar amount of time and personnel is also required to install the power supplies in the racks, attaching the WIECs to the CE flanges, and routing and connecting the warm cables.



### 4.5.2 Internal calibration and initial commissioning

While the cryostat is being closed (and any time there is welding on the cryostat), the electronics should be turned off and all cables between the detector racks, including the low-voltage power and bias voltage, fans, and heater power, should be disconnected from the WIECs. Once the cryostat is closed, the waveform baseline and noise level of all channels should be measured. Dead electronics channels should be identified by measuring the response of all channels to the internal electronics calibration pulser at a nominal setting, such as  $\pm 600$  mV, which distinguishes between induction and collection channels. The noise levels should be measured with the wire bias voltages fully enabled on the  $G$ ,  $U$ , and  $X$  planes of the APAs. It should also be measured with the cathode high voltage on at a very low value, e.g. 50 V. The non-responsive channels, identified as having very low noise levels, and the channels that have noise levels that significantly exceed the average value should be flagged and recorded. Sources of excess noise should be identified and, if possible, fixed. Any warm electronics components with issues should be replaced with spares.

Once the cryostat is filled with gaseous argon, the waveform baseline and noise level of all of the channels will be measured again, and any new non-responsive channels in the electronics should be identified by injecting  $\pm 600$  mV with the internal calibration pulser. As the cryostat is cooled down, the temperature at the electronics and the noise level of all channels should be monitored periodically. Any new non-responsive channels should be flagged and excess noise sources that are exposed as the electronics cools down should be identified and, if possible, fixed.

Once the electronics is fully submerged in LAr, a full set of electronics diagnostic tests should be run, including waveform baseline and noise level measurements as well as a full gain calibration on all channels using the internal calibration pulser at settings up to the saturation of the FE inputs. The shaping time should be measured on all channels by injecting the  $\pm 600$  mV internal pulser at each of the four settings and fitting the pulse shape. Any new non-responsive channels during the pulser runs should be flagged. Any new disconnected channels should be flagged and excess noise sources should be identified. These tests can be performed on the electronics installed on the bottom APAs even while the corresponding wires are in the gaseous argon.

## 4.6 Interfaces

Table 4.6 contains a brief summary of all of the interfaces between the TPC electronics consortium and other consortia or groups, with references to the current version of the interface documents. In some cases, the interface documents involve more than one consortium (one example is the bias voltage distribution system where the interface involves both the APA and the HV consortia). In such cases, the goal is to have all of the corresponding interface documents consistent. At this stage, most of the interface documents are not yet complete; drawings of the mechanical interfaces and diagrams of the electrical interfaces are still under development. The interface documents should be further refined during the first half of 2020 before the engineering design reviews of the detector. All interface documents specify the responsibilities of different consortia or groups during all phases of the experiment, including design and prototyping, integration, installation, and commissioning. In the remainder of this section, the most important interfaces, specifically those with the APA, DAQ, and HV consortia, as well as the interface with technical coordination, are discussed in detail. Finally, a brief overview of the remaining interfaces is also presented.

**Table 4.6.** TPC electronics system interfaces.

| Interfacing System   | Description  | Linked Reference |
|----------------------|--|------------------|
| APA                  | Mechanical (cable trays, cable routing, connections of CE boxes and frames) and electrical (bias voltage, FEMB–CR boards connection, grounding scheme)                     | [9]              |
| DAQ                  | Data output from the WIB to the DAQ back-end, clock signal distribution, controls and data monitoring responsibilities   | [68]             |
| CISC                 | Rack layout, controls and data monitoring  | [69]             |
| HV                   | Grounding, bias voltage distribution, installation and testing   | [30]             |
| PD system            | Electrical (cable routing and installation), cold flange   | [70]             |
| Facility             | Cable trays inside the cryostat, cryostat penetrations, rack layout and power distribution on the detector mezzanine, cable and optical fiber trays on top of the cryostat | [71]             |
| Installation Team    | Integration and installation activities at SURF, equipment required for TPC electronics consortium activities, cold boxes for APA tests, material handling                 | [72]             |
| Physics              | Responsibilities for simulation and reconstruction software  | [73]             |
| Software & Computing | Database needs for storing detector calibration and configurations, computing needs for calibration and monitoring   | [74]             |
| Calibration          | Access to low-level electronics calibration for high-level physics calibration   | [75]             |

#### 4.6.1 APA

The most important interface is between the TPC electronics and the APA consortia. The design of the FEMBs and of the APAs are intertwined, both from the mechanical and electrical points of view. The CE boxes, which house the FEMBs, are supported by the APA and are attached to the CR boards of the APA through a connector that passes all signals from the wires to the FE amplifiers. The cable trays that house both the CE and the PD system cold cables are initially attached to the yoke of the upper APA. The CE cables for the lower APA must be routed through the frames of both the bottom and top APAs. The TPC electronics consortium provides the bias voltage for the APA wires as well as for the electron diverters and the FC termination electrodes (the latter are a

responsibility of the HV consortium) using the SHV boards mounted on the APAs. The grounding requirements discussed in section 4.2.1 inform the design of all mechanical and electrical interfaces between the CE components and APAs as well as the design of the connections between the top and bottom APAs and between the top APA and the DSS. All integration and installation activities at SURF must be carefully coordinated by the two consortia and where appropriate also with the PD system consortium and technical coordination.

### 4.6.2 DAQ

The DAQ system receives the data produced by the TPC electronics detector components, further processes this data to form trigger decisions, and finally transfers the data to permanent storage for analysis. The DAQ system is also responsible for delivering the clock and control signals to the WIECs. The interfaces are realized through optical fibers, ensuring that no electrical noise is fed into the WIECs. One fiber per WIEC delivers the clock and control signals to the PTC, which then rebroadcasts the information to the WIBs in that crate. Each WIB reads out the data from four FEMBs and transmits the data through two 10 Gbps links to the DAQ back-end.

The data signals from the WIECs to the DAQ system are carried on multi-mode optical fibers, compatible with either the OM3 or OM4 standards. Individual fibers will be merged into bundles of 12 fibers with MTP connectors near the CE cryostat penetrations. These bundles will be merged in trunks of 144 fibers on the detector mezzanine, which will then be fanned out to individual optical fibers inside the CUC. The feasibility of this data transmission scheme using optical fibers with a length up to 300 m has been demonstrated at BNL in summer 2018 using ProtoDUNE-SP components. The data format used for DUNE will be a modification of the one adopted for ProtoDUNE-SP, taking into account the need for an extended address space to accommodate the larger number of FEMBs in the detector. The DAQ consortium is also responsible for providing the software environment used for downloading the detector configuration.

### 4.6.3 HV

The HV consortium interface is driven by the fact that the CE flange provides the return path for the small current that flows from the high-voltage power supply through the cathode panels, the FC, and finally the termination electrodes. The hardware interface uses the SHV boards mounted on the APAs, which are the responsibility of the APA consortium. The SHV boards also distribute the bias voltage to the FC termination electrodes. The TPC electronics consortium is responsible for bringing the bias voltage for the FC termination electrodes to the SHV boards. Appropriate rules for avoiding ground loops are also included in the interface document.

### 4.6.4 Technical coordination

In this section, we consider the interfaces with LBNF and with the DUNE technical coordination, including the interfaces with the Joint Project Office (JPO) that oversees the integration and installation activities that take place at SURF. The TPC electronics consortium has several interfaces with the facility, namely the cable trays inside the cryostat, the cryostat penetrations used by the TPC electronics and PD system consortia, and the racks and trays on top of the cryostat. The TPC electronics consortium is responsible for the design, procurement, and installation of the cable trays

inside the cryostat and the cryostat penetrations. The DUNE technical coordination is responsible for providing the racks where the low-voltage power supplies and the bias voltage supplies are installed, including their power, cooling, and monitoring systems, as well as the hardware interlock system. Technical coordination is also responsible for the trays connecting these racks to the corresponding WIEC and for the network switches that connect the controls for the TPC electronics to the DAQ and slow controls back-ends. Finally, technical coordination will provide the DDSS that will protect the TPC electronics detector components. The TPC electronics consortium will work with technical coordination to establish the action matrix for the DDSS and the hardware interlocks, and also to resolve any electronics noise problems that may be caused by improper grounding of detector components.

The TPC electronics consortium will work with the teams responsible for the underground integration and installation in order to plan all activities that take place at SURF. This includes developing plans to outline the responsibilities of the consortium and those of technical coordination personnel for the activities at SURF, including all shipments, transport, and logistics, as well as all integration and installation. Cold boxes for testing the APAs after integration with the FEMBs will be provided by technical coordination at SURF. All other testing equipment will be provided either by the TPC electronics consortium or by other consortia. Equipment required to minimize risk of ESD damage to the detector components will be provided by the TPC electronics consortium.

### 4.6.5 Other interfaces

The interface with the PD system consortium is relatively simple. The PD system detector component should be isolated from the CE detector component other than sharing a common reference voltage point (detector ground) at the chimneys. Inside the cryostat, the PD system and CE cables will be housed together in cable trays that are the responsibility of the TPC electronics consortium. The TPC electronics consortium will also assume the responsibility for routing the PD system cables through the cryostat penetration and for connecting them to the PD system flange. The TPC electronics consortium will also connect the cables that run from the flange to the mini-racks housing the PD system warm electronics. The flange itself will be designed and built by the PD system consortium, but its integration on the spool piece of the cryostat penetration will be the responsibility of the TPC electronics consortium.

The CISC consortium provides the software infrastructure for the slow control and monitoring of the status of the TPC electronics components. The CISC and TPC electronics consortia may also have hardware interfaces because they may share the same racks on top of the cryostat. The most important aspect of the interface between these two consortia is the requirement from the TPC electronics consortium to have all relevant parts of the slow control and monitoring equipment functional at the beginning of the installation for SURF.

The TPC electronics consortium is responsible for many parts of the DUNE simulation and reconstruction software, which constitute the interface with the Physics group. These include the simulation of the material of the detector components (FEMBs, cables, and cable trays) inside the LAr, the simulation of the response of the electronics, from the signal formation to its digitization, and finally the methods for the deconvolution of the electronics response to be used in the event reconstruction software (the latter responsibility is shared with the APA consortium). Many of these software tools already exist and have been used for the simulation and the reconstruction of

ProtoDUNE-SP. In the coming years they will be updated to reflect the changes to the detector design relative to ProtoDUNE-SP. Similarly, the TPC electronics consortium has an interface with the Software and Computing consortium that covers mostly the need for data storage and data access. This includes both database needs (for storing detector calibration constraints and detector configurations) and disk space needs (for storing the data from special calibration runs that are used to obtain the calibration data). The calibration data on the response shape of the electronics and on its gain are also relevant to the Calibration consortium, which is tasked with obtaining high-level calibrations of the detector response. When doing this, the most up-to-date electronics calibrations, or in some cases special electronics calibrations, will be required.

### 4.7 Safety

Personnel safety during construction, testing, integration, and installation of the TPC electronics components for the DUNE SP FD is crucial for the success of the project. The members of the TPC electronics consortium will respect the safety rules of the institutions where the work is performed, which may be one of the national laboratories, SURF, or one of the universities participating in the project. A preliminary analysis of the risks involved in the design, construction, integration, and installation of the detector components provided by the TPC electronics consortium has been performed using the approach discussed in Volume III, DUNE far detector technical coordination, chapter 10.

#### 4.7.1 Personnel safety during construction

The main risks for consortium personnel are exposure to the LN<sub>2</sub> used for cooling down components during testing (risk HA-8 in table 11.25 in Volume III, DUNE far detector technical coordination, chapter 11), falls from heights (risk HA-1), electrical shocks (risk HA-6), and oxygen deficiency hazards, possibly caused by leaks of either LN<sub>2</sub> or LAr from test setups (risk HA-8). The leadership of the TPC electronics consortium will work with the LBNF/DUNE ES&H manager and other relevant responsible personnel at the various institutions to ensure all the members of the consortium, including students and postdocs, receive the appropriate training for the work they are performing and that all preventive measures to minimize the risk of accidents are in place. Where appropriate, we will adopt the strictest standard and requirements among those of different institutions. Hazard analyses will be performed, and the level of PPE will be determined appropriately for each task. PPE includes appropriate gloves for handling LN<sub>2</sub> dewars, fall protection equipment for work at height, and steel-toed shoes and hard hats for integration work with the APA. Oxygen monitors should be used in areas with large potential concentrations of cryogenic gases.

ES&H plans for the activities to be performed in various locations, including all universities, national laboratories, and SURF, will be discussed in the various reviews (Preliminary Design, Engineering Design, Production Readiness, Production Progress) that will take place during the construction of the detector. This will include inspections by a LBNF/DUNE ES&H representative at all the sites where detector components will be assembled or tested to ensure conformance to all of the safety rules.

#### 4.7.2 Detector safety during construction

In addition to personnel safety during detector construction, including all testing, integration, installation, and commissioning, we have also considered how to protect the detector components and minimize any chances of damaging them during handling. We identified two main risks to the safety of the detector during construction and one risk during operation. The most important risk during construction is damage induced by ESD in the electronics components. The second risk is mechanical damage to parts during transport and handling. For operation risks, we must consider the risk of damage to the electronics caused by accumulated dust inside the components installed on the top of the detector. In this section, we discuss these three risks and ways to minimize their possible effect. In the following section, we discuss how to prevent damage during operation to the TPC electronics components by using the interlocks of the detector safety system.

ESD can damage any of the electronics components mounted on the FEMBs, WIECs, the bias voltage supplies, or the power supplies. If the damage occurs early in construction, the outcome is a reduction of the yield for some of components, which must be addressed by keeping a sufficient number of spares on hand to prevent schedule delays associated with procuring new parts. ESD damage on the FEMBs after the APAs have been installed inside the cryostat could result in a permanent reduction of the fraction of operating channels in the detector. Even if most components, including the custom ASICs designed for use in the FEMBs, contain some level of protection against ESD, the possibility of this kind of damage cannot be ignored, and appropriate preventive measures must be taken during assembly, testing, installation, and shipping of all of the detector components provided by the TPC electronics consortium. These measures include using appropriate ESD-safe packing materials, appropriate clothing and gloves, wearing conducting wrist or foot straps to prevent charges from accumulating on workers' bodies, anti-static mats to conduct harmful electric charges away from the work area, and humidity control. All laboratories with detector components provided by the TPC electronics consortium will implement these measures, including SURF.

Additional measures include using custom-made terminations for power, control, and readout cold cables when these are being routed through the APA frames or through the cryostat penetrations. Storage cabinets where ASICs and FEMBs are stored should have ESD mats on the shelves and humidity control. Most importantly, all personnel must be trained to take the appropriate preventive measures. We will require that all the personnel working on the TPC electronics consortium components take a training class originally developed at Fermilab for handling the charge-coupled devices of the Dark Energy Survey (DES) experiment (the material for this training class can also be used at remote sites). The scientists in charge of the TPC electronics activities at each site involved in the project will be responsible for monitoring the training of personnel at universities, national laboratories, and SURF.

Most of the damage to detector components happens during transport among the various sites where assembly, testing, integration, and installation take place. When appropriate, measures to prevent ESD damage must also be taken for shipments. Appropriate packaging will be used to ensure that parts are not damaged during transport. We will perform tests upon receiving FEMBs as well as integration tests for cold cables as part of the quality control process discussed in section 4.4.4 in order to ensure the full functionality of these parts, which are very hard to replace after detector integration and installation. For components on the top of the cryostat that can be replaced if damaged during transport, we will perform integration tests after installation.

In addition to damage during shipping, we must also consider the possibility of damage caused by handling of the detector parts. Additional precautions are being considered for operations where the risk of damage to TPC electronics detector components is high. For testing ASICs and FEMBs in LN<sub>2</sub>, this has resulted in developing the CTS discussed in section 4.3.1 to prevent condensation on components after they are extracted from the LN<sub>2</sub> at the end of a test. For the cold cables, this includes modifying the size of the tubes used for the APA frames, adding a conduit inside the frames, and placing a mesh around the cables. Special tooling will be designed for arranging the cold cables on the spools used when cables are routed through the APA frames. Similarly, tooling will be developed to support the cold cables while they are being routed through the cryostat penetrations. All cables and optical fibers will be installed in cable trays on top of the cryostat, and for the fibers, additional protection in the form of sleeves or tubes may also be used.

To ensure that the DUNE detector will be operational for a long time, we also will attempt to minimize damage that could happen to detector components inside the experimental cavern, which can come from two sources: incorrect operation of the detector and environmental conditions. We will discuss the former in the next section. Once the cryostat is filled with LAr, the environmental conditions inside the cryostat are extremely stable. Experience from previous experiments using electronics inside LAr indicates that, apart from initial problems, little loss of readout channels occurred over long periods.

Therefore, the main safety concern is related to the electronics installed on top of the cryostat. The main problem in this case is dust accumulation on detector components. Over the long term, dust could damage the cooling fans used in the WIECs and the TPC electronics racks, cause breakdown on the surface of diodes used in bias voltage supplies, and, if the dust contains any chemical residue that may create deposits on printed circuit boards, create leakage paths between traces on printed circuit boards. While the experimental cavern should be a very dry environment, protections should still be in place to prevent water from dripping on the WIECs and on the racks containing the TPC electronics power and bias voltage supplies. Appropriate filters will be added to the air supply used to cool the WIECs and the TPC electronics power and bias voltage supplies, thereby minimizing the accumulation of dust. The air humidity in the cavern will be controlled to prevent condensation.

### 4.7.3 Detector safety during operation

In this section, we discuss where we will use the detector safety system described in Volume III, DUNE far detector technical coordination, chapter 10. To avoid unsafe conditions for the TPC electronics detector during operations, hardware interlocks will be put in place in test setups at SURF to prevent operating or even powering up detector components unless conditions are safe both for the detector and for personnel. Interlocks will be used on all low-voltage power and on bias voltage supplies, including inputs from environmental monitors both inside and outside the cryostat. Examples of these interlocks include turning off the power to the WIECs if the corresponding cooling fans are not operational or if the temperature inside the crates exceeds a preset value. Similar interlocks will be used for low-voltage power and bias voltage supplies in TPC electronics racks. Interlocks may be needed to connect the value of the bias voltage on the FC termination electrodes to the high voltage applied on the TPC cathode. Interlocks will turn off transmitters on the WIECs if the readout fibers' bundles are cut. One problem we must address

is the connection between the PLC used by the detector safety system and the WIECs to avoid introducing noise inside the detector. We can easily decouple the environmental sensors required by the detector safety system inside the WIECs by following the appropriate grounding rules. The connection used to provide the enable/disable signals from the PLC to the WIECs will require optical fibers to avoid possible ground loops. Interlocks connected to the detector safety system will also be used during tests of the APAs in the cold boxes at CERN, Fermilab, and SURF. The CTS has its own interlock system to prevent condensation from forming on the FEMBs once they have warmed to room temperature. We cannot exclude the possibility that for some of the smaller test stands we will have to rely on software interlocks for detector safety, but this should be kept to a minimum, and no software interlock should be used for the cold boxes at CERN, Fermilab, and SURF.

#### 4.8 Risks

In this section, we discuss the risks that could be encountered during design and construction of the DUNE SP FD, as well as the risks that can be encountered later during commissioning and operation. For every risk, we will describe the mitigating actions being put in place even now at the design stage of the experiment, and the possible responses that we will take should a specific risk be realized. Table 4.7 contains a list of all risks that we are considering. For each risk, we assess a probability for a risk to be realized (P), as well as cost (C) and schedule (S) impacts, after the mitigation activities discussed in the text are put in place. It should be noted that in the case of poor lifetime of the components installed inside the cryostat, there is no cost or schedule impact, as they cannot be accessed and replaced. All of these risks are discussed in detail in the remainder of this section.

**Table 4.7:** TPC electronics risks (P=probability, C=cost, S=schedule) The risk probability, after taking into account the planned mitigation activities, is ranked as L (low < 10 %), M (medium 10 % to 25 %), or H (high > 25 %). The cost and schedule impacts are ranked as L (cost increase < 5 %, schedule delay < 2 months), M (5 % to 25 % and 2–6 months, respectively) and H (> 20 % and > 2 months, respectively).

| ID            | Risk  | Mitigation   | P | C | S |
|---------------|---|--|---|---|---|
| RT-SP-TPC-001 | Cold ASIC(s) not meeting specifications                                     | Multiple designs, use of appropriate design rules for operation in LAr   | H | M | L |
| RT-SP-TPC-002 | Delay in the availability of ASICs and FEMBs                                | Increase pool of spares for long lead items, multiple QC sites for ASICs, appropriate measures against ESD, monitoring of yields | M | L | L |
| RT-SP-TPC-003 | Damage to the FEMBs / cold cables during or after integration with the APAs | Redesign of the FEMB/cable connection, use of CE boxes, ESD protections, early integration tests                                 | M | L | L |
| RT-SP-TPC-004 | Cold cables cannot be run through the APAs frames                           | Redesign of APA frames, integration tests at Ash River and at CERN, further reduction of cable plant                             | L | L | L |



|               |  |  |   |     |     |
|---------------|--|--|---|-----|-----|
| RT-SP-TPC-005 | Delay and/or damage to the TPC electronics components on the top of the cryostat | Sufficient spares, early production and installation, ESD protection measures  | L | L   | L   |
| RT-SP-TPC-006 | Interfaces between TPC electronics and other consortia not adequately defined    | Early integration tests, second run of ProtoDUNE-SP with pre-production components   | M | L   | L   |
| RT-SP-TPC-007 | Insufficient number of spares  | Early start of production, close monitoring of usage of components, larger stocks of components with long lead times   | M | L   | L   |
| RT-SP-TPC-008 | Loss of key personnel  | Distributed development of ASICs, increase involved of university groups, training of younger personnel  | H | L   | M   |
| RT-SP-TPC-009 | Excessive noise observed during detector commissioning                           | Enforce grounding rules, early integration tests, second run of ProtoDUNE-SP with pre-production components, cold box testing at SURF                          | L | L   | M   |
| RT-SP-TPC-010 | Lifetime of components in the LAr  | Design rules for cryogenic operation of ASICs, measurement of lifetime of components, reliability studies  | L | n/a | n/a |
| RT-SP-TPC-011 | Lifetime of components on the top of the cryostat                                | Use of filters on power supplies, stockpiling of components that may become obsolete, design rules to minimize parts that need to be redesigned / refabricated | L | M   | L   |

#### 4.8.1 Design and construction risks

Despite the successful operation of ProtoDUNE-SP, we cannot build and operate the DUNE SP FD using the same ASICs; we are improving the design of the FE amplifier, redesigning the ADC, and replacing the FPGA on the FEMB with a dedicated data serialization and transmission ASIC (COLDATA). The project schedule has sufficient time for a second submission of all of these ASICs in the current development cycle. We nevertheless must consider the risk (RT-SP-TPC-001 in table 4.7) that, even after the second iteration, we may not have a set of ASICs that meets all the DUNE requirements.

To reduce the probability of this happening, we are pursuing the development of the CRYO ASIC, and we will also perform system tests of the COTS solution for the ADC that is planned for use in the SBND experiment. Should this risk become reality, an additional development cycle would be required, which would delay the availability of FEMBs for approximately 12 months. Based on the current schedule, this would not be a problem for the detector integration and installation. More importantly, such a delay would require that, during the first part of the APA production, a sufficient number of FEMBs with non-final electronics be available for integration tests on the APAs. These boards would then have to be replaced later by the final boards.

The second risk (RT-SP-TPC-002) is a general delay in the availability of the ASICs and/or FEMBs, which would then not be available for integration on the APAs. This risk has several possible triggers: a lower fabrication yield than expected for ASICs and FEMBs, significant downtime at one of the QC sites, or losses during handling and transport, in addition to the issues with the

design already covered in the previous risk. Our planning includes several ways to mitigate this risk. By procuring spares for the ASICs and the discrete components to be mounted on the FEMBs, we can continue integration with the APAs; we are also splitting the QC process among various sites. We will also emphasize, as discussed in section 4.7.2, the use of appropriate measures that minimize the probability of any ESD damage. We will then monitor the use of spare components and, if needed, fabricate additional parts. Appropriate monitoring of the production yield and spares should minimize delays in APA integration. As in the case of the first risk, should this second risk become reality, we do not expect to have delays in the installation of the detector inside the cryostat.

The third risk (RT-SP-TPC-003) is the possibility of damage to the FEMBs during or after integration with the APAs. This could happen while the FEMBs are being installed or, more likely, during the installation of the cold cables, something that has already taken place during the installation of ProtoDUNE-SP. This damage could also happen when the APAs are moved into the cryostat or during the final cabling of the detector. The damage to the FEMBs and cold cables could be either mechanical damage during handling or ESD damage. We are redesigning the connection between the FEMBs and the cold cables to minimize the probability of the former and putting procedures in place to minimize the probability of the latter. The risk of mechanical damage is further reduced by housing the FEMBs inside the CE boxes and by having appropriate strain relief on the cold cables. To minimize the possibility of ESD damage, we will follow all appropriate procedures, and in addition, we will use plugs on all the cold cables while they are routed through the APA frames and cryostat penetrations in order to avoid injecting charge on the FEMBs that could cause ESD damage. Finally, we are planning for extensive testing of the CE several times during integration and installation that would allow us to replace the FEMBs or the cold cables if necessary. This includes significant time for testing the entire readout chain after the APAs are placed in their final position inside the cryostat, when repairs are still possible.

We still consider risk (RT-SP-TPC-004) a possibility: that the cold cables cannot be routed through the frames of the APAs. In that case, the cables for the FEMBs attached to the bottom APA would have to be routed along the walls of the cryostat, requiring a significant redesign of the entire detector. To minimize this risk, we have significantly redesigned the APA frame to use larger tubes, and many studies have been performed in recent months. These studies are based on the assumption that there can be a small reduction in the cable plant size compared to ProtoDUNE-SP. The probability of this risk being realized has been significantly reduced following the cable insertion tests performed at Ash River using a stacked pair of APAs, discussed in sections 2.3.3 and 4.2.5. This risk has not yet been retired, since the expected reduction of the cable plant needs to be demonstrated with the design and test of new FEMBs. Should this risk be realized, we will consider other ways for reducing the cable plant, instead of the considering the option of routing the cables along the walls of the cryostat. For example, the control signals could be shared between multiple FEMBs.

The next risk (RT-SP-TPC-005) involves delays in the availability of or damage to the TPC electronics components installed on top of the cryostat. As discussed in section 4.5.1, we plan to have all TPC electronics detector components on top of the cryostat, including those required to power, control, and readout one pair of APAs, installed and available before inserting the APAs into the cryostat. This allows extensive testing of APAs to mitigate the risk of damage to the readout chain. To mitigate the risk associated with delays in installing the TPC electronics components

on top of the cryostat, we plan to have sufficient spares and to use appropriate ESD prevention measures. If only a subset of all components is available, cables and fibers on the top of the cryostat would have to be re-routed to allow integrating and installing the APAs to continue without delays, and tests will have to be repeated when all the components become available and are installed. The worst possible consequence is a delay in closing the cryostat and beginning operation.

Another risk (RT-SP-TPC-006) is that incompatibilities between various components of the DUNE FD go undetected until these components are integrated during prototyping, during integration at the SURF, or during installation. These incompatibilities could result in reworking or redesigning some of the components and therefore in delays of the project. This risk clearly diminishes as long as integration tests, including mock-ups and prototypes, come early in design and construction. The schedule for the design and construction of the TPC electronics detector components foresees many integration tests to reduce this risk as much as possible. These tests include integration tests with components provided by the APA, PD system, and DAQ consortia, as well as integration tests of cable routing in the cable trays and through the cryostat penetrations. The second run of ProtoDUNE-SP, using pre-production detector components, will further help in mitigating this risk. At that point, any design change or any deviation from established procedures will need to go through very extensive vetting to avoid the introduction of new incompatibilities between detector components.

Another issue that can arise during the detector integration and installation is a delay caused by the excessive usage of spare detector parts (RT-SP-TPC-007). For ASICs and FEMBs, this kind of risk has already been considered (RT-SP-TPC-002). For the other TPC electronics detector components, the risk should be considered separately, since the other components are needed at an earlier point in time and have completely different fabrication and testing schedules. Some of the actions required to mitigate this risk are similar, including an early start to the production, careful monitoring of yields during the QC process, and a larger number of spares in the case of long lead items.

The final risk we consider for the construction of the TPC electronics detector components is the loss of key personnel (RT-SP-TPC-008). The number of scientists and engineers that have become involved with the TPC electronics has significantly increased since the construction of ProtoDUNE-SP, and in some sense this has already contributed to reducing significantly the probability and possible impacts of this risk. In some areas, like ASIC design, the addition of large teams of engineers involved in the design of the new ASICs means that the probability of this risk is now negligible. There are areas where the experience from the construction and operation of ProtoDUNE-SP resides with a few expert scientists and engineers, and areas where only a single engineer is responsible for the design of a set of detector components. The mitigation of this risk involves enlarging the team(s) that are responsible for the design and prototyping of the detector components. This has already been done for the ASICs and plans are already in place to involve university groups in the design of the FEMBs and of the WIEC. Succession plans for the consortium leadership need to be put in place, including training younger personnel.

### 4.8.2 Risks during commissioning

The biggest risk during the commissioning phase (RT-SP-TPC009 in table 4.7) is excessive noise caused by some detector component not respecting the DUNE grounding rules. This risk was

realized at least twice during the integration and commissioning of the ProtoDUNE-SP detector. During the integration of the first APA, a source of noise was discovered in the electronics used for the readout of the photon detector, which required a simple fix on all of the readout boards. Later, a large noise source was discovered in the temperature monitors. The overall noise in ProtoDUNE-SP was reduced compared to previous LAr experiments or prototypes, such as MicroBooNE or the 35 ton prototype. Even if some unresolved source of noise is still apparent in the ProtoDUNE-SP data, this should not preclude using the collected data for calibration and for physics analyses. Further studies are planned for 2020 to investigate the remaining sources of noise.

The main problem in going from ProtoDUNE-SP to the DUNE FD is one of scale. Even if the detector design addresses all possible noise sources, the simple fact that the detector is 25 times larger and has a correspondingly larger number of cryostat penetrations requires much more attention to detail during installation and commissioning. Observations of excessive noise in DUNE would result in a delay in commissioning and data taking until the source of the noise is found and mitigated. To minimize excessive electronic noise, we plan to enforce the grounding rules throughout the design phase, based on the lessons learned from the operation of the ProtoDUNE-SP detector. We also plan to perform integrated tests to discover possible problems as early as possible. This includes system tests at the ICEBERG test stand at Fermilab for each generation of the FEMBs and photon detectors. We plan to perform noise measurements in the cold boxes at SURF, and later during the insertion of the APAs inside the cryostat before the TCO closure, including repeating the measurements directly before the LAr fill. We expect that the extensive testing will allow a quick transition to detector operations, first with cosmics and later with beam, as soon as the cryostat has been completely filled.

### 4.8.3 Risks during operation

The expectation for the DUNE FD is that data taking will continue for at least two decades. Assuming that the detector operates as designed after commissioning, two additional risks must still be considered. These are related to the lifetime of the CE components installed inside (RT-SP-TPC-010 in table 4.7) and on top (RT-SP-TPC-011) of the cryostat. The components inside the cryostat are not replaceable, and therefore any malfunction of a detector component will result in a loss of sensitive volume. The components on top of the cryostat (with the exception of the flange at the transition from the cold to the warm volume) can be replaced, and as long as we have sufficient spares, this will not result in any loss beyond the amount of time required for replacing the component. The risk of losing components installed inside the cryostat has been considered from the earliest stage of the design of ASICs. As discussed in section 4.3.3, we have formed a reliability committee to ensure that all appropriate measures are considered in the design and that our QA process includes the relevant tests of component lifetime. These lifetime measurements should make sure that we will see only minimal losses of sensitivity in the detector during operations.

As discussed in section 4.7.3, we are taking measures (like adding air filters to the WIECs and bias voltage and low-voltage power supplies) to minimize damage from environmental conditions to the detector components on top of the cryostat. We have discussed in section 4.4.1 our plan for spare detector components. We cannot exclude the possibility that we will not have enough spares, which we plan to build during construction, for the lifetime of the experiment. In this case, it may become necessary to fabricate new boards or procure new supplies during operations. One possible issue

related to this is the continued availability of certain components, in particular FPGAs and optical transmitters and receivers, which may become obsolete and no longer be available when we need to fabricate new parts. While it will always be possible to design new boards using more modern components, we wish to keep the maintenance costs for the detector to a minimum, and this may involve following the technology evolution and stockpiling components that may become obsolete and/or hard to procure. We are also considering placing the FPGAs and the optical components on mezzanine cards to minimize redesign and procurement costs should these components become unavailable during the lifetime of the experiment.

#### 4.9 Organization and management

In this section we first discuss the organization of the TPC electronics consortium that at the moment consists entirely of US institutions: fifteen university groups plus groups from four DOE national laboratories. Table 4.8 provides a list of the participating institutions. Later we discuss the assumptions that have been made in developing the construction plan for the detector components that will be provided by the TPC electronics consortium, including the responsibilities of the different institutions that are part of the consortium. Finally, we present a schedule for the construction, integration, and installation of the TPC electronics into the detector.

**Table 4.8.** Institutions participating in the TPC electronics consortium (all from the US).

| Institution                           |
|---------------------------------------|
| Boston University                     |
| Brookhaven National Laboratory        |
| University of Cincinnati              |
| Colorado State University             |
| University of California, Davis       |
| Fermilab                              |
| University of Florida                 |
| University of Hawaii                  |
| Iowa State University                 |
| University of California, Irvine      |
| Lawrence Berkeley National Laboratory |
| Louisiana State University            |
| Michigan State University             |
| University of Pennsylvania            |
| University of Pittsburgh              |
| SLAC National Accelerator Laboratory  |
| Stony Brook University                |

#### 4.9.1 Consortium organization

The present consortium organization structure includes a consortium leader and a technical lead (both currently from Fermilab), with personnel from BNL helping with system design. A working group structure has been recently provided with subgroups responsible for the detector components inside the cryostat (ASICs, FEMBs, and cold cables), outside the cryostat (mostly the WIECs with their boards), and all equipment used for testing the detector components. When appropriate, a subgroup responsible for integration and installation activities at SURF will be formed (for now, the technical lead oversees these activities). In addition, another subgroup will be in charge of software and physics preparation activities, including calibrations and simulations. Mechanical design activities span detector components both inside and outside the cryostat, requiring strong contacts between technical coordination and other consortia (mainly the APA consortium). The lead engineer (from BNL) on mechanical aspects of the cold electronics (mechanical interfaces with the APAs, cabling, including cable trays, and cryostat penetrations) works directly with the technical coordination team. The TPC electronics consortium will also have contact people for the overall LBNF/DUNE management for ES&H and for QA/QC. For the moment, the technical lead oversees these activities, although oversight will be transferred in part to each subgroup leader for testing activities. The leadership positions in the consortium are listed in table 4.9 and a diagram of the organization of the consortium and of its relationships with other groups in the LBNF and DUNE organizations is shown in figure 4.49.

**Table 4.9.** Current leadership positions in the TPC electronics consortium.

| Position                     |
|------------------------------|
| Consortium Leader            |
| Technical Lead               |
| System Aspects               |
| Cold Components              |
| Warm Components              |
| Test Setups                  |
| Integration and Installation |
| Mechanical Design            |
| Reliability Task Force       |
| TDR Editor                   |
| ES&H contact                 |
| QA/QC contact                |

In addition to the working groups, task forces for specific issues will be formed as necessary. A first example is the task force charged with studying reliability issues in the TPC electronics components and preparing recommendations for the choice of ASICs, the design of printed circuit boards, and testing; this was discussed in section 4.3.3. Later on, this task force will help in developing the QC program for the TPC electronics detector components in collaboration with the

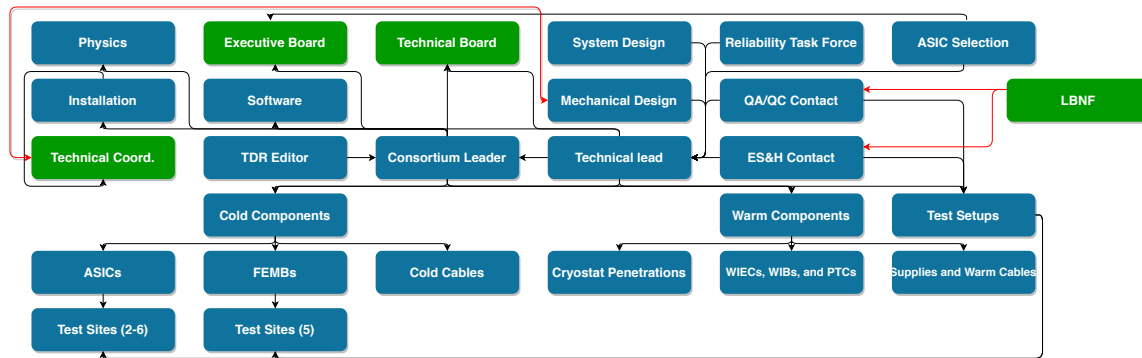


**Figure 4.49.** Organization chart of the TPC electronics consortium and relations to other groups in the LBNF and DUNE organizations (shown in green).

testing group leadership, with the ProtoDUNE-SP experience as a starting point. Later, a second task force, with possible personnel overlap with the first task force and possibly including experts from outside of the DUNE Collaboration, will be tasked with establishing the criteria for the ASIC selection. This task force will be also asked to propose a recommendation that will then go to the DUNE Executive Board for the final approval, as discussed in section 4.2.3.5.

#### 4.9.2 Planning assumptions

In section 4.9.4, we describe the current schedule for the construction, integration, and installation of the TPC electronics detector components for the first SP TPC FD module. This schedule, as well as the costs associated with detector construction, are based on experience with constructing and commissioning the ProtoDUNE-SP detector in addition to assumptions for the remaining R&D program and the production planning discussed here. Section 4.4.1 details the number of spare parts that we plan to fabricate in order to account for known yield issues during detector construction and to address possible problems. Table 4.10 gives a summary of all fabricated components required for the first SP FD module. To develop a schedule for detector construction, we must consider the current state of development of the ASICs, FEMBs, and all other components in order to estimate the time required for the final production.

A second detector module may be built using the SP technology, and in that case the construction of the TPC electronics components for the second module would immediately follow construction of the first one. The total number of components for the second module will be less than the amount for the first detector, assuming that for components inside the cryostat the spare parts from the first module can be used for the second. Similarly, for the components on the top of the cryostat, the pool of spares from the first module should be sufficient to cover the second. Given the timeline for the construction of the detector components and their integration on the APAs or their installation at SURF, an insufficient number of spares presents a risk only for the second detector module, as discussed in section 4.8.1.

The critical path for the construction of the first SP TPC FD module is driven by the availability of FEMBs, which in turn depends on completing the design of the ASICs. Thus, construction of the APAs could start as early as spring 2020, while the decision on the ASICs to be used on the FEMBs may come as late as January 2021. The schedule for this decision depends on the TPC electronics

consortium, which is planning a second design iteration on all ASICs followed by system tests of various flavors of FEMBs. The first version of all ASICs underwent standalone tests in spring / summer 2019 and will go through the sequence of system tests (with the 40% APA prototype at BNL, the seventh ProtoDUNE-SP APA in the cold box at CERN, and the TPC in the ICEBERG cryostat at Fermilab) in early 2020. At the same time, lifetime tests will be performed on all ASICs. Designs of the ASICs and FEMBs, including results from the system test stands and from lifetime tests, will be reviewed in early 2020. This will trigger any further design changes on the ASICs, to be followed by a second round of prototyping and testing. This gets us to the January 2021 date for the final ASIC decision. Consequently, the initial tests of the DUNE prototype APAs must be performed with preliminary versions of FEMBs, which will still be using the first generation of ASICs (although the final mechanical and electrical connections to the APAs will be available and used).

**Table 4.10.** Number of TPC electronics components required for a full SP module (accounting for spares and yields during QC).

| Detector component                             | Number required                             |
|--|---|
| LArASIC  | 30,000 chips (at least 43 wafers)           |
| ColdADC and COLDATA                            | 30,000 and 7,500 chips (at least 33 wafers) |
| CRYO   | 7,500 chips (at least 35 wafers)            |
| FEMB   | 3,200                                       |
| Cold signal cables                             | 1,650 and 1,575 (bottom and top APA)        |
| Cold power cables                              | 1,650 and 1,575 (bottom and top APA)        |
| Cold bias voltage cables                       | 660 and 630 (bottom and top APA)            |
| Cryostat penetrations                          | 80  |
| CE flanges                                     | 160   |
| WIEC   | 155   |
| WIB  | 775   |
| PTC  | 155   |
| Warm power cables                              | 165 (three different lengths)               |
| Warm bias voltage cables                       | 1,320 (three different lengths)             |
| Wiener PL506 power box                         | 30  |
| Wiener MPOD crate                              | 30  |
| Wiener MPOD modules with 8 HV channels         | 180   |
| Power supplies and cables for heaters and fans | 30  |

After the January 2021 review, an additional six months may be required for a final iteration of the FEMB design and a final round of system tests before beginning fabrication of the ASICs and FEMBs. Engineering runs for the ASICs and FEMBs should then take place in the second half of 2021, with most production starting in spring 2022. Production and testing of all chips required for constructing the first SP TPC FD module would be completed by August 2023. The first batch



of production FEMBs would then be available for installation on the APAs in February 2023, and production would be completed in January 2024, roughly eight months before the beginning of the integration of the FEMBs on the APAs at SURF. The final FEMBs for the first SP module are expected to be available at the SDWF fourteen months ahead of their for installation on the last APA to be installed inside the cryostat. There are therefore between eight and fourteen months of float in the schedule for the ASICs and FEMBs, which would allow for a third iteration of design and prototyping if needed. It should be noted that, for the detector components to be installed on the top of the cryostat, there are between ten and fourteen months of float.

The schedule presented above assumes that during the construction of the APAs, integration tests will be performed using preliminary versions of the FEMBs that must then be replaced with final versions at a later date. It also assumes that for the second run of ProtoDUNE-SP, expected to take place in the second half of 2021, prototype FEMBs using the second iteration of prototype ASICs will be used. Using the ASICs from the pre-production, fabricated using the masks that will be used during the production phase, would require a delay of one year in the second run of ProtoDUNE-SP. The difference in the masks used for the fabrication of the ASICs (multipurpose wafer run instead of a dedicated run) does not negate the usefulness of the second run of ProtoDUNE-SP as a final validation of the DUNE SP module design.

If a second SP TPC FD module is built, the critical path will transition from the FEMBs to the APAs, assuming that construction of both APAs and FEMBs will continue without interruption after construction of the first module. This is because constructing one APA requires more time than constructing the corresponding FEMBs. Therefore, toward the end of the constructing this possible second module, we expect that all required FEMBs will be at the SDWF waiting for the delivery of the APAs before integration can take place.

All other detector components that are the responsibility of the TPC electronics consortium can be produced relatively quickly in less than two years. The procurement, assembly, and testing of these components can be scheduled so that we have sufficient time in the schedule to address possible problems during production. Changes in all of these components, unlike those used in the ProtoDUNE-SP detector, are less important than those affecting the ASICs and FEMBs. We are assuming that final designs for the rest of the detector components will be available in the second half of 2020 and that the corresponding production readiness reviews will occur, at the latest, six months before the ASIC design choice. The first components to be installed on the detector are the cryostat penetrations, which must be installed before the detector support structure inside the cryostat is completed. In this way, the cryostat can be completely sealed, other than the manholes used to feed clean air into the cryostat and the TCO that is used as an exhaust portal and as an entry point for the detector components. The rest of the TPC electronics components, which are installed on top of the cryostat (WIECs with all of their boards, supplies, cables, and fibers), should be installed before installing the corresponding rows of APAs and properly connecting the cables linking the APAs to power, control, and readout. The APAs should be tested as soon as they are installed.

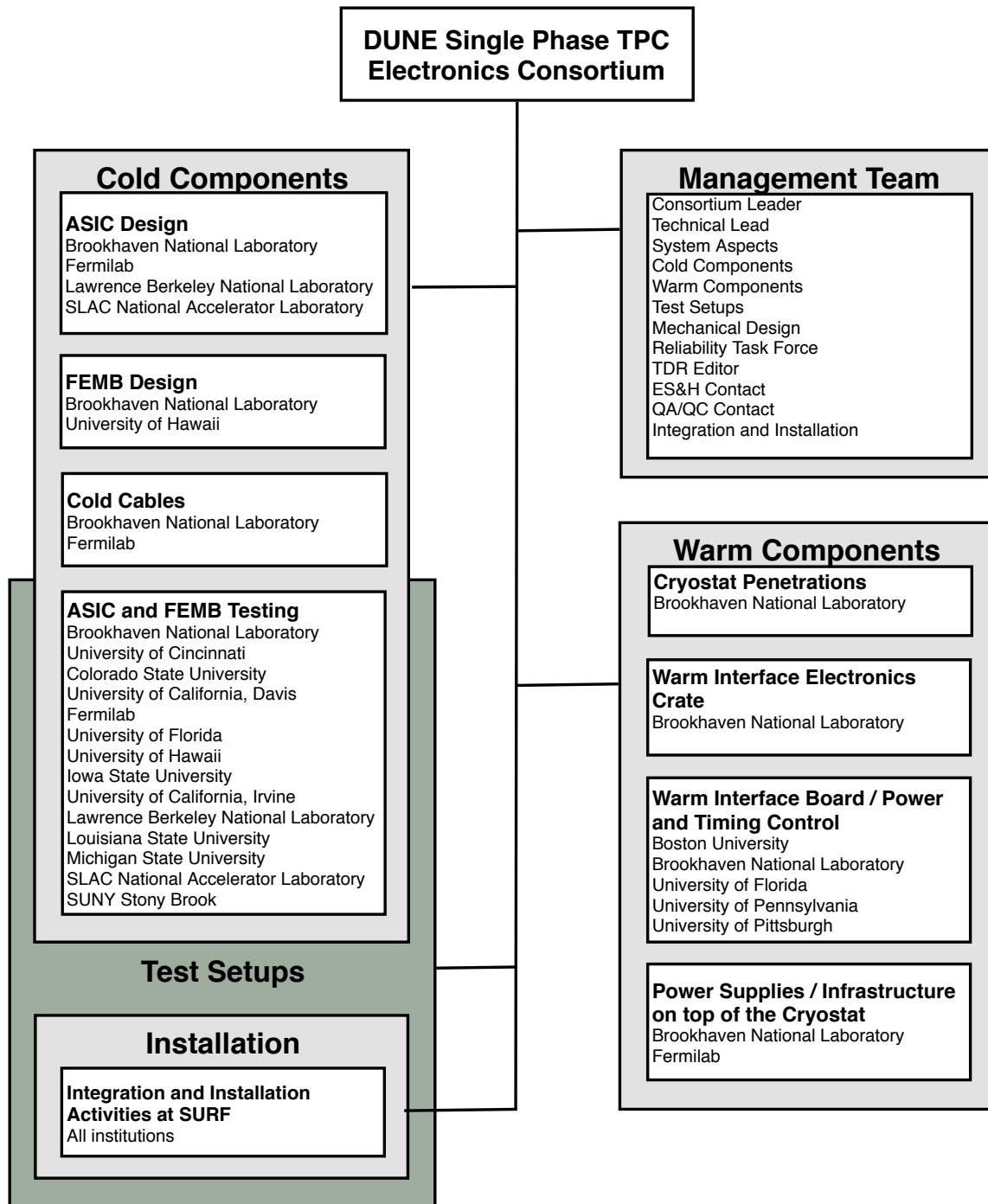
### 4.9.3 Institutional responsibilities

Design and prototyping for the SP DUNE FD have been concentrated so far at the DOE national laboratories, mostly because the focus has been on designing the new generation of ASICs. The

design of the LArASIC was done at BNL, the CRYO chip was done at SLAC, and the new ColdADC was a joint effort of BNL, Fermilab, and LBNL. The COLDATA ASIC was designed at Fermilab, with some components provided by engineers from the Electrical Engineering Department at Southern Methodist University (not a consortium member). The CTS was designed at Michigan State University. Most of the design and construction work for the ProtoDUNE-SP detector was done at BNL, with other institutions contributing to testing, installation, and commissioning. Given the extent of the project, particularly testing, additional institutions have begun to contribute to all of the activities for constructing the DUNE SP FD, which began in the middle of 2018. Almost all the engineering of detector components, except for the boards to be installed on the WIECs and most boards and setups for testing, will remain a responsibility of the DOE national laboratories. Testing of ASICs, FEMBs, cables, power and bias voltage supplies, and WIECs with their boards will be done at various universities that are members of the consortium. All institutions are expected to contribute to the integration and installation activities at SURF, which is very demanding in terms of personnel. A detailed list of the institutions contributing to the development, production, and testing of the various detector components is given in figure 4.50.

### 4.9.4 High-level cost and schedule

In section 4.9.2, we discussed how the project will evolve from the current design and prototyping phase to production for the ASICs and FEMBs by spring 2022. During the same period, the engineering of all other detector components will be completed and prototypes fabricated. The procurement and qualification of cold cables, cryostat penetrations, WIECs, and power and bias voltage supplies can then begin in spring 2021. Integrating FEMBs on the APAs would then take place over 18 months beginning in early 2023. At this moment, the installation and testing of APAs in the cryostat and corresponding activities of the TPC electronics consortium, including installing all detector components on top of the cryostat, are scheduled to take four months starting in April 2024. Table 4.11 shows a preliminary list of milestones, including the current plan to complete the design, R&D, and engineering phases; and then later the production setup, production, integration, and installation activities. The schedule for the completion of the design and prototyping, the pre-production, the construction of the detector components (including the QC process), and their integration and installation at SURF is displayed in figure 4.51.

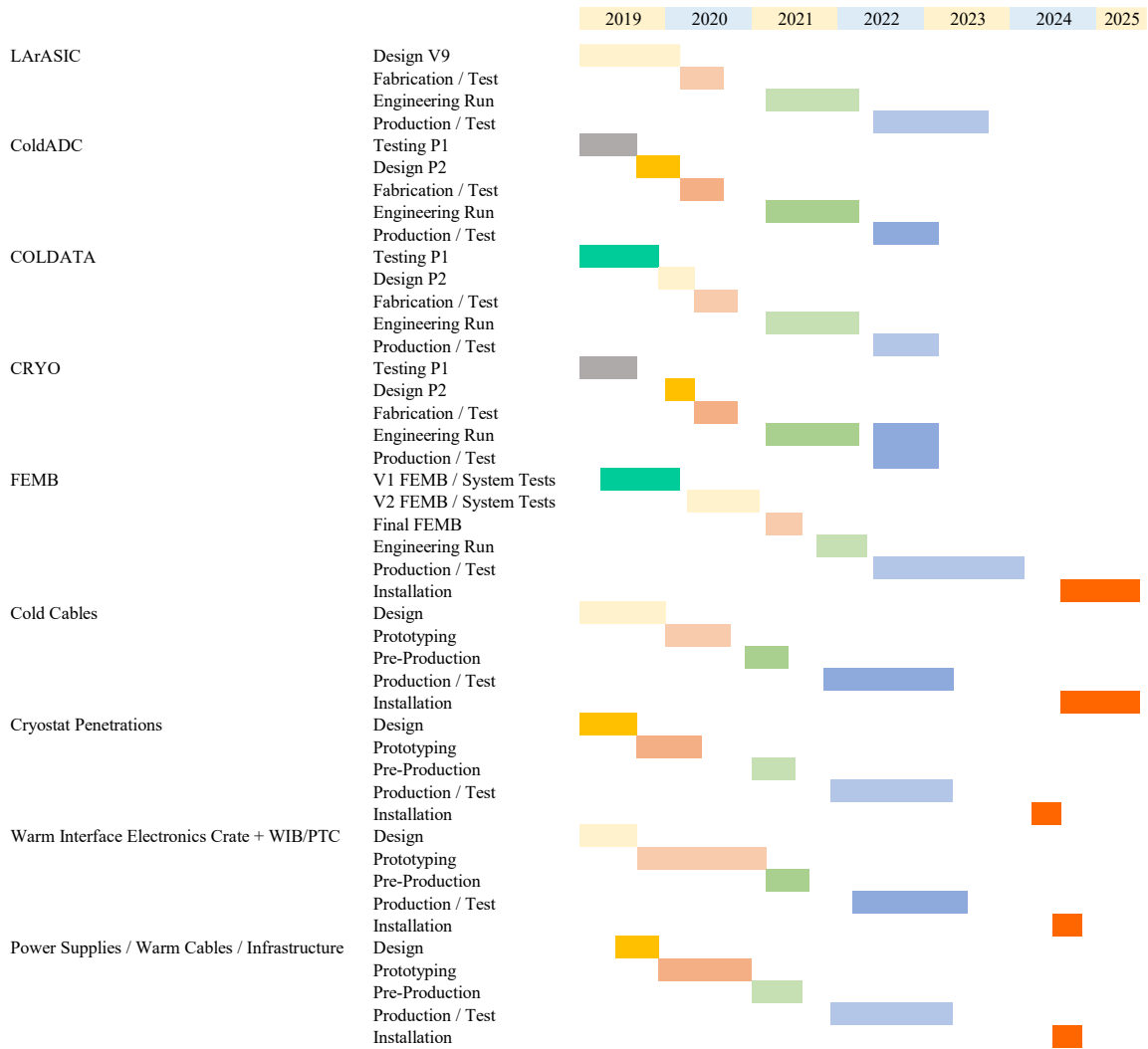


2020 JINST 15 T08010

**Figure 4.50.** Responsibilities of the institutions in the TPC electronics consortium, matched to the organization chart of the consortium.

**Table 4.11.** Milestones of the TPC electronics consortium.

| Milestone   | Date           |
|---|----------------|
| Complete the submission of the first generation of ASICs                                | April 2019     |
| Complete the standalone testing of the first generation of ASICs                        | October 2019   |
| Complete system and lifetime tests on the first generation of ASICs and FEMBs           | May 2020       |
| Submission of second generation of ASICs  | June 2020      |
| Complete the standalone testing of the second generation of ASICs                       | September 2020 |
| Complete system and lifetime tests on the second generation of ASICs and FEMBs          | January 2021   |
| Decision on the ASIC(s) to be used for construction                                     | January 2021   |
| Start of ProtoDUNE-SP-II installation   | March 2021     |
| Complete characterization of final prototypes of ASICs and FEMBs including system tests | July 2021      |
| Complete Engineering Design Reviews and launch pre-production of detector components    | September 2021 |
| Start of procurement of cold cables   | December 2021  |
| Start of production of cryostat penetrations  | December 2021  |
| Start of production of WIECs, WIBs, and PTCs  | December 2021  |
| Start of procurement of power supplies and warm cables                                  | December 2021  |
| Complete testing of pre-production of all ASICs   | January 2022   |
| Complete testing of pre-production FEMBs  | April 2022     |
| South Dakota Logistics Warehouse available  | April 2022     |
| Complete testing of prototypes and Production Readiness Reviews                         | May 2022       |
| Start of ASICs production   | May 2022       |
| Start of FEMBs production   | May 2022       |
| Beneficial occupancy of cavern 1 and CUC  | October 2022   |
| Completion of cryostat penetrations procurement   | February 2023  |
| Completion of the procurement and QC of cold cables                                     | March 2023     |
| CUC counting room accessible  | April 2023     |
| Completion of the WIECs, WIBs, and PTCs production and QC                               | May 2023       |
| Completion of the procurement of power supplies and warm cables                         | June 2023      |
| Completion of ASICs production and QC   | August 2023    |
| Completion of FEMBs production and QC   | January 2024   |
| Begin installation of the TPC electronics components on top of the cryostat             | April 2024     |
| Complete installation of the TPC electronics components on top of the cryostat          | July 2024      |
| Start of detector module #1 TPC installation  | August 2024    |
| Begin integration of the FEMBs on the APAs at SURF                                      | August 2024    |
| Complete integration of the FEMBs on the APAs at SURF                                   | March 2025     |
| End of detector module #1 TPC installation  | May 2025       |



2020 JINST 15 T08010

**Figure 4.51.** Schedule for the completion of the design and prototyping, the pre-production, the construction of the TPC electronics detector components (including the QC process), and their integration and installation at SURF.

## Chapter 5

# Photon detection system

### 5.1 Introduction

The DUNE FD consists of detector systems for charge and light produced by an ionization event in the LArTPC. The charge detection system permits both calorimetry and position determination, with two of the three spatial coordinates ( $y$  and  $z$ ) established by the position of the APA wires receiving the charge and the third ( $x$ ) by the arrival time of the charge. Locating the  $x$  position requires independently determining the time of the ionization event, a clock start time. Two systems provide this in DUNE: the Fermilab accelerator system for neutrino beam related events and the PD system.

Neutrino CPV and other elements of the DUNE long-baseline neutrino program are possible without data from the PD system. The neutrino beam timing allows full functionality of the APAs, and the deep underground location reduces the possibility of in-time background events from cosmic rays and other sources to a negligible level. Similarly, DUNE can detect SNBs originating within the galaxy without the PD system because the presence of thousands of low-energy neutrino events, even if they consist only of few millimeter long tracks, provides an unambiguous signal in the TPC. By contrast, DUNE's nucleon decay physics cannot be executed without the PD system. The inability to establish a clock start time ( $t_0$ ) makes it impossible to determine whether a candidate proton decay event was fully contained in the detector volume or associated with objects entering the detector from the outside. Determining  $t_0$  also allows the energy reconstructed by the TPC to be corrected for charge lost due to electron capture and other transport effects in the TPC. This physics sets the requirement on minimum light yield in the dimmest regions of the detector far from the photon detectors and timing resolution, described further in appendix section 5.16.1.2.

While only absolutely required for proton decay searches, the PD system directly enhances physics capabilities for all three DUNE physics drivers, opens up prospects for further physics explorations, and contributes to a more robust set of operating points of the detector that help all physics. For SNB neutrino events, the PD system allows proper location of the event vertex, and improves energy resolution by allowing position-dependent energy corrections and complementary direct calorimetric measurements, improving energy resolution and possibly sensitivity to underlying supernova dynamical models. The PD system also enables a complementary triggering scheme for the burst itself, increasing reliability, reducing dead time, and extending the sensitivity further

out to nearby dwarf galaxies (see appendix section 5.16.1.3). Applications to supernova physics set the average light yield requirement.

The PD system can also measure energy calorimetrically for all classes of events, working as a crosscheck of the energy measured by the TPC or improving the resolution when both measurements are used together (see appendix section 5.16.1.4). In the event that the DUNE TPC cannot operate at its goal electric field of 500 V/cm, the PD system energy measurements could compensate for reduced charge detector performance because light production increases relative to the free charge for lower E field.

The PD system could open new areas of investigation. The few-MeV scale solar neutrino interactions occur as isolated events in time and space. Suppressing radiological and noise related backgrounds to pull out a signal for these events likely requires redundant measurements with charge and light. The PD system may also provide a means for identifying events with Michel electrons produced from the decay of a stopped muon. Tagging these electrons can be used to estimate the antineutrino content of the beam flux or further reduce nucleon decay backgrounds (see appendix section 5.16.1.4).

Volume II, DUNE physics, of this TDR describes the detailed physics simulations of the main DUNE physics drivers. The PD system performance specifications have been established and validated in part by simulation. Details of this simulation, which includes non-uniformity in light yield due to the optical properties of the argon, electronics response, and realistic reconstruction, are presented in appendix section 5.16.1.

## 5.2 Design specifications and scope

### 5.2.1 Specifications

Based on the physics drivers and additional simulation studies described in appendix section 5.16.1, table 5.1 summarizes the PD system specifications necessary to achieve the DUNE science objectives. In the remainder of this chapter, we present a design that meets or exceeds the specifications. Section 5.8 summarizes an extensive set of prototypes that validate the assumptions used in the design.

**Table 5.1:** PDS specifications.

| Label   | Description     | Specification (Goal)                     | Rationale   | Validation  |
|---------|-----------------|--|---|---|
| SP-FD-3 | Light yield     | > 20 PE/MeV (avg),<br>> 0.5 PE/MeV (min) | Gives PDS energy resolution comparable to that of the TPC for 5-7 MeV SN $\nu$ s, and allows tagging of > 99 % of nucleon decay backgrounds with light at all points in detector. | Supernova and nucleon decay events in the FD with full simulation and reconstruction. |
| SP-FD-4 | Time resolution | < 1 $\mu$ s<br>(< 100 ns)                | Enables 1 mm position resolution for 10 MeV SNB candidate events for instantaneous rate < 1 m <sup>-3</sup> ms <sup>-1</sup> .  |   |

## Chapter 5. Photon detection system

|          |  |   |   |  |
|----------|--|---|---|--|
| SP-FD-15 | LAr nitrogen contamination   | < 25 ppm  | Maintain 0.5 PE/MeV PDS sensitivity required for triggering proton decay near cathode.                | In situ measurement  |
| SP-PDS-1 | Clean assembly area  | Class 100,000 clean assembly area   | Demonstrated as satisfactory in ProtoDUNE-SP, and is the DUNE assembly area standard.                 | ProtoDUNE-SP and in Fermilab materials test stand  |
| SP-PDS-2 | Spatial localization in $y$ - $z$ plane  | < 2.5 m   | Enables accurate matching of PD and TPC signals.  | SNB neutrino and NDK simulation in the FD  |
| SP-PDS-3 | Environmental light exposure   | No exposure to sunlight. All other unfiltered sources: < 30 minutes integrated across all exposures | Shown to prevent damage to WLS coatings due to UV.  | Studies in ProtoDUNE-SP, and at IU   |
| SP-PDS-4 | Environmental humidity limit   | < 50 % RH at 70 °F  | Demonstrated to prevent damage to WLS coatings due to humidity.                                       | PD optical coating studies   |
| SP-PDS-5 | Light-tight cryostat   | Cryostat light leaks responsible for < 10 % of data transferred from PDS to DAQ                     | Minimizing false triggers due to cryostat light leaks helps limit the data transfer rate to DAQ.      | ProtoDUNE-SP and ICEBERG   |
| SP-PDS-7 | Mechanical deflection (static)   | < 5 mm  | Minimize motion of PD modules inside the APA (due to static and dynamic loads) to avoid damaging APA. | PD FEA, ProtoDUNE-SP, ICEBERG; Ash River integration tests and CERN pre-production integration tests pending |
| SP-PDS-8 | Clearance for installation through APA side tubes                                  | > 1 mm  | Maintain required clearance to allow PD insertion into APA following wire wrapping.                   | PD FEA, ProtoDUNE-SP, ICEBERG; Ash River integration tests and CERN pre-production integration tests pending |
| SP-PDS-9 | No mechanical interference with APA, SP-CE and SP-HV detector elements (clearance) | > 1 mm  | PD mounting and securing element tolerances must prevent interference with APA and CE cable bundles.  | ICEBERG, Ash River integration tests, and the CERN pre-production integration tests                          |

2020 JINST 15 T08010



|           |  |                                      |  |   |
|-----------|--|--------------------------------------|--|---|
| SP-PDS-10 | APA intrusion limit for PD cable routing             | < 6 mm                               | PD modules must install into APA frames following wire wrapping. PD modules must not occlude APA side tubes. | ICEBERG, Ash River integration tests, and the CERN pre-production integration tests |
| SP-PDS-11 | PD cabling cannot limit upper-lower APA junction gap | 0 mm separation mechanically allowed | PD cable connections must not limit the minimum upper and lower APA separation.                              | ICEBERG, Ash River integration tests, and the CERN pre-production integration tests |
| SP-PDS-12 | Maintain PD-APA clearance at LAr temperature         | > 0.5 mm                             | PD mounting frame and cable harness must accommodate thermal contraction of itself and APA frame.            | Thermal modeling, ProtoDUNE, ICEBERG, CERN pre-production integration tests         |
| SP-PDS-13 | Data transfer rate from SP-PD to DAQ                 | < 8 Gbps                             | PD data transfer must not exceed DAQ data throughput capability.   | Maximum bandwidth out of the PD electronics is 80 Mbps                              |
| SP-PDS-14 | Signal-to-noise in SP-PD                             | > 4                                  | Keep data rate within electronics bandwidth limits.  | ProtoDUNE-SP, ICEBERG and ProtoDUNE-SP-2  |
| SP-PDS-15 | Dark noise rate in SP-PD                             | < 1 kHz                              | Keep data rate within electronics bandwidth limits.  | Pre-production photosensor testing, ProtoDUNE-SP, ICEBERG and ProtoDUNE-SP-2        |
| SP-PDS-16 | Dynamic Range in SP-PD                               | < 20 %                               | Keep the rate of saturating channels low enough for effective mitigation.                                    | Pre-production photosensor testing, ProtoDUNE-SP, ICEBERG and ProtoDUNE-SP-2        |

### 5.2.2 Scope

The scope of the SP PD system, provided by the SP PD consortium, includes selecting and procuring materials for, and the fabrication, testing, delivery and installation of light collectors (X-ARAPUCA), photosensors (SiPMs), electronics, and a calibration and monitoring system. This TDR chapter will describe the design, validation, assembly, and QA/QC testing of the PD system for a single 10 kt DUNE SP module. The baseline components for a SP module are listed in table 5.2.

Although the configuration of the SP and DP modules led to significantly different solutions for the PD system, a number of scientific and technical issues affect them in a similar way, and the consortia for these two systems cooperate closely on these. See Volume V, The DUNE Far Detector Dual-Phase Technology, chapter 5.

Table 5.2. PD system baseline configuration.

| Component                  | Description                             | Quantity   |
|----------------------------|---|--|
| Light collector            | X-ARAPUCA                               | 10 modules per APA; 1500 total (1000 single-sided; 500 double-sided) |
| Photosensor                | Hamamatsu MPPC 6 mm × 6 mm              | 192 SiPMs per module; 288,000 total                                  |
| SiPM signal summing        | 6 passive × 8 active                    | 4 circuits per module; 6000 total                                    |
| Readout electronics        | Based on commercial ultrasound chip     | 4 channels/module; 6000 total  |
| Calibration and monitoring | Pulsed UV via cathode-mounted diffusers | 45 diffusers/CPA side; 180 diffusers for 4 CPA sides                 |

### 5.3 Photon detector system overview

#### 5.3.1 Principle of operation

Liquid argon (LAr) is an abundant scintillator and emits about 40 photons/keV when excited by minimum ionizing particles [76] in the absence of external E fields. An external E field suppresses the electron recombination that leads to the excimers responsible for most of the VUV luminescence in LAr and hence reduces the photon yield; for the nominal DUNE SP module field of 500 V/cm, the yield is approximately 24 photons/keV [77]. As depicted in figure 5.1, the passage of ionizing radiation in LAr produces excitations and ionization of the argon atoms that ultimately result in the formation of the excited dimer  $\text{Ar}_2^*$ . Photon emission proceeds through the de-excitation of the lowest lying singlet and triplet excited states,  $^1\Sigma$  and  $^3\Sigma$ , to the dissociative ground state. The de-excitation from the  $^1\Sigma$  state is very fast and has a characteristic time of the order of  $\tau_{\text{fast}} \approx 6$  ns. The de-excitation from the  $^3\Sigma$  state is much slower because it is forbidden by the selection rules; it has a characteristic time of  $\tau_{\text{slow}} \approx 1.5$   $\mu\text{sec}$ . In both decays, photons are emitted in a 10 nm band centered around 127 nm, which is in the VUV region of the electromagnetic spectrum [78]. The relative intensity of the fast versus the slow component is related to the ionization density of LAr and depends on the ionizing particle: 0.3 for electrons, 1.3 for alpha particles and 3 for neutrons [79]. This phenomenon is the basis for the particle discrimination capabilities of LAr exploited by experiments that can separate the two components, but its utility in a large detector is effectively restricted to events with single charged particles. This limits its effectiveness in DUNE, where most events in which such particle ID (PID) would be beneficial are multi-particle, but it could be a powerful supplement to the charge measurement in some cases.

#### 5.3.2 Design considerations

The principal task of the SP PD system is to measure the VUV scintillation light produced by ionizing tracks in the TPC within the geometrical constraints of the APA structure. The modular arrangement of the SP module calls for a configuration across the width of the cryostat starting

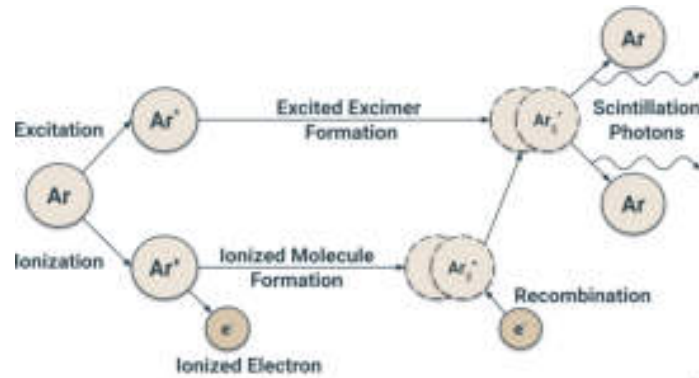


**Figure 5.1.** Schematic of scintillation light production in argon.

with an APA plane against one cryostat wall, and following with APAs and CPAs in the order APA-CPA-APA-CPA-APA. The structure of the APA, along with the imperative to maximize the active volume of LAr, precludes the use of traditional large area photomultiplier tubes (PMTs).

A solution that reduces the impact of the PD system on the active volume to zero is to place the light collector modules in the inactive space between the innermost wire planes of the APAs. To satisfy APA fabrication constraints and mechanical integrity, we must install the modules through slots in a (wound) APA frame (see chapter 2). Individual PD modules are restricted to a profile of dimensions  $23 \text{ mm} \times 118 \text{ mm} \times 2097 \text{ mm}$ . There are ten PD modules per APA, equally-spaced by 592 mm, for a total of 1500 per SP module. Of these, 500 are mounted in central APA frames and must collect light from both directions (dual-face), and 1000 are mounted in frames near the vessel walls and collect light from only one direction (single-face). Figure 5.2 illustrates the baseline configuration of PD modules and APAs in an SP module.

To detect scintillation light over a large area in a compact space requires a multi-step process. First, the VUV scintillation photons are converted to longer wavelength by chemical wavelength shifters.<sup>1</sup> These photons are then channeled as efficiently as possible toward much smaller photosensors that produce an electrical signal. Because of the severe space constraints, these must be silicon photosensors with dimensions of just a few millimeters, not a traditional photomultiplier. Another requirement, distinct from most previous HEP applications of these devices, is that they must operate reliably for many years at LAr temperatures.

An operational consideration for the PD system design is the presence in the LArTPC of the long-lived cosmogenic radioisotope  $^{39}\text{Ar}$ , which has a specific activity in argon extracted from the atmosphere of approximately 1 Bq/kg [80]. The isotope undergoes beta decay at a mean beta energy of 220 keV with an endpoint of 565 keV and makes up  $\sim 70\%$  of the radiological background signal. In the 10 kt FD modules, this leads to a rate of more than 10 MHz of very short ( $\sim 1 \text{ mm}$ ) tracks uniformly distributed throughout the module, each of which produces several thousand VUV scintillation photons. This continuous background affects the DAQ, trigger, and spatial granularity required of the PD system. Spatial granularity helps even more with rare but more energetic

<sup>1</sup>The most widely used wavelength shifter for LAr detectors is 1,1,4,4-Tetraphenyl-1,3-butadiene (TPB), which absorbs VUV photons and re-emits them with a spectrum centered around 420 nm, close to the wavelength of maximum quantum efficiency for photo-conversion in most commercial photosensors.

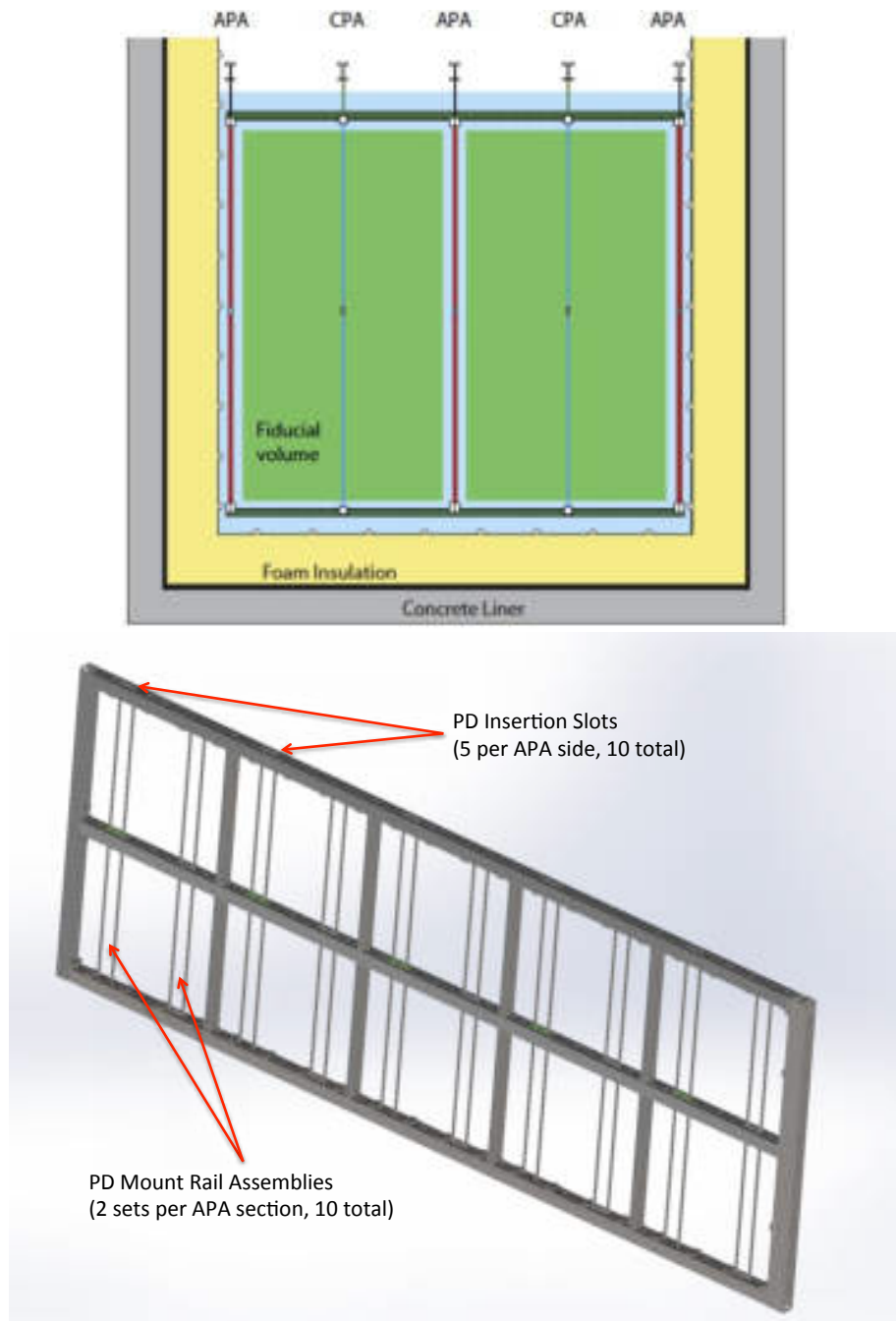


**Figure 5.2.** End-on schematic view of the active argon volume showing the four drift regions and anode-cathode plane ordering of the TPC inside the SP module (top). The three rows of APAs across the width of the SP module are two frames high and 25 frames deep. Schematic of an APA frame (on its side) showing the ten pairs of PD module support rails (almost vertical in figure) (bottom). Notice the five slots on the frame's side that the PD modules fit through (top of figure). The other five slots are on the frame's opposite side, at the bottom of the figure.

radiological backgrounds that can produce multi-photon signals, but only a single detector. Low energy neutrinos, on the other hand, will produce coincident signals on multiple channels, allowing them to be easily identified.

### 5.3.3 Design overview

The large-area light collectors are the core modular elements of the PD system. They convert incident 127 nm scintillation photons into photons in the visible range ( $>400$  nm) that compact SiPM photosensors, in turn, convert to an electrical signal. The light collector design must optimize the costs of various components of the system while meeting the performance requirements. Even though production cost and key performance parameters of SiPMs have improved significantly in recent years, covering the light detector surfaces with enough of them to meet the physics requirements of the PD system would be cost-prohibitive. The light collector design should maximize the active VUV-sensitive area of the PD system while minimizing the necessary photocathode (SiPM) coverage. This is detailed in section 5.4.

#### 5.3.3.1 Light collectors

DUNE investigated many PD light collector module options before forming the SP PD consortium; we selected four for further development. Two designs, S-ARAPUCA<sup>2</sup> and X-ARAPUCA, use a relatively new scalable concept designed to provide significantly better performance than the other approaches. Functionally, ARAPUCA is a light trap that captures wavelength-shifted photons inside boxes with highly reflective internal surfaces until they are eventually detected by SiPMs or are lost. The two other designs are based on the use of wavelength-shifters and long plastic light guides coupled to SiPMs at the ends. Their performance could meet the basic physics requirements but with only a small safety margin, and their performance is not easily scalable within the geometric constraints of the SP module.

The performance of the light collector is characterized by the *collection efficiency* of the device, which is defined as the ratio of the number of detected photons and the number of 127 nm scintillation photons incident on the light collector window. For the ARAPUCA, this depends on three distinct aspects of the design:

- The efficiency of the conversion of incident VUV photons to photons trapped inside the cavity. This depends primarily on the wavelength shifter(s) efficiency and the fraction of converted photons that enter the cavity.
- The efficiency for the captured photons to eventually fall on the photosensor. This depends primarily on the reflectivity of the surfaces of the cavity, the geometry of the cavity, and the ratio of the photosensitive area to the light collector window area.
- The efficiency for the photosensor to convert incident photons to an electronic signal. This depends on the energy of the converted photons in the cavity and properties of the commercial sensor.

The *effective area* of a PD module is another useful figure-of-merit that is defined to be the photon collection efficiency multiplied by the photon collecting area of a PD module.

---

<sup>2</sup>*Arapuca* is the name of a simple trap for catching birds originally used by the Guarani people of Brazil.

*S-ARAPUCA*: in an S-ARAPUCA cell, enhanced photon trapping is attained when using the wavelength-shifting plates and the technology of the dichroic short-pass optical filter. These commercially available interference filters use multi-layer thin films highly transparent to photons with a wavelength below a tunable cutoff, with transmission typically more than 95%, yet almost perfectly reflective to photons with a wavelength above the cutoff. Such a filter forms the entrance window to a cell whose internal surfaces are covered by highly reflective acrylic foils except for a small fraction occupied by SiPMs.

For the collector to act as a photon trap, the external face of the dichroic filter is coated with a wavelength shifting coating with an emission wavelength less than the cutoff wavelength of the filter. The transmitted photons pass through the filter where they encounter a second wavelength-shifter coated on either the inside surface of the filter plate or on the rear surface of the box. This second wavelength-shifter has emission spectra which exceed the cutoff wavelength, thus trapping the photon inside the box. Trapped photons reflect off the inner walls and the filter surface(s) (of reflectivity typically greater than 98 %) and have a high probability of impinging on a SiPM before being lost to absorption.

Several iterations of the S-ARAPUCA design were tested in small cryostats (section 5.8.2.1) and ProtoDUNE-SP (section 5.8.2.2), establishing the viability of the concept for DUNE.

*X-ARAPUCA*: the X-ARAPUCA, adopted as the baseline design and detailed in section 5.4, is an evolution of the first generation S-ARAPUCA. In the X-ARAPUCA, the secondary WLS layer of the S-ARAPUCA (a vacuum-deposited layer of WLS applied to the inner surfaces of the cell) is replaced by a WLS plate with an emission wavelength higher than the filter plate transmission frequency. Wavelength shifted photons from this plate have two mechanisms for transport to the photosensors inside the cell: either they are transported along the WLS plate to the photosensors via total internal reflection, or those escaping the plate are captured due to reflection from the dichroic filter by the standard ARAPUCA effect. The concept is illustrated in figure 5.3. Validation of the X-ARAPUCA design is described in sections 5.8.3.1 and 5.8.3.2.

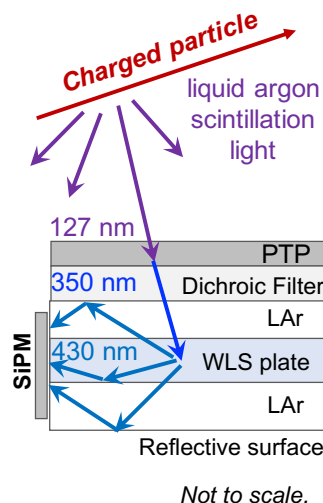


**Figure 5.3.** Schematic representation of a single-sided readout X-ARAPUCA operating principle. This example assumes a filter cutoff of 400 nm. (Note: in the original ARAPUCA concept, the second wavelength-shifter was coated on the inner surface of the filter and the WLS plate shown in the figure was absent.)

While the S-ARAPUCA modules deployed in ProtoDUNE-SP collect light from only one direction, the next generation X-ARAPUCA can be deployed as either single-face or dual-face readout by using either an opaque reflector plate (single) or a second dichroic filter window (dual) on the second face. Figure 5.4 shows how a light-collector module is incorporated into an APA. One module spans the width of an APA. Figure 5.5 (left) shows a detail of the module where the 24 X-ARAPUCA cells are visible on either side of a signal summing and interface board that becomes enclosed by the hollow central beam of the APA frame. Figure 5.5 (right) illustrates how a module is inserted into an APA frame.

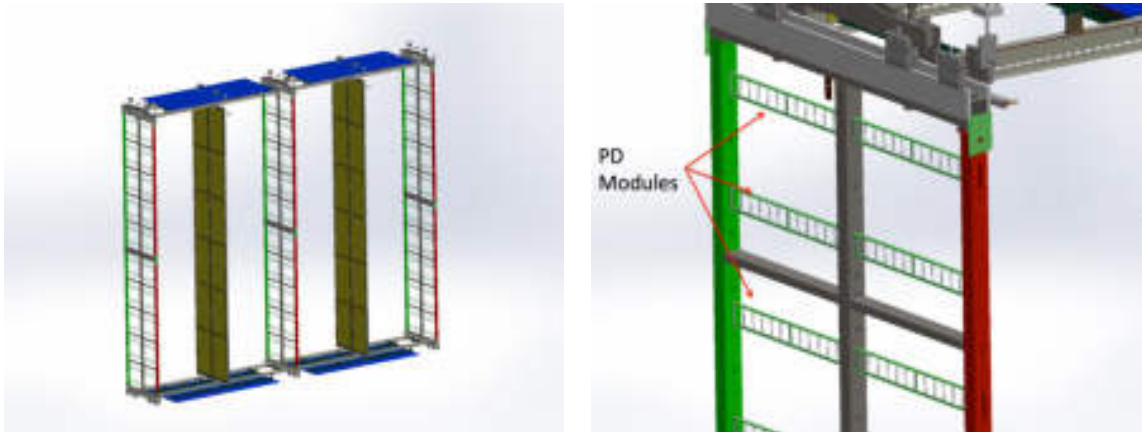


**Figure 5.4.** 3D model of PDs in the APA. The model on the left shows the full width of a one APA deep slice of the TPC illustrating the APA-CPA-APA-CPA-APA system configuration. The figure on the right shows a detail of the top far side of the TPC where three photon collector modules are visible.

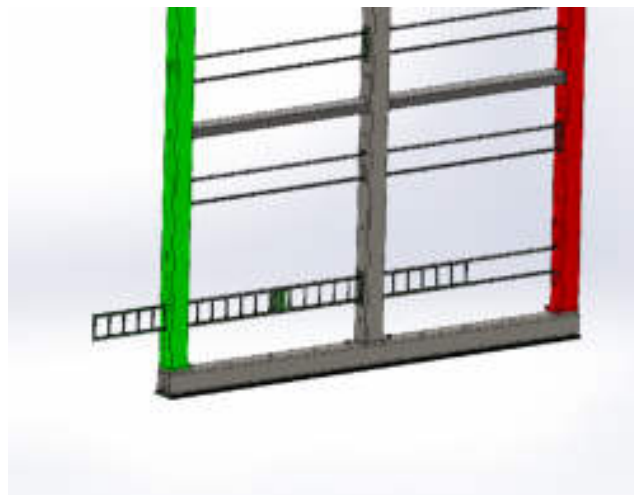


**Figure 5.5.** Solid model of a PD module being inserted into an APA frame (wires not shown), which is done after the APA assembly is completed.

The X-ARAPUCA light collector design has the flexibility to accommodate greater demands, such as might be desired for Short-Baseline Neutrino (SBN) physics, without major changes. One example of this flexibility is the ability to increase the number of SiPMs to increase light yield, which

could be incorporated quite late in the final design stages because it would not involve significant mechanical changes.

### 5.3.3.2 Silicon photosensors

The SP PD system uses a multi-step approach to scintillation light detection with the final stage of conversion into electrical charge performed by SiPMs. Robust photon conversion efficiency, low operating voltages, small size, and ruggedness make their use attractive in the SP design where the PDs must fit inside the APA frames.

Based on extensive testing and experience with the vendor, we have selected a 6 mm × 6 mm MPPC produced by Hamamatsu<sup>3</sup> (Japan) as the baseline SiPM device. We are also vigorously pursuing an alternative based on the design of a device developed for operation in LAr by the DarkSide experiment collaboration and Fondazione Bruno Kessler (FBK)<sup>4</sup> (Italy).

The baseline PD system design has 192 MPPCs per PD module with groups of 48 MPPCs electrically ganged into four electronics readout channels, which provides some spatial granularity within a module and helps to reduce the impact of radiological noise. This configuration has a total of 288,000 MPPCs per SP module.

### 5.3.3.3 Readout electronics

The PD system design requires an electronics readout system that collects and processes electric signals from photosensors in LAr to (1) provide the interface to trigger and timing systems, and (2) enable data transfer to an offline storage system for physics analysis. The quantitative requirements for the system are driven by many FD level specifications that affect signal size sensitivity, S/N, timing resolution, event size and data transfer limits from the DAQ, power needs and dissipation limits, channel density and channel count, and cost.

As described in section 5.3.3.2, each electronics signal from a PD module is formed from an ensemble of 48 Hamamatsu MPPCs summed into a single channel by a combination of passive and active ganging. A cold amplifier adjusts the MPPC output signal level before transmitting the signal over ~20 m long<sup>5</sup> twisted-pair cables to the input of FE ADCs outside the cryostat. The twisted pair cable is impedance-matched to the receiver amplifiers for the ADCs to optimize common-mode noise rejection at the input of the front-end digitizer.

The digitizer is a low-cost solution based on commercial ultrasound ASIC chips rather than digitizers based on flash ADCs used in ProtoDUNE-SP. Inspiration for this FE comes from the system developed for the Mu2e experiment cosmic ray tagger (CRT) readout system as described in section 5.6.2.

The FE will continuously digitize the input signals for each channel and store waveforms alongside event metadata that meet the trigger conditions. In an externally triggered waveform mode, the configured waveform window at the time of the external trigger is also stored. These internally or externally triggered waveforms are transmitted to the DAQ board reader processes for storage. The DAQ system and data storage limitations impose constraints on the data bandwidth, readout rates, and zero suppression.

---

<sup>3</sup>Hamamatsu™ Photonics K.K., <http://www.hamamatsu.com/>.

<sup>4</sup>Fondazione Bruno Kessler™, <https://www.fbk.eu>.

<sup>5</sup>Cable lengths are not uniform across all PDs, ranging from 15 m at the shortest to 27.25 m at the longest, averaging 20 m.



Single photoelectron signals from  $^{39}\text{Ar}$  and radiological backgrounds will dictate threshold level adjustments. We will configure the photon readout to trigger on signals from the central trigger and timing systems for a variety of configurable events, e.g., beam events, cosmic muons, periodic triggering, random triggering, or any combination of these. A special trigger condition needed for SNB observation will enable readout of all digitized data over predefined periods. The interface design will define the power, grounding, and rack schemes.

### 5.3.4 Options to improve uniformity of response

Because the PD modules are installed only in the APA, light collection is not uniform over the entire active volume of the TPC. Though not necessary to meet the basic DUNE performance specifications, improving the uniformity of the response would increase the trigger efficiency, simplify the analysis for SNB neutrinos and increase the light yield of the detector, which could enable enhanced calorimetric measurements based on light emitted by the ionizing particles.

The primary source of non-uniformity of response is that the Rayleigh scattering length for 127 nm scintillation photons is relatively short compared to the size of the TPC active volume. In parallel to the baseline design, we are pursuing two options that convert 127 nm scintillation photons to longer wavelength photons that have a longer Rayleigh scattering length, significantly improving light collection uniformity:

- Use of a wavelength-shifter-coated cathode plane; see appendix section 5.16.2.1.
- Use of trace amount of xenon in the LAr; see appendix section 5.16.2.2.

### 5.3.5 Overview summary

As described in sections 5.16.1.2 and 5.16.1.3, the performance required for the PD system to achieve 99% for tagging nucleon decay events is a light yield of 0.5 PE/MeV at the furthest point (near the CPA), while the requirement to enable a calorimetric energy measurement with the PD system for low-energy events like SNBs is 20 PE/MeV averaged over the active volume (FD-SP-3 in table 5.1). The relationship between these two different light yields and the collection efficiency of the PD system depends on the assumed Rayleigh scattering length. Conservatively assuming that this length is 60 cm, the 0.5 PE/MeV at the CPA corresponds to a collection efficiency of 1.3% and the 20 PE/MeV averaged over the active volume corresponds to an efficiency of 2.6%.

Although full validation of the SP PD system light collection system is still in progress, initial results on the X-ARAPUCA prototype are very encouraging — the single cell prototype (section 5.8.3.1) has achieved a collection efficiency of 3.5%. This is significantly higher than the requirement.

A measured collection efficiency in excess of the specification ensures a safety margin against degradation in performance of the optical components over time and failures of a fraction of inaccessible active components during long term operation of the detector. It also opens broader opportunities for the photon detection system to extend the physics reach of the experiment, perhaps in unanticipated ways.

## 5.4 Light collectors

The X-ARAPUCA, adopted as the baseline design, is an evolution of the ARAPUCA concept that further improves the collection efficiency, while retaining the same working principle, mechanical form factor and active photosensitive coverage. In the original ARAPUCA concept, two wavelength-shifters were coated on either side of the dichroic filter window. In contrast, the X-ARAPUCA replaces the inner surface coating with a wavelength-shifter-doped polystyrene light guide<sup>6</sup> occupying a portion of the cell volume, with the silicon photosensor readout mounted along the narrow sides of the cell, as illustrated in figure 5.6. The model shown is a single cell design used for prototypes that allows for photons to enter from either face, however one window can be replaced with an opaque reflecting surface for sensitivity through just one face.

Photons entering the light guide plate are absorbed and wavelength-shifted with high efficiency, and some fraction (those incident on the plate surface at greater than the critical angle) are transported to the readout via total internal reflection. The LAr gaps between the plate and the surfaces of the cavity ensure the discontinuity of the refractive index that contributes to effective trapping of the photons ( $n_{\text{plate}}=1.58$  and  $n_{\text{LAr}}=1.24$  for the wavelengths emitted by the plate). Those exiting the plate reflect off the filter or other highly reflecting surfaces of the cell, with some fraction eventually incident on a SiPM, as in a standard ARAPUCA cell. X-ARAPUCA is thus effectively a hybrid solution between the S-ARAPUCA and the WLS light guide concepts implemented in ProtoDUNE-SP.

This solution minimizes the number of reflections on the internal surfaces of the cell and thus minimizes the probability of photon loss. We have performed a full numerical description of the X-ARAPUCA using the Geant4 framework, following previous studies done for the S-ARAPUCA device [81]. The comparison between the two kinds of devices is dependent on the value of absorption length of the bar, which was not known precisely, so the gain in efficiency for the X-ARAPUCA with the dimensions tested at UNICAMP is estimated to be between 15 and 40% when compared to the S-ARAPUCA with same dimensions and number of SiPMs. Results from prototype measurements are presented in sections 5.8.3.1 and 5.8.3.2 and are consistent with the simulations.

The PD module designed for the DUNE SP module, illustrated in figure 5.7, consists of four supercells, each containing a rectangular light guide inside the cell positioned behind an array of six dichroic filters that form the entrance window. This design is easily configurable to detect light from just one side, as required for the side APAs, or from both sides for the central APAs.

For dual-sided X-ARAPUCA modules, dichroic filters are placed on both sides of the cell facing the drift volumes. In the case of the single-sided device, the back side of the cell has a layer of highly reflective Vikuiti<sup>7</sup> to act as a reflector. In both cases, the SiPM arrays are installed on two of the narrow sides of the cell perpendicular to the windows, parallel to and up against the light guide thin ends. Half of the SiPM active detection area collects photons from the light guide, a quarter of the area on either side of the guide is free to collect the fraction of photons reflected off the cell walls and windows. This fraction of photosensor coverage for photons emerging from the light guide ends is a result of using a standard  $6 \times 6 \text{ mm}^2$  SiPM placed symmetrically with respect

<sup>6</sup>Eljen EJ-286™.

<sup>7</sup>3M Vikuiti™ ESR.

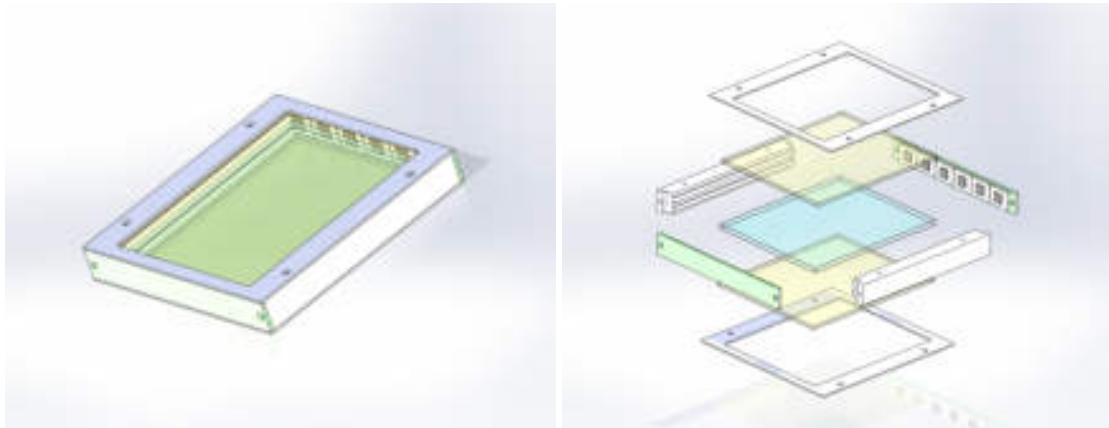


**Figure 5.6.** Simplified conceptual model depicting a X-ARAPUCA cell design sensitive to light from both sides: assembled cell (left), exploded view (right). The yellow plates represent the dichroic filters (coated on their outside surfaces with PTP WLS), the pale blue plate represents the wavelength shifting plate, and the photosensors are visible on the right side of the cell. The size and aspect ratio of the cells can be adjusted to match the spatial granularity required for a PD module.

to the mid-plane of the bar. Simulation of two additional SiPM geometries with the same active area ( $4 \times 9 \text{ mm}^2$  and  $3 \times 12 \text{ mm}^2$ ) showed no substantial difference in the detection efficiency that would justify a custom geometry for the SiPM.

The basic mechanical design of the X-ARAPUCA-based PD modules is similar to that of the two prototypes produced for ProtoDUNE-SP. The prototype design was modified to include mechanical changes to allow both single-sided and dual-sided readout; an increase in the light collection area made possible by larger slots in the APA; and a modified cabling and connector plan necessary to move the PD cables out of the APA side tubes while reducing cable requirements to one Cat-6 cable per PD module.

An X-ARAPUCA module is assembled in a bar-like configuration with external dimensions inside the APA frame of  $2092 \text{ mm} \times 118 \text{ mm} \times 23 \text{ mm}$ , allowing insertion between the wire planes through each of the ten slots (five on each side) in an APA. In addition, there is a header block  $5 \text{ mm}(\text{long}) \times 135 \text{ mm}(\text{wide})$  at the insertion side of the module used to fix the module inside the APA frame, bringing the maximum length to  $2097 \text{ mm}$  and the maximum width to  $135 \text{ mm}$ . The module contains four X-ARAPUCA supercells, each with six dichroic filter-based optical windows (for the single-sided readout) or twelve windows (double-sided readout) with an exposed area of  $78 \text{ mm} \times 93 \text{ mm}$ . The total window area for each (single-sided) supercell X-ARAPUCA is  $43,524 \text{ mm}^2$ . The internal dimensions of a supercell are approximately  $488 \text{ mm} \times 100 \text{ mm} \times 8 \text{ mm}$ . A WLS plate (Eljen EJ-286) of dimensions  $487 \text{ mm} \times 93 \text{ mm} \times 3.5 \text{ mm}$  is centered in the supercell midway between the dichroic windows.

The thickness of  $3.5 \text{ mm}$  for the plate is chosen to allow the almost complete absorption of the photons wavelength-shifted by the PTP and to ensure the nominal conversion efficiency. This thickness allows a  $2 \text{ mm}$  LAr gap on both sides of the plate, which prevents any physical contact of the surfaces even considering the tolerances on material thicknesses and plate flatness.

To reduce production costs and simplify fabrication, most of the PD components are designed to be water-jet cut from sheets of FR-4 G-10 material, with minimal post-cutting machining required

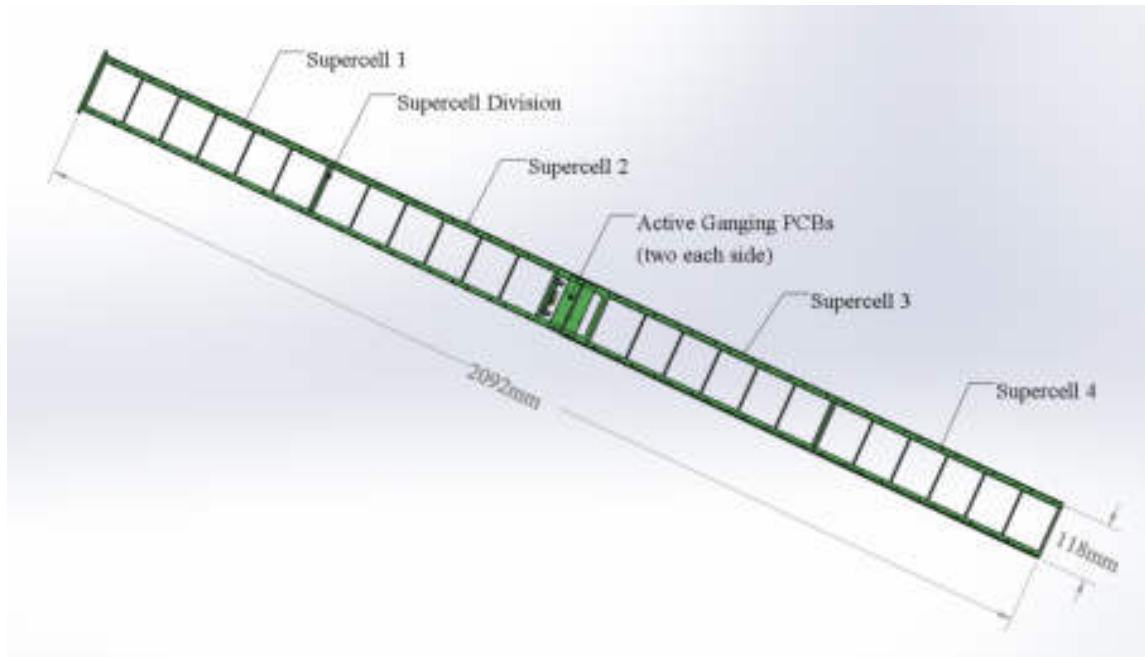


**Figure 5.7.** X-ARAPUCA module overview. A module, which spans the width of an APA, includes 24 X-ARAPUCA cells, grouped into a set of four supercells of six cells each. In the center, active ganging PCBs collect the signals and mechanically connect the supercells.

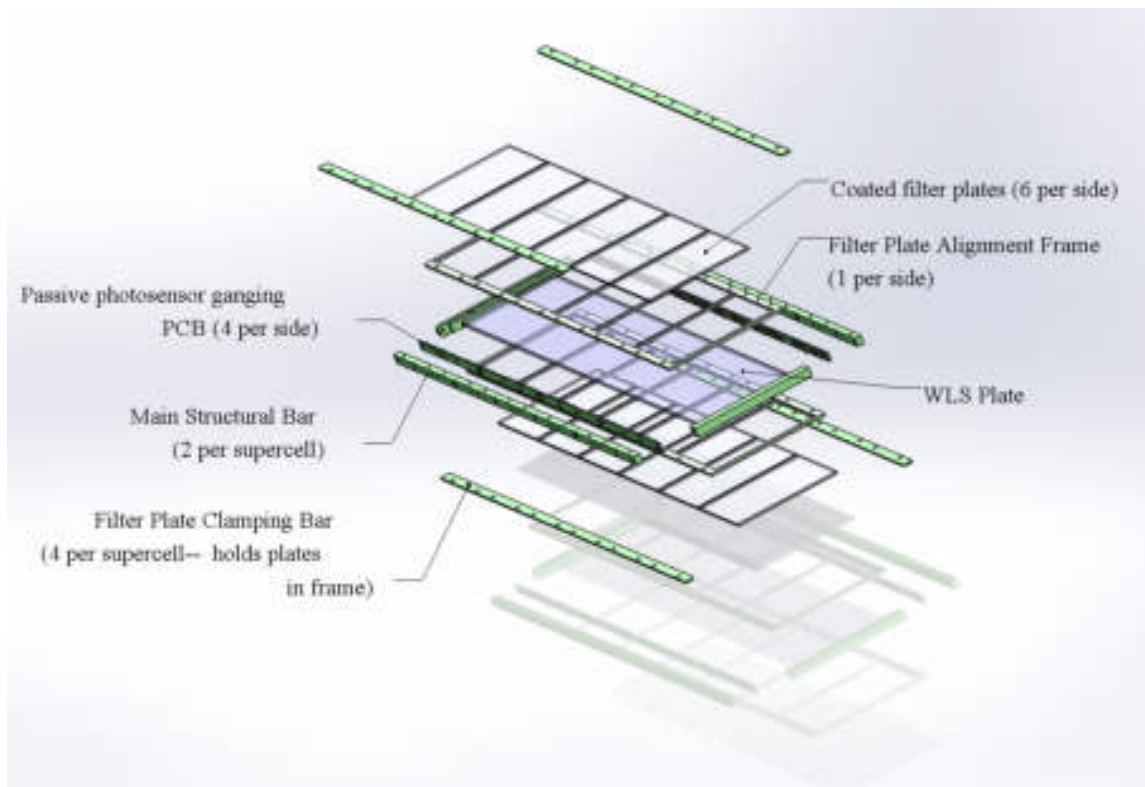


**Figure 5.8.** Detailed exploded view of X-ARAPUCA supercell. Note that components are designed to be cut from FR-4 G-10 sheets to simplify fabrication.

2020 JINST 15 T08010

(mostly the tapping of pre-cut holes). The current design contains many small fasteners; we will investigate replacing some of the fasteners with epoxy lamination of cut sheets where appropriate and cost effective.

The SiPMs are mounted to PCBs called “photosensor mounting boards” that are positioned on the long sides of the supercell. Six SiPMs are mounted to a single photosensor mounting board. The mounting boards incorporate spacers that position the face of the photosensors a nominal 0.5 mm from the face of the WLS plate. All six are electrically connected in parallel (“passively ganged”).

Before mounting the boards into the X-ARAPUCA module, the boards are tested at room and LN<sub>2</sub> temperatures. Each supercell uses eight photosensor mounting boards, each with six SiPMs (figure 5.9 (top)), to accommodate the 48 SiPMs. The ganged signal outputs from these boards are connected to traces in signal routing boards at the edge of the PD module. These signal routing boards also act as mechanical elements in the design, mechanically joining the supercells and providing for rigidity. The routing boards PCBs are four-layer boards, 1046 mm × 23 mm × 1.5 mm.

The passively ganged signals are then routed through these boards to an active-ganging PCB at the center of the module, where all eight passively ganged signals from a single supercell are actively ganged into one output channel (figure 5.9 (bottom)). This summed output from a single supercell is then connected to a single twisted pair in the Cat-6 readout cable for the module. The active ganging PCBs (one per supercell, four per module) are positioned in the module so that they are located inside the central APA mechanical support tube when fully installed.

The internal surface on the lateral sides of the cell are lined with the Vikuiti™ adhesive-backed dielectric mirror foil that has been laser cut with openings at the locations of the SiPMs (i.e., the PCB surfaces surrounding the SiPMs visible in figure 5.9 will be highly-reflective). In the case of the single-sided readout, the dichroic filter windows on the non-active side of the cell are replaced by a blank FR-4 G-10 sheet lined in the cell interior with a Vikuiti™ reflector foil. These types of foils have been used extensively in the WArP<sup>8</sup> and LArIAT<sup>9</sup> experiments, where they performed well optically; no issues were reported related to adhesion of the film or dissolution of the wavelength shifter in LAr.

In DUNE, we have demonstrated that the foils adhere very strongly to FR-4 G10 surfaces cleaned following the PD standard cleaning procedures. Tests by the PD group have demonstrated adhesion is maintained through multiple cryogenic (LN<sub>2</sub>)/warm thermal cycles. The mechanical design provides additional mechanical constraints on the Vikuiti™ sheets after module assembly, so the foils will be held in place mechanically even if the adhesive fails. Samples of the adhesive have been used in other experiments with no negative impact on the LAr purity observed. Samples will be tested in the Fermilab materials test stand, and in ICEBERG, SBND, and ProtoDUNE-SP-2 to confirm that the adhesive does not negatively impact LAr purity or detector performance.

To allow for air to vent out of the cell and LAr to completely fill the cell during the detector fill, holes are provided at the end of each supercell (four holes total, top and bottom of the cell when mounted in the APAs).

The optical window(s) of each supercell are dichroic filters with a cut-off at 400 nm. While the filters used for the ProtoDUNE-SP prototypes have been acquired from Omega Optical Inc.,<sup>10</sup>

<sup>8</sup>Wimp ARgon Program at Gran Sasso: <http://warp.lngs.infn.it/>.

<sup>9</sup>Liquid Argon Time Projection Chamber at Fermilab: <https://lariat.fnal.gov/>.

<sup>10</sup>Omega Optical Inc., Brattleboro, VT USA: <http://www.omegafilters.com/>.

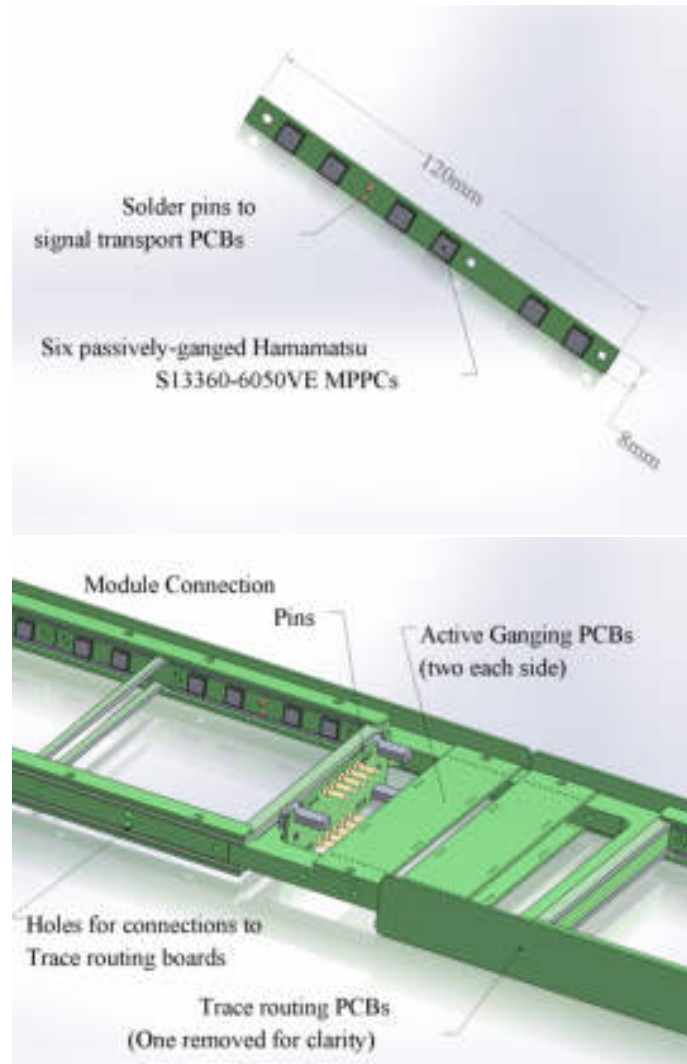


**Figure 5.9.** Model of photosensor mounting board (top) and signal routing PCB (bottom) for X-ARAPUCA module. Six Hamamatsu MPPCs are passively ganged and the ganged signals transmitted along the routing board to the active ganging circuits in the center of the module.

Opto Eletronica S.A.<sup>11</sup> (in Brazil) is our current primary candidate vendor for DUNE production filters. Opto is a well-established company with a long history of involvement in research optical components for harsh environments and large thermal gradients (including camera optics for satellite photography). We plan an extensive suite of testing of their filters at UNICAMP, in ICEBERG, and in ProtoDUNE-SP-2. Other vendors are also being investigated.<sup>12</sup>

The filters are coated on the external side facing the LAr active volume with PTP.<sup>13</sup> The coatings for the ProtoDUNE-SP modules have been made at the thin film facility facility at Fermilab using a vacuum evaporator. Each coated filter was dipped in LN<sub>2</sub> to check the stability of the evaporated coating at cryogenic temperature.

<sup>11</sup>Opto Eletronica S.A.: <http://www.opto.com.br/>.

<sup>12</sup>ASHAI — Japan, Andover — USA, and Edmunds Optics-USA.

<sup>13</sup>p-TerPhenyl, supplier: Sigma-Aldrich@.

For the FD, filter coatings will be done by the vacuum deposition facility at UNICAMP (see section 5.8.3.1).

### 5.5 Silicon photosensors

The physics goals, the design of the light collectors, and the trigger and DAQ system constraints determine the suite of specifications for the silicon photosensors such as the number of devices, spectral sensitivity, dynamic range, triggering threshold and rate, and zero-suppression threshold. An initial survey of commercial products and a 12-month period of R&D indicated that the performance characteristics of devices from several vendors effectively meet the PD system needs. However, a key additional requirement is to ensure the mechanical and electrical integrity of these devices in a cryogenic environment. Catalog devices for most vendors are certified for operation only down to  $-40^{\circ}\text{C}$  and though one candidate device performed well initially, after an unadvertised production process change a large fraction cracked when submerged in LAr.<sup>14</sup> This highlighted the need to be in close communication with vendors in the SiPM design, fabrication, and packaging certification stages to ensure robust and reliable long-term operation in a cryogenic environment.

Nearly one thousand SiPMs, of several types, are used in ProtoDUNE-SP's PD system,<sup>15</sup> providing an excellent test bed for evaluation and monitoring of SiPM performance in a realistic environment over a period of months. Results from ProtoDUNE-SP are summarized in section 5.8.

The SP module baseline PD system design has  $192 \times 6 \times 6 \text{ mm}^2$  MPPCs per PD module with groups of 48 MPPCs electrically ganged into four electronics readout channels. This leads to a total of 288,000 MPPCs.

Two entities have expressed interest to engage with the consortium with an explicit intent to provide a product specifically for cryogenic operation: (1) Hamamatsu Photonics K.K., a large well-known commercial vendor in Japan, and (2) Fondazione Bruno Kessler (FBK)<sup>16</sup> in Italy. FBK is an experienced developer of solid state photosensors that typically licenses its technology; it is partnering with the DarkSide<sup>17</sup> collaboration to develop devices with specifications very similar to DUNE's. Table 5.3 summarizes the key characteristics of the baseline device, Hamamatsu S13360, and two other devices from Hamamatsu and FBK that are under consideration.

While the devices from Hamamatsu have been tested extensively by the consortium, those from FBK are relatively new to us. The technologies they have developed that are suitable for the needs of DUNE are the NUV-HD-SF (standard field) and NUV-HD-LF (low field) [82]. In particular, the LF technology (see table 5.3) offers the lowest dark current rate and has been successfully employed for the DarkSide experiment. NUV-HV-SF sensors developed by FBK specifically for DUNE have been tested in Milano (Italy), CSU (CO, US), and NIU (IL, US). The sensors were characterized both at room and cryogenic temperatures (77 K) and underwent more than 50 thermal cycles. The tests confirmed the nominal performance of the photosensors and proved the reliability of the sensors at low temperature. Extensive thermal tests and characterization of sensors in the NUV-HD-LF technology are in progress.

---

<sup>14</sup>SensL MicroFC-60035C-SMT.

<sup>15</sup>ProtoDUNE-SP uses 516 SensL MicroFC-60035C-SMT, 288 Hamamatsu MPPC 13360-6050CQ-SMD with cryogenic packaging, and 180 Hamamatsu MPPC 13360-6050VE.

<sup>16</sup>Hamamatsu Photonics K.K.: <https://www.fbk.eu/en/>.

<sup>17</sup>Darkside project: <http://darkside.lngs.infn.it/>.

The milestone for photosensor selection for the first SP module is early 2021. Though a baseline photosensor that meets the requirements has been identified, the addition of experienced INFN groups to the PD system effort has enabled us to pursue the promising FBK option in a way that was not possible previously. We are carrying out targeted investigations on the performance, cost, and production capability to establish the viability of the alternatives for all or part of the sensors required for either the first or subsequent SP modules. Two photosensor types (one from each vendor) will be selected in early 2020 to be used in ProtoDUNE-SP-2.

As described in section 5.4, the size and sensitivity of currently available SiPMs requires that multiple devices are needed for each X-ARAPUCA cell. The spatial granularity of each device is much smaller than required for DUNE so, along with limitations on the number of readout channels, it is required that the signal output of the SiPMs must be electrically ganged. The terminal capacitance of the sensors strongly affects the S/N when devices are ganged in parallel, which led to a design that passively gangs several sets of SiPMs in parallel, which are then summed with active components, as described in section 5.6.1.

**Table 5.3.** Candidate photosensors characteristics.

|                                    | Hamamatsu (Baseline)                    | Hamamatsu-2                              | FBK                                     |
|------------------------------------|---|--|---|
| Series part #                      | S13360                                  | S14160                                   | NUV-HD-LF                               |
| $V_{br}$ (typical)                 | 50 V to 52 V                            | 36 V to 38 V                             | 31 V to 33 V                            |
| $V_{op}$ (typical)                 | $V_{br}+3$ V                            | $V_{br}+2.5$ V                           | $V_{br}+3$ V                            |
| Temperature dependence of $V_{br}$ | 54 mV/K                                 | 35 mV/K                                  | 25 mV/K                                 |
| Gain at $V_{op}$ (typical)         | $1.7 \times 10^6$                       | $2.5 \times 10^6$                        | $0.75 \times 10^6$                      |
| Pixel size                         | 50 $\mu\text{m}$                        | 50 $\mu\text{m}$                         | 25 $\mu\text{m}$                        |
| Size                               | 6 mm x 6 mm                             | 6 mm x 6 mm                              | 4 mm x 4 mm                             |
| Wavelength                         | 320 to 900 nm                           | 280 to 900 nm                            | 280 to 700 nm                           |
| PDE peak wavelength                | 450 nm                                  | 450 nm                                   | 450 nm                                  |
| PDE at peak                        | 40%                                     | 50%                                      | 50%                                     |
| DCR at $0 \cdot 5\text{PE}$        | $< 50 \text{ kHz} \cdot \text{mm}^{-2}$ | $< 100 \text{ kHz} \cdot \text{mm}^{-2}$ | $< 25 \text{ kHz} \cdot \text{mm}^{-2}$ |
| Crosstalk                          | $< 3\%$                                 | $< 7\%$                                  | $< 3\%$                                 |
| Terminal capacitance               | 35 pF $\cdot \text{mm}^{-2}$            | 55 pF $\cdot \text{mm}^{-2}$             | 50 pF $\cdot \text{mm}^{-2}$            |
| Lab experience                     | Mu2e and DUNE prototypes                |  | Darkside                                |

## 5.6 Electronics

The electronic readout system for the PD system must (1) collect and process electrical signals from SiPMs reading out the light collected by the X-ARAPUCAs, (2) provide an interface with the trigger and timing systems supporting data reduction and classification, and (3) transfer data to



offline storage for physics analysis. Figure 5.10 provides a simple overview of the signal path and key elements.

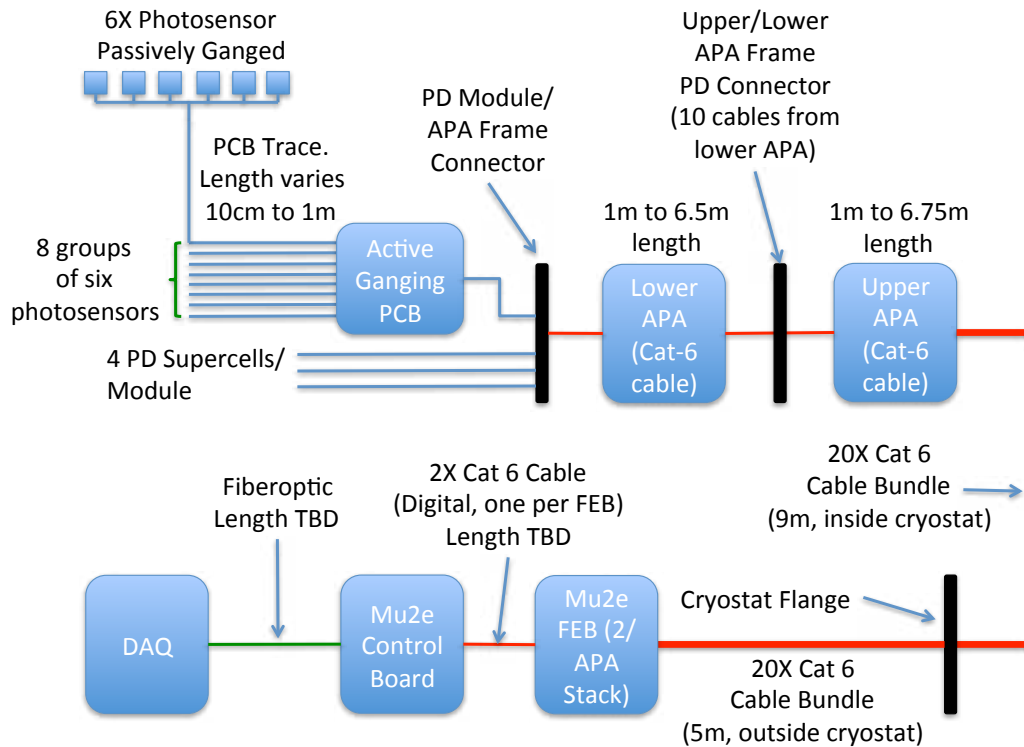


**Figure 5.10.** Overview of the PD system signal path.

As specified in the requirements table 5.1, the readout system must enable the  $t_0$  measurement of non-beam events; this capability will also enhance beam physics by recording interaction time of events within beam spill more precisely to help separate against potential cosmic background interactions. A highly capable readout system was developed for use with ProtoDUNE-SP and prototype development as described in section 5.8.2.2. However, a more cost-effective waveform digitization system developed for the Mu2e experiment has been identified and selected as the baseline choice for the PD system.

### 5.6.1 SiPM signal ganging

The ganging of electrical signals from SiPM arrays is implemented to minimize the electronics channel count while maintaining adequate redundancy and granularity, as well as to improve the readout system performance. Technical factors that affect performance of the ganging system are the characteristic capacitance of the SiPM and the number of SiPMs connected together, which together dictate the S/N and affect the system performance and design considerations.

We have demonstrated a feasible purely passive summing scheme with twelve Hamamatsu MPPC sensors now operational in ProtoDUNE-SP. For optimal performance in DUNE, we have shown that an ensemble of 48 Hamamatsu 6 mm  $\times$  6 mm MPPCs can be summed into a single channel by a combination of passive and active ganging (see section 5.8.1). In this scheme, an amplifier is used to adjust the MPPC output signal level to the input of an ADC; the active summing

is realized with an OpAmp THS4131. This combination of passive and active ganging with cold signal summing and amplification, illustrated in figure 5.11, is the baseline for the PD system.

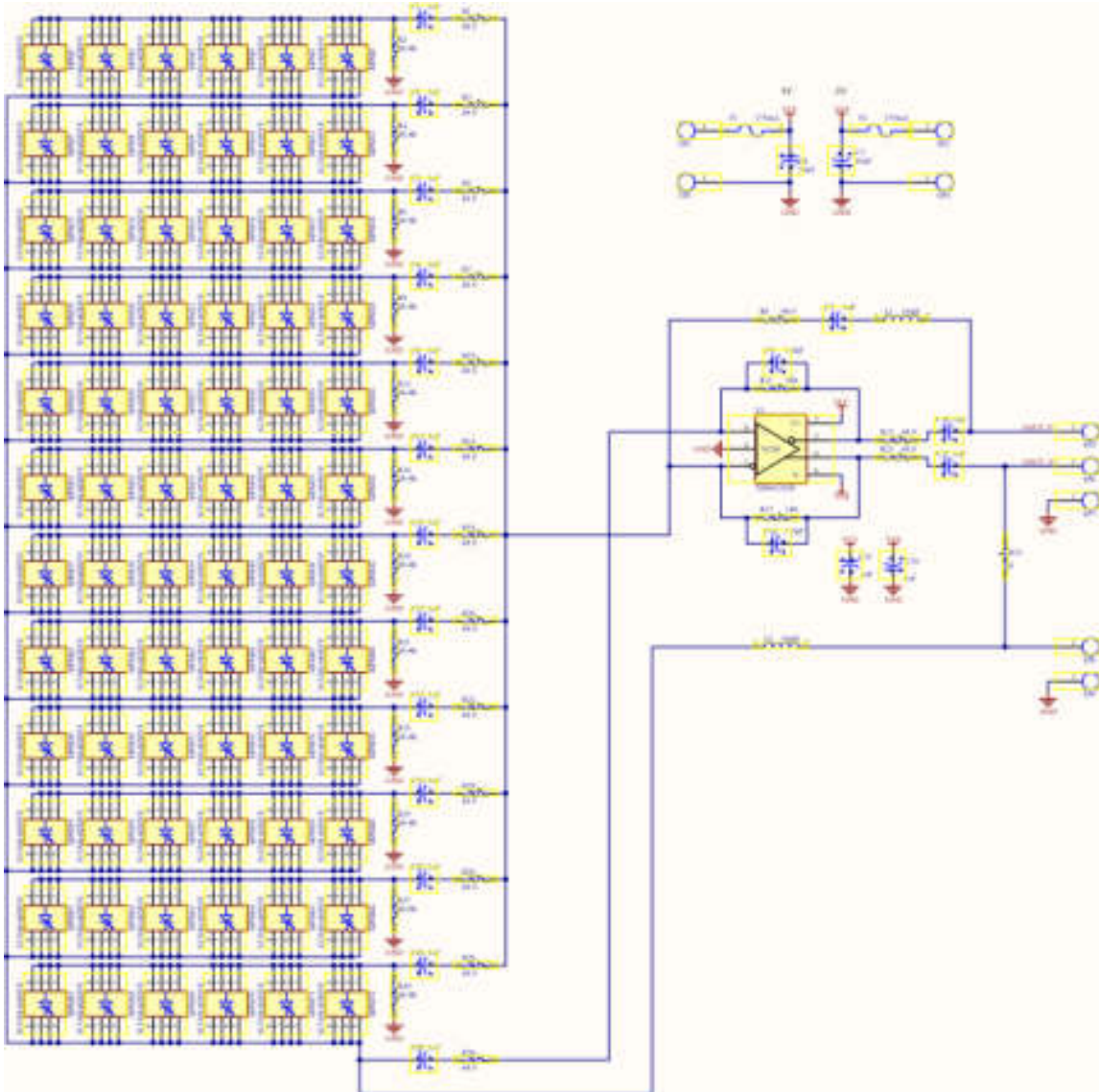


**Figure 5.11.** SiPM signal summing board circuit: 6 passive x 8 active, 48 SiPMs total.

### 5.6.2 Front-end electronics baseline design

The FE electronics for the development and prototype stages of the PD system, including ProtoDUNE-SP, was provided by a custom-designed SiPM Signal Processor (SSP, see DocDB 3126 [83]). This system was highly configurable and provided detailed information on the photosensor signal, which allowed a thorough understanding of the photon system performance. For the much larger SP module, a system is required that meets the performance requirements yet optimizes the cost. To this end, we have developed a solution based on lower-sampling-rate commercial ultrasound ASIC chips rather than digitizers based on flash ADCs used in the SSP. Inspiration for this cost-effective

FE comes from the system developed for the Mu2e experiment cosmic ray tagger readout system. Both SSP and the new design are used in the PD validation process summarized in section 5.8 to allow direct comparison.

Development of the readout electronics to date has been primarily by US groups. However, since fabrication of the DUNE readout electronics will be conducted by a collaboration of Latin American institutions (including groups in Peru, Colombia, Paraguay, and Brazil), further development is being performed by these groups, with support from the US groups. The engineers met and worked together at Fermilab in summer 2019, and that collaboration is continuing. We expect the first DAPHNE prototypes to be complete and tested in ICEBERG in April/May 2020. Pre-production Mu2e-based electronics readout will also be tested in the ProtoDUNE-SP-2 run at CERN in 2021–2022.

### 5.6.2.1 Front-end board and controller

The readout and digitization of the signals from the active summing board described in section 5.6.1 will rely on a set of FE board (FEB) readout electronics boards and controller boards, originally designed for the Mu2e experiment [7] at Fermilab. As discussed in section 5.8.1, preliminary results indicate that the active-summing board and Mu2e electronics FEB combination will perform well together and, in general, meet the readout requirements for the experiment. Figure 5.12 shows the 64 channel FEB design carried over from Mu2e. The board has a number of notable features, discussed below. Most importantly, the board is designed to utilize commercial, off-the-shelf parts only, and is therefore quite inexpensive compared to other designs. In particular, the digitization implements the low-noise, high-gain, and high-dynamic-range commercial ADCs used in ultrasonic transducers.

The FEB is the centerpiece of the baseline readout electronics system. The current 64 channel<sup>18</sup> FEB relies on commercial ultrasound chips,<sup>19</sup> with programmable anti-alias filters and gain stages, to read out the MPPC signals from the active ganging boards inside the PD modules. The board currently takes HDMI inputs, with four channels per input. Each of the eight ultrasound chips on an FEB handles eight channels (120 mW per channel) of data using a low-noise preamplifier, a programmable gain amplifier, and a programmable low-pass filter. The information is buffered with a total of 1 GB DDR SDRAM, divided in four places, and a set of Spartan 6™ FPGAs are used for parallelizing the serial ADC data, zero suppression, and timing. Each of the four FPGAs on a board, corresponding to 16 channels, handles two ADC chips with an available 256 MB DDR SDRAM.

After digitization, the data from each FEB, in the form of pulses (time-stamp and pulse height), is sent via Ethernet to a master controller that aggregates the signals from 24 FEBs, or  $64 \times 24 = 1536$  channels. The 24 FEBs corresponding to a single controller will come in sets of 12, with each set of 12 FEBs referenced to a single chassis as shown in figure 5.13. A trigger decision (e.g., accelerator timing signal) can be produced and/or received by the controller and, depending on the decision, each event’s digital information is sent to the controller and then to DAQ computers for

<sup>18</sup>This text assumes 64 channels/FEB when presenting the FEB and controller. However, we envision 40 channels/FEB in the final design, corresponding to a single APA as described in section 5.6.3.

<sup>19</sup>Texas Instruments™ 12 bit, 80 megasamples/s (MS/s); AFE5807.

processing and storage. The controller-to-DAQ connection will rely on a fiber connection, although an Ethernet-based controller output option is available.

### 5.6.2.2 Bandwidth, readout rates, and zero suppression

DAQ system and data storage limitations impose constraints on the data flow from the FE electronics system. For example, if it were necessary to read out a  $5.5\ \mu\text{s}$  waveform in order to include more of the longer time constant scintillation light component, the 80 megasamples/s (MS/s), 12-bit ADC device would produce a 5.3 kbit waveform. For an envisioned dark count (DC) rate of 250 Hz/channel, this corresponds to a data transfer rate of 53 MB/s/APA (1 APA=40 channels) or 6.6 MB/s FEB-to-controller DC rate. This rate approaches the crucial bottleneck in the electronics readout system with a maximum rate of 10 MB/s (per FEB). However, zero-suppression techniques and multi-channel coincidence/threshold requirements at the FEB firmware level can be used to significantly mitigate this issue, noting that each on-FEB FPGA handles 16 channels.

The design is flexible enough to accommodate modest changes in system requirements, such as the suppression factor determined by parameters like the readout window length and limits on the overall trigger rate. Firmware and zero-suppression technique development is in progress and can easily adapt to the physics and calibration requirements of the PD. In addition to its bandwidth and DC rate readout capabilities, the system can also manage a highly coincident event in which a large number (or all) channels fire at once. For example, the controllers' 24-board write speed of 150 MB/s could handle even the unlikely all-detector event featuring 6000 channels firing at once (corresponding to 4 MB event size).

The baseline electronics readout system performance is consistent with the DAQ interface specification of 8 Gb/s per connection, given that each FEB signal corresponds to a maximum of 10 MB/s (240 MB/s total).

### 5.6.2.3 Power, grounding, and rack schemes

Figure 5.14 shows the grounding, power, and data link schemes for the system. The FEBs are powered via power-over-Ethernet (600 mA, 48 V supply) from the controller. One Cat-6 cable from the controller to each FEB handles the signal and power simultaneously. The reference planes of the controller and FEB are isolated on both sides. The grounding scheme calls for each set of twelve FEBs referenced to a single chassis, with each chassis and corresponding controller on detector ground and the DAQ, connected to each controller via fiber, on building ground.

The rack space and power consumption required by the system assume a total of 6000 channels with 40 channels/FEB. This system requires 13 chassis (12 FEB/chassis) at 6U each and seven controllers (controlling 24 FEB each) at 1U each; these can be accommodated in just over two 42U capacity racks. The power supply on a controller is 700 W, with each FEB taking 20 W.

### 5.6.3 Electronics next steps

The FEBs, developed for the Mu2e cosmic ray veto and proposed for use in DUNE, can read out an array of MPPCs with an adequate S/N ration to be sensitive to single photons. However, we want to optimize and further develop them by pursuing the following tasks:

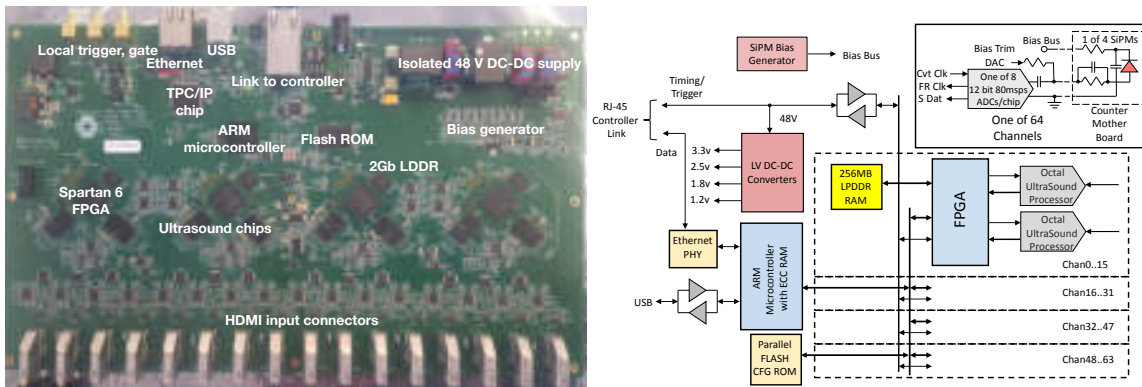


Figure 5.12. Photograph of the 64-channel PD system FE board (80 MS/s, 12 bit ADC) (left); schematic of the FE board (right).

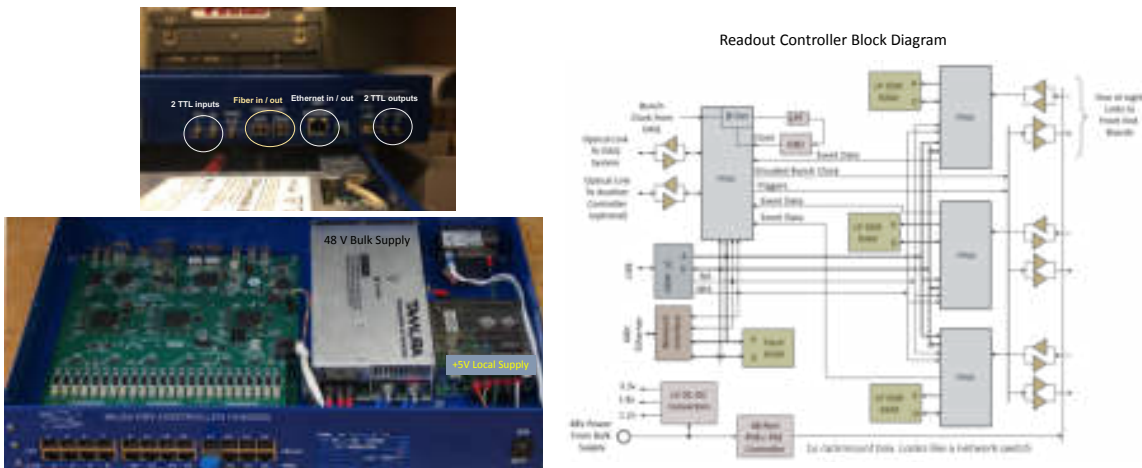


Figure 5.13. The front (left-bottom) and back views of the controller module (left-top); it is capable of accepting signals from 24 FEBs; schematic of the controller (right).

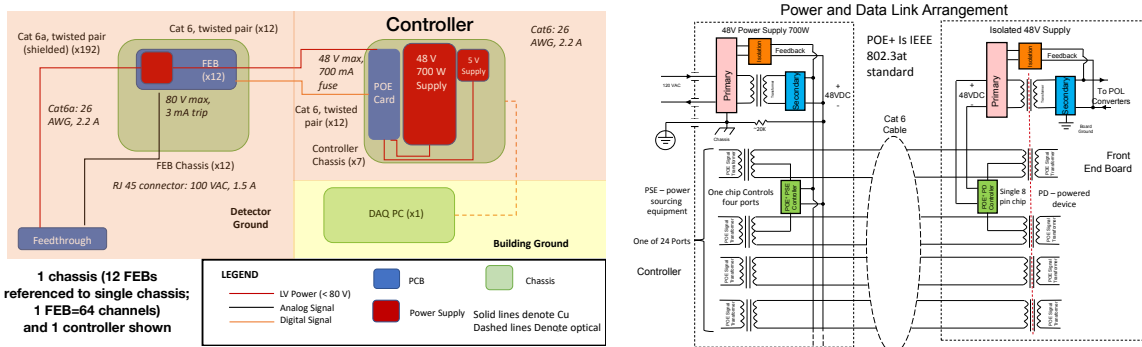


Figure 5.14. Grounding scheme with 1 chassis, containing 12 FEBs, a controller module, and a DAQ PC, as an example (left); power and data link arrangement of the FEB and controller (right).

1. To better match the 40 ProtoDUNE-SP channels per APA, the system presented here assumes that only 40 out of the 64 channels on the existing Mu2e FEB are populated with active electronics. A prototype board will test this configuration and validate the associated cost model.
2. The Mu2e warm readout electronics use last-generation (Xilinx™ Spartan-6) FPGAs and other components that have since been superseded by newer devices. Design and prototyping work will incorporate newer FPGAs (Xilinx Spartan-7 or Artix-7) into the electronics, improving their performance and maintainability over the lifetime of the DUNE experiment. The Artix-7 FPGAs have been implemented in the SSP readout system used in ProtoDUNE-SP, and therefore the expertise with these system components has been established.
3. Results from the ICEBERG test stand can determine whether there are sufficient logic resources in the FPGAs to meet a broad range of possible DAQ requirements expected from the warm readout electronics. To that end, the low-cost FE solution will be compared to existing 14 bit, 150 MS/s SSP readout. Straightforward zero suppression schemes that can be implemented on the Mu2e board with the current Spartan-6 FPGA will be tested with respect to potential DAQ data rate limitations. However, increases in the number of logic cells can be accommodated by switching to more capable, but still pinout-compatible, devices within the same Xilinx FPGA family as discussed above.
4. It may be desirable to increase the dynamic range of the ADCs used on the FEBs in order to achieve desired physics goals related to the energy resolution of beam neutrino events. To this end, we plan to investigate replacing the TI AFE5807 ultrasound chip with the TI AFE5808 ultrasound chip, which is pinout-compatible but incorporates a 14-bit ADC. Ultimately, a prototype board will incorporate all relevant optimizations and improvements.

The final requirements for the system will be informed by analysis of the data from the readout system implemented in ProtoDUNE-SP and subsequent data from operating ICEBERG from August 2019 through the end of the year.

Additional testing of the system will continue through ProtoDUNE-SP-2 operations. The specifications for the readout electronics system will be reconsidered based on that experience and established before the PD final design review (see the high-level schedule in section 5.15.1).

### 5.7 Calibration and monitoring

Calibration and monitoring is an essential component of the PD system. The primary system is a pulsed UV-light source that will allow calibration of the PD gain, linearity, and timing resolution and monitoring the stability of the photon response of the system over time. In many experiments, a pulsed light system is a valuable well-defined, controllable light source for monitoring but for (near) surface detectors, often a supplement to using tracked cosmic ray muons, which provide a much closer replica of the signal from events of interest. However, at DUNE, the muon rate per individual photon detector will be very low and insufficient to monitor changes in the system response. In this situation, the pulsed system will play an essential role in achieving and maintaining the PD performance required for neutrino calorimetry. This system will also be a valuable detector

commissioning tool prior to sealing the cryostat, in the cool-down phase, and during the LAr fill. Other complementary calibration systems, such as radioactive sources, are described in chapter 6.

The system design is almost identical to that deployed in ProtoDUNE-SP, as described in section 5.8.5; the primary differences are the number of diffusers, the lengths of the optical fibers, and the addition of a monitoring diode.

The system hardware consists of both warm and cold components but has no active components within the cryostat. The active component consists of a 1U rack mount light calibration module (LCM) located outside the cryostat. The LCM generates UV (245 nm to 280 nm) pulses that propagate through a quartz fiber-optic cable to diffusers at the CPA that distribute the light uniformly across the PDs mounted within the APA. It consists of an FPGA-based control logic unit coupled to an internal LED pulser module (LPM) and an additional bulk power supply. The LPM has multiple digital outputs from the control board to control the pulse amplitude, pulse multiplicity, repetition rates, and pulse duration; programmable DACs control the LPM pulse amplitude. ADC channels internal to the LCM are used to read out a reference photodiode used for pulse-by-pulse monitoring of the LED light output. The output of the monitoring diode is available for normalizing the response of the SiPMs in the detector to the monitoring pulse.

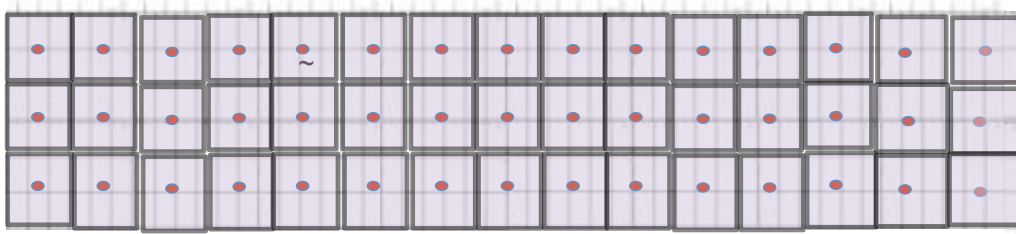


**Figure 5.15.** Schematic of a complete SP cathode plane ( $60\text{ m} \times 12\text{ m}$ ) showing the locations of the calibration and monitoring system diffusers. Each diffuser illuminates a region of about  $4\text{ m} \times 4\text{ m}$  (indicated by the squares) on APAs  $3.6\text{ m}$  away.

Quartz fibers,  $10\text{ m}$  to  $30\text{ m}$  long, are used to transport light from the optical feedthrough (at the cryostat top) through the FC GP, and through FC strips to the CPA top frame. These fibers are then optically connected to diffusers located on the CPA panels using fibers that are  $2\text{ m}$  to  $10\text{ m}$  long. The diffusers,  $2.5\text{ cm}$  in diameter, are mounted on the cathode plane panels acting as light sources to illuminate PDs embedded in the APAs. There will be 45 diffusers uniformly distributed across each of the SP module cathode planes facing APAs, as indicated in figure 5.15. Each diffuser will illuminate an area of approximately  $4\text{ m} \times 4\text{ m}$  on the APAs that are  $3.6\text{ m}$  away.

The diffusers reside at the CPA potential, so the HV system places a requirement on the fiber electrical resistance to protect the cathode from experiencing electrical breakdown along this path. This requirement is easily met by the fibers.

As demonstrated in ProtoDUNE-SP, the system performs the required calibration and monitoring tasks with minimal impact on the TPC design and function.

## 5.8 Design validation

This section summarizes the most important sets of measurements, completed, ongoing, and planned, that validate the SP PD system design.

### 5.8.1 Photosensors and active ganging

As described in section 5.6.1, the active ganging of SiPMs aims to increase the active photo-detecting area while keeping the number of readout channels at a reasonable number. Several active ganging detectors were designed and tested during 2017–2018. The systems were based on an active summing node mounted near the photosensors in the LAr. Several incarnations of the cold summing node were designed and tested using SensL and Hamamatsu SiPMs, as were several types of operational amplifiers. Some of these designs were tested and validated in the S-ARAPUCA prototype measurements. We describe here only the most recent design that demonstrated that 48 Hamamatsu MPPCs in the baseline design can be ganged together on a single differential output with excellent signal performance, low noise, and low power dissipation.

Figure 5.16 (left) shows a matrix array of 72 MPPCs organized as 12 rows of six 13360-6050VE MPPCs each. The six MPPCs per row are connected in parallel, giving a total output capacitance of 7.8 nF. The 12 rows are connected to the summing node of an operational amplifier, THS4131, as illustrated in figure 5.16 (right). Since the DUNE baseline design is based on 48 MPPCs/X-ARAPUCA module, only eight rows of six MPPCs were used for the tests. The performance of the cold summing electronics was done by illuminating the MPPC array with an LED and digitizing the output with a high-speed oscilloscope and with the SSP readout electronics (see section 5.8.2.2).

As shown in figure 5.17 (left), the mean signal has a rise time of 60 ns and a recovery time of 660 ns, well within the DUNE PD specifications.

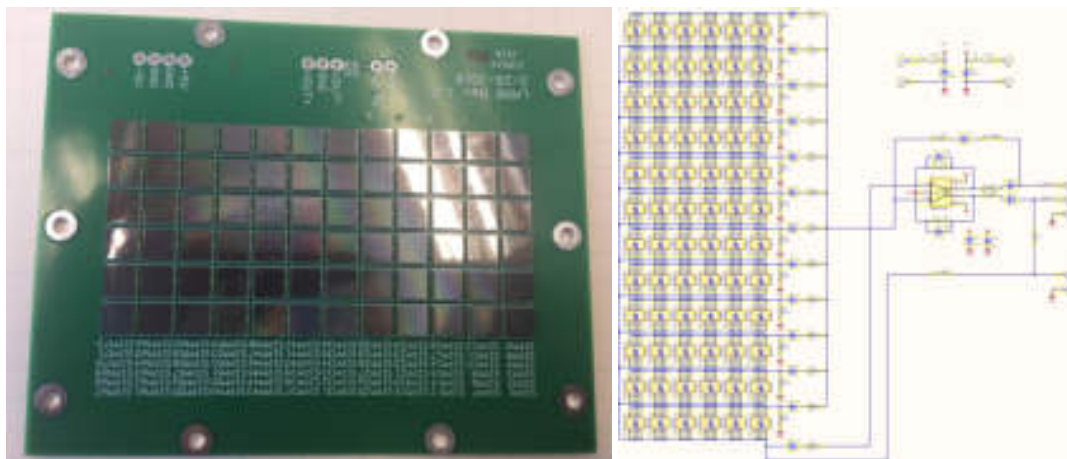


**Figure 5.16.** Summing board with a total of 72 MPPCs used to demonstrate the optimal combination of passive and active ganging with 48 Hamamatsu 6 mm×6 mm MPPCs (left). Schematic of the summing circuit with a THS4131 operational amplifier (right).

Figure 5.17 (right) shows a histogram of light collection signals from the array for a bias voltage equivalent to 2 volts above the mean breakdown voltage. Since there are 48 MPPCs in the array,



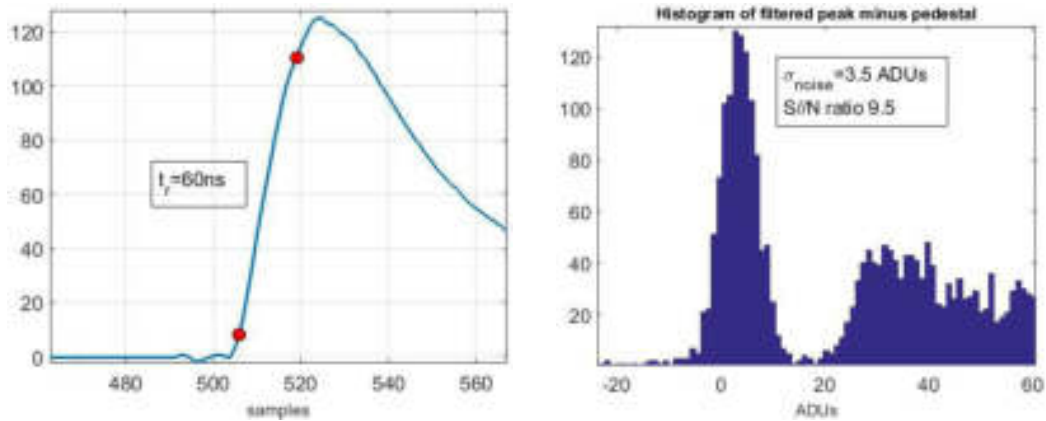


**Figure 5.17.** Waveform signal from 48 MPPCs/ARAPUCA module, summed with the THS4131 operational amplifier and digitized with the SSP FEB (left); histogram of signals with a 47 V bias illustrating the first photoelectron peak well-separated from the pedestal with an  $S/N = 9.5$  (right).

and a single common bias, there is a spread in the gains. Even when the Hamamatsu MPPCs have a small spread in breakdown voltages, it is enough to smear the peaks in the histogram. It is worth distinguishing the difference between noise and gain spread. The circuit noise can be measured as full width at half maximum (FWHM) or RMS around the 0 photoelectron signal (3.5 ADC counts in the figure); the first photoelectron peak is at 33 ADC counts, resulting in an optimal signal to noise ratio of about ten.

Since the breakdown voltage of the MPPCs is provided by the manufacturer for each device, the gain spread can be reduced by picking groups of 48 MPPCs with similar breakdown values for each module. The differential output of the CE impedance is matched to the readout electronics and able to reject more than 60 dB of common mode noise. This is particularly important since the MPPCs and output wiring are inside a high voltage TPC. The timing properties of the 48 ganged electronics were also measured in LAr using a  $^{241}\text{Am}$  alpha source. Figure 5.18 shows the time walk for a constant discrimination threshold which, as expected, is not a linear function of the signal height. The error distribution, which is not Gaussian, has a FWHM of 80 ns. This value is well within the DUNE specification (table 5.1).

**FBK sensors.** FBK has published detailed measurements on photosensors developed in collaboration with the DarkSide cryogenic experiment [82]. Figure 5.19 (left) shows that the photon detection efficiency of candidates devices as function of wavelength is very well matched to the needs of the X-ARAPUCA.

An extensive program of evaluation of the key performance characteristics is underway by the DUNE PD system team. In the first phase, a sample of (4 mm×4 mm, 40  $\mu\text{m}$  cell-pitch) devices has been tested at INFN-Milano in a dedicated setup optimized for the measurement of very low dark currents. The sensors were operated at 77 K and can be biased from 21 V (breakdown voltage) up to 31 V (maximum overvoltage range at cryogenic temperature is +10 V). The dark count rate at 4 V overvoltage is  $\sim 0.2\text{ Hz/mm}^2$ , which meets the DUNE requirements (see figure 5.19 (right)). These devices have undergone numerous temperature cycles during the testing with no deterioration in characteristics. Another sample at CSU has undergone more than 50 thermal cycles with no evidence of mechanical failures.

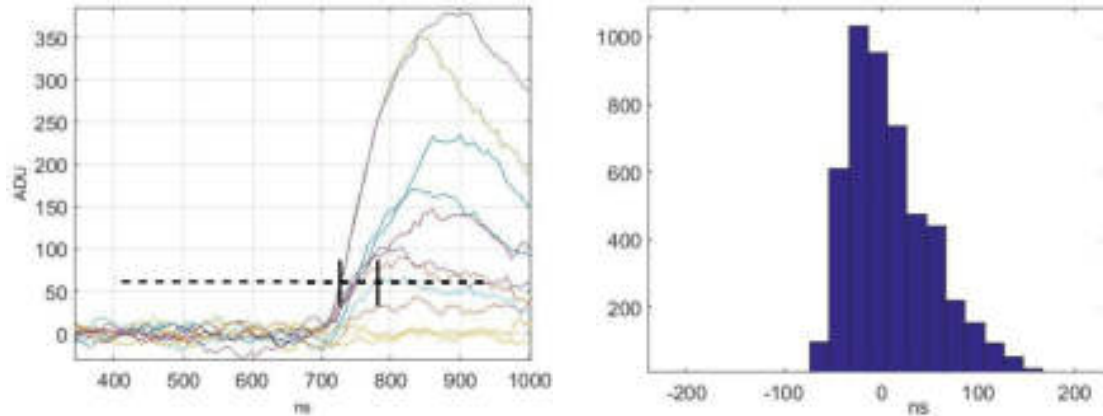


**Figure 5.18.** Oscilloscope trace (left) and histogram (right) illustrating time walk from 48 ganged MPPCs measured with the constant discrimination threshold on the SSP board.

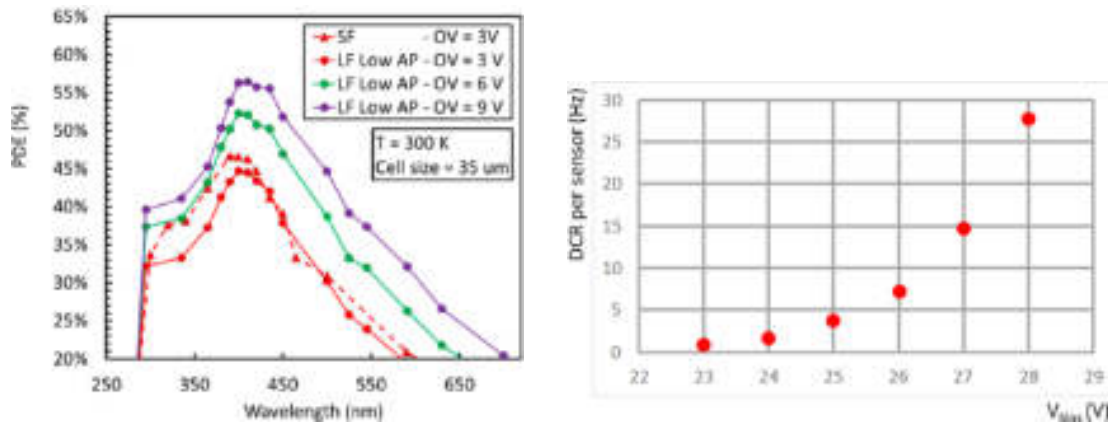


**Figure 5.19.** PDE measured at 293 K for FBK NUV-HD-Cryo and NUV-HD SiPMs (left); dark count rate for NUV-HD-SF SiPMs at 77 K (right).

**Mu2e electronics.** The Mu2e electronics have undergone a series of end-to-end warm and cold tests to demonstrate single-photon sensitivity in various parallel/series ganging and SiPM/MPPC configurations. Here we summarize the results with the 72-MPPC active ganging array described in section 5.8.1 at LN<sub>2</sub> temperatures. A balun<sup>20</sup> is used to convert from the differential actively-ganged MPPC array output to the single-ended FEB.

A trigger allowed data to be collected in time with an LED flasher, with samples taken every 12.5 ns for the length of the readout window ( $\sim 3\mu\text{s}$ , in this case). Figure 5.20 shows the system used and a histogram of the maximum ADC value during each trigger window. The first peak above zero corresponds to the electronic noise and the second peak corresponds to a one-PE signal. The signal to noise from these tests was measured to be 4, calculated from the ratio of the single photon peak (20 ADC, after subtracting the noise peak) to the spread in the noise ( $\sigma_{\text{noise}} = 5 \text{ ADC}$ ); this is similar to the value found when using the SSPs for readout ( $S/N = 5$ ).

<sup>20</sup>A transformer used to convert differential (BALanced) signals to single-ended (UNbalanced) ground referenced signal.

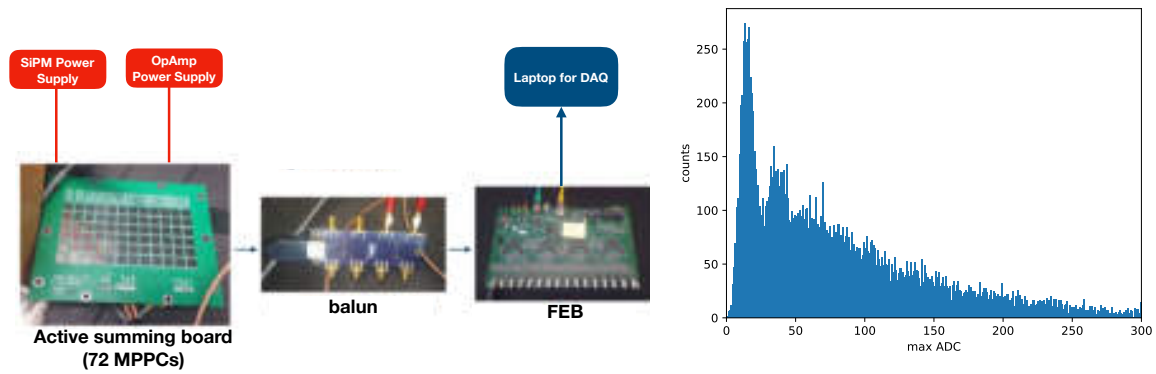


**Figure 5.20.** The Mu2e electronics readout board was used to read out a 72-MPPC active ganging array ( $V_b = 47.2$  V) (left). The maximum ADC results are shown, with the first and second peaks representing 0 and 1 photoelectron signals (right).

## 5.8.2 Standard ARAPUCA (S-ARAPUCA)

### 5.8.2.1 Development prototypes

As outlined in section 5.3.3.1, the design for the S-ARAPUCA features a dichroic filter window coated with a wavelength-shifter on the LAr active volume face and a second wavelength shifter coated onto the dichroic filter on the surface inside the cell. The proof-of-concept measurements of this design were performed on a small cell with internal dimensions of  $3.5 \text{ cm} \times 2.5 \text{ cm} \times 0.6 \text{ cm}$ , with a window formed from a dichroic filter of dimensions  $3.5 \text{ cm} \times 2.5 \text{ cm}$  and a wavelength cut-off at 400 nm. The external side was coated with PTP and the internal side was coated with tetra-phenyl butadiene (TPB). The trapped light was detected by a single  $6 \text{ mm} \times 6 \text{ mm}$  SensL MicroFC-60035C-SMT SiPM.<sup>21</sup> The cell was exposed to scintillation light produced in pure LAr by an alpha source<sup>22</sup> that emits three alpha lines with energies of 4.187 MeV, 4.464 MeV, and 4.759 MeV with relative abundances of 48.9%, 2.2%, and 48.9%. The observed spectrum was fit using the predicted photon yield from the three alpha lines to extract the overall collection efficiency for this configuration of  $1.10\% \pm 0.15\%$  [84] for this configuration, consistent with Monte Carlo (MC) expectations [81]. This corresponds to a gain in the effective photosensors area of approximately a factor of 3.7.

A series of subsequent prototypes with filters from different manufacturers, different reflectors, and different dimensions were evaluated with similar results.

The final set of prototypes prior to ProtoDUNE-SP were tested in the TallBo facility using an external set of cosmic ray counters as a readout trigger. These consisted of an array of eight S-ARAPUCA cells each with a photon collection area of  $80 \text{ cm}^2$ , but the SensL SiPMs used in previous prototypes were replaced with four  $6 \text{ mm} \times 6 \text{ mm}$  Hamamatsu S13360-6050VE MPPCs. Two double-shift light guide modules were also included in the test and served as a reference for the S-ARAPUCA results.

The measured collection efficiency range for the eight ARAPUCA cells was 0.72% to 0.80%, with an effective S-ARAPUCA gain of about 4.5 times the photosensor area. These tests demonstrate

<sup>21</sup>SensL SiPM: <http://sensl.com/products/c-series/>.

<sup>22</sup>A <sup>238</sup>U-Al alloy in the form of a metallic foil.

that the effective area gain is maintained when the area for light collection of the cell is scaled up by almost an order of magnitude.

### 5.8.2.2 ProtoDUNE-SP

The most comprehensive set of data on the S-ARAPUCA will come from the fully instrumented modules in the ProtoDUNE-SP experiment [6] that completed first beam running in November 2018. Since ProtoDUNE-SP will remain filled with LAr for much of the CERN long shutdown, it will provide a long-term cold test of full-scale PD modules for the first time, so it may be possible to quantify any deterioration in their performance.

Three prototype photon collector designs are present in ProtoDUNE-SP: 29 double-shift guides, 29 dip-coated guides, and two S-ARAPUCA arrays. The TPC provides precise reconstruction in 3D of the track of any ionizing event inside the active volume, and matching the track with the associated light signal will enable an accurate comparison of the relative photon collection efficiencies of the different PD modules. The large number of modules and independent channels that record each event can be used to constrain the parameters of the LAr that regulate VUV light propagation in the simulation and are poorly determined in the literature. In principle, absolute calculations of the relative and absolute detection efficiencies are possible using MC simulations. The precision of this approach may be limited by the precision of the constraints on the parameters but in any case will result in a consistent simulation constrained by measurements.

Figure 5.21 shows an event display from ProtoDUNE-SP overlaid with colored bars indicating the positions of PD modules that are on the beam entry side of the TPC. Of the two S-ARAPUCA arrays in ProtoDUNE-SP, the first is installed in APA 3 in the fourth position from the top, near the level at which the beam particles enter this drift volume. This module and the surrounding light guide modules are illuminated with a significant amount of light from each beam particle interaction. This module is visible near the center of the photograph of APA 3 in figure 5.22. The second is installed in APA 6, in the 6th position from the top, in the drift region on the opposite side of the opaque cathode plane, which does not see entering beam particles; this module does not see significant light from beam events (only from showering particles that pass through the cathode), but it observes photons from a large collection of triggered cosmic rays.

Each ProtoDUNE-SP S-ARAPUCA module array is composed of sixteen cells, where each cell is an S-ARAPUCA box with window dimensions of 7.8 cm  $\times$  9.8 cm; half of the cells have twelve MPPCs installed on the bottom side of the cell and half have six MPPCs. The MPPCs used are the Hamamatsu model 13360-6050CQ-SMD, which are functionally the same as the 13360-6050VE used for the ganging tests (section 5.8.1) and also on some of the light guide bars in ProtoDUNE-SP, but this model incorporates a package specifically designed for cryogenic operation.<sup>23</sup> The MPPCs have active dimensions 0.6 cm  $\times$  0.6 cm and account for 5.6% (12 MPPCs) or 2.8% (6 MPPCs) of the area of the window. The MPPCs are passively ganged together, so that only one readout channel is needed for each S-ARAPUCA grouping of 12 MPPCs (the boxes with six MPPCs are ganged together to form 12-MPPC units), so a total of 12 channels is required per PD module. The total

<sup>23</sup>A thin glass window mounted in front of uncoated silicon photosensitive surface, as opposed to the thin coating directly on the silicon for the 13360-6050VE.

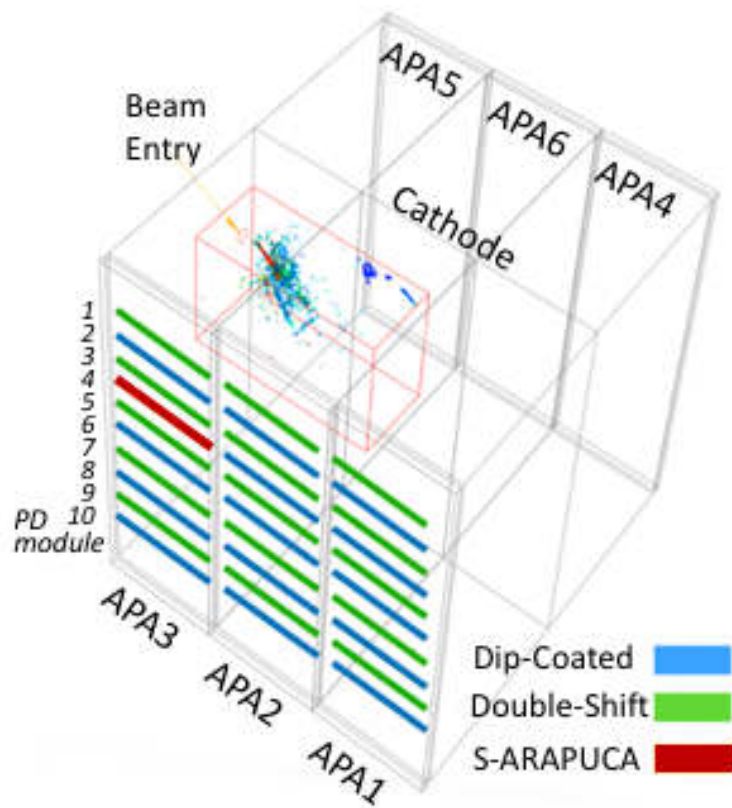


**Figure 5.21.** Event display from ProtoDUNE-SP showing the location of the PD modules on the beam entry side of the TPC. Reconstructed TPC hits from a test beam electron are visible at approximately the same height in the TPC as the S-ARAPUCA module mounted in APA 3.

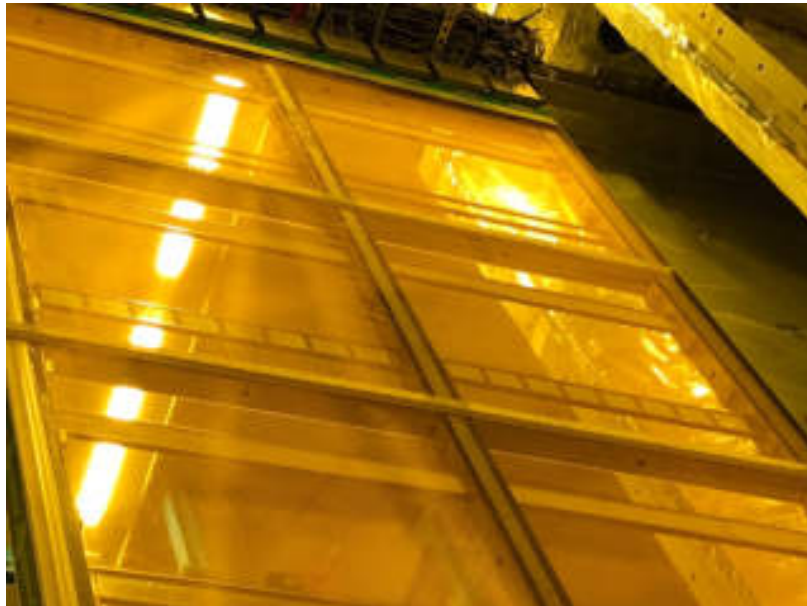


**Figure 5.22.** Visible in the center of the photograph of APA 3 is the 16-cell S-ARAPUCA array installed in ProtoDUNE-SP.

width of a module is 9.6 cm, while the active width of an S-ARAPUCA is 7.8 cm, the length is the same as the light guide modules (~210 cm).<sup>24</sup>

An S-ARAPUCA array during assembly is shown in figure 5.23; the array installed in ProtoDUNE-SP is shown in figure 5.22. A simulation of the S-ARAPUCA cells, using code that was validated by the earlier prototype measurements (section 5.8.2), predicts a photon collection efficiency for the module on the beam side of the cathode of 1.5%, and for the module on the non-beam side with an optimized configuration, (12 SiPMs and PTP coated on the filter substrate), it could be as high as 3.0%. A full S-ARAPUCA module with the optimized configuration would have an effective area equivalent to a detector with 36 cm<sup>2</sup> active area with 100% collection efficiency and produce an average light yield across the TPC of 20 PE/MeV.



**Figure 5.23.** ProtoDUNE-SP S-ARAPUCA module being assembled in a class 100,000 clean area. Front face of assembled module (left) shows the 16 coated dichroic filter plates. Assembly photos show the reflective rear side (top right) and inner coated surface (right bottom) of Vikuiti reflective foils. Note the cutouts in foil for MPPC active area.

As described above, for the S-ARAPUCA modules, the SiPMs are passively summed in groups of 12 to produce 12 signal channels per module. The 58 light guide-style light collectors each have 12 SiPMs, which are passively summed in groups of three such that each light guide has four signal channels. The unamplified summed analog signals from the SiPMs are transmitted directly to outside the cryostat for processing and digitization by a SSP.

The SSP consists of 12 readout channels packaged in a self-contained 1U module, where each channel contains a fully-differential voltage amplifier and a 14-bit, 150-MSPS ADC that digitizes the SiPM signal waveforms. The SSP also provides a programmable bias voltage to the sensors. The entire set of photon collector arrays are read out by 24 SSP units (a total of 288 channels).

<sup>24</sup>Since ProtoDUNE-SP was constructed, the slot opening in the APA opening for PD module installation has been enlarged allowing for a module with larger collection area.

**ProtoDUNE-SP PD system measurements.** The ProtoDUNE-SP beam run provides several distinct sets of data for understanding PD system performance: beam data sets with triggers determined by the beam instrumentation; cosmic ray data sets from triggers randomly or in coincidence with the CRT modules; and calibration module data sets, with triggers in coincidence or free running with a programmed light pulse. The single avalanche response and gain for all 256 readout channels has been extracted from ProtoDUNE-SP data, including runs using the pulsed UV-light calibration system.

The analysis is ongoing, but here we summarize some initial results that illustrate the performance and stability of the PD system:

- Figure 5.24 shows the response<sup>25</sup> to tagged electrons (left) and muons (right) with a momentum of 7 GeV/c for each of the PD modules on the beam side of the cathode; the S-ARAPUCA module is in position APA 3, PD module 4. The observed energy is mostly contained within the first APA width of LAr for electrons but is distributed through the whole width of the TPC for the minimum ionizing muons. Although a detailed simulation is not completed, the ratio of the average signal (in photoelectrons) in the S-ARAPUCA module to the adjacent double-shifter bars, is approximately a factor of five for both the electron and muon samples. This is consistent with the detection efficiency ratio measured in earlier prototypes.
- Figure 5.25 provides two examples of the timing capability of the PD system. The left plot shows the excellent correlation between the TPC and PD system track time. The TPC track time is the track  $t_0$  time and the PD system time is the matched flash time for a 4500 track sample. The right plot shows the measured time difference in the PD system response to two consecutive flashes from the calibration system, demonstrating timing resolution of 14 ns, well below the 0.1  $\mu$ s to 1  $\mu$ s physics requirement.
- Figure 5.26 shows the response<sup>26</sup> of the S-ARAPUCA in APA 3 to the tagged electron beam as a function of incident electron kinetic energy. The observed energy is mostly contained within the first APA (APA 3) width of LAr. The observed number of photons have not been corrected for geometry, attenuation, or scattering effects but nonetheless shows a linear response over the 0.3 GeV to 7.0 GeV beam energy range.
- Figure 5.27 shows the stability of the measured light yield in the S-ARAPUCA on the non-beam drift side of the TPC (APA 6) using the calibration system (left) and a triggered cosmic ray muon sample (right). The left plot shows the response to the calibration flashes over time period spanning November 2018 – June 2019 normalized to the average response over the period; different colors correspond to different readout channels (error bars not shown to increase visibility of points; average of the errors is 1.4% with a maximum of 4%). The right plot shows the summed PD light yield (all modules of the same type) as a response to cosmic-ray muon samples partitioned by collector and sensor technology over the same period.

The S-ARAPUCA variation across the entire time period is less than 2%, but statistical uncertainties are larger than those of the other technologies because there is only a single

<sup>25</sup>In units of photoelectrons, not corrected for SiPM after-pulsing and crosstalk.

<sup>26</sup>In units of detected photons, corrected for SiPM after-pulsing and crosstalk.

S-ARAPUCA module with a much smaller light collection area than the combination of approximately 15 times more similar-sized modules for each of the other technologies.

The ProtoDUNE-SP PD modules have been operated for more than six months. In this time, no failures of SiPM readout channels have been detected beyond the few seen immediately after installation; none of those failures were in the MPPC readout channels, which is the baseline photosensor.

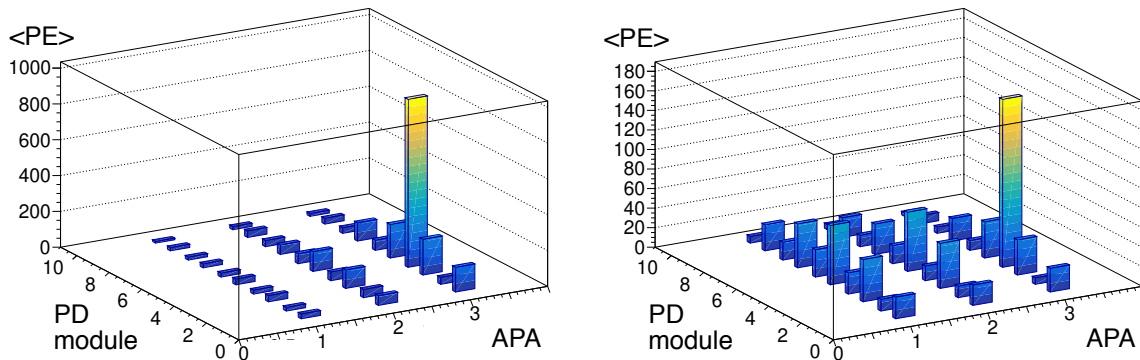


**Figure 5.24.** PD system response (in photoelectron) to 7 GeV/c momentum electrons (left) and muons (right) in ProtoDUNE-SP.

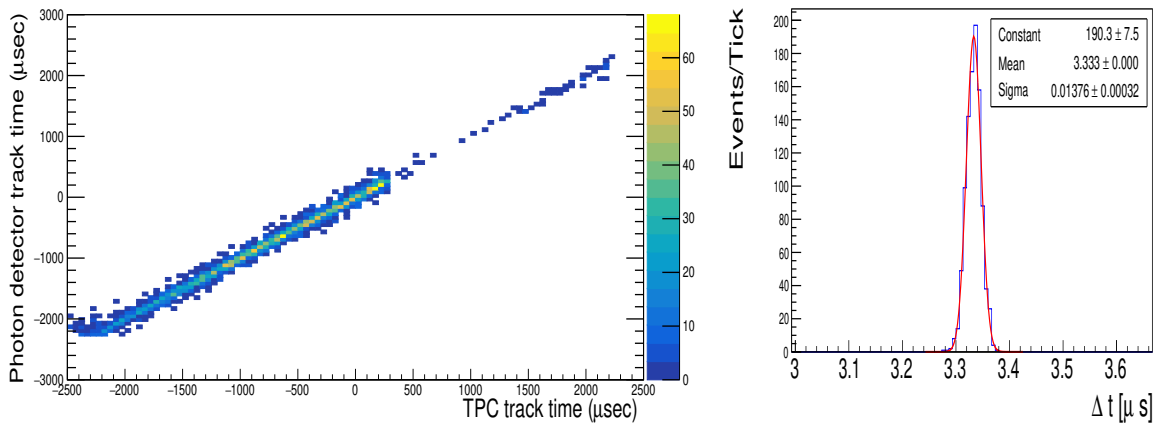


**Figure 5.25.** PD system timing measurements: correlation between the TPC and the PD system track time (left); time difference between two consecutive calibration flashes, demonstrating a resolution of 14 ns (right).

### 5.8.3 Extended ARAPUCA (X-ARAPUCA)

The X-ARAPUCA is an evolution of the S-ARAPUCA concept that moves the second wavelength-shifter from the inner surface of the dichroic filter to a wavelength-shifter-doped plate that acts as a light guide. This design change was motivated by simulations that indicated a significant increase in collection efficiency for this configuration.

This section describes in detail the first measurements that demonstrate the validity of the design, followed by a description of ongoing efforts to validate the final design.



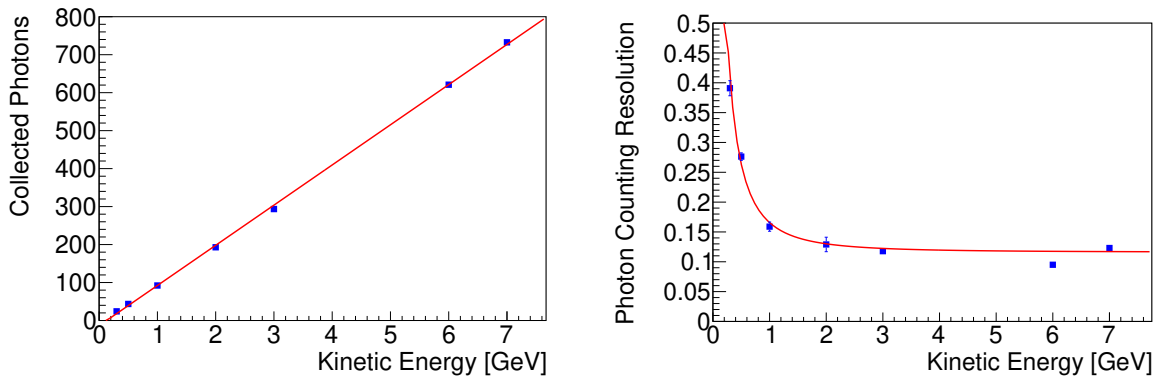


**Figure 5.26.** Mean number of collected photons as a function of incident electron kinetic energy (left); photon counting resolution of the S-ARAPUCA array as response to test beam electrons (right).

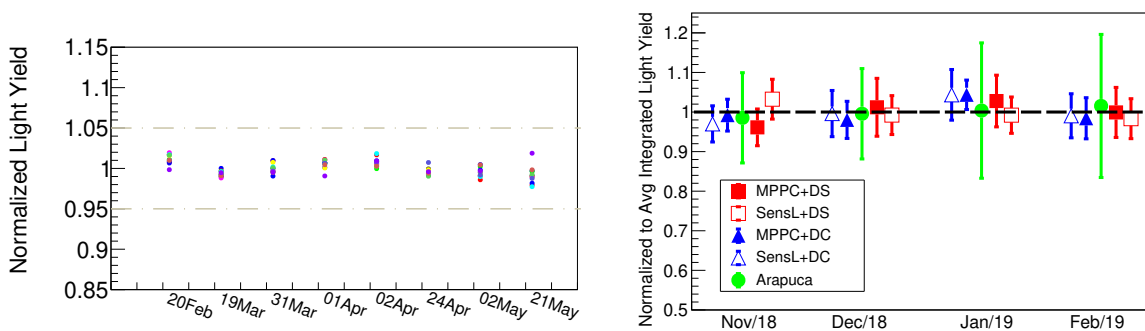


**Figure 5.27.** Stability of the S-ARAPUCA response in APA 6 measured with the UV-light calibration system (left) and the stability measurements of all PD system channels in APAs 4–6 with cosmic-ray muons tagged by the CRT (right).

### 5.8.3.1 Single cell X-ARAPUCA measurements

The first tests of an X-ARAPUCA cell were made at UNICAMP, Brazil, at the end of November 2018. The structure of the cell allowed it to operate as either an S-ARAPUCA or an X-ARAPUCA, with both single- or double-sided readout in both. This flexibility will allow relative and absolute measurements of performance in the same cryostat and so provide a crucial step to validating the baseline design.

Building on the experience with the ProtoDUNE-SP prototypes, the frames for the test cell were fabricated from FR-4 G-10 in a configuration very similar to that planned for the SP module but with some small modifications necessitated by the requirements for holding a single window. The overall dimensions of the cell are  $12.3 \text{ cm} \times 10.0 \text{ cm} \times 1.56 \text{ cm}$ . Figure 5.28 shows an exploded design drawing and the completed cell.

The dichroic windows for the prototype are the same size as one of the six windows in a FD-design X-ARAPUCA supercell:  $10.0 \text{ cm} \times 7.8 \text{ cm}$ . The filter plate was coated with PTP by vacuum evaporation (film thickness  $\sim 400 \mu\text{g}/\text{cm}^2$ ) using an in-house deposition system at UNICAMP (see figure 5.29). The thickness of the film needs to have a minimal value in order to ensure that the VUV light is fully absorbed. This minimum value is in the range of  $100 \mu\text{g}/\text{cm}^2$  to  $200 \mu\text{g}/\text{cm}^2$ . The  $400 \mu\text{g}/\text{cm}^2$  is chosen in order to ensure that the minimum thickness is reached everywhere on

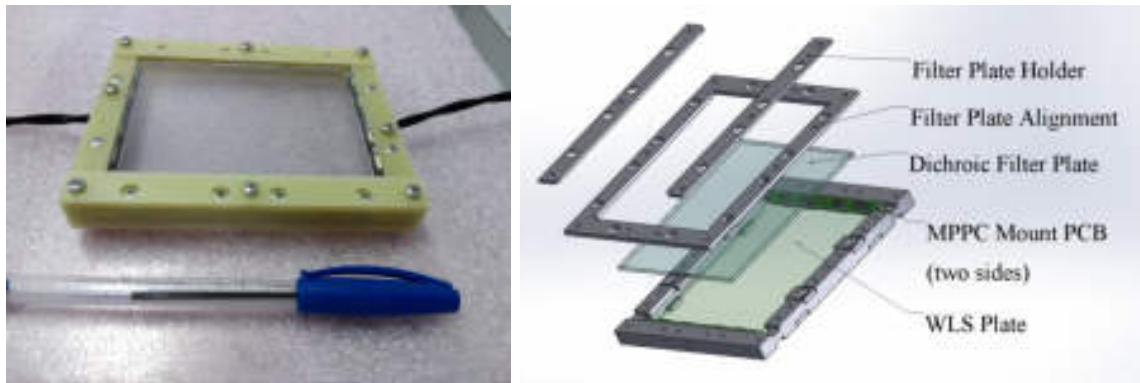


**Figure 5.28.** X-ARAPUCA test cell: assembled cell (left); exploded model (right). Note that exploded components can be duplicated on the back side (not shown) for double-sided test cell.

the filter even in presence of exceptional fluctuations (measured RMS of the order of  $30 \mu\text{g}/\text{cm}^2$ ). When the minimal thickness is reached the maximum conversion efficiency is obtained.

Adhesion was tested by submerging the coated filter in  $\text{LN}_2$  several times. The coating was visually inspected after each submersion, and no visible effect was observed. At the end of the test, the coated filter was weighed with a precision balance, and no loss of material was measured. The film was also analyzed with an optical microscope, and no signs of degradation could be observed.

The wavelength shifting plate in the X-ARAPUCA configuration is made from Eljen EJ-286 blue WLS plate, with dimensions  $9.3 \text{ cm} \times 7.8 \text{ cm} \times 0.35 \text{ cm}$ .

The WLS plate thickness of 0.35 cm was initially selected to optimize collection of light both by total internal reflection within the WLS plate and light trapped between the filter plates and the WLS plate. Simulation has demonstrated that the detection efficiency performance of the detector reaches a shallow maximum at approximately this value.

The side walls of the test cell are lined with Vikuiti reflector, with cutouts at the positions of the photosensors.

The photosensors in the test cell are of the baseline type:  $0.6 \text{ cm} \times 0.6 \text{ cm}$  Hamamatsu S13360-6050VE MPPCs. The photosensors are arranged in the same configuration as in the baseline design, with four MPPCs (passively ganged) mounted to two sides of the test cell, with positioning relative to the WLS plates and dichroic filters identical to the baseline design. In a departure from the baseline design, the two passively ganged groups of four MPPCs are read out separately; no active ganging circuit is implemented for these tests.

The test cell is installed at the bottom of a vacuum-tight stainless-steel cylinder (height  $\sim 30 \text{ cm}$ ) closed by two CF160 flanges and exposed to an alpha source<sup>27</sup> placed at 3 cm from the center of the dichroic window. Figure 5.30 shows photographs of the test cryostat and the test cell in the support structure; the alpha source holder is visible through the windows. The stainless-steel cylinder is deployed in a small open Dewar that is filled with commercial-grade LAr to act as a thermal bath.

The spectrum of the detected number of photons is shown in figure 5.31 with a black line. The same fit procedure as in section 5.8.2 allows an estimate of the number of detected photons for each alpha line. The result of the fit is shown with a red line in figure 5.31. Comparing the

<sup>27</sup>The same as used in the S-ARAPUCA proof-of-principle tests described in section 5.8.2.



**Figure 5.29.** Coated dichroic filter plates (left) and UNICAMP thin film coating facility (right).

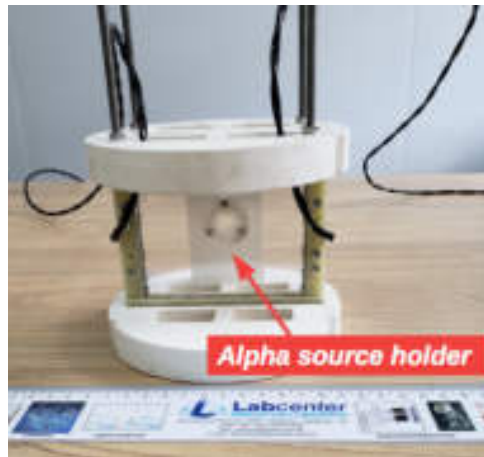


**Figure 5.30.** Test cryostat (left) and X-ARAPUCA test cell mounting structure (right). Note the alpha test source in holder.

number of detected photons with the number of photons impinging on the X-ARAPUCA provides an estimate the global photon collection efficiency of the device as  $3.5 \pm 0.5\%$ . This result includes the correction for the crosstalk and after-pulsing of the two arrays of MPPC at their operating voltage. The efficiency was stable for the duration of several days of this measurement.

The same test was repeated with the double-sided version of the X-ARAPUCA. Exactly the same set-up and the same device were used with the exception that the back plane coated with Vikuiti was replaced with a dichroic filter coated with PTP. The same testing and analysis procedures were followed, and the global detection efficiency was found to be only 10% less than the single sided version.

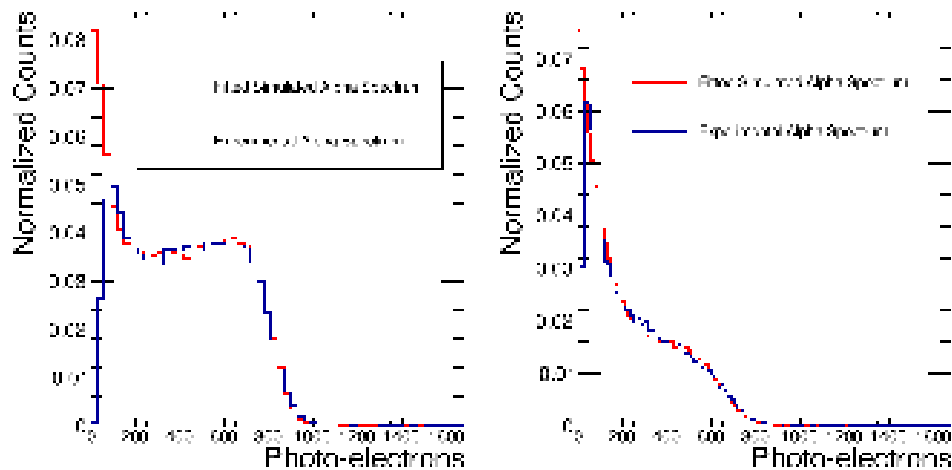


**Figure 5.31.** Spectrum of the total number of photoelectron collected with the alpha source (blue line) fitted with the Monte Carlo prediction for the single-sided (left) and double-sided (right) X-ARAPUCA. Higher background activity at low energy was found for the second case.

The measured global collection efficiencies translate into an equivalent surface area<sup>28</sup> of 70 cm<sup>2</sup> for a single sided X-ARAPUCA module and of 63 cm<sup>2</sup> for the double-sided, which exceed the specifications for our system by a substantial factor (section 5.16.1).

### 5.8.3.2 ICEBERG test stand

The ICEBERG test-stand is a small-scale TPC, using smaller FD APA and cathode designs, constructed primarily to provide a platform for DUNE CE testing at Fermilab. The test stand consists of a 94.7 cm × 79.9 cm APA, with an approximately 30 cm drift length to a cathode plane on each side (figure 5.32). It can accommodate up to two almost 1/2-length PD modules<sup>29</sup> in a mounting structure nearly identical to the final DUNE FD configuration, allowing for testing of PD prototype performance, electrical connections, and interfaces with the CE and APA systems (figure 5.33). In addition, the test stand will be used to allow comparisons between Mu2e-based warm electronics and ProtoDUNE-SP SSP system, as well as testing newer versions of photosensors active ganging circuit designs.

The ICEBERG facility will enable the primary validation of the X-ARAPUCA design prior to a full-scale test envisioned at a future ProtoDUNE-SP run in late 2021.

At least three test campaigns are planned for the ICEBERG TPC with PD modules:

1. The initial photon detector configuration consisted of one full-length S-ARAPUCA supercell and one full-length X-ARAPUCA supercell. Both of these supercells have single-side windows to allow comparisons of measurements with S-ARAPUCA and X-ARAPUCA prototypes in summer and fall 2018 ProtoDUNE-SP. The first test run occurred in February-March 2019. This run demonstrated that both module prototypes and the cryogenic active ganging circuitry were operational and saw signals from both modules using a Mu2e front end

<sup>28</sup>The equivalent surface area is defined as the product of the physical acceptance window of the device multiplied by its global collection efficiency.

<sup>29</sup>To enable the use of existing components for the APA frame, the PD modules are 50 mm shorter than final modules, which required a slight modification to the PD module design.

electronics system modified for use by the DUNE PD (in a separate stream from the TPC DAQ). Significantly, no crosstalk between the PD and CE readout electronics was observed. Unfortunately, difficulties with the TPC CE and HV systems prevented readout of ionization tracks required to allow direct comparisons between the PD modules and required the test to end before significant progress was made.

2. A second campaign took place late July through December 2019. It used the same PD modules as the first campaign. The data will facilitate comparisons of SSP and Mu2e readout systems for similar events as indicated by hodoscope events. Two short runs (ICEBERG 2A and 2B) occurred in August and September 2019, during which the DAPHNE and SSP were commissioned and initial photosensor bias voltage studies were conducted. These runs were cut short due to problems with the cryogenic filtering system for the ICEBERG cryostat.
3. A third campaign is planned for spring of 2020. This run (ICEBERG run 3) will incorporate four X-ARAPUCA supercells, though it is partially occluded in the frame due to the limitations in APA size mentioned above. Two supercells will be single-sided and two double-sided, allowing for additional comparisons of PD technologies. This campaign will also demonstrate readout of Mu2e electronics by the ICEBERG DAQ. In addition, we plan to incorporate a prototype of the DUNE SP monitoring system.

The test stand will provide testing and validation of the PD system Mu2e-based electronics system, including a side-by-side comparison with the ProtoDUNE-SP SSP electronics readout. In addition, concurrent data taking with the TPC and light collection system will allow us to study TPC-induced noise on the PD, PD-induced noise on the TPC, grounding scheme configuration, controller-DAQ and controller-FEB interfaces, bandwidth and rates issues, online and offline PD-TPC interfaces, zero-suppression techniques, firmware development, accepting and producing triggers, and, in general, will inform possible upgrade paths for the system.

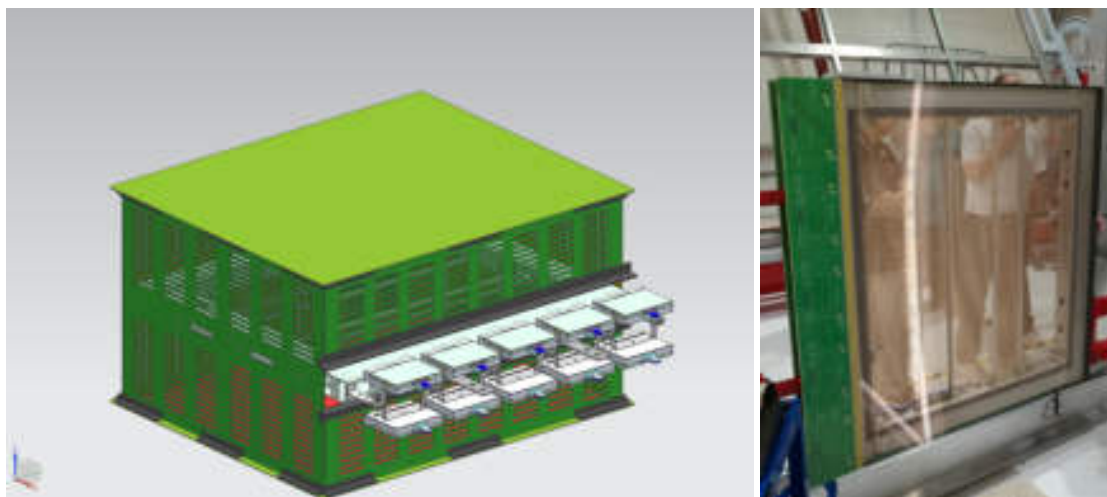


**Figure 5.32.** Solid model of ICEBERG TPC (left), and assembled ICEBERG APA (right). Note the two sets of PD module mounting rails, which are vertical in this image but horizontal during operation. The centrally-mounted APA allows for testing of double-sided readout photon detector modules.

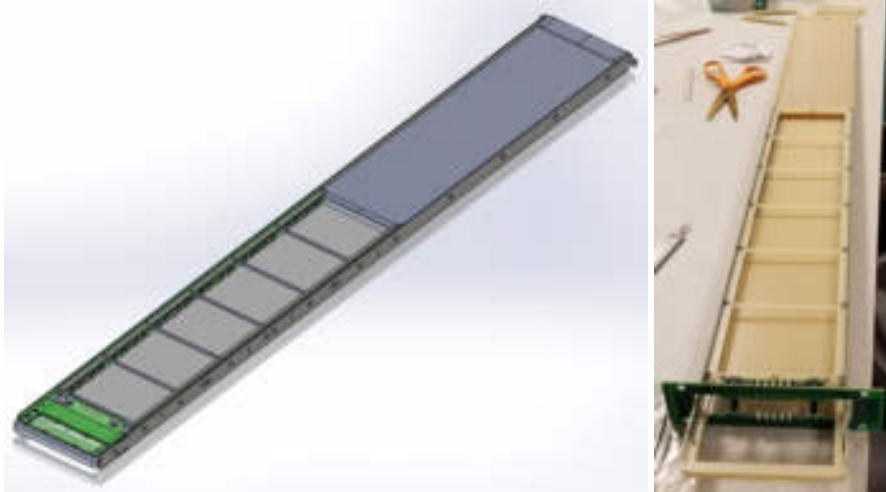


**Figure 5.33.** Software solid model of a single supercell ICEBERG PD module (left) and fabricated components during assembly (right). The connector board (green) in the right photo is mounted to the APA frame prior to wire wrapping.

Delays in the ICEBERG commissioning schedule unrelated to the ProtoDUNE-SP system prevented having significant results available in time for this TDR. However, test stand data are still expected to provide critical input for the 60% design review scheduled for May of 2020. Additional runs in 2020 will assist in preparing for the final design review and ProtoDUNE-SP-2 module designs.

### 5.8.3.3 SBND

The baseline PD system for the SBND experiment includes three types of detector: TPB-coated cryogenic photomultipliers, an array of dipped light-collector bars similar to those used in ProtoDUNE-SP, and a small array of X-ARAPUCA modules. Eight modified X-ARAPUCA modules will provide an opportunity for a long-term system test of a significant number of key components prior to the SBND PD system production readiness reviews. Each SBND X-ARAPUCA will consist of two dichroic filter plates with dimensions  $100\text{ mm} \times 78\text{ mm} \times 1.5\text{ mm}$  that are coated with PTP at the UNICAMP vacuum deposition facility. These filters will be produced by Opto Electronics S.A. in Brazil, the leading vendor candidate for the DUNE PD modules. Also, each SBND module will contain an Eljen WLS plate  $200\text{ mm} \times 78\text{ mm} \times 4\text{ mm}$ . FR-4 G-10 frame components will be fabricated at local vendors, representing candidates for eventual DUNE fabrication. A software solid model of the design is shown in figure 5.34.

The eight SBND X-ARAPUCA modules will be assembled at UNICAMP using the DUNE PD consortium assembly plan, which will provide valuable experience with fabrication of multiple modules at that site.

In the summer of 2019, the SBND collaboration re-opened the question of the composition of their light collection system, eliminating the dipped bar modules in favor of 200 additional X-ARAPUCA modules. These modified modules will use WLS plates and coated filter plates identical to those proposed for DUNE, and frame components very similar to those in the final DUNE PD

system. The modification to the SBND system will provide a larger scale, long-term test of critical PD components and will significantly enhance the value of the test as a development run for the UNICAMP facility.

We expect that module assembly for SBND will be complete with installation in the detector beginning in spring of 2020. Filling with LAr and operation will occur in summer 2020, and we expect initial results from the PD system in fall 2020. SBND will be the first large-scale operational testing for X-ARAPUCA modules very similar to those to be used in DUNE. SBND will also use coated reflector foils, which will provide additional valuable information on that DUNE PD system option.

While not part of the DUNE project, and not part of the validation schedule for the ProtoDUNE-SP, SBND results will inform our preparations for the final design review of these components and the fabrication of modules for ProtoDUNE-SP-2.

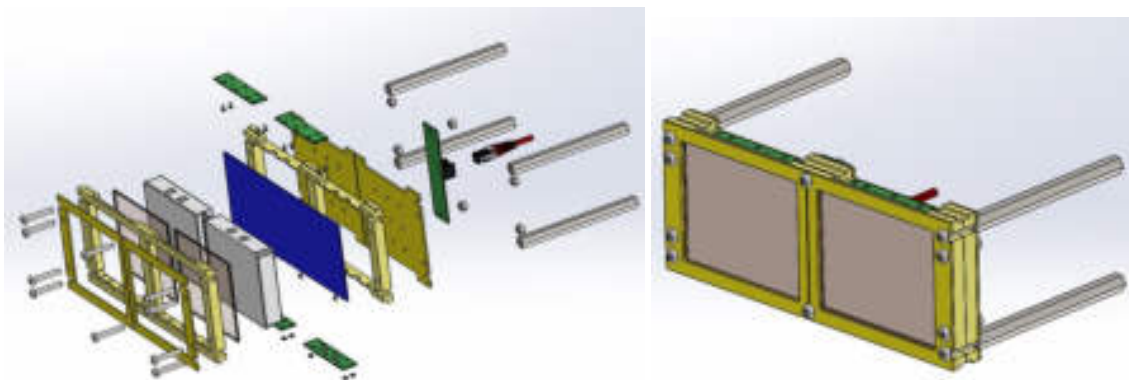


**Figure 5.34.** Software solid model of two-cell X-ARAPUCA modules for SBND, exploded (left) and assembled (right).

#### 5.8.3.4 ProtoDUNE-SP-2

Following completion of the initial run of ProtoDUNE-SP, a second test run called ProtoDUNE-SP-2 is planned in the same cryostat. This test will serve as a final validation of all pre-production SP module detector designs, verifying their performance and ensuring they perform in concert with no interference. We intend to replace three complete APA assemblies with pre-production modules to allow testing 40 final-design PD modules.

ProtoDUNE-SP-2 will allow for the first end-to-end test of the final PD system, with significantly redesigned elements:

- full-size X-ARAPUCA modules read out in conjunction with a TPC;
- 48-channel photosensor active ganging;
- final design electrical connectors for PD modules mounted inside full-scale APAs;
- pre-installed cable harnesses inside APAs including final module supports;
- readout of full-scale X-ARAPUCA modules using modified Mu2e electronics, including integrating TPC and PD event matching into the DAQ system.

Two candidate photosensors will be tested (20 modules built with each sensor type), and the experience gained while fabricating ProtoDUNE-SP-2 will be an important factor for selecting between the candidate sensors or deciding to incorporate both in the PD system final design. All other components will be final design components, so at least half of the PD modules in ProtoDUNE-SP-2 will represent the “Module 0” level of design.

While all of these elements will have been tested previously individually and/or at smaller scale, ProtoDUNE-SP-2 will represent the final pre-production testing of all the final design components as an integrated system.

The schedule for ProtoDUNE-SP-2 calls for PD modules to be installed into APA modules at CERN at the end of summer 2021. However, some components, including module support rails, electrical connectors, and cable harness components, must be mounted inside APA frames prior to wire wrapping and so must be available by mid-2020. Re-filling of the ProtoDUNE-SP cryostat will begin in the winter of 2022, with operations beginning in late 2023. Operation of ProtoDUNE-SP-2 will continue for at least one year. This schedule allows for initial operation of the complete system prior to the PD production readiness review and the beginning of mass-production of SP modules in summer 2022, although some components (including dichroic filter plates and photosensors) will have begun procurement by that time. These components are physically smaller and more amenable to testing in smaller cryostats, reducing the exposure due to this delay. These scheduling issues will be addressed in more detail in 5.15.1.

If the decision has been taken to proceed with our performance enhancement alternates (xenon doping or CPA-mounted reflector foils, see section 5.16.2), they will be tested in ProtoDUNE-SP-2 as well.

### 5.8.3.5 Long term cryogenic aging

It is difficult to accelerate aging effects due to long-term immersion of components in cryogenic liquids. While mechanical aging due to thermal expansion/contraction can be readily accelerated by cycling the components to be tested through multiple cycles, long term aging not related to rapid thermal stresses are not amenable to easy acceleration. An example of such a process might be dissolution of PTP coatings over time.

Mitigation of these risks involves some level of long-term exposure to liquid cryogen with extrapolation to the DUNE timescales. Several such tests are planned for the PD system:

- ProtoDUNE-SP will provide a long-term test of two S-ARAPUCA modules for a period of up to one year at the time of draining in the Winter of 2020. The system will be continuously monitored for gain and response of the detectors, and will provide information regarding aging of FR-4 G-10 structures, photosensors, and coated filter plates. Other ProtoDUNE-SP detectors (Double-shift bar designs) will give some indication of aging of similar WLS plates to those used in the X-ARAPUCA modules.
- SBND will provide a multi-year test of many X-ARAPUCA components, such as coated filter plates, WLS plates, and photosensors. SBND will run for at least three years, starting in late 2020. As part of a running experiment, the system will be continuously monitored for gain and response of the detectors and will provide information regarding aging of FR-4



G-10 structures, photosensors, and coated filter plates as well as WLS plates to be used in the X-ARAPUCA modules.

In addition, TPB-coated reflector foils will be tested in SBND. While coated reflector foils are not part of the baseline PD system, this will provide validation for the concept we currently present as an option (section 5.16.2.1).

- ProtoDUNE-SP-2 will provide a long term test of full-scale X-ARAPUCA modules in the final DUNE configuration. While this test will begin shortly before DUNE PD module production fabrication, it will provide long-term validation of all X-ARAPUCA components during module production prior to integration into the APA frames, allowing for possible insights and improvements into the X-ARAPUCA design.

### 5.8.4 Materials selection, testing and validation

#### 5.8.4.1 PD module mechanical frame

The APA mechanical frame components are fabricated from FR-4 G-10 (Garolite®), a glass-epoxy laminate commonly used in printed circuit boards and other mechanical applications where an electrically insulating component with low thermal expansion coefficient is required. G-10 is widely used in cryogenic applications, including most of the other DUNE subsystems (See DocDB 10452 [37] for an extensive discussion in the context of the HV system cathode planes). FR-4 has been certified at the Fermilab materials test stand as an acceptable material for use in DUNE from the standpoint of LAr contamination.

Thermal contraction of FR-4 is similar to that of stainless steel, simplifying design of the module interface with the APA frame. It allows us to use long printed circuit boards for routing photosensor electrical signals along the detector sides without incurring thermal expansion issues. As an excellent insulator, it simplifies electrically isolating the PD system from the APA frame, as required by the DUNE grounding scheme. However, selecting FR-4 as our main module structural material comes at the cost of some additional difficulty machining components.

All fasteners used in the PD are stainless steel alloy 304, widely used in cryogenic applications. This alloy has also been certified at the Fermilab materials test stand as an acceptable material for use in DUNE from the standpoint of LAr contamination.

#### 5.8.4.2 PD module-APA frame mechanical support structure

All PD mechanical supports (including rails, brackets and fasteners are to be manufactured from stainless steel alloy 304. This has the benefit of matching thermal contraction coefficients with the APA frame and being approved for use in LAr by the materials test stand.

#### 5.8.4.3 Dichroic filter/filter coating

The dichroic filters used in X-ARAPUCA consist of a fused silica substrate, coated on one face to provide the required dichroic properties and on the opposite face with a thin evaporated layer of PTP. Fused silica was selected in part due to its excellent low-temperature properties. It is widely used as an optical window in low temperature applications, due to its stability and low coefficient of thermal contraction; fused silica dichroic filters have performed well in many S-ARAPUCA validation tests.

Stability of the PTP coating is of greater concern. Initial validation of the S-ARAPUCA in TallBo, ProtoDUNE-SP, and in repeated cryogenic immersion tests at Fermilab and other facilities has demonstrated that while it is possible to generate highly-reliable PTP coatings on fused silica substrates, careful surface preparation and deposition procedures are required to prevent failure of the coating. Dissolution of similar wavelength-shifting coatings into LAr has been reported but in a technology-dependent fashion [85], so continued investigation of the design specific to DUNE is necessary to confirm robustness.

A test stand has been developed at Syracuse University to investigate the long-term stability of X-ARAPUCA optical coatings in LAr that will subject coated materials to a continuous flow. This will stress the adhesion of the coating to the plates to simulate the convective flow of LAr in the SP module.

The test stand consists of a 74 L LAr cryostat with a frame suspending coated filters beneath an impeller driving a continuous flow of LAr across them. Filters will be inspected monthly for degradation in their opacity, transparency, and wavelength-shifting response. A dark box containing a visible-light and near-UV scanning bed will measure wavelength shifting performance of the tested elements before and after suspension within the argon flow.

Testing began in late 2019, when coated filter plates become available, and is expected to run through late 2022.

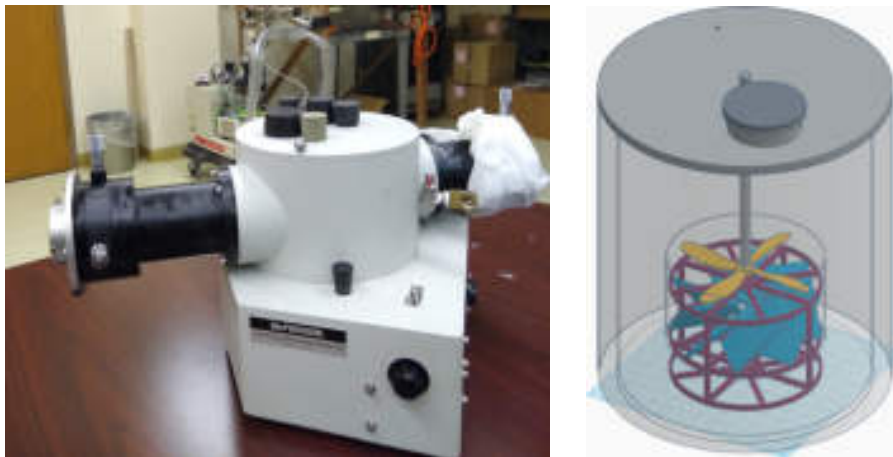


**Figure 5.35.** Two components of the PD coating test stand. (1) VUV monochromator (foreground) and 2-axis scanning chamber (background) currently undergoing recommissioning (left); and (2) solid model of 74 L LAr cryostat for quality control studies and future detector development (right).

### 5.8.4.4 WLS plates

The X-ARAPUCA wavelength shifting plates are fabricated by the same vendor as the light guide bars utilized in the double-shift ProtoDUNE-SP modules. The plates are made with the same transparent matrix material, but have a different wavelength shifting dopant chosen to provide a better match to the spectral sensitivity of the PD SiPM (around 430 nm). It also has an emission spectrum very similar to TPB, used in the S-ARAPUCA, which ensures the same performance of the dichroic filter and of the reflective coatings.

While it is possible that the cryogenic properties of this modified WLS material may be altered by the change in doping agent, it is expected that the tests done for the double-shift bar prototypes are a valuable guide for their expected performance. As part of the design verification, samples of these bars were manually thermocycled to verify they didn't craze. In addition, we used a LAr test stand with an alpha source behind a small sample of the WLS plate to scan the attenuation length of a short sample. Finally, we built a darkbox with a  $\sim 420$  nm LED scanning down the length of a full bar to verify the attenuation length and to compare the results to the LAr data. (This formed the basis of the threshold requirements on in-air attenuation length measurement for the ProtoDUNE-SP batch.) This same sequence will be undertaken for the light guides selected for X-ARAPUCA.

As with most other components, it is not possible to simulate long-term exposure to LAr of a length similar to that expected in DUNE operation, but we will substitute continuous long term exposure by running samples through repeated thermal cycling to maximize thermal stresses in the material. Finally, samples of the WLS plates will be certified for use in DUNE in the materials test stand at Fermilab.

### 5.8.5 Calibration and monitoring

All major components of the SP module PD system calibration and monitoring system have been designed, fabricated, tested, and operated in ProtoDUNE-SP. Figure 5.36 shows the hardware components of the system. Although at a longer wavelength (245 nm to 280 nm) than LAr scintillation light (127 nm), the UV light from the calibration system exercises the full chain of measurement steps initiated by a physics event in the detector module, starting from the wavelength conversion, photon capture in the S-ARAPUCA, photon detection, and the FE electronics readout.

A substantial ProtoDUNE-SP data set has been collected and the data analysis is underway. Goals of the analysis are to verify that the CPA includes an optimal distribution of light diffusers for the SP module; to demonstrate capability of the system evaluate gain and timing resolution; to perform relative comparisons of photon channels; and to characterize and monitor stability of the PD system over the duration of ProtoDUNE-SP. Here we present preliminary results that demonstrate the timing performance of the system, the stability of the two types of SiPM, and the photon detection rate over several months.

Figure 5.37 (left) shows a typical double waveform recorded by an ProtoDUNE-SP SSP module as a response to calibration system light pulses illuminating an S-ARAPUCA channel; the figure on the right demonstrates that the calibration system has the precision and stability to meet the system requirements.

Figure 5.38 shows the SiPM gain (charge per photoelectron-induced avalanche) extracted from the calibration data normalized to the average gain during the period. The left figure shows the results over a period of three months for the MPPCs mounted on the S-ARAPUCA modules; the right figure shows the results over a period of six months for the SensL SiPMs that are mounted on a set of double-shift and dip-coated light collector bars. The colors correspond to different readout channels for the left figure and to the average of the sensors in PD modules for the right figure. All sensors are stable at the level of a few percent, with no significant systematic decline.

Figure 5.39 shows the measured signal (average number of photons, normalized to the average signal over the three-month period) from the double-shift and dip-coated light collector bars in

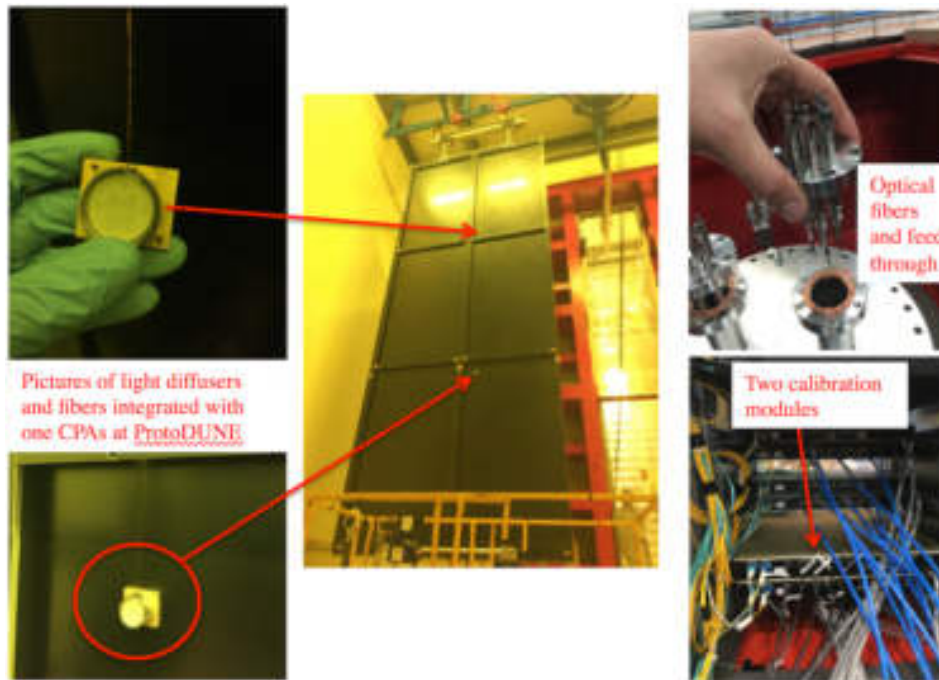


**Figure 5.36.** The photographs show the hardware components of the ProtoDUNE-SP calibration and monitoring system.

APA 6 that are read out with MPPC SiPMs (left), and those in APA 4 that are read out with SensL SiPMs (right), in response to the calibration flashes. The colors correspond to the average of the sensors in PD modules. The measured signal is sensitive to stability in the intensity of the calibration system light and the response of the light collectors (including effects such as changes in wavelength shifter properties and SiPM response). The ratio is stable at the few percent level.

These results verify operation and performance of both the PD system and the UV-light calibration system. This monitoring will continue for the duration of the ProtoDUNE-SP operation.

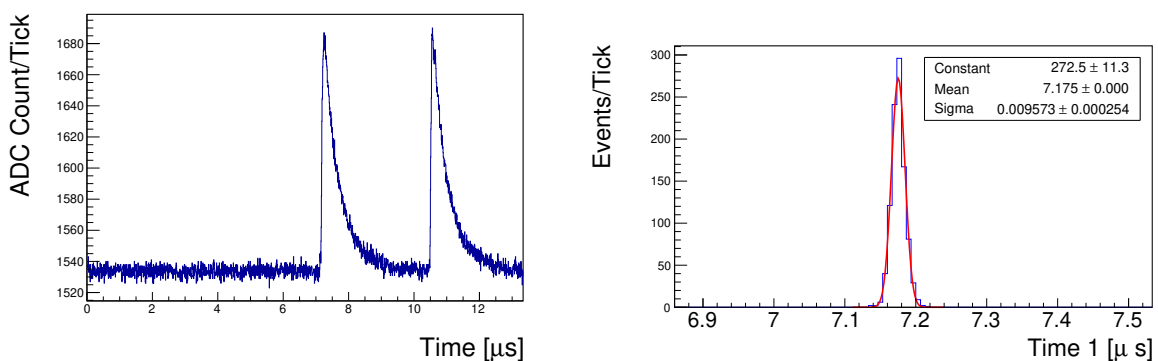


**Figure 5.37.** Double waveforms recorded by ProtoDUNE-SP SSP as a response to calibration system light pulses collected by an S-ARAPUCA channel (left). Distribution of measured times of the first light pulse in the two-pulse waveform for 1000 pulse pairs (right).

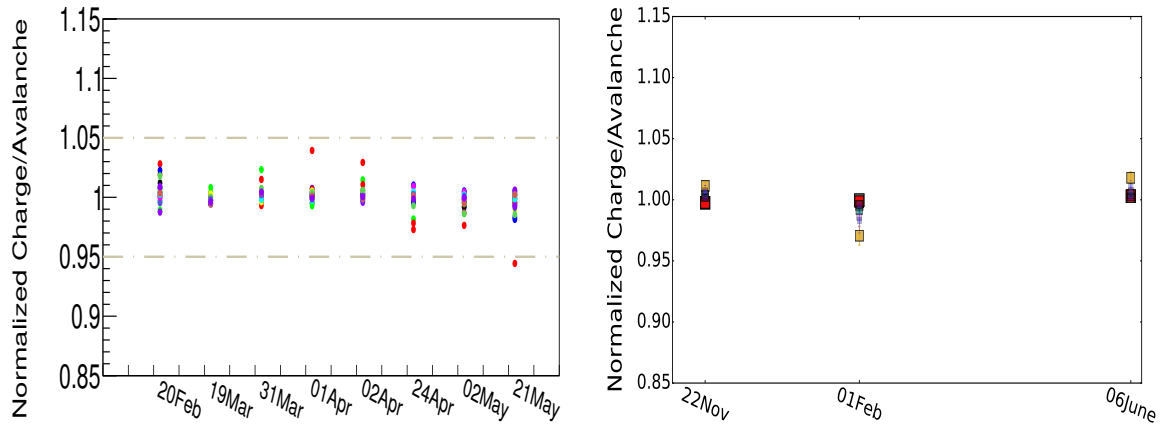


**Figure 5.38.** Normalized gain measurements using the calibration system light pulses: MPPC SiPMs on the S-ARAPUCA modules (left); SensL SiPMs on the dip-coated and double-shift bars in APA 3 (right). This demonstrates the stability of the gain for both types of device operating in LAr.

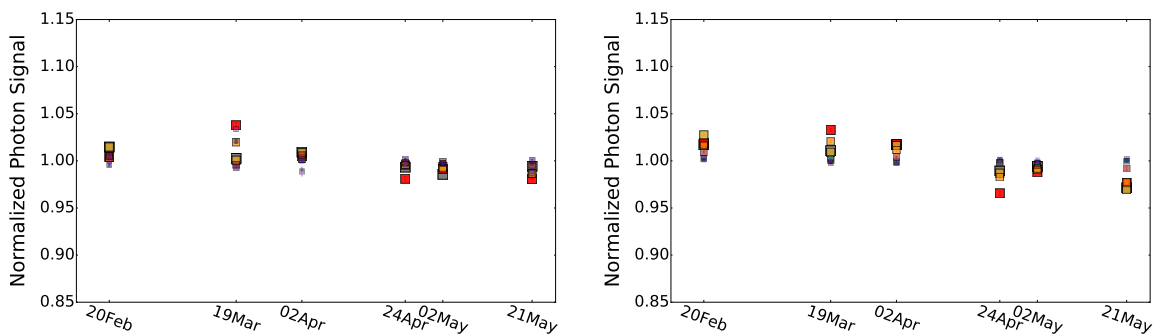


**Figure 5.39.** Measurement of the signal from the calibration system using the dip-coated and double-shift bars in APA 6 that have MPPC SiPMs (left) and in APA 4 that have SensL SiPMs. The signal is normalized to the average response over the entire period.

## 5.9 Production and assembly

The SP PD system consortium is a geographically diverse group of institutions, collaborating across three continents to fabricate a single integrated system. As such, careful planning and control of component fabrication, assembly and testing must be maintained. This section describes the planning for fabrication, assembly, and testing, focusing primarily on the PD light collector modules, photosensors and photosensor modules, and electronics. It also covers planning for calibration and monitoring.

This section first describes the fabrication procedure for each of the major PD system components. It concludes (in section 5.9.7), by outlining the work flow and responsible institutions for the assembly plan.

### 5.9.1 Light collector module component fabrication

The PD light collector modules were designed with ease of fabrication in mind. The module components can be fabricated and QC tested at physically separated facilities, later to be collected and assembled at one or more assembly facilities.

Each SP module detector requires the fabrication of 1500 photon detector modules, a significant production effort. Many of the components for these modules are commercially available or relatively easy to fabricate, but some, such as photosensors (288,000 required), filter plates (48,000 required), and WLS plates (6000 required), are specialized items requiring close interfaces with industrial partners. These issues will be discussed in the relevant sub-sections below.

#### 5.9.1.1 Dichroic filter and reflector foils fabrication and coating

The baseline design for dichroic filters is a fused silica plate, 10 cm  $\times$  7.8 cm  $\times$  0.2 cm, commercially coated (as described in section 5.4) to provide the dichroic properties of the filter. The filter plates will be purchased from a commercial vendor (certified by the vendor for performance), and the performance of a representative sample will be tested at a collaboration institution as part of our QC program.

Prior to coating, the filters are cleaned using the procedure outlined in section 5.9.2.3. For PD production, the evaporation process will be performed in Brazil, where a large vacuum evaporator with an internal diameter of one meter is now available. The conversion efficiency of the film deposited on the filters will be measured for a representative sample, with a dedicated set-up that will use the 127 nm light produced by a VUV monochromator.

Vikuiti reflector foils required for the rear reflector surface of single-sided X-ARAPUCA supercells and the sides of all modules will be purchased and laser-cut to the form factor required by a vendor. Mechanical and optical QC tests will be performed on a representative sample upon receipt.

Coated filter plates and reflector foils represent one of the more challenging fabrication tasks for the consortium. A total of 48,000 filter plates will be required, and fabrication will need to occur at a rate of approximately 1200 per month. Dichroic filters will be purchased as part of the Brazilian effort. A Brazilian candidate vendor for the filters (Opto Eletronica S.A<sup>30</sup>), has been selected for

---

<sup>30</sup>[www.opto.com.br](http://www.opto.com.br).

the filter manufacturing. Preliminary contact has been made, a budgetary estimate received, and initial discussions suggest that they will be capable of meeting our production schedule. Coating of filter plates will be conducted at UNICAMP. Prototype studies suggest a coating cycle time of less than two hours per 24 filter plates, which meets the needs of the project.

### 5.9.1.2 Wavelength shifting plates

The baseline design for the wavelength-shifting plates are Eljen EJ-286 plates of dimensions 48.7 cm  $\times$  9.3 cm  $\times$  0.35 cm. The edges of a plate will be simultaneously cut and polished with a diamond-edged cutter to increase internal reflectivity, following a proprietary process developed by Eljen. Plates will be delivered to the consortium institution responsible for this component, where QC testing of a representative sample will be performed.

Eljen, Inc. has been involved in PD module development for many years and has proven a reliable partner. We have a budgetary estimate for the plates, indicating a total production time of approximately 18 months for all 6000 wavelength-shifting plates required.

### 5.9.1.3 Mechanical components

The mechanical components of the PD module frames are fabricated from FR-4 G-10. This material will mitigate thermal expansion issues (see thermal expansion discussion in section 5.9.3.2), but is abrasive and somewhat difficult and expensive to work with using traditional machining processes.

To mitigate these difficulties, most of the PDs frame components were designed so that they can be fabricated using water-jet cutting technology. In some cases, post-cutting fabrication is required, e.g., tapping of pre-cut holes, or (rarely) drilling and tapping holes into the sides of the components where the water jet could not pre-cut pilot holes.

Water jet cutting of FR-4 G-10 components will be conducted in-house at UNICAMP to allow for improved quality and schedule control. A dedicated water-jet cutting machine is being purchased now, and fabrication processes will be validated during SBND and ProtoDUNE-SP-2 fabrication. Secondary machining operations (hole tapping, etc.) will also be conducted at UNICAMP. QC tests will be conducted on a representative sample of finished components.

## 5.9.2 Photon detector module assembly

SP module PD module assembly will occur at a PD assembly facility at UNICAMP. Assembly procedures are described below. Final assembly planning for PD modules is guided by the experience gained during the assembly of 60 ProtoDUNE-SP PD modules.

### 5.9.2.1 Incoming materials control

Each PD sub-component assembly site will have a quality control supervisor, who will be responsible for overseeing all quality-related activities at that site, maintaining all production records and assembly travelers, and uploading them to the production database as appropriate. This local supervisor will report directly to the PD consortium lead.

All materials for PD module assembly will be delivered to the UNICAMP module assembly facility with a QC traveler (in the case of materials custom fabricated for DUNE) generated prior to arrival at the assembly site or will have an incoming materials traveler generated immediately

upon receipt of the component (for commercial components). These travelers will be scanned (or uploaded if in electronic format) upon receipt at the assembly facility, and the data stored in the DUNE QC database. Materials will either arrive with a pre-existing DUNE inventory control batch/lot number, or will have one assigned prior to entering the assembly area. Bar code labels attached to storage containers for all components in the assembly area will facilitate traceability throughout the assembly process.

Immediately upon receipt, all materials will undergo an incoming-materials inspection, including confirmation of key dimensional tolerances as specified on their incoming materials documentation. The results of these inspections will be included on the traveler for that batch/lot and entered into the database.

In the case of deviations from specification noted in these inspections, the deviation from nominal will be recorded in an exception section of the traveler, as will the resolution of the discrepancy.

### 5.9.2.2 Assembly area requirements

Assembly will occur in a class 100,000 or better clean assembly area (see specification SP-PDS-1 in table 5.1).

Photosensitive components (e.g., TPB-coated surfaces) are sensitive to near-UV light exposure and will be protected by blue-filtered light in the assembly area (>400 nm or better filters<sup>31</sup>); it has been determined that this level of filtering is sufficient to protect coated surfaces during exposures of up to several days. For exposures of weeks or months, such as in the ProtoDUNE-SP cryostat assembly area, a higher cutoff yellow filter is used.<sup>32</sup>

Exposure of photosensitive components will be strictly controlled, per requirement SP-PDS-3 in table 5.1. Work flow restrictions will ensure no component exceeds a total exposure of 8 hours to filtered assembly area lighting (including testing time).

### 5.9.2.3 Component cleaning

All components will be cleaned following manufacturer's specifications and DUNE materials test stand recommendations. All incoming materials will have written cleaning procedures, and their travelers will document the completion of these procedures.

### 5.9.2.4 Assembly procedures

As was done for ProtoDUNE-SP, detailed step-by-step written procedure documents will guide the assembly for each PD module, with a QC traveler completed and recorded in the database. Travelers will be based on those used for ProtoDUNE-SP, modified as need to capture additional data needed for X-ARAPUCA module fabrication.

ProtoDUNE-SP experience suggests that a two-person assembly team is necessary. Our current assembly plan envisions a pair of two-person assembly teams working simultaneously, with a fifth person acting as shift leader. This labor force will allow for production of 20 PD modules per week, meeting our production requirements.

---

<sup>31</sup>For example, GAMTUBE T1510™ from GAM Products, Inc., <http://www.gamonline.com/catalog/gamtube/index.php>.

<sup>32</sup>F007-010™ Amber with Adhesive — [http://www.epakelectronics.com/uv\\_filter\\_materials\\_flexible.htm](http://www.epakelectronics.com/uv_filter_materials_flexible.htm).



The shift leader acts as a QC officer responsible primarily for ensuring the distribution of materials to the assembly teams, documenting the batch and lot numbers for each PD on the travelers, and ensuring that the teams follow the documented assembly procedures.

Assembly fixtures mounted to 2.4 m long flat tables will support and align PD components during assembly. All workers handling PD components will wear gloves, hair nets, shoe covers, and clean-room disposable laboratory jackets at all times.

### 5.9.2.5 Post-assembly quality control

Post-assembly QC planning is also based on ProtoDUNE-SP experience, modified as appropriate for larger-scale production. Each PD module goes through a series of go/no-go gauges designed to control tolerances of critical interface points. Following this, each module is inserted into a test APA support model, representing the tightest slot allowed by APA mechanical tolerances. It is then scanned at a fixed set of positions with 275 nm UV LEDs. The PD response at each position is measured using PD readout electronics and the data compared to reference set of values. Figure 5.40 shows the scanner used for ProtoDUNE-SP modules. These performance data will serve as a baseline for the PD module, and will be compared against those taken in an identical scanner shortly before installation into an APA in the SP module, as for ProtoDUNE-SP. All data collected are recorded to the module traveler and to the DUNE QC database. Post-assembly immersion into a LN<sub>2</sub> cryostat followed by a repeat scan of each PD module (as in ProtoDUNE-SP) is under consideration as a final QC check.



**Figure 5.40.** PD module scanner.

### 5.9.3 APA frame mounting structure and module securing

PD modules are inserted into the APA frames through ten slots (five on each side) and are supported inside the frame by stainless steel guide channels. The slot dimensions for the SP module APA frames are 136.0 mm × 25.0 mm<sup>33</sup> (see figure 5.41 (left)). The guide channels are positioned into the APA frame prior to application of the wire mesh, and are not accessible following wire wrapping. Following insertion, the PD modules are fixed in place using two stainless steel captive screws.

<sup>33</sup>For ProtoDUNE-SP they were only 108.0 mm × 19.2 mm; the increase allows for larger PD modules and an increase in light collection area of nearly 50% over the ProtoDUNE-SP design.

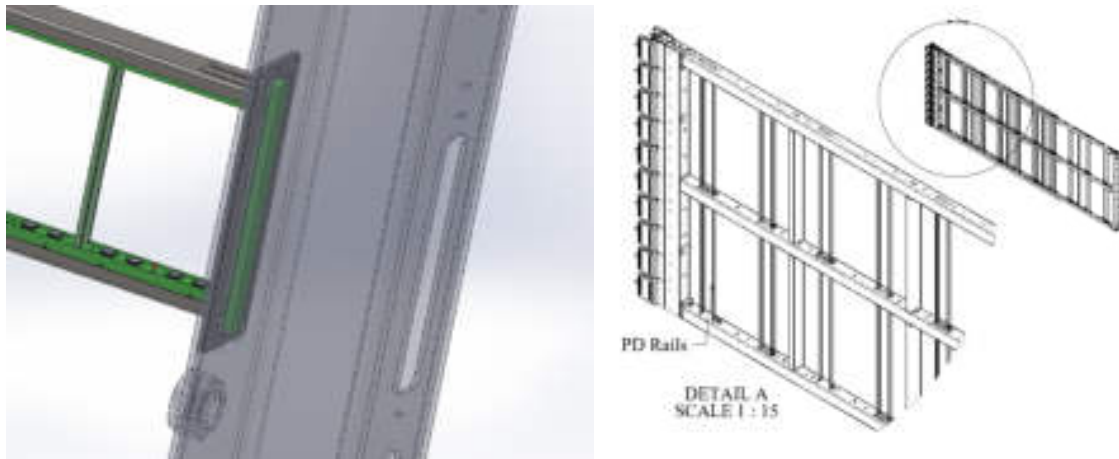


**Figure 5.41.** PD mounting in APA frame: fixed end of PD module inside transparent APA side tube showing clearance for CE cables (left) and showing PD mounting rails in an APA frame (right).

### 5.9.3.1 Signal cable and connections

For the ProtoDUNE-SP, PD cables were run inside the APA side tubes, five cables per side. For the SP module, however, this space will be filled by the cable harness for the lower APA cold electronics (CE) cables. This change required a revised plan for placing the PD cables. In addition, it was observed during ProtoDUNE-SP PD system installation that running the PD cables and making electrical connections to the modules during PD integration was time-consuming and introduced risk to the process.

For the SP module, the PD cables will be positioned in the APA frames prior to installing the mesh and wire-wrapping the frame. An APA in the lower position will house the cables for only the PDs in that lower APA whereas those in the top position will house the cables for the upper APA PDs and the pass-through cables from the lower APA. The cabling thus requires two different styles of APA frame. All cables terminate at the header of the top APA after assembly (see figure 5.42).

The cable connections between the upper and lower APAs are made during APA installation into the cryostat, while the APA stack is being assembled. The same in-line multi-pin connectors used at the flange penetration in ProtoDUNE-SP<sup>34</sup> are used for this connection. Superior-Essex<sup>35</sup> Category 6A U/FTP (STP) with FEP jacket (part no. 6S-220-xP) was validated in ProtoDUNE-SP. Similar cable will be used in DUNE, but custom-fabricated by the same vendor with two additional twisted pair contained within the external jacket for powering the photosensor active ganging board.

The PD signal cables are expected to contract approximately 2% relative to the APA frame during cool-down of the detector module to cryogenic temperatures. The design accounts for this by leaving cable loops in place between the anchor points to the APA frame, allowing for the required relative motion.

To remove interference with the CE cables, the electrical connections between the PD modules and the PD cable harness are moved to the face of the central APA tube. Printed circuit boards with spring-loaded electrical sockets are positioned on the inside face of the tube as part of the PD rail

<sup>34</sup>Hirose LF 10WBP-12S connectors <https://www.hirose.com>.

<sup>35</sup><http://superioressexcommunications.com>.

installation as shown in figure 5.43 (left). During PD integration into the APA frames, a PCB with pin contacts mounted to the PD module (see figure 5.9 right) engages into the PCB mounted to the APA frame, automatically making the electrical connection as shown in figure 5.43 (right).

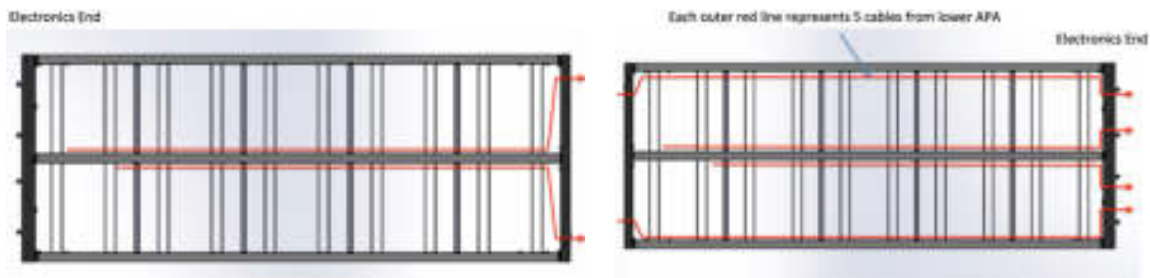


**Figure 5.42.** PD cable routing in APA frames: bottom APA (left) and top APA (right).

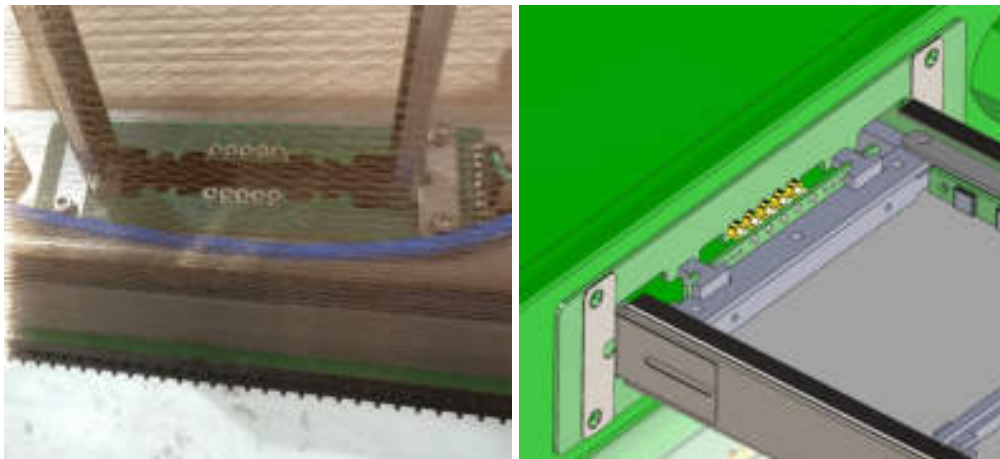


**Figure 5.43.** PD cable connectors in APA frames: PD connector plate mounted in APA frame (ICEBERG model, left) and a computer model of the mated PD and connector assembly in an APA (right). Note that active ganging PCBs are buried inside the central tube.

### 5.9.3.2 Thermal contraction and load deformation

**Thermal contraction.** During cool-down from room to LAr temperatures, significant relative shrinkage of module components is possible. Mitigating these effects was a major consideration in the X-ARAPUCA module design.

Thermal expansion coefficients (CTE) for the stainless steel APA frames and fused-silica filter plates drove the materials selection for the X-ARAPUCA modules. As shown in table 5.4, the relative shrinkage of FR-4 G-10 and stainless steel are well-matched and fall between the fused silica filter plates and the polystyrene WLS plates. The frame components are fabricated from FR-4 G-10, resulting in a shrinkage of the stainless steel frame structure relative to the frame of approximately 1.2 mm along the long (~2000 mm) axis of the bar, minimizing the motion needed to be accounted for in the electrical connectors to the wiring harness. The shrinkage of the frame

relative to the filter plate is < 0.2 mm. Both these relative shrinkage factors are accounted for in the dimensions and tolerances of the design.

The largest relative contraction of mechanical components is between the FR-4 frame and the polystyrene WLS plates. The most critical relative shrinkage is between the face of the photosensors and the WLS plate, where the 92 mm width of the plate will shrink significantly more than the PD module structure, resulting in more separation (approximately 1.3 mm) between the sensor face and the plate. Simulation indicates that X-ARAPUCA performance is not strongly affected by this gap size (reducing the gap to zero, direct contact, would be beneficial but would introduce unacceptable risk of damage). The WLS plate contracts relatively more along the long axis, by 5.8 mm for the 487.0 mm long plate, but this affects the performance of the detector less; the WLS bar mounting structure addresses this issue.

Another important potential thermal contraction interference to track in the PD design is the relative contraction of the slots in the APA frame and the separation of the photon detector support rails relative to the photon detector cross section. This requirement is listed in table 5.1 as specification SP-PD-12, which requires that a minimum gap between the PD module and the APA frame of 0.5 mm be maintained after cool-down. Specification SP-PD-08 in the same table that requires a minimum clearance of 1.0 mm between the modules and the APA frame at room temperature, together with the relative thermal contractions of the stainless steel APA frame and G-10 PD frames ensures that this specification is met.

**Table 5.4.** Shrinkage of PD module materials for a 206°C temperature drop.

| Material                     | Shrinkage Factor (m/m) |
|------------------------------|------------------------|
| Stainless Steel (304)        | $2.7 \times 10^{-3}$   |
| FR-4 G-10 (In-plane)         | $2.1 \times 10^{-3}$   |
| Fused Silica (Filter Plates) | $1.1 \times 10^{-4}$   |
| Polystyrene (WLS Bars)       | $1.4 \times 10^{-2}$   |

Mitigation of these contractions is detailed in table 5.5.

**PD mount frame deformation under static PD load.** FEA modeling of the PD support structure was conducted to study static deflection prior to building ProtoDUNE-SP prototypes. Modeling was conducted in both the vertical orientation (APA upright, as installed in cryostat) and also horizontal orientation. Basic assumptions used were fully-supported fixed end conditions for the rails, with uniform loading of  $3 \times$  PD mass (5 kg) along the rails. Figure 5.44 illustrates the rail deflection for the APA in the horizontal (left) and vertical (right) orientations. Prototype testing confirmed these calculations. Similar modeling of final-design DUNE PD modules will be completed prior to 60% design review.

**Table 5.5.** Relative Shrinkage of PD components and APA frame, and mitigations.

| Interface  | Relative shrinkage                           | Mitigation   |
|--|--|--|
| PD Length to APA width                                   | PD expands 1.2 mm relative to APA frame      | PD affixed only at one end of APA frame, free to expand at other end. 3 mm nominal clearance (beyond tolerance allowance) for expansion in design. |
| Width of PD in APA Guide Rails                           | PD expands 0.1 mm relative to slot width     | PD not constrained in C-channels. C channels and tolerances designed to contain module across thermal contraction range.                           |
| Width of module end mount board to stainless steel frame | Stainless frame shrinks 0.1 mm more than PCB | Diameter of shoulder screws and FR-4 board clearance holes selected to allow for motion.   |
| Length of WLS bar relative to FR-4 PD frame              | WLS bar shrinks 5.8 mm relative to PD frame  | Allowed for in WLS bar mount fixtures.   |

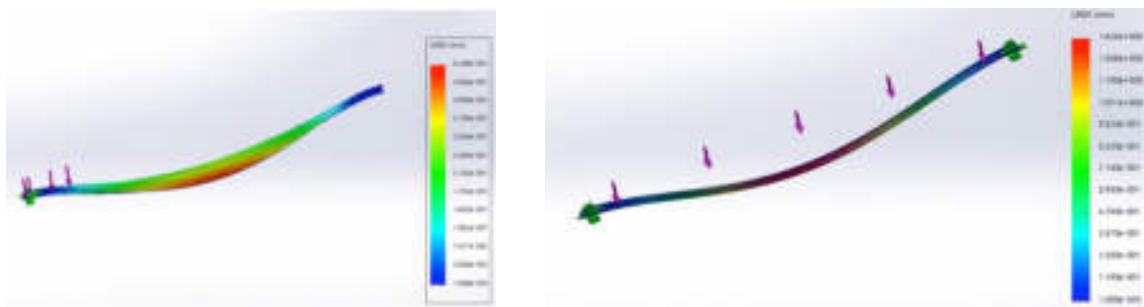


**Figure 5.44.** PD mechanical support analysis: rail deflection for the APA in the horizontal (left) and vertical (right) orientations.

#### 5.9.4 Photosensors and photosensor modules

The use of SiPMs in noble liquids is relatively new but growing rapidly with experiments such as GERDA, MEG II, DarkSide, and nEXO which are in various stages of preparation. The collaborators of DUNE will learn from these experiments, but in principle, DUNE has a more stringent accessibility and longevity constraints. Risk mitigation through reliability engineering, process control, and vendor and collaboration testing will be a key feature of the DUNE SiPM production process.

*Reliability Engineering:* the primary issue is the change in material properties and thermal stresses induced in the packaging due to differential coefficients of thermal expansion (CTEs). This is especially critical for interfaces, in particular die to substrate, substrate to potting mold, potting mold to encapsulation, and solder joints to everything else. Analysis of these interfaces and

collaboration with vendors to match CTEs as much as possible at these interfaces will contribute substantially to the long-term reliability of the photosensors.

*Process Control:* small and seemingly innocuous changes in the photosensor fabrication process can have a big impact on the robustness of these devices at extreme temperatures. This is one of the reasons why in space applications, for instance, same-day same-batch components are utilized. Given the photosensor quantities involved, this is not feasible for the DUNE PD system, but it will be important to establish a memorandum of understanding (MoU) with the vendor regarding strict process control once the pre-production batch has been qualified.

*Procurement:* potential vendors have verified that delivery of 100,000 devices per year is a reasonable expectation so long as the purchase contract is initiated early enough. Vendor visits to Hamamatsu and FBK in June-July 2019 will be used as an opportunity to confirm this guidance.

*Quality Assurance:* this will be an essential component in the photosensor risk mitigation strategy consisting of restricting the number of production batches, clearly communicating desired device and packaging parameters to the vendor, and vendor testing to guarantee device operation down to liquid nitrogen temperatures. Before shipment to the consortium, the vendor must qualify a randomly selected sample of devices from each production batch. The qualification would entail thermally stressing the devices with visual and electrical measurements made before and after.

*Quality Control:* the above strategies, while significantly lowering the risk, do not obviate the need for a strict testing regimen. Every sensor will be tested multiple times, at various stages of assembly, before installation in the SP module.

SiPMs are mounted in groups of six passively-ganged sensors to mounting boards, with eight mounting boards per supercell. Passive ganging (sensors in parallel) is implemented with traces on the SiPM mounting board (PD module), as was done for ProtoDUNE-SP. The SiPMs are mounted using a pick-and-place machine and standard surface-mount device soldering procedures. The outputs from these mounting boards are then routed to active ganging circuits in the center of the PD module, where they are collected into a summing amplifier and reduced to a single output channel.

The ganged analog signals exit via long cables (approximately 20 m) for digitization outside the cryostat. ProtoDUNE-SP has provided essential operational experience with a passive ganging board and signal transport provided by Teflon Ethernet Cat-6 cables, as described in section 5.9.3.

### 5.9.5 Electronics

The PD system consortium gained extensive experience in manufacturing processes for electronic systems during the development of the ProtoDUNE-SP SSPs. A general description of the readout system of ProtoDUNE-SP can be seen in the section 5.6. Compatibility between elements designed by different institutions is guaranteed when standard procedures are followed, so the circuit design must be done in accordance with mutually agreed-upon specification documents. A sufficient number of units must be produced to allow for testing both locally and in the central facility; for example, in ProtoDUNE-SP five 12-channel SSPs were produced and delivered to CERN for integration testing. Twenty-four were fabricated for ProtoDUNE-SP operation. Similar manufacturing test programs are envisioned for DUNE.

The readout electronics of the PD system will be designed and produced with similar tools and protocols as for ProtoDUNE-SP. For example, PCB layout is performed in accordance with

IPC<sup>36</sup> specifications. Bare PCB manufacturing requirements are embedded within the Gerber file fabrication documents (e.g., layers, spacing, impedance, finish, testing, etc.). Components are assembled on circuit boards either by trained PD consortium technical staff or by external assembly vendors, based on volume, and in accordance with per-design assembly specification documents. Testing occurs at collaboration institutions in accordance with a per-design test procedure that typically includes a mix of manual, semi-automated and automated procedures in an engineering test bench followed by overall characterization in a system or subsystem test stand. Other considerations and practices relevant to readout electronics production and assembly are itemized here:

- **Components:** schematic capture is done using appropriate tools (such as OrCAD 16.6.<sup>37</sup> or similar toolset) available within a design facility. Design is hierarchical with common FE page referenced multiple times, such as for all input channels. The schematic contains the complete bill of materials (BOM) including all mechanical parts. An electronics schematics subversion repository or similar tool is typically used for version control and backup. Multiple internal design reviews are held before the schematic is released for layout. The BOM, stored directly within the schematic, is extracted to a spreadsheet when ordering parts. Every part specifies both manufacturer and distributor information. Distributor information may be overridden by a technician at order time due to price or availability. Standard search engines such as Octopart,<sup>38</sup> ECIA<sup>39</sup> and PartMiner<sup>40</sup> are used to check price or availability across all standard distributors. A parts-availability check is performed prior to handoff from schematic to layout since obsolete or long lead-time parts may have been removed from the design and replaced. BOM information includes dielectric, tolerance, temperature coefficient, voltage rating, and size (footprint) to ensure that all parts are fully described.
- **Boards:** standard tools (such as the Allegro<sup>41</sup> toolset) are available for the PCB layout. Conventional PCBs are controlled-impedance multi-layer boards with many sets of delay-matched nets where necessary. In usual practice, multiple previously qualified vendors bid competitively. The consortium electronics group provides the complete impedance and delay characteristics within the layout tool, and the selected vendor cross-checks these values prior to manufacture and performs full electrical and impedance testing. Multiple internal design reviews are held prior to release of the design.
- **Cable plant:** the cabling designed will take into consideration the APA space and will be done in close collaboration with the TPC CE consortium to avoid crosstalk effects. Before making a final decision on cable procurement, we are investigating the possibility of cable manufacturing in a PD system consortium institution versus the cost of a commercial solution.
- **Manufacturer list:** in addition to the general laboratory procedures for QA, the general practice will be to use only PCB manufacturers and external assembly vendors whose workmanship

---

<sup>36</sup>IPC™, Association Connecting Electronics Industries, <http://www.ipc.org/>.

<sup>37</sup>OrCAD™ schematic design tool for PCB design <http://www.orcad.com>.

<sup>38</sup>Octopart <https://octopart.com/>.

<sup>39</sup>ECIA <https://www.eciaauthorized.com>.

<sup>40</sup>PartMiner <https://www.part-miner.com/>.

<sup>41</sup>Cadence Allegro®PCB design solution <https://www.cadence.com>.

and facilities have been personally inspected by experienced production team members. All external assemblers are required to quote in accordance with an assembly specifications document describing the IPC class and specific solder chemistry requirements of the design. The BOM document will show selected and alternate suppliers where available for every component of the FE boards.

- **FE electronics firmware:** this will be specified and updated iteratively in collaboration with other systems. The electronics working group will be responsible for responding to requests for additional firmware development, including for example, modifications to timing interface, modifications to trigger interface, and implemented sensitivity to in-spill versus not-in-spill conditions. Documents describing firmware architecture for each major change will be written and distributed to PD and DAQ working groups before implementation. An FE electronics users manual containing all details of new firmware will be distributed with production units when manufactured.
- **Mechanical assembly:** with the mechanical assembly of electronics readout boards, it is common practice to use a 3D model generated by the layout software. All relevant dimensions of the PCB including connector and indicator placement is extracted as a base DXF file from which an overall exploded mechanical diagram of chassis and other mechanical parts is made. Mechanical items such as shield plates will also be provided. It is assumed that external vendors will make the FE chassis (one for the chassis, one for front and back panels) from drawings provided by the consortium.

### 5.9.6 Calibration and monitoring

The consortium gained extensive experience in manufacturing, testing, and assembly processes during the development of the calibration and monitoring system for ProtoDUNE-SP. A general description of the proposed calibration and monitoring system can be seen in section 5.7.

The design and production of the calibration modules including electronics circuitry, FPGA implementation for light-source controls, optical timing/trigger and DAQ communication protocols, and UV light sources, closely follows the process described in section 5.9.5.

Design and selection of cold diffuser components and selection of cold and warm quartz fiber components follows requirements derived from interface considerations with HV, CPA and cryostat systems, and was tested in ProtoDUNE-SP. Installation, QA and QC of optical fibers is performed during the CPA installation process, with diffusers and CPA fibers pre-installed on the CPAs.

Installation of fibers that connect CPAs to the optical feedthrough penetrations at the cryostat will be defined with the DSS and cryostat teams, based on installation experience in ProtoDUNE-SP.

### 5.9.7 Outline of PD system assembly plan

The SP PD consortium is composed of many institutions in North and South America and Europe and fabrication of the system will occur at many locations. Here we present an outline of our assembly plan. The schedule interfaces implicit in this assembly program will be detailed in the overall project schedule.



- Photosensors, mounting and active ganging: Italian groups funded by INFN (and their associated universities) will procure, test, and assemble the active ganging circuits for the PD system. Photosensor mounting board assembly will likely be outsourced to a yet-to-be selected external firm.

The groups most involved are Bologna, Genova, Milano, Milano-Bicocca, and Laboratori Nazionali del Sud. Other Italian groups have also expressed interest in joining. We will allocate tasks among the interested groups prior to the final design review.

Following assembly, these components and their associated QC documentation will be shipped to UNICAMP for assembly into PD modules.

- Light collector modules: light collector modules will be fabricated primarily in Brazil.

Dichroic filters and wavelength shifting plates will be procured and received by a combination of CTI Campinas and the National Laboratory of Synchrotron Light (also in Campinas), where they will undergo reception QC testing.

Following testing, the dichroic filters will be delivered to UNICAMP for coating with PTP in their in-house vacuum deposition system.

The module mechanical components are also the responsibility of UNICAMP. This includes the FR-4 G-10 components (which will be fabricated in-house at UNICAMP), signal routing circuit boards, module electrical connectors, and other miscellaneous components (purchased externally) required to fabricate the modules.

Module assembly and initial QC testing will happen at UNICAMP.

Following assembly, the tested modules and all the associated QC documentation will be shipped to a reception center in the USA, where they will be retested and stored in the SDWF until required for integration into the APAs underground.

- APA support rails and electrical connectors: stainless steel rails and associated hardware for supporting the PD modules inside the APA will be fabricated by vendor in the USA. Components for cable connection between the upper and lower APAs, and cable management pieces, will be procured from vendors, assembled, and tested in the USA.

Following assembly and testing, these components will be shipped to APA frame assembly sites for integration into the frames prior to wire wrapping.

- Readout electronics and DAQ interface: the FE electronics and DAQ interfaces will be built by a collaboration of Latin American countries, particularly Colombia, Peru, and Paraguay, with engineering support from Fermilab and the University of Michigan in the US.

The FE electronics, communications boards, and external cabling between them and the DAQ will be designed by collaboration engineers, fabricated, or purchased from external vendors, and tested at collaboration institutions. While the exact distribution of effort is still being settled, interested institutions in Colombia include Universidad Antonio Nariño (UAN) and Universidad EIA. In Peru, they include the Universidad Nacional de Ingeniería de Peru.

DAQ/PD interface firmware development will be conducted by Paraguay, particularly the Universidad National de Asuncion (FIUNA), in conjunction with UAN in Colombia.

Following assembly and testing, components will be shipped to a reception center in the US for inspection then stored at the SDWF until needed.

- **Cables:** materials for cables and connectors inside the APA frames will be purchased, assembled and tested in the USA. Cables between the APA and the cryostat flange, as well as those between the flange and the DAPHNE electronics, will be purchased by UNICAMP and assembled and tested at their facilities. Following testing, the cables and their associated QC documentation will be assembled into groups of 20 cable sets (one APA stack) and shipped to the SDWF for storage until needed for installation. Cables intended to be routed inside the APA frames will be shipped directly to the APA frame assembly facilities.
- **Monitoring system:** the monitoring system including LED drivers, optical fibers, and diffusers will be designed, fabricated and tested in the US by the South Dakota School of Mines and Technology and Argonne National Laboratory.

Following assembly and testing, the system will be stored at the SDWF until needed for installation.

### 5.10 System interfaces

#### 5.10.1 Overview

Table 5.6 contains a summary and brief description of all the interfaces between the SP module PD system consortium and other consortia, working groups, and task forces, with references to the current version of the interface documents describing those interfaces. Drawings of the mechanical interfaces and diagrams of the electrical interfaces are included in the interface documents as appropriate. It is expected that further refinements of the interface documents will take place prior to the final production readiness review for the detector. The interface documents specify the responsibility of different consortia or groups during all phases of the experiment including design and prototyping, integration, installation, and commissioning.

Additional details describing the interface between the SP PD system and the other consortia, task forces (TF) and subsystems are given below.

#### 5.10.2 Anode plane assembly

The interface with the Anode Plane Assembly (APA) represents the most significant mechanical interface for the PD system. Interfaces with the APA are involved in meeting specifications SP-PDS-2, SP-PDS-7, SP-PDS-8, SP-PDS-9, SP-PDS-10, SP-PDS-11, and SP-PDS-12 (see table 5.1). The interface document will be written to monitor these specifications.

The APA frame is designed to provide:

- mechanical support and alignment for the PD modules, including access slots through the side of the frame for insertion of modules after the APAs are wrapped in wire;

**Table 5.6.** Single Phase PD system interface links.

| Interfacing System                         | Description   | Linked Reference |
|--|---|------------------|
| Detector Subsystems                        |   |                  |
| APA  | Mechanical support for PDs, PD installation slots, PD cabling support, access slots   | DocDB 6667 [10]  |
| CE   | Electrical signal interference, grounding, cable routing, cryostat flange, installation and testing   | DocDB 6718 [70]  |
| HV   | Mounting of PD monitoring system, possible reflector foil support, electrical discharge or corona effect light contamination  | DocDB 6721 [31]  |
| DAQ  | Data format, data timing, trigger information, timing and synchronization   | DocDB 6727 [86]  |
| CISC                                       | Rack layout, flange heaters, power supply selection, power and signal cable selection, monitoring cameras and camera lighting, purity monitor lighting, controls and data monitoring                | DocDB 6730 [87]  |
| Technical Coordination                     |   |                  |
| Facility interfaces                        | Cable trays inside the cryostat, cryostat penetrations, rack layout and power distribution on the detector mezzanine, cable and fiber trays on top of the cryostat                                  | DocDB 6970 [88]  |
| Installation interfaces                    | Sequence of integration and installation activities at SURF, equipment required for PD consortium activities, environmental controls in the cryostat during installation, post-installation testing | DocDB 6997 [89]  |
| Calibration task force interfaces          | Interface of SP module DP monitoring system into calibration system.  | DocDB 7051 [90]  |
| Physics, Software and Computing interfaces | Covers interfaces between the PD group and the joint computing task force, including specifications required for physics, data handling, and computing and storage requirements.                    | DocDB 7105 [91]  |

- mounting support for the PD electrical connections between the PD modules and the cable harness mounted inside the APA frame;
- mechanical support and strain relief for PD cables located inside the completed APA frame; and
- provision to connect the PD cables from the lower APA to the upper APA in an assembled APA stack and to connect the cables from the top of the APA stack to the cryostat flange.

Work on the two-APA connection and inspection in the underground assembly area will be performed by the APA group. Work on cabling prior to installation is performed by PD system and TPC electronics groups under supervision of the APA installation group. Once the APAs are moved inside the cryostat, the PD system and electronics consortia will be responsible for the routing of the cables in the trays hanging from the top of the cryostat.

Careful interface control will be required to ensure a successful assembly, which will be guided by the interface control document between the PD and APA consortia.

### 5.10.3 TPC cold electronics

Interfaces with the TPC CE are involved in meeting specifications SP-FD-2, SP-PDS-8, and SP-PDS-10 (see table 5.1). The interface between the PD and CE systems primarily consists of:

- ensuring no electrical cross-talk between the electronics and cabling harnesses of the PD and CE systems;
- ensuring there be no electrical contact between the PD system and CE components except for sharing a common reference voltage point (ground) at the feedthroughs;
- developing a common cable routing plan allowing the systems to share a common cable tray system on top of the APA frame and routing the cables to the cryostat flanges; and
- managing the interface between the PD and CE flanges in the cryostat cabling tees.

The CE and PD use a common cable tray system but separate flanges for the cold-to-warm transition, and each consortium is responsible for the design, procurement, testing, and installation, of their flange on the feedthrough, together with LBNF, which is responsible for the design of the cryostat. The installation of the racks on top of the cryostat is a responsibility of the facility, but the exact arrangement of the various crates inside the racks will be reached after common agreement between the CE, PD, CISC, and possibly DAQ consortia. The PD and CE consortia will retain all responsibility for selecting, procuring, testing, and installing their respective racks unless space and cost requires an agreement on shared crates to house the low-voltage or high-bias voltage modules for both systems.

### 5.10.4 Cathode plane assembly and high voltage system

Interfaces with the HV system should meet mechanical specification SP-PDS-9 (see table 5.1). In addition, light produced in electrical discharges in the HV system may increase the PD system data volume and impact the DAQ system. Communication between the three systems has been established on this issue.

The primary interface between the PD and HV systems is summarized as follows:

- providing an optical fiber routing path and strain relief system to the cryostat calibration hatch;
- mounting the PD monitoring system light diffusers to the CPA faces; and
- minimizing background light due to electrical discharge (corona effects).

This interface has strong overlap with the calibration consortium; this is described in more detail in section 5.10.8.

If the light reflector foil option were to be implemented, production of the FR-4+resistive Kapton CPA frames will be the responsibility of the HV consortium, together with design of the

structure for mounting the PD reflector foils to the CPA structure. The HV consortium will also provide mounting attachment points in the CPA frame structure. The reflector foils themselves, TPB coating of the WLS foils, and any required hardware for mounting the foils will be the responsibility of the PD consortium, with the understanding that all designs and procedures will be approved by the HV consortium.

### 5.10.5 Data acquisition

Interfaces with the DAQ system are involved in meeting specifications SP-PDS-5 and SP-PDS-13 (see table 5.1). The PD system interfaces with the DAQ system are described in DocDB 6727 [86] and include

- Data physical links: data are passed from the PD to the DAQ on 25 optical links following the 1000Base-SX standard. The links run from the PD readout system on the cryostat to the DAQ system in the CUC.
- Data format: data are encoded using UDP/IP. The data format consists of a header containing the word count, event time stamp, and channel ID, followed by the digitized waveform in 80 MHz samples. The data format has also been specified to use compression (zero suppression) and custom communication protocol.
- Data timing: the data must contain enough information to identify the time at which it was taken.
- Trigger information: the PD may provide summary information useful for data selection. If present, this will be passed to the DAQ on the same physical links as the remaining data.
- Timing and synchronization: clock and synchronization messages will be propagated from the DAQ to the PD using a backwards compatible development of the ProtoDUNE-SP timing system protocol [60]. There will be at least one timing fiber available for each data link coming from the PD system.
- Power-on initialization and start-of-run setup: the PDS may require initialization and setup on power-on and start of run. Power on initialization should not require communication with the DAQ. Start run/stop run and synchronization signals such as accelerator spill information will be passed by the timing system interface.

The data format has been determined but it is possible to include additional summary information to the header that depends on the outcome of triggering studies underway. This minor potential modification can be accommodated easily.

Excessive PD data may be generated by background effects such as light leaks in the cryostat or light generated due to sporadic short duration current discharge from the HV system (referred to as “micro-discharges” or as “streamers” in ProtoDUNE-SP). The HV consortium is trying to reduce the rate at which the discharges happen, but it is not expected to be completely eliminated.

In the case of light leaks, specification SP-PD-05 limits the acceptable data generated by these leaks to less than 10% of the total data transfer rate from the PD to the DAQ. Light flashes due to HV micro-discharges may be harder to mitigate, but the experience of streamers producing light in

ProtoDUNE-SP informs what we are likely to experience in DUNE and indicates that there is low risk that it will be a serious problem:

- They occur at a relatively low rate: once per few hours in ProtoDUNE-SP, likely much less underground due to the much lower cosmic ray rate that generates charge in the TPC.
- When they occur, they produce a significant amount of light but in a localized region (this was observed in the ProtoDUNE-SP PD system).

There is an automatic mitigation scheme in the HV system slow control that can identify when micro-discharges occur and stop them, but the power supply data is read relatively slowly (a few Hz) compared to the timescale of the PD/DAQ. Data corresponding to the PD response to the light flash will have already been recorded by the DAQ before the HV system can respond, so the mitigation will likely need to be a function of the DAQ.

In summary, since electrical discharges from the HV system are not under the control of the PD system it is not directly a specification for the PD system. Following consultation with the DAQ and HV consortia, we determined that it is also not appropriate as a specification on the HV system but is better addressed in the DAQ/PD interface document.

### 5.10.6 Cryogenics instrumentation and slow control

The primary interactions between the PD and the CISC include

- warm electronics rack controls, power supplies, rack safety equipment;
- warm cable and connector selection;
- cryogenic camera systems for detector monitoring, including lighting systems;
- purity monitor lighting requirements;
- cryostat flanges required for PD signal cable and monitoring systems; and
- PD slow control (including bias voltage) and data monitoring.

Additional interaction may occur in the case that the xenon doping performance enhancement is selected for inclusion in the detector. This system requires pre-mixing xenon gas and argon gas to introduce xenon doping into the LAr volume.

Any required hardware for this enhancement will be the responsibility of the PD consortium, with the understanding that all designs and procedures will be approved in advance by the cryogenics group.

A proposal is under consideration to mount CISC temperature sensors inside the APA frames, sharing a readout cable routing inside the APA frames and upper-to-lower APA connection point with the PD. This decision will be reached prior to the 60% design review. In case this plan is adapted, all PD cables and connectors will be the responsibility of the PD consortium, and all CISC components, cables, and connectors will be the responsibility of the CISC consortium. Cable routing plans, junction plates, and cable fixation will be the responsibility of the PD consortium.

### 5.10.7 Facility, integration and installation interfaces

The interface document with the project interface and installation working group covers the interface of the PD group with the technical coordination groups who oversee the integration of the PD modules and electronics into the APA and DAQ. Interfaces with the facility, integration, and installation group are involved in meeting specifications SP-PDS-1, SP-PDS-3, SP-PDS-4, and SP-PDS-5 (see table 5.1). The interfaces are distributed among the facility, integration, and installation working groups and primarily consist of

- electrical racks, cable trays, and cryostat penetrations, and power distribution on the mezzanine;
- storage for arriving PD modules prior to their integration;
- planning of pre-integration tests of PD components at the integration area and required equipment/tools;
- sequence of integration and installation activities at SURF (including environmental controls);
- quality management testing of PD modules during integration and installation;
- equipment required for PD consortium activities; and
- environmental controls in the cryostat during installation, and post-installation testing.

The PD consortium retains responsibility for providing quality management tooling and test plans at the integration area, as well as specialized labor and supervisory personnel for PD module integration and installation. Distribution of these responsibilities is described in DocDB 6970 [88].

The installation is described in detail in chapter 9.

### 5.10.8 Calibration and monitoring

This subsection concentrates on the description of the interface between the SP-PD system, calibration, and CISC consortia. Main interface items are

- cold components: light sources (diffusers and fibers) placed on the cathode planes to illuminate the detectors;
- warm components: a controlled pulsed-UV source and warm optics; and
- the optical feedthrough: used to PD bring monitoring system fiber optics through the calibration and monitoring flange. The flange itself is a shared interface between the PD system, the calibration task force, and CISC.

Hardware components required for PD monitoring and calibration systems will be designed and fabricated by the SP-PD system consortium.

Cold components (diffusers and fibers) interface with HV and are described in a separate interface document (DocDB 6721 [31]). Warm components interface the PD calibration and monitoring subsystem with the CISC DocDB 6730 [87] and DAQ DocDB 6727 [86] subsystems.

A joint development effort with HV/CPA groups will define the optimization of materials and location of the photon diffusers, fiber routes, connectors location and also the installation procedure of the diffusers and fiber. The feedthrough ports/locations and fiber routing along DSS will be determined jointly by SP-PD system and cryostat/DSS groups. The calibration and PD system consortia will share rack spaces. Multi-purpose ports are planned to be shared between various groups, calibration devices such as lasers and cameras will make use of them. SP-PD system, calibration, and CISC will define the ports for deployment. An interlock system to avoid turning on light sources when the PD system is in operation will be provided.

### 5.10.9 Physics, software and computing

Interfaces with physics, software, and computing are involved in meeting specifications SP-FD-3, SP-FD-4, SP-PDS-2, SP-PDS-5, SP-PDS-14, SP-PDS-15, and SP-PDS-16 (see table 5.1). The physics topics covered by the SNB/low energy and NDK/HEP working groups are the most closely connected to the SP PD system. The connection stems from the need for self-triggering for DUNE non-beam physics addressed by these two groups. However, there are connections to all physics working groups involving FD observables, as scintillation light information will improve event reconstruction/classification beyond what is achievable by TPC information only.

Below is a summary of interfaces between the SP PD system and FD and ProtoDUNE-SP simulation and reconstruction groups:

- generating photon libraries, and the tools for doing so;
- simulating and evaluating performance of physics events;
- SP PD system reconstruction performance studies;
- algorithms for matching flashes to TPC tracks; and
- analyzing the light produced by various species of charged particles.

It is critical that the performance specifications for the PD system meet the needs of the physics and reconstruction teams, both in terms of detector performance and background (including false triggers from radiologicals and light contamination from cryostat light leaks, HV system corona discharges, and calibration system effects such as purity monitors, laser flashers and cameras. These interfaces will be captured here. Light contamination of any nature must be studied quantitatively so that the impact on error budget due to misclassification of events can be calculated. Quantitative indicators should be established using ProtoDUNE-SP data, which should also provide the basis for identification algorithms of spurious signals caused by light leakage.

The SP PD system shares interfaces with the DUNE core computing systems, primarily with databases. The two databases that will have direct interfaces with the SP PD system are the hardware/QC and calibration databases. All the off-line calibration values will be stored in the DUNE calibration database. Additionally, the system will interface with the DUNE hardware database. During all stages of production/procurement and QC evaluations of PD system components, as well as integration and installation of the system, tracking of the hardware, and test results will be stored in the DUNE hardware/QC database. The SP PD system consortium will work with the database



group to ensure that all schema, applications, and procedures for the database interfaces are developed. As components of the system will originate at multiple institutions, well defined procedures and management will be required to ensure that all data is archived in the DUNE hardware/QC database.

### 5.11 Risks

Table 5.7 contains a list of all the risks that we are currently holding in the PD risk register. Each line includes the official DUNE risk register identification number, a description of the risk, the proposed mitigation for the risk, and finally three columns rating the post-mitigation (P)robability that the risk described comes to pass, the degree of (C)ost risk for that line, and the degree of (S)chedule risk. Risk levels are defined as (L)ow (<10% probability of occurring, <5% cost impact, <2 month schedule impact), (M)edium (10 to 25% probability of occurring, 5% to 20% cost impact, 2 to 6 month schedule impact), or (H)igh (>25% probability of occurring, >20% cost impact, >6 month schedule impact). Most of these risks are reduced to a “Low” level following mitigation (as shown in the table), although several of them currently hold a higher risk levels (pre-mitigation), due to the early stage of development of the PD system relative to other systems.

In the following sections, we present a narrative description of each of the risks and the proposed mitigation.

**Table 5.7:** PD system risks (P=probability, C=cost, S=schedule) The risk probability, after taking into account the planned mitigation activities, is ranked as L (low < 10 %), M (medium 10 % to 25 %), or H (high > 25 %). The cost and schedule impacts are ranked as L (cost increase < 5 %, schedule delay < 2 months), M (5 % to 25 % and 2–6 months, respectively) and H (> 20 % and > 2 months, respectively).

| ID           | Risk  | Mitigation   | P | C | S |
|--------------|---|--|---|---|---|
| RT-SP-PD -01 | Additional photosensors and engineering required to ensure PD modules collect enough light to meet system physics performance specifications.   | Extensive validation of X-ARAPUCA design to demonstrate they meet specification.                                 | L | M | L |
| RT-SP-PD-02  | Improvements to active ganging/front end electronics required to meet the specified 1 $\mu$ s time resolution.                                  | Extensive validation of photosensor ganging/front end electronics design to demonstrate they meet specification. | L | L | L |
| RT-SP-PD-03  | Evolutions in the design of the photon detectors due to validation testing experience require modifications of the TPC elements at a late time. | Extensive validation of X-ARAPUCA design to demonstrate they meet specification and control of PD/APA interface. | L | L | L |

|             |  |  |   |   |   |
|-------------|--|--|---|---|---|
| RT-SP-PD-04 | Cabling for PD and CE within the APA frame or during the 2-APA assembly/installation procedure require additional engineering/development/testing. | Validation of PD/APA/CE cable routing in prototypes at Ash River.  | L | L | L |
| RT-SP-PD-05 | Experience with validation prototypes shows that the mechanical design of the PD is not adequate to meet system specifications.                    | Early validation of X-ARAPUCA prototypes and system interfaces to catch problems ASAP.   | L | L | L |
| RT-SP-PD-06 | pTB WLS filter coating not sufficiently stable, contaminates LAr.  | Mechanical acceleration of coating wear. Long-term tests of coating stability.   | L | L | L |
| RT-SP-PD-07 | Photosensors fail due to multiple cold cycles or extended cryogen exposure.  | Execute testing program for cryogenic operation of photosensors including multiple cryogenic immersion cycles.                   | L | L | L |
| RT-SP-PD-08 | SiPM active ganging cold amplifiers fail or degrade detector performance.  | Validation testing if photosensor ganging in multiple test beds.   | L | L | L |
| RT-SP-PD-09 | Previously undetected electro-mechanical interference discovered during integration.   | Validation of electromechanical design in Ash River tests and at ProtoDUNE-SP-2.   | L | L | L |
| RT-SP-PD-10 | Design weaknesses manifest during module logistics-handling.   | Validation of shipping packaging and handling prior to shipping. Inspection of modules shipped to site immediately upon receipt. | L | L | L |
| RT-SP-PD-11 | PD/CE signal crosstalk.  | Validation in ProtoDUNE-SP, ICEBERG and ProtoDUNE-SP-2.  | L | L | L |
| RT-SP-PD-12 | Lifetime of PD components outside cryostat.  | Specification of environmental controls to mitigate detector aging.  | L | L | L |

### 5.11.1 Physics performance specification risks

Risk RT-SP-PD-01 in the table 5.7 addresses the performance specification that the PD system detect 0.5 pe/MeV of deposited energy. The system as designed may not reach this requirement during validation, necessitating additional engineering time and possibly additional system cost. Current design validation (section 5.8) provides firm indication that this specification will be met by the X-ARAPUCA. Mitigation of this risk is being achieved by allocating enough development resources to the PD to continue developing improved light collection modules; increasing the APA slot size to allow for larger modules; or increasing the number of photosensors per X-ARAPUCA supercell. The cost risk is rated M because photosensors are a significant cost driver for the project and increasing their number presents a significant medium level cost risk to the system.

Risk RT-SP-PD-02 addresses the performance specification that the PD system provide 1  $\mu$ s time resolution. While the timing resolution specification has been met by the ProtoDUNE-SP SSP-based S-ARAPUCA, cost-saving modifications to the readout electronics could degrade the performance of the PD system below the 1  $\mu$ s requirement. In addition, the combination of active and passive ganging of 48 photosensors could degrade timing performance. Current design validation

(section 5.8) provides firm indication that this specification will be met by the X-ARAPUCA and our baseline electronics, so a risk level of L is assigned to this risk. Mitigation of this risk is being achieved by allocating enough engineering resources to proceed rapidly with the design modifications of our reduced-cost baseline system; extensive testing of passive ganging prototypes, including parallel development of two design options for the active ganging circuit; and testing of timing performance in software simulation and multiple validation test stands.

### 5.11.2 Design risks

Risk RT-SP-PD-03 addresses the interface of the APA and PD designs, and the possibility that in order to meet detector performance or reliability specifications, the PD design may evolve in a direction requiring modification of the APA. Our current design validation (section 5.8) provides firm indication that these specifications will be met by the X-ARAPUCA, but we have not yet completed the validation process. While the design validation at this point is sufficient to reduce the overall risk to low following validation, this remains one of the principle risks we consider due primarily to the significant potential costs (financial and schedule) associated with such a change following the TDR. Mitigation of this risk involves close interaction between the APA and PD consortia and assigning significant resources to PD validation efforts.

Risk RT-SP-PD-04 covers the plans for running PD cables within the APA frames. Lessons learned during the ProtoDUNE-SP led to the re-design of the PD cabling layout, moving the cables inside the APA frame where they will be unreachable following installation of the APA wires. Additionally, installation of the APAs into the cryostat will require making PD cable connections between the upper and lower APAs underground. This risk addresses the concern that difficulties with these APA/PD interfaces will require changes to the cabling plan. Mitigation consists of extensive validation tests, including full-scale integration tests at the Ash River installation site.

Risk RT-SP-PD-05 concerns the possibility that continuing validation tests demonstrate that the PD mechanical design is in some way not adequate to meet DUNE specifications. While validation is ongoing and the possibility of a required design change remains, the impact and cost of such a change is likely relatively low. Mitigation includes continued design validation testing and sufficient engineering resources.

Risk RT-SP-PD-06 concerns the possibility that continuing validation tests demonstrate that the coatings required on the dichroic filter plates are not sufficiently robust in cryogenic applications and flake or dissolve off the surface and contaminate the LAr, possibly impacting electron lifetime or optical performance of the detector. Experience in ProtoDUNE-SP suggested that coatings of the filters is a delicate operation, and the possibility exists to produce unstable coatings. Mitigation includes continued validation testing of coated filters and sufficient engineering resources. This is one of the more significant outstanding risks, due to the possibility of negatively impacting the performance of the TPC.

Risk RT-SP-PD-07. One of the most significant lessons of the ProtoDUNE-SP for the PD system was the failure of a significant number of photosensors during module assembly QC due to an unannounced change in the manufacturer's photosensor packaging procedures. Problems developed with initially reliable photosensors mid-way through fabrication, requiring rapid changes to the PD design. This risk addresses the possibility of a re-occurrence of this or a similar problem. Mitigation includes (but is not limited to) extensive QA testing prior to selecting the final

photosensor candidate, careful coordination with photosensor vendor(s), and rigorous QC testing procedures (including tracking wafer fabrication and packaging batch information from the vendor) for photosensors. We are in close contact with both candidate photosensor candidates to develop a QA/QC plan sufficient to address our concerns.

Risk RT-SP-PD-08 addresses the possibility of a degradation in PD performance or outright failure due to the cold amplifiers required by the active ganging circuitry. In order to reach the baseline design of 48 ganged photosensors per X-ARAPUCA supercell, a mix of active and passive ganging is required. While initial validation testing is very promising, these circuits remain quite new. Mitigation of this risk involves additional validation testing in bench-top testing and in the ICEBERG test stand.

### 5.11.3 Risks during integration

Risk RT-SP-PD-09 addresses the possibility that a previously undetected flaw in the PD module design or the integration plan with the APAs manifests itself during the integration process. Steps taken to mitigate this risk include close coordination between the PD, APA, CE, and the integration task force coordinated by the project, including extensive full-scale testing at Ash River and at other integration test sites.

Risk RT-SP-PD-10 covers risks associated with integration into DUNE detectors. Fabrication and initial testing of PDs will occur in Brazil, follow-on testing will occur at the US reception facility prior to storage at the SDWF, and additional logistics and handling will occur prior to the modules arriving at the underground integration facility. This risk addresses the possibility that previously undetected weaknesses will be discovered in QC testing following receipt of the modules. Mitigation of this risk includes careful design engineering and testing of shipping and handling procedures.

### 5.11.4 Risks during installation/commissioning/operations

The biggest risk that could be realized during the commissioning and operations phase is the observation of excessive noise caused by failure to follow the DUNE grounding rules. Risk RT-SP-PD-11 addresses the possibility of discovering such a failure during installation QC testing or commissioning of the detector. The observation of excessive noise in DUNE would result in a delay of the commissioning and of data taking until the source of the noise is found and remedial actions are taken. In order to minimize the probability of observing excessive electronic noise, we plan to enforce the grounding rules throughout the design phase, based on the lessons learned from the operation of the ProtoDUNE-SP detector. In addition, testing at ICEBERG between PD and all generations of CE electronics will minimize this risk.

Risk RT-SP-PD-12 addresses PD maintenance during operation. During operation, most PD components are inaccessible due to being submerged in LAr. However, some components such as the warm readout electronics remain accessible. It is valuable to assign a risk to the need of their requiring spares beyond those planned for, or replacement due to a previously undetected flaw. Mitigation steps include two aspects: (1) designing the warm systems to facilitate repair, and (2) performing a careful mean time between failure analysis to predict failure rates over the lifetime of the experiment that will allow the procurement of sufficient spares in the production phase.

## 5.12 Transport and handling

A storage facility near or at the FD site (the SDWF) will be established to allow storage of materials for detector assembly until needed. Transport of assembled and tested PD modules, electronics, cabling, and monitoring hardware to the SDWF is the responsibility of the PD consortium.

Following assembly and quality management testing in Brazil, the PD modules will be packaged and shipped to an intermediate testing facility in the US for post-shipping checkout. Following this, the modules will be stored in their shipping containers in the SDWF. Cables, readout electronics, and monitoring hardware will be shipped directly to the SDWF and stored until needed underground for integration.

Packaging plans are informed by the ProtoDUNE-SP experience. Each SP module will be individually sealed into a light-tight anti-static plastic bag. Bagged modules will be packaged in groups of ten modules (matching the need for a single APA transported in a single shipping box), approximately 20 cm × 20 cm × 250 cm long. These shipping boxes will be gathered into larger crates to facilitate shipping. The optimal number per shipment is being considered.

Documentation and tracking of all components and PD modules will be required during the full logistics process. Well defined procedures are in place to ensure that all components/modules are tested and examined prior to, and after, shipping. Information coming from such testing and examinations will be stored in the DUNE hardware database. Each PD module shipping bag will be labeled with a text and barcode label, referencing the unique ID number for the module contained, and allowing linkage to the hardware database upon unpacking prior to integration into the APAs underground.

Tests have been conducted and continue to validate environmental requirements for photon detector handling and shipping. The environmental condition specifications for lighting (SP-PDS-3 in table 5.1), humidity (SP-PDS-4 in table 5.1), and work area cleanliness (SP-PDS-1 in table 5.1) apply for surface and underground transport, storage and handling, and any exposure during installation and integration underground.

Details of PD integration into the APA and installation into the cryostat, including quality management testing equipment, tests, and documentation are included in chapter 9.

## 5.13 Quality assurance and quality control

The QA and QC programs for the FD are based on our experience with the ProtoDUNE-SP. Our design-phase quality management system is based upon that experience. Following completion of the 60-percent design review, we will develop a quality final assurance program focused on final specifications and drawings, and developing a formal set of fabrication procedures along with detailed QC and test plans.

During fabrication, integration into the detector, and detector installation into the cryostat, our QC plan will be carefully followed, including incoming materials and other inspection reports, fabrication travelers, and formal test result reports entered into the DUNE QA/QC database.

Particular steps in this process are detailed below.

### 5.13.1 Design quality assurance

PD design QA focuses on ensuring that the detector modules meet the following goals:

- physics goals as specified in the DUNE requirements document;
- interfaces with other detector subsystems as specified by the subsystem interface documents; and
- materials selection and testing to ensure non-contamination of the LAr volume.

The PD system consortium will perform the design and fabrication of the components in accordance with the applicable requirements of the LBNF-DUNE QA plan. If the institute (working under the supervision of the consortium) performing the work has a documented QA program, the work may be performed in accordance with their own program.

Upon completion of the PD system design and QA/QC plan, there will be a pre-production review process, with the reviewers charged to ensure that the design demonstrates compliance with the goals above.

### 5.13.2 Production and assembly quality assurance

The PD system will undergo a QA review for all components prior to completion of the design and development phase of the project. The ProtoDUNE-SP test will represent the most significant test of near-final PD components in a near-DUNE configuration, but additional tests will also be performed. The QA plan will include, but not be limited to, the following areas:

- materials certification (in the Fermilab materials test stand and other facilities) to ensure materials compliance with cleanliness requirements;
- cryogenic testing of all materials to be immersed in LAr, to ensure satisfactory performance through repeated and long-term exposure to LAr. Special attention will be paid to cryogenic behavior of fused silica and plastic materials (such as filter plates and wavelength-shifters), SiPMs, cables and connectors. Testing will be conducted both on small-scale test assemblies (such as the small test cryostat at CSU) and full-scale prototypes (such as the full-scale CDDF cryostat at CSU).
- mechanical interface testing, beginning with simple mechanical go/no-go gauge tests, followed by installation into the ProtoDUNE-SP-2 system, and finally full-scale interface testing of the PD system into the final pre-production TPC system models; and
- full-system readout tests of the PD readout electronics, including trigger generation and timing, including tests for electrical interference between the TPC and PD signals.

Prior to beginning construction, the PD system will undergo a final design review, where these and other QA tests will be reviewed and the system declared ready to move to the pre-production phase.

### 5.13.3 Production and assembly quality control

Prior to the start of fabrication, a manufacturing and QC plan will be developed detailing the key manufacturing, inspection, and test steps. The fabrication, inspection, and testing of the components will be performed in accordance with documented procedures. This work will be documented on travelers and applicable test or inspection reports. Records of the fabrication, inspection and testing will be maintained. When a component has been identified as being in noncompliance to the design, the nonconforming condition shall be documented, evaluated, and dispositioned as: *use-as-is* (does not meet design but can meet functionality as it is), *rework* (bring into compliance with design), *repair* (will be brought to meet functionality but will not meet design), and *scrap*. For products with a disposition of accept, as is, or repair, the nonconformance documentation shall be submitted to the design authority for approval.

All QC data (from assembly and pre- and post-installation into the APA) will be directly stored to the DUNE database for ready access of all QC data. Monthly summaries of key performance metrics (to be defined) will be generated and inspected to check for quality trends.

Based on the ProtoDUNE-SP model, we expect to conduct the following production testing. Prior to shipping from assembly site:

- dimensional checks of critical components and completed assemblies to insure satisfactory system interfaces;
- post-assembly cryogenic checkouts of SiPM mounting PCBs (prior to assembly into PD modules);
- module dimensional tolerances using go/no-go gauge set; and
- warm scan of complete module using motor-driven LED scanner (or UV LED array).

Following shipping to the US reception and checkout facility but prior to storage at SDWF:

- mechanical inspection;
- warm scan (using identical scanner to initial scan); and
- cryogenic testing of completed modules (in CSU CDDF or similar facility).

Following delivery to integration clean room underground, prior to and during integration and installation:

- warm scan (using identical scanner to initial scan);
- complete visual inspection of module against a standard set of inspection points, with photographic records kept for each module;
- end-to-end cable continuity and short circuit tests of assembled cables; and
- an FE electronics functionality check.

#### 5.13.4 Installation quality control

PD system pre-installation testing will follow the model established for ProtoDUNE-SP. Prior to installation in the APA, the PD modules will undergo a warm scan in a scanner identical to the one at the PD module assembly facility and the results compared. In addition, the module will undergo a complete visual inspection for defects and a set of photographs of selected critical optical surfaces taken and entered into the QC record database. Following installation into the APA and cabling, an immediate check for electrical continuity to the SiPMs will be conducted.

Following the mounting of the TPC CE and the PDs, the entire APA will undergo a cold system test in a gaseous argon cold box, similar to that performed during ProtoDUNE-SP. During this test, the PD system system will undergo a final integrated system check prior to installation, checking dark and LED-stimulated SiPM performance for all channels, checking for electrical interference with the cold electronics, and confirming compliance with the detector grounding scheme.

#### 5.14 Safety

Safety management practices will be critical for all phases of the photon system assembly, and testing. Planning for safety in all phases of the project, including fabrication, testing, and installation will be part of the design process. The initial safety planning for all phases will be reviewed and approved by safety experts as part of the initial design review. All component cleaning, assembly, testing, and installation procedure documentation will include a section on safety concerns relevant to that procedure and will be reviewed during the appropriate pre-production reviews.

Areas of particular importance to the PD system include

- Hazardous chemicals (particularly WLS chemicals such as PTP used in filter plate coating) and cleaning compounds: all potentially hazardous chemicals used will be documented at the consortium management level, with materials data safety sheets (MSDS) and approved handling and disposal plans in place.
- Liquid and gaseous cryogenics used in module testing: full hazard analysis plans will be in place at the consortium management level for all module or module component testing involving cryogenic hazards, and these safety plans will be reviewed in the appropriate pre-production and production reviews.
- High voltage safety: some of the candidate SiPMs require bias voltages above 50 VDC during warm testing (although not during cryogenic operation), which may be a regulated voltage as determined by specific laboratories and institutions. Fabrication and testing plans will demonstrate compliance with local HV safety requirements at the particular institution or laboratory where the testing or operation is performed, and this compliance will be reviewed as part of the standard review process.
- UV and VUV light exposure: some QA and QC procedures used for module testing and qualification may require use of UV and/or VUV light sources, which can be hazardous to unprotected operators. Full safety plans must be in place and reviewed by consortium management prior to beginning such testing.



- Working at heights, underground: some aspects of PD system module fabrication, testing and installation may require working at heights or deep underground. Personnel safety will be an important factor in the design and planning for these operations, all procedures will be reviewed prior to implementation, and all applicable safety requirements at the relevant institutions will be observed at all times.

### 5.15 Organization and management

The SP PD consortium benefits from the contributions of many institutions and facilities in Europe and North and South America. Table 5.8 lists the member institutions.

**Table 5.8:** PDS consortium institutions.

| Member Institute                                  | Country        |
|---|----------------|
| Federal University of ABC                         | Brazil         |
| State University of Feira de Santana              | Brazil         |
| Federal University of Alfenas Poços de Caldas     | Brazil         |
| Centro Brasileiro de Pesquisas Físicas            | Brazil         |
| Federal University of Goiás                       | Brazil         |
| Brazilian Synchrotron Light Laboratory LNLS/CNPEM | Brazil         |
| University of Campinas                            | Brazil         |
| CTI Renato Archer                                 | Brazil         |
| Federal Technological University of Paraná        | Brazil         |
| Universidad del Atlantico                         | Colombia       |
| Universidad Sergio Ablada                         | Colombia       |
| University Antonio Nariño                         | Colombia       |
| Institute of Physics CAS                          | Czech Republic |
| Czech Technical University in Prague              | Czech Republic |
| Universidad Nacional de Assuncion                 | Paraguay       |
| Pontificia Universidad Catolica Perú              | Perú           |
| Universidad Nacional de Ingeniería                | Perú           |
| University of Warwick                             | UK             |
| University of Sussex                              | UK             |
| University of Manchester                          | UK             |
| Edinburgh University                              | UK             |
| Argonne National Laboratory                       | USA            |
| Brookhaven National Laboratory                    | USA            |
| California Institute of Technology                | USA            |
| Colorado State University                         | USA            |
| Fermilab  | USA            |

|   |       |
|---|-------|
| Duke University                             | USA   |
| Idaho State University                      | USA   |
| Indiana University                          | USA   |
| University of Iowa                          | USA   |
| Louisiana State University                  | USA   |
| Massachusetts Institute of Technology       | USA   |
| University of Michigan                      | USA   |
| Northern Illinois University                | USA   |
| South Dakota School of Mines and Technology | USA   |
| Syracuse University                         | USA   |
| University of Bologna and INFN              | Italy |
| University of Milano Bicocca and INFN       | Italy |
| University of Genova and INFN               | Italy |
| University of Catania and INFN              | Italy |
| Laboratori Nazionali del Sud                | Italy |
| University of Lecce and INFN                | Italy |
| INFN Milano                                 | Italy |
| INFN Padova                                 | Italy |

The SP PD system consortium follows the typical organizational structure of DUNE consortia:

- A consortium lead provides overall leadership for the effort and attends meetings of the DUNE Executive and Technical Boards.
- A technical lead provides technical support to the consortium lead, attends the Technical Board and other project meetings, oversees the project schedule and work breakdown structure (WBS), and oversees the operation of the project working groups.
- A Project Management Board composed by the project leads from the participating countries, the consortium leadership team and few ad hoc members, which maintains tight communication between the countries participating in the consortium construction activity.

Below the leadership, the consortium is divided up into six working groups, each led by two or three working group conveners (see table 5.9). Each working group is charged with one primary area of responsibility within the consortium, and the conveners report directly to the Technical Lead regarding those responsibilities.

The working group conveners are appointed by the PD system consortium lead and technical lead; the structure may evolve as the consortium matures and additional needs are identified.

### 5.15.1 High-level schedule

Table 5.10 lists key milestones in the design, validation, construction, and installation of the SP PD system. These milestones include external milestones indicating linkages to the main DUNE

**Table 5.9.** PD working groups and responsibilities.

| Working Group                   | Responsibilities  |
|---------------------------------|---|
| Light Collector WG              | Mechanical design, materials selection for PD modules                 |
| Photosensors WG                 | Selection, validation, procuring of photosensors, cold active ganging |
| Readout electronics WG          | Warm electronics, cable harness, DAQ interface                        |
| Integration and Installation WG | Internal (inter-WG) and external (inter-consortia) interfaces         |
| Physics and Simulation WG       | Physics and simulations studies to determine PD specifications        |
| ProtoDUNE Analysis WG           | Validation of PD system in ProtoDUNE-SP and ProtoDUNE-SP-2            |

schedule (highlighted in color in the table), as well as internal milestones such as design validation and technical reviews.

In general, the flow of the schedule commences with a 60% design review based on module performance testing at UNICAMP and at ICEBERG and integration testing at Ash River. Additional similar design validation follows, leading to a final design review (FDR). Following the FDR, 30 modules and required electronics, cabling, and PD monitoring system components for ProtoDUNE-SP-2 will be built, installed, and validated during a second ProtoDUNE run at CERN. Once the data from this test have undergone initial analysis, production readiness reviews will be conducted and module fabrication will begin.

Some parts of the PD system system, such as the support rails and electrical connectors required in mid-2020 for APA assembly and photosensors and filter plates which have a long procurement cycle, will require an abbreviated design review process as detailed in the narrative earlier in this document and shown in the milestone table.

**Table 5.10:** PDS consortium schedule.

| Milestone  | Date           |
|--|----------------|
| 60 percent design validation testing complete                | May 2020       |
| 60 percent design review                                     | May 2020       |
| production readiness review for PD rails, cables, connectors | May 2020       |
| Final design review for PD rails, cables, connectors         | July 2020      |
| Fabrication of PD rails, cables, connectors begins           | August 2020    |
| Final design validation testing complete                     | September 2020 |
| Down selection to two photosensor candidates                 | September 2020 |
| Final design review for remaining PD components              | September 2020 |
| Start of module 0 component production for ProtoDUNE-SP-2    | March 2021     |
| Start of ProtoDUNE-SP-II installation                        | March 2021     |

|  |                     |
|--|---------------------|
| End of module 0 component production for ProtoDUNE-SP-2          | August 2021         |
| End of module 0 installation for ProtoDUNE-SP-2                  | August 2021         |
| Start of PD installation in ProtoDUNE-SP-II                      | September 2021      |
| Begin procurement of filter plates                               | October 2021        |
| ProtoDUNE-SP-2 initial results available                         | December 2021       |
| production readiness review for photosensors                     | March 2022          |
| Begin procurement of production photosensors                     | April 2022          |
| production readiness review for remaining PD components          | May 2022            |
| Begin fabrication/procurement of remaining module components     | June 2022           |
| Begin assembly of PD monitoring system                           | January 2022        |
| <b>Start of ProtoDUNE-DP-II installation</b>                     | <b>March 2022</b>   |
| Begin assembly of front-end electronics modules                  | March 2022          |
| <b>SDWF available</b>  | <b>April 2022</b>   |
| Begin assembly of X-ARAPUCA modules                              | July 2022           |
| <b>Beneficial occupancy of cavern 1 and CUC</b>                  | <b>October 2022</b> |
| Initial batch (80 PD modules) assembled                          | March 2023          |
| <b>CUC counting room accessible</b>                              | <b>April 2023</b>   |
| Initial batch (80 PD modules) arrive at US PD Reception Facility | June 2023           |
| Second batch (160 PD modules) assembled                          | July 2023           |
| Initial batch (80 PD modules) arrive at SDWF                     | September 2023      |
| Second batch (160 PD modules) arrive at US PD Reception Facility | October 2023        |
| PD monitoring system at SDWF                                     | October 2023        |
| Third batch (320 PD modules) assembled                           | November 2023       |
| Second batch (160 PD modules) arrive at SDWF                     | December 2023       |
| <b>Top of detector module #1 cryostat accessible</b>             | <b>January 2024</b> |
| Third batch (320 PD modules) arrive at US PD Reception Facility  | January 2024        |
| Front end electronics modules at SDWF                            | February 2024       |
| Fourth batch (320 PD modules) assembled                          | February 2024       |
| Third batch (320 PD modules) arrive at SDWF                      | April 2024          |
| Fourth batch (320 PD modules) arrive at US PD Reception Facility | May 2024            |
| Fifth batch (320 PD modules) assembled                           | June 2024           |
| <b>Start of detector module #1 TPC installation</b>              | <b>August 2024</b>  |
| Fourth batch (320 PD modules) arrive at SDWF                     | August 2024         |
| Fifth batch (320 PD modules) arrive at US PD Reception Facility  | September 2024      |
| Final batch (300 PD modules) assembled                           | December 2024       |
| Fifth batch (320 PD modules) arrive at SDWF                      | December 2024       |
| Final batch (300 PD modules) arrive at US PD Reception Facility  | February 2025       |
| Final batch (300 PD modules) arrive at SDWF                      | April 2025          |

|  |              |
|--|--------------|
| End of detector module #1 TPC installation   | May 2025     |
| Top of detector module #2 accessible         | January 2025 |
| Start of detector module #2 TPC installation | August 2025  |
| End of detector module #2 TPC installation   | May 2026     |

### 5.15.2 High-level cost narrative

In the fall of 2018, we completed an initial cost estimate for fabrication of PD modules for one 10kt DUNE module and updated the estimate extensively in March/April of 2019. The estimates are based on ProtoDUNE-SP costs, modified as necessary for an X-ARAPUCA design. Vendor quotations or vendor estimates are used for all the major components. For fabrication costs, the biggest uncertainties center around the photosensor fabrication; this constitutes approximately half the total PD system cost. We have estimates from Hamamatsu for photosensors which would reduce this line by nearly a factor of two, significantly reducing the system cost. We also have preliminary indications that similar cost savings may also be available from using FBK photosensors. As noted earlier in this TDR, a major focus of our remaining development work is focused on realizing these potential savings.

The dichroic filter procurement and coating represent the other major cost driver for the project. The costing for the filter plates is based on initial contacts with a Brazilian filter firm. Initial samples of filter substrates have been received at UNICAMP and have been successfully coated and tested through multiple cryogenic cycles with no indication of failure. Extensive additional validation of the Brazilian filters will occur during late 2019 as part of the SBND module fabrication.

These filter plates are significantly cheaper than the filters manufactured by Omega, Inc. that were tested in our earlier validation studies. Until these tests are complete, the filter plates remain a significant cost and schedule risk.

Extensive use of design-for-fabrication techniques throughout the module development phase, as well as multiple rounds of prototype development, have allowed us to minimize the component cost for the remaining components. In-house fabrication and assembly using university shop facilities and student labor for assembly (particularly at UNICAMP) have also reduced costs.

Modification of an existing and well understood readout electronics system has very significantly reduced initial cost estimates for that portion of the system.

## 5.16 Appendix

### 5.16.1 Simulation

The broad performance specifications for the PD system are determined by a series of physics deliverables addressing the major physics goals of DUNE: nucleon decay searches, supernova burst neutrinos, and beam neutrinos. Detailed subdetector specifications, such as light yield of the light collectors, are determined using a full simulation, reconstruction, and analysis chain developed for the Liquid Argon Software (LArSoft) framework.

### 5.16.1.1 Simulation and reconstruction steps

The first step in the simulation specific to the PD system is the simulation of the production of light and its transport within the volume to the PDs. Argon is a strong scintillator, producing 24,000  $\gamma$ s/MeV at our nominal drift field. Even accounting for the efficiency of the PDs, it is prohibitive to simulate every optical photon with Geant4 in every event. So, prior to the full event simulation, the detector volume is voxelized and many photons are produced in each voxel. The fraction of photons from each voxel reaching each photosensor is called the visibility, and these visibilities are recorded in a 4-dimensional library. This library includes Rayleigh scattering length ( $\lambda_R = 60$  cm [92]), absorption length ( $\lambda_A = 20$  m), and the measured collection efficiency versus position of the double-shift light-guide bars. There is significant uncertainty on the scattering length in the literature, so the value is conservatively chosen at the low end of those reported. With these optical properties, there is a factor of 20 difference in total amount of light collected between events right in front of the photon detectors and those on the far side of the drift volume 3.6 m away.

When a particle trajectory is simulated, the amount of charge and light it produces is calculated in small steps. The light produced in each step is distributed onto the various PDs using the photon library as a look-up table, and the 30% early (6 ns) plus 70% late (1.5  $\mu$ s) scintillation time constants are applied. Transport time of the light through the LAr is not currently simulated but is under development. It is not expected to make a significant difference in the studies presented here.

The second step is the simulation of the sensor and electronics response. For the studies shown here, the SensL SiPM and SiPM signal processor (SSP) readout electronics used for PD development and in ProtoDUNE-SP is assumed (see section 5.6). However, a range of S/N and dark rates are considered in order to set requirements on the needed performance of the electronics. Crosstalk (where a second cell avalanches when a neighbor is struck by a photon generated internal to the silicon) is introduced by adding a second photoelectron 16.5% of the time when an initial photoelectron is added to the waveform. Additional uncorrelated random noise is added to the waveform with an RMS of 0.1 photoelectron. The response of the SSP self-triggering algorithm, based on a leading-edge discriminator, is then simulated to determine if and when a 7.8  $\mu$ s waveform will be read out, or in the case of the simulation, stored and passed on for later processing.

The third step is reconstruction, which proceeds in three stages. The first is a “hit finding” algorithm that searches for peaks on individual waveforms channel-by-channel, identifying the time (based on the time of the first peak) and the total amount of light collected (based on the integral until the hit goes back below threshold). The second step is a “flash finding” algorithm that searches for coincident hits across multiple channels. All the coincident light is collected into a single object that has an associated time (the earliest hit), an amount of light (summed from all the hits), and a position on the plane of the APA ( $y$ - $z$ ) that is a weighted average of the positions of the photon collectors with hits in the flash. The final step is to “match” the flash to the original event by taking the largest flash within the allowed drift time that is within 240 cm in the  $y$ - $z$  plane. Since the TPC reconstruction is still in active development, especially for low-energy events, we match to the true event vertex of the event in the analyses presented here. This is a reasonable approximation since the position resolution of the TPC will be significantly better than that of the PD system.

These tools (or subsets of them) are then used to evaluate how the performance of the PD system affects the following set of physics deliverables.

### 5.16.1.2 Nucleon decay

Nucleon decays are rare events, so excluding backgrounds is of the utmost importance. Since some backgrounds can be generated by cosmic rays passing outside the active detector area, setting a fiducial volume to exclude such events is critically important.

**Fiducialization with  $t_0$ .** The physics deliverable: the PDs must be able to determine  $t_0$  with approximately 1  $\mu$ s resolution (SP-FD-4: time resolution) for events with visible energy greater than 200 MeV throughout the active volume and do so with  $> 99\%$  efficiency (SP-FD-3: light yield), as described in Volume II, DUNE physics, chapter 6, section 6.1.4. This energy regime is relevant for nucleon decay and atmospheric neutrinos. The time measurement is needed for event localization for optimal energy resolution and rejection of entering backgrounds. This resolution is required for comparable spatial resolution to the TPC along the drift direction.

**Table 5.11.** Efficiency for tagging nucleon decay events with the PD system at the CPA, the dimmest region of the detector, which is 3.6 m from the PDs, shown for range of light yields (LY) at that position. Also shown is the total PD module collection efficiency required for that light yield with the simulated scattering length, 60 cm.

| CPA Light yield (PE/MeV) | Collection Efficiency (%) | Efficiency at the CPA (%) |
|--------------------------|---------------------------|---------------------------|
| 0.09                     | 0.24                      | $93.8 \pm 0.4$            |
| 0.28                     | 0.75                      | $97.7 \pm 0.4$            |
| 0.33                     | 0.88                      | $98.4 \pm 0.2$            |
| 0.50                     | 1.3                       | $98.9 \pm 0.2$            |

The physics here feeds down to a requirement on the minimum light yield (SP-FD-3: light yield), determined by measuring how often the correct flash was not assigned to nucleon decay events<sup>42</sup> in the dimmest region of the detector, near the CPA. A minimum light yield of 0.5 PE/MeV is required to meet the requirement of 99% efficiency, as shown in table 5.11.

A light collector with 1.3% collection efficiency (defined as the probability that a photon reaching the surface of the light collector will be recorded as a photoelectron) achieves this light yield with the simulated 60 cm scattering length. This efficiency is equivalent to having 23 cm<sup>2</sup> of active area per module with 100% efficiency. At this scattering length, there is a factor of 20 difference in light yield between the brightest and dimmest regions of the detector, so techniques to improve light yield uniformity (discussed in appendix 5.16.2) would reduce the inefficiency still further and ease understanding the detector systematic uncertainties.

### 5.16.1.3 Supernova neutrinos

Supernova bursts are also rare events, though here the event is made up of many interactions (spread over several seconds) instead of a single interaction. For distant supernovae (at the far side of the Milky Way or in the Large Magellanic Cloud), the top priority is to ensure that the detector can

<sup>42</sup>The most relevant sample is actually the *background* to nucleon decay events. However, efficiently simulating background that can mimic nucleon decays is challenging since they can be quite rare topologies. It is therefore easier to simulate the nucleon decay signal that should be representative of the background.

identify a burst when it happens and trigger the detector readout. For nearby supernovae, triggering will not be a challenge, and instead the goal is to record as much information as possible about the burst.

**Burst triggering.** The physics deliverable: the PD system must be able to trigger on SNBs which produce 50 neutrino interactions in a 10 kt volume<sup>43</sup> with almost 100% efficiency with a false positive rate of less than one per month. This deliverable is most important for distant supernovae where the most important requirement is that we trigger and record the data. If both the PD system and TPC triggers have good efficiency, they can provide redundancy against one another or be combined to increase efficiency or lower the background rate. The once-per-month false positive rate is determined by limits in data handling.

The PD system trigger performance was studied for a plausible but challenging signal: a supernova burst in the Large Magellanic Cloud, which we conservatively assumed would produce only 10 signal events in the far detector. The trigger efficiency was studied with variations in light yield, dark rate, and signal-to-noise ratio, keeping the requirement from the DAQ that the fake rate be held to less than one per month. The burst trigger efficiency for 10 supernova neutrino events in one 10 kt module (a pessimistic prediction for a supernova in the LMC), was found to be approximately 80%, and it is relatively insensitive to all these parameters for average light yield  $>7$  PE/MeV (equivalent to 0.9% collection efficiency with the simulated optical properties), dark rate  $<1$  kHz, and signal-to-noise  $> 3$ . The uncorrelated noise from dark rate and low signal-to-noise was easily excluded from trigger primitives by the clustering scheme, and the increased light yield makes both backgrounds and signal brighter together, so performance stays basically constant. Thus this physics deliverable, while important, does not constrain any detector requirements.

**TPC energy measurement and time resolution with  $t_0$ .** The physics deliverable: the PDs must be able to provide  $t_0$  determination with 1  $\mu$ s resolution (SP-FD-4: time resolution) for at least 60% of the neutrinos in a typical SNB energy spectrum. The  $t_0$  measurements are used in concert with the TPC-reconstructed event in two ways: to correct for the attenuation of the charge signal as a function of how far the charge drifts through the TPC and to provide more precise absolute event times for resolving short time features in the SNB neutrino event rate. This deliverable is important primarily for nearby supernovae where the number of events is large enough that time and energy resolution will be the limiting factors in extracting physics, as described in Volume II, DUNE physics, chapter 7.

The 60%  $t_0$  tagging requirement comes from two studies of a typical SNB neutrino spectrum under varying PD performance assumptions: the resolution of the energy reconstructed with the TPC and drift-corrected using the time from the PDs, and the observability of the in-fall ‘notch’ in the SNB event time distribution. Both studies show significant improvement when going from no PDs to a system that has a collection efficiency of at least 0.25% (equivalent to 0.5 PE/MeV for 60% of the detector volume), but only marginal improvements past that point, as can be seen in figure 5.45. The light yield required here is sufficiently low that this deliverable does not set any additional detector requirements.

<sup>43</sup>About the amount expected for a burst at the far side of our galaxy.



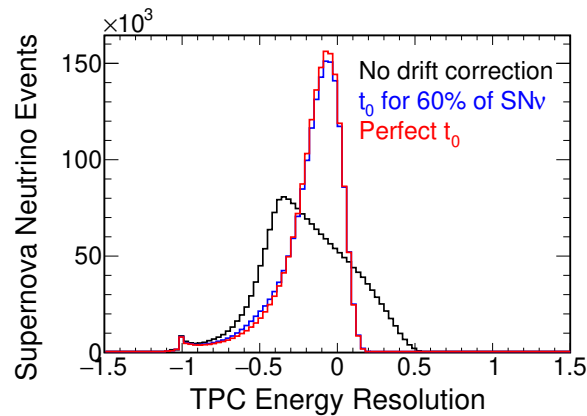


**Figure 5.45.** The energy resolution for supernova neutrino events when reconstructed by the TPC with the drift distance corrected using three assumptions on the performance of the PD system. The options considered range from drift correction for no events (black), to 60% of events (blue), to 100% of events (red).

**Calorimetric energy.** Physics deliverable: the PD system should be able to provide a calorimetric energy measurement for low-energy events, like SNBs, complementary to the TPC energy measurement. Improving the energy resolution will enable us to extract the maximum physics from a SNB (see Volume II, DUNE physics, chapter 7), and with the goal to achieve energy resolution comparable to the TPC, we can take full advantage of the anti-correlation between the emission of light and charge signals imposed by the conservation of energy. In addition, this requirement allows the photon detection system to provide redundancy if a supernova occurs during adverse detector conditions. If the argon purification system is offline, the photon signal is significantly less sensitive to electronegative impurities, and if the drift field is low, the reduced charge signal can be partially recovered by increased light.

The calorimetric energy performance was studied for supernova burst neutrino events simulated in the far detector for a range of different detector performance assumptions. The energy reconstruction was simple, correcting the total observed amount of photons for the average number of photons expected per MeV as a function of position along the drift direction. Events were required to be well away from the side walls to avoid any possible edge effects. The energy resolution vs. true energy is shown in figure 5.46. There is a significant benefit to achieving a photon detector with an average light yield of 20 PE/MeV, where the PD system and TPC have comparable resolution for the lowest energy (<7 MeV) supernova neutrinos. Past this light yield, the improvement appears to plateau in this analysis. This physics deliverable thus sets a requirement, FD-SP-3: light yield, of 20 PE/MeV averaged over the active volume.

While options that can improve the uniformity of the detector are not essential to achieve required resolution, they are likely to improve the calorimetric energy reconstruction above and beyond total light yield. A detector that is more uniform will be easier to calibrate, and the impact of uncertainties on the optical parameters of the liquid argon will be reduced. This effect is potentially important for supernova neutrinos, and certainly more important for the beam neutrino events described in the next section. In addition, for Xe-doping specifically, speeding up the late light will allow for flashes that are narrower in time, reducing the amount of radiological contamination mixed in with the signal, which is of particular importance with these relatively small signals.

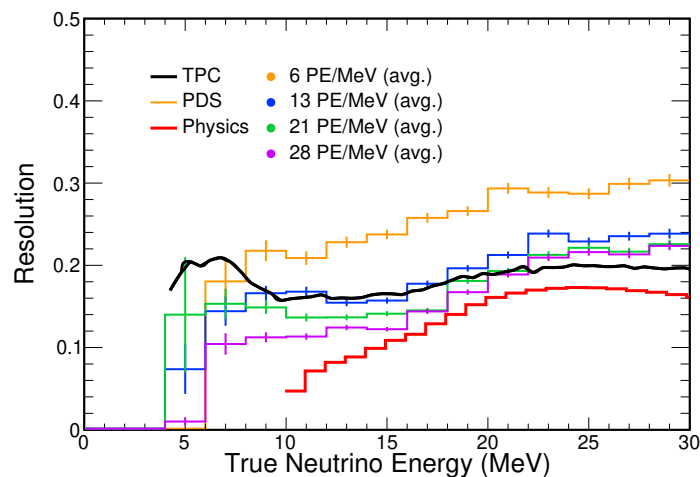


**Figure 5.46.** The energy resolution (determined from the distribution widths of the fraction of difference between reconstructed and true to true neutrino energy for simulated events) for supernova neutrino events when reconstructed directly through PD system calorimetry for a range of light yields, represented by different colors. The red line labeled *Physics* shows the energy smearing inherent to the neutrino interactions and thus serves as a theoretical minimum resolution. The black line shows the energy resolution achieved by the TPC, defined in a similar way. The performance improves significantly up until approximately 20 PE/MeV where the PD system and TPC give comparable resolution below approximately 7 MeV.

#### 5.16.1.4 Beam neutrinos

The PD system is not required for fiducializing beam neutrino events since the pulsed beam will provide sufficient precision to place the interactions in space. However, the PDs can potentially contribute to the energy measurement, and the better timing resolution can help identify Michel electrons from muon and pion decay.

**Calorimetric energy.** Physics deliverable: the PD system should be able to provide a calorimetric energy measurement for high-energy events, like neutrinos from the LBNF beam, complementary to the TPC energy measurement. Neutrino energy is an observable critical to the success of the oscillation physics program (see Volume II, DUNE physics, chapter 5), and a second independent measurement can provide a cross-check that reduces systematic uncertainties or directly improves resolution for some types of events.

In order to provide a meaningful cross-check, the resolution and uncertainty of the PD system measurement must be comparable to the calorimetric resolution of the TPC. The limit on this measurement will likely come from how well the efficiency of the detector and the optical properties of the argon can be determined (both must be known to approximately 5% to have a comparable measurement of electron shower energy), which define a program of measurements between now and the operation of the detector rather than requirements on the system itself. The requirement that does flow down from this is that the dynamic range of the system be sufficient to allow for accurate measurement of the amount of light reaching the PD system.

Some amount of saturation is tolerable since it can be corrected for using the pulse shape or the neighboring unsaturated channels. However, if the saturation is too large, and too many channels are

saturated, the corrections become difficult, so we require that no more than 20% of beam neutrino events have saturating channels (SP-PDS-16: dynamic range), consistent with but looser than the TPC requirement of 10%.

We studied the likelihood of channels saturating by simulating beam neutrino events in the far detector. The likelihood of saturation depends on the digitization frequency, the dynamic range, and the collection efficiency of the detector design. Assuming the baseline electronics, a 12-bit and 80 MHz digitizer, we find the likelihood of saturation vs. average light yield shown in table 5.12.

**Table 5.12.** The fraction of beam events which have saturating PD system channels for different light yields, and the corresponding PD system collection efficiencies.

| Avg. Light Yield (PE/MeV) | Collection Efficiency (%) | Saturation Fraction (%) |
|---------------------------|---------------------------|-------------------------|
| 6                         | 0.88                      | 6                       |
| 13                        | 1.8                       | 13                      |
| 21                        | 2.6                       | 20                      |
| 28                        | 3.5                       | 24                      |

**Michel electron tagging.** Physics deliverable: the PD system should be able to identify events with Michel electrons from muon and pion decays. The identification of Michel electrons can improve background rejection for both beam neutrinos and nucleon decay searches. Some Michel electrons are difficult to identify with the TPC since they appear simultaneous within the time resolution of the TPC and colinear with their parent. However, because the PD system can observe the fine time structure of events in the detector, it can identify Michel electrons that appear separated in time from the main event. While DUNE-specific studies of Michel electron tagging have not been performed, the LArIAT experiment has demonstrated that Michel electrons can be identified and studied using photon signals.

### 5.16.2 Options to enhance light yield uniformity

Due to a combination of geometric effects and the impact of Rayleigh scattering, the baseline SP PD system design will result in non-uniformity of light collection along the drift direction. Light emitted from interactions close to the APAs has an order of magnitude larger chance of being detected compared to interactions close to the CPA.

Though the designs described in the previous sections will meet the PD performance requirements, two options for enhancing both the light yield and light yield uniformity are under consideration. Both approaches mitigate the impact of a short Rayleigh scattering length by converting 127 nm scintillation photons to longer wavelength photons with a significantly longer Rayleigh scattering length. An increase in uniformity will enhance the ability to do calorimetric reconstruction with scintillation light, thus enhancing the charge-based energy reconstruction and increasing the efficiency of triggering on low energy signals.

These options will be pursued in parallel with the baseline design and may be implemented after appropriate review if resources are available and if they do not interfere with, or produce unacceptable risk for, the baseline design schedule.

### 5.16.2.1 Coated reflector foils on the TPC cathode

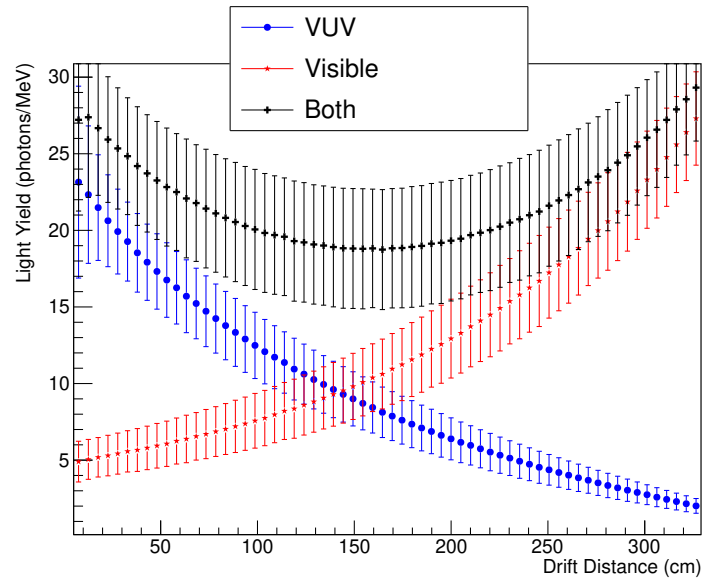
In this option, scintillation light falling on the cathode plane is converted into the visible wavelengths and reflected. Installing the foils on the cathode represents the option with the minimal impact on the current design of the HV system (field cage and cathode) and ensures a good uniformity of the light yield across the detector. This light could then be detected by the PDs embedded in the APA, improving the overall collection efficiency. This option would require at least a fraction of the light collectors be sensitive to visible light. This sensitivity to visible light can be achieved in two ways: (1) by coating the X-ARAPUCA with TPB instead of PTP, which results in the same WLS combination as the double shift bars (whose performance is measured in ProtoDUNE-SP) and/or (2) by leaving some of the X-ARAPUCA detectors without a WLS coating but with an appropriate dichroic filter. In the former case, the PDs are sensitive to both the direct and reflected light, in the latter case only to the reflected light.

Figure 5.47 shows the simulated results of a configuration where 50% of the APA light collectors can record both direct scintillation light and the reflected visible light from the CPA, and 50% are left uncoated to maximize uniformity. This results in an enhancement of the total light collection close to the cathode (black points).

Introducing the foils on the cathode may also enable drift position resolution using only scintillation light. This requires the PDs to differentiate direct VUV light from re-emitted visible light (i.e., requires two types of PD) and sufficient timing of arrival of first light.

Coated reflector foils are manufactured through low-temperature evaporation of TPB on dielectric reflectors e.g., 3M DM2000 or Vikuiti ESR. Foils prepared in this manner have been successfully used in dark matter detectors such as WArP [93]. Recently, they have been shown to work in LArTPCs at neutrino energies, namely in the LArIAT test beam detector [94]. In LArIAT, they have been installed on the field cage walls and, during the last run, on the cathode. An alternative solution would be to use Polyethylene Naphthalate (PEN) instead of TPB. This wavelength-shifter has a similar emission spectrum to TPB [95] but is provided in sheets, which could greatly simplify the production and installation. The choice of using PEN depends on demonstrating that its performance holds in LAr; these studies are ongoing. The method of foil installation is being developed in collaboration with the DUNE HV consortium, with the objective of minimizing the impact on the CPA design.

A run has been performed using the CERN FLIC 501 prototype TPC, with the DUNE-like resistive cathode covered with a non-perforated DM2000 foil evaporated with TPB. No obvious HV problems were observed, but the data is still being analyzed to understand whether any field distortions were present. A second run with the cathode coated with PEN was performed in March 2019. The comparison of effects on the electric field between the two solutions is in progress. Preliminary studies show that PEN seems to work as a wavelength-shifter at liquid argon temperatures but may not be as efficient as TPB. A future run will involve running with a perforated TPB-coated foil. The presence of the holes maintains the resistive character of the cathode and minimizes the effect of electric field distortions.



**Figure 5.47.** Predicted light yield in the PD system with WLS-coated reflector foils on the CPA. Blue points represent direct VUV light impinging on the PDs assuming a 2.5% photon detection efficiency and 70% wire mesh transmission and half of the detectors left uncoated; red stars — represent scintillation light that has been wavelength-shifted and reflected on the CPA assuming the same photon detection efficiency folded in with an 80% transmittance of the filters to visible light. Black points show the sum of these two contributions.

### 5.16.2.2 Doping liquid argon with trace parts of xenon

This option exploits the conversion of the LAr 127 nm light to 175 nm by doping the LAr volume with 20–100 ppm of xenon. While there are indications that the absolute light yield in xenon-doped argon may be higher than in pure argon, in the current estimates, we assume the yields are the same. In this case, the source of the improved performance described here is the much longer Rayleigh scattering length for 175 nm light. The improvement is illustrated in figure 5.48 from a DUNE PD simulation, assuming an absorption length for the scintillation light of 20 m. The gain in average yield for events near the CPA is about a factor of five.

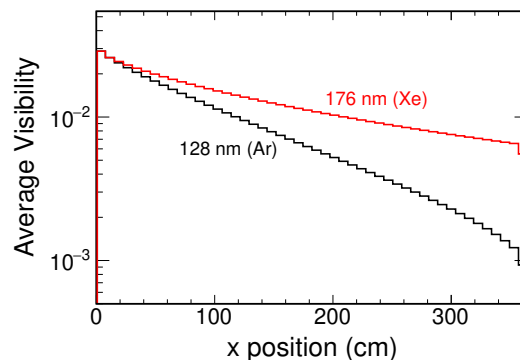


**Figure 5.48.** Simulation of visibility of 128 nm (LAr with xenon doping) and 176 nm (LAr scintillation) light in a SP module.

Doping with xenon also affects the time structure of the scintillation light and in particular reduces the fraction of late light. Having a light signal of shorter duration can bring advantages both in physics, such as making it easier to tag Michel electrons from pions and electrons, and in the electronics required. The longer wavelength of the scintillation light resulting from the Xe doping allows the possibility of simplifying the design of the PD system light collectors (X-ARAPUCA) by dispensing with the use of the outer layer of wavelength shifting material, thereby reducing costs and simplifying the handling of the light collectors during storage and installation.

Doping the argon with xenon is facilitated by the fact that at the DUNE FD the argon is transported from the surface to underground as gas before it is re-condensed for delivery to the cryostats. Xenon and argon can therefore be mixed in gas form before condensation; in consultation with the cryogenic experts, we have identified locations where this mix could be achieved. Since the operations take place at room temperature, the implementation is relatively straightforward.

**Critical issues and R&D work.** Xenon doping must not adversely affect the performance of the TPC, and while the doping is expected to be neutral or even beneficial, its effects on charge yield, drift lifetime, and HV stability need to be established. There is experience in xenon doping of argon both at CERN and Fermilab, and tests for the TPC effects are being designed. More detailed R&D is needed to optimize the xenon doping fraction and its interaction with the light-detection system. This can be conducted on a time scale of about a year by a small number of dedicated investigators using resources that, mostly, are expected to be available at Fermilab and CERN.

## Chapter 6

# Calibration hardware for single-phase

### 6.1 Introduction

A detailed understanding of the overall detector response is essential for achieving DUNE physics goals. The precision with which each calibration parameter must be measured is spanned by the requirements on the systematic uncertainties for the LBL and SNB physics programs at DUNE. The calibration program must generally provide measurements at the few-percent-or-better level stably across an enormous volume and over a long period and provide sufficient redundancy. This chapter focuses on describing the dedicated calibration hardware systems to be deployed for the DUNE SP module that provide necessary information beyond the reach of external measurements and existing sources and monitors.

A detailed description of the calibration strategy for the DUNE FD is provided in Volume II, DUNE physics, chapter 4 of this TDR. In brief, the calibration strategy uses existing sources of particles, external measurements, and dedicated external calibration hardware systems. Existing calibration sources for DUNE include beam or atmospheric neutrino-induced samples, cosmic rays, argon isotopes, and instrumentation devices such as LAr purity and temperature monitors. Dedicated calibration hardware systems consist of laser and neutron source deployment systems. External measurements by ProtoDUNE-2 and SBN experiments will validate techniques, tools, and the design of systems applicable to the DUNE calibration program. These sources and systems provide measurements of the detector response model parameters, or provide tests of the response model itself. Calibration measurements can also provide corrections to data, data-driven efficiencies, systematics, and particle responses.

The dedicated calibration hardware systems for the SP module include an ionization laser system, a photoelectron laser system, and a pulsed neutron source system. The possibility of deploying a radioactive source system is also currently being explored. The responsibility of the calibration hardware systems falls under the joint SP and DP calibration consortium, which was formed in November 2018.

Section 6.2 discusses general aspects driving the calibration program: scope, requirements and data taking strategy. The baseline calibration hardware designs are described in section 6.3 and respective subsections.

Section 6.3.2 describes the baseline design for the ionization laser system that provides an independent, fine-grained measurement of the electric field throughout the detector, which is an essential parameter that affects the spatial and energy resolution of physics signals. Volume II, DUNE physics, of this TDR assumes that the FV is known to the 1 % level. Through measurements of the spatial distortions and drift velocity map, the laser calibration system mainly helps define the detector FV, thus allowing for the correct prediction of the FD spectra. The laser system also offers many secondary uses such as alignment checks, stability monitoring, and diagnosing detector performance issues. Possible electron lifetime measurements are under study. With the goal of knowing precisely the direction of the laser beam tracks, an independent laser beam location system (LBLS) is also planned, and is described in section 6.3.3. Alternative designs for the ionization laser system that may improve the physics capability and/or reduce overall cost are also under development and are described in appendix, section 6.7.1. Section 6.3.4 describes the photoelectron laser system that can be used to rapidly diagnose electronics or TPC response issues along with many other useful measurements such as integrated field across drift, drift velocity, and electronics gain.

Section 6.3.5 describes the baseline design for the pulsed neutron source (PNS) system, which provides a triggered, well defined, energy deposition from neutron capture in Ar detectable throughout the detector volume. Neutron capture is an important component of signal processes for SNB and LBL physics, enabling direct testing of the detector response spatially and temporally for the low-energy program and the efficiency of the detector in reconstructing the low-energy spectra. A spatially fine-grained measurement of electron lifetime is also planned with this source. The proposed radioactive source deployment system (RSDS) described in the appendix, section 6.7.3, is in many ways complementary to the PNS system, and can provide at known locations inside the detector a source of gamma rays in the same energy range of SNB and solar neutrino physics. The RSDS is the only calibration system that could probe the detection capability for single isolated solar neutrino events and study how well radiological backgrounds can be suppressed. In contrast, the PNS is externally triggered and does not provide such a well defined source location for gamma rays inside the detector. On the other hand, the PNS can probe the uniformity of the full detector, while the RSDS could only scan the ends of the detector.

For all the calibration hardware systems, the goal is to deploy prototype designs and validate them at ProtoDUNE-2 during the post long shutdown 2 (LS2) running at CERN. The validation plan for calibration systems at ProtoDUNE-2 and other experiments is described in section 6.3.6.

Section 6.4 describes interfaces calibration has with other DUNE consortia, especially with DAQ which are described in more detail in section 6.4.1.

Sections 6.5 and 6.6 conclude the chapter with descriptions of the aspects related to construction and installation of the systems, as well as organizational aspects, including schedule and milestones, discussed in section 6.6.4.

## 6.2 Calibration overview

This section focuses on the general aspects of calibrations in DUNE: the scope of the consortium activities and planned systems; the physics and performance requirements driving the design; and the overall strategy for usage of the systems, in combination with natural sources.



### 6.2.1 Scope

The scope of the calibration consortium includes a laser ionization system, a photoelectron laser system, a laser beam location system, and a pulsed neutron source system. In addition, the consortium is evaluating a radioactive source deployment system. The calibration consortium is responsible for design through commissioning in the SP module for these calibration devices and their associated feedthroughs. Validating the designs of calibration systems at ProtoDUNE-2 (and other experiments as relevant) is also included under the scope of the consortium. Figure 6.1 shows the subsystems included under the calibration consortium.

Chapters 3, 4, 5, and 8 of Volume IV, The DUNE far detector single-phase technology, of this TDR describe other hardware essential for calibration such as CE external charge injection systems, HV monitoring devices, PD system stability monitoring devices, and cryogenics instrumentation and detector monitoring devices, respectively. The scope of these systems is described by their respective consortia, and the calibration consortium has substantial interfaces with these consortia. The use of other calibration sources such as external measurements and existing sources of particles (e.g., muons, pions) is discussed in the calibration section of TDR Volume II, DUNE physics, chapter 4.

We are pursuing the effects of calibration on physics and related studies. Calibrations also require simulations (e.g., E field) to identify desirable locations for calibration devices in the cryostat, away from regions of high E field, so that their presence does not induce large field distortions. The design of the calibration systems and understanding the related physics requires coordination with other consortia and groups. This is discussed in section 6.4.

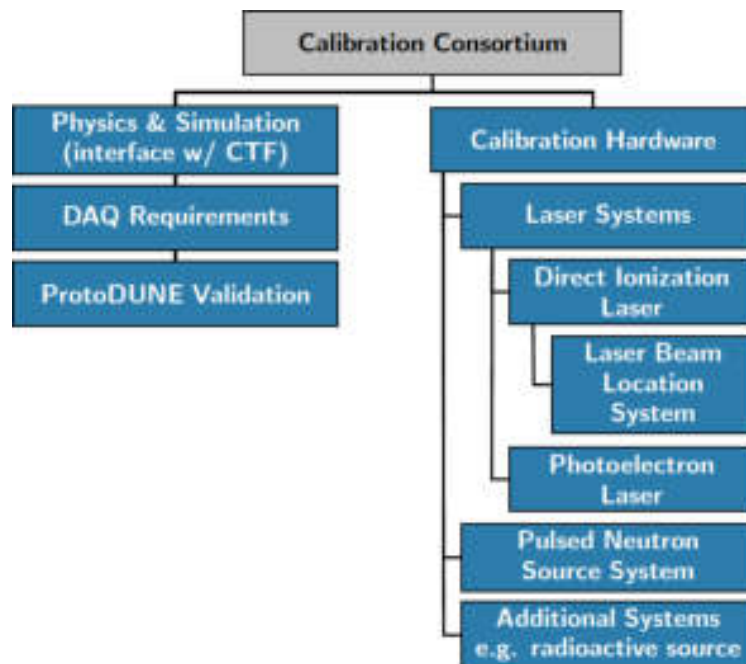


**Figure 6.1.** Calibration consortium subsystem chart. CTF stands for Calibration Task Force.

## 6.2.2 Design considerations and requirements

Some common design considerations for calibration devices include stability, reliability, and longevity, so calibration systems can be operated for the lifetime of the experiment (20 years). Such longevity is uncommon for any device, so the overall design permits replacing devices where possible, namely the parts that are external to the cryostat. The systems must also adhere to relevant global requirements of the DUNE detector. Table 6.1 shows the top-level overall requirements for calibration subsystems along with global DUNE requirements that are relevant for calibration. For example, DUNE requires the E field on any instrumentation device inside the cryostat to be less than 30 kV/cm to minimize the risk of dielectric breakdown in LAr. Another consideration important for event reconstruction is understanding the maximum tolerable level of noise on the readout electronics due to calibration devices and implementing proper grounding schemes to minimize it. ProtoDUNE-SP is evaluating this. In table 6.1, two values are quoted for most of the parameters: 1) specification, which is the minimum requirement to guarantee baseline performance, and 2) goal, an ideal requirement for achieving improved precision.

For the ionization laser system, the energy and position reconstruction requirements for physics measurements lead to requirements for the necessary precision in measuring the TPC E field as well as its spatial coverage and granularity. The precision of the E field measurement with the laser system must be about 1 % so that the effect from E field on the collected charge, via the dependence of the recombination factor on E field, is well below 1 %. This is also motivated by consistency with the high level DUNE specification of 1 % on field uniformity throughout the volume for component alignment and the HV system. For laser coverage, to keep the E field measurement at the  $\sim 1$  % level, we are aiming for a coverage of 75 % or more of the total FV. The requirement on granularity for the laser is estimated based on the FV uncertainty requirements (1 %) and corresponding uncertainty requirements (1.5 cm) in each coordinate. A specification is set for a voxel size of  $30 \times 30 \times 30$  cm<sup>3</sup>, that should be sufficient to satisfy the FV uncertainty requirements. A goal is set for  $10 \times 10 \times 10$  cm<sup>3</sup>, which could allow for a refinement in precision in some detector regions.

The laser beam location must also meet the level of reconstruction requirement in each coordinate, approximately 5 mm. In order to reach that over distances of up to 20 m, where the latter is the maximum distance that any beam needs to travel to cover all detector voxels, this results in a stringent alignment requirement of  $0.015^\circ$  (or 0.25 mrad) on the pointing precision. The laser beam location system is also designed to check the beam location with a precision of 5 mm over distances of up to 20 m. The data volume for the ionization laser system must be no more than 184 TB/year/10 kt, assuming 800k laser pulses,  $10 \times 10 \times 10$  cm<sup>3</sup> voxel sizes, a 100  $\mu$ s zero suppression window, and two dedicated calibration campaigns per year.

For the PNS system, the system must provide sufficient neutron event rate to make spatially separated precision measurements across the detector of a comparable size to the voxels probed by the laser ( $30 \times 30 \times 30$  cm<sup>3</sup>) for most regions of the detector (75 %). For the SNB program, the sensitivity to distortions of the neutrino energy spectrum depends on the uncertainties in the detection threshold and the reconstructed energy scale and resolution. Studies discussed in the physics TDR present target ranges for the uncertainties in these parameters [96] as a function of energy. The measurements with the PNS system aim to provide response corrections and performance estimates, so those uncertainty targets are met throughout the whole volume. This ensures that each voxel has sufficient neutron event rate (percent level statistical uncertainty).

In terms of data volume requirements, the PNS system requires at least 144 TB/year/10 kt assuming  $10^5$  neutrons/pulse, 100 neutron captures/m<sup>3</sup>, and 130 observed neutron captures per pulse, and two calibration runs per year.

Table 6.2 shows the full set of requirements related to all calibration subsystems. More details on each of the requirements can be found under dedicated subsections.

**Table 6.1:** Calibration specifications.

| Label    | Description                                       | Specification (Goal)   | Rationale   | Validation                            |
|----------|---|--|---|---------------------------------------|
| SP-FD-1  | Minimum drift field                               | > 250 V/cm<br>(> 500 V/cm)   | Lessens impacts of $e^-$ -Ar recombination, $e^-$ lifetime, $e^-$ diffusion and space charge. | ProtoDUNE                             |
| SP-FD-2  | System noise                                      | < 1000 $e^-$   | Provides >5:1 S/N on induction planes for pattern recognition and two-track separation.       | ProtoDUNE and simulation              |
| SP-FD-5  | Liquid argon purity                               | < 100 ppt<br>(< 30 ppt)  | Provides >5:1 S/N on induction planes for pattern recognition and two-track separation.       | Purity monitors and cosmic ray tracks |
| SP-FD-7  | Drift field uniformity due to component alignment | < 1 % throughout volume  | Maintains APA, CPA, FC orientation and shape.   | ProtoDUNE                             |
| SP-FD-9  | APA wire spacing                                  | 4.669 mm for U,V;<br>4.790 mm for X,G  | Enables 100% efficient MIP detection, 1.5 cm $yz$ vertex resolution.                          | Simulation                            |
| SP-FD-11 | Drift field uniformity due to HVS                 | < 1 % throughout volume  | High reconstruction efficiency.   | ProtoDUNE and simulation              |
| SP-FD-13 | Front-end peaking time                            | 1 $\mu$ s  | Vertex resolution; optimized for 5 mm wire spacing.   | ProtoDUNE and simulation              |
| SP-FD-22 | Data rate to tape                                 | < 30 PB/year   | Cost. Bandwidth.  | ProtoDUNE                             |
| SP-FD-23 | Supernova trigger                                 | > 95 % efficiency for a SNB producing at least 60 interactions with a neutrino energy >10 MeV in 12 kt of active detector mass during the first 10 seconds of the burst. | > 95% efficiency for SNB within 20 kpc  | Simulation and bench tests            |
| SP-FD-24 | Local electric fields                             | < 30 kV/cm   | Maximize live time; maintain high S/N.  | ProtoDUNE                             |
| SP-FD-25 | Non-FE noise contributions                        | << 1000 $e^-$  | High S/N for high reconstruction efficiency.  | Engineering calculation and ProtoDUNE |
| SP-FD-26 | LAr impurity contributions from components        | << 30 ppt  | Maintain HV operating range for high live time fraction.                                      | ProtoDUNE                             |

## Chapter 6. Calibration hardware for single-phase

|            |   |  |  |  |
|------------|---|--|--|--|
| SP-FD-27   | Introduced radioactivity                          | less than that from $^{39}\text{Ar}$   | Maintain low radiological backgrounds for SNB searches.  | ProtoDUNE and assays during construction |
| SP-FD-29   | Detector uptime                                   | > 98%<br>(> 99%)   | Meet physics goals in timely fashion.  | ProtoDUNE                                |
| SP-FD-30   | Individual detector module uptime                 | > 90%<br>(> 95%)   | Meet physics goals in timely fashion.  | ProtoDUNE                                |
| SP-CALIB-1 | Ionization laser E field measurement precision    | 1 %  | E field affects energy and position measurements.  | ProtoDUNE and external experiments.      |
| SP-CALIB-2 | Ionization laser E field measurement coverage     | > 75 %<br>(100 %)  | Allowable size of the uncovered detector regions is set by the highest reasonably expected field distortions, 4 %. | ProtoDUNE                                |
| SP-CALIB-3 | Ionization laser E field measurement granularity  | $30 \times 30 \times 30 \text{ cm}^3$<br>( $10 \times 10 \times 10 \text{ cm}^3$ ) | Minimum measurable region is set by the maximum expected distortion and position reconstruction requirements.      | ProtoDUNE                                |
| SP-CALIB-4 | Laser beam location precision                     | 0.5 mrad<br>(< 0.5 mrad)   | The necessary spatial precision does not need to be smaller than the APA wire gap.                                 | ProtoDUNE                                |
| SP-CALIB-5 | Neutron source coverage                           | > 75 %<br>(100 %)  | Set by the energy resolution requirements at low energy.   | Simulations                              |
| SP-CALIB-6 | Ionization laser data volume per year (per 10 kt) | > 184 TB/yr/10kt<br>(> 368 TB/yr/10kt)   | The laser data volume must allow the needed coverage and granularity.  | ProtoDUNE and simulations                |
| SP-CALIB-7 | Neutron source data volume per year (per 10 kt)   | > 144 TB/yr/10kt<br>(> 288 TB/yr/10kt)   | The pulsed neutron system must allow the needed coverage and granularity.  | Simulations                              |

### 6.2.3 Strategy

Once the far detector is filled and at the desired high voltage, it immediately becomes live for all non-beam physics signals, so it is important to tune the detector response model with calibration data as early as possible. Moreover, since both beam and non-beam physics data will have a fairly uniform rate, regular calibrations in order to monitor space and time dependencies are also needed.

Following those considerations, the strategy for calibration data taking will be organized around three specific periods:

**Commissioning.** As soon as the detector is full, with HV on and the DAQ operational, it is useful to take laser calibration data. The main goal is to help identify problems in the APA wires or the electronics channels, or large cool-down distortions. Depending on how long the ramp-up will take, it could be useful to take data before the HV reaches the nominal level, because we can identify problems earlier and possibly learn about dependency of various detector parameters with E field.

**Table 6.2.** Full list of Specifications for the Calibration Subsystems.

| Quantity/Parameter                               | Specification                     | Goal                        |
|--|-----------------------------------|-----------------------------|
| Noise from calibration devices                   | $\ll 1000$ enc                    |                             |
| Max. E field near calibration devices            | $< 30$ kV/cm                      | $< 15$ kV/cm                |
| <b>Direct Ionization Laser System</b>            |                                   |                             |
| E field measurement precision                    | 1%                                | $< 1\%$                     |
| E field measurement coverage                     | $> 75\%$                          | 100%                        |
| E field measurement granularity                  | $< 30 \times 30 \times 30$ cm     | $10 \times 10 \times 10$ cm |
| Top field cage penetrations (alternative design) | to achieve desired laser coverage |                             |
| Data volume per 10 kton                          | 184 TB/year                       | 368 TB/year                 |
| Longevity, internal parts                        | 20 years                          | $> 20$ years                |
| Longevity, external parts                        | 5 years                           | $> 20$ years                |
| <b>Laser Beam Location System</b>                |                                   |                             |
| Laser beam location precision                    | 0.5 mrad                          | 0.5 mrad                    |
| Longevity  | 20 years                          | $> 20$ years                |
| <b>Photoelectron Laser System</b>                |                                   |                             |
| Longevity, internal parts                        | 20 years                          | $> 20$ years                |
| Longevity, external parts                        | 5 years                           | $> 20$ years                |
| <b>Pulsed Neutron Source System</b>              |                                   |                             |
| Coverage   | $> 75\%$                          | 100%                        |
| Data volume per 10 kton                          | 144 TB/year                       | 288 TB/year                 |
| Longevity  | 3 years                           | $> 20$ years                |

**Early data.** During the early stages of data-taking, the goal is to do the fullest possible fine-grained laser and neutron calibration (E field map, lifetime, low energy scale/resolution response) as early as possible, so that all the physics can benefit from a calibrated detector from day 1. These results should be combined at a later stage with detector-wide average measurements with cosmics.

**Stable data-taking.** The main goal of calibrations during stable data-taking is to track possible variations of detector response parameters, and contribute to constraining the detector systematics. We expect to combine fine-grained, high statistics scans at regular time intervals — twice a year for laser, six times for the pulsed neutron source — with more frequent coarse-grained scans (e.g., photoelectron laser, large voxel ionization laser scan). These, combined with analysis of cosmic ray and radiological backgrounds data, can alert to the need of additional fine scans in particular regions.

### 6.3 Calibration systems

DUNE plans to build two primary systems dedicated to calibrate the SP module — a laser system and a pulsed neutron source system — both of which require interfaces with the cryostat, that are described in section 6.3.1.

The laser system is aimed at determining the essential detector model parameters with high spatial and time granularity. The primary goal is to provide maps of the drift velocity and E field, following a position-based technique already proven in other LArTPC experiments. Two laser sub-systems are planned. With high intensity coherent laser pulses, charge can be created in long straight tracks in the detector by direct ionization of LAr with the laser beams. This is described in section 6.3.2. An auxiliary system aimed at an independent measurement and cross-check of the laser track direction is described in section 6.3.3. On the other hand, laser excitation of targets placed on the cathode creates additional charge from well-defined locations that can be used as a general TPC monitor and to measure the integrated drift time. This is described in section 6.3.4.

The PNS system provides a “standard candle” neutron capture signal (6.1 MeV multi-gamma cascade) across the entire DUNE volume that is directly relevant to the supernova physics signal characterization thus validating the performance of the detector in the low energy regime. The PNS system is described in detail in section 6.3.5.

The physics motivation, requirements and design of these systems are described in the following subsections. Alternative designs for the ionization laser system, pulsed neutron source system, as well as the proposed radioactive source deployment system, are described in sections 6.7.1, 6.7.2, and 6.7.3 of the appendix, respectively.

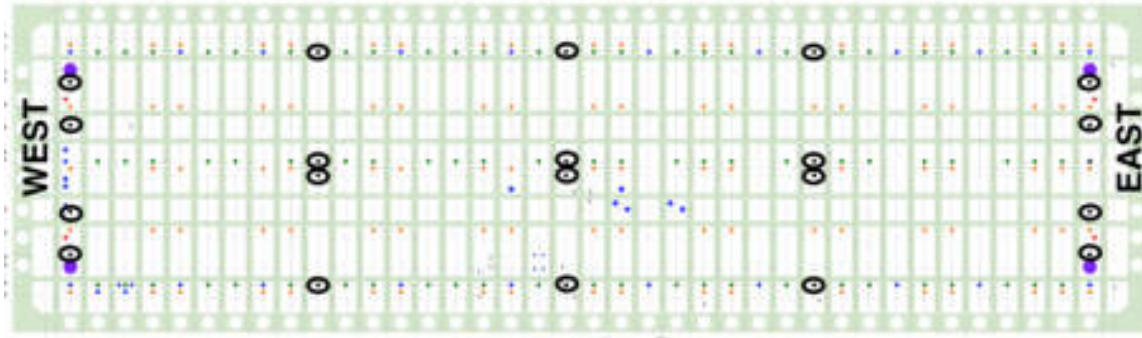
#### 6.3.1 Cryostat configuration for calibration systems

Figure 6.2 shows the current cryostat design for the SP module with penetrations for various subsystems. The penetrations dedicated to calibration are the highlighted black circles.

In addition to these dedicated ports, there are plans to use the DSS and cryogenics ports (orange and blue dots in figure 6.2) as needed to route cables for other calibration systems, e.g., fiber optic cables for the PD calibration system, which is described in chapter 5. DSS and cryogenics ports can be accommodated by feedthroughs with a CF63 side flange for this purpose.

The current plan is to use the calibration ports for several different purposes, but their placement is largely driven by requirements for the ionization track laser. The ports toward the center of the cryostat are placed near the APAs, where the E field is small, to minimize any risks due to HV discharge. HV is not an issue for the far east and west ports since they are located outside the FC and the penetrations are located close to mid-drift (a location favorable for possible source deployment). Implementing the baseline ionization track laser system as described in section 6.3.2 requires 12 feedthroughs, the three central ones in each of the four TPC drift volumes; this arrangement allows lasers to be used for full volume calibration of the E field and associated diagnostics (e.g., HV).

The distance between any two consecutive feedthrough columns shown in figure 6.2 is approximately 15 m. Since the MicroBooNE laser system has shown that tracks will propagate over that detector’s full 10 m length, this distance is considered reasonable. Assuming that the effects of Rayleigh scattering and self-focusing (Kerr effect) do not limit the laser track length, this laser arrangement could illuminate the full volume with crossing tracks in the central region, and single



**Figure 6.2.** Top view of the SP detector module cryostat showing various penetrations. Circles highlighted in black are multi-purpose calibration penetrations. The green dots are TPC signal cable penetrations. The blue ports are cryogenics ports. The orange ports are DSS penetrations. The larger purple ports at the four corners of the cryostat are human access ports.

tracks in the region closer to the end-walls. At this time, the maximum usable track length is unknown, and it may be that the full 60 m detector module length could be covered by the laser system after optimization.

Throughout this chapter, the following convention for the coordinate axes will be used:  $x$  is parallel to the drift direction,  $y$  is the vertical, and  $z$  is parallel to the beamline. This is illustrated in chapter 8 figure 8.3.

### 6.3.2 Laser calibration: ionization system

Through its effect on drift velocity, recombination, and lifetime, the E field is a critical parameter for physics signals as it ultimately affects the spatial resolution and energy response of the detector. The primary purpose of a laser system is to provide an independent, fine-grained estimate of the E field in space and time. It would be extremely valuable to achieve measurements of electron lifetime with the laser system, but the feasibility of that is still under discussion. The R&D plan in ProtoDUNE-2 will address the feasibility of carrying out charge-based measurements which, if successful, would open up the possibility of using the laser to measure electron lifetime. So, except where specifically indicated, the rest of this section will focus on drift velocity and E field measurement.

#### 6.3.2.1 Physics motivation

Because it measures spatial distortions of straight tracks, the laser system actually measures the local drift velocity field directly and helps define the detector FV, and this in itself is an important input for the LBL analysis. However, it is still important to use information independent of the charge in order to disentangle effects like lifetime and recombination from E field distortions. The laser system can do this, by using the position information to derive the E field from the local velocity map, taking into account the colinearity between both vectors, and the relatively well studied relation between the magnitude of the drift velocity and the E field, considering a temperature dependence (see [97] and references [29, 45-58] therein). A laser system also has the intrinsic advantage of being immune to recombination effects, thus eliminating particle-dependent effects.

Several sources may distort the E field temporally and/or spatially in the detector. Current simulation studies indicate that positive ion accumulation and drift (space charge) due to ionization sources such as cosmic rays or  $^{39}\text{Ar}$  is small in the DUNE FD, causing E field distortions of at most 0.1 % [98]. However, not enough is known yet about the fluid flow pattern in the FD to exclude the possibility of stable eddies that may amplify the effect for both SP and DP modules. This effect can be further amplified significantly in the DP module due to accumulation in the liquid of ions created by the electron multiplication process in the gas phase. Additionally, other sources in the detector (especially detector imperfections) can cause E field distortions. For example, FC resistor failures, non-uniform resistivity in the voltage dividers, CPA misalignment, CPA structural deformations, and APA and CPA offsets and deviations from flatness can create localized E field distortions. These effects are presented in figures 6.3 and 6.4, showing the effect of a few % on the E field from 2 cm CPA position tilts and up to 4 % from FC single resistor failures.

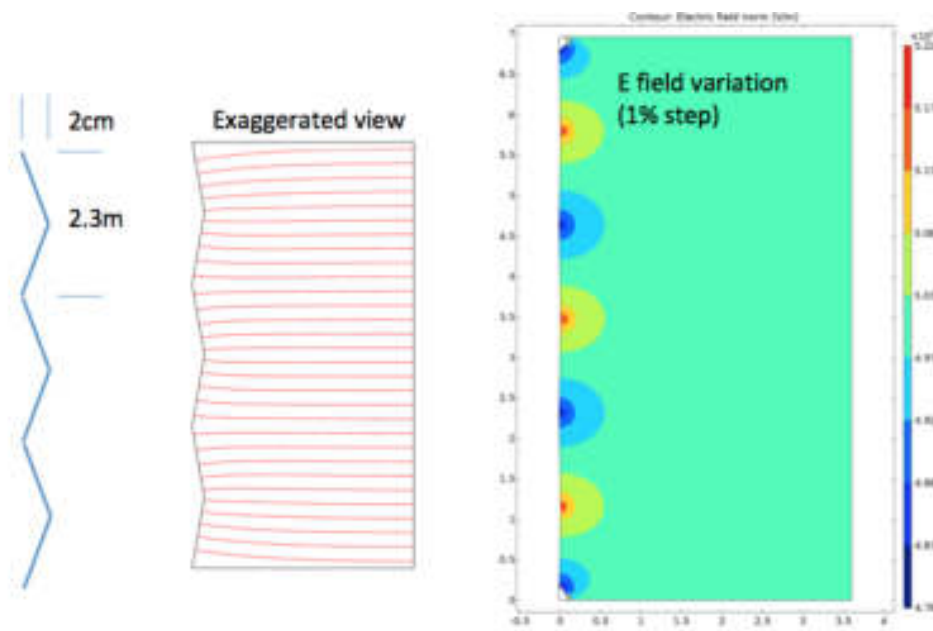


**Figure 6.3.** Illustration of a possible distortion of the CPA position [99], assuming a 2 cm swing, and its impact on E field (right).

In both SP and DP modules, a resistor failure will create significant, local E field distortions that must be identified. In the DP module, four resistors would have to fail to cause a failure across the FC gap, but even one failure in the SP module can have an effect; this may be partly, but not completely, mitigated by modifying the HV. While the resistor failure will be detected temporally, its location in space is not possible to determine from slow controls monitoring data. Misalignments of detector objects or deformations may also create E field distortions; while individual effects may be small, it is possible to have a combined, significant effect. Each individual E field distortion may add in quadrature with other effects, and can aggregate up to 4 % under certain conditions. Understanding all these effects requires in situ measurement of E field for proper calibration.

Useful secondary uses of laser include alignment (especially modes that are weakly constrained by cosmic rays), stability monitoring, and diagnosing detector performance issues (e.g., HV). Mis-



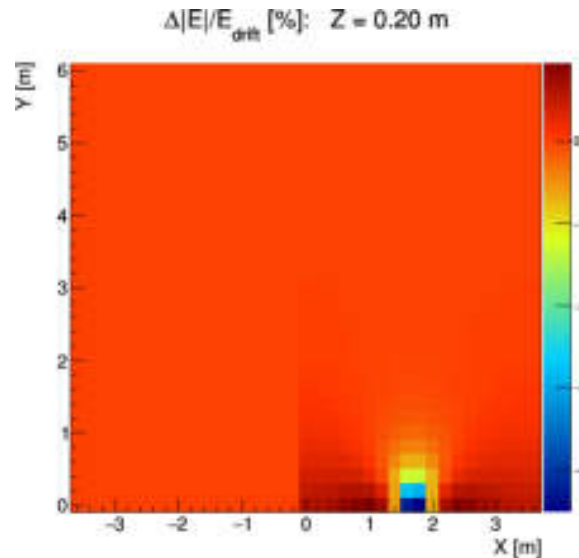


**Figure 6.4.** Impact on E field magnitude distortions of a single FC resistor failure [100].

alignment may include physical deformation and/or rotations of objects within the detector. Given the expected low rate of cosmic ray events (about 3500/day/10-kt, inclusive) at the underground location, calibration with cosmic rays is not possible over short time scales. Even over long time scales, certain alignment directions are difficult to assess with cosmic rays alone, such as distortions of the detector that preserve the gap widths and do not shift the APAs in  $x$  near the gaps relative to one another. These distortions include global shifts and rotations in the locations of all detector elements, and crumpling modes where the edges of the APAs hold together but angles are slightly different from nominal.

With respect to electron lifetime, the preliminary results from ProtoDUNE-SP purity monitors and cosmic ray analyses indicate significant variations with time and space, both between monitors at different vertical coordinates (see chapter 8), and between the regions inside and outside the TPC. The possibility of carrying out such measurements with the ionization laser is therefore quite interesting. The ArgonTUBE experiment obtained lifetime measurements with laser [101] compatible with the cosmic ray ones, but it is not clear yet if this is possible at very large scales, since the modelling of the density of ionization charge created along the tracks presents challenges related to the previously mentioned self-focusing. Therefore the characterization of the ionization charge density from laser tracks will be an important goal of the development plan in ProtoDUNE-2.

### 6.3.2.2 Requirements

The energy and position reconstruction requirements for physics measurements lead to requirements on the necessary precision of the laser E field measurement, its spatial coverage and granularity. The next sections discuss the rationale behind each requirement, which we take as the DUNE specification.

**E field precision:** in the LBL and high-energy range, Volume II, DUNE physics, chapter 5 of this TDR states that the calibration information must provide approximately 1 to 2% understanding of

normalization, energy scale and resolution, and position resolution within the detector. Because a smaller E field leads to higher electron-ion recombination and therefore a lower collected charge, distortions of the E field can introduce energy scale bias. To connect this to a specification for the necessary precision of the E field measurement, we note that, via recombination studies [98], we expect a 1 % distortion on E field to lead to a 0.3 % bias on collected charge. Because other effects will contribute to the lepton energy scale uncertainty budget, we consider a goal for the laser system to measure the E field to a precision of  $\sim 1\%$  so that its effect on the collected charge is well below 1 %. This is also motivated by consistency with the high level DUNE specification on field uniformity throughout the volume due to component alignment and HV system, that is set at 1 %. Together with two other high-level DUNE specifications, the APA wire spacing (4.7 mm) and the front end peaking time (1  $\mu$ s), the effect of this E field precision requirement on engineering parameters of the calibration laser system is discussed further in section 6.3.2.3.1.

**E field measurement coverage:** in practice, measuring the E field throughout the whole volume of the TPC will be difficult, so we must establish a goal for the coverage and granularity of the measurement. Until a detailed study of the propagation of the coverage and granularity into a resolution metric is available, a rough estimate of the necessary coverage can be made as follows.

Assuming 4 % as the maximum E field distortion that is expected from a compounding of multiple possible effects in the DUNE FD as described in the previous section, we can then ask what would be the maximum acceptable size of the spatial region uncovered by the calibration system, if a distortion of that magnitude (systematically biased in the same direction) were present in that region. Our criterion of acceptability is to keep the overall E field distortion, averaged over the whole detector, at the 1 % level. To meet this requirement, the aforementioned spatial region should be no larger than 25 % of the total fiducial volume. Therefore, we aim to have a coverage of 75 % or more.

In addition, we need to consider that the method used to estimate E field distortions is based on obtaining position displacement maps [102], and that the comparison between the reconstructed and true direction of a single track does not unambiguously determine a specific displacement map. Having tracks coming from different origins crossing in the same position is a direct way to eliminate that ambiguity, since the displacement vector is given simply by the vector connecting the intersections of the two reconstructed and the two true tracks. A joint iterative analysis of several close-by tracks is the default method for all other positions, but the system design should allow for the maximum possible number of positions for crossing tracks from different beams.

**E field measurement granularity:** volume II (DUNE physics) of this TDR states that a FV uncertainty of 1 % is required. This translates to a position uncertainty of 1.5 cm in each coordinate (see chapter 2). In the  $y$  and  $z$  coordinates, position uncertainty is given mainly by the APA wire pitch, and since this is about 4.7 mm, the requirement is met. In the drift ( $x$ ) direction, the position is calculated from timing, and considering the electronics peaking time of 1  $\mu$ s, the uncertainty should be even smaller.

The position uncertainty, however, also depends on the E field, via the drift velocity. Because the position distortions accumulate over the drift path of the electron, it is not enough to specify an uncertainty on the field. We must accompany it by specifying the size of the spatial region of that

distortion. For example, a 10 % distortion would not be relevant if it was confined to a 2 cm region and if the rest of the drift region was at nominal field. Therefore, what matters is the product of [size of region]  $\times$  [distortion]. Moreover, one can distinguish distortions into two types:

1. Those affecting the magnitude of the field. Then the effect on the drift velocity  $v$  is also a change of magnitude. According to the function provided in [103], close to  $500 \text{ V} \cdot \text{cm}^{-1}$ , the variation of the velocity with the field is such that a 4 % variation in field  $E$  leads to a 1.5 % variation in  $v$ .
2. Those affecting the direction of the field. Nominally, the field  $E$  should be along  $x$ , so  $E = E_L$  (the longitudinal component). If we consider that the distortions introduce a new transverse component  $E_T$ , in this case, this translates directly into the same effect in the drift velocity, which gains a  $v_T$  component,  $v_T = v_L E_T / E_L$ , i.e., a 4 % transverse distortion on the field leads to a 4 % transverse distortion on the drift velocity.

Thus, a 1.5 cm shift comes about from a constant 1.5 % distortion in the velocity field over a region of 1 m. In terms of E field, that could be from a 1.5 % distortion in  $E_T$  over 1 m or a 4 % distortion in  $E_L$  over the same distance.

E field distortions can be caused by space-charge effects due to accumulation of positive ions caused by  $^{39}\text{Ar}$  decays (cosmic ray rate is low in FD), or detector defects, such as CPA misalignments (figure 6.3), FC resistor failures (figure 6.4), resistivity non-uniformities, etc. These effects added in quadrature can be as high as 4 %. The space charge effects due to  $^{39}\text{Ar}$  [98] can be approximately 0.1 % for the single-phase (SP), and 1 % for the DP (dual-phase), so in practice these levels of distortions must cover several meters to be relevant. Other effects due to CPA or FC imperfections can be higher because of space charge, but they are also much more localized. If we assume there are no foreseeable effects that would distort the field more than 4 %, and considering the worst case scenario (transverse distortions), then the smallest region that would produce a 1.5 cm shift is  $1.5 \text{ cm} / 0.04 = 37.5 \text{ cm}$ . This provides a target for the granularity of the measurement of the E field distortions in  $x$  to be smaller than approximately 30 cm, with, of course, a larger region if the distortions are smaller. Given the above considerations, then a voxel size of  $10 \times 10 \times 10 \text{ cm}^3$  appears to be enough to measure the E field with the granularity needed for a good position reconstruction precision. In fact, because the effects that can likely cause bigger E field distortions are problems or alignments in the CPA (or APA) or in the FC, it is conceivable to have different size voxels for different regions, saving the highest granularity of the probing for the walls/edges of the drift volume.

### 6.3.2.3 Design

The design of the laser calibration system for DUNE is largely based on the design of the system built for MicroBooNE [4], which in turn was based on several previous developments [104–107]. A similar system was also built for CAPTAIN [108] and in the near future, will be built for SBND [109]. Operation of the MicroBooNE system has already taken place. A preliminary report was given in [110], and more details on the data analysis are available in [102].

**Design overview.** Ionization of LAr by laser can occur via a multiphoton process in which two-photon absorption [111] leads the atom to the excited states band, and a third photon subsequently

causes ionization. This can only occur with high photon fluxes, and so the lasers must provide pulse energies of 60 mJ or more within a few ns. Unlike muons, the laser beams do not suffer multiple scattering and travel along straight lines determined by the steering mirror optics. The basic measurement consists of generating laser ionization tracks in the TPC and comparing the reconstructed tracks with the direction known from the steering hardware. An apparent curvature of the measured track is attributed to drift velocity, and therefore E field, distortions (either in direction or magnitude).

While the Rayleigh scattering length for 266 nm light is approximately 40 m, additional optics effects may limit the maximum practical range of laser beams of that wavelength to a distance smaller than that. Those can include the Kerr effect due to the dependency of the refractive index on the E field. In the presence of an intense field, such as that caused by the laser beam itself, the change in refractive index can lead to lensing, or focusing, that distorts the coherence of the beam.<sup>1</sup> Despite this, laser beams with lengths of 10 m in LAr have been observed in MicroBooNE, and beams with 20 m lengths (possibly more) can be reasonably expected to obtain with a similar system. This has determined the choice of locating five calibration ports in the cryostat roof at 15 m intervals along each of the four drift volumes of the SP module, for a total of 20 ports. In fact, there are four ports just outside each of the FC end-walls, and 12 ports located over the top FC, close to the APA of each drift volume, as shown in figure 6.2. As is discussed further below, the number of ports currently assigned for the ionization laser system in the baseline design is 12, a compromise between having the maximum possible coverage with crossing tracks and cost considerations.

**Mechanical and optical design for a single port sub-system.** For each of the used calibration ports, a laser sub-system can be schematically represented by figure 6.5 (left) and consists of the following elements:

- a laser box (see figure 6.5, right) that provides
  - a Nd:YAG laser, with the fourth harmonic option providing 266 nm in intense 60 mJ pulses with about 5 ns width, with a divergence of 0.5 mrad. The Surelite SL I-10 laser<sup>2</sup> is a possible choice since it has been successfully used in the past in other experiments.
  - an attenuator and a collimator to control the intensity and size of the beam;
  - a photodiode that gives a TPC-independent trigger signal;
  - a low-power red laser, aligned with the UV laser, to facilitate alignment operations; and
  - a Faraday cage to shield the surrounding electronics from the accompanying electromagnetic pulse.

---

<sup>1</sup>The Kerr effect is so far believed to be the cause of non-homogeneity of the ionization along the laser beam observed in MicroBooNE, which prevents the use of the charge information. Its effect on the position measurement and E field uncertainty has been studied by MicroBooNE.

<sup>2</sup>Amplitude Surelite™ <https://amplitude-laser.com/wp-content/uploads/2019/01/Surelite-I-II-III>.

- a feedthrough (see figure 6.6, left) into the cryostat that provides
  - the optical coupling that allows the UV light to pass through into the cryostat directly into the liquid phase, avoiding distortions due to the gas-liquid interface and the gas itself;
  - a rotational coupling that allows the whole structure to rotate while maintaining the cryostat seal;
  - a periscope structure (see figure 6.6; right) mounted under the rotating coupling that supports a mirror within the LAr;
  - the additional theta rotation of the mirror accomplished by a precision mechanism coupled to an external linear actuator; and
  - both the rotation and linear movements of the steering mechanism read out by precision encoders.

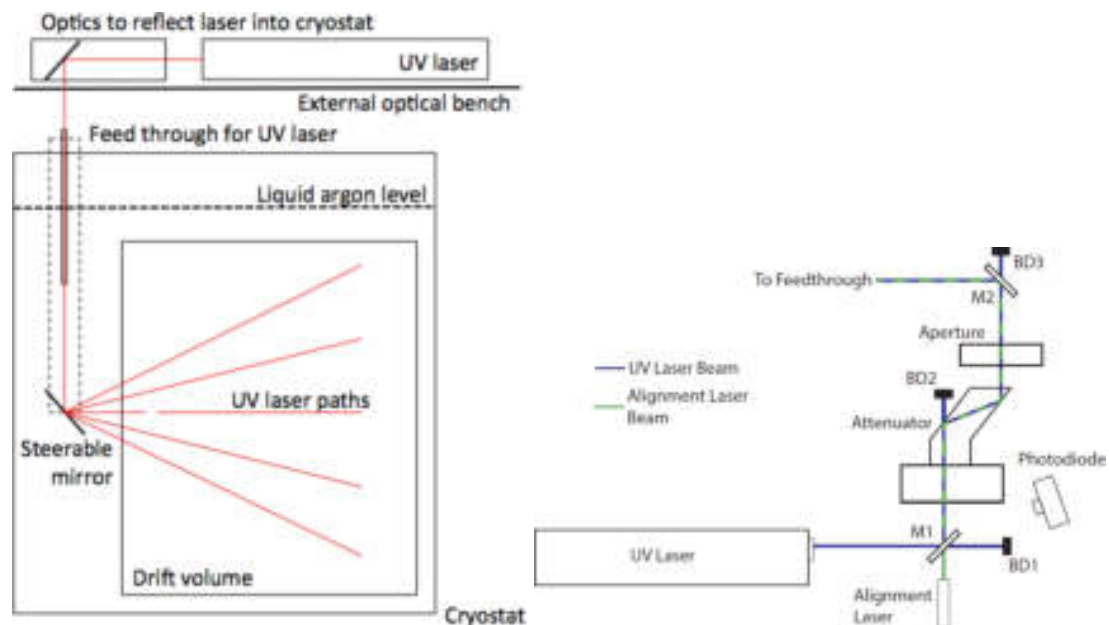


**Figure 6.5.** Left: schematics of the ionization laser system in one port [109]. Right: schematics of the laser box [4].

The goal of the mechanical design of the system is to achieve a precision close to that of the TPC position measurements, so that no single factor dominates the overall systematics. The TPC precision of about 5 mm in the  $y, z$  coordinates is given primarily by the wire spacing of 4.7 mm and 4.8 mm. The precision of about 2 mm on the  $x$  coordinate comes essentially from the  $1 \mu\text{s}$  peaking time of the front-end electronics and the typical drift velocity ( $1.6 \text{ mm}/\mu\text{s}$ ).

The starting point of the laser beams is given by the position of the mirror in the periscope, which is known from construction drawings, warm surveys and cool down calculations. The angle of the beam is given by the angles  $(\theta, \phi)$  of the mirror, which are set by the periscope motors and read out by the encoders. For MicroBooNE, reference [110] quotes a very good 0.05 mrad precision

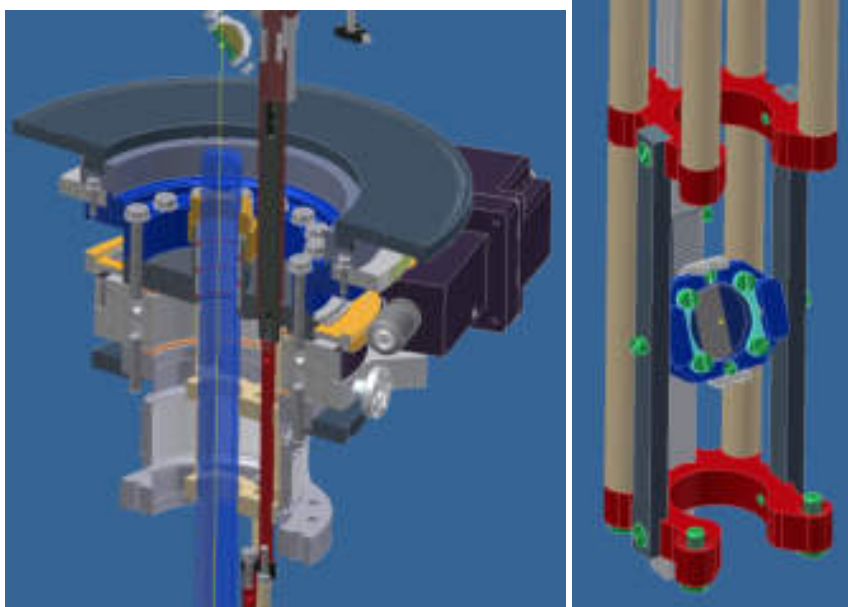


**Figure 6.6.** CAD drawings of the MicroBooNE laser calibration system [4]. Left: calibration port feedthrough. Right: laser beam periscope.

(0.5 mm at 10 m) from the encoders alone, and an overall pointing precision of 2 mm at 10 m, driven mostly by beam size and divergence. In fact, with a 0.5 mrad divergence, we expect the beam to be 5 mm wide at 10 m.

In DUNE, we aim to reach a similar precision. This will require a number of design and installation considerations: having encoders of similar high accuracy, carrying out surveys in various reference frames, and a capability to do location checks with a precision of about 5 mm at 20 m from the beam origin. Therefore we aim to have a system that can locate the beam end point in few positions and attached to different references, at least one per drift volume and laser beam. The independent laser beam location system is described in section 6.3.3.

**Coverage estimations and top FC penetration.** A crucial aspect of the design of the full array is the position of the periscope and the cold mirror with respect to the FC, since its profiles can induce significant shadows and limit the beam's coverage. In order to address this aspect and motivate the design choices, we carried out a set of shadowing calculation studies.

Given that the FC profiles are 4.6 cm wide with only a small 1.4 cm gap between them, the shadows produced if the laser source is located outside the FC would be substantial. We estimate that the maximum angle at which beams can go through is about  $45^\circ$ . Given the limitations of the region above the FC (shown in figure 6.7, left), especially the geometry of the ground plane, it is likely that the mirror cannot be placed much higher up than 40 cm away from the FC. With those assumptions, we have carried out a rough estimation of the fraction of voxels that would be crossed by any unblocked track. For simplicity, we are considering only a single vertical plane, so the coverage is actually overestimated since it does not consider the effect of the FC I-beams, transverse to the FC profiles. Figure 6.7 (right) shows an example of those calculations. Assuming 10 cm voxels and no track directed at the APA, the coverage is at most 30%. Assuming 30 cm voxels and allowing all tracks directed at the APA, the maximum coverage would be 58%.

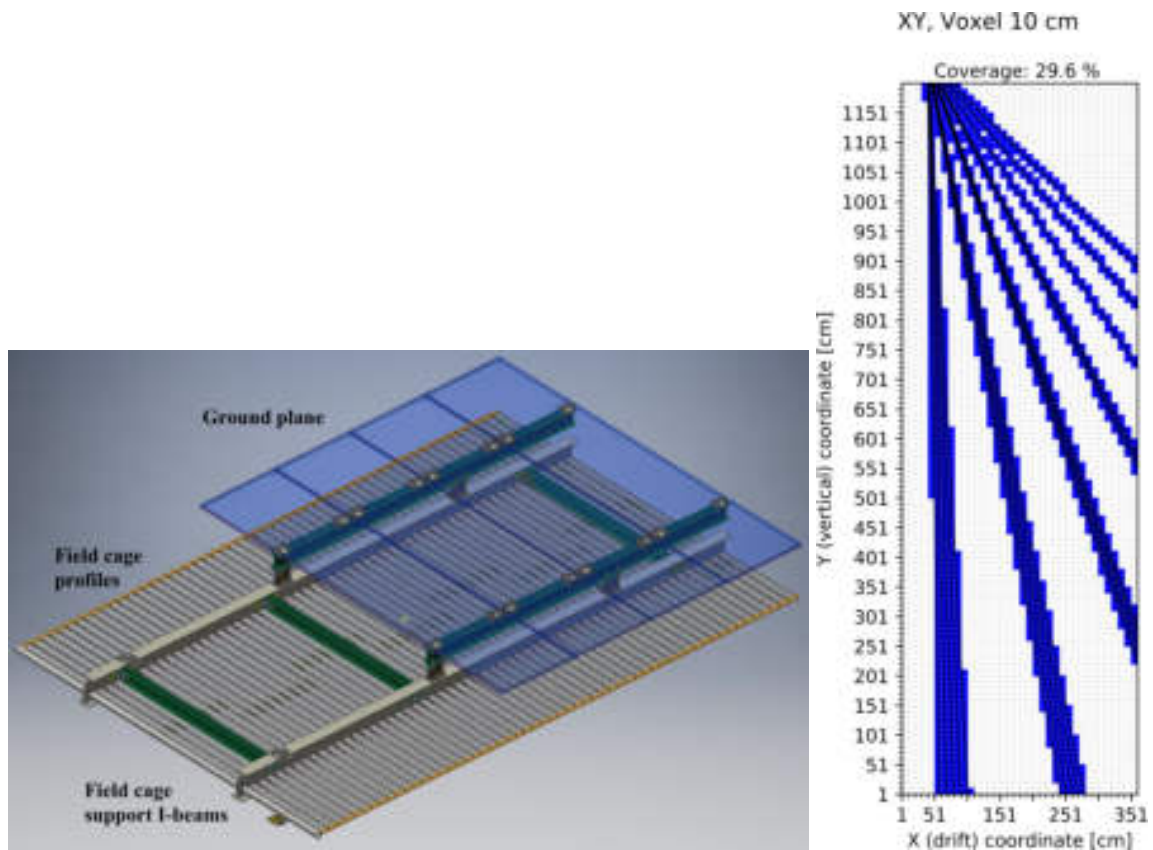


**Figure 6.7.** View of the top field cage (left) and laser 2D voxel coverage estimation for one drift volume (right).

Penetration of the FC would eliminate most of these shadows and allow for a practically unimpeded coverage. Depending on the depth of the periscope within the TPC, some partial shadowing from the field cage support I-beam would still remain. Figure 6.8 shows a possible way to accomplish this for the top-of-TPC ports [112]. A CAD model of the SBND laser calibration system periscope was used as reference design for DUNE. The SBND periscope, when rotating over its axis, requires a 12 cm diameter circular region free of impediments. In order to take into account a tolerance for the estimated 0.3 % shrinkage of the FC at cryogenic temperatures, we chose an opening of three profiles, equivalent to 18 cm. Still, in order to minimize any risk associated with the presence of material close to the FC, ongoing design studies will evaluate the feasibility of implementing vertically retractable periscopes, with a travel range sufficient for them to clear the top of the FC.

Simulations of the effect of FC penetrations on the E field were carried out [113], and are illustrated in figure 6.9. These have shown that the effect of a 12 cm  $\times$  12 cm opening (equivalent to two profiles), located at 40 cm (along the  $x$  direction) from the APA, is small and tolerable, with a maximum  $10 \text{ kV} \cdot \text{cm}^{-1}$  E field caused by the opening and periscope. These simulations need to be redone with a larger opening of 18 cm  $\times$  18 cm (i.e., three profiles). Still, if we were to choose, conservatively, to discard from the physics data analysis the volume within the TPC determined by the periscope lateral size, a vertical penetration of 10 cm, and the full drift length

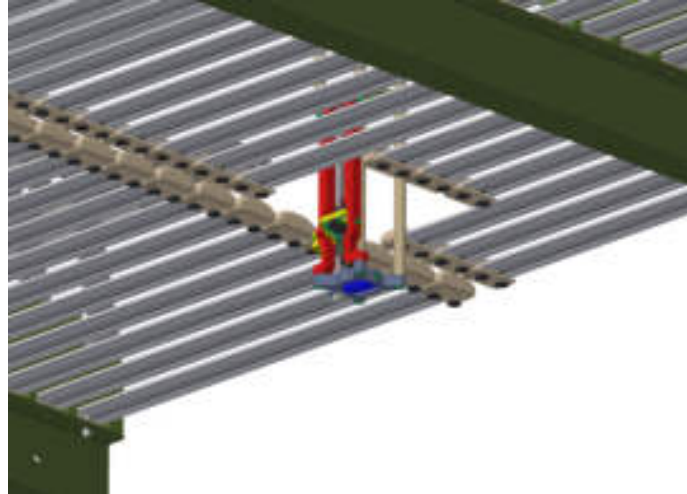


**Figure 6.8.** CAD drawing of one way the periscope could penetrate the FC [112].

(12 cm × 10 cm × 360 cm = 431 for each of the 12 periscopes), it would represent only a very small fraction of  $5 \times 10^{-6}$  of the full detector volume.

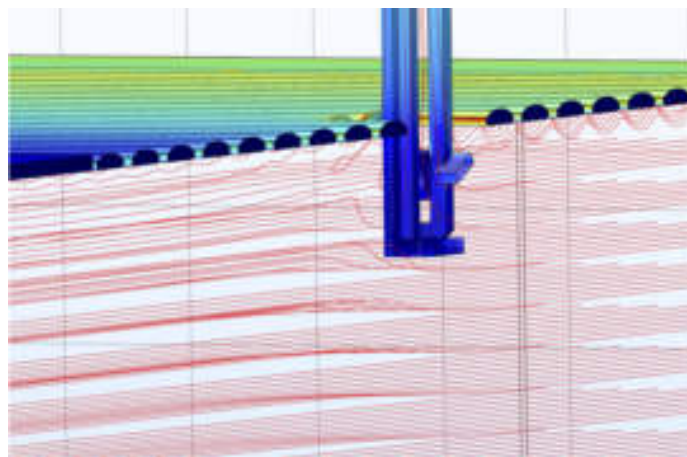


**Figure 6.9.** Simulation of the effect on the E field of a laser periscope penetration of the FC. In this case, an opening of only two profiles was considered.

**Full array scope considerations.** As mentioned earlier (section 6.3.2.2), the system should allow for crossing laser beam tracks wherever possible. In order to collect them in the full SP module volume, that would require using all the available 20 calibration ports. Since it is possible to use an iterative method to obtain displacement maps in regions where no crossing tracks are available, to minimize the overall cost of the system, the baseline design will use only the 12 central ports, providing crossing tracks in essentially 50% of the detector volume. In addition, for the six most central ports, close to the central APA, the distance between them is small enough that we can consider having the same laser box serve two feedthroughs to reduce the costs associated with the laser and its optics. In that case, the total number of lasers needed would be nine.



Usage of the end-wall ports, which are not on top of the TPC, is therefore not part of the baseline design, and is considered only as an alternative in section 6.7.1. A coverage calculation for possible end-wall periscopes, taking into account the shadowing of both the FC profiles and the support beams, gives a maximum of 56 % coverage for 30 cm voxels (allowing all tracks directed at the APA). In this case the laser beams would enter the FC laterally and FC penetration would be harder to consider, so an alternative mechanical design aimed at improving the coverage, is considered in section 6.7.1.

A scan of the full detector using  $10 \times 10 \times 10 \text{ cm}^3$  volume elements would require a number of tracks approximately  $8 \times 10^5$  and can take about three days. Shorter runs could be done to investigate specific regions. The sampling granularity, and therefore the amount of data taken, depends on DAQ requirements. In fact, even to be able to record the desired  $8 \times 10^5$  tracks, a dedicated data reduction algorithm must be devised, so that only a drift window of about  $100 \mu\text{s}$  of data is recorded, and the position of that window depends on the beam position and direction and which wires are being read out. More details on this are given in section 6.4.1.

### 6.3.2.3.1 Measurement program

This section describes the methods used to measure parameter maps and their expected precision, given the design outlined above.

**E field and drift velocity measurement.** The method for E field measurement is based on the measurement of apparent position displacements of the straight laser tracks. The laser produces straight tracks with a known starting position and direction. If, when reconstructed under the assumption of uniform and homogeneous drift velocity, any deviations from that are observed, they are attributed to E field distortions.

The first step in the analysis [102] is to obtain a field of position displacements by comparing the known and reconstructed tracks. If two crossing tracks are used, the displacement vector is simply given by the vector connecting the point where the reconstructed tracks cross and the point where the known tracks cross. However, since those displacements can vary both in direction and magnitude, there will be ambiguity in that determination if only one track is used in a given spatial region. An iterative procedure was developed by the MicroBooNE collaboration [102, 110] to obtain a displacement map from a set of several non-crossing tracks from opposite directions. Following this, a set of drift velocity field lines, which are the same as E field lines, can be obtained from the displacement map, assuming that all charge deposits along a field line will be collected in the same position. Using the relationship between E field and drift velocity [97, 103], we can then also obtain the magnitude of the E field.

Since the observed position distortion in one location depends on E field distortions in many locations along the drift path, this method of analysis clearly requires the acquisition of data from many different tracks crossing each detector drift volume at many different angles.

As already indicated in the previous section (section 6.3.2.3), the pointing precision will be on average 2 mm (at average distances of 10 m), and the TPC precision is 2 mm in  $x$  and 5 mm in  $y$ ,  $z$ . Conservatively taking those in quadrature, we get  $\sigma_x = 3 \text{ mm}$  and  $\sigma_{yz} = 5.4 \text{ mm}$ . If we would use

only one track per direction, in regions of size  $l = 300$  mm, we would therefore be sensitive to drift velocity field distortions of  $\sigma/l$ , i.e., 1 % in  $x$  and 1.8 % in  $y, z$ .

In order to estimate the E field precision, we must distinguish between the  $x$  and  $y, z$  coordinates. To first order, distortion in  $y, z$  do not affect the magnitude of the field, and so the relative distortions on E field are equal to the relative distortions of the velocity. Along  $x$ , we must consider the relation between the magnitudes of the drift velocity and E field. Using the formula from [97, 103] we can see that, at 500 V/cm, a 1 % change in E field leads to a corresponding change of 0.375 % in drift velocity. We therefore reach the values of 2.7 % ( $= 1./0.375$ ) in  $x$  and 1.8 % in  $y, z$  for a conservative estimate of E field precision using a single track per direction.

This is a conservative estimate because it does not take into account the fact that the centroid of the beam should be known better than its full width, and because it is based on the assumption of a single track per direction. As observed in MicroBooNE [102], using several tracks improves the precision, and in most of the volume an accuracy of 1 % was reached so the amount of statistics needed to reach 1 % will be an important question to address in the development plan.

On one side, this gives us an ultimate limit to the E field precision achievable with the laser system, but on the other side, since these TPC precision considerations apply to physics events also, it tells us that an E field precision much better than 1 % should not have an effect on the physics.

**Charge-based measurements.** Electron drift-lifetime [114, 115] is the parameter that governs the dependence of the amount of collected charge on the drift time. A possible measurement of electron drift-lifetime would therefore require a very good control over the charge profile of the ionization laser tracks. This was achieved in a small scale experiment that measured lifetime with laser beams [101], but is harder with longer distances. The charge produced by the laser tracks along its path depends on distance because the light intensity is reduced due to beam divergence and scattering, as well as non-linear effects such as the self-focusing, or Kerr effect. For this reason, the first steps in any laser-based charge measurement are a fine-tuning of the laser intensity in order to reduce self-focusing to a minimum, and “charge profile calibration scan” which consists of acquiring tracks parallel to the APA. In order to get good statistical precision, several tracks could be acquired, in the same or different direction, but always parallel to the APA in order to factorize out any effect from electron drift-lifetime. This set of data provides a calibrated laser beam charge profile that can then be used to analyse and normalize the measured charge profile from tracks that do have an angle with respect to the APA and therefore span different drift times.

As for electron-ion recombination, since the  $dE/dx$  for laser beams is much smaller than for charged particles, the effect should also be much smaller. However, that small effect has been observed [111], so a similar method than described above could be used to evaluate any dependence of the electron-ion recombination factor on the angle  $\phi$  between the track and the electric field, that is predicted in some models [116]. This would entail taking data with tracks as parallel as possible to the E field, in order to enhance the angular dependence term on the recombination expression (that goes with  $1/\sin \phi$ ), and to compensate for the smaller  $dE/dx$  for laser beams.

### 6.3.3 Laser calibration: beam location system

Because the precision of the E field measurement relies heavily on a precise knowledge of the laser beam tracks, an independent measurement of their direction for some specific positions is

required. The laser beam location system (LBLS) addresses this requirement. While the direction of the laser beam will be very well known based on the reading from the encoders on the laser beam steering mechanism, residual uncertainty or unpredictable shift in the pointing direction will remain. Keeping in mind the long length of the ionization track of more than 15 m, even a small offset in the pointing direction can lead to vastly different ionization track locations, especially close to the end of the track. Such inaccuracies will directly affect our ability to precisely calibrate any variations in the E field.

### 6.3.3.1 Design

The LBLS is designed to provide precise and accurate knowledge of the laser track coordinates. Two complementary systems are planned, one based on PIN diodes and another based on mirrors.

**PIN diode system for laser beam location.** The design for the system using PIN diodes is based on the existing system that was built for the miniCAPTAIN experiment [108].

The LBLS consists of groups of 9 PIN diodes, operating in passive, photovoltaic mode. These are GaP diodes with a sensitivity range extending down to 200 nm wavelength; thus, detecting 266 nm light is straightforward. PIN diodes are placed at the bottom of the cryostat and receive direct laser light<sup>3</sup> passing through the gaps between the FC profiles to minimize interference with the FC. Drawings of one such group of PIN diodes are shown in figure 6.10. With the group of 9 photodiodes, we can detect not only the beam but also crudely characterize its profile, giving a more precise location of the central beam pulse axis.

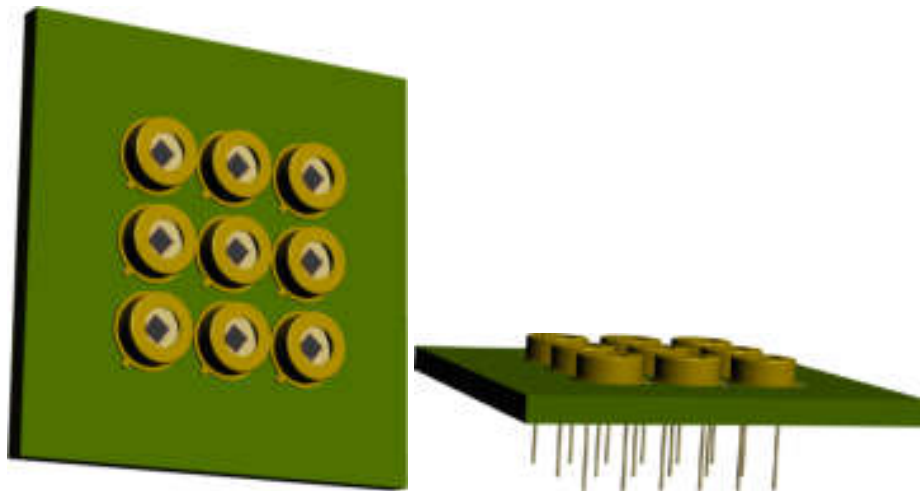


**Figure 6.10.** (Left) LBLS cluster mounted on the opposite wall from the laser periscope to detect and accurately determine the end point of the laser beam. (Right) Profile of the LBLS group mounted on the PCB. GaP diodes come with pins that use pair of twisted wires to transport the signal.

There will be two LBLS pads per laser, with each pad visible by two different lasers, to maximize precision and ensure sufficient redundancy in the system. There will be a total of 16 locations (4 per volume) for a total of 32 pads. Pads will be placed on the central line of each of

<sup>3</sup>This is a difference with respect to the miniCAPTAIN system, which does not observe direct light, but detects fluorescence in the FR-4.

the four volumes, in the middle between each pair of adjacent lasers, located under the FC. The locations of the pads will be carefully surveyed after installation and prior to closing of the cryostat. The laser should always send the first pulse in the direction of the LBL before proceeding into a calibration sequence. In this way, the absolute location of the initial laser track will be determined with high accuracy. The location of the other laser tracks will also be determined with high accuracy with respect to the initial track thanks to the high precision of the rotary encoders.

**Mirror-based beam location system:** in addition to the PIN diode system, we will also have clusters of small mirrors that allow measuring the beam end position via its reflections.

Figure 6.11 shows a conceptual sketch with a cluster of 6 mirrors located close to each other, but with different angles. When the beam hits one of the mirrors, it will be reflected back into the TPC, and the reflection angle unambiguously identifies which mirror was actually hit. With small mirrors, 5 mm in diameter, the required positioning precision would be met if these mirrors are placed at distances of more than 10 m. The preferred location is, therefore, at the bottom FC. Because the cluster can be small (a few cm), it can fit inside the FC profiles. For each drift volume segment seen by two lasers, we plan to install at least two clusters, for redundancy, so the total number of clusters would be 32.

The simplest solution would be to use polished aluminum as the reflecting surface, so that the cluster could be a single block. Tests of the actual reflectivity of the (oxidized) surface will be part of the development plan. An alternative would be small dielectric mirrors.

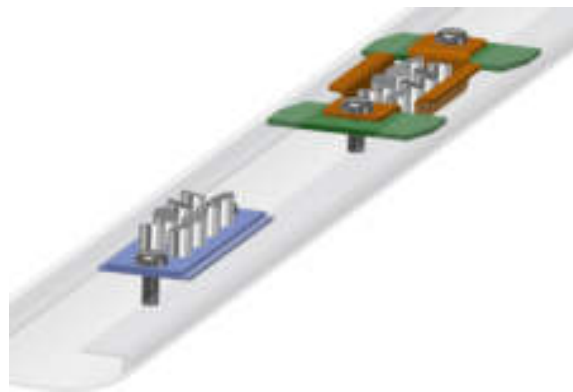


**Figure 6.11.** View of the mirror cluster for the beam location system inserted in the FC profiles [112].

### 6.3.3.2 Development plan

Further optimization of the PIN diode assembly to reduce electronic noise and cross-talk is required. Also, the size and shape of the cluster that would best collect the light coming through the field cage gaps needs to be optimized. Another important aspect is durability of the system that will require extensive running in the cryogenic conditions with a large number of cool-downs to validate GaP for extended use in DUNE. Finally, alternatives to GaP diodes such as SiPMs are under consideration. While SiPMs require power, their sensitivity to single photons makes them a desirable candidate for low light signals and more accurate beam direction reconstruction.

As for the mirror-based system, the capability of the TPC to identify the reflected beam will depend on how diffuse the reflectivity on the aluminum surfaces will be. A full test must be carried out at ProtoDUNE-SP, including alternative options such as using mirrors. Small dielectric mirrors for 266 nm with 6.35 mm diameter are commercially available.

### 6.3.4 Laser calibration: photoelectron system

Well localized electron sources represent excellent calibration tools for the study of electron transport in the LArTPC. A photoelectron laser system can provide such sources at predetermined locations on the cathode, leading to precise measurements of total drift time and integrated spatial distortions when the charge is not collected in the expected wires. These are achieved by simply measuring the time difference between the laser pulse trigger time and the time when the electron cloud reaches the APA. Such measurement will result in an improved spatial characterization of the E field, and consequent reduction of detector instrumentation systematic errors.

Being an operationally simpler system compared to the ionization laser system, the photoelectron laser can be used as a “wake-up” system to quickly diagnose if the detector is alive, and to provide indications of detector regions that may require a fine-grained check with the ionization system. This is especially important due to the low cosmic ray environment in the detector underground. The photoelectric laser system will utilize the ionization laser for target illumination, thus eliminating the additional cost associated with the laser purchase.

#### 6.3.4.1 Design

In order to produce localized clouds of electrons using a photoelectric effect, small metal discs will be placed on the cathode plane assembly and used as targets. Photoelectric laser systems have been successfully used at T2K [117] and in the Brookhaven National Laboratory (BNL) LAr test-stand [118] to generate well-localized electron clouds for E field calibration.

The baseline material choice for the metal targets is aluminum, while silver is being considered as an alternative. At 266 nm (Nd:YAG quadrupled wavelength) the single photon energy of 4.66 eV is sufficient to generate photoelectrons from aluminum and silver. However, aluminum and silver are prone to oxidization. In the case of aluminum, a thick layer of aluminum oxide forms the surface, but this does not increase the work function of the material. Table 6.3 lists the relevant features of metals under consideration.

The main factor driving the electron yield from the photoelectric targets is the quantum efficiency of the material. Although electrons will be released from the metal whenever photons hit the metal surface, most of the ejected electrons carry forward momentum and therefore are never released from the metal. Only a small fraction of released electrons back-scatters or knocks another electron out of the surface. The quantum efficiency for various metals is typically between  $10^{-5}$  and  $10^{-6}$ , thus quite low. All material candidates will be studied in the lab to verify the electron yield, and tested in ProtoDUNE-2 in order to verify the quantum efficiency for different materials.

Disc targets will be fabricated with two different diameters: 5 mm and 10 mm to provide a test of the vertex reconstruction precision. In addition to circular targets, metal strips  $0.5 \times 10$  cm are being considered to calibrate the rate of transverse diffusion in LAr. However, their impact on the cathode field will be carefully studied before being incorporated into target list, to prevent any disruptions to the cathode electric field.

**Table 6.3.** Work function and other features of candidate metal targets for laser photoelectron system.

| Target Material | Work function (eV)               | $\lambda_{\max}$ (nm) | $\lambda_{\text{laser}}$ required (nm) | Oxidizing in air | Type of oxidation |
|-----------------|----------------------------------|-----------------------|--|------------------|-------------------|
| Aluminum        | 4.06                             | 305                   | 266                                    | Yes              | Surface layer     |
| Silver          | 4.26-4.73<br>(lattice dependent) | 291                   | 266                                    | Yes              | Surface layer     |

The targets will be fastened to field shaping strips located on the rim around the resistive panel of the cathode plane assembly. Figure 6.12 illustrates locating the photoelectric targets on the rim around the resistive panel. The distance between the dots will be 10 cm with 5 targets at each corner, while the strips will be fastened at the center of each long side of the resistive plane. The total number of disc targets per resistive panel is 20 and the total number of strips per resistive panel is 2 as illustrated in figure 6.13. Given that there are 600 resistive panels per SP module, there will be a total of 12,000 disc targets and 1200 strip targets per module. The photoelectric dots and strips layout will be further refined based on the calibration requirements and performance simulation results. It will be essential to conduct a survey of the photocathode disc locations on the cathode after installation and prior to detector closing. In this way, the absolute spatial calibration of the E field will be achieved.

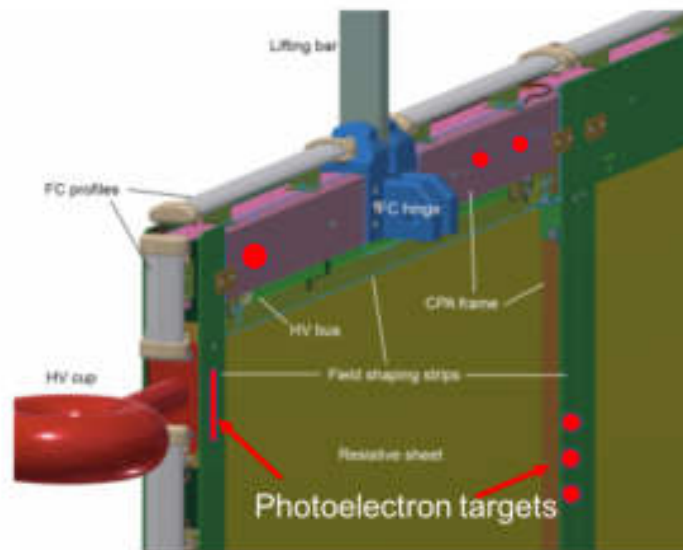


**Figure 6.12.** The best place to place the photo targets without being intrusive for the E field, is the surface of the field shaping strips around the rim of the resistive panel. Circular targets will be implemented, while the strip targets are still under consideration.

A few thousand electrons are required per spill from each dot to produce the signal above the noise level on the wire and this number will be achieved with high intensity lasers (pulses of the order of 100 mJ). The laser beams used to illuminate the targets will be injected into the cryostat via cryogenic optical fibers guided into mounting points in the APA, where they are coupled with

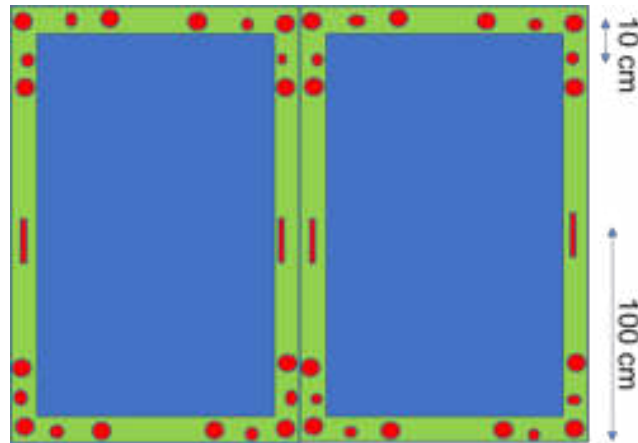


**Figure 6.13.** There are a total of 5 circular targets in each corner, for a total of 20 circular targets: 12 large and 8 small diameter targets total. In addition, 2 strips at the center along the long sides of the resistive panels may be added if not disruptive to the high voltage on the cathode plane.

defocusing elements that will illuminate 10 m diameter surface on the CPA with a single fiber. Fibers will be fastened along the central line of the APA in the space between the top and bottom APA, on the top of the upper APA and on the bottom of the lower APA. With the aid of the defocusing elements, the entire single phase module can be illuminated with a total of 72 fibers, corresponding to just 6 fibers along the central line along with 6 fibers on top and bottom for a total of 18 fibers per each of the four drift volumes. Figure 6.14 shows the conceptual view of the CPA illumination.

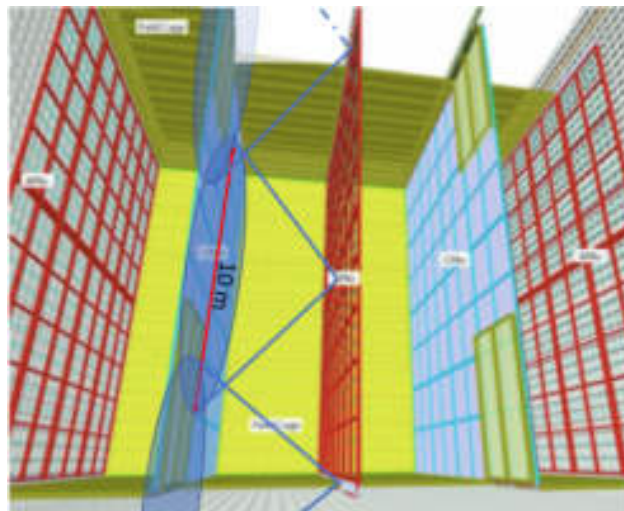


**Figure 6.14.** Conceptual view of the CPA illumination with fibers placed on the top and bottom of the APA for better coverage and overlap.

While the current plan aims for illumination of the entire CPA, the Kapton material that composes the resistive panels undergoes photoelectric effect, albeit with three orders of magnitude lower quantum efficiency at cryogenic temperatures when compared to phototargets at 266 nm. While the noise produced is expected to be tolerable, in case the noise is higher than anticipated, the solution is to illuminate only the areas where phototargets are placed reducing the resistive panel exposure. In this case, instead of defocusing elements, bare fibers will be utilized. The bare fiber opening angle is  $10^\circ$  and 1.3 m diameter exposure. Assuming parallel running of lasers, photoelectron targets in 3 out of 4 volumes can be illuminated at once, assuming that laser firing can be coordinated and calibrated with sufficient precision and that volumes 2 and 3 share lasers. Lasers typically operate at 10 Hz frequency. If 10000 pulses per laser are assumed, about 15 minutes of running is needed per laser for a single calibration run as the photoelectron clouds from different dots are very well localized. With the help of commercial multiplexers per each volume, 1 hour per volume will be sufficient for a single calibration campaign. If the DAQ or lasers themselves prevent parallel running, the entire calibration campaign will take between 15 minutes or up to 1–5 hours. The calibration run duration will depend on the final calibration scheme.

The photoelectron system will use the same lasers used for argon ionization. Stability of the laser pulses will be monitored with a power meter. Dielectric mirrors reflective to 266 nm light will guide the laser light to injection points, but a fraction of the light will be transmitted instead of reflected to the power meter behind the mirror. The laser will also send a forced trigger signal to the DAQ based on the photodiode that will be triggered on the fraction of the light passing through the dielectric mirror.

### 6.3.4.2 Development plan

The photoelectron system will require the following tasks to complete the design that can be done in ProtoDUNE-2 or in the lab:

- test the mounting of the targets on the CPA;
- use different target materials to compare their performance;
- verify the potential of targets to generate several 1000 electron clouds and their ability to diagnose electric field distortions and vertex reconstruction;
- allocate ports to insert laser fibers used for illumination;
- validate interface with ionization laser in order to inject UV photons into fibers;
- validate efficiency of laser light injection in the optical fiber;
- validate light attenuation in fibers;
- validate design interface with APA and optimized locations of fibers between top and bottom APAs;
- validate diffuser design and light losses in the diffuser as well as its ability to illuminate large areas of CPAs;



- validate bare fiber CPA illumination; and
- survey of the dots position to the required level of precision.

### 6.3.4.3 Measurement program

Photoelectron systems have been used in other experiments to diagnose electronics issues by using the known time period between the triggered laser signal and read out times, and to perform rapid checks of the readout of the TPC itself.

A photoelectron laser is an effective diagnostic and calibration tool, that can quickly and accurately sample the electron drift velocity in the entire detector. In addition, it can be used to identify electric field distortions due to space charge effects. Exact knowledge of the timing and position of the generated electron clouds is useful for vertex calibration. In addition to electronics issues, discrepancies between the measured and expected drift time can point to either distortions in the position of the detector elements or to a different drift velocity magnitude.

Another planned measurement is the comparison between the expected and measured  $y$ ,  $z$  position of the collected charge, that can point to transverse distortions of the E field.

### 6.3.5 Pulsed neutron source system

The SNB signal includes low-energy electrons, gammas and neutrons, which capture on argon. Each signal channel will have specific detector threshold effects, energy scale, and energy resolution. As noted in Volume II, DUNE physics, chapter 7, the sensitivity to SNB physics depends on the uncertainties of relevant detector response parameters, and so a calibration method to constrain those uncertainties is needed. Local detector conditions may change with time due to a variety of causes that include electronics noise, misalignments, fluid flow, LAr purity, electron lifetime and E field. While these are intended to be characterized from other systems via inputs to the detector model, “standard candles” provide a method to assess if our detector model is incomplete or insufficient. An ideal standard candle matches one of the relevant signal processes and will provide spatial and/or temporal information. The pulsed neutron source (PNS) system, as described below, will provide a standard candle neutron capture signal (6.1 MeV multi-gamma cascade) across the entire DUNE volume that is directly relevant to the supernova physics signal characterization. The PNS is also capable of providing a spatially fine-grained measurement of electron lifetime.

Liquid argon is near transparent to neutrons with an energy near or at 57 keV due to an anti-resonance in the cross-section caused by the destructive interference between two high level states of the  $^{40}\text{Ar}$  nucleus (see figure 6.15). The cross-section at the anti-resonance “dip” is about 10 keV wide, and at the bottom the cross section of  $1.6 \times 10^{-4}$  b implies an elastic scattering length of over 2000 m. Natural argon has three major isotopes:  $^{36}\text{Ar}$  (0.3336 %),  $^{38}\text{Ar}$  (0.0834 %), and  $^{40}\text{Ar}$  (99.6035 %) each with a slightly different anti-resonance. The average elastic scattering length of the 57 keV neutrons in natural liquid argon is about 30 m.

The neutrons at the anti-resonance energy could be injected into liquid argon in the TPC, provided no materials (e.g., hydrocarbons) block the path. Those that do scatter lose energy, leave the anti-resonance, quickly slow down and are captured. Each capture releases exactly the binding energy difference between  $^{40}\text{Ar}$  and  $^{41}\text{Ar}$ , about 6.1 MeV in the form of  $\gamma$  rays. As will be described below, by using a *DD* Generator (where *DD* stands for “deuterium-deuterium”), a triggered pulse

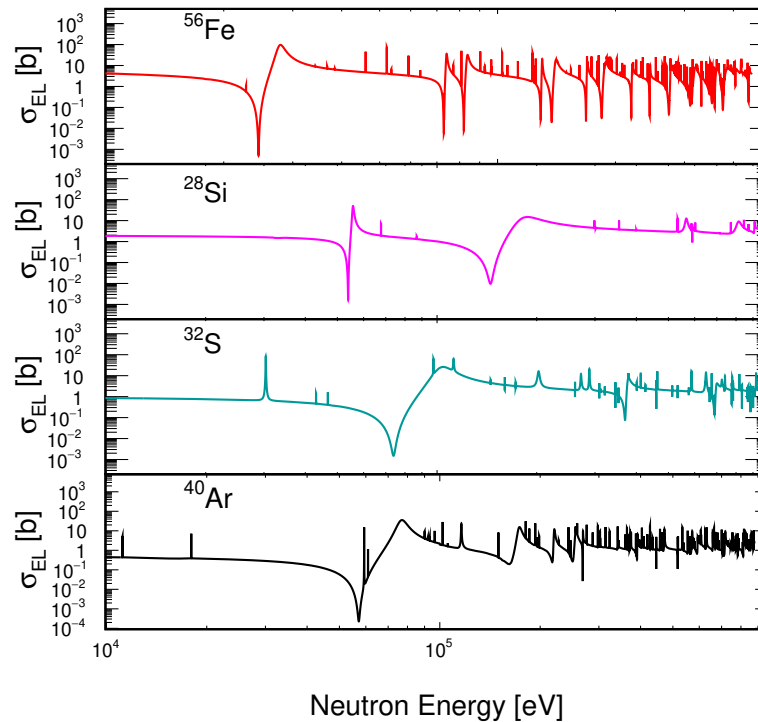


**Figure 6.15.** Illustration of interference anti-resonance dips in the cross section of  $^{56}\text{Fe}$ ,  $^{28}\text{Si}$ ,  $^{32}\text{S}$ , and  $^{40}\text{Ar}$ . Elastic scattering cross-section data is obtained from ENDF VIII.0 [188].

of neutrons can be generated outside the TPC, then injected via a dedicated opening in the insulation into the liquid argon, where it spreads through the 58 m volume of the detector to produce 6.1 MeV energy depositions.

One important property of the neutron capture reaction  $^{40}\text{Ar}(n,\gamma)^{41}\text{Ar}$  is that the deexcitation of  $^{41}\text{Ar}$  nucleus produces a cascade of prompt  $\gamma$ s. Because of the detector threshold effect, the multiplicity and the total energy of the  $\gamma$ s within the cascades could be effectively decreased to below the expected values of the neutron capture process. As a consequence, the neutron capture identification and the assessment of neutron tagging efficiency in liquid argon strongly depends on a precise model of the full  $\gamma$  energy spectrum from thermal neutron capture reaction. The neutron capture cross-section and the  $\gamma$  spectrum have been measured and characterized by the Argon Capture Experiment at DANCE (ACED), where DANCE is the Detector for Advanced Neutron Capture Experiments. Recently, the ACED collaboration performed a neutron capture experiment using DANCE at the Los Alamos Neutron Science Center (LANSCE). The result of neutron capture cross-section was published [119] and will be used to prepare a database for the neutron capture studies. The data analysis of the energy spectrum of correlated  $\gamma$  cascades from neutron captures is underway and will be published soon. The  $\gamma$  energy spectrum and the branching ratios in the ENDF library will be updated with the ACED result.

Figure 6.16 shows an example of the energy spectra of individual  $\gamma$  clusters measured by ACED [119]. The most common  $\gamma$  cascade emitted from  $^{41}\text{Ar}$  decay has 167 keV, 1.2 MeV and 4.7 MeV  $\gamma$ s. The peak energy of these  $\gamma$ s can be clearly seen in the background subtracted data in ref. [119]. In liquid argon detectors, the  $\gamma$ s are detected through calorimetric measurement.

Assuming the  $\gamma$  cascade from a neutron capture is fully contained in the active volume, it is possible to detect the individual  $\gamma$ s from the neutron capture. The correlation of the measured  $\gamma$  is a strong indication of neutron capture events. Low energy  $\gamma$  reconstruction algorithms are being investigated to identify the neutron capture events that could be used for detector response calibration.

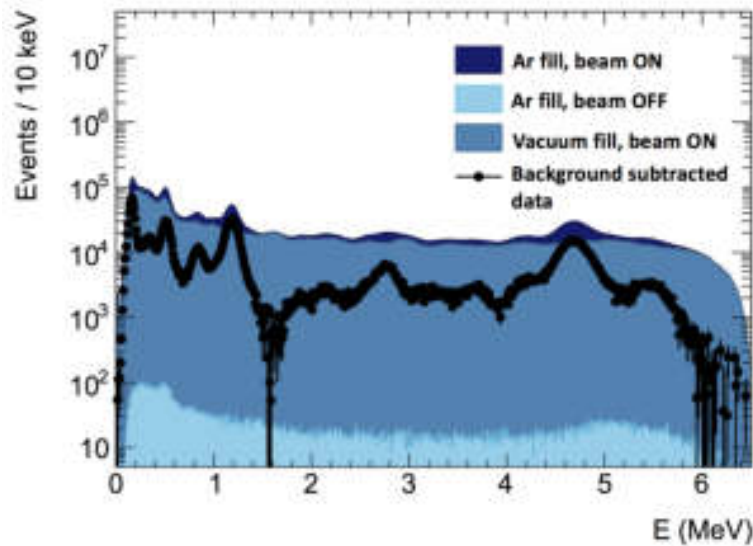


**Figure 6.16.** Energy spectra of individual  $\gamma$  clusters measured by ACED. Only events detected in the 0.02 eV to 0.04 eV neutron energy window are selected.

### 6.3.5.1 Design

The basic design concept of sources like the pulsed neutron source are based on successful boron neutron capture therapy [120]. The design of the PNS system used for energy calibration is shown in figure 6.17. The system will consist of four main components: a *DD* generator, an energy moderator reducing the energy of the *DD* neutrons down to the desired level, shielding materials, and a neutron monitor to confirm neutron flux and safe operation.

**DD generator source:** *DD* generators are commercial devices that can be readily obtained from several vendors at a cost of about \$125k each, which includes all control electronics. The pulse width is adjustable and can be delivered from about 10  $\mu$ s to 1000  $\mu$ s (which affects the total neutron output).

**Moderator:** a feasible moderator has been designed using a layered moderator (Fe or Si)-filter (S)-absorber (Li) configuration. The 2.5 MeV neutrons from the *DD* generator are slowed to less than 1 MeV by the energy moderator. Natural iron and silicon are found to be efficient moderators for this purpose. Then an energy filter made of sulfur powder is used to further select the neutrons with the desired anti-resonance energy. The neutron anti-resonance energy in  $^{32}\text{S}$  is 73 keV, right above the 57 keV anti-resonance energy in  $^{40}\text{Ar}$ . The neutrons at this energy lose about 3.0 keV per elastic scattering length. After a few elastic scattering interactions, most of the 73 keV neutrons selected by the sulfur filter will fall into the 57 keV anti-resonance energy region in LAr. These materials

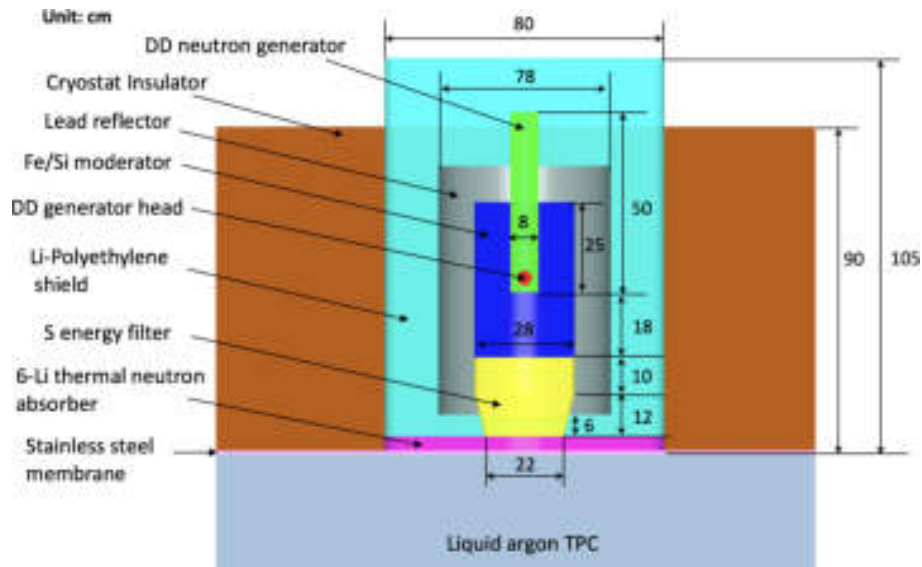


**Figure 6.17.** Conceptual design of the pulsed neutron source. The whole device is placed outside the TPC volume on top of the cryostat.

require no cooling or special handling. Finally, a thermal absorbing volume of lithium is placed at the entry to the argon pool in order to capture any neutrons that may have fallen below the 57 keV threshold. A reflecting volume is added around the *DD* generator and the neutron moderator to increase downward neutron flux. Figure 6.18 shows the energy spectrum of the neutrons moderated and injected into the TPC.

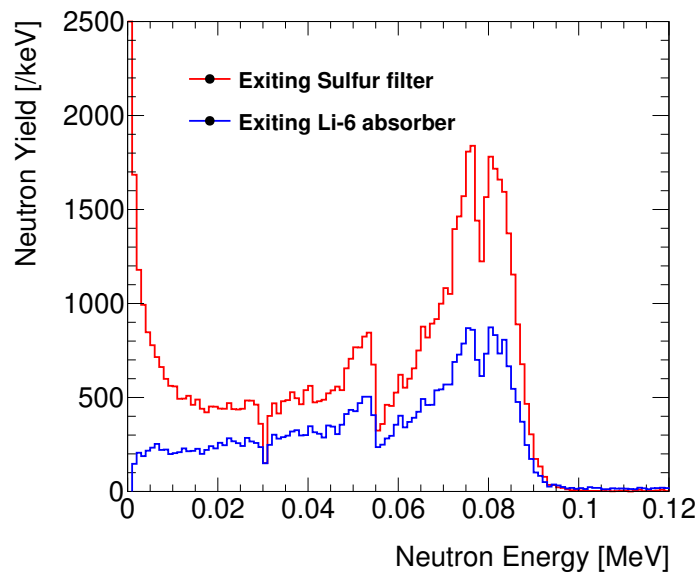


**Figure 6.18.** Energy of moderated neutrons produced by the pulsed neutron source. The total number of initial *DD* generator neutrons is  $1 \times 10^6$ .

**Shielding:** the source will be encased in a shielding volume. The goal of the shield is to block both scattered neutrons and gammas that are produced in the source. Lithium-polyethylene (7.5 %) is chosen to be the material for the neutron shield because it is rich in hydrogen and lithium atoms which yield a high neutron absorption cross section. Lithium-polyethylene is also light weight, commercially available, and relatively inexpensive. The energy spectrum entering the shield has multiple peaks between 0.5 MeV and 1.5 MeV, and one major spike at 2.2 MeV. The shield can effectively block the lower energy peaks but can only degrade the intensity of the 2.2 MeV because 2.2 MeV gammas are a characteristic signature for neutron captures on hydrogen. A safe thickness of the lithium-polyethylene shield must be found, one that can degrade the dose of 2.2 MeV gammas to safe levels. The dose of radiation from 2.2 MeV gammas was calculated assuming a person standing 1 m away. Simulation indicates that a shield with 12 cm thick lithium-polyethylene satisfies basic safety requirements.<sup>4</sup>

**Neutron Monitor:** the system will need a monitoring system to confirm that the source is operating as expected. A neutron monitoring detector consisting of an Eljen EJ-420 coupled to an ADIT L51B16S 2-inch PMT will be placed just outside of the moderating material surrounding the *DD* generator and will be read out with a CAEN waveform digitizer with neutron/ $\gamma$  pulse-shape discriminating firmware. The monitoring detector will provide relative flux information to the calibration users and will ensure that the intensity of the source is constant, thereby allowing a comparison of data taking at different times. A small collimator will be placed in front of the neutron detector, and inside the shielding material of the *DD* source. The collimator dimensions and material specifications (likely a combination of iron, lead, and polyethylene) will be optimized from Monte Carlo simulations.

Based on the general concept described above, figure 6.19 shows a conceptual layout of the neutron injection system. It is referred to as the “large format moderator” design. The neutron source is about 0.8 m wide and 1 m high. It would sit above the cryostat insulator. Beneath the neutron source, a cylindrical insulator volume with a diameter of more than 50 cm has to be removed to allow the neutrons enter the cryostat. Such an interface is provided by the human access ports near the endwalls of the detector. The top flange of the human access port is sealed, and the neutron source sits on top, providing heat insulation. The neutron source weighs about 1.6 t and will be supported by the I-beams. This design allows a permanent deployment of the neutron source. GEANT4 simulation has shown that 0.13 % of the neutrons generated by the *DD* generator are expected to be captured inside the TPC. It is also possible to place the neutron source inside the human access ports which would allow a factor of 6 increase of the neutron flux but will require a modification of the interface flange. This is currently being investigated.

Simulation studies were done placing the PNS system on top of a cryostat with the same size as the DUNE 10 kt TPC. Initial simulation results indicate that one PNS could cover 1/3 of the TPC volume, so three identical neutron sources on top of the cryostat would illuminate the whole TPC volume of the DUNE FD. However, this would require opening three additional neutron injection ports which are not included in the current cryostat design.<sup>5</sup> The baseline configuration of the PNS

---

<sup>4</sup>These calculations will be redone assuming a 30 cm personnel safety distance and shielding thickness reestimated to meet DUNE safety requirements.

<sup>5</sup>Ideally, opening three identical neutron injection ports for each 10 kt TPC would make full use of the neutron source.

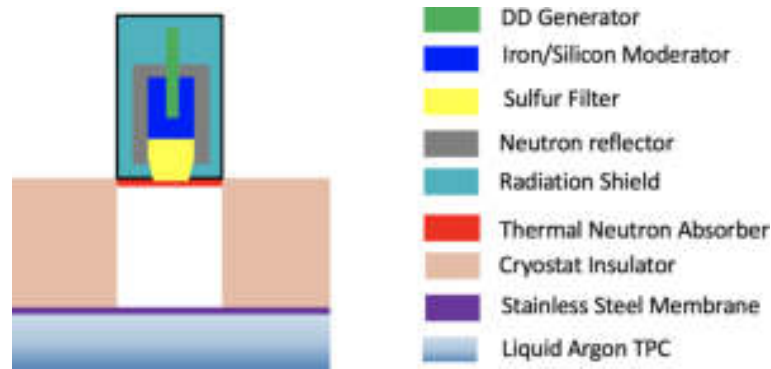


**Figure 6.19.** Large format neutron source deployed above/inside the human access holes.

system consists of two large format neutron sources permanently located at the corner human access ports at the opposite ends on top of the cryostat.

Figure 6.20 shows the position distribution of the neutron captures under baseline configuration. The distribution shows that the baseline deployment can cover a large fraction of the TPC volume, but, as evident from the figure, not many neutrons reach the central region of the TPC. Neutrons with long scattering lengths can reach the center of the TPC but, much longer operation time maybe needed to achieve the required statistics. Assuming a minimum number of 100 neutron captures per  $\text{m}^3$  in order to carry out a localized energy calibration, and the typical *DD* generator pulse intensity of  $10^5$  neutrons/pulse, the number of pulses needed to calibrate the high rate regions is of the order of 1000, and at least 10 times that for the low rate regions. But given the 0.5 Hz DAQ limitation, this would mean calibration runs will increase from 40 minutes to about 7 hours to cover the low rate regions. More details on this are given in section 6.4.1. If the neutron capture events at the center of the TPC are not sufficient, the detector response calibration would depend on simulations and extrapolation using results from the regions with high neutron coverage. To increase the low coverage at the center of the TPC, an alternative deployment strategy is proposed using a small format neutron source design described in section 6.7.2.

The system is expected to have a long lifetime of operation, as the PNS system sits on top of the cryostat, with no opening to the LAr, so it is possible to replace the system in case of failure with only crane support.

### 6.3.5.2 Measurement program

The 6.1 MeV  $\gamma$  cascade will provide a uniform signal for neutron capture, part of the supernova signal. The source may also be used to determine the relative efficiency across the detector for neutron capture, and provide measurements of energy resolution and energy scale spatially and temporally. Simulation studies are currently underway.

The first goal of the simulation is to provide the expected distribution of signals, with a normalization given by the pulse width of PNS operation, and neutrons energy and angular correlated distribution, depending on the source filter and shield design. It is envisaged that the calibration can be done in two modes. First, a short PNS pulse can provide isolated neutron captures closer

While this is not possible for the first FD module as the cryostat design is frozen, it informs the importance of these ports for subsequent FD modules.

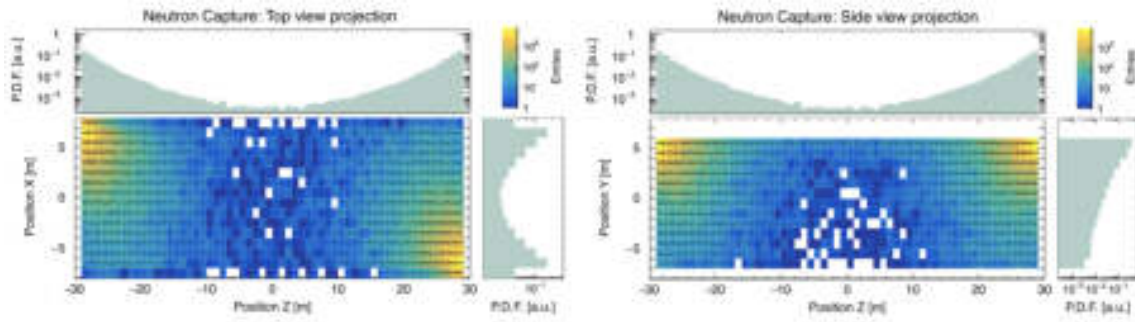


**Figure 6.20.** Neutron capture positions inside a DUNE-sized TPC, assuming baseline configuration with two large format neutron sources located at the corner human access ports at the opposite corners on top of the cryostat.  $L=60$  m (along  $Z$  axis, horizontally parallel to the beam direction),  $W=14.5$  m (along  $X$  axis, horizontally perpendicular to the beam direction),  $H=10$  m (along  $Y$  axis, vertically perpendicular to the beam direction).  $1.8 \times 10^7$   $DD$  generator neutrons with  $2.5$  MeV energy were simulated in each moderator and propagated inside the TPC. Top (left) and side (right) views of neutron capture positions are shown.

to the entrance path; and then a longer pulse, for which the same region is saturated, but captures happen in the full volume.

By using an external trigger coupled to the PNS operation and running the usual trigger algorithms in parallel, the calibration will provide the efficiency of the trigger and DAQ systems as a function of total fluxes. Changing the pulse width can result in higher or lower detector activity. The source will be used for SNB calibration to test the capabilities of triggering for low energy signals, but also to identify them in different pile-up conditions. The transmission of the global timing from the external PNS trigger to the DAQ provides a strong constraint on the initial timing for the TPC as the neutron capture times are of the order of  $0.15$  ms, much lower than typical drift time for the TPC. The PD system, with resolution of  $100$  ns, can discriminate between different neutron captures. The calibration will measure the efficiency of the PD system response for low energy events, depending on the distance due to Rayleigh scattering in LAr. We will then study the usage of the PD system time information for improving the position reconstruction of TPC signals. In the absence of the PD system system, the global timing from the PNS translates to an uncertainty of around  $10$  cm.

Individual event positions can be translated into response maps of both the photon detectors and the LArTPC to standard candles of  $6.1$  MeV electromagnetic depositions. When the cascades can be more precisely reconstructed, individual  $\gamma$ s within the cascades can be identified, and this provides a lower energy “standard candle” close to the solar electron-neutrino threshold. Comparing the collected charge for equal energy signals at different distances from the TPC gives a measurement of the electron lifetime, a key detector response parameter. High PNS flux runs can generate momentary local space charge effects, in the upper regions of the detector, that will need to be characterized; low flux runs should be taken before to ensure expected space charge distributions. The global simulation will be tested in the (smaller scale) ProtoDUNE detectors. The neutron mean free path will be larger than the ProtoDUNE size, and so external events and interactions with materials of the PD system, APA, and CPA systems will be more prominent. These effects must be simulated.

Note that captures of external background neutrons, entering the active volume is a main background for low energy physics; a comparison of simulations of PNS events and external neutron backgrounds will be interesting, as will a comparison of simulated supernova and solar neutrino signals. For the high energy beam events, the number and energy distributions of neutrons depend on the type of neutrino interaction and are significantly different for neutrinos and anti-neutrinos. Measuring the number and distance of neutron captures around the main hadronic cascades can thus help in identifying which extra proton scattering signals to associate to the hadronic cascades. This can also help make a statistical correction to the energy reconstruction of the neutrino and anti-neutrino events.

### 6.3.6 Validation of calibration systems

All calibration designs presented in the previous section require full system validation before being deployed in the DUNE FD. Here, we describe the validation of a complete baseline design and some of the alternative designs described in the appendix, section 6.7.

Although laser calibration systems are being operated in other LArTPC experiments (e.g., MicroBooNE, future SBND runs), they have stringent requirements in terms of mechanical and optical precision, long-term reliability, laser track length, performance of the LBLS, DAQ interface, and effect on E field, especially due to the FC penetration. All of these lead to corresponding goals for a test installation and operation in ProtoDUNE-SP that could be done in the post-LS2 run. As figure 6.21 shows, ProtoDUNE-SP has ports of the same size as the DUNE FD that could be used for these tests. If a pair of ports can be used, then one could even have crossing tracks within a single drift volume. If one of the ports external to the TPC can be used, then we would test the double-rotary alternative system described in section 6.7.1 and aimed at improving the coverage from the end-wall locations.

The goal for validation would be to test all aspects of the system design, installation, alignment, operation, interfaces with DAQ, and analysis, among others. ProtoDUNE-SP, because it is located at the surface, could measure the E field map with cosmic rays to compare with the one from the laser system to improve the analysis methods or identify weak aspects in the design. An important design parameter is the length of a laser track. Our design assumes that 20 m is possible. MicroBooNE has demonstrated only up to 10 m, but the track could be longer, depending on laser intensity. Measurements are limited by the size of the detector, but one way to gain information on longer tracks is to make a scan with low laser intensities, so that the end of the track is visible, and register how the maximum obtained track length scales with intensity. An extrapolation to the DUNE FD laser intensity would tell us the maximum length possible. Such a measurement could also be done at MicroBooNE or SBND.

An important aspect of the development plan, to be carried out at ProtoDUNE-SP-2, is the characterization of the charge created by the laser beam ionization as a function of distance travelled in the LAr and the laser beam intensity. This dependence is thought to be affected by self-focusing effects due to the high light intensity, but it can be studied by measuring the collected charge distribution from a series of tracks close, and parallel, to the APAs in order to break any correlations with the electron lifetime. This measured charge function could then be used with tracks in different directions to obtain a measurement of electron lifetime, which would significantly increase the capabilities of the laser system.



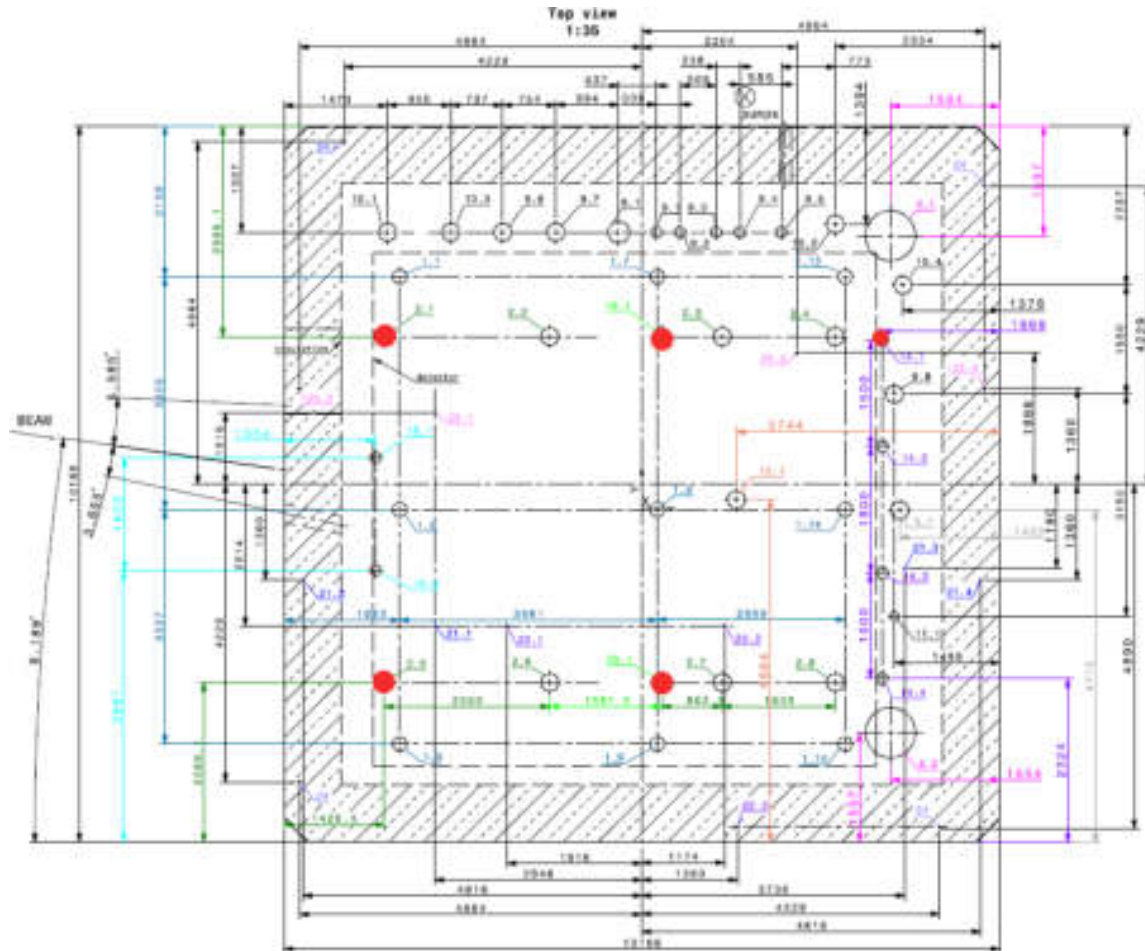


**Figure 6.21.** Top view of the ProtoDUNE-SP cryostat showing various penetrations. Ports marked in red are free and could be used to test the calibration systems. The four largest ports have the same diameter (250 mm) as the calibration ports of DUNE FD, and are located over the TPC. The largest ports at the right side corners of the cryostat are the human access ports.

The pulsed neutron source is a new idea never used in other experiments, so a ProtoDUNE-SP-2 test is essential. The corner human access ports similar to the ones in the DUNE FD could be used for this test.

In addition to dedicated hardware validation runs at ProtoDUNE-SP-2, other LAr experiments provide ample opportunities to develop and validate calibration tools and techniques, especially those relevant to the hardware being deployed. For example, the MicroBooNE experiment is currently leading the development of analysis methods using laser data to extract an E field map. Energy calibration techniques and related software tools are also being developed at various experiments (MicroBooNE, ICARUS, LArIAT, ProtoDUNE) that involve estimating and propagating uncertainties like E field distortions, recombination, and other effects into physics signals. Other calibration related developments include DAQ and calibration database design, all of which are being improved at SBN and ProtoDUNE.

## 6.4 Interfaces with other consortia

Interfaces between calibration and other consortia have been identified and appropriate documents have been developed. The documents are currently maintained in the CERN Engineering and Equipment Data Management Service (EDMS) database, with a TDR snapshot kept in the DUNE document database (DocDB). A brief summary is provided in this section. Table 6.4 lists the interfaces and corresponding DocDB document numbers. The main systems calibration has interfaces with are HV, PD system, and DAQ, and the important issues that must be considered are listed below.

**HV** Evaluate the effect of the calibration hardware on the E field due to laser system periscopes and FC penetration. Evaluate the effect of the incident laser beam on the CPA material (Kapton); integrate the hardware of the photoelectron laser system (targets) and the LBLs (diodes) within the HV system components. Ensure that the radioactive source deployment is in a safe field region and cannot do mechanical harm to the FC.

**PDS** Evaluate long term effects of laser light, even if just diffuse or reflected, on the scintillating components (TPB plates) of the PD system; establish a laser run plan to avoid direct hits; evaluate the effect of laser light on alternative PD system ideas, such as having reflectors on the cathode plane assemblies; validate light response model and triggering for low energy signals.

**DAQ** Evaluate DAQ constraints on the total volume of calibration data that can be acquired; develop strategies to maximize the efficiency of data taking with data reduction methods; study how to implement a way for the calibration systems to receive trigger signals from DAQ to maximize supernova live time. More details on this are presented in section 6.4.1.

Integrating and installing calibration devices will interfere with other devices, requiring coordination with the appropriate consortia as needed. Similarly, calibration will have significant interfaces at several levels with cryostat and facilities in coordinating resources for assembly, integration, installation, and commissioning (e.g., networking, cabling, safety). Rack space distribution and interaction between calibration and systems from other consortia will be managed by technical coordination in consultation with those consortia.

### 6.4.1 Calibration data volume estimates

The calibration systems must interface with the DUNE DAQ system, discussed in detail in chapter 7. Trigger decisions for physics events are made hierarchically: trigger primitives are generated from TPC and PD system “hits”, and these trigger primitives are then used to create trigger candidates which are collections of trigger primitives satisfying selection criteria such as exceeding a threshold number of adjacent collection wire hits, or total collection wire charge recorded, etc. These trigger candidates are passed on to a module level trigger (MLT) which then makes decisions about whether a given trigger candidate is accepted as a detector-wide trigger. If so, the MLT sends trigger commands to the data flow orchestrator (DFO) which in turn passes them to an available event builder (EB) that then requests data from the FE readout of the DAQ (servers that host FELIX

**Table 6.4.** Calibration consortium interface links.

| Interfacing System     | Description   | Reference        |
|------------------------|---|------------------|
| HV                     | effect of calibration hardware (laser and radioactive source) on E field and field cage; laser light effect on CPA materials, field cage penetrations; attachment of positioning targets to HV supports | DocDB 7066 [33]  |
| PD system              | effect of laser light on PD system, reflectors on the CPAs (if any); validation of light response and triggering for low energy signals   | DocDB 7051 [90]  |
| DAQ                    | DAQ constraint on total volume of the calibration data; receiving triggers from DAQ   | DocDB 7069 [121] |
| CISC                   | multi-functional CISC/calibration ports; space sharing around ports; fluid flow validation; slow controls and monitoring for calibration quantities   | DocDB 7072 [122] |
| TPC Electronics        | Noise, electronics calibration  | DocDB 7054 [75]  |
| APA                    | APA alignment studies using laser and impact on calibrations  | DocDB 7048 [17]  |
| Physics                | tools to study impact of calibrations on physics  | DocDB 6865 [123] |
| Software and Computing | Calibration database design and maintenance   | DocDB 6868 [124] |
| TC Facility            | Significant interfaces at multiple levels   | DocDB 6829 [125] |
| TC Installation        | Significant interfaces at multiple levels   | DocDB 6847 [126] |

cards). The management of trigger decisions — whether they are generated by candidates from the TPC, PD system, calibrations, or other systems — is done in the MLT.

The trigger commands are in the form of absolute time stamps that are used to extract snapshots of the data stored in the FE readout buffers. For physics triggers, all TPC information for a snapshot of time (roughly twice the drift time, or 5.4 ms) are read out, without any additional zero suppression or localization. For calibration events, this approach would create an unmanageable amount of data and, in any case, is unnecessary because calibration events create interactions or tracks at known positions or times, or both.

To reduce data volume from calibrations, therefore, calibration systems that can be triggered externally are desirable. Like the distribution of trigger commands to the FE readout buffers, the external trigger for a calibration system will take the form of an absolute time stamp. The time

stamp is generated by the MLT, thus ensuring that (for example) a calibration event does not occur during a candidate supernova burst. The distribution of these time stamps will be done through the DAQ’s timing and synchronization system. Thus triggerable calibration systems (like the laser or PNS) will have to be synchronized to the rest of the DAQ system and be capable of accepting time stamps. There will be differences in the details of how different calibration systems are handled, as discussed later in this section.

Table 6.5 shows the estimated data volume needs for various calibration systems assuming each system is run twice per year. For the ionization laser system, as noted earlier, a scan of the full detector can take about three days, resulting in a total of about six days or a week per year per 10 kt module. For the PNS system, as noted later in this section, a single run can take about seven hours; doing that twice, or even four times, per year will result in a total of about one day per year per 10 kt module. It is expected that once the detector launches into stable operations, the need for full calibration campaign runs will reduce to one nominal run per year. We also expect some shorter runs may be needed in smaller, targeted regions of the detector, or for detector diagnostic issues.

**Table 6.5.** Estimated data volume needs per year per 10 kt for various calibration systems.

| System                  | Data Volume (TB/year) | Assumptions   |
|-------------------------|-----------------------|---|
| Ionization Laser System | 184                   | 800k laser pulses, $10 \times 10 \times 10 \text{ cm}^3$ voxel sizes, a $100 \mu\text{s}$ zero suppression window (lossy readout), and 2 times/year |
| Neutron Source System   | 144                   | $10^5$ neutrons/pulse, 100 neutron captures/ $\text{m}^3$ , 130 observed neutron captures per pulse, 2 times/year                                   |

#### 6.4.1.1 Laser system

The E field vector from ionization laser calibration is determined by looking at the deflection of crossing laser tracks within detector voxels. Because any given laser track illuminates many such voxels, one laser pulse can be used for several measurements; essentially, what matters is how many voxels it takes to cover three walls of a given drift volume — CPA, bottom and end-wall FC, taking into account that we divide that volume by 4 because of beam coverage.

Considering a small voxel size of  $10 \times 10 \times 10 \text{ cm}^3$ , the total number of independent track directions is estimated to be 800,000: about half the rate of cosmic rays and thus nominally a substantial total data volume. However, with the specification voxel size of  $30 \times 30 \times 30 \text{ cm}^3$ , that number would be 27 times smaller, so that would allow a larger number of tracks per direction. Keeping to the overall estimate of 800,000 tracks per scan, the choice of voxel granularity and track statistics per direction can be made until the commissioning period.

Fortunately, unlike every other event type in the detector, the laser track has both a reasonably well known position and time; thus the trigger command issued to the FE buffers can be much narrower than the window used for physics triggers. A  $100 \mu\text{s}$  zero suppression window should be wide enough to avoid windowing problems in the induction plane wire deconvolution process.

To ensure that the interesting part of each waveform is recorded, the DAQ will need to know the current position of the laser, which will be transmitted from the laser system to the MLT via the DAQ control, configuration and monitoring subsystem (CCM).

From the standpoint of data volume, therefore, the total assuming the 100  $\mu$ s zero-suppression window is

$$800,000/\text{scan}/10 \text{ kt} \times 100 \mu\text{s} \times 1.5\text{Bytes}/\text{sample} \times 2 \text{ MHz} \times 384,000 \text{ channels} = 92 \text{ TB}/\text{scan}/10 \text{ kt}. \quad (6.1)$$

If such a calibration scan were done twice a year, then the total annual data volume for the laser is 184 TB/year/10 kt and four times a year would result in 368 TB/year/10 kt

#### 6.4.1.2 Pulsed neutron source

The pulsed neutron source (PNS) system creates a burst of neutrons that are captured throughout a large fraction of the total cryostat volume. For triggering and data volume, this is very convenient: the existing scheme of taking 5.4 ms of data for each trigger means all these neutrons will be collected in a single DUNE event. Thus, the data volume is simply 6.22 GB times the total number of such pulses, but these are likely to be few: a single burst can produce thousands of neutrons whose  $t_0$  is known up to the neutron capture time of 200  $\mu$ s or so.

To trigger the PNS, the MLT will provide a time stamp for the source to fire, and then send a trigger command to the FE readout buffers (via the DFO and EB) that will look like a physics trigger command. The MLT itself then tags that trigger command with the expected trigger type (in this case, PNS).

Typically, a commercial *DD* neutron generator produces  $10^5 - 10^8$  neutrons/pulse, depending on the adjustable pulse width. The current assumption for neutron yield from the *DD* generator is  $10^5$  neutrons per pulse.<sup>6</sup> With the current baseline deployment design in figure 6.19, approximately 130 neutron captures per *DD* generator pulse should be observed inside a 10 kt module. As shown in figure 6.20, the deployment of two large format neutron sources at the corner human access ports could approximately provide calibration for about half of the total TPC volume (30 kt). As the suggested number for localized energy calibration is 100 neutron captures per  $\text{m}^3$ , a total number of 2300 pulses would be needed to calibrate regions under high neutron coverage. Assuming two identical pulsed neutron sources operating in synchronization mode, 1150 triggers are needed for each calibration run. Therefore, the total data volume per run would be

$$1150 \text{ Triggers} \times 1.5 \text{ Bytes} \times 2 \text{ MHz} \times 5.4 \text{ ms} \times 384,000 \text{ channels} = 7.2 \text{ TB}/\text{run}. \quad (6.2)$$

The recommended trigger rate of the PNS system is 0.5 Hz which is limited by the bandwidth of the DAQ event builder. Assuming that the spatial distribution of the neutron capture is near-uniform for the regions that are covered by the two large format neutrons sources, the operation time per calibration run would be 40 minutes. Running the PNS calibration system twice a year would result in a total data volume of 14.4 TB per 10 kt per year. For realistic neutron capture distribution that is non-uniform, we expect to operate the PNS system for a period of 10 times longer than that

<sup>6</sup>Realistic assumption based on commercially available *DD* generators that produce the most neutron yield with a pulse width less than 100  $\mu$ s. *DD* generators with higher neutron yield are being developed in laboratories; commercial devices may require further development to reach a higher level of performance.

under the ideal assumption (7.2 TB/run). As a consequence, the data size per calibration run would be 72 TB/run and running the PNS calibration twice a year would result in a total data size of 144 TB/year/10 kt and four times a year results in 288 TB/year/10 kt.

### 6.5 Construction and installation

#### 6.5.1 Quality control

The manufacturer and the institutions in charge of devices will conduct a series of tests to ensure the equipment can perform its intended function as part of QC. QC also includes post-fabrication tests and tests run after shipping and installation. The overall strategy for the calibration devices is to test the systems for correct and safe operation in dedicated test stands, then at ProtoDUNE-SP-2, then as appropriate near SURF at South Dakota School of Mines and Technology (SDSMT), and finally underground. Electronics and racks associated to each full system will be tested before transporting them underground.

- **Ionization Laser System:** the first important test is design validation in ProtoDUNE-SP-2. For assembly and operation of the laser and feedthrough interface, this will be carried out on a mock-up flange for each of the full hardware sets (periscope, feedthrough, laser, power supply, and electronics). All operational parts (UV laser, red alignment laser, trigger photodiode, attenuator, diaphragm, movement motors, and encoders) will be tested for functionality before being transported underground.
- **Photoelectron Laser System:** the most important test is to measure the light transmission of all fibers at 266 nm. A suitable transmission acceptance threshold will be established based on studies during the development phase. Studies to estimate the number of photoelectrons emitted as a function of intensity (based on distance of fiber output to the metallic tab) will also be undertaken.
- **Laser Beam Location System:** for the LBLS, the main test is checking that the PIN diodes are all functional, and with a light detection efficiency within a specified range, to ensure uniformity across all clusters. For the mirror-based system, the reflectivity of all mirrors will also be tested prior to assembly.
- **Pulsed Neutron Source System:** the first test will be safe operation of the system in a member institution radiation-safe facility. Then, the system will be validated at ProtoDUNE-SP-2. The same procedure will be carried out for any subsequent devices before the devices are transported to SURF and underground. System operation will be tested with shielding assembled to confirm safe operating conditions and sufficient neutron yields using an external dosimeter as well as with the installed neutron monitor. The entire system, once assembled, can be brought down the Ross shaft.

#### 6.5.2 Installation, integration and commissioning

This section describes the installation plans for calibration systems. Most of the hardware is to be installed outside the cryostat so, space on mezzanine surrounding each calibration port is important

for powering and operating the calibration systems. However, some sub-systems have internal components which will be installed following a specific installation sequence, coordinated with other consortia.

### 6.5.2.1 Ionization laser system

Checking the alignment of the optical components is an essential step of the ionization laser system installation. The system includes a low power visible laser that can be used for the several mirror alignment operations, but before that use, both the UV and the visible lasers in the laser box need to be aligned. Alignment of the visible and UV (Class 4) lasers requires special safety precautions and must be carried out once for each periscope/laser system before installing further TPC components. For that reason, the laser boxes must be installed on the cryostat roof as soon as that area becomes accessible.

The periscopes are the only components of the ionization laser system that will be inside the cryostat, but they will be installed from the top of the cryostat and not from the TCO, including the alternative options. However, this installation should be done very carefully in the presence of an operator inside the cryostat, to ensure there are no collisions of the long laser periscopes with other detector components, especially FC elements and CE cable trays. The periscopes should be installed after the relevant structural elements, especially the top FC modules. Installation should proceed in sequence with the assembly of other components, with the furthest from TCO assembled first.

The relevant QC is essentially an alignment test. The LBLS can be used to align the periscopes as they are installed, so it is important that the LBLS is also installed in the same sequence as the periscopes.

A support beam structure closest to the TCO temporarily blocks the calibration ports, but it is removed after the last TPC component is installed. After that, the final calibration components can be installed, including the periscopes on the TCO end wall.

### 6.5.2.2 Laser beam location system

This system has several parts that need to be installed inside the TCO, and some must be integrated with the HV system during installation underground.

The PIN diode system uses a set of diodes that fire when the laser beam hits them. Because the laser shoots from above and the diodes must be in a low voltage region, the plan is to place the diodes below the bottom FC, facing upward, simply on a tray close to the cryostat membrane.

For the pointing measurement, the beams will pass through the FC electrodes and hit the diodes below. There will be 32 of these diode clusters to be installed. The installation will consist of positioning the cluster trays in pre-determined locations, and routing the cables to the respective feedthroughs (work is still underway to decide how to route cables and which flanges to use).

The second laser beam location system consists of a set of 32 mirror clusters: a plastic or aluminum piece holding four to six small mirrors 6 mm in diameter, each at a different angle; the ionization laser will point to these mirrors to obtain an absolute pointing reference. These clusters will be attached to the bottom FC profiles facing into the TPC. This attachment/assembly of the mirror clusters on corresponding FC profiles will be done during FC assembly underground.

### 6.5.2.3 Photoelectron laser system

A large number of photoelectric targets (about 4000) must be attached to the cathode. Experience from other experiments indicates that targets can be glued to the cathode surface, which can be done after cathode assembly but before the cathode is installed in the cryostat.

Once the cathode plane assemblies are in place, the photoelectric target locations will need a high precision survey, which is necessary for the absolute calibration of the electric field with the photoelectron laser.

The third part of the installation is quartz optical fibers on the APA, needed to illuminate the photoelectric targets with light from the Nd:YAG laser. Fiber tips must be properly fastened and oriented for effective illumination, and fiber bundle routing will bring the fiber bundles to the outside of the cryostat where Nd:YAG laser injection points will be located.

### 6.5.2.4 Pulsed neutron source system

The PNS will be installed after the human access ports are closed because the source sits above the cryostat. Installing the system should take place in two stages. In the first stage, the assembly of the system would be independent of the TPC installation. The whole system will be assembled on the ground outside the cryostat at a dedicated radiation safe area. Once assembled, the neutron source will be lifted by crane and integrated with the cryostat structure. Final QC testing for the system will be operating the source and measuring the flux with integrated monitor and dosimeter.

### 6.5.3 Safety

This section discusses risks to personnel safety. Detector safety and risks involving damage to detector components are discussed in section 6.6.3.

Human safety is of critical importance during all phases of the calibration work, including R&D, laboratory testing, prototyping (including ProtoDUNE-SP deployment), and integration and commissioning at the DUNE FD site. DUNE ES&H personnel review and approve the work planning for all phases of work as part of the initial design review, as well as before implementation. All documentation of component cleaning, assembly, testing, installation, and operation will include hazard analysis and work planning documentation and will be reviewed appropriately before production begins. In addition, in the case of planned ProtoDUNE-2 tests, the consortium will interface with CERN safety system to ensure all requirements are met.

Several areas are of particular importance to calibration are

- **Underground laboratory safety:** all personnel working underground or in other installation facilities must follow appropriate safety training and be provided with the required PPE. Risks associated with installing and operating the calibration devices include, among others, working at heights, confined space access, falling objects during overhead operations, and electrical hazards. Appropriate safety procedures will include aerial lift and fall protection training for working at heights. For falling objects, the corresponding safety procedures, including hard hats (brim facing down) and a well restricted safety area, will be part of the safety plan. More details on PPE are provided in TDR Volume III, DUNE far detector technical coordination, chapter 10.



- **Laser safety:** the laser system requires operating a class IV laser [127, 128]. This requires an interlock on the laser box enclosure for normal operation, with only trained and authorized personnel present in the cavern for the one-time alignment of the laser upon installation in the feedthroughs. The trained personnel will be required to wear appropriate laser protective eye wear. A standard operating procedure will be required for the laser which will be reviewed and approved by the Fermilab laser safety officer.
- **Radiation safety for PNS:** a *DD* neutron generator will be used as a calibration device. The design of safety systems for this system include key control, interlock, moderator, and shielding. Lithium-polyethylene (7.5 %) is chosen to be the material for the neutron shield which is rich in hydrogen. The gammas from neutron capture on hydrogen in the shielding material could cause potential radiation hazards. The design of the radiation safety systems (custom shielding and moderator) will be designed to meet Fermilab Radiological Control Manual (FRCM) safety requirements and will be reviewed and approved by Fermilab radiological control organization. Material safety data sheets will be submitted to the DUNE ES&H to understand other safety hazards such as fire. Before beginning any operations at ProtoDUNE-SP, the entire system will be assembled in a neutron shielded room and tested to confirm no leaking of neutrons will occur. The system will also have a neutron monitor that can provide an interlock.
- **High voltage safety:** some of the calibration devices will use high voltage. Fabrication and testing plans will show compliance with local HV safety requirements at any institution or laboratory that conducts testing or operation, and this compliance will be reviewed as part of the design process.
- **Hazardous chemicals:** hazardous chemicals (e.g., epoxy compounds used to attach components of the system) and cleaning compounds will be documented at the consortium management level, with a material safety data sheet as well as approved handling and disposal plans in place.
- **Liquid and gaseous cryogenics:** cryogenics (e.g., liquid nitrogen and LAr) will most likely be used in testing of calibration devices. Full hazard analysis plans will be in place at the consortium management level for full module or module component testing that involves cryogenics. These safety plans will be reviewed appropriately by DUNE ES&H personnel before and during production.

## 6.6 Organization and management

### 6.6.1 Consortium organization

The calibration consortium was formed in November 2018 as a joint single and dual phase consortium, with a consortium leader and a technical leader. Figure 6.22 shows the organization of the consortium. The calibration consortium board currently comprises institutional representatives from 11 institutions as shown in table 6.6. The consortium leader is the spokesperson for the

consortium and responsible for the overall scientific program and management of the group. The technical leader of the consortium is responsible for managing the project for the group.

The consortium’s initial mandate is the design and prototyping of a laser calibration system, a neutron generator, and possibly a radioactive source system, so the consortium is organized into three working groups, each dedicated to one system. Each group has a designated working group leader.

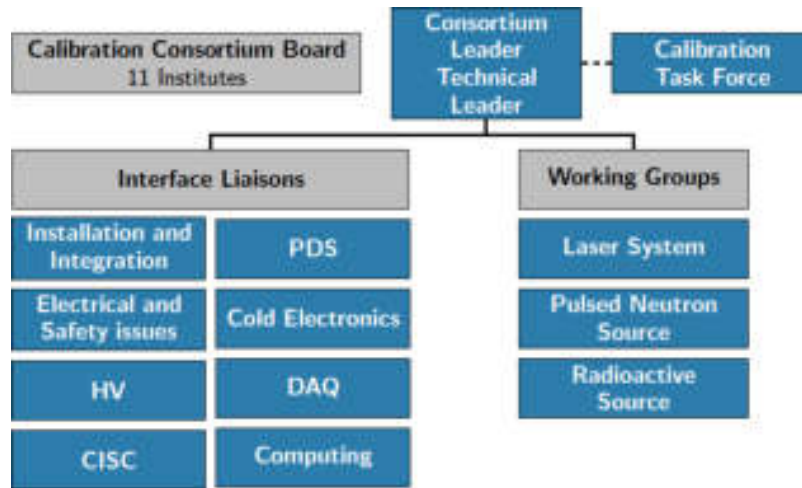


Figure 6.22. Organizational chart for the calibration consortium.

Table 6.6. Current calibration consortium board institutional members and countries.

| Member Institute                                    | Country     |
|---|-------------|
| LIP   | Portugal    |
| University of Bern (Bern)                           | Switzerland |
| Los Alamos National Lab (LANL)                      | USA         |
| Michigan State University (MSU)                     | USA         |
| Colorado State University (CSU)                     | USA         |
| University of Iowa                                  | USA         |
| University of Hawaii (Hawaii)                       | USA         |
| University of Pittsburgh (Pitt)                     | USA         |
| Boston University (BU)                              | USA         |
| University of California, Davis (UC Davis)          | USA         |
| South Dakota School of Mines and Technology (SDSMT) | USA         |

In addition, figure 6.22 shows several liaison roles currently being established to facilitate connections with other groups and activities:

- Detector integration and installation,
- Electrical and safety issues,

- DAQ,
- Computing,
- Cryogenic instrumentation and slow controls (CISC),
- Cold electronics,
- High voltage,
- Photon Detection System.

Currently, new institutions are added to the consortium following an expression of interest from the interested institute and upon obtaining consensus from the current consortium board members.

### 6.6.2 Institutional responsibilities

Calibrations will be a joint effort for SP and DP. Design validation, testing, calibration, and performance of calibration devices will be evaluated using ProtoDUNE data.

Following the conceptual funding model for the consortium, various responsibilities have been distributed across institutions within the consortium. Table 6.7 shows the current institutional responsibilities for primary calibration subsystems. For physics and simulations studies and validation with ProtoDUNE, a number of institutions are interested.

**Table 6.7.** Institutional responsibilities in the calibration consortium.

| Subsystem                          | Institutional Responsibility                                       |
|------------------------------------|--|
| Ionization Laser System            | Bern, LIP, LANL, Hawaii  |
| laser beam location system         | Hawaii, LIP  |
| Photoelectron Laser System         | LANL, Hawaii   |
| Pulsed Neutron Source System       | BU, CSU, UC Davis, Iowa, LIP, MSU, LANL, SDSMT                     |
| Proposed Radioactive Source System | SDSMT  |
| Physics & Simulation               | BU, CSU, Hawaii, LANL, LIP, MSU, SDSMT, UC Davis, Pittsburgh, Iowa |

### 6.6.3 Risks

Table 6.8 lists the possible risks identified by the calibration consortium along with corresponding mitigation strategies and impact on probability, cost, and schedule post-mitigation. The table shows all risks are medium or low level, mitigated with necessary steps and precautions. More discussion on each risk is provided below.

- *Risk 1:* the ProtoDUNE-SP design tests being inadequate for the FD is an important one because this requires early validation from ProtoDUNE data so we can perform R&D of alternate designs and/or improvements on a reasonable time scale. In addition, the calibration ports will be designed to be multipurpose to enable deployment of new systems if they are developed. Therefore, in general, the calibration systems mitigate risk to the experiment as the systems sit above the cryostat and/or use multipurpose ports and may be removed.
- *Risk 2:* this is a medium-level risk where the elements of the calibration system fail engineering requirements, such as laser beam divergence and precision of the mechanical system, in which case the as-built system will not meet the physics requirements. The mitigation strategy for this involves testing the same designs envisioned for the FD in dedicated lab tests and ProtoDUNE-SP-2, to identify any issues and address them. The pre-installation QC will also allow us to reject parts that do not meet requirements.
- *Risk 3:* if the ionization laser beam directly hits the elements of the PD system system for an extended time, the scintillation efficiency might be degraded. The mirror movement controller of the laser system must avoid the beam directly hitting the PD system. An automated system will block or turn off the laser beam in case of saturation at one of the PD system channels. The laser electrical system must allow the later implementation of a hardware interlock if that is found to be necessary.
- *Risk 4:* this is a low level risk, where the laser beam location system fails; this would reduce the precision of the E field measurement but will not prevent the measurement from being made. Pre-fill QC will be carried out to minimize this risk. Additionally, redundancy will be built into the system, with alternative targets, including some passive ones. A possible alternative way to obtain an absolute measurement is to use reflections off of the aluminum FC profiles, with a very slow angular scan.
- *Risk 5:* this risk relates to the laser beam misalignment. If the laser beam becomes misaligned with the mirror sequence, then that specific ionization laser module becomes unusable for calibration. To mitigate this, the ionization laser system includes a visible (red) laser specifically for the purpose of alignment. If the misalignment is not just with the warm mirrors, but also with the cold ones, cryostat cameras might be needed to check arrival of red light to the TPC.
- *Risk 6:* if the effective attenuation length of 57 keV neutrons in LAr turns out to be significantly smaller than 30 m, then PNS system will not cover the whole detector, or additional modules will be needed. This will be resolved in the next year by a measurement at the Los Alamos National Lab (LANL); the ProtoDUNE run will also provide a full end-to-end demonstration.
- *Risk 7:* if the neutron flux from the *DD* generator of the PNS system is enough to activate the moderator and cryostat insulation, then a new source of radiological backgrounds might be created. This can be mitigated by neutron activation studies of insulation material, and ProtoDUNE testing at neutron flux intensities and durations well above the run plan, as well as simulation studies done in collaboration with the DUNE Background Task Force.

- *Risk 8:* if the neutron yield from the *DD* generator is not high enough to provide sufficient neutron captures inside the TPC, then either the neutron calibration cannot be done or a higher flux generator must be obtained, or additional sources must be used. Investigation is being done on both commercially available and custom *DD* generators. Additionally, operating the *DD* generator with wider pulse is under consideration, which would require the PD system to provide the neutron capture time  $t_0$ . Another possibility is to carry out dedicated runs at higher pulse rate and, to ensure that the DAQ can handle it, one would acquire only the data from the APAs farthest from the source. All of this will be tested in the ProtoDUNE-2 run. Placing the neutron source closer to the TPC may increase the neutron yield by a factor of 6. An alternative design (figure 6.24) with neutron source inside the calibration feedthrough ports (centrally located on the cryostat) is being studied. This compact neutron source would be light enough to be moved across different feedthroughs and will provide additional coverage.
- *Risk Opportunity 9:* the ionization laser system assumes that the laser beams will be sufficiently narrow for a measurement up to 20 m distances. However, as the Rayleigh scattering is of the order 40 m, it is possible the laser may travel further than 20 m. This may reduce the number of lasers needed and therefore the overall cost. The maximum laser distance will be assessed in ProtoDUNE-2.

**Table 6.8:** Calibration risks (P=probability, C=cost, S=schedule) The risk probability, after taking into account the planned mitigation activities, is ranked as L (low < 10 %), M (medium 10 % to 25 %), or H (high > 25 %). The cost and schedule impacts are ranked as L (cost increase < 5 %, schedule delay < 2 months), M (5 % to 25 % and 2–6 months, respectively) and H (> 20 % and > 2 months, respectively).

| ID           | Risk   | Mitigation   | P | C | S |
|--------------|--|--|---|---|---|
| RT-SP-CAL-01 | Inadequate baseline design                         | Early detection allows R&D of alternative designs accommodated through multipurpose ports        | L | M | M |
| RT-SP-CAL-02 | Inadequate engineering or production quality       | Dedicated small scale tests and full prototyping at ProtoDUNE; pre-installation QC               | L | M | M |
| RT-SP-CAL-03 | Laser impact on PDS                                | Mirror movement control to avoid direct hits; turn laser off in case of PDS saturation           | L | L | L |
| RT-SP-CAL-04 | Laser beam location system stops working           | QC at installation time, redundancy in available targets, including passive, alternative methods | L | L | L |
| RT-SP-CAL-05 | Laser beam misaligned                              | Additional (visible) laser for alignment purposes  | M | L | L |
| RT-SP-CAL-06 | The neutron anti-resonance is much less pronounced | Dedicated measurements at LANL and test at ProtoDUNE   | L | L | L |
| RT-SP-CAL-07 | Neutron activation of the moderator and cryostat   | Neutron activation studies and simulations   | L | L | L |

|              |  |   |   |   |   |
|--------------|--|---|---|---|---|
| RT-SP-CAL-08 | Neutron yield not high enough                          | Simulations and tests at ProtoDUNE; alternative, movable design | L | M | M |
| RO-SP-CAL-09 | Laser beam is stable at longer distances than designed | tests at ProtoDUNE  | M | H | L |

#### 6.6.4 Schedule and milestones

Table 6.9 shows the schedule and key milestones for the calibration consortium that lead to commissioning the first FD module. The demonstration of calibration systems design, operation, and performance at the ProtoDUNE-SP-II running is a key part of calibration schedule; those milestones are also listed in the table. The technology design decisions on calibration subsystems should be made by January 2020 for the laser system and by March 2020 for the neutron source system followed by technical design reviews. The production of design prototypes to be deployed at ProtoDUNE-SP-II running should be finished by February 2021 followed by assembly and deployment in ProtoDUNE-SP in March 2021. The radioactive source deployment system (RSDS)

design will follow a demonstration R&D program outlined in detail in table 6.11 in the appendix, with major milestones highlighted in this section. The major steps for systems approval are the design review in May 2020 and the deployment test at ProtoDUNE-SP-II in April 2022.

Production of calibration systems for the FD should start in March 2022, followed by assembly of the systems underground once the detector cavern becomes available in early 2023. Installing the laser system can begin as soon as the cryostat roof is accessible and conclude once the TPC is ready to install. If it is approved, the RSDS guide system can begin installation just before TPC is installed. The purge-boxes on top of the cryostat can be done later. Installing the main components of the PNS will begin once the human access ports are no longer needed for TPC installation in June 2025.

**Table 6.9.** Key calibration construction schedule milestones leading to commissioning the first FD module. (\*) Schedule items related to the radioactive source deployment system (RSDS) are to be considered pending system approval.

| Milestone   | Date (Month YYYY) |
|---|-------------------|
| Laser systems design decision (including ionization, beam location and photoelectron systems) | January 2020      |
| Laser systems design review   | February 2020     |
| PNS design decision   | March 2020        |
| PNS design review   | April 2020        |
| RSDS design review  | May 2020          |
| Start of module 0 component production for ProtoDUNE-II                                       | April 2020        |
| End of module 0 component production for ProtoDUNE-II   | February 2021     |
| Start of ProtoDUNE-SP-II installation   | March 2021        |
| Start of ProtoDUNE-DP-II installation   | March 2022        |
| production readiness review dates   | March 2022        |
| South Dakota Logistics Warehouse available  | April 2022        |
| RSDS demonstration test at ProtoDUNE-SP-II (*)  | April 2022        |
| Start of Laser and PNS production   | May 2022          |
| Beneficial occupancy of cavern 1 and CUC  | October 2022      |
| End of PNS production   | March 2023        |
| End of Laser system production  | July 2023         |
| End of RSDS production (*)  | August 2023       |
| CUC counting room accessible  | April 2023        |
| Start assembly of calibration production units in the cavern                                  | May 2023          |
| Top of detector module #1 cryostat accessible   | January 2024      |
| Start installation and alignment of Laser boxes   | May 2024          |
| Start of detector module #1 TPC installation  | August 2024       |
| Start installation of Laser System periscopes   | August 2024       |
| Start installation of RSDS guide system (*)   | August 2024       |
| End of detector module #1 TPC installation  | May 2025          |
| Installation of RSDS purge-boxes (*)  | May 2025          |
| Installation of the PNS main components   | June 2025         |
| Top of detector module #2 accessible  | January 2025      |
| Start of detector module #2 TPC installation  | August 2025       |
| End of detector module #2 TPC installation  | May 2026          |

2020 JINST 15 T08010

## 6.7 Appendix

### 6.7.1 Laser system alternative designs

#### 6.7.1.1 End-wall coverage enhancement

The eight calibration ports closer to the end-walls (four on each side) are not positioned on top of the TPC, but instead located about 40 cm away from the FC along the  $z$  (beamline) direction. If positioned on top, FC penetration would be quite complicated, having to come from the sides. Use of the periscope baseline design for the end-wall periscopes would severely limit the volume coverage, similar to the coverage limitation mentioned in section 6.3.2.3.

We describe here an alternative design for the end-wall ports that would improve the laser beam coverage without requiring FC penetration.

The periscope is exactly the same as the baseline design but, at the top of the calibration port, is mounted on a flange that has an additional rotation degree of freedom. Figure 6.23 presents a preliminary drawing of the concept. The 250 mm diameter calibration port has on top of it the main rotary flange that, itself, has another smaller port off-centered by 40 mm with respect to the main one. On this smaller port, a secondary rotary flange is installed and it is this one that holds the laser periscope, including the optical feedthrough and the linear stage for mirror movement. When the main flange rotates, the periscope also moves along a circular (40 mm diameter) trajectory. Consequently, within the cryostat, the relative position between the beam mirror and the FC profiles changes as well, and so the shadowed regions also change, by parallax. Using different main rotary flange angles, it should be possible to locate the mirror in enough different positions in order to cover all the previously shadowed angles.

Calculations similar to the ones showed earlier show that, using only 3 different positions (separated by  $90^\circ$ ), a coverage of 94 % should be possible for 30 cm voxels and allowing all tracks directed at the APA.

### 6.7.2 PNS system alternative designs

#### 6.7.2.1 Small format moderator

An alternative method for delivering the neutrons is to use the existing calibration feedthroughs. In the current cryostat design, 20 calibration feedthroughs with a 25 cm outer diameter will be available on top of the cryostat. One can design the neutron source with an ultra-thin  $DD$  generator that fits the size of the feedthrough as shown in figure 6.24 (right). The problem is that there will be no space in the feedthrough for the shielding materials to fit in, so additional shielding will need to be placed around the feedthrough. The weight of this compact neutron source will be about 140 kg, so minimal special mounting is needed. In addition, the source may be moved as well, allowing further flexibility. The effective neutron flux is expected to be similar to that of the baseline deployment.

The volume coverage at the center of the detector can be significantly increased by using a small format neutron source deployed on top at the center of the cryostat using the multi-purpose feedthroughs. Figure 6.25 shows the position distribution of the neutron captures using two large format sources at the corner human access ports and one additional small format source in the middle of the cryostat. The small format source is important to complement the coverage at the center of the TPC. The alternative small format neutron source is very compact and lightweight, so



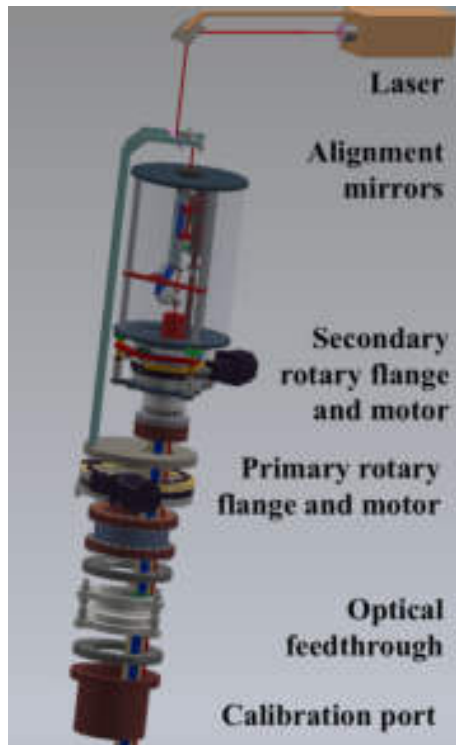


**Figure 6.23.** Exploded CAD drawing (preliminary) of the double rotary flange for the end-wall laser calibration ports. The calibration port is shown in brown at the bottom; the primary and secondary rotary flanges are shown in yellow, with the (black) motors next to them. The optical feedthrough is shown in the center, in blue. On top, the mirror arrangement allows the laser beam to be aligned with the optical feedthrough no matter the angle of each of the rotary flanges.

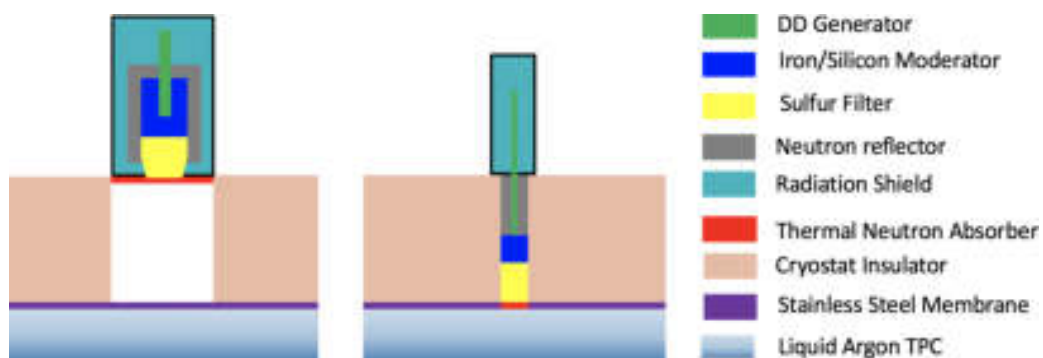


**Figure 6.24.** (right) Small format neutron source deployed inside the calibration feedthrough ports. (left) For comparison, large format neutron source deployed above/inside the human access ports is shown on the left.

further coverage improvement is possible by moving the source to different calibration feedthroughs. The deployment of the small format source would require sharing of the feedthrough ports with other calibration systems, which is currently under investigation.

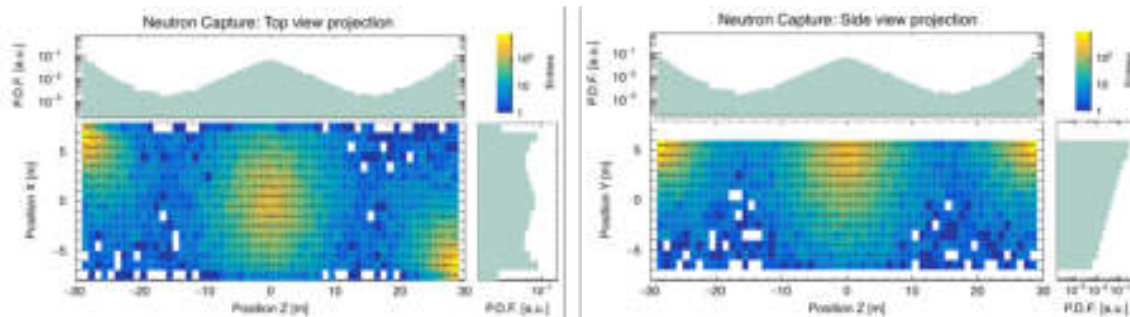


**Figure 6.25.** Neutron capture positions inside a DUNE-sized TPC, assuming alternative configuration with two large format neutron sources located at the corner human access ports and one small format neutron source located at the center of the cryostat, which compensates the missing volume coverage of the two large format sources at the center of the detector.  $L=60$  m (along  $Z$  axis, horizontally parallel to the beam direction),  $W=14.5$  m (along  $X$  axis, horizontally perpendicular to the beam direction),  $H=10$  m (along  $Y$  axis, vertically perpendicular to the beam direction).  $2.7 \times 10^7$   $DD$  generator neutrons with 2.5 MeV energy were simulated in each moderator and propagated inside the TPC. Top (left) and side (right) views of neutron capture positions are shown.

In principle, for the baseline deployment plan as shown in figure 6.20, we can run the neutron source for a longer time to increase the coverage at the central region of the detector. However, this would result in a huge data volume. So, the best way to complement the coverage at the center of the detector is to use the alternate deployment as discussed here. This design would require a total number of 4600 pulses to calibrate the entire 10 kt module. Assuming that three neutron sources with identical neutron capture yield are operated in synchronization mode, 1500 triggers are needed for each calibration run. Therefore, the total data volume per run would be

$$1500 \text{ Triggers} \times 1.5 \text{ Bytes} \times 2 \text{ MHz} \times 5.4 \text{ ms} \times 384,000 \text{ channels} = 9.5 \text{ TB/run.} \quad (6.3)$$

The recommended trigger rate of the PNS system is 0.5 Hz which is limited by the bandwidth of the DAQ event builder. Assuming that the spatial distribution of the neutron capture is uniform across the whole detector volume, the operation time per calibration run would be 50 minutes. Running the PNS calibration system twice a year would result in a total data volume of 19 TB per 10 kt per year. For realistic neutron capture distribution that is non-uniform, we expected to operate the PNS system for a period of 10 times longer than that under the ideal assumption (9.5 TB/run). As a result, the data size per calibration run would be 95 TB/run and running the PNS calibration twice a year would result in a total data size of 190 TB/year and four times a year would result in 380 TB/year.

### 6.7.3 Proposed radioactive source calibration system

Radioactive source deployment provides an in-situ source of physics signals at a known location and with a known activity that can be chosen such that there is only one calibration event per

drift time window. The primary source design probes de-excitation products ( $\gamma$ -rays) which are directly relevant for detection of supernova neutrinos and  $^8\text{B}/\text{hep}$  solar neutrinos. The radioactive source deployment system (RSDS) is the only calibration system that could probe the detection capability for single isolated solar neutrino events and study how well radiological backgrounds can be suppressed. The trigger efficiency could be studied as a function of threshold.

Other measurements with the primary source include electro-magnetic (EM) shower characterization for long-baseline  $\nu_e$  CC events, electron lifetime and electric field as a function of detector module vertical position, individual light detector response, and determination of radiative components of the Michel electron energy spectrum from muon decays. Aside from the primary nickel source that produces 9 MeV  $\gamma$ -rays via the  $^{58}\text{Ni}(n,\gamma)^{59}\text{Ni}$  reaction, other sources could be deployed with the same multi-purpose system, for example an  $(\alpha,\gamma)$  source, and  $^{252}\text{Cf}$  and/or AmBe neutron sources that probe the impact of various radiological backgrounds, like radon (causing  $(\alpha,\gamma)$  events) or radiological neutrons, or simply measure the neutron tagging efficiency, useful for improved calorimetry of beam neutrino interactions. In contrast to the primary nickel source with 9 MeV gamma-rays, the  $(\alpha,\gamma)$  source producing gamma-ray energies around 15 MeV via the  $^{40}\text{Ar}(\alpha,\gamma)^{44}\text{Ca}$  reaction could even be deployed outside of the cryostat, to probe the upper visible energy range and trigger efficiency for  $^8\text{B}/\text{hep}$  solar neutrinos.

Both the RSDS and the PNS systems are needed to address the integrated response of the detector for low energy physics, especially SNB and  $^8\text{B}/\text{hep}$  solar neutrinos. The RSDS primarily probes for trigger efficiency, the PNS tests mostly for uniformity. Response in argon may change rapidly as a function of photon energy due to underlying nuclear physics mechanisms. A combination of 6 MeV (direct neutron capture response), 9 MeV (from the nickel source), 15 MeV (from the  $(\alpha,\gamma)$  source) is needed to map the low energy response. In terms of complementarity, radioactive sources provide a known position, known-energy single photon events that could be triggered on, while the pulsed neutron source provides a simple, potentially, non-invasive design with externally triggered multi-photon energy signature which is visible across the entire detector with a known time signature.

### 6.7.3.1 Design considerations

A composite source can be used that consists of  $^{252}\text{Cf}$ , a strong neutron emitter, and  $^{58}\text{Ni}$ , which, via the  $^{58}\text{Ni}(n,\gamma)^{59}\text{Ni}$  process, converts one of the  $^{252}\text{Cf}$  fission neutrons, suitably moderated, to a monoenergetic 9 MeV photon [129]. The source is envisaged to be inside a cylindrical moderator with mass of about 15 kg and a diameter of 20 cm such that it can be deployed via the multipurpose instrumentation ports discussed in section 6.3.1. The activity of the radioactive source is chosen such that no more than one 9 MeV capture  $\gamma$ -event occurs during a single drift period. This forms the main requirement for this system as this allows one to use the arrival time of the measured light as a  $t_0$  and then measure the average drift time of the corresponding charge signal(s). Table 6.10 lists the full set of requirements for the radioactive source deployment system.

The sources would be deployed outside the FC within the cryostat to avoid regions with a high electric field, about 30 cm from the field cage. The  $\gamma$ -ray would need to travel about two attenuation lengths (including the 10 cm radius of the source body). Such high  $\gamma$ -energies are typically only achieved by thermal neutron capture, which invokes a neutron source surrounded by a large amount of moderator, thus driving the size of the source.

**Table 6.10.** Full list of Specifications for radioactive source deployment system.

| Quantity/Parameter   | Specification                    | Goal                              |
|--|----------------------------------|-----------------------------------|
| Distance of the source from the field cage                                       | 30 cm                            |                                   |
| Rate of 9 MeV capture $\gamma$ -events inside the source (top-level requirement) | < 1 Hz                           |                                   |
| Data volume per 10 kt  | 50 TB $\cdot$ year <sup>-1</sup> | 100 TB $\cdot$ year <sup>-1</sup> |
| Longevity  | 20 years                         | > 20 years                        |

A gamma source based on the  $^{58}\text{Ni}(n,\gamma)^{59}\text{Ni}$  reaction, and triggered by an AmBe neutron source, has been successfully built [129], yielding high  $\gamma$ -energies of 9 MeV. DUNE proposes to use a  $^{252}\text{Cf}$  (or AmLi as backup) neutron source with lower neutron energies, which requires less than half of the surrounding moderator, and making the  $^{58}\text{Ni}(n,\gamma)$  source only 20 cm or less in diameter. The multipurpose instrumentation feedthroughs at either end of the cryostat are sufficient for this, and have an outer diameter of 25 cm. The moderator material chosen for DUNE is Delrin,<sup>7</sup> which has a large enough density to avoid flotation. Further, the end caps of the source body are round to avoid distorting the electric field and to eliminate the risk of the source getting stuck during deployment. Figure 6.26 depicts the primary source design of a cylindrical Delrin moderator with a diameter of 20 cm, a height of 40 cm including half-spheres at either end with radius of 10 cm, deployed at  $z=40$  cm leaving a gap of 30 cm towards the FC and at a distance to the APA of  $x=220$  cm, which is slightly further than mid-drift.

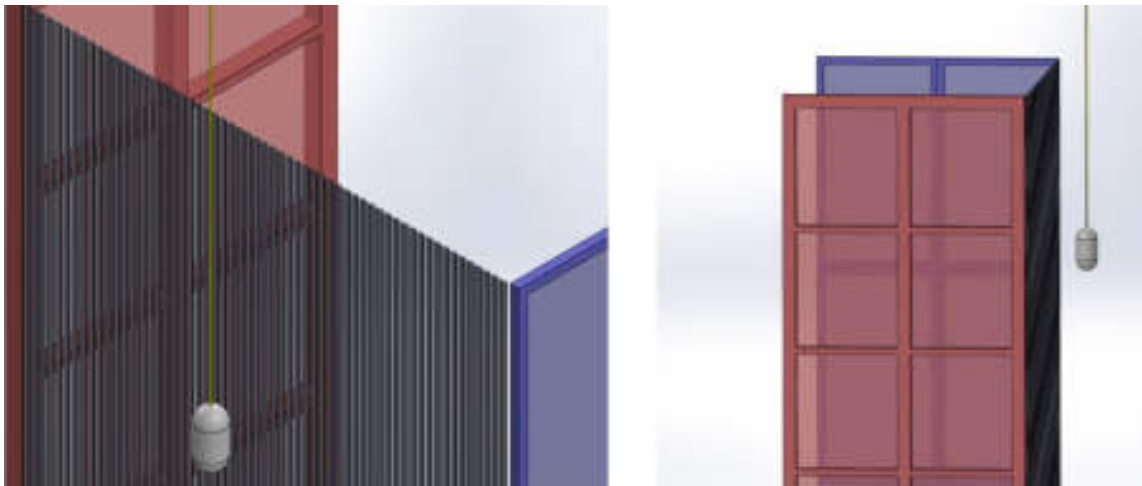


**Figure 6.26.** Fish-line deployment scheme in DUNE for a radioactive source encapsulated inside a cylindrical Delrin moderator body 20 cm in diameter and 40 cm high, including half-spheres with a radius of 10 cm at either end. A  $^{252}\text{Cf}$  neutron source and a natural Ni target are sealed inside at the center. The fish-line is deployed 40 cm outside of the FC and 220 cm away from the APA (red plane).

<sup>7</sup>DuPont™Delrin®, <https://www.dupont.com/products/delrin.html>.

A successfully employed multipurpose fish-line calibration system for the Double Chooz reactor neutrino experiment has become available after the decommissioning of Double Chooz in 2018. The system can be easily refitted for use in DUNE. The system will be housed inside a purge-box that is connected via a neck to a multipurpose calibration feedthrough with a closed gate valve on top of the cryostat. Before deployments, the source will be gently cooled-down by blowing liquid argon boil-off onto it inside a sealed purge-box. After the source has reached near-LAr temperatures, the purge-box will be evacuated by a vacuum pump to remove any residual oxygen and nitrogen which is monitored at the ppm level. Then, the entire purge-box interior is purged with boil-off liquid argon, and the pressure equalized with the gas pressure inside the detector, before the gate-valve is opened and deployments can commence. This procedure ensures that no significant impurities are introduced into the detector during a deployment and that no significant amount of liquid argon is boiled-off from the detector.

Deployed near mid-drift (in each TPC module) the 9 MeV  $\gamma$ -ray source can illuminate the full drift length from APA to CPA. The sources are retrieved from the detector after each deployment and stored outside the cryostat following approved safety protocols, and the gate-valves are kept closed after deployments. More details on radiation safety and handling procedures are presented in section 6.7.3.9.

### 6.7.3.2 Development plan

The major development plans for the radioactive source deployment system include the following.

- Continue development of relevant simulation tools including geometry representation of the source deployment system and impact from various radiological contaminants on detector response.
- Conduct studies to suppress radiological backgrounds for the calibration source.
- Conduct simulation studies to understand data and trigger rates.
- Study a baseline design source with Delrin moderator,  $^{252}\text{Cf}$  neutron source, and natural nickel target, both sealed inside at the moderator's center.
- Validate 9 MeV capture  $\gamma$ -ray yield of source using spectroscopic measurements with the 'RABBIT' germanium detector at South Dakota School of Mines and Technology (SDSMT), that has an assay chamber large enough to fit the bulky moderator.
- Validate with  $^3\text{He}$  based hodoscope at SDSMT to ensure that the flux of neutrons escaping the moderator is not an issue; otherwise use lower energetic AmLi neutron source instead and/or more moderator material, and/or different geometric configuration of nickel target.
- Test gentle GAr cooling of source and validate material integrity. Measure tensile strength of braided SS-304 wire-ropes at cryogenic temperatures and ensure a safety factor of one order of magnitude by adjusting number of steel braids and their diameters. Validate cryogenic shrinkage of sectional teflon sleeves, that enclose the braided steel wire-ropes and electrically insulate it towards the FC.

- Validate that anticipated fluid flow in LAr does not cause oscillations of the source; otherwise design vertical guide wires to be pre-installed during detector installation which will keep source in stable position during deployment along the vertical axis.
- Explore other radioactive sources beyond the primary 9 MeV  $\gamma$ -ray nickel source, such as the previously mentioned 15 MeV  $\gamma$ -ray source based on the  $^{40}\text{Ar}(\alpha, \gamma)^{44}\text{Ca}$  process with  $^{241}\text{Am}$  as the alpha emitter. This is currently being assembled at SDSMT. Furthermore, investigate hybrid neutron sources ( $^{252}\text{Cf}$  and AmBe) that emulate the kinetic neutron energy spectrum of radiological neutrons and probe the neutron tagging efficiency.

A successful demonstration of the RSDS in ProtoDUNE-2 running is the main priority for this system towards making a decision on deploying this system for the FD. A schedule with main steps towards ProtoDUNE-2 deployment is shown in table 6.11.

**Table 6.11.** Key milestones towards commissioning the radioactive source deployment system in ProtoDUNE-2.

| Milestone   | Date (Month YYYY) |
|---|-------------------|
| Baseline RSDS design validation                             | January 2020      |
| RSDS mock-up deployment test at SDSMT                       | March 2020        |
| RSDS Design review  | May 2020          |
| RSDS Production readiness review (PRR)                      | July 2020         |
| Start of module 0 RSDS component production for ProtoDUNE-2 | September 2020    |
| End of module 0 RSDS component production for ProtoDUNE-2   | February 2021     |
| <b>Start of ProtoDUNE-2 (SP) installation</b>               | <b>March 2021</b> |
| Start of RSDS installation                                  | April 2021        |
| RSDS demonstration test at ProtoDUNE-2                      | April 2022        |

### 6.7.3.3 Measurement program

The proposed primary 9 MeV single  $\gamma$  source may also be used to test the  $\gamma$  component of the SNB and  $^8\text{B}/\text{hep}$  solar neutrino signal along the full drift but only in the endwall regions of the detector. The source may also be used to determine the relative charge and light extraction efficiency in the vertical direction for measurements of energy resolution and energy scale.

Figure 6.27 depicts in a top view of the detector the simulated charge extraction efficiency for the 9 MeV  $\gamma$ -ray source deployed 40 cm outside of the FC, near mid-drift i.e., 220 cm away from the APA in the  $x$  direction, in the presence of expected background before (a) and after (b) applying selection cuts. The selection cuts are based on the amplitude and location of wire hits, and require a coincidence with a suitable signal in the PD system. Figure 6.27(b) shows that the selection cuts can reject radiological backgrounds almost entirely, and that the RSDS should allow the study of the trigger efficiency for isolated solar neutrino events, and its threshold dependence.

Figure 6.28 shows exemplary simulated RSDS measurements of the E field strength (a) and of the electron lifetime (b), each for three different scenarios. The analysis is based on fitting the

measured distribution of drift-time, i.e., the time difference between the PD system signal and the recorded hit times on collection wires, passing the selection cuts. Figure 6.28(a) illustrates that with this method the E field strength could be measured at  $\sim 1\%$  precision at each vertical deployment position at the endwalls. Likewise, figure 6.28(b) illustrates that the electron lifetime could be measured at about  $\sim 10\%$  precision (possibly better at higher lifetimes) at each vertical deployment position at the endwalls.

Figure 6.28(c) illustrates that it is not convincingly possible to unambiguously measure both the electron lifetime and the electric field strength with a recorded charge spectrum (after selection cuts) alone, since both parameters simply shift the upper falling edge of the charge spectrum up or down. However, when combined with the drift-time measurement, the charge measurement would provide an additional constrain that could possibly break correlations.

Aside from the primary 9 MeV  $\gamma$ -ray nickel source, other sources could be deployed with the same multi-purpose system, for example a  $^{40}\text{Ar}(\alpha, \gamma)^{44}\text{Ca}$  gamma-ray source, a  $^{252}\text{Cf}$  and/or AmBe neutron source that probe the impact of various radiological backgrounds, like radon ( $\alpha, \gamma$ ) or radiological neutrons, or simply measure the neutron tagging efficiency, useful for improved calorimetry of beam neutrino interactions. In contrast to the nickel source, the 15 MeV ( $\alpha, \gamma$ ) could be deployed outside of the cryostat.

An external ProtoDUNE-2 deployment can demonstrate the feasibility of the non-invasive 15 MeV  $^{40}\text{Ar}(\alpha, \gamma)^{44}\text{Ca}$   $\gamma$ -ray source despite the lack of overburden to shield cosmic rays. In contrast to cosmic muons, 15 MeV  $\gamma$ -ray induced hit clusters will start inside the detector volume, and are not tracks that begin at the detector edges. Thus, the RSDS calibration events could therefore be easily selected and the detected charge can be analyzed. The detected light, however, will be obscured from the high light level in each drift period from cosmic muons hitting ProtoDUNE.

### 6.7.3.4 RSDS design validation

The cosmic induced background rate at ProtoDUNE is too high at the surface to detect responses to the DUNE  $\gamma$ -ray source; a higher intensity source could be deployed to test the detector response and analysis method. However, tests of functionality, reliability, and safety of the mechanical deployment system are essential to show the source can be deployed and retrieved with no issues, so these will be the main goals of the ProtoDUNE-2 deployment. As mentioned earlier, tests of the source design itself, in terms of  $\gamma$  activity, will be done at SDSMT.

### 6.7.3.5 DAQ requirements

Section 6.4.1 provides an overall discussion of the Calibration and DAQ interface. Here, the DAQ requirements for the radioactive source deployment system are discussed. The radioactive source will not be triggerable by the MLT. Rather, it will deliver a tag to the MLT and that tag will include a time stamp that can be used by the MLT to issue a trigger command to the FE readout. The trigger command will have a standard readout window size of 5.4 ms, but to keep data rates manageable, the command will only be send to FE readout buffers that are expected to be illuminated by the source. The localization of trigger commands thus reduces the data volume by 150, if only one APA is read out.

Nevertheless, if the rate of such a source is anywhere close to one per 5.4 ms, the detector would be running continuously in the current scheme. Therefore we assume that the interaction rate in the

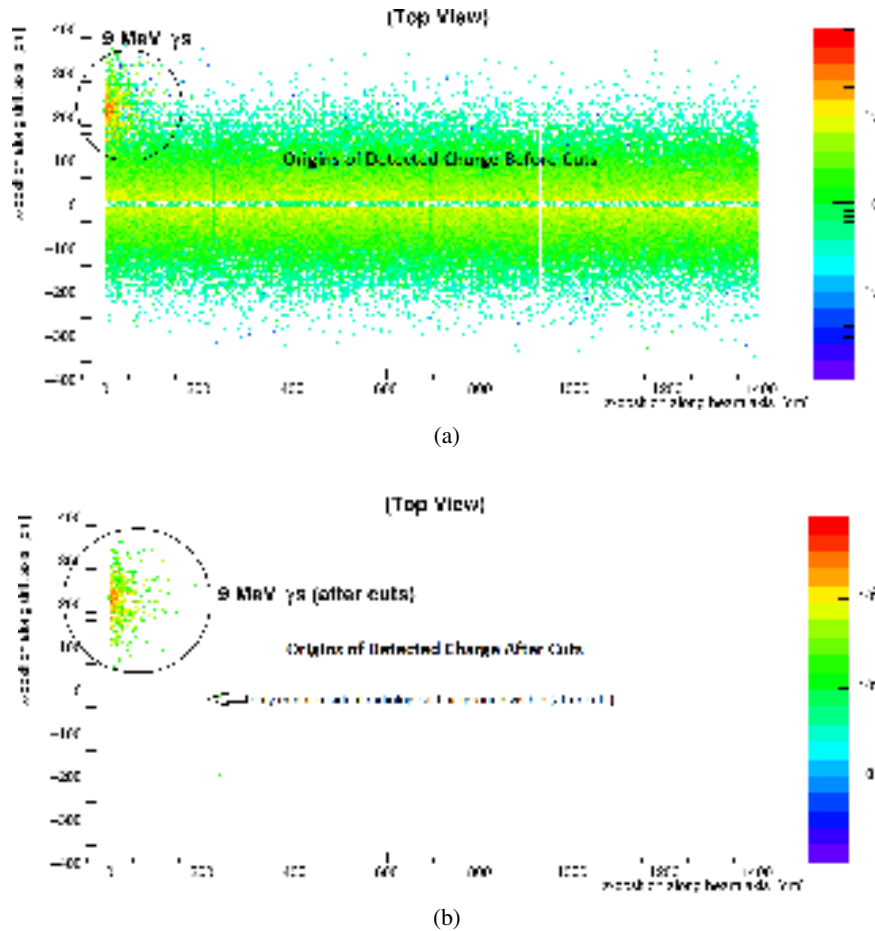


**Figure 6.27.** Detected charge (a) without cuts and (b) with selection cuts for a simulated 9 MeV  $\gamma$ -ray source deployed at  $z = -40$  cm outside of the FC,  $x = 220$  cm away from the APA, and  $y = 300$  cm half-height of an upper endwall APA with simulated expected radiological background, that gets almost eliminated by selection cuts.

detector is 10 Hz or less. The tag from the source will likely be much higher than this, because not all  $\gamma$ s interact in the active TPC volume. Thus the radioactive source trigger will be a coincidence in the Module-Level Trigger between a low-energy trigger candidate from the illuminated APA, and a source tag with a relevant time stamp. With this rate, and with localization of events to one APA, the total data volume would be

$$8 \text{ hours} \times 4 \text{ FTs} \times 10 \text{ Hz} \times 1.5 \text{ Bytes} \times 2 \text{ MHz} \times 5.4 \text{ ms} \times 2560 \text{ channels} = 50 \text{ TB/scan.} \quad (6.4)$$

Running this calibration four times/year would yield 200 TB of data in 10 kt per year. Table 6.12 summarizes the data volume requirements for RSDS.

### 6.7.3.6 Risks

The risks associated with the radioactive source system are described in table 6.13 along with appropriate mitigation strategies and the impact (low, medium or high risk levels) on probability, cost, and schedule post-mitigation. There are three residual medium-level risks in the table, more discussion on them is provided below:



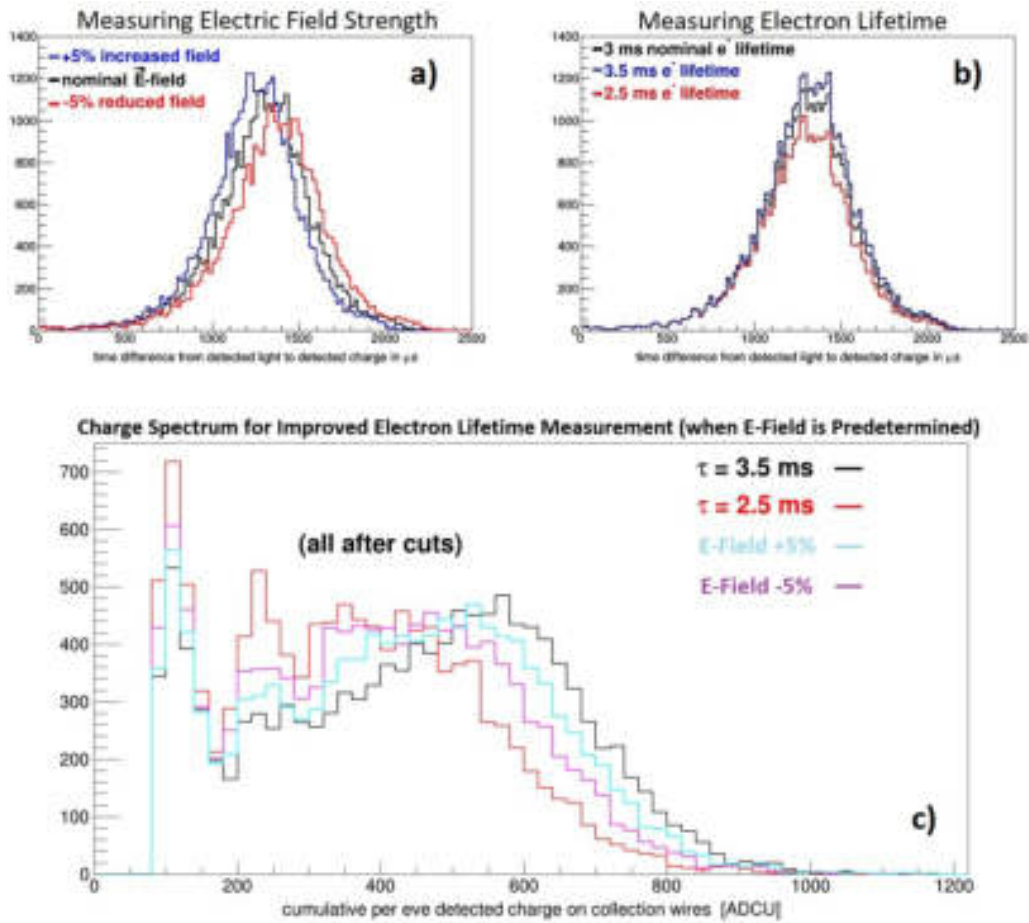


**Figure 6.28.** Simulated measurements of (a) E field strength from drift-time distribution, (b) electron lifetime from drift-time distribution, and (c) electron lifetime from charge distribution when electric field is unambiguously known from drift-time distribution. All spectra were created with applied selection cuts for a simulated 9 MeV  $\gamma$ -ray source with radiological backgrounds deployed at  $z = -40$  cm outside of the FC,  $x = 220$  cm away from the APA, and  $y = 300$  cm half-height of an upper endwall APA. (Colors of histograms are matching colors of corresponding labels in each histogram.)

**Table 6.12.** Estimated data volume per year per 10 kt for the radioactive source system.

| System                             | Data Volume<br>(TB $\cdot$ year <sup>-1</sup> ) | Assumptions   |
|------------------------------------|---|---|
| Proposed Radioactive Source System | 200   | Source rate < 10 Hz; single APA readout, lossless readout; 4 times/year |

- *Radioactivity leak*: if radioactivity leaks into the detector during a deployment, radiological backgrounds in the detector might increase. Rigorous source certification under high pressure and cryogenic temperatures mitigates this risk.
- *Source stuck or lost*: if the source gets stuck or is lost in the detector, then it becomes a permanent localized radiological background source. Fish-line an order of magnitude stronger than needed to hold the weight, round edges of the moderator and a torque limit of the stepper motor will mitigate this risk.
- *Oxygen and nitrogen contamination*: if the purge-box has a small leak, oxygen and nitrogen could get into the LAr. Leak checks before deployments will mitigate this risk.

**Table 6.13:** Radioactive source calibration system risks (P=probability, C=cost, S=schedule) The risk probability, after taking into account the planned mitigation activities, is ranked as L (low < 10 %), M (medium 10 % to 25 %), or H (high > 25 %). The cost and schedule impacts are ranked as L (cost increase < 5 %, schedule delay < 2 months), M (5 % to 25 % and 2–6 months, respectively) and H (> 20 % and > 2 months, respectively).

| ID           | Risk   | Mitigation   | P | C | S |
|--------------|--|--|---|---|---|
| RT-SP-CAL-10 | Radioactive source swings into detector elements | Constrain the system with guide-wires  | L | L | L |
| RT-SP-CAL-11 | Radioactivity leak                               | Obtain rigorous source certification under high pressure and cryogenic temperatures  | L | L | M |
| RT-SP-CAL-12 | Source stuck or lost                             | Safe engineering margins, stronger fish-line and a torque limit in deployment system | L | M | L |
| RT-SP-CAL-13 | Oxygen and nitrogen contamination                | Leak checks before deployments   | L | M | M |
| RT-SP-CAL-14 | Light leak into the detector through purge-box   | Light-tight purge box with an infrared camera for visual checks                      | L | L | L |
| RT-SP-CAL-15 | Activation of the cryostat insulation            | Activation studies and simulations   | L | L | L |

### 6.7.3.7 Installation, integration, and commissioning

The first elements of the radioactive source guide system are installed before the TPC elements on the end wall farthest from the TCO and as the last system, concurrent and coordinated with the alternative laser system (if any deployed), once the TPC is installed before closing the TCO. The radioactive source deployment system is installed at the top of the cryostat and can be installed when DUNE becomes operational.

The commissioning plan for the source deployment system will include a dummy source deployment (within 2 months of the commissioning) followed by first real source deployment (within 3 to 4 months of the commissioning) and a second real source deployment (within 6 months of the commissioning). Assuming stable detector conditions, the radioactive source will be deployed every half a year. Ideally, a deployment before and after a run period are desired so at least two data

points are available for calibration. This also provides a check if the state of the system has changed before and after the physics data run. It is estimated that it will take a few hours (e.g. 8 hours) to deploy the system at one feedthrough location and a full radioactive source calibration campaign might take a week.

### 6.7.3.8 Quality control

A mechanical test of the Double Chooz fish-line deployment system with a LAr mock-up column will be done in the high bay laboratory at SDSMT. The ultimate test of the system will be done at ProtoDUNE. Safety checks will also be done for the source and for appropriate storage on the surface and underground.

### 6.7.3.9 Safety

A composite source is used for the radioactive source system that consists of  $^{252}\text{Cf}$ , a strong neutron emitter, and  $^{58}\text{Ni}$ , which, via the  $^{58}\text{Ni}(n,\gamma)^{59}\text{Ni}$  process, converts one of the  $^{252}\text{Cf}$  fission neutrons, suitably moderated, to a monoenergetic 9 MeV gamma. This system also poses a radiation risk, which will be mitigated with a purge-box for handling, and a shielded storage box and an area with lockout-tagout procedures, also applied to the gate-valve on top of the cryostat. Material safety data sheets will be submitted to DUNE ES&H and specific procedures will be developed for storage and handling of sources to meet Fermilab Radiological Control Manual (FRCM) requirements. These procedures will be reviewed and approved by SURF and Fermilab radiation safety officers. Sources that get deployed will be checked monthly to ensure they are not leaking. A designated shielded storage area will be assigned for sources and proper handling procedures will be reviewed periodically. A custodian will be assigned to each shielded source.

## Chapter 7

# Data acquisition

### 7.1 Introduction

The far detector (FD) data acquisition (DAQ) system receives, processes, and records data from the Deep Underground Neutrino Experiment (DUNE) FD. It provides timing and synchronization for all detector modules and subdetectors; receives, synchronizes, compresses, and buffers data streaming from the subdetectors; extracts information from the data at a local level to subsequently make local, module, and cross-module data selection decisions; builds event records from selected space-time data volumes and relays them to permanent storage; and carries out subsequent data reduction and filtering as needed.

This chapter provides a description of the design of the DUNE FD DAQ system developed by the DUNE FD DAQ consortium. This consortium brings together resources and expertise from European Organization for Nuclear Research (CERN), Colombia, Czech Republic, France, Italy, Japan, the Netherlands, the UK, and the USA. Its members bring considerable experience from ICARUS, MicroBooNE, SBND, and the DUNE prototype liquid argon time-projection chambers (LArTPCs), as well as from ATLAS at the LHC and other major HEP experiments across the world.

The system is designed to service all FD detector module designs interchangeably. However, some aspects of the DAQ design described in this chapter are tailored to meet the specific needs of the single-phase (SP) detector module technology. Adaptations to detector technology are implemented in the upstream part of the DAQ, leaving the remainder generic. The individual detector modules are serviced by the DAQ independently and the two modules are only loosely coupled through a cross-module triggering mechanism.

The chapter begins with an overview of the DAQ design (section 7.2), including requirements that the design must meet and specifications for interfaces between the DAQ and other DUNE FD systems. Subsequently, section 7.3, which comprises the bulk of this chapter, describes the design of the FD DAQ in greater detail. Section 7.4 describes design validation efforts to date, as well as future design development and validation plans. At the center of these efforts is the ProtoDUNE DAQ system (described in section 7.4.1), which has demonstrated several key aspects of the DUNE FD DAQ design and continues to serve as a platform for further developing and validating the final design. The chapter finishes with two sections (sections 7.5 and 7.6), which detail the management of the DAQ project, including the schedule for completing the design, production, and installation of the system, as well as safety considerations.

## 7.2 Design overview

Figure 7.1 provides an overview of the DUNE FD DAQ system servicing a single FD detector module. The system is physically located at the FD site, split between the underground DUNE caverns and the surface level at Sanford Underground Research Facility (SURF). Specifically, DAQ uses space and power both in the underground central utility cavern (CUC) and the above-ground main communications room (MCR). The upstream part of the system, responsible for raw detector data reception, buffering, and pre-processing, resides in the CUC. The DAQ back-end subsystem (DAQ BE), which is responsible for event-building, run control, and monitoring, resides on the surface. Data flows through the DAQ from upstream to the back-end parts of the DAQ and then offline. Most raw data is processed and buffered underground, thus controlling consumption of available data bandwidth to the surface.

A hierarchical DAQ data selection subsystem (DAQ DS) consumes minimally-processed information from the upstream DAQ and, through further data processing, carries out a module-level trigger decision leading to a trigger command. The command is subsequently executed by a data flow orchestrator (DFO) residing in the DAQ BE by retrieving the required data from memory buffers maintained by the upstream DAQ. The results are aggregated across the detector module into a cohesive record and saved to non-volatile storage. During or after aggregation, an optional down-selection of the data is possible via high level filtering. Finally, the data is transferred offsite and archived by the DUNE offline group. All detector modules and their subcomponents are synchronized and timed against a global, common clock, provided by the timing and synchronization subsystem. Cross-module communication and communication to the outside world for data selection (trigger) purposes is facilitated through an external trigger interface (ETI), which is part of the DAQ DS. The specifics of design implementation and data flow are described in section 7.3.

### 7.2.1 Requirements and specifications

The DUNE FD DAQ system is designed to meet the DUNE top-level as well as DAQ-level requirements summarized in table 7.2. The DAQ-level requirements ensure that the system can record all necessary information for offline analysis of data associated with on- and off-beam physics events, as directed by the DUNE physics mission, with minimal compromise to DUNE's physics sensitivity. The requirements must be met following the specifications provided in the same table. Those specifications are associated with trigger functionality, readout, and operations and are described further in the following subsections.

#### 7.2.1.1 How DUNE's physics mission drives the DAQ design

The DUNE FD has three main physics drivers: measuring neutrino charge-parity symmetry violation (CPV) and related long baseline oscillation using the high intensity beam provided by Fermilab; measuring off-beam atmospheric neutrinos and searches for rare processes such baryon-number-violating decays; and detecting neutrinos from a nearby supernova neutrino burst (SNB). The DUNE FD DAQ system must facilitate data readout to deliver on these main physics drivers while keeping within physical (space, power) and resource constraints for the system. In particular, the off-beam measurements require continuous readout of the detector, and the lack of external triggers for such events requires real-time or online data processing and self-triggering capabilities. Because

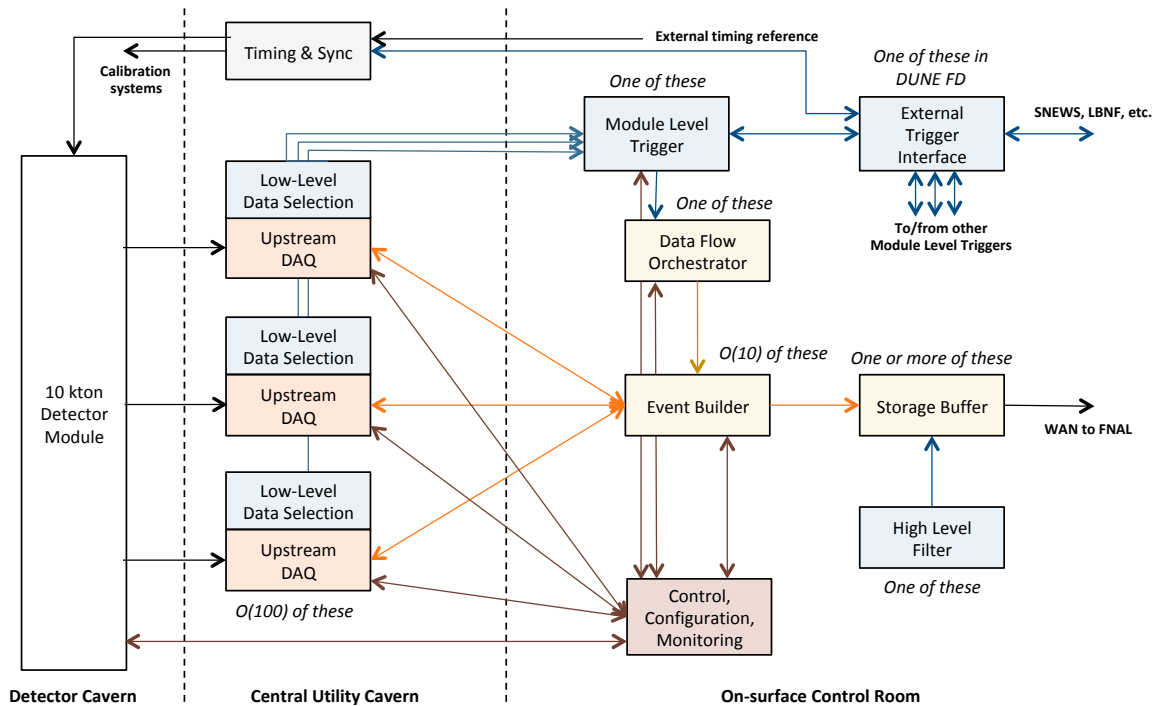


**Figure 7.1.** DAQ conceptual design overview focusing on a single 10 kt module. Included are the upstream DAQ subsystem in orange, the DAQ DS in blue, and the DAQ BE subsystem in yellow, which includes the DFO, EB, and storage buffer. Also shown, in brown, is the subsystem for timing and synchronization, in gray, and the subsystem for control, configuration, and management.

the continuous raw data rate of the far detector module, as received by the DAQ system, reaches multiple terabits per second, significant data buffering and processing resources are needed as part of the design, as specified in later sections of this chapter.

The DUNE FD modules use two active detector components from which the DAQ system must acquire data: the time projection chamber (TPC) and the photon detection system (PD system). The two components access the physics by sensing and collecting signals associated with very different sensing time scales.

Ionization charge measurement by the TPC for any given activity in the detector requires a nominal recording of data over a time window of approximately 1 ms to 10 ms. This time scale is determined by the ionization electron drift speed in liquid argon (LAr) and the detector dimension along the drift direction, nominally set to 5.4 ms, corresponding to  $2.4 \times 2.25$  ms. The latter (2.25 ms) assumes a drift electric field of 500 V/cm. The 2.4 factor ensures capturing ionization information from at least a full drift before and after the trigger time associated with the activity. Early commissioning data will be used to evaluate and optimize this nominal readout time.

On the other hand, the PD system measures argon scintillation light emission, which occurs and is detected over a timescale of multiple ns to  $\mu$ s for any given event and/or subsequent subevent process. Unlike the TPC, the PD system data is zero-suppressed in the PD system electronics (see chapter 5). Although the PD system system readout sampling frequency is higher than the TPC, the combination of zero-suppression and expected activity levels should have significantly lower data

2020 JINST 15 T08010

rates than the TPC. Therefore, the total raw data volume received by the DAQ system should be dominated by the TPC data, which is sent out from the TPC electronics as a continuous stream.

Figure 7.2 provides the expected activity rates in a single far detector module as a function of true energy associated with given types of signal. At low energy ( $<10$  MeV), activity is dominated by radiological backgrounds intrinsic to the detector and low-energy solar neutrino interactions. Supernova burst neutrinos, expected to arrive at a galactic SNB rate of once per century, would span the 10 MeV to 30 MeV range. At higher energies (generally more than 100 MeV), rates are dominated by cosmic rays, beam neutrino interactions, and atmospheric neutrino interactions. With the exception of supernova burst neutrinos, the activity associated with any of these physics signals is localized in space and particularly in time. Supernova burst activity, on the other hand, is characteristically distinct, because it can manifest as up to several thousands of low-energy neutrino interactions arriving over multiple seconds. Supernova burst neutrinos are thus associated with activity that extends over the entirety of the detector and over a relatively long time.

The nature and rates of these signatures necessitate a data selection strategy that handles two distinct cases: a localized high-energy activity trigger, prompting an event record readout for activity associated with a minimum of 100 MeV of deposited energy; and an extended low-energy activity trigger, prompting an event record readout when multiple localized low-energy activity candidates with low deposited energy each (approximately 10 MeV) are found over a short (less than 10 s) time and over the entirety of a 10 kt module. Because of the high granularity of the detector readout elements, a hierarchical DAQ DS is used to provide data processing and triggering and to facilitate optional data reduction and filtering.

The DAQ system must have  $>99\%$  efficiency for particles depositing  $>100$  MeV of energy in the detector for localized high-energy triggers. The system's architecture must also provide a mechanism for triggering on galactic supernova bursts with  $>95\%$  efficiency for a supernova burst producing at least 60 interactions with a neutrino energy  $>10$  MeV in 12 kt of active detector mass, during the first 10 s of the burst, per DUNE requirements. This requirement ensures sensitivity to the great majority of SNBs in our galaxy as well as some bursts in small nearby galaxies, as described in this document's SNB physics requirements section. The DAQ architecture must also provide a mechanism for recording neutrino interactions associated with those bursts over a 30 s period, with a goal of 100 s. During this period, the full raw data information must be stored. The rationale for the latter is that most models of SNBs show structure in the neutrino flux for up to 30 s, and there is potential for interesting measurements to be made up to 100 s.

Offline considerations require the DAQ to reduce the full FD data volume for offline permanent storage to 30 PB/year. An FD composed of four single-phase modules using a strategy by which the entire FD is read out for 5.4 ms, given the presence of a localized high energy trigger, will be limited by this offline permanent storage constraint to an average readout rate of 0.3 Hz. Strategies will be developed and validated during commissioning and early running that will limit the readout to some subset of the detector module, which should allow an increase in this rate limit by about an order of magnitude. The instantaneous readout rate can be much higher, for example to accommodate calibrations.

For planning, the DAQ will allot an average SNB trigger rate of one per month. Given current understanding of SNB rates and the  $>95\%$  expected efficiency for a SNB with at least 60 interactions each of minimum 10 MeV in true neutrino energy, most such triggers will be due to fluctuations of

low energy radiological backgrounds and, potentially, excess noise. Such triggers will prompt 100 s of data from the entire module to be read out. At this average rate and if saved to offline storage, the SNB triggers will produce 1.8 PB/year uncompressed from one single-phase module. There is, however, no requirement to permanently store SNB data that is deemed, after further offline analysis, to be due to fake triggers.

The capability of recording data losslessly is built into the design as a conservative measure; a particular concern is charge reconstruction efficiency and resolution in the case of zero suppression, in particular for TPC induction wire readout channels. MicroBooNE is currently investigating the effect of zero suppression on reconstruction efficiency and energy resolution for low-energy events [130]. Expected data rates from physics signals of interest that fit the requirement of 30 PB/year sent to permanent storage are summarized in table 7.1 and detailed in DocDB 9240 [131]. Potential bottlenecks are analyzed in DocDB 11461 [132].

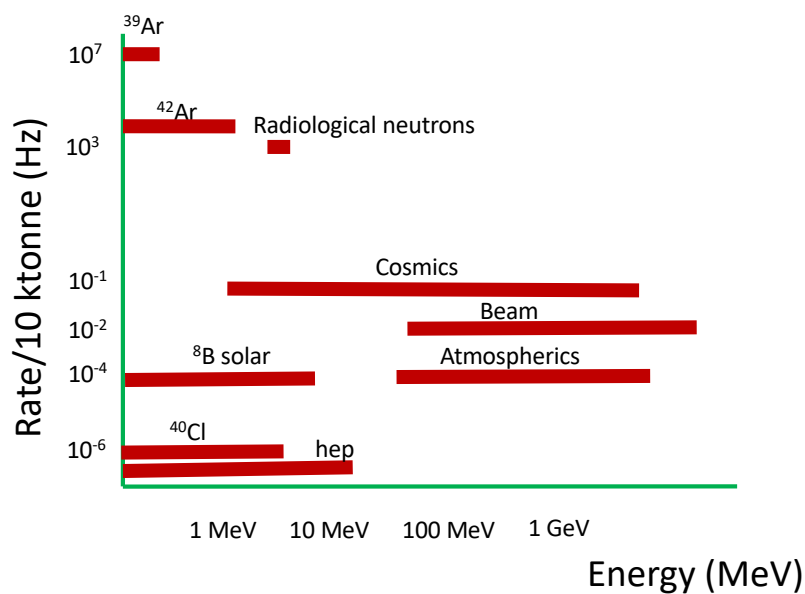


**Figure 7.2.** Expected physics-related activity rates in a single 10 kt module.

Self-triggering on SNB activity is a unique challenge for the DUNE FD, and an aspect of the design that has never been demonstrated in a LArTPC. The challenge of SNB triggering is two-fold. First, the activity of the individual SNB neutrino interactions should be relatively low energy (5 MeV to 30 MeV), often indistinguishable from pile up of radiological background activity in the detector. Triggering on an ensemble of  $O(100)$  events expected on average in the case of a galactic supernova burst is, therefore, advantageous; however, this ensemble of events will likely be rare over the entire detector and over an extended period of  $O(10)$ s, so sufficient buffering capability must be designed into the system to capture the corresponding signals. Furthermore, to ensure high efficiency in collecting SNB interactions that, individually, are below low-energy activity threshold, data from all channels in the detector will be recorded over an extended and contiguous period, which is specified to 30 s to 100 s, around every SNB trigger. This time has been defined in consultation with the DUNE physics groups.



**Table 7.1.** Summary of expected data volumes produced yearly for initial single-module running. The numbers assume TPC only rates with no compression and are given for a single 10 kt module, assuming the parameters listed in table 7.3. (A 2-4x lossless compression factor is expected.) Trigger primitives (see section 7.3.3), fake SNB data as well as additional data recorded for detector performance studies and debugging need not be stored offline permanently.

| Source  | Annual Data Volume | Assumptions  |
|---|--------------------|--|
| Beam interactions                                   | 27 TB              | 10 MeV threshold in coincidence with beam time, including cosmic coincidence; 5.4 ms readout                                 |
| Cosmics and atmospheric neutrinos                   | 10 PB              | 5.4 ms readout   |
| Radiological backgrounds                            | < 2 PB             | < 1 per month fake rate for SNB trigger; 100 s readout   |
| Cold electronics calibration                        | 4 TB               | scaled from ProtoDUNE-SP experience  |
| Radioactive source calibration                      | 100 TB             | < 10 Hz source rate; single APA readout; 5.4 ms readout  |
| Laser calibration                                   | 200 TB             | $10^6$ total laser pulses; half the TPC channels illuminated per pulse; lossy compression (zero-suppression) on all channels |
| Random triggers                                     | 60 TB              | 45 per day; 5.4 ms readout   |
| Trigger primitives and detector performance studies | < 15 PB            | $^{39}\text{Ar}$ dominated   |

**Table 7.2:** DAQ specifications.

| Label    | Description  | Specification (Goal)   | Rationale  | Validation  |
|----------|--|--|--|---|
| SP-FD-22 | Data rate to tape  | < 30 PB/year   | Cost. Bandwidth.   | ProtoDUNE   |
| SP-FD-23 | Supernova trigger  | > 95 % efficiency for a SNB producing at least 60 interactions with a neutrino energy >10 MeV in 12 kt of active detector mass during the first 10 seconds of the burst. | > 95% efficiency for SNB within 20 kpc   | Simulation and bench tests  |
| SP-DAQ-1 | DAQ readout throughput: The DAQ shall be able to accept the continuous data stream from the TPC and Photon detectors.  | 1.5 TB/s per single phase detector module  | Specification from TPC and PDS electronics   | Modular test on ProtoDUNE; overall throughput scales linearly with number of APAs   |
| SP-DAQ-2 | DAQ storage throughput: The DAQ shall be able to store selected data at an average throughput of 10 Gb/s, with temporary peak throughput of 100 Gb/s.  | 10 Gb/s average storage throughput; 100 Gb/s peak temporary storage throughput per single phase detector module  | Average throughput estimated from physics and calibration requirements; peak throughput allowing for fast storage of SNB data ( $\sim 10^4$ seconds to store 120 TB of data).  | ProtoDUNE demonstrated steady storage at $\sim 40$ Gb/s for a storage volume of 700 TB. Laboratory tests will allow to demonstrate the performance reach. |
| SP-DAQ-3 | DAQ readout window: The DAQ shall support storing triggered data of one or more APAs with a variable size readout window, from few $\mu$ s (calibration) to 100 s (SNB), with a typical readout window for triggered interactions of 5.4 ms. | $10 \mu$ s < readout window < 100 s  | Storage of the complete dataset for up to 100 s is required by the SNB physics studies; the typical readout window of 5.4 ms is defined by the drift time in the detector; calibration triggers can be configured to readout data much shorter time intervals. | Implementation techniques to be validated on the ProtoDUNE setup and in test labs.  |

|          |  |  |  |
|----------|--|--|--|
| SP-DAQ-4 | <p>Calibration trigger:<br/>The DAQ shall provide the means to distribute time-synchronous commands to the calibration systems, in order to fire them, at a configurable rate and sequence and at configurable intervals in time. Those commands may be distributed during physics data taking or during special calibration data taking sessions. The DAQ shall trigger and acquire data at a fixed, configurable interval after the distribution of the commands, in order to capture the response of the detector to calibration stimuli.</p> | <p>Calibration is essential to attain required detector performance comprehension.</p> | <p>Techniques for doing this have been run successfully in MicroBooNE and ProtoDUNE.</p> |
| SP-DAQ-5 | <p>Data record:<br/>Corresponding to every trigger, the DAQ shall form a data record to be transferred to offline together with the metadata necessary for validation and processing.</p>  | <p>Needed for offline analysis.</p>  | <p>Common experimental practice.</p>   |
| SP-DAQ-6 | <p>Data verification:<br/>The DAQ shall check integrity of data at every data transfer step. It shall only delete data from the local storage after confirmation that data have been correctly recorded to permanent storage.</p>  | <p>Data integrity checking is fundamental to ensure data quality.</p>                  |  |

|          |   |                                 |  |
|----------|---|---------------------------------|--|
| SP-DAQ-7 | High-energy Trigger: >100 MeV<br>The DAQ shall trigger and acquire data on visible energy deposition >100 MeV. Data acquisition may be limited to the area in which activity was detected.  | Driven by DUNE physics mission. | Physics TDR. 100 MeV is an achievable parameter; lower thresholds are possible.  |
| SP-DAQ-8 | Low-energy Trigger: >10 MeV<br>The DAQ shall trigger and acquire data on visible energy deposition > 10 MeV of single neutrino interactions. Those triggers will normally be fired using a pre-scaling factor, in order to limit the data volume. | Driven by DUNE physics mission. | Physics TDR. 10 MeV is an achievable parameter; lower thresholds are possible.   |
| SP-DAQ-9 | DAQ deadtime:<br>While taking data within the agreed conditions, the DAQ shall be able to trigger and acquire data without introducing any deadtime.  | Driven by DUNE physics mission. | Zero deadtime is an achievable inter-event deadtime but a small deadtime would not significantly compromise physics sensitivity. |

### 7.2.1.2 Considerations for design

The DAQ system is designed as a single, scalable system that can service all FD modules. It is also designed so the system can record and store full detector data with zero dead time, applying appropriate data reduction through data selection and compression. The system should be evolutionary, taking advantage of the staged construction of the DUNE FD, thus beginning very conservatively for the first DUNE FD module, but aggressively reducing the design conservatism with further experience of detector operations. At the same time, the system is designed to be able to add capacity as required. Most processing and buffering of raw detector data is done underground, in the upstream DAQ and low level data selection parts of the system (see figure 7.1), with only event building and data storage on surface.

Power, cooling, and space are constrained both in the CUC and on the surface, limited to 500 kV·A and 56 racks (out of 60 racks total) in the CUC, and 50 kV·A and 8 racks on the surface for DAQ for all four FD modules. The underground computing required for the DAQ to service the SP detector module should require less than a quarter of the total power and rack space provided for all four detector modules. The hardware for upstream DAQ, low level data selection, various

services, networking, and the timing system, including spares, all kept in the CUC, should consume less than 63 kW and all fill less than 300U of rack space [133].

There are five key challenges for the DUNE FD DAQ system:

- First, the high overall experiment uptime goal requires DAQ to be stringently designed for reliability, fault tolerance, and redundancy, criteria that aim to reduce overall downtime.

The DAQ system is fully configurable, controllable, and operable from remote locations, with authentication and authorization implemented to allow exclusive control. The DAQ monitors the quality of the detector data and of its own operational status, as well as automated error detection and recovery capabilities.

- Second, the system must be able to evolve to accommodate newly commissioned sub-components as they are installed into a detector module that is under construction. The DAQ must also continue to service existing modules that are operational while simultaneously accommodating subsequent detector modules as they are installed and commissioned. To support this ongoing variability, the DAQ will support operating as multiple independent instances or partitions.

Partitioning will also be supported within a single detector module for special calibration or debugging runs that are incompatible with physics data taking, while the rest of the detector remains in physics data taking mode. Partitioning, i.e., allowing several instances of the DAQ to operate independently with different configurations on different parts of the detector, will also be important during the installation and commissioning, so experts can work in parallel, e.g., for photon detectors (PDs) and TPC.

- Third, the SNB physics requirements require heavy buffering in the upstream DAQ. Implementing a buffer element in the upstream DAQ allows the formation and capture of delayed, data-driven data selection decisions: the trigger accumulates low energy signals over an extended period while carrying out the trigger decision, thus identifying activity compatible with SNB. The depth of this buffer is determined in consultation with physics groups and driven primarily by the need to retain all unbiased data while processing up to 10 s of data for the trigger decision preceding a SNB trigger. Collecting data containing information on other types of interactions and decays does not pose additional requirements on the upstream DAQ buffer because the latency required for triggers should be well below 10 s.
- Fourth, the DAQ must support a very wide range of readout windows and trigger rates. This includes acquiring localized events in both time and space up to the very large and rare SNB detector-wide readouts over 100 s.
- Finally, the DAQ must reduce the volume of data to be permanently stored offline to a maximum of 30 PB/year. The DAQ system should be able to select interesting time windows in which activity was detected, apply lossless compression to data records, and filter records to remove unnecessary data regions.

A programmable trigger priority scheme ensures that the readout for the main physics triggers is never or rarely inhibited, thus making it easy to determine the live-time of these triggers.

Table 7.3 summarizes the important parameters driving the DAQ design. These parameters set the scale of data buffering, processing, and transferring resources that must be built into each FD module.

**Table 7.3.** Summary of important parameters driving the DAQ design. The PD system system parameters are under study, but the PD system raw data volume that must be handled by the DAQ should be an order of magnitude smaller than the TPC raw data volume.

| Parameter   | Value       |
|---|-------------|
| TPC Channel Count per Module                        | 384,000     |
| TPC Collection Channel Count per Subdetector (APA)  | 960         |
| TPC Induction Channel Count per Subdetector (APA)   | 1600        |
| PDS Channel Count per Module                        | 6000        |
| PDS Channel Count per Subdetector (PDS per APA)     | 40          |
| TPC analog-to-digital converter (ADC) Sampling Rate | 2 MHz       |
| TPC ADC Dynamic Range                               | 12 bits     |
| PDS ADC Sampling Rate                               | Under study |
| PDS ADC Dynamic Range                               | Under study |
| PDS ADC Readout Length                              | Under study |
| Localized Event Record Window                       | 5.4 ms      |
| Extended Event Record Window                        | 100 s       |
| Full size of Localized Event Record per Module      | 6.5 GB      |
| Full size of Extended Event Record per Module       | 120 TB      |

### 7.2.2 Interfaces

The DAQ system scope begins at the optical fibers streaming raw digital data from the detector active components (TPC and PD system) and ends at a wide-area network interface that distributes the data from on site at SURF to offline centers off site. The DAQ also provides common computing and network services for other DUNE systems, although slow control and safety functions fall outside DAQ's scope.

Consequently, the DUNE FD DAQ system interfaces with the TPC cold electronics (CE), PD system readout, computing, cryogenic instrumentation and slow controls (CISC), and calibration systems of the FD, as well as with facilities and underground installation. The interface agreements with the FD systems are listed in table 7.4 and described briefly in the following subsections. Interface agreements with facilities and underground installation are described in section 7.5.

**TPC CE.** The DAQ and TPC CE interface is described in DocDB 6742 [68]. The physical interface is in the CUC where optical links from the warm interface boards (WIBs) transfer the raw TPC

Table 7.4. Data Acquisition System Interface Links.

| Interfacing System         | Description  | Reference          |
|----------------------------|--|--------------------|
| TPC CE                     | Data rate and format, number and type of links, timing, inherent noise   | DocDB 6742 [68]v6  |
| PDS Readout                | Data rate and format, number and type of links, timing   | DocDB 6727 [86]v2  |
| Computing                  | Off-site data transfer rates, methods, data file content, disk buffer, software development and maintenance        | DocDB 7123 [134]   |
| CISC                       | Information exchange, hardware and software for rack and server monitoring   | DocDB 6790 [135]v1 |
| Calibration                | Constraint on total volume of the calibration data; trigger and timing distribution from the DAQ                   | DocDB 7069 [121]   |
| Timing and Synchronization | Clients, clock frequency, protocols, transports, accuracy, synchronization precision, monitoring                   | DocDB 11224 [136]  |
| Facilities                 | Detector integration, coordination, cables, racks, safety, conventional facilities, lack of impact on cryo and DSS | DocDB 6988 [137]v1 |
| Installation               | Prototyping, planning, transport, underground equipment and activity, safety                                       | DocDB 7015 [138]   |

data to the DAQ front-end readout (Front-End Link eXchange (FELIX); see section 7.3.2). This ensures the DAQ is electrically decoupled from the detector cryostat. Ten 10 Gbit/s links are expected per anode plane assembly (APA) and have been specified as 300 m OM4 multi-mode fibers from small form-factor pluggable (SFP)+ at the WIB to miniature parallel optical device (MiniPOD) on FELIX. (The optical fibers themselves are the responsibility of the DAQ consortium.) The data format has been specified as a custom communication protocol with no compression.

**PD system readout.** The DAQ and PD system readout interface is described in DocDB 6727 [86]. It should require no more than 150 10 Gbit/s OM4 fibers from one FD module. This is similar to the interface to the TPC CE, except the overall data volume is lower by an order of magnitude. The data format has been specified to use compression (zero suppression) and a custom communication protocol.

**Computing.** The DAQ and computing interface is described in DocDB 7123 [134]. The computing consortium is responsible for the online areas of WAN connection between SURF and Fermilab providing 100 Gbit/s bandwidth, while the DAQ consortium is responsible for disk buffering to handle any temporary WAN disconnects and the infrastructure needed for real-time data quality monitoring. The computing consortium is also responsible for the offline development and operation of the tools for data transfers to Fermilab. The primary constraint in defining the DAQ and offline computing interface is the requirement to produce less than 30 PB/year into final storage at Fermilab. The DAQ and computing consortia are jointly responsible for data format definition and data access libraries, as well as real-time data quality monitoring software. The former is specified in the form of a data model documented in DocDB 7123 [134].

**CISC.** The DAQ and CISC interface is described in DocDB 6790 [135]. The DAQ provides a network in the CUC for CISC, operation information and hardware monitoring information to CISC, and power distribution and rack status units in DAQ racks. The information from CISC feeds back into the DAQ for run control operations.

**Calibration.** The DAQ and calibration interface is described in DocDB 7069 [121]. Two calibration systems are envisioned for the FD: a laser calibration system and a neutron generator. Two-way communication between the calibration system and the DAQ is needed. Specifically, the calibration system must notify the data selection system, thus informing trigger decision when activity has been induced in the detector. At the same time, the DAQ must provide input to the calibration system, so it can avoid inducing activity in the detector during certain periods such as SNB readout time or during a beam spill. This second communication will be initiated by the data selection system and distributed via the ETI and subsequently through the DAQ timing system.

**Timing and Synchronization.** The timing system of the DUNE FD connects with almost all detector systems and with the calibration system. It has a uniform interface to each of them. A single interface document DocDB 11224 [136] describes all timing interfaces.



Accuracy of timestamps delivered to detector endpoints will be  $\pm 500$  ns with respect to UTC. Synchronization between any two endpoints in the detector will be less than 10 ns. Between detector modules, synchronization will be less than 25 ns.

### 7.3 Data acquisition system design

This section begins with an overview of the DAQ design followed by descriptions of the subsystem designs and implementation specifics.

#### 7.3.1 Overview

The DAQ system comprises five distinct subsystems: (1) upstream DAQ (section 7.3.2), (2) DAQ DS (section 7.3.3), (3) DAQ BE (section 7.3.4), (4) DAQ control, configuration and monitoring subsystem (CCM) (section 7.3.5), and (5) DAQ timing and synchronization subsystem (DAQ TSS) (section 7.3.7). Figure 7.1 shows the physical extent of the subsystems: the upstream DAQ and DAQ TSS live underground in the CUC; DAQ DS occupies both underground and above-ground spaces; DAQ BE is above-ground and includes data flow orchestration, event building, and buffering before distribution of data to offline storage; and CCM extends throughout the entire physical layout of the system, supported on a private network throughout the DAQ system. Each of these subsystems is described in further detail in the following subsections.

Front-end readout is carried out by the upstream DAQ using custom data receiver and co-processing field programmable gate array (FPGA) and commodity computing hardware, all of which is hosted in 80–85 servers in the CUC. A corresponding number of additional servers execute subsequent software-based low-level processing of trigger primitives generated in the upstream DAQ for the purposes of data selection. The trigger candidates constructed from trigger primitives are propagated to a central server responsible for further processing and module-level triggering. The module level trigger also interfaces to a second server that receives and propagates cross-module and external trigger and timing information. The module level trigger considers trigger candidates and external trigger inputs in issuing a trigger command to the DAQ BE subsystem. The DAQ BE subsystem facilitates event building in a few servers and buffering for built events on non-volatile storage. Upon receiving a trigger command, the DAQ BE queries data from the upstream DAQ buffers and builds that into an event record, which is temporarily stored in (a number of) files. Event records are optionally processed in a high-level filter/data reduction stage, which is part of overall data selection, before event records are shipped to DUNE offline. Pervasively, the DAQ control, configuration and monitoring subsystem (CCM) orchestrates data taking (section 7.3.5), and the DAQ timing and synchronization subsystem (DAQ TSS) provides synchronization and synchronous command distribution (section 7.3.7). Figure 7.3 provides a conceptual illustration of the overall DAQ system functionality.

Key to implementing the DAQ design is the requirement that the system can be partitioned. Specifically, the system can operate in as multiple independent DAQ instances, each executed across all DAQ subsystems and uniquely mapped among subsystem components. More specifically, a given partition may span the entire detector module or some subset of it; its extent is configurable at run start. This ensures continual readout of most of the detector in normal physics data-taking run

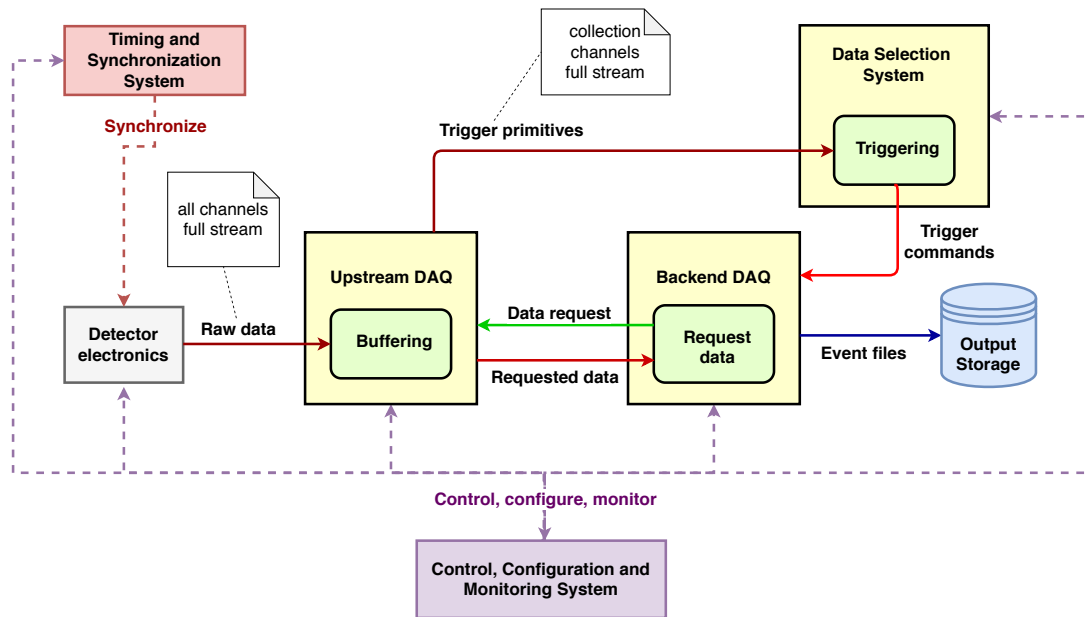


Figure 7.3. Conceptual Overview of DAQ system functionality for a single 10 kt module.

mode, while enabling simultaneous calibration or test runs of small portion of the detector without interrupting normal data taking.

### 7.3.2 Upstream DAQ

The upstream DAQ provides the first link in the data flow chain of the DAQ system; it receives raw data from detector electronics. The upstream DAQ implements a receiver, buffer, and a portion of low-level data selection (trigger primitive generation; see section 7.3.3) as detailed in figure 7.4. It is physically connected to the detector electronics via optical fiber(s) and buffers and serves data to other DAQ subsystems, namely the DAQ DS and the DAQ BE.

The upstream DAQ system comprises many similar DAQ readout units (DAQ RUs), each connected to a subset of electronics from a detector module and interfacing with the DAQ switched network. In the case of the TPC, 75 functionally identical DAQ RU are each responsible for the readout of raw data from two APAs. In the case of the PD system, up to eight DAQ RU are each responsible for the readout of raw data from a collection of PD system subdetectors. Each DAQ RU consists of a DAQ front-end computer (DAQ FEC), commodity server that hosts a collection of custom hardware, firmware, and software that collectively implement a set of functional blocks.

In the baseline design, used also for system costing, each DAQ RU is composed of

1. one dual socket multicore 2U server, with two 10 Gbit/s and two 1 Gbit/s ethernet ports for redundant data transmission and control, with at least 256 GB of DDR4 RAM, and sufficient PCIe lanes to host 2 TB of SSD disks;
2. two FELIX cards [139], each with a PCIe 3.0 x16 interface and supporting ten 9.6 Gbit/s bidirectional serial optical links;

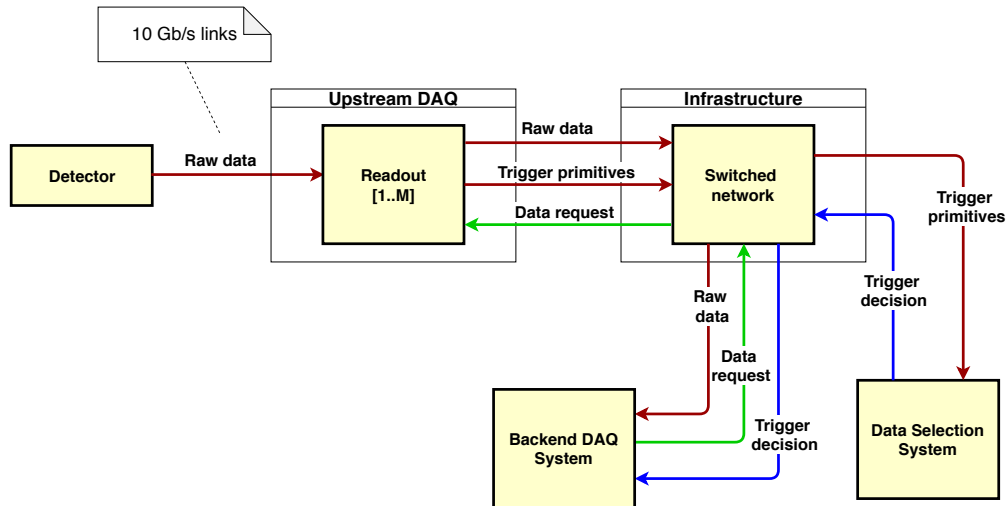


Figure 7.4. DUNE upstream DAQ subsystem and its connections.

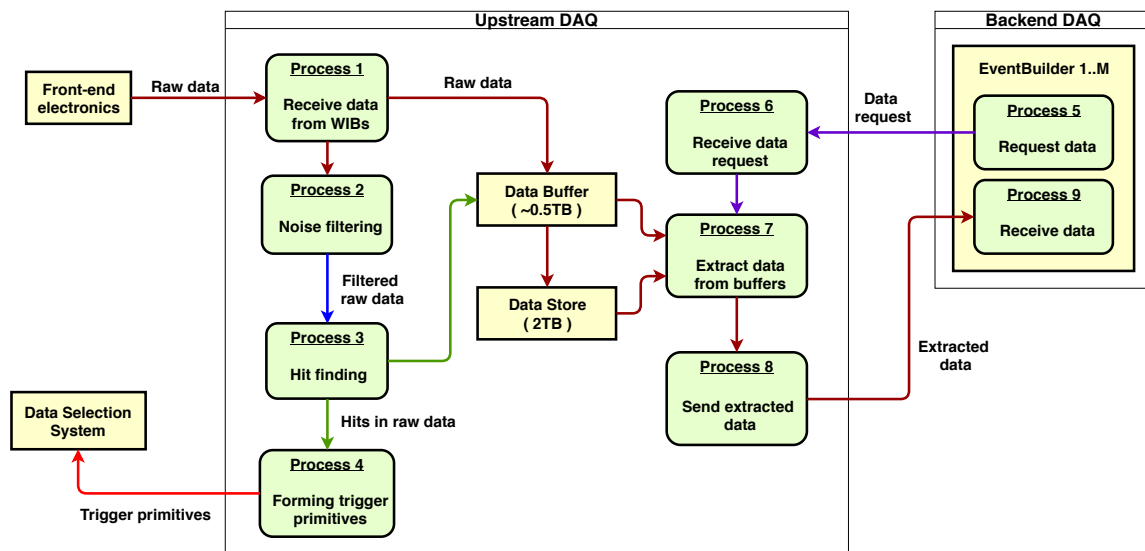


Figure 7.5. DUNE upstream DAQ subsystem functional blocks.

- only for the TPC readout, four custom-designed co-processor cards mounted onto the two FELIX cards for additional processing power and data buffering.

The main functional blocks of the upstream DAQ are described below:

- The physical interface between the detector electronics and the DAQ are 9.6 Gbit/s point-to-point serial optical links running a simple (e.g., 8/10 bit encoded) protocol. Each APA has ten such links connecting its WIBs to the DAQ. To reduce space and power consumption in the CUC, high data aggregation is needed. In the baseline design, the 20 fibers from two APAs are aggregated into one DAQ FEC with each APA connected to one FELIX FPGA PCIe 3.0 board. If commodity computing technology advances sufficiently, a PCIe 4.0 version of FELIX may be produced to increase the data aggregation, so each board would accept 20

links, and a total of 40 links per DAQ FEC would be accommodated. Tests were performed to verify OM3 and OM4 fibers support 10 Gbit/s links over a run of 300 m. Higher-speed fiberoptic links may be used to reduce the number of fibers if run lengths can be reduced. The FELIX board and firmware were developed initially by and for the ATLAS experiment and is now proposed or already in use by several other experiments including ProtoDUNE.

- The upstream DAQ subsystem provides access to the DAQ DS and DAQ BE through a commodity switched network as illustrated in figure 7.4. The network communication protocol is described in section 7.3.5.5. The data flow is handled by the DAQ RUs via software. Dedicated hardware or firmware development is not required.
- The data processing functional block is tasked with identifying and forming trigger primitives (see section 7.3.3.1), after a stage of data reorganization and noise filtering for both the TPC and PD system. Trigger primitives summarize time periods on a channel where the digitized waveform is no longer consistent with noise. These regions of interest are then used as input to the DAQ DS where they begin the process of forming a trigger decision.

In the baseline design, this functional block is implemented in FPGA. R&D studies are ongoing to evaluate alternative implementations (in GPUs or CPUs) that may have advantages in flexibility or cost.

- In DUNE, the upstream DAQ system is in charge of buffering all detector data until the DAQ DS has issued a trigger command (see section 7.3.3) and until the DAQ BE (section 7.3.4) has requested and received the corresponding selected data. In addition, in the case of a SNB trigger, data received after the issuing of the trigger must be buffered for longer to avoid loss of data due to any possible downstream bottlenecks. Localized and extended trigger activity are associated with two rather different time scales and data throughput metrics, and those collectively dictate the temporary storage technology and scale.

A trigger decision based on localized activity should require buffering the full data stream for no more than one second. Extended triggers present a far more challenging set of buffering requirements; early activity from a SNB may occur at a rate near that of radiological activity. Theoretical estimates indicate 10 s of integration time may be needed for the SNB interaction rate to be deemed significantly enough above background rate to form a trigger decision. In order to locate interactions in this low-rate period, the full data rate must be buffered until an SNB trigger may be formed. The throughput and endurance required by this buffer is satisfied by RAM technology like DDR4.

A second challenge in recording data during an SNB is to assure essentially 100% efficiency for collecting the individual, low-energy interactions during any given SNB burst. To achieve this, the full-stream of data is recorded for a time duration that should cover the time envelope of the burst. Guided by SNB models, this duration is set to 100 s. This requires extracting as much as 120 TB from the TPC upstream DAQ across one single-phase detector module. It is not cost effective to design the DAQ to extract such extended data record along the same path as nominal readout, so additional buffering is needed.

The technology and scale of this additional buffering must satisfy several requirements. Each DAQ RU must accept the full data rate of the portion of the detector module it services. The media must have sufficient capacity and allow sufficient extraction throughput to make it unlikely to ever be too full to accept another extended data record: 4 Tbit/s guarantee the ability to store two SNB events simultaneously. Furthermore, assuming that, on average, an SNB trigger condition will be satisfied once per month, the optimal technology is solid-state Non-volatile memory express (NVMe) devices, which, at the scale required to provide suitable input bandwidth, can provide a capacity to write the data from several extended activity triggers. The recorded data will be transferred to the DAQ BE system in less than a day.

For both types of activity, the buffering requirements may be reduced by using lossless compression to the data before it enters the buffer. A factor of at least two to four compression is expected, based on MicroBooNE [130] and ProtoDUNE experience using a modified Huffman encoding of differential ADC values. Efforts are currently underway to understand the costs and technology requirements in exploiting this benefit.

Figure 7.5 shows the flow diagram of data and control messages within the upstream DAQ as well as the main interaction of the upstream DAQ with other subsystems.

### 7.3.3 Data selection

The DAQ DS is a hierarchical, online, primarily software-based system. It is responsible for immediate and continuous processing of a substantial fraction of the entire input data stream. This includes data from TPC and PD system subdetectors. From that input, as well as external inputs provided by the accelerator and detector calibration systems, the DAQ DS must form a trigger decision, which in turn produces a trigger command. This command summarizes the observed activity that led to the decision and provides addresses (in channel-time space) of the data in the upstream DAQ buffers that capture raw data corresponding to the activity. This command is sent to, then consumed, and executed by the DAQ back-end subsystem (DAQ BE) as described in section 7.3.4. It may also be propagated to an external trigger logic (ETL) stage, and from there, it may be distributed to other detector modules or other detector systems (e.g., calibration) for further consideration.

To facilitate partitioning, the DAQ DS can be instantiated several times, and multiple instances can operate in parallel. Within any given partition, the DAQ DS will also be informed and aware of current detector configuration and conditions and apply certain masks and mapping on subdetectors or their fragments in its decision making. This information is delivered to the DAQ DS by the CCM system (section 7.3.5).

Following DUNE FD and DAQ requirements, the DAQ DS must select, with sufficiently high (>99%) efficiency, data associated with calibration signals, as well as beam interactions, atmospheric neutrinos, rare baryon-number-violating events, and cosmic ray events that deposit visible energy in excess of 100 MeV. It must also select data associated with potential SNBs producing 60 neutrino interactions over a span of 10 s in 12 ktons of active liquid argon mass each with 10 MeV in neutrino energy, with >95% efficiency. Furthermore, to meet the requirement that the DUNE FD maintain <30 PB/year to permanent storage, the DAQ DS must make data selection

decisions in a way that allows the DAQ system to effectively reduce its input data by almost four orders of magnitude, without compromising the above efficiencies.

To meet its requirements, the DAQ DS design follows a hierarchical data selection strategy, where low-level decisions are fed forward into higher-level ones until a module-level trigger is activated. The hierarchy is illustrated in figure 7.6. At the lowest level, trigger primitives are formed on a per-channel basis, and represent, for the baseline design, a hit on a wire/channel activity summary. Trigger primitives are aggregated into trigger candidates, which represent information associated with higher-level constructs derived from trigger primitives, for example “clusters of hits”. Trigger candidate information is subsequently used to inform a module-level trigger decision, which generates a trigger command; this takes the form of either a localized high energy trigger or an extended SNB trigger, and each prompts the corresponding readout of an event record. Details on the exact algorithm implementation for trigger primitive, trigger candidate, and trigger command generation can be found in DocDB 11215 [140] and DocDB 14522 [141] and references therein. After event-building, further data selection is carried out in the form of down-selection of event records through a high level filter. Details on a possible post-event-building filtering algorithm implementation can be found in DocDB 11311 [142].

This data selection strategy is applicable to both the PD system and the TPC, operating in parallel up to the module level trigger stage, where PD system and TPC information can be combined to form a module level trigger decision. Data selection design efforts have taken the approach of validating and demonstrating a TPC-based data selection. Nevertheless, the data selection design by construction allows an additional PD system-based data selection component to be accommodated within the same design, which will augment data selection capabilities, efficiency, and robustness.

The DAQ DS subsystem structure is illustrated in figure 7.7. The structure reflects the three stages of data selection: (1) low level trigger, which consists of trigger primitive generation (facilitated in upstream DAQ; see section 7.3.2) and subsequent trigger candidate generation; (2) module level trigger; and (3) high level filter. Each stage is described in further detail in subsequent sections. An additional subsystem component is the ETI, which serves as a common interface for the module level trigger of each of the FD detector modules and between the module level trigger and other systems (calibration, accelerator, and timing system) within a single detector module. An additional responsibility of the ETI is to send SNB triggers to global coincidence trigger recipients like SuperNova Early Warning System (SNEWS) [143] after sufficient confirmation of trigger quality.

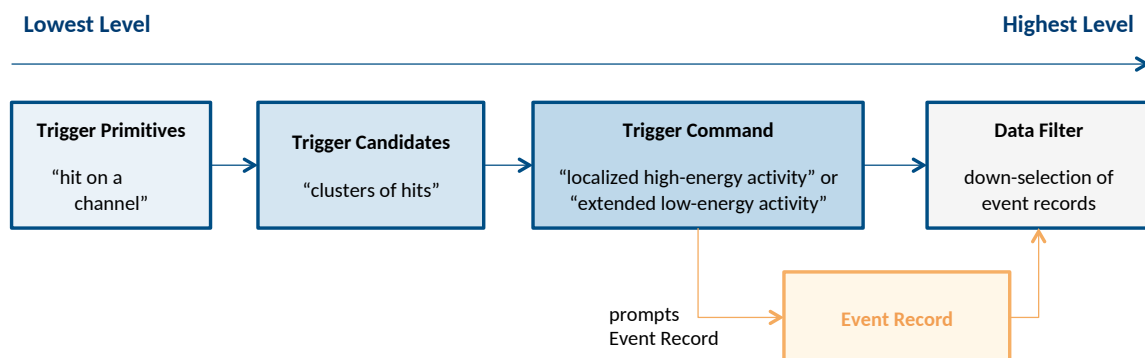


**Figure 7.6.** Data selection strategy and hierarchy.

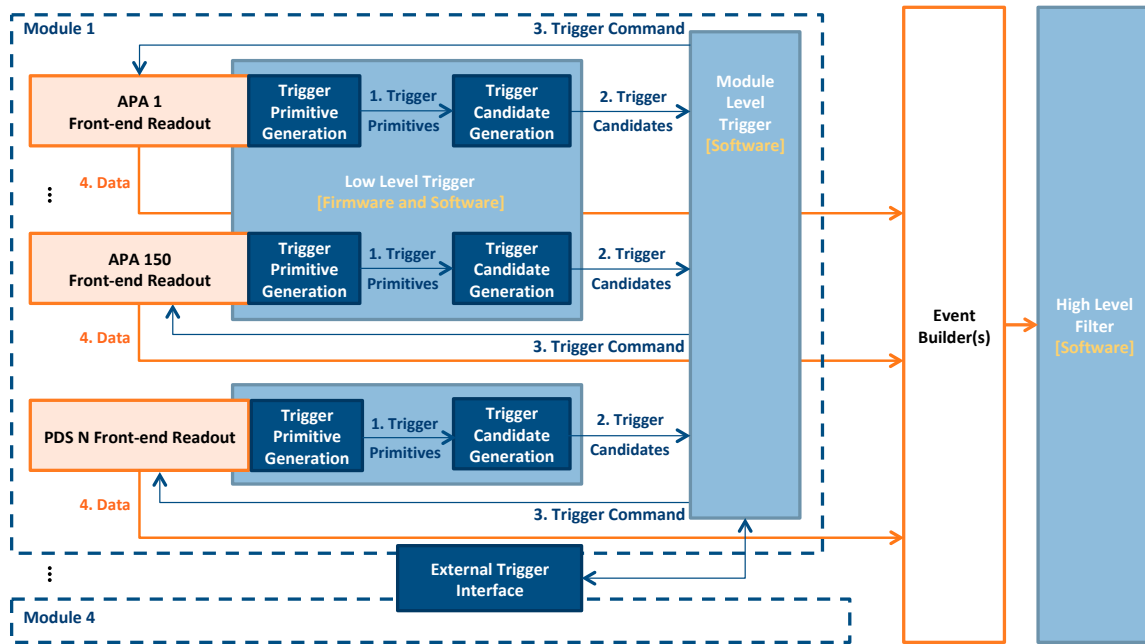


**Figure 7.7.** Block diagram of the DUNE DAQ DAQ DS illustrating hierarchical structure of subsystem design, subsystem functionality, and data flow.

The first stage of DUNE FD operations will trigger on two general classes of physics, each handled differently at the trigger level:

**High-energy interactions.** High-energy interactions include cosmic muons, neutrino beam interactions, atmospheric neutrinos, and nucleon decays. The trigger efficiency for these interactions must be  $>99\%$  for any given particle type (electron, muon, photon, etc.) that has a localized (confined to a limited number of neighboring channels) visible energy deposition above 100 MeV. To achieve this requirement, algorithms for creating high-energy trigger candidates target a trigger efficiency of 50% at 10 MeV visible energy, thus ensuring  $>99\%$  efficiency or higher at 100 MeV. This type of trigger is referred to as localized high energy trigger. Pushing the high-energy threshold down could enable detection of diffuse supernova neutrinos and solar neutrinos if radiological and neutron backgrounds are low enough.

**Low-energy interactions.** The primary physics target for low-energy interactions is a neutrino burst from a nearby supernova. Low-energy trigger candidates (with thresholds at or below 10 MeV visible energy) are generated and are input to an extended low-energy trigger data selection algorithm that looks for bursts inconsistent with fluctuations in low-energy background events. The time window for detecting such bursts is tuned to ensure nearly 100% efficiency out to the galactic edge, and the pre-burst buffers are sized to handle the associated latency for detection.

Each trigger type prompts readout of the entire module but over significantly different time ranges: localized triggers prompt readout of 5.4 ms event records; extended triggers prompt readout of 100 s event records.

Ultimately, each trigger decision culminates in a command sent to the DAQ BE subsystem. This command contains all logical detector addresses and time ranges required, so an EB can

properly query the upstream DAQ buffers and finally collect and output the corresponding detector data and the corresponding trigger data. The details for forming this command are described next, while the operation of the DAQ BE is described in section 7.3.4.

Viable data selection algorithms for the low level and module level triggers already exist, including algorithms for a module level SNB trigger. Monte Carlo simulations have demonstrated that the resulting SNB trigger efficiency reaches >99% for any SNBs occurring within our galaxy, and efforts to extend this reach to the Large Magellanic Cloud using refined algorithms are currently under way [140, 141]. At the same time, the pipelines of processing required for data selection can be executed using different firmware and software implementations. Development is actively ongoing to demonstrate and compare performance of different implementations. In satisfying the philosophy and strategies of the DAQ design, there is built-in flexibility in defining whether each element of a pipeline executes on FPGA, CPU, GPU, or, in principle, some other future hardware architecture. A purely software implementation of data selection (including trigger primitive generation) is being implemented for demonstration at ProtoDUNE; it will be then modified to match the baseline design in which trigger primitives are generated in upstream DAQ FPGA.

### 7.3.3.1 Low level trigger: trigger primitive generation

A trigger primitive is defined nominally on a per-channel basis. In the case of the SP module TPC, it is identified as a collection-channel signal rising above a (configurable) noise-driven threshold for a (configurable) minimum period of time (here called a hit). A trigger primitive takes the form of an information packet that summarizes the above-threshold waveform information in terms of its threshold crossing times and statistical measures of its ADC samples. In addition, these packets carry a flag indicating the occurrence of any failures or other exceptional behavior during trigger primitive processing.

Algorithms for generating trigger primitives are under development [144]. Trigger primitive generation proceeds by establishing a waveform baseline for a given channel, subtracting this baseline from each sample, maintaining a measure of the noise level with respect to the baseline, and searching for the waveform to cross a threshold defined in terms of the noise level. The trigger primitive or hit is said to span the time period when the waveform is above the noise threshold. Such algorithms (e.g., [145]) have been validated using both Monte Carlo simulations and real data from ProtoDUNE. Trigger primitive generation performance is summarized in section 7.4.2.

The format and schema of trigger primitives are subject to further optimization because they are further tightly coupled with the generation of trigger candidates, discussed in the following subsection. Nominally, each trigger primitive comprises the channel address (32 bit), hit start time (64 bit), the time over threshold (16 bit), the integral ADC value (32 bit), an error flag (16 bit), and possibly also the waveform peak (12 bit) associated with the hit. Thus, 20 B to 22 B provides a generous data representation of trigger primitive information. The trigger primitive rate will be dominated by the rate of decay of naturally occurring  $^{39}\text{Ar}$ , which is about 10 MHz per module. Radioactive isotopes of krypton may also contribute to the trigger primitive rate, but based on results from dark matter experiments, this rate is much smaller than the intrinsic  $^{39}\text{Ar}$  rate. This leads to a detector module trigger primitive aggregate rate of 200 MB/s. The subsequent stage of the data selection must continuously absorb and process this rate providing trigger candidates as described next.



### 7.3.3.2 Low level trigger: trigger candidate generation

At the trigger candidate generation stage of the low level trigger, trigger primitives from individual, contiguous fragments of the detector module are cross-channel and time correlated, and further selection criteria are applied. This may result in the output of trigger candidates. More specifically, once activity is localized in time and channel space, we can apply a rough energy-based threshold based on the combined metrics carried by the cross-correlated trigger primitives; satisfying this criteria defines a trigger candidate.

A trigger candidate packet carries information about all the trigger primitives used in its formation. In particular, the packet provides a measure of the total activity represented by these primitives, as well as a measure of their collective time, channel location, and extent within the module. These measures are used downstream by the module level trigger, as described more in the next section.

While the selection applied in the previous stage (trigger primitive generation) is driven by a measure of noise, at the trigger candidate generation stage, before applying any thresholds, the rate is driven by background activity. In particular,  $^{39}\text{Ar}$  decays would provide 50 kHz of trigger candidates per APA face if the threshold was set very low, i.e., at 0.1 MeV. Next, activity from the  $^{42}\text{Ar}$  decay chain would be substantial for a threshold below 3.5 MeV. Nominally, individual candidates, or groups of candidates nearby in detector space and time, with measures of energy higher than these two types of decays, will be passed to the module level trigger.

This stage of data selection is implemented 75 (TPC) plus eight (PD system) CPU servers, which receive the trigger primitive stream from the upstream DAQ and distribute trigger candidates to the module level trigger stage, described next, via the 10 Gbit/s DAQ network. Studies are underway to demonstrate CPU resource use and latency, as are efforts to demonstrate online trigger candidate generation at ProtoDUNE. Trigger candidate generation performance is summarized in section 7.4.2.

### 7.3.3.3 Module level trigger

Data selection is further facilitated as trigger candidates are consumed by the module level trigger in order to form the ultimate trigger decision that prompts the readout of data records from buffers kept by the upstream DAQ. The physical (channel and time) location, extent, and energy measure of the candidates are used at this stage to categorize the activity in terms of a localized high energy trigger or an extended low energy trigger. Specifically, a suitable number of isolated, low energy candidates found in coincidence over the integration period of up to 10 s across the full detector module indicate the latter; individual high energy candidates, found otherwise, indicate the former.

When a particular condition in a category is satisfied, the trigger decision is made and a trigger command is formed. The trigger command packet includes information about the candidates (and primitives) that were used to form it. The decision also provides direction as to what set of detector subcomponents should be read out and over what time period (localized or extended as described above). The module level trigger publishes a stream of trigger commands and the primary subscriber should be the DFO of the DAQ BE as described in section 7.3.4.

The module level trigger is implemented in  $O(1)$  CPU server (with 100% redundancy), which receives the trigger candidate stream from the low level trigger stage of the data selection and

distributes trigger commands to the DAQ BE via the 10 Gbit/s DAQ network. Studies are underway to demonstrate CPU resource use and latency, as are efforts to demonstrate online trigger command generation at ProtoDUNE. Trigger command generation performance is summarized in section 7.4.2.

### 7.3.3.4 External trigger interface

The ETI provides a loose coupling between the module level triggers (MLTs), sources of external information such as beam spill times and information to or from components of DUNE FD calibration systems. As an interface between MLTs, the ETI receives and distributes information about module-level SNB trigger commands. This allows any detector module, which alone may not have satisfied a SNB trigger requirement, to nonetheless perform an SNB readout. The ETI is also responsible for forming a coincidence between module-level SNB trigger commands and publishing the results, e.g., for consumption by the SNEWS.

The ETI also receives information about beam spill times from the accelerator. These times can drive a model of the beam timeline to predict when beam spills, and consequently beam-related interactions, should occur. These predictions can then be sent to the MLTs, so they can either alter trigger decision criteria or merely include the information in contemporaneous trigger decisions. The beam time information can also be distributed to components of the calibration system to avoid producing activity in the detector that may interfere with activity from beam neutrinos.

The external trigger interface is implemented in  $O(1)$  CPU server (with 100% redundancy), with 10 Gbit/s networking and interfacing hardware components (to White Rabbit (WR) and DUNE timing system) for timing and external trigger signal I/O.

### 7.3.3.5 High level filter

The last processing stage in the DAQ DS is the high level filter, which resides in the DAQ BE, and physically, on the surface at SURF. The high level filter acts on triggered, read out, and aggregated data. It therefore serves primarily to down-select and thus limit the total triggered data rate to offline storage, thereby keeping efficiency high in collecting information on activities of interest, while maintaining low selection and content bias, reducing the output data rate. It may do so using further filtering, lossy data reduction, and/or further event classification. Because it benefits from operating on relatively low-rate data, it can accommodate a higher level of sophistication in algorithms for data selection decisions.

More specifically, the high level filter may further reduce the rate of data output to offline storage by applying refined selection criteria that may otherwise be impossible to apply to the pre-trigger data stream. For example, instrumentally-generated signals (e.g., correlated noise) may produce trigger candidates that cannot be rejected by the module level trigger and, if left unmitigated, may lead to an undesirably high output data rate. Post processing the triggered data may reduce this unwanted contamination. Furthermore, the high level filter can also reduce the triggered data set by further identifying and localizing interesting activity. A likely candidate hardware implementation of this level of data selection is a GPU-based system residing on surface at SURF.

To fully understand how much and what type of data reduction may be beneficial, simulation studies are ongoing [142], summarized in section 7.4.2, and will must be validated with initial data

analysis after the first DUNE FD operation. Development efforts are also ongoing to determine the scale of processing required by the FD.

### 7.3.4 Back-end DAQ

The DAQ BE moves data of interest identified by the data-selection system from the readout DAQ buffers, serving them to the high level filter and storing the filtered data into the output buffer. From there, data will be transferred to permanent storage off-site.

The DAQ BE system accepts trigger commands produced by the DAQ DS as described in section 7.3.3. It queries the upstream DAQ buffers and accepts returned data as described in section 7.3.2. Finally, it records trigger commands and the corresponding detector data to the output storage buffer.

The principal components of the DAQ BE are the data flow orchestrator (DFO), event builder (EB) and the output storage buffer (OB) in figure 7.1.

#### 7.3.4.1 Data flow orchestration

The EB stage is implemented as a pool of redundant EB processes to maximize the system tolerance to faults and to handle the readout of long SNB events in parallel to nominal readout requests. This asynchronous, parallel readout will be coordinated by a DFO. Its operation is illustrated in figure 7.8 and is discussed here:

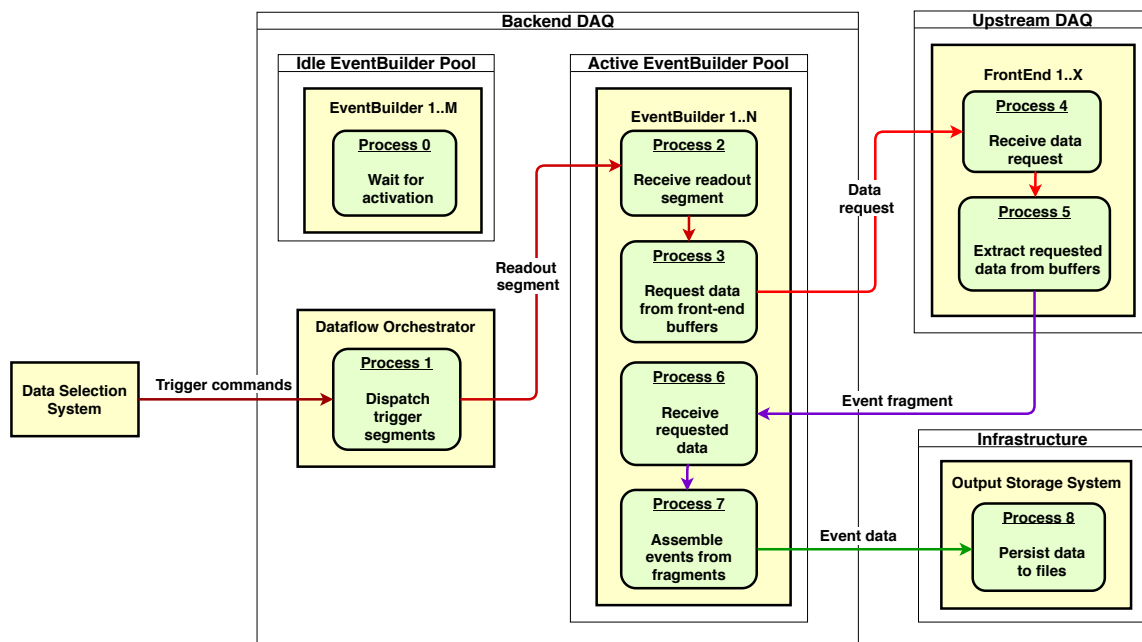


Figure 7.8. Illustration of DUNE DAQ BE operation.

- DFO accepts a stream of trigger commands and dispatches each to an available EB process as described in section 7.3.4.2 for execution.

- In atypical situations in which there are insufficient event builder resources available to handle the rate of triggers produced by the data selection subsystem, the DFO will alert the DS subsystem that the rate of triggers needs to be reduced. When such reductions are requested, the DAQ DS will update the calculation of the module-level DAQ livetime appropriately.
- The DFO will provide relevant data flow status and statistics information to the monitoring processes that are described in section 7.3.5.4. Given its central role and knowledge of the state of available event builder buffers, it will be able to provide important information about the health and performance of the system.

### 7.3.4.2 Event builder

The DAQ BE will provide the instances of the event builder (EB) most likely as `artdaq` [146] components of the same name. As described above, each EB instance will:

- Receive a readout segment for execution. Execution entails interpreting the trigger command segment and querying the appropriate upstream DAQ units to request data from the period of time.
- Requests and their replies may be sent synchronously, and replies are expected even if data has already been purged from the upstream DAQ units. (In that case, an empty fragment will be generated with appropriate error flags set).
- The received data then processed and aggregated, is finally saved to one or more files on the output storage system before it is transferred offline.

As part of this, the EB subsystem will provide book-keeping functionality for the raw data. This will include the documenting of simple mappings, such as which trigger is stored in which raw data file, as well as more sophisticated quality checks. For example, it will know which time windows and geographic regions of the detector are requested for each trigger, and in the unlikely event that some fraction of the requested detector data can not be stored in the event record, it will document that mismatch.

### 7.3.4.3 Output buffer

The output buffer system is composed by the physical hardware resource to host the incoming data and by the software services handling the final processing stages through the High Level Filter and the transfer off-site to permanent storage.

It has two primary purposes. First, it decouples the production of data from filtering and the transfer of filtered data offline. It provides the elasticity needed by the DAQ to deal with perturbations in the flow of data, therefore minimizing the impact of temporary loss in filtering performance due to hardware or software issues. Second, it provides local storage sufficient for uninterrupted DAQ operation in the unlikely event that the network connection between the FD and Fermilab is lost. A capacity of at least a few PB is envisioned, sufficient to buffer the nominal output of the entire FD for about one week even in the case of SNB events. Based on prior experience of

the consortium with unusual losses of connectivity at other far detector experiment sites, this is a conservative storage capacity value.

The output buffer system will provide the relevant data flow status and statistics information to the monitoring processes that are described in section 7.3.5.4. The knowledge of the health and performance of the of the buffer system will enable the monitoring system to promptly identify and address developing faults before they can have an impact on data taking.

### 7.3.4.4 Data network

Upstream DAQ, DAQ DS and DAQ BE DAQ are interconnected by a 10/100 Gbit/s ethernet network for data exchange. In particular the upstream DAQ and DAQ DS servers are connected through redundant 10 Gbit/s links to top-of-rack switches with 10 Gbit/s uplinks. The EB and Output buffer hardware will support 100 Gbit/s directly. The DAQ data network is connected to the Fermilab network via a WAN interface.

### 7.3.4.5 Data model

The data model for the DUNE far detector describes the format and characteristics of the triggered data at each stage in the analysis chain, the grouping of the data into logical units such as runs, and the characteristics of ancillary data such as detector configuration parameters and calibration results.

The requirements that these place on the DAQ are primarily in the areas of flexibility and traceability. The DAQ will have the flexibility to handle the readout of triggers that have a time window that is on the order of a single TPC drift time (for example a trigger associated with a beam gate window), triggers that have a time window of many seconds (such as for a supernova burst trigger), and windows between those two extremes (for detector and electronics studies). In the area of traceability, the DAQ system will provide the necessary level of detail regarding the conditions that triggered each event, the expected and actual regions of the detector that contributed raw data to each event, the conditions of the detector and electronics during data taking, the version and configuration of the software components used in the DAQ chain, etc.

### 7.3.5 Control, configuration, and monitoring

The DAQ control, configuration and monitoring subsystem (CCM), illustrated in figure 7.9, consist of the software subsystems to control, configure, and monitor the DAQ system, as well as the detector components participating to data taking. It provides a central access point for the highly distributed DAQ components, allowing them to be treated and managed as a single, coherent system, though their corresponding subsystem interfaces. It is responsible for error handling and recovery, which is achieved by designing a robust and autonomous fault-tolerant control system. The main goal is to maximize system up-time, data-taking efficiency and data quality when the system faces programmatic (i.e. calibrations) and unforeseen (hardware failures or software faults) change of data-taking conditions. The DAQ control, configuration and monitoring subsystem (CCM) provides an access point, which is delegating user's actions to the corresponding interfaces. The detector components and infrastructure elements access the DAQ control, configuration and monitoring subsystem (CCM) subsystems through their provided interfaces.

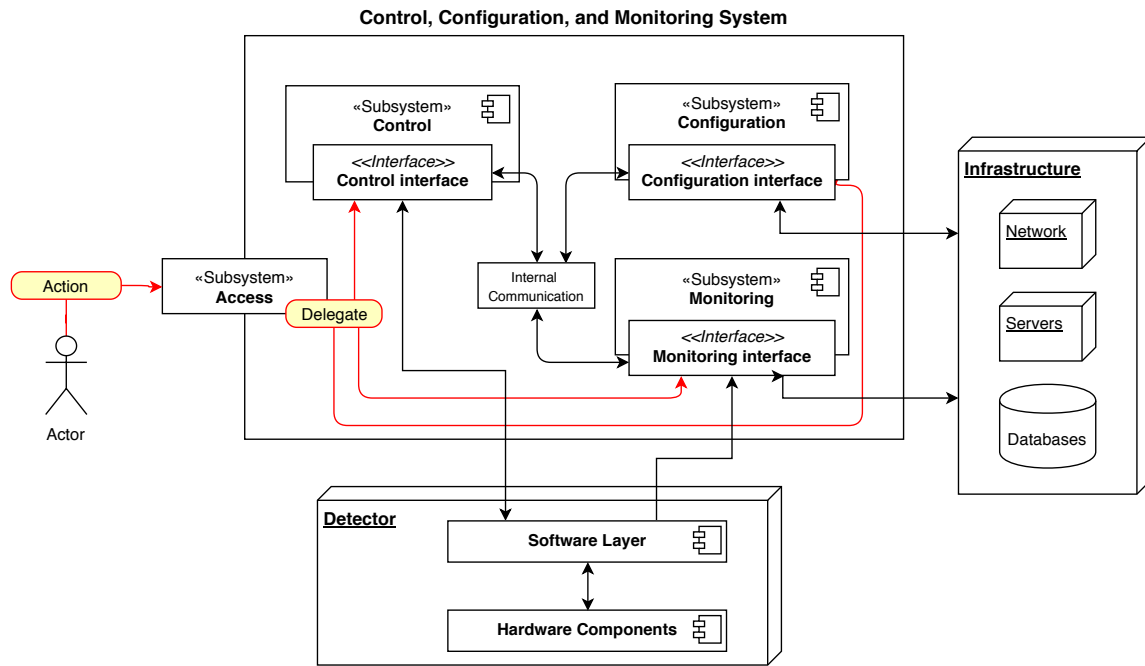


Figure 7.9. Main interaction among the three CCM subsystems.

The following sections describe each DAQ control, configuration and monitoring subsystem (CCM) subsystem, covering internal functions and dependencies between each other.

### 7.3.5.1 Access

Actions are defined as any kind of human interaction with the DAQ control, configuration and monitoring subsystem (CCM). The access subsystem is responsible for the action delegation to internal function calls and procedures. Its implementation is driven by the control, configuration and monitoring interface specifications, and protects the direct access to detector and infrastructural resources. It also controls authentication and authorization, which locks different functionalities to certain actor groups and subsystems. As an example, only the detector experts can modify front-end configuration through the configuration interfaces, or only an expert user can exclude an APA's readout from data taking.

### 7.3.5.2 Control

The control subsystem consists of several components and utilities, and also has additional subsystems to carry out dedicated roles. It enforces the implementation of required interfaces and actively manages DAQ process lifetimes. It operates in a distributed, fault-tolerant manner due to protocols that will drive the FSM for state sharing.

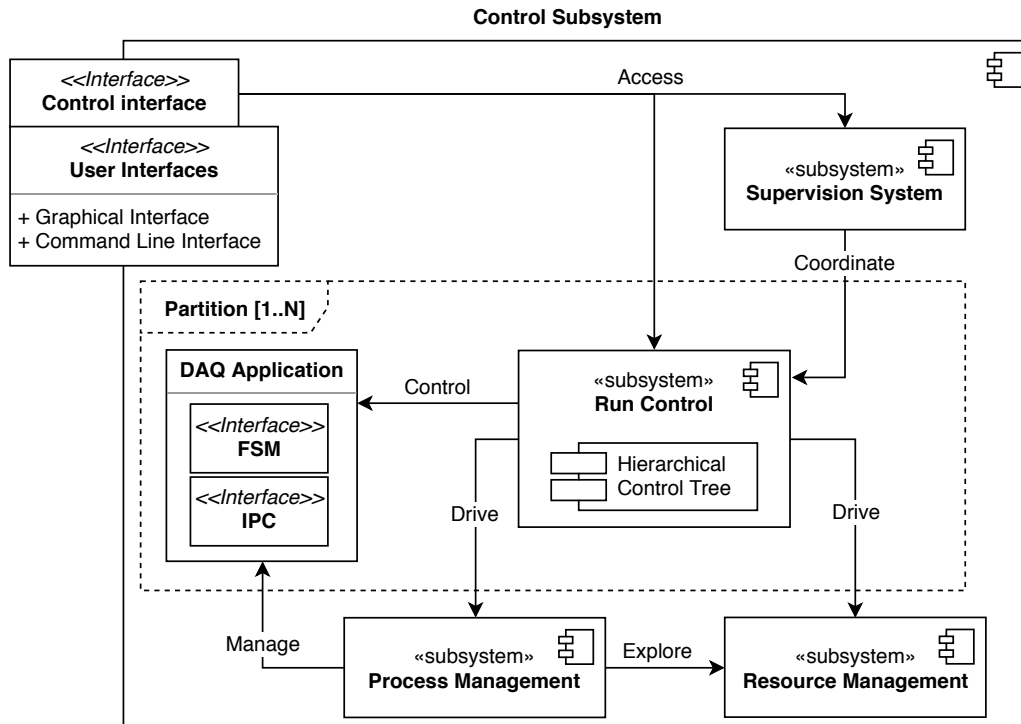


Figure 7.10. Roles and services that compose the DAQ control subsystem.

It contains the following core components:

- **Supervision System** — It is responsible for manual and automated control and supervision of DAQ components at any given time. In autonomous mode, the system makes attempts for fault-recovery, failover to backup instances of subsystems, and isolation of problematic regions of the control tree. This is carried out by a hierarchical rule-based planning or fuzzy logic system.
- **DAQ Application** — The CCM provides interfaces in order to communicate with processes of the DAQ, and the ability to control and communication with the CCM. The Inter Process Communication (IPC) supports a mechanism to interact with all actors participating to data taking. The Finite State Machine (FSM) enforces the possible states and transitions that are specific to the experiment's components, and also describes them in a uniform way.
- **Run Control** — This part of the control subsystem coherently steers the data taking operations. It interacts with all actors participating to data taking in a given partition. It consists of a hierarchical control tree, which can subdivide the DAQ components into separated regions that may be acted upon independently.
- **Resource Management** — It provides a global scope of available resources for the DAQ components. This includes the mapping between the detector front-end readout units, processes, servers where they are spawned and required resources for the processes.
- **Process Management** — It is responsible for managing process lifetime.

### 7.3.5.3 Configuration

The configuration subsystem provides several key elements for the configuration management of DAQ components and detector front-end electronics. It provides a description of system configurations, the ability to define and modify configurations, and graphical user interfaces for the human user to access the data. Data access libraries will hide the technology used for the databases implementation. The subsystem is also responsible for the serialization, persistency, and bookkeeping of configurations.

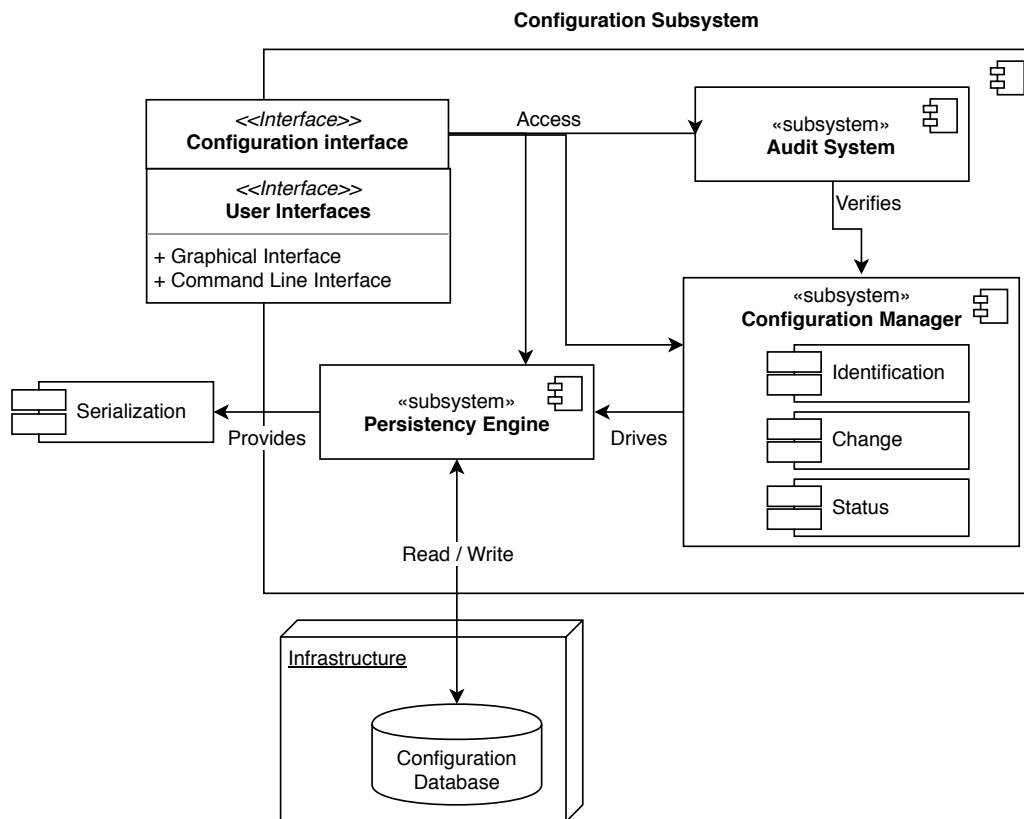


**Figure 7.11.** Main components of the CCM configuration subsystem.

The main components of the configuration subsystem are the following:

- **Configuration Manager** — It consists of the three main components of configuration management systems. The Identification Engine is a set of functionalities that are responsible for the definition of DAQ components and their corresponding configuration specification. The Change Manager is responsible for providing control over altering the configuration specifications of components. The Status Engine is providing status and information about configuration specifications of individual, or set of DAQ elements.
- **Audit System** — This important subsystem is supporting the experts and decision making systems to verify the consistency of configuration specifications against the DAQ and detector components. It provides results on mis-configurations and potential problems on configuration alignment and dependencies between components.



- Persistence Engine — This component provides a single and uniform serialization module, which is strictly followed by every DAQ component. Also responsible for configuration schema evolution and communication with the configuration database. The storage engine privileges will be only read and write operations, not allowing updates and removal of configurations. It also provides a redundant session layer for high-availability and load distribution.

The configuration system will mainly consist of standard configuration management components, with a high emphasis on the audit system, in order to verify that the global configuration of the CCM complies with the detector, physics and operational requirements.

### 7.3.5.4 Monitoring

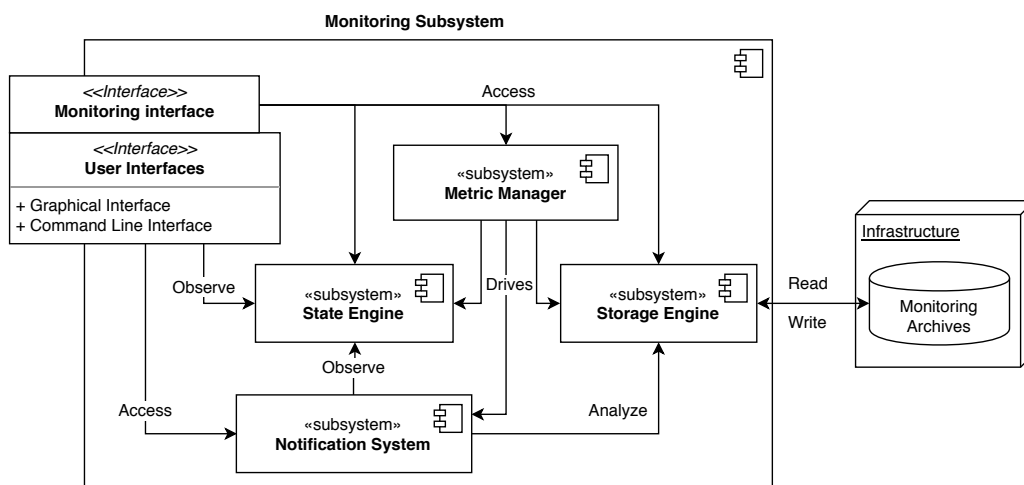


Figure 7.12. Roles and services that compose the DAQ monitoring subsystem.

Highly-scalable and efficient operational monitoring is essential during data-taking periods. Any malfunctioning component of the experiment must be identified and reported as soon as possible. Therefore, the aim of the monitoring subsystem is probing and notifying the status of CCM components, services, and resources. There is also a requirement of CCM infrastructure monitoring and log aggregation. The types of monitoring information vary greatly depending on operational complexity, which require flexibility from the monitoring infrastructure for seamless additions, modifications and aggregated view on service degradation. It consists of the following main components, also shown in figure 7.12:

- Metric Manager — It is responsible for the registration of metric data streams and corresponding aggregator functions. This central element is the collection of features and services that provides support for configurable operational monitoring of CCM services. CCM components and services that are registered via the Metric Manager, are reporting monitoring data to the State and the Storage Engines in a publish-subscribe fashion.
- State Engine — This engine is responsible for providing the global state of the system at the current time. It subscribes to a set of registered metrics in the Metric Manager, and records

the actual global state of the set for decision making systems (supervision, notification, and visualization).

- **Storage Engine** — Metrics may have different persistency requirements, for which the engine is responsible for archiving the data with the settings of interval, smoothing, etc. It also provides an implementation for the most common communication protocols for the database back ends (SQL, REST, etc.).
- **Notification System** — It is a rule-based system of scheduled and aimed notifications that occur in the case of state combinations. It defines soft and hard states of events and grace periods of alarms.
- **User Interfaces** — Provides graphical and command line user interfaces for monitoring configuration management and visualization of metric data.

Monitoring being a key requirement in the industry for computer clusters and their applications, the proposed solution is the adaptation of mature, robust, and open-source third party tools, with the extension of DUNE CCM specific interface implementations and configurations of these monitoring systems.

### 7.3.5.5 Inter-process communication

The DUNE FD DAQ is an asynchronous, parallel distributed data processing system. It is composed of many independent processes which ingest and produce messages. The mechanisms of such message passing are generally called inter-process communication (IPC). Referring to figure 7.1, IPC is used for both in-band detector data flow between upstream DAQ and back-end EBs and for out-of-band messages as part of CCM. The IPC used by the DAQ DS spans both descriptions as it passes derivations of a subset of detector data (trigger primitives, candidates) and culminates in a source of out-of-band message (trigger commands) to direct the readout by EB and other components of detector data that is held in the upstream DAQ buffers.

The ZeroMQ [147] smart socket library is the basis of a system being developed and evaluated for parts of both in-band and out-of-band IPC. As part of the CCM, this includes the issuing of control and reconfiguration commands to and receiving of monitoring messages from essentially all DAQ components. As part of DAQ DS, this includes the transfer of trigger primitive, candidate and command messages. In the upstream DAQ this includes the upstream DAQ buffer interface (UBI) that provides access to the upstream DAQ primary buffers for queries by EB and other components. IPC must be implemented broadly across many DAQ systems and ZeroMQ allows their problems to be solved in common, shared software. As CCM has the most complex IPC needs, this work is organizationally considered part of this system.

As described in 7.3.4, artdaq [146] utilizes IPC between its back-end components. It has been well tested with ProtoDUNE and other experiments. artdaq may be used for some portions of the IPC described above. For example, if the UBI is implemented as an artdaq Board Reader it would necessarily use artdaq IPC. This would limit the types of clients that could query for data in the buffers to be artdaq modules. Understanding how to optimally select an IPC for such parts of the DAQ connection graph is an area of ongoing R&D effort.

### 7.3.5.6 Hardware

The CCM software suite will run on approximately 15 servers interconnected by a 1 Gbit/s ethernet network to upstream DAQ, DAQ DS, DAQ BE as well as detector and calibration daq interface elements. While this network has a lower throughput compared to the data network, it has many more endpoints  $O(2000)$ .

### 7.3.6 Data quality monitoring

While the CCM contains an element of monitoring (section 7.3.5.4), here data quality monitoring (DQM) refers to a subsystem that quickly analyzes the data in order to determine the general quality of the detector and DAQ operation. This is in order to allow operators to promptly detect and respond to any unexpected changes and assure high exposure times for later physics analyses. A DAQ data quality monitoring (DQM) will be developed (including necessary infrastructure, visualization, and algorithms), which will process a subset of detector data in order to provide prompt feedback to the detector operators. This system will be designed to allow it to evolve as the detector and its data is understood during commissioning and early operation and to cope with any evolution of detector conditions.

### 7.3.7 Timing and synchronization

The DAQ timing and synchronization subsystem (DAQ TSS) provides synchronous time services to the DAQ and the detector electronics. All components of the FD use clocks derived from a single Global Positioning System (GPS) disciplined source, and all module components are synchronized to a common 62.5 MHz clock. This rate is chosen in order for this common clock to satisfy the requirements of the detector electronics of both the single-phase and the dual-phase far detector modules. To make full use of the information from the PD system, the common clock must be aligned within a single detector module with an accuracy of  $O(10\text{ ns})$ . For a common trigger for a SNB between modules, the timing must have an accuracy of order 1 ms. However, a tighter constraint is the need to calibrate the common clock to universal time derived from GPS so the data selection algorithm can be adjusted inside an accelerator spill, which again requires an absolute accuracy of order 1  $\mu\text{s}$ . The design of the timing system allows for an order-of-magnitude better synchronization precision than these requirements, allowing a substantial margin of safety and the possibility for future upgrades to front-end electronics.

The DUNE FD uses a improved version of the ProtoDUNE timing system, where a design principle is to transmit synchronization messages over a serial data stream with the clock embedded in the data. The format is described in DocDB 1651 [60]. The timing system design is described in detail in DocDB 11233 [61].

Central to the timing system are four types of signals:

- a 10 MHz reference used to discipline a stable master clock,
- a one-pulse-per-second signal (1PPS signal) from the GPS,
- a Precision Time Protocol (PTP) signal providing an absolute time for each 1PPS signal, and

- an inter-range instrumentation group (IRIG) time code signal used to set the timing system 64 bit time stamp.

The timing system synchronization codes are distributed to the DAQ readout components in the central utility cavern (CUC) and the readout components on the cryostat via single mode fibers and passive splitters/combiners. All custom electronic components of the timing system are contained in two Micro Telecommunications Computing Architecture ( $\mu$ TCA) shelves; at any time, one is active while the other serves as a hot spare. The 10 MHz reference clock and the 1PPS signal are received through a single-width advanced mezzanine card (AMC) at the center of the  $\mu$ TCA shelf. This master timing AMC is a custom board and produces the timing system signals, encoding them onto a serial data stream. This serial data stream is distributed over a backplane to a number of fanout AMCs. The fanout AMC is an off-the-shelf board with two custom FPGA mezzanine cards (FMCs). Each FMC has four SFP cages where fibers connect the timing system to each detector component (e.g., APA) or where direct attach cables connect to other systems in the CUC.

To provide redundancy, two independent GPS systems are used, one with an antenna at the surface at the Ross shaft, and the other with an antenna at the surface at the Yates shaft. Signals from either GPS are fed through single-mode optical fibers to the CUC, where either GPS signal can act as a hot spare while the other is active. Differential delays between these two paths are resolved by a second pair of fibers, one running back from the timing system to each antenna, allowing closed-loop delay estimation.

### 7.4 Design validation and development plans

The following strategy is being followed in order to validate and develop the DUNE FD DAQ:

- use ProtoDUNE and other test stands as a basis for prototyping, development and validation of the DAQ design;
- use Monte Carlo simulations and emulations in order to augment actual hardware demonstrations and validate triggering schemes in the FD environment; and
- benefit from experience in LArTPC data processing by other experiments.

The design and implementation of the DAQ is being carried out using an iterative prototyping model, which is well suited for a system that largely relies on commercial off-the-shelf hardware components, on communication and information technologies that are rapidly evolving, and that mainly requires software and firmware development effort. The advantage of the prototyping model is also that it facilitates the identification of and collaboration among experts from a large number of institutions, through focussed efforts to achieve the short-term objectives established through each prototyping iteration.

Once the identification of applicable technologies are completed and the overall system requirements are refined, the project will switch to an iterative incremental model, ensuring that, step-by-step, functional and performance requirements will be met by each of the sub-components individually, and by the DAQ system globally. The overall schedule, summarized in section 7.6.2,

reflects the different development and production time scales that are envisioned for the various DAQ components.

While DUNE data processing challenges are unique in both form and scale, other ongoing or planned near-term LArTPC experiments, including MicroBooNE, SBND [148], and ICARUS, are exercising a number of relevant data processing and data reduction techniques, and already providing valuable inputs to the DUNE FD DAQ design. For example, MicroBooNE has demonstrated successful implementations of lossless Huffman compression and of continuous readout via use of lossy compression (dynamic and fixed-baseline zero-suppression) [130]; this has provided guidance and confidence on anticipated achievable data reduction factors and data compression impact on physics performance.

The following subsections summarize past, ongoing, and planned development and validation studies and identify how anticipated outcomes will be used to finalize the DAQ design.

### 7.4.1 ProtoDUNE test beam

The FD DAQ consortium constructed and operated the DAQ system [149] for ProtoDUNE, which included two parallel DAQ readout architectures, one based on FELIX, developed by ATLAS [139], and the other on reconfigurable computing element (RCE), developed at SLAC. DAQ design and construction for ProtoDUNE began in Q3 of 2016, and the system became operational at the start of the beam data run in Q4 of 2018. The detector is continuing to run at the time of writing, recording cosmic ray activity, and providing further input for DAQ development toward DUNE.

Figure 7.13 depicts the ProtoDUNE DAQ system. The DAQ is split between the FELIX and reconfigurable computing element (RCE) [150] implementations. The two architectures share the same back end and timing and trigger systems. Neither of these tested architectures explicitly represents the baseline design for the DUNE FD. Instead, each roughly maps onto one of two data processing approaches: one in which the data is processed exclusively in custom-designed FPGA firmware and carrier board, and the other in which the data is processed primarily with custom software run in commodity servers. The baseline design presented here merges elements of the two approaches. Specifically, it uses FELIX as the hardware platform for data receiving and handling, and a co-processor FELIX daughter card (analogous to the RCE platform used at ProtoDUNE) to provide additional, dedicated data processing resources.

Besides overall readout architecture, the ProtoDUNE and DUNE DAQ systems exhibit two key differences. First, the ProtoDUNE DAQ is externally triggered (and at a trigger rate over an order of magnitude higher than that anticipated for DUNE). Because of this, the ProtoDUNE DAQ does not facilitate online data processing from the TPC or PD system for self-triggering. Second, the ProtoDUNE system sits at the surface with a much higher data occupancy due to cosmic ray activity. Overcoming the first key difference in order to demonstrate data selection capability for the FD DAQ design is a main component of current and future DAQ development plans.

#### 7.4.1.1 ProtoDUNE outcomes

The ProtoDUNE-SP DAQ supported a test-beam experiment, and the requirements of the DUNE DAQ are substantially different in scale and performance. However, the successful operation of the ProtoDUNE-SP DAQ has provided several key demonstrations for final system, in particular the data flow architecture, run configuration and control, and back-end functionality.

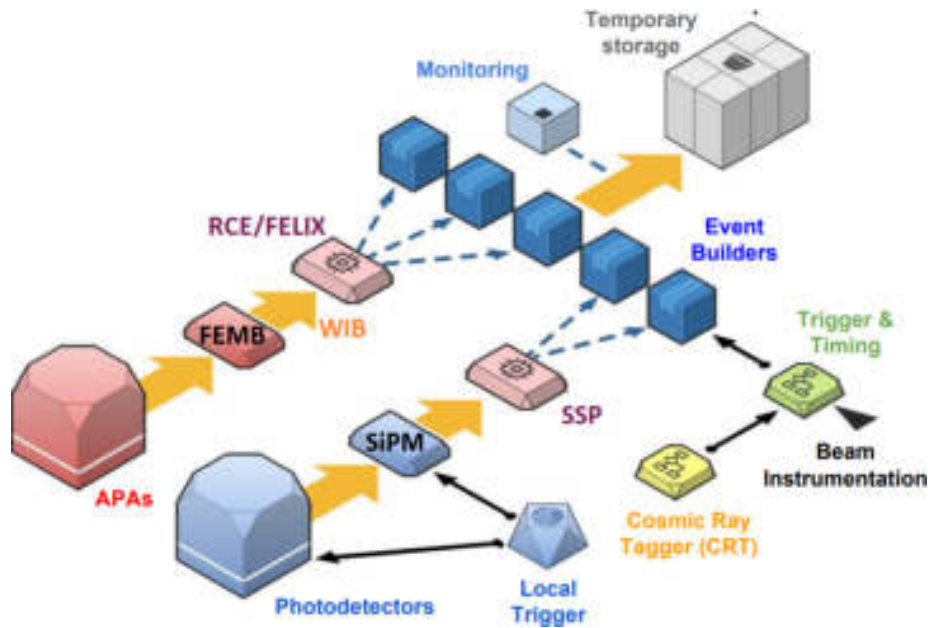


Figure 7.13. The ProtoDUNE DAQ system.

Specifically, ProtoDUNE-SP has demonstrated:

- Upstream DAQ: front-end readout hardware and data flow functionality servicing two out of the six APAs. The data from each APA was continuously streamed to a single FELIX board hosted in a dedicated computer which then transferred it to two other computers for buffering and readout. The baseline upstream DAQ for DUNE FD will retain one APA per FELIX board but place two FELIX boards and the buffering and readout functionality all together in a single DAQ FEC. In addition to data flow functionality, ProtoDUNE front-end readout also demonstrates the interface to the front-end TPC electronics, and scalability to DUNE. It also supports host server requirements and specifications. Finally, it serves as platform for further development involving co-processor implementation and data selection aspects.
- DAQ BE, CCM and software infrastructure: successful DAQ BE implementation, including event builder farm and disk buffering, as well as an initial implementation of CCM functions. This has allowed the development and exercising of system partitioning, and provides a basis for scalability to DUNE. ProtoDUNE also serves as a platform for further system development, in particular in CCM and for the data flow orchestrator part of the DAQ BE.
- Data selection and timing: successful operation of the timing distribution system, and external trigger distribution to the front-end readout.

Besides demonstrating end-to-end data flow, an important outcome of ProtoDUNE has been the delineation of cross-system interfaces, i.e. understanding the exact DAQ scope and the interfaces to TPC, PD system, and offline computing. The use of commodity solutions where possible, and leverage of professional support from CERN IT substantially expedited the development and success of the project, as did the strong on-site presence of experts from within the consortium during early

installation and commissioning. Outcomes specific to ProtoDUNE subsystems are discussed in greater detail in [151].

### 7.4.2 Ongoing development

DAQ subsystem development is ongoing at ProtoDUNE at the time of writing. A detailed schedule for 2019 is available in [152]. Major development plan milestones, a number of which have already been achieved at the time of this writing, are:

- optimization and tuning of the front-end readout;
- optimization and tuning of the artdaq based dataflow software;
- enhancement of monitoring and troubleshooting capabilities;
- introduction of CPU-based hit finding (necessary for PD system readout);
- introduction of FPGA-based hit finding (for TPC readout);
- implementation of online software data selection beyond trigger primitive stage (introduction of trigger candidate generation, trigger command generation), and tests on well identified interaction topologies (e.g., long horizontal tracks, or Michel electrons from muon decay);
- integration of online trigger command and modified data flow to event builder to facilitate self-triggering of detector;
- implementation of extended FPGA-based front-end functionality (e.g., compression); and
- prototyping of fake SNB data flow in front end and the back end.

Below, we focus on ongoing developments related to upstream DAQ, data selection, and CCM prototyping, which is relevant to all DAQ subsystems. These are the key areas where new technologies, beyond ProtoDUNE, remain to be designed and tested.

#### 7.4.2.1 Upstream DAQ development

The use of FELIX as the front-end readout technology for DUNE was successfully prototyped at ProtoDUNE, initially for the readout of one APA. In ProtoDUNE, FELIX allows streaming of data arriving on multiple 10 Gbit/s optical point-to-point links into commercial host memory and, from there, storing, dispatching or processing of the data via software.

In ProtoDUNE, a single APA FELIX-based readout consists of two servers with a point-to-point 100 Gbit/s network connection to the FELIX host computer. The FELIX I/O card interfaces with its host PC through 16-lane PCIe 3.0 (theoretical bandwidth of 16 GB/s). It transfers the incoming WIB data directly into the host PC memory using continuous DMA transfer. The FELIX host PC runs a software process that publishes the data to any client subscribing to it. Subscriptions may identify from which input optical links the received data stream will be sourced. The clients consuming these streams are “BoardReader” processes implemented in the artdaq data acquisition toolkit. In order to sustain the data rate, modest modifications of the firmware and software were carried out specifically for ProtoDUNE: each FELIX host receives and publishes data at ~75 Gbit/s. The

BoardReader hosts are equipped with embedded Intel QuickAssist (QAT)<sup>1</sup> technology for hardware accelerated data compression. The ProtoDUNE application of the FELIX front-end readout is shown in figure 7.14.

In DUNE only a very small fraction of the data received via the FELIX system will ever need to leave the host: thus it is not required to implement very high speed networked data dispatching. On the other hand it may be interesting to carry out data processing and buffering on the host. While this is not the baseline design for DUNE, R&D is ongoing at ProtoDUNE-SP to evaluate the feasibility of implementing hit finding, data buffering, and possibly even local trigger candidates generation on the FELIX host.

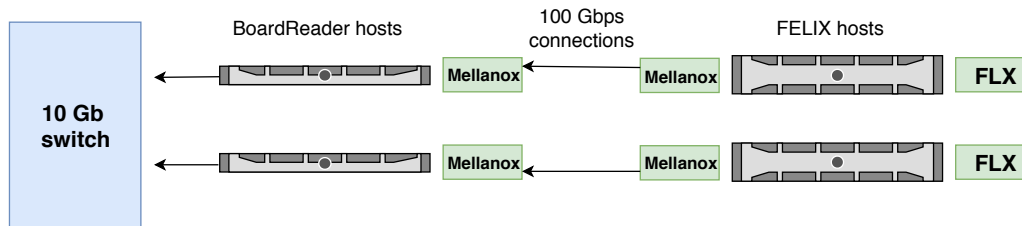


**Figure 7.14.** The topology of the FELIX-based upstream DAQ of ProtoDUNE (from [153]). The FELIX host servers are publishing the data from the WIBs over 100 Gb/s network interfaces. The BoardReader hosts are carrying out trigger matching, data compression and forwarding of fragments to the event builder.

The DAQ team is investing substantial effort into the introduction of a triggering chain based on the TPC data into ProtoDUNE, which will allow to carry out pre-design prototyping studies of the complete flow of data of the DUNE DAQ. The FELIX-based readout system will be adapted to support the different studies, from co-processor based data handling in firmware (including trigger primitive generation, compression, and buffering) to software-based processing, on a single server. Benchmarking and optimization of the FELIX firmware and software will also continue, with the aim of further compacting the readout by supporting two APAs on a single server.

#### 7.4.2.2 Co-processor development

Upstream DAQ development efforts at ProtoDUNE include a parallel test platform for trigger primitive generation, compression, and buffering firmware validation for the FPGA co-processor board. The platform for these tests will initially be a Xilinx ZCU102 development board. Passive optical splitters will be inserted into the fiber path downstream of the WIBs, providing duplicate data inputs for the test hardware, without disrupting the main readout path of ProtoDUNE. Tests using the development board will first focus on generation of trigger primitives, which will be read out over the network via IPBus [154]. The ZCU102 includes 512MBytes of DDR4 RAM connected to the FPGA programmable logic, as well as a four lane PCIe Gen 2 socket which will host an NVMe SSD on an adapter. This combination of hardware will allow tests of buffering and compression of readout data, in parallel with trigger primitive generation. The ZCU102 will subsequently be replaced with a “FELIX demonstrator” using a Xilinx Virtex-7 Ultrascale+ FPGA, connected to a custom FPGA co-processor board via an FMC+ connector. These boards represent the first prototypes for the final system hardware.

<sup>1</sup>Intel® QuickAssist Technology.



Tests using the development board will focus on functionality rather than data throughput. However, the tests will provide estimates of FPGA logic and memory resources that can be scaled up to the full system. Tests using the FELIX Demonstrator and PBM at ProtoDUNE will focus on scaling the functional tests performed using the ZCU102 to a full demonstration of trigger and readout functionality for a full APA. In addition, this platform will facilitate integration with the prototype DAQ DS and DAQ BE subsystems at ProtoDUNE.

### 7.4.2.3 Data selection development

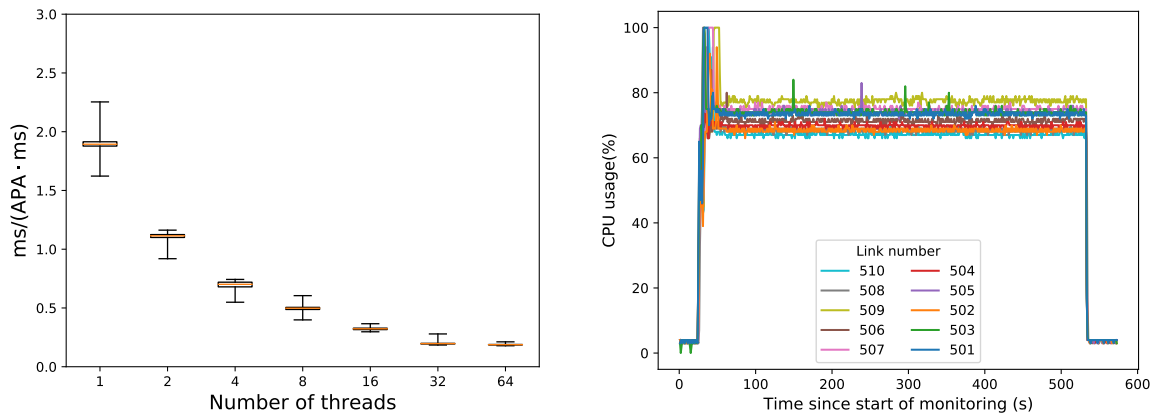


**Figure 7.15.** CPU core-time (left) required to find primitives in simulated signal and noise data across 960 collection channels. In this test, the data has been pre-formatted to facilitate the use of SIMD hardware accelerated functions (AVX2). Per thread CPU utilization (right) to process live data from a ProtoDUNE APA. Processing includes data reformatting, trigger primitive generation, and output message formation. Each thread, one per FELIX link, requires about 75% CPU core utilization to keep up. Variation in utilization reflects the variations in levels of ionization and noise activity in the input data and is due to output message formation. The peak usage at the start arises from input buffering while the process is initializing. Once operational state is achieved, this brief backlog is processed.

During early stages of design, significant effort has been dedicated to trigger primitive generation studies through simulations. Specifically, charge collection efficiency and fake rates due to noise and radiologicals have been studied as a function of hit threshold, demonstrating that data rate requirements can be met, given sufficiently low electronics noise levels and radiological rates [145]. Ongoing efforts within DUNE’s radiologicals task force aim to validate or provide more accurate background predictions, against which this performance will be validated. In addition, offline studies demonstrate the performance of trigger primitive generation algorithms as a function of the number of CPU cores used. The results are summarized in figure 7.15 and show that four cores are sufficient to keep up with 960 channels. The test does not include reformatting of the data required to put it in a form that allows AVX2 hardware SIMD acceleration. In tests with live ProtoDUNE data, it is found that ten cores at an average 65% usage were enough to handle both reformatting and trigger primitive generation. Effort on understanding and removing contribution from cosmics/cosmogenics and (known) noisy channels is ongoing. These results are summarized in figure 7.17 Additional details may be found in DocDB 14062 [155].

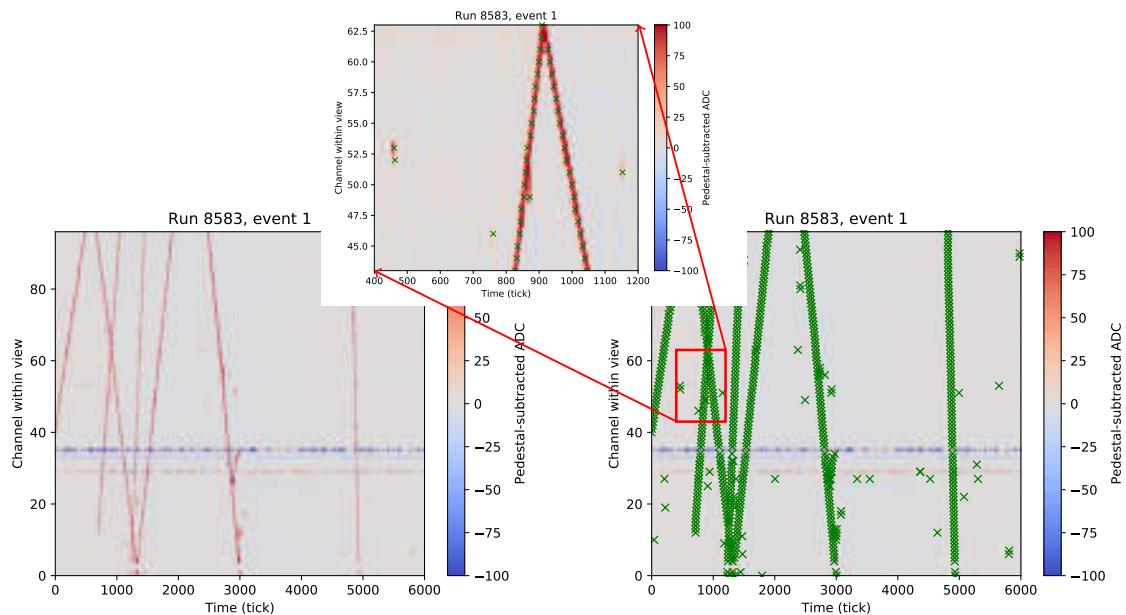


**Figure 7.16.** Example result of the trigger-primitive software (“hit finder”) applied to ADC waveform data spanning 96 collection channels that are sensitive to activity in the drift volume of ProtoDUNE-SP. At left, the figure shows the ADC sample values relative to pedestal which are input to the algorithm. At right, these same data are shown with a green  $\times$  marking each trigger primitive found. The inset is a zoomed region showing in detail the alignment of the input waveforms and the derived trigger primitives. In this test, the algorithm runs on the continuous stream of ADC waveforms prior to readout while actual readout was prompted by an external trigger.

Trigger candidate generation, building on trigger primitives information and considering integral ADC and trigger primitive proximity by channel and time (in  $50\mu\text{s}$ ) space, has also been studied with Monte Carlo simulations [140]. Trigger candidates with sufficient total integral ADC can be accepted to generate corresponding trigger commands for localized high energy activity, such as for beam, atmospheric neutrinos, baryon number violating signatures, and cosmics. Simulation studies demonstrate that this scheme meets efficiency requirements for localized high energy triggers. Specifically, simulations demonstrate that  $> 99\%$  efficiency is achievable for  $> 100\text{ MeV}$  visible energy deposited by single particles (shown in figure 7.18 for  $e^-$ ), and that the corresponding effective threshold for localized triggers for the system is at  $\sim 10\text{ MeV}$ . This translates to all-inclusive efficiencies for beam  $\nu_e$  and  $\nu_\mu$  events in excess of  $99\%$  for visible energies above  $100\text{ MeV}$ , as shown in figure 7.19.

Low-energy trigger candidates furthermore can serve as input to the SNB trigger. Simulations demonstrate that the trigger candidate efficiency for any individual SNB neutrino interaction is on the order of  $20\text{--}30\%$ . However, a multiplicity-based SNB trigger decision that integrates low-energy trigger candidates over an up to  $10\text{ s}$  integration window yields high trigger efficiency out to the galactic edge while keeping fake SNB trigger rates to one per month. An energy-weighted multiplicity count scheme can be applied to further increase efficiency and minimize background [141]. This is illustrated in figure 7.20, demonstrating nearly  $100\%$  efficiency out to

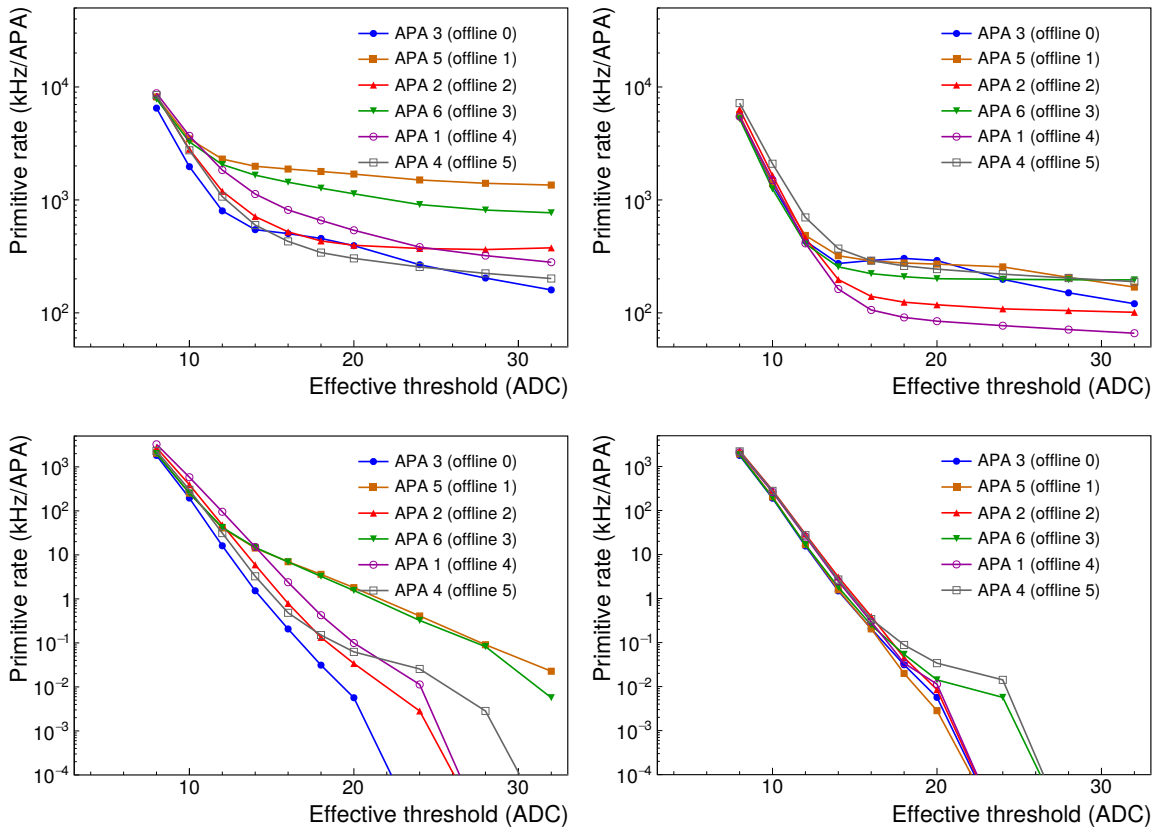


**Figure 7.17.** Trigger primitive rates in ProtoDUNE-SP as a function of threshold in four categories: all data (top left), after removal of particularly noisy channels (top right), with HV off so no contribution to signal (bottom left) and HV off and noisy channels excluded (bottom right).

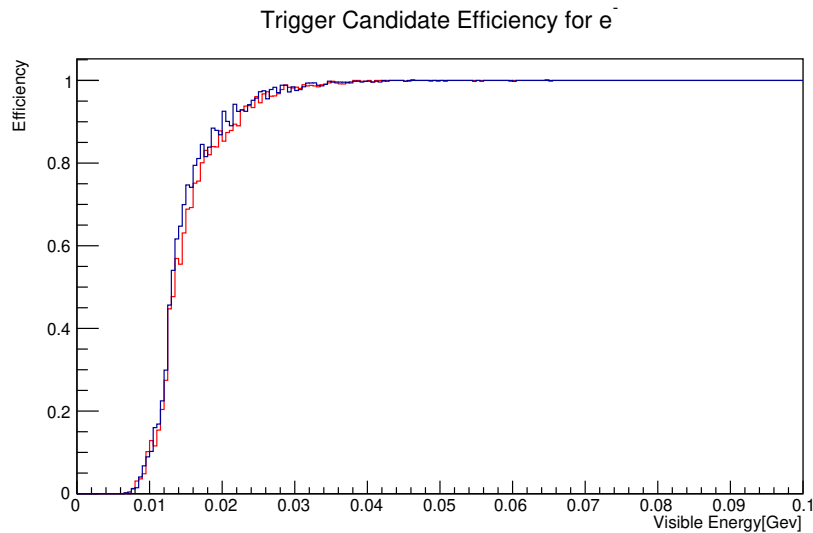


**Figure 7.18.** Efficiency for forming trigger candidates as input trigger primitives from two algorithms, online (blue) and offline (red).

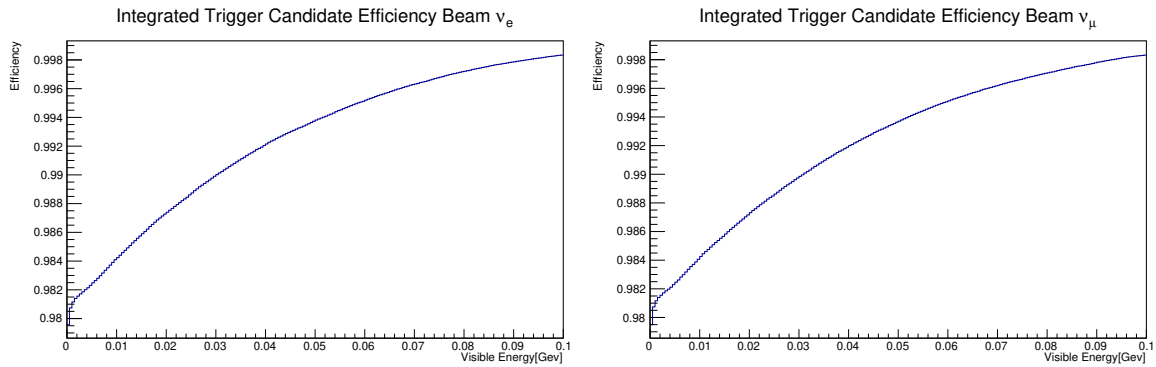


**Figure 7.19.** All-inclusive efficiency for forming trigger candidates from ionization activity from beam  $\nu_e$  (left) and beam  $\nu_\mu$  (right) interactions at or above a given visible energy. At smaller energies, somewhat more events with their visible energy dispersed in space and time fail the trigger candidate selection criteria. High efficiency is obtained at 100 MeV visible. The trigger candidate algorithm used is the offline version, see figure 7.18 for comparison with online version.

the edge of the galaxy, and 70% efficiency for a SNB at the Large Magellanic Cloud (or for any SNB creating 10 events). This performance is obtained by considering the sum ADC distribution of trigger candidates over 10 s and comparing to a background-only vs. background plus SNB hypothesis. The efficiency gain compared to a simpler, trigger candidate counting-based approach is quite significant; using only counting information, the efficiency for a SNB at the Large Magellanic Cloud is 6.5%. The DAQ consortium is working on further refining these algorithms to further improve SNB trigger efficiency for more distant SNBs. For additional efficiency increase, the design provides flexibility for a slightly higher fake SNB trigger rate to be handled by the DAQ BE, combined with more aggressive data reduction applied at the high level trigger stage so as to respect the data rate to offline storage requirement.

The dominant contributor to fake SNB triggers is radiological backgrounds from neutrons, followed by radon. It is crucial to continue working closely with the radiological task force to validate radiological the background assumptions.

In the case of the high level filter, the consortium is exploring the use of machine learning techniques, specifically image classification with the use of convolutional neural networks (CNNs) on GPUs, as a way to classify and down-select individual sections of TPC channel vs. time (“frames”), with extent of one APA’s worth of collection plane channels by one drift length (2.25 ms, or, 4500 samples). CNNs have been trained on Monte Carlo (MC) simulations of frames with each of the following off-beam event topologies: atmospheric neutrino interactions, baryon number violating interactions (proton decay or neutron-antineutron oscillation), cosmic ray interactions, supernova neutrino interactions, or no interactions at all — all with radiological and noise background included in the simulations. Preliminary studies show that a CNN can be successfully trained classify any given input frame as one of three categories: empty, containing a SNB neutrino interaction, or containing a high-energy (atmospheric neutrino, baryon number violating, or cosmic ray) interaction. Specifically, empty frames can be rejected with an efficiency of >99%, while frames containing or partially containing a supernova neutrino, an atmospheric/cosmic interaction, or a baryon number-violating interaction can be preferentially selected with efficiency

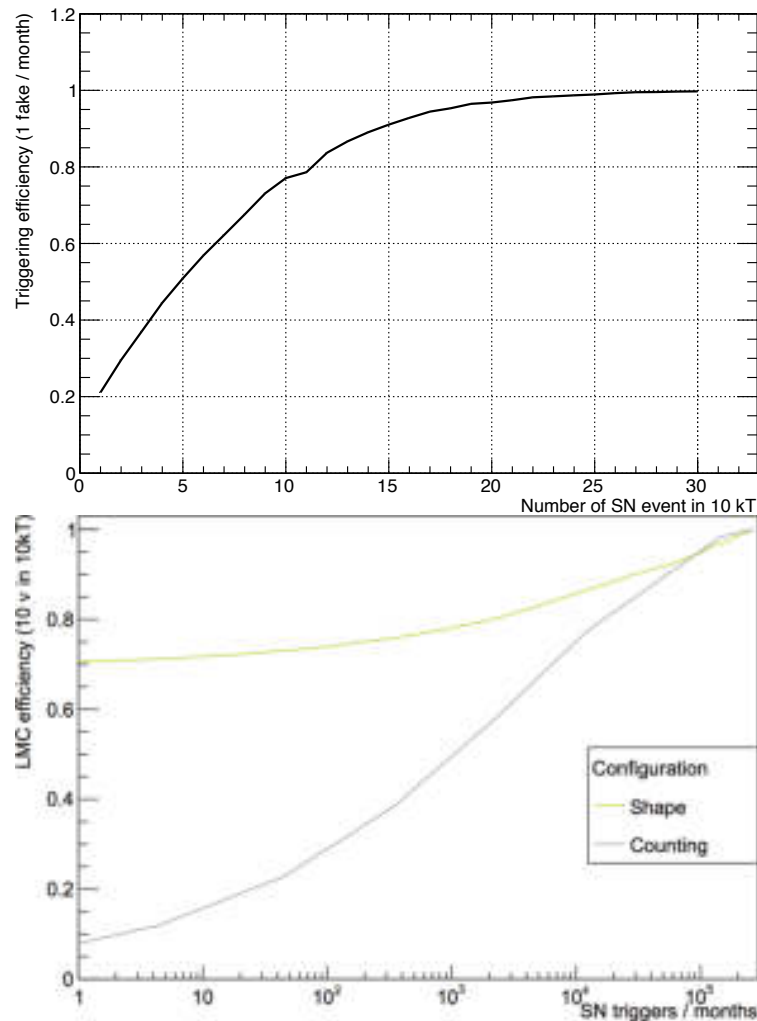


**Figure 7.20.** Top: SNB trigger efficiency as a function of the number of supernova neutrino interactions in the 10 kt module, for a likelihood trigger approach that utilizes sum ADC shape information of trigger candidates input into the trigger decision. Bottom: for a SNB at the Large Magellanic Cloud, where 10 neutrino interactions are expected, the efficiency gain over a counting-only trigger is significantly improved.

>88%, >92%, or >99%, respectively. Such a filter could potentially be applied to reduce the event record size by more than two orders of magnitude. Details may be found in DocDB 11311 [142]. The speed at which machine learning inference may be applied is under study [156].

#### 7.4.2.4 Prototype trigger message passing

A prototype trigger message passing (PTMP) system using elements of the IPC mechanism described in section 7.3.5.5 is currently under development and testing at ProtoDUNE. The primary goals of this prototype is to add a self-triggering mechanism to the ProtoDUNE detector that includes many of the features needed for the far detector DAQ. Throughput and latency of the mechanism is being evaluated and optimized. Message schema and application level protocols have been designed and are being improved. Future work will include prototyping CCM functionality including discovery

and presence.

PTMP has been successfully exercised to transfer trigger primitives from the software based hit finder. The short-term goal will be to successfully aggregate information from across an APA and feed the result to a trigger candidate finder which identifies horizontal muons. From this output a trigger decision can be made.

### 7.4.3 Plan for future development

As mentioned in the introduction of this section, at present, the development model chosen for the DAQ system is the one of iterative prototyping. This model is widely used in projects in which requirements are still being refined and particularly for systems relying on rapidly evolving technologies, such as today's information and computing sector. This model will be used throughout 2019, making use of the ProtoDUNE setup to explore architectural options, software solutions, etc. At a later stage, the DAQ development will move to a more streamlined incremental model, ensuring that careful design precedes the final implementation of individual components. Most of the development will be carried out emulating the data inputs. On the other hand, the DAQ will be validated regularly via test stand integration with detectors, such as ProtoDUNE or pre-installation sites. The overall development schedule with the main DAQ milestones is shown in section 7.6.2.

## 7.5 Production, assembly, installation and integration

The DAQ system relies largely on commercial off-the-shelf components, with the exception of the timing system and the first stage of the upstream DAQ. Therefore, the production and assembly aspects are simpler than for other systems, while of course the installation and integration stages are very important and have to be planned carefully, due to the large number of interfaces of the DAQ system with other parts of the experiment.

### 7.5.1 Production and assembly

#### 7.5.1.1 Timing system

A prototype of the timing system already exists and has been used at ProtoDUNE-SP. The final hardware prototype will be used in the second run of ProtoDUNE-SP in 2021 and production is planned right afterwards, allowing detector communities to have an early integration with the timing hardware and firmware.

#### 7.5.1.2 Upstream DAQ

The upstream DAQ will have FPGA mezzanine cards connecting to the detector electronics readout fibres, and processing and storing data temporarily. Prototype cards implementing parts of the required functionality exist already, but more prototypes are planned before the production readiness review planned in December 2022. While the hardware design will be done at the institutions working in this area, the production of prototypes and final cards will be outsourced to companies, allowing for early identification of those companies that can guarantee a high quality cards production.

### 7.5.1.3 Racks, servers, storage and network

While commercial devices do not need to be produced or assembled, enough time has to be planned, once the proper devices are identified, for the tendering and procurement procedures. Racks and fibers will be procured in order to be available early in 2023; servers and switches will be purchased in two batches, one to be ready for supporting the installation and commissioning of the detector components and DAQ infrastructure and one to reach nominal performance, in time for the start of data taking.

### 7.5.2 Installation and integration

The DAQ will be installed in an enclosure in the west end of the CUC (“Data Room” in figure 7.21. Roughly half of this space will be office space (including control workstations) and the other will be a computer room to hold the DAQ front-end computing and network equipment (figure 7.22). Further details of the interface of DAQ with underground facilities may be found in DocDB 6988 [137], and the installation interface document for DAQ in DocDB 7015 [138].

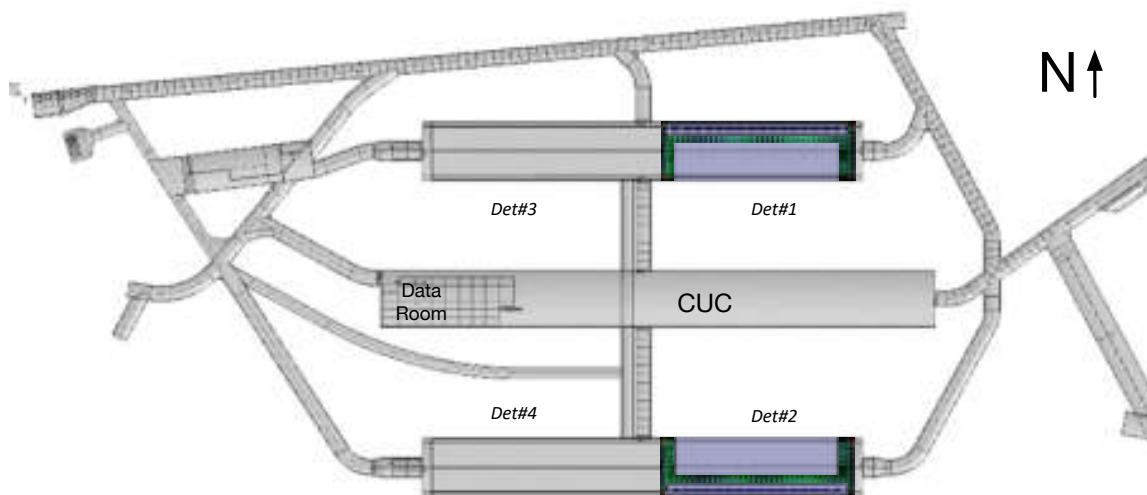


**Figure 7.21.** Top view of the layout at the 4850L at SURF. Shown are the three large excavations and the location of detectors in the north (upper) and south caverns. The CUC in the middle houses the DUNE data room where the DAQ will be installed and the underground utilities.

Infrastructure in the CUC will be installed starting in Q4 2022 (table 7.6). At that point, CF will have handed the DAQ group an empty room with cooling water and power connections. Over the next nine months, racks for the DAQ computing will be installed, plumbed into cooling water, and connected to power and networking. The network connection from this data room to the fiber trunks going up the shaft will also be made, as will preparations to receive the multi-mode fiber connections from the WIB to the FELIX cards housed in servers in these racks. There is space for 60 racks racks, with four set aside for other consortia, 12 per module for upstream DAQ electronics, and the remaining space for networking and other DAQ computing needs. An initial engineering design of the computer room is shown in figure 7.23, which meets all requirements for capacity, cooling, safety and installation schedule.

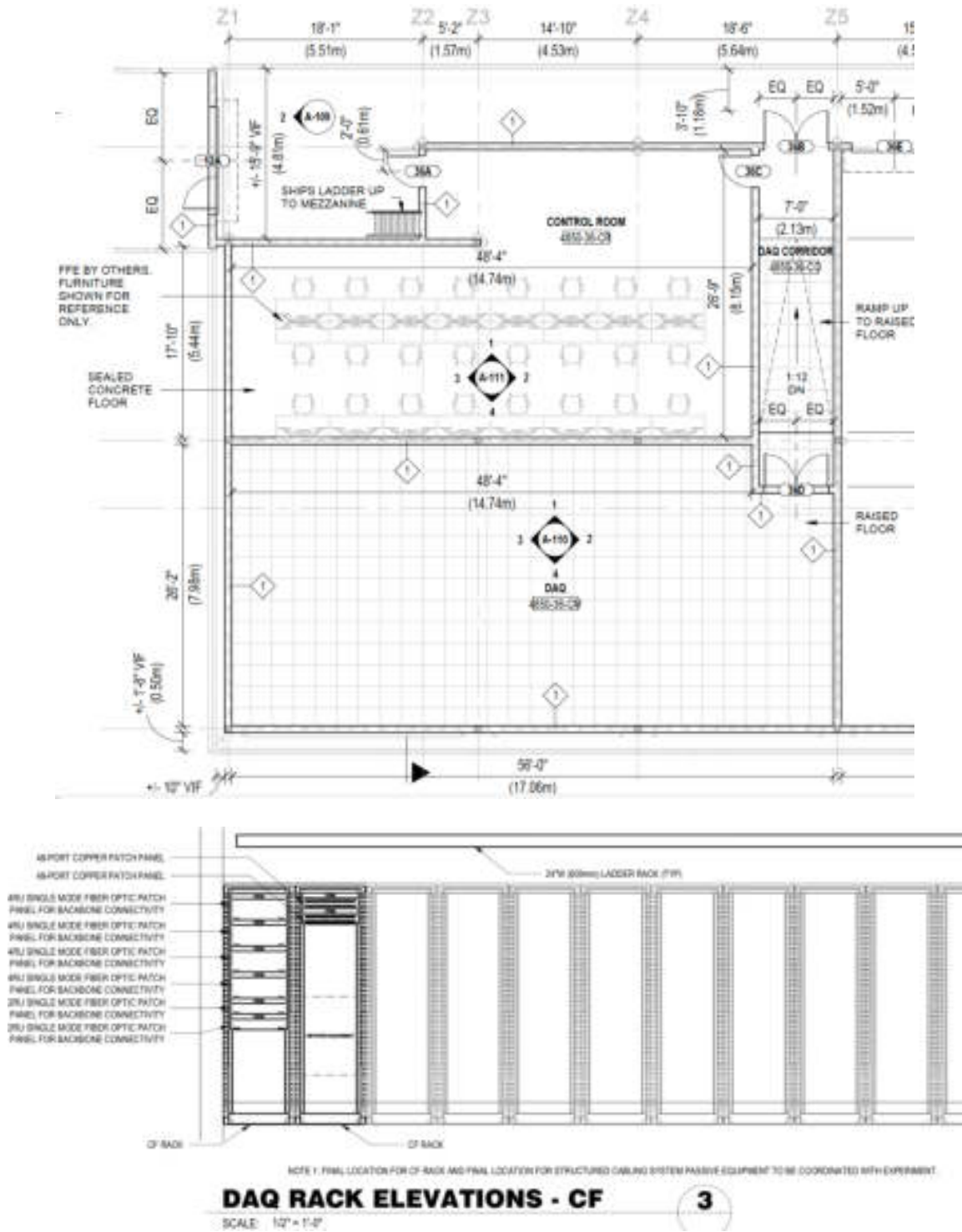


**Figure 7.22.** Top: the overall layout of the DUNE spaces in the CUC. A110 is the DUNE data room, which houses the underground computing, and A111 is a general-purpose work area (not a control room, as labeled) that we call the experimental work area. Bottom: the first row of ten racks in the data room is shown. The first two represent the CF interface racks. The images were taken from the ARUP 90% design drawings U1-FD-A-108 and U1-FD-T-701 [157].



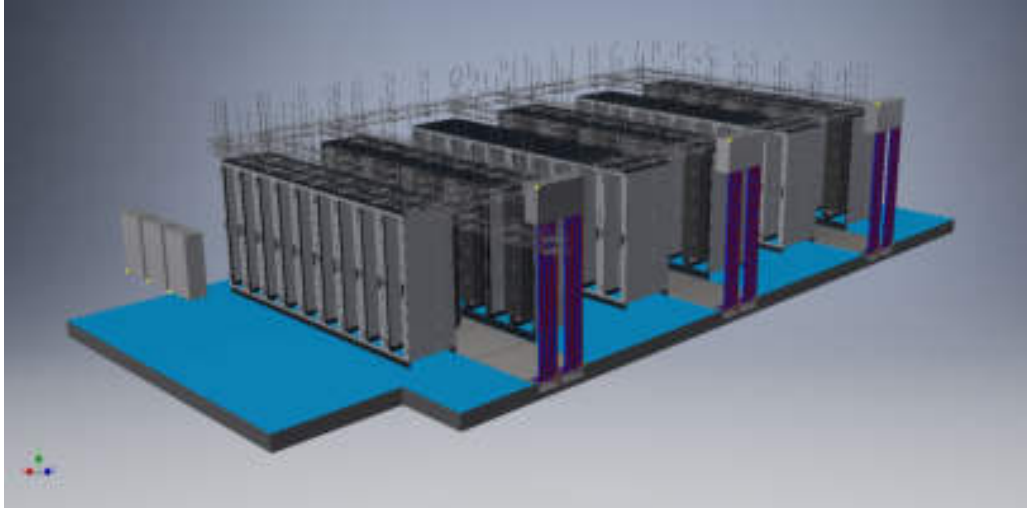


**Figure 7.23.** Initial engineering design for the DAQ counting room in the CUC.

Starting in Q3 2023, the data room will be ready for the installation of the DAQ servers servicing the first module described in section 7.2.1.2. This will proceed over the next year, with servers being installed, cabled up, and tested. As much configuring and commissioning work as possible will be done over the network from the surface (or home institutions), to limit the number of people underground. Note that this data room is sized for all four modules of DAQ computing, so one quarter will be installed at this point. If more computing power is needed for the commissioning of the first module (for example, to deal with unexpected noise levels), space and power will be borrowed from the provision for future modules until the problems are alleviated. Additional space for eight racks will be on the surface in the Ross Dry Room. This will house the back-end computers, high level filter servers, and associated network equipment.

Starting in Q3 2024, the DAQ will thus be ready to connect fibers to the WIBs on the detector top as planes are installed, to allow their commissioning.

The underground installation phase of the DAQ system has the largest safety implications, which are discussed in section 7.6.3.

## 7.6 Organization and project management

### 7.6.1 Consortium organization

The DAQ consortium was formed in 2017 as a joint single and dual phase consortium, with a consortium leader and a technical leader. The current organization of the consortium is shown in figure 7.24. The DAQ institution board currently comprises representatives from 34 institutions as shown in table 7.5. The consortium leader is the spokesperson for the consortium and responsible for the overall scientific program and management of the group. The technical leader of the consortium is responsible for managing the project for the group. The leadership is assisted in its duties by the Project Office, populated by the Resource Manager, the Software and Firmware coordinator and the Integration and Support Coordinator, providing support in the corresponding areas. The consortium is organized into working groups addressing the design, R&D, integration, and, in

the future, construction, commissioning and installation of the key DAQ systems. The Physics Performance and Facility working groups are not associated to a specific system but provide oversight of the general DAQ performance in the physics context and the on the interface with the facility infrastructure. The DAQ working group mandates are detailed in DocDB 14938 [158].

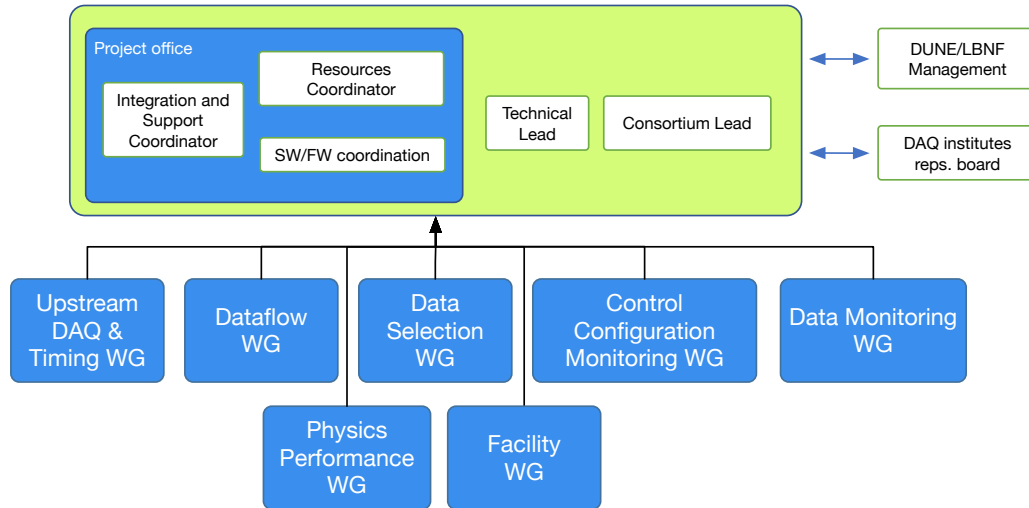


Figure 7.24. Organizational chart for the DAQ Consortium.

### 7.6.2 Schedule and milestones

The high-level DAQ milestones are listed in table 7.6, interleaved with the top-level DUNE project milestones, and illustrated in figure 7.25. Since the DAQ project is largely based on commercial off-the-shelf components, it can be seen in the overall timeline that many of the components are procured relatively late in the project schedule.

### 7.6.3 Safety and risks

Personnel safety during design, construction, testing, installation, and commissioning of the system is crucial for the success of the project. Detector safety during installation, commissioning and operations is also key to project success. The consortium will strictly follow ES&H guidelines for the project as well as follow the safety rules of the institutions where the work is performed, including national laboratories, SURF, and participating universities.

Two overall safety plans will be followed by the FD DAQ. General work underground will comply with all safety procedures in place for working in the detector caverns and in the CUC underground at SURF. DAQ-specific procedures for working with racks full of electronics or computers, as defined at Fermilab, will be followed, especially with respect to electrical safety and the fire suppression system chosen for the counting room. For example, a glass wall between the server room space and the other areas in the CUC will be necessary to prevent workers in the server room from being unseen if they are in distress, and an adequate hearing protection regime must be put in place.

There are no other special safety items for the DAQ system not already covered by the more general safety plans. The long-term emphasis is on remote operations capability from around the

**Table 7.5.** DAQ Consortium Board institutional members and countries.

| <b>Member Institute</b>                             | <b>Country</b> |
|---|----------------|
| CERN  | CERN           |
| Universidad Sergio Arboleda (USA)                   | Colombia       |
| Czech Technical University                          | Czech Republic |
| Lyon  | France         |
| INFN Bologna  | Italy          |
| Iwate   | Japan          |
| KEK   | Japan          |
| NIT Kure  | Japan          |
| NIKHEF  | Netherlands    |
| University of Birmingham                            | UK             |
| Bristol University                                  | UK             |
| University of Edinburgh                             | UK             |
| Imperial College London                             | UK             |
| University College London (UCL)                     | UK             |
| University of Liverpool                             | UK             |
| Oxford University                                   | UK             |
| Rutherford Appleton Lab (RAL)                       | UK             |
| University of Sussex                                | UK             |
| University of Warwick                               | UK             |
| Brookhaven National Lab (BNL)                       | USA            |
| Colorado State University (CSU)                     | USA            |
| Columbia University                                 | USA            |
| University of California, Davis (UCD)               | USA            |
| Duke University                                     | USA            |
| University of California, Irvine (UCI)              | USA            |
| Fermi National Accelerator Laboratory (Fermilab)    | USA            |
| Iowa State University                               | USA            |
| University of Minnesota, Duluth (UMD)               | USA            |
| University of Notre Dame                            | USA            |
| University of Pennsylvania (Penn)                   | USA            |
| South Dakota School of Mines and Technology (SDSMT) | USA            |
| Stanford Linear Accelerator Lab (SLAC)              | USA            |

**Table 7.6.** DAQ Consortium Schedule.

| <b>Milestone</b>  | <b>Date (Month YYYY)</b> |
|---|--------------------------|
| Upstream DAQ Architecture Technology Decision             | June 2020                |
| Engineering Design Review for Timing System               | June 2020                |
| Start of ProtoDUNE-SP-II installation                     | March 2021               |
| Production Readiness Review for Timing System             | June 2021                |
| Preliminary Software Design Review                        | January 2022             |
| Engineering Design Review for Hardware/Firmware           | March 2022               |
| Start of ProtoDUNE-DP-II installation                     | March 2022               |
| South Dakota Logistics Warehouse available                | April 2022               |
| Start of Racks Procurement                                | July 2022                |
| Start of DAQ Server Procurement (I)                       | September 2022           |
| Beneficial occupancy of cavern 1 and CUC                  | October 2022             |
| Production Readiness Review for Readout Hardware/Firmware | December 2022            |
| End of Racks Procurement                                  | March 2023               |
| Start of DAQ Custom Hardware Production                   | March 2023               |
| CUC counting room accessible                              | April 2023               |
| End of DAQ Server Procurement (I)                         | May 2023                 |
| Start of DAQ Installation                                 | May 2023                 |
| DAQ Software Final Design Review                          | June 2023                |
| End of DAQ Custom Hardware Production                     | December 2023            |
| Top of detector module #1 cryostat accessible             | January 2024             |
| Start of detector module #1 TPC installation              | August 2024              |
| Start of DAQ Server Procurement (II)                      | September 2024           |
| Top of detector module #2 accessible                      | January 2025             |
| End of DAQ Server Procurement (II)                        | May 2025                 |
| End of DAQ installation                                   | May 2025                 |
| End of detector module #1 TPC installation                | May 2025                 |
| Start of detector module #2 TPC installation              | August 2025              |
| End of DAQ Standalone Commissioning                       | December 2025            |
| End of detector module #2 TPC installation                | May 2026                 |
| DAQ Server Procurement (III)                              | July 2026                |
| End of DAQ Commissioning                                  | December 2026            |

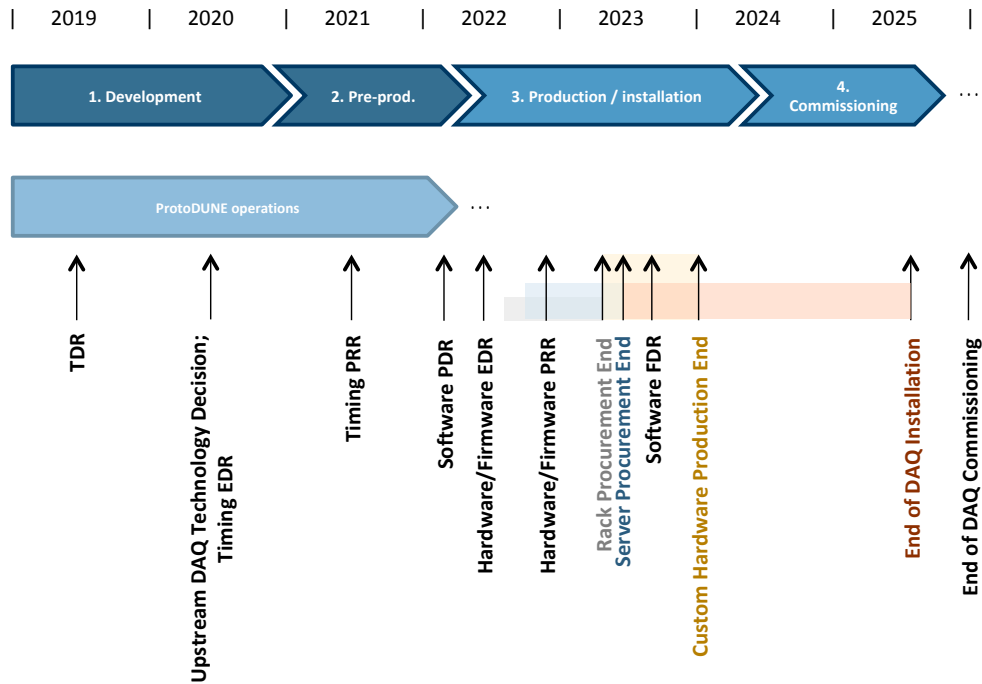


Figure 7.25. DAQ schedule for first 10 kt module.

world, limiting the need for physical presence at SURF, and with underground access required only for urgent interventions or hardware replacement.

A set of risks to the successful construction and operation of the DAQ system has been identified by the consortium, and is provided, together with mitigation strategies and pre-mitigation risk level, in table 7.7. Post-mitigation risk levels are currently being re-evaluated. Risk is quantified with respect to probability, cost impact, and schedule impact. High (H), medium (M), and low (L) probability is identified as > 25%, 10 – 25%, and < 10%, respectively; high (H), medium (M), and low (L) cost impact is identified as > 20%, 5 – 20%, and < 5% cost increase, respectively; and high (H), medium (M), and low (L) schedule impact is identified as > 6 months, 2 – 6 months, and < 2 months delay, respectively.

**Table 7.7:** DAQ risks (P=probability, C=cost, S=schedule) The risk probability, after taking into account the planned mitigation activities, is ranked as L (low < 10 %), M (medium 10 % to 25 %), or H (high > 25 %). The cost and schedule impacts are ranked as L (cost increase < 5 %, schedule delay < 2 months), M (5 % to 25 % and 2–6 months, respectively) and H (> 20 % and > 2 months, respectively).

| ID           | Risk                         | Mitigation   | P | C | S |
|--------------|------------------------------|--|---|---|---|
| RT-SP-DAQ-01 | Detector noise specs not met | ProtoDUNE experience with noise levels and provisions for data processing redundancy in DAQ system; ensure enough headroom of bandwidth to FNAL. | L | L | L |

|              |  |  |   |   |   |
|--------------|--|--|---|---|---|
| RT-SP-DAQ-02 | Externally-driven schedule change                    | Provisions for standalone testing and commissioning of production DAQ components, and schedule adjustment  | L | L | L |
| RT-SP-DAQ-03 | Lack of expert personnel                             | Resource-loaded plan for DAQ backed by institutional commitments, and schedule adjustment using float  | L | L | H |
| RT-SP-DAQ-04 | Power/space requirements exceed CUC capacity         | Sufficient bandwidth to surface and move module 3/4 components to an expanded surface facility   | L | L | L |
| RT-SP-DAQ-05 | Excess fake trigger rate from instrumental effects   | ProtoDUNE performance experience, and provisions for increase in event builder and high level filter capacity, as needed; headroom in data link to FNAL. | L | L | L |
| RT-SP-DAQ-06 | Calibration requirements exceed acceptable data rate | Provisions for increase in event builder and high level filter capacity, as needed; headroom in data link to FNAL.                                       | L | L | L |
| RT-SP-DAQ-07 | Cost/performance of hardware/computing excessive     | Have prototyping and pre-production phases, reduce performance using margin or identify additional funds   | L | L | L |
| RT-SP-DAQ-08 | PDTS fails to scale for DUNE requirements            | Hardware upgrade   | L | L | L |
| RT-SP-DAQ-09 | WAN network  | Extensive QA and development of failure mode recovery and automation, improved network connectivity, and personnel presence at SURF as last resort.      | L | M | M |
| RT-SP-DAQ-10 | Infrastructure                                       | Design with redundancy, prior to construction, and improve power/cooling system.   | M | M | L |
| RT-SP-DAQ-11 | Custom electronics manufacturing issues              | Diversify the manufacturers used for production; run an early pre-production and apply stringent QA criteria.  | L | M | M |

The following risks and mitigation strategies have been identified:

**Detector noise specs not met.** Excessive noise will make it impossible for the DAQ DS to meet physics goals while generating reasonable data volumes. Prior (to construction) mitigation includes studying noise conditions at ProtoDUNE, and leaving provisions in the system for additional front-end filtering (in the form of the upstream DAQ upgradable processing resources) and/or post-event builder processing (in the form of the high level filter). Mitigation (post-construction) includes augmenting filtering resources using a larger computing system for the high level filter.

**Externally-driven schedule change.** The DAQ has schedule links during testing, construction, and installation phases with most other subsystems. Schedule slip elsewhere will potentially cause delay to the DAQ. Prior mitigation includes making provisions for stand-alone testing

and commissioning of DAQ components, in the form of vertical and horizontal slice tests, at ProtoDUNE or elsewhere. Mitigation includes adjusting schedule for stand-alone testing and commissioning phases.

**Lack of expert personnel.** A significant number of experts in hardware, software, firmware are needed, and must be sustained throughout the project. Lack of personnel will increase technical risks and cause delay. Prior mitigation includes developing a full resource-loaded plan for DAQ, backed by national and institutional commitments, and avoiding single points of failure. Mitigation includes adaptation of the DAQ schedule, using schedule float.

**Power/space requirements exceed CUC capacity.** The CUC has fixed space and power allocation for DAQ that cannot be exceeded. Prior mitigation includes allowing sufficient bandwidth up the shafts to move the upstream DAQ components for subsequent DUNE far detector modules (modules 3 and 4) to the surface, or moving some of the DAQ components to the detector caverns, and carrying out a feasibility study for doing so. Mitigation includes expending additional resources on an expanded surface facility.

**Excess fake trigger rate from instrumental effects.** Instrumental effects (beyond excessive noise) can cause fake triggers. Prior mitigation includes studying ProtoDUNE performance in detail, and monitoring detector performance during installation. Mitigation includes substantially increasing data volume, and increasing processing resources in the high level filter.

**Calibration requirements exceed acceptable data rate.** Calibration schemes may require substantial data volumes, far in excess of triggered data volume, beyond currently envisioned; e.g., due to offline analysis inefficiencies. Prior mitigation includes allowing for back-end (EB) system expansion to cope with the increased data rate, and allowing for a high-level filter data selections stage to carry out online analysis and data reduction. Mitigation includes increasing the back-end DAQ and high level filter system capacity.

**Cost/performance of hardware/computing excessive.** Costs of system-as-designed may exceed available budget, due to the IT technology (FPGA, servers, storage) market evolving in an unfavorable way. Prior mitigation includes the planning of prototyping and pre-construction phases to allow realistic appraisal of system costs, and applying sufficient margin in performance estimates. Mitigation includes reducing performance or identifying additional funds.

**ProtoDUNE timing system fails to scale for DUNE requirements.** The ProtoDUNE timing system concept may not scale to DUNE in scale or performance. Prior mitigation includes testing the system at realistic scale before the final design. Mitigation includes replacing the system with upgraded hardware.

**WAN network.** The network connectivity to the experiment from remote locations may be proven unstable, making remote control and monitoring inefficient. Prior mitigation includes ensuring that minimal human intervention is needed on the system for steady data taking and that automated error recovery is well developed. Mitigation includes effort to further improve automated data taking, and increased cost for improving network connectivity. In the worst case, one would foresee presence of personnel at SURF.

**Infrastructure.** The power/cooling systems on which the DAQ relies on cause more frequent than expected downtime. Prior mitigation includes designing, wherever possible, independent and redundant systems. Mitigation includes adding more uninterruptible power supplies, and improving the water cooling system to overcome otherwise degraded experiment uptime.

**Custom electronics manufacturing issues.** Large-scale production of high-speed custom electronics proves challenging, resulting in DAQ installation delays. Prior mitigation includes diversifying manufacturers used for prototype production; assess manufacturer capability to meet specifications. Mitigation includes running early pre-production with selected manufacturers, applying stringent QA criteria to ensure compliance with specifications.



## Chapter 8

# Cryogenics instrumentation and slow controls

### 8.1 Introduction

The cryogenic instrumentation and slow controls (CISC) consortium provides comprehensive monitoring for all detector components and for LAr quality and behavior as well as a control system for many detector components. The SP and dual-phase (DP) modules both use the same control system and have nearly identical cryogenics instrumentation except for differences in location due to the different TPC geometries and the addition of dedicated instrumentation for monitoring temperature and pressure in the gas phase for the DP module. Volume V, The DUNE Far Detector Dual-Phase Technology, chapter 6 of this technical design report (TDR) is virtually the same as this chapter apart from those few differences.

The consortium responsibilities are split into two main branches: cryogenics instrumentation and slow controls, as illustrated in figure 8.1.

Each element of CISC contributes to the DUNE physics program primarily through the maintenance of high detector live time. As described in Volume II, DUNE physics, of this TDR, neutrino CPV and resolution of the neutrino mass hierarchy over the full range of possible neutrino oscillation parameters will require at least a decade of running the FD. Similar requirements apply to searches for nucleon decay and SNB events from within our galaxy. Throughout this long run-time the interior of any DUNE cryostat remains completely inaccessible. No possibility exists for repairs to any components that could be damaged within the TPC structure; hence environmental conditions that present risks must be detected and reported quickly and reliably.

Detector damage risks peak during the initial fill of a module with LAr, as temperature gradients take on their highest values during this phase. Thermal contractions outside of the range of design expectations could result in broken APA wires, silicon photomultipliers (SiPMs) in PDs that detach from the X-ARAPUCA light detectors, or poor connections at the cathode high voltage (HV) feedthrough point that could lead to unstable E fields. These considerations lead to the need for a robust temperature monitoring system for the detector, supplemented with liquid level monitors, and a high-performance camera system to enable visual inspection of the interior of the cryostat during the filling process. These systems are fully described in section 8.2.1 of this chapter.

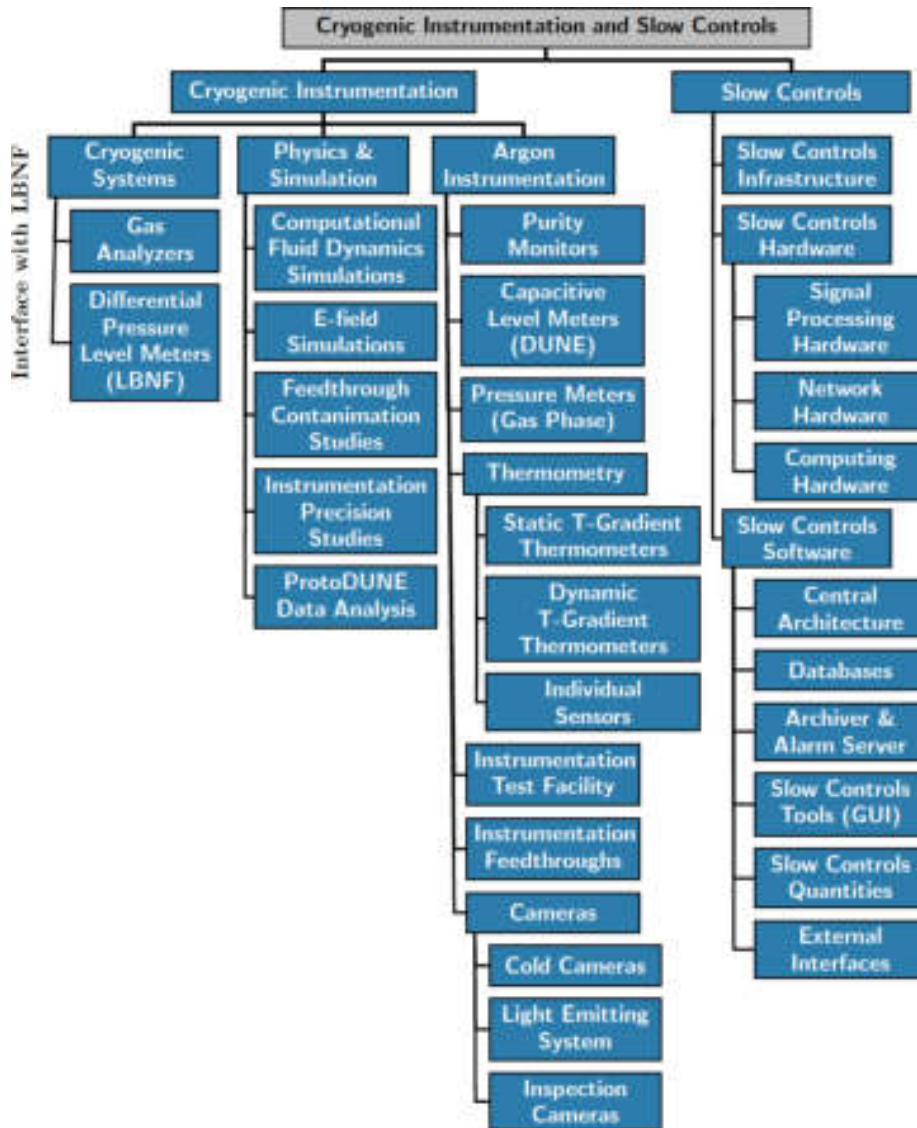


Figure 8.1. CISC subsystem chart.

Argon purity must be established as early as possible in the filling process, a period in which gas analyzers are most useful, and must maintain an acceptable value, corresponding to a minimum electron drift lifetime of 3 ms, throughout the data-taking period. Dedicated purity monitors (section 8.2.2) provide precise lifetime measurements up to values of 10 ms, the range over which electron attenuation most affects signal-to-noise (S/N) in the TPC. The purity monitors and gas analyzers remain important even after high lifetime has been achieved as periodic detector “top-off” fills occur; the new LAr must be of very high quality as it is introduced into the cryostat.

The CISC system must recognize and prevent fault conditions that could develop in the detector module over long periods of running. For example, the liquid level monitors must register any drop in liquid level; a drop in the level could place top sections of the field cage (FC) or bias HV points for the APAs close enough to the gas-liquid boundary to trigger sparking events. Very slow-developing

outgassing phenomena could conceivably occur, with associated bubble generation creating another source of HV breakdown events. The cold camera system enables detection and identification of bubbling sites, and the development of mitigation strategies such as lower HV operation for some period of time. A more subtle possibility is the formation of quasi-stable eddies in argon fluid flow that could prevent positive argon ions from being cleared from the TPC volume, resulting in space charge build up that would not otherwise be expected at the depth of the FD. The space charge could in turn produce distortions in the TPC drift field that degrade tracking and calorimetry performance. The high-performance thermometry of the DUNE CISC system creates input for well developed complex fluid flow models described in section 8.1.3 that should enable detection of conditions associated with these eddies.

Finally, a high detector live-time fraction over multi-year operation cannot be achieved without an extensive system to monitor all aspects of detector performance, report this information in an intelligent fashion to detector operators, and archive the data for deeper offline studies. Section 8.1.1.2 details the DUNE slow controls system designed for this task.

The baseline designs for all the CISC systems have been used in ProtoDUNE-SP, and most design parameters are extrapolated from these designs. The ProtoDUNE-SP data (and in some cases ProtoDUNE-DP data) will therefore be used to validate the instrumentation designs and to understand their performance.

### 8.1.1 Scope

#### 8.1.1.1 Cryogenics instrumentation

Cryogenics instrumentation includes purity monitors, various types of temperature monitors, and cameras with their associated light emitting systems. Also included are gas analyzers and LAr level monitors that are directly related to the external cryogenics system, which have substantial interfaces with the Long-Baseline Neutrino Facility (LBNF). LBNF provides the needed expertise for these systems and is responsible for the design, installation, and commissioning, while the CISC consortium provides the resources and supplements labor as needed.

A cryogenic instrumentation test facility (CITF) for the instrumentation devices is also part of the cryogenics instrumentation. CISC is responsible for design through commissioning in the SP module of LAr instrumentation devices: purity monitors, thermometers, capacitive level meters, cameras, and light-emitting system, and their associated feedthroughs.

Cryogenics instrumentation requires significant engineering, physics, and simulation work, such as E field simulations and cryogenics modeling studies using computational fluid dynamics (CFD). E field simulations identify desirable locations for instrumentation devices in the cryostat, away from regions of high E field, so that their presence does not induce large field distortions. CFD simulations help identify expected temperature, impurity, and velocity flow distributions and guide the placement and distribution of instrumentation devices inside the cryostat.

#### 8.1.1.2 Slow controls

The slow controls portion of CISC consists of three main components: hardware, infrastructure, and software. The slow controls hardware and infrastructure comprises networking hardware, signal processing hardware, computing hardware, and associated rack infrastructure. The slow controls

software provides, for every slow control quantity, the central slow controls processing architecture, databases, alarms, archiving, and control room displays.

CISC provides software and infrastructure for controlling and monitoring all detector elements that provide data on the health of the detector module or conditions important to the experiment, as well as some related hardware.

Slow controls base software and databases are the central tools needed to develop control and monitoring for various detector systems and interfaces. These include:

- base input/output software;
- alarms, archiving, display panels, and similar operator interface tools; and
- slow controls system documentation and operations guidelines.

Slow controls for external systems collect data from systems external to the detector module and provide status monitoring for operators and archiving. They collect data on beam status, cryogenics status, DAQ status, facilities systems status, interlock status bit monitoring (but not the actual interlock mechanism), ground impedance monitoring, and possibly building and detector hall monitoring, as needed.

The DUNE detector safety system (DDSS) can provide inputs to CISC on safety interlock status, and CISC will monitor and make that information available to the experiment operators and experts as needed. However, DDSS and CISC are separate monitors, and the slow controls portion of CISC does not provide any inputs to DDSS. A related question is whether CISC can provide software intervention before a hardware safety interlock. In principle such intervention can be implemented in CISC, presumably by (or as specified by) the hardware experts. For example, at ProtoDUNE-SP, the automatic lowering of HV to clear streamers was implemented in the software for the HV control using CISC-level software.

Slow controls covers software interfaces for detector hardware devices, including:

- monitoring and control of all power supplies,
- full rack monitoring (rack fans, thermometers and rack protection system),
- instrumentation and calibration device monitoring (and control to the extent needed),
- power distribution unit and computer hardware monitoring,
- HV system monitoring through cold cameras, and
- detector components inspection using warm cameras.

CISC will develop, install, and commission any hardware related to rack monitoring and control. Most power supplies may only need a cable from the device to an Ethernet switch, but some power supplies might need special cables (e.g., GPIB or RS232) for communication. The CISC consortium is responsible for providing these control cables.

CISC has additional activities outside the scope of the consortium that require coordination with other groups. This is discussed in section 8.4.4.

### 8.1.2 Design considerations

Important design considerations for instrumentation devices include stability, reliability, and longevity, so that devices can survive for at least 20 years. Such longevity is uncommon for any device, so the overall design allows replacement of devices where possible. Some devices are critical for filling and commissioning but less critical for later operations; for these devices we specify a minimum lifetime of 18 months and 20 years as a desirable goal. DUNE requires the E field on any instrumentation devices inside the cryostat to be less than 30 kV/cm to minimize the risk of dielectric breakdown in LAr.

A consideration important for event reconstruction is the maximum noise level induced by instrumentation devices that the readout electronics can tolerate. ProtoDUNE-SP is evaluating this. Table 8.1 shows the top-level specifications that determine the requirements for CISC together with selected high-level specifications for CISC subsystems. The physics-driven rationale for each requirement and the proposed validation are also included in the table. Tables 8.2 and 8.3 show the full set of specifications for the CISC subsystems. In all these tables two values are quoted for most of the design parameters: (1) specification, which is the intended value or limits for the parameter set by physics and engineering needs, and (2) goal, an improved value offering a benefit which the collaboration aims to achieve where it is cost-effective to do so.

Data from purity monitors and different types of thermometers will be used to validate the LAr fluid flow model. A number of requirements drive the design parameters for the precision and granularity of monitor distribution across the cryostat. For example, the electron lifetime measurement precision must be 1.4 % to keep the bias on the charge readout in the TPC below 0.5 % at 3 ms lifetime. For thermometers, the parameters are driven by the CFD simulations based on ProtoDUNE-SP design. The temperature measurement resolution must be less than 2 mK, and the relative precision of those measurements must be less than 5 mK. The resolution is defined as the temperature root mean square (RMS) for individual measurements and is driven by the electronics. The relative precision also includes the effect of reproducibility for successive immersions in LAr. The relative precision is particularly important in order to characterize gradients below 20 mK. As will be described below, the laboratory calibration data and the recent analysis of thermometer instrumentation data from ProtoDUNE-SP shows that a 2.5 mK relative precision is achievable.

The level meters must have a precision of 0.1% over 14 m (i.e., 14 mm) for measurement accuracy during filling. This precision is also sufficient to ensure that the LAr level stays above the ground planes (GPs) of a single-phase (SP) module. As shown in table 8.3, several requirements drive the design of cold and warm cameras and the associated light emitting system. The components of the camera systems must not contaminate the LAr or produce bubbles so as to avoid increasing the risk of HV discharge. Both cold and warm cameras must provide coverage of at least 80 % of the TPC volume with a resolution of 1 cm for cold cameras and 2 mm for warm cameras on the TPC.

For the CITF, a cryostat with a capacity of only 0.5 to approximately 3 m<sup>3</sup> will suffice and will keep turn-around times and filling costs lower. For gas analyzers, the operating range must allow establishment of useful electron lifetimes; details are in table 8.2.

For slow controls, the system must be sufficiently robust to monitor a minimum of 150,000 variables per detector module, and support a broad range of monitoring and archiving rates; the estimated variable count, data rate, and archive storage needs are discussed in section 8.3.4. The

system must also interface with a large number of detector subsystems and establish two-way communication with them for control and monitoring. For the alarm rate, 150 alarms/day is used as the specification as it is the maximum to which humans can be expected to respond. The goal for the alarm rate is less than 50 alarms/day. The alarm logic system will need to include features for managing “alarm storms” using alarm group acknowledgment, summaries, delays, and other aids.

**Table 8.1:** CISC specifications.

| Label      | Description                               | Specification (Goal)  | Rationale   | Validation                            |
|------------|---|---|---|---------------------------------------|
| SP-FD-5    | Liquid argon purity                       | < 100 ppt<br>(< 30 ppt)   | Provides >5:1 S/N on induction planes for pattern recognition and two-track separation. | Purity monitors and cosmic ray tracks |
| SP-FD-15   | LAr nitrogen contamination                | < 25 ppm  | Maintain 0.5 PE/MeV PDS sensitivity required for triggering proton decay near cathode.  | In situ measurement                   |
| SP-FD-18   | Cryogenic monitoring devices              |   | Constrain uncertainties on detection efficiency, fiducial volume.                       | ProtoDUNE                             |
| SP-FD-25   | Non-FE noise contributions                | $\ll 1000 e^-$  | High S/N for high reconstruction efficiency.  | Engineering calculation and ProtoDUNE |
| SP-FD-29   | Detector uptime                           | > 98%<br>(> 99%)  | Meet physics goals in timely fashion.   | ProtoDUNE                             |
| SP-FD-30   | Individual detector module uptime         | > 90%<br>(> 95%)  | Meet physics goals in timely fashion.   | ProtoDUNE                             |
| SP-CISC-1  | Noise from Instrumentation devices        | $\ll 1000 e^-$  | Max noise for 5:1 S/N for a MIP passing near cathode; per SBND and DUNE CE              | ProtoDUNE                             |
| SP-CISC-2  | Max. E field near instrumentation devices | < 30 kV/cm<br>(< 15 kV/cm)  | Significantly lower than max field of 30 kV/cm per DUNE HV                              | 3D electrostatic simulation           |
| SP-CISC-3  | Precision in electron lifetime            | < 1.4%<br>(< 1%)  | Required for accurate charge reconstruction per DUNE-FD Task Force report.              | ProtoDUNE-SP and CITF                 |
| SP-CISC-4  | Range in electron lifetime                | 0.04 ms to 10 ms in cryostat, 0.04 ms to 30 ms inline                                       | Slightly beyond best values observed so far in other detectors.                         | ProtoDUNE-SP and CITF                 |
| SP-CISC-11 | Precision: temperature reproducibility    | < 5 mK<br>(2 mK)  | Enables validation of CFD models, which predicts gradients below 15 mK                  | ProtoDUNE-SP and CITF                 |
| SP-CISC-14 | Temperature stability                     | < 2 mK at all places and times<br>(Match precision requirement at all places, at all times) | Measure the temp map with sufficient precision during the entire duration               | ProtoDUNE-SP                          |

|            |                         |  |  |   |
|------------|-------------------------|--|--|---|
| SP-CISC-27 | Cold camera coverage    | > 80% of HV surfaces (100%)                  | Enable detailed inspection of issues near HV surfaces.                               | Calculated from location, validated in prototypes.  |
| SP-CISC-51 | Slow control alarm rate | < 150/day (< 50/day)                         | Alarm rate low enough to allow response to every alarm.                              | Detector module; depends on experimental conditions |
| SP-CISC-52 | Total No. of variables  | > 150,000 (150,000 to 200,000)               | Scaled from ProtoDUNE-SP   | ProtoDUNE-SP and CITF                               |
| SP-CISC-54 | Archiving rate          | 0.02 Hz (Broad range 1 Hz to 1 per few min.) | Archiving rate different for each variable, optimized to store important information | ProtoDUNE-SP  |

### 8.1.3 Fluid dynamics simulation

Proper placement of purity monitors, thermometers, and liquid level monitors within the detector module requires knowing how LAr flows within the cryostat, given its fluid dynamics, heat and mass transfer, and distribution of impurity concentrations. Fluid flow is also important in understanding how the positive and negative ion excess created by various sources (e.g., ionization from cosmic rays and  $^{36}\text{Ar}$ ) is distributed across the detector as it affects E field uniformity. Finally, CFD simulations are crucial to predict the purity of the argon in regions where experimental data is unavailable. The overall goal of the CFD simulations is to better understand and predict the fluid (in either liquid or vapor state) motions and the implications for detector performance.

Fluid motion within the cryostat is driven primarily by small changes in density caused by thermal gradients within the fluid although pump flow rates and inlet and outlet locations also contribute. Heat sources include exterior heat from the surroundings, interior heat from electronics, and heat flow through the pump inlet. In principle, purity monitors can be placed throughout the cryostat to determine if the argon is pure enough for experimentation. However, some areas inside the cryostat are off limits for such monitors.

The fluid flow behavior can be determined by simulating LAr flow within a detector module using Siemens Star-CCM+,<sup>1</sup> a commercially available CFD code. Such a model must properly define the fluid characteristics, solid bodies, and fluid-solid interfaces, as well as provide a way to measure contamination, while still maintaining reasonable computation times. In addition, these fluid dynamics simulations can be compared to available experimental data to assess simulation accuracy and credibility.

Although simulation of the detector module presents challenges, acceptable simplifications can accurately represent the fluid, the interfacing solid bodies, and variations of contaminant concentrations. Because of the magnitude of thermal variation within the cryostat, modeling of the LAr is simplified by using constant thermophysical properties, calculating buoyant force with the Boussinesq Model (using a constant density for the fluid with application of a temperature-dependent buoyant force), and a standard shear stress transport turbulence model. Solid bodies that touch the LAr include the cryostat wall, cathode planes, anode planes, GP, and FC. As in

<sup>1</sup><https://mdx.plm.automation.siemens.com/star-ccm-plus>.

**Table 8.2.** List of specifications for the different CISC subsystems (1).

| Quantity/Parameter   | Specification  | Goal  |
|--|--|---|
| Noise from Instrumentation devices   | $\ll 1000 e^-$   |   |
| Max. E field near instrumentation devices  | <30 kV/cm  | <15 kV/cm                                       |
| <b>Purity Monitors</b>   |  |   |
| Precision in electron lifetime   | <1.4% at 3 ms, <4% at 9 ms, relative differences <2.5%   | < 1%  |
| Range in electron lifetime   | 0.04 - 10 ms   | (0.04 – 30 ms inline)                           |
| Longevity  | 20 years   | > 20 years                                      |
| Stability  | Match precision requirement at all places/times          |   |
| Reliability  | Daily Measurements                                       | Measurements as needed                          |
| <b>Thermometers</b>  |  |   |
| Vertical density of sensors for T-gradient monitors                              | > 2 sensor/m   | > 4 sensors/m                                   |
| 2D horizontal density for top/bottom individual sensors                          | 1 sensor/5(10) m   | 1 sensor/3(5) m                                 |
| Swinging/deflection of T-Gradient monitors                                       | < 5 cm   | < 2 cm  |
| Resolution of temperature measurements   | < 2 mK   | <0.5 mK   |
| Precision: temperature reproducibility   | < 5 mK   | 2 mK  |
| Reliability  | 80% (in 18 months)                                       | 50% (during 20 years)                           |
| Longevity  | > 18 months  | > 20 years                                      |
| Stability  | < 2 mK at all places and times                           | Match precision requirement at all places/times |
| Discrepancy between lab and in situ calibrations for temperature sensors         | < 5 mK   | < 3 mK  |
| Discrepancy between measured temperature map and CFD simulations in ProtoDUNE-SP | < 5 mK   |   |
| <b>Gas Analyzers</b>   |  |   |
| Operating Range O2   | 0.2 (air) to 0.1 ppt                                     |   |
| Operating Range H2O  | Nom. air to sub-ppb; contaminant-dependent               |   |
| Operating Range N2   | Nominally Air Nom. air to sub-ppb; contaminant-dependent |   |
| Precision: 1 sigma at zero   | per gas analyzer range                                   |   |
| Detection limit: 3 sigma   | Different analyzer modules needed to cover entire range  |   |
| Stability  | < <sup>σ</sup> % of full scale range.                    |   |
| Longevity  | >10 years  |   |
| <b>Pressure Meters (GAr)</b>   |  |   |
| Relative precision (DUNE side)   | 0.1 mbar   |   |
| Absolute precision (DUNE side)   | <5 mbar  |   |



**Table 8.3.** List of specifications for the different CISC subsystems (2).

| Quantity/Parameter                                    | Specification  | Goal                               |
|---|--|------------------------------------|
| <b>Level Meters</b>                                   |  |                                    |
| Precision (LBNF scope)                                | 0.1% over 14 m (14 mm)   |                                    |
| Precision (capacitive level meters, DUNE scope)       | 1 cm   | <5 mm                              |
| Longevity (all)                                       | 20 years   | > 20 years                         |
| <b>Cold cameras</b>                                   |  |                                    |
| Coverage  | 80% of the exterior of HV surfaces   | 100%                               |
| Frames per second                                     | yet to be defined  |                                    |
| Resolution  | 1 cm on the TPC  | yet to be defined                  |
| Duty cycle  | yet to be defined  |                                    |
| longevity   | > 18 months  | > 20 years                         |
| <b>Inspection cameras</b>                             |  |                                    |
| Coverage  | 80% of the TPC   | yet to be defined                  |
| Frames per second                                     | yet to be defined  |                                    |
| Resolution  | 2 mm on the TPC  | yet to be defined                  |
| heat transfer   | no generation of bubbles   |                                    |
| longevity   | > 18 months  | > 20 years                         |
| <b>Light emitting system</b>                          |  |                                    |
| radiant flux  | > 10 mW/sr   | 100 mW/sr                          |
| power   | < 125 mW/LED   |                                    |
| wavelength  | red/green  | IR/white                           |
| longevity   | > 18 months (for cold cameras)   | > 20 years                         |
| <b>cryogenic instrumentation test facility (CITF)</b> |  |                                    |
| Dimensions  | 0.5 to 3 cubic meters  |                                    |
| Temperature stability                                 | ±1K  |                                    |
| Turn-Around time                                      | ~9 days  | 9 days                             |
| LAr purity  | O <sub>2</sub> , H <sub>2</sub> O: low enough to measure drifting electrons of devices under test, ~0.5 ms.<br>N <sub>2</sub> : ppm for scintillation light tests. | >1.0 ms                            |
| <b>Slow Controls</b>                                  |  |                                    |
| Alarm rate  | <150/day   | < 50/day                           |
| Total No. of variables per detector module            | 150,000  | 150,000 – 200,000                  |
| Server rack space                                     | 2 racks  | 3 racks                            |
| Archiving rate  | 0.02 Hz  | Broad range 1 Hz to 1 per few min. |
| Near Detector Status                                  | Beam conditions and detector status  | Full beam and detector status      |

previous CFD models of the DUNE 35 ton prototype and ProtoDUNE-SP [159], the FC planes, anode planes, and GP can be represented by porous bodies. Because impurity concentration and electron lifetime do not affect fluid flow, these variables can be simulated as passive scalars, as is commonly done for smoke released [160] in air or dyes released in liquids.

Discrepancies between real data and simulations may affect detector performance. Simulation results contribute to decisions about where to place sensors and monitors, and to the definitions of various calibration quantities. Methods of mitigating such risks include well established convergence criteria, sensitivity studies, and comparison to results of previous CFD simulation work. Moreover, the simulation will be improved with input from LAr temperature and purity measurements and validation tests from ProtoDUNE-SP.<sup>2</sup>

Taking into account that the CFD model can predict both temperature and impurity levels, the procedure for validating and tuning the CFD model will be the following: (1) use temperature measurements in numerous locations in the cryostat to constrain temperature predictions and improve the CFD model, (2) use the improved model to predict the LAr impurity level at the purity monitor locations, and (3) compare the predictions to the actual purity monitor measurements to further constrain the CFD model.

Figure 8.2 shows an example of the temperature distribution on a plane intersecting a LAr inlet and at a plane halfway between an inlet and an outlet; the geometry used for this simulation is shown in figure 8.3.<sup>3</sup> Note the plume of higher temperature LAr between the walls and the outer APA on the inlet plane. The current placement of instrumentation in the cryostat as shown in figure 8.5 was determined using temperature and impurity distributions from previous simulations.

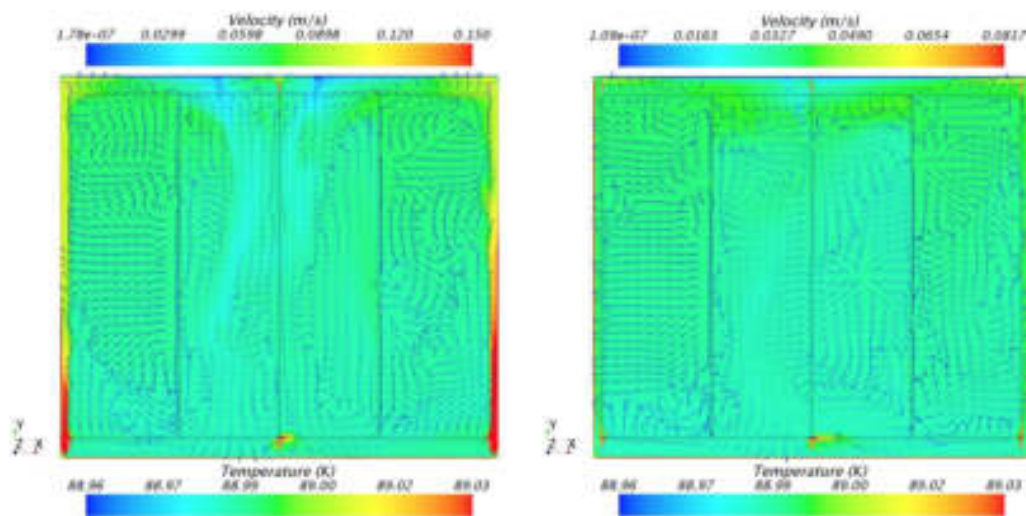


**Figure 8.2.** Distribution of temperature on a plane intersecting an inlet (left) and halfway between an inlet and an outlet (right), as predicted by previous CFD simulations (from [159]). (See figure 8.3 for geometry.)

<sup>2</sup>Because ProtoDUNE-DP was not instrumented with high-precision thermometers in the liquid phase and because the cryogenics design is the same for SP and DP modules of the DUNE FD, ProtoDUNE-SP data will be used to validate the liquid CFD model.

<sup>3</sup>The inlet and outlet map has recently changed; it now consists of two rows of 64 inlets each at each longer side of the cryostat and four outlets along the shorter sides (drift direction) of the cryostat.

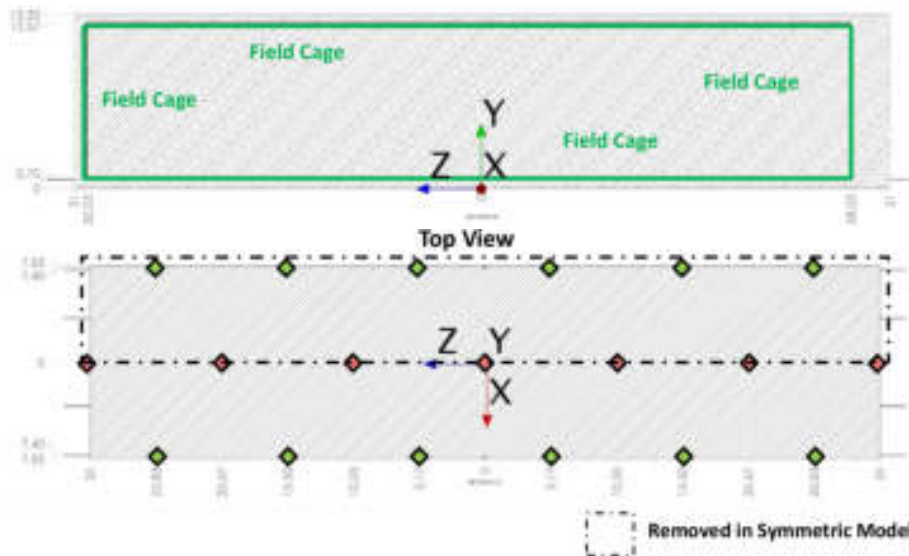


**Figure 8.3.** Layout of the SP module within the cryostat (top) and positions of LAr inlets and outlets (bottom) as modeled in the CFD simulations [159]. The  $y$  axis is vertical and the  $x$  axis is parallel to the TPC drift direction. Inlets are shown in green and outlets are shown in red.

The strategy for future CFD simulations begins with understanding the performance of the ProtoDUNE-SP cryogenics system and modeling the detector modules to derive specifications for instrumentation. We are pursuing a prioritized set of studies to help determine the requirements for other systems. We plan to

- Review the DUNE FD cryogenics system design and verify the current implementation in simulation to ensure that the simulation represents the actual design.
- Model the ProtoDUNE-SP liquid and gas regions with the same precision as the FD. Presently, we have only the liquid model, which is needed to interpret the thermometer data. The gas model is needed to see how to place thermometers in the ullage and verify the design of the gaseous argon purge system.
- Verify the CFD model for the SP module in a simulation performed by LBNF; this defines the requirements for instrumentation devices (e.g., thermometry).

### 8.1.3.1 Validation in ProtoDUNE

ProtoDUNE-SP has collected data to validate the CFD using:

- static and dynamic T-gradient thermometers,
- individual temperature sensors placed in the return LAr inlets,
- two 2D grids of individual temperature sensors installed below the bottom ground planes and above the top ground planes,
- a string of three purity monitors vertically spaced from near the bottom of the cryostat to just below the LAr surface,

- two pressure sensors (relative and absolute) in the argon gas,
- H<sub>2</sub>O, N<sub>2</sub>, and O<sub>2</sub> gas analyzers,
- LAr level monitors, and
- standard cryogenic sensors including pressure transducers, individual temperature sensors placed around the cryostat on the membrane walls, and recirculation flow rates transducers.

The data, which have been logged through the ProtoDUNE-SP slow control system [161], are available for offline analysis.

In parallel, CISC has produced a ProtoDUNE-SP CFD model with input from ProtoDUNE-SP measurements (see table 8.4). Streamlines<sup>4</sup> from the current simulation (figure 8.4) show the flow paths from the four cryostat inlets to the outlet. The validation of this model consists of an iterative process in which several versions of the CFD simulation, using different input parameters, eventually converge to a reasonable agreement with data from instrumentation devices. Those comparisons will be shown in section 8.2.1.4.

**Table 8.4.** CFD input parameters for ProtoDUNE-SP.

| Parameter               | Value            | Comments  |
|-------------------------|------------------|---|
| Cryostat height         | 7.878 m          | Measured with laser (1 cm error approx.)          |
| LAr surface height      | 7.406 m          | Measured by capacitive level meter (< 1 cm error) |
| Ullage pressure         | 1.045 bar        | Measured by pressure gauges                       |
| LAr surface temperature | 87.596 K         | Computed using ullage pressure and [162]          |
| LAr inlet temperature   | bulk LAr + 0.2 K | Estimated from pressure settings in cryo-system   |
| LAr flow rate per pipe  | 0.417 kg/s       | Estimated from cryostat filling rate              |

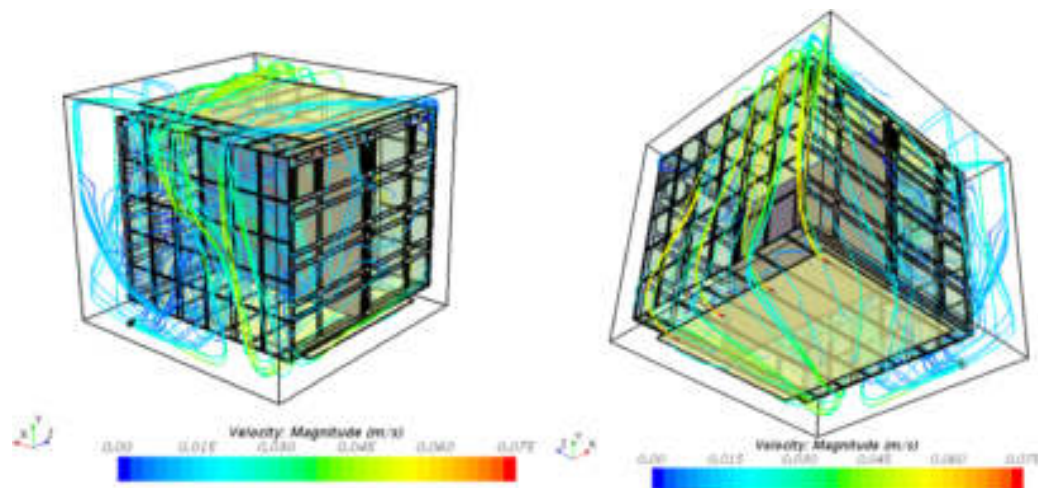


**Figure 8.4.** Streamlines for LAr flow inside ProtoDUNE-SP.

<sup>4</sup>In fluid mechanics, a streamline is a line that is everywhere tangent to the local velocity vector. For steady flows, a streamline also represents the path that a single particle of the fluid will take from inlet to exit.

Once the ProtoDUNE-SP CFD model predicts the fluid temperature in the entire cryostat to a reasonable level under different conditions, we will use it to produce maps of impurity levels in the detector module. These can be easily converted into electron lifetime maps, which we will compare to the ProtoDUNE-SP purity monitor data.

### 8.2 Cryogenics instrumentation

Instrumentation inside the cryostat must accurately report the condition of the LAr so that we can ensure that it is adequate to operate the TPC. This instrumentation includes purity monitors to check the level of impurity in the argon and to provide high-precision electron lifetime measurements, as well as gas analyzers to verify that the levels of atmospheric contamination do not rise above certain limits during the cryostat purging, cooling, and filling. Temperature sensors deployed in vertical arrays and at the top and bottom of the detector module monitor the cryogenics system operation, providing a detailed 3D temperature map that helps predict the LAr purity across the entire cryostat. The cryogenics instrumentation also includes LAr level monitors and a system of internal cameras to help find sparks in the cryostat and to monitor the overall cryostat interior.

The proper placement of purity monitors, thermometers, and liquid-level monitors in the detector module requires understanding the LAr fluid dynamics, heat and mass transfer, and the distribution of impurity concentrations within the cryostat. Both this and coherent analysis of the instrumentation data require CFD simulation results.

ProtoDUNE-SP is testing the performance of purity monitors, thermometers, level monitors and cameras for the SP module, validating the baseline design.

#### 8.2.1 Thermometers

As discussed in section 8.1.3, a detailed 3D temperature map is important for monitoring the cryogenics system for correct functioning and the LAr for uniformity. Given the complexity and size of purity monitors, they can only be installed on the sides of the cryostat to provide a local measurement of LAr purity. A direct measurement of the LAr purity across the entire cryostat is not feasible, but a sufficiently detailed 3D temperature map based on CFD simulations can predict it. The vertical coordinate is especially important because it will relate closely to the LAr recirculation and uniformity.

The baseline sensor distribution and the cryostat ports used to extract cables (with indication of number of cables per port) are shown in figure 8.5. The baseline distribution will evolve as more information becomes available (precise CFD simulations, better understanding of detector support system (DSS) ports, installation interfaces with other groups), but the baseline suffices to establish the overall strategy.

High-precision temperature sensors will be distributed near the TPC walls in two ways: (1) forming high density ( $> 2$  sensors/m) vertical arrays (called T-gradient monitors) and (2) in coarser ( $\sim 1$  sensor/5 m) 2D arrays (called individual sensors) at the top and bottom of the detector module, where it is most crucial to know the temperature.

Expected temperature variations inside the cryostat are very small (0.02 K; see figure 8.2), so sensors must be cross-calibrated to better than 0.005 K. Most sensors will be calibrated in the laboratory before installation (installation is described in section 8.4.5.2). Calibration before

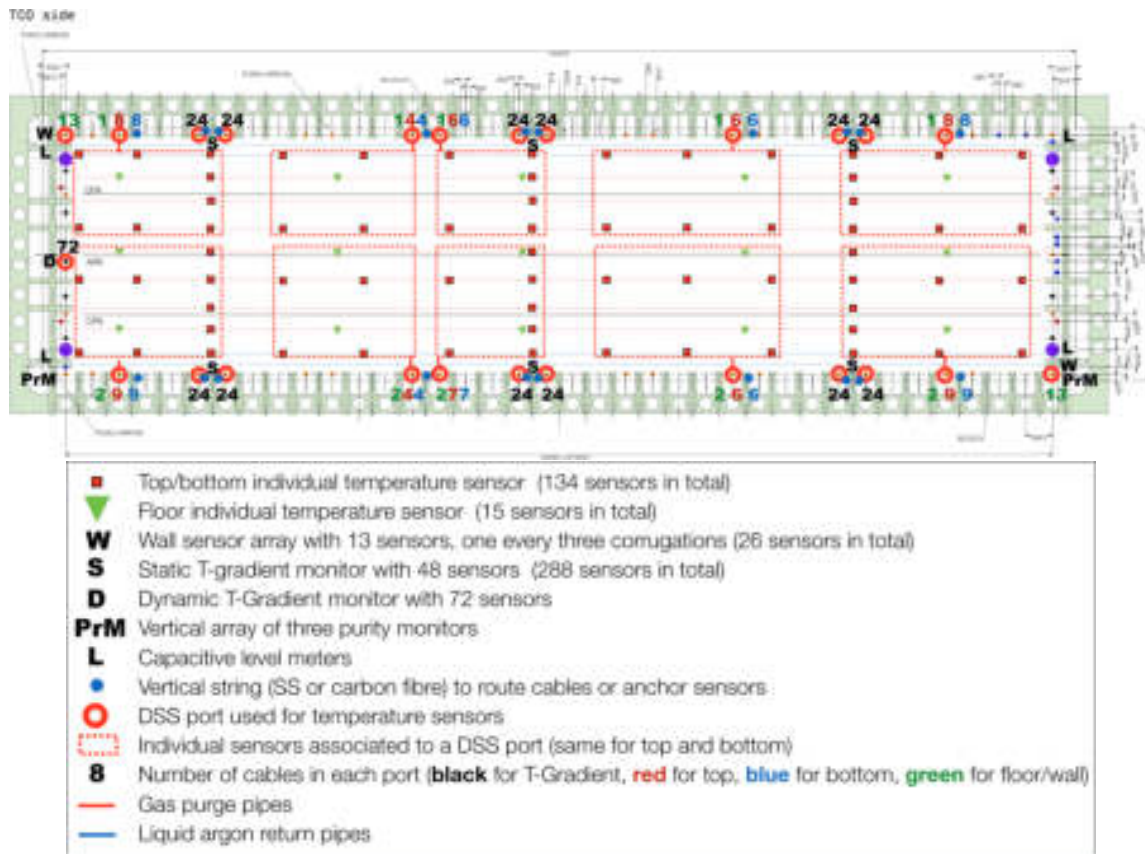


Figure 8.5. Distribution of temperature sensors inside the cryostat.

installation is the only option for sensors installed on the long sides of the detector and the top and bottom of the cryostat, where space is limited. Given the precision required and the unknown longevity of the sensors — possibly requiring another calibration after some time — an additional method will be used for T-gradient monitors installed on the short ends of the detector in the space between the field cage end walls and the cryostat walls. There is sufficient space in this area for a movable system, which can be used to cross calibrate the temperature sensors in situ, as described in 8.2.1.1.

The baseline design for all thermometer systems have three elements in common: sensors, cables, and readout system. We plan to use Lake Shore PT100-series<sup>5</sup> platinum sensors with 100  $\Omega$  resistance because in the temperature range 83 K to 92 K they show high reproducibility of  $\sim 5$  mK and absolute temperature accuracy of 100 mK. Using a four-wire readout greatly reduces issues related to lead resistance, any parasitic resistances, connections through the flange, and general electromagnetic noise pick-up. Lakeshore PT102 sensors (see figure 8.13, right) were used in the 35 ton prototype and ProtoDUNE-SP, giving excellent results. For the inner readout cables, a custom cable made by Axon<sup>6</sup> is the baseline. It consists of four teflon-jacketed copper wires (American wire gauge (AWG) 28), forming two twisted pairs, with a metallic external shield and an outer teflon jacket. The readout system is described in section 8.2.1.5.

<sup>5</sup>Lake Shore Cryotronics™ platinum RTD series, <https://www.lakeshore.com/>.

<sup>6</sup>Axon™ Cable, <http://www.axon-cable.com>.

Another set of lower-precision sensors epoxied into the bottom membrane of the cryostat will monitor the cryostat filling in the initial stage. Finally, the inner walls and roof of the cryostat will have the same types of sensors to monitor the temperature during cool-down and filling (“W” sensors in figure 8.5).

### 8.2.1.1 Dynamic T-gradient monitors

To address concerns about potential differences in sensor readings prior to and after installation in a detector module, and potential drifts over the lifetime of the module that may affect accuracy of the vertical temperature gradient measurement, a dynamic temperature monitor allows cross-calibration of sensor readings in situ. Namely, this T-gradient monitor is motorized, allowing vertical motion of the temperature sensor array in the detector module, enabling precise cross-calibration between the sensors, as illustrated in figure 8.6.

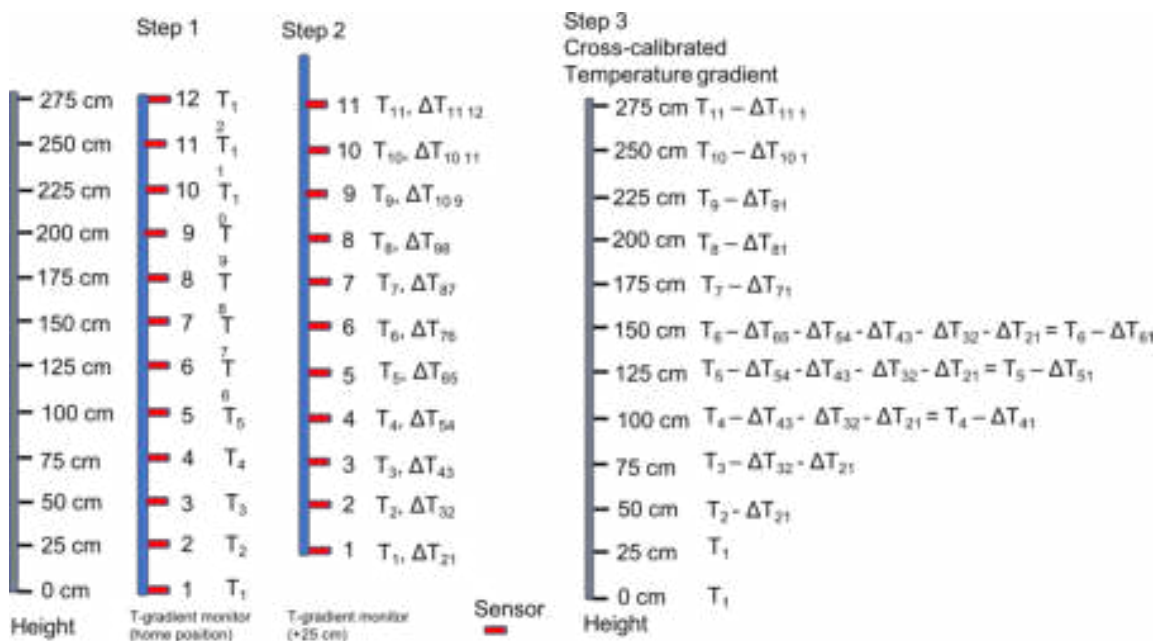


**Figure 8.6.** In step 1, sensor temperature measurements are taken with the T-gradient monitor in the home position. In step 2, the entire system is moved up 25 cm and another set of temperature readings is taken by all sensors. Then, the offsets between pairs of sensors are calculated for each position. In step 3, offsets are linked together, providing cross-calibration of all sensors, to obtain the entire vertical temperature gradient measurement with respect to a single sensor (number 1 in this case).

The procedure for cross-calibrations is the following: in step 1, the temperature reading of all sensors is taken at the home (lowest) position of the carrier rod. In step 2, the stepper motor moves the carrier rod up 25 cm. Since the sensors along the entire carrier rod are positioned 25 cm apart, when the system is moved up 25 cm, each sensor is positioned at the height that was occupied by another sensor in step 1. Then a second temperature reading is taken. In this manner, except for the lowest position, two temperature measurements are taken at each location with different sensors. Assuming that the temperature at each location is stable over the few minutes required to make the measurements, any difference in the temperature readings between the two different sensors is

due to their relative measurement offset. This difference is then calculated for all locations. In step 3, readout differences between pairs of sensors at each location are linked to one another, expressing temperature measurements at all heights with respect to a single sensor. In this way, temperature readings from all sensors are cross-calibrated in situ, canceling all possible offsets due to electromagnetic noise or any parasitic resistances that may have prevailed despite the four-point connection to the sensors that should cancel most of the offsets. These measurements are taken with a very stable current source, which ensures high precision of repeated temperature measurements over time. The motion of the dynamic T-monitor is stepper-motor operated, delivering measurements with high spatial resolution.

A total of 72 sensors will be installed with 25 cm spacing, decreased to 10 cm spacing for the top and bottom 1 m of the carrier rod. The vertical displacement of the system is such that every sensor can be moved to the nominal position of at least five other sensors, minimizing the risks associated with sensor failure and allowing for several points of comparison. The total expected motion range of the carrier rod is 1.35 m.

This procedure was tested in ProtoDUNE-SP, where the system was successfully moved up by a maximum of 51 cm, allowing cross-calibration of all sensors (22 sensors with 10.2 cm spacing at top and bottom and 51 cm in the middle).

Figure 8.7 shows the temperature profile after calibration when the recirculation pumps are off. Under these conditions the temperature should be very homogeneous except near the surface. This is indeed what is observed in that figure, demonstrating the reliability of the method.

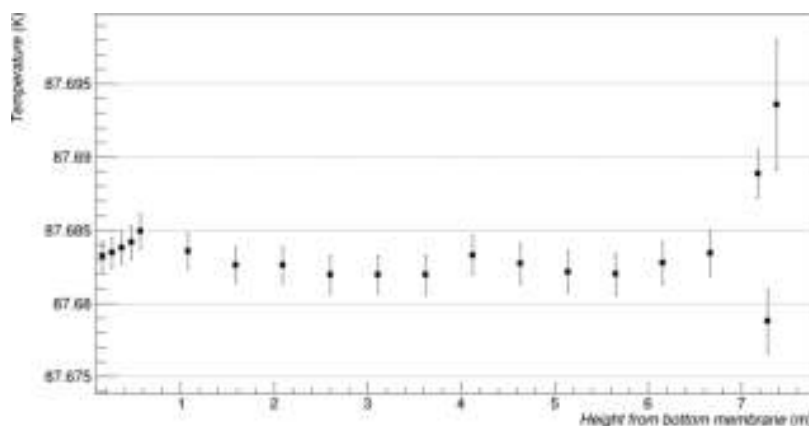


**Figure 8.7.** Temperature profile as measured by the dynamic T-gradient monitor after cross-calibration, when the recirculation pumps are off. Temperature variation is of the order of 3 mK except close to the top and the gas phase interface, as expected.

A dynamic T-gradient monitor has three parts: a carrier rod on which sensors are mounted; an enclosure above the cryostat housing space that allows the carrier rod to move vertically 1.5 m over its lowest location; and the motion mechanism. The motion mechanism consists of a stepper motor connected through a ferrofluidic dynamic seal to a gear and pinion motion mechanism. The sensors have two pins soldered to a PCB. Two wires are individually soldered to the common soldering pad for each pin. A cutout in the PCB around the sensor allows free flow of argon for more accurate temperature readings. Stepper motors typically have very fine steps that allow highly



precise positioning of the sensors. Figure 8.8 shows the overall design of the dynamic T-gradient monitor. The enclosure has two parts connected by a six-cross flange. One side of this flange will be used for signal wires, another will be used as a viewing window, and the two other ports will be spares. Figure 8.9, left shows the PCB mounted on the carrier rod and the sensor mounted on the PCB along with the four point connection to the signal readout wires. Figure 8.9, right shows the stepper motor mounted on the side of the rod enclosure. The motor remains outside the enclosure, at room temperature, as do its power and control cables.



**Figure 8.8.** A schematic of the dynamic T-gradient monitor.

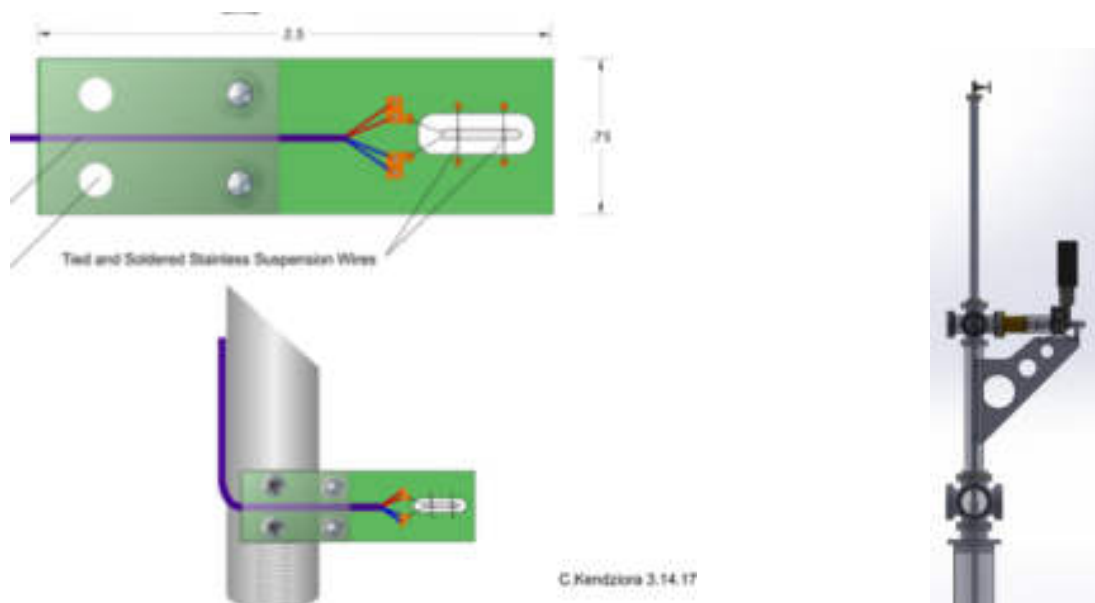


**Figure 8.9.** Left: sensor mounted on a PCB board and PCB board mounted on the rod. Right: the driving mechanism of the dynamic T-gradient monitor, consisting of a stepper motor driving the pinion and gear linear motion mechanism.

### 8.2.1.2 Static T-gradient monitors

Several vertical arrays of high-precision temperature sensors cross-calibrated in the laboratory will be installed behind the APAs. The baseline design assumes six arrays with 48 sensors each. Spacing between sensors is 20 cm at the top and bottom and 40 cm in the middle area. This configuration is similar to the one used in ProtoDUNE-SP but with nearly double the spacing. As shown in figure 8.10 a configuration with 48 sensors was appropriate in ProtoDUNE-SP, as it should be in the SP module where the expected total gradient is no larger than in ProtoDUNE-SP (see figure 8.2).

Sensors will be cross-calibrated in the laboratory using a controlled environment and a high-precision readout system, described in section 8.2.1.5. The accuracy of the calibration for ProtoDUNE-SP was estimated to be 2.6 mK, as shown in figure 8.11. Preliminary results for the

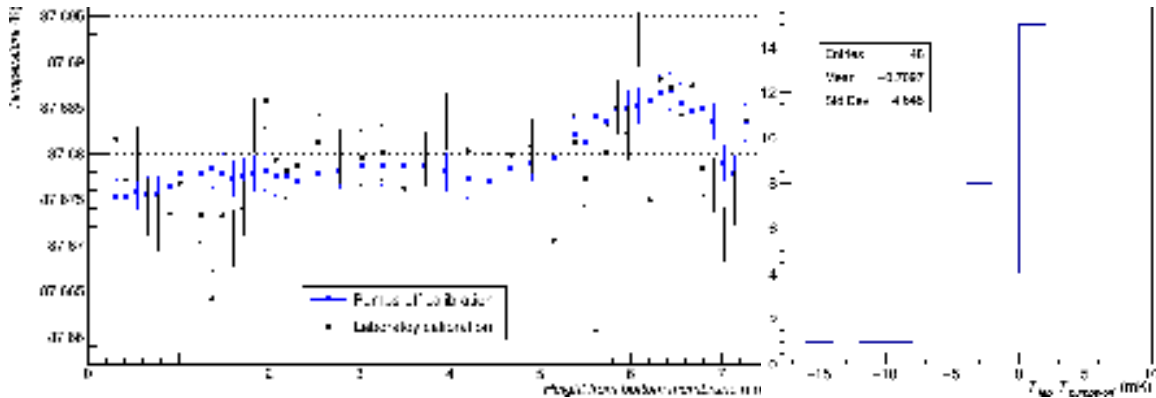


**Figure 8.10.** Left: temperature profile as measured by the static T-gradient monitor for two different calibration methods. Right: distribution of the difference between both methods.

analysis of ProtoDUNE-SP static T-gradient monitor data are shown in figure 8.10. The temperature profile has been computed using both the laboratory calibration and the so-called “in-situ pump-off calibration,” which consists of estimating the offsets between sensors assuming the temperature of LAr in the cryostat is homogeneous when the re-circulation pumps are off (the validity of this method is demonstrated in section 8.2.1.1). The RMS of the difference between both methods is 4.6 mK, slightly larger than the value quoted above for the accuracy of the laboratory calibration, due to the presence of few outliers (under investigation) and to the imperfect assumption of homogeneous temperature when pumps are off (see figure 8.7).

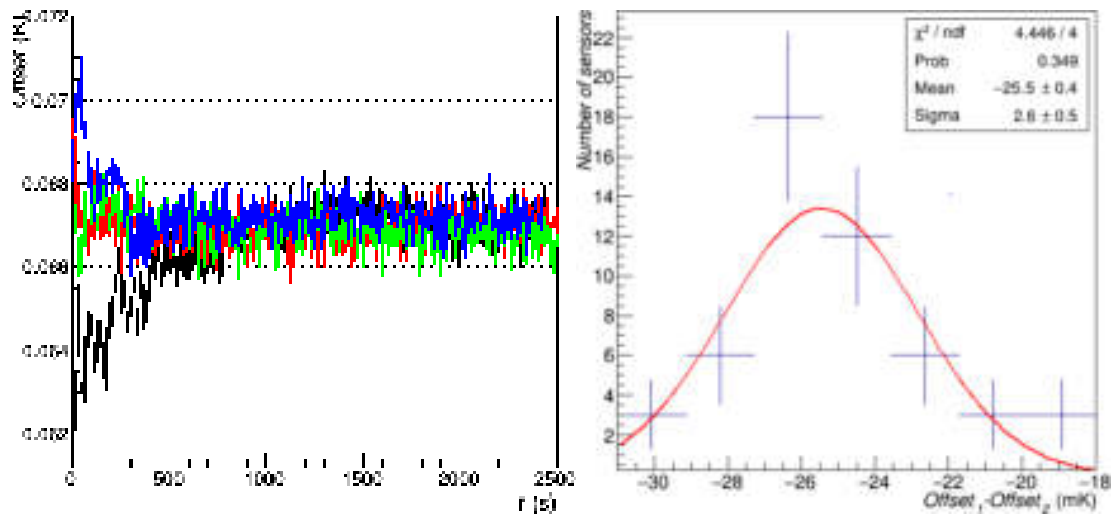


**Figure 8.11.** Left: temperature offset between two sensors as a function of time for four independent immersions in LAr. The reproducibility of those sensors, defined as the RMS of the mean offset in the flat region, is  $\sim 1$  mK. The resolution for individual measurements, defined as the RMS of one offset in the flat region, is better than 0.5 mK. Right: difference between the mean offset obtained with two independent calibration methods for the 51 calibrated sensors. The standard deviation of this distribution is interpreted as precision of the calibration.

Figure 8.12 shows the baseline mechanical design of the static T-gradient monitor. Two strings (stainless steel or carbon fibre) are anchored at the top and bottom corners of the cryostat using the available M10 bolts (see figure 8.13, left). One string routes the cables while the other supports the temperature sensors. Given the height of the cryostat, an intermediate anchoring point to reduce swinging is under consideration. A prototype is being built at IFIC, Spain, where the full system will be mounted using two dummy cryostat corners.

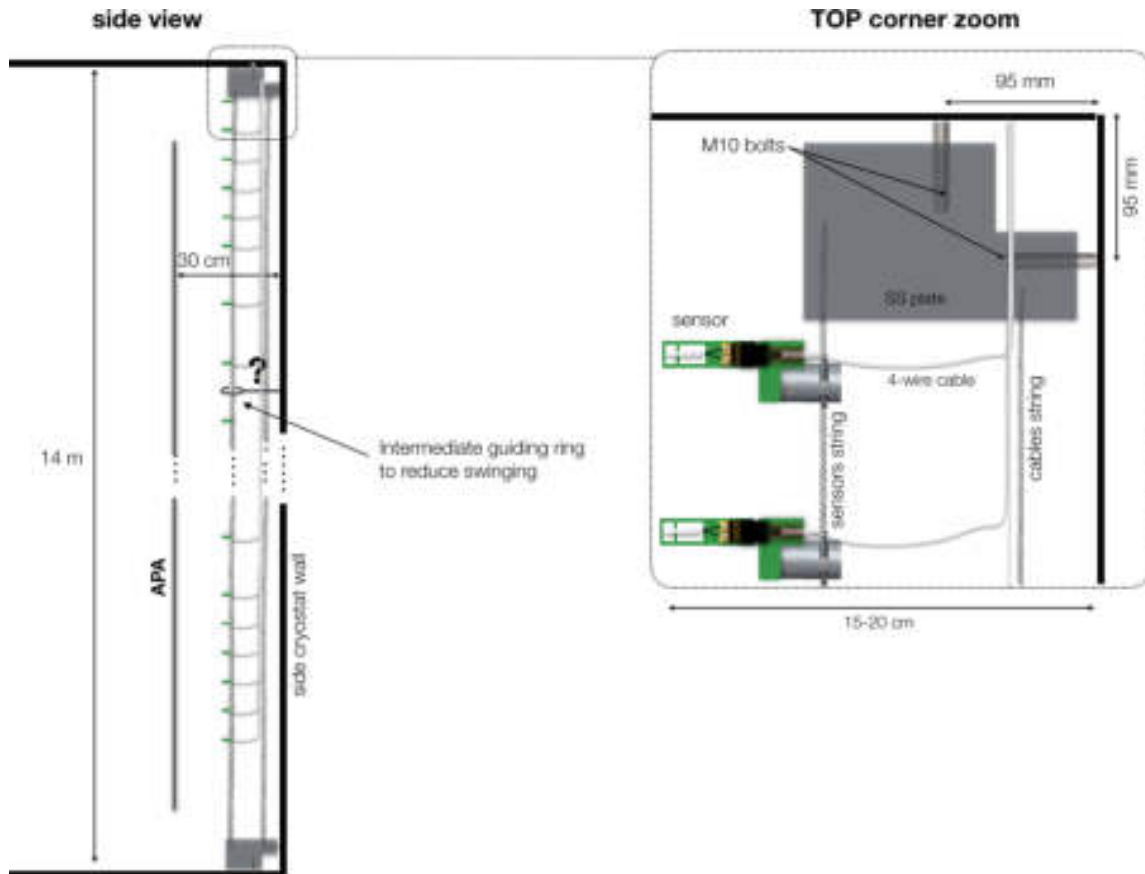


**Figure 8.12.** Conceptual design of the static T-gradient monitor.

Figure 8.13 (right) shows the baseline design of the ( $52 \times 15 \text{ mm}^2$ ) PCB support for temperature sensors with an IDC-4 male connector. A narrower connector (with two rows of two pins each) is being studied. This alternative design would reduce the width of the PCB assembly and allow more sensors to be calibrated simultaneously. Each four-wire cable from the sensor to the flange will have an IDC-4 female connector on the sensor end; the flange end of the cable will be soldered or crimped to the appropriate connector, whose type and number of pins depend on the final design of the DSS ports that will be used to extract the cables. SUBD-25 connectors were used in ProtoDUNE-SP.

### 8.2.1.3 Individual temperature sensors

T-gradient monitors will be complemented by a coarser 2D array (every 5 m) of precision sensors at the top and bottom of the detector module, as shown in figure 8.5. Following the ProtoDUNE-SP design, bottom sensors will use the cryogenic pipes as a support structure, while top sensors will



**Figure 8.13.** Left: bolts at the bottom corner of the cryostat. Right: lakeshore PT102 sensor mounted on a PCB with an IDC-4 connector.

be anchored to the GPs. Although sensors at the top will have a similar distribution to those at the bottom, suitable anchoring points at the top and bottom will differ.

As in ProtoDUNE-SP, another set of standard sensors will be evenly distributed and epoxied to the bottom membrane. They will detect the presence of LAr when cryostat filling starts. Finally, two vertical arrays of standard sensors will be epoxied to the lateral walls in two opposite vertical corners, with a spacing of 102 cm (every three corrugations), to monitor the cryostat membrane temperature during the cool-down and filling processes.

Whereas in ProtoDUNE-SP cables were routed individually (without touching neighboring cables or any metallic elements) to prevent grounding loops in case the outer Teflon jacket broke, such a failure has been proved to be very unlikely. Thus, in the detector modules, cables will be routed in bundles, simplifying the design enormously. As figure 8.5 shows, up to 20 sensors will use the same DSS port, large enough for a cable bundle 16 mm in diameter.

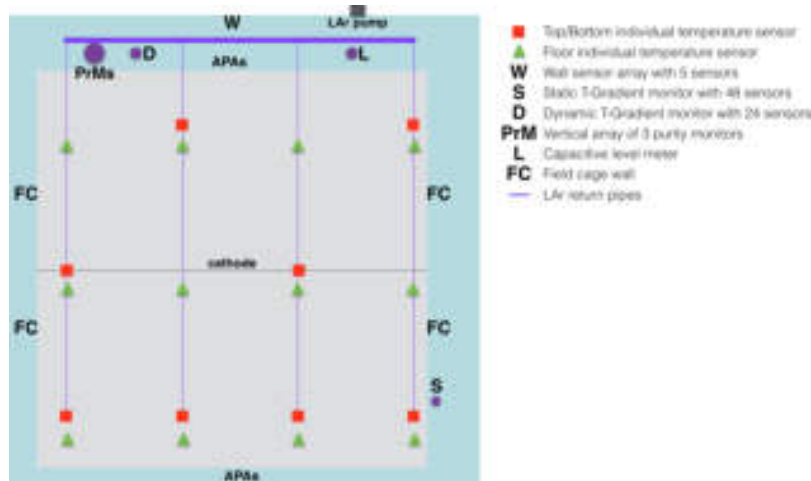
Cable bundles of several sizes will be configured using custom made Teflon pieces that will be anchored to different cryostat and detector elements to route cables from sensors to DSS ports. For sensors at the bottom (on pipes and floor), cables will be routed towards the cryostat bottom horizontal corner using stainless steel split clamps anchored to pipes (successfully prototyped in ProtoDUNE-SP), and from there, to the top of the cryostat using vertical strings (as with static T-gradient monitors). For sensors on the top GPs, cables bundles will be routed to the corresponding DSS port using Teflon supports attached to both the FR-4 threaded rods in the union between two GP modules and to the DSS I-beams (both successfully prototyped in ProtoDUNE-SP). Sensors on the walls will use bolts in the vertical corners for cable routing.

For all individual sensors, PCB sensor support, cables, and connection to the flanges will be the same as for the T-gradient monitors.

#### 8.2.1.4 Analysis of temperature data in ProtoDUNE-SP

Temperature data from ProtoDUNE-SP has been recorded since LAr filling in August 2018. The analysis of this data and the comparison with CFD simulations is actively underway, but interesting preliminary results are available and are described below. Figure 8.14 shows the distribution of temperature sensors in the ProtoDUNE-SP cryostat.

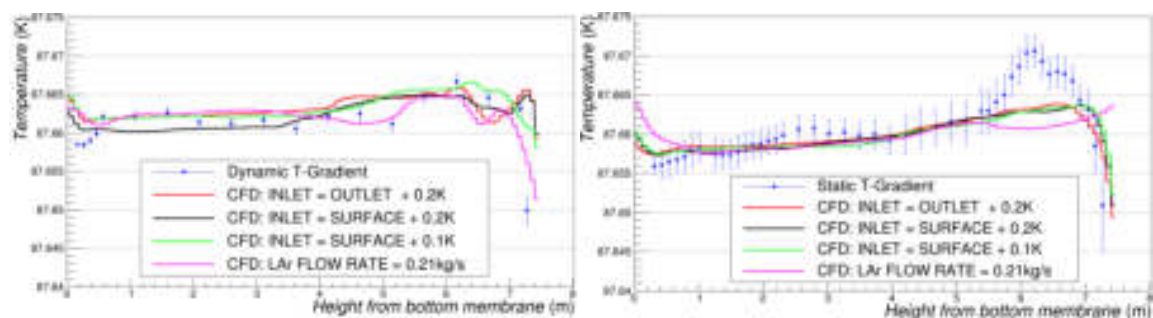
All precision temperature sensors (for the static and dynamic T-gradient monitors, and the 2D arrays at top and bottom) were calibrated in the laboratory prior to installation, as described in section 8.2.1.2. However, since the calibration method was still under development when those sensors were installed, this calibration was only satisfactory (2.6 mK precision) for the static T-gradient



**Figure 8.14.** Distribution of temperature sensors in the ProtoDUNE-SP cryostat. Notice that four of the bottom sensors are located right above the LAr inlets. Purity monitors and level meters are also indicated.

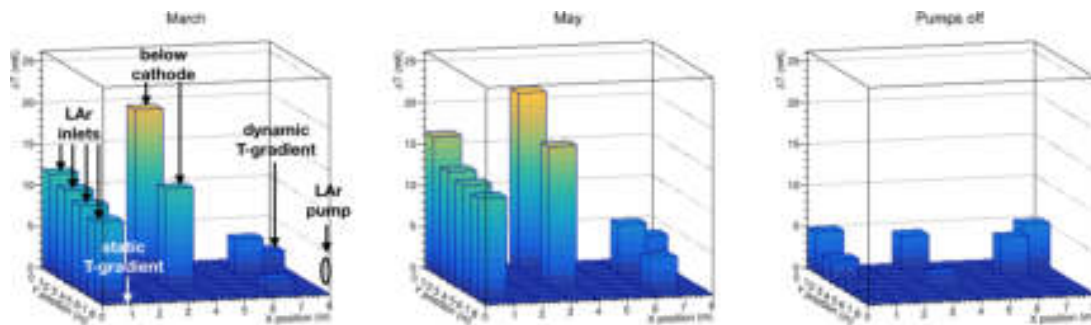
monitor, for which the sensors were calibrated last and plugged in just few days prior to installation in the cryostat. In section 8.2.1.2, an additional calibration method, the so-called “pumps-off calibration,” is described and the agreement with the laboratory calibration was demonstrated (see figure 8.10). Since this is the only reliable calibration for individual sensors, this method is used for the data analysis presented in this section, for all sensors except for the dynamic T-gradient monitor, for which the calibration based on the movable system is more precise (see section 8.2.1.1).

Figure 8.15 shows the vertical temperature profiles as measured by the dynamic and static T-gradient monitors during a 10 minute period in May 2019. The stability of these profiles has been carefully studied: the relative variation between any two sensors on the same profiler remained below 3 mK during the entire data taking period, demonstrating that the shape of the profiles is nearly constant in time. In figure 8.15 it is clear that the shapes of the two profiles are similar, with a bump at 6.2 m, but the magnitude of variation of the static profile almost doubles compared to the dynamic profile. This effect is attributed to the fact that the dynamic T-gradient monitor is in the path of the LAr flow, which makes the temperature more uniform, while the static profiler is on the side.



**Figure 8.15.** Temperature profiles measured by the T-gradient monitors and comparison to the CFD model with different boundary conditions. Left: dynamic T-gradient monitor; right: static T-gradient monitor.

We can use temperature measurements by the bottom sensor grid to connect the two different regions covered by the T-gradient monitors. Figure 8.16 shows the temperature difference between bottom sensors and the second sensor of the static T-gradient monitor, 40 cm from the floor, which is used as a reference. Also shown in the figure is the dynamic T-gradient monitor's third sensor, located at a similar height. Three different periods are shown in the figure: two periods with pumps-on and one period with pumps-off. It is observed that when the pumps are working, the temperature decreases towards the LAr pump, and is higher in the sensors below the cathode. The horizontal gradient observed in this situation is of the order of 20 mK — larger than the vertical gradient. When the pumps are off the horizontal gradient decreases, although a residual gradient of 5 mK is observed. This gradient is attributed to the inertia of the liquid once the pumps are switched off: it takes more than one day to recover the horizontal homogeneity.



**Figure 8.16.** Temperature difference between bottom sensors at 40 cm from the floor and static T-gradient sensor at same height. The third dynamic T-gradient sensor, at the same height, is also shown. Two pumps-on periods (left and middle panels) and one pump-off period (right panel) are shown.

CFD simulations have been produced using different inputs. We have identified two parameters as potential drivers of the convection regime: (1) the incoming LAr flow rate, and (2) the incoming LAr temperature. Figure 8.15 shows the result of varying these parameters. The CFD model reasonably predicts the main features of the data, but some details still need to be understood, in particular the bump at 6.2 m and the lower measured temperature at the bottom. It is worth noting that the simulation depends minimally on the LAr temperature while the flow rate has more impact, especially in the regions where discrepancies are larger. All simulations use the nominal LAr flow rate, 0.42 kg/s, except the one explicitly indicated in the plots that uses half that rate. More simulations with other LAr flow rates are still in progress.

The CFD reassuringly predicts a reasonable response for more than one set of initial conditions. It is still important to measure the instrumentation response to help establish the validity of the CFD model. We did not run tests with differing initial conditions during the beam run because even controlled changes of the cryostat environment could have undesirable effects. However, recently we ran dedicated tests to validate the CFD under various deliberate changes of the cryostat. These additional tests included pump and recirculation manipulations (such as pump on-off, change of pumping speed, and bypassing of filtration), and changing the cryostat pressure set point to a higher (or lower) value<sup>7</sup> to induce changes in the pressure for a specified time while monitoring

<sup>7</sup>The HV was ramped down for this exercise because dropping the pressure too fast might provoke boiling of the LAr near the surface.

the instrumentation. Any change in pressure could change the temperatures everywhere in the cryostat. Studying the rate of this change, as detected at various heights in the cryostat, might provide interesting constraints on the CFD model.

### 8.2.1.4.1 Comparison of calibration methods

Three different calibration methods have been described above: a laboratory calibration prior to installation, the “pumps off” calibration, and the movable system calibration. The underlying assumption is that reliable temperature monitoring at the few mK level is desirable during the entire lifetime of the experiment, both to guarantee the correct functioning of the cryogenics system and to compute offline corrections based on temperature measurements and CFD simulations. This is only possible if an in situ calibration method is available, since relative calibration between sensors is expected to diverge with time. Two in situ methods have been used. The pumps-off calibration method is very powerful since it is the only way of cross-calibrating all sensors in the cryostat at any point in time. However, it relies on the assumption that the temperature is uniform when the recirculation pumps are off. The validity of this assumption has to be bench-marked with real data, and this is done in ProtoDUNE-SP using the calibration based on the movable system (see figure 8.7). The movable system calibration method is the most precise and the one that sustains all other methods, providing a reliable reference during the entire lifetime of the experiment. This method is even more crucial for the FD. Indeed, recirculation pumps will be located on one side of the cryostat, very far (almost 60 m) from some regions of the LAr volume, where the inertia will be more pronounced and the homogeneous temperature assumption becomes less valid.

### 8.2.1.5 Readout system for thermometers

A high-precision and very stable system is required to achieve a readout level of  $< 5$  mK. The proposed readout system was used in ProtoDUNE-SP and relies on a variant of an existing mass PT100 temperature readout system developed at CERN for an LHC experiment; it has already been tested and validated in ProtoDUNE-SP. The system has an electronic circuit that includes

- a precise and accurate current source<sup>8</sup> for the excitation of the temperature sensors measured using the four-wires method,
- a multiplexing circuit connecting the temperature sensor signals and forwarding the selected signal to a single line, and
- a readout system with a high-accuracy voltage signal readout module<sup>9</sup> with 24 bit resolution over a 1 V range.

This readout system also drives the multiplexing circuit and calculates temperature values. The CompactRIO device is connected to the detector Ethernet network, sending temperature values to the DCS software through a standard OPC-UA driver.

---

<sup>8</sup>The actual current delivered is monitored with high-precision resistors such that the effect of ambient temperature can be disentangled.

<sup>9</sup>National Instrument CompactRIO™ device with a signal readout NI9238™ module.

The current mode of operation averages more than 2000 samples taken every second for each sensor. Figure 8.11 shows the system has a resolution higher than 1 mK, the RMS of one of the offsets in the stable region.

### 8.2.2 Purity monitors

A fundamental requirement of a LArTPC is that ionization electrons drift over long distances in the liquid. Part of the charge is inevitably lost due to electronegative impurities in the liquid. To keep this loss to a minimum, monitoring impurities and purifying the LAr during operation is essential.

A purity monitor is a small ionization chamber used to infer independently the effective free electron lifetime in the LArTPC. It illuminates a cathode with UV light to generate a known electron current, then collects the drifted current at an anode a known distance away. Attenuation of the current is related to the electron lifetime. Electron loss can be parameterized as  $N(t) = N(0)e^{-t/\tau}$ , where  $N(0)$  is the number of electrons generated by ionization,  $N(t)$  is the number of electrons after drift time  $t$ , and  $\tau$  is the electron lifetime.

For the SP module, the drift distance is 3.5 m, and the E field is  $500 \text{ V} \cdot \text{cm}^{-1}$ . Given the drift velocity of approximately  $1.5 \text{ mm} \cdot \mu\text{s}^{-1}$  in this field, the time to go from cathode to anode is roughly  $\sim 2.4 \text{ ms}$  [103]. The LArTPC signal attenuation,  $[N(0) - N(t)]/N(0)$ , must remain less than 20% over the entire drift distance [163]. The corresponding electron lifetime is  $2.4 \text{ ms}/[-\ln(0.8)] \approx 11 \text{ ms}$ .

Residual gas analyzers can be used to monitor the gas in the ullage of the tank and would be an obvious choice for analyzing argon gas. Unfortunately, suitable and commercially available mass spectrometers have a detection limit of  $\sim 10$  parts per billion (ppb), whereas DUNE requires a sensitivity of parts per trillion (ppt). Therefore, specially constructed and distributed purity monitors will measure LAr purity in all phases of operation. These measurements, along with an accurate CFD model, enable the determination of purity at all positions throughout the detector module.

Purity monitors are placed inside the cryostat but outside of the TPC. They are also placed within the recirculation system outside the cryostat, both in front of and behind the filtration system. Continuous monitoring of the LAr supply lines to the detector module provides a strong line of defense against contamination from sources both in the LAr volume and from components in the recirculation system. Similarly, gas analyzers (described in section 8.2.5) protect against contaminated gas.

Furthermore, using several purity monitors to measure lifetime with high precision at carefully chosen points provides key input, e.g., vertical gradients in impurity concentrations, for CFD models of the detector module.

Purity monitors were deployed in previous LArTPC experiments, e.g., ICARUS, MicroBooNE, and the 35 ton prototype. During the first run of the 35 ton prototype, two of the four purity monitors stopped working during cool-down, and a third operated intermittently. We later found that this was due to poor electrical contacts between the resistor chain and the purity monitor. A new design was implemented and successfully tested in the second run.

ProtoDUNE-SP and ProtoDUNE-DP use purity monitors to measure electron lifetime at different heights, and they use a similar design.

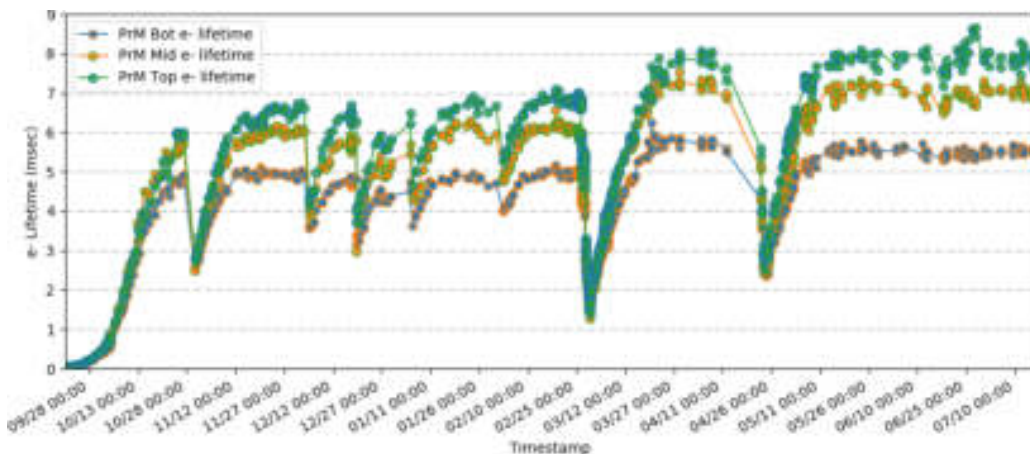


Figure 8.17 shows the assembly of the ProtoDUNE-SP purity monitors. The design reflects improvements to ensure electrical connectivity and improve signals. ProtoDUNE-SP uses a string of purity monitors connected with stainless steel tubes to protect the optical fibers.



**Figure 8.17.** The ProtoDUNE-SP purity monitoring system.

ProtoDUNE-SP implements three purity monitors. The purity monitors continuously monitored LAr purity during all commissioning, beam test and operation periods of ProtoDUNE-SP. Figure 8.18 shows the ProtoDUNE-SP data taken using its three purity monitors from commissioning of ProtoDUNE-SP starting in September 2018, through the entire beam running period, to July 2019.



**Figure 8.18.** The electron lifetimes measured by three purity monitors in ProtoDUNE-SP as a function of time, September 2018 through July 2019. The purity is low prior to start of circulation in October. Reasons for later dips include recirculation studies and recirculation pump stoppages.

2020 JINST 15 T08010

Although ProtoDUNE-SP receives ample cosmic ray data to perform electron lifetime measurements, the purity monitor system was found to be essential for providing quick, reliable real-time monitoring of purity in the detector and to catch purity-related changes in time due to LAr recirculation issues. Each purity monitor electron lifetime measurement is based on purity monitor anode-to-cathode signal ratios from 200 UV flashes within 40 seconds at the same location. The statistical error on this lifetime measurement is less than 0.03 ms when the purity is 6 ms.

The purity monitor system at ProtoDUNE-SP measured electron lifetime every hour during commissioning and daily during the beam test. During this time, it alerted the experiment to problems several times. The first time was for filter saturation during LAr filling, and the others were for recirculation pump stoppages, false alarms, and problems from the cryostat-level gauges. The dips in figure 8.18 show these sudden changes in purity caught by purity monitors. Given the high sensitivity, the ProtoDUNE-SP purity monitors were immediately able to alert the experiment to the purity drops, preventing situations which otherwise would have continued unnoticed for some time, with potentially serious consequences for the ability to take any data.

During the commissioning and beam test of ProtoDUNE-SP, the purity monitors operated with different high voltages to change electron drift time, ranging from 150  $\mu\text{s}$  to 3 ms. This allowed the ProtoDUNE-SP purity monitors to measure electron lifetime from 35  $\mu\text{s}$  to about 10 ms with high precision, a dynamic range greater than 300. This measurement was also valuable for the ProtoDUNE-SP lifetime calibration. Because purity monitors have much smaller drift volumes than the TPC, they are less affected by the space charge caused by cosmic rays.

A similar operation plan is planned for the SP module, with modifications to accommodate the relative positions of the instrumentation port and the purity monitor system, and the different geometric relationships between the TPC and cryostat.

### 8.2.2.1 Purity monitor design

The SP module baseline purity monitor design follows that of the ICARUS experiment (figure 8.19) [164]. It consists of a double-gridded ion chamber immersed in the LAr volume with four parallel, circular electrodes, a disk holding a photocathode, two grid rings (anode and cathode), and an anode disk. The cathode grid is held at ground potential. The cathode, anode grid, and anode each hold separate bias voltages and are electrically accessible via modified vacuum-grade HV feedthroughs. The anode grid and the field-shaping rings are connected to the cathode grid by an internal chain of 50 M $\Omega$  resistors to ensure the uniformity of the E fields in the drift regions. A stainless mesh cylinder is used as a Faraday cage to isolate the purity monitor from external electrostatic background.

The purity monitor measures the electron drift lifetime between its anode and cathode. The purity monitor's UV-illuminated photocathode generates the electrons via the photoelectric effect. Because the electron lifetime in LAr is inversely proportional to the electronegative impurity concentration, the fraction of electrons generated at the cathode that arrives at the anode ( $Q_A/Q_C$ ) after the electron drift time  $t$  gives a measure of the electron lifetime  $\tau$ :  $Q_A/Q_C \sim e^{-t/\tau}$ .

Once the electron lifetime becomes much larger than the drift time  $t$  the purity monitor reaches its sensitivity limit. For  $\tau \gg t$ , the anode-to-cathode charge ratio becomes  $\sim 1$ . Because the drift time is inversely proportional to the E field, in principle, lowering the field should make it possible to measure lifetimes of any length, regardless of the length of the purity monitor. On the other

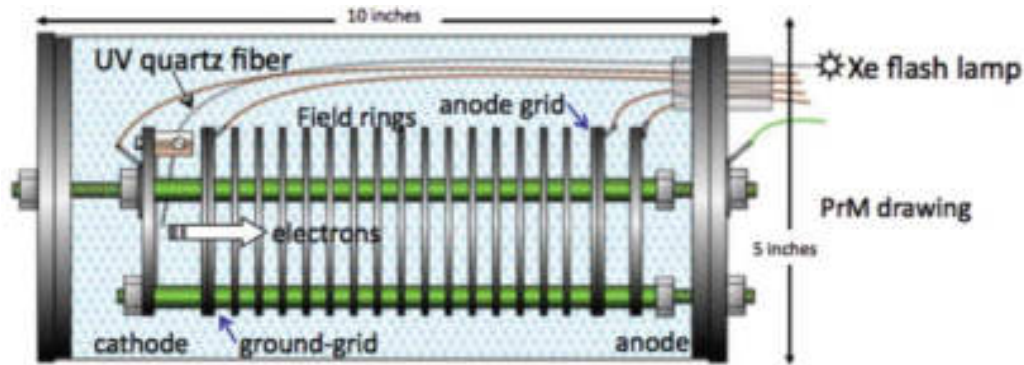


**Figure 8.19.** Schematic diagram of the basic purity monitor design [164].

hand, increasing the voltage will shorten the drift time, allowing measurement of a short lifetime when purity is low.

The electron lifetime of the purest commercial LAr, after the first filtering and during the filling process, is typically higher than  $40\ \mu\text{s}$ . However, when the filter starts to saturate, the lifetime decreases to less than  $30\ \mu\text{s}$ . To reduce the energy loss due to impurities, the SP module requires an electron lifetime greater than 3 ms.

Varying the operational HV on the anode from 250 V to 4000 V in the ProtoDUNE-SP's 24 cm (9.5 inch) long purity monitor allowed us to make the  $35\ \mu\text{s}$  to 10 ms electron lifetime measurements. Purity monitors with different lengths (drift distances) are needed to extend the measurable range to below  $35\ \mu\text{s}$  and above 10 ms.

The photocathode that produces the photoelectrons is an aluminum plate coated first with  $50\ \text{\AA}$  of titanium followed by  $1000\ \text{\AA}$  of gold, and is attached to the cathode disk. A xenon flash lamp is the light source in the baseline design, although a more reliable and possibly submersible light source, perhaps LED-driven, could replace this in the future. The UV output of the lamp is quite good, approximately  $\lambda = 225\ \text{nm}$ , which corresponds closely to the work function of gold (4.9 eV to 5.1 eV). Several UV quartz fibers carry the xenon UV light into the cryostat to illuminate the photocathode. Another quartz fiber delivers the light into a properly biased photodiode outside the cryostat to provide the trigger signal when the lamp flashes.

### 8.2.2.2 Electronics, DAQ, and slow controls interfacing

The purity monitor electronics and DAQ system consist of front-end (FE) electronics, waveform digitizers, and a DAQ PC. Figure 8.20 illustrates the system.

The baseline design of the FE electronics follows that used in the 35 ton prototype, Liquid Argon Purity Demonstrator (LAPD), and MicroBooNE. The cathode and anode signals are fed into two charge amplifiers contained within the purity monitor electronics module. This electronics module includes a HV filter circuit and an amplifier circuit, both shielded by copper plates, to allow the signal and HV to be carried on the same cable and decoupled inside the purity monitor electronics module. A waveform digitizer that interfaces with a DAQ PC records the amplified anode and cathode outputs. The signal and HV cable shields connect to the grounding points of the cryostat and are separated from the electronic ground with a resistor and a capacitor connected in

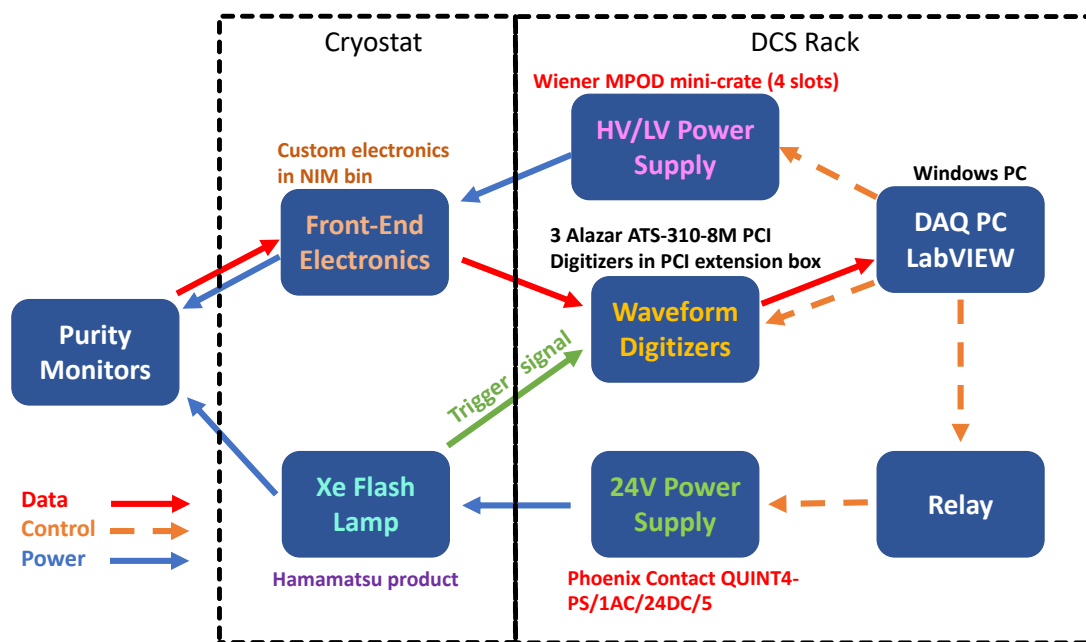


Figure 8.20. Block diagram of the purity monitor system.

parallel, mitigating ground loops between the cryostat and the electronics racks. Amplified output is transmitted to an AlazarTech ATS310 waveform digitizer<sup>10</sup> containing two input channels, each with 12 bit resolution. Each channel can sample a signal at a rate of  $20 \text{ MS} \cdot \text{s}^{-1}$  to  $1 \text{ kS} \cdot \text{s}^{-1}$  and store up to 8 MS in memory. One digitizer is used for each purity monitor, and each digitizer interfaces with the DAQ PC across the PCI bus.

A custom LabVIEW<sup>11</sup> application running on the DAQ PC has two functions: it controls the waveform digitizers and the power supplies, and it monitors the signals and key parameters. The application configures the digitizers to set the sampling rate, the number of waveforms to be stored in memory, the pre-trigger data, and a trigger mode. A signal from a photodiode triggered by the xenon flash lamp is fed directly into the digitizer as an external trigger to initiate data acquisition. LabVIEW automatically turns on the xenon flash lamp by powering a relay when data taking begins and then turns it off when finished. The waveforms stored in the digitizers are transferred to the DAQ PC and used to obtain averaged waveforms to reduce the electronic noise in them.

The baseline is estimated by averaging the waveform samples prior to the trigger. This baseline is subtracted from the waveforms prior to calculating peak voltages of the cathode and anode signals. The application performs these processes in real time. The application continuously displays the waveforms and important parameters like measured electron lifetime, peak voltages, and drift time in the purity monitors, and shows the variation in these parameters over time, thus pointing out effects that might otherwise be missed. Instead of storing the measured parameters, the waveforms and the digitizer configurations are recorded in binary form for offline analysis. HV modules<sup>12</sup> in

<sup>10</sup>AlazarTech ATS310™ — 12 bit, 20 MS/s, <https://www.alazartech.com/Product/ATS310>.

<sup>11</sup>National Instruments, LabVIEW™, <http://www.ni.com/en-us.html>.

<sup>12</sup>iseg Spezialelektronik GmbH™ high voltage supply systems, <https://iseg-hv.com/en>.

a WIENER MPOD mini crate<sup>13</sup> supply negative voltages to the cathode and positive voltages to the anode. The LabVIEW application controls and monitors the HV systems through an Ethernet interface.

The xenon flash lamp and the FE electronics are installed close to the purity monitor flange, to reduce light loss through the optical fiber and prevent signal loss. Other pieces of equipment that distribute power to these items and collect data from the electronics are mounted in a rack separate from the cryostat. The slow control system communicates with the purity monitor DAQ software and controls the HV and LV power supplies of the purity monitor system. The optical fiber must be placed within 0.5 mm of the photocathode for efficient photoelectron extraction, so little interference with the PD system is expected. The purity monitors could induce noise in the TPC electronics, in particular via the current surge through a xenon lamp when it is flashed. This source of noise can be controlled by placing the lamp inside its own Faraday cage with proper grounding and shielding. At ProtoDUNE-SP, after careful checks of the grounding, this noise has remained well below the noise generated by other sources.

In the SP module we can make use of triggering to prevent any potential noise from the purity monitor's flash lamp from affecting TPC and PD system signals. The LArTPC trigger rate is a few hertz, and each trigger window is one or a few milliseconds. The pulse from a flash lamp is very short (a microsecond or so, much shorter than the gaps between LArTPC trigger windows). Thus, a LArTPC trigger signal may be sent to a programmable pulse generator, which generates a trigger pulse that does not overlap with LArTPC trigger windows. This trigger pulse is then sent to the external trigger port on the flash lamp HV controller so that the lamp flashes between LArTPC trigger windows. In this way, the electronic and light noises from the flash lamp do not affect data taking at all.

### 8.2.2.3 Production and assembly

The CISC consortium will produce the individual purity monitors, test them in a test stand, and confirm that each monitor operates at the required level before assembling them into the strings of three monitors each that will be mounted in the SP module cryostat using support tubes. The assembly process will follow the methodology developed for ProtoDUNE.

A short version of the string with all purity monitors will be tested at the CITF. The full string will be assembled and shipped to South Dakota. A vacuum test in a long vacuum tube will be performed on-site before inserting the full assembly into the SP module cryostat.

### 8.2.3 Liquid level meters

The goals for the LAr level monitoring system are basic level sensing when filling, and precise level sensing during static operations.

Filling the cryostat with LAr will take several months. During this operation several systems will be used to monitor the LAr level. The first 5.5 m will be covered by cameras and by the vertical arrays of resistance temperature detectors (RTDs) at known heights, since temperature will change drastically when the cold liquid reaches each RTD. Once the liquid reaches the level of the cryogenics pipes going out of the cryostat, the differential pressure between that point and the

---

<sup>13</sup>WIENER MPOD™ Universal Low and High Voltage Power Supply System, <http://www.wiener-d.com/>.

bottom of the cryostat can be converted to depth using the known density of LAr. Fine tuning of the final LAr level will be done using several capacitive level meters at the top of the cryostat.

During operation, liquid level monitoring has two purposes: the LBNF cryogenics system uses monitoring to tune the LAr flow, and DUNE uses monitoring to guarantee that the top GPs are always submerged at least 20 cm below the LAr surface to mitigate the risk of dielectric breakdown. This was the value used for the HV interlock in ProtoDUNE-SP.

The LAr flow is tuned using two differential pressure level meters, installed as part of the cryogenics system, one on each side of the detector module. They have a precision of 0.1 %, which corresponds to 14 mm at the nominal LAr surface. Cryogenic pressure sensors will be purchased from commercial sources. Installation methods and positions will be determined as part of the cryogenics internal piping plan.

For HV integrity, multiple 4 m long capacitive level sensors (with a precision of less than 5 mm) will be deployed along the top of the fluid for use during stable operations, and checked against each other. One capacitive level sensor at each of the four corners of the cryostat will provide sufficient redundancy to ensure that no single point of failure compromises the measurement.

Figure 8.21 shows the evolution of the ProtoDUNE-SP LAr level over two months as measured by the differential pressure and capacitive level meters.

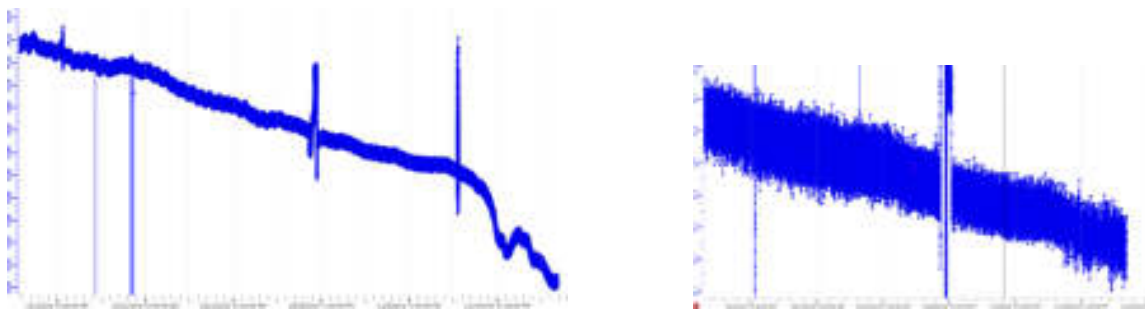


**Figure 8.21.** Evolution of the ProtoDUNE-SP LAr level over two months. Left: measured by the capacitive level meter. Right: measured by the differential pressure level meter. The units in the vertical axis are percentages of the cryostat height (7878 mm).

ProtoDUNE-SP uses the same design for differential pressure level meters as the SP module. In the case of capacitive level meters, ProtoDUNE-SP is using commercially bought 1.5 m long level meters while ProtoDUNE-DP is using 4 m long level meters that are custom-built by CERN. We plan to use the longer capacitive level meters custom-built by CERN for both SP and DP modules.

#### 8.2.4 Pressure meters

The absolute temperature in the liquid varies with the pressure in the argon gas in the ullage of the cryostat, therefore, precise measurements of pressure inside the cryostat allow for a better understanding of temperature gradients and CFD simulations. In ProtoDUNE-SP, pressure values were also used to understand the strain gauge signals installed in the cryostat frame.

Standard industrial pressure sensors can be used to measure the pressure of the argon gas. For the DUNE FD, the plan is to follow the same design and configuration used in ProtoDUNE-SP. ProtoDUNE uses two types of pressure sensors and a pressure switch,

- a relative pressure sensor (range: 0–400 mbar, precision: 0.01 mbar),
- an absolute pressure sensor (range: 0–1600 mbar, precision: 0.05 mbar), and
- a mechanical relative pressure switch adjustable from 50 to 250 mbar.

Both sensors and the pressure switch are installed in a dedicated flange as shown in figure 8.22 and are connected directly to a slow controls system PLC circuit. Dedicated analog inputs are used to read the current values (4 mA to 20 mA) which are then converted to pressure according to the sensors range. Given the much larger size of the DUNE detector modules, the system described above will be doubled for redundancy: two flanges in opposite cryostat sides will be instrumented with three sensors each.

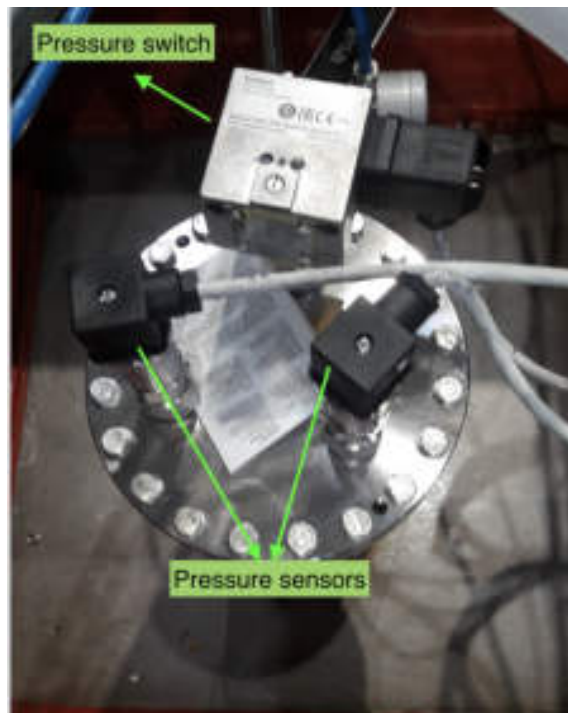


**Figure 8.22.** Photograph of the pressure sensors installed on a flange in ProtoDUNE-SP.

Further, relative and absolute pressure sensors (with comparatively lower precision) are installed by LBNF that are also recorded by the slow controls system. The availability of two types of sensors from LBNF and CISC provides redundancy, independent measurements, and cross checks.

### 8.2.5 Gas analyzers

Gas analyzers are commercially produced modules that measure trace quantities of specific gases contained within a stream of carrier gas. The carrier gas for DUNE is argon, and the trace gases of interest are oxygen ( $O_2$ ), water ( $H_2O$ ), and nitrogen ( $N_2$ ).  $O_2$  and  $H_2O$  affect the electron lifetime in LAr and must be kept below 0.1 ppb ( $O_2$  equivalent) while  $N_2$  affects the efficiency of scintillation light production at levels higher than 1 ppm. The argon is sampled from either the argon vapor in the ullage or from the LAr by using small diameter tubing run from the sampling point to the

gas analyzer. Typically, the tubing from the sampling points are connected to a switchyard valve assembly used to route the sample points to the desired gas analyzers (see figure 8.23).

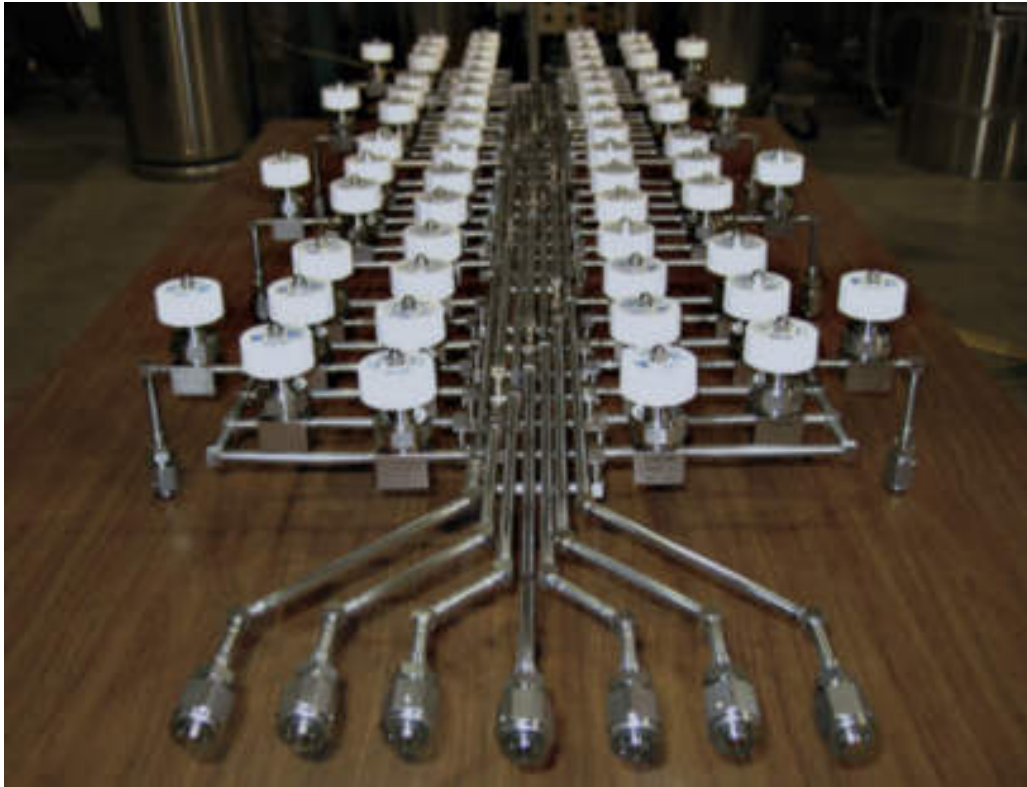


**Figure 8.23.** A gas analyzer switchyard that routes sample points to the different gas analyzers.

The gas analyzer would be predominantly used during three periods:

1. Once the detector is installed and after the air atmosphere is eliminated from the cryostat to levels low enough to begin cool-down. This purge and gas recirculation process is detailed in section 8.4.5.3. Figure 8.24 shows the evolution of the  $N_2$ ,  $O_2$ , and  $H_2O$  levels from gas analyzer data taken during the purge and recirculation stages of the DUNE 35 ton prototype phase 1 run.
2. Before other means of monitoring impurity levels (e.g., purity monitors, or TPC tracks) are sensitive, to track trace  $O_2$  and  $H_2O$  contaminants from tens of ppb to hundreds of ppt. Figure 8.25 shows an example plot of  $O_2$  levels at the beginning of LAr purification from one of the later 35 ton prototype HV runs.
3. During cryostat filling to monitor the tanker LAr delivery purity. This tracks the impurity load on the filtration system and rejects any deliveries that do not meet specifications. Specifications for the delivered LAr are in the 10 ppm range per contaminant.

Since any one gas analyzer covers only one contaminant species and a range of 3 to 4 orders of magnitude, several units are needed both for the three contaminant gases and to cover the ranges



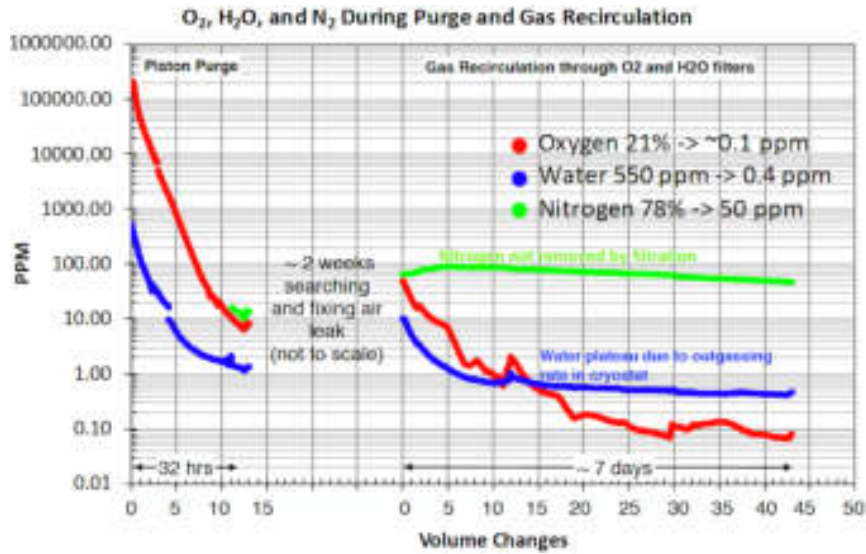


**Figure 8.24.** Plot of the O<sub>2</sub>, H<sub>2</sub>O, and N<sub>2</sub> levels during the piston purge and gas recirculation stages of the 35 ton prototype Phase 1 run.

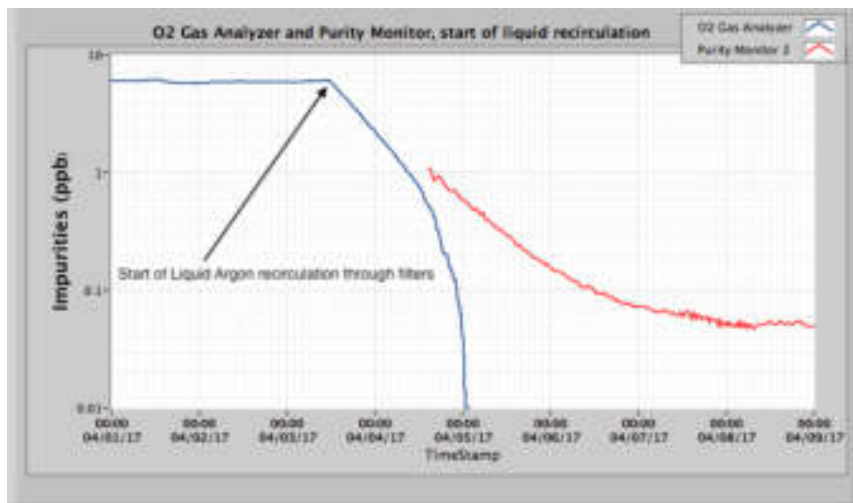


**Figure 8.25.** O<sub>2</sub> as measured by a precision O<sub>2</sub> analyzer just after the 35 ton prototype cryostat was filled with LAr, continuing with the LAr pump start and beginning of LAr recirculation through the filtration system. As the gas analyzer loses sensitivity, the purity monitor can pick up the impurity measurement. Note that the purity monitor is sensitive to both O<sub>2</sub> and H<sub>2</sub>O impurities giving rise to its higher levels of impurity.

seen between cryostat closure and the beginning of TPC operations: 20 % to  $\lesssim$  100 ppt for O<sub>2</sub>, 80 % to  $\lesssim$  1 parts per million (ppm) for N<sub>2</sub>, and  $\sim$ 1 % to  $\lesssim$  1 ppb for H<sub>2</sub>O. Because the total cost of these analyzers exceeds \$100 k, we want to be able to sample more than a single location or cryostat with the same gas analyzers. At the same time, the tubing run lengths from the sample point should be as short as possible to maintain a timely response for the gas analyzer. This puts some constraints on sharing devices because, for example, argon is delivered at the surface, so a separate gas analyzer may be required there.

### 8.2.6 Cameras

Cameras provide direct visual information about the state of the detector module during critical operations and when damage or unusual conditions are suspected. Cameras in the WA105 DP demonstrator showed spray from cool-down nozzles and the level and state of the LAr as it covered the charge-readout plane (CRP) [165]. A camera was used in the LAPD cryostat [164] to study HV discharges in LAr and in EXO-100 while a TPC was operating [166]. Warm cameras viewing LAr from a distance have been used to observe HV discharges in LAr in fine detail [167]. Cameras are commonly used during calibration source deployment in many experiments (e.g., the KamLAND ultra-clean system [168]).

In DUNE, cameras will verify the stability, straightness, and alignment of the hanging TPC structures during cool-down and filling; ensure that no bubbling occurs near the GPs (SP) or CRPs (DP); inspect the state of movable parts in the detector module (calibration devices, dynamic thermometers); and closely inspect parts of the TPC after any seismic activity or other unanticipated event. For these functions, a set of fixed cold cameras are used; they are permanently mounted at fixed points in the cryostat for use during filling and commissioning, and a movable, replaceable warm inspection camera can be deployed through any free instrumentation flange at any time during the life of the experiment.

Eleven cameras were deployed in ProtoDUNE-SP at the locations shown in figure 8.26. They successfully provided views of the detector during filling and throughout its operation.

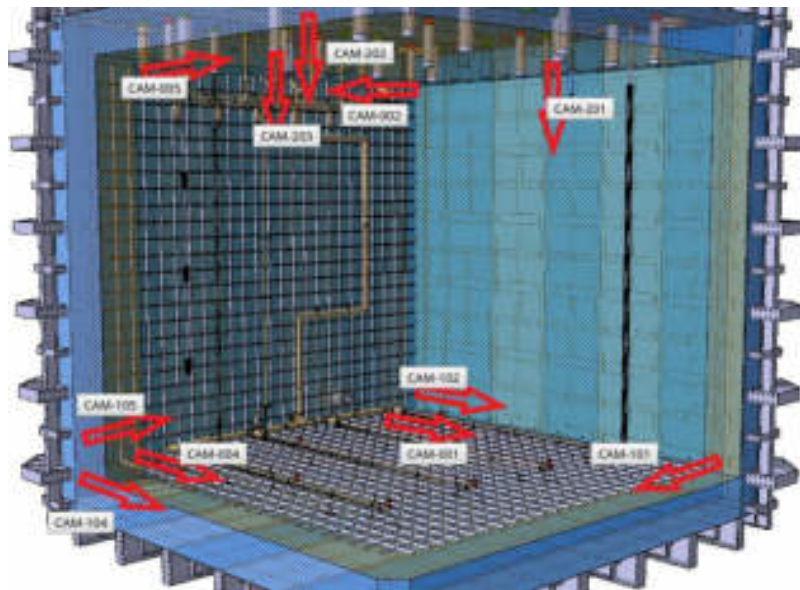


**Figure 8.26.** A 3D view showing the locations of the 11 cameras in ProtoDUNE-SP.

The following sections describe the design considerations for both cold and warm cameras and the associated lighting system. ProtoDUNE-SP camera system designs and performance are also discussed. The same basic designs can be used for both the SP module and the DP module.

### 8.2.6.1 Cryogenic cameras (cold)

The fixed cameras monitor the following items during filling:

- positions of corners of APA, cathode plane assembly (CPA), FCs, GPs (1 mm resolution);
- relative straightness and alignment of APA, CPA, and FC ( $\lesssim 1$  mm);
- relative positions of profiles and endcaps (0.5 mm resolution); and
- the LAr surface, specifically, the presence of bubbling or debris.

One design for the DUNE fixed cameras uses an enclosure similar to the successful EXO-100 design [166], which was also successfully used in the LAPD and ProtoDUNE-SP (see figure 8.27). Cameras 101, 102, 104, and 105, shown in figure 8.26, use this enclosure. A thermocouple in the enclosure allows temperature monitoring, and a heating element provides temperature control. SUB-D connectors are used at the cryostat flanges and the camera enclosure for signal, power, and control connections.

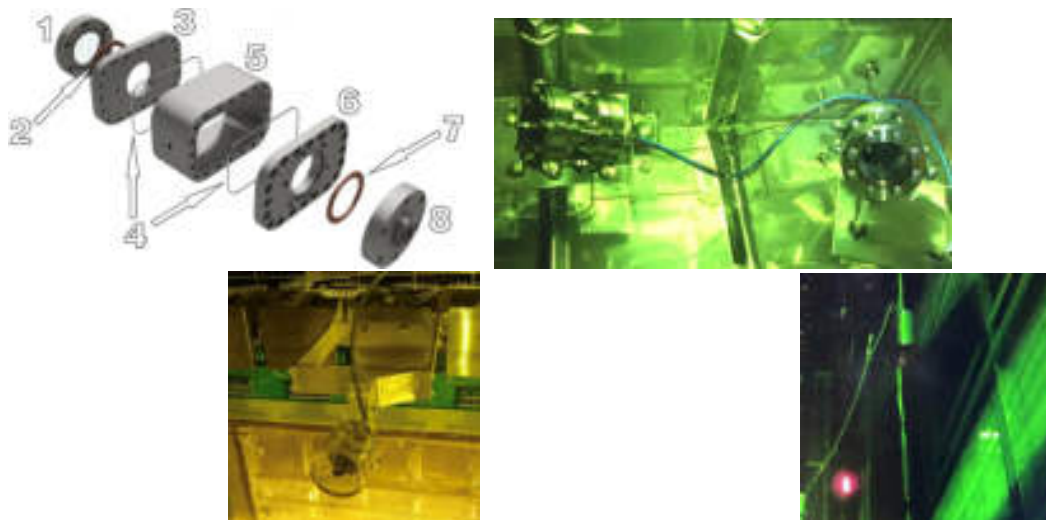


**Figure 8.27.** Top left: a CAD exploded view of a vacuum-tight camera enclosure suitable for cryogenic applications [166]. (1) quartz window, (2 and 7) copper gasket, (3 and 6) flanges, (4) indium wires, (5) body piece, (8) signal feedthrough. Top right: two of the ProtoDUNE-SP cameras using a stainless steel enclosure. Bottom left: one of the ProtoDUNE-SP cameras using acrylic enclosure. Bottom right: a portion of an image taken with ProtoDUNE-SP camera 105 showing a purity monitor mounted outside the APA on the beam left side. This photo was taken with ProtoDUNE-SP completely filled.

An alternative design uses an acrylic enclosure. This design was used successfully in ProtoDUNE-SP (see figure 8.27, bottom left). Cameras 001, 002, 004, and 005, shown in figure 8.26, use acrylic enclosures. All operate successfully, including those at the bottom of the cryostat. The FD modules will be twice as deep as ProtoDUNE, and therefore cameras observing the lowest surfaces of the FC must withstand twice the pressure.

Improved designs for the cold cameras will be tested in ProtoDUNE-DP and CITF for improved imaging including focus adjustment, and in CITF for pressure resistance, during 2020.

### 8.2.6.2 Inspection cameras (warm)

The inspection cameras are intended to be as versatile as possible. The following inspections have been identified as likely uses:

- status of HV feedthrough and cup,
- status of FC profiles, endcaps (0.5 mm resolution),
- vertical deployment of calibration sources,
- status of thermometers, especially dynamic thermometers,
- HV discharge, corona, or streamers on HV feedthrough, cup, or FC,
- relative straightness and alignment of APA, CPA, and FC (1 mm resolution),
- gaps between CPA frames (1 mm resolution),
- relative position of profiles and endcaps (0.5 mm resolution), and
- sense wires at the top of outer wire planes in SP APA (0.5 mm resolution).

Unlike the fixed cameras, the inspection cameras must operate only as long as any inspection; the cameras can be replaced in case of failure. It is also more practical to keep the cameras continuously warmer than  $-150\text{ }^{\circ}\text{C}$  during deployment; this allows use of commercial cameras, e.g., cameras of the same model were used successfully to observe discharges in LAr from 120 cm away [167].

The inspection cameras use the same basic enclosure design as for cold cameras, but the cameras are mounted on a movable fork so that each camera can be inserted and removed from the cryostat, using a design similar to the dynamic temperature probes: see figure 8.28 (left) and figure 8.9. To avoid contaminating the LAr with air, the entire system is sealed, and the camera can only be deployed through a feedthrough equipped with a gate valve and a purging system, similar to the one used in the vertical axis calibration system at KamLAND [168]. The entire system is purged with pure argon gas before the gate valve is opened.

Motors above the flange allow the fork to be rotated and moved vertically to position the camera. A chain drive system with a motor mounted on the end of the fork allows the camera assembly to tilt, creating a point-tilt mount that can be moved vertically. With the space above the cryostat flanges and the thickness of the cryostat insulation, cameras can be moved vertically up to 1 m inside the cryostat. The motors for rotation and vertical motion are outside the sealed volume, coupled mechanically using ferrofluidic seals, thus reducing any risk of contamination and allowing manual rotation of the vertical drive if the motor fails.

An alternative design was demonstrated in ProtoDUNE-SP. In this design, the warm camera is contained inside a gas-tight acrylic tube inserted into the feedthrough, so a gate valve or a gas-tight rotatable stage is not needed, and the warm cameras can be removed for servicing or upgrade at any time. Figure 8.28 (right) shows an acrylic tube enclosure and camera immediately before deployment. These acrylic tube enclosures for removable cameras were deployed in ProtoDUNE-SP at the positions marked 201, 202, and 203 in figure 8.26; they operated successfully. Cameras

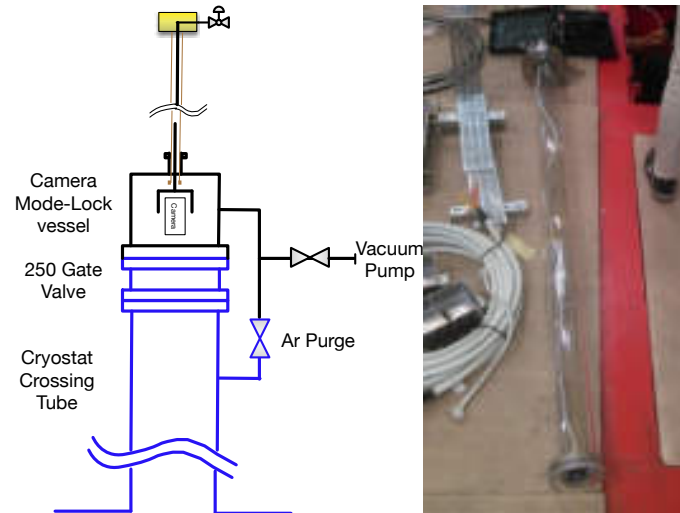


**Figure 8.28.** Left: an overview of the inspection camera design using a sealed deployment system opening directly into the cryostat. Right: a photo of the ProtoDUNE-SP warm inspection camera acrylic tube, immediately before installation; the acrylic tube is sealed with an acrylic dome at the bottom and can be opened at the top.

with fisheye lenses were used in these tubes during initial operation. One camera was removed without any evidence of contamination of the LAr. We plan to use other cameras during post-beam running.

Improved designs for the inspection cameras will be tested in the CITF and ProtoDUNE-SP during 2020 and 2021, focusing particularly on longevity, camera replaceability, and protection of the LAr.

### 8.2.6.3 Light-emitting system

The light-emitting system uses LEDs to illuminate the parts of the detector module in the camera's field of view with selected wavelengths (IR and visible) that cameras can detect. Performance criteria for the light-emission system include the efficiency with which the cameras can detect the light and the need to avoid adding heat to the cryostat. Very high-efficiency LEDs help reduce heat generation; one 750 nm LED [169] has a specification equivalent to 33 % conversion of electrical input power to light.

While data on how well LEDs perform at cryogenic temperatures is sparse, some studies of NASA projects [170] indicate that LEDs are more efficient at low temperatures and that emitted wavelengths may change, particularly for blue LEDs. In ProtoDUNE-SP, amber LEDs were observed to emit green light at LAr temperature (bottom right photo in figure 8.27). To avoid degradation of wavelength-shifting materials in the PD system, short wavelength LEDs are not used in the FD; LEDs will be tested in LN<sub>2</sub> to ensure their wavelength is long enough.

LEDs are placed in a ring around the outside of each camera, pointing in the same direction as the lens, to illuminate nearby parts of the detector module within the camera's field of view. Commercially available LEDs exist with a range of angular spreads that can be matched to the needs of the cameras without additional optics.

Additionally, chains of LEDs connected in series and driven with a constant-current circuit are used for broad illumination, with each LED paired in parallel with an opposite polarity LED and a resistor (see figure 8.29). This allows two different wavelengths of illumination using a single chain simply by changing the direction of the drive current, and allows continued use of an LED chain even if individual LEDs fail.

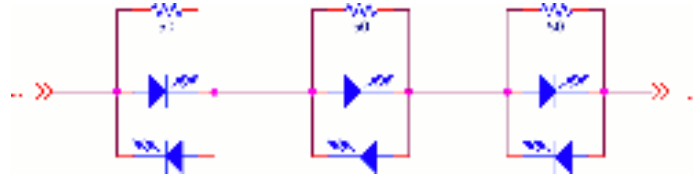


Figure 8.29. Example schematic for LED chain, allowing failure tolerance and two LED illumination spectra.

### 8.2.7 Cryogenics instrumentation test facility

The CISC consortium plans to build a cryogenic instrumentation test facility (CITF) at Fermi National Accelerator Laboratory (Fermilab) to facilitate testing of various cryogenics instrumentation devices and small-scale assemblies of CISC systems. In the past and recent times, various test facilities at Fermilab have provided access to small (< 1 ton) to intermediate (~1 ton) volumes of purified TPC-grade LAr, required for any device intended for drifting electrons for millisecond periods.

The Proton Assembly Building (PAB) facility at Fermilab houses the ICEBERG R&D cryostat and electronics (ICEBERG) 3000 liter cryostat, which enables fast turnaround testing for the DUNE CE.

The PAB facility also includes TallBo (450 liter), Blanche (500 liter), and Luke (250 liter) cryostats. In the recent past, Blanche has been used for HV studies, TallBo for PD studies, and Luke for the material test stand work. These studies have contributed to the design and testing of ProtoDUNE-SP components.

### 8.2.8 Validation in ProtoDUNE

Design validation and testing of many planned CISC systems for the SP module will be done using the data from ProtoDUNE-SP and ProtoDUNE-DP as discussed below.

- Level Meters: the same differential pressure level meters which are already validated in ProtoDUNE-SP will be used in the SP module. The same capacitive level meters currently used in ProtoDUNE-DP will be used in the SP module. These will be validated in the upcoming ProtoDUNE-DP run.
- Pressure Meters (GAR): the same high-precision pressure sensors that are already validated in ProtoDUNE-SP will be used in SP FD.
- Gas Analyzers: the same gas analyzers currently used in ProtoDUNE-SP will be used in the SP module, so they have already been validated.

- High-precision thermometer arrays in LAr: the static and dynamic T-gradient thermometers discussed in the previous sections are validated using ProtoDUNE-SP data.
- Purity Monitors: the same purity monitor basic design used in ProtoDUNE-SP will be used in the SP module. ProtoDUNE-2 at CERN provides opportunities to test any improvements to the design.
- Cameras: various types of cameras are being actively developed in both ProtoDUNE-SP and ProtoDUNE-DP so these detectors will perform validation of the designs. Future improvements can be tested in ProtoDUNE-2 at CERN.

### 8.3 Slow controls

The slow controls system collects, archives, and displays data from a broad variety of sources and provides real-time status, alarms, and warnings for detector operators. The slow control system also provides control for items such as HV systems, TPC electronics, and PD systems. Data is acquired via network interfaces. Figure 8.30 shows connections between major parts of the slow controls system and other systems.

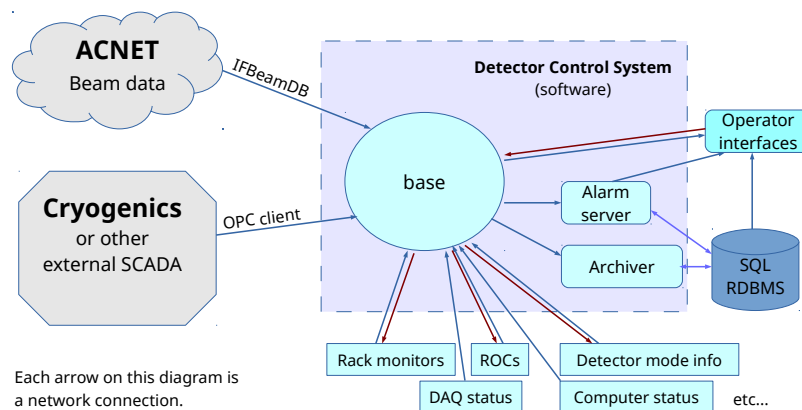


**Figure 8.30.** Typical slow controls system connections and data flow.

The ProtoDUNE-SP detector control system [161] fully met its operational requirements. Section 8.3.6 provides a short description of the ProtoDUNE-SP slow controls and its performance.

#### 8.3.1 Slow controls hardware

Slow controls is expected to need a modest amount of dedicated hardware, largely for rack monitoring, and a small amount of dedicated network and computing hardware. Slow controls also relies on common infrastructure as described in section 8.3.2.

##### 8.3.1.1 Dedicated monitoring hardware

Every rack (including those in the CUC) should have dedicated hardware to monitor rack parameters like rack protection system, rack fans, rack air temperatures, thermal interlocks with power supplies, and any interlock bit status monitoring needed for the racks. For the racks in the CUC server room,

this functionality is built into the proposed water cooled racks, as already in place at ProtoDUNE. For the racks on the detector itself, the current plan is to design and install a custom-built 1U rack-mount enclosure containing a single-board computer to control and monitor various rack parameters. Such a system has been successfully used in MicroBooNE. The design is being improved for the SBND experiment (see figure 8.31). Other slow controls hardware includes interfacing cables like adapters for communication and debugging and other specialized cables like GPIB or National Instruments cables. The cable requirements must be determined in consultation with other groups once hardware choices for various systems are finalized.

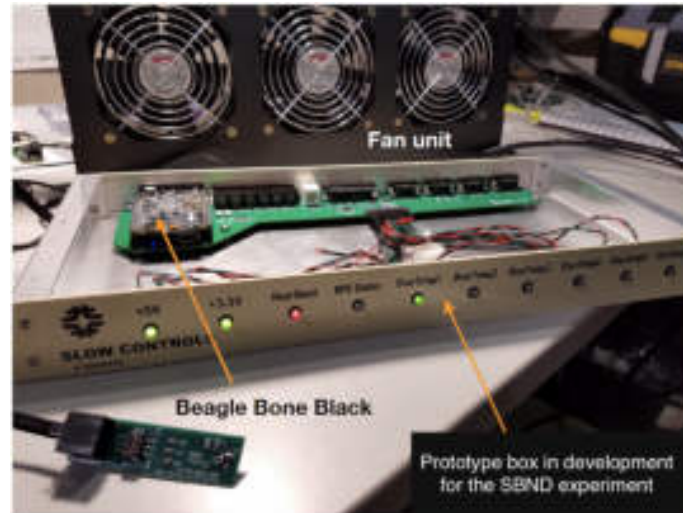


**Figure 8.31.** Rack monitoring box prototype in development for the SBND experiment based on the original design from MicroBooNE.

### 8.3.1.2 Slow controls network hardware

The slow controls data originates from the cryogenics instrumentation and from other systems as listed in table 8.5. This data is collected by software running on servers (section 8.3.1.3) housed in the underground data room in the CUC, where data is archived in a central CISC database. The instrumentation data is transported over conventional network hardware from any sensors located in the cryogenics plant. However, the readouts that are in the racks on top of the cryostats must be cautious about grounding and noise. Therefore, each rack on the cryostat has a small network switch that sends any network traffic from that rack to the CUC via a fiber transponder. This is the only network hardware specific to slow controls and will be provided by SURF's general computing infrastructure. The network infrastructure requirements are described in section 8.3.2.

### 8.3.1.3 Slow controls computing hardware

Two servers (a primary server and a replicated backup) suitable for the relational database discussed in section 8.3.3 are located in the CUC data room, with an additional two servers to service the FE monitoring interface. These additional servers would cover assembling dynamic CISC monitoring web pages from adjacent databases. Yet another server will be needed to run back-end I/O. Any special purpose software, such as iFix used by the cryogenics experts, would also run here. One or



two additional servers should accommodate these programs. Replicating this setup on a per-module basis would make commissioning and independent operation easier, accommodate different module design (and the resulting differences in database tables), and ensure sufficient capacity. These four sets of networking hardware would fit tightly into one rack or very comfortably into two.

### 8.3.2 Slow controls infrastructure

The data rate will be in the range of tens of kilobytes per second, given the total number of slow controls quantities and the update rate (see section 8.3.4), placing minimal demands on local network infrastructure. Network traffic out of SURF to Fermilab will primarily be database calls to the central CISC database, either from monitoring applications or from database replication to the offline version of the CISC database. This traffic requires little bandwidth, so the proposed general purpose links both out of the underground area at SURF and back to Fermilab can accommodate the traffic.

Up to two racks of space and appropriate power and cooling are available in the CUC's DAQ server room for CISC use. This is ample space as described in section 8.3.1.3.

### 8.3.3 Slow controls software

To provide complete monitoring and control of detector subsystems, the slow controls software includes

- the control systems base for input and output operations and defining processing logic, scan conditions, and alarm conditions;
- an alarm server to monitor all channels and send alarm messages to operators;
- a data archiver for automatic sampling and storing values for history tracking; and
- an integrated operator interface providing display panels for controls and monitoring.

In addition, the software must be able to interface indirectly with external systems (e.g., cryogenics control system) and databases (e.g., beam database) to export data into slow controls process variables (or channels) for archiving and status displays. This allows us to integrate displays and warnings into one system for the experiment operators and provides integrated archiving for sampled data in the archived database. As one possibility, an input output controller running on a central DAQ server could provide soft channels for these data. Figure 8.30 shows a typical workflow of a slow controls system.

The key features of the software require highly evolved software designed to manage real-time data exchange, scalable to hundreds of thousands of channels sampled at intervals of hours to seconds as needed. The software must be well documented, supported, and reliable. The base software must also allow easy access to any channel by name. The archiver software must allow data storage in a database with adjustable rates and thresholds so data for any channel can be easily retrieved using channel name and time range. Among other key features, the alarm server software must remember the state, support an arbitrary number of clients, and provide logic for delayed alarms and acknowledging alarms. A standard naming convention for channels will be part of the software to help handle large numbers of channels and subsystems.

The ProtoDUNE-SP detector control system software [161] provides a prototype for the FD slow controls software. In ProtoDUNE-SP, the unified control system base is WinCC OA [171], a commercial toolkit used extensively at CERN, with device interfaces supported using several standardized interface protocols. A more detailed description is in section 8.3.6 below. WinCC OA is our baseline for the FD slow control software. EPICS [172] is an alternative controls system which also meets the specifications; it is used in other neutrino experiments including MicroBooNE [4] and NOvA [173].

### 8.3.4 Slow controls quantities

The final set of quantities to monitor will ultimately be determined by the subsystems being monitored, documented in appropriate interface control documents (ICDs), and continually revised based on operational experience. The total number of quantities to monitor has been roughly estimated by taking the total number monitored in ProtoDUNE-SP[161], 7595 as of Nov. 19, 2018, and scaling by the detector length and the number of planes, giving approximately 150,000 per detector module. Quantities should update on average no more than once per minute. Transmitting a single update for each channel at that rate translates to a few thousand updates per second, or a few tens of thousands of bytes per second. While this is not a significant load on a network with an efficient slow controls protocol, it would correspond to approximately 1 TB per year per detector module if every timestamp and value were stored. The actual data volume will be lower because values are stored only if they vary from previous values by more than an amount that is adjustable channel-by-channel. Database storage also allows data to be sparsified later. No slow controls data is planned to be written to the DAQ stream. With careful management of archiving thresholds for each quantity monitored and yearly reduction of stored sample time density, the retained data volume can be reduced to a few TB over the life of the experiment.

The subsystems to be monitored include the cryogenics instrumentation described in this chapter, the other detector systems, and relevant infrastructure and external devices. Table 8.5 lists the quantities expected from each system.

### 8.3.5 Local integration

The local integration of the slow controls consists entirely of software and network interfaces with systems that are outside of the scope of the detector module. This includes the following:

- readings from the LBNF-managed external cryogenics systems, for status of pumps, flow rates, inlet, and return temperature and pressure, which are implemented via OPC-UA or a similar SCADA interface;
- beam status, such as protons-on-target, rate, target steering, and beam pulse timing, which are retrieved via IFbeam; and
- near detector status, which can be retrieved from a common slow controls database.

Integration occurs after both the slow controls and non-detector systems are in place. The LBNF-CISC interface is managed by the cryogenics systems working group in CISC (see section 8.4), which includes members from both CISC and LBNF. The IFbeam DB interface for slow controls is

Table 8.5. Slow controls quantities.

| System                                     | Quantities   |
|--|--|
| <b>Detector cryogenics instrumentation</b> |  |
| Purity monitors                            | anode and cathode charge, bias voltage and current, flash lamp status, calculated electron lifetime  |
| Thermometers                               | temperature, position of dynamic thermometers  |
| Liquid level                               | liquid level   |
| Gas analyzers                              | purity level readings  |
| Pressure meters                            | pressure readings  |
| Cameras                                    | camera voltage and current draw, temperature, heater current and voltage, lighting current and voltage   |
| <b>Other detector systems</b>              |  |
| Cryogenic internal piping                  | feedthrough gas purge flow and temperature   |
| HV systems                                 | drift HV voltage and current, end-of-field cage current and bias voltage, electron diverter bias, ground plane currents  |
| TPC electronics                            | voltage and current to electronics   |
| PD   | voltage and current for photodetectors and electronics   |
| DAQ  | warm electronics currents and voltages, run status, DAQ buffer sizes, trigger rates, data rates, GPS status, computer and disk health status, other health metrics as defined by DAQ group |
| CRP / APA                                  | bias voltages and currents   |
| <b>Infrastructure and external systems</b> |  |
| Cryogenics (external)                      | status of pumps, flow rates, inlet and return temperature and pressure (via OPC or similar SCADA interface)  |
| Beam status                                | protons on target, rate, target steering, beam pulse timing (via IFbeam)   |
| Near detector                              | near detector run status (through common slow controls database)   |
| Rack power and status                      | power distribution unit current and voltage, air temperature, fan status if applicable, interlock status   |
| <b>Detector calibration systems</b>        |  |
| Laser                                      | laser power, temperature, operation modes, other system status as defined by calibration group   |
| External neutron source                    | safety interlock status, power supply monitoring, other system status as defined by calibration group  |
| External radioactive source                | system status as defined by calibration group  |

an already well established method used in MicroBooNE, NOvA, and other Fermilab experiments. An internal near detector (ND)/FD working group can be established to coordinate detector status exchange between the near and far sites.

### 8.3.6 Validation in ProtoDUNE

The ProtoDUNE-SP detector control system has met all requirements for operation of ProtoDUNE-SP [161] and will be used for ProtoDUNE-DP. The requirements for ProtoDUNE are nearly identical to those for the SP module other than total channel count. Of particular note, the ProtoDUNE slow control system unified a heterogenous set of devices and data sources through several protocols into a single control system, as illustrated in figure 8.32. In addition to what the figure shows, data were also acquired from external cryogenics and beam systems. The topology and data flow of the system matches the general shape shown in figure 8.30.

In this control system, the unified control system base is WinCC-OA [171], a commercial SCADA system for visualizing and operating of processes, production flows, machines, and plants, used in many businesses. It was chosen at CERN as a basis for developing the control systems of the LHC experiments, the accelerators and the laboratory infrastructure for its flexibility and scalability, as well as for the openness of the architecture, allowing it to interface with many different types of hardware devices and communication protocols. Additional software developed at CERN is also used, including Joint COntrols Projects [174] and UNified Industrial COntrol System (UNICOS) [175]. WinCC-OA and the additional software developed on top of it in the past 20 years, have grown into a fairly complex ecosystem. While multiple collaboration members have experience using the ProtoDUNE-SP control system, customizing and using WinCC-OA in an effective way for developing the control system of DUNE requires proper training and a non-negligible learning effort.

As noted in sections 8.3.3 and 8.3.4, the slow control archiver will gradually accumulate terabytes of data, requiring a sizable database to store the value history and allow efficient data retrieval. Individually adjustable rates and thresholds for each channel are key to keeping this database manageable. The ProtoDUNE-SP operations provided not only a test of these features as implemented in the ProtoDUNE slow control system, but also insight into reasonable values for these archiving parameters for each system.

## 8.4 Organization and management

The organization of the CISC consortium is shown in figure 8.33. The CISC consortium board currently comprises institutional representatives from 19 institutes as shown in table 8.6. The consortium leader is the spokesperson for the consortium and responsible for the overall scientific program and managing the group. The technical leader of the consortium is responsible for managing the project for the group. Currently, the consortium has five working groups:

**Cryogenics Systems:** gas analyzers and liquid level monitors; CFD simulations;

**Argon Instrumentation:** purity monitors, thermometers, pressure meters, capacitive level meters, cameras and light emitting system, and CITF, also feedthroughs, E field simulations, instrumentation precision studies, ProtoDUNE data analysis coordination and validation;

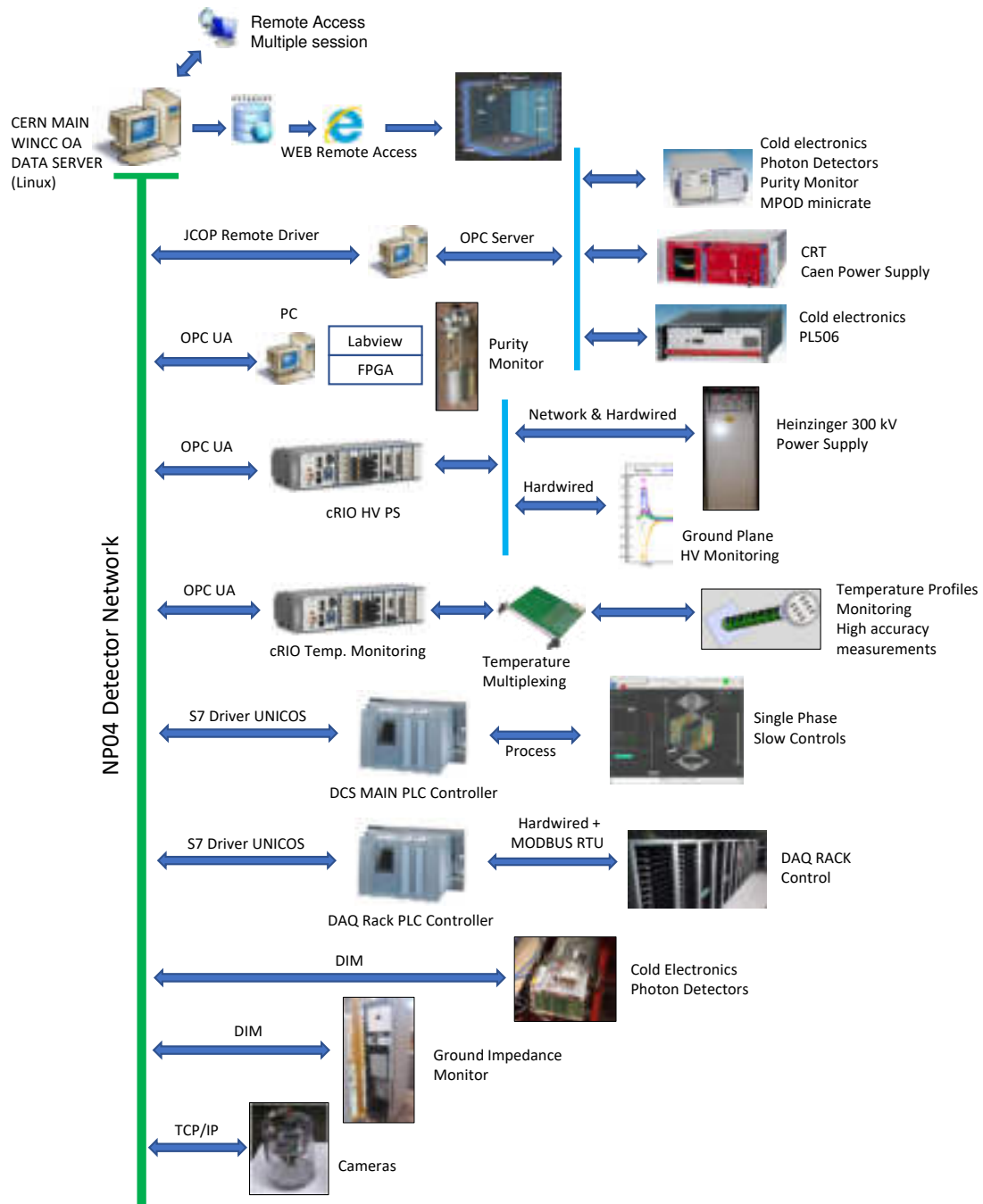


Figure 8.32. Diagram of the ProtoDUNE-SP control system topology, from [161].

2020 JINST 15 T08010

**Slow Controls Base Software and Databases:** base I/O software, alarms and archiving databases, and monitoring tools, also variable naming conventions, and slow controls quantities;

**Slow Controls Detector System Interfaces:** signal processing software and hardware interfaces (e.g., power supplies), firmware, rack hardware and infrastructure

**Slow Controls External Interfaces:** interfaces with external detector systems (e.g., cryogenics system, beam, facilities, DAQ, and near detector status).

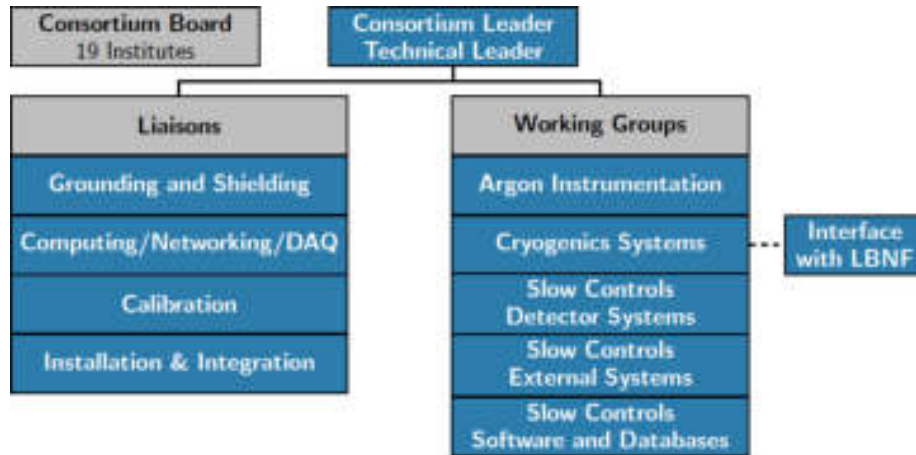


Figure 8.33. CISC Consortium organizational chart.

Moreover, because the CISC consortium broadly interacts with other groups, liaisons have been named as shown in figure 8.33. A short-term task force was recently formed to explore the need for cryogenics modeling for the consortium. A work plan for CFD simulations for both ProtoDUNE and FD was developed based on input from the task force.

#### 8.4.1 Institutional responsibilities

The CISC consortium will be a joint effort for SP and DP. A single slow controls system will be implemented to serve both the SP module and the DP module.

Design and installation of cryogenics systems (e.g., gas analyzers, liquid level monitoring) will be coordinated with LBNF, with the consortium providing resources and effort, and expertise provided by LBNF. ProtoDUNE designs for LAr instrumentation (e.g., purity monitors, thermometers, cameras) will be the basis for detector module designs. Design validation, testing, calibration, and performance will be evaluated through ProtoDUNE data.

Following the conceptual funding model envisioned for the consortium, various responsibilities have been distributed across institutions within the consortium pending final funding decisions. Table 8.7 shows the current institutional responsibilities for primary CISC subsystems. Only lead institutes are listed in the table for a given effort. For physics and simulations studies and for validation using ProtoDUNE, a number of institutes are involved. A detailed list of tasks and institutional responsibilities are presented in [176].

**Table 8.6.** Current CISC consortium board members and their institutional affiliations.

| Member Institute                           | Country |
|--|---------|
| CIEMAT                                     | Spain   |
| Instituto de Fisica Corpuscular (IFIC)     | Spain   |
| University of Warwick                      | UK      |
| University College London (UCL)            | UK      |
| Argonne National Lab (ANL)                 | USA     |
| Brookhaven National Lab (BNL)              | USA     |
| University of California, Irvine (UCI)     | USA     |
| Drexel University                          | USA     |
| Fermi National Accelerator Lab (Fermilab)  | USA     |
| University of Hawaii                       | USA     |
| University of Houston                      | USA     |
| Idaho State University (ISU)               | USA     |
| Kansas State University (KSU)              | USA     |
| University of Minnesota, Duluth (UMD)      | USA     |
| Notre Dame University                      | USA     |
| South Dakota State University (SDSU)       | USA     |
| University of Tennessee at Knoxville (UTK) | USA     |
| Virginia Tech (VT)                         | USA     |
| Boston University (BU)                     | USA     |

#### 8.4.2 Schedule

Table 8.8 shows key construction milestones for the CISC consortium leading to commissioning of the first FD module. CISC construction milestones align with the overall construction milestones of the first FD module (highlighted in orange in the table). The technology design decisions for CISC systems should be made by April 2020 followed by final design reviews in June 2020. Design decisions will largely be based on how a given system performed (technically and physics-wise) in ProtoDUNE. This is currently actively ongoing with the ProtoDUNE-SP instrumentation data. As noted in section 8.2.8, the current plan is to deploy improved designs of static and dynamic T-gradient thermometers, purity monitors, long (DP-style) level meters and cameras to be validated in ProtoDUNE-2. The production of systems aimed for ProtoDUNE-2 SP should be finished by January 2021 followed by assembly and deployment in March 2021.

Designs may need review based on performance in ProtoDUNE-2 and any modifications will be incorporated into the final design before the start of production of CISC systems for the FD in April 2023. This will be followed by assembly of the systems underground in the detector cavern in July 2024. Installation of instrumentation devices will start in September 2024 following the beneficial occupancy of the interior of the cryostat. Installing gas analyzers, level meters, individual temperature sensors, static T-gradient thermometers, and support structure for all instrumentation

**Table 8.7.** Institutional responsibilities in the CISC consortium.

| CISC Sub-system                       | Institutional Responsibility             |
|---------------------------------------|--|
| Purity Monitors                       | UCI, Houston                             |
| Static T-gradient monitors            | IFIC                                     |
| Dynamic T-gradient monitors           | Hawaii                                   |
| Individual Sensors                    | IFIC                                     |
| Readout System for Thermometers       | IFIC, Hawaii, CIEMAT                     |
| Pressure Meters                       | UTK                                      |
| Cold Cameras                          | KSU, BNL                                 |
| Warm Cameras                          | KSU, BNL                                 |
| Light-emitting System (for cameras)   | Drexel                                   |
| Gas Analyzers                         | FNAL, LBNF                               |
| Differential Pressure Level Meters    | LBNF                                     |
| Capacitive Level Meters               | Notre Dame                               |
| CITF                                  | FNAL, ANL                                |
| CFD Simulations                       | SDSU, ANL                                |
| Other Simulation & Validation Studies | Number of Institutes                     |
| Slow Controls Hardware                | UMD, UTK, Drexel                         |
| Slow Controls Infrastructure          | UMD, UTK                                 |
| Slow Controls Base Software           | KSU, UTK, BU, Drexel, Warwick, ANL, IFIC |
| Slow Controls Signal Processing       | A number of institutes                   |
| Slow Controls External Interfaces     | VT, UTK, UMD                             |

devices will be finished before installing TPC, but installation of dynamic T-gradient thermometers, purity monitors, pressure meters and cameras will occur afterward. CISC will work closely with LBNF to coordinate installation of the cryogenics systems and instrumentation devices. For slow controls, the goal is to have the full slow controls system commissioned and integrated into remote operations at least three months before the SP module is ready for operations.

### 8.4.3 Risks

Table 8.9 lists the possible risks identified by the CISC consortium along with corresponding mitigation strategies. A more detailed list of risks with additional descriptions can be found in [177]. The table shows 18 risks, all at medium or low level, mitigated with necessary steps and precautions. More discussion on all medium-level risks are provided in the text below.

- Risk 01: the risk associated with ProtoDUNE-SP-based designs being inadequate for FD, is important because this requires early validation from ProtoDUNE data so R&D of alternate designs can be timely. With ProtoDUNE-SP data now available, the consortium is focused on validating instrumentation designs.



**Table 8.8.** CISC construction schedule milestones leading to commissioning of the first FD module. Key DUNE dates and milestones, defined for planning purposes in this TDR, are shown in orange. Dates will be finalized following establishment of the international project baseline.

| Milestone   | Date (Month YYYY) |
|---|-------------------|
| Technology Decision Dates   | April 2020        |
| Final Design Review Dates   | June 2020         |
| Start of module 0 component production for ProtoDUNE-2                                      | August 2020       |
| End of module 0 component production for ProtoDUNE-2  | January 2021      |
| Start of ProtoDUNE-SP-II installation   | March 2021        |
| Start of ProtoDUNE-DP-II installation   | March 2022        |
| South Dakota Logistics Warehouse available  | April 2022        |
| production readiness review dates   | September 2022    |
| Beneficial occupancy of cavern 1 and CUC  | October 2022      |
| Start procurement of CISC hardware  | December 2022     |
| CUC counting room accessible  | April 2023        |
| Start of production of CISC hardware  | April 2023        |
| Top of detector module #1 cryostat accessible   | January 2024      |
| End of CISC hardware production   | April 2024        |
| Start integration of CISC hardware in the cavern  | July 2024         |
| Start of detector module #1 TPC installation  | August 2024       |
| Installation of gas analyzers and support structure for all instrumentation devices         | September 2024    |
| Installation of individual sensors, static T-gradient thermometers, and level meters        | November 2024     |
| Top of detector module #2 cryostat accessible   | January 2025      |
| All slow controls hardware, infrastructure, & networking installed                          | February 2025     |
| Slow controls software for I/O, alarms, archiving, displays installed on production systems | May 2025          |
| End of detector module #1 TPC installation  | May 2025          |
| Install dynamic T-gradient monitors, cameras, purity monitors, and pressure meters          | June 2025         |
| Install all feedthroughs for instrumentation devices  | July 2025         |
| Start of detector module #2 TPC installation  | August 2025       |
| Install slow control expert interfaces for all systems in time for testing                  | September 2025    |
| End of detector module #2 TPC installation  | May 2026          |
| Full slow controls systems commissioned and integrated into remote operations               | July 2026         |

2020 JINST 15 T08010

- Risk 06: temperature sensors in the dynamic T-gradient monitor are calibrated using two methods: lab calibration to 0.002 K (as in the static T-gradient monitor case) and in situ cross-calibration moving the system vertically. Disagreement between the two methods can occur. In order to mitigate this we need to investigate and improve both methods, specifically the laboratory calibration since this is the only one possible for sensors behind APAs, and top/bottom of the detector.
- Risk 10: this risk involves an inability to build a working prototype for cold cameras during R&D phase that meets all the requirements & safety, e.g., that cold camera prototypes fail longevity tests or show low performance (e.g. bad resolution). This risk originates from past experience with cold cameras that became non-operational after a period of time in LAr or showed low performance. In order to address this, we plan to pursue further R&D to improve thermal insulation and heaters, develop alternative camera models, etc. If problems persist one can use the cameras in the ullage (cold or inspection) with the appropriate field of view and lighting such that elements inside LAr can be inspected during filling.
- Risk 12: cameras are delicate devices and some of them located near HV devices can be destroyed by HV discharges. This can be mitigated by ensuring that most important cold cameras have enough redundancy such that the loss of one camera does not compromise the overall performance. In the case of inspection cameras, we can simply replace them.
- Risk 17: the gas analyzers and level meters may fail as these are commercial devices purchased at some point in their product cycle and cannot be required to last 20 years. Typical warranties are ~1 year from date of purchase. The active electronics parts of both gas analyzers and level meters are external to the cryostat so they can be replaced. To mitigate this, provisions will be made for future replacement in case of failure or loss of sensitivity. Also, the risk is not high since we have purity monitors in the filtration system that can cover the experiment during the time gas analyzers are being replaced or repaired.

Related to risks 12, 16 and 18, ageing is an important aspect for several monitors, especially for those that are inaccessible. The ProtoDUNE tests demonstrate that the devices survive the commissioning phase, and we continue to learn from ProtoDUNE experience. In addition to ProtoDUNE, other tests are planned. For example, in the case of purity monitors, photocathodes are expected to survive the first five years and if we prevent running them with high frequency at low purity (lifetime < 3 ms), ageing can be prevented for a longer time. To understand long-term ageing, R&D is planned at CITF and at member institute sites for many of the devices. Systems that are replaceable, such as inline purity monitors, gas analyzers, and inspection cameras, can be replaced when failures occur and maintained for the lifetime of the experiment.

**Table 8.9:** CISC risks (P=probability, C=cost, S=schedule) The risk probability, after taking into account the planned mitigation activities, is ranked as L (low < 10 %), M (medium 10 % to 25 %), or H (high > 25 %). The cost and schedule impacts are ranked as L (cost increase < 5 %, schedule delay < 2 months), M (5 % to 25 % and 2–6 months, respectively) and H (> 20 % and > 2 months, respectively).

| ID            | Risk   | Mitigation  | P | C | S |
|---------------|--|---|---|---|---|
| RT-SP-CISC-01 | Baseline design from ProtoDUNEs for an instrumentation device is not adequate for DUNE far detectors | Focus on early problem discovery in ProtoDUNE so any needed redesigns can start as soon as possible.  | L | M | L |
| RT-SP-CISC-02 | Swinging of long instrumentation devices (T-gradient monitors or PrM system)                         | Add additional intermediate constraints to prevent swinging.  | L | L | L |
| RT-SP-CISC-03 | High E-fields near instrumentation devices cause dielectric breakdowns in LAr                        | CISC systems placed as far from cathode and FC as possible.   | L | L | L |
| RT-SP-CISC-04 | Light pollution from purity monitors and camera light emitting system                                | Use PrM lamp and camera lights outside PDS trigger window; cover PrM cathode to reduce light leakage. | L | L | L |
| RT-SP-CISC-05 | Temperature sensors can induce noise in cold electronics   | Check for noise before filling and remediate, repeat after filling. Filter or ground noisy sensors.   | L | L | L |
| RT-SP-CISC-06 | Disagreement between lab and <i>in situ calibrations for ProtoDUNE-SP dynamic T-gradient monitor</i> | Investigate and improve both methods, particularly laboratory calibration.                            | M | L | L |
| RT-SP-CISC-07 | Purity monitor electronics induce noise in TPC and PDS electronics.                                  | Operate lamp outside TPC+PDS trigger window. Surround and ground light source with Faraday cage.      | L | L | L |
| RT-SP-CISC-08 | Discrepancies between measured temperature map and CFD simulations in ProtoDUNE-SP                   | Improve simulations with additional measurements inputs; use fraction of sensors to predict others    | L | L | L |
| RT-SP-CISC-09 | Difficulty correlating purity and temperature in ProtoDUNE-SP impairs understanding cryo system.     | Identify causes of discrepancy, modify design. Calibrate PrM differences, correlate with RTDs.        | L | L | L |
| RT-SP-CISC-10 | Cold camera R&D fails to produce prototype meeting specifications & safety requirements              | Improve insulation and heaters. Use cameras in ullage or inspection cameras instead.                  | M | M | L |
| RT-SP-CISC-11 | HV discharge caused by inspection cameras  | Study E-field in and on housing and anchoring system. Test in HV facility.                            | L | L | L |
| RT-SP-CISC-12 | HV discharge destroying the cameras  | Ensure sufficient redundancy of cold cameras. Warm cameras are replaceable.                           | L | M | L |

|               |   |   |   |   |   |
|---------------|---|---|---|---|---|
| RT-SP-CISC-13 | Insufficient light for cameras to acquire useful images                           | Test cameras with illumination similar to actual detector.  | L | L | L |
| RT-SP-CISC-14 | Cameras may induce noise in cold electronics                                      | Continued R&D work with grounding and shielding in realistic conditions.                          | L | L | L |
| RT-SP-CISC-15 | Light attenuation in long optic fibers for purity monitors                        | Test the max. length of usable fiber, optimize the depth of bottom PrM, number of fibers.         | L | L | L |
| RT-SP-CISC-16 | Longevity of purity monitors  | Optimize PrM operation to avoid long running in low purity. Technique to protect/recover cathode. | L | L | L |
| RT-SP-CISC-17 | Longevity: Gas analyzers and level meters may fail.                               | Plan for future replacement in case of failure or loss of sensitivity.                            | M | M | L |
| RT-SP-CISC-18 | Problems in interfacing hardware devices (e.g. power supplies) with slow controls | Involve slow control experts in choice of hardware needing control/monitoring.                    | L | L | L |

#### 8.4.4 Interfaces

CISC subsystems interface with all other detector subsystems and potentially impact the work of all detector consortia, as well as some working groups (e.g., physics, software and computing, beam instrumentation), and technical coordination, requiring interactions with all of these entities. We also interact heavily with LBNF beam and cryogenics groups. Detailed descriptions of CISC interfaces are maintained in the DUNE DocDB. A brief summary is provided in this section. Table 8.10 lists the IDs of the different DocDB documents as well as their highlights. Descriptions of the interfaces and interactions that affect many systems are given below.

CISC interacts with the detector consortia because CISC will provide status monitoring of all important detector subsystems along with controls for some components of the detector. CISC will also consult on selecting different power supplies to ensure monitoring and control can be established with preferred types of communication. Rack space distribution and interaction between slow controls and other modules from other consortia will be managed by technical coordination in consultation with those consortia.

CISC will work with LBNF to determine whether heaters and RTDs are needed on flanges. If so, CISC will specify the heaters and RTDs, and will provide the readout and control, while the responsibility for the actual hardware will be discussed with the different groups.

Installing instrumentation devices will interfere with other devices and must be coordinated with the appropriate consortia. On the software side, CISC must define, in coordination with other consortia/groups, the quantities to be monitored/controlled by slow controls and the corresponding alarms, archiving, and GUIs.

#### 8.4.5 Installation, integration, and commissioning

##### 8.4.5.1 Purity monitors

The purity monitor system will be built in modules, so it can be assembled outside the cryostat leaving few steps to complete inside the cryostat. The assembly itself comes into the cryostat with the individual purity monitors mounted to support tubes, with no HV cables or optical fibers yet installed. The support tube at the top and bottom of the assembly is then mounted to the brackets

**Table 8.10.** CISC system interface links.

| Interfacing System      | Description  | Linked Reference |
|-------------------------|--|------------------|
| APA                     | static T-gradient monitors, cameras, and lights  | DocDB 6679 [13]  |
| PD system               | PrMs, light emitting system for cameras  | DocDB 6730 [87]  |
| TPC Electronics         | noise, power supply monitoring   | DocDB 6745 [69]  |
| HV Systems              | shielding, bubble generation by inspection camera, cold camera locations, ground planes                                | DocDB 6787 [34]  |
| DAQ                     | description of CISC data storage, allowing bi-directional communications between DAQ and CISC.                         | DocDB 6790 [135] |
| Calibration             | multifunctional CISC/CITF ports; space sharing around ports  | DocDB 7072 [122] |
| Physics                 | indirect interfaces through calibration, tools to extract data from the slow controls database                         | DocDB 7099 [178] |
| Software & Computing    | slow controls database design and maintenance  | DocDB 7126 [179] |
| Cryogenics              | must be designed and implemented. purity monitors, gas analyzers, interlock mechanisms to prevent contamination of LAr | -                |
| Beam                    | beam status  | -                |
| TC Facility             | significant interfaces at multiple levels  | DocDB 6991 [180] |
| TC Installation         | significant interfaces at multiple levels  | DocDB 7018 [181] |
| TC Integration Facility | significant interfaces at multiple levels  | DocDB 7045 [182] |

inside the cryostat, and the brackets attached to the cables trays and/or the detector support structure. At much the same time, the FE electronics and light source can be installed on the top of the cryostat, and the electronics and power supplies can be installed in the electronics rack.

Integration begins by running the HV cables and optical fibers to the purity monitors, through the top of the cryostat. These cables are attached to the HV feedthroughs with sufficient length to reach each purity monitor inside the cryostat. The cables are run along cable trays through the port reserved for the purity monitor system. Each purity monitor will have three HV cables that connect it to the feedthrough and then further along to the FE electronics. The optical fibers are then run through the special optical fiber feedthrough, into the cryostat, and guided to the purity monitor system either using the cables trays or guide tubes, depending on which solution is adopted. This should protect fibers from breaking accidentally as the rest of the detector and instrumentation installation continues. The optical fibers are then run inside the purity monitor support tube and to the appropriate purity monitor, terminating the fibers at the photocathode of each monitor while protecting them from breaking near the purity monitor system itself.

Integration continues as the HV cables are connected through the feedthrough to the system FE electronics; then optical fibers are connected to the light source. The cables connecting the FE electronics and the light source to the electronics rack are also run and connected at this time. This allows the system to be turned on and the software to begin testing the various components and connections. Once all connections are confirmed successful, integration with the slow controls system begins, first by establishing communication between the two systems and then transferring data between them to ensure successful exchange of important system parameters and measurements.

Commissioning the purity monitor system begins once the cryostat is purged and a gaseous argon atmosphere is present. At this time, the HV for the purity monitors is ramped up without risk of discharge through the air, and the light source turned on. Although the drift electron lifetime in the gaseous argon would be very large and therefore not measurable with the purity monitors themselves, the signal strength at both the cathode and anode will give a good indication of how well the light source generates drift electrons from the photocathode. Comparing the signal strengths at the anode and cathode will indicate whether the electrons successfully drift to the anode. Although quality assurance (QA) and quality control (QC) should make it unlikely for a purity monitor to fail this final test, if that does happen then the electric and optical connections can be fixed before filling.

### 8.4.5.2 Thermometers

Static T-gradient monitors must be installed before the outer APAs, ideally right after the pipes are installed. The profilers are preassembled before they are delivered to SURF. Installation will follow these steps:

1. anchor the stainless steel bottom plates to the four bolts on the bottom corner of the cryostat,
2. anchor the stainless steel support holding the two strings to the four bolts on the top corner of the cryostat,
3. unroll the array with the help of the scissor lift,
4. anchor the strings to the bottom stainless steel support,
5. check and adjust tension and verticality,
6. review all cable and sensor supports,
7. route cable from the top anchoring point to the two DSS ports, and
8. plan to plug sensors into IDC-4 connectors later, just before moving the corresponding APA into its final position.

Individual temperature sensors on pipes and cryostat floor are installed immediately after installing the static T-gradient monitors. First, vertical stainless steel strings for cable routing are installed following a procedure similar to the one described above for the static T-gradient monitors. Next, we anchor all cable supports to pipes. Then each cable is routed individually starting from the sensor end (with IDC-4 female connector but without the sensor) to the corresponding cryostat

port. Once all cables going through the same port have been routed, we cut the cables to the same length, so they can be properly assembled into the corresponding connector(s). To avoid damaging the sensors, they are installed later (by plugging the IDC-4 male connector on the sensor PCB to the IDC-4 female connector on the cable end), just before unfolding the bottom GPs.

For the SP, individual sensors on the top GP must be integrated with the GPs. For each CPA (with its corresponding four GP modules) going inside the cryostat, cable and sensor supports will be anchored to the GP threaded rods as soon as possible. Once the CPA is moved into its final position and its top GPs are ready to be unfolded, sensors on these GPs are installed. Once unfolded, cables exceeding the GP limits can be routed to the corresponding cryostat port using either neighboring GPs or DSS I-beams.

Dynamic T-gradient monitors are installed after the TPC components are in place. Figure 8.8 shows the design of the dynamic T-gradient monitor with its sensor carrier rod, enclosure above the cryostat, and stepper motor and figure 8.9 shows detailed views of key components. Each monitor comes in several segments with sensors and cabling already in place. Additional slack will be provided at segment joints to make installation easier. Segments of the sensor carrier rod with preattached sensors are fed into the flange one at a time. Each segment, as it is fed into the cryostat, is held at the top with a pin that prevents the segment from sliding all the way in. The next segment is connected at that time to the previous segment. Then the pin is removed, the first segment is pushed down, and the next segment top is held with the pin at the flange. This process is repeated for each segment until the entire sensor carrier rod is in place. Next, the enclosure is installed on top of the flange, starting with the six-way cross at the bottom of the enclosure. (See figure 8.9, right.) Again, extra cable slack at the top will be provided to ease connection to the D-sub flange and to allow the entire system to move vertically. The wires are connected to a D-sub connector on the feedthrough on one side port of the cross. Finally, a crane positions the remainder of the enclosure above the top of the cross. This enclosure includes the mechanism used to move the sensor rod, which is preassembled with the motor in place on the side of the enclosure, and the pinion and gear used to move the sensor inside the enclosure. The pinion gets connected to the top of the rod. The enclosure is then connected to top part of the cross, which finishes the installation of the dynamic T-gradient monitor.

Commissioning all thermometers will occur in several steps. In the first stage, only cables are installed, so the readout performance and the noise level inside the cryostat is tested with precision resistors. Once sensors are installed, the entire chain is checked again at room temperature. Spare cables, connectors and sensors are available for replacement at SURF if needed. The final commissioning phase takes place during and after cryostat filling.

### 8.4.5.3 Gas analyzers

The gas analyzers are installed before the piston purge and gas recirculation phases of the cryostat commissioning. They are installed near the tubing switchyard to minimize tubing run length and for convenience when switching the sampling points and gas analyzers. Because each is a standalone module, a single rack with shelves is adequate to house the modules.

For integration, the gas analyzers typically have an analog output (4 mA to 20 mA or 0 V to 10 V), which maps to the input range of the analyzers. They also usually have several relays to indicate the scale they are currently running. These outputs can be connected to the slow controls for

readout. However, using a digital readout is preferable because this gives a direct analyzer reading at any scale. Currently, the digital output connections are RS-232, RS-485, USB, and Ethernet. The preferred option is chosen at the time of purchase. The readout usually responds to a simple set of text query commands. Because of the natural time scales of the gas analyzers and lags in gas delivery times (which depend on the length of the tubing run), sampling every minute is adequate. Our current plan is to record both analog and digital signals to have both outputs available.

The analyzers must be brought online and calibrated before beginning the gas phase of the cryostat commissioning. Calibration varies by module because they are different, but calibration often requires using argon gas with zero contaminants, and argon gas with a known level of the contaminant to check the scale. Contaminants are usually removed with a local inline filter for the first gas sample. This gas phase usually begins with normal air, with the more sensitive analyzers valved off at the switchyard to prevent overloading their inputs (and potentially saturating their detectors). As the argon purge and gas recirculation progress, the various analyzers are valved back in when the contaminant levels reach the upper limits of the analyzer ranges.

#### **8.4.5.4 Liquid level monitoring**

Installing differential pressure level meters is the responsibility of LBNF, but the capacitive level meters fall within CISC's scope. The exact number of capacitive level meters must still be decided. There will be at least four, located at the four corners of the cryostat. They will be attached to the M10 bolts in the cryostat corners after the detector is installed. Cables will be routed to the appropriate DSS port. If additional capacitive level meters are needed in the central part of the cryostat, those will be installed before the nearby APAs.

#### **8.4.5.5 Pressure meters**

Installing pressure meters is the responsibility of CISC. A total of six sensors will be mechanically installed in two dedicated flanges (three sensors each) at opposite sides of the cryostat after the detector is installed. Cables will be routed through the same dedicated port assigned for these devices. The pressure signals (absolute and relative) are read and converted to standard 4–20 mA current loop signals. A twisted pair shielded cable connects the sensors to the slow controls PLC controller using software to convert electrical signals to pressure values.

#### **8.4.5.6 Cameras and light emitting system**

Installing fixed cameras is simple in principle, but involves a considerable number of interfaces. The enclosure of each camera has exterior threaded holes to facilitate mounting on the cryostat wall, cryogenic internal piping, or DSS. Each enclosure is attached to a gas line to maintain appropriate underpressure in the fill gas, therefore an interface with cryogenic internal piping will be necessary. Each camera has a cable (coaxial or optical) for the video signal and a multiconductor cable for power and control. These get run through cable trays to flanges on assigned instrumentation feedthroughs.

The inspection camera is designed to be inserted and removed on any instrumentation feedthrough equipped with a gate valve at any time during operation. Installing the gate valves and purge system for instrumentation feedthroughs falls under cryogenic internal piping.



Installing fixed lighting sources separate from the cameras requires mounting on cryostat wall, cryogenic internal piping, or DSS, and multiconductor cables for power run through cable trays to flanges on assigned instrumentation feedthroughs.

#### **8.4.5.7 Slow controls hardware**

Slow controls hardware installation includes installing multiple servers, network cables, any specialized cables needed for device communication, and possibly some custom-built hardware to monitor racks. The installation sequence will be planned with the facilities group and other consortia. The network cables and rack monitoring hardware will be common across many racks and will be installed first as part of the basic rack installation, to be led by the facilities group. Specialized cables needed for slow controls and servers are installed after the common rack hardware. The selection and installation of these cables will be coordinated with other consortia, and servers will be coordinated with the DAQ group.

#### **8.4.5.8 Transport, handling, and storage**

Most instrumentation devices will be shipped in pieces to SURF via the South Dakota Warehouse Facility (SDWF) and mounted on-site. Instrumentation devices are in general small, except for the support structures for purity monitors and dynamic T-gradient monitors, which will cover the entire height of the cryostat. The load on those structures is relatively small ( $< 100$  kg), so they can be fabricated in sections of less than 3 m, which can be easily transported to SURF, down the shaft, and through the tunnels. All instrumentation devices except the dynamic T-gradient monitors can be moved into the cryostat without the crane. The dynamic T-gradient monitors, which are introduced into the cryostat from above, require a crane for the installation of the external enclosure (with preassembled motor, pinion and gear).

#### **8.4.6 Quality control**

The manufacturer and the institution in charge of device assembly will conduct a series of tests to ensure the equipment can perform its intended function as part of QC. QC also includes post-fabrication tests and tests run after shipping and installation. For complex systems, the entire system will be tested before shipping. Additional QC procedures can be performed underground after installation.

The planned tests for each subsystem are described below.

##### **8.4.6.1 Purity monitors**

The purity monitor system will undergo a series of tests to ensure the system performs as intended. These tests include electronic tests with a pulse generator, mechanical and electrical connectivity tests at cryogenic temperatures in a cryostat, and vacuum tests for short and full assemblies in a dewar and in a long vacuum tube.

The QC tests for FD purity monitors begin with testing individual purity monitors in vacuum after each is fabricated and assembled. This test checks the amplitude of the signal generated by the drift electrons at the cathode and the anode to ensure the photocathode can provide sufficient numbers of photoelectrons to measure the signal attenuation with the required precision, and that

the field gradient resistors all work properly to maintain the drift field. A smaller version of the assembly with all purity monitors installed will be tested at the CITF to ensure the full system performs as expected in LAr.

Next, the entire system is assembled on the full-length mounting tubes to check the connections along the way. Ensuring that all electric and optical connections are operating properly during this test reduces the risk of problems once the full system is assembled and ready for the final test in vacuum. The fully assembled system is placed in the shipping tube, which serves as a vacuum chamber, and tested at SURF before the system is inserted into the cryostat. During insertion, electrical connections are tested continuously with multimeters and electrometers.

#### 8.4.6.2 Thermometers

**Static T-gradient thermometers.** Static T-gradient monitors undergo three type of tests at the production site before shipment to SURF: a mechanical rigidity test, a calibration of all sensors, and a test of all electrical cables and connectors. The mechanical rigidity is tested by mounting the static T-gradient monitor between two dummy cryostat corners mounted 15 m apart. The tension of the strings is set to match the tension that would occur in a vertical deployment in LAr, and the deflection of the sensor and electrical cable strings is measured and compared to the expected value; this is to ensure any swinging or deflection of the deployed static T-gradient monitor will be  $< 5$  cm, mitigating any risk of touching the anode plane assemblies. The laboratory calibration of sensors will be performed as explained in section 8.2.1. The main concern is reproducibility of results because sensors could change resistance and hence their temperature scale when undergoing successive immersions in LAr. In this case, the calibration procedure itself provides QC because each set of sensors goes through five independent measurements. Sensors with RMS variation outside the requirement (2 mK for ProtoDUNE-SP) are discarded. This calibration also serves as QC for the readout system (similar to the final one) and of the PCB-sensor-connector assembly. Finally, the cable-connector assemblies are tested; sensors must measure the expected values with no additional noise introduced by either cable or connector.

An integrated system test is conducted at a LAr test facility at the production site, which has sufficient linear dimension ( $>2$  m) to test a good portion of the system. This ensures that the system operates in LAr at the required level of performance. The laboratory sensor calibration is compared with the in situ calibration of the dynamic T-gradient monitors by operating both dynamic and static T-gradient monitors simultaneously.

The last phase of QC takes place after installation. The verticality of each array is checked, and the tensions in the stainless steel strings adjusted as necessary. Before closing the flange, the entire readout chain is tested. This allows a test of the sensor-connector assembly, the cable-connector assemblies at both ends, and the noise level inside the cryostat. If any sensor presents a problem, it is replaced. If the problem persists, the cable is checked and replaced as needed.

**Dynamic T-gradient thermometers.** The dynamic T-gradient monitor consists of an array of high-precision temperature sensors mounted on a vertical rod. The rod can move vertically to cross-calibrate the temperature sensors in situ. We will use the following tests to ensure that the dynamic T-gradient monitor delivers vertical temperature gradient measurements with a precision of a few mK.

- Before installation, temperature sensors are tested in LN<sub>2</sub> to verify correct operation and to set the baseline calibration for each sensor with respect to the absolutely calibrated reference sensor.
- Warm and cold temperature readings are taken with each sensor after it is mounted on the PCB and the readout cables are soldered.
- The sensor readout is taken for all sensors after the cold cables are connected to electric feedthroughs on the flange and the warm cables outside of the cryostat are connected to the temperature readout system.
- The stepper motor is tested before and after connecting to the gear and pinion system.
- The fully assembled rod is connected to the pinion and gear and moved with the stepper motor on a high platform many times to verify repeatability, possible offsets, and any uncertainty in the positioning. Finally, repeating this test so many times will verify the sturdiness of the system.
- The full system is tested after it is installed in the cryostat; both motion and sensor operation are tested by checking sensor readout and vertical motion of the system.

**Individual sensors.** To address the quality of individual precision sensors, the same method as for the static T-gradient monitors is used. The QC of the sensors is part of the laboratory calibration. After mounting six sensors with their corresponding cables, a SUBD-25 connector is added, and the six sensors tested at room temperature. All sensors must give values within specifications. If any of the sensors present problems, they are replaced. If the problem persists, the cable is checked and replaced as needed.

For standard RTDs to be installed on the cryostat walls, floor, and roof, calibration is not an issue. Any QC required for associated cables and connectors is performed following the same procedure as for precision sensors.

#### 8.4.6.3 Gas analyzers

The gas analyzers will be guaranteed by the manufacturer. However, once received, the gas analyzer modules are checked for both *zero* and the *span* values using a gas-mixing instrument and two gas cylinders, one having a zero level of the gas analyzer contaminant species and the other cylinder with a known percentage of the contaminant gas. This verifies the proper operation of the gas analyzers. When they are installed at SURF, this process is repeated before commissioning the cryostat. Calibrations will need to be repeated per manufacturer recommendations over the gas analyzer lifetime.

#### 8.4.6.4 Liquid level monitoring

The manufacturer will provide the QC for the differential pressure level meters; further QC during and after installation is the responsibility of LBNF.

The capacitive sensors will be tested with a modest sample of LAr in the laboratory before they are installed. After installation, they are tested in situ using a suitable dielectric in contact with the sensor.

#### 8.4.6.5 Pressure meters

The manufacturer will provide the QC for the pressure meters; further QC during and after installation is the responsibility of CISC.

The pressure sensors will be tested with a modest sample of gaseous argon in the laboratory before they are installed. After installation, they are tested in situ at atmospheric pressure. The whole pressure readout chain, (including slow controls PLC and software protocol) will also be tested and cross-checked with LBNF pressure sensors.

#### 8.4.6.6 Cameras

Before transport to SURF, each cryogenic camera unit (comprising the enclosure, camera, and internal thermal control and monitoring) is checked for correct operation of all features, for recovery from 87 K non-operating mode, for leakage, and for physical defects. Lighting systems are similarly checked. Operations tests will verify correct current draw, image quality, and temperature readback and control. The movable inspection camera apparatus are inspected for physical defects and checked for proper mechanical operation before shipping. A checklist is created for each unit, filed electronically in the DUNE logbook, and a hard copy sent with each unit.

Before installation, each fixed cryogenic camera unit is inspected for physical damage or defects and checked at the CITF for correct operation of all features, for recovery from 87 K non-operating mode, and for contamination of the LAr. Lighting systems are similarly checked. Operations tests verify correct current draw, image quality, and temperature readback and control. After installation and connection of wiring, fixed cameras and lighting are again checked for operation. The movable inspection camera apparatus is inspected for physical defects and, after integration with a camera unit, tested in the facility for proper mechanical and electronic operation and cleanliness before being installed or stored. A checklist will be completed for each QC check and filed electronically in the DUNE logbook.

#### 8.4.6.7 Light-emitting system

The entire light-emitting system is checked before installation to ensure functionality of light emission. Initial testing of the system (see figure 8.29) begins with measuring the current when low voltage (1 V) is applied, to check that the resistive LED failover path is correct. Next, the forward voltage is measured using nominal forward current to check that it is within 10% of the nominal forward voltage drop of the LED, that all of the LEDs are illuminated, and that each LED is visible over the nominal angular range. If the LEDs are infrared, a video camera with the IR filter removed is used for a visual check. This procedure is then duplicated with the current reversed for LEDs oriented in the opposite direction. Initial tests are performed at room temperature and then repeated in LN<sub>2</sub>. Color shifts in the LEDs are expected and will be noted. A checklist is completed for each QC check and filed electronically in the DUNE logbook.

Room temperature tests are repeated during and immediately after installation to ensure that the system has not been damaged during transportation or installation. Functionality checks of the LEDs are repeated after the cameras are installed in the cryostat.

#### 8.4.6.8 Slow controls hardware

Networking and computing systems will be purchased commercially, requiring manufacturer's QA. However, the new servers are tested after delivery to confirm they suffered no damage during shipping. The new system is allowed to burn in overnight or for a few days, running a diagnostics suite on a loop in order to validate the manufacturer's QA process.

The system is shipped directly to SURF where an on-site expert boots the systems and does basic configuration. Specific configuration information is pulled over the network, after which others may log in remotely to do the final setup, minimizing the number of people underground.

#### 8.4.7 Safety

Safety is of critical importance during all phases of the CISC project, including R&D, laboratory calibration and testing, mounting tests, and installation. Safety experts review and approve the initial safety planning for all phases as part of the initial design review, as well as before implementation. All documentation of component cleaning, assembly, testing, and installation will include a section on relevant safety concerns and will be reviewed during appropriate pre-production reviews.

Several areas are of particular importance to CISC.

- Hazardous chemicals (e.g., epoxy compounds used to attach sensors to cryostat inner membrane) and cleaning compounds: all chemicals used will be documented at the consortium management level, with a material safety data sheet and approved handling and disposal plans in place.
- Liquid and gaseous cryogens used in calibrating and testing: LN<sub>2</sub> and LAr are used to calibrate and test instrumentation devices. Full hazard analysis plans will be in place at the consortium management level for full module or module component testing that involves cryogens. These safety plans will be reviewed in appropriate pre-production and production reviews.
- High voltage safety: purity monitors have a voltage of ~2 kV. Fabrication and testing plans will show compliance with local HV safety requirements at any institution or laboratory that conducts testing or operation, and this compliance will be reviewed as part of the standard review process.
- Working at heights: some fabrication, testing, and installation of CISC devices require working at heights. Both T-gradient monitors and purity monitors, which span the height of the detector, require working at heights exceeding 10 m. Temperature sensors installed near the top cryostat membrane and cable routing for all instrumentation devices also require working at heights. The appropriate safety procedures including lift and harness training will be designed and reviewed.
- Falling objects: all work involving heights have associated risks of falling objects. The corresponding safety procedures, including proper helmet use and a well restricted safety area, will be included in the safety plan.

## Chapter 9

# Detector installation

### 9.1 Introduction

This chapter covers all the work and infrastructure required to install the SP module.

We first provide a reminder of the scale of the task, beginning with the two facts that drive all others: a DUNE FD module is enormous, with outer cryostat dimensions of 65.8 m(L)  $\times$  18.9 m(W)  $\times$  17.8 m(H); and every piece of a detector module must descend 1500 m down the Ross Shaft to the 4850L of SURF and be transported to a detector cavern.

The SP module's 150 anode plane assemblies, each 6.0 m high and 2.3 m wide, and weighing 600 kg with 3500 strung sense and shielding wires, must be taken down the shaft as special "slung loads" and moved to the area just outside the DUNE cryostat. The APAs are moved into a 30 m  $\times$  19 m clean room (a portion of which is 17 m high) where they are outfitted with PD units and passed through a series of qualification tests. Here, two APAs are linked into a vertical 12 m high double unit and connected to readout electronics. They receive a cold-test in place, then move into the cryostat to be connected at the proper location on the previously installed DSS, and have their cabling connected to feedthroughs. Additional systems are installed in parallel with the APAs, e.g., the FC and their HV connections, elements of the CISC, and detector calibration systems. The cathode plane, FC, and APA together define the TPC active volume.

After twelve months of detector component installation, which follows twelve months of detector infrastructure installation, the cryostat closes (with the last installation steps occurring in a confined space accessed through a narrow human-access port). Following leak checks, final electrical connection tests, and installation of the neutron calibration source, the process of filling the cryostat with 17,000,000 kg of LAr begins.

The installation requires meticulous planning and execution of thousands of tasks by well trained teams of technicians, riggers, and detector specialists. High-level requirements for these tasks are spelled out in table 9.1<sup>1</sup> and the text that follows it. In all the planning and future work, the pre-eminent requirement in the installation process is safety. DUNE's goal is zero accidents resulting in personal injury, damage to detector components, or harm to the environment.

---

<sup>1</sup>APAs are produced well in advance of their installation date. They are shipped to the storage facility immediately after fabrication and testing in order to control the risk of damage in shipping.

**Table 9.1:** Installation specifications.

| Label     | Description   | Specification (Goal)                              | Rationale  | Validation                             |
|-----------|---|---|--|--|
| SP-INST-1 | Compliance with the SURF Material Handling Specification for all material transported underground | SURF Material Handling Specification              | Loads must fit in the shaft be lifted safely.                                      | Visual and documentation check         |
| SP-INST-2 | Coordination of shipments with CMGC; DUNE to schedule use of Ross Shaft                           | 2 wk notice to CMGC                               | Both DUNE and CMGC need to use Ross Shaft  | Deliveries will be rejected            |
| SP-INST-3 | Maintain materials buffer at logistics facility in SD   | > 1 month   | Prevent schedule delays in case of shipping or customs delays                      | Documentatation and progress reporting |
| SP-INST-4 | APA stroage at logistics facility in SD   | 700 m <sup>2</sup>                                | Store APAs during lag between production and installation                          | Agree upon space needs                 |
| SP-INST-5 | Installation cleanroom Specificaiton  | ISO 8   | Reduce dust (contains U/Th) to prevent induced radiological background in detector | Monitor air purity                     |
| SP-INST-6 | UV filter in installation cleanrooms for PDS sensor protection                                    | filter < 400 nm for > 2 wk exp; < 520 nm all else | Prevent damage to PD coatings  | Visual or spectrographic inspection    |

Installation of the SP module presents hazards that include manipulation of heavy loads in the tight spaces at the 4850L and in the detector module, working at considerable heights above the floor, repeated utilization of large volumes of cryogenes, multiple tests with HV, commissioning of a Class IV laser system, and deployment of a high-activity neutron source. Mitigation of these hazards begins with the strong professional on-site environment, safety and health (ES&H) teams of the Fermilab South Dakota Services Division (SDSD) and SURF.

All installation team members, both at the surface and underground, will undergo rigorous formal safety training. Daily safety meetings will ensure that all workers are aware of the scope of the planned underground work and any related safety considerations. Any team member can stop work at any time for safety purposes. The overall DUNE safety plan is described in Volume III, DUNE far detector technical coordination, chapter 10 of this TDR. Individual sections within this chapter provide details on the evolving safety plan for installation. This plan has been informed by the successful safety experience of SURF with other underground experiments (e.g., LUX, Majorana Demonstrator, LZ), DUNE members in executing projects at other underground locations (e.g., MINOS at Soudan, Minnesota, USA), at other locations remote from major international laboratories (e.g., Daya Bay, China and the NOvA far detector (Ash River, Minnesota, USA), and at the home laboratories of both Fermilab and CERN).

As part of the DUNE design process the detector components and the TPC have been prototyped at various stages. ProtoDUNE-SP, which was assembled from full-scale components has been completed and has taken data. This process has been extremely important in planning the SP module installation and a detailed list of lessons learned from ProtoDUNE-SP construction and installation was compiled [183]. These lessons and other experience from the team planning the installation were used to develop a list of risks for the SP module installation and to formulate mitigation strategies to reduce the risks. The highest-impact risks — those requiring a mitigation strategy — are listed in table 9.2. These mitigation strategies and all the lessons learned from ProtoDUNE-SP will be factored into the detailed installation plan. A description of each of the high level risks follows.

**Table 9.2:** SP module installation risks (P=probability, C=cost, S=schedule) The risk probability, after taking into account the planned mitigation activities, is ranked as L (low < 10 %), M (medium 10 % to 25 %), or H (high > 25 %). The cost and schedule impacts are ranked as L (cost increase < 5 %, schedule delay < 2 months), M (5 % to 25 % and 2–6 months, respectively) and H (> 20 % and > 2 months, respectively).

| ID         | Risk                              | Mitigation   | P | C | S |
|------------|-----------------------------------|--|---|---|---|
| RT-INST-01 | Personnel injury                  | Follow established safety plans.   | M | L | H |
| RT-INST-02 | Shipping delays                   | Plan one month buffer to store materials locally. Provide logistics manual.                    | H | L | L |
| RT-INST-03 | Missing components cause delays   | Use detailed inventory system to verify availability of necessary components.                  | H | L | L |
| RT-INST-04 | Import, export, visa issues       | Dedicated Fermilab SDSDDivision will expedite import/export and visa-related issues.           | H | M | M |
| RT-INST-05 | Lack of available labor           | Hire early and use Ash River setup to train JPO crew.  | L | L | L |
| RT-INST-06 | Parts do not fit together         | Generate 3D model, create interface drawings, and prototype detector assembly.                 | H | L | L |
| RT-INST-07 | Cryostat damage                   | Use cryostat false floor and temporary protection.   | L | L | M |
| RT-INST-08 | Weather closes SURF               | Plan for SURF weather closures   | H | L | L |
| RT-INST-09 | Detector failure during cool-down | Cold test individual components then cold test APA assemblies immediately before installation. | L | H | H |

**Personal Injury:** the installation of the detector module requires on the order of fifty person-years of effort. Substantial work at heights, rigging of heavy equipment, use of custom tooling, and some work in confined spaces is necessary. It is critical that all safety measures be implemented and proper oversight be in place. DUNE will follow the Fermilab safety program, and if any additional measures are needed to comply with the SURF program, they will be adopted. However, even with an excellent safety program, given the large number of hours, the risk of injury remains significant for a project of this scale and needs to be accounted for in the project risk evaluation.



**Shipping Delays:** delays in shipping and availability of components presented problems at ProtoDUNE-SP, and in fact the delays, not technical limitations, ended up driving the installation plan. To avoid this for the SP module installation, a one-month buffer of equipment is required from the consortia. The one month period was determined by the maximum delay in customs from a shipment for ProtoDUNE-SP, which was three weeks. In addition, a detailed shipping manual will be prepared to provide guidance to collaborators and the LBNF/DUNE logistics manager will be available to provide direct assistance. The residual risk that components are delayed is still considered high, but the total schedule impact is expected to be on the few-week scale.

**Missing components cause delay:** often during ProtoDUNE-SP installation, parts would arrive at CERN with small pieces missing, e.g., brackets or hardware. For the SP module, detailed interface drawings will define the interfaces clearly and the work packages will list all parts. A part-breakdown structure will be defined to clarify the ownership of each part and track the location of all hardware. With these systems in place we expect to minimize the number of instances of pieces missing when they are needed. The residual risk is considered highly likely, but with minimal impact.

**Import export and VISA issues:** Fermilab has established a new SDS to expedite customs and visa issues. This risk will need re-evaluation after the new division has had time to evaluate the issues.

**Lack of available labor:** unemployment in the Lead area remains low. At the time work is ramping up it may be difficult to find local people with the requisite skills. To mitigate the risk, we plan to hire the core team early and train them at SURF and Ash River. In addition, a longer hiring period will be planned (6–12 months) so there will be ample time to hire and train the crew. The residual risk is considered low.

**Parts do not fit together:** integration is a critical component of any complex project. DUNE has implemented a process to generate a complete 3D model of the detector module that can be used to detect conflicts. Interface drawings are being generated to clearly define the interfaces between components. Beyond this, an installation prototype of the full assembly is being planned at the NOvA far detector building in Ash River. This installation prototype will test the installation of the detector components using full-scale mechanical mockups. For ProtoDUNE-SP, the Ash River test was critical for finding mismatches between components and identifying installation difficulties due to limited space. After all the installation steps have been tested it is expected the residual risk will be low. It is highly likely that some small conflict will be found but the impact on the overall schedule will be low.

**Cryostat Damage:** the cryostat membrane is a 1.2 mm thick stainless steel membrane. A screw driver dropped from 12 m, for example, would likely cause damage, and much larger pieces of equipment than that will be used. Equipment must also move within the cryostat. To protect the cryostat, a false floor will be constructed. When the false floor is removed, measures will be taken to prevent items from dropping on the membrane. Where possible, all bolts, brackets, and components will be attached to nearby structures so they cannot be dropped. The residual risk of damaging the cryostat is considered small, but in the unlikely event it occurs, it would have a moderate schedule impact.

**Weather closes SURF:** weather events in South Dakota that lead to closing SURF for one or two days occur several times each winter. This risk is accepted, and the average number of snow days is added to the project schedule.

Detector failure during cool-down: as the detector module cools, thermal stresses will develop that the design must be sufficiently robust to withstand. Risk of breakage due to these stresses is particularly critical as it occurs after all components are installed. This risk is minimized by thoroughly testing each component individually in the cold, then cold testing each APA-PD-CE assembly just prior to moving it into the cryostat. This test of the final assembled components is considered critical in reducing the risk of failure during cool down. The residual risk is classed as low probability, but would have a high impact if it should occur.

The remainder of this chapter is divided into three main sections. The first section describes how material will be delivered to the South Dakota region and forwarded to the Ross Headframe on the SURF site. The second section describes the infrastructure needed to install and operate the SP module. This includes a cleanroom and its contents, as well as electronics racks, cable trays, storage facilities, and machining facilities. The third section describes the installation process itself, which is divided into three phases: the CUC setup phase, the installation setup phase, and the detector installation phase. These are summarized in section 9.4.

### 9.2 Logistics

Access to the underground installation area for DUNE, LBNF, and Joint Project Office (JPO) personnel, as well as for LBNF and DUNE materials and equipment, will be provided solely by the 1500 m-deep Ross Shaft. Coordinating transport and ensuring on-time delivery of all items are therefore among the more challenging aspects of the LBNF and DUNE endeavor. The JPO (see Volume III, DUNE far detector technical coordination, chapter 4 of this TDR) oversees the SDWF where deliveries are received before transport to the Ross Headframe.

Due to the enormous cost of the LBNF-CF contracts and the risk of increased construction costs due to delays in delivery of materials, the shaft scheduling must be tightly controlled by LBNF-CF during construction. The shaft is outfitted with hoists that control the cage and two skips. The cage is used to transport people, equipment and materials, and the skips to bring up muck and transport over-sized equipment and materials. The LBNF-CF construction manager/general contractor (CMGC) will coordinate overall usage of the Ross Shaft during this period, until the end of the excavation work. At that time the JPO will take over the management of the shaft usage.

To facilitate the flow of non-CF LBNF and DUNE materials and equipment to the Ross Headframe, the JPO will lease a warehouse facility within a maximum one-day roundtrip<sup>2</sup> from SURF by truck. It is expected that the lease of this facility, referred to as the SDWF, will include warehouse space, personnel, and a warehouse management system (WMS) to inventory all incoming materials and equipment. A facility has not yet been selected.

Most materials and equipment will be shipped to the SDWF; CF material, and likely cryogenics equipment, are exceptions and will ship directly to SURF. The SDSO logistics organization will (1) receive and inventory all goods shipped to the SDWF, (2) coordinate with the CF-CMGC to transport this material to the Ross Headframe in a just-in-time manner, and (3) transport it underground and into the cavern. Figure 9.1 shows a high-level overview of the material flow to the Ross Headframe.

---

<sup>2</sup>For purposes of warehouse selection “one-day roundtrip” is considered three hours of transportation each way and two hours of unloading and loading at the Ross Headframe.

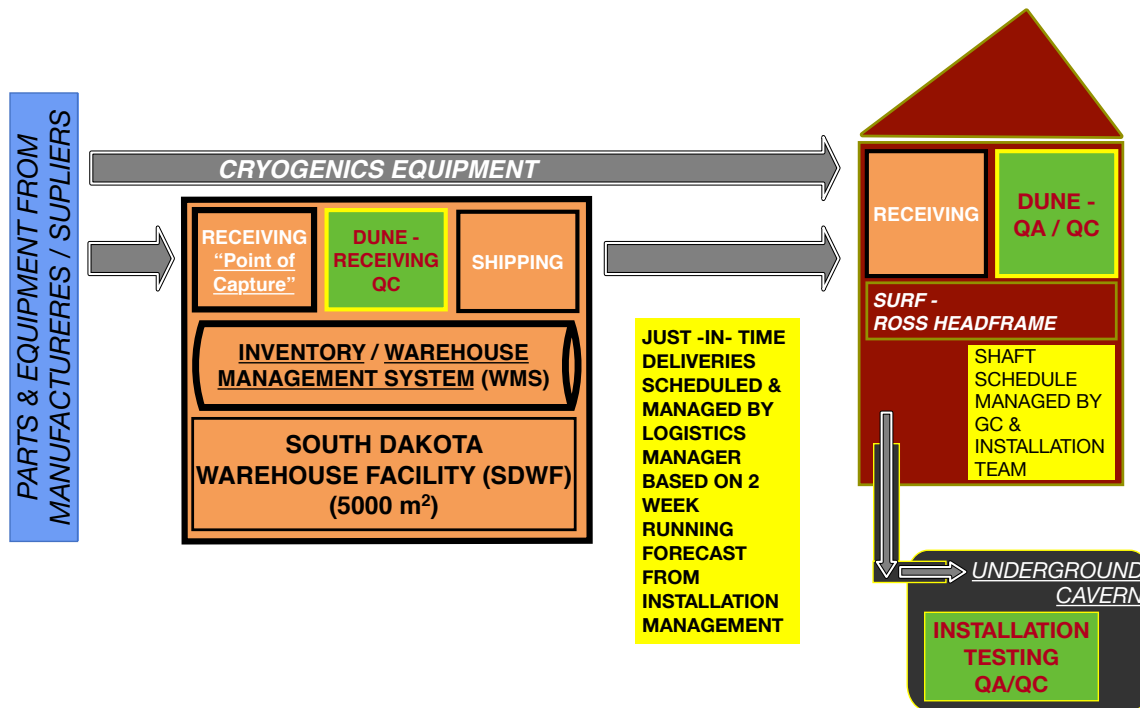
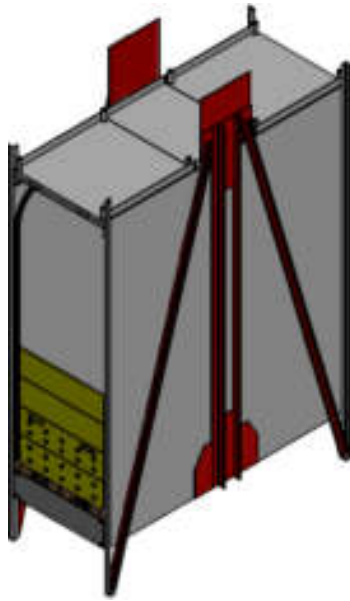


Figure 9.1. Material flow diagram for LBNF and DUNE.

### 9.2.1 Logistics planning

The JPO/SDSD logistics team oversees transportation of the cryostat (steel, foam, and membrane), the cryogenics system, the DUNE detector components, and all related infrastructure not provided by the CF. LBNF specifically oversees the cryostat and cryogenics system, which LBNF will discuss in its TDR. Because LBNF materials dominate the logistics, we present a summary of them here, along with an overview of the DUNE materials. The steel structure for a single DUNE cryostat requires roughly 1,800 individual steel pieces, some of which weigh up to 7.5 t, as well as 125 t of bolts to assemble the steel frame. The internal structure for the cryostat, which includes the foam insulation and the thin stainless steel membrane, requires transporting roughly 4,000 boxes of approximate size 1.5 m × 3.5 m × 1.2 m. The current plan calls for warehousing all these boxes at the SDWF before installation begins. The logistics operation will require roughly 5000 m<sup>2</sup> of area available approximately two years before installation of the first detector module begins, to stage construction of the cryostat, cryogenics system, and detector. By the time detector components start arriving, most of the cryostat boxes will have been delivered to SURF, leaving ample space for the detector and the cryogenics components. Additional warehouse space may be required if the boxes for the second cryostat arrive before detector module #1 installation is complete; a few buildings of the required size are available in the general area around SURF.

The SURF Facility Access Specification [184] defines the limitations on dimensions and weights for all materials to be transported underground, the most stringent of which are set by the Ross Shaft and Cage. It is possible to bring material down the shaft underneath the cage or in the skip compartment as a slung load, but this is a much slower process and requires careful



Ross Cage Specifications

|                 |                          |
|-----------------|--------------------------|
| Inside height   | 3.6 m                    |
| Inside depth    | 3.7 m                    |
| Inside width    | 1.38 m                   |
| Weight limit    | 5,897 kg                 |
| Round trip time | 17 min (incl. unloading) |

Figure 9.2. Simplified Ross Cage model and specifications.

planning and review of detailed procedures for each trip. The APAs, for example, require this special handling because they are too tall to fit in the cage.

Most material will be brought underground inside the cage. Figure 9.2 illustrates the new Ross Cage and summarizes its parameters. The roundtrip travel time for the Ross Cage is 17 minutes (actual travel time is 3.6 minutes each way), dominated by loading and unloading time. Slung loads will require more than an hour round trip.

The Ross Headframe has no loading dock so careful planning of material loading and unloading of shipments is required. All materials must arrive at SURF on a flatbed or curtain-sided chassis, and a forklift will be available for unloading. All deliveries, either from the SDWF or direct to the Ross Headframe, require (1) coordination with the logistics organization, and (2) minimum two weeks prior notice, per an advance delivery plan.

Logistics will provide to DUNE institutions a shipping manual that specifies guidelines on required shipping data and cargo consignment. Adherence to the guidelines will enable the logistics organization to monitor shipping progress and ensure that no delays occur due to incomplete or missing documentation.

In ProtoDUNE-SP’s experiences with trans-oceanic international shipping highlighted the need to increase delivery schedule duration beyond the shipper-quoted average, which was sometimes exceeded by as much as three weeks. For LBNF/DUNE materials, we will plan shipping and transport so that items arrive in South Dakota a minimum of four weeks before they are expected underground. This buffer will allow sufficient advanced planning for the underground work, with confidence that the installation plan can be maintained.

Sufficient space must be made available at the SDWF and in the underground area to house this material. The SDWF staff will deconsolidate or consolidate arriving cargo into appropriately sized boxes and crates, as needed, for delivery to SURF, to make the most efficient use of available trucks and the Ross Shaft.

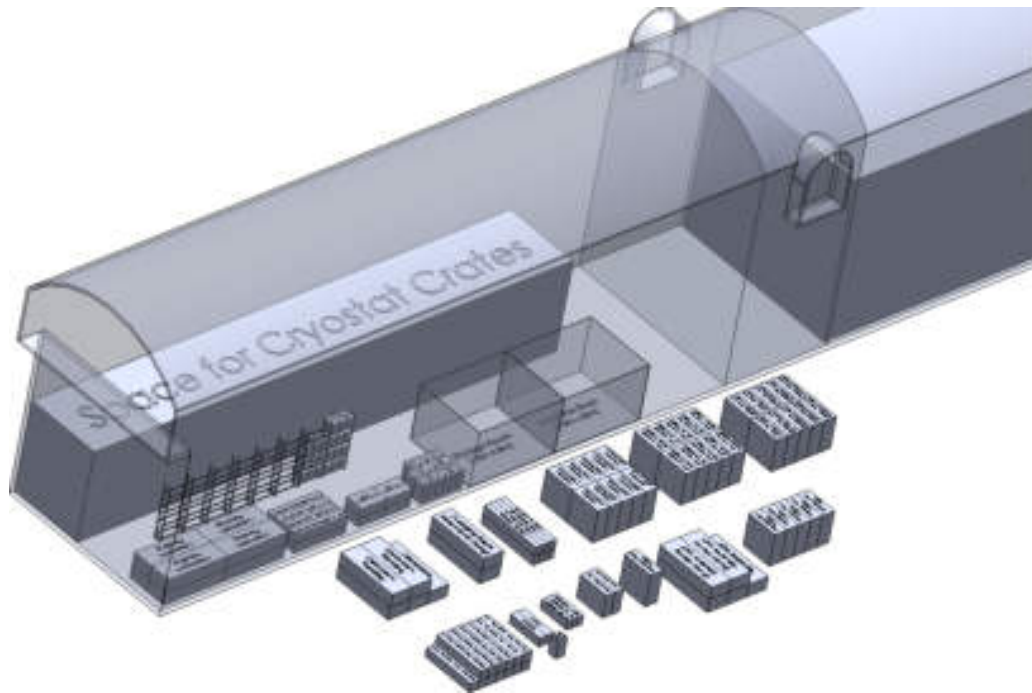


**Figure 9.3.** CAD image showing the empty half of the north cavern as used during the installation setup phase of the first detector module. The entire cavern is 145 m long, 20 m wide, and 28 m high; the half shown is therefore approximately 73 m long. Half of this empty space will be used for the cryostat work and half for storage of the detector infrastructure. The material shown outside the cavern must be stored in the SDWF.

To determine the storage space requirements and how much hoist time must be dedicated to DUNE, a detailed inventory of all DUNE detector equipment and infrastructure is needed. A complete list of materials has been solicited from all consortia and technical coordination. The entries in the inventory spreadsheet are organized as “loads” for the Ross Shaft where a load is a crate or set of boxes that will be transported underground in one trip, either in the cage or as a slung load [185]. Information captured in the load spreadsheet includes the number of trips, type of trip (slung load or cage), package dimensions, weight, and type of package (crate, pallet, box, or carton).

The load list at present predicts 1,600 hoist trips and approximately two months of cage time, most of which is spread over one year. Detector installation (see figure 9.21) for the SP module will span two years, so we divide the logistics planning into three phases (summarized in section 9.4: (1) the CUC setup phase, (2) the installation setup phase, and (3) the detector installation phase. For each phase, a 3D model was generated to show how much material can be stored underground outside the work area and how much material must be stored at the SDWF, thus setting the surface space requirements. The phase with the largest amount of material to transport is the installation setup phase. Figure 9.3 shows the model of the underground area and the required boxes for surface storage for the first month of this phase. The crates outside the cavern were used to estimate DUNE’s storage needs in the surface storage facility. Roughly 1000 m<sup>2</sup> of warehouse space will be needed at this time to buffer DUNE installation equipment. The SDWF will also need space to store up to 150 APAs, adding another 700 m<sup>2</sup>. The remaining 3300 m<sup>2</sup> is available for LBNF storage. The

amount of warehouse space actually leased can be adjusted to match LBNF/DUNE needs, and after the second cryostat construction is complete it will be reduced.

Managing the hoist and planning all the transport of materials underground is one of the primary responsibilities of the CMGC. This task will be challenging and the installation plan with warehouse space on the surface and storage space underground will give critical flexibility in the timing of the delivery of materials. With month-long buffers above and below ground, and a two-week advanced notification of the installation needs, the CMGC has freedom to schedule deliveries around the needs of other contractors.

### 9.2.2 Logistics quality control

The ProtoDUNE-SP experience offers a couple of significant lessons regarding logistics.

1. A central inventory system is essential for tracking shipments.
2. It is important to apply realistic shipping durations based on experience into the overall planning so that work can proceed on a predictable schedule.

The central inventory system implemented at the SDWF and minimum one-month material buffer are the plans we have in place to prevent repetition of the ProtoDUNE-SP schedule problems. The full list of lessons learned from ProtoDUNE-SP is in [183].

Component testing at the SDWF is presently not planned, however a DUNE QC procedure will be followed to detect any damage incurred during transportation and determine remedial action. Any request from the consortia to perform work in the SDWF will be addressed on a case-by-case basis.

In critical cases where the shipping dimensions approach the shaft dimensions, a test transportation using a dummy component will be done. At present the APA shipping/transport box is planned to be tested in this fashion.

The logistics organization in coordination with the SDWF will inventory all received shipments and ensure that all materials fit in the Ross Cage, or if a slung load is needed, that the necessary procedures are in place and approved before any material is transported to the Ross Headframe. JPO representatives will verify that no obvious damage occurred in transport.

The contribution-in-kind model of this project complicates logistics oversight and inventory control, since components will be delivered from many institutions and from different countries. Similarly, during production and testing, QC information must be gathered from and made accessible to all collaborators. Because of the complexity of the project and the different requirements for QC and logistics oversight, two different databases will be used. A commercial WMS will control the inventory process at both the SDWF (items both received and shipped) and at SURF (items received at the Ross Headframe). A separate database, the DUNE construction database (DCDB), will store test and other QC data, e.g., shipping reports and any reported damage. The WMS will need to provide location and QC information to the DCDB, which will ultimately archive both sets of data. The DCDB has not yet been designed.

Until materials arrive at the SDWF (or SURF if directly shipped), the contributors' freight forwarding system will control the logistics supply chain, which will depend on the contractual circumstances and the contributor's choice. However, assuming the shipment is consigned as

outlined in the shipping manual (so that the logistics organization has access to the shipping data), the logistics manager will monitor the cargo progress and step in if a problem arises. The QC and shipping data flow is shown in figure 9.4.

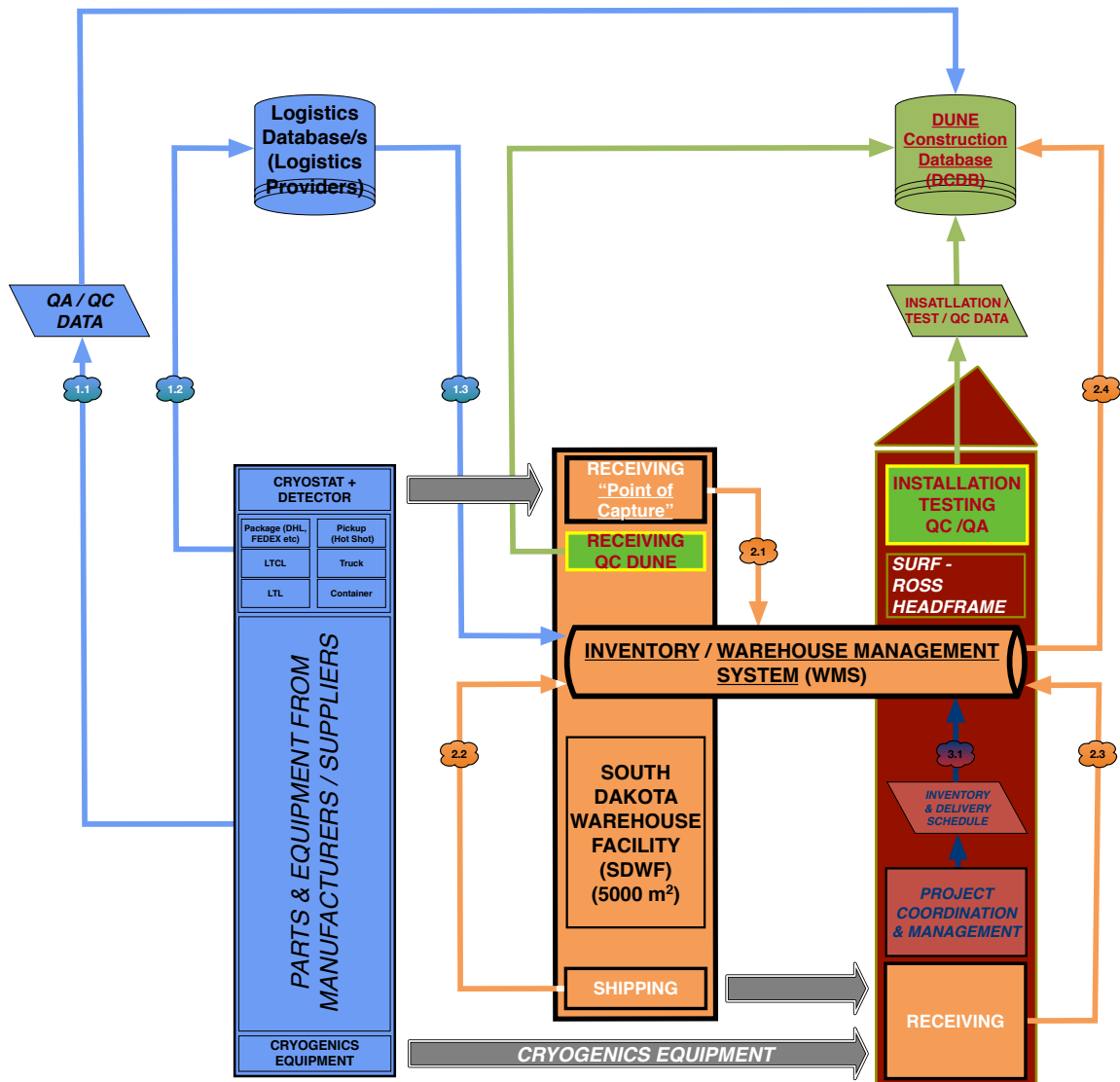


Figure 9.4. QC and shipping data flow diagram for the LBNF and DUNE logistics.

The JPO installation management team will provide a shipping (supply) report to the SDSD logistics organization and SDWF for scheduling delivery of parts and equipment two weeks in advance of the required delivery date. All deliveries will be inventoried upon receipt at the Ross Headframe in the WMS.

### 9.2.3 Logistics safety

The SDWF will be managed and operated by an independent contractor under the supervision of the DUNE logistics manager.

2020 JINST 15 T08010

The facility will be operated under the contractor's ES&H program, which must conform to federal regulations and will be reviewed by Fermilab's ES&H management prior to entering a contractual relationship.

### 9.3 Detector infrastructure

The JPO will provide the infrastructure needed to install the SP module. The major items, described below, include the detector support system (DSS), the electronics mezzanine on the cryostat roof (including racks), cable trays, an underground cleanroom with appropriate installation equipment, piping inside the cryostat, and cold boxes with associated cryogenics supply.

Other items, not described here but also in the JPO scope, include a small machine shop, scissor lifts, rigging equipment, hand tools, diagnostic equipment (including oscilloscopes, network analyzers, and leak detectors), local storage with some critical supplies, and personnel protective equipment (PPE).

#### 9.3.1 Detector support system

The DSS provides the structural support for the detector inside the cryostat. It also provides the necessary infrastructure inside the cryostat to move the detector elements into place during assembly. The DSS is a new design, quite different from the ProtoDUNE-SP DSS. The detector elements supported by the DSS include the endwall field cages (endwall FCs), the APAs, and the cathode plane assemblies with top and bottom FC panels. The nominal load of the detector elements both dry (in air) and wet (in LAr)<sup>3</sup> are shown in table 9.3. The weights listed are the current design weights. The DSS, however, is designed to accommodate significant design changes — even if the detector weight were to double the DSS still meets the design code requirements. The feedthroughs can be adjusted to compensate for deflections due to load.

The DSS shown in figure 9.5 consists of five rows of I-beams inside the detector that support the five rows of APAs and CPAs. The I-beams themselves are supported from the cryostat outer steel structure through a series of vertical supports or mechanical feedthroughs, also shown in figure 9.5. The DSS constrains the location of the detector inside the cryostat and also accommodates the detector elements' movement and contraction during cooling. The layout of the DSS sets, in turn, the overall layout of the detector module since the module's elements become a unified mechanical structure only after they are mounted to the DSS and internally connected.

During installation the detector components are moved along the I-beams using both simple and motorized trolleys. The end of the DSS nearest the temporary construction opening (TCO) is also designed as a switchyard. An additional set of north-south beams allow a short section of the I-beam rail to be shifted between the five rows of DSS beams that correspond to the five alternating rows of detector elements (APA-CPA-APA-CPA-APA). With this the 12 m tall detector elements can enter the cryostat on an I-beam through the TCO, be loaded on the short switchyard beam, moved to the required row of DSS and then be pushed into position.

---

<sup>3</sup>The "wet" load takes into account the buoyancy of the liquid argon. As G10 is almost neutral buoyant the difference is substantial for some sub-systems.



**Table 9.3.** The expected dry and wet static loads for the DSS.

|                                     |         | Weight before fill (Dry) |       |              |         |
|-------------------------------------|---------|--------------------------|-------|--------------|---------|
|                                     |         | Unit Weight              |       | Total Weight |         |
| Detector Component                  | # Units | (kg)                     | (lbs) | (kg)         | (lbs)   |
| DSS                                 | 1       | NA                       | NA    | 12318        | 27100   |
| APA (Installed APA pair, no cables) | 75      | 1184                     | 2604  | 88768        | 195290  |
| CPA                                 | 100     | 233                      | 513   | 23331        | 51327   |
| Top or Bottom FC module (FC TB)     | 400     | 149                      | 328   | 59679        | 131294  |
| TPC Electronics and Cables          | 3000    | 4.9                      | 10.8  | 14700        | 32400   |
| endwall FC                          | 8       | 904                      | 1989  | 7234         | 15914   |
| <b>Total</b>                        |         |                          |       | 206,000      | 454,000 |
|                                     |         | Weight after fill (Wet)  |       |              |         |
| DSS (not in liquid)                 | 1       | NA                       | NA    | 12318        | 27100   |
| APA (Installed APA pair/No cables)  | 75      | 850                      | 1874  | 64000        | 140000  |
| CPA                                 | 100     | 45                       | 99    | 4520         | 9943    |
| Top or Bottom FC module (FC TB)     | 400     | 68                       | 150   | 27359        | 60191   |
| TPC Electronics and Cables          | 3000    | 2.9                      | 6.4   | 8700         | 19200   |
| endwall FC                          | 8       | 283                      | 622   | 2263         | 4978    |
| <b>Total</b>                        |         |                          |       | 110,000      | 242,000 |

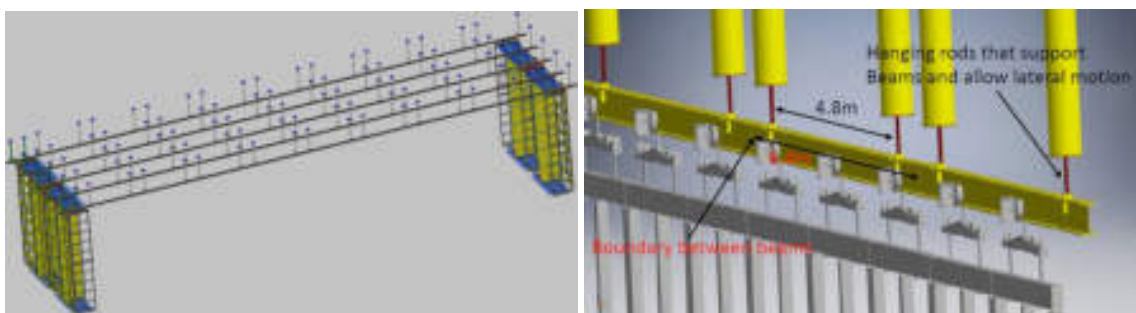


**Figure 9.5.** 3D model of the DSS showing the entire structure on the left along with one APA row and one CPA-FC row at each end. The right panel is a zoomed image showing the connections between the vertical supports and the horizontal I-beams.

The DSS is designed to meet the following requirements:

- support the weight of the detector;
- accommodate cryostat roof movement during filling, testing, and operation;
- accommodate variation in feedthrough locations and variation in the flange angles due to installation tolerances and loading on the warm structure;
- accommodate shrinkage of the detector and DSS from ambient temperature to LAr temperature;
- define the positions of the detector components relative to each other;
- provide electrical connection to the cryostat ground and remain electrically isolated from the detector;
- allow support penetrations to be purged with gaseous argon to prevent contaminants from diffusing back into the liquid;
- ensure that the instrumentation cabling does not interfere with the DSS;
- consist entirely of components that can be installed through the TCO;
- meet AISC-360 codes;
- meet seismic requirements one mile underground at SURF;
- consist entirely of materials compatible with operation in ultrapure LAr;
- ensure that the DSS beams either sit completely submerged in LAr or sit completely in gas while leaving a 4–5 % ullage at the top of the cryostat;
- maintain the centerline of the APA near the cryostat at 400 mm from the membrane flat surface;
- ensure that the supports do not interfere with the cryostat I-beam structures;
- ensure that the detector's lower GP lies over the cryogenic piping; and
- include the infrastructure necessary to move the APA and CPA-FC assemblies from outside the cryostat through the TCO to the correct position.

Each row of the DSS consists of a series of ten 6.4 m long W10 × 26 stainless steel I-beam sections, for a total of 50 I-beam segments for the five rows. The length of the beam segments was chosen to be a multiple of the 1.6 m pitch of the major cryostat beams, which allows the regular placement of the support feedthrough across the cryostat roof. With a W10 × 26 I-beam and 6.4 m between the supports, the beam deflections due to the loads can be kept below 5 mm. Each I-beam is suspended on both ends by the mechanical feedthroughs that penetrate the cryostat roof. During cool-down each I-beam shrinks while the mechanical supports outside the cryostat remain fixed,

causing gaps to form between APAs that are adjacent but supported on separate beams. APAs that are supported on the same beam will not have gaps develop because both the beam and APA frames are stainless steel and will shrink together. The gap between two adjacent DSS beams after cool-down will be 17 mm; this is considered acceptable. Increasing the beam length beyond 6.4 m was not considered because the deformation of the I-beam under load would increase, as would the gap between APAs on adjacent beams and the difficulty of installing the beams.

The DSS I-beams are supported on both ends from a vertical support feedthrough shown in figure 9.6. A 25 mm solid stainless steel rod, which is threaded at both ends, runs down the center of the feedthrough and carries the detector load. The support rod connects on the bottom end to a clevis which is then pinned to the DSS beams shown in figure 9.7. At the top the rod bolts to an X-Y table sitting on the top Conflat flange that allows a lateral adjustment of  $\pm 2.5$  cm (1 in). A swivel washer is used in the bolted connection to the X-Y table to allow the support rod to swing freely. The bolted connection also allows the DSS I-beams to be adjusted vertically. The vacuum seal is established at the top with a bellows between the rod and the top flange. The top flange of the DSS support feedthrough is a Conflat flange that connects to the cryostat crossing tube's mating flange. The crossing tube is welded to the cryostat roof and the top flange is mechanically supported from the cryostat's 1.1 m tall support I-beams. The cryostat crossing tubes are shown in figure 9.12.

During installation the detector components will be pushed along the DSS I-beams, placing a lateral load on the DSS. A 15.2 cm (6 in) outer diameter (OD) tube is welded to the top flange of the DSS feedthrough. This lateral support tube extends through the cryostat insulation and has a clamping collar at the bottom that is used to fix the I-beam support clevises in position during installation. The bottom of the lateral support tube is seen in figure 9.7. The long bolts press on the flat sides of the clevis to fix the support rod's location. There is a nominal 10 mm gap between the OD of the support tube and the inner diameter (ID) of the clearance tube in the cryostat. The clevis can be positioned anywhere inside the 15.2 cm tube.

After the detector has been installed all restraints on the clevis are released to allow motion as the detector contracts during cool-down. The two support rods that support each DSS beam will contract and move toward each other by 13.1 mm along the axis of the detector. The drift distance will shrink by 7.4 mm caused by the contraction of the field cage. The detector is symmetric in the drift direction around the center APA. The drifts on either side of the center APA will shrink toward the center while the center APA remains unmoved. This results in the CPAs moving 7.4 mm toward the center and the outer APAs moving 14.8 mm ( $2 \times 7.4$  mm) toward the center. The hanging rod is designed to have a range of motion of 15 mm in the drift direction to accommodate this shrinkage.

Detector components are installed using a shuttle beam system as illustrated in figure 9.8. The last two columns of feedthroughs (western-most) support temporary beams that run north-south, perpendicular to the main DSS beams. A shuttle beam has trolleys mounted to it and traverses north-south until it aligns with the required row of DSS beams. The last APA or CPA in a row is supported by the shuttle beam, which is bolted directly to the feedthroughs once it is in place. As the last CPA or APA in each row is installed, the north-south beams are removed. This system will be thoroughly tested as part of the Ash River testing program described in 9.4.2.

The shuttle beam and each detector component are moved using a motorized trolley as seen in figure 9.9. A commercially available motorized trolley will be modified as needed for the installation. A mechanical stop will prevent the trolley from passing the end of the shuttle beam

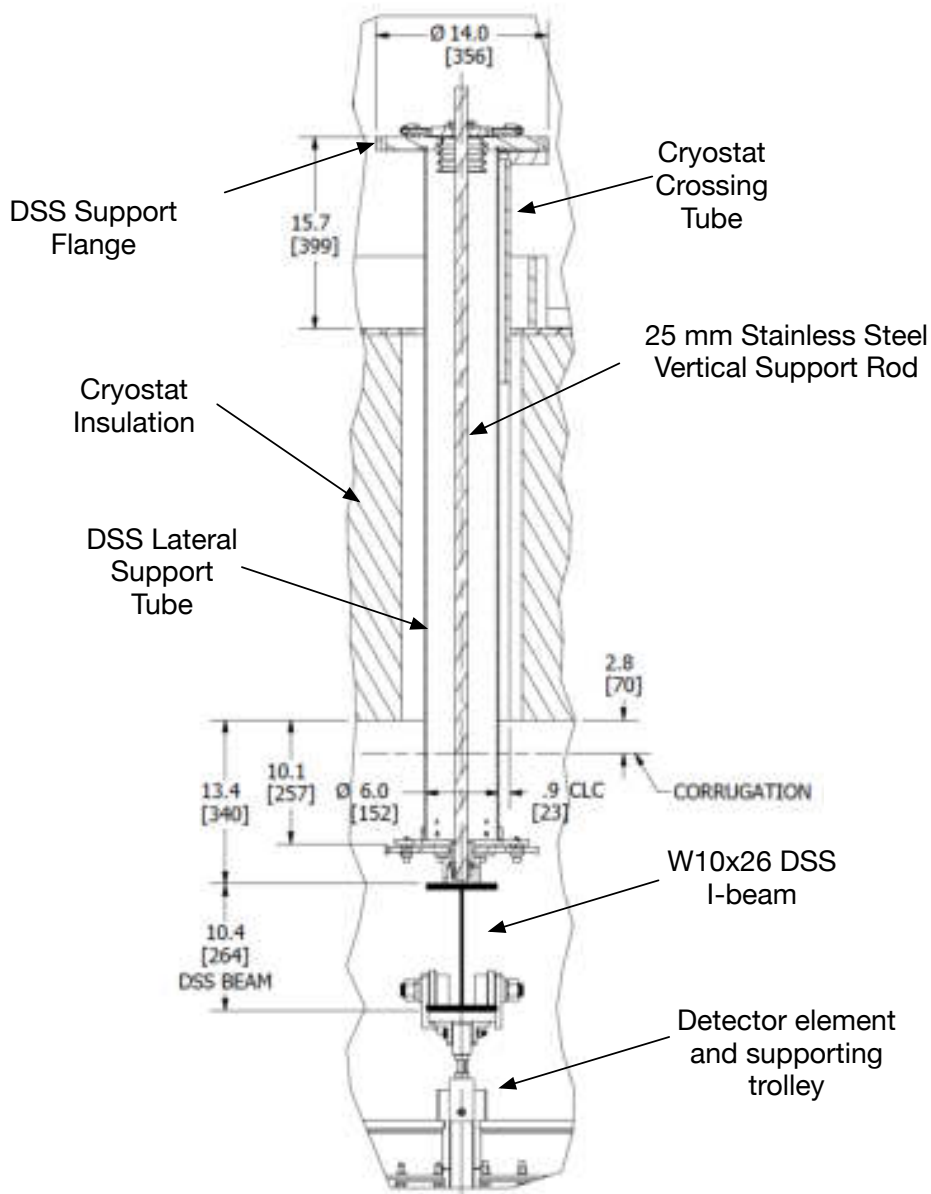


**Figure 9.6.** Drawing of the DSS vertical support feedthrough. The detector load is carried by the 25 mm inner support rod. The outer lateral support tube prevents swinging during installation. The feedthrough mounts to the cryostat crossing tube, which is an integral part of the cryostat.

Note: a few of the DSS vertical support feedthroughs have a short vacuum chamber with side ports inserted between the DSS support flange and the cryostat crossing tube. These chambers are used to bring the CISC cables out of the cryostat and are shown in the CISC section in figure 9.28.

2020 JINST 15 T08010

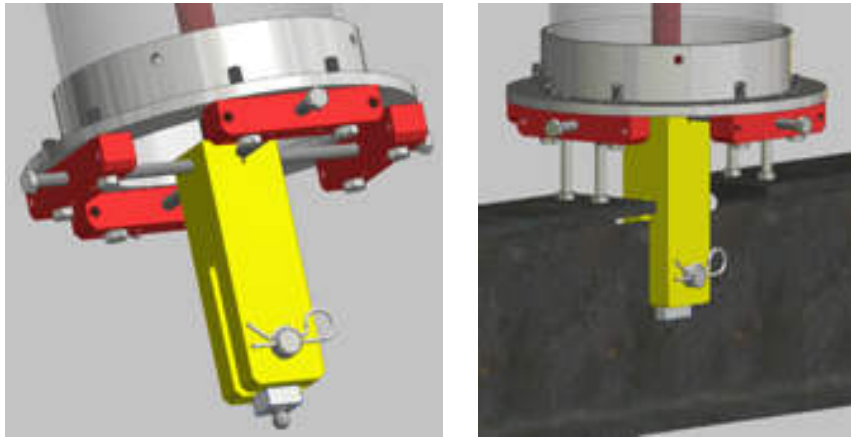


**Figure 9.7.** Left panel shows how the central support rod is locked in position during detector installation. The outer 15.2 cm (6 in) tube is used to fix the support clevis in position. The right panel shows the system as it is connected to the I-Beam.

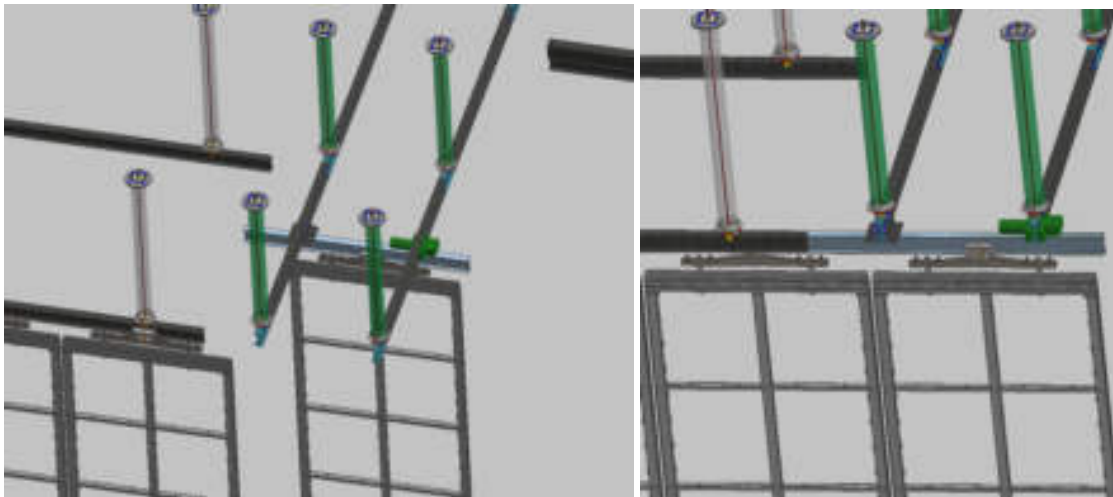


**Figure 9.8.** 3D models of the shuttle beam end of the DSS. The figures show how an APA is translated into position using the north-south beams until it lines up with the correct row of I-beams.

unless the beam is aligned with a corresponding DSS beam. A detailed engineering design report for the DSS is available [186] and the preliminary design review is complete.

A mock-up of the shuttle system will be constructed to test the mechanical interlock and drive systems for the shuttle beam for each detector module. Tests will be conducted to evaluate the level of misalignment between beams that can be tolerated and the amount of positional control that can be achieved with the motorized trolley. We plan to construct a full scale prototype of a section of the switchyard and perform tests at floor level. Later, the test program will be expanded at Ash River, where a full-scale installation test will be performed; see section 9.4.2.



**Figure 9.9.** Prototype of the motorized DSS trolley that will push the APA and CPA along the I-beams and through the switchyard.

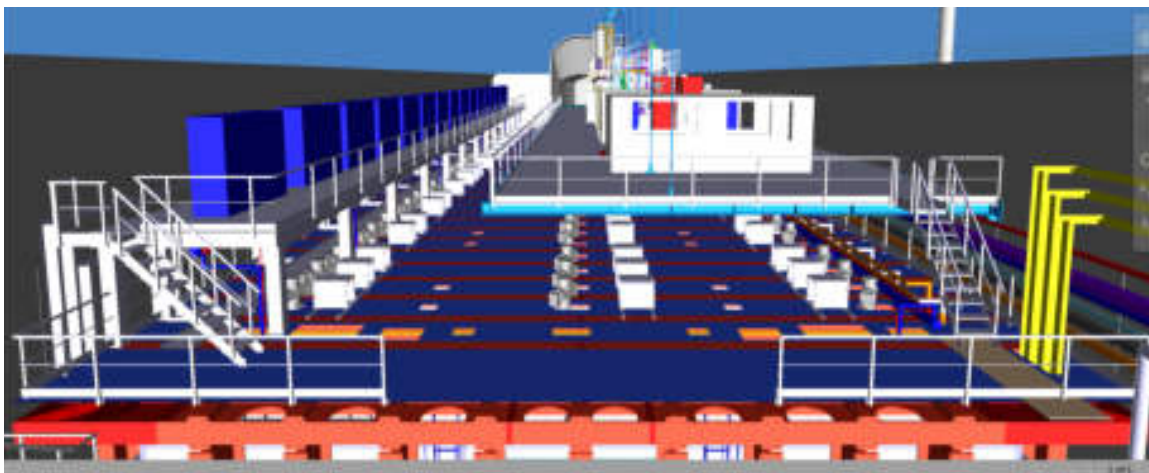
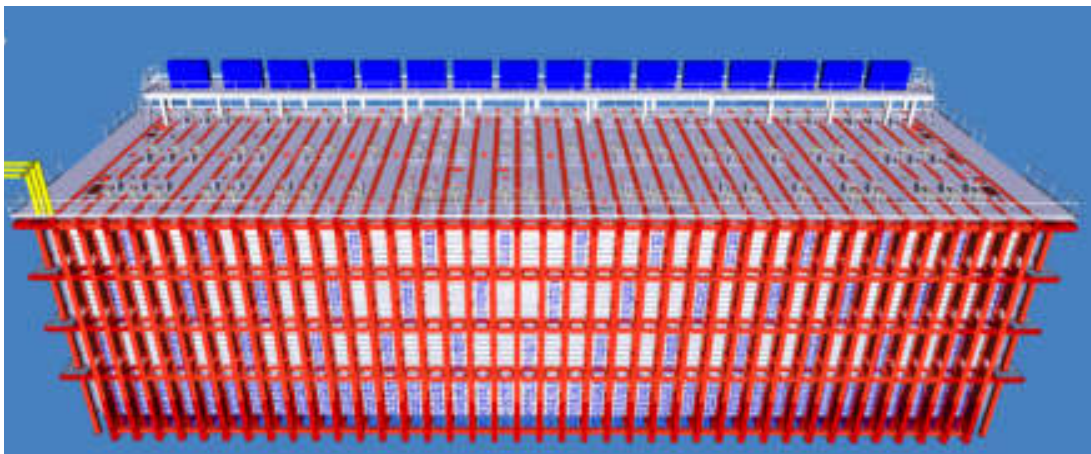


**Figure 9.10.** The electronics racks sit on the DUNE electronics mezzanine. The top image is a view from above the detector looking at the racks from the side. In this view the cavern and cryogenics mezzanine are hidden. The bottom view is from the end of the cryostat looking over the roof. The access stairs to the mezzanine are shown.

2020 JINST 15 T08010

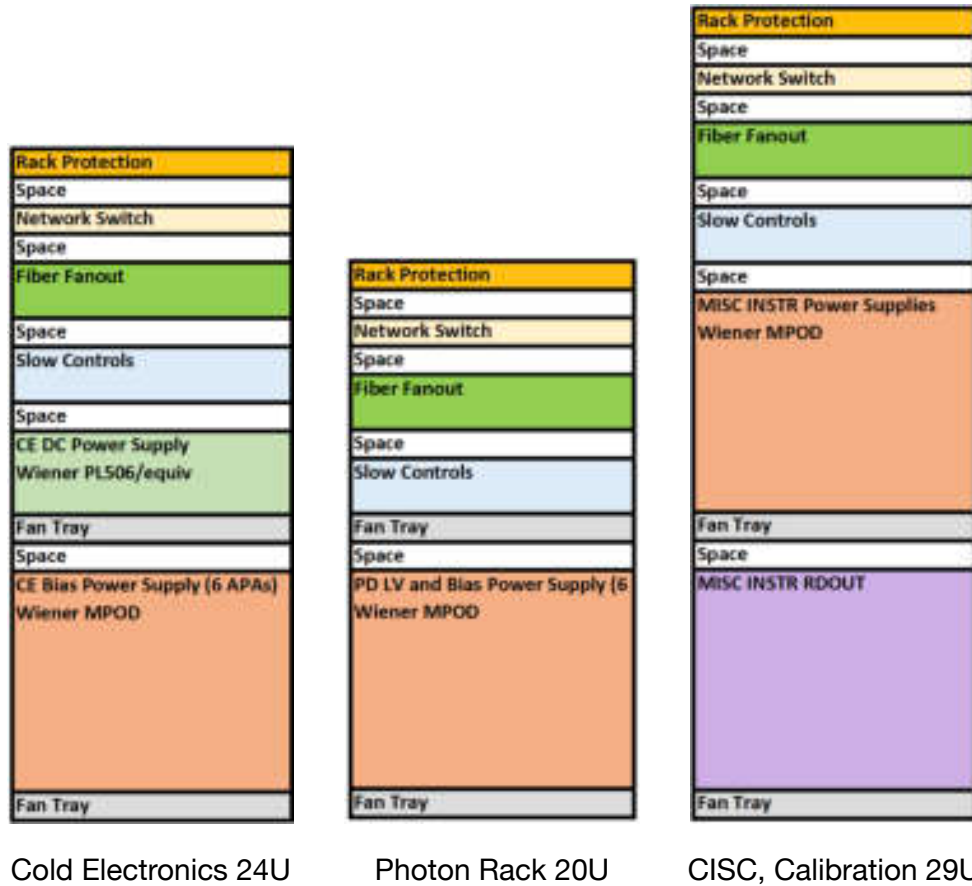


**Figure 9.11.** The nominal contents of the electronics racks on the mezzanine is shown. Each rack is configured to consume less than 3.5 kW.

### 9.3.2 Cryostat roof infrastructure

The top image in figure 9.10 shows the DUNE electronics mezzanine with the 42U tall racks placed on top. During the initial design steps, it became clear that the constraints placed on the rack location by the many DSS support feedthroughs, the electronics feedthrough, and the I-beams themselves make distributing the racks on the roof very challenging. By constructing a fixed mezzanine for the electronics above the cryostat at the same height as the cryogenic mezzanine, the electronics feedthroughs are kept clear. This configuration also makes working on the electronics much easier because there are no local obstacles and all the racks are in one place.

Since the electronics modules in the racks are connected to the detector readout electronics, they are by definition at detector ground. The mezzanine must therefore also be connected to detector ground, which is accomplished by bolting the mezzanine to the cryostat I-beams.

Figure 9.10 (top) shows 16 groups of five racks each on the mezzanine for a total of 80 racks. The electronics inside the detector racks will be air-cooled and the heat exhausted into the cavern air. The HVAC system for the detector cavern has a 400 kW capacity, which is sufficient for the first detector module. Note that as the majority of the heat is generated by the CE and PD electronics located near the cryostat feedthroughs distributed across the cryostat roof, a water-cooling scheme

would be difficult to engineer. CF will provide sufficient chilled water capacity at the entrance to the north cavern to accommodate the maximum heat load for two detector modules. When detector #3 is selected and the heat loads are known, the added cooling for this module will be designed.

Of the 80 racks, CE LV power requires 25, and another 25 will be made available collectively for APA wire bias voltage, PD power, and miscellaneous additional CE, PD system, and APA electronics modules. The remaining 30 will be available for slow control, calibration, and other electrical equipment. Small 12U-high mini-racks will be placed near the electronics feedthroughs for the PD readout electronics and optical patch panels. If this is not enough, additional racks can be placed on the cryostat roof. The present rack configuration for this layout is shown in figure 9.11. The electronics modules inside the racks are distributed to keep the AC power requirement for each rack below 3.5 kW. The racks are 42U high, which provides significant extra rack space [187].

The 12U-high mini-racks near the feedthrough flanges will be relatively empty because the PD readout should need only approximately 2U in height while the CE patch panel needs less than 1U. The mini-racks are shown in the lower panel of figure 9.10; they are the gray rectangles near the electronics crosses.

The north-south cable trays (transverse to the beam) that run from the electronics mezzanine to the electronics feedthrough are routed under the floor of the cryostat roof (shown in gray in figure 9.10) next to the I-beams. This keeps the roof reasonably clear, allowing equipment to be transported across it. The gap between the web of the I-beams is 1.2 m so a 200 mm to 300 mm wide cable tray installed along the beams leaves enough space for people to work on the electronics crates while standing directly on the cryostat's outer steel skin (figure 9.25). The cable trays between the CUC and the electronics mezzanine will run along the west end of the cryostat under the floor of the cryostat roof. We estimate that only half of the 1.6 m space is needed, so the cable tray quantity could in principal be doubled, if necessary.

The flooring material for the top of the SP module will be similar to the 25 mm thick plywood used at ProtoDUNE-SP. It is important that it be easy to cut so that it can be fit around many obstacles and pipes on the roof. It must be light enough to lift up to allow access under the floor, and it must support the load of a person and a small cart. We will investigate fire-retardant options available in the USA and other possible materials, with input from the Fermilab fire life-safety group.

Air filters for the cleanroom and inside the cryostat will also be placed on the cryostat roof. The present plan is to place fan filter units near the access holes on the east end of the cryostat. Initial calculations indicate sufficient airflow is possible to support one air exchange per hour inside the cryostat. The air handling system has yet to be designed in detail.

The cryostat crossing tubes are among the most critical components of the roof infrastructure since they penetrate the cryostat roof and connect to the cold cryostat membrane. The top flange of the crossing tube supports either the electronics feedthrough or the detector support feedthrough and must be directly tied to the cryostat's steel I-beams for support. Accurate placement and true vertical installation of the crossing tubes is important to ensure proper interfacing to the cryostat membrane. A draft assembly drawing of the crossing tube is shown in figure 9.12. The crossing tube consists of a 464 mm long stainless steel pipe with a 1 cm thick wall. One end of the thick-walled section is welded to a 800 mm long 250 mm diameter thin-walled tube which is also welded to the cryostat membrane. A custom Conflat flange at the top end of the crossing tube connects to the



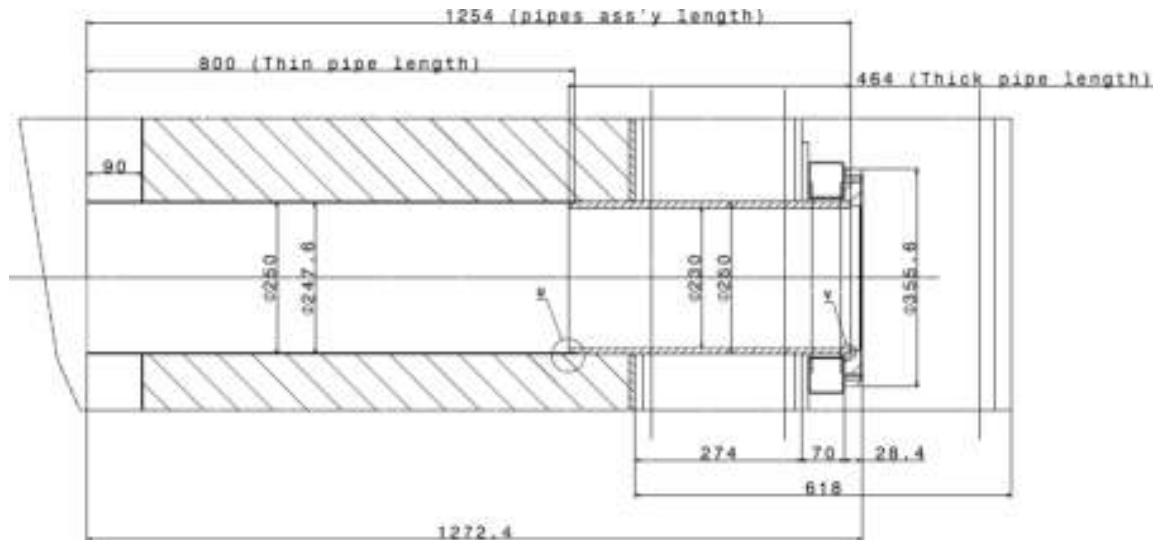


**Figure 9.12.** Draft drawing of the cryostat crossing tubes. The hatched region is the cryostat insulation. Units are mm. Points labeled “u” and “v” are welds.

feedthrough. The thick tube section is also welded to the steel roof plates (the thin cross-hatched segments in figure 9.12).

Each of the 250 crossing tubes has a small side port that connects to the cryogenic gas-handling system through a network of pipes on the cryostat roof. During the initial purge gaseous argon (GAr) is withdrawn from each port and analyzed to assess progress and determine when the system is ready to be cooled down. Five GAr streams, each collecting gas from 50 crossing tubes, are connected independently to the gas analyzers. This provides some redundancy and position-dependant information on the contamination level of the gas at the top of the cryostat during the purge.

During filling and normal operation the collection and analysis of the gas from the crossing tubes will continue in order to monitor impurities (mainly water, oxygen and nitrogen) produced by outgassing from the cables in the feedthroughs and the warmer metal surfaces in the ullage. These impurities can be removed from the GAr by the cryogenics system. If the gas analyzers find no significant nitrogen contamination, the GAr from all or a subset of ports can be sent to the condenser, re-condensed, and purified along with the rest of the LAr. Simple  $O_2$  sensors monitor the return gas for traces of oxygen, which would indicate development of a leak in the room-temperature feedthroughs.

A 500 kVA transformer provides power to each detector module and the total power budget available for use by detector electronics is derated to 400 kW at the power distribution panels. The CE is the SP module’s largest power consumer, dissipating 306 W per APA. The LV power supplies’ controller needs about 35 W per APA and has an efficiency of approximately 85%. This leads to a load of approximately 400 W per APA, or a total load of 60 kW per detector module. The APA wire-bias power supplies have a maximum load of 465 W per set of six APAs, for a total budget of about 12 kW. Cooling fans and heaters near the feedthroughs will use a nominal amount of power, so the overall power budget for the CE and APAs is expected to be less than 75 kW.

The PD system electronics is based on the Mu2e cosmic ray veto electronics, which reports a power load of approximately 6 kW. DUNE plans a power budget of 8 kW because of cable drops and power supply inefficiencies.

Each of the approximately 80 detector racks will have fan units, Ethernet switches, rack protection, and slow controls modules, adding a load of about 500 W per rack, for a total of 40 kW.

Twenty-five racks are reserved for cryogenics instrumentation with a per-rack load conservatively estimated at 2 kW, for a total of 50 kW.

The detector module will thus use an estimated 173 kW of power. These numbers provide a safety factor of about two on our power estimates relative to available power.

### 9.3.3 Cryostat internal infrastructure

The internal cryogenics comprises three sets of pipe distribution networks and two sets of sprayers. All pipes enter the cryostat from the top; some go all the way down to the floor, and others remain in the ceiling. On the floor are:

- **Argon gas distribution:** a set of pipes for GAr. These pipes are used only prior to filling to remove air in the cryostat. They will all have either a longitudinal slit or calibrated holes to distribute GAr uniformly along the length of the cryostat. We have run CFD simulations showing that air will be removed from the system as long as GAr is flowing in at the right speed, calculated and experimentally verified as 1.2 m/hr (vertical meters in the cryostat).
- **LAr distribution:** two sets of pipes are required for flowing LAr over a broad range of flow rates. These pipes are used to fill the cryostat and, during steady state operations, to return the LAr from the purification system. The pipes have calibrated holes to return the LAr uniformly throughout the length of the cryostat which is very important to maintain uniform purity. Four pumps circulate the LAr inside the cryostat all of which operate initially to achieve purity. Once the target purity is achieved only one or two pumps remain in service. Individual pumps can be isolated for routine maintenance.

On the ceiling are:

- **Cool down sprayers:** two sets of cool down sprayers are distributed along the long sides of each cryostat. One set distributes LAr using liquid sprayers that generate a conical profile of small droplets of liquid. The other set of sprayers distributes GAr to move the LAr droplets within the interior and thus cool down the detector and cryostat uniformly. These sprayers are being tested in ProtoDUNE-DP. They are a variation of those implemented in ProtoDUNE-SP.

Figure 9.13 shows the current layout of the internal cryogenics. The GAr pipes are in red, the LAr pipes in blue.

Infrastructure inside the cryostat includes the cryostat false floor, the UV-filtered lighting, and the battery-operated scissor lifts. The floor must support the load of the scissor lift used to work on the electronic cabling on the inside of the cryostat near the ceiling and allow the scissor lift to get close enough to the APAs to work comfortably at the top. The floor must be laid out so that the panels can be removed in sections as equipment is installed. This is especially important for the

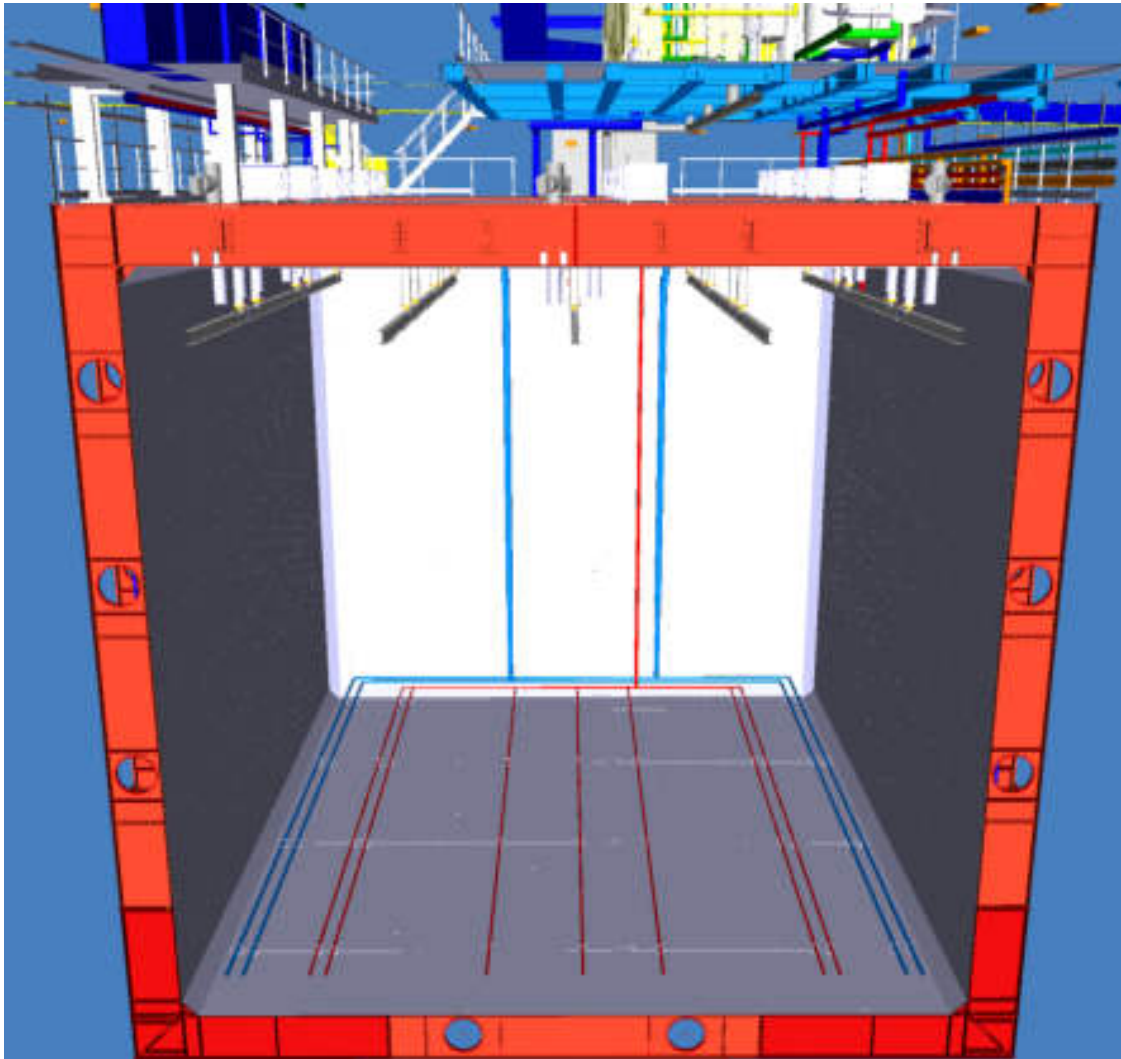


**Figure 9.13.** Endview of the inside of the cryostat after the cryogenic piping has been installed. The GAR pipes used during the piston purge are in red and the pipes which return the purified LAr to the cryostat are in blue.

APAs since inadequate room exists between the bottom of the APAs and the floor to allow removal of panels after installation.

The cryostat lighting, using UV-filtered<sup>4</sup> LED lamps, is expected to be fairly simple. Options for the lighting will be developed during tests at the Ash River facility. Floor-mounted lights with task lighting will be investigated. If needed, lighting can also be mounted to the DSS and removed as the detector is installed.

We plan to use a commercially available battery-operated scissor lift with a 12 m reach. Tests at Ash River will verify the stability of the lift at height. If the lift is determined to be suitable, then the remaining issue to resolve is how to install and remove it from the cryostat. Commercially available scissor lifts are too wide to fit easily through the TCO opening where one of the large

<sup>4</sup>Light is filtered according to the requirement SP-INST-6.

cryostat support I-beams protrudes above the TCO floor level, so custom lifting equipment will be needed to insert the lifts into the cryostat from above. At the end of the installation process, the last lift may require dismantling before it can be removed from the cryostat.

### 9.3.4 Cleanroom and cleanroom infrastructure

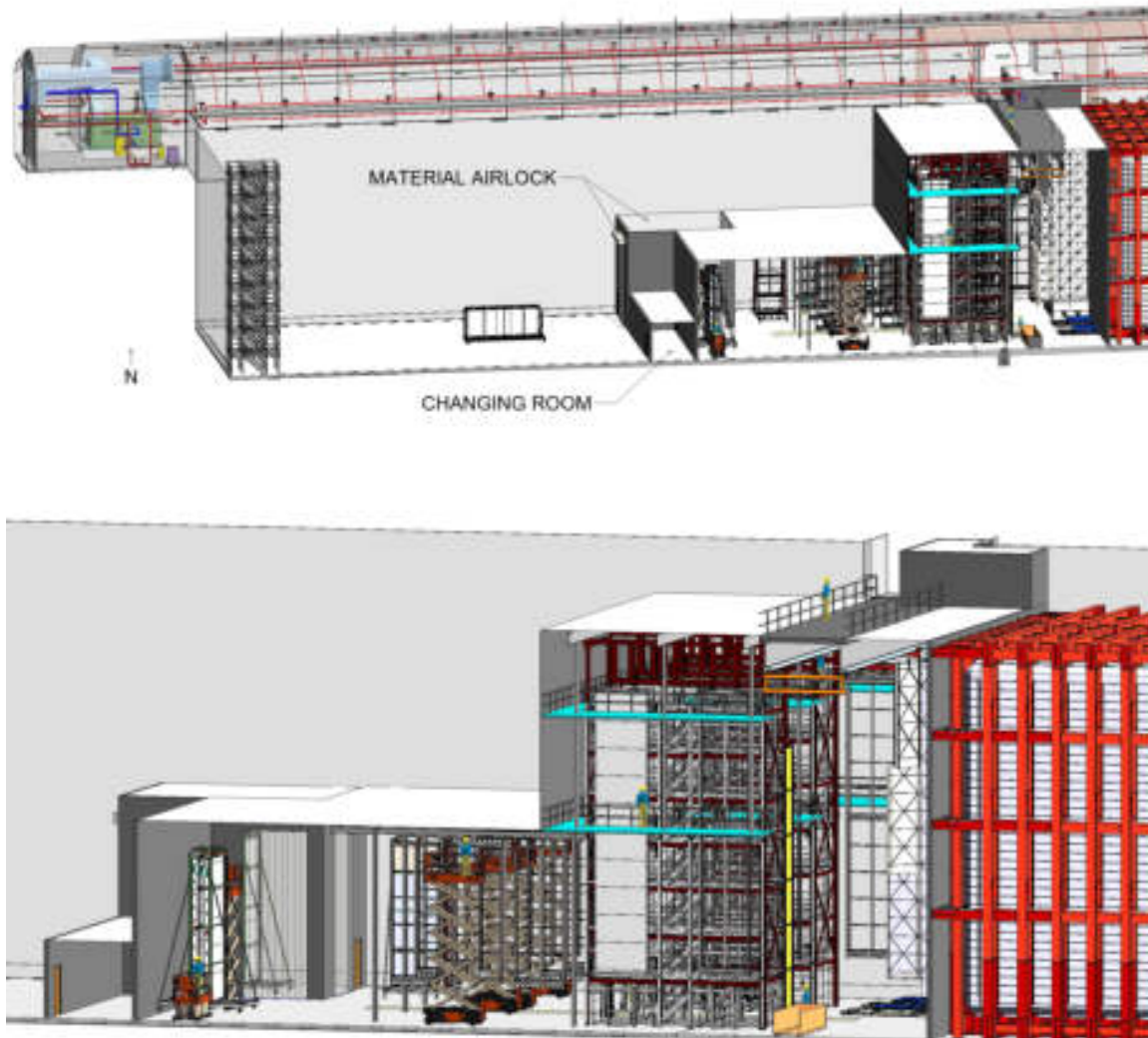


**Figure 9.14.** Two views of the installation cleanroom. The top view shows the cleanroom in position in the north cavern. The location of the material airlock and the changing room are indicated. The lower image is a closer view showing the equipment in the cleanroom. The 17.8 m tall cryostat is shown in red.

Since the 12 m tall full anode plane assemblies would be too large and fragile to be brought down the Ross Shaft, they will be assembled in front of the cryostat itself, where there is ample vertical space. A cleanroom meeting the ISO-8 cleanroom standard (3.5 M particles per m<sup>3</sup> or 0.1 M per ft<sup>3</sup>) is required for any work on the detector components in order that the accumulated U/Th contamination due to dust in the detector produce a background rate lower than the (unavoidable)

Ar<sup>39</sup> decay background. We therefore plan to construct a large ISO-8 cleanroom in the assembly area (figure 9.14) to meet the DUNE cleanliness requirements.

Upon arrival in the cavern, the detector elements first pass through a materials airlock (figure 9.14) before entering the cleanroom. This airlock has large entry doors of dimensions 3 m wide and 8 m tall, large enough to allow the tallest item — an APA transport box (2.6 m by 6.6 m) — to enter in a vertical orientation while bolted to a custom pallet and be moved with electric pallet jacks. The airlock itself is 7 m wide, 9 m deep, and 9 m tall. All materials must be brought through the material airlock and cleaned prior to entering the cleanroom proper. The materials airlock, cleanroom, and inside the cryostat will be outfitted with UV-filtered lights to protect the PDs. Personnel must enter the cleanroom through a changing room. The changing room on the 4910 level is 13 m wide and 4 m deep, large enough to allow 50 people to gown up for the cleanroom within a reasonable time (roughly 15 people can change at a time). A smaller changing room on the 4850L allows easier access to the elevated work platform.

The cleanroom infrastructure consists of the cleanroom itself, the cold boxes and cryogenics plant for testing the assembled APAs, the assembly towers, rails and a switchyard to allow the APAs to move inside the cleanroom, and the PD integration infrastructure.

A combination of contractors, the lead worker, and rigger teams will set up the infrastructure; they will also assist in detector assembly. The attire requirements for work in an ISO-8 cleanroom are a cleanroom lab coat, clean shoes, and nets for hair and beards. This basic cleanroom attire will be augmented with a clean hard hat and gloves, for safety reasons.

To keep the cleanroom at least at ISO-8, air is first filtered then forced into the cryostat's east end. From there it flows through the cryostat and into and through the cleanroom and the airlocks.

The size of the installation cleanroom depends on the work performed inside it and the required equipment. The dimensions have been defined and are described below, but optimization will continue through fall of 2019. After the tests at Ash River modifications may be necessary. Figure 9.14 illustrates the conceptual design. The top figure shows the cleanroom situated in the cavern next to the cryostat; the materials airlock and the changing room are on the west end. The bottom image is a closer view showing some of the equipment in the cleanroom.

The cleanroom proper can be divided into several work areas as follows:

- materials and personnel airlocks,
- PD integration area,
- four APA assembly lines, where the lower rails are for wire tension measurements and the upper rails are for APA assembly and cabling,
- the switchyard area used to move the assembled APAs around the cleanroom and into the cryostat,
- the cold box area where the APAs are cold tested, and
- the HV assembly area.

The PDs are integrated into the APAs and the initial QA tests upon receipt are performed in the 10 m high PD integration area at the west end of the cleanroom.

Because APA preparation is time-consuming, four assembly lines will operate in the cleanroom to keep up with the cold tests and installation. Three lines will be in continuous usage and the fourth will remain available for repairs or contingency. Each assembly line has a lower and upper set of rails for moving the APAs. The wire tension is measured and the lower CE front-end mother boards (FEMBs) are installed at the lower rail section. The PD integration area and the lower rail section of the assembly lines measure 19.5 m wide by 18 m deep, with a 9 m ceiling. A design for this area similar to that used for the ProtoDUNE-SP cleanroom is under consideration, as the height is similar. If needed, the rail system inside the integration work area can be used to support the roof.

The APA assembly and cabling area in the cleanroom is where the top and bottom APAs are connected together to form the 12 m doublets, and the CE cables are inserted and connected to the FEMBs.

The ceiling in this area is 17.8 m, placing the ceiling at the same level as the bridge and the roof of the cryostat. A 9.5 m by 19.5 m area next to the bridge is sufficient to house the two large assembly towers needed to support the assembly lines. Above the towers, I-beams running north-south, i.e., transverse to the neutrino beam, are needed to support work platforms that allow access to both faces of the APAs. These beams can be used to support the cleanroom roof, which can be a light-weight frame with a fire-retardant fabric attached. The outer towers' steel structure provides a strong surface to which to attach a polymer sheet intended to serve as the vertical wall connecting the 17.8 m area to the 10 m tall area.

The switchyard area is the region under the north-south bridge where a bridge crane is mounted. It is used to move the APA from the assembly lines to the cold boxes and into the cryostat, and is similar to the shuttle beam system in the DSS shown in figure 9.8. The cold boxes and the HV assembly area are between the bridge and the cryostat.

The cleanroom spans the width of the cavern excavation. The side walls of the cleanroom will be constructed by hanging reinforced fire-retardant plastic sheets against the walls, providing a low-cost, easy-to-install solution.

Given the substantial size and the significant occupancy of the cleanroom, it will require electrical outlets, Wi-Fi, and fire protection. Monitoring for oxygen deficiency hazard (ODH) will be installed as required by the safety analysis of the cold box cryogenics system.

Equipment in the integration work area adjacent to the materials airlock will consist of a station for integrating the PDs into the APA, two pairs of rails for preparing the APA for assembly, and several scissor lifts for working around the APAs. In the PD integration area an APA transport box will be positioned between two fixed lifts that will be raised until the PD paddles can easily be inserted into the side of the APA. Figure 9.15 illustrates the rail setup in the integration work area. The APAs are removed from their transport box and mounted to the rails at the far end of the assembly rails near the PD integration area and material airlock. They then move along the rails using simple trolleys running on the I-beams. The rails are long enough to hold three APAs at a time. This setup is conceptual and the engineering design of the rail supports has not yet started. Cross-bracing of the vertical posts will be added during the design stage.

In the 17 m tall APA assembly and cabling area of the cleanroom two large work towers (shown in figure 9.16) support the four assembly lines. These towers are designed to be wide enough to hold two APAs side-by-side with enough space between them to walk through or work. The tower is seven stories tall with work areas at each landing. Rails at mid-height and at the top of the towers

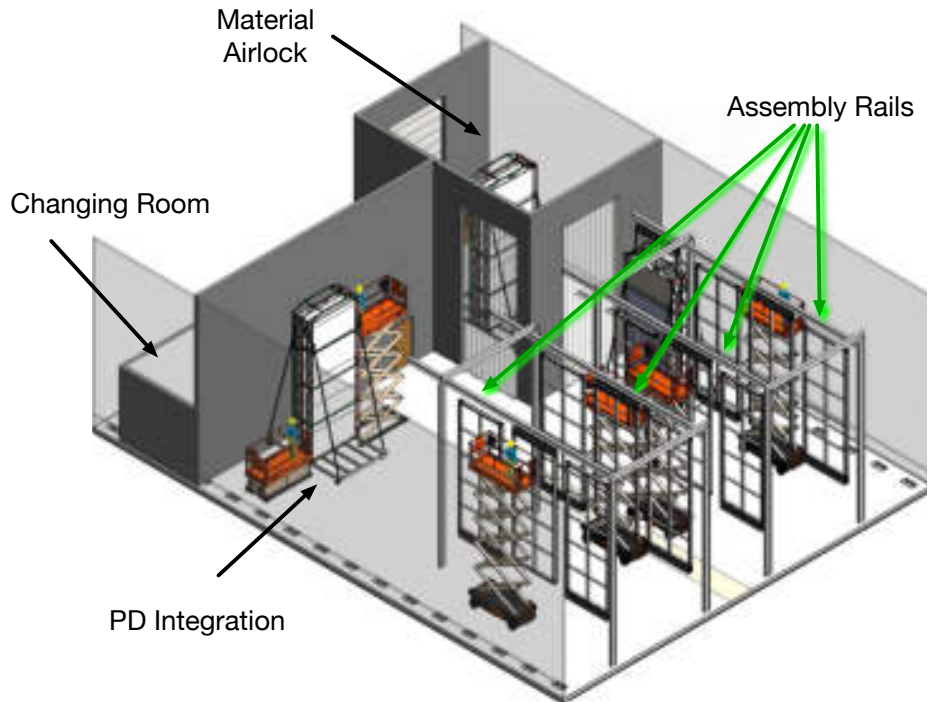


**Figure 9.15.** Two pairs of rails are used to prepare the APA for assembly. Each rail holds three APAs. This is where the wire tension measurements are performed and the CE FEMBs are installed on the lower APAs. The lower CE is easily reachable from the floor in this arrangement. This view is from the assembly towers looking west along the assembly lines.

are used to move the APAs to the different locations along the tower. The towers also provides support for the tooling needed to hold the upper and lower APA during assembly and to bring the two modules together so they can be connected. This tooling is called the APA assembly fixture and is provided by the APA consortium.

The tower is conceived as a steel outer frame that supports the APAs and the rails. Inside the steel frame is standard scaffolding that allows workers to access the APAs at different heights. The scaffolding is wide enough for people to work simultaneously on both sides and it accommodates a stairway in the middle that meets OSHA standards. North-south beams spanning the width of the cavern will be placed on top of the towers to support the cleanroom roof and the work platforms shown in figure 9.17. The image shown in figure 9.16 is a modified model based on a single-wide APA tower that has passed all safety reviews and has already been constructed at Ash River. The double-wide tower will need to be re-engineered to ensure that all the beam dimensions and bracing are appropriate for the larger spans and loads. It will then go through the full safety review and an initial prototype will be fabricated for use at Ash River. The size and the layout of the top level of the tower will be optimized based on input from the Ash River tests.

Because the cables can only be inserted through the APA frames after the top and bottom APAs have been assembled, quite a bit of work must be performed at the 14.8 m height of the TCO beam.

The commercial scaffolding inside the APA assembly towers provide a solid, safe work platform for working on the side of the APA facing the tower. However, access to both faces of the APA is

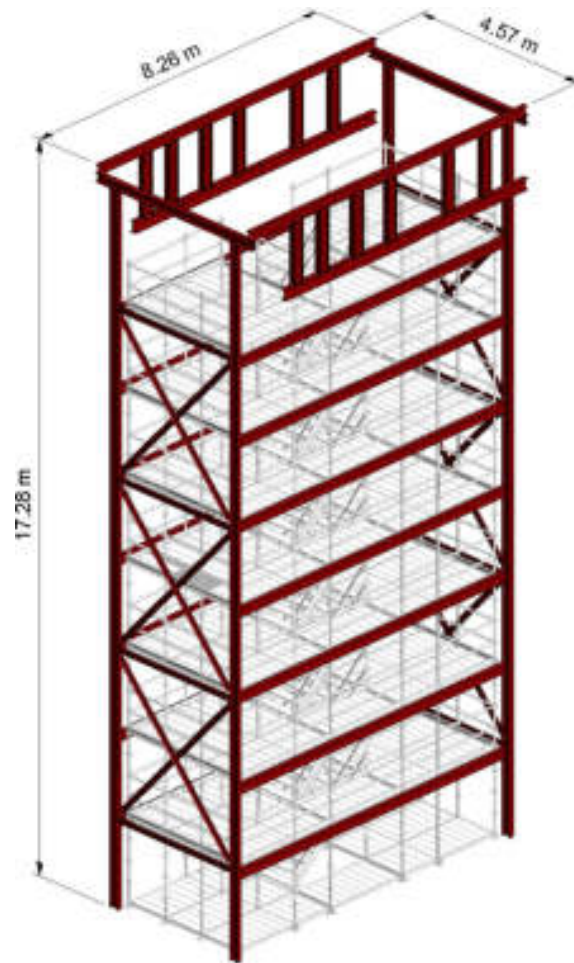


**Figure 9.16.** Isometric view of the APA assembly and cabling tower. The steel outer structure is shown in red. The inner scaffolding in gray permits work at different heights. The tower is designed to be two APAs wide to allow work on two of them side-by-side simultaneously. Both the north and south faces are equipped with assembly rails so that a single tower can support two assembly lines.

required to connect the cables to the FEMB and to properly bundle the cable into the cable trays in a way that allows the cables to be installed easily once the assembly is in the cryostat. Given the large number of person-hours needed for work at height, all measures will be taken to ensure that this work is safe. For this reason a large stable workdeck will be constructed as shown in figure 9.17. By running north-south I-beams from the cavern walls across the assembly towers, strong rigid support points are provided. Vertical posts down from these beams can then support the fixed workdeck as needed. Access to the workdeck is provided by a walkway along the west end of the platform that connects to both the assembly towers. A second means of egress is provided by a connection to the permanent stairs.

Once a top-bottom APA pair is assembled it can be moved onto the switchyard under the bridge. This switchyard, illustrated schematically in figure 9.17, is essentially a bridge crane running under the north-south bridge in the cavern. Several bridge beams (called shuttle beams) driven by electric trolleys move on the runway beams of the crane. A rail at the bottom of the crane mates with the



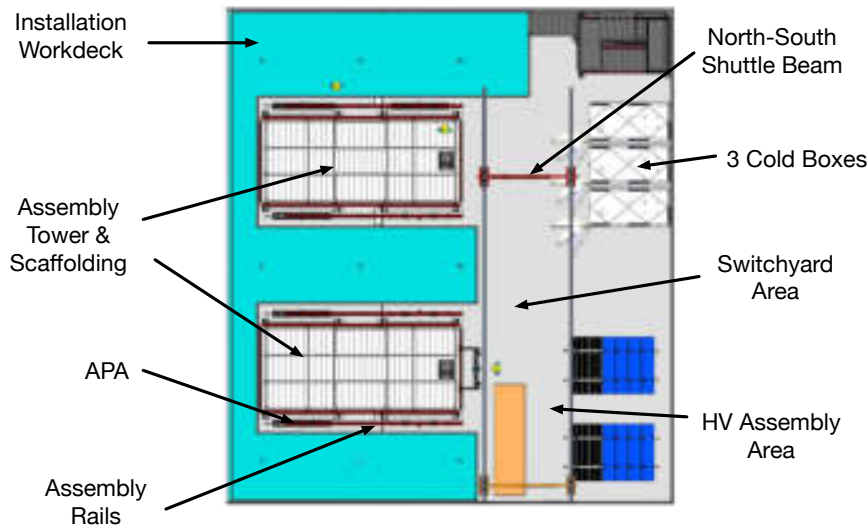


**Figure 9.17.** Installation workdeck, assembly towers and rails, switchyard, cold boxes and HV assembly area in the installation cleanroom. Plan view.

fixed beams from the assembly lines, the cold boxes, the TCO beams and the HV assembly area. By aligning the bridge beams with a set of fixed beams supported from the cleanroom roof, the APAs and CPAs can be transferred from the fixed beams to the bridge crane and moved to different locations in the cleanroom. The 12 m tall CPA panels will be assembled directly under the bridge crane and transferred directly from the assembly fixture to the switchyard crane.

The division of responsibilities between the installation and the consortia deliverables are defined in interface documents, but they are governed by a simple concept. Any part which bolts, pins or connects to a consortia deliverable is the responsibility of the consortia. General infrastructure, hoists, and cranes are the responsibility of the installation team. Thus, for example, the installation towers are installation's responsibility, while the fixtures that bolt to the towers and to the APAs are the responsibility of the APA consortium.

### 9.3.5 Cryogenics and Cold boxes

After an APA pair is fully assembled and cabled but before installation in the detector cryostat, it is thermally cycled in a tall narrow test cryostat, called a cold box, shown in figure 9.18). To test APAs at a rate necessary to keep up with the installation plan, we will use three identical cold boxes in the cleanroom. The cold boxes require a dedicated cryogenics system that uses a fine mist of cold nitrogen to cool down close to LAr temperature. This system is designed so that no liquid nitrogen will accumulate.

A cold box has external dimensions of 14.0 m by 3.2 m by 1.3 m (H×L×W). With three layers of 100 mm thick foam insulation, the internal dimensions are 13.4 m by 2.6 m by 0.7 m. A rail section similar to those used elsewhere in the cleanroom will be mounted inside each cold box to allow the cleanroom switchyard and trolleys to push an APA into a cold box. The cold boxes will be light-tight when closed to support PD testing. A support base under the cold boxes will adjust the height to mate with the cleanroom switchyard.

The cold box electronics feedthroughs will be similar to what is used on the top of the DUNE cryostat, except that short cables will be run from the warm interface electronics crate (WIEC) to a patch panel inside the cold box. This will allow the cable on the APA to connect directly to the test readout without having to remove any cabling. The cold box design is nearly the same as the successful ProtoDUNE-SP cold box. The outer shell is similarly constructed of a stainless steel plate with reinforcing ribs welded on. The height is of course doubled, and a hinged door is planned. Unbolting the door and lifting it off the ProtoDUNE-SP cold box required significant effort, and lacking full crane coverage in this case, doors that can be opened and closed using a scissor lift are necessary. The DUNE cold boxes will collectively need about 11 t of stainless steel, according to initial estimates. The finished boxes are too big to fit down the Ross Shaft. As the design continues, we will investigate whether the boxes can be brought underground partially assembled, or if they must be fully assembled in place.

The cold boxes and associated cryogenics system are the responsibility of the JPO and the design of the cold boxes will be provided by the CERN team, which designed the ProtoDUNE test cryostats. The cryogenics system will be designed by the LBNF cryogenics team.

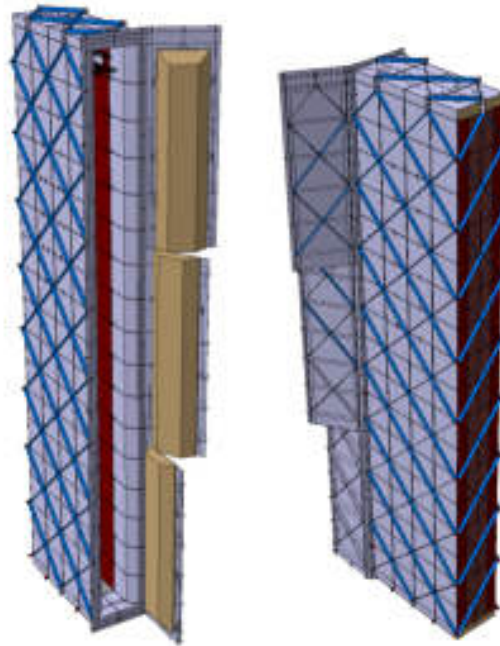


**Figure 9.18.** Cold boxes used to thermally cycle the fully assembled APA pairs.

The cold boxes will be used to test the APAs underground prior to installation. The cryogenics supporting the cold boxes must ensure their reliable and safe operation; to that end, the system must

- support three cold boxes operating in parallel: one in cool-down mode, two either in steady-state or warm-up modes;
- allow personnel in the cleanroom during all phases of the purge, cool-down, operation, and warm-up modes;
- test the detector modules at near LAr temperature;

- operate 24 hours a day;
- allow remote operations; and
- be located in the vicinity of the TCO, as space is available on top of the cryogenics mezzanine on the roof of the cryostat.

It must operate in the following modes:

- **purge:** during this mode, air is removed from the system (cold box and cryogenics system) and replaced with dry nitrogen. The concentration of moisture is monitored, and when it no longer decreases, the cool-down can commence.
- **cool-down:** cold nitrogen is introduced into the system to cool the inside of the cold box and the APA inside it. This should take 24 hours, during which time the temperature decreases from room temperature to about 90 K.
- **steady-state operations:** after reaching approximately 90 K, the detector is turned on and fully tested. This takes about 2 shifts.
- **warm-up:** after completing the test, the system is warmed up to room temperature over a period of 24 hours.

**Table 9.4.** Table of parameters for the cold box cryogenics system.

| Parameter                           | Value        |
|-------------------------------------|--------------|
| Dual APA thermal mass               | 1,600 kg     |
| Temperature uniformity              | +60 K / -0 K |
| Electronics load                    | 300 W        |
| Cold box insulation thickness       | 0.3 m        |
| Target cool-down temperature        | 90 K         |
| Target cool-down duration           | 24 hr        |
| Target steady-state duration        | 24 hr        |
| Target warm-up duration             | 24 hr        |
| Maximum cooling power               | 13 kW        |
| Maximum liquid nitrogen consumption | 300 l/hr     |

The evaporation of liquid nitrogen provides the cooling power for the system. Warm nitrogen and a heater provide the heating power. At peak consumption, the expected maximum heat load is 8.5 kW. Assuming a 50% margin on the refrigeration load, the cryogenics system requires 13 kW of net cooling power at peak consumption, which equals about 300 l/hr of evaporating liquid nitrogen.

Two layouts are currently under consideration: (1) a closed-loop with mechanical refrigeration, in which liquid nitrogen is generated in situ, circulated, and the spent nitrogen recondensed before being put back into the system; and (2) open-loop, in which liquid nitrogen is transported

underground by means of portable dewars, circulated, and the spent nitrogen vented away. For the closed-loop, we would need a mechanical refrigeration capable of supplying 13 kW of cooling. For the open-loop, it is possible to use a 2000 l dewar, which is commercially available and transportable up and down the Ross Shaft inside the cage. To supply the required amount of nitrogen, four trips per day are needed over the two-year period of detector installation.

The current versions of the closed-loop and open-loop systems are presented in figures 9.19 and 9.20, respectively. Both options are viable and a decision will be taken on which to adapt after the analysis is complete.

A full ODH analysis will be performed once the design has progressed to the point where the process flow and pipe dimensions are fixed (These are a necessary input to the analysis). Since no liquid is accumulated and the room volume is large, our initial assessment is that standard ODH safety measures will be adequate.

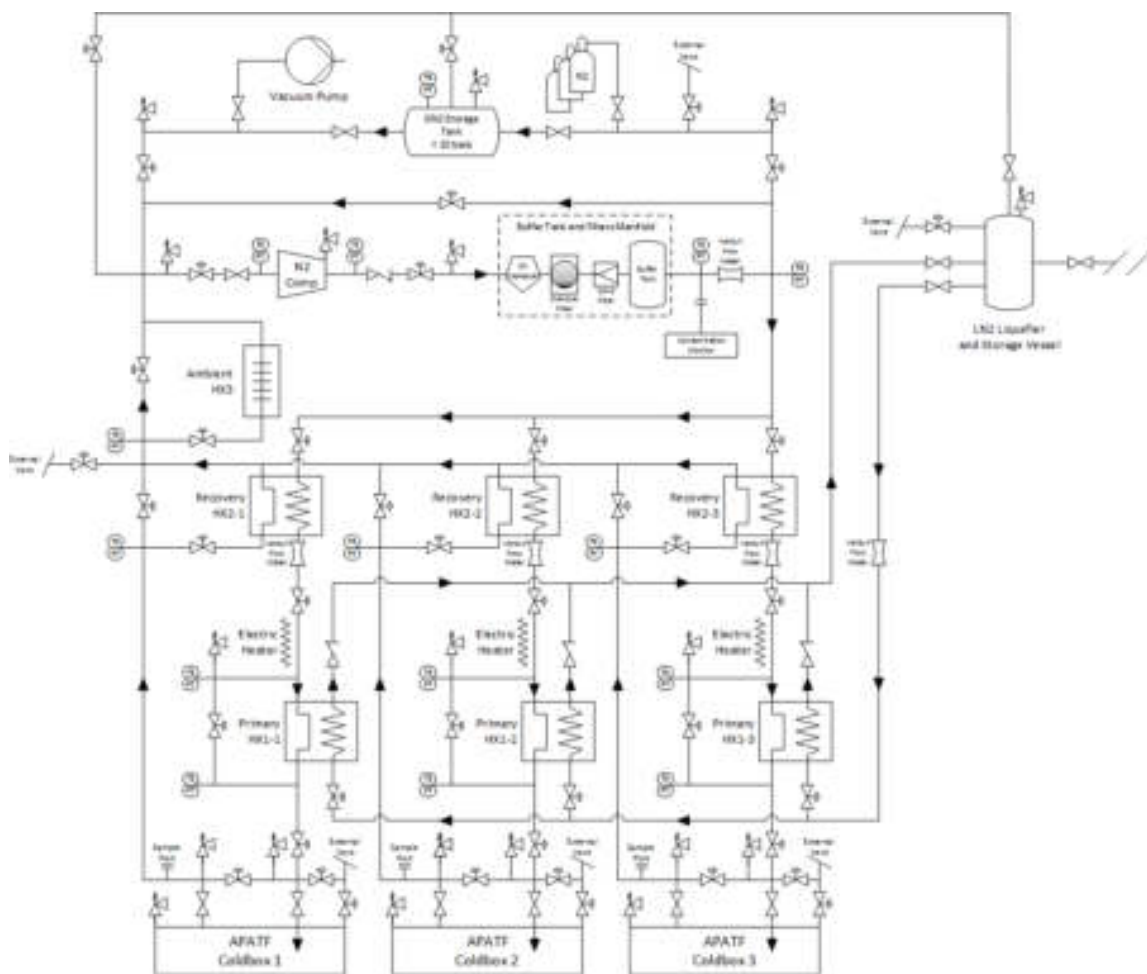


**Figure 9.19.** Layout of the cryogenics supporting the APA test facility with mechanical refrigeration (closed-loop).

2020 JINST 15 T08010

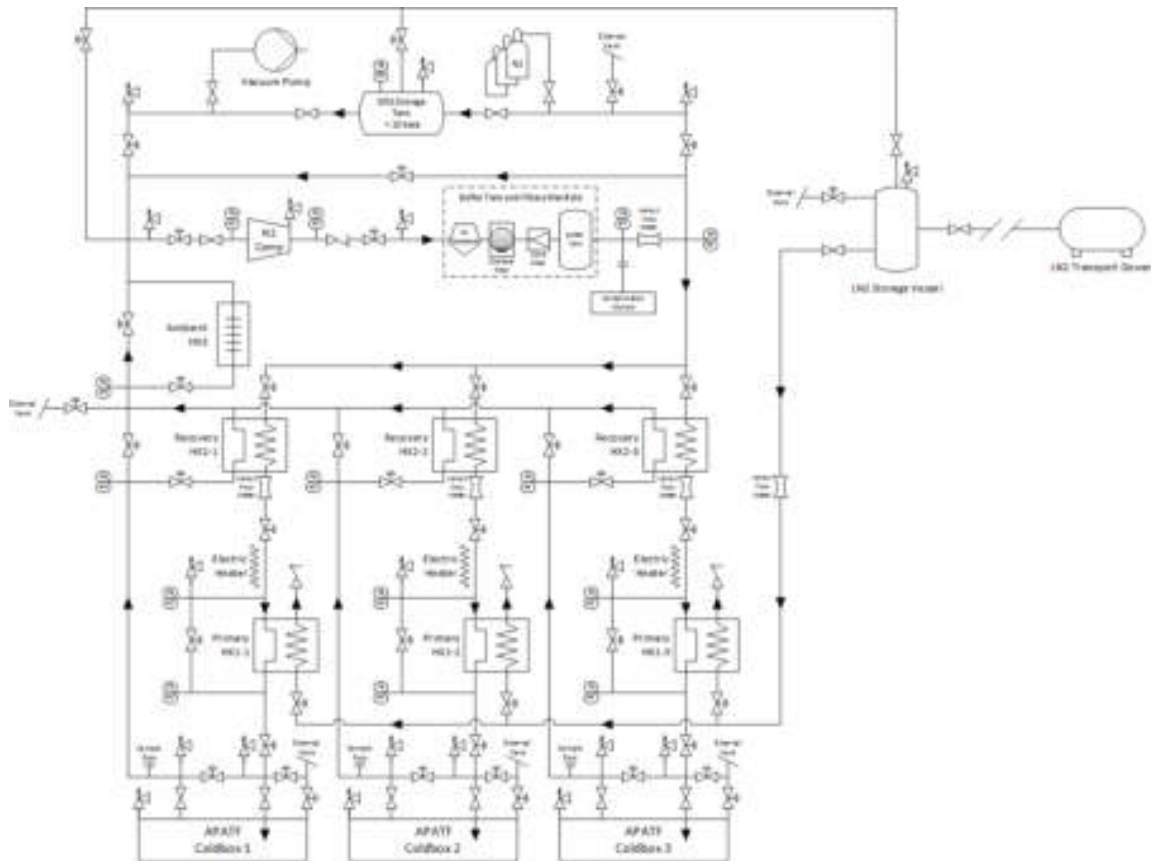


**Figure 9.20.** Layout of the cryogenics supporting the APA test facility with open-loop refrigeration (open-loop).

### 9.3.6 Prototyping and testing (QA/QC)

Installing all this new equipment underground during the installation setup phase involves many new techniques and unique work. While most of the procedures will have been tested during the trial assembly at Ash River, everything must be properly approved. The main APA and CPA towers will already be structurally approved, but all lifting fixtures, shuttle beams, crane tower connections, and cold box connections must undergo load tests.

The load test program for the lifting fixtures, shuttle beams, crane tower connections, and cold box connections will be documented in test procedures in accordance with the LBNF DUNE QA program. These test procedures will (1) list prerequisites for testing, (2) identify fixtures and test equipment, and (3) provide step-by-step instructions, acceptance criteria, and documentation requirements. They will be in place prior to the start of testing. The test results will be documented and approved by the systems engineering team prior to use of the lifting fixtures, shuttle beams, and crane tower connections.

The cold boxes and cryogenics system will also be tested, which may require restricting access to the cleanroom for several days for system checks. The cold boxes and the associated cryogenic system test program will be similar to the test program that was instituted for ProtoDUNE-SP. This test program will also be documented in procedures in accordance with the LBNF DUNE QA

program. These test procedures will (1) list prerequisites for testing, (2) identify test equipment, and (3) provide step-by-step instructions, acceptance criteria, and documentation requirements. The test results will be documented and approved by the systems engineering team prior to use of the cold box and cryogenics system.

### 9.4 Detector installation

As mentioned in section 9.2, the DUNE detector installation will proceed in three phases: CUC set up, installation set up, and the detector installation. The schedule in figure 9.21 shows the major underground activities and gives an idea of what work occurs in each phase.

The first phase, CUC set up, begins when the underground area for the north cavern and CUC become available to LBNF and DUNE. At this time, the LBNF cryostat construction begins in the north cavern, and DUNE equipment installation begins in the CUC, specifically, infrastructure in the DUNE data room. Figure 9.22 shows a top view of the underground areas and the location of the dataroom at the west end of the CUC.

The detector installation setup phase (referred to as Infrastructure Det#1 in the table in figure 9.21) begins during the cryostat membrane installation period. In this phase, the equipment needed for detector installation is erected in the north cavern. This includes the bridge across the cavern, the cleanroom, lifting equipment and work platforms, the cold boxes and cryogenics system for APA testing, and the DSS and switchyard. The detector itself is installed in the third phase of the installation.

#### 9.4.1 Installation process description

##### 9.4.1.1 CUC installation phase

Once the LBNF CF outfitting of the north cavern and the CUC is complete, LBNF begins the first cryostat installation in the north cavern and DUNE can begin to install equipment in the data room and work area room in the CUC. See figure 9.23. DUNE will not have access to the north cavern due to the heavy steel work for the cryostat. At this point LBNF CF will have installed redundant single-mode fiber up the shafts to provide external connectivity, and in the empty data room, an 18 in false floor, a 500 kVA power disconnect, and connections for sufficient chilled water to cool the racks. The data room, like the adjacent CF electronics room, will be outfitted with a dry fire-extinguishing system.

The water-cooled racks, cable trays, power distribution, and water distribution in the data room are the responsibility of DUNE and will be installed once the space becomes available. Installation of the racks must be coordinated with CF since the first two racks are for CF use and must be in place before the first phase of work underground is complete. Some small overlap will be needed between CF and DUNE at this time. The general-purpose network will be installed by Fermilab's SDS and connected to the Ross Shaft fiber optics. This is required for most subsequent work in the underground area. The DAQ fiber trunk between the detector cavern and the CUC data room will be installed after the cable trays, electronics mezzanine, and racks are available in the north cavern.

Data from the detector electronics will be transmitted over a multimode fiber trunk from the WIBs on top the SP module to the DAQ data room in the CUC, shown in figure 9.23. The data



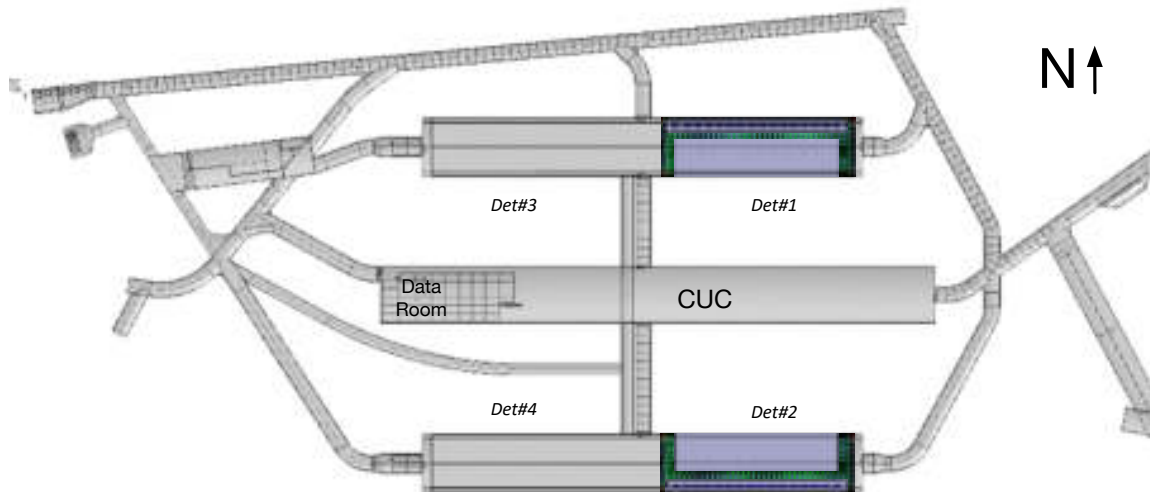


**Figure 9.22.** Top view of the layout at the 4850L at SURF. Shown are the three large excavations and the location of detectors in the north (upper) and south caverns. The detector caverns (north and south) are 145 m long, 20 m wide, and 28 m high. The CUC in the middle houses the DUNE data room where the DAQ will be installed and the underground utilities. The north, middle and south caverns are also referred to as cavern#1, cavern#2 and cavern#3 in figure 9.21.

room will contain 60 water-cooled racks, two of which are reserved for CF use, two for CISC servers, and the rest for DAQ servers and networking. Racks for all four modules will be installed at the beginning of the CUC commissioning phase because they must be plumbed into the cooling water below the data room’s drop floor and wired into power distribution from the ceiling. DAQ equipment will populate the racks as needed for servicing the detector commissioning. For the first detector module, details of this configuration will be informed by DAQ vertical slice tests done at other institutions.

At the same time, the eight above-ground DAQ racks that receive data from the underground data room and transmit the data to Fermilab will be installed, connected to the network, and connected to the single-mode fiber in the Ross and Yates Shafts. With this infrastructure in place, the DAQ group can begin constructing and testing the final DUNE DAQ, starting with the timing system. Enough DAQ back-end servers to support the first APAs will be operational before the APAs are installed. The remainder of the DAQ will grow in parallel with APA installation.

The underground experimental work area (shown as “CONTROL ROOM” in figure 9.23) must serve a variety of purposes during the DUNE installation. Initially, the area will be outfitted with office equipment for the installation team, workstations for DAQ, and a basic conference area for meetings. The room is 17 m wide with portions that are 5.5 m and 8 m deep.

During this early installation stage, the machine shop and DUNE storage area will be set up in the detector excavation area and shared with the cryostat team.



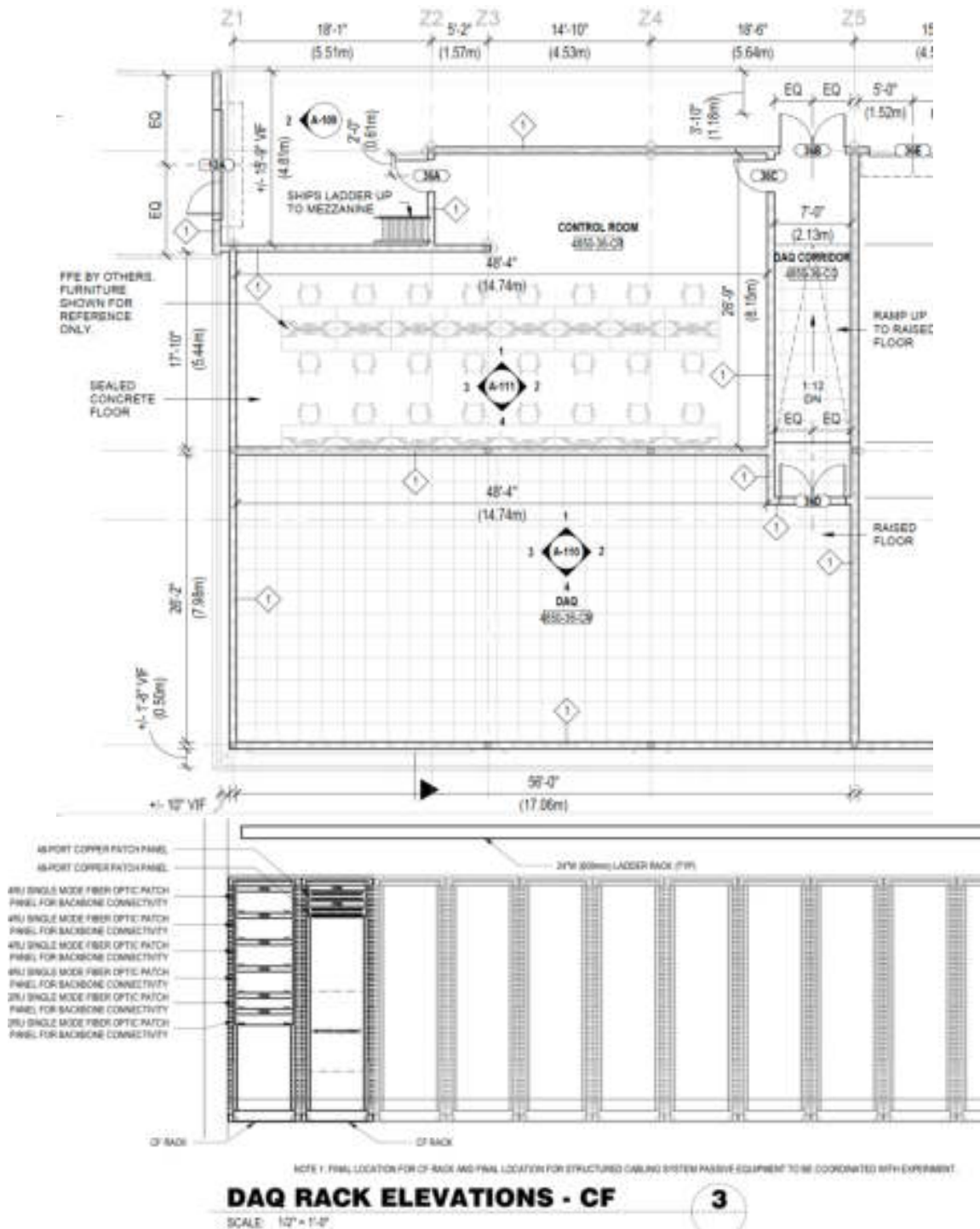


**Figure 9.23.** Top: the overall layout of the DUNE spaces in the CUC. A110 is the DUNE data room, which houses the underground computing, and A111 is a general-purpose work area (not a control room, as labeled) that we call the experimental work area. Bottom: the first row of ten racks in the data room is shown. The first two represent the CF interface racks. The images were taken from the ARUP 90% design drawings U1-FD-A-108 and U1-FD-T-701 [157].

2020 JINST 15 T08010

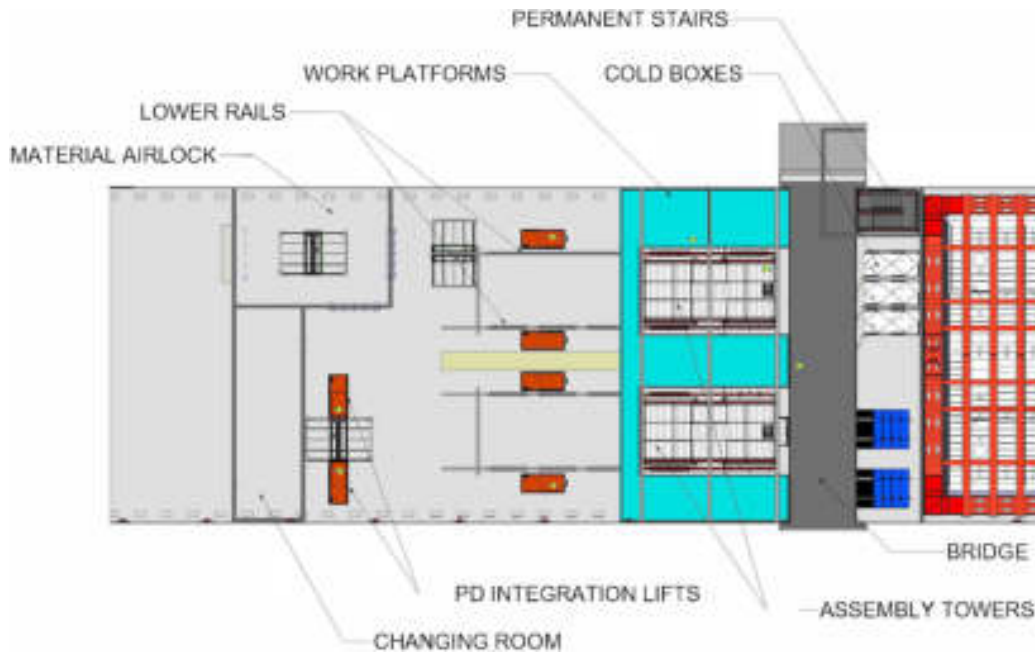


**Figure 9.24.** Top view of the installation area highlighting the infrastructure. The 18.9 m wide cryostat is on the right. The cleanroom roof and cavern walls are removed in this view.

#### 9.4.1.2 Installation setup phase

Once the steel structure of the cryostat is complete, the remaining work by the LBNF cryostat team will be focused inside the cryostat, installing the insulation and membrane. LBNF activity outside the cryostat will consist mainly of transporting the 4,000 crates of foam and other materials from the cavern to inside the cryostat. Since the cryostat outer steel structure will be in position, DUNE can begin installing the infrastructure needed outside the cryostat to support detector installation. Figure 9.24 shows the major pieces of infrastructure supporting the detector installation. The first piece of equipment is the bridge between the north and south drifts. This will allow the cryogenics equipment to travel from the north drift to the CUC and will provide part of the structure for the cleanroom. It also provides an additional means of egress in an emergency.

As part of the bridge construction, the crane under the bridge will be mounted. This will be used to lift crates off the floor and bring them into the cryostat, freeing the cavern crane for work elsewhere. The decking on top of the cryostat is also installed in this early stage to provide a safe work surface.

The largest and most time-consuming pieces of equipment to construct in this phase are the three cold boxes and their associated cryogenics system. The cold boxes, visible in figures 9.18 and 9.24, will likely need to be constructed in place due to their size (see section 9.3.5) and fabrication will begin as early as possible. If it is possible to bring them down the shaft partially assembled, then once the first detector module is complete, we can break them down to their pre-assembled parts and move them to the second detector module area.

After the bridge crane under the north-south bridge is in place the APA assembly and cabling towers are installed. The two towers have enough space between them, as described in section 9.3.4,

to walk through or perform work. With the towers in place, the north-south support beams and the fixed platforms can be installed. This work is done at height so it will only cause temporary interruptions to the material transport along the floor to the cryostat; the lower set of rails and the CPA assembly equipment can be installed at the convenience of the cryostat installation crew.

When the cryostat membrane work is complete the cryogenic piping inside the cryostat can be installed, the cryostat cleaned, and the false floor installed. After the cryostat is cleaned the HEPA filters will be installed in air handling units for the cryostat and purified air will begin flowing. A curtain over the TCO can be used to prevent dust from the cavern from entering the cryostat until the cleanroom walls are constructed.

In parallel to the installation of the cryogenic piping, the walls of the cleanroom can be assembled and AC power and fire suppression installed. Finally, the floor is painted and cleaned, making the cleanroom ready for operation.

On the cryostat roof the installation of the cryostat crossing tubes proceeds in parallel with the cryostat membrane assembly sequence. The crossing tubes are welded to the 1 cm thick steel cryostat roof and cross braced to the large I-beams. The thin-walled tubes that penetrate the foam insulation are welded to the cryostat inner membrane.

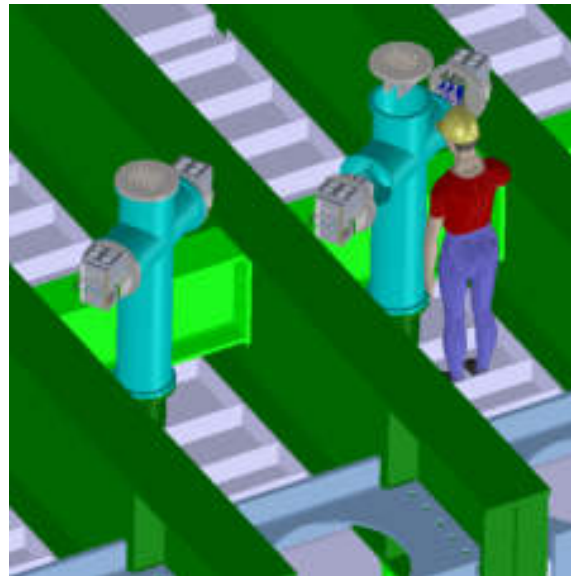


**Figure 9.25.** Installation of the crosses to which the TPC electronics warm readout and the PD cables are connected. In this figure the cryostat roof decking is not shown. During the cross installation a section of decking will be removed so people can access the required flanges and work at a comfortable height.

Once the crossing tubes are installed and leak-checked, we connect the TPC electronics crosses and mount the feedthrough flanges for the CE and PDs onto the crosses. The height of the crosses was chosen to allow a person to work comfortably on the WIECs and PD flanges while standing on the cryostat roof. A fully assembled cross is shown on the left of figure 9.25, and a cross with a WIEC extracted in “assembly position” is shown on the right. The present plan is to install the crosses shortly after the cryostat crossing tubes are installed. This allows us to seal the large openings in the cryostat roof to prevent dust from entering. For this stage, temporary rubber seals

are used for the flanges; they must be removed during the cabling process later in the installation. When the WIEC installation is complete the TPC electronics is ready for the installation of power and fiber optics for readout.

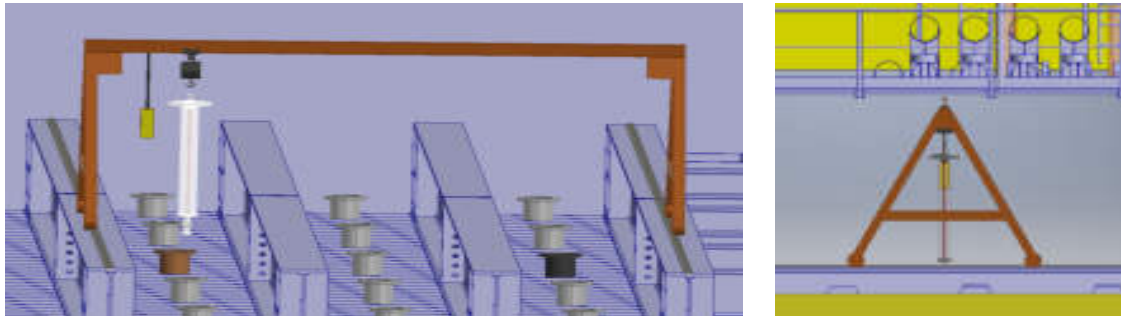


**Figure 9.26.** The DSS support feedthroughs are installed using a gantry crane running along the roof of the cryostat. The cryostat decking is not shown. The gantry can move freely on the cryostat roof decking. The gantry crane is selected to fit under the mezzanine as shown in the right panel.

The DSS support feedthroughs can be installed in parallel to the TPC electronics crosses. This is the first step in the DSS installation. A gantry crane on top of the cryostat picks up the feedthroughs and lowers them into the cryostat crossing tubes as shown in figure 9.26. There are 20 feedthroughs per row and five rows, for a total of 100 feedthroughs. A fixture with a tooling ball is attached to the clevis of each feedthrough. The horizontal *XY* and the vertical *Z* positions of this tooling ball are defined, a survey is performed to determine the location of each tooling ball center, and adjustments are made to get the tooling ball centers to within  $\pm 3$  mm of the nominal position. The 6.4 m long I-beams are then raised and pinned to the clevis. Each beam weighs roughly 160 kg (350 lbs). A lifting tripod is placed over each feedthrough's supporting beam, and a 0.64 cm (0.25 in) cable is fed through the top flange of the feedthrough down 14 m to the cryostat floor where it is attached to the I-beam. The cable access port and lifting cable are shown in figure 9.27. The winches on each tripod raise the beam in unison to position it at the correct height for pinning to the feedthrough clevis. Once the beams are mounted, a final survey of the beams ensures proper placement and alignment.

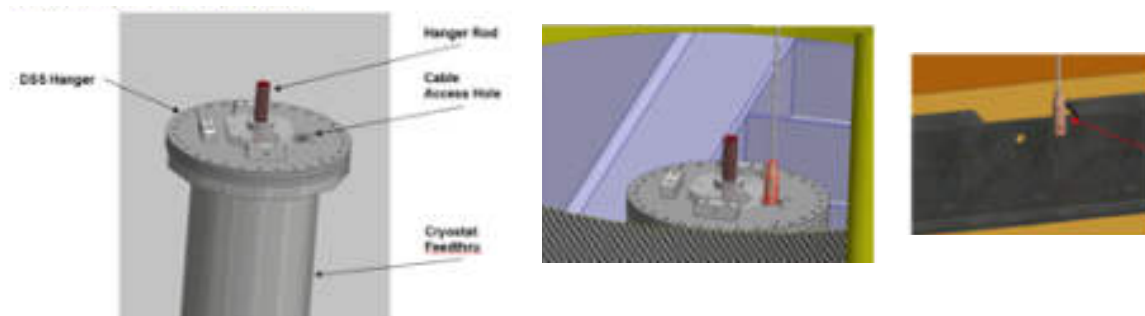


**Figure 9.27.** A cable access port is included in the DSS flange. This is used to feed a cable from the roof through the flange and attach it to the I-beams during DSS installation.

Next it is time to install the mezzanines for the cryogenics system and the detector electronics racks, followed by the cable trays, piping, lighting, and cryostat roof flooring. At this point, the cryostat roof is ready for DAQ and cryogenics system installations to begin; this will proceed in parallel with the detector installation.

### 9.4.1.3 Detector installation phase

At the start of the detector installation phase, the cleanroom and all equipment inside are operational, the DSS is installed, and the cryostat is clean and ready for installation. Figure 9.24 shows the layout (plan view with the roof removed) of the cleanroom during the detector installation phase; the cryostat is on the right and the open cavern on the left. In the north-east corner of the figure (upper right corner), the access (permanent) stairway is shown. This stairway is inside the cleanroom and allows people easy access to both the work platforms and the cleanroom floor. The doors to the stairway will never be locked; the stairway is considered a means of egress in emergency, as it leads to an exit through the mucking drift. A second stairway and an industrial elevator at the west entrance to the cavern provide access to the cavern floor for personnel and equipment. The primary changing room is in the southwest corner of the cleanroom and a smaller changing room (shown in figure 9.14) will be situated near the stairs at the 4850L for people accessing the work platforms.

In the north-west corner of the cleanroom is the material airlock where all materials enter through tall doors. Outfitting the airlock with a removable roof is under consideration. It would allow entry of equipment via the cavern crane, which could facilitate the process.

Labor for the detector installation phase is split between the JPO and the DUNE consortia.

The detector installation team includes the detector installation manager, one installation shift supervisor per shift, the JPO technical support team, and DUNE consortia scientific and technical personnel. (See figure 4.5 in Volume III, DUNE far detector technical coordination, chapter 4.) The detector installation manager is responsible for communicating with the underground cavern coordinator for all logistics, shipping, and inventory issues. They organize the daily underground detector installation tasks and lead the detector installation part of the shift-change meeting. The detector installation team is divided into several work crews operating in the cleanroom and cryostat. They are responsible for moving all detector components into the materials airlock, cleanroom, cold box (if needed), and cryostat. Additional activities in the cleanroom include linking the APAs together, installing PDs, installing and cabling the electronics, and removing APA protective covers. Inside the cryostat, the detector installation team installs the TPC components.

Each of the DUNE FD consortia has specific tasks related to its subsystem. The installation activities are planned estimating both the JPO and consortia labor contributions.

The first detector equipment to be installed are CISC T-gradient thermometers, an array of purity monitors, and cameras, all at the east end of the cryostat. This equipment will be used to monitor the cool-down, filling, and commissioning of the detector. Some equipment for the laser calibration system is also installed at this time, including some positioning diodes and possibly an optical mirror-based switching system. The signals exit the cryostat via electrical feedthroughs distributed across the cryostat roof and integrated with the DSS support structure, as shown in figure 9.28. Because all these components are small, they can be installed using a scissor lift with 12 m reach. At present, this is the tallest battery operated (thus cleanroom compatible) scissor lift rated for use in the USA that we have identified.

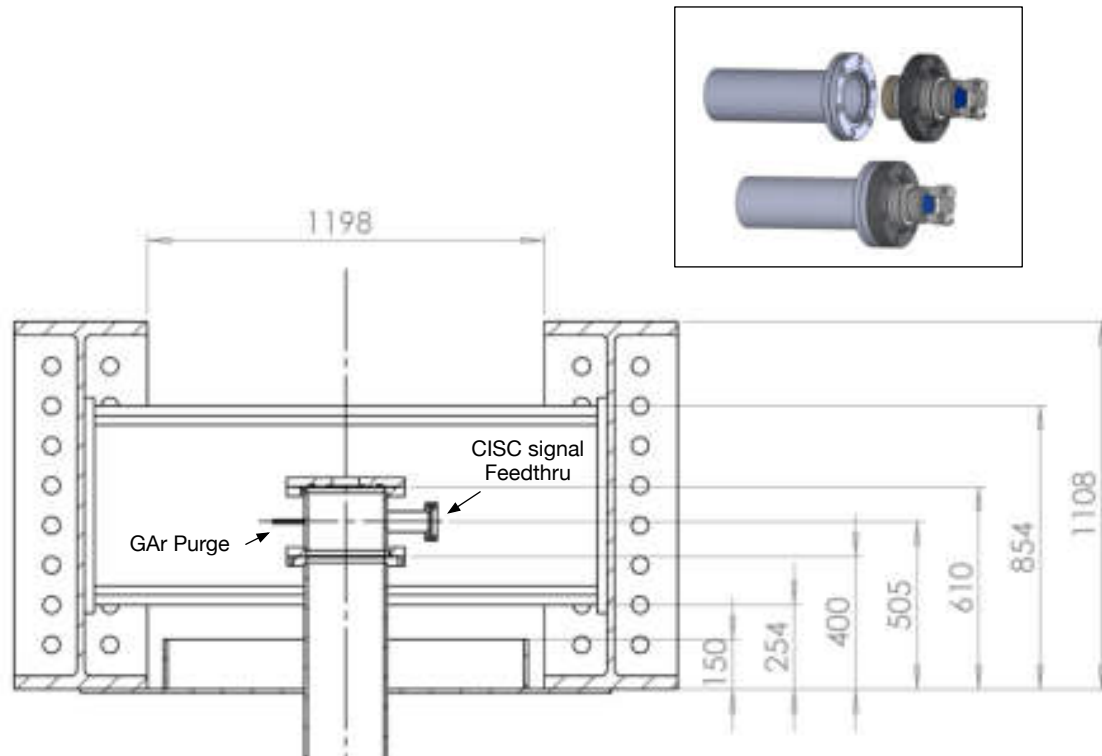


**Figure 9.28.** Design of the instrumentation feedthroughs. The signal feedthrough is integrated with the DSS support feedthroughs. A side port on a short spool piece in the DSS support structure allows the instrumentation cables to be fed through the cryostat walls where needed.

Cabling for the remaining static T-gradient monitors is also installed before the start of TPC installation. The thermometer cables and mechanical supports are anchored to the cryostat using the bolts running along the cryostat's top and bottom edges and can be installed once the cryostat is clean. To avoid damaging the small and fragile thermometers, they are not plugged into the small IDC-4 connectors until just before the corresponding APA is moved into its final position. Cables and supports for the thermometers on the pipes below the detector and on the cryostat floor are installed immediately after installing the static T-gradient monitors on the walls. Again, the thermal sensors themselves are installed later, just before unfolding the bottom GPs, to avoid damage.

Individual sensors on the top GP must be integrated with the other GPs. For each CPA (with its corresponding four GP modules), cable and sensor supports will be anchored to the GP threaded rods. Once the CPA is moved into its final position and its top GPs are ready to be unfolded, sensors on these GPs are installed.

Installing fixed cameras is, in principle, simple but involves a large number of interfaces. The enclosure for each camera has exterior threaded holes to facilitate its mounting on the cryostat wall, the cryogenic internal piping, or the DSS. Each enclosure is attached to a gas line to maintain appropriate underpressure in the fill gas, requiring an interface with cryogenic internal piping. Camera cables are run through cable trays to flanges on assigned instrumentation feedthroughs.

A summary of all the cryogenics instrumentation provided by the CISC consortium is shown in figure 9.29.

At this point the quartz optical fibers required for the PD monitoring system are run from the optical flange locations (still being finalized) to locations on the CPA support beams of the DSS, to be connected later to the diffusers mounted on the CPAs.

The residual gas analyzers that monitor impurities in the GAr system must be installed before the piston purge and gas recirculation phases of cryostat commissioning. However the actual installation time depends on the schedule for outfitting the mezzanine and installing the GAr purge piping. These instruments are installed near the tubing switchyard to minimize tubing run length and for convenience when switching the sampling points and gas analyzers.

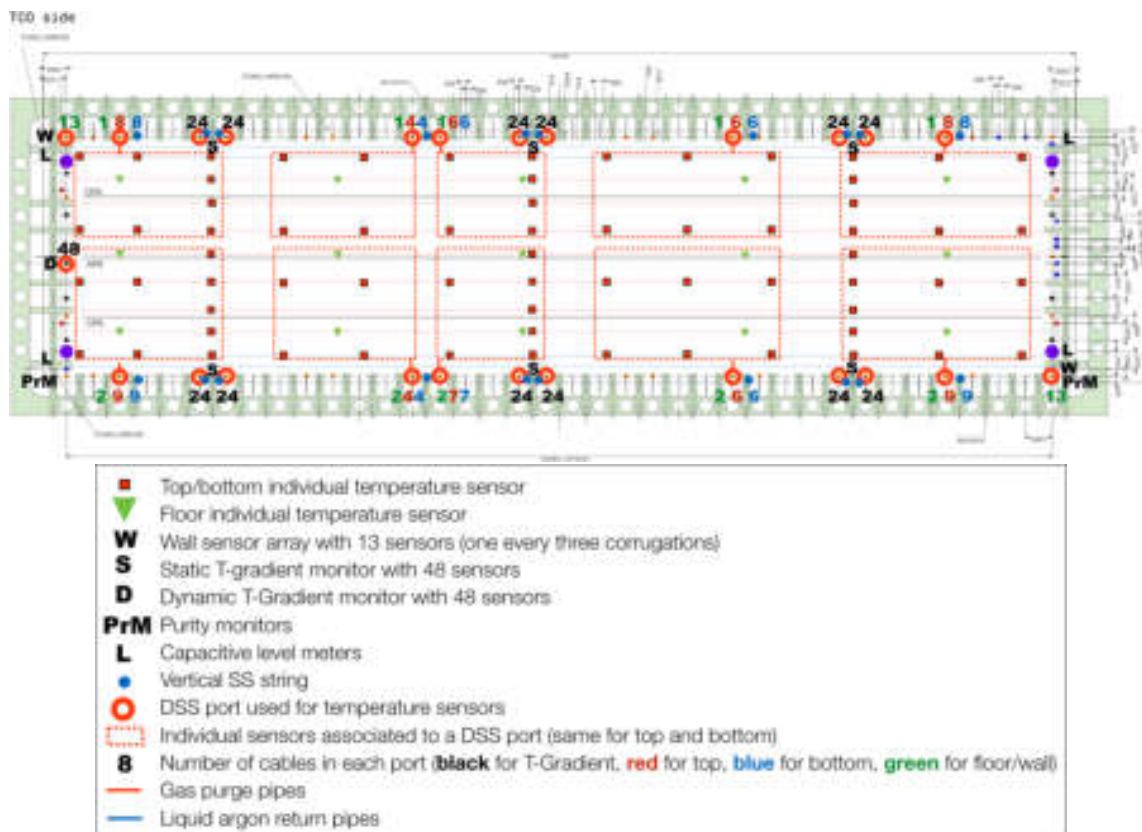
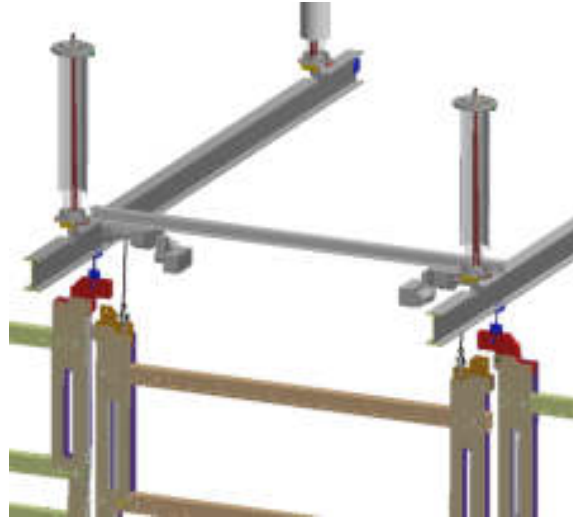


Figure 9.29. Distribution of various CISC devices inside the cryostat.

Next the east endwall FC is installed. The endwall planes are brought underground in custom crates. Each of the eight crates holds four endwall modules. Eight modules are needed to build one complete 12 m tall plane. First a custom hoist is installed on the end of the DSS beam for lifting and assembling the modules in place, as shown in figure 9.30. The endwall FC transport crates are then brought to the material airlock using a forklift where they are cleaned. Once clean, the crates are moved into the cleanroom and placed next to the TCO. Then a hoist running on the rails through the TCO lifts the endwall modules onto the transport cart, which is then rolled into the cryostat. Figure 9.31 shows an endwall module being transferred to the transport cart. The top endwall module is then attached to the installation hoist and lifted out of the cart. When the module

is free of the cart, the cart is re-positioned so the second module can be attached to the first, and the pair is then lifted. This process is repeated until the full 12 m endwall FC plane is assembled and can be attached to the DSS. Figure 9.30 shows an endwall plane being lifted into position. All the HV connections inside the plane can now be tested. The process is then repeated for the remaining three endwall planes comprising the east endwall FC.



**Figure 9.30.** Image showing the hoisting equipment used to lift the endwall into position. The field shaping strips are removed in this image. This shows one of the 3.5 m endwall planes in place and a second being positioned.

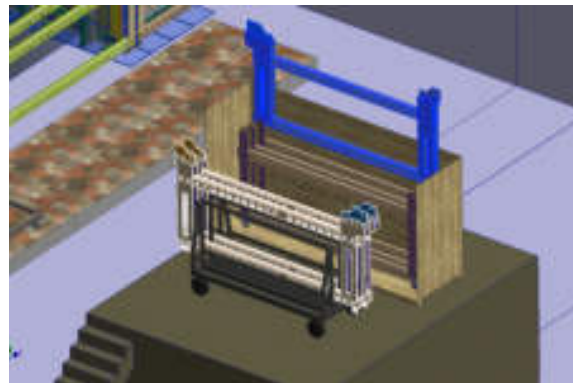


**Figure 9.31.** The endwalls are lifted out of the transport crates using the one of the hoists on the installation switchyard. Each module is placed on a custom cart that is rolled into the cleanroom. The pedestal in front of the TCO is at the height of the cryostat floor so carts can be used to bring material into the cryostat. The guard rails are not shown.

The installation of an APA and CPA with top and bottom FC modules is the most labor-intensive part of the detector installation. Figure 9.32 represents one of the 25 rows of TPC. DUNE aims to perform work in parallel to the extent possible and finish installing one row every week. This requires that several separate teams work in the cleanroom, inside the cryostat, and on the cryostat roof simultaneously — positioning the equipment, integrating PD into the APA, mounting



the CE FEMB on the APA connecting the cables, cold testing APA, installing APA in the cryostat, assembling and installing CPA-FC, and deploying the FCs. Figure 9.33 shows the labor breakdown and activities in the airlock, cleanroom, and cryostat for the APA installation. These labor estimates will be refined during time and motion studies at Ash River. This complicated installation process will be described in steps: first the APA assembly work in the cleanroom, followed by the CPA assembly, and finally the installation process inside the cryostat.

While the APAs, CPA, and FC are installed, the area outside the cleanroom in the north cavern is available for storage; this area has sufficient capacity to store one full month's worth of equipment. As it is called for, equipment will be brought into the cleanroom's materials airlock through a roll-up or curtain door in the west wall using either an electric forklift or electric pallet jacks.

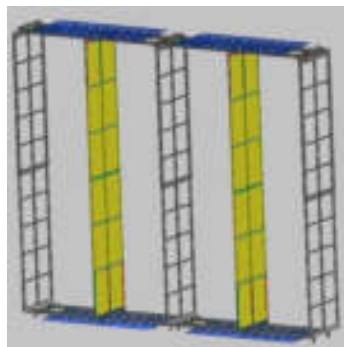


**Figure 9.32.** One row of the APA and CPA with associated FCs. The FCs are shown deployed in the final orientation. The equipment in the figure represents 1/25 of the total TPC.

|             |                               | Week 1  |       |         |         |          |      |         |       |            |       |         |       |         |       |         |       |       |      |       |       |       |            |
|-------------|-------------------------------|---------|-------|---------|---------|----------|------|---------|-------|------------|-------|---------|-------|---------|-------|---------|-------|-------|------|-------|-------|-------|------------|
|             |                               |         |       |         |         | Day 1    |      |         |       | Day 2      |       |         |       | Day 3   |       |         |       | Day 4 |      |       |       |       |            |
|             |                               | Shift 1 |       | Shift 2 |         | Shift 1  |      | Shift 2 |       | Shift 1    |       | Shift 2 |       | Shift 1 |       | Shift 2 |       |       |      |       |       |       |            |
| Task        | APA                           | CE      | Shift | HV      | Riggers | Location | 6:00 | 11:00   | 16:00 | 21:00      | 6:00  | 11:00   | 16:00 | 21:00   | 6:00  | 11:00   | 16:00 | 21:00 | 6:00 | 11:00 | 16:00 | 21:00 |            |
| APA Pair #1 | # FTE                         | # FTE   | # FTE | # FTE   | # FTE   |          |      |         |       |            |       |         |       |         |       |         |       |       |      |       |       |       |            |
| 1           | Move APA Pair into SAS        | 3       |       |         | 3       | SAS      | 6    | 3       | 3     | APA, 3 Rig |       |         |       |         |       |         |       |       |      |       |       |       |            |
| 2           | Install Bot APA PD/Test       | 3       |       |         | 3       | SAS      | 6    | 6       | 3     | APA, 3 Rig |       |         |       |         |       |         |       |       |      |       |       |       |            |
| 3           | Install Bot APA PD/Test       | 3       |       |         | 3       | SAS      |      |         | 6     | 6          | 3A-3R |         |       |         |       |         |       |       |      |       |       |       |            |
| 4           | Move APA to Work Station      | 3       |       |         | 3       | SAS      |      |         |       | 6          |       |         |       |         |       |         |       |       |      |       |       |       |            |
| 5           | Cable work/Test               |         | 4     |         |         | WS-1     |      |         |       |            | 4     | 4       | 4     | 4       | CE    |         |       |       |      |       |       |       |            |
| 6           | Cable management/CB Cable     |         | 4     |         |         | WS-1     |      |         |       |            |       |         |       | 4       | 2A-2R |         |       |       |      |       |       |       |            |
| 7           | Remove Protective panels      | 2       |       |         | 2       | WS-1     |      |         |       |            |       |         |       |         |       |         |       |       |      |       | 2     | 2     | 2-Surveyor |
| 8           | Photogrammetry/Survey         | 2       |       |         |         | WS-1     | 2    | 2       | 2     | 2          | 2     | 2       | 2     |         |       |         |       |       |      |       | 2     | 2     | 2          |
| 9           | Close up Cold Box/Warm test   | 1       | 1     |         | 2       | CB-1     | 2    | 2       | 4     | 4          |       |         |       |         |       |         |       |       |      |       |       | 4     | 4          |
| 10          | Cool Down                     |         | 2     |         |         | CB-1     |      |         |       |            | 2     | 2       | 2     | 2       |       |         |       |       |      |       |       |       |            |
| 11          | Cold Tests                    |         | 2     |         |         | CB-1     |      |         |       |            |       |         |       | 2       | 2     |         |       |       |      |       |       |       |            |
| 12          | Warm Up                       |         | 2     |         |         | CB-1     |      |         |       |            |       |         |       |         | 2     | 2       | 2     | 2     |      |       |       |       |            |
| 13          | Open Cold Box-Remove          | 1       | 1     |         | 2       | CB-1     |      |         |       |            |       |         |       |         |       |         |       |       |      |       |       | 4     | 4          |
| 14          | Move to cryostat-Position     |         |       |         | 4       | Cryo     |      |         |       |            |       |         |       |         |       |         |       |       |      |       |       |       |            |
| 15          | Final Cable-Cryostat-in & out |         | 4     |         |         | Cryo     |      |         |       |            |       |         |       |         |       |         |       |       |      |       |       |       |            |
| 16          | DAQ Test                      |         | 4     |         |         | Cryo     |      |         |       |            |       |         |       |         |       |         |       |       |      |       |       |       |            |
| 17          | Deploy                        |         |       |         | 4       | Cryo     |      |         |       |            |       |         |       |         |       |         |       |       |      |       |       |       |            |
| 18          | Final Test                    |         | 4     |         |         | Cryo     |      |         |       |            |       |         |       |         |       |         |       |       |      |       |       |       |            |

**Figure 9.33.** Typical APA schedule for SP module. As described in section 9.6, two 10 hour shifts are planned Monday to Thursday and a smaller shift Friday to Sunday for cryogenic and other tests.

An APA transport crate that holds two APAs is first rotated to the vertical orientation and bolted to a custom-weighted skid or cart used for moving the crate in the cleanroom. Battery powered pallet jacks move the crate into the materials airlock where the outer covers are removed and the outer frame cleaned. After the air purity has recovered, the transport box can be brought into the cleanroom proper.

2020 JINST 15 T08010

The APAs are first moved to the PD integration area where the PDs are inserted into the sides of the APAs. The layout of the PD integration area is seen in figure 9.34. The APA transport boxes and APA protective covers are designed to keep the slots in the sides for the PDs clear so the PD modules can be inserted in the sides of the APAs without removing them from the transport box. The APA transport box is placed between two fixed scissor lifts so that two-person teams in the lifts can easily hold a PD module on the side of the lift. The lift is raised to align the paddle with one of the five slots in the side of the APA. The paddle can then slide into the side of the APA. The guides inside the APA frame ensure that the electrical connectors in the middle of the APA mate easily. The PDs are locked into position with two captured screws. After each PD is installed it can be tested electrically by accessing the connectors at the top using a scissor lift. Once the ten PD paddles are installed on the first APA, the transport crate is shifted slightly and the PDs can be inserted into the second APA and tested. The APA transport crate may need to come out from between the lifts to install the lower PD modules.

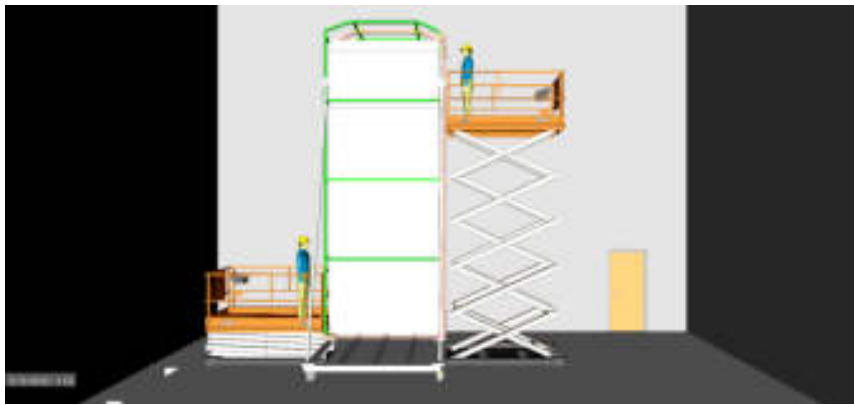


**Figure 9.34.** Area where the PDs are integrated into the APA modules. Floor-mounted scissor lifts are used to access the sides of the APA.

After the PD integration and testing is complete the transport box with the two APAs is moved to the start of one of the four assembly lines (figure 9.35 A). The initial time-and-motion studies indicate that three lines are sufficient to keep up with the cold testing and installation in the cryostat; we add a fourth as a spare that can also be used for any needed repair.

First a top APA is removed from the transport box and mounted to trolleys on the assembly line rails (figure 9.35 B). The APA is shifted over to the top APA tension measuring station, the protective covers are removed, and a visual inspection performed. The bottom of this APA cannot support the load of the lower APA, so heavy-duty rods are inserted into the sides of the APA and bolted to the side tubes using the bolts designed for the linkage connecting the APA pair. The lower APA can then be hoisted out of the transport box and connected to the rail. Either the trolleys can be mounted directly to the rods or a crossbar can be placed between the support rods to hold them. Then the lower APA is shifted to its tension-measuring location where it is locked in position and its protective covers are removed (figure 9.35 C). Wire tension data is collected according to the QA plan, similarly to ProtoDUNE-SP. The protective covers are re-installed after the tension measurements to protect the wires during the subsequent assembly steps. The top APA is moved to the first station on the APA assembly tower and attached to a rail section that can be hoisted to the upper level (figure 9.35 D).

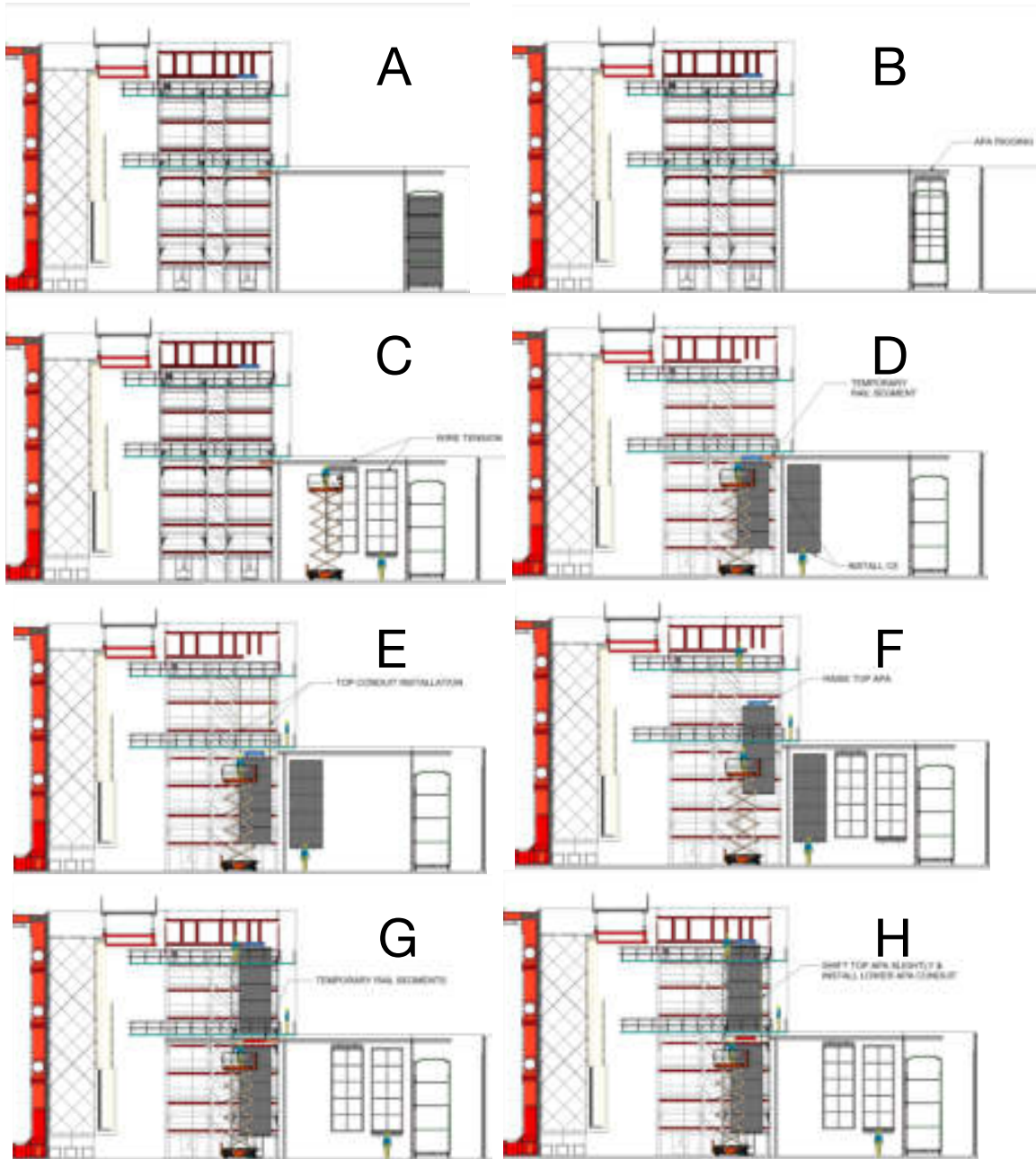
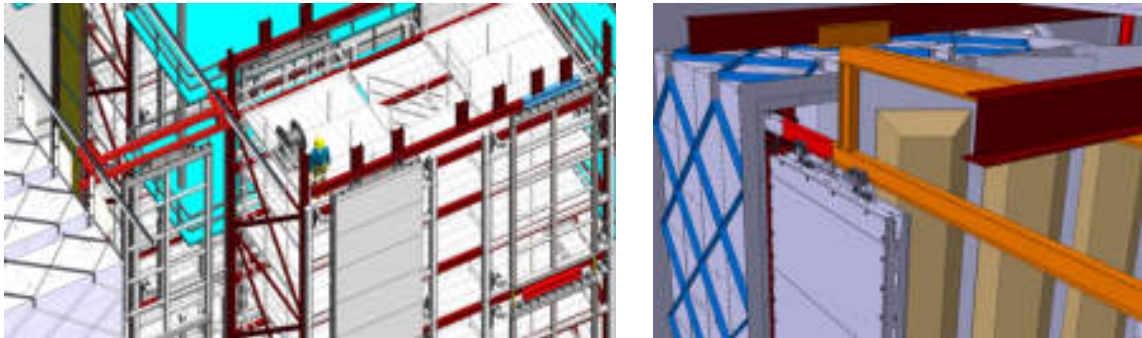


Figure 9.35. Initial APA testing and assembly into pairs. Follow row by row from top-left.

2020 JINST 15 T08010

The two short sections of the I-beam rail can be removed to the right and left of the beam segment now supporting the top APA and the (6 m) cable conduits, needed to install the CE cables, are installed (figure 9.35 E). Once the conduit is in place, the I-beam segment supporting the APA is attached to a hoist, lifted to the upper rails, and attached. Locking pins in the APA assembly fixture then hold the top APA rigidly in position. The lower APA is then moved into position to be connected to the assembly fixtures. At this point the lower APA is supported from the bottom, and guides connected to the sides of the APA provide mechanical stability while allowing jacks integrated into the lower support to lift the APA and the trolleys and rails it was riding on can be removed.

The cable conduit is installed by freeing the top APA and shifting it slightly to allow its insertion from the top through the foot tube, after which the APA is moved back into position and again locked to the APA assembly fixture (figure 9.35 H). We then test the lower APA PD paddles to ensure that everything is working. At this point, the upper APA is supported by the trolleys that move the APAs along the upper transport rails, and it is stabilized using the APA assembly frame. There is a 300 mm to 500 mm gap between the upper and lower APA, and the PD cables between upper and lower APA can now be connected. The connection from the top connectors to the SiPMs can also be checked. To connect the two APA modules mechanically, a metal linkage with electrical insulators is inserted into the upper APA and bolted into place. Then the lower APA is raised until the linkage can be bolted to the lower APA. At this point the APA pair can be released from the assembly tower supports and jacks; it is now supported from the top, where the upper APA connects to the transport rail system. The CE boxes can be installed at the top and bottom of the APA pair and a simple test of the electronics is performed. The APAs can now be shifted over to the second station on the assembly tower where the cabling is done.



**Figure 9.36.** Left: APA pair moving on the cleanroom switchyard and cables being inserted on the tower. Right: the APAs being inserted into the cold box.

The next assembly step is to install and test the electronics cabling. The left image in figure 9.36 shows the APA cabling area on the APA assembly tower. The electronics cables are delivered to the cleanroom on reels, pre-bundled and tested. The switchyard crane lifts the lower APA cable reels to the top of the assembly tower, and a cable is spooled over to a motorized deployment spool. The cable guide is then attached and fed through a guide sheave and into the conduit on the side of the APA. The cable bundle is carefully fed through the conduit and anchored in place using a cryogenic-compatible cable grip. The cable is connected to the electronics at the bottom and is laid

into the cable trays on top. This process is repeated for the second lower APA cable bundle. Finally, the upper CE and PD cables can be installed and prepared for transport.

At this time, the functionality of all the electronics is checked. After the APA electrical test, the APA pair is moved onto the switchyard where the protective covers are removed and the assembly is surveyed using photogrammetry. The APA pair is then transported to a cold box where it undergoes a thermal cycle and complete systems test. (The cold boxes were described in section 9.3.5.) The right image in figure 9.36 shows the APA being inserted into the cold box. The cold box is also a Faraday cage, so noise levels can be measured and the PD system checked for photon sensitivity. After the cold test is complete, an APA will either move back to a cabling station (if a repair is needed), or into the cryostat for installation. Recall that three assembly lines are needed to keep up with the cold testing but four assembly lines are available. The fourth line will be used for repair and eventually dis-assembly if required. Possible repairs would include repairing electrical connections, replacing electronics modules, replacing photon modules, removing damaged APA wires.

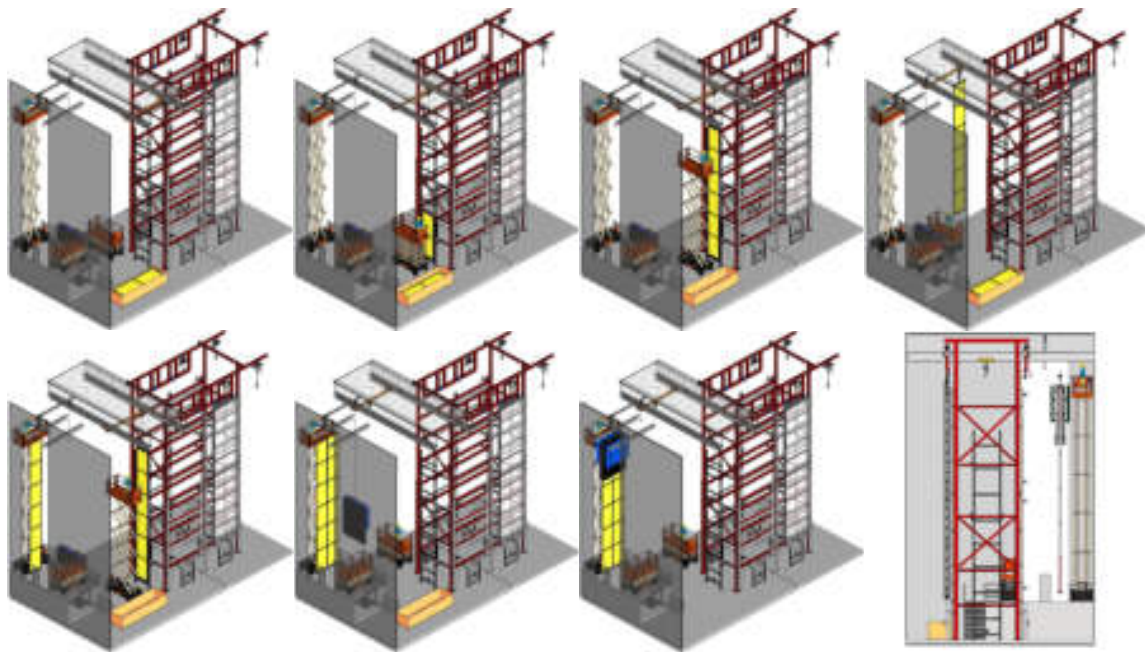


**Figure 9.37.** The CPA assembly steps are shown. Top row from left: CPAs are delivered to the CPA assembly fixture in the cleanroom. The 3 m sub-panels are lifted onto the assembly frame and connected. The CPA sub-panel is moved in front of the TCO. Bottom row from left: a second sub-panel is assembled. The two sub-panels are combined to make a CPA panel. The FC modules are attached to the top. The assembly is then moved into the cryostat through the TCO.

The CPA and top FC modules are assembled in parallel to the APA assembly. Figure 9.37 shows the assembly sequence. The CPA units are delivered to the airlock in crates that hold six 4 m long 1.15 m wide units. After cleaning, the crates are brought into the cleanroom and opened. The CPA units inside are bagged to provide additional dust protection. They are lifted out of the crate and placed on the assembly frame using the cleanroom switchyard hoist. The first two of the 4 m tall units are assembled together vertically, followed by third one. The 12 m tall CPA panel

is then lifted, connected to the installation switchyard, and moved to the TCO beam. The second 12 m tall panel is then assembled like the first from the three remaining CPA units in the crate. The two 1.15 m wide panels are then connected to make the 2.3 m wide cathode plane. A complete set of QC measurements is taken of all electrical connections between units and panels. The cathode plane is then moved to a location in the switchyard where the diffuser fibers and top FC modules are then attached. Finally, the CPA-FC assembly is moved into the cryostat. In figure 9.37, the completed assembly is shown outside the cryostat with the lower FC modules also attached. This is an option, but present planning is to install the lower FC modules once it is inside the cryostat.

PD monitoring system optical diffusers and short optical fibers must be connected to the CPA panels before the panels are installed in the cryostat. Discussions are underway about the optimal site for this installation: at the CPA assembly facility before shipping to the site, or as part of the assembly of CPA stacks in the underground cleanroom. Whichever solution is adopted, quartz optical fibers must be routed from the diffuser to the top of the CPA assembly to be connected later to the pre-installed fibers in the cryostat; this connection will occur upon final positioning of the CPA.

Work inside the cryostat proceeds in parallel with the work in the cleanroom. It is critical that the cryostat function as a Faraday cage which shields the TPC from external noise sources. A permanent ground monitor will be connected to the cryostat immediately after the construction is complete to monitor if any connections are made between the detector ground and the cavern ground. An acoustical alarm will sound if forbidden connections are detected. This system was used quite successfully at ProtoDUNE.

The large detector components like APA pairs and CPA modules enter the cryostat using the TCO rails that connect to the DSS switchyard. Inside the cryostat, the modules are pushed onto one of the switchyard shuttle beams shown in figure 9.8. The DSS shuttle beam is then moved to the appropriate row of the DSS, and the module is pushed down the length of the cryostat into position. The position of the DSS beams are well defined and accurately surveyed so that the APA and CPA modules can be accurately located by precisely positioning them along the DSS beams. A small correction in the height of the modules may be needed to accommodate deflections in the DSS due to load. Figure 9.38 shows the typical situation during the APA installation and CE cabling.

After the APA is moved into position, the permanent support rod is connected to the DSS beam, and the trolleys are removed. The crawler used to push the APA along the rails is then moved back through the shuttle area and can be used for the next module. After the APA is locked into position, the cable tray feedthrough to the CE is installed, after which CE cabling can start. Even when a CPA module is in position, more than 3 m of space remains free between the APA and CPA, and a scissor lift can easily be positioned in front of the APA. The two right images in figure 9.38 show the situation at the top of the cryostat during cabling. The cables are not shown, so the cable trays and their support infrastructure can be seen.

When cabling begins, all the cables are in the cable trays. Two people are in the scissor lift in front of the APA, and another two people are on top of the cryostat. The CE cables from the bottom APA emerge from the APA side-tube and are split into two bundles in the cable tray for a total of four cable bundles. The top APA also has CE cables organized into four bundles. The photon cables from both the top and bottom APAs are bundled into two cable bundles. During the cabling process, each bundle is partly removed from the cable tray and fed up through the cryostat crossing

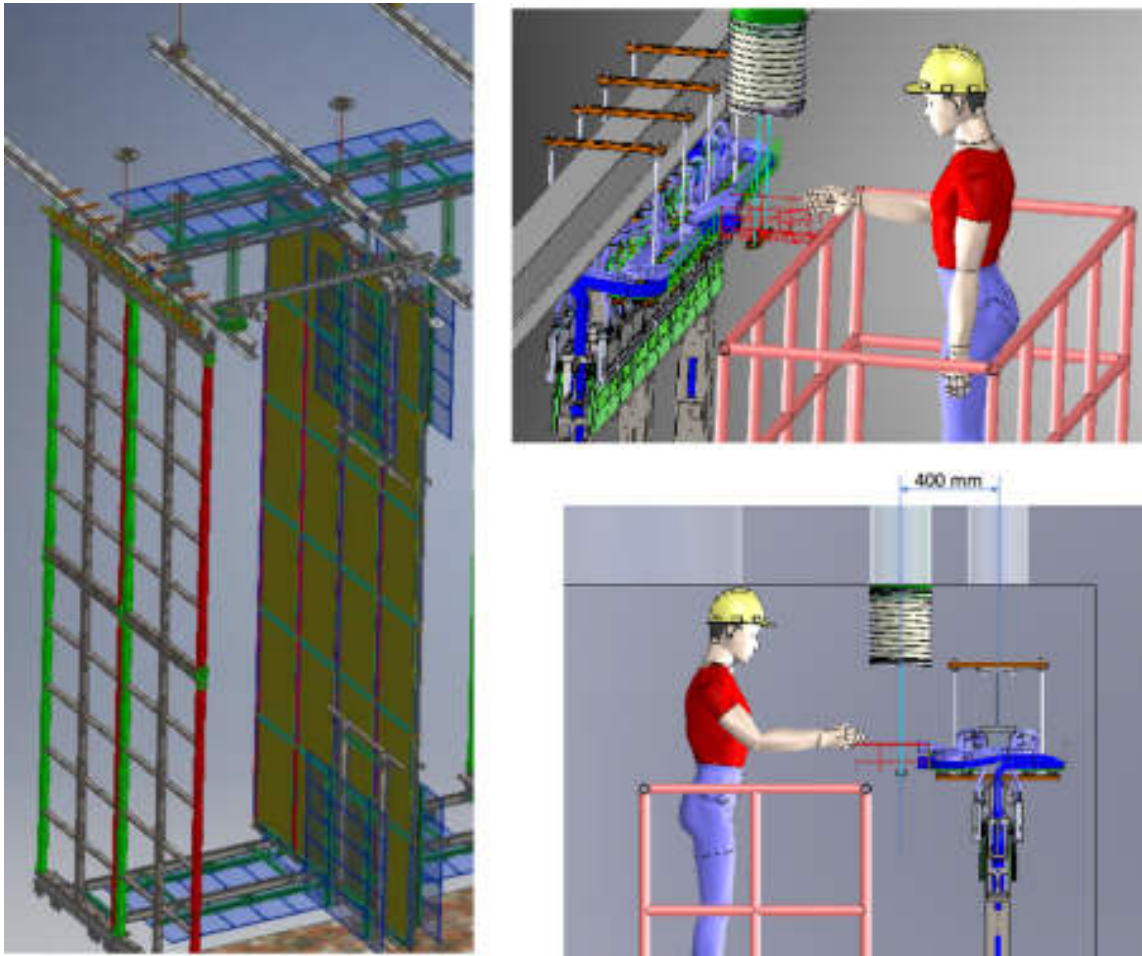


**Figure 9.38.** The installation of the APA and cabling of the cold electronics. The left panel shows the APA installation process. One row of APA and HV equipment is installed, and a second APA is ready for electrical cabling. The top right image shows the cable trays that will hold the CE cables; one worker is in the scissor lift. The left bottom image shows the work space with the geometry of the APA, the cryostat roof, and the cable feedthrough.

tube. At the top and bottom of the crossing tube the cables are strain relieved. This is repeated for each of the ten cable bundles needed for the APA pair. When all cables are installed through the cryostat crossing tube, any excess length is returned to the cable tray at the top of the APA. On the roof, the short individual cables are connected to the feedthrough flange, and all electronics and electrical connections are checked. At this point the flange connecting the WIEC can be sealed to the cryostat feedthrough flange, and the cable installation is complete.

Similarly, the PD warm cables are connected to the readout module, and the flange sealed after testing. Once testing is complete, the support for the tray holding the excess cabling is transferred to the DSS beam. This minimizes any uneven load on the APA pair, so they hang more vertically. The electronics for each APA is continuously monitored after installation.

Placement and routing of the cables is complex. Figure 9.39 shows the working 3D model of the cable routing, showing how the cables will be bundled and placed in the trays. A mock up the

cabling configuration is planned at Brookhaven National Laboratory (BNL), and the installation of the cables will be tested as part of the Ash River testing program.

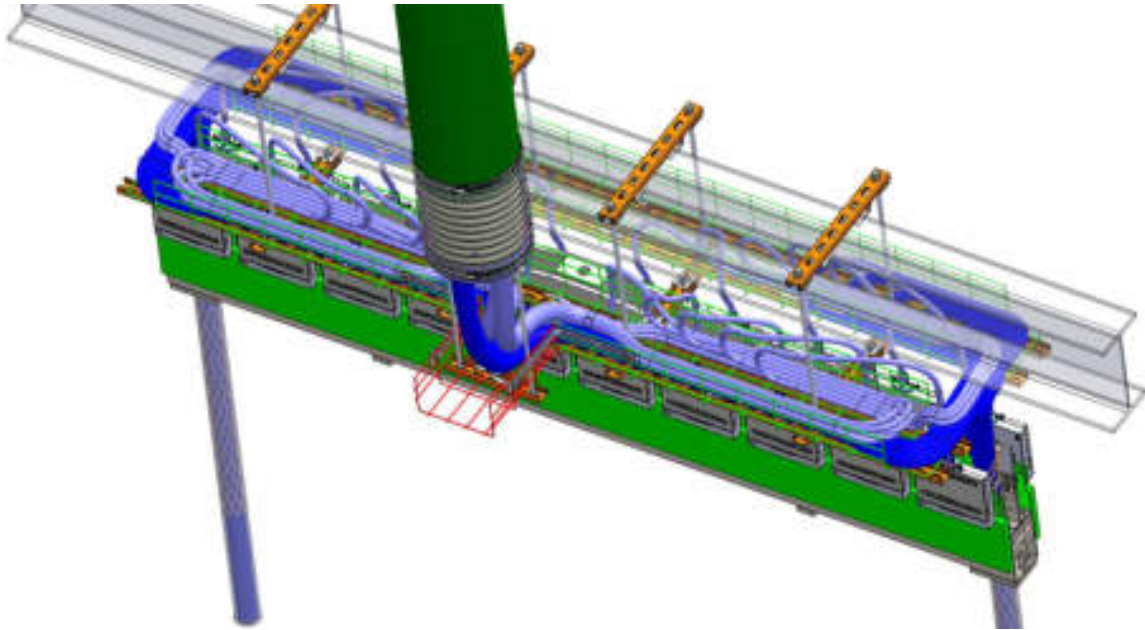


**Figure 9.39.** Working model of the cable trays and routing of the PD cables in the trays. The scale is set by the 2.3 m APA width.

The cathode FC assemblies are brought into the cryostat like the APA pairs, using the overhead rails through the TCO. Inside the cryostat, they are moved into position using the DSS switchyard and DSS I-beams. Once in position, the load is transferred directly to the DSS beam, and the trolleys are removed. The CPA will wait in position until its APA pairs are fully tested, after which the FC modules could be deployed. The deployment sequence of the FC has not yet been fixed. If the FC modules are immediately deployed then the APA and FC can be tested in the final position. If we wait to deploy them, the CE can undergo a longer burn-in test and we have an opportunity to clean the cryostat near the end of the installation. The decision on the best time to deploy the FC will be made during final design.

Figure 9.40 shows the equipment for deploying the FCs. The top FC modules are raised by connecting a cable to the module and then using a pulley-winch assembly to lift the module, which latches to the APA mounts. A scissor lift is used to connect the cable to the module and also to control the winch. Once the FC are latched at the APA ends and the FC termination connections are made and verified on the APAs.

After the module is in place, the deployment tool is moved to the next APA and CPA sets. The lower FC is deployed using a custom frame that can be wheeled into position. The cable from a small hoist is then attached to the FC module, and the module can be lowered. The hoist is on a linear slide, so the cable is always directly over the connection point, keeping the CPA from swinging due to an induced moment. When the module is down, it latches to the APA frame much like the upper FC. The electrical connections to the HV bus are tested, and deployment is complete.



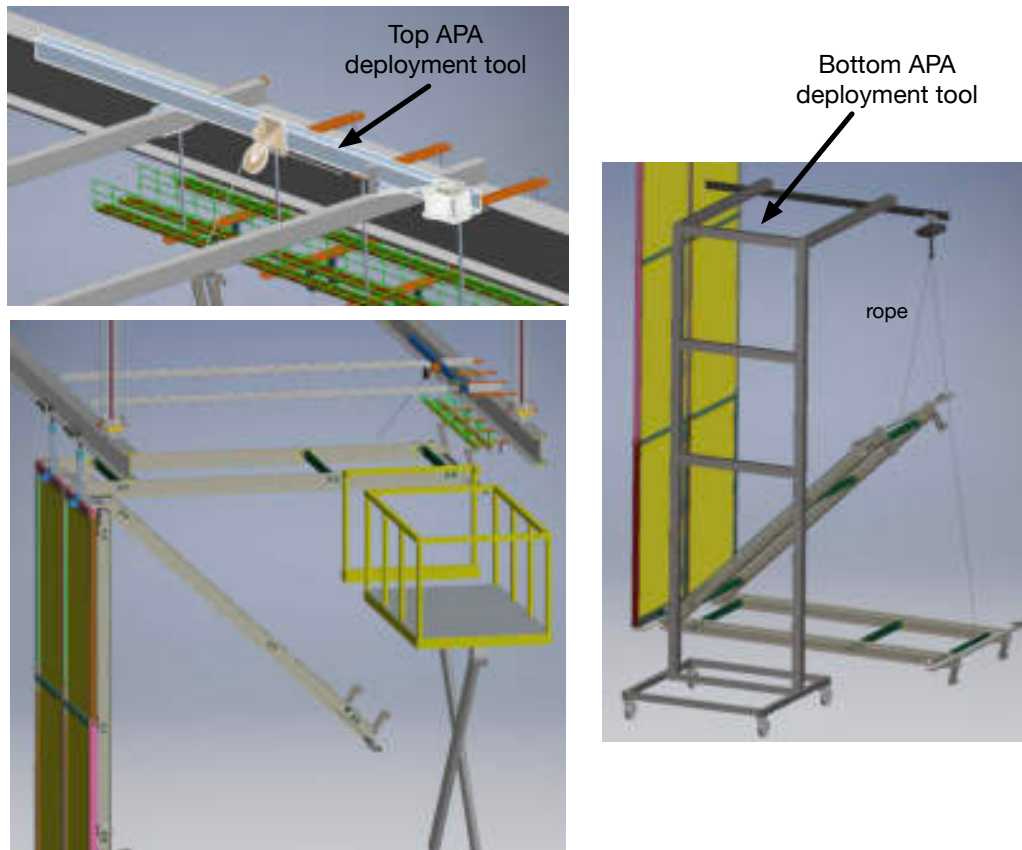


**Figure 9.40.** The top FC assemblies are deployed using a custom tool that mounts to the DSS beams as seen in the top-left panel. The FC is lifted using the electric winch controlled by an operator in the nearby scissor lift. The lower FC is lowered using a hoist mounted on a wheeled frame. The hoist is on a linear slide to keep it aligned above the connection point.

In principle, the CPA-FC assemblies can be constructed faster than the APAs and the CPA-FC assembly process could start later than the start of APA assembly if the deployment is postponed. The sequence will be baselined prior to completion of preliminary design.

Weekly during the TPC installation the TCO will be optically closed and the cryostat made dark to allow testing of the PDs and noise measurements of the TPC electronics. These tests will be performed on the weekend shift.

The periscopes for the laser calibration system on the top of the TPC can be installed after the nearby FC elements are deployed. The lasers are immediately aligned with the alignment laser system. Once for each periscope/laser system, prior to the installation of further TPC components, the cavern will need to be cleared for the optical alignment as both UV (Class 4) and visible lasers are used. This will require special safety precautions, outlined in Volume III, DUNE far detector technical coordination, chapter 10 of this TDR. It may be possible to align all lasers at roughly the same time, to minimize the disruption.

The last row of detector elements is installed much like previous rows except that the north-south runway beams in the switchyard need to be removed to allow the last row of the detector to contract as it cools down. Figure 9.41 shows the top of the detector as this last row is installed.

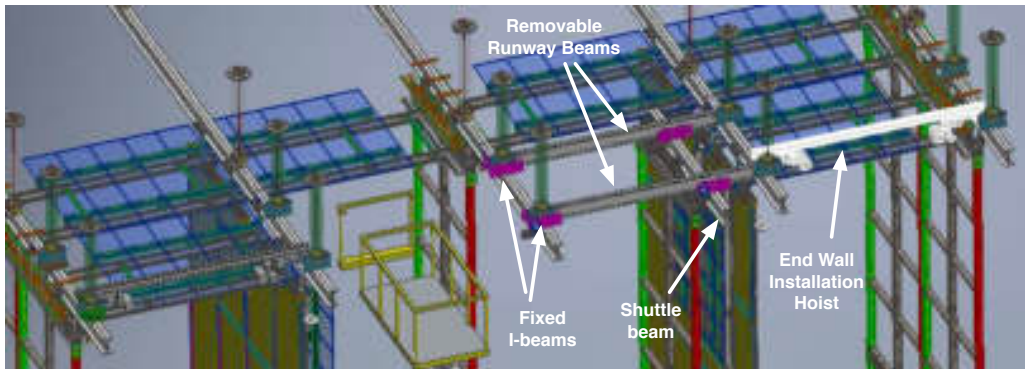


**Figure 9.41.** Detector installation as the last row of detector components is installed. At this time, the switchyard runway beams are removed, and the temporary hoists for the endwall FCs are installed.

When the shuttle beam with the detector component is aligned to the correct APA or CPA row, it is bolted to a short I-beam section of the runway beam which is in turn permanently fixed to the DSS support feedthrough. When the shuttle beams at both ends of a runway beam section are fixed in position, a section of the runway beam is removed and the endwall FC insertion hoist mounted. The last FC modules could then be deployed but they are kept in the folded state to give space for the endwall FC.

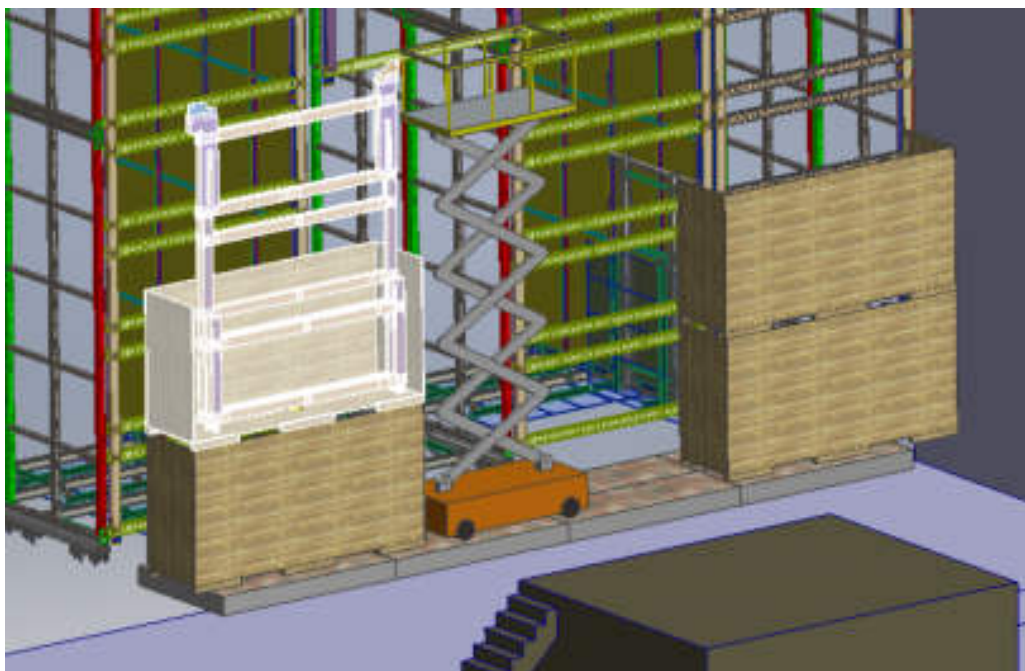


**Figure 9.42.** Installation of the final endwall FC before closing the TCO.

The west endwall FCs are installed like the first endwall FCs except there is now only 2 m of space in which to work. Figure 9.42 is an image showing the inside of the cryostat at the time the endwall FCs is installed. The crates holding the endwall FCs panels will take much of the available space, but there is room for a person to connect the hoist cables to the endwall FCs and the hoist

2020 JINST 15 T08010

can be operated from the scissor lift. After the north and south endwall FCs panels are installed the center APA is rolled into the cryostat, the shuttle beam is bolted to the DSS, and the runway beams are removed. The two center drift volumes FCs are then deployed. The last two endwall FCs are constructed, and the TPC is effectively finished.

At this point, a frame supported by the shuttle beams is covered with flame-retardant plastic and installed to create a work area for the TCO closure. A scaffold for egress to the access holes through the roof must be in place before the TCO is closed. The scissor lift must be removed at this time since the TCO beams are required to lift it over a piece of the cryostat's structural steel support. The TCO is closed working from the scaffolding inside. Once access through the TCO is blocked, the cryostat is classed as a confined space and the corresponding safety measures are required. The east end of the cryostat is then cleaned and the plastic sheeting is removed.

The dynamic T-gradient monitor is installed after the TCO is closed. The monitor comes in several segments with pre-attached sensors and cabling already in place. Each segment is fed into the crossing tube flange one at a time until the entire sensor carrier rod is in place. The remainder of the system (the motor system that moves the sensor rod and the sensors) that goes on top of the flange is installed using the bridge crane.

The purity monitor system will be built in modules so that it can be assembled outside the cryostat, leaving only a few steps to complete inside the cryostat. The assembly itself comes into the cryostat with the three individual purity monitors mounted to support tubes that are then mounted to the brackets inside the cryostat. The brackets get attached to the appropriate elements (cables trays, DSS, and bolts in the cryostat corner are under consideration). Also at this time, the remaining level monitors are installed.

The periscopes at the end of the detector are installed and aligned.

Once all this work is completed, the scaffolding is taken apart and hoisted out the access holes along with all remaining flooring sections. The area is cleaned, and the last two workers in the cryostat are hoisted out.

The warm inspection cameras and other possible calibration instruments can be installed from the roof while the TCO is being closed. At this point, the cryostat is classified as a confined space and the corresponding safety measures are required (these measures include a search of the area before closure, confined-space training for workers, and controlled access into and out of the cryostat). After the TCO is closed the four access holes (two for ventilation and two for personnel access) can be closed and the pulsed neutron source can be placed in position above two of the access holes. The east end of the cryostat is then cleaned and the plastic sheeting is removed. The pulsed neutron source can be tested to confirm neutron yields with integrated monitors and dosimeters in dedicated runs.

### **9.4.2 Installation prototyping and testing (QA/QC)**

This section describes the planned QA process for developing the installation process and qualifying the installation equipment; the QC testing planned during the detector installation follows.

#### **9.4.2.1 Detector installation quality assurance**

An extensive prototyping program designed to develop and test the ProtoDUNE-SP installation process was executed in the NOvA assembly area at Ash River prior to the final design of the

ProtoDUNE detector. The NOvA Far Detector Laboratory at Ash River is owned and operated by the University of Minnesota using grants from the DOE and Fermilab. A mechanical mock-up of one sixth of the detector was fabricated from test components where the interface infrastructure was considered final. Here all the mounting points, external dimensions, loads, latches and hinges were expected to be exactly as planned for the final ProtoDUNE-SP detector. A mock-up cryostat roof and wall were constructed to understand how some tasks could be performed physically in the space available. Initially, all the components failed the installation test and had to be modified. A series of hands-on working group meetings with the different consortia were held to resolve installation issues and revise the detector design. In some cases, two iterations were required before the components could be assembled together in the space available, and dedicated tooling had to be developed. Having the mock-up of the cryostat roof and walls was critical in developing the installation procedures and eventually assembling ProtoDUNE-SP on schedule; only when handling these objects in the space available did all the constraints become obvious. The experience gained during the ProtoDUNE Ash River trial assembly was critical for both verifying the mechanical design and interface, and also for developing the tools and procedures needed for the installation.

The DUNE TPC will have half the available work space, both above and below the TPC inside the cryostat, compared to ProtoDUNE-SP. We learned from ProtoDUNE-SP that access at the top and bottom of the detector was already difficult, as was properly connecting the bottom latches between the FC and the APA during the FC deployment.

The process of test-installing the detector mock-up allowed refinement of the hazard analysis and development of the detailed procedure documentation for the assembly process. Having complete, well developed procedures prior to the delivery of the components at CERN allowed the safety approval process to begin early. Along with the test installation, this created a safe work environment.

Mechanical tests at the DUNE trial assembly at Ash River will be key to developing the installation process. We will also perform the time-and-motion studies that are required to develop a reliable schedule. Other important prototyping tasks performed at universities, national laboratories, and CERN will contribute to the installation plan. For example, Argonne National Laboratory (ANL) is testing the APA shuttle beam drive system and the CPA assembly tower connections before they are shipped to Ash River, and BNL is planning a test setup to develop the cable management process on top of the detector. The ProtoDUNE-SP experience has led to many small improvements in the assembly process, and the SP module prototyping effort will help us develop it further.

Full-scale mechanical testing of the assembly and installation of all the TPC components, including the DSS, will be critical for the success of the SP module. A prototype of the installation equipment for the SP module will be constructed at the NOvA neutrino experiment FD site in Ash River, and the installation process tested with full-scale mechanical models detector elements. This assembly area at Ash River, shown in figure 9.43, meets the requirements of both space and available equipment, and experienced technicians that helped construct the ProtoDUNE-SP detector are available. It has both the elevation and floor space available to do a full-scale test of both the component assembly outside the cryostat and a test installation of the TPC components inside the cryostat. Also available are a 75 ft × 100 ft loading dock and ramp access, two 10 t cranes, a machine shop, and a wide assortment of tools.

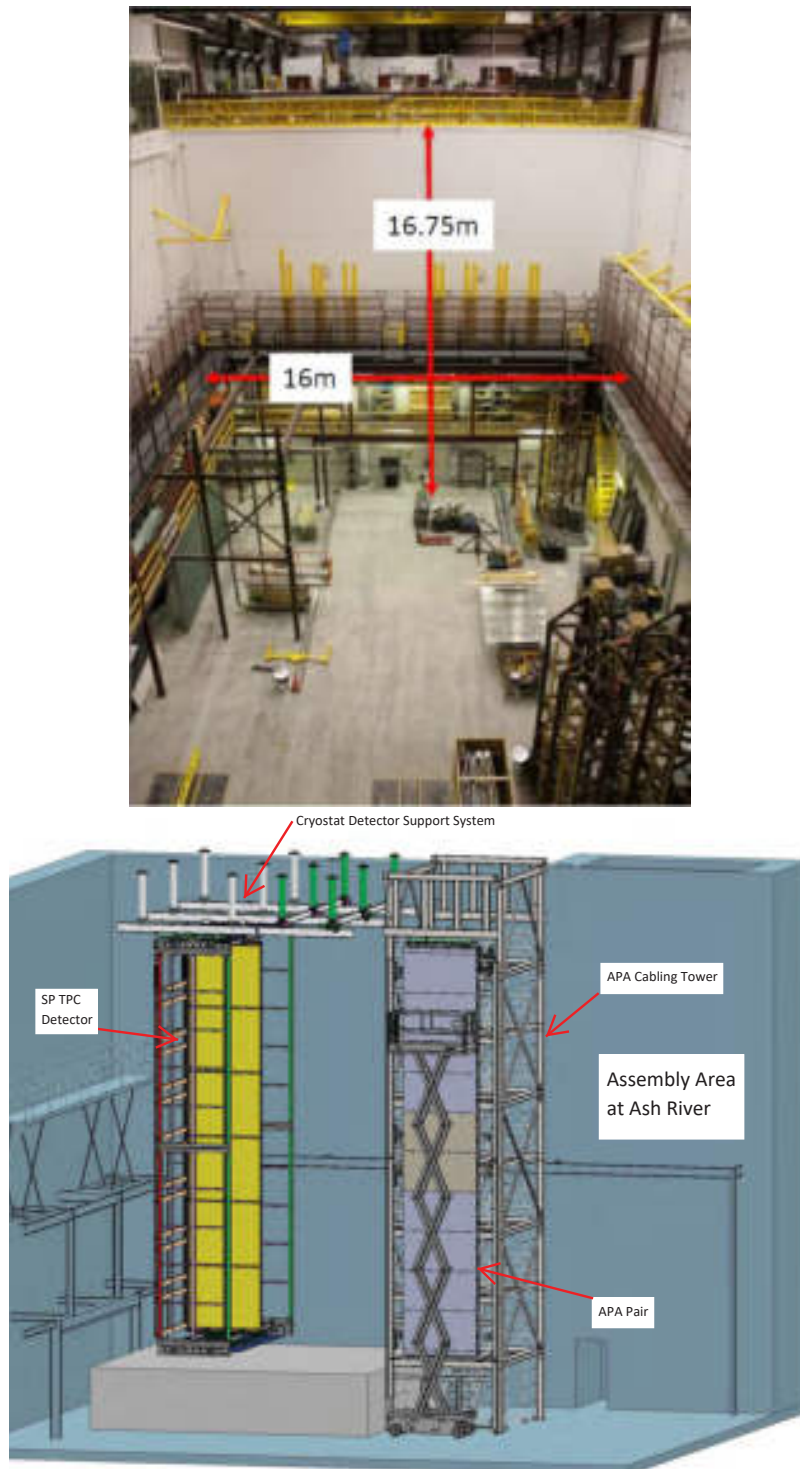


**Figure 9.43.** Top panel shows the NOvA Assembly Area and the bottom panel shows the 3D model of the installation prototype.

While the University of Minnesota has jurisdiction over the safety program at Ash River, the facility also follows the Fermilab Safety Program and works together with Fermilab to ensure a safe working environment. A key deliverable of the ProtoDUNE-SP work was a set of documentation including e.g., component design, hazard analysis, and final assembly procedures, for approval by the CERN Health Safety and Environment division. For Ash River and DUNE, this is all part of the operational readiness clearance (ORC) review process. Documentation for both the trial assembly process at Ash River and for DUNE will be stored on the engineering document management system (EDMS) at CERN. Though many of the TPC components are mechanically similar to the ProtoDUNE-SP components, the access equipment will be different and the need to work at 14 m height will make construction of the SP module much more challenging.

The DUNE FD trial assembly program at Ash River has the following goals:

1. Validate the APA design.
2. Test all full-scale TPC components during both the initial assembly stages in the cleanroom outside the cryostat and the deployment stages inside the cryostat:
  - APA assembly: manipulation of APA shipping frames, joining an APA pair together, CE cabling, removal and re-installation of the APA protection covers, movement on shuttle beam, cryostat cabling, and final deployment in cryostat.
  - Integration and installation testing of PD components: cable harness routing and cryogenic cable strain relief, module integration into APA frames, and electrical connections between upper and lower APAs. Mounting of PD monitoring system components and optical fiber routing on the CPA.
  - DSS and shuttle beam system, including final detector configuration.
  - Assembly of HV system: construction of an endwall FC, CPA pairs, movement on shuttle beam, and final deployment in cryostat.
3. Write full set of hazard analyses and assembly procedure documents; gather all component documentation.
4. Test access equipment (scaffold, scissor lifts, work platforms) and lifting fixtures.
5. Study assembly time and motion, including labor estimates.
6. Train lead workers as DUNE begins set up (in the installation setup phase).
7. Test mechanical modifications.
8. Train the installation team prior to the start of DUNE installation (in the installation phase).
9. Possibly (in future) run assembly tests of the DP module components.

We have developed a staged testing program to meet the above goals. The initial phase is dedicated to qualifying the APA and FC designs. The main difference (other than the number of units) between ProtoDUNE-SP and the DUNE SP module is that one APA will hang beneath

another, doubling the height. The cables from the lower APA will need to be routed through the upper APA, thus requiring a redesign.

To date, an APA pair has never been assembled and cabled. It is critical to complete tests of these operations before finalizing the APA design. The initial phase of the installation testing is focused on this; it is time critical in order that APA production can begin in 2020. The assembly and deployment of the CPAs can be tested in parallel since they will not require large amounts of additional infrastructure.

The second phase of the prototyping program is focused on developing the installation plan and verifying all the detector interfaces. We will construct a full-scale model of the major installation equipment in the cleanroom and the inside of the cryostat, and conduct a dry run of the assembly, component transport and deployment in the cryostat. This is especially important because the space in the SP module cryostat above and below the detector is only half that of ProtoDUNE-SP, where some of the installation steps were already challenging.

The final prototyping stage includes a mock-up of the top of the cryostat to test the final cabling steps at height and perform accurate time-and-motion studies to benchmark the installation schedule. Detailed procedures will be drafted and in place before the start of actual installation. The installation team will train to work underground at this time.

Testing the installation process early allows identification of hazards and remediation measures — without the time pressure associated with the actual installation. This is critical for reducing risks. Detector installation is by definition on the critical path, making it vital that the work be performed efficiently and with the lowest possible risk.

This prototyping program is summarized in table 9.5 and the 3D model representing the final layout is shown in figure 9.43.

QC activities during the integration of the CE, APAs and PDs underground are intended to ensure that the detector is fully functional once the cryostat is filled with LAr. The testing of all detector components will continue throughout the installation of all the elements of the TPC, until the cryostat is ready to be filled with LAr. All these consortium-provided detector components that arrive underground will have gone through a qualification process to ensure that they are fully functional and that they meet the DUNE specifications. Additional tests and checks will be performed during installation to ensure that the components have not been damaged during the transport or during the installation itself, and most importantly that all the parts are properly connected.

The individual consortia will retain responsibility for providing quality management, tooling, and test plans at the integration area, as well as specialized labor and supervisory personnel for component integration and installation.

Following the mounting of the TPC CE and the PDs, the entire APA will undergo a cold system test in a gaseous argon cold box, similar to that performed during ProtoDUNE-SP. During this test, the system will undergo a final integrated system check prior to installation, checking dark and LED-stimulated SiPM performance for all channels, checking for electrical interference with the CE, and confirming compliance with the detector grounding scheme. The QC process will be documented through the development of procedures which will define the integration and installation tests required including the appropriate acceptance criteria. The integration and installation process will be documented on travelers or manufacturing and inspection plan documents. Test results will

**Table 9.5.** Summary of the tests at Ash River.

| Testing phase    | Deliverables   |
|------------------|--|
| FY-19 20 Phase 0 |  |
|                  | Build an APA cabling tower for full scale APA pair assembly          |
|                  | Check vertical cabling with a pair of APA side tubes                 |
|                  | Test APA shipping frame and underground handling                     |
|                  | Build a CPA assembly stand and test assembly process                 |
|                  | Test FC deployment and ground plane installation                     |
| FY-20 21 Phase 1 |  |
|                  | Build support structure for DSS shuttle, 3 sections of DSS beam      |
|                  | Test movement of CPA and APA from cleanroom to final destination     |
|                  | Test APA, CPA, endwall and FC deployment in one drift section        |
|                  | Test assembly sequence of final section of TPC                       |
|                  | Removal of DSS shuttle beam runway rails                             |
|                  | Final deployment after TCO is closed up                              |
| FY-21 22 Phase 2 |  |
|                  | Include the top of the cryostat (no warm structure) with feedthrough |
|                  | Test DSS installation  |
|                  | Test CE cable installation using feedthrough                         |
|                  | Design feedthrough to support Dual Phase installation test           |
|                  | Test shipping and construction using first factory TPC components    |
|                  | Train lead workers for underground at SURF                           |

either appear on these documents or we will have individual test reports including the test data. All documents will be retained in the EDMS.

#### 9.4.2.2 DAQ QC testing

Testing is required at several stages of DAQ installation. The first is the installation of the data room infrastructure, where, upon installation, professional data center building contractors will test rack airflow, power distribution, and check for cooling-water leaks.

The distance between the detector and the data room is not negligible for multimode fibers and 10 Gb/s transmission. In order to avoid any issue with signal integrity, path of the detector-to-data room fiber runs will be minimized, high quality multimode OM4 fibers will be purchased, installed professionally and carefully tested in place. Covered cable trays will protect them after installation. As APAs and servers are commissioned, pre-tested fibers will be connected to the newly installed hardware.

The DAQ servers in the CUC data room will be initially received and integrated off site. Upon installation in the CUC, only a simple functionality test is needed. Sufficient spare capacity will be



installed, and the main commissioning work will be software-related, which can be done over the network from the surface or remotely.

### 9.4.2.3 APA QC testing

After the APA transport boxes are brought into the material airlock the outer covers are removed and a visual inspection can be performed. Next the APAs are moved to the PD integration area, tests here are described in the PD section.

When the PD integration is complete the APA transport box is moved to one of the APA assembly lines. Individual APAs are removed from the transport frame, mounted to the assembly line rails, and the protective covers are removed. A second detailed visual inspection is performed now that the wires are visible. A spot check of the wire tensions will be done to verify that no change has occurred since the APA left the factory.

In the current plan, the tension measurements are performed using a laser focused on individual wires, the same method used at the production site. The wire is plucked to induce a vibration, and a photodiode under the wire records the frequency of vibration, which directly translates into the tension value. The measured values are stored in the wire DCDB database. While this method is robust and has been extensively used by LArTPC experiments, it is very time consuming and thus prohibits measuring every wire. Two people over three shifts will be able to measure approximately 350 wires, 10% of the total. In ProtoDUNE-SP 10% of the wires were measured prior to cold testing and no wires were found to be out of tolerance.

An alternative method, using electrical signals, is currently under development and could replace the laser method, potentially allowing measurement of all the wires. With this electrical method, where adjacent wires under certain voltages induce the middle wire to vibrate, the resonance frequency vibration of the measured wire correlates directly to the wire tension.

The current requirement for tension values are  $6 \pm 1$  N, however this tolerance is currently under study with ProtoDUNE data. If wires are found in DUNE that are outside the tolerance specification then the wire will be removed and a more detailed study of the APA performed. No more than 25 missing wires will be permitted. APA wires are also tested for continuity, to make sure they are intact and properly connected to the readout boards. This test is done as part of the TPC electronics testing below. Photogrammetry is used to measure the final assembled dimensions of the APA, either while the wire tension is being measured or immediately before entering the cold box. A measurement of the wire-plane spacing is also performed using a scanning laser combined to a Faro arm (a portable coordinate measuring machine). The exact wire-plane spacing values will be stored in the wire DCDB database. In the case of any deviations from the required tolerance of 0.5 mm, different bias voltage values may be used to make corrections to the wire plane transparency.

Once the APAs have been installed, the TPC electronics will be continuously read out; this will directly inform wire continuity and the full function of the channels.

### 9.4.2.4 TPC electronics QC testing

Many of the activities of the CE consortium at SURF aim to ensure the full functionality of the TPC once the cryostat is filled with LAr. All the detector components provided by the CE consortium that arrive at SURF will have gone through a qualification process to ensure that they are fully functional and that they meet the DUNE specifications. Additional tests and checks are performed

at SURF to ensure that the components have not been damaged during the transport or during the installation itself, and most importantly that all the parts are properly connected.

FEMBs are tested multiple times during this process, first after they are received and then after installation on the APAs. Further tests are performed before and after the APAs are installed in the cryostat, using the final cables to connect the FEMBs and the detector flanges. Results of these tests at SURF are compared with the results of the tests performed during the qualification of ASICs and FEMBs to detect possible deviations that could signal damage in the boards or problems in the connections. All test results will be stored in the same database system used for results obtained during the qualification of components.

The post-installation APA tests, performed at room temperature, involve connecting up to four FEMBs to a WIB that is connected directly to a laptop computer for readout over 1 Gbps Ethernet, with power provided by a portable 12 V supply. For the reception test, the FEMBs are attached to a capacitive load to simulate the presence of wires, which allows a test of connectivity, and measurement of the baseline and RMS of the noise for each channel. Dead channels are identified using the calibration pulse internal to the FE ASIC as well as the measured noise level relative to that associated with the temporary capacitive load. Overall, the reception test and the test performed after attaching the FEMBs to the APAs each require approximately half an hour per FEMBs, including the time for connecting and disconnecting test cables. The CE consortium plans to have a cryogenic test stand available in a laboratory on the surface at SURF or at a nearby institution to perform checks at LN<sub>2</sub> temperature of FEMBs that fail the QC procedures at SURF, and eventually for sample checks on the FEMBs as they are received at SURF.

Once the pair of APAs is in the cold box an initial test of the readout is performed at room temperature, to ensure the final cables are properly connected to the FEMBs. This test is done using elements of the final DAQ system. Fast Fourier transforms of the noise measurements made in the closed cold box will be inspected for indications of coherent noise. All FE gain and shaping time settings will be exercised, and the gain will be measured using the integrated pulser circuit in the FE ASIC and/or the WIB. The connectivity and noise measurements, as well as the check for dead channels, are repeated later after the APA pair cools down to a temperature close to that of LN<sub>2</sub> in the cold box. The bias voltage connections and the PD system are also checked at this time.

Results of all these tests will be compared with results obtained in earlier QC tests. If problems are found, it will be possible to fix them by re-seating cables or replacing individual FEMBs. Noise levels are also monitored during the cool-down and warm-up operations of the cold boxes. These tests also ensure that the power, control, and readout cables are properly connected on the FEMB side and that this connection will withstand temperature cycles. Although the connection between the cables and the FEMB has been redesigned to address a problem seen in ProtoDUNE-SP, repeating these tests during integration and installation of the TPC is important because a single connection problem would result in the loss of one entire FEMB. In addition, the tests performed in the cold box at SURF will demonstrate that the power, control, and readout cables for the bottom APAs are not damaged when they are routed through the APA frames. The FEMBs are tested immediately after installation, after the cables are installed, and during and after thermal cycling. This ensures that the connections are robust before the APA enters the cryostat. Testing at LN<sub>2</sub> temperature, done with the final cables attached, indicates clearly the capacitance of the wires and it verifies that the connections to the FEMBs and the cables is maintained during thermal cycling. After

installation in the cryostat the FEMBs are monitored continuously. Additional measurements of the noise level inside the cryostat will be performed regularly by closing the TCO temporarily with an radio frequency (RF) shield electrically connected to the cryostat steel.

All readout tests are repeated after the APAs are put in their final positions inside the cryostat and after the power, control, and readout cables are connected to the warm flange attached to the cryostat penetration. At this point, the connection between the cables and the flange is validated, and the entire power, control, and readout chain, including the final DAQ BE used during normal operations, are exercised. The installation plan for the TPC components inside the cryostat (APAs, cathode plane assemblies, and deployment of the FCs) allows for minor repairs on some FEMBs without extracting the APAs from the cryostat. The testing of all components will continue throughout the installation of the TPC, until the cryostat is ready to be filled with LAr. When the APAs are in their final position, replacing FEMBs or cold cables will be more difficult and may require extracting the APAs from the cryostat. This operation will be performed only if major problems occur with the FEMBs.

In addition to measurements on the APA readout, the CE consortium will also test the bias voltage system together with the APA and HV consortia. These tests should show that the cables providing the bias voltage to the APA wires, the FC termination electrodes, and the electron diverters are connected properly with no short circuits. These tests will commence as soon as the first APA pair is in its final position, but after connecting the bias voltage cables to the safe high voltage (SHV) boards on the APA. The connection will use a resistive load for the FC termination electrodes and the electron diverters. This ensures the continuity of the bias voltage distribution system from the bias voltage supplies to the APAs. The test must be repeated for the FC termination electrodes and the electron diverters after the FC modules are deployed.

Additional tests will be performed on the other components provided by the TPC electronics consortium prior to insertion into the APAs. After the cryostat penetrations are put in place, helium leak checks will be performed. These tests will be repeated after all cables have been routed through the cryostat penetration. As soon as the bias voltage and the power supplies are installed on the cryostat mezzanine and cables are put in place between the corresponding racks and cryostat penetrations, tests will be performed to ensure that the proper power and bias voltage can be delivered to the WIECs before installing them. Even before connecting the WIECs to the warm flanges, tests will be performed to ensure that they can be properly powered up, controlled, and read out by the DUNE DAQ. Tests will be performed on the readout fiber plant to ensure that all fiber connections are functional and properly mapped. Additional tests will be performed on the slow control system and on the detector safety system several times during the installation of the detector. These tests will take place before the corresponding APAs are installed, after their installation, after all the corresponding cables and fibers are connected, and finally during the integrated tests that take place before the TCO is closed and the cryostat is filled. Negative results in any of these tests will halt integration, installation, and commissioning activities. The results will then be used in reviews that must take place before the closure of the TCO is authorized, the LAr filling operation takes place, and the detector is commissioned.

#### 9.4.2.5 HV QC testing

The endwall FCs are assembled in eight panel units, four on each end of the TPC. As each of the eight panels is removed from the shipping crate and placed on the installation cart, the endwall panel checklist is filled out [37]. This checklist includes a visual inspection of the frames, profiles, and connections, as well as continuity and resistance measurements of the divider boards and their connections. After completing an eight-panel endwall in the cryostat, the complete endwall checklist is filled out. This includes hanging position, straightness measurements, and continuity checks between panels.

The CPA panels are assembled from a set of three units removed from the shipping crates. After each unit is removed from its bag, a visual inspection confirms structural integrity and the connections between FSSs, HV bus pieces, and profiles, if present. After inspection, the unit is positioned on the CPA assembly tower. After all three units are connected on the tower, the CPA panel checklist is filled out. This includes inspecting all mechanical connections, continuity checks of the FSS, resistive panel (RP), profile, and HV bus connections, and resistance measurements of the four mini-resistor board connections from the RP to the FSS. This is repeated for the second panel in a CPA plane. Then the two panels are paired, each hanging from trolleys on the transport beam. Visual inspection of the alignment and hanging straightness is made, and HV bus connections at the top and bottom are made and checked for continuity (CPA plane checklist).

The FC top and bottom units are removed from their crates. The FC unit checklist is filled out with a visual inspection of the frames, profiles, and connections, as well as continuity and resistance measurements of the divider boards and their connections. After hanging the top FC units on the CPA plane, the four jumpers from the first FC profile on each side of the CPA and the CPA FSS is connected, and the resistance is measured, completing the CPA-FC top assembly checklist. The FC bottom units are not attached to the CPA but are taken into the cryostat independently after filling out the FC unit checklist.

The CPA-FC top assembly is moved into its position in the cryostat. After deploying the FC top units, the resistor board/jumper between the FC and the CPA FSS are visually inspected. Also, the latch connecting the FC to the APA is visually inspected. After deploying the FC bottoms, visual inspection verifies the resistor board/jumper connection from the FC to the CPA. Also, the latch connecting the FC bottom to the APA is visually inspected. These are included in the CPA-FC cryostat checklist.

#### 9.4.2.6 CISC QC testing

Cryogenics instrumentation systems must undergo a series of tests to guarantee they will perform as expected:

- Purity monitors: each of the fully assembled purity monitor arrays is placed in its shipping tube, which serves as a vacuum chamber to test all electric and optical connections at SURF before the system is inserted into the cryostat. During insertion, electrical connections are tested continuously with multimeters and electrometers.
- Static T-gradient thermometers: right after each sensor array is installed, its verticality is checked, and the tensions in the stainless steel strings adjusted as necessary. Once cables are

routed to the corresponding DSS ports, the entire readout chain is tested. This allows a test of the sensor, the sensor-connector assembly, the cable-connector assemblies at both ends, and the noise level inside the cryostat. If any sensor presents a problem, it is replaced. If the problem persists, the cable is checked and replaced as needed.

- Dynamic T-gradient thermometers: the full system is tested after it is installed in the cryostat. Two aspects are particularly important: the vertical motion of the system using the step motor, which is controlled through the slow controls system, and the full readout chain, which is tested mainly for failures in sensors, cables, and connectors inside the cryostat.
- Individual sensors: to address the quality of individual precision sensors, the same method is used as for the static T-gradient monitors. For standard RTDs to be installed on the cryostat walls, floor, and roof, calibration is not an issue. Any QC required for associated cables and connectors is performed following the same procedure as for precision sensors.
- Gas analyzers: once the gas analyzer modules are installed at SURF and before the cryostat is commissioned, the analyzers are checked for both *zero* and the *span* values using a gas-mixing instrument and two gas cylinders, one with a zero level of the gas analyzer contaminant species and the other with a known percentage of the contaminant gas. This verifies that the gas analyzers are operating properly.
- Liquid level monitoring: once installed in the four cryostat corners, the capacitive level meters are tested in situ using a suitable dielectric in contact with the sensors.
- Cameras: after installing and connecting the wiring, fixed cameras, movable inspection cameras, and the light-emitting system are checked for operation at room temperature. Good quality images should be obtained of all cryostat and detector areas chosen from the system's design.

### 9.4.2.7 Photon detector QC testing

PD modules will arrive underground in custom crates. Each crate will contain the ten modules required for one APA, each individually packaged in a static-resistant sealed plastic bag filled with clean dry nitrogen. Each PD module is initially removed from its shipping bag, inspected visually, then (if it passes inspection) loaded into the optical scanner for operational testing shown in figure 9.44.

The optical scanner tests the operation of the photosensor readout chain to ensure all electrical connections are operational, and measures light-collection performance at several positions along the length of the module. Identical optical scanners are used at the module assembly facility, to test the module just before shipping so the underground test will detect any changes in performance due to shipping or storage. This technique was used successfully in ProtoDUNE-SP.

The optical scanner consists of a light-tight aluminum box, approximately 2.5 m long, with a 0.75 m<sup>2</sup> cross section. The box acts as a Faraday cage to minimize electrical interference with measurements. In the DUNE test configuration, two PD modules are inserted through slots on the face of the box, guided by support rails of the type used for the APAs, which provides a final mechanical check of the PD module dimensions. The insertion slots are closed and optically sealed.

The PD module uses an electrical connector identical to the ones in the APA frames, and that important interface is also checked in the scanner. Once the scan begins, DUNE PD readout electronics is used to bias and read out the photosensors, while a UV LED is scanned along the length of the modules via an automated stepper-motor-driven translation stage. Measurements are made at 16 positions along the length (on two sides for double-sided PD modules), checking the performance of each dichroic filter. The response is compared to that measured earlier at the assembly facility. Figure 9.44 shows the scanner used to test the ProtoDUNE-SP PDs.



**Figure 9.44.** Picture of the 2.5 m long scanner used for operational tests of the ProtoDUNE-SP PD modules prior to insertion into an APA.

Access to the PDs inside the APAs is severely limited once the CE cable conduit is in place, so identifying problems early in the process is necessary to minimize schedule issues caused by required PD maintenance or repair due to problems detected during installation.

Following the optical scan, the PD modules are inserted into an APA at the PD integration area in the cleanroom. The connection to the cable harness, which is pre-installed in the APA before wire wrapping, is automatic. An electrical continuity check follows insertion to verify continuity between the PD module and the PD cable end connector at the end of the APA.

As the upper and lower APAs are joined on the assembly tower, PD cables from the upper to the lower APA will be connected, and at that time, continuity checks will be made.

Once the upper and lower APAs are joined, the assembled unit will be moved into a cold box in front of the cryostat for final testing. This is an opportunity to make a final low-temperature check of the complete PD CE and cabling chain before installation into the cryostat. PD FE electronics boards will be used to read out the photon system during the cold test, and results will be compared to previous QA test results.

The APA stack is rolled into position in the cryostat following the cold box test, and the PD and CE cables connected to the cryostat flange. At this point, a final continuity check is made from the flange bulkhead to the PD module.

Discussions are underway with the installation team to arrange for a one-shift dark test of the installed PDs in the cryostat following final installation, verifying end-to-end system operation.

### 9.4.2.8 Calibration system testing

The laser system is aligned and tested as the lasers are installed. This requires an initial alignment with the alignment laser followed by testing with the UV laser under controlled conditions. Details of the testing procedures have not yet been developed. The pulsed neutron source will be calibrated offline to verify the shielding design and neutron flux. The source will be operated in test mode in situ to verify the functionality.

## 9.5 Detector commissioning

Once the SP module is installed in the cryostat and the TCO is closed, a warm commissioning phase can begin in order to test the fully assembled detector. After completion of the cryogenics installation, cold commissioning of both the cryogenics system and the detector can commence. Cold commissioning of the cryogenics steps through specific operating modes: purge, cool-down, fill, and circulate. During these steps DUNE conducts its own cold commissioning procedures.

Before the purging starts, a series of tests is performed to verify that the detector is operating nominally.

1. A pedestal and RMS characterization of all CE channels verifies that all APA FE boards are responding and no dead channel or new noise sources arose following the TCO closing.
2. A noise scan of all PD channels is performed as a last check.
3. Each APA wireplane is checked to verify it is isolated from the APA frame and properly connected to its HV power supply through the following steps:
  - The SHV connector of each wire plane bias channel gets unplugged at the power supply, and both the resistance and capacitance between inner conductor and ground is measured. The resistance should show that the wireplane is electrically isolated from the ground, while the capacitance value should match that of the cold HV cable and the capacitance of the circuit on the APA top frame.
  - 50 V is applied to each wireplane and the drawn current is checked against the expected value.
  - Nominal voltages are applied to each wireplane, and the drawn current is checked against the expected value.
4. A low HV (i.e., 1 kV to 2 kV) is applied to the cathode, and the drawn current is checked against the expected value to ensure the integrity of the HV line.

Cryogenics plant commissioning begins after installation is complete and the cryogenics system, including cryogenics controls and safety ODH systems, are approved for operation. The system first purges the air inside the cryostat by injecting pure GAr at the bottom at a rate that fills the cryostat volume uniformly, but faster than the diffusion rate. This “piston purge” process produces a column of GAr that rises through the volume and pushes the air up and out through the GAr purge lines and the GAr venting lines. When the piston purge is complete, misting nozzles inject a liquid-gas mix into the cryostat that cools the detector components at a controlled rate.

Once the detector is cold, the filling process begins. LAr stored at the surface is vaporized, brought down the shaft in gaseous form, and re-condensed underground. The LAr then flows through filters to remove any H<sub>2</sub>O and O<sub>2</sub> before entering the cryostat. Given the volume of the cryostat and the limited cooling power for recondensing, 12 months will be required to fill the first detector module. The detector readout electronics will monitor the status of the detector during the filling period.

A number of the following tests (and likely others) will take place during the cool-down and fill phases:

1. Each APA wireplane isolation and proper connection to its HV power supply will be checked at regular time intervals as was done before sealing the cryostat.
2. 1 kV to 2 kV will be held on the cathode, and the drawn current will be monitored constantly to observe the trend in temperature of the total resistance.
3. CE noise figures (pedestal, RMS) will be measured at regular intervals and their trends with temperature recorded.
4. PD system noise (pedestal, RMS) will be measured at regular intervals and its trend with temperature recorded.
5. Values of the temperature sensors deployed in several parts of the cryostat will be monitored constantly to watch the progress of the cool-down phase and to relate the temperature to the behavior of the other SP module subsystems.

Regular monitoring of CE and PD noise, as well as checks of wire plane isolation and proper connections to the bias supply system will continue throughout the fill period, recording noise variations as a function of the progressively reduced temperature. In addition,

1. as each purity monitor is submerged in liquid, it will be turned on every eight hours to check LAr purity.
2. as soon as top GPs are submerged, HV on the cathode will be raised up to 10 V-50 V to check that the current drawn by the system agrees with expectations.

Once the detector module is full, the drift HV will be carefully ramped up following these steps:

1. Evaluate need for a filter regeneration before starting any operation.



2. Once filter regeneration is completed (if needed), examine the LAr surface using cameras to verify that the surface is flat, with no bubbles or turbulence;
3. Start LAr recirculation while monitoring the LAr surface again to see if activating the recirculation system introduced any turbulence into the liquid.
4. Wait one day after beginning recirculation to stabilize the LAr flow inside the detector module, then start the HV ramp up.

Ramping up of the cathode HV represents the final step in the detector commissioning period; the full operating design parameters of the TPC detector can be accessed only after the cathode is at full voltage. We raise the cathode voltage in steps over three days. On the first day, cathode voltage is first raised to 60 kV, then to 90 kV after waiting two hours, and finally to 120 kV after waiting another two hours. It is left at this value overnight. On the second day, cathode voltage is first raised to 140 kV, then to 160 kV after waiting four hours, and left at this value overnight. On the third day, cathode voltage is first raised to 170 kV and then to the nominal operating voltage of 180 kV after waiting four hours. During each HV ramp up, all CE current draws are monitored, and the procedure is stopped if any of the current draws go out of the allowed range. During each waiting period, regular DAQ runs monitor CE and PD noise and response, while cathode HV and current draw stability are constantly monitored.

In ProtoDUNE-SP, this process took three days, after which the system was ready for data-taking. With a detector twenty times larger, the process will take longer, but the turn on time should still be relatively short.

### 9.6 Schedule

The detector installation planning hinges on the date that the JPO is permitted to begin work underground. According to the DUNE CF schedule, the JPO receives the acceptance for use and possession (AUP) for the north cavern and CUC in October 2022. The SDWF will be in place approximately six months before the warm structure installation begins, i.e., in spring 2022. Building the schedule for the detector module #1 installation after AUP is complicated and depends on many entities including CF, LBNF, and South Dakota Science and Technology Authority (SDSTA). The maximum number of people allowed underground is 144, which is based a one-hour time limit to evacuate all the underground personnel using all available paths. As a backup, the underground refuge must have capacity to accommodate this number of people. This number places a hard bound on how much work can be performed underground at any time and is particularly critical during the excavation of the third cavern when CF is still active. Figure 9.45 shows the main activities for the detector module #1 installation and the high-level milestones are shown in table 9.6.

The cost, schedule, and labor estimates are based on two 10 hour shifts per day, four days a week (Monday through Thursday). Work efficiency should be a maximum of 70%. The cage ride, shift meetings, lunch, coffee breaks, and cleanroom gowning takes up to three hours per day. Some low level of effort is planned on Friday, Saturday, and Sunday to monitor the cold boxes and take data.

**Table 9.6.** SP installation, integration, and commissioning schedule.

| Milestone  | Date (Month YYYY) |
|--|-------------------|
| Ash River phase 0 complete   | March 2020        |
| Start of ProtoDUNE-SP-II installation                              | March 2021        |
| Ash River phase 1 complete   | June 2021         |
| Installation Preliminary Design Review                             | August 2021       |
| Start of ProtoDUNE-DP-II installation                              | March 2022        |
| South Dakota Logistics Warehouse available                         | April 2022        |
| Ash River phase 2 complete   | July 2022         |
| Installation production readiness review                           | August 2022       |
| Start production of installation infrastructure for module #1      | August 2022       |
| Installation Final Design Review                                   | September 2022    |
| Beneficial occupancy of cavern 1 and CUC                           | October 2022      |
| Start construction warm structure cryostat #1                      | October 2022      |
| Start outfitting of CUC  | October 2022      |
| CUC counting room accessible                                       | April 2023        |
| Start installation of cold structure cryostat #1                   | August 2023       |
| Start installing Detector#1 infrastructure                         | August 2023       |
| Top of detector module #1 cryostat accessible                      | January 2024      |
| Start installation of detector module #1                           | June 2024         |
| Start of detector module #1 TPC installation                       | August 2024       |
| Complete installation of east FC endwall & first APA for module #1 | September 2024    |
| Complete installation of APA #75 for detector module #1            | January 2025      |
| Top of detector module #2 accessible                               | January 2025      |
| Complete installation of APA #150 (last) for detector module #1    | April 2025        |
| End of detector module #1 TPC installation                         | May 2025          |
| TCO of detector module #1 closed                                   | July 2025         |
| Start of cryogenic operation for detector module #1                | August 2025       |
| Start of detector module #2 TPC installation                       | August 2025       |
| End of detector module #2 TPC installation                         | May 2026          |
| Start of detector module #1 commissioning                          | January 2027      |



We have defined three schedule phases for installation of the first SP module:

- **CUC Installation Phase:** this period, described in detail in section 9.4.1.1, starts once AUP has been received for the north cavern and the CUC. This is the same time that excavation of the south cavern and installation of the warm structure by LBNF begins. Since the FTEs underground is limited to 144 at a time, access will be minimal for DUNE personnel and their work will only take place inside the CUC and surface dataroom. Installing the basic rack infrastructure in the dataroom will take an estimated three months. Installation and testing of the DAQ (required at the start of detector installation) will continue over the next 12 month period. Ten DAQ workers are planned on each shift in this period.
- **Installation Setup Phase:** described in detail in section 9.4.1.2, this period includes installation of the majority of the infrastructure. The setup phase is a critical training period, so getting lead workers, riggers, and equipment operators familiar with the tasks is a priority, as is adjusting the crews to ensure balanced teams. The training process will have begun already at Ash River. There are many parallel underground activities planned in this phase making it a difficult phase to schedule, and frequent schedule adjustments may be required. Immediately after the cryostat warm structure is complete the north-south bridge is constructed. Following this the bridge crane under the bridge can be installed. A few months after the cryostat warm structure is complete the CF work will also complete. Eighty of the 144 underground workers will become available to the JPO, and the underground installation team (UIT) team doubles in size. The JPO will start two 10 hour shifts per day. Due to space constraints, peripheral work only on the cleanroom structure and assembly towers can begin. Once the cryostat cold structure is approximately six months into its installation schedule, most of the foam will have been installed and floor space becomes available in the north cavern. The cold box construction must begin immediately at this point because the welding takes approximately six months. In parallel, the machine shop area can be set up. As the membrane installation nears completion, the walls of the cleanroom can be installed as can the remaining equipment. Installation of the DSS could begin during the final installation stages of the cryostat cold structure because they both require full-height scaffolding for the welding on the top of the cryostat. The ProtoDUNE-SP DSS was installed this way. This requires a crew on top of the cryostat installing the DSS support feedthroughs from the top, as shown in figure 9.26. The details have not yet been worked out with the contractor, and work may be done in stages.
- **Detector Installation Phase:** the final detector installation phase begins with an operational readiness review to check that all documentation and procedures are in place. After the east endwall FCs are installed, a start-up period of 1.5 months begins for the first two rows of TPC components. To meet this schedule, three assembly lines, three cold boxes, and separate crews in the cryostat, all working in parallel, are needed. It will take 5.5 months to install rows 3 through 24 and about one month for row 25. Closing the TCO will take approximately two months for the cryostat cold structure contractor; during this time, there is no access to the cryostat. Once this is completed, we can complete the final instrumentation, and the purge can begin. During this period, up to 50 people will be working in the cleanroom and cryostat.

The total time to install the detector including the time for the setup phase is two years. Coincidentally, this was roughly the time needed to install MINOS and NOvA.

### 9.7 Environmental, safety, and health (ES&H)

Volume III, DUNE far detector technical coordination, chapter 10 of the DUNE TDR outlines the requirements and regulations that DUNE work must comply with, whether (1) at Fermilab, (2) in areas leased by Fermilab or the DOE, (3) in leased space at SURF, or (4) at collaborating institutions.

#### 9.7.1 Documentation approval process

DUNE implements an engineering review and approval process for all required documentation, including structural calculations, assembly drawings, load tests, hazard analysis (HAs), and procedural documents for a comprehensive set of identified individual tasks. As for ProtoDUNE-SP, all these documents are stored in EDMS. For the larger operations and systems like TPC component factories, the DSS, cleanroom, and assembly infrastructure, DUNE safety also reviews the documentation then visits the site to conduct an operational readiness review, which includes a demonstration of the final operations. The operational readiness reviews are listed in project schedule.

Structural calculations, assembly drawings and proper documentation of load tests, hazard analyses, and procedures for various items and activities will require review and approval before operational readiness is granted.

#### 9.7.2 Support and responsibilities

The ES&H coordinator for each shift, who will report to the DUNE project ES&H manager, has overall ES&H oversight responsibility for the DUNE activities at the SDWF and on the SURF site. This person coordinates any ES&H activities and facilitates the resolution of any issues that are subject to the requirements of the DOE Workers Safety and Health Program, Title 10, Code Federal Regulations (CRF) Part 851 (10 CFR 851) (see Volume III). The on-site ES&H coordinator facilitates training and runs weekly safety meetings. This person is also responsible for managing ES&H-related documentation, including training records, HA documents, weekly safety reports, records on materials-handling equipment, near-miss and accident reports, and equipment inspections.

If the ES&H coordinator is absent, the shift supervisor acts in this capacity.

All workers have work stop authority in support of a safe working environment.

#### 9.7.3 Safety program

The on-site ES&H coordinators will guide the FD installation safety program, using the following:

1. the Fermilab Environment, Safety and Health Manual (FESHM);
2. the DUNE Installation ES&H Plan, which includes the fire evacuation plan, fire safety plan, lockdown plans, and the site plan;

3. work planning and controls documentation which includes both hazard analysis and procedures;
4. Safety Data Sheets (SDS);
5. the respiratory plan, as required for chemical or ODH hazards; and
6. the training program, which covers required certifications and training records.

During the installation setup phase, as new equipment is being installed and tested, new employees and collaborators will be trained to access the facility and use the equipment. At the end of this phase, we will require two shifts per day.

The cold box and cryogenics system will not be tested during the trial assembly work at Ash River. While the new cold box design is very similar to ProtoDUNE-SP's, it will be operated under DOE and FESHM regulations. Procedures for operating the cold box will be written according to the established requirements.

The DUNE installation team will develop an ES&H plan for detector installation that defines the ES&H requirements and responsibilities for personnel during assembly, installation, and construction of equipment at SURF. It will cover at least the following areas:

**Work Planning and HA:** the goal of the work planning and HA process is to initiate thought about the hazards associated with work activities and plan how to perform the work. Work planning ensures the scope of the job is understood, appropriate materials and tools are available, all hazards are identified, mitigation efforts are established, and all affected employees understand what is expected of them. The work planning and HA program is documented in chapter 2060 in the FESHM.

The shift supervisor and the ES&H coordinator will lead a work planning meeting at the start of each shift to (1) coordinate the work activities, (2) notify the workers of potential safety issues, constraints, and hazard mitigations, (3) ensure that employees have the necessary ES&H training and PPE, and (4) answer any questions.

**Access and training:** all DUNE workers requiring access to the SURF site must (1) register through the Fermilab Users Office to receive the necessary user training and a Fermilab identification number, and (2) they must apply for a SURF identification badge. The workers will be required to complete SURF surface and underground orientation classes. Workers accessing the underground must also complete 4850L and 4910L specific unescorted access training, and obtain a trip action plan (TAP) for each trip to the underground area; this is required as part of SURF's Site Access Control Program. A properly trained guide will be stationed on all working levels.

**PPE:** the host laboratory is responsible for supplying appropriate PPE to all workers.

**ERT:** the SDSTA will maintain an emergency response incident command system and an ERT. The guides on each underground level will be trained as first responders to help in a medical emergency.

**Guides:** the shift supervisor and lead workers will be trained as guides.

**House cleaning:** all workers are responsible for keeping a clean organized work area. This is particularly important underground. Flammable items must be in proper storage cabinets, and items like empty shipping crates and boxes must be removed and transported back to the surface to make space.

Equipment operation: all overhead cranes, gantry cranes, fork lifts, motorized equipment, e.g., trains and carts, will be operated only by trained operators. Other equipment, e.g., scissor lifts, pallet jacks, hand tools, and shop equipment, will be operated only by people trained and certified for the particular piece of equipment. All installation equipment will be electrically powered.

2020 JINST 15 T08010

# Acknowledgments

This document was prepared by the DUNE collaboration using the resources of the Fermi National Accelerator Laboratory (Fermilab), a U.S. Department of Energy, Office of Science, HEP User Facility. Fermilab is managed by Fermi Research Alliance, LLC (FRA), acting under Contract No. DE-AC02-07CH11359.

The DUNE collaboration also acknowledges the international, national, and regional funding agencies supporting the institutions who have contributed to completing this Technical Design Report.

2020 JINST 15 T08010



# Glossary

- Micro Telecommunications Computing Architecture ( $\mu$ TCA)** The computer architecture specification followed by the crates that house charge and light readout electronics in the DP module. 407, 564
- S/N** signal-to-noise ratio. 178, 179, 569
- one-pulse-per-second signal (1PPS signal)** An electrical signal with a fast rise time and that arrives in real time with a precise period of one second. 7, 15, 406, 407, 571
- 35 ton prototype** A prototype cryostat and SP detector built at Fermilab before the ProtoDUNE detectors. 93, 131, 215, 437, 441, 451, 454, 459, 460
- 4850L** The depth in feet (1480 m) of the top of the cryostats underground at SURF; used more generally to refer to the DUNE underground area. Called the “4850 level” or “4850L”. 66, 70, 418, 489, 490, 512, 523, 528, 561
- AC** capacitive coupling. 142, 146
- analog-to-digital converter (ADC)** A sampling of a voltage resulting in a discrete integer count corresponding in some way to the input. 12, 13, 52, 133, 134, 136, 137, 139, 143, 146–155, 157, 158, 160–163, 169, 173, 175, 177, 179, 181–187, 189, 192, 194, 199, 200, 212, 235, 244–247, 249, 250, 252–254, 257, 385, 392, 395, 413, 568–570, 572, 578, 580
- advanced mezzanine card (AMC)** Holds digitizing electronics and lives in  $\mu$ TCA crates. 407
- Argonne National Laboratory (ANL)** US national laboratory in Lemont, IL. 122, 543
- anode plane assembly (APA)** A unit of the SP detector module containing the elements sensitive to ionization in the LAr. It contains two faces each of three planes of wires, and interfaces to the cold electronics and photon detection system. 6–9, 11–16, 19–34, 36–75, 77–82, 86–90, 96, 97, 100, 101, 103–107, 110, 113, 114, 126, 129, 131, 132, 134–143, 146–148, 157, 164–170, 172–175, 177–179, 182, 183, 185, 186, 188–193, 195, 198, 200–215, 217–221, 223, 225, 229–231, 234–240, 246, 247, 249, 250, 255–258, 260, 263–268, 271, 272, 276–280, 282, 284–287, 289, 290, 293–296, 298, 299, 302, 305, 310, 311, 319, 321, 323–327, 329–333, 336–339, 346, 347, 355, 360, 363, 367–372, 387, 389, 390, 396, 407, 409–412, 415, 428, 429, 437, 444, 462, 463, 470, 477, 480, 481, 483, 485, 489, 495–497, 499–502, 504, 505, 507–521, 523, 525, 528, 529, 531–543, 545–555, 557, 568
- ARAPUCA** A PD system design that consists of a light trap that captures wavelength-shifted photons inside boxes with highly reflective internal surfaces until they are eventually detected by SiPM detectors or are lost. 232, 233, 237, 254, 577, 581
- ArgoNeuT** The ArgoNeuT test-beam experiment and LArTPC prototype at Fermilab. 3, 132
- artdaq** A data acquisition toolkit for data transfer, aggregation and processing. 191, 399, 405, 410

- Ash River** The Ash River, Minnesota, USA NOvA experiment far site, used as an assembly test site for DUNE. 16, 50, 51, 70, 74, 75, 77, 79, 98, 116, 126, 168, 492, 510, 512, 514, 520, 532, 539, 542, 543, 545, 559, 561
- ASIC** application-specific integrated circuit. 6, 9, 13, 39, 40, 46, 52, 88, 89, 126, 134, 137, 139–141, 143–148, 151, 153–157, 159–170, 172, 173, 175, 177, 179, 181, 184–189, 192–196, 198–200, 202, 209, 210, 212–215, 217–221, 223, 235, 245, 549, 566, 570, 572, 577
- Advanced Telecommunications Computing Architecture (ATCA)** An advanced computer architecture specification developed for the telecommunications, military, and aerospace industries that incorporates the latest trends in high-speed interconnect technologies, next-generation processors, and improved reliability, availability and serviceability. 191
- ATLAS** One of two general-purpose detectors at the LHC. It investigates a wide range of physics, from the search for the Higgs boson to extra dimensions and particles that could make up dark matter (DM). 126, 144, 375, 391
- acceptance for use and possession (AUP)** Required for beneficial occupancy of the underground areas at SURF for LBNF and DUNE. 556, 559
- American wire gauge (AWG)** U.S. standard set of non-ferrous wire conductor sizes. 441
- Brookhaven National Laboratory (BNL)** US national laboratory in Upton, NY. 71, 94, 147, 148, 151, 157, 158, 164, 188, 192, 193, 199, 206, 217, 219, 221, 539, 543
- bottom field cage (bottom FC)** The horizontal portions of the SP FC on the bottom of the TPC. 81, 87, 89, 94, 99, 103, 105, 115, 116
- CAPTAIN** Experimental program sited at Los Alamos National Laboratory (LANL) that is designed to make measurements of scientific importance to long-baseline (LBL) neutrino physics and physics topics that will be explored by large underground detectors. 326, 334
- charged current (CC)** Refers to an interaction between elementary particles where a charged weak force carrier ( $W^+$  or  $W^-$ ) is exchanged. 2, 25
- DAQ control, configuration and monitoring subsystem (CCM)** A system for controlling, configuring and monitoring other systems in particular those that make up the DAQ where the CCM encompasses run control (RC). 352, 388, 392, 400, 401, 403–406, 409, 410, 416
- cold electronics (CE)** Analog and digital readout electronics that operate at cryogenic temperatures. 6, 11–13, 16, 19, 21–23, 31, 33–35, 41, 45, 50–53, 55, 64, 70, 73, 74, 77, 84, 85, 104, 113, 114, 126, 131, 132, 134, 137, 139–141, 164–167, 169, 170, 173, 175, 177, 179, 181, 184, 185, 187, 189, 192–194, 201, 203, 205–207, 213, 215, 219, 252, 263, 264, 277, 282, 286, 287, 295, 299, 316, 354, 385, 387, 465, 506–508, 513, 514, 526, 532, 535–539, 545, 546, 548–550, 553–556, 570, 576
- European Organization for Nuclear Research (CERN)** The leading particle physics laboratory in Europe and home to the ProtoDUNEs. (In French, the Organisation Européenne pour la Recherche Nucléaire, derived from Conseil Européen pour la Recherche Nucléaire. 7, 14, 21, 23, 31, 41, 42, 44, 50–52, 74, 77, 91, 97, 105, 112, 120, 122, 123, 147, 189–193, 202, 211, 219, 246, 255, 267, 281, 302, 311, 313, 315, 349, 355, 375, 450, 457, 466, 469, 471, 490, 492, 517, 543, 545, 569, 572, 576, 580
- conventional facilities (CF)** Pertaining to construction and operation of buildings and conventional infrastructure, and for LBNF and DUNE project (LBNF/DUNE), CF includes the excavation caverns. 419, 493, 494, 507, 521, 523, 524, 556, 559, 571

- computational fluid dynamics (CFD)** High performance computer-assisted modeling of fluid dynamical systems. 430, 432, 434, 437–440, 447, 449–451, 457, 471, 473, 509
- cryogenic instrumentation and slow controls (CISC)** Includes equipment to monitor all detector components and LAr quality and behavior, and provides a control system for many of the detector components. 114, 207, 287, 289–291, 385, 387, 428–432, 439, 456, 458, 465, 467–469, 471, 473–476, 479, 480, 483, 487–489, 503, 523, 528, 530
- cryogenic instrumentation test facility (CITF)** A facility at Fermilab with small ( $< 1$  ton) to intermediate ( $\sim 1$  ton) volumes of instrumented, purified TPC-grade LAr, used for testing devices intended for use in DUNE. 430, 432, 436, 456, 462, 464, 465, 471, 477, 480, 485, 487
- construction manager/general contractor (CMGC)** The organizational unit responsible for management of the construction of conventional facilities at the underground area at the SURF site. 493, 497
- CMOS** Complementary metal-oxide-semiconductor. 131, 134, 139, 140, 145, 148, 151, 153, 154, 156–159, 184, 194
- convolutional neural network (CNN)** A deep learning technique most commonly applied to analyzing visual imagery. 415
- cluster on board (COB)** An ATCA motherboard housing four RCEs. 191, 577
- ColdADC** A newly developed 16-channels ASIC providing analog to digital conversion. 137, 143, 145, 147–149, 151–156, 159, 167, 173, 181, 184, 185, 187, 189, 194, 195, 219, 221
- COLDATA** A 64-channel control and communications ASIC. 13, 137, 139, 143, 145, 151, 153–156, 159, 165–167, 173, 184, 185, 187, 189, 194, 195, 212, 219, 221
- commercial off-the-shelf (COTS)** Items, typically hardware such as computers, that may be purchased whole, without any custom design or fabrication and thus at normal consumer prices and availability. 143, 157, 158, 163, 169, 181, 185, 186, 189, 192, 194, 202, 212
- charge parity (CP)** Product of charge and parity transformations. 2, 83
- cathode plane assembly (CPA)** The component of the SP detector module that provides the drift HV cathode. 6, 8–10, 16, 81, 82, 85–87, 89, 91, 93–96, 98–108, 112–118, 121–123, 125, 126, 129, 130, 230, 236, 250, 267, 270, 283, 287, 288, 291, 306, 310–312, 323, 326, 338–340, 346, 349, 351, 355, 368, 462, 463, 499–502, 505, 516, 520, 526, 529–532, 536, 537, 539–541, 543, 545, 546, 550, 551, 566, 577
- CPA/FC** A pair of CPA panels and the top and bottom FC portions that attach to the pair; an intermediate assembly for installation into the SP module. 121
- charge-parity symmetry violation (CPV)** Lack of symmetry in a system before and after charge and parity transformations are applied. For CP symmetry to hold, a particle turns into its corresponding antiparticle under a charge transformation, and a parity transformation inverts its space coordinates, i.e., produces the mirror image. 19, 25, 83, 225, 376, 428
- CR** Capacitance-Resistance. 22, 33, 35, 45, 52, 53, 61, 64, 137, 142, 143, 165, 168, 190, 205
- charge-readout plane (CRP)** In the DP technology, a collection of electrodes in a planar arrangement placed at a particular voltage relative to some applied E field such that drifting electrons may be collected and their number and time may be measured. 461, 470
- cosmic ray tagger (CRT)** Detector external to the TPC designed to tag TPC-traversing cosmic ray particles. 235, 258, 260

- CRYO** Integrated ASIC including FE circuitry providing signal amplification and pulse shaping, analog to digital conversion, and control and communication functionalities for 64 channels. 143, 145, 157, 159–164, 168–170, 172, 173, 181, 185, 187–189, 194, 195, 198, 199, 212, 219, 221
- CTE** coefficient of thermal expansion. 31, 34, 35, 89, 280, 281
- CTS** Cryogenic Test System. 161, 188, 199, 200, 202, 210, 211, 221
- central utility cavern (CUC)** The utility cavern at the 4850L of SURF located between the two detector caverns. It contains utilities such as central cryogenics and other systems, and the underground data center and control room. 4, 6, 13, 17, 75, 206, 223, 288, 303, 362, 376, 383–385, 387, 388, 390, 407, 418, 419, 421, 423, 466–468, 476, 493, 496, 507, 521, 523–525, 547, 556, 557, 559
- convolutional visual network (CVN)** An algorithm for identifying neutrino interactions based on their topology and without the need for detailed reconstruction algorithms. 133
- DAC** digital-to-analog converter. 146, 160, 163, 250
- DAPHNE** Detector electronics for Acquiring PHotons from NEutrinos is a custom-developed warm front-end waveform digitizing electronics module derived from the readout system developed at Fermilab for the Mu2e experiment. 246, 264, 285
- data acquisition (DAQ)** The data acquisition system accepts data from the detector FE electronics, buffers the data, performs a trigger decision, builds events from the selected data and delivers the result to the offline secondary DAQ buffer. 6, 7, 13–16, 111, 131, 133, 134, 137, 165, 169, 172, 173, 175, 188, 190–192, 201–207, 214, 230, 235, 242, 246–249, 264, 266, 283–290, 307, 315, 319, 332, 339, 345–349, 351, 352, 358, 360, 370, 375–378, 383–411, 415–418, 420, 421, 423–427, 431, 454–456, 468–470, 473, 480, 484, 521, 523, 528, 547, 549, 550, 556, 559, 565, 567–570, 574, 577, 580
- DAQ back-end subsystem (DAQ BE)** The portion of the DAQ that is generally toward its output end. It is responsible for accepting and executing trigger commands and marshaling the data they address to output storage buffers. 13, 15, 376, 377, 388, 389, 391, 392, 394–400, 406, 409, 412, 415, 550
- DAQ data selection subsystem (DAQ DS)** The subsystem of the DAQ responsible for forming a trigger decision based on a portion of the input data stream. The majority subset of the DAQ trigger subsystem (DAQ TS). 376–378, 388, 389, 391–394, 397–400, 405, 406, 412, 425
- DAQ front-end computer (DAQ FEC)** The portion of one DAQ partition that hosts the DAQ data receiver (DDR), DAQ primary buffer and data selector. It hosts the DAQ front-end readout (FER) and corresponding portion of the DAQ primary buffer. 389–391, 409, 567, 570
- DAQ front-end fragment** The portion of one DAQ partition relating to a single DAQ FEC and corresponding to an integral number of detector units. See also data fragment. 567, 568, 570
- DAQ partition** A cohesive and coherent collection of DAQ hardware and software working together to trigger and read out some portion of one detector module; it consists of an integral number of DAQ front-end fragments. Multiple DAQ partitions may operate simultaneously, but each instance operates independently. 567
- DAQ primary buffer** The portion of the DAQ front-end fragment that accepts full data stream from the corresponding detector unit and retains it sufficiently long for it to be available to produce a data fragment. 567, 568
- DAQ readout unit (DAQ RU)** The first element in the data flow of the DAQ. 14, 389, 391, 392
- DAQ trigger subsystem (DAQ TS)** The subsystem of the DAQ responsible for forming a trigger decision. 567

- DAQ timing and synchronization subsystem (DAQ TSS)** The portion of the DAQ that provides for timing and synchronization to various components. 388, 406
- data fragment** A block of data read out from a single DAQ front-end fragment that span a contiguous period of time as requested by a trigger command. 567, 568
- data selection** The process of forming a trigger decision for selecting a subset of detector data for output by the DAQ from the content of the detector data itself. Not to be confused with data selector. 378, 388, 392, 393, 395, 397, 406, 408, 568
- data selector** The portion of the DAQ front-end fragment that accepts trigger commands and returns the corresponding data fragment. Not to be confused with data selection. 567, 568
- Daya Bay** a neutrino-oscillation experiment in Daya Bay, China, designed to measure the mixing angle  $\Theta_{13}$  using antineutrinos produced by the reactors of the Daya Bay and Ling Ao nuclear power plants. 490
- DC** direct coupling. 142, 147, 154, 170, 573, 578
- DUNE construction database (DCDB)** Database used by DUNE to track the history and testing of all parts of each detector module. 497, 548
- DCS** Distributed Communications System. 450
- DAQ data receiver (DDR)** The portion of the DAQ front-end fragment that accepts data from the FER, emits trigger candidates produced from the input trigger primitives, and forwards the full data stream to the DAQ primary buffer. 567
- DUNE detector safety system (DDSS)** The system used to manage key aspects of detector safety. 16, 175, 207, 431
- detector module** The entire DUNE far detector is segmented into four modules, each with a nominal 10 kt fiducial mass. 19–21, 60, 62, 64, 74, 75, 81, 82, 86, 87, 125, 131, 132, 164, 223, 270, 277, 303, 304, 362, 366, 375, 376, 388, 392, 393, 396, 423, 429, 431, 432, 434, 436, 438, 440, 442, 446, 447, 451, 457, 458, 461, 464, 469, 473, 476, 489–494, 496, 504, 506–509, 523, 525, 555–558, 568–570, 579, 580
- detector unit** A portion of a detector module may be further partitioned into a number of similar parts. For example the SP TPC is made up of APA units (and other elements). 567, 574
- data flow orchestrator (DFO)** The process by which trigger commands are executed in parallel and asynchronous manner by the back-end output subsystem of the DAQ. 349, 352, 376, 377, 396, 398
- discovery and presence** As used in the context of the IPC, a system that provides mechanisms for a node on a communication network to learn of the existence of peers and their identity (discovery) as well as determine if they are currently operational or have become unresponsive (presence). 416
- dark matter (DM)** The term given to the unknown matter or force that explains measurements of galaxy motion that are otherwise inconsistent with the amount of mass associated with the observed amount of photon production. 19, 565
- differential non-linearity (DNL)** A commonly used measure of performance in ADCs. The DNL error is defined as the difference between an actual step width and the ideal value of one least significant bit (LSB). 152, 157, 163
- DOE** U.S. Department of Energy. 543, 560, 561
- dual-phase (DP)** Distinguishes one of the DUNE far detector technologies by the fact that it operates using argon in both gas and liquid phases. 82, 123, 286, 314, 428, 437, 457, 473, 566, 576, 580

- DP module** dual-phase DUNE FD module. 123, 228, 323, 428, 461, 473, 545, 564
- data quality monitoring (DQM)** Analysis of the raw data to monitor the integrity of the data and the performance of the detectors and their electronics. This type of monitoring may be performed in real time, within the DAQ system, or in later stages of processing, using disk files as input. 406
- detector support system (DSS)** The system used to support a SP detector module within its cryostat. 16, 37–39, 51, 101, 113, 114, 121, 206, 283, 291, 321, 322, 440, 446, 447, 481, 483, 484, 489, 499–506, 510, 513, 521, 527–531, 537–543, 545, 552, 559, 560
- Deep Underground Neutrino Experiment (DUNE)** A leading-edge, international experiment for neutrino science and proton decay studies. 1–4, 9, 14–16, 18–22, 25–27, 29, 31, 39, 41, 42, 51, 53, 55, 60, 61, 64, 66, 71, 74, 75, 81, 84, 131–136, 139–147, 154, 158, 159, 163, 164, 168, 170–173, 175, 177, 181, 182, 184–194, 196, 199, 200, 202, 206–208, 210–212, 214, 215, 217–221, 225, 226, 228, 229, 232, 233, 236, 237, 240–244, 246, 247, 249, 251, 252, 263–270, 274–277, 279–281, 289, 291, 292, 294–298, 301, 304, 310–315, 317, 321, 323–326, 329, 330, 340, 344, 346–349, 352, 355, 356, 359, 365, 367, 368, 370, 373, 375–379, 383–385, 387, 388, 390–392, 394, 397, 398, 406–409, 418, 419, 436–438, 451, 458, 459, 461, 462, 465, 471, 479, 487, 489–498, 505, 506, 509, 512, 517, 520, 521, 523–525, 528, 531, 543, 545, 546, 548, 550, 552–554, 556, 559–561, 565, 566, 570, 573, 577, 579
- event builder (EB)** A software agent that executes trigger commands for one detector module by reading out the requested data. 349, 352, 377, 394, 398–400, 405, 426
- executive board (EB)** The highest level DUNE decision-making body for the collaboration. 164
- engineering document management system (EDMS)** A computerized document management system developed and supported at CERN in which some DUNE documents, drawings and engineering models are managed. 545, 547, 560
- equivalent noise charge (ENC)** The equivalent noise charge is the input charge that corresponds to a  $S/N = 1$ . 132, 134, 158, 175–178, 192
- endwall field cage (endwall FC)** The vertical portions of the SP FC near the wall. 81, 86, 87, 89, 93, 94, 96, 98–101, 103, 105–107, 112, 113, 117–119, 126, 499, 500, 530, 531, 541, 542, 545, 551, 559
- effective number of bits (ENOB)** The effective number of bits is a measure of the dynamic range of an ADC and its associated circuitry. The resolution of an ADC is specified by the number of bits used to represent the analog value, in principle giving  $2N$  signal levels for an  $N$ -bit signal. However, all real ADC circuits introduce noise and distortion. ENOB specifies the resolution of an ideal ADC circuit that would have the same resolution as the circuit under consideration. 152, 157, 163
- ERT** emergency response team. 561
- environment, safety and health (ES&H)** A discipline and specialty that studies and implements practical aspects of environmental protection and safety at work. 70, 91, 208, 217, 355, 356, 490, 499, 560, 561
- ESD** electrostatic discharge. 88, 196, 207, 209, 213, 214
- external trigger interface (ETI)** Interface between module trigger logics (MTLs) and external source and sinks of relevant trigger information. 376, 387, 393, 397
- external trigger logic (ETL)** Trigger processing that consumes detector module level trigger notification information and other global sources of trigger input and emits trigger command information back to the MTLs. 392, 574, 580

- external trigger candidate** Information provided to the MTL about events external to a detector module so that it may be considered in forming trigger commands. 574
- Fondazione Bruno Kessler (FBK)** FBK is a research non-profit entity in Trento, Italy that partners in the development of technology with applications in various fields including High Energy Physics. 242, 243, 252, 253, 281, 304
- field cage (FC)** The component of a LArTPC that contains and shapes the applied E field. 4, 6, 10, 16, 20, 21, 51, 81, 82, 85–89, 91–100, 102–109, 111–114, 116–123, 125, 126, 130, 141, 168, 175, 190, 191, 203, 205, 206, 210, 250, 321, 323, 324, 326, 327, 329–332, 334, 335, 347, 349, 351, 354, 359, 363, 366–369, 371, 372, 429, 434, 437, 462, 463, 489, 499–501, 531, 532, 536, 537, 539–543, 545, 550, 551, 565, 566, 569, 571, 579
- far detector (FD)** The 70 kt total (40 kt fiducial) mass LArTPC DUNE detector, composed of four 17.5 kt total (10 kt fiducial) mass modules, to be installed at the far site at SURF in Lead, SD, USA. 1, 4, 5, 7, 11, 15, 16, 18, 20, 25, 26, 28, 78, 83, 91, 93, 98, 122, 124, 175, 184, 187–196, 199, 202, 208, 211, 212, 214, 215, 218–221, 225, 230, 235, 242, 260, 263, 291, 296, 313–315, 323, 325, 326, 344, 345, 347, 348, 355, 359, 361, 362, 369, 375–379, 383–385, 387, 392–394, 397–399, 406–408, 428, 430, 437, 438, 450, 457, 462, 464, 465, 469, 471, 473–475, 484, 489, 528, 543, 545, 560, 569, 573, 574, 578, 579
- front-end (FE)** The front-end refers a point that is “upstream” of the data flow for a particular subsystem. For example the SP front-end electronics is where the cold electronics meet the sense wires of the TPC and the front-end DAQ is where the DAQ meets the output of the electronics. 6, 21, 52, 66, 84, 88, 89, 109, 126, 131, 135–137, 139–141, 146, 147, 159, 161, 163, 175–177, 181, 187, 192, 199, 204, 205, 212, 235, 245–249, 270, 282–284, 298, 349–352, 370, 454, 456, 467, 480, 481, 549, 553, 554, 567, 570, 572, 580
- finite element analysis (FEA)** Simulation of a physical phenomenon using the numerical technique called Finite Element Method (FEM), a numerical method for solving problems of engineering and mathematical physics. 40, 130, 184, 279
- FEB** front-end board. 246–249, 252, 253, 264
- Front-End Link eXchange (FELIX)** A high-throughput interface between FE and trigger electronics and the standard PCIe computer bus. 7, 14, 349, 387, 389–391, 408–412, 418
- front-end mother board (FEMB)** Refers a unit of the SP CE that contains the FE amplifier and ADC ASICs covering 128 channels. 13, 14, 25, 45, 52, 133, 134, 137, 139–144, 146, 147, 153, 155, 157–159, 163–165, 167–177, 179, 182–186, 188–190, 192, 193, 195, 196, 198–203, 205–207, 209–215, 217–221, 223, 513–515, 532, 549, 550, 580
- DAQ front-end readout (FER)** The portion of a DAQ front-end fragment that accepts data from the detector electronics and provides it to the DAQ FEC. 567, 568
- Fermi National Accelerator Laboratory (Fermilab)** U.S. national laboratory in Batavia, IL. It is the laboratory that hosts DUNE and serves as its near site. 4, 70, 89, 91, 119, 123, 145, 147, 148, 151, 153, 157, 188, 190, 192, 209, 211, 215–217, 219, 221, 240, 241, 246, 263, 268–270, 284, 297, 313, 356, 465, 468, 471, 490–492, 499, 507, 521, 523, 543, 545, 560, 561, 564, 572–574, 577, 579
- Fermilab Environment, Safety and Health Manual (FESHM)** The document that contains Fermilab’s policies and procedures designed to manage environment, safety, and health in all its programs. 560, 561
- FFT** fast Fourier transform. 152

**FIFO** First-In-First-Out. 156

**FPGA mezzanine card (FMC)** Boards holding FPGAs and other integrated circuitry that attach to a motherboard. 407

**field programmable gate array (FPGA)** An integrated circuit technology that allows the hardware to be reconfigured to execute different algorithms after its manufacture and deployment. 64, 65, 137, 143, 161, 170, 172–175, 185, 186, 191, 196, 199, 212, 216, 246, 247, 249, 250, 283, 388, 391, 395, 408, 410–412, 571, 577

**FRP** fiber-reinforced plastic. 86, 89, 95, 96, 99–101, 106, 111, 116–118, 123

**far site conventional facilities (FSCF)** The CF at the DUNE far detector site, SURF. 579

**FSS** field shaping strips. 94, 96, 103, 105, 115, 116, 551

**FTE** full-time equivalent. A unit of labor for the project. One year of work from one person. 559

**fiducial volume (FV)** The detector volume within the TPC that is selected for physics analysis through cuts on reconstructed event position. 20, 83, 315, 317, 322, 325

**full width at half maximum (FWHM)** Width of a distribution measured between those points at which the distribution is equal to half of its maximum amplitude. 252

**gaseous argon (GAr)** argon in its gas phase. 508–510, 530, 555

**Geant4** A software toolkit for the simulation of the passage of particles through matter using MC methods. 305

**ground plane (GP)** An electrode held electrically neutral relative to Earth ground voltage; it is mounted on the FC in a SP module to protect the cryostat wall. 23, 81, 82, 85, 87–89, 93, 95–100, 105, 107–109, 111, 117, 123, 126, 250, 432, 434, 437, 447, 457, 461, 462, 482, 501, 529, 555

**GPIB** general purpose interface bus. 467

**Global Positioning System (GPS)** A satellite-based system that provides a highly accurate 1PPS signal that may be used to synchronize clocks and determine location. 7, 15, 406

**hazard analysis (HA)** A first step in a process to assess risk; the result of hazard analysis is the identification of the hazards present for a task or process. 70, 560, 561

**HEP** high energy physics. 193, 194, 291, 375

**high voltage (HV)** Generally describes a voltage applied to drive the motion of free electrons through some media, e.g., LAr. 10, 20, 46, 49, 51, 81–94, 98, 102–105, 107–116, 118, 120, 122–126, 129, 164, 179, 190, 204–206, 250, 264, 268, 283, 286–291, 299, 311, 313, 316, 317, 319, 321, 323, 325, 349, 354, 356, 428–432, 453–457, 459, 461, 463, 465, 466, 470, 477, 479–481, 488–490, 512, 513, 516, 531, 538, 539, 545, 550, 551, 554–556, 578

**high voltage system (HVS)** The detector subsystem that provides the TPC drift field. 81, 89, 113, 119–123, 126–129, 140

**Inter-Integrated Circuit (I2C)** I<sup>2</sup>C or I2C is a synchronous, multi-master, multi-slave, packet switched, single-ended, serial computer bus widely used for attaching lower-speed peripheral ICs to processors and microcontrollers in short-distance, intra-board communication. 151, 153, 155, 156, 161, 166



**ICARUS** A neutrino experiment that was located at the Laboratori Nazionali del Gran Sasso (LNGS) in Italy, then refurbished at CERN for re-use in the same neutrino beam from Fermilab used by the MiniBooNE, MicroBooNE and SBND experiments. The ICARUS detector is being reassembled at Fermilab. 84, 86, 87, 91, 96, 126, 375, 408, 451, 453, 577

**ICEBERG R&D cryostat and electronics (ICEBERG)** Integrated Cryostat and Electronics Built for Experimental Research Goals: a new double-walled cryostat built and installed at Fermilab for liquid argon detector R&D and for testing of DUNE detector components. 147, 157, 188–193, 215, 219, 240, 241, 246, 249, 263–265, 295, 302, 465

**inner diameter (ID)** Inner diameter of a tube. 502

**IFbeam** Database that stores beamline information indexed by timestamp. 469, 470

**IFIC** Instituto de Fisica Corpuscular (in Valencia, Spain). 446

**integral non-linearity (INL)** A commonly used measure of performance in ADCs. It is the deviation between the ideal input threshold value and the measured threshold level of a certain output code. 152, 157, 163

**integration office** The office that incorporates the onsite team responsible for coordinating integration and installation activities at SURF. 572

**inter-process communication (IPC)** A system for software elements to exchange information between threads, local processes or across a data network. An IPC system is typically specified in terms of protocols composed of message types and their associated data schema. 405, 416, 568

**inter-range instrumentation group (IRIG)** A standards body that defined a time-code standard for transferring timing information. 407

**Joint Project Office (JPO)** The framework through which team members from the LBNF project office, integration office, and DUNE technical coordination work together to provide coherence in project support functions across the global enterprise. Its functions include global project configuration and integration, installation planning and coordination, scheduling, safety assurance, technical review planning and oversight, development of partner agreements, and financial reporting. 206, 493, 494, 497–499, 517, 528, 556, 559

**LabVIEW** Laboratory Virtual Instrument Engineering Workbench is a system-design platform and development environment for a visual programming language from National Instruments. 455, 456

**Los Alamos National Laboratory (LANL)** US national laboratory in Los Alamos, NM. 565

**Liquid Argon Purity Demonstrator (LAPD)** Cryostat at Fermilab for long-term studies requiring a large volume of argon. 454, 461, 462

**liquid argon (LAr)** Argon in its liquid phase; it is a cryogenic liquid with a boiling point of  $-90^{\circ}\text{C}$  (87 K) and density of 1.4 g/ml. 2, 3, 6, 7, 13, 15, 16, 19, 21, 36, 42, 52, 66, 82–84, 86, 89, 94, 96, 97, 99, 103, 107–111, 114, 120, 126, 130–133, 136, 137, 139, 140, 142, 144, 145, 156, 161, 164, 167, 168, 177–179, 188–190, 192–194, 204, 207, 208, 210, 215, 229, 230, 235–238, 240–242, 250–252, 254, 255, 258, 261, 266, 268–270, 272, 278, 294, 295, 297, 312, 314, 317, 321, 326–328, 336, 340, 342, 345, 347, 348, 356, 359, 368, 369, 373, 374, 377, 428–430, 432, 434, 437–440, 445, 447–454, 456–466, 473, 477, 485–489, 499, 501, 508–510, 516, 517, 546, 548, 550, 555, 556, 566, 575, 579

**LArASIC** A 16-channel FE ASIC that provides signal amplification and pulse shaping. 137, 143, 145–149, 151–154, 156, 159, 161, 167, 168, 175, 181, 182, 184, 185, 187, 194, 195, 198, 219, 221

- LArIAT** The repurposed ArgoNeuT LArTPC, modified for use in a charged particle beam, dedicated to the calibration and precise characterization of the output response of these detectors. 3, 240, 310, 311, 348
- Liquid Argon Software (LArSoft)** A shared base of physics software across LArTPC experiments. 304
- liquid argon time-projection chamber (LArTPC)** A TPC filled with liquid argon; the basis for the DUNE FD modules. 1–4, 15, 18, 19, 81–83, 87, 91, 113, 126, 131, 175, 177, 189, 225, 230, 311, 321, 346, 347, 375, 379, 408, 451, 456, 548, 564, 570, 573, 579
- long-baseline (LBL)** Refers to the distance between the neutrino source and the FD. It can also refer to the distance between the near and far detectors. The “long” designation is an approximate and relative distinction. For DUNE, this distance (between Fermilab and SURF) is approximately 1300 km. 16, 314, 315, 322, 324, 565
- laser beam location system (LBLS)** Auxiliary calibration system providing an independent location measurement of the ionization laser beams direction. 315, 334, 335, 347, 349, 353, 354
- Long-Baseline Neutrino Facility (LBNF)** The organizational entity responsible for developing the neutrino beam, the cryostats and cryogenics systems, and the conventional facilities for DUNE. 2, 4, 15, 16, 206, 208, 217, 218, 287, 309, 430, 457, 458, 469, 473, 475, 479, 483, 486, 487, 493–498, 517, 520, 521, 525, 556, 559, 573, 579
- LBNF and DUNE project (LBNF/DUNE)** The overall global project, including LBNF and DUNE. 70, 208, 217, 565
- Lawrence Berkeley National Laboratory (LBNL)** US national laboratory in Berkeley, CA. 148, 151, 221
- LCM** light calibration module. 250
- low-dropout regulator (LDO)** A low-dropout or LDO regulator is a DC linear voltage regulator that can regulate the output voltage even when the supply voltage is very close to the output voltage. 160, 161, 168
- LED** Light-emitting diode. 250, 251, 253, 270, 276, 285, 298, 299, 454, 464, 465, 487, 510, 546, 553
- LHC** Large Hadron Collider. 199, 375, 450, 471, 565
- LN<sub>2</sub>** liquid nitrogen. 63, 94, 96, 142, 145, 146, 152, 156, 157, 161, 240, 241, 253, 261, 276, 464, 486–488, 549
- LPM** light pulser module. 250
- least significant bit (LSB)** The bit with the lowest numerical value in a binary number. 568
- LUX** Large Underground Xenon (LUX) dark matter detector at SURF. 490
- LV** low voltage. 52, 137, 139, 153, 154, 167, 169–171, 174–176, 192, 456, 507, 508
- LVDS** low-voltage differential signaling. 151, 156, 165
- LZ** Experiment sited at SURF that seeks to detect faint interactions between galactic dark matter and regular matter. 490
- Majorana Demonstrator** Experiment sited at SURF that seeks to determine whether neutrinos are their own antiparticles. 490
- Monte Carlo (MC)** Refers to a method of numerical integration that entails the statistical sampling of the integrand function. Forms the basis for some types of detector and physics simulations. 254, 255, 415, 571

- main communications room (MCR)** Space at the FD site for cyber infrastructure. 376
- mass hierarchy (MH)** Describes the separation between the mass squared differences related to the solar and atmospheric neutrino problems. 83
- MicroBooNE** The LArTPC-based MicroBooNE neutrino oscillation experiment at Fermilab. 3, 10, 84, 87, 91, 130, 177, 180, 181, 183, 184, 186, 215, 321, 326–329, 332, 333, 347, 348, 375, 379, 392, 408, 451, 454, 467, 469, 471, 572, 577
- miniature parallel optical device (MiniPOD)** a family of types of multi-channel optical transceivers. 387
- MINOS** A long-baseline neutrino experiment, with a near detector at Fermilab and a far detector in the Soudan mine in Minnesota, designed to observe the phenomena of neutrino oscillations (ended data runs in 2012). 490, 560
- minimum ionizing particle (MIP)** Refers to a particle traversing some medium such that the particle's mean energy loss is near the minimum. 19, 22, 25, 26, 132
- master in slave out (MISO)** The Master In Slave Out is a logic signal on the Serial Peripheral Interface (SPI) bus on which the data from the slave are transmitted once a request from the master is received. 154
- module level trigger (MLT)** The DAQ component responsible for producing a trigger decision that will be used to command the readout of a detector module. 349–352, 370, 397
- master out slave in (MOSI)** The Master Out Slave In is a logic signal on the SPI bus on which the data from the master is transmitted. 154
- memorandum of understanding (MoU)** A document summarizing an agreement between two or more parties. 281
- MPPC** 6 mm×6 mm Multi-Pixel Photon Counters produced by Hamamatsu™ Photonics K.K. 229, 235, 241, 242, 244, 246, 247, 251–255, 257, 259, 261, 262, 270–272
- module trigger logic (MTL)** Trigger processing that consumes detector unit level trigger command information and emits trigger commands. It provides the ETL with trigger notifications and receives back any external trigger candidates. 569, 570, 580
- Mu2e** An experiment sited at Fermilab that searches for charged-lepton flavor violation and seeks to discover physics beyond the standard model (SM). 235, 244, 246, 247, 249, 253, 254, 263, 264, 266, 509
- NASA** U.S. National Aeronautics and Space Administration. 145, 194
- neutral current (NC)** Refers to an interaction between elementary particles where a neutrally charged weak force carrier ( $Z^0$ ) is exchanged. 25
- near detector (ND)** Refers to the detector(s) installed close to the neutrino source at Fermilab. 83, 471
- nucleon decay (NDK)** The hypothetical, baryon number violating decay of a proton or a bound neutron into lighter particles. 19, 291
- Enriched Xenon Observatory (nEXO)** Experiment at Lawrence Livermore National Laboratory (U.S. national lab in Livermore, CA) searching for new physics with neutrinoless double-beta decay. 157, 159
- NOvA** The NOvA off-axis neutrino oscillation experiment at Fermilab. 16, 120, 469, 471, 490, 492, 542–544, 560, 565

- Non-volatile memory express (NVMe)** A specification for an interface to storage media attached via PCIe. 392, 411
- outer diameter (OD)** Outer diameter of a tube. 502
- oxygen deficiency hazard (ODH)** a hazard that occurs when inert gases such as nitrogen, helium, or argon displace room air and thus reduce the percentage of oxygen below the level required for human life. 513, 519, 555, 561
- OM3** Type of multi-mode fiber optic cable, typically capable of 10 Gbps data transmission at lengths up to 300 m. 206, 391
- OM4** Type of multi-mode fiber optic cable, typically capable of 10 Gbps data transmission at lengths up to 550 m. 206, 391
- OPC-UA** OPC Unified Architecture is a machine to machine communication protocol for industrial automation developed by the OPC Foundation. OPC stands for Object Linking and Embedding for Process Control. 450, 469
- operational readiness review** A project management device by which the operational readiness is reviewed. 559, 560
- operational readiness clearance (ORC)** Final safety approval prior to the start of operation. 545
- OSHA** Occupational Safety and Health Administration (USA Department of Labor) formed by the Occupational Safety and Health Act of 1970. 514
- Proton Assembly Building (PAB)** Home of several LAr facilities at Fermilab. 465
- PCB** printed circuit board. 35, 142, 144, 165, 168, 169, 182, 194, 239–241, 278, 281–283, 298, 443, 444, 446, 447, 482, 485, 486
- PCI** Peripheral Component Interconnect. 455
- photon detector (PD)** The detector elements involved in measurement of the number and arrival times of optical photons produced in a detector module. 3, 7–9, 12, 14, 16, 21, 22, 28, 29, 41, 48, 53, 54, 56, 66, 109, 110, 126, 129, 133, 138, 142, 165, 166, 190, 228, 230–232, 234–238, 240, 242, 244, 246, 247, 249–251, 255–259, 263–271, 273–290, 292–300, 302–307, 309–312, 321, 384, 428, 465, 466, 470, 489, 506, 507, 512, 513, 516, 526, 528, 530, 531, 533, 535–540, 545, 546, 548, 552–556
- photon detection system (PD system)** The detector subsystem sensitive to light produced in the LAr. 28, 50, 51, 53, 55, 56, 70, 74, 77, 109, 114, 137, 140, 142, 165, 173, 179, 184, 188–190, 192, 193, 201, 203, 205–207, 214, 225, 226, 228–230, 232, 235, 236, 242–245, 248, 249, 251, 252, 258–260, 264–268, 270, 271, 273, 277, 281, 282, 284–291, 293, 297, 299–302, 304–310, 312, 313, 316, 346, 349, 350, 359, 360, 369, 370, 377, 385, 387, 389, 391–393, 396, 406, 408–410, 456, 464, 480, 507, 509, 536, 549, 564
- particle ID (PID)** Particle identification. 229
- PLC** programmable logic controller. 211, 458, 483, 487
- Phase-Locked Loop (PLL)** A control system that generates an output signal whose phase is related to the phase of an input signal. 143, 155, 156, 173
- photomultiplier tube (PMT)** A device that makes use of the photoelectric effect to produce an electrical signal from the arrival of optical photons. 230, 344

- PNP** Type of bipolar junction transistor consisting of a layer of N-doped semiconductor sandwiched between two layers of P-doped material. 148
- pulsed neutron source (PNS)** Calibration system based on neutron capture gamma showers spread out in the whole detector. 315, 317, 318, 321, 340, 342, 344–347, 351–353, 355, 356, 359, 361, 362, 365, 366
- parts per billion (ppb)** A concentration equal to one part in  $10^{-9}$ . 451, 459, 460
- personnel protective equipment (PPE)** Equipment worn to minimize exposure to hazards that cause serious workplace injuries and illnesses. 70, 119, 208, 355, 499, 561
- parts per million (ppm)** A concentration equal to one part in  $10^{-6}$ . 460
- parts per trillion (ppt)** A concentration equal to one part in  $10^{-12}$ . 451, 459, 460
- production readiness review** A project management device by which the production readiness is reviewed. 17, 265, 267, 285, 302, 303, 362, 476, 557
- ProtoDUNE** Either of the two DUNE prototype detectors constructed at CERN. One prototype implements SP technology and the other DP. 3, 8–11, 15, 16, 18, 84, 89, 95, 98, 113, 122, 125, 126, 147, 302, 346, 348, 358, 359, 370, 374, 375, 391, 392, 395–397, 405–412, 416, 417, 425, 426, 439, 456, 457, 462, 467, 471, 473–475, 477, 517, 537, 543, 548, 564, 576
- ProtoDUNE-2** The second run of a ProtoDUNE detector. 127, 314–316, 322, 324, 336, 339, 355, 360, 369, 370, 466, 474, 476
- ProtoDUNE-DP** The DP ProtoDUNE detector at CERN. 122, 126, 303, 362, 423, 430, 437, 451, 457, 462, 465, 466, 471, 476, 509, 557
- ProtoDUNE-SP** The SP ProtoDUNE detector at CERN. 20–22, 27, 31, 33, 35, 36, 39, 41–52, 54–62, 64, 66, 70, 71, 74, 75, 78, 79, 84, 85, 89, 91, 92, 94, 95, 97, 98, 102, 105–108, 110–112, 115, 116, 118, 120, 122, 123, 125, 126, 130–132, 140–144, 146, 147, 156, 163–165, 168, 170–175, 177–179, 181–193, 198–203, 206, 208, 212–215, 218–221, 223, 233–235, 237, 238, 240–242, 244, 245, 249, 250, 254–260, 263–267, 269–271, 274–277, 279, 281, 283, 288, 289, 291, 293–299, 302–305, 311, 317, 324, 336, 347, 348, 355, 356, 359, 361, 362, 380, 408, 409, 411, 413, 414, 417, 423, 430–432, 435, 437–441, 443–448, 450–454, 456–458, 461–466, 469, 471, 472, 474–476, 485, 491, 492, 495, 497, 499, 507, 509, 513, 517, 520, 533, 542, 543, 545, 546, 548, 549, 552, 553, 556, 557, 559–561
- ProtoDUNE-SP-2** A second test run in the single-phase ProtoDUNE test stand at CERN, acting as a validation of the final single-phase detector design. 74, 240, 241, 243, 246, 249, 265–268, 274, 297, 302, 303, 347, 348, 353, 359
- power and timing backplane (PTB)** Backplane used to connect the WIBs and the power and timing card (PTC)s on the WIEC. Also connects the CE flange on the cryostat penetration. 13, 139, 169, 170
- power and timing card (PTC)** Cards that provide further processing and distribution of the signals entering and exiting the SP cryostat. 13, 134, 139, 169–174, 185, 186, 189, 191, 196, 201, 202, 206, 219, 223, 576
- Precision Time Protocol (PTP)** A networking protocol that allows synchronizing of clocks to within a few  $\mu$ s of a time standard on a local network. 406
- p-terphenyl (PTP)** A wavelength-shifting (WLS) material. 238, 241, 254, 257, 260, 262, 265, 267–269, 284, 299, 311

- quality assurance (QA)** The set of actions taken to provide confidence that quality requirements are fulfilled, and to detect and correct poor results. 17, 18, 61, 77, 123, 125, 132, 186, 187, 194, 198, 215, 217, 228, 282, 283, 294–297, 299, 481, 488, 512, 520, 533, 542, 553, 579
- quality control (QC)** An aggregate of activities (such as design analysis and inspection for defects) performed to ensure adequate quality in manufactured products. 17, 18, 41, 55, 59, 62–64, 66, 111, 112, 120–123, 125, 146, 187, 188, 194–196, 198–202, 212–214, 217, 219, 221, 223, 224, 228, 273–276, 283–285, 291, 292, 294–299, 353–355, 359, 481, 484–487, 497, 498, 537, 542, 546, 549, 552
- QFP** Quad Flat Package. 146
- RC** resistive-capacitive (circuit). 83, 88, 142, 183
- run control (RC)** The system for configuring, starting and terminating the DAQ. 565
- reconfigurable computing element (RCE)** Data processor located outside of the cryostat on a cluster on board (COB) that contains FPGA, RAM and solid-state disk (SSD) resources, responsible for buffering data, producing trigger primitives, responding to triggered requests for data and syncing SNB dumps. 191, 408, 580
- radio frequency (RF)** Electromagnetic emissions that are within the (radio) frequency band of sensitivity of the detector electronics. 550
- root mean square (RMS)** The square root of the arithmetic mean of the squares of a set of values, used as a measure of the typical magnitude of a set of numbers, regardless of their sign. 150, 252, 261, 305, 432, 445, 451, 549, 554, 555, 578, 579
- resistive panel (RP)** Resistive panels form the constant potential surfaces for a SP module CPA; they are composed of a thin layer of carbon-impregnated Kapton and laminated to both sides of a FR-4 sheet. 86, 93, 94, 104, 105, 115, 116, 129, 551
- radioactive source deployment system (RSDS)** Proposed calibration system based on the deployment of radioactive sources inside the DUNE cryostat. 315, 361, 362, 366, 369–371
- resistance temperature detector (RTD)** A temperature sensor consisting of a material with an accurate and reproducible resistance/temperature relationship. 456, 479, 486, 552
- S-ARAPUCA** Standard ARAPUCA design with different WLS coatings on both faces of the dichroic filter window(s) of the cell. 232–234, 237, 251, 254–261, 263, 267–272, 293
- signal-to-noise (S/N)** signal-to-noise ratio. 4, 8–10, 12, 19, 83, 84, 132, 235, 243, 244, 247, 252, 253, 305, 429
- SACI** SLAC National Accelerator Laboratory (SLAC) ASIC Control Interface. 161, 169
- SAR** successive approximation register. 157, 160
- Short-Baseline Neutrino (SBN)** A Fermilab program consisting of three collaborations, MicroBooNE, SBND, and ICARUS, to perform sensitive searches for  $\nu_e$  appearance and  $\nu_\mu$  disappearance in the Booster Neutrino Beam. 234, 314, 348
- SBND** The Short-Baseline Near Detector experiment at Fermilab. 96, 130–132, 157, 158, 163, 169, 177, 181, 184, 186, 188, 212, 240, 265–268, 274, 304, 326, 330, 347, 375, 408, 467, 572, 577
- SCADA** supervisory control and data acquisition. 469, 471
- Fermilab South Dakota Services Division (SDSD)** A Fermilab division responsible providing host laboratory functions at SURF in South Dakota. 490, 492–494, 498, 521

- South Dakota Science and Technology Authority (SDSTA)** The legal entity that manages SURF, in Lead, S.D. 556, 561
- South Dakota Warehouse Facility (SDWF)** Warehousing operations in South Dakota responsible for receiving LBNF and DUNE goods and coordinating shipments to the Ross shaft at SURF. 66, 67, 70, 114, 115, 118, 121–123, 198, 201, 202, 220, 284, 285, 295, 296, 298, 484, 493–498, 556, 560
- secondary DAQ buffer** A secondary DAQ buffer holds a small subset of the full rate as selected by a trigger command. This buffer also marks the interface with the DUNE Offline. 567
- spurious free dynamic range (SFDR)** Spurious free dynamic range is the ratio of the RMS value of the signal to the RMS value of the worst spurious signal regardless of where it falls in the frequency spectrum. The worst spur may or may not be a harmonic of the original signal. 152
- small form-factor pluggable (SFP)** a particular standard for optical transceivers. 387, 407
- signal feedthrough (SFT)** A cryostat penetration allowing for the passage of cables or other extended parts. 141
- safe high voltage (SHV)** Type of bayonet mount connector used on coaxial cables that has additional insulation compared to standard BNC and MHV connectors that makes it safer for handling HV by preventing accidental contact with the live wire connector in an unmated connector or plug. 33, 49, 113, 165, 168, 175, 191, 206, 550, 554
- silicon photomultiplier (SiPM)** A solid-state avalanche photodiode sensitive to single photoelectron signals. 7–9, 133, 228, 229, 232–235, 237, 238, 240, 242–245, 250, 251, 253, 254, 257–259, 269–272, 280, 281, 297–299, 305, 428, 535, 546, 564
- SLAC National Accelerator Laboratory (SLAC)** US national laboratory in Menlo Park, CA. 145, 157, 161, 170, 221, 577
- standard model (SM)** Refers to a theory describing the interaction of elementary particles. 574
- supernova neutrino burst (SNB)** A prompt increase in the flux of low-energy neutrinos emitted in the first few seconds of a core-collapse supernova. It can also refer to a trigger command type that may be due to this phenomenon, or detector conditions that mimic its interaction signature. 2, 8, 14–16, 19, 83, 133, 225, 236, 291, 307, 308, 314, 315, 317, 340, 346, 366, 369, 376, 378–380, 384, 387, 391–393, 395, 397, 406, 410, 413, 415, 416, 428, 577, 578
- signal to noise and distortion ratio (SNDR)** Also known as SINAD. Ratio of the RMS signal amplitude to the mean value of the root-sum-square of all other spectral components, including harmonics, but excluding DC levels. It is a good indication of the overall dynamic performance of an ADC because it includes all components which make up noise and distortion. 152, 163
- SuperNova Early Warning System (SNEWS)** A global supernova neutrino burst trigger formed by a coincidence of SNB triggers collected from participating experiments. 393, 397
- single-phase (SP)** Distinguishes one of the DUNE far detector technologies by the fact that it operates using argon in its liquid phase only. 2–4, 16, 18–20, 53, 62, 75, 81, 82, 123, 131, 132, 136, 140, 164, 189, 193, 195, 196, 199, 202, 208, 211, 212, 218–221, 228, 229, 232, 235, 236, 251, 264, 267, 283, 285, 290, 291, 296, 300, 301, 310, 314, 375, 383, 428, 432, 437, 457, 465, 473, 482, 557, 558, 564, 565, 568–570, 576, 579, 580
- SP module** single-phase DUNE FD module. 4, 19–22, 25, 28, 33, 37, 48, 53, 55, 59, 71, 81, 82, 84, 86, 87, 89, 91, 97–99, 102, 105, 106, 112, 115, 116, 119, 120, 122–128, 131–133, 139–141, 143, 147, 154, 157, 159, 161, 163, 164, 167, 170–173, 177, 179, 182, 184, 189, 219, 220, 228–232, 235, 237, 242,

243, 245, 250, 260, 266, 269, 270, 273, 274, 276, 277, 281, 285, 286, 312, 314, 316, 321, 323, 327, 331, 395, 430, 438, 440, 444, 451, 453, 454, 456, 457, 461, 465, 466, 471, 473, 475, 489–493, 496, 499, 507, 508, 521, 532, 543, 545, 546, 554, 555, 559, 566, 571, 577

**Serial Peripheral Interface (SPI)** The Serial Peripheral Interface is a synchronous serial communication interface specification used for short distance communication, primarily in embedded systems. 154, 574

**SPICE** SPICE (“Simulation Program with Integrated Circuit Emphasis”) is a general-purpose, open-source analog electronic circuit simulator. It is a program used in integrated circuit and board-level design to check the integrity of circuit designs and to predict circuit behavior. 145, 148, 156

**solid-state disk (SSD)** Any storage device that may provide sufficient write throughput to receive, both collectively and distributed, the sustained full rate of data from a detector module for many seconds. 577

**SSP** SiPM signal processor. 245, 246, 249, 251–253, 257, 263, 264, 270, 271, 281, 293, 305

**Sanford Underground Research Facility (SURF)** The laboratory in South Dakota where the LBNF far site conventional facilities (FSCF) will be constructed and the DUNE FD will be installed and operated. 4, 6, 13, 17, 24, 66–68, 70, 75, 79, 115, 121, 122, 126, 186, 189, 196, 198, 201–203, 206–211, 214, 215, 217, 218, 220, 221, 223, 224, 290, 353, 374, 376, 385, 387, 397, 418, 467, 468, 481, 482, 484–495, 497, 501, 523, 548, 549, 551, 552, 560, 561, 567, 573, 578–580

**TallBo** A cylindrical cryostat at Fermilab primarily used for developing scintillation light collection technologies for LArTPC detectors. 254, 269, 465

**trip action plan (TAP)** A document required for any trip by a worker to the underground area at SURF, per that site’s access control program; it describes the work to be accomplished during the trip. 561

**temporary construction opening (TCO)** An opening in the side of a cryostat through which detector elements are brought into the cryostat; utilized during construction and installation. 16, 17, 106, 198, 215, 220, 354, 373, 499, 501, 510, 511, 514, 516, 518, 526, 530, 537, 539–542, 547, 550, 554, 557, 559

**technical design report (TDR)** A formal project document that describes the experiment at a technical level. 1, 17, 19, 84, 179, 226, 228, 265, 294, 304, 314–317, 324, 325, 349, 355, 428, 490, 493, 494, 540, 560

**technical coordination** The DUNE organization responsible for overall integration of the detector elements and successful execution of the detector construction project; areas of responsibility include general project oversight, systems engineering, QA and safety. 122, 132, 206, 207, 217, 349, 479, 572

**total harmonic distortion (THD)** Total harmonic distortion is the ratio of the RMS value of the fundamental signal to the mean value of the root-sum-square of its harmonics. 152

**top field cage (top FC)** The horizontal portions of the SP FC on the top of the TPC. 81, 87, 89, 94, 97–100, 105, 115, 117

**tetra-phenyl butadiene (TPB)** A WLS material. 254, 265, 269, 275, 288, 311, 349

**time projection chamber (TPC)** A type of particle detector that uses an E field together with a sensitive volume of gas or liquid, e.g., LAr, to perform a 3D reconstruction of a particle trajectory or interaction. The activity is recorded by digitizing the waveforms of current induced on the anode as the distribution of ionization charge passes by or is collected on the electrode. 6, 9–11, 14–16, 19, 21–23, 25, 27, 28, 33, 37, 48, 51–53, 66, 81–84, 88, 89, 94, 97, 99, 102, 103, 105, 106, 108, 110, 111, 113, 114, 116,



120, 129–134, 136, 137, 139–142, 145, 147, 157, 163, 165, 169, 170, 172, 175, 177–179, 184, 186, 187, 189–196, 198, 199, 201–210, 213, 214, 216–226, 229, 231, 234, 236, 252, 255–259, 263, 264, 266, 286, 287, 289, 291, 294, 297, 299, 305–311, 313, 315, 317, 321, 322, 324, 325, 327, 328, 330, 332, 333, 335, 336, 340, 341, 343–350, 352, 354, 355, 359–361, 363, 365, 371, 373, 377–380, 384, 385, 387, 389–393, 395, 396, 408–411, 415, 428–430, 432, 436, 438, 440, 453, 456, 461, 465, 466, 470, 475, 476, 480, 482, 489, 491, 500, 526–529, 531, 532, 537, 540, 542, 543, 545, 546, 548–551, 556, 559, 560, 565, 568, 571, 573, 579

**trigger candidate** Summary information derived from the full data stream and representing a contribution toward forming a trigger decision. 349, 393, 395–397, 411, 413, 415, 416, 580

**trigger command** Information derived from one or more trigger candidates that directs elements of the detector module to read out a portion of the data stream. 376, 388, 391–393, 396–399, 405, 410, 413, 568–570, 574, 578, 580

**trigger decision** The process by which trigger candidates are converted into trigger commands. 350, 376, 384, 387, 391–394, 396, 397, 413, 417, 567, 574, 580

**trigger notification** Information provided by MTL to ETL about trigger decision processing. 569, 574

**trigger primitive** Information derived by the DAQ FE hardware that describes a region of space (e.g., one or several neighboring channels) and time (e.g., a contiguous set of ADC sample ticks) associated with some activity. 349, 391, 393, 395, 396, 405

**TSMC** Taiwan Semiconductor Manufacturing Company. 145, 148, 157

**Universal Asynchronous Receiver/Transmitter (UART)** A universal asynchronous receiver-transmitter is a computer hardware device for asynchronous serial communication in which the data format and transmission speeds are configurable. 151

**upstream DAQ buffer interface (UBI)** The process which provides read-only access to data residing in the upstream DAQ buffers to processes on the network. 405

**UHMWPE** ultra-high molecular weight polyethylene. 92, 93, 95, 97, 113, 115

**underground installation team (UIT)** An organizational unit responsible for installation in the underground area at the SURF site. 559

**UNICAMP** University of Campinas, Sao Paulo, Brazil. 237, 241, 242, 260, 262, 265, 266, 274, 284, 285, 302, 304

**VUV** vacuum ultra-violet. 3, 7, 229, 230, 232, 255, 260, 273, 299, 311, 312

**WA105 DP demonstrator** The  $3 \times 1 \times 1 \text{ m}^3$  WA105 DP prototype detector at CERN. 461

**work breakdown structure (WBS)** An organizational project management tool by which the tasks to be performed are partitioned in a hierarchical manner. 301

**warm interface board (WIB)** Digital electronics situated just outside the SP cryostat that receives digital data from the FEMBs over cold copper connections and sends it to the RCE FE readout hardware. 13, 134, 137, 139, 144, 153–155, 165, 167, 169–175, 185, 186, 189, 196, 199–202, 205, 206, 219, 223, 385, 387, 390, 411, 418, 420, 521, 549, 576, 580

**warm interface electronics crate (WIEC)** Crates mounted on the signal flanges that contain the WIBs. 13, 134, 137, 139, 140, 153, 169, 170, 172–175, 185, 186, 189, 191, 192, 196, 201–204, 206, 207, 209–211, 214, 215, 217, 219–221, 223, 517, 526, 527, 538, 550, 576

**wavelength-shifting (WLS)** A material or process by which incident photons are absorbed by a material and photons are emitted at a different, typically longer, wavelength. 8, 129, 233, 237, 238, 240, 261, 265, 267–270, 273, 278, 279, 288, 299, 311, 312, 576, 577, 579, 581

**warehouse management system (WMS)** Commercial software package used to track shipments and interface to freight forwarders. This includes a database for shipping. 493, 497, 498

**White Rabbit (WR)** A component of the timing system that forwards clock signal and time-of-day reference data to the master timing unit. 397

**X-ARAPUCA** Extended ARAPUCA design with WLS coating on only the external face of the dichroic filter window(s) but with a WLS doped plate inside the cell. 9, 228, 229, 232–234, 236–241, 243, 251, 252, 259–270, 273, 275, 278, 279, 293–295, 304, 311, 313, 428

# Bibliography

- [1] C. Rubbia, *The Liquid Argon Time Projection Chamber: A New Concept for Neutrino Detectors*, Tech. Rep. CERN-EP-INT-77-08 (1977).
- [2] ICARUS collaboration, *Design, construction and tests of the ICARUS T600 detector*, *Nucl. Instrum. Meth. A* **527** (2004) 329 [INSPIRE].
- [3] C. Anderson et al., *The ArgoNeUT Detector in the NuMI Low-Energy beam line at Fermilab*, 2012 *JINST* **7** P10019 [arXiv:1205.6747] [INSPIRE].
- [4] MICROBoONE collaboration, *Design and Construction of the MicroBoONE Detector*, 2017 *JINST* **12** P02017 [arXiv:1612.05824] [INSPIRE].
- [5] LArIAT collaboration, *LArIAT: Liquid Argon In A Testbeam*, arXiv:1406.5560 [INSPIRE].
- [6] DUNE collaboration, *The Single-Phase ProtoDUNE Technical Design Report*, arXiv:1706.07081 [INSPIRE].
- [7] Mu2E collaboration, *Mu2e Technical Design Report*, arXiv:1501.05241 [INSPIRE].
- [8] F. Feyzi and D. Wenman, *Structural analysis plans and results*, CERN EDMS 2100877 (2019).
- [9] D. Christian, A. Marchionni, S. Soldner-Rembold and M. Verzocchi, *DUNE Interface Document: APA / TPC Electronics*, DUNE doc 6670, DUNE (2018), <https://docs.dunescience.org/cgi-bin/ShowDocument?docid=6670&asof=2019-11-1>.
- [10] A. Marchionni, E. Segreto, C. Touramanis and D. Warner, *DUNE Interface Document: SP-APA/PDS*, DUNE doc 6667, DUNE (2018), <https://docs.dunescience.org/cgi-bin/ShowDocument?docid=6667&asof=2019-11-1>.
- [11] A. Marchionni, F. Pietropaolo, S. Soldner-Rembold, and B. Yu, *DUNE Interface Document: HVS/APA*, DUNE doc 6673, DUNE (2018), <https://docs.dunescience.org/cgi-bin/ShowDocument?docid=6673&asof=2019-11-1>.
- [12] G. Karagiorgi, A. Marchionni, D. Newbold, and S. Soldner-Rembold, *DUNE FD Interface Document: SP APA to Joint DAQ*, DUNE doc 6676, DUNE (2018), <https://docs.dunescience.org/cgi-bin/ShowDocument?docid=6676&asof=2019-11-1>.
- [13] A.C. Villanueva et al., *DUNE FD Interface Document for Single Phase/Joint: SP APA to Joint CISC*, <https://docs.dunescience.org/cgi-bin/ShowDocument?docid=6679>.
- [14] E. James, S. Kettell, A. Marchionni, M. Marshak, and S. Soldner-Rembold, *DUNE FD Interface Document: Integration Facility to SP APA*, DUNE doc 7021, DUNE (2019), <https://docs.dunescience.org/cgi-bin/ShowDocument?docid=7021&asof=2019-11-1>.
- [15] E. James, S. Kettell, A. Marchionni, M. Marshak, and S. Soldner-Rembold, *DUNE FD Interface Document: Integration Facility to SP APA*, DUNE doc 6967, DUNE (2019), <https://docs.dunescience.org/cgi-bin/ShowDocument?docid=6967&asof=2019-11-1>.

- [16] E. James, S. Kettell, A. Marchionni, M. Marshak, and S. Soldner-Rembold, *DUNE FD Interface Document: Integration Facility to SP APA*, DUNE doc 6994, DUNE (2019), <https://docs.dunescience.org/cgi-bin/ShowDocument?docid=6994&asof=2019-11-1>.
- [17] S. Gollapinni, K. Mahn, A. Marchionni, and S. Soldner-Rembold, *DUNE FD Interface Document: Calibration to SP APA*, DUNE doc 7048, DUNE (2018), <https://docs.dunescience.org/cgi-bin/ShowDocument?docid=7048&asof=2019-11-1>.
- [18] A. Marchionni, A. Norman, H. Schellman, and S. Soldner-Rembold, *DUNE FD Interface Document: Software and Computing to SP APA*, DUNE doc 7102, DUNE, 2018. <https://docs.dunescience.org/cgi-bin/ShowDocument?docid=7102&asof=2019-11-1>.
- [19] A. Marchionni, R. Patterson, S. Soldner-Rembold, and E. Worcester, *DUNE FD Interface Document: DUNE Physics to SP APA*, DUNE doc 7075, DUNE (2018), <https://docs.dunescience.org/cgi-bin/ShowDocument?docid=7075&asof=2019-11-1>.
- [20] L. Greenler, *Layer Distortion Summary 6m Frame*, DUNE doc 1300, DUNE (2017), <https://docs.dunescience.org/cgi-bin/ShowDocument?docid=1300&asof=2019-11-1>.
- [21] MICROBooNE collaboration, *Construction and Assembly of the Wire Planes for the MicroBooNE Time Projection Chamber*, 2017 *JINST* **12** T03003 [arXiv:1609.06169] [INSPIRE].
- [22] D. Garcia-Gamez, V. Basque, T.G. Brooks, J.J. Evans, M. Perry, S. Söldner-Rembold et al., *A Novel Electrical Method to Measure Wire Tensions for Time Projection Chambers*, *Nucl. Instrum. Meth. A* **915** (2019) 75 [arXiv:1804.05941] [INSPIRE].
- [23] M. Andrews, *Integrated Environment, Safety and Health Management Plan*, DUNE doc 291 (2016), <https://docs.dunescience.org/cgi-bin/ShowDocument?docid=291&asof=2019-11-1>.
- [24] S. Rescia and B. Yu, *Cathode HV Discharge Mitigation Design*, tech. rep. (2016), <https://docs.dunescience.org/cgi-bin/ShowDocument?docid=1320&version=1>.
- [25] V. Guarino, G. Horton-Smith, S. Magill and B. Yu, *CPA Electrical Connections Cold Test*, tech. rep. (2017), <https://docs.dunescience.org/cgi-bin/ShowDocument?docid=2338&version=2>.
- [26] V. Guarino, *CPA and FC Design*, tech. rep. (2018), <https://docs.dunescience.org/cgi-bin/ShowDocument?docid=1504&version=20>.
- [27] J. Nelson, *Mechanical Specifications for ProtoDUNE-SP field cage test in 35 ton*, tech. rep. (2016), <https://docs.dunescience.org/cgi-bin/ShowDocument?docid=1601&version=1>.
- [28] A. Blatter et al., *Experimental study of electric breakdowns in liquid argon at centimeter scale*, 2014 *JINST* **9** P04006 [arXiv:1401.6693] [INSPIRE].
- [29] F. Pietropaolo, *DUNE FD Interface Document: DSS to SP HV*, DUNE doc 16766, CERN (2019), <https://docs.dunescience.org/cgi-bin/ShowDocument?docid=16766&asof=2019-11-1>.
- [30] D. Christian, F. Pietropaolo, M. Verzocchi, and B. Yu, *DUNE Interface Document: Single Phase TPC Cold Electronics and Joint Far Detector HV System*, DUNE doc 6739, DUNE (2018), <https://docs.dunescience.org/cgi-bin/ShowDocument?docid=6739&asof=2019-11-1>.
- [31] D. Duchesneau, I. Gil-Botella, E. Segreto, and D. Warner, *DUNE FD Interface Document: SP Photon Detector to joint High Voltage*, DUNE doc 6721, DUNE, 2018. <https://docs.dunescience.org/cgi-bin/ShowDocument?docid=6721&asof=2019-11-1>.
- [32] F. Feyzi, E. James, F. Pietropaolo, T. Shaw, and B. Yu, *DUNE FD Interface Document: SP TPC Electronics to joint DAQ*, DUNE doc 6985, DUNE (2018), <https://docs.dunescience.org/cgi-bin/ShowDocument?docid=6985&asof=2019-11-1>.

- [33] S. Gollapinni, K. Mahn, F. Pietropaolo, and B. Yu, *DUNE FD Interface Document: Calibration to Joint HV*, DUNE doc 7066, DUNE (2018),  
<https://docs.dunescience.org/cgi-bin/ShowDocument?docid=7066&asof=2019-11-1>.
- [34] A. C. Villanueva et al., *DUNE FD Interface Document: High Voltage to CISC*,  
<https://docs.dunescience.org/cgi-bin/ShowDocument?docid=6787>.
- [35] E. James, M. Marshak, F. Pietropaolo, and B. Yu, *DUNE FD Interface Document: Integration Facility to Joint HV*, DUNE doc 7039, DUNE (2018),  
<https://docs.dunescience.org/cgi-bin/ShowDocument?docid=7039&asof=2019-11-1>.
- [36] R. Patterson, F. Pietropaolo, E. Worcester, and B. Yu, *DUNE FD Interface Document: DUNE Physics to Joint HV*, DUNE doc 7093, DUNE (2018),  
<https://docs.dunescience.org/cgi-bin/ShowDocument?docid=7093&asof=2019-11-1>.
- [37] V. Guarino and S. Magill, *FD HV Design*, DUNE doc 10452 (2019),  
<https://docs.dunescience.org/cgi-bin/ShowDocument?docid=10452&asof=2019-11-1>.
- [38] G. De Geronimo et al., *Front-end ASIC for a Liquid Argon TPC*, *IEEE Trans. Nucl. Sci.* **58** (2011) 1376 [INSPIRE].
- [39] O. Palamara, M. Stancari, and D. Schmitz, *Technical Requirements of the SBND TPC Front-End Electronics*, SBND doc 1921 (2017),  
<http://sbn-docdb.fnal.gov/cgi-bin/ShowDocument?docid=1921>.
- [40] ARGO-NeUT collaboration, *Demonstration of MeV-Scale Physics in Liquid Argon Time Projection Chambers Using ArgoNeuT*, *Phys. Rev. D* **99** (2019) 012002 [arXiv:1810.06502] [INSPIRE].
- [41] MICROBooNE collaboration, *Study of Reconstructed  $^{39}\text{Ar}$  Beta Decays at the MicroBooNE Detector*, tech. rep., MICROBOONE-NOTE-1050-PUB (2018).
- [42] A. Hairapetian, D. Gitlin and C.R. Viswanathan, *Low-temperature mobility measurements on CMOS devices*, *IEEE Trans. Electron Dev.* **36** (1989) 1448.
- [43] C. Hu, S.C. Tam, F.-C. Hsu, P.-K. Ko, T.-Y. Chan and K. W. Terrill, *Hot-electron-induced mosfet degradation — model, monitor, and improvement*, *IEEE Trans. Electron Dev.* **32** (1985) 375.
- [44] V. Radeka, *Shielding and grounding in large detectors*, in proceedings of 4th workshop *Electronics for LHC experiments*, Rome, Italy, 21–25 September 1998, pp. 14–18.
- [45] T.M. Shaw, *Dune grounding and shielding rules*, tech. rep., Fermilab (2019),  
<https://edms.cern.ch/document/2095958>.
- [46] R. Patterson and A. Hammoud, *Effect of temperature on the performance and stability of recent cots silicon oscillators*, *NASA Electronic Parts and Packaging Program* (2010)  
[https://nepp.nasa.gov/files/19908/10\\_281\\_GRC\\_Patterson\\_Si%20Oscillators%207\\_12\\_10.doc](https://nepp.nasa.gov/files/19908/10_281_GRC_Patterson_Si%20Oscillators%207_12_10.doc).
- [47] TSMC Company, *65nm Technology*,  
<http://www.tsmc.com/english/dedicatedFoundry/technology/65nm.htm>.
- [48] L.W. Nagel and D.O. Pederson, *SPICE (Simulation Program with Integrated Circuit Emphasis)*, (April 1973).
- [49] TSMC Company, *0.13-micron Technology*,  
<https://www.tsmc.com/english/dedicatedFoundry/technology/0.13um.htm>.
- [50] TSMC Company, *0.18-micron Technology*,  
<https://www.tsmc.com/english/dedicatedFoundry/technology/0.18um.htm>.

- [51] D.W. Cline and P.R. Gray, *A power optimized 13-b 5 msamples/s pipelined analog-to-digital converter in 1.2 micron cmos*, *IEEE J. Solid-State Circuits* **31** (1996) 294.
- [52] E.G. Soenen and R.L. Geiger, *An architecture and an algorithm for fully digital correction of monolithic pipelined adcs*, *IEEE Trans. Circuits and Systems II: Analog and Digital Signal Processing* **42** (1995) 143.
- [53] *I2C Info – I2C Bus, Interface and Protocol*, <http://i2c.info>.
- [54] H. Chen et al., *Lifetime Study of COTS ADC for SBND LAr TPC Readout Electronics*, in *21st IEEE Real Time Conference* (2018), arXiv:1806.09226 [INSPIRE].
- [55] S. Li, J. Ma, G. De Geronimo, H. Chen and V. Radeka, *LAr TPC Electronics CMOS Lifetime at 300 K and 77 K and Reliability Under Thermal Cycling*, *IEEE Trans. Nucl. Sci.* **60** (2013) 4737 [INSPIRE].
- [56] *EXO-200. The Enriched Xenon Observatory*, <https://www-project.slac.stanford.edu/exo/about.html>.
- [57] Y. Zhu, C. Chan, U. Chio, S. Sin, S. U, R.P. Martins and F. Maloberti, *A 10-bit 100-ms/s reference-free sar adc in 90 nm cmos*, *IEEE J. Solid-State Circuits* **45** (2010) 1111.
- [58] W. Yeh et al., *Efficient suppression of substrate noise coupling in cmos technology*, *International Conference on Solid State Devices and Materials* (2003), pp. 408–409.
- [59] SLAC, *SLAC ASIC Control Interface (SACI)*, <https://confluence.slac.stanford.edu/pages/viewpage.action?pageId=219252577>.
- [60] D. Newbold, *ProtoDUNE-SP Timing System: Interfaces and Protocol*, tech. rep., Bristol (2016), <https://docs.dunescience.org/cgi-bin/ShowDocument?docid=1651>.
- [61] D. G. Cussans and D. Newbold, *DUNE Far Detector Timing and Synchronization System*, DUNE doc 11233 (2018), <https://docs.dunescience.org/cgi-bin/ShowDocument?docid=11233&asof=2019-11-1>.
- [62] MICROBooNE collaboration, *Noise Characterization and Filtering in the MicroBooNE Liquid Argon TPC*, 2017 *JINST* **12** P08003 [arXiv:1705.07341] [INSPIRE].
- [63] DUNE collaboration, *First results on ProtoDUNE-SP LArTPC performance from a test beam run at the CERN Neutrino Platform*, in preparation, to be submitted to *JINST*.
- [64] M. Verzocchi, *Lessons learned from ProtoDUNE, details for the SP-CE consortium*, DUNE doc 12367, DUNE (2019), <https://docs.dunescience.org/cgi-bin/ShowDocument?docid=12367&asof=2019-11-1>.
- [65] M. Takhti, A. Sodagar and R. Lotfi, *Domino adc: A novel analog-to-digital converter architecture*, in proceedings of 2010 IEEE Int. Symp. Circuits and Systems, Paris, France, 30 May–2 June 2010, pp. 4057 – 4060.
- [66] LBNE collaboration, *Cryogenic Lifetime Studies of 130 nm and 65 nm nMOS Transistors for High-Energy Physics Experiments*, *IEEE Trans. Nucl. Sci.* **62** (2015) 1255 [INSPIRE].
- [67] A. Teverovsky, *Reliability of electronics at cryogenic temperatures*, (2005), <https://nepp.nasa.gov/DocUploads/1BCC6326-46F7-4C5E-94D476A8B6176ED1/Approach%20to%20Reliability%20Testing%20at%20cryo%20NEPP.pdf>.
- [68] D. Christian, G. Karagiorgi, D. Newbold, and M. Verzocchi, *DUNE FD Interface Document: SP TPC Electronics to joint DAQ*, DUNE doc 6742, DUNE (2018), <https://docs.dunescience.org/cgi-bin/ShowDocument?docid=6742&asof=2019-11-1>.

- [69] A. Cervera Villanueva, D. Christian, S. Gollapinni, and M. Verzocchi, *DUNE Interface Document: CISC / SP-TPC Cold Electronics*, DUNE doc 6745, DUNE, 2018.  
<https://docs.dunescience.org/cgi-bin/ShowDocument?docid=6745&asof=2019-11-1>.
- [70] D. Christian, E. Segreto, M. Verzocchi, and D. Warner, *DUNE Interface Document: Single Phase TPC Cold Electronics and Single Phase TPC Photon System*, DUNE doc 6718, DUNE (2018),  
<https://docs.dunescience.org/cgi-bin/ShowDocument?docid=6718&asof=2019-11-1>.
- [71] D. Christian, F. Feyzi, E. James, T. Shaw, and M. Verzocchi, *DUNE Interface Document: Single Phase TPC Cold Electronics and Detector and Facilities Infrastructure (LBNF) and Technical Coordination (DUNE)*, DUNE doc 6973, DUNE (2018),  
<https://docs.dunescience.org/cgi-bin/ShowDocument?docid=6973&asof=2019-11-1>.
- [72] D. Christian, E. James, S. Kettel, J. Stewart, and M. Verzocchi, *DUNE Interface Document: TPC Electronics / Underground Installation Team*, DUNE doc 7000, DUNE (2018),  
<https://docs.dunescience.org/cgi-bin/ShowDocument?docid=7000&asof=2019-11-1>.
- [73] D. Christian, R. Patterson, M. Verzocchi, and E. Worcester, *DUNE Interface Document: DUNE Physics to SP TPC Electronics*, DUNE doc 7081, DUNE (2018),  
<https://docs.dunescience.org/cgi-bin/ShowDocument?docid=7081&asof=2019-11-1>.
- [74] D. Christian, M. Kirby, A. McNab, H. Schellman, and M. Verzocchi, *DUNE Interface Document: Software and Computing to SP TPC Electronics*, DUNE doc 7108, DUNE (2018),  
<https://docs.dunescience.org/cgi-bin/ShowDocument?docid=7108&asof=2019-11-1>.
- [75] D. Christian, S. Gollapinni, K. Mahn, and M. Verzocchi, *DUNE Interface Document: Calibration to SP TPC Electronics*, DUNE doc 7054, DUNE (2018),  
<https://docs.dunescience.org/cgi-bin/ShowDocument?docid=7054&asof=2019-11-1>.
- [76] T. Doke, K. Masuda and E. Shibamura, *Estimation of absolute photon yields in liquid argon and xenon for relativistic (1 MeV) electrons*, *Nucl. Instrum. Meth. A* **291** (1990) 617 [INSPIRE].
- [77] S. Kubota, M. Hishida, M. Suzuki and J.-z. Ruan(Gen, *Dynamical behavior of free electrons in the recombination process in liquid argon, krypton and xenon*, *Phys. Rev. B* **20** (1979) 3486 [INSPIRE].
- [78] T. Heindl, T. Dandl, M. Hofmann, R. Krucken, L. Oberauer, W. Potzel et al., *The scintillation of liquid argon*, *EPL* **91** (2010) 62002 [arXiv:1511.07718] [INSPIRE].
- [79] A. Hitachi, T. Takahashi, N. Funayama, K. Masuda, J. Kikuchi and T. Doke, *Effect of ionization density on the time dependence of luminescence from liquid argon and xenon*, *Phys. Rev. B* **27** (1983) 5279 [INSPIRE].
- [80] WARP collaboration, *Measurement of the specific activity of ar-39 in natural argon*, *Nucl. Instrum. Meth. A* **574** (2007) 83 [astro-ph/0603131] [INSPIRE].
- [81] F. Marinho, L. Paulucci, A.A. Machado and E. Segreto, *Numerical characterization of the ARAPUCA: a new approach for LAr scintillation light detection*, *J. Phys. Conf. Ser.* **1056** (2018) 012036 [arXiv:1804.03764] [INSPIRE].
- [82] A. Gola, F. Acerbi, M. Capasso, M. Marcante, A. Mazzi, G. Paternoster, C. Piemonte, V. Regazzoni and N. Zorzi, *NUV-Sensitive Silicon Photomultiplier Technologies Developed at Fondazione Bruno Kessler*, *Sensors* **19** (2019) 308.
- [83] J. T. Anderson, R. Dharmapalan, Z. Djurcic, G. Drake, A. Farbin, and M. Oberling, *ProtoDUNE ANL Photon Detector Readout PRR Documents*, DUNE doc 3126, DUNE (2018),  
<https://docs.dunescience.org/cgi-bin/ShowDocument?docid=3126&asof=2019-11-1>.

- [84] E. Segreto et al., *Liquid Argon test of the ARAPUCA device*, 2018 *JINST* **13** P08021 [arXiv:1805.00382] [INSPIRE].
- [85] J. Asaadi, B.J.P. Jones, A. Tripathi, I. Parmaksiz, H. Sullivan and Z.G.R. Williams, *Emanation and bulk fluorescence in liquid argon from tetraphenyl butadiene wavelength shifting coatings*, 2019 *JINST* **14** P02021 [arXiv:1804.00011] [INSPIRE].
- [86] D. Duchesneau, I. Gil-Botella, G. Karagiorgi, and Newbold, *DUNE FD Interface Document: DP Photon Detector to joint DAQ*, DUNE doc 6727, DUNE (2018), <https://docs.dunescience.org/cgi-bin/ShowDocument?docid=6727&asof=2019-11-1>.
- [87] A. C. Villanueva et al., *DUNE FD Interface Document: SP Photon Detector to Joint CISC*, DUNE doc 6730, DUNE (2018), <https://docs.dunescience.org/cgi-bin/ShowDocument?docid=6730&asof=2019-11-1>.
- [88] F. Feyzi, E. James, E. Segreto, and T. Shaw, *DUNE FD Interface Document: Facility Interfaces to SP Photon Detection*, DUNE doc 6970, DUNE (2018), <https://docs.dunescience.org/cgi-bin/ShowDocument?docid=6970&asof=2019-11-1>.
- [89] E. James, E. Segreto, J. Stewart, and D. Warner, *DUNE FD Interface Document: Installation Interfaces to SP Photon Detector*, DUNE doc 6997, DUNE (2018), <https://docs.dunescience.org/cgi-bin/ShowDocument?docid=6997&asof=2019-11-1>.
- [90] S. Gollapinni, K. Mahn, E. Segreto, and D. Warner, *DUNE FD Interface Document: Calibration to SP Photon Detector*, DUNE doc 7051, DUNE (2018), <https://docs.dunescience.org/cgi-bin/ShowDocument?docid=7051&asof=2019-11-1>.
- [91] A. Norman, H. Schellman, E. Segreto, and D. Warner, *DUNE FD Interface Document: Software and Computing to SP Photon Detector*, DUNE doc 7105, DUNE (2018), <https://docs.dunescience.org/cgi-bin/ShowDocument?docid=7105&asof=2019-11-1>.
- [92] E. Grace and J.A. Nikkel, *Index of refraction, Rayleigh scattering length and Sellmeier coefficients in solid and liquid argon and xenon*, *Nucl. Instrum. Meth. A* **867** (2017) 204 [arXiv:1502.04213] [INSPIRE].
- [93] WARP collaboration, *Effects of Nitrogen contamination in liquid Argon*, 2010 *JINST* **5** P06003 [arXiv:0804.1217] [INSPIRE].
- [94] SBND collaboration, *Light Detection System simulations for SBND*, *J. Phys. Conf. Ser.* **888** (2017) 012094 [INSPIRE].
- [95] M. Kuźniak, B. Broerman, T. Pollmann and G.R. Araujo, *Polyethylene naphthalate film as a wavelength shifter in liquid argon detectors*, *Eur. Phys. J. C* **79** (2019) 291 [arXiv:1806.04020] [INSPIRE].
- [96] E. Conley, *Fitting supernova neutrino spectral parameters with the Deep Underground Neutrino Experiment*, DUNE doc 14068, DUNE (2019), <https://docs.dunescience.org/cgi-bin/ShowDocument?docid=14068&asof=2019-11-1>.
- [97] Y. Li et al., *Measurement of Longitudinal Electron Diffusion in Liquid Argon*, *Nucl. Instrum. Meth. A* **816** (2016) 160 [arXiv:1508.07059] [INSPIRE].
- [98] M. Mooney, *Space charge effects in lartpcs*, *Workshop on Calibration and Reconstruction for LArTPC Detectors* (2018). <https://indico.fnal.gov/event/18523/session/19/contribution/29/material/slides/0.pdf>.
- [99] B. Yu, *Drift field distortions due to cpd/field cage imperfections*, *DUNE Calibration Task Force meeting* (2017). <https://indico.fnal.gov/event/15245/contribution/1/material/slides/>.



- [100] M. Mooney, *Field cage resistor chain failure study*, DUNE Calibration Task Force meeting (2019), <https://indico.fnal.gov/event/19386/contribution/4/material/slides/0.pdf>.
- [101] A. Ereditato, C.C. Hsu, S. Janos, I. Kreslo, M. Messina, C. Rudolf von Rohr et al., *Design and operation of ARGONTUBE: a 5 m long drift liquid argon TPC*, 2013 *JINST* **8** P07002 [arXiv:1304.6961] [INSPIRE].
- [102] MICROBoONE collaboration, *A Method to Determine the Electric Field of Liquid Argon Time Projection Chambers Using a UV Laser System and its Application in MicroBoONE*, to be published in *JINST*, arXiv:1910.01430 [INSPIRE].
- [103] W. Walkowiak, *Drift velocity of free electrons in liquid argon*, *Nucl. Instrum. Meth. A* **449** (2000) 288 [INSPIRE].
- [104] B. Rossi et al., *A Prototype liquid Argon Time Projection Chamber for the study of UV laser multi-photon ionization*, 2009 *JINST* **4** P07011 [arXiv:0906.3437] [INSPIRE].
- [105] M. Zeller et al., *First measurements with ARGONTUBE, a 5m long drift Liquid Argon TPC*, *Nucl. Instrum. Meth. A* **718** (2013) 454 [INSPIRE].
- [106] A. Ereditato, I. Kreslo, M. Lüthi, C. Rudolf von Rohr, M. Schenk, T. Strauss et al., *A steerable UV laser system for the calibration of liquid argon time projection chambers*, 2014 *JINST* **9** T11007 [arXiv:1406.6400] [INSPIRE].
- [107] A. Ereditato, D. Goeldi, S. Janos, I. Kreslo, M. Luethi, C. Rudolf von Rohr et al., *Measurement of the drift field in the ARGONTUBE LAr TPC with 266 nm pulsed laser beams*, 2014 *JINST* **9** P11010 [arXiv:1408.6635] [INSPIRE].
- [108] CAPTAIN collaboration, *The CAPTAIN Detector and Physics Program*, in *Community Summer Study 2013: Snowmass on the Mississippi*, 9, 2013, arXiv:1309.1740 [INSPIRE].
- [109] MICROBoONE, LAr1-ND, ICARUS-WA104 collaborations, *A Proposal for a Three Detector Short-Baseline Neutrino Oscillation Program in the Fermilab Booster Neutrino Beam*, arXiv:1503.01520 [INSPIRE].
- [110] Y. Chen, *Laser calibration at lar tpcs*, *Workshop on Calibration and Reconstruction for LArTPC Detectors* (2018), <https://indico.fnal.gov/event/18523/session/17/contribution/35/material/slides/0.pdf>.
- [111] I. Badhrees et al., *Measurement of the two-photon absorption cross-section of liquid argon with a time projection chamber*, *New J. Phys.* **12** (2010) 113024 [arXiv:1011.6001] [INSPIRE].
- [112] B. Yu, *Fc penetrations and laser interface*, DUNE Calibration Consortium meeting (2019), <https://indico.fnal.gov/event/20390/contribution/0/material/slides/>.
- [113] B. Yu, *E field distortion from a laser port opening on the field cage*, DUNE Calibration Task Force meeting (2017), <https://indico.fnal.gov/event/15246/contribution/0/material/slides/>.
- [114] MICROBoONE collaboration, *A Measurement of the Attenuation of Drifting Electrons in the MicroBoONE LArTPC*, MICROBOONE-NOTE-1026-PUB, (2017), <http://microboone.fnal.gov/wp-content/uploads/MICROBOONE-NOTE-1026-PUB.pdf>.
- [115] M. Antonello et al., *Experimental observation of an extremely high electron lifetime with the ICARUS-T600 LAr-TPC*, 2014 *JINST* **9** P12006 [arXiv:1409.5592] [INSPIRE].
- [116] ARGONEuT collaboration, *A Study of Electron Recombination Using Highly Ionizing Particles in the ArgoNeuT Liquid Argon TPC*, 2013 *JINST* **8** P08005 [arXiv:1306.1712] [INSPIRE].

- [117] T2K ND280 TPC collaboration, *Time Projection Chambers for the T2K Near Detectors*, *Nucl. Instrum. Meth. A* **637** (2011) 25 [arXiv:1012.0865] [INSPIRE].
- [118] Y. Li et al., *A 20-Liter Test Stand with Gas Purification for Liquid Argon Research*, 2016 *JINST* **11** T06001 [arXiv:1602.01884] [INSPIRE].
- [119] V. Fischer et al., *Measurement of the neutron capture cross-section on argon*, *Phys. Rev. D* **99** (2019) 103021 [arXiv:1902.00596] [INSPIRE].
- [120] H. Koivunoro, D. Bleuel, U. Nastasi, T. Lou, J. Reijonen and K.-N. Leung, *Bnct dose distribution in liver with epithermal d-d and d-t fusion-based neutron beams*, *Appl. Rad. Isot.* **61** (2004) 853.
- [121] S. Gollapinni, G. Karagiorgi, K. Mahn, and D. Newbold, *DUNE FD Interface Document: Calibration to Joint DAQ*, DUNE doc 7069, DUNE (2018), <https://docs.dunescience.org/cgi-bin/ShowDocument?docid=7069&asof=2019-11-1>.
- [122] S. Gollapinni et al., *DUNE FD Interface Document: Calibration to Joint CISC*, <https://docs.dunescience.org/cgi-bin/ShowDocument?docid=7072>.
- [123] S. Gollapinni, K. Mahn, R. Patterson, and E. Worcester, *DUNE FD Interface Document: Calibration Task Force to DUNE Physics*, DUNE doc 6865, DUNE, 2019. <https://docs.dunescience.org/cgi-bin/ShowDocument?docid=6865&asof=2019-11-1>.
- [124] S. Gollapinni, K. Mahn, A. Norman, and H. Schellman, *DUNE FD Interface Document: Calibration Task Force to DUNE Software and Computing*, DUNE doc 6868, DUNE (2019), <https://docs.dunescience.org/cgi-bin/ShowDocument?docid=6868&asof=2019-11-1>.
- [125] F. Feyzi, S. Gollapinni, E. James, K. Mahn, and T. Shaw, *DUNE FD Interface Document: Facility to Calibration Task Force*, DUNE doc 6829, DUNE (2019), <https://docs.dunescience.org/cgi-bin/ShowDocument?docid=6829&asof=2019-11-1>.
- [126] S. Gollapinni, E. James, K. Mahn, and J. Stewart, *DUNE FD Interface Document: Installation to Calibration Task Force*, DUNE doc 6847, DUNE, 2019. <https://docs.dunescience.org/cgi-bin/ShowDocument?docid=6847&asof=2019-11-1>.
- [127] M. Quinn, *Lasers*, FESHM 4260, Fermi National Accelerator Laboratory (January, 2019), <http://esh-docdb.fnal.gov/cgi-bin/RetrieveFile?docid=385>.
- [128] TIS/RP, *Rules for the safe use of lasers at cern*, Safety Instruction IS 22, CERN (January 1994), [https://edms.cern.ch/ui/file/335744/LAST\\_RELEASED/IS22\\_E.pdf](https://edms.cern.ch/ui/file/335744/LAST_RELEASED/IS22_E.pdf).
- [129] J.G. Rogers, M.S. Andreaco, C. Moisan and I. M. Thorson, *A 7–9 MeV isotopic gamma-ray source for detector testing*, *Nucl. Instrum. Meth. A* **413** (1998) 249.
- [130] MicroBooNE collaboration, *The MicroBooNE Continuous Readout Stream for Detection of Supernova Neutrinos*, *J. Phys. Conf. Ser.* **1312** (2019) 012006 [arXiv:1907.02195] [INSPIRE].  
MicroBooNE collaboration, *The Continuous Readout Stream of the MicroBooNE Liquid Argon Time Projection Chamber for Detection of Supernova Neutrinos*.
- [131] J. Klein, *DUNE Far Detector Data Volumes*, DUNE doc 9240, Univ. of Pennsylvania (2018), <https://docs.dunescience.org/cgi-bin/ShowDocument?docid=9240&asof=2019-11-1>.
- [132] B. Viren, *What are the DUNE FD DAQ Bottlenecks?*, DUNE doc 11461 (2018), <http://docs.dunescience.org/cgi-bin/ShowDocument?docid=11461&asof=2019-11-1>.
- [133] G. Lehmann-Miotto and A. Thea, *DUNE FD SP DAQ rack layout and power consumption estimate draft*, DUNE doc 15544 (2019), <https://docs.dunescience.org/cgi-bin/ShowDocument?docid=15544>.

- [134] G. Karagiorgi, D. Newbold, A. Norman, and H. Schellman, *DUNE FD Interface Document: Software and Computing to Joint DAQ*, DUNE doc 7123, Columbia, Bristol, Fermilab, and Oregon State (2018), <https://docs.dunescience.org/cgi-bin/ShowDocument?docid=7123&asof=2019-11-1>.
- [135] A.C. Villanueva et al., *DUNE FD Interface Document: DAQ to CISC*, <https://docs.dunescience.org/cgi-bin/ShowDocument?docid=6790&version=1>.
- [136] D.G. Cussans, J.R. Klein, and D. Newbold, *DUNE FD Interface Document: Timing/Synchronization*, DUNE doc 11224 (2018), <https://docs.dunescience.org/cgi-bin/ShowDocument?docid=11224&asof=2019-11-1>.
- [137] F. Feyzi, E. James, G. Karagiorgi, D. Newbold, and T. Shaw, *DUNE FD Interface Document: Facility Interfaces to Joint DAQ*, DUNE doc 6988, DUNE, 2018. <https://docs.dunescience.org/cgi-bin/ShowDocument?docid=6988&asof=2019-11-1>.
- [138] E. James, G. Karagiorgi, S. Kettell, D. Newbold, and J. Stewart, *DUNE FD Interface Document: Installation Interfaces to Joint DAQ*, DUNE doc 7015, DUNE (2018), <https://docs.dunescience.org/cgi-bin/ShowDocument?docid=7015&asof=2019-11-1>.
- [139] W. Wu, *FELIX: the New Detector Interface for the ATLAS Experiment* (2018), arXiv:1806.10667.
- [140] D. Last and D. Rivera, *Data Selection for DUNE Beam and Atmospheric Events*, DUNE doc 11215 (2018), <https://docs.dunescience.org/cgi-bin/ShowDocument?docid=11215&asof=2019-11-1>.
- [141] P. Lasorak, *DUNE Supernovae Triggering*, DUNE doc 14522 (2019), <https://docs.dunescience.org/cgi-bin/ShowDocument?docid=14522&asof=2019-7-23>.
- [142] G. Ge, Y. jae Jwa, and G. Karagiorgi, *ML-based triggering for DUNE*, DUNE doc 11311 (2018), <https://docs.dunescience.org/cgi-bin/ShowDocument?docid=11311&asof=2019-11-1>.
- [143] P. Antonioli et al., *SNEWS: The Supernova Early Warning System*, *New J. Phys.* **6** (2004) 114 [astro-ph/0406214] [INSPIRE].
- [144] A. Booth, G. Karagiorgi, J. R. Klein, P. J. Lasorak, D. Last, D. Rivera, P. Rodrigues, and B. Viren, *DUNE-SP Data Selection Summary*, DUNE doc 11275, DUNE (2018), <https://docs.dunescience.org/cgi-bin/ShowDocument?docid=11275&asof=2019-11-1>.
- [145] P. Rodrigues, *Single phase TPC trigger primitive algorithms for TDR*, DUNE doc 11236, DUNE (2018), <https://docs.dunescience.org/cgi-bin/ShowDocument?docid=11236&asof=2019-11-1>.
- [146] K. Biery, E. Flumerfelt, J. Freeman, W. Ketchum, G. Lukhanin and R. Rechenmacher, *artdaq: DAQ Software Development Made Simple*, *J. Phys. Conf. Ser.* **898** (2017) 032013 [INSPIRE].
- [147] P. Hintjens, *ZeroMQ, Messaging for Many Applications*, O'Reilly Media (2012), <http://zguide.zeromq.org/>.
- [148] SBND collaboration, *Liquid Argon TPC Trigger Development with SBND*, in *Meeting of the Division of Particles and Fields of the American Physical Society (DPF2019)*, Boston, Massachusetts, 29 July – 2 August 2019, arXiv:1910.08218 [INSPIRE].
- [149] DUNE collaboration, *The DAQ for the Single Phase DUNE Prototype at CERN*, *IEEE Trans. Nucl. Sci.* **66** (2019) 1210 [arXiv:1806.09310] [INSPIRE].
- [150] G. Barr, M. Graham, R. Herbst, and L. Ruckman, *ProtoDUNE RCE-Based TPC Readout*, DUNE doc 1881 (2018), <https://docs.dunescience.org/cgi-bin/ShowDocument?docid=1881&asof=2019-7-23>.
- [151] K. Hennessy, *Dune cdr review - protodune-sp lessons learned*, in *DUNE CDR: DAQ Review*, 3 December 2018, <https://indico.fnal.gov/event/18505/contribution/10/material/slides/0.pdf>.

- [152] G. Lehmann-Miotto, “ProtoDUNE DAQ Schedule 2019, DUNE doc 14095, DUNE, 2019. <https://docs.dunescience.org/cgi-bin/ShowDocument?docid=14095&asof=2019-11-1>.
- [153] A. Borga et al., *FELIX based readout of the Single-Phase ProtoDUNE detector*, *IEEE Trans. Nucl. Sci.* **66** (2019) 993 [arXiv:1806.09194] [INSPIRE].
- [154] C. Ghabrous Larrea, K. Harder, D. Newbold, D. Sankey, A. Rose, A. Thea et al., *IPbus: a flexible Ethernet-based control system for xTCA hardware*, 2015 *JINST* **10** C02019 [INSPIRE].
- [155] J. Klein, *ProtoDUNE Data Selection Tests*, DUNE doc 14062 (2018), <https://docs.dunescience.org/cgi-bin/ShowDocument?docid=14062&asof=2019-11-1>.
- [156] Y.-J. Jwa, G. Di Guglielmo, L.P. Carloni and G. Karagiorgi, *Accelerating Deep Neural Networks for Real-time Data Selection for High-resolution Imaging Particle Detectors*, in *New York Scientific Data Summit (NYSDS)*, IEEE (2019).
- [157] J. Wilhite, *LBNF BSI - 90 Pct Final Design*, LBNF DocDB 14242, LBNF (2018), <https://docs.dunescience.org/cgi-bin/ShowDocument?docid=14242>.
- [158] G.L. Miotto and A. Thea, *DAQ Consortium Working Group Mandates*, DUNE doc 14938 (2019), <https://docs.dunescience.org/cgi-bin/ShowDocument?docid=14938&asof=2019-11-1>.
- [159] G. J. Michna et al., *CFD Analysis of Fluid, Heat, and Impurity Flows in DUNE FAR Detector to Address Additional Design Considerations*, DUNE doc 5915, South Dakota State University (2017), <https://docs.dunescience.org/cgi-bin/ShowDocument?docid=5915&asof=2019-11-1>.
- [160] P. Strons and J.L. Bailey, *Flow visualization methods for field test verification of CFD analysis of an open gloveport*, *Enclosure* (2017). <https://www.osti.gov/pages/servlets/purl/1402050>.
- [161] A. Kehrl, G. L. Miotto, X. Pons, S. Ravat, and M. J. Rodriguez, *The protoDUNE Single Phase Detector Control System*, in *Proceedings of CHEP 2018*, tech. rep. (2018), <https://docs.dunescience.org/cgi-bin/ShowDocument?docid=11098>.
- [162] The Liquid Argon Technology @BNL, *Basic properties*, <https://lar.bnl.gov/properties/basic.html> (accessed 15 January 2019).
- [163] L. Whitehead, *DUNE Far Detector Task Force Final Report*, DUNE doc 3384, 2018. <https://docs.dunescience.org/cgi-bin/ShowDocument?docid=3384&asof=2019-11-1>.
- [164] M. Adamowski et al., *The Liquid Argon Purity Demonstrator*, 2014 *JINST* **9** P07005 [arXiv:1403.7236] [INSPIRE].
- [165] WA105 collaboration, *Status of the WA105-3x1x1 m<sup>3</sup> dual phase prototype*, tech. rep. (2017), <https://indico.fnal.gov/event/12345/session/1/contribution/5/material/slides/0.pdf>.
- [166] S.C. Delaquais, R. Gornea, S. Janos, M. Lüthi, C. Rudolf von Rohr, M. Schenk et al., *Development of a camera casing suited for cryogenic and vacuum applications*, 2013 *JINST* **8** T12001 [arXiv:1310.6601] [INSPIRE].
- [167] M. Auger, A. Blatter, A. Ereditato, D. Goeldi, S. Janos, I. Kreslo et al., *On the Electric Breakdown in Liquid Argon at Centimeter Scale*, 2016 *JINST* **11** P03017 [arXiv:1512.05968] [INSPIRE].
- [168] T.I. Banks et al., *A compact ultra-clean system for deploying radioactive sources inside the KamLAND detector*, *Nucl. Instrum. Meth. A* **769** (2015) 88 [arXiv:1407.0413] [INSPIRE].
- [169] Lumileds, *LUXEON C Color Line* (datasheet), <https://www.lumileds.com/uploads/571/DS144-pdf> (accessed 19 November 2018).
- [170] J. Carron, A. Philippon, L.S. How, A. Delbergue, S. Hassanzadeh, D. Cillierre, P. Danto and M. Boutillier, *Cryogenic characterization of LEDs for space application*, *Proc. SPIE, Sixteenth*

- International Conference on Solid State Lighting and LED-based Illumination Systems* **10378** (2017) 20.
- [171] Siemens AG, *SIMATIC WinCC open architecture*, <http://www.siemens.com/wincc-open-architecture> (accessed 27 November 2018).
- [172] *EPICS - Experimental Physics and Industrial Control System*, <https://epics-controls.org/> (accessed 19 July 2019).
- [173] G. Lukhanin, K. Biery, S. Foulkes, M. Frank, A. Hatzikoutelis, J. Kowalkowski et al., *Application of control system studio for the NOvA detector control system*, *J. Phys. Conf. Ser.* **396** (2012) 062012 [INSPIRE].
- [174] *About JCOP*, <http://jcop.web.cern.ch/> (accessed 19 July 2019).
- [175] *UNICOS*, (2015), <http://unicos.web.cern.ch/>.
- [176] A.C. Villanueva and S. Gollapinni, *DUNE FD WBS: Slow Control*, DUNE doc 5609, DUNE (2018), <https://docs.dunescience.org/cgi-bin/ShowDocument?docid=5609&asof=2019-11-1>.
- [177] S. Gollapinni et al., *DUNE FD Risks: CISC*, <https://docs.dunescience.org/cgi-bin/ShowDocument?docid=7192&asof=2019-11-1>.
- [178] S. Gollapinni et al., *DUNE FD Interface Document: DUNE Physics to Joint CISC*, <https://docs.dunescience.org/cgi-bin/ShowDocument?docid=7099&version=1>.
- [179] S. Gollapinni et al., *DUNE FD Interface Document: Software and Computing to Joint CISC*, <https://docs.dunescience.org/cgi-bin/ShowDocument?docid=7126>.
- [180] F. Feyzi et al., *DUNE FD Interface Document: Facility Interfaces to Joint CISC*, <https://docs.dunescience.org/cgi-bin/ShowDocument?docid=6991>.
- [181] S. Gollapinni et al., *DUNE FD Interface Document: Installation Interfaces to Joint CISC*, <https://docs.dunescience.org/cgi-bin/ShowDocument?docid=7018>.
- [182] S. Gollapinni et al., *DUNE FD Interface Document: Integration Facility to Joint CISC*, <https://docs.dunescience.org/cgi-bin/ShowDocument?docid=7045&version=1>.
- [183] R. Rameika, *ProtoDUNE - SP Lessons Learned*, DUNE doc 8255, DUNE (2018), <https://docs.dunescience.org/cgi-bin/ShowDocument?docid=8255&asof=2019-11-1>.
- [184] D. Montanari, E. Costopoulos, and J. Willhite, *Far Site Shaft Hoisting Assumptions and Parameters*, DUNE doc 328, DUNE (2018), <https://docs.dunescience.org/cgi-bin/ShowDocument?docid=328&asof=2019-11-1>.
- [185] J. Stewart, *DUNE Load List for Ross*, DUNE doc 8426, DUNE (2018), <https://docs.dunescience.org/cgi-bin/ShowDocument?docid=8426&asof=2019-11-1>.
- [186] V. Guarino, *DUNE Installation Integration*, DUNE doc 6260, DUNE (2019), <https://docs.dunescience.org/cgi-bin/ShowDocument?docid=6260&asof=2019-11-1>.
- [187] T. Shaw, *Detector Racks – DUNE working document*, DUNE doc 4499, DUNE (2018), <https://docs.dunescience.org/cgi-bin/ShowDocument?docid=4499&asof=2019-11-1>.
- [188] D.A. Brown et al., *ENDF/B-VIII.0: The 8th Major Release of the Nuclear Reaction Data Library with CIELO-project Cross Sections, New Standards and Thermal Scattering Data*, *Nucl. Data Sheets* **148** (2018) 1.

# The DUNE collaboration

B. Abi,<sup>1</sup> R. Acciarri,<sup>2</sup> M.A. Acero,<sup>3</sup> G. Adamov,<sup>4</sup> D. Adams,<sup>5</sup> M. Adinolfi,<sup>6</sup> Z. Ahmad,<sup>7</sup> J. Ahmed,<sup>8</sup>  
 T. Alion,<sup>9</sup> S. Alonso Monsalve,<sup>10</sup> C. Alt,<sup>11</sup> J. Anderson,<sup>12</sup> C. Andreopoulos,<sup>14,13</sup> M. Andrews,<sup>2</sup>  
 F. Andrianala,<sup>15</sup> S. Andringa,<sup>16</sup> A. Ankowski,<sup>17</sup> M. Antonova,<sup>18</sup> S. Antusch,<sup>19</sup> A. Aranda-Fernandez,<sup>20</sup>  
 A. Ariga,<sup>21</sup> L.O. Arnold,<sup>22</sup> M.A. Arroyave,<sup>23</sup> J. Asaadi,<sup>24</sup> A. Aurisano,<sup>25</sup> V. Aushev,<sup>26</sup> D. Autiero,<sup>27</sup>  
 F. Azfar,<sup>1</sup> H. Back,<sup>28</sup> J.J. Back,<sup>8</sup> C. Backhouse,<sup>29</sup> P. Baesso,<sup>6</sup> L. Bagby,<sup>2</sup> R. Bajou,<sup>30</sup> S. Balasubramanian,<sup>31</sup>  
 P. Baldi,<sup>32</sup> B. Bambah,<sup>33</sup> F. Barao,<sup>16,34</sup> G. Barenboim,<sup>18</sup> G. Barker,<sup>8</sup> W. Barkhouse,<sup>35</sup> C. Barnes,<sup>36</sup>  
 G. Barr,<sup>1</sup> J. Barranco Monarca,<sup>37</sup> N. Barros,<sup>16,38</sup> J.L. Barrow,<sup>39,2</sup> A. Bashyal,<sup>40</sup> V. Basque,<sup>41</sup> F. Bay,<sup>42</sup>  
 J. Bazo Alba,<sup>43</sup> J.F. Beacom,<sup>44</sup> E. Bechetoille,<sup>27</sup> B. Behera,<sup>45</sup> L. Bellantoni,<sup>2</sup> G. Bellettini,<sup>46</sup> V. Bellini,<sup>48,47</sup>  
 O. Beltramelio,<sup>10</sup> D. Belver,<sup>49</sup> N. Benekos,<sup>10</sup> F. Bento Neves,<sup>16</sup> J. Berger,<sup>50</sup> S. Berkman,<sup>2</sup> P. Bernardini,<sup>51</sup>  
 R.M. Berner,<sup>21</sup> H. Berns,<sup>52</sup> S. Bertolucci,<sup>54,53</sup> M. Betancourt,<sup>2</sup> Y. Bezawada,<sup>52</sup> M. Bhattacharjee,<sup>55</sup>  
 B. Bhuyan,<sup>55</sup> S. Biagi,<sup>56</sup> J. Bian,<sup>32</sup> M. Biassoni,<sup>57</sup> K. Biery,<sup>2</sup> B. Bilki,<sup>58</sup> M. Bishai,<sup>5</sup> A. Bitadze,<sup>41</sup>  
 A. Blake,<sup>59</sup> B. Blanco Siffert,<sup>60</sup> F. Blaszczyk,<sup>2</sup> G. Blazey,<sup>61</sup> E. Blucher,<sup>62</sup> J. Boissevain,<sup>63</sup> S. Bolognesi,<sup>64</sup>  
 T. Bolton,<sup>65</sup> M. Bonesini,<sup>57,66</sup> M. Bongrand,<sup>67</sup> F. Bonini,<sup>5</sup> A. Booth,<sup>9</sup> C. Booth,<sup>68</sup> S. Bordoni,<sup>10</sup>  
 A. Borkum,<sup>9</sup> T. Boschi,<sup>69</sup> N. Bostan,<sup>70</sup> P. Bour,<sup>71</sup> S. Boyd,<sup>8</sup> D. Boyden,<sup>61</sup> J. Bracinek,<sup>72</sup> D. Braga,<sup>2</sup>  
 D. Brailsford,<sup>59</sup> A. Brandt,<sup>24</sup> J. Bremer,<sup>10</sup> C. Brew,<sup>14</sup> E. Brianne,<sup>41</sup> S.J. Brice,<sup>2</sup> C. Brizzolari,<sup>57,66</sup>  
 C. Bromberg,<sup>73</sup> G. Brooijmans,<sup>22</sup> J. Brooke,<sup>6</sup> A. Bross,<sup>2</sup> G. Brunetti,<sup>74</sup> N. Buchanan,<sup>45</sup> H. Budd,<sup>75</sup>  
 D. Caiulo,<sup>27</sup> P. Calafiura,<sup>76</sup> J. Calcutt,<sup>73</sup> M. Calin,<sup>77</sup> S. Calvez,<sup>45</sup> E. Calvo,<sup>49</sup> L. Camilleri,<sup>22</sup> A. Caminata,<sup>78</sup>  
 M. Campanelli,<sup>29</sup> D. Caratelli,<sup>2</sup> G. Carini,<sup>5</sup> B. Carlus,<sup>27</sup> P. Carniti,<sup>57</sup> I. Caro Terrazas,<sup>45</sup> H. Carranza,<sup>24</sup>  
 A. Castillo,<sup>79</sup> C. Castromonte,<sup>80</sup> C. Cattadori,<sup>57</sup> F. Cavalier,<sup>67</sup> F. Cavanna,<sup>2</sup> S. Centro,<sup>74</sup> G. Cerati,<sup>2</sup>  
 A. Cervelli,<sup>54</sup> A. Cervera Villanueva,<sup>18</sup> M. Chalifour,<sup>10</sup> C. Chang,<sup>81</sup> E. Chardonnet,<sup>30</sup> A. Chatterjee,<sup>50</sup>  
 S. Chattopadhyay,<sup>7</sup> J. Chaves,<sup>82</sup> H. Chen,<sup>5</sup> M. Chen,<sup>32</sup> Y. Chen,<sup>21</sup> D. Cherdack,<sup>83</sup> C. Chi,<sup>22</sup> S. Childress,<sup>2</sup>  
 A. Chiriacescu,<sup>77</sup> K. Cho,<sup>84</sup> S. Choubey,<sup>85</sup> A. Christensen,<sup>45</sup> D. Christian,<sup>2</sup> G. Christodoulou,<sup>10</sup>  
 E. Church,<sup>28</sup> P. Clarke,<sup>86</sup> T.E. Coan,<sup>87</sup> A.G. Cocco,<sup>88</sup> J. Coelho,<sup>67</sup> E. Conley,<sup>89</sup> J. Conrad,<sup>90</sup> M. Convery,<sup>17</sup>  
 L. Corwin,<sup>91</sup> P. Cotte,<sup>64</sup> L. Cremaldi,<sup>92</sup> L. Cremonesi,<sup>29</sup> J.I. Crespo-Anadón,<sup>49</sup> E. Cristaldo,<sup>93</sup> R. Cross,<sup>59</sup>  
 C. Cuesta,<sup>49</sup> Y. Cui,<sup>81</sup> D. Cussans,<sup>6</sup> M. Dabrowski,<sup>5</sup> H. Da Motta,<sup>94</sup> L. Da Silva Peres,<sup>60</sup> Q. David,<sup>27</sup>  
 G.S. Davies,<sup>92</sup> S. Davini,<sup>78</sup> J. Dawson,<sup>30</sup> K. De,<sup>24</sup> R.M. De Almeida,<sup>95</sup> P. Debbs,<sup>70</sup> I. De Bonis,<sup>96</sup>  
 M. Decowski,<sup>42,97</sup> A. De Gouvea,<sup>98</sup> P.C. De Holanda,<sup>99</sup> I.L. De Icaza Astiz,<sup>9</sup> A. Deisting,<sup>100</sup>  
 P. De Jong,<sup>42,97</sup> A. Delbart,<sup>64</sup> D. Delepine,<sup>37</sup> M. Delgado,<sup>101</sup> A. Dell'Acqua,<sup>10</sup> P. De Lurgio,<sup>12</sup>  
 J.R. De Mello Neto,<sup>60</sup> D.M. DeMuth,<sup>102</sup> S. Dennis,<sup>103</sup> C. Densham,<sup>14</sup> G. Deptuch,<sup>2</sup> A. De Roeck,<sup>10</sup>  
 V. De Romeri,<sup>18</sup> J. De Vries,<sup>103</sup> R. Dharmapalan,<sup>104</sup> M. Dias,<sup>105</sup> F. Diaz,<sup>43</sup> J. Diaz,<sup>106</sup> S. Di Domizio,<sup>78</sup>  
 L. Di Giulio,<sup>10</sup> P. Ding,<sup>2</sup> L. Di Noto,<sup>78</sup> C. Distefano,<sup>56</sup> R. Diurba,<sup>107</sup> M. Diwan,<sup>5</sup> Z. Djurcic,<sup>12</sup>  
 N. Dokania,<sup>108</sup> M. Dolinski,<sup>109</sup> L. Domine,<sup>17</sup> D. Douglas,<sup>73</sup> F. Drielsma,<sup>17</sup> D. Duchesneau,<sup>96</sup> K. Duffy,<sup>2</sup>  
 P. Dunne,<sup>110</sup> T. Durkin,<sup>14</sup> H. Duyang,<sup>111</sup> O. Dvornikov,<sup>104</sup> D. Dwyer,<sup>76</sup> A. Dyshkant,<sup>61</sup> M. Eads,<sup>61</sup>  
 D. Edmunds,<sup>73</sup> J. Eisch,<sup>112</sup> S. Emery,<sup>64</sup> A. Ereditato,<sup>21</sup> C. Escobar,<sup>2</sup> L. Escudero Sanchez,<sup>103</sup> J.J. Evans,<sup>41</sup>  
 E. Ewart,<sup>106</sup> A.C. Ezeribe,<sup>68</sup> K. Fahey,<sup>2</sup> A. Falcone,<sup>57,66</sup> C. Farnese,<sup>74</sup> Y. Farzan,<sup>113</sup> J. Felix,<sup>37</sup>  
 E. Fernandez-Martinez,<sup>114</sup> P. Fernandez Menendez,<sup>18</sup> F. Ferraro,<sup>78</sup> L. Fields,<sup>2</sup> A. Filkins,<sup>115</sup>  
 F. Filthaut,<sup>42,116</sup> R.S. Fitzpatrick,<sup>36</sup> W. Flanagan,<sup>117</sup> B. Fleming,<sup>31</sup> R. Flight,<sup>75</sup> J. Fowler,<sup>89</sup> W. Fox,<sup>106</sup>  
 J. Franc,<sup>71</sup> K. Francis,<sup>61</sup> D. Franco,<sup>31</sup> J. Freeman,<sup>2</sup> J. Freestone,<sup>41</sup> J. Fried,<sup>5</sup> A. Friedland,<sup>17</sup> S. Fuess,<sup>2</sup>

I. Furic,<sup>118</sup> A.P. Furmanski,<sup>107</sup> A. Gago,<sup>43</sup> H. Gallagher,<sup>119</sup> A. Gallego-Ros,<sup>49</sup> N. Gallice,<sup>121,120</sup>  
V. Galymov,<sup>27</sup> E. Gamberini,<sup>10</sup> T. Gamble,<sup>68</sup> R. Gandhi,<sup>85</sup> R. Gandrajula,<sup>73</sup> S. Gao,<sup>5</sup> D. Garcia-Gamez,<sup>122</sup>  
M.Á. García-Peris,<sup>18</sup> S. Gardiner,<sup>2</sup> D. Gastler,<sup>123</sup> G. Ge,<sup>22</sup> B. Gelli,<sup>99</sup> A. Gendotti,<sup>11</sup> S. Gent,<sup>124</sup>  
Z. Ghorbani-Moghaddam,<sup>78</sup> D. Gibin,<sup>74</sup> I. Gil-Botella,<sup>49</sup> C. Giererd,<sup>27</sup> A. Giri,<sup>125</sup> D. Gnani,<sup>76</sup> O. Gogota,<sup>26</sup>  
M. Gold,<sup>126</sup> S. Gollapinni,<sup>63</sup> K. Gollwitzer,<sup>2</sup> R.A. Gomes,<sup>127</sup> L. Gomez Bermeo,<sup>79</sup> L.S. Gomez Fajardo,<sup>79</sup>  
F. Gonnella,<sup>72</sup> J. Gonzalez-Cuevas,<sup>93</sup> M.C. Goodman,<sup>12</sup> O. Goodwin,<sup>41</sup> S. Goswami,<sup>128</sup> C. Gotti,<sup>57</sup>  
E. Goudzovski,<sup>72</sup> C. Grace,<sup>76</sup> M. Graham,<sup>17</sup> E. Gramellini,<sup>31</sup> R. Gran,<sup>129</sup> E. Granados,<sup>37</sup> A. Grant,<sup>130</sup>  
C. Grant,<sup>123</sup> D. Gratieri,<sup>95</sup> P. Green,<sup>41</sup> S. Green,<sup>103</sup> L. Greenler,<sup>131</sup> M. Greenwood,<sup>40</sup> J. Greer,<sup>6</sup> C. Griffith,<sup>9</sup>  
M. Groh,<sup>106</sup> J. Grudzinski,<sup>12</sup> K. Grzelak,<sup>132</sup> W. Gu,<sup>5</sup> V. Guarino,<sup>12</sup> R. Guenette,<sup>133</sup> A. Guglielmi,<sup>74</sup>  
B. Guo,<sup>111</sup> K. Guthikonda,<sup>134</sup> R. Gutierrez,<sup>101</sup> P. Guzowski,<sup>41</sup> M.M. Guzzo,<sup>99</sup> S. Gwon,<sup>135</sup> A. Habig,<sup>129</sup>  
A. Hackenburg,<sup>31</sup> H. Hadavand,<sup>24</sup> R. Haenni,<sup>21</sup> A. Hahn,<sup>2</sup> J. Haigh,<sup>8</sup> J. Haiston,<sup>91</sup> T. Hamernik,<sup>2</sup>  
P. Hamilton,<sup>110</sup> J. Han,<sup>50</sup> K. Harder,<sup>14</sup> D.A. Harris,<sup>2,136</sup> J. Hartnell,<sup>9</sup> T. Hasegawa,<sup>137</sup> R. Hatcher,<sup>2</sup>  
E. Hazen,<sup>123</sup> A. Heavey,<sup>2</sup> K.M. Heeger,<sup>31</sup> K. Hennessy,<sup>13</sup> S. Henry,<sup>75</sup> M. Hernandez Morquecho,<sup>37</sup>  
K. Herner,<sup>2</sup> L. Hertel,<sup>32</sup> A.S. Hesam,<sup>10</sup> J. Hewes,<sup>25</sup> A. Higuera Pichardo,<sup>83</sup> T. Hill,<sup>138</sup> S.J. Hillier,<sup>72</sup>  
A. Himmel,<sup>2</sup> J. Hoff,<sup>2</sup> C. Hohl,<sup>19</sup> A. Holin,<sup>29</sup> E. Hoppe,<sup>28</sup> G.A. Horton-Smith,<sup>65</sup> M. Hostert,<sup>69</sup>  
A. Hourlier,<sup>90</sup> B. Howard,<sup>106</sup> R. Howell,<sup>75</sup> J. Huang,<sup>139</sup> J. Huang,<sup>52</sup> J. Hugon,<sup>140</sup> G. Iles,<sup>110</sup> A.M. Iliescu,<sup>54</sup>  
R. Illingworth,<sup>2</sup> A. Ioannisian,<sup>141</sup> R. Itay,<sup>17</sup> A. Izmaylov,<sup>18</sup> E. James,<sup>2</sup> B. Jargowsky,<sup>32</sup> F. Jediny,<sup>71</sup>  
C. Jesús-Valls,<sup>142</sup> X. Ji,<sup>5</sup> L. Jiang,<sup>143</sup> S. Jiménez,<sup>49</sup> A. Jipa,<sup>77</sup> A. Joglekar,<sup>81</sup> C. Johnson,<sup>45</sup> R. Johnson,<sup>25</sup>  
B. Jones,<sup>24</sup> S. Jones,<sup>29</sup> C. Jung,<sup>108</sup> T. Junk,<sup>2</sup> Y. Jwa,<sup>22</sup> M. Kabirnezhad,<sup>1</sup> A. Kaboth,<sup>14</sup> I. Kadenko,<sup>26</sup>  
F. Kamiya,<sup>144</sup> G. Karagiorgi,<sup>22</sup> A. Karcher,<sup>76</sup> M. Karolak,<sup>64</sup> Y. Karyotakis,<sup>96</sup> S. Kasai,<sup>145</sup> S.P. Kasetti,<sup>140</sup>  
L. Kashur,<sup>45</sup> N. Kazaryan,<sup>141</sup> E. Kearns,<sup>123</sup> P. Keener,<sup>82</sup> K.J. Kelly,<sup>2</sup> E. Kemp,<sup>99</sup> W. Ketchum,<sup>2</sup> S. Kettell,<sup>5</sup>  
M. Khabibullin,<sup>146</sup> A. Khotjantsev,<sup>146</sup> A. Khvedelidze,<sup>4</sup> D. Kim,<sup>10</sup> B. King,<sup>2</sup> B. Kirby,<sup>5</sup> M. Kirby,<sup>2</sup>  
J. Klein,<sup>82</sup> K. Koehler,<sup>131</sup> L.W. Koerner,<sup>83</sup> S. Kohn,<sup>147,76</sup> P.P. Koller,<sup>21</sup> M. Kordosky,<sup>115</sup> T. Kosc,<sup>27</sup>  
U. Kose,<sup>10</sup> V. Kosteletzky,<sup>106</sup> K. Kothekar,<sup>6</sup> F. Krennrich,<sup>112</sup> I. Kreslo,<sup>21</sup> Y. Kudenko,<sup>146</sup> V. Kudryavtsev,<sup>68</sup>  
S. Kulagin,<sup>146</sup> J. Kumar,<sup>104</sup> R. Kumar,<sup>148</sup> C. Kuruppu,<sup>111</sup> V. Kus,<sup>71</sup> T. Kutter,<sup>140</sup> A. Lambert,<sup>76</sup> K. Lande,<sup>82</sup>  
C.E. Lane,<sup>109</sup> K. Lang,<sup>139</sup> T. Langford,<sup>31</sup> P. Lasorak,<sup>9</sup> D. Last,<sup>82</sup> C. Lastoria,<sup>49</sup> A. Laundrie,<sup>131</sup>  
A. Lawrence,<sup>76</sup> I. Lazanu,<sup>77</sup> R. LaZur,<sup>45</sup> T. Le,<sup>119</sup> J. Learned,<sup>104</sup> P. LeBrun,<sup>27</sup> G. Lehmann Miotto,<sup>10</sup>  
R. Lehnert,<sup>106</sup> M. Leigui de Oliveira,<sup>144</sup> M. Leitner,<sup>76</sup> M. Leyton,<sup>142</sup> L. Li,<sup>32</sup> S. Li,<sup>5</sup> S. Li,<sup>17</sup> T. Li,<sup>86</sup> Y. Li,<sup>5</sup>  
H. Liao,<sup>65</sup> C. Lin,<sup>76</sup> S. Lin,<sup>140</sup> A. Lister,<sup>131</sup> B.R. Littlejohn,<sup>149</sup> J. Liu,<sup>32</sup> S. Lockwitz,<sup>2</sup> T. Loew,<sup>76</sup>  
M. Lokajicek,<sup>150</sup> I. Lomidze,<sup>4</sup> K. Long,<sup>110</sup> K. Loo,<sup>151</sup> D. Lorca,<sup>21</sup> T. Lord,<sup>8</sup> J. LoSecco,<sup>152</sup> W.C. Louis,<sup>63</sup>  
K. Luk,<sup>147,76</sup> X. Luo,<sup>153</sup> N. Lurkin,<sup>72</sup> T. Lux,<sup>142</sup> V.P. Luzio,<sup>144</sup> D. MacFarland,<sup>17</sup> A. Machado,<sup>99</sup>  
P. Machado,<sup>2</sup> C. Macias,<sup>106</sup> J. Macier,<sup>2</sup> A. Maddalena,<sup>154</sup> P. Madigan,<sup>147,76</sup> S. Magill,<sup>12</sup> K. Mahn,<sup>73</sup>  
A. Maio,<sup>16,38</sup> J.A. Maloney,<sup>155</sup> G. Mandrioli,<sup>54</sup> J.C. Maneira,<sup>16,38</sup> L. Manenti,<sup>29</sup> S. Manly,<sup>75</sup> A. Mann,<sup>119</sup>  
K. Manolopoulos,<sup>14</sup> M. Manrique Plata,<sup>106</sup> A. Marchionni,<sup>2</sup> W. Marciano,<sup>5</sup> D. Marfatia,<sup>104</sup> C. Mariani,<sup>143</sup>  
J. Maricic,<sup>104</sup> F. Marinho,<sup>156</sup> A.D. Marino,<sup>157</sup> M. Marshak,<sup>107</sup> C. Marshall,<sup>76</sup> J. Marshall,<sup>8</sup> J. Marteau,<sup>27</sup>  
J. Martin-Albo,<sup>18</sup> N. Martinez,<sup>158</sup> D.A. Martinez Caicedo,<sup>91</sup> S. Martynenko,<sup>108</sup> K. Mason,<sup>119</sup>  
A. Mastbaum,<sup>159</sup> M. Masud,<sup>18</sup> S. Matsuno,<sup>104</sup> J. Matthews,<sup>140</sup> C. Mauger,<sup>82</sup> N. Mauri,<sup>54,53</sup>  
K. Mavrokoridis,<sup>13</sup> R. Mazza,<sup>57</sup> A. Mazzacane,<sup>2</sup> E. Mazzucato,<sup>64</sup> E. McCluskey,<sup>2</sup> N. McConkey,<sup>41</sup>  
K.S. McFarland,<sup>75</sup> C. McGrew,<sup>108</sup> A. McNab,<sup>41</sup> A. Mefodiev,<sup>146</sup> P. Mehta,<sup>160</sup> P. Melas,<sup>161</sup>  
M. Mellinato,<sup>57,66</sup> O. Mena,<sup>18</sup> S. Menary,<sup>136</sup> H. Mendez,<sup>158</sup> A. Menegolli,<sup>162</sup> G. Meng,<sup>74</sup> M. Messier,<sup>106</sup>  
W. Metcalf,<sup>140</sup> M. Mewes,<sup>106</sup> H. Meyer,<sup>163</sup> T. Miao,<sup>2</sup> G. Michna,<sup>124</sup> T. Miedema,<sup>42,116</sup> J. Migenda,<sup>68</sup>  
R. Milincic,<sup>104</sup> W. Miller,<sup>107</sup> J. Mills,<sup>119</sup> C. Milne,<sup>138</sup> O. Mineev,<sup>146</sup> O.G. Miranda,<sup>164</sup> S. Miryala,<sup>5</sup>  
C. Mishra,<sup>2</sup> S. Mishra,<sup>111</sup> A. Mislivec,<sup>107</sup> D. Mladenov,<sup>10</sup> I. Mocioiu,<sup>165</sup> K. Moffat,<sup>69</sup> N. Moggi,<sup>54,53</sup>  
R. Mohanta,<sup>33</sup> T.A. Mohayai,<sup>2</sup> N. Mokhov,<sup>2</sup> J.A. Molina,<sup>93</sup> L. Molina Bueno,<sup>11</sup> A. Montanari,<sup>54</sup>  
C. Montanari,<sup>162</sup> D. Montanari,<sup>2</sup> L.M. Montano Zetina,<sup>164</sup> J. Moon,<sup>90</sup> M. Mooney,<sup>45</sup> A. Moor,<sup>103</sup>  
D. Moreno,<sup>101</sup> B. Morgan,<sup>8</sup> C. Morris,<sup>83</sup> C. Mossey,<sup>2</sup> E. Motuk,<sup>29</sup> C.A. Moura,<sup>144</sup> J. Mousseau,<sup>36</sup> W. Mu,<sup>2</sup>  
L. Mualem,<sup>166</sup> J. Mueller,<sup>45</sup> M. Muether,<sup>163</sup> S. Mufson,<sup>106</sup> F. Muheim,<sup>86</sup> A. Muir,<sup>130</sup> M. Mulhearn,<sup>52</sup>  
H. Muramatsu,<sup>107</sup> S. Murphy,<sup>11</sup> J. Musser,<sup>106</sup> J. Nachtman,<sup>70</sup> S. Nagu,<sup>167</sup> M. Nalbandyan,<sup>141</sup>

R. Nandakumar,<sup>14</sup> D. Naples,<sup>50</sup> S. Narita,<sup>168</sup> D. Navas-Nicolás,<sup>49</sup> N. Nayak,<sup>32</sup> M. Nebot-Guinot,<sup>86</sup> L. Necib,<sup>166</sup> K. Negishi,<sup>168</sup> J.K. Nelson,<sup>115</sup> J. Nesbit,<sup>131</sup> M. Nessi,<sup>10</sup> D. Newbold,<sup>14</sup> M. Newcomer,<sup>82</sup> D. Newhart,<sup>2</sup> R. Nichol,<sup>29</sup> E. Niner,<sup>2</sup> K. Nishimura,<sup>104</sup> A. Norman,<sup>2</sup> R. Northrop,<sup>62</sup> P. Novella,<sup>18</sup> J.A. Nowak,<sup>59</sup> M. Oberling,<sup>12</sup> A. Olivares Del Campo,<sup>69</sup> A. Olivier,<sup>75</sup> Y. Onel,<sup>70</sup> Y. Onishchuk,<sup>26</sup> J. Ott,<sup>32</sup> L. Pagani,<sup>52</sup> S. Pakvasa,<sup>104</sup> O. Palamara,<sup>2</sup> S. Palestini,<sup>10</sup> J.M. Paley,<sup>2</sup> M. Pallavicini,<sup>78</sup> C. Palomares,<sup>49</sup> E. Pantic,<sup>52</sup> V. Paolone,<sup>50</sup> V. Papadimitriou,<sup>2</sup> R. Papaleo,<sup>56</sup> A. Papanestis,<sup>14</sup> S. Paramesvaran,<sup>6</sup> S. Parke,<sup>2</sup> Z. Parsa,<sup>5</sup> M. Parvu,<sup>77</sup> S. Pascoli,<sup>69</sup> L. Pasqualini,<sup>54,53</sup> J. Pasternak,<sup>110</sup> J. Pater,<sup>41</sup> C. Patrick,<sup>29</sup> L. Patrizzii,<sup>54</sup> R.B. Patterson,<sup>166</sup> S. Patton,<sup>76</sup> T. Patzak,<sup>30</sup> A. Paudel,<sup>65</sup> B. Paulos,<sup>131</sup> L. Paulucci,<sup>144</sup> Z. Pavlovic,<sup>2</sup> G. Pawloski,<sup>107</sup> D. Payne,<sup>13</sup> V. Pec,<sup>68</sup> S.J. Peeters,<sup>9</sup> Y. Penichot,<sup>64</sup> E. Pennacchio,<sup>27</sup> A. Penzo,<sup>70</sup> O.L. Peres,<sup>99</sup> J. Perry,<sup>86</sup> D. Pershey,<sup>89</sup> G. Pessina,<sup>57</sup> G. Petrillo,<sup>17</sup> C. Petta,<sup>48,47</sup> R. Petti,<sup>111</sup> F. Piastra,<sup>21</sup> L. Pickering,<sup>73</sup> F. Pietropaolo,<sup>10,74</sup> J. Pillow,<sup>8</sup> R. Plunkett,<sup>2</sup> R. Poling,<sup>107</sup> X. Pons,<sup>10</sup> N. Poonthottathil,<sup>112</sup> S. Pordes,<sup>2</sup> M. Potekhin,<sup>5</sup> R. Potenza,<sup>48,47</sup> B.V. Potukuchi,<sup>169</sup> J. Pozimski,<sup>110</sup> M. Pozzato,<sup>54,53</sup> S. Prakash,<sup>99</sup> T. Prakash,<sup>76</sup> S. Prince,<sup>133</sup> G. Prior,<sup>16</sup> D. Pugner,<sup>27</sup> K. Qi,<sup>108</sup> X. Qian,<sup>5</sup> J. Raaf,<sup>2</sup> R. Raboanary,<sup>15</sup> V. Radeka,<sup>5</sup> J. Rademacker,<sup>6</sup> B. Radics,<sup>11</sup> A. Rafique,<sup>12</sup> E. Raguzin,<sup>5</sup> M. Rai,<sup>8</sup> M. Rajaoalisoa,<sup>25</sup> I. Rakhno,<sup>2</sup> H. Rakotondramanana,<sup>15</sup> L. Rakotondravohitra,<sup>15</sup> Y. Ramachers,<sup>8</sup> R. Rameika,<sup>2</sup> M. Ramirez Delgado,<sup>37</sup> B. Ramson,<sup>2</sup> A. Rappoldi,<sup>162</sup> G. Raselli,<sup>162</sup> P. Ratoff,<sup>59</sup> S. Ravat,<sup>10</sup> H. Razafinime,<sup>15</sup> J. Real,<sup>170</sup> B. Rebel,<sup>131,2</sup> D. Redondo,<sup>49</sup> M. Reggiani-Guzzo,<sup>99</sup> T. Rehak,<sup>109</sup> J. Reichenbacher,<sup>91</sup> S.D. Reitzner,<sup>2</sup> A. Renshaw,<sup>83</sup> S. Rescia,<sup>5</sup> F. Resnati,<sup>10</sup> A. Reynolds,<sup>1</sup> G. Riccobene,<sup>56</sup> L.C. Rice,<sup>50</sup> K. Rielage,<sup>63</sup> Y. Rigaut,<sup>11</sup> D. Rivera,<sup>82</sup> L. Rochester,<sup>17</sup> M. Roda,<sup>13</sup> P. Rodrigues,<sup>1</sup> M. Rodriguez Alonso,<sup>10</sup> J. Rodriguez Rondon,<sup>91</sup> A. Roeth,<sup>89</sup> H. Rogers,<sup>45</sup> S. Rosauero-Alcaraz,<sup>114</sup> M. Rossella,<sup>162</sup> J. Rout,<sup>160</sup> S. Roy,<sup>85</sup> A. Rubbia,<sup>11</sup> C. Rubbia,<sup>171</sup> B. Russell,<sup>76</sup> J. Russell,<sup>17</sup> D. Ruterbories,<sup>75</sup> R. Saakyan,<sup>29</sup> S. Sacerdoti,<sup>30</sup> T. Safford,<sup>73</sup> N. Sahu,<sup>125</sup> P. Sala,<sup>121,10</sup> N. Samios,<sup>5</sup> M. Sanchez,<sup>112</sup> D.A. Sanders,<sup>92</sup> D. Sankey,<sup>14</sup> S. Santana,<sup>158</sup> M. Santos-Maldonado,<sup>158</sup> N. Saoulidou,<sup>161</sup> P. Sapienza,<sup>56</sup> C. Sarasty,<sup>25</sup> I. Sarcevic,<sup>172</sup> G. Savage,<sup>2</sup> V. Savinov,<sup>50</sup> A. Scaramelli,<sup>162</sup> A. Scarff,<sup>68</sup> A. Scarpelli,<sup>30</sup> T. Schaffer,<sup>129</sup> H. Schellman,<sup>40,2</sup> P. Schlabach,<sup>2</sup> D. Schmitz,<sup>62</sup> K. Scholberg,<sup>89</sup> A. Schukraft,<sup>2</sup> E. Segreto,<sup>99</sup> J. Sensenig,<sup>82</sup> I. Seong,<sup>32</sup> A. Sergi,<sup>72</sup> F. Sergiampietri,<sup>108</sup> D. Sgalaberna,<sup>11</sup> M. Shaevitz,<sup>22</sup> S. Shafaq,<sup>160</sup> M. Shamma,<sup>81</sup> H.R. Sharma,<sup>169</sup> R. Sharma,<sup>5</sup> T. Shaw,<sup>2</sup> C. Shepherd-Themistocleous,<sup>14</sup> S. Shin,<sup>173</sup> D. Shooltz,<sup>73</sup> R. Shrock,<sup>108</sup> L. Simard,<sup>67</sup> N. Simos,<sup>5</sup> J. Sinclair,<sup>21</sup> G. Sinev,<sup>89</sup> J. Singh,<sup>167</sup> J. Singh,<sup>167</sup> V. Singh,<sup>174,175</sup> R. Sipos,<sup>10</sup> F. Sippach,<sup>22</sup> G. Sirri,<sup>54</sup> A. Sitraka,<sup>91</sup> K. Siyeon,<sup>135</sup> D. Smargianaki,<sup>108</sup> A. Smith,<sup>89</sup> A. Smith,<sup>103</sup> E. Smith,<sup>106</sup> P. Smith,<sup>106</sup> J. Smolik,<sup>71</sup> M. Smy,<sup>32</sup> P. Snopok,<sup>149</sup> M. Soares Nunes,<sup>99</sup> H. Sobel,<sup>32</sup> M. Soderberg,<sup>176</sup> C.J. Solano Salinas,<sup>80</sup> S. Söldner-Rembold,<sup>41</sup> N. Solomey,<sup>163</sup> V. Solovov,<sup>16</sup> W.E. Sondheim,<sup>63</sup> M. Sorel,<sup>18</sup> J. Soto-Oton,<sup>49</sup> A. Sousa,<sup>25</sup> K. Soustruznik,<sup>177</sup> F. Spaggiardi,<sup>1</sup> M. Spanu,<sup>5</sup> J. Spitz,<sup>36</sup> N.J. Spooner,<sup>68</sup> K. Spurgeon,<sup>176</sup> R. Staley,<sup>72</sup> M. Stancari,<sup>2</sup> L. Stanco,<sup>74</sup> H. Steiner,<sup>76</sup> J. Stewart,<sup>5</sup> B. Stillwell,<sup>62</sup> J. Stock,<sup>91</sup> F. Stocker,<sup>10</sup> T. Stokes,<sup>140</sup> M. Strait,<sup>107</sup> T. Strauss,<sup>2</sup> S. Striganov,<sup>2</sup> A. Stuart,<sup>20</sup> D. Summers,<sup>92</sup> A. Surdo,<sup>51</sup> V. Susic,<sup>19</sup> L. Suter,<sup>2</sup> C. Sutura,<sup>48,47</sup> R. Svoboda,<sup>52</sup> B. Szczerbinska,<sup>178</sup> A. Szcelc,<sup>41</sup> R. Talaga,<sup>12</sup> H. Tanaka,<sup>17</sup> B. Tapia Oregui,<sup>139</sup> A. Tapper,<sup>110</sup> S. Tariq,<sup>2</sup> E. Tatar,<sup>138</sup> R. Tayloe,<sup>106</sup> A. Teklu,<sup>108</sup> M. Tenti,<sup>54</sup> K. Terao,<sup>17</sup> C.A. Ternes,<sup>18</sup> F. Terranova,<sup>57,66</sup> G. Testera,<sup>78</sup> A. Thea,<sup>14</sup> J.L. Thompson,<sup>68</sup> C. Thorn,<sup>5</sup> S. Timm,<sup>2</sup> A. Tonazzo,<sup>30</sup> M. Torti,<sup>57,66</sup> M. Tortola,<sup>18</sup> F. Tortorici,<sup>48,47</sup> D. Totani,<sup>2</sup> M. Touns,<sup>2</sup> C. Touramanis,<sup>13</sup> J. Trevor,<sup>166</sup> W.H. Trzaska,<sup>151</sup> Y.T. Tsai,<sup>17</sup> Z. Tsamalaidze,<sup>4</sup> K. Tsang,<sup>17</sup> N. Tsverava,<sup>4</sup> S. Tufanli,<sup>10</sup> C. Tull,<sup>76</sup> E. Tyley,<sup>68</sup> M. Tzanov,<sup>140</sup> M.A. Uchida,<sup>103</sup> J. Urheim,<sup>106</sup> T. Usher,<sup>17</sup> M. Vagins,<sup>179</sup> P. Vahle,<sup>115</sup> G. Valdivieso,<sup>180</sup> E. Valencia,<sup>115</sup> Z. Vallari,<sup>166</sup> J.W. Valle,<sup>18</sup> S. Vallecorsa,<sup>10</sup> R. Van Berg,<sup>82</sup> R.G. Van de Water,<sup>63</sup> D. Vanegas Forero,<sup>99</sup> F. Varanini,<sup>74</sup> D. Vargas,<sup>142</sup> G. Varner,<sup>104</sup> J. Vassel,<sup>106</sup> G. Vasseur,<sup>64</sup> K. Vaziri,<sup>2</sup> S. Ventura,<sup>74</sup> A. Verdugo,<sup>49</sup> S. Vergani,<sup>103</sup> M.A. Vermeulen,<sup>42</sup> M. Verzocchi,<sup>2</sup> H. Vieira de Souza,<sup>99</sup> C. Vignoli,<sup>154</sup> C. Vilela,<sup>108</sup> B. Viren,<sup>5</sup> T. Vrba,<sup>71</sup> T. Wachala,<sup>181</sup> A.V. Waldron,<sup>110</sup> M. Wallbank,<sup>25</sup> H. Wang,<sup>182</sup> J. Wang,<sup>52</sup> Y. Wang,<sup>182</sup> Y. Wang,<sup>108</sup> K. Warburton,<sup>112</sup> D. Warner,<sup>45</sup> M. Wascko,<sup>110</sup> D. Waters,<sup>29</sup> A. Watson,<sup>72</sup> P. Weatherly,<sup>109</sup> A. Weber,<sup>14,1</sup> M. Weber,<sup>21</sup> H. Wei,<sup>5</sup> A. Weinstein,<sup>112</sup> D. Wenman,<sup>131</sup> M. Wetstein,<sup>112</sup> M.R. White,<sup>91</sup> A. White,<sup>24</sup> L.H. Whitehead,<sup>103</sup> D. Whittington,<sup>176</sup> M.J. Wilking,<sup>108</sup> C. Wilkinson,<sup>21</sup> Z. Williams,<sup>24</sup> F. Wilson,<sup>14</sup>



R.J. Wilson,<sup>45</sup> J. Wolcott,<sup>119</sup> T. Wongjirad,<sup>119</sup> K. Wood,<sup>108</sup> L. Wood,<sup>28</sup> E. Worcester,<sup>5</sup> M. Worcester,<sup>5</sup> C. Wret,<sup>75</sup> W. Wu,<sup>2</sup> W. Wu,<sup>32</sup> Y. Xiao,<sup>32</sup> G. Yang,<sup>108</sup> T. Yang,<sup>2</sup> N. Yershov,<sup>146</sup> K. Yonehara,<sup>2</sup> T. Young,<sup>35</sup> B. Yu,<sup>5</sup> J. Yu,<sup>24</sup> J. Zalesak,<sup>150</sup> L. Zambelli,<sup>96</sup> B. Zamorano,<sup>122</sup> A. Zani,<sup>121</sup> L. Zazueta,<sup>115</sup> G. Zeller,<sup>2</sup> J. Zennamo,<sup>2</sup> K. Zeug,<sup>131</sup> C. Zhang,<sup>5</sup> M. Zhao,<sup>5</sup> E. Zhivun,<sup>5</sup> G. Zhu,<sup>44</sup> E.D. Zimmerman,<sup>157</sup> M. Zito,<sup>64</sup> S. Zucchelli,<sup>54,53</sup> J. Zuklin,<sup>150</sup> V. Zutshi<sup>61</sup> and R. Zwaska<sup>2</sup>

- 1 University of Oxford, Oxford, OX1 3RH, United Kingdom
- 2 Fermi National Accelerator Laboratory, Batavia, IL 60510, USA
- 3 Universidad del Atlantico, Carrera 30 Número 8- 49 Puerto Colombia - Atlántico, Colombia
- 4 Georgian Technical University, 77 Kostava Str. 0160, Tbilisi, Georgia
- 5 Brookhaven National Laboratory, Upton, NY 11973, USA
- 6 University of Bristol, H. H. Wills Physics Laboratory, Tyndall Avenue Bristol BS8 1TL, United Kingdom
- 7 Variable Energy Cyclotron Centre, 1/AF, Bidhannagar Kolkata - 700 064 West Bengal, India
- 8 University of Warwick, Coventry CV4 7AL, United Kingdom
- 9 University of Sussex, Brighton, BN1 9RH, United Kingdom
- 10 CERN, European Organization for Nuclear Research 1211 Genève 23, Switzerland, CERN
- 11 ETH Zurich, Institute for Particle Physics, Zurich, Switzerland
- 12 Argonne National Laboratory, Argonne, IL 60439, USA
- 13 University of Liverpool, L69 7ZE, Liverpool, United Kingdom
- 14 STFC Rutherford Appleton Laboratory, OX11 0QX Harwell Campus, Didcot, United Kingdom
- 15 University of Antananarivo, BP 566, Antananarivo 101, Madagascar
- 16 Laboratório de Instrumentação e Física Experimental de Partículas, Av. Gama Pinto, n.2, Lisboa, Complexo Interdisciplinar (3is) 1649-003 Portugal
- 17 SLAC National Acceleratory Laboratory, Menlo Park, CA 94025, USA
- 18 Instituto de Física Corpuscular, Catedrático Jose Beltran, 2 E-46980 Paterna (Valencia), Spain
- 19 University of Basel, Klingelbergstrasse 82, CH-4056 Basel, Switzerland
- 20 Universidad de Colima, 340 Colonia Villa San Sebastian Colima, Colima, Mexico
- 21 University of Bern, Sidlerstrasse 5, CH-3012 Bern, Switzerland
- 22 Columbia University, New York, NY 10027, USA
- 23 Universidad EIA, Via José María Córdoba #km 2 + 200, Envigado, Antioquia
- 24 University of Texas at Arlington, Arlington, TX 76019, USA
- 25 University of Cincinnati, Cincinnati, OH 45221, USA
- 26 Kyiv National University, 64, 01601 Kyiv, Ukraine
- 27 Institut de Physique des 2 Infinis de Lyon, Rue E. Fermi 4 69622 Villeurbanne, France
- 28 Pacific Northwest National Laboratory, Richland, WA 99352, USA
- 29 University College London, London, WC1E 6BT, United Kingdom
- 30 Université de Paris, CNRS, Astroparticule et Cosmologie, F-75006, Paris, France
- 31 Yale University, New Haven, CT 06520, USA
- 32 University of California Irvine, Irvine, CA 92697, USA
- 33 University of Hyderabad, Gachibowli, Hyderabad - 500 046, India
- 34 Instituto Superior Técnico - IST, Univ. de Lisboa, Portugal
- 35 University of North Dakota, 3501 University Ave Grand Forks, ND 58202-8357, USA
- 36 University of Michigan, Ann Arbor, MI 48109, USA
- 37 Universidad de Guanajuato, Gto., C.P. 37000, Mexico
- 38 Faculdade de Ciências - FCUL, Univ. de Lisboa, Portugal
- 39 University of Tennessee at Knoxville, TN, 37996, USA
- 40 Oregon State University, Corvallis, OR 97331, USA
- 41 University of Manchester, Oxford Road, Manchester M13 9PL, United Kingdom
- 42 Nikhef National Institute of Subatomic Physics, Science Park, Amsterdam, Netherlands
- 43 Pontificia Universidad Católica del Perú, Apartado 1761, Lima, Perú
- 44 Ohio State University, 191 W. Woodruff Ave. Columbus, OH 43210, USA
- 45 Colorado State University, Fort Collins, CO 80523, USA

- 46 *Università di Pisa, Theor. Division; Largo B. Pontecorvo 3, Ed. B-C, I-56127 Pisa, Italy*
- 47 *Istituto Nazionale di Fisica Nucleare Sezione di Catania, Via Santa Sofia 64, I-95123 Catania, Italy*
- 48 *Università di Catania, Dipartimento di Fisica e Astronomia “E. Majorana”, Italy*
- 49 *CIEMAT, Centro de Investigaciones Energéticas, Medioambientales y Tecnológicas, Av. Complutense, 40, E-28040 Madrid, Spain*
- 50 *University of Pittsburgh, Pittsburgh, PA 15260, USA*
- 51 *Università del Salento and Istituto Nazionale Fisica Nucleare, Via Provinciale per Arnesano, 73100 Lecce, Italy*
- 52 *University of California Davis, Davis, CA 95616, USA*
- 53 *University of Bologna, Department of Physics and Astronomy, viale Berti Pichat 6/2, 40127 Bologna, Italy*
- 54 *Istituto Nazionale di Fisica Nucleare Bologna, 40127 Bologna BO, Italy*
- 55 *Indian Institute of Technology Guwahati, Guwahati, 781 039, India*
- 56 *Laboratori Nazionali del Sud, Via S. Sofia 62, 95123 Catania, Italy*
- 57 *Istituto Nazionale di Fisica Nucleare Sezione di Milano Bicocca , Piazza della Scienza, 3 - I-20126 Milano, Italy*
- 58 *Beykent University, Istanbul*
- 59 *Lancaster University, Bailrigg, Lancaster LA1 4YB, United Kingdom*
- 60 *Universidade Federal do Rio de Janeiro, Rio de Janeiro - RJ, 21941-901, Brazil*
- 61 *Northern Illinois University, Department of Physics, DeKalb, Illinois 60115, USA*
- 62 *University of Chicago, Chicago, IL 60637, USA*
- 63 *Los Alamos National Laboratory, Los Alamos, NM 87545, USA*
- 64 *CEA/Saclay, IRFU Institut de Recherche sur les Lois Fondamentales de l’Univers, F-91191 Gif-sur-Yvette CEDEX, France*
- 65 *Kansas State University, Manhattan, KS 66506, USA*
- 66 *University of Milano-Bicocca, Dep. of Physics “G. Occhialini”, Piazza della Scienza 3, Milano, Italy*
- 67 *Laboratoire de l’Accélérateur Linéaire , Bâtiment 200, 91440 Orsay, France*
- 68 *University of Sheffield, Department of Physics and Astronomy, Sheffield S3 7RH, United Kingdom*
- 69 *Durham University, South Road, Durham DH1 3LE, United Kingdom*
- 70 *University of Iowa, Department of Physics and Astronomy 203 Van Allen Hall Iowa City, IA 52242, USA*
- 71 *Czech Technical University in Prague, Břehová 78/7, 115 19 Prague 1, Czech Republic*
- 72 *University of Birmingham, Edgbaston, Birmingham B15 2TT, United Kingdom*
- 73 *Michigan State University, East Lansing, MI 48824, USA*
- 74 *Universtà Degli Studi di Padova, Dip. Fisica e Astronomia G. Galilei and INFN Sezione di Padova, I-35131 Padova, Italy*
- 75 *University of Rochester, Rochester, NY 14627, USA*
- 76 *Lawrence Berkeley National Laboratory, Berkeley, CA 94720, USA*
- 77 *University of Bucharest, Faculty of Physics, Bucharest, Romania*
- 78 *Università degli studi di Genova, Istituto Nazionale di Fisica Nucleare Genova, 16126 Genova GE, Italy*
- 79 *Universidad Sergio Arboleda, Cll 74 -14 -14, 11022 Bogotá, Colombia*
- 80 *Universidad Nacional de Ingeniería, Av. Tupac Amaru 210, Lima 25, Perú*
- 81 *University of California Riverside, 900 University Ave, Riverside CA 92521*
- 82 *University of Pennsylvania, Philadelphia, PA 19104, USA*
- 83 *University of Houston, Houston, TX 77204, USA*
- 84 *Korea Institute of Science and Technology Information, Daejeon, 34141, South Korea*
- 85 *Harish-Chandra Research Institute, Jhansi, Allahabad 211 019, India*
- 86 *University of Edinburgh, Edinburgh EH8 9YL, United Kingdom*
- 87 *Southern Methodist University, Dallas, TX 75275, USA*
- 88 *Istituto Nazionale di Fisica Nucleare Sezione di Napoli, Complesso Universitario di Monte S. Angelo, I-80126 Napoli, Italy*
- 89 *Duke University, Durham, NC 27708, USA*
- 90 *Massachusetts Institute of Technology, Cambridge, MA 02139, USA*
- 91 *South Dakota School of Mines and Technology, Rapid City, SD 57701, USA*
- 92 *University of Mississippi, P.O. Box 1848, University, MS 38677 USA*
- 93 *Universidad Nacional de Asunción, San Lorenzo, Paraguay*

- 94 *Centro Brasileiro de Pesquisas Físicas, Rio de Janeiro, RJ 22290-180, Brazil*
- 95 *Fluminense Federal University, Rua Miguel de Frias, 9 Icaraí Niterói - RJ, 24220-900, Brazil*
- 96 *Laboratoire d'Annecy-le-Vieux de Physique des Particules, CNRS/IN2P3 and Université Savoie Mont Blanc, CNRS/IN2P3 and Université Savoie Mont Blanc, 74941 Annecy-le-Vieux, France*
- 97 *University of Amsterdam, Science Park 105, NL-1098 XG Amsterdam, The Netherlands*
- 98 *Northwestern University, Evanston, IL 60208, USA*
- 99 *Universidade Estadual de Campinas, Campinas - SP, 13083-970, Brazil*
- 100 *Royal Holloway College London, Egham, Surrey, TW20 0EX*
- 101 *Universidad Antonio Nariño, Cra 3 Este No 47A-15, Bogotá, Colombia*
- 102 *Valley City State University, Valley City, ND 58072, USA*
- 103 *University of Cambridge, JJ Thomson Avenue, Cambridge CB3 0HE, United Kingdom*
- 104 *University of Hawaii, Honolulu, HI 96822, USA*
- 105 *São Paulo Federal University, Departamento de Física-Campus Diadema, 09913-030, São Paulo, Brazil*
- 106 *Indiana University, Bloomington, IN 47405, USA*
- 107 *University of Minnesota Twin Cities, Minneapolis, MN 55455, USA*
- 108 *Stony Brook University, SUNY, Stony Brook, New York 11794, USA*
- 109 *Drexel University, Philadelphia, PA 19104, USA*
- 110 *Imperial College of Science Technology and Medicine, Blackett Laboratory Prince Consort Road, London SW7 2BZ, United Kingdom*
- 111 *University of South Carolina, Columbia, SC 29208, USA*
- 112 *Iowa State University, Ames, Iowa 50011, USA*
- 113 *Institute for Research in Fundamental Sciences, Farmanieh St. Tehran, 19538-33511, Iran*
- 114 *Madrid Autonoma University and IFT UAM/CSIC, Ciudad Universitaria de Cantoblanco 28049 Madrid, Spain*
- 115 *College of William and Mary, Williamsburg, VA 23187, USA*
- 116 *Radboud University, Heyendaalseweg 135, NL-6525 AJ Nijmegen, The Netherlands*
- 117 *University of Dallas, Irving, TX 75062-4736, USA*
- 118 *University of Florida, PO Box 118440 Gainesville, FL 32611-8440, USA*
- 119 *Tufts University, Medford, MA 02155, USA*
- 120 *Università degli Studi di Milano, Dipartimento di Fisica, I-20133 Milano, Italy*
- 121 *INFN sezione di Milano, via Celoria 16, 20133 Milano, Italy*
- 122 *University of Granada & CAFPE, Campus Fuentenueva (Edif. Mecenas), 18002 Granada, Spain*
- 123 *Boston University, Boston, MA 02215, USA*
- 124 *South Dakota State University, Brookings, SD 57007, USA*
- 125 *Indian Institute of Technology Hyderabad, Hyderabad, 502285, India*
- 126 *University of New Mexico, 1919 Lomas Blvd. N.E. Albuquerque, NM 87131, USA*
- 127 *Universidade Federal de Goiás, Goiania, GO 74690-900, Brazil*
- 128 *Physical Research Laboratory, Ahmedabad 380 009, India*
- 129 *University of Minnesota Duluth, Duluth, MN 55812, USA*
- 130 *Daresbury Laboratory, Daresbury Warrington, Cheshire WA4 4AD, United Kingdom*
- 131 *University of Wisconsin Madison, Madison, WI 53706, USA*
- 132 *University of Warsaw, Faculty of Physics ul. Pasteura 5 02-093 Warsaw, Poland*
- 133 *Harvard University, 17 Oxford St. Cambridge, MA 02138, USA*
- 134 *K L University, K L E F, Green Fields, Guntur - 522 502, AP, India*
- 135 *Chung-Ang University, Dongjak-Gu, Seoul 06974, South Korea*
- 136 *York University, Physics and Astronomy Department, 4700 Keele St. Toronto M3J 1P3, Canada*
- 137 *High Energy Accelerator Research Organization (KEK), Ibaraki, 305-0801, Japan*
- 138 *Idaho State University, Department of Physics, Pocatello, ID 83209, USA*
- 139 *University of Texas at Austin, Austin, TX 78712, USA*
- 140 *Louisiana State University, Baton Rouge, LA 70803, USA*
- 141 *Yerevan Institute for Theoretical Physics and Modeling, Halabian Str. 34, Yerevan 0036, Armenia*
- 142 *Institut de Física d'Altes Energies, Campus UAB, Facultat Ciències Nord, 08193 Bellaterra, Barcelona, Spain*
- 143 *Virginia Tech, Blacksburg, VA 24060, USA*

- 144 *Universidade Federal do ABC, Av. dos Estados 5001, Santo André - SP, 09210-580 Brazil*
- 145 *National Institute of Technology, Kure College, Kure College, Hiroshima, 737-8506, Japan*
- 146 *Institute for Nuclear Research of the Russian Academy of Sciences, prospekt 60-letiya Oktyabrya 7a, Moscow 117312, Russia*
- 147 *University of California Berkeley, Berkeley, CA 94720, USA*
- 148 *Punjab Agricultural University, Department of Math. Stat. & Physics, Ludhiana 141004, India*
- 149 *Illinois Institute of Technology, Chicago, IL 60616, USA*
- 150 *Institute of Physics, Czech Academy of Sciences, Na Slovance 2, 182 21 Praha 8, Czech Republic*
- 151 *University of Jyväskylä, P.O. Box 35, FI-40014, Finland*
- 152 *University of Notre Dame, Notre Dame, IN 46556, USA*
- 153 *University of California Santa Barbara, Santa Barbara, California 93106 USA*
- 154 *Laboratori Nazionali del Gran Sasso, I-67010 Assergi, AQ, Italy*
- 155 *Dakota State University, Madison, SD 57042, USA*
- 156 *Universidade Federal de São Carlos, Araras - SP, 13604-900, Brazil*
- 157 *University of Colorado Boulder, Boulder, CO 80309, USA*
- 158 *University of Puerto Rico, Mayaguez, 00681, USA*
- 159 *Rutgers University, Piscataway, NJ, 08854, USA*
- 160 *Jawaharlal Nehru University, School of Physical Sciences, New Delhi 110067, India*
- 161 *University of Athens, University Campus, Zografou GR 157 84, Greece*
- 162 *Università degli studi di Pavia, Istituto Nazionale di Fisica Nucleare Sezione di Pavia, I-27100 Pavia, Italy*
- 163 *Wichita State University, Physics Division, Wichita, KS 67260, USA*
- 164 *Centro de Investigacion y de Estudios Avanzados del IPN (Cinvestav), Mexico City*
- 165 *Pennsylvania State University, University Park, PA 16802, USA*
- 166 *California Institute of Technology, Pasadena, CA 91125, USA*
- 167 *University of Lucknow, Lucknow 226007, Uttar Pradesh, India*
- 168 *Iwate University, Morioka, Iwate 020-8551, Japan*
- 169 *University of Jammu, Physics Department, JAMMU-180006, India*
- 170 *University Grenoble Alpes, CNRS, Grenoble INP, LPSC-IN2P3, 38000 Grenoble, France*
- 171 *Gran Sasso Science Institute, Viale Francesco Crispi 7, L'Aquila, Italy*
- 172 *University of Arizona, 1118 E. Fourth Street Tucson, AZ 85721, USA*
- 173 *Jeonbuk National University, 414, Natural Science Building #5 Department of Physics 567 Baekjedaero, Deogjin-gu Jeonju, Jeonrabuk-do 54896*
- 174 *Central University of South Bihar, Department of Physics SH-7, Gaya Panchanpur Road, Gaya - 824236*
- 175 *Banaras Hindu University, Department of Physics, Varanasi - 221 005, India*
- 176 *Syracuse University, Syracuse, NY 13244, USA*
- 177 *Institute of Particle and Nuclear Physics of the Faculty of Mathematics and Physics of the Charles University in Prague, V Holešovičkách 747/2, 180 00 Praha 8-Libeň, Czech Republic*
- 178 *Texas A&M University (Corpus Christi), Corpus Christi, TX 78412, USA*
- 179 *Kavli Institute for the Physics and Mathematics of the Universe, Kashiwa, Chiba 277-8583, Japan*
- 180 *Universidade Federal de Alfenas, Poços de Caldas - MG, 37715-400, Brazil*
- 181 *H. Niewodniczański Institute of Nuclear Physics, Polish Academy of Sciences, Cracow, Poland*
- 182 *University of California Los Angeles, Los Angeles, CA 90095, USA*